

RECORD
of the
11th Symposium on
Electron, Ion, and Laser Beam Technology

Boulder, Colorado, 12-14 May 1971

R. F. M. THORNLEY
Editor

IEEE Catalog No. 71 C 23-ED

Sponsored by
Group on Electron Devices of the
Institute of Electrical and Electronics Engineers, Inc.
American Vacuum Society
University of Colorado



San Francisco Press, Inc.

547 Howard Street, San Francisco, California 94105

RECORD

Copyright © 1971 by Institute of Electrical and Electronics Engineers, Inc.

All rights reserved

11th Symposium on
Electron Ion and Laser Beam Technology
Boulder, Colorado, 12-14 May 1971

R. J. M. THORNTON
Editor

IEEE Catalog No. 71-03-10

Sponsored by
Group on Electron Devices of the
Institute of Electrical and Electronics Engineers, Inc.
American Vacuum Society
University of Colorado

Library of Congress catalog card 62-51780

Printed in the United States of America

SBN 911302-17-X

San Francisco Press, Inc.
201 Howard Street, San Francisco, California 94102

PREFACE

The 11th Symposium on Electron, Ion and Laser Beam Technology was held in the Memorial Center of the University of Colorado in Boulder, Colorado, on 12-14 May 1971. Highlights of the program included work on electron-beam fabrication of microcircuits, computer lens-design techniques, and beam-addressed memories. The Symposium attendance expanded from 130 at the previous meeting to 160 at this one, largely as a result of the increased activity in these fields. The attendance may also have been influenced by the mountain scenery adjacent to Boulder, and the excellent skiing conditions which certainly persuaded many participants to come early or to extend their stay in Colorado.

Altogether 80 papers were presented. Of these, 42 were concerned with the theory and applications of electron beams. Laser applications and technology accounted for 18 papers, with the balance representing work on ion beams, ion sources, analysis of information storage devices, and generation of charged liquid particles.

The increased degree of interest in electron-beam fabrication was demonstrated in sessions on fabrication technology and on computer-controlled microfabrication, in which the basic technology has been extended to make conductors 500 Å wide, and to the very complex structures characteristic of integrated solid-state circuits. The Symposium also attracted many papers on information storage, with two complete sessions being devoted to this subject. Many different technologies were discussed but no single approach emerged as the preferred method of achieving a beam-addressed memory.

Diners at the conference banquet were entertained by Dr. Robert Adler, Zenith Corp. vice president and director of research, who spoke on the topic, "Will buggywhips ever be practical?" with several illuminating examples drawn from his own experience.

The conference was held under the general chairmanship of Prof. F. S. Barnes of the University of Colorado. The practical aspects of the Conference were ably handled by the Department of Conferences and Institutes of the University, whose staff showed, by their exemplary performance, the degree of skill and expertise that they have developed in conference organization. The availability of such professional assistance rendered unnecessary many of the subcommittees usually associated with technical conferences, leaving only the problems of defining the program for the organizers.

The conference was sponsored by the Electron Devices Group of the IEEE, the American Vacuum Society, and the University of Colorado. Additional support from the National Science Foundation is gratefully acknowledged; this enabled several overseas speakers to contribute to the meeting.

The Steering Committee, whose members include F. S. Barnes, L. Marton, T. E. Everhart, C. Süsskind, B. W. Schumacher, and J. Forester, are to be complimented on setting an excellent stage for the 1971 Symposium. For the technical content of the meeting, I should like to thank the members of the program committee (L. S. Birks, A. N. Broers, F. Chernow, T. E. Everhart, W. C. Nixon, B. W. Schumacher, M. L. Stitch, J. R. Werning, and R. Wolfgang) for their efforts in evaluating a record number of submitted papers. The many sessions were moderated by J. R. Werning, J. V. Walker, C. Süsskind, M. L. Stitch, T. E. Everhart, A. N. Broers, L. Marton, J. Kelly, J. McMahon (for J. L. Emmett), R. F. W. Pease, E. D. Wolf, P. H. Rose, F. Chernow, and H. E. Klauser. My thanks are due them for a con-

sistently perfect discharge of their duties. Finally, I should like to thank all the participants in the Symposium, whether as speakers or listeners, for their essential part in making the Symposium a success.

R. F. M. THORNLEY

Boulder, Colorado, 1971

TABLE OF CONTENTS

Page

INFORMATION STORAGE

1

Berkowitz, Hughes, Lawson, Meiklejohn, "An electron beam-magnetic film memory system," 1; Ferber, "Ionizing-radiation-produced nonvolatile metal-oxide-semiconductor (MOS) memory," 9; Swinney, "Laser recording real-time imagery," 17; Tschang, "The effects of imagewise electrostatic charge buildup in electron beam recording," 27; Wagner, "Vesicular films in electron and laser beam recording," 35; Engberg, "State-of-the-art wide-bandwidth electron-beam analog recorder and reproducer," 43; Pass, Teeple, "A 100-MHz multichannel laser recorder and readout system," 53; Reynolds, "An optical storage subsystem," 60; Elser, Gayle, "Analysis of an imbedded element storage array," 61; Levene, Siryj, "Equipment applications for material transfer recording," 69.

ANALYSIS

77

Eisen, Rosenstein, Silverman, "The application of radiochromic dye film dosimetry to medium-Z absorbers," 77; Perry, Buxton, "Energy deposition profiles in thermoelastic media from a 45-kA, 3-MeV electron beam," 81; Schroeder, Phillips, Southward, Grannemann, "High-dose-rate electron-beam irradiations using a telescoping drift tube," 89; Phillips, Grannemann, Southward, "Removing the spectrum dependence from electron-beam dosimetry measurements by using a magnetic electron deflection tube," 93; Gamo, Iwaki, Masuda, Namba, Ishihara, Kimura, "Concentration profiles and enhanced diffusion in ion implanted silicon studied by radioactivation analysis," 103; Flemming, Ahmed, "Low-energy electron-beam equipment for microelectronic device evaluation," 111; Hewitt, Barker, Amme, "Ion bombardment of mineral surfaces," 115; Carlson, "Spectroscopic studies of the emission from plasmas generated by an intense electron beam," 121; Crawford, Kudirka, "Electron micro-beam testing for large microcircuit arrays," 131.

BEAM PHYSICS

141

Andrews, Nahman, "Electron-beam deflection in traveling-wave oscilloscopes," 141; Takagi, Yamada, "A new type of traveling-wave deflection system," 147; Ashley, "Hybrid computer-aided synthesis of thick electrostatic electron lenses," 157; Boers, "Digital-computer solution of Laplace's equation including dielectric interfaces and small floating electrodes," 167; Kuyatt, Natali, Di Chio, "Third-order aberration coefficients of electron lenses," 177; Seliger, "E x B mass separator design," 183; Wang, "Aberration analysis of electrostatic small angle deflection," 193; Amboss, Wold, "Double-deflection aberrations in a scanning electron microscope," 195; Broers, Pfeiffer, "Minimum beam diameter obtainable in electron-probe apparatus," 205; Fraser, Meyers, Elser, "A computer analysis of the spherical aberration of three electrostatic immersion lenses," 209; Heritage, "Third-order aberrations of magnetic electron lenses," 219; Parks, "Analytical solution of the axial potential for a three-element electrostatic lens," 229; Pfeiffer, "Experimental investigation of energy broadening in electron optical instruments," 239.

LASER TECHNOLOGY

247

Eckbreth, Burwell, Davis, "Electric-discharge CO₂ lasers," 247; Flinchbaugh, "High-power visible lasers featuring an externally charged plasma-discharge bore for stable, long-life operation," 259; McMahon, Emmett, "Development of high-power Nd: glass laser systems," 269; Miley, "Gas laser excitation with a relativistic electron beam," 279; Namba, Masuyama, Kawabe, Masuda, "Internal Q-switching and long time delay phenomena in electron beam excited GaAs lasers," 291; Miley, Verdeyen, Ganley, Guyot, Thiess, "Pumping and enhancement of gas lasers via ion beams," 299; George, "A beam profile analyzer for high-power laser beams," 307.

FABRICATION TECHNOLOGY

313

Johnston, Cochran, Herrmannsfeldt, Fritzsche, "Fabrication of a superconducting linear accelerator by electron-beam welding," 313; Shepherd, "The influence of ion kinetic energy on the surface reactivity of ion-beam-deposited Cu," 323; Wolf, Ozdemir, Perkins, Coane, "Response of the positive electron resist Elvacite 2041 to kilovolt electron beam exposure," 331; Hatzakis, Broers, "Electron-beam techniques for fabricating fine metal lines," 337; Ting, "Electron scattering and the sensitivity of positive electron resist," 345; Wilson, Shifrin, "Ion implantation system for device production," 351; Sample, Bollini, Decker, "Generation of beams of charged liquid particles," 359.

MOLECULAR LASER INTERACTIONS

367

Asmus, "Continuous synthesis of polymer fuels through high-temperature laser beam interactions," 367; Kim, Taki, Namba, "Laser-induced chemical reaction: decomposition of various compounds and reaction of decomposed fragments with low hydrocarbons," 375; Kobayasi, Inaba, "Laser beam technology for remotely sensing invisible molecules in the polluted atmosphere," 385; Vanderborgh, Ristau, Coloff, "Laser-induced degradation of inorganic systems," 403; Hutcheson, Roth, Barnes, "Laser-generated acoustic waves in liquids," 413.

GENERATION OF HIGH-POWER ELECTRON BEAMS

421

Yonas, Smith, Spence, Putnam, Champney, "Development and application of a 1-MV, 1-MA mylar dielectric pulsed electron accelerator and concepts for higher energy modular generator systems," 421; Ecker, Benford, Stallings, Putnam, Spence, "Intense beam generation at megampere currents and beam transport in pulsed external magnetic field configurations," 433; Johnson, "REBA, a pulsed electron beam generator," 445; Parker, Anderson, "The behavior of low-impedance, field emission diodes," 453.

COMPUTER-CONTROLLED MICROFABRICATION

463

Ozdemir, Wold, Buckey, "Computer-controlled scanning electron microscope system for high resolution microelectronic pattern fabrication," 463; Chang, Wallman, "A computer-controlled electron-beam

machine for micro-circuit fabrication," 471; Herzog, Greeneich, Everhart, Van Duzer, "Computer-controlled resist exposure in the scanning electron microscope," 483; Dix, Ballantyne, Nixon, "Paper tape-controlled electron probe resist exposure and direct metallic deposition," 495; Livesay, Fritz, "Electron image projection systems for microcircuit lithography," 505.

RELATIVISTIC ELECTRON BEAMS

513

Block, Burton, Frame, Hammer, Kolb, Levine, Lupton, Oliphant, Shipman, Vitkovitsky, "NRL relativistic electron beam program," 513; Boers, "Digital computer simulation of high current, relativistic, and field emission electron tubes," 527; Boris, Lee, "Computational studies of relativistic electron beams," 535; Bradley, Martin, Prestwich, Boers, Johnson, "Characteristics of high v/γ electron-beam propagation," 553; Putnam, "Intense relativistic electron beam-plasma interactions in finite cavities," 561.

ION SOURCES

577

Graybill, McNeill, Uglum, "Acceleration of ions by relativistic electron-beam-formed plasmas," 577; Meckel, "Large-diameter ion source with variable-beam cross-section configurations," 585; Douglas-Hamilton, "High pressure recombination rate measurements," 591; Takagi, Yamada, Ishikawa, "Beam-plasma type ion source," 597; Aubert, DuBarry, Gautherin, Septier, "The duoplasmatron as a negative hydrogen ion source," 605; Byers, Reader, "Electron-bombardment ion source operation using various gases," 615; Takagi, Yamada, Ishikawa, "Electron-bombardment type simplified ion source," 623; Aberth, Spindt, Rogers, "Multipoint field ionization beam source," 631.

THERMAL EFFECTS OF BEAMS

637

Mori, Nemoto, "New electron beam evaporator and its characteristics," 637; Bas, Hafner, Latif, Wulff, "An electron-beam floating-zone melting device for working pressures in the range 10^{-7} to 15 Torr," 643; Bakish, "Electron-beam welding in transition," 653; Linlor, "Interaction of high-intensity laser radiation with matter," 659; Thurber, "Laser welding: theory, status, and prospects," 665; Banas, Walch, "Materials processing with carbon dioxide laser," 685.

AUTHOR INDEX

695

SESSION ON INFORMATION STORAGE

AN ELECTRON BEAM-MAGNETIC FILM MEMORY SYSTEM

A. E. BERKOWITZ, W. C. HUGHES, J. L. LAWSON, and W. H. MEIKLEJOHN

General Electric Corporate Res. & Dev., Schenectady, New York

The flying spot scanner¹ was an early example of an electron-beam (EB) memory system. The concept of the "fly's eye" lens,² the development of better cathodes,³ and the introduction of Curie point writing⁴ have led to a number of proposals⁵⁻⁷ for a high-density and large-capacity EB memory.

The EB memory described in this paper uses the "fly's eye" lens to address the bit sites, and a perforated target covered with a low-Curie point magnetic material to record the information. The electron beam is used both to store the digital information by thermomagnetic recording and to read out the stored information nondestructively. This memory is not considered to be a direct replacement for an extended core, disk, or drum memory, but rather has disk-like capacity, core-like data rates, and intermediate access times. One tube might contain 500 megabits that can be written at a rate of 1 megabit/sec and read at an average data rate of 5 megabits/sec, which includes an access time of 0.1 ms to the beginning of a word.

The proposed system is based upon calculations of the electron trajectories in both the reading and writing modes and some experimental measurements of the electron deflections due to the magnetic field at the bit sites.

DESCRIPTION OF THE MEMORY SYSTEM

A site in the storage plane consists of a 1- μ m-diameter hole surrounded by a thin film of magnetic material. An 8-kV electron beam is used to heat an annular region around the hole to a temperature above the Curie point of the magnetic material. The heated magnetic region cools in a magnetic field applied in one direction to store a "1" and in the opposite direction to store a "0." The direction of the magnetization is detected during the read mode by passing a low-voltage (100-V) electron beam through the hole and detecting the direction of deflection of the beam by the magnetic field produced by the magnetized annular region.

A schematic diagram of the system is shown in Fig. 1. During the reading mode the electrons from the cathode pass through a suitable optical system (illumination control), which adjusts the accelerating voltage to about 100 volts. The lenslet selector directs the electron beam to the desired lenslet of the fly's eye lens (FEL); the fine-deflection plates direct the beam to the selected site on the target. The beam is deflected by the magnetic field in the hole as it passes through the target. The signal-current director deflects the beam to the split detector. If a "1" had been stored at the bit site the beam falls on one side of the detector; and on the other side of the detector for a stored "0." The servo system is necessary to correct for unwanted deflections caused by stray magnetic fields.

A portion of the storage plane is shown diagrammatically in Fig. 2. In practice many lenslet fields of 10^4 bits would be contained between a set of strip lines. An enlarged view of two bit sites is shown in one of the lenslet fields. Two storage sites per bit are used to improve the ratio

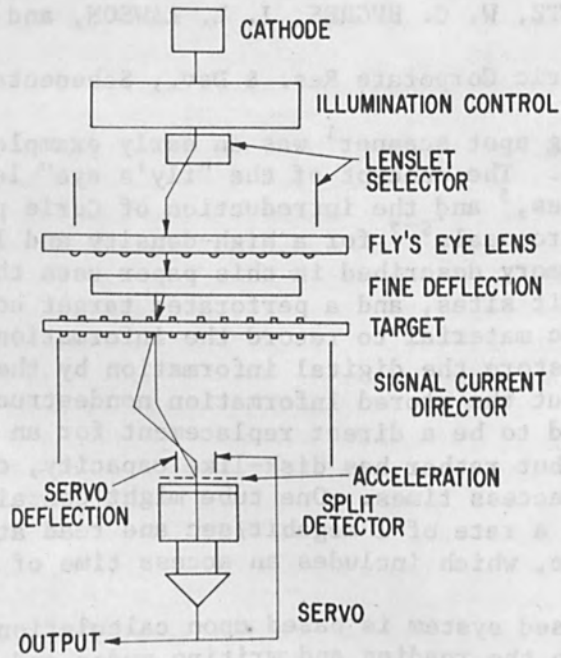


FIG. 1.--Schematic diagram of memory system.

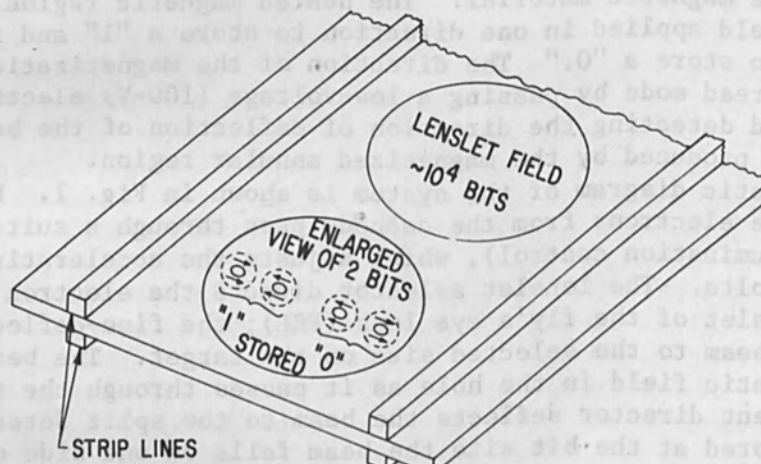


FIG. 2.--Schematic diagram of storage plane.

of signal to noise of the system. As the 8-kV beam scans across a row of storage sites, the strip lines are pulsed to produce the magnetization pattern shown in Fig. 2 for a recorded "1" and a recorded "0."

CALCULATION OF BEAM DEFLECTIONS

The angular deflection of the electron beam was calculated from the model shown in Fig. 3(a). The round hole in the storage plane with its annular magnetization region was approximated by a rectangular hole of length d and width L and a magnetized region of length D and a thickness t . If a divergence of the magnetization (M) only on the faces a , b , c , and e is assumed, the magnetic field at any point in space may be calculated. The field due to the sheet of free magnetic poles of surface density σ , shown in Fig. 3(b), is given by the following expression:

$$H_x/\sigma = \tan^{-1}(Y_1 Z_1 / X_1 R_{111}) - \tan^{-1}(Y_2 Z_2 / X_1 R_{121}) - \tan^{-1}(Y_1 Z_2 / X_1 R_{112}) + \tan^{-1}(Y_2 Z_2 / X_1 R_{122})$$

$$H_y/\sigma = \ln(Z_2 + R_{112})(Z_1 + R_{121}) - \ln(Z_1 + R_{111})(Z_2 + R_{122}) \quad (1)$$

$$H_z/\sigma = \ln(Y_2 + R_{121})(Y_1 + R_{112}) - \ln(Y_1 + R_{111})(Y_2 + R_{122})$$

where

$$X_1 = X - X_0, \quad Y_1 = Y - (t/2), \quad Y_2 = Y + (t/2), \quad Z_1 = Z - (L/2),$$

$$Z_2 = Z + (L/2)$$

$$R_{ijk}^2 = X_i^2 + Y_j^2 + Z_k^2$$

The magnetic field throughout all space due to the magnetized region around one hole is given by four sets of the equations shown above with the proper sign for the magnetic pole density σ and the appropriate value for X_0 .

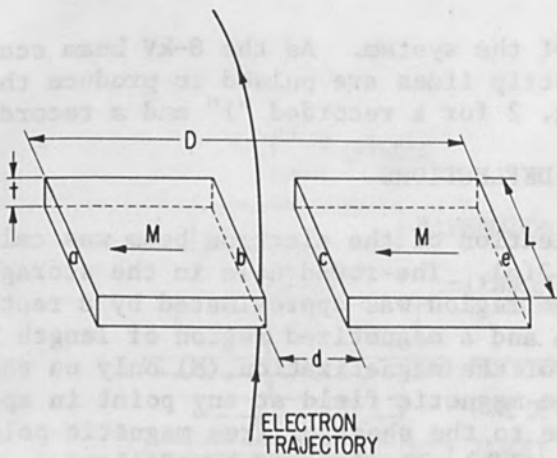
From the equations of motion for an electron

$$\begin{aligned} m\ddot{\vec{r}} &= q(\vec{E} + \vec{v} \times \vec{H}) \\ \vec{E} &= -\nabla V \end{aligned} \quad (2)$$

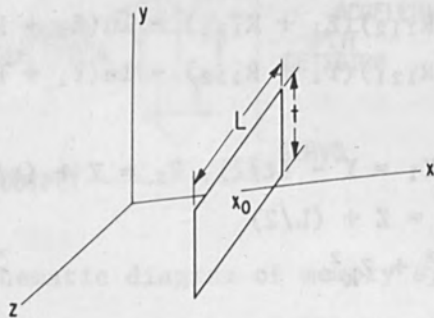
the trajectories of the electrons were determined by computer calculations.

The calculated angular deflection of a 100-volt electron beam passing through a 1- μm -diameter hole in a 5- μm magnetic film is shown in Fig. 4. The angular deflection is shown as a function of the ratio of the diameter of the magnetized region to the diameter of the hole (D/d). Although there is no analytical expression to show that the deflection is proportional to D/d , such a dependence is borne out by numerical calculations for the useful range of values of D/d . For a constant value of $D/d = 2$ where $D = 2, 4, \text{ and } 6 \mu\text{m}$, the calculated deflections agree within 0.5 per cent.

A major problem in the calculations is to determine the proper value for the magnetic pole density σ . The procedure used for the data shown in Fig. 4 was to select a value for σ which produced calculated values for the horizontal field H_x that were in agreement with the calculated⁸ and measured⁹ magnetic fields near the surface of magnetic tape. A check on this value for σ was obtained from the magnetization M which is assumed to be 100 gauss, a value typical of magnetic tape. Since it is assumed in the model that the regions are permanently magnetized and that there is a divergence of M only at the end faces, the magnetic field near the pole faces



(a)



(b)

FIG. 3.--(a) Model of magnetized region used for calculation of beam deflection; (b) model used to develop magnetic fields given by Eq.(2).

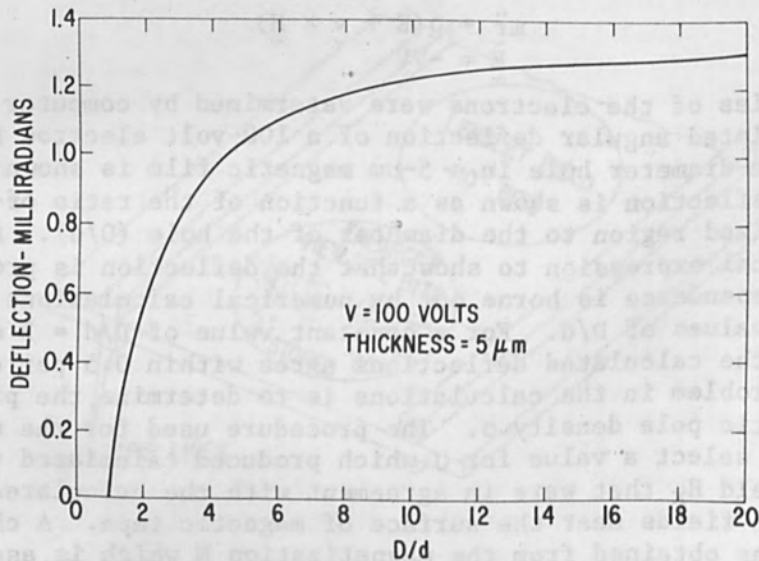


FIG. 4.--Angular deflections calculated for 100-volt electrons passing through hole in magnetized region. Magnetic moment of material is 100 gauss and thickness is 5 μm .

outside the magnetic material is equal to $2\pi M$. When σ is adjusted to produce this value of H , the angular deflections are about 4 times the value shown in Fig. 4. This value for σ is somewhat unrealistic since the divergence of M is not confined to the end faces in a real material.

To check the calculated deflections shown in Fig. 4, a specimen of CrO_2 tape¹⁰ was prepared containing thirty 1-mil-diameter holes on 4-mil centers. The magnetic material around each hole was heated above the Curie point with a laser beam and cooled in a magnetic field. The diameter of the magnetized region was found to be 4 mils by a Bitter solution. The specimen was then flooded with a 5-kV electron beam and the image was formed on a fluorescent screen. The deflection pattern is shown in Fig. 5, where the deflections should occur only along the lettered column directions.

Considering only column C, the region around the holes of rows 1, 3, and 5 were magnetized so as to cause an upward deflection; rows 2 and 4 were magnetized for a downward deflection. As a result the image spacings between rows 1 and 2 and between rows 3 and 4 have increased, whereas the spacings between rows 2 and 3 and rows 4 and 5 have decreased. The angular deflection obtained from this experiment when corrected for the voltage and the interaction between bits was 25×10^{-4} radian. This value is greater than the deflection of 10×10^{-4} radian shown in Fig. 4 for $D/d = 4$, but less than the upper limit of 40×10^{-4} radian obtained when σ was determined from the magnetization.

Another result of the numerical calculations is that all electrons passing through the hole in the storage plane experience the same angular deflection to within 1 per cent of the average value. This was an unexpected result since the magnetic fields near the magnetic material may be one to two orders of magnitude greater than the field at the center of the hole. Experimental evidence for the validity of this calculation is shown in Fig. 5. The circular holes in the magnetized storage plane are imaged as circular holes on the phosphor screen.

The angular deflections shown in Fig. 4 were determined for a magnetic film thickness of 5 μm . The numerical calculations show that the deflection is proportional to the film thickness in the useful range from 1 to 10 μm .

WRITING PROCESS

Thermomagnetic recording requires the heating of a magnetic material above its Curie point and then cooling the material in a magnetic field. Experiments show that an external magnetic field of 60 oersted applied during the cooling of a 1-mil-diameter region of CrO_2 tape from above the Curie temperature will satisfactorily magnetize the spot.

However, when the magnetized regions are spaced closely together, there is an additional demagnetizing field from all the other bits. The magnetic field applied by the strip lines must be increased above this value of 60 oersted by the maximum demagnetizing field from all other bits. This interaction field was calculated by means of the model shown in Fig. 3(a) for the nearest and next nearest neighbors. These bits were magnetized so as to produce a maximum demagnetizing field at the bit; this field was calculated to be 3.4 oersteds for 2- μm -diameter magnetized regions on 4- μm centers. Each of the remaining 10^4 bits in the lenslet field were assumed to produce a dipole field at the selected bit site. The sum of these 10^4 dipole fields at the bit site was about 3 oersted. Thus the demagnetizing

outside the magnetic material is equal to $2\pi H$. When θ is adjusted so that this value of H , the angular deflection is about 1 times the value shown in Fig. 4. This value for θ is somewhat unobtainable since the divergence of H is not constant in the end tubes in a real material.

To check the calculated deflection angles in Fig. 4, a specimen of CrO₂ tape was prepared containing thirty 1-mil-diameter holes on 4-mil centers. The magnetic material around each hole was heated above the Curie point with a laser beam and cooled in a magnetic field. The direction of the magnetized region was found to be 45° by a laser interferometer. The specimen was then imaged with a 5-kV electron beam and the image was formed on a fluorescent screen. The deflection pattern is shown in Fig. 5.

where the deflection angles occur only along the lattice column directions.

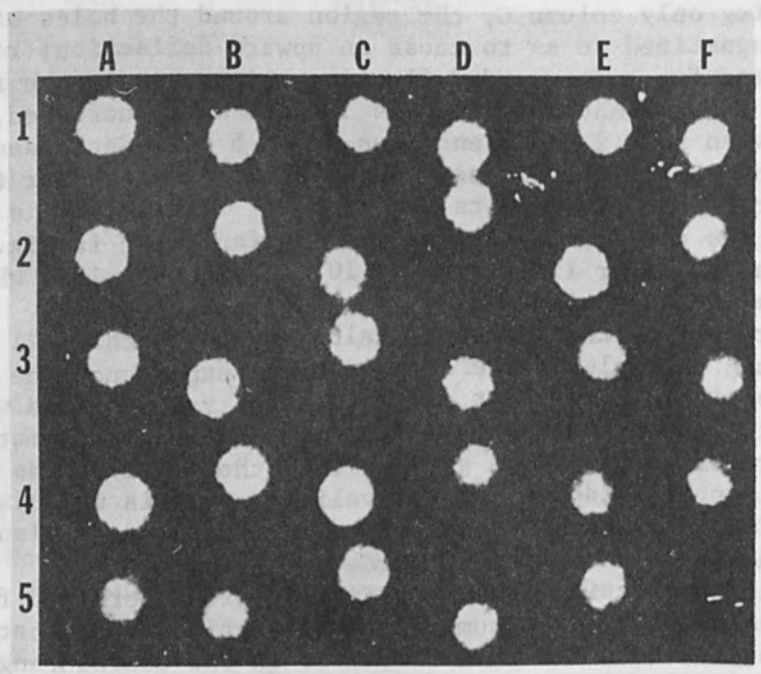


FIG. 5.--5-kv electron beam image of 1-mil-diameter holes on 4-mil centers. Diameter of magnetized region around each hole is 4 mils.

Thermomagnetic recording requires the heating of a magnetic material above its Curie point and then cooling the material in a magnetic field. Experiments show that an external magnetic field of 50 oersted applied during the cooling of a 1-mil-diameter region of tape does not raise the Curie temperature still substantially above the room temperature. However, when the magnetized regions are spaced closely together, there is an additional demagnetizing field from all the other holes. The magnetic field applied by the strip lines must be increased above this value of 50 oersted by the maximum demagnetizing field from all other holes. This maximum demagnetizing field was calculated by means of the model shown in Fig. 3(a) for the nearest and next nearest neighbors. These calculations are so as to produce a maximum demagnetizing field of 10 oersted. This field was calculated to be 3.4 oersted for 3-mil-diameter magnetized regions on 4-mil centers. Each of the remaining 10 holes in the lattice field were assumed to produce a dipole field at the center of the hole. The sum of these 10 dipole fields at the center of the hole is 10 oersted. Thus the demagnetizing field at the center of the hole is 13.4 oersted. This value is used in the calculation of the required magnetic field.

field for the "worst case" magnetization of all the bits is less than 10 oersteds. The strip lines must produce a magnetic field of 70 oersteds at all of the bit sites to insure the recording of a bit. Calculations show that this field can be obtained with 30-mil square strip lines with a 24-A pulse current.

During the writing process the electron beam scans across the bit sites within a lenslet field and dwells long enough to heat the spot above 150°C. Calculations show that an 8-kV beam of 1-μA for a duration of 1 μsec heats a ferrite material to 150°C. The spot cools below a critical setting temperature (0.9 T_c) in 0.3 μsec. Slightly higher beam currents or voltages are required for a 1-MHz writing rate.

SYSTEM PERFORMANCE

The data on the deflection angle shown in Fig. 4 permit a calculation of signal to noise (S/N), bit rate, and capacity.

To optimize the density, 1-μm-diameter holes with 2-μm-diameter magnetized region around the hole were chosen. Figure 4 shows that for this condition (D/d = 2) the deflection angle θ for a "1" or "0" is 5.8 × 10⁻⁴ radian for 100-volt electrons. In terms of the voltage and thickness, the deflection angle is given by

$$\theta = 11t \times 10^{-4} / \sqrt{V} \quad (3)$$

where t is in micrometers and V is in volts.

The two fundamental sources of readout error are the shot noise in the reading beam and the crosstalk from adjacent bit sites.

The shot noise in the system dictates that one selects a suitable ratio of electrons arriving at the detector for a recorded "1" to those electrons arriving for a recorded "0." With 150 electrons in a "1" and 10 electrons in a "0" it can be shown that an error probability of less than 10⁻¹⁷ can be obtained with an ideal detector.

The minimum beam current (amperes) required to obtain 150 electrons during the read cycle is given by

$$I = 2.5 \times 10^{-17} \times \text{bit rate} \quad (4)$$

where the bit rate is in Hertz.

The amount of current that can be obtained in an electron spot is proportional to the square of the maximum angle of arrival, the cathode potential, and the cathode loading. For 1-μm holes we obtain

$$I = 6.2 \times 10^{-8} \theta_1^2 V j_0 \quad (5)$$

where θ₁ is the half angle of convergence in radians of the electron beam, V is the cathode potential (volts), and j₀ is the cathode loading (amp/cm²).

Substitution of Eq. (3) into Eq. (5) with θ = 2θ₁ yields

$$I = j_0 \times 10^{-12} \quad (6)$$

Equating equations (4) and (6), we obtain the bit rate (Hertz) as a function of the cathode loading

$$\text{bit rate} = 4 \times 10^4 \times j_0 \quad (7)$$

For a cathode loading of 125 amp/cm², the bit rate is 5 megabits/sec.

The crosstalk between bit sites has been examined by numerical calculations. The deflection angles of the electrons given in Fig. 4 were also calculated when the nearest and next nearest neighbors were magnetized so as to cause a maximum influence at the recorded bit site. The extreme signal variation was 40 per cent for a 4- μm bit spacing and 16 per cent for a 6- μm bit spacing. This does not cause errors directly unless the variation exceeds 100 per cent, so that it appears that the bits could be located on 4- μm centers or at a density of 10^7 bits/in.².

ACKNOWLEDGMENTS

The authors greatly appreciate the experimental beam-deflection measurements made by J. F. Norton and H. H. Lemmerman, the beam heating calculations of D. W. Skelly, the materials preparation by C. E. VanBuren and J. J. Bartfai, and the magnetic measurements by B. Valachovic.

REFERENCES

1. C. W. Hoover Jr. and G. Haughk, The flying spot store, in Large Capacity Memory Techniques for Computer Systems (M. C. Youits, ed.), Macmillan Co., 1962; pp. 79-98.
2. S. P. Newberry, An electron optical technique for large-capacity random-access memories, Proc. Fall Joint Computer Conf. AFIPS 29: 717-728, 1966; S. P. Newberry, T. H. Klotz Jr., and E. C. Buschmann, Advances in fly's eye electron optics, Proc. National Electronics Conf. 23: 746-751, 1967.
3. W. C. Hughes, Long, high brightness sources for demountable guns, 10th Symposium on Electron, Ion, and Laser Beam Technology, San Francisco Press, 1969; 441-452; W. W. Dolan and W. P. Dyke, Phys. Rev. 95: 327, 1954.
4. L. Mayer, Magnetic writing with an electron beam, J. Appl. Phys. 29: 1454-1456, 1958.
5. M. S. Cohen, Feasibility of Lorentz readout of a high density fast magnetic memory, IEEE Trans. MAG-4: 639-645, 1968.
6. C. D. Mee and G. J. Fan, IEEE Trans. MAG-3: 72-76, 1967.
7. D. O. Smith, IEEE Trans. MAG-3: 593-599, 1967.
8. D. E. Speliotis and J. H. Judy, IEEE Trans. MAG-6: 653, 1970.
9. R. F. M. Thornley and J. D. Hutchison, Appl. Phys. Letters 13: 249-250, 1968.
10. R. K. Waring Jr., J. Appl. Phys. 42: 1763, 1971.

IONIZING-RADIATION-PRODUCED NONVOLATILE METAL-OXIDE-SEMICONDUCTOR (MOS) MEMORY

R. R. FERBER

Westinghouse Electric Corporation, East Pittsburgh, Pa.

A technique of "burning in" a preferred state in metal-oxide-semiconductor (MOS) memory cells using ionizing radiation (electron bombardment, for example) has been demonstrated. When the power is removed and reapplied, the memory always configures itself to the preset pattern while still allowing normal electrical alteration of stored information in either random access memory (RAM) or shift register configuration memory chips. In some respects, this technique yields results similar to those of the "read MOSTLY memory" technique developed recently by other workers.¹ Potential applications of this data "burn in" technique are as an additional or improved method of fabrication of read-only semiconductor memories (ROM) and reprogrammable read-only memories. Considerable application also exists for a memory which can be preprogrammed to turn on in a particular memory pattern each time power is interrupted and reapplied, and still operate as an ordinary electrically alterable memory. A conceptual reprogrammable electron beam scanned MOS memory array tube which uses this ionizing radiation induced predisposition is described as a memory design example.

BACKGROUND

The stored information volatility of conventional metal-oxide-semiconductor (MOS) memories of both random access and shift register types has limited their use in many applications. Where information must be preserved, elaborate power supply continuity safeguards must be employed with MOS memories, or, as an alternate, other memory types such as magnetic core or plated wire must be utilized. The memory-processing technique described in this paper provides at least a partial solution to the problem of memory volatility inherent in MOS devices since when power is removed and reapplied, the memory elements all revert to their preprogrammed states.

There are other techniques that can produce similar read-only type memory cell behavior such as that discussed by Sho Nakanuma et al.² This programming generally depends on high electric field charge transport through aluminum oxide or the oxide in a multilayer Si_3N_4 - SiO_2 gate insulator structure and the accumulation or trapping of this charge in the nitride-oxide interface region. The floating-gate avalanche-injection metal oxide semiconductor (FAMOS) device³ is another recently announced electrically programmable read-only memory device. These methods generally require rather high potentials to accomplish adequate charge transfer (20 to 100 V), and extra processing steps are generally required during memory fabrication. The ionizing-radiation-induced presetting technique described here is equally applicable to both oxide (MOS) and oxidenitride (MNOS) gate insulator memory devices and requires no special device processing. In addition, none of the other methods described above allows the use of the memory as a normal electrically alterable random-access or shift register unit while power is applied, as is the case here.

DESCRIPTION OF OPERATION

The memory considered here has, as a basic building block, a bistable flip-flop which consists of two cross-coupled inverter stages (Fig. 1). A CMOS cell is shown but the principle is equally applicable to other MOS memory devices. The desired characteristic of nonvolatility in a MOS memory is attained through exposure of the memory to ionizing radiation while a particular stored information configuration is being held in its various cells.

In the usual MOS memory, i.e., a memory that has not been exposed to radiation, the application of a supply potential at B+ (Fig. 1) places a voltage across the two input transistors of the flip-flop. The likelihood of Q₁ or Q₂ turning on first depends on many variables, all of which contribute to the randomness of the resultant logic state.

For a memory cell to assume a preferred state, either Q₁ or Q₂ must be biased to such a degree as to insure its turning on first. One method of realizing this is to utilize the effects of ionizing radiation. The basic mechanism by which an MOS transistor's characteristics can be altered in a radiation environment is the buildup of trapped charge in the oxide layer of the device. Characteristically, SiO₂, which is the most common oxide used in commercial MOS devices, traps positive charges due to exposure to ionizing radiation. The result of this charge trapping is a shift ΔV_T in the threshold voltage V_T of both N and P-channel devices toward a more negative threshold voltage (Fig. 2). However, it has been shown⁴ that the amount of charge trapping (and hence the amount of threshold voltage shift of a MOS device) depends upon the magnitude and polarity of the gate voltage and its duty cycle during irradiation. Devices irradiated with a positive gate bias with respect to the source exhibit a great deal more charge trapping near the oxide-silicon interface than those with a negative or zero bias (Fig. 3). Thus, in general, the devices irradiated with a positive bias on the gate show a greater threshold voltage shift than those irradiated with a negative bias. Devices irradiated with zero gate bias tend to exhibit the smallest threshold shifts.

The operation of this phenomenon of "burning in" of a particular preferred state through the use of ionizing radiation can be described by considering a CMOS random access memory of the type shown in Fig. 4. It is made up of cells like those shown in Fig. 1. Table 1 shows the bias conditions for each transistor of the memory flip-flop (Q₁ through Q₄) for each of the two memory states. It may be seen that gate bias voltages (V_{gs}) of B+, 0, and -(B+) can exist in the cell during normal operation.

TABLE 1.--Bias conditions for individual memory cell transistors.

Transistor	Type	MEMORY STATE 0		MEMORY STATE 1	
		Gate bias voltage V_{gs}	State	Gate bias voltage V_{gs}	State
Q ₁	P Channel	-(B+)	on	B+	off
Q ₂	N Channel	0	off	B+	on
Q ₃	P Channel	B+	off	-(B+)	on
Q ₄	N Channel	B+	on	0	off

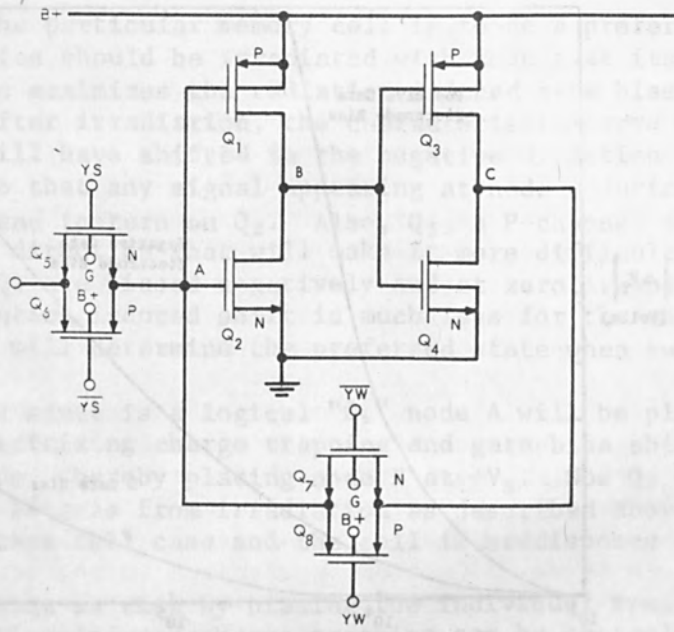


FIG. 1.--Basic memory cell.

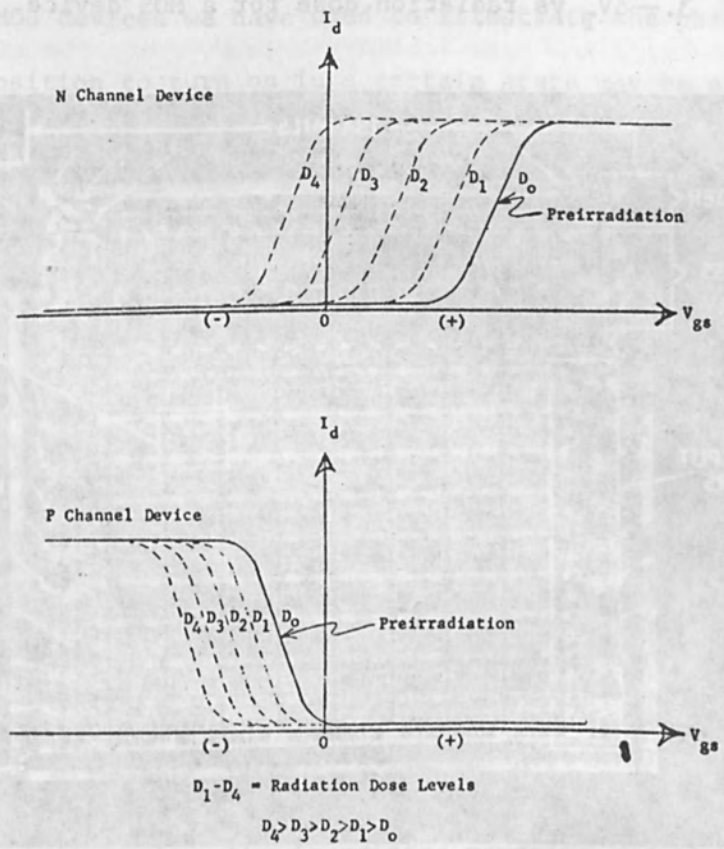


FIG. 2.--Gate characteristic shift with radiation.

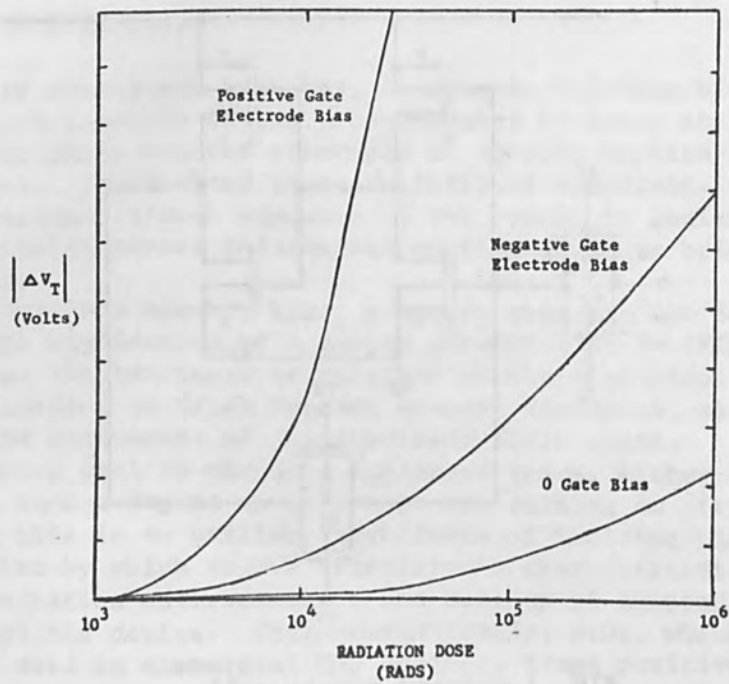


FIG. 3.-- ΔV_T vs radiation dose for a MOS device.

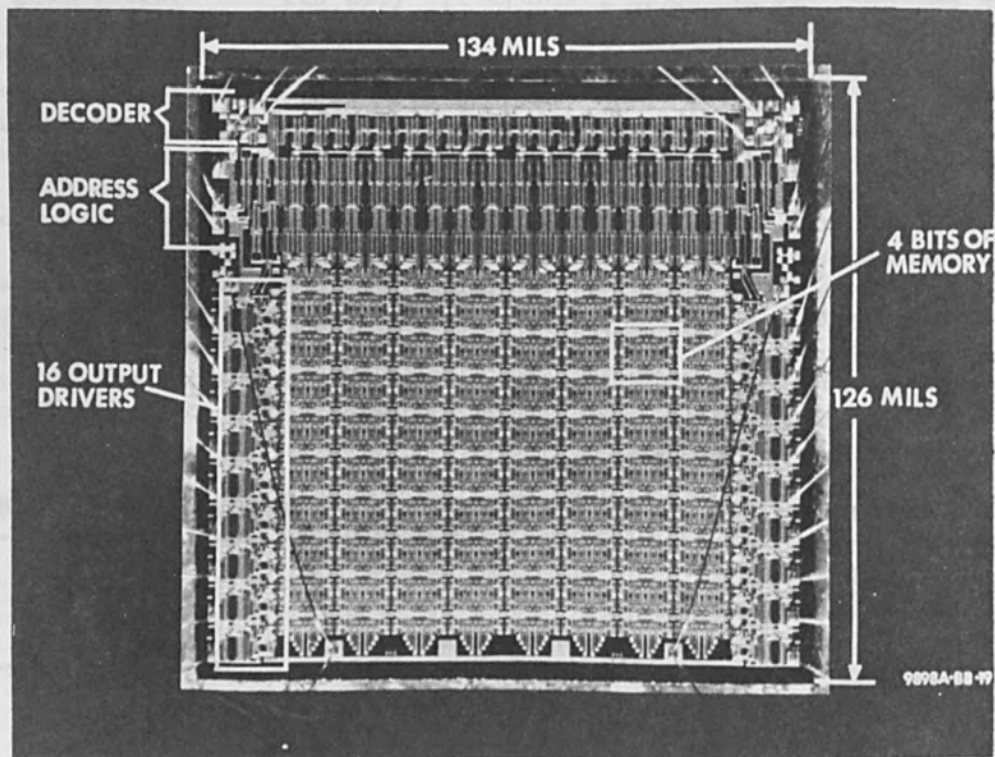


FIG. 4.--288-bit CMNOS memory chip.

Therefore, if the particular memory cell is to be a preferred "1" state cell, the device should be irradiated with node A at its positive state. This process maximizes the radiation-induced gate bias shift in the first stage. After irradiation, the characteristic curve of Q_2 , an N-channel device, will have shifted in the negative direction as predicted by Fig. 2, so that any signal appearing at node A during the turn on transient will tend to turn on Q_2 . Also, Q_1 , a P-channel device, will have shifted in the direction that will make it more difficult to turn on. Transistors Q_3 and Q_4 are biased negatively and at zero, respectively. Therefore, the radiation induced shift is much less for the second stage, and the first stage will determine the preferred state when supply voltage is applied.

If the preferred state is a logical "0," node A will be placed at ground potential, minimizing charge trapping and gate bias shifts on Q_1 and Q_2 ; Q_1 will be on, thereby placing node B at $+V_S$. Now Q_3 and Q_4 exhibit the maximum effects from irradiation as described above for Q_1 and Q_2 in the "1" state cell case and the cell is predisposed to turn on in a "0" state.

The over-all result is that by biasing the individual transistors, the degree of radiation-induced charge trapping can be controlled and used to force each cell of the memory to come up in a preferred state each time power is interrupted and reapplied. However, the total dose must be kept below the level that effectually renders Q_1 and Q_3 inoperable. This level is approximately 5×10^5 rads (Si) for the particular oxide-nitride CMOS devices we have used to illustrate the phenomenon described herein.

The predisposition to turn on in a certain state may be erased by annealing at about 250°C , which effectively removes the charge trapped in the oxide. It would then be possible to irradiate again with a different memory state configuration in the cells and thus alter the predisposition pattern.

EXPERIMENTAL VERIFICATION

Irradiations have been made on several CMNOS memories of the type shown in Fig. 4 both with a Van de Graaff accelerator electron beam and with a 1000-Curie Cs_{137} gamma ray source. For the particular devices tested, which are rather "hard" to radiation damage, the dose required to cause absolute predisposition of each cell to turn on in a preferred state is between 1 and 2×10^5 rads. This is well below the dose required to cause radiation-damage-induced malfunction of the memory. SiO_2 gate insulator MOS memories, which are not as radiation "hard" as the oxide-nitride gate insulated memories, require exposures of between 10^4 and 10^5 rads to insure turn on predisposition of the memory cells.

It was found by examining the behavior of various data lines that the behavior of all memory cells with radiation exposure was quite similar and the "burn in" phenomenon was stable for radiation exposures from 1×10^5 rads to 4×10^5 rads. The memory predisposition characteristics were also stable with time--memories were checked up to 6 weeks after irradiation with no apparent change in predisposition behavior.

Anneals were performed on the irradiated memories and it was found that the "burned in" predisposition pattern was stable to at least 125°C . A one-hour anneal at 250°C , however, removed the predisposition burned in

pattern as would be expected from the results of other workers on MOS device radiation effects and annealing. Thus, the "burned in" pattern may be erased.

APPLICATION EXAMPLE

A memory using this principle, which can have the preset information altered at will, may be envisioned along the following lines. Consider a cathode-ray-tube-like structure with an accelerating potential between 5 and 10 kV with the space normally occupied by the phosphor screen covered with MOS memory chips with the active surface facing the electron beam. This memory chip array also has a heater that can raise the temperature to 250°C or so. Then 10^5 rads exposure in the gate insulator structures may be accumulated very quickly by use of an electron beam of sufficient energy to penetrate the gate insulator structure. It is desirable to limit the accelerating potential to values of the order of 100 kV to remain below the electron displacement damage threshold but this is no problem since the gate metallization, protective layer, and gate insulator are generally less than 10^4 Å thick. To enter and "freeze in" a particular data pattern, it is merely necessary to enter the desired data into the memory and then irradiate a part of or all of the memory to the proper dosage by the electron beam. If, at some later time, the predisposed initial data conditions need to be altered, the heater may be used to remove the gate insulator trapped charge by holding the array at 250°C for an hour or so with operating voltages removed. After cooling to normal operating temperature, a new data set may be entered and the electron beam radiation exposure repeated.

Consider now the structure of Fig. 5, which is typical of MOS and CMOS device cross sections. In this case, the gate regions for both N and P devices have a thin layer of SiO_2 (about 40 Å) next to the silicon with about 600 Å of Si_3N_4 making up the gate insulator. On top of this are the aluminum gate metallization of about 2000 Å and a protective SiO_2 overlayer of 1000 Å or so. This is the total thickness to be penetrated by the electron beam. If we assume the various material thicknesses quoted above, then the total mass to be penetrated is about 10^{-4} g/cm². But SiO_2 , Si_3N_4 , and Al have very similar electron interaction cross sections and so to the accuracies necessary for consideration here, we may use the electron range-energy relationship for aluminum⁵ shown in Fig. 6 to determine the necessary electron-beam energy for penetration of the gate structure. For a 100 µg/cm² aluminum equivalent, a 5-keV beam would penetrate the gate structure. However, it is desirable to use a somewhat higher energy to insure a relatively uniform rate of ionization through the gate insulator. Thus, an 8- to 10-keV beam energy might be chosen in this case.

The electron exposure could be made using either a scanned, focused beam or an unscanned flood beam. The use of a scanned, focused beam and a control grid would allow selective "burning in" of a particular memory predisposition pattern in any portion of the memory. Here, the beam could be modulated to produce radiation exposure to any desired pattern of memory cells while leaving others unexposed.

The "burning in" exposure time is quite short. If we assume a 10 × 10 cm array of memory chips on a ceramic substrate which forms the scanned area of a cathode-ray-tube type of structure and assume a beam current of

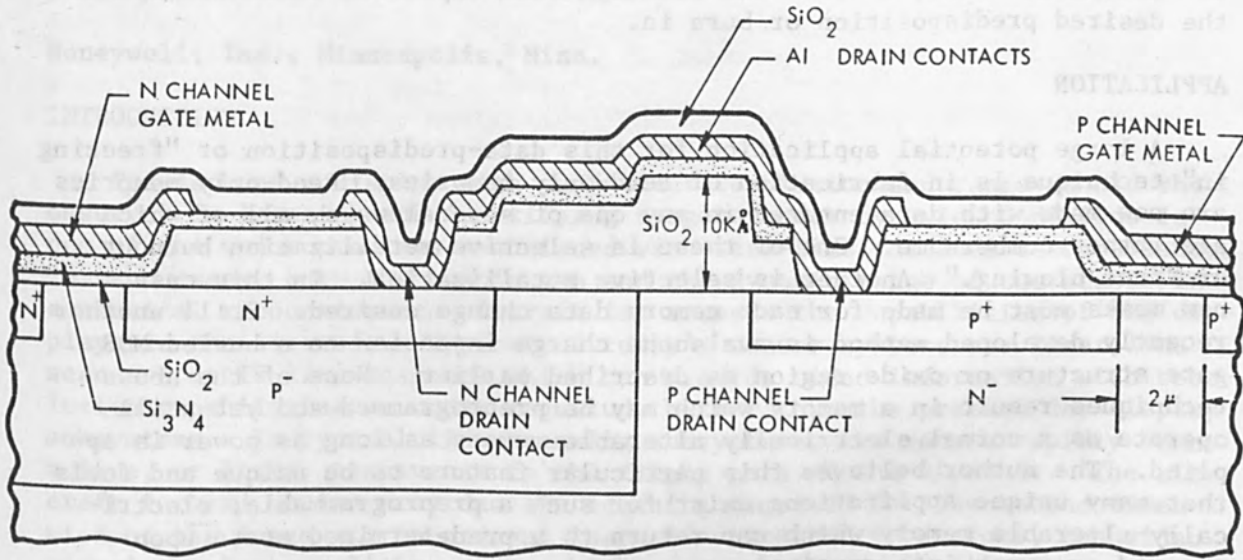


FIG.5.--CMOS chip cross section.

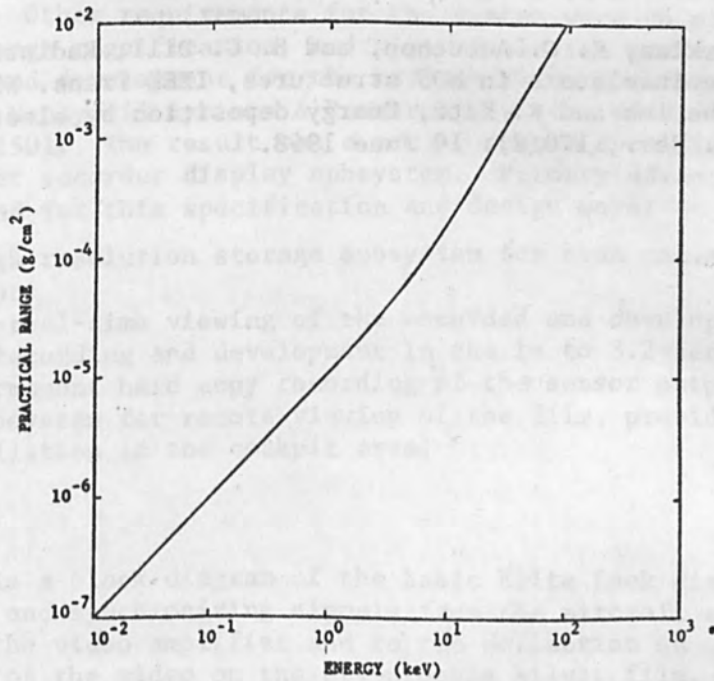


FIG. 6.--Practical range vs energy for electrons in aluminum.

1 μ mamp distributed over the array either by scanning or flood gun technique, then the dose in the gate insulator region is of the order of 10^5 rads/sec. Thus, 1- to 2-sec electron-beam exposures would accomplish the desired predisposition or burn in.

APPLICATION

A large potential application for this data-predisposition or "freezing in" technique is in fabrication of read-only memories. Read-only memories are now made with data entered in any one of several ways, all of which are rather cumbersome. One of these is selective metallization burnout or "fuse blowing." Another is selective metallization. In this case, new masks must be made for each memory data change desired. Still another recently developed method is avalanche charge injection to a buried MOS gate structure or oxide region as described earlier. None of the above techniques result in a memory which may be preprogrammed and yet still operate as a normal electrically alterable memory as long as power is applied. The author believes this particular feature to be unique and feels that many unique applications exist for such a preprogrammable, electrically alterable memory which can return to a predetermined state upon command or power interruption.

REFERENCES

1. D. Frohmann-Bentchkowsky, 1971 International Solid State Circuits Conference, Philadelphia, Pa., February 17-19, 1971.
2. S. Nakanuma et al., Read only memory using MAS transistors, IEEE Journal of Solid-State Circuits, SC-5(5), 1970.
3. FAMOS electrically programmable ROM spotlighted at ISSCC, EEE 19(4), 1971.
4. C. W. Perkins, K. G. Aubuchon, and H. G. Dill, Radiation effects in modified oxide insulators in MOS structures, IEEE Trans. NS-15(6), 1968.
5. E. J. Kobetich and R. Katz, Energy deposition by electron beams and δ rays, Phys. Rev., 170(2): 10 June 1968.

LASER RECORDING REAL-TIME IMAGERY

S. I. SWINNEY

Honeywell, Inc., Minneapolis, Minn.

INTRODUCTION

The lack of a display with sufficient resolution and range to aid the observer in locating and identifying targets under dynamic conditions is one of the major problems associated with real-time tactical reconnaissance. In many cases, both the resolution and the dynamic range of the sensor in a tactical reconnaissance aircraft far exceeds the capabilities of the displays in the aircraft. Typical of today's sensor systems are laser line scanners or IR line scanners which can provide video information with resolution capabilities on order magnitude better than the present day display subsystems. In typical line-scanning subsystems, the sensor rapidly scans a line, or lines, transverse to the flight path of the aircraft. The aircraft forward motion provides the scanning required for the second dimension of the imagery. In present laser line-scanner subsystems, the video signal modulates a light source which scans photographic film in synchronism with the laser scanner. The film moves at a velocity proportional to the aircraft velocity. The exposed film must then be ground processed, usually by wet film-processing techniques, for use by an observer or photo interpreter.

The work described in this paper is based on an earlier work performed under the Elite Look (Improved Reconnaissance Display Techniques) program. The Elite Look program was to develop the design and specifications for equipment to provide for the transformation, storage, and display of line-scan imagery. Other requirements for the system were to provide stop action capability, image magnification, and high resolution near-real-time viewing. The research and development for the earlier Elite Look program was completed by the Honeywell Systems & Research Division under Air Force contract F33-615-67-C-1501. The result was a set of system specifications and drawings of a laser recorder display subsystem. Primary advantages of the approach selected for this specification and design were:

- (1) A high-resolution storage subsystem for scan conversion of a line scanning sensor.
- (2) Near-real-time viewing of the recorded and developed imagery with demonstrated recording and development in the 1- to 3.2-sec time range.
- (3) A permanent hard copy recording of the sensor output.
- (4) A subsystem for remote viewing of the film, providing for a minimum display installation in the cockpit area.

BASIC SYSTEM

Figure 1 is a block diagram of the basic Elite Look display system. Video signals and synchronizing signals from the aircraft sensor subsystem are fed into the video amplifier and to the deflection subsystem to provide the recording of the video on the dry-process silver film. The dry process film is driven at a rate proportional to the V/H signal received from the aircraft and the image is written on the film in a continuous line-scan mode. The film passes through a heat processor, where it is developed and

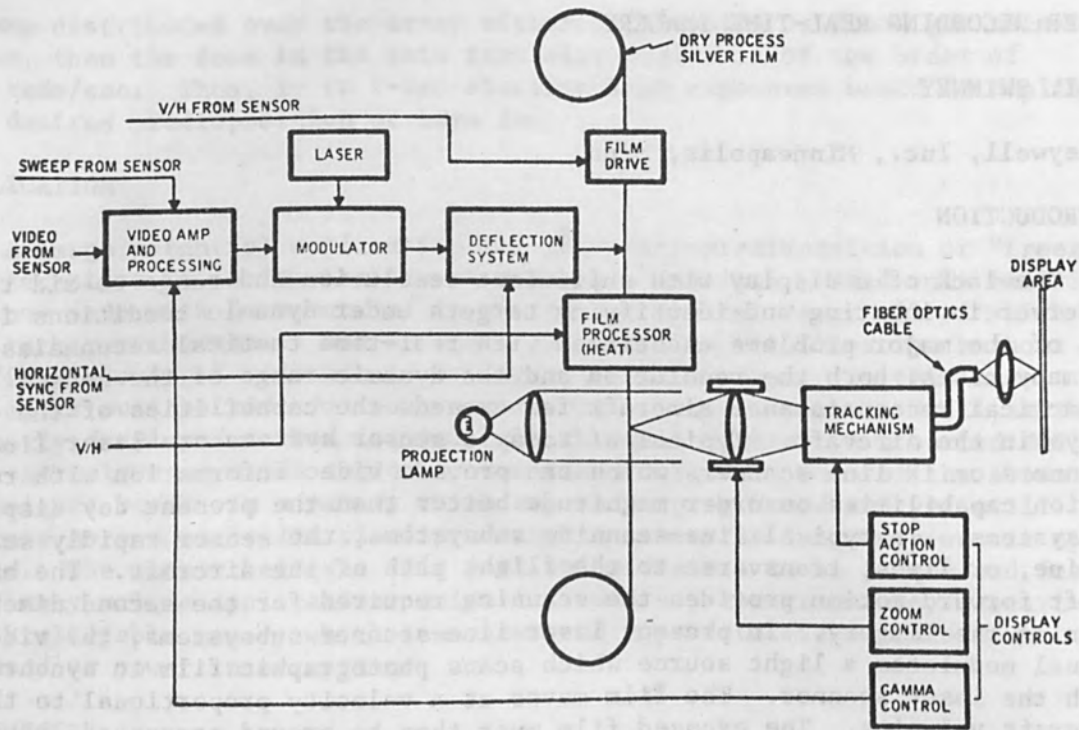


FIG. 1.--Elite Look subsystem.

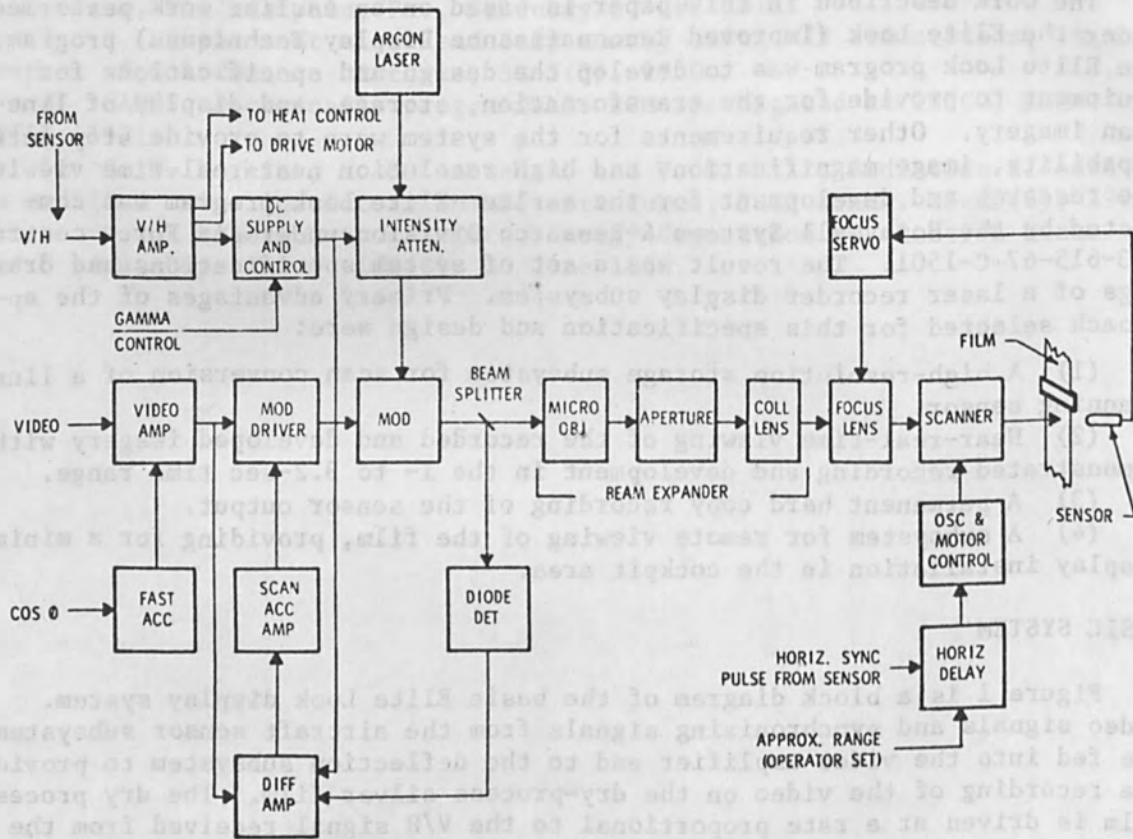


FIG. 2.--Recording subsystem.

passes into the projection area where projection optics and a fiber-optics cable transfer the image to a display subsystem in the cockpit.

Figure 2 is a block diagram for the basic film-recording or write-in subsystem. The argon gas laser yields 25 mW minimum at 4880 Å in a cw TEM₀₀ mode. The beam diameter is 2 mm maximum with a beam divergence of 1.0 millirad full angle.

The modulator has a nominal voltage sensitivity of 160 V ac peak-to-peak at 4880 Å. The extinction ratio is 110:1 with a 2.1-mm beam diameter. The input light-power handling capability of the modulator is 100 mW average with a transmission efficiency of 70 per cent minimum. The frequency response of the modulator is 1 Hz to 30 MHz at 1 db. Also shown in Fig. 2 are the optics for beam forming to provide focus at the film plane, the scanner for deflection of the film, and the AGC circuits required for beam compensation of variations in the video level from the sensor during the sweep.

Figure 3 shows the write-in subsystem (the subsystem which has been further developed beyond the Elite Look work). In the Elite Look system, the major components contributing to the size, weight, and power requirements of the system were the argon gas laser, its power supplies, and the cooling required for the laser. New components and the use of new dry silver-film materials may lead to a significant improvement in the over-all physical parameters of the system.

LASER

The RCA Model LB 2101 argon ion laser was reexamined to determine whether a newer, more compact, more efficient laser could be used. Beam profiles for the RCA argon ion laser show that at the output aperture of the laser the beam diameter (between 1/e² points) is 1.29 mm; 1.75 m away, the beam diameter increases to 2.31 mm, a full angle divergence of 0.58 millirad.

Spectral-line measurements were also made on the argon ion laser; the results are tabulated below.

Wavelength(Å)	4578	4658	4727	4765	4880	4965	5017	5145
Power(W)	0.05	0.11	0.05	0.27	0.83	0.18	0.11	0.85

FILM

The film used in the Elite Look System was 3M 784 UC dry silver film, a heat-developed product that meets the very short development and display time requirements. A spectral sensitivity curve for this film (Fig. 4) shows that it is sensitive in the ultraviolet region and also has a good sensitivity in the green visible region. Figure 5 shows density of the 784 film when exposed by a monochromatic source. Both the 4880 and the 5145 Å line of the argon ion laser were used to test the film, which is seen to be more sensitive to the 5145-Å line. Peak sensitivity occurs at 5350 Å; the response curve is actually a broad peak between 4800 and 5600 Å. Base fog for the film is on the order of 0.05 to 0.1 of transmission density. Minimum density varies between 0.1 and 3.0. The gamma range is 0.7 to 2.4. Density and gamma increase with both exposure time and temperature. A basic limitation in rapid processing of the 784 film is the thermal response of the film base. One experimental approach consists in preheating the film to a bias temperature of 250°F. At this temperature care must be taken to

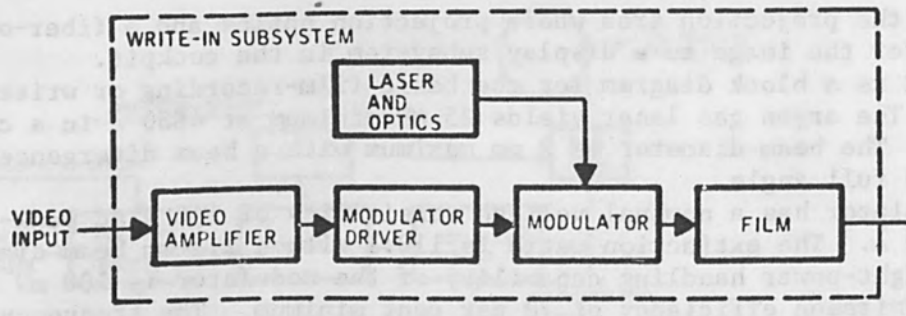


FIG. 3.--Write-in subsystem.

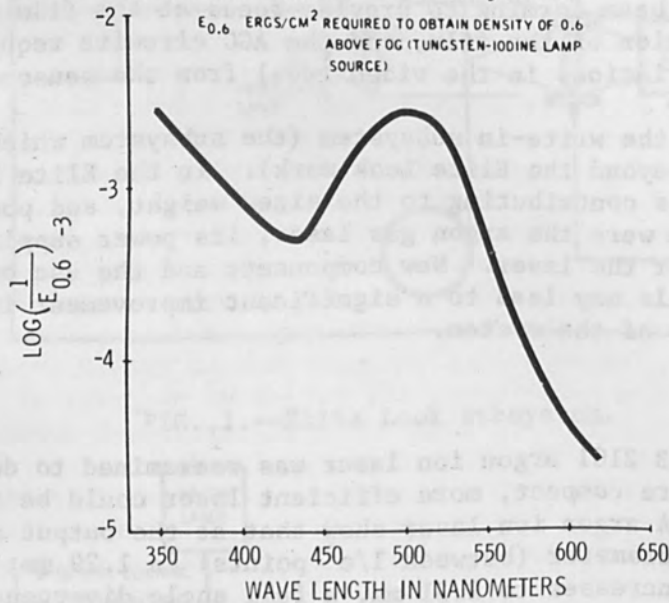


FIG. 4.--784 film spectral sensitivity.

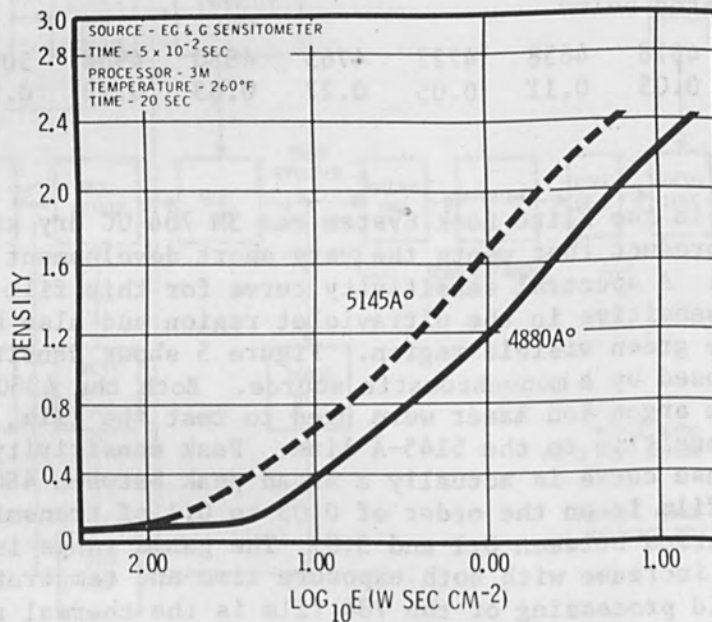


FIG. 5.--Monochromatic processing.

prevent dwell of the film during the preheat. After exposure by the laser, the film is raised in temperature to 275-320°F, depending on the time required for development, and is then immediately cooled below the bias temperature and is ready for viewing.

Figure 6 shows three different samples of the 784 film developed for 3.2 seconds at temperatures of 275, 280, and 320°F. Samples of the film were exposed at the 4880-Å line and then developed as shown. Reasons for the 275°F curve crossing the other two have not been fully investigated at this time. Preliminary conclusions are that the sample of film was not representative of the standard 784 film characteristics. During the development of the film, the temperatures in the development chamber were measured at the film plane with a thermocouple and bridge.

MTF ANALYSIS

A signal of noise analysis and modulation transfer function analysis was conducted on the total Elite Look System to determine display capabilities. Figure 7 shows the system as it is used for noise analysis and MTF. An important question was what would happen to the 784 film MTF under high-heat (rapid-development) conditions. Other noise contributors to the display system are also shown. Primary noise sources were noise on the laser beam and thermal noise in the video amplifier. A test section of the 784 film was exposed or written with a square-wave pattern and then developed at 3.2 sec. Modulation response of the film was then measured using a Joyce Loebel microdensitometer. The resulting MTF curve for the film is shown in Figure 8. The critical area for the film in the total system was the 100 line pairs per millimeter spot. The 784 film is seen to have an excellent MTF characteristic even under extreme conditions of development. Measured response of the film at 100 lp/mm was 58 per cent.

ELITE LOOK SUMMARY

The performance of the Elite Look System met the objective of the program as follows:

Recording spot size	5 μ
Scan rates	2000 lines/sec nominal 5000 lines/sec max.
Development time	1-3.2 sec
Shades of gray	19 2 steps
Display control	Zoom and stop action

The physical characteristics of the Elite Look System were less satisfactory:

Size	Recorder, 7.75 ft ³ Display, 1 ft ³
Weight	Recorder, 330 lb Display, 10 lb
Power	Recorder and display, 3190 W

Results of the Elite Look proved that the technology was available to provide a high-resolution recording display capable of matching performance requirements of high-resolution sensors, but only at the cost of greater power, weight, and size.

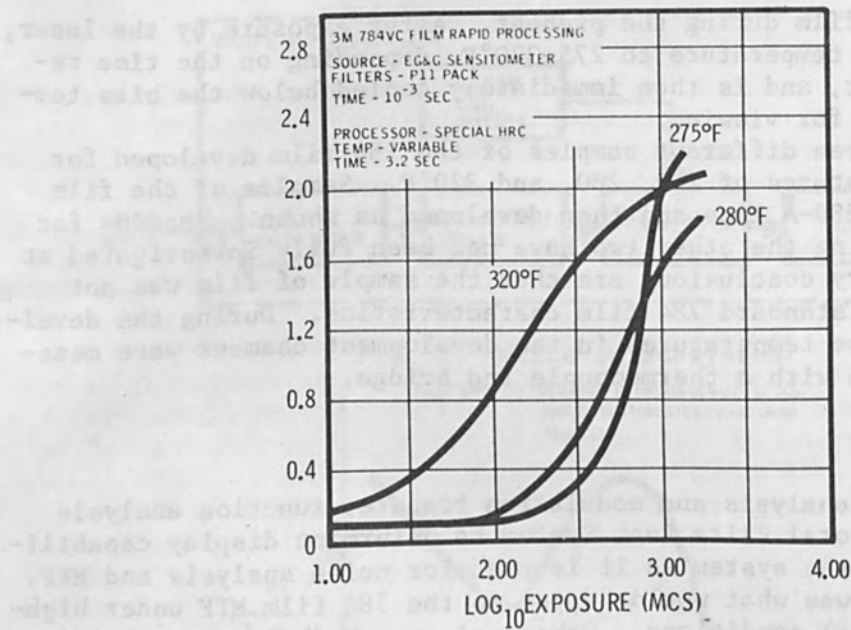


FIG. 6.--Rapid-processing sensitometry with varying temperature.

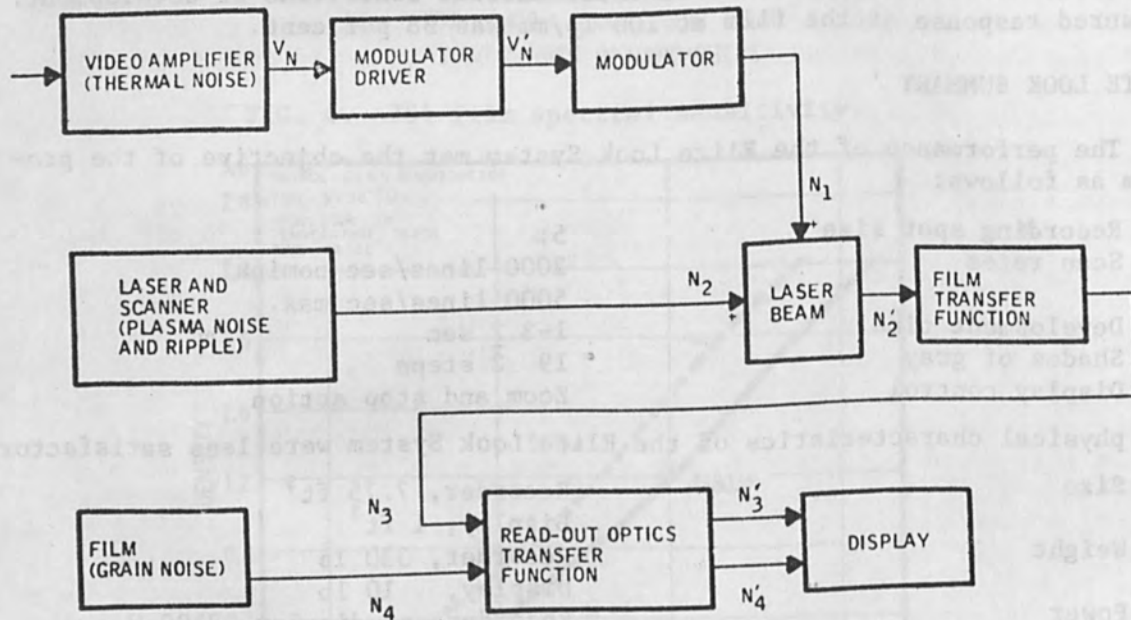


FIG. 7.--Noise analysis.

IMPROVED RECORDER SYSTEM

New developments, primarily in laser technology, have provided a way of building a laser recording and display subsystem that maintain the performance characteristics of the Elite Look subsystem and allow significant reductions in the size, weight, and power requirements. Continued development work on the laser writing subsystem at Honeywell has shown that a solid-rod laser can be used to replace the argon ion laser and to provide significant physical improvements without loss of performance. A neodymium YAG laser and frequency is used. The Nd-YAG laser is optically pumped by a gas flashtube. Output of the laser is normally $1.06 \mu(10\ 600 \text{ \AA})$. A lithium niobate crystal in the laser cavity doubles the output frequency (reduces the output wavelength to 5300 \AA), which is just 50 \AA from the 5350-\AA peak sensitivity of the film.

With the doubled Nd-YAG laser and an output of 100 mW, a significant reduction in size over the original argon ion laser results, as shown in Table I. Lifetime of the Nd-YAG laser depends primarily on the life of the flashtube, which must be replaced approximately every 100 to 150 hr.

TABLE I.--Comparison of argon ion and Nd-YAG lasers.

	Argon Ion	Nd-YAG
Laser head size (in.)	$24 \times 8 \times 10$	$8 \times 6 \times 4$
Cooler size (in.)	$24 \times 15 \times 19$	$12 \times 8 \times 6$
Input power (W)	2500	100 - 150

A newer development in the optical pumping of Nd-YAG lasers, which promises even higher efficiency, is the use of gallium arsenide diodes to pump the Nd-YAG rod. Their output optically matches the absorption band of the Nd-YAG rod for most efficient pumping. (Developmental work on this type of laser is currently being carried on at Honeywell.) The advantages:

- Efficiency of the pumping is increased by a factor of 2 over flashtube
- Pump lifetime is increased by a factor of 10 over flashtube
- Power input can be reduced to 50-75 W
- Cooler size can be reduced

Use of the Nd-YAG laser with flashtube pumping or with the solid-state GaAs pump array thus provide significant improvements over the argon ion laser. Another useful improvement would result from improvements in the 784 film. Figure 9 shows a density-vs-exposure curve for the newest 784 film. Speed of the film has been increased and the D_{\max} of the film has also been increased slightly. Base fog level or D_{\min} remains about the same.

Figure 10 is a comparison of the relative sensitivity of the 784 film and a new red-sensitive dry-silver material. Current plans retain the 784 film; however, further study of the red-sensitive film with a different writing source is under way.

Figure 11 shows the characteristics of the 784 film with and without antihalation undercoating (AHU). The 784 AHU film is used at the present time to prevent scattering and spreading of the laser recording spot. This film also maintains or improves the MTF as tested in the Elite Look program. Sensitivity of the 784 AHU is slightly lower than without AHU, but is more than compensated by the improvements in the laser system mentioned above.

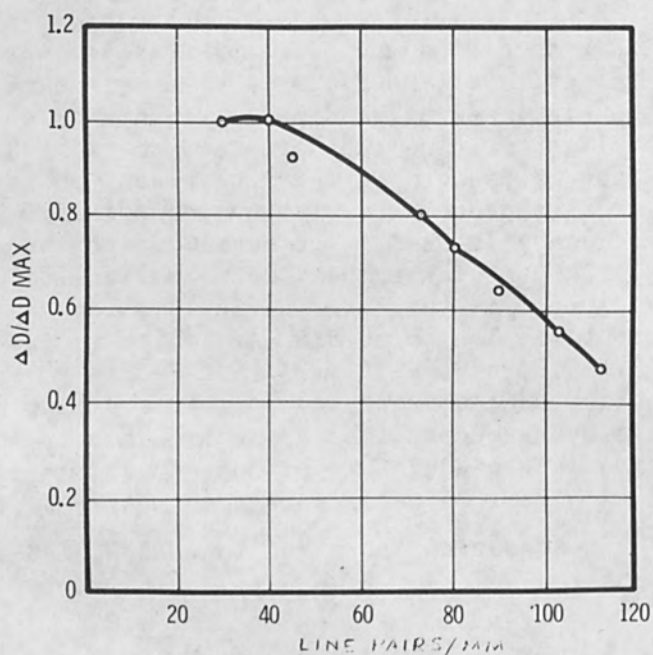


FIG. 8.--Square-wave modulation response of 784 film 3.2-sec processing.

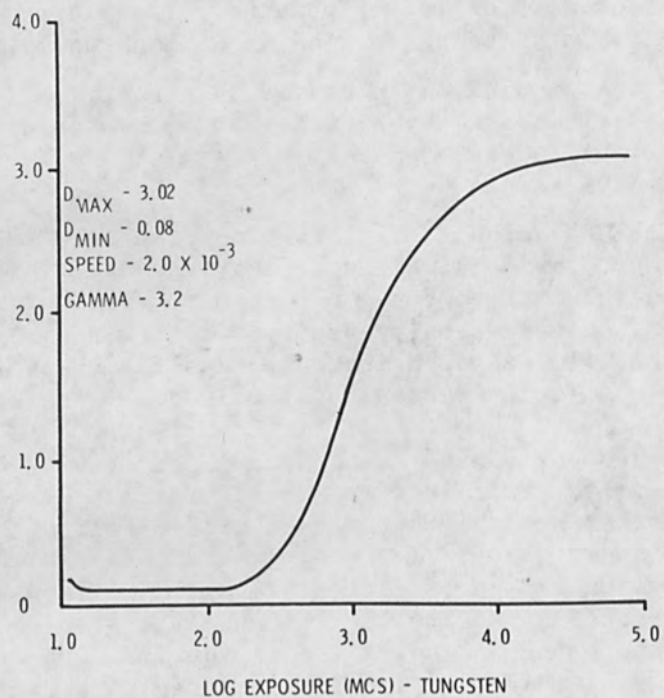


FIG. 9.--D log E values of new 784 film.

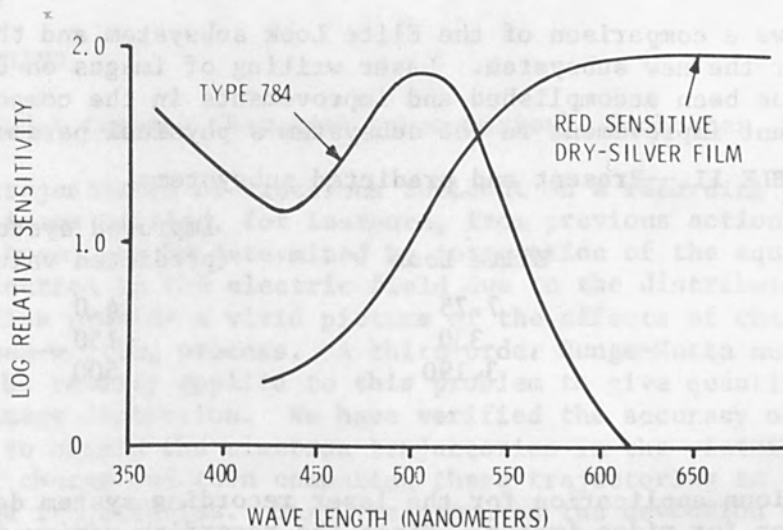


FIG. 10.--Relative sensitivity of 3M films.

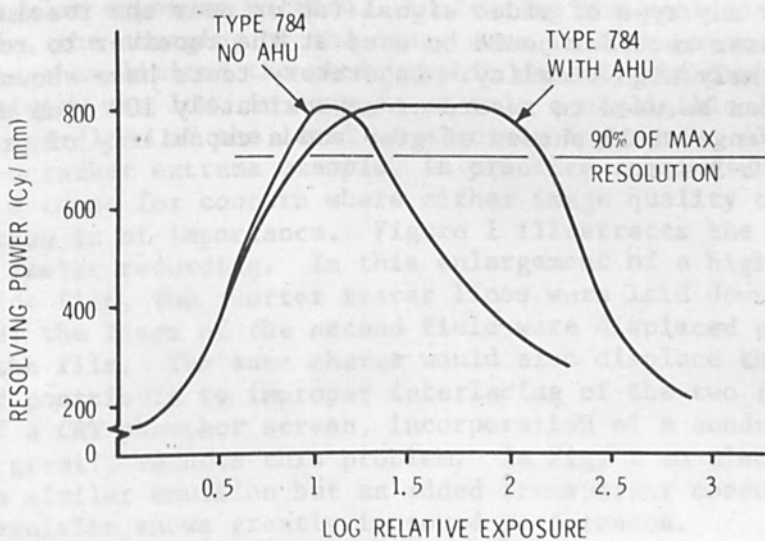


FIG. 11.--Resolving power of 784 and 784 AHU.

SUMMARY

Table II shows a comparison of the Elite Look subsystem and the predicted values for the new subsystem. Laser writing of images on dry-silver film materials has been accomplished and improvements in the components provide significant improvement in the subsystem's physical parameters.

TABLE II.--Present and predicted subsystems.

	Elite Look	Improved system (predicted values)
Size (ft ³)	7.75	4.0
Weight (lb)	330	150
Power (W)	3.190	500

APPLICATIONS

The most obvious application for the laser recording system described is scan conversion for video images. Since the recording medium is a film which retains a permanent record, an image can be recorded from either a line-scanning sensor or from a slow-framerate sensor and stored on the film material. Readout of the film can then be accomplished by projection techniques or by scanning with a television camera. The method of readout is determined by the resolution requirements of the system.

Another application would be the recording for permanent storage of slow-scan video being sent via a communications link from a satellite to the ground. In addition, this type of system would provide an extremely high-quality remote-recording station. When it becomes necessary to transmit a picture or any type of video signal (at or near the resolution of the original) the laser recorder could be used at the receiver to record the video with extremely high fidelity. Laboratory tests have shown that the laser and film can be used to record at approximately 100 line pairs/mm with a dynamic range of 19 shades of grey and a capability of processing in the range of 1-3 sec.

THE EFFECTS OF IMAGEWISE ELECTROSTATIC CHARGE BUILDUP IN ELECTRON BEAM RECORDING

P. S. TSCHANG

Eastman Kodak Company (Research Laboratories), Rochester, N.Y.

The trajectories of electrons incident on a recording medium carrying a charge image arising, for instance, from previous action of the writing electron beam, can be determined by integration of the equations of motion for an electron in the electric field due to the distributed charge. Such trajectories provide a vivid picture of the effects of charge accumulation on the beam-writing process. A third-order Runge-Kutta numerical integration can be readily applied to this problem to give quantitative information on image distortion. We have verified the accuracy of this method by using it to obtain the electron trajectories in the vicinity of a stationary point charge and then comparing these trajectories to the analytically integrated trajectories. Next, we computed the deviation of an electron beam directed to land near a rectangular charge pattern on a dielectric slab whose back plane was at ground potential. The computed deviation is in close agreement with results of an experiment.

INTRODUCTION

It has been known since the early days of electron-beam recording that film charging was responsible for the barrel-shaped appearance of an otherwise rectangular exposure pattern. In testing the sensitivity of photographic film, the charging of the image area in time prevented further exposure and thus limited the photographic density obtainable. When the film sensitivity was low, in some cases only a negligible density could be developed regardless of the level of electron exposure. Although this represents a rather extreme example, in practice considerably less charging can be a cause for concern where either image quality or precision of image location is of importance. Figure 1 illustrates the effect of a television raster recording. In this enlargement of a high-resolution silver halide film, the shorter raster lines were laid down during the first field; the lines of the second field were displaced upward by the charge on the film. The same charge would also displace the lines transversely and contribute to improper interlacing of the two fields. As in the case of a CRT phosphor screen, incorporation of a conducting layer on the target greatly reduces this problem. In Fig. 2 an electron recording film with a similar emulsion but an added transparent conductive coating below the emulsion shows greatly improved performance.

RUNGE-KUTTA'S METHOD

Given the classical equations of motion for an electron in a potential field ϕ

$$\ddot{x}_i(t) = \frac{e}{m} \frac{\partial \phi}{\partial x_i} \equiv f_i(x_1, x_2, x_3), \quad i = 1, 2, 3 \quad (1)$$

the third-order Runge-Kutta integration^{1,2} predicts $x_i(t + \delta)$ and $\dot{x}_i(t + \delta)$ from $x_i(t)$ and $\dot{x}_i(t)$ and ϕ

$$x_i(t + \delta) = x_i(t) + \delta \left[\dot{x}_i(t) + 1/4 k_i^0 + 1/4 k_i^1 \right] \quad (2)$$

$$\dot{x}_i(t + \delta) = \dot{x}_i(t) + 1/4 k_i^0 + 3/4 k_i^1 \quad (3)$$

where $k_i^0 = \delta f_i[x_1(t), x_2(t), x_3(t)] \quad (4)$

$$k_i^1 = \delta f_i(\tilde{x}_1, \tilde{x}_2, \tilde{x}_3) \quad (5)$$

$$\tilde{x}_j \equiv x_j(t) + 2/3 \dot{x}_j(t)\delta + 2/9 k_j^0\delta$$

A repeated application of this process generates x_i and \dot{x}_i with t as the independent variable. Without going into the relative merits of other numerical schemes, we may state that the Runge-Kutta procedure is easily programmed for the computer and, where ϕ can be formulated, requires relatively little computer storage.

SOME USEFUL FORMULAS

From an isolated point charge Q the potential is

$$\phi = \frac{Q}{4\pi\epsilon_0 r} \quad (\text{mks units}) \quad (6)$$

From an isolated uniform surface charge density σ , within a $2\alpha \times 2\beta$ rectangle (Fig. 3) the derivatives of the potential are:

$$f_1 = \frac{e}{m} \frac{\partial \phi}{\partial x} = \frac{e\sigma}{4\pi\epsilon_0} \left\{ \tan^{-1} \left[\frac{(\alpha - z)(\beta - y)}{C_1 x} \right] + \tan^{-1} \left[\frac{(\alpha + z)(\beta - y)}{C_2 x} \right] + \tan^{-1} \left[\frac{(\alpha - z)(\beta + y)}{C_3 x} \right] + \tan^{-1} \left[\frac{(\alpha + z)(\beta + y)}{C_4 x} \right] \right\} \quad (7)$$

$$f_2 = \frac{e}{m} \frac{\partial \phi}{\partial y} = \frac{e\sigma}{4\pi\epsilon_0} \log \left\{ \frac{C_1 + (\alpha - z)}{C_3 + (\alpha - z)} \frac{C_4 - (\alpha + z)}{C_2 - (\alpha + z)} \right\} \quad (8)$$

$$f_3 = \frac{e}{m} \frac{\partial \phi}{\partial z} = \frac{e\sigma}{4\pi\epsilon_0} \log \left\{ \frac{C_1 + (\beta - y)}{C_2 + (\beta - y)} \frac{C_4 - (\beta + y)}{C_3 - (\beta + y)} \right\} \quad (9)$$

$$C_1 = \sqrt{(\alpha - z)^2 + (\beta - y)^2 + x^2}$$

$$C_2 = \sqrt{(\alpha + z)^2 + (\beta - y)^2 + x^2}$$

$$C_3 = \sqrt{(\alpha - z)^2 + (\beta + y)^2 + x^2}$$

$$C_4 = \sqrt{(\alpha + z)^2 + (\beta + y)^2 + x^2}$$

For the same surface-charge configuration with a backing dielectric slab of dielectric constant ϵ and thickness ℓ , whose other face is held at ground potential, we have^{3,4}

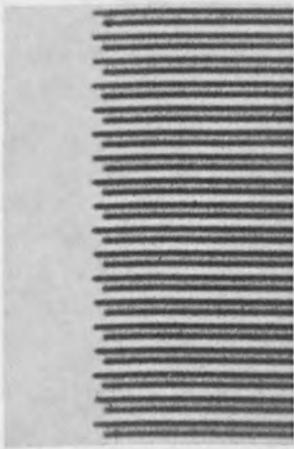


FIG. 1.--Enlargement of a portion of standard interlaced television raster scan on silver halide film. Spacing of two fields should be about $14 \mu\text{m}$.

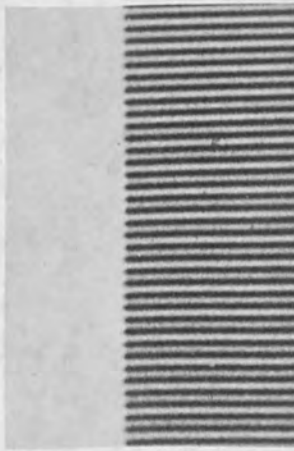


FIG. 2.--Same as Fig. 1 except that film has transparent conductive layer under emulsion.

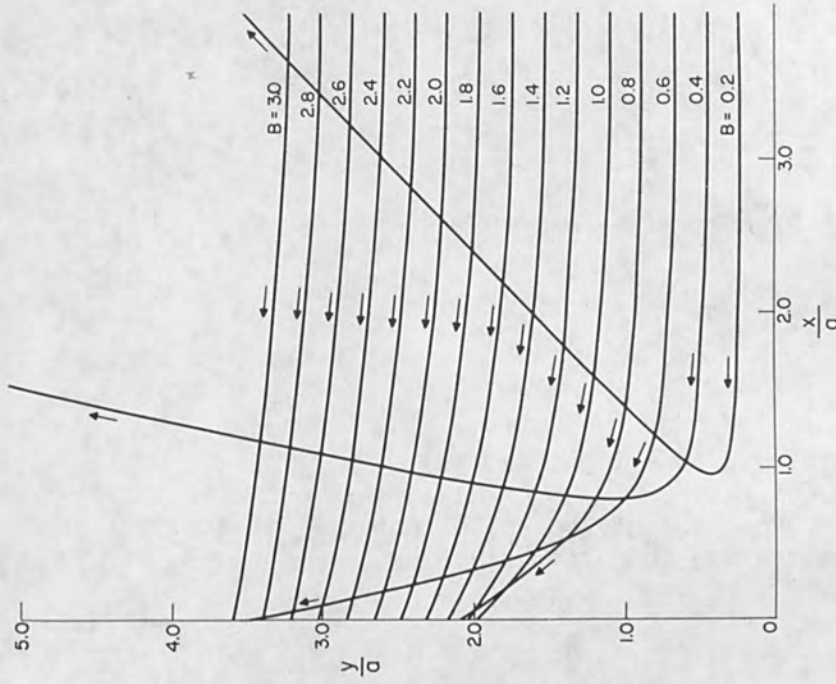


FIG. 4.--Deflection of electrons by negative point charge located at origin computed by third-order Runge-Kutta method.

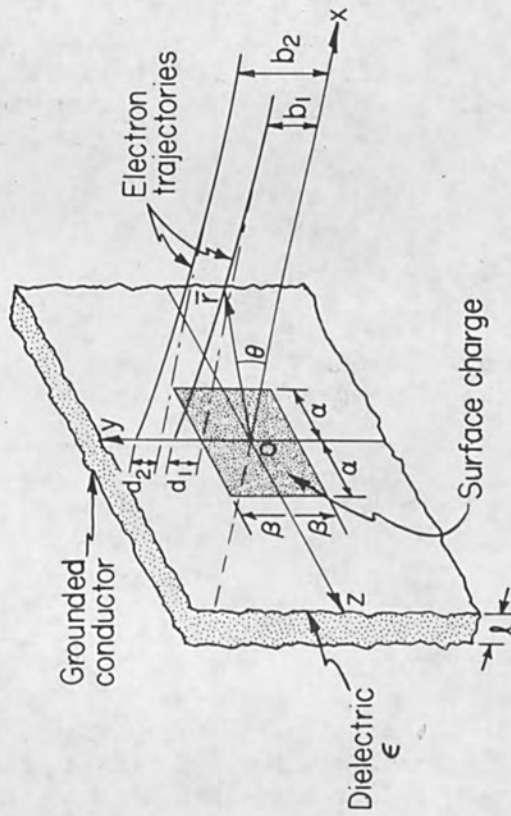


FIG. 3.--Configuration of charging study.

$$f_i = (K + 1)f_i^{(1)} - (1 - K^2) [f_i^{(2)} + Kf_i^{(3)} + K^2f_i^{(4)} + \dots + K^{N-2}f_i^{(N)}] \quad (10)$$

$$\text{where } K = \frac{1 - \epsilon}{1 + \epsilon}$$

$f_i^{(1)}$ is given by Eqs. (7), (8), and (9)

$$f_i^{(2)} = f_i^{(1)}(x_1 + 2\ell, x_2, x_3)$$

.

.

$$f_i^{(N)} = f_i^{(1)}(x_1 + 2(N-1)\ell, x_2, x_3)$$

For $x \gg \alpha, \beta, y, z$, Eq. (10) may be approximated by the derivatives of a central inverse-square law potential given by

$$\phi = \frac{1 + K}{1 - K} \frac{4\alpha\beta\sigma}{4\pi\epsilon_0} \frac{2\ell}{r^2} \quad (11)$$

The trajectories of electrons in a central potential field $\phi(r)$ are described by⁵

$$\frac{dr}{d\theta} = \pm \frac{r^2}{b} \sqrt{1 - \frac{b^2}{r^2} - \frac{\phi(r)}{U}} \quad (12)$$

in polar coordinates. Here b is the so-called impact parameter and U is the kinetic energy of the electron removed from the scattering center.

When Eq. (6) is substituted in Eq. (12) one obtains, after integration

$$\frac{r}{a} = \frac{2B^2}{2B \sin \theta + \cos \theta - 1} \quad (13)$$

$$a = \frac{|Q|}{4\pi\epsilon_0 U}, \quad B = \frac{b}{a}$$

for repulsive scattering.

Likewise, when Eq. (11) is used one obtains

$$\frac{r}{c} = \sqrt{(D^2 + 1) \left\{ \tan^2 \left[\frac{\sqrt{D^2 + 1}}{D} \theta + \frac{\pi}{2} \right] + 1 \right\}} \quad (14)$$

$$D = \frac{b}{c}, \quad c = \sqrt{2\ell a} \cdot \sqrt{\frac{1 + K}{1 - K}}$$

COMPUTER PROGRAM

The essential parameters used for the computer program are defined in Fig. 3. Here, an electron with initial velocity corresponding to kinetic energy eU is traveling parallel to the $-x$ axis with impact parameter b and in the plane $z = 0$. A point charge Q located at the origin or a surface charge of σ is placed within a $2\alpha \times 2\beta$ rectangle on the front face of the dielectric with thickness ℓ and with the back face of the dielectric at

ground potential. To avoid excessive computation, the starting point for the Runge-Kutta steps is established at $x = x_0$, where x_0 is some convenient finite length such that Eq. (13) or Eq. (14) can be used to give y_0 and $dy/dx|_0$. The kinetic energy of the electron at the starting point is then computed and from that one can compute \dot{x}_0 and \dot{y}_0 . From this point the computation proceeds according to Eqs. (2), (3), (4), and (5) in conjunction with the appropriate potential derivatives until the trajectory is terminated by one of the following conditions:

$$x \leq 0, \quad y > y_{\max}, \quad x > x_{\max}$$

RESULTS

For the test case of an isolated negative point charge the Runge-Kutta electron trajectories normalized to a are plotted in Fig. 4 for a range of B . Note the sharp bends in trajectory of the two backscattered electrons. A similar plot obtained from the exact solution (Eq. 13) is indistinguishable from Fig. 4 in every detail, including the sharp bends. This is a good indication of the accuracy attained with the Runge-Kutta method and suggests its application to other, much more demanding types of electron-optical computations.

If practical values are used for the various parameters, a plot of electron trajectories for the case of surface charge distributed on a dielectric would not exhibit the zone around the origin of Fig. 4 which is clear of all trajectories. All rays would be at best slightly curved and such a plot would not be very informative. In this instance the most significant thing by far would be the deviation from the unperturbed path,

$$d = (y - b) \Big|_{x=0}$$

at the point where the electron enters the dielectric. This is a quantity that can be measured on a phosphor screen or on electron recording film. Figure 5 gives the computed d (for electrons directed at the edge, i.e., $b = \beta$) as a function of $\alpha (= \beta)$, with σ ranging from 10^{-9} to 10^{-5} coulomb/cm². Two families of curves are shown: one for $\ell = 100 \mu\text{m}$, $\epsilon = 3.0$ to represent a typical film base material, and the other for $\ell = 4 \mu\text{m}$, $\epsilon = 1.5$ to represent an emulsion with an underlying conductive layer. The first model should closely approximate the charging behavior of a film without a conductive layer below the emulsion since the emulsion thickness would be insignificant compared with the film-base thickness. The second model should give a conservative prediction of charging since the electrons, e.g., at 15 kV, are actually expected to penetrate a considerable distance below the surface, whereas some would be collected by the conductive sublayer.

EXPERIMENTAL EVALUATION

An experimental facility to verify some of the computed d values and to provide additional evidence of charging effects can be readily set up with raster-type electron-beam recording equipment. By means of appropriate raster-size control, electronic timing, and logic circuitry for beam modulation (blank/unblank), a test pattern such as that shown in Fig. 6 can be obtained. Here the normal (unblanked) raster is rather

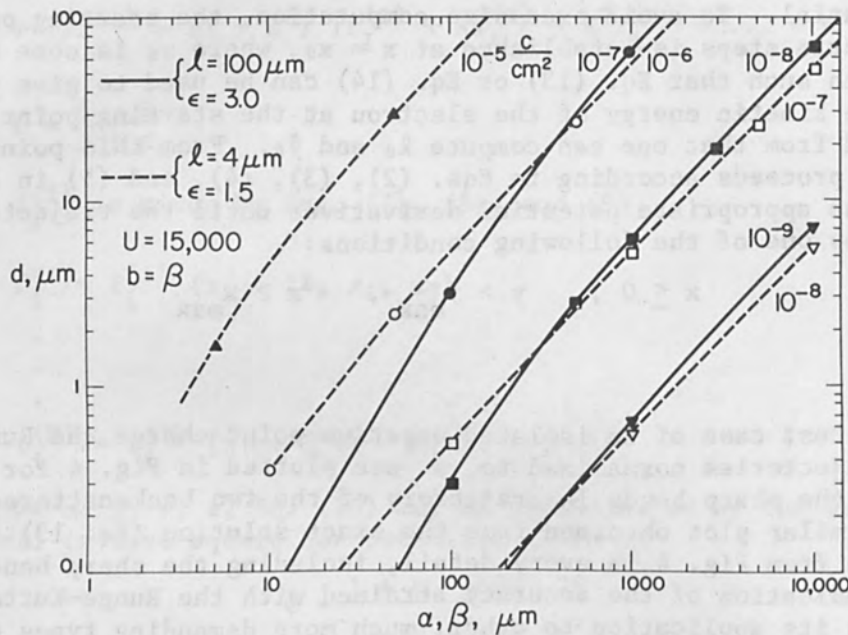


FIG. 5.--Deviation parameter d plotted against the side dimension of square charge pattern on dielectrics.

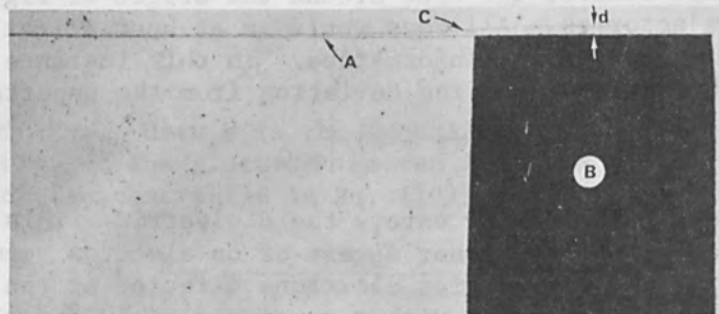


FIG. 6.--Electron exposure pattern for experimental study of film charging. Experimental film without conductive sublayer.

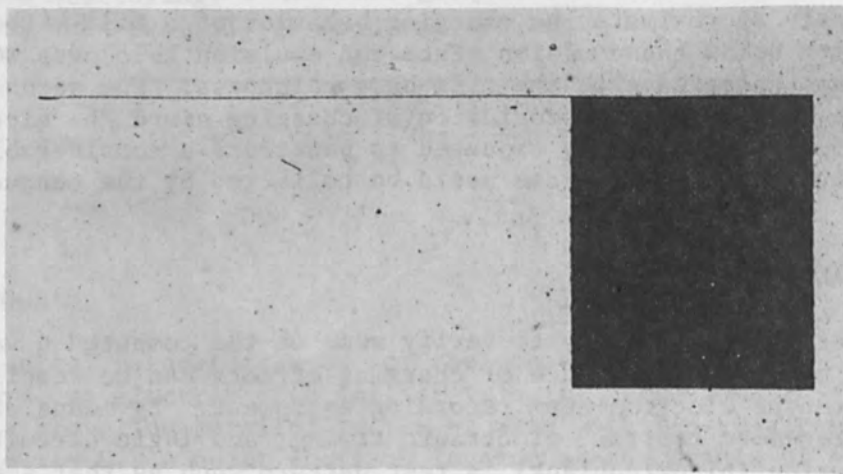


FIG. 7.-- Same as Fig. 6 except that film has transparent conductive sublayer.

compressed in the vertical direction. The first full horizontal line (A) is laid down, followed immediately by the rest of the horizontal lines in this vertical interval except that a large fraction of horizontal scan (in this case about 66 per cent) has been blanked off. This results in an abbreviated raster (B). Finally, after a controlled time interval, another full horizontal line (C) corresponding to line (A) in the raster position is laid down. Since the charge in (B) dominates the whole picture (1000-line raster) any deviation of (C) from (A) is attributed to the effects of charge remaining in (B). Figure 6 depicts quite clearly the extent of charge-induced beam deflection for an experimental film which has no conductive sublayer. In this case we measure $d = 68 \mu\text{m}$ whereas the computed result indicates $75 \mu\text{m}$. Even though the 10-percent discrepancy is quite acceptable for most purposes, we believe a closer control of experimental and computer input parameters should minimize this difference.

Referring again to Fig. 6 we see that the shape of the abbreviated raster (B) has been significantly affected by its continuously evolving charge pattern. Thus, the base width is as much as 5 per cent greater than the top width. We may note also the curved sides and in particular the sharp break in curvature about 1/10 the distance from the top. The location of this break point seems most closely related to the film thickness. In contrast, Fig. 7 depicts a similar film but with a conductive sublayer added. No charge effects are now evident at this level of magnification.

FIGURE OF MERIT M

For small deflection, $d/b \ll 1$, and large ratio of image dimension to film thickness, $\beta/\ell > 1$, the following expression is a useful approximation:

$$\frac{d}{\beta} \approx 3 \times 10^{12} \frac{\sigma_{\text{eff}} \ell}{\epsilon U}$$

where σ_{eff} is the effective average charge density (coulomb/cm²), ℓ is in cm, $\epsilon = 1.0-5.0$, and $U = 10-20$ kV.

The degree of freedom from charge distortion can be represented by a figure of merit M defined as

$$M \equiv 2\beta/d$$

This is the ratio of image width to the deviation of the edge position. Thus, M is certainly the upper bound to the number of image elements per column, or row, if precise locating of the elements is important, as in the case of IC mask generation. For standard interlaced television-raster recording, if one were to have $M = 525$, then the top and bottom adjacent lines of the two fields would be totally paired. Making $M = 1500$, for instance, would result in a much more pleasing raster display. The table below gives M for a number of situations, together with representative electron exposure values for three broad classes of films:

	I	II
M	$\epsilon = 3.0$ $\ell = 0.01 \text{ cm}$	$\epsilon = 1.5$ $\ell = 0.0004 \text{ cm}$
	$U = 15 \text{ kV}$	
$\sigma_{\text{eff}} = 10^{-10} \text{ coul/cm}^2$	30 000	400 000*
10^{-9}	3 000	40 000*
10^{-8}	300	4 000*
10^{-7}	30	400*

* $\sigma_{\text{eff}} \ll \text{electron exposure}$

Electron Exposure for $\bar{D} = 1.0$	Film Type
$3 \times 10^{-10} \text{ coul/cm}^2$	Fine-grain silver halide film
$3 \times 10^{-9} - 3 \times 10^{-8}$	Ultra-fine-grain silver halide film
$10^{-8} - 10^{-5}$	Nonsilver halide film

From this table one can draw conclusions as to when a film with a conductive sublayer will be desirable. Note here that because of electron penetration, for an emulsion of 4- μm thickness, exposed to 15-kV electrons, σ_{eff} is much smaller than the electron exposure. In practice, a factor of 10 improvement in M can be expected this way.

CONCLUSION

We have indicated the usefulness of the third-order Runge-Kutta method for determining electron trajectories in the presence of point or rectangular charge patterns on a dielectric. Other charge patterns can be also incorporated. Serious charge-induced distortion can occur in recording materials of comparatively low sensitivity. A conductive sublayer mitigates this distortion substantially. We believe the proposed figure of merit M can be a useful guideline in the early stage of the design of electron-beam information-recording systems. For a more specific determination of charging effects the general procedure outlined in this paper can be further tailored to account for the particular system configuration, writing sequence, etc., for the electrostatic force is indeed long range.

REFERENCES

1. A. Septier (ed.), Focusing of Charged Particles, Vol. 1, Academic Press, New York/London, 1967; Chap. 1,2 by C. Weber.
2. J. A. Zonneveld, Automatic Numerical Integration, Mathematisch Centrum, Amsterdam, 1964.
3. H. E. J. Neugebauer, Applied Optics, 3: 385-393, 1964.
4. W. R. Smythe, Static and Dynamic Electricity, McGraw Hill, New York, 1950; p. 182.
5. E. W. McDaniel, Collision Phenomena in Ionized Gases, Wiley, New York, 1964; Chap. 3.

VESICULAR FILMS IN ELECTRON AND LASER BEAM RECORDING

V. L. WAGNER JR.

Kalvar Corp., New Orleans, La.

Kalvar[®] vesicular films have been in use for several years now and have found applications in many fields. There are several good reviews on vesicular film mechanics, sensitometry, and densitometry.^{1,2} In vesicular photography, exposure is normally achieved using ultraviolet light, which eliminates the need for a darkroom, and development is accomplished simply by the application of heat. Access to the final processed image is immediate. Processors for roll vesicular films have achieved speeds in excess of 200 ft/min and processors at higher speeds are planned.

Attenuation of light by a vesicular image is achieved by the scattering of light. If the light incident on the film is collimated, the scattered rays emerge from the image at varying angles and the relative aperture is very important in determining photographic density, as seen in Fig. 1. If aperture A is either made wider or moved closer to the film plane, thus reducing the f number and numerical aperture, the number of scattered rays collected increases and the greater collected light flux results in a lower photographic density. A typical effect of the change of aperture is shown in Fig. 2, in which the difference between f/4.5 and f/0.0 (diffuse density) is exemplified for a Type 10 film developed at a relatively low temperature. (Most of the H & D curves in the present paper show abscissas numbered from 28 to 0, representing successive steps of a silver-step tablet in which each step varies by a density equal to 0.15, and give the f number used for the particular density measurement.)

TYPICAL FILM TYPES

The sensitometric characteristics of Kalvar films of Types 10(103)--still the most widely used vesicular material for duplication of computer output microfilm originals--and 16(614) are shown in Fig. 3. Type 16 has achieved great acceptance and is in volume use in the duplication of COM originals, micropublishing, and also for front-screen projection of motion picture duplicates. An improved version of Type 16, the Type 14, is a full stop faster at the same exposure range and density scale and also has an aesthetically more pleasing color than Type 16 (more neutral gray as opposed to the blue color of Type 16). However, both types project as black and white, as do all vesicular films. Another film, Type 23(233), fully meets the requirements for film to be used in television applications and has achieved good acceptance in the large-scale duplication of such television film originals. The photographic characteristics of Types 14 and 23 are presented in Fig. 4. Density measurements for the latter were obtained at f/1.6 which is typical for the television application. In addition, Type 23 makes very pleasing projection duplicates (Fig. 5). In graphic arts applications Type 16 may be used for color separation work where good continuous-tone film is desirable. For line and half-tone work Type 41(415) has gained wide acceptance (Fig. 6). Given in Fig. 6 are diffuse densities to ultraviolet radiation, which is a realistic method of evaluation since it is characteristic to the application. Still another film, also shown in Fig. 6, is Type 90, a hard-copy material

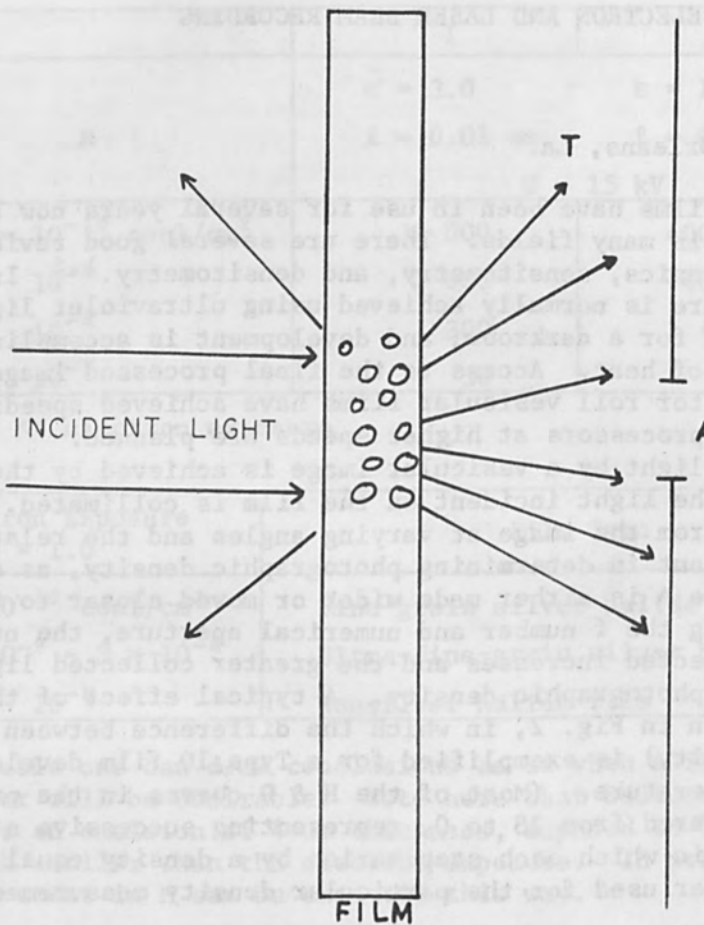


FIG. 1.--Schematic of Kalvar density in use.

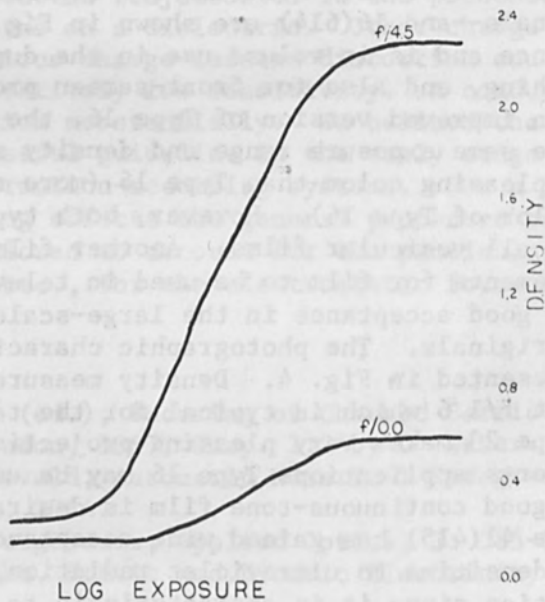
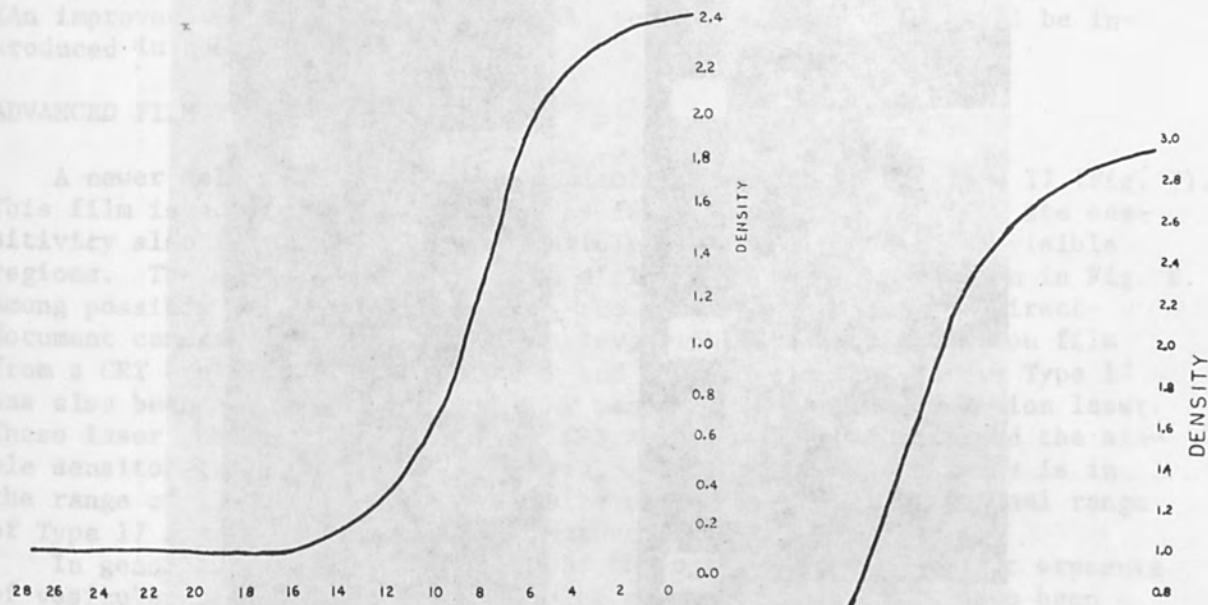


FIG. 2.--The effect of aperture on density.

that produces
 an improved
 produced in
 ADVANCED FILM

A newer
 This film is
 activity also
 regions. The
 Among possible
 document cards
 from a CRT
 has also been
 These Laser
 ple sensitive
 the range
 of Type 17



(a)
 FIG. 3.--(a) Type 10;
 (b) Type 16.

are the nitrogen pulsed laser (6328 Å) and the helium-neon laser (6330 and 6331 Å).

An experimental film having a resolution of 100 lines/mm has been used in the duplication of holograms. The film is sensitive to the green light of a He-Ne laser (6330 Å) and the red light of a He-Ne laser (6331 Å).

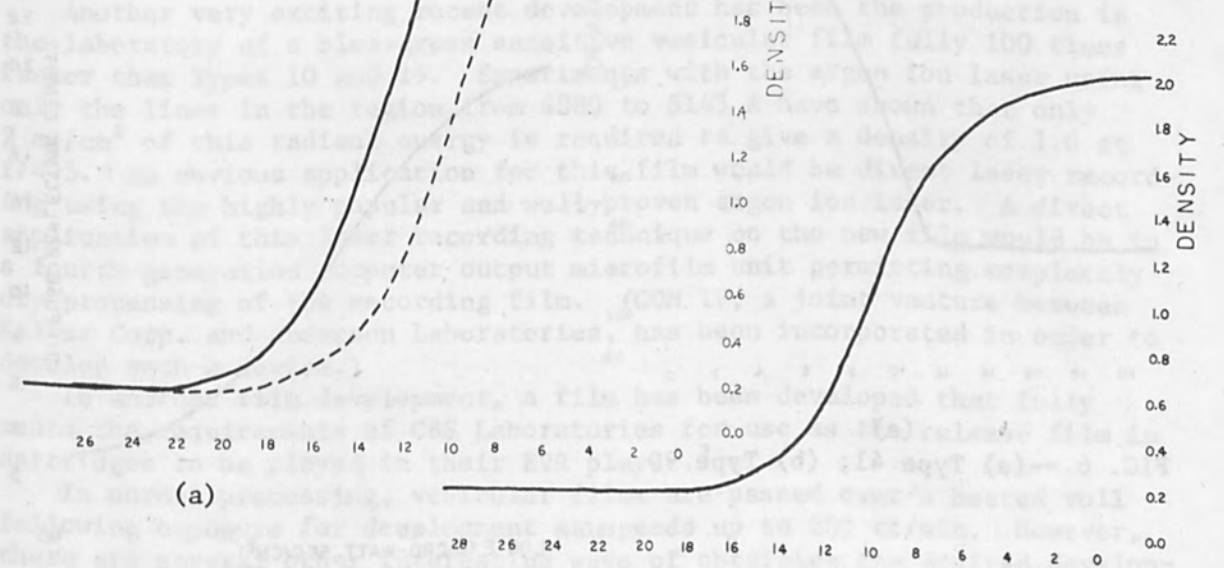
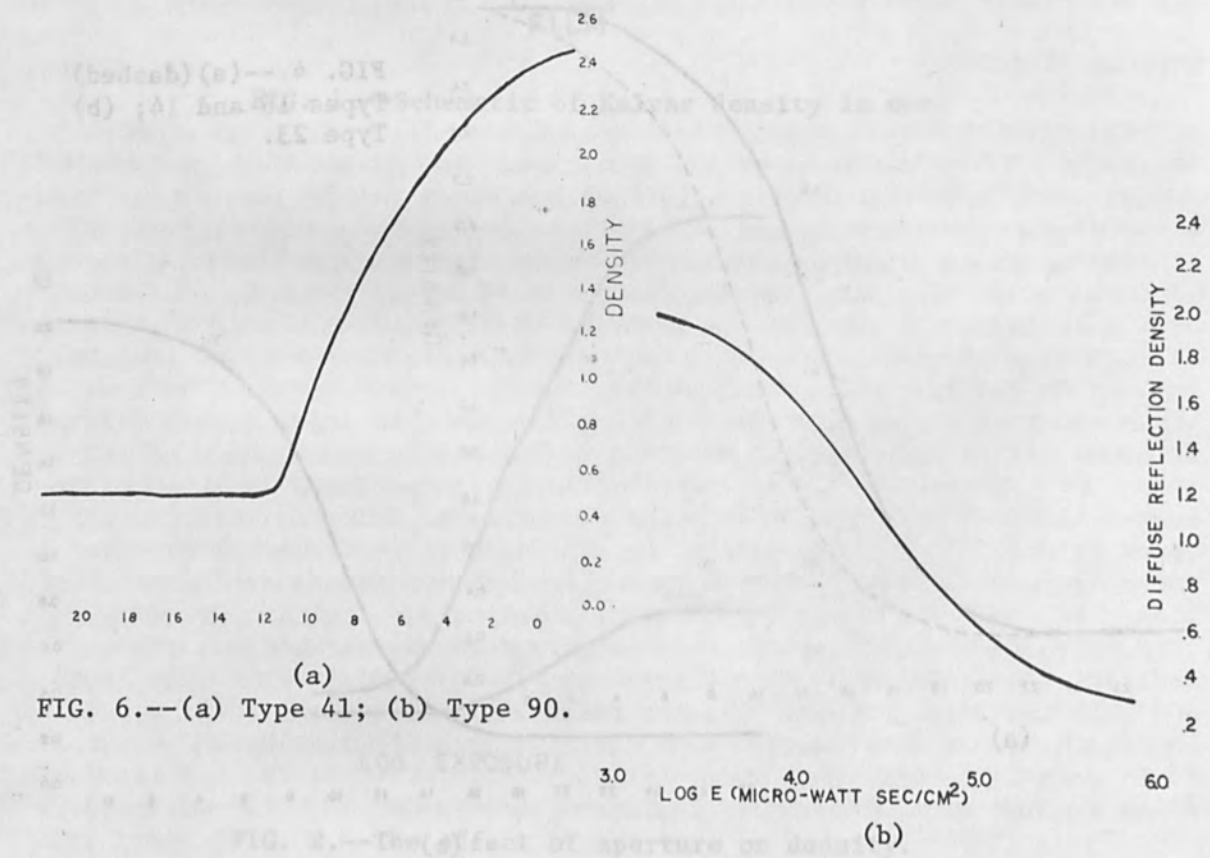


FIG. 4.--(a) (dashed)
 Types 16 and 14; (b)
 Type 23.



FIG. 5.--Release Prints: Kalvar Type 23 (left) and Silver halide cine positive of same negative.



that produces a positive from a positive and a negative from a negative. (An improved version of this material, to be called Type 91, will be introduced in the very near future.)

ADVANCED FILM TYPES

A newer Kalvar film under development at present in KDR Type 17 (Fig. 7). This film is approximately 10 times as fast as Types 10 and 16. Its sensitivity also lies in the near ultraviolet and short-wavelength visible regions. The spectral sensitivities of Types 10 and 17 are shown in Fig. 8. Among possible applications would be the use of this film in a direct-document camera, and in applications involving direct recording on film from a CRT employing a P-16 phosphor and fiber optic faceplate. Type 17 has also been successfully exposed by means of the argon double-ion laser. These laser results, as well as the CRT exposures, have confirmed the simple sensitometric results given in Fig. 7. Required input energy is in the range of 15-20 mj/cm^2 for a density of 1.6 at $f/4.5$. The tonal range of Type 17 and its speed are important assets.

In general, no lasers operating at the optimum wavelength for exposure of vesicular films have been available, but some experiments have been carried out that demonstrate the feasibility of utilizing laser beams for this purpose. The zinc oxide solid-state laser which has been reported, though still inefficient, has an ideal output wavelength for exposure of Type 10 film. Other lasers used successfully to expose Types 10 and 17 are the nitrogen pulse laser (Avco-Everett) which emits at 3371 Å, the helium-cadmium laser (3250 and 4416 Å), and the argon double-ion laser (3511 and 3638 Å).

An experimental film having extremely high contact resolution has been used in the duplication of holograms. Advantages are: (1) no laser is needed for the contact copy; (2) the entire exposure, development, and fixing takes place in less than 1 min without recourse to a darkroom; (3) the process as with all vesicular films is completely dry. Holograms may be thus massproduced inexpensively and used in advertising or other commercial or scientific applications. The sensitometric curve for the film designated as Type XC is shown in Fig. 9.

Another very exciting recent development has been the production in the laboratory of a blue-green sensitive vesicular film fully 100 times faster than Types 10 and 16. Experiments with the argon ion laser using only the lines in the region from 4880 to 5145 Å have shown that only 2 mj/cm^2 of this radiant energy is required to give a density of 1.6 at $f/4.5$. An obvious application for this film would be direct laser recording using the highly popular and well-proven argon ion laser. A direct application of this laser recording technique on the new film would be in a fourth-generation computer output microfilm unit permitting completely dry processing of the recording film. (COM IV, a joint venture between Kalvar Corp. and Anderson Laboratories, has been incorporated in order to develop such a device.)

In another film development, a film has been developed that fully meets the requirements of CBS Laboratories for use as the release film in cartridges to be played in their EVR player.³

In normal processing, vesicular films are passed over a heated roll following exposure for development at speeds up to 200 ft/min. However, there are several other interesting ways of obtaining the desired development energy (about 0.13 cal/cm^2 per mil of film thickness). One is the

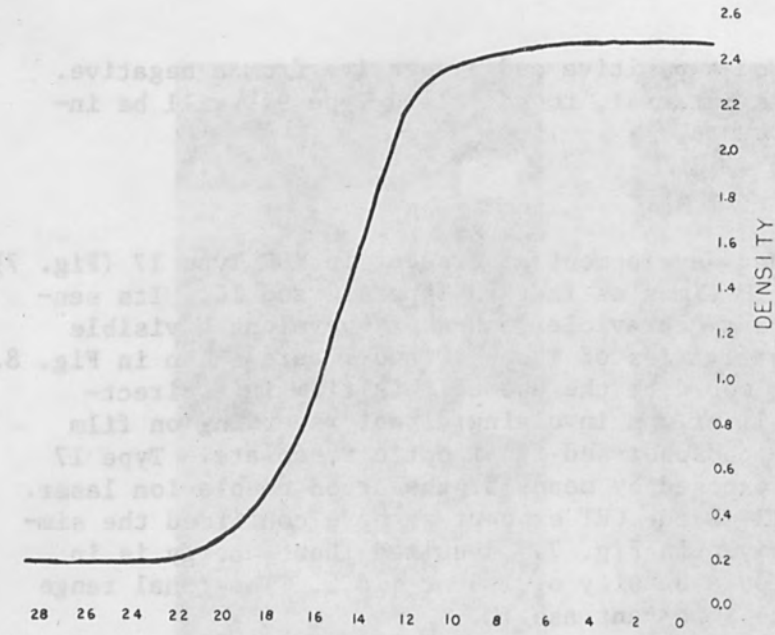


FIG. 7.--Type 17.

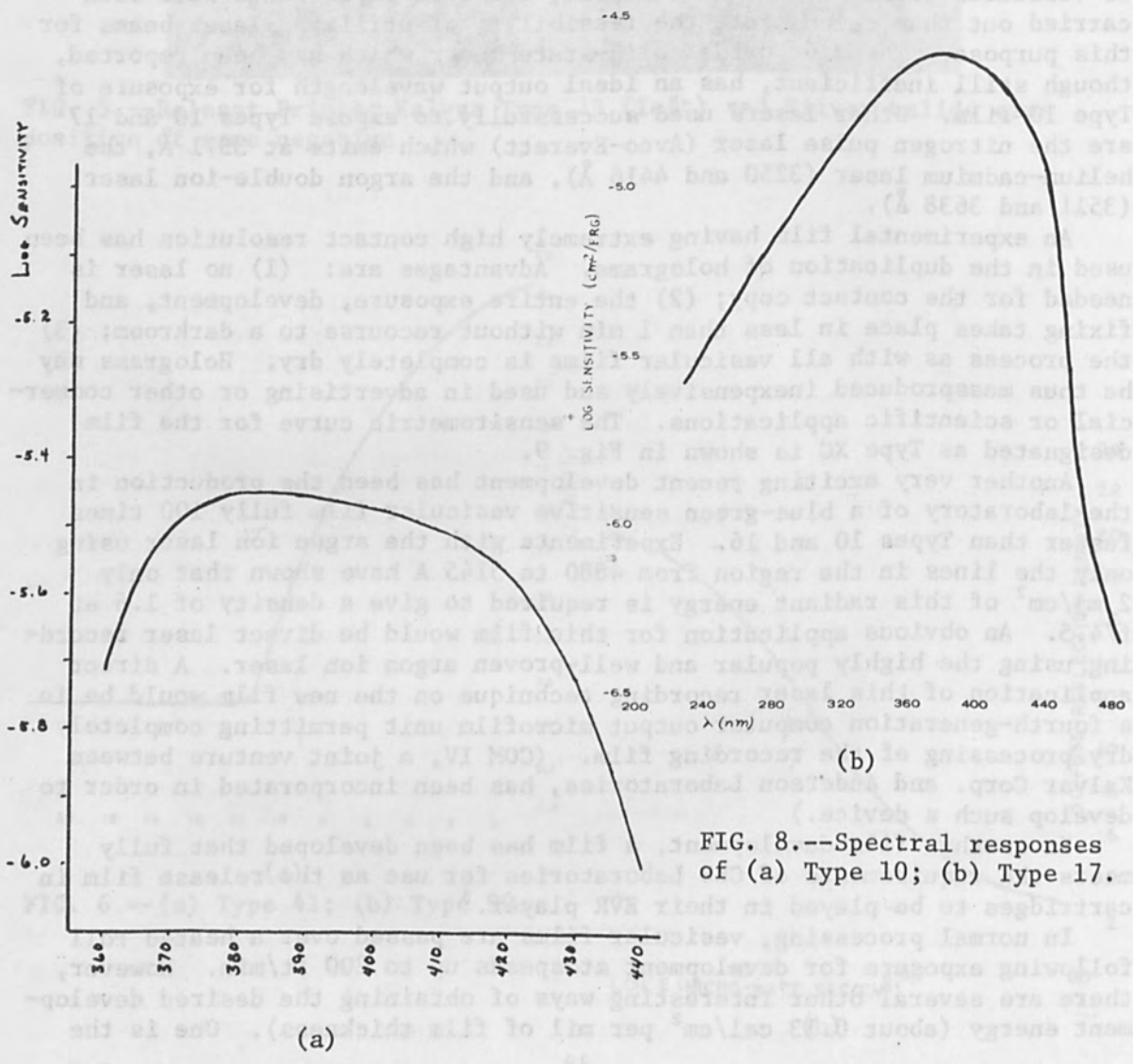


FIG. 8.--Spectral responses of (a) Type 10; (b) Type 17.

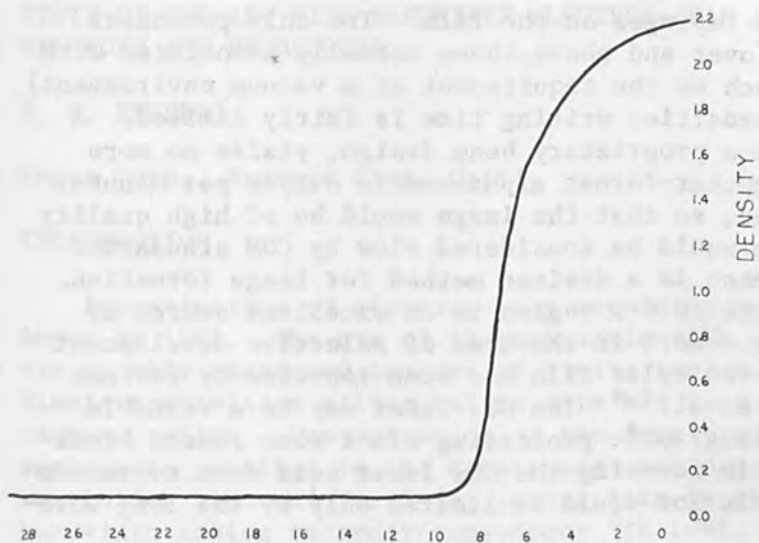


FIG. 9.--Type XC.

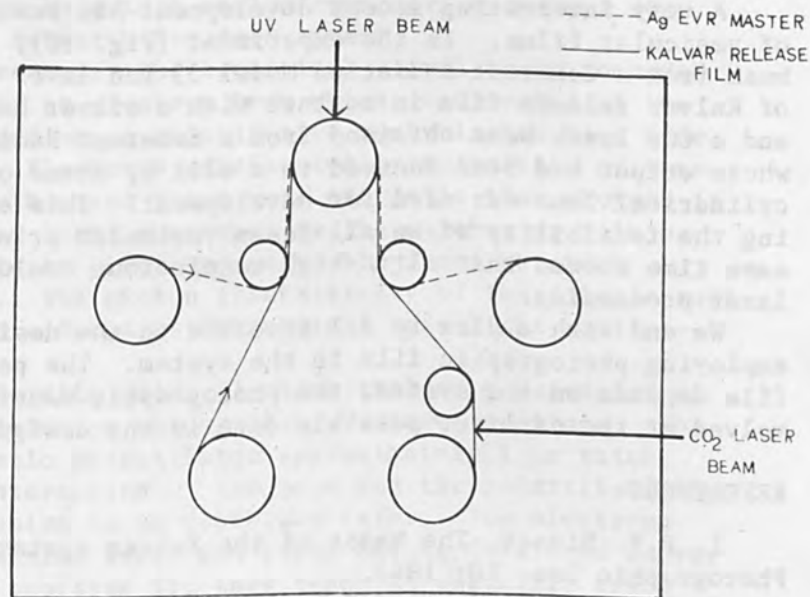


FIG. 10--Simplified schematic diagram of experimental vesicular laser printer processor.

absorption of energy from an rf field, a dielectric process that does not involve contact with any heat sink; however, the method is fairly inefficient because of poor coupling between film and field at the radio frequencies tested so far. We have also successfully developed film in a microwave field at 2450 MHz. This seems to be a reasonably practical method of development and further experimental work is being done along these lines. A hot-air knife utilizing high-velocity air is yet another noncontact technique for development of vesicular films. Noncontact techniques may also result in improved resolution of the finished image.

Vesicular films cannot be directly exposed by electron beams as can silver halide films; however, the heat generated by the electron beam may be used for selective development of previously exposed vesicular films. Development of film by impingement of an electron beam onto the fully exposed material is an interesting technique because it is a real-time process. The film is ready for use immediately since the initial exposure step has also served to fix the film and selective development is achieved

only where the electron beam impinges on the film. The only potential drawback of this technique (over and above those normally associated with electron-beam technology, such as the requirement of a vacuum environment) is that with normal beam intensities writing time is fairly limited. A recent calculation, based on a proprietary beam design, yields no more than ten 16-mm frames of computer-format alphanumeric output per minute; a 1000 line raster is assumed, so that the image would be of high quality even though the writing rate would be considered slow by COM standards.

Where selective development is a desired method for image formation, the CO₂ laser operating in the 10.6- μ region is an excellent source of selective development energy. Work in the area of selective development and thus image formation of vesicular film has been reported by Forkner and Lowenthal⁴ and by Inaba et al.^{5,6} The CO₂ laser may be a valuable future tool in real-time photographic processing since some recent breakthroughs have been achieved in focusing the CO₂ laser beam down to reasonable spot size, so that resolution would be limited only by the long wavelength involved.

A very interesting recent development has been the laser processing of vesicular films. In the experiment (Fig. 10), a defocused UV laser beam from a Coherent Radiation Model 53 ion laser was used for exposure of Kalvar release film in contact with a silver halide original EVR master and a CO₂ laser beam obtained from a Coherent Radiation Model 42 laser whose output had been focused to a slit by means of a beam expander and cylindrical lens was used for development. This experiment, besides proving the feasibility of an all-laser vesicular printer processor, at the same time showed that ultra-high resolutions could be achieved by such laser processing.

We end with a plea to all involved in the design of future systems employing photographic film in the system. The performance of a given film depends on the system; the photographic manufacturer should be involved at the earliest possible date in the design process.

REFERENCES

1. R.T. Nieset, The basis of the Kalvar system of photography, J. Photographic Soc. 10: 1962.
2. V.L. Wagner Jr. and I.H. DeBarbieris, Direct and reversal imaging in vesicular photography, 2nd Intern. Congress of Reprography, Cologne, October 1967; in Reprographie 2: 147-151, 1969.
3. P.C. Goldmark et al., Color electronic video recording, J.SMPTE 79: 677, 1970.
4. J.F. Forkner and D. Lowenthal, A photographic recording medium for 10.6 μ laser irradiation, Appl. Optics 6: August 1967.
5. H. Inaba, T. Kobayashi, K. Yumawaki, and A. Serigiyama, Direct observation of output beam patterns from N₂-CO₂ laser at 10.6 μ by thermal development method, Infrared Phys. 7: 1967.
6. H. Inaba and H. Ito, Observation of power-dependent distortion of an infrared beam at 10.6 μ m from a CO₂ laser during propagation in liquids, J. Quantum Electronics 4: February 1968.

STATE-OF-THE-ART WIDE-BANDWIDTH ELECTRON-BEAM ANALOG RECORDER AND REPRODUCER

E. W. ENGBERG

Ampex Corp., Redwood City, Calif.

INTRODUCTION

Investigation of electron-beam recording and reproducing began at Ampex in 1961. The use of thermoplastic film as the recording medium was quickly abandoned because of limitations in signal-to-noise ratio. Electron-sensitive silver halide film has been used since then for the storage medium. Demonstration of the feasibility of electron-beam techniques resulted in the development and delivery of a high-resolution scanner¹ for 5-in. aerial film in 1965, and a 5-MHz-bandwidth analog recorder/reproducer² in 1968, followed in 1969 by demonstration of a 100-MHz-bandwidth analog/recorder/reproducer developed for the Advanced Research Projects Agency.

In an electron beam recorder the electrical signal to be recorded modulates the intensity of an electron beam which is directed at the silver halide recording medium; a quantitative analysis has been made by Tarnowsky and Evans.³ Electrons accelerated by potentials of tens of kilovolts are several thousand times more energetic than photons in the visible portion of the light spectrum, so that a shorter film exposure suffices. Exposure by electrons generally requires about 3.5×10^{10} electrons/cm². The photon insensitivity of the film is such that it may be handled in a comparatively bright safe-light environment.

A cross section of the film (Fig. 1) shows that it consists of an Estar base 50 to 100 μm thick on which there are three coatings. The surface coating is a plastic scintillator approximately 1 μm thick. Photons created by the interaction of the beam and the scintillator provide the readout mechanism to be described later. The electrons next pass through the emulsion layer and after having delivered energy to the emulsion, thereby exposing it, they reach an optically transparent conductive layer and are dissipated throughout the film. This method prevents the local accumulation of static charges, which would exert unwanted influences upon the impinging electron beam.

During recording (Fig. 2), a focused electron beam 10 μm in diameter is scanned transversely back and forth across the 35-mm film over a width of 28 mm. The beam makes a short transition in the longitudinal direction each time it reaches the end of the scanning pattern, near the edge of the film, and begins to reverse. The film motion itself provides the major component of deflection in the longitudinal direction. Thus a pattern of parallel lines perpendicular to the edge of the film is created with a line-to-line spacing of 24 μm .

As the beam scans the film, the signal to be recorded modulates the beam's intensity, thereby varying the exposure along the scan line. The exposed film is removed from the recorder and chemically processed very much like ordinary photographic film. After processing, the film appears as shown in Fig. 3. The signal has been recorded as a variation of the photon transmission by the film along the scan line.

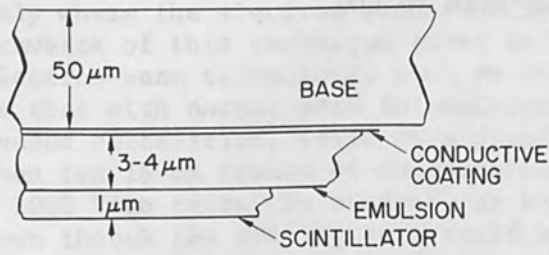


FIG. 1.--Film cross section.

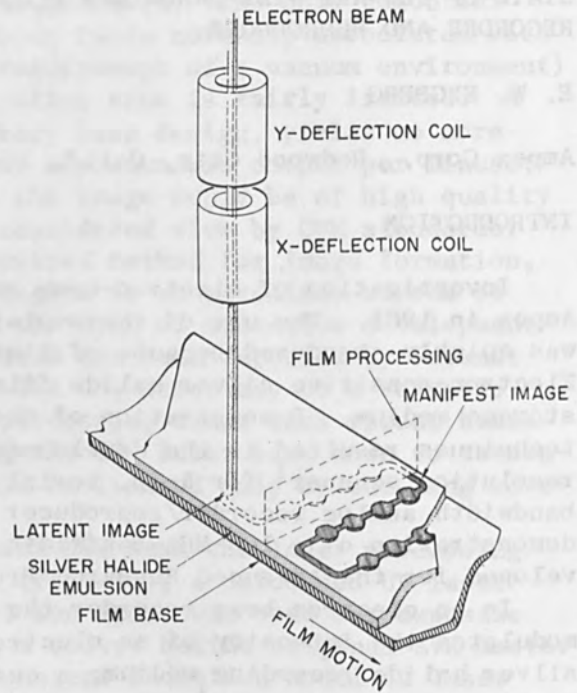


FIG. 2.--Recording process.

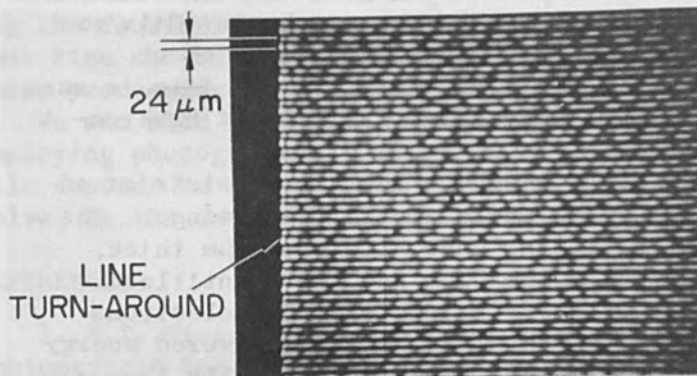


FIG. 3.--Microscope photograph of recorded film.

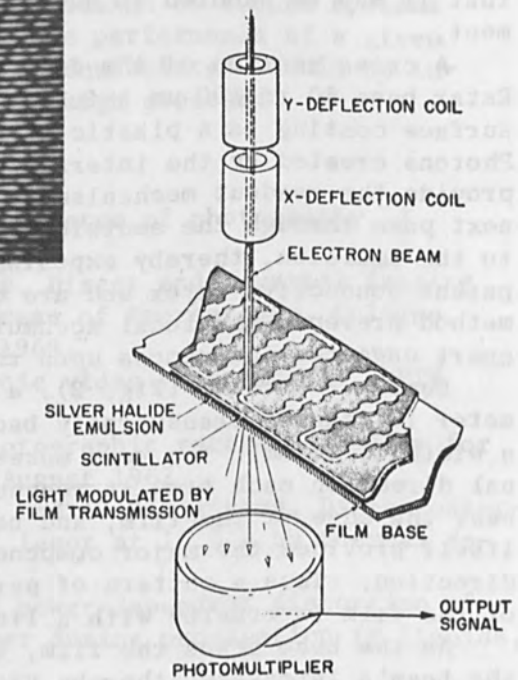


FIG. 4.--Readout process.

In the readout process (Fig. 4), the same scanning pattern is used as that used to record. This time, the electron beam is maintained at a constant current. As the beam strikes the film, a spot of light equal in size to the cross section of the beam is generated by the scintillator coating over the emulsion. The intensity of the light, when viewed through the film base, is modulated by the emulsion as the spot is scanned along the recorded line. A multiplier phototube collects the photons that have traveled through the film base and converts them to electrons. The resulting electrical output from the multiplier phototube is then a replica of the signal originally recorded.

SYSTEM DESCRIPTION

An over-all view of the AER-1020 Electron Beam Recorder is shown in Fig. 5. A close-up view of the electron gun and the film transport is shown in Fig. 6. The triode section of the electron gun is located at the top of the gun housing. A hairpin tungsten filament generates the electron beam which is accelerated downward. The gun housing is divided into two regions by a small aperture, through which the beam passes on its way to the film and which permits evacuation of the cathode region to a pressure lower than that in the electron-optics area below. After being focused and deflected in the optics area, the beam passes through another opening to hit the film moving by at the center section of the film transport. The playback multiplier phototube supports the back of the film at the point where it is struck by the electron beam, so that it can collect as much of the light given off by the film's scintillator as possible. Film speed is controlled by a capstan in the transport center section and tension by two tension-sensing arms. The capstan and tension servos allow precise and gentle control of the film motion.

Below the transport, there are three sloping control panels (Fig. 6). The left panel is the transport control through which the operator controls film motion by push-button commands. The right panel contains the controls that the operator must use in making a recording or play it back. The center panel contains the push buttons used to select the mode in which the recorder is to be used (i.e., record or playback). At the center of this panel are indicators which alert the operator to malfunctions within the recorder. The two operating modes of the vacuum system are also controlled from this panel. Other vacuum-system operations are controlled from the vacuum control panel located at the upper left section of the recorder.

The right-hand section of the recorder contains the instrumentation equipment necessary to evaluate the performance of the recorder: oscilloscope, digital voltmeter, and frequency spectrum analyzer.

The major subsystems of the recorder are shown in Fig. 7. The signal to be recorded is first applied to the signal-processing electronics, where its amplitude is controlled, and pilot signals are added to it. Then it is coupled to the control grid of the electron gun, modulating the intensity of the electron beam and thus varying film exposure. After development of the film, the recording operation is complete.

To play back, the developed film is again scanned by the electron beam, as described earlier, and the resulting signal from the multiplier phototube is applied to the Reproduce signal processing. The pilots, which were added to the signal, are separated and analyzed for

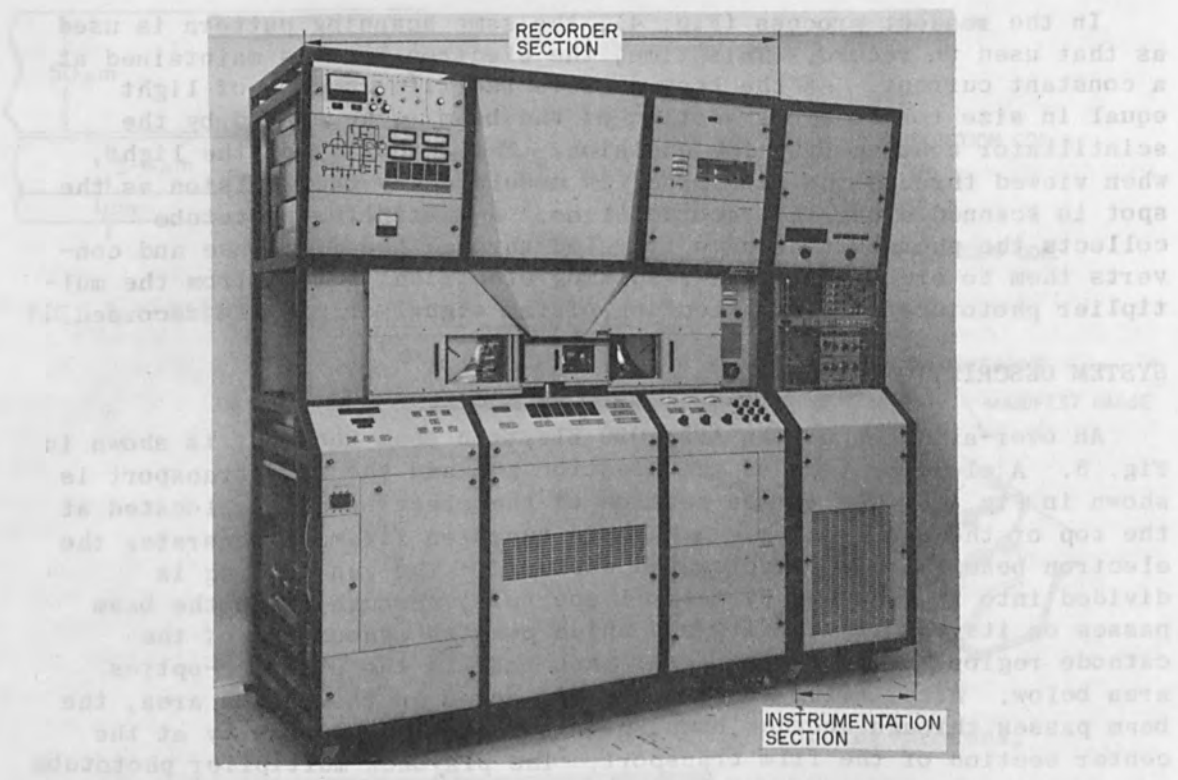


FIG. 5.--AER-1020 electron-beam recorder.

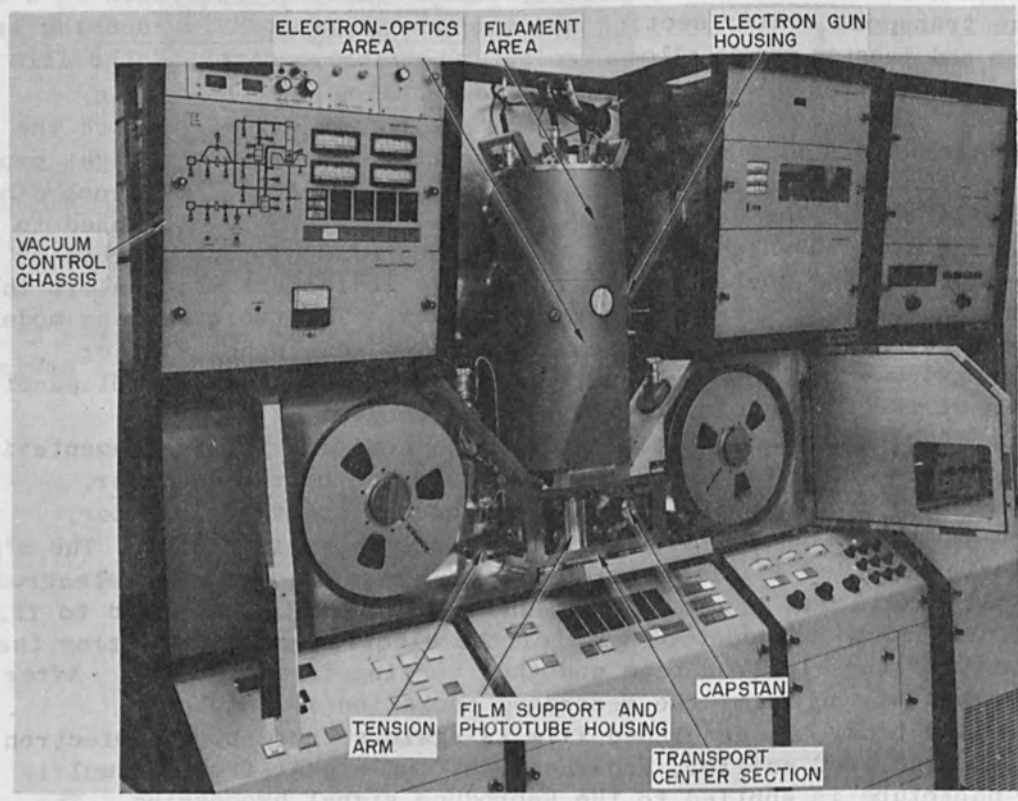


FIG. 6.--Electron gun and transport.

amplitude and timing errors. As amplitude errors are detected the error signal is fed back to the control grid of the electron gun. This adjusts the play back intensity of the beam in such a manner as to cancel the original error. Detected timing errors are likewise fed back to the appropriate deflection amplifier to adjust the scanning rate of the electron beam, thereby cancelling the error. During playback, fourteen closed-loop servos are simultaneously controlling the electron beam to obtain the highest fidelity of the reproduced signal.

VACUUM SYSTEM

Interaction of the operator with the vacuum system has been minimized. The operator has only two pushbuttons to control the vacuum system in normal recording and playback operations. The vacuum system is totally automatic and as fail-safe as practical. Major vacuum valves are pneumatically operated and air stored in a ballast tank can return them to the safest condition in the event of power failure.

A combination of digital and analog circuitry developed at Ampex over the past 10 years has been incorporated into the memory, logic, decision, and control functions for the vacuum system. To prevent tampering, the vacuum-system control panel (Fig. 8) is normally behind a cover, which is removed only when a vacuum system malfunction is reported to the operator at the system status panel.

The control panel contains a vacuum system diagram that has a lamp at each valve location to indicate the state of that valve. Switches beside each valve and major component location in the diagram control the application of power to that valve or component. Normally, all switches are left in the automatic position. However, for diagnostic procedures, the switches may be manually used to force the application or removal of power. A diagram similar to the one on the control panel is shown in Fig. 9. As on the control panel, all valves and major components are schematically placed.

Four vacuum pumps are used in the system--two rotary-vane mechanical pumps and two oil-diffusion pumps. When the electron gun is to be evacuated to high vacuum, a 20-CFM mechanical pump is first used to rough-pump both gun areas. After the pressure in each gun area has decreased to 10^{-2} torr, the evacuation of that area is automatically switched over to an oil-diffusion pump. The 4-in. diffusion pump for the electron-optics area has a capacity of 600 liters/sec; the 2-in. diffusion pump for the filament area, 150 liters/sec. Both diffusion pump pumps are continually forepumped by a second mechanical pump which has a capacity of 5 CFM. After both gun areas have switched over and are being evacuated by the diffusion pumps, the roughing pump is switched to continuous evacuation of the transport area.

The outgassing rate of the contained film and not the volume of the transport determines the required capacity of the roughing pump, which must thus be many times larger than would be necessary for evacuation of an empty transport. When the pressure inside the transport has decreased to 300 microns (normally after about 45 sec), the gate valve (which seals the electron gun from the transport) is opened. The pressure in the transport during normal operation may range between 1 and 200 microns depending upon the outgassing rate of the film. Because the pressure in the transport affects the pressure in the

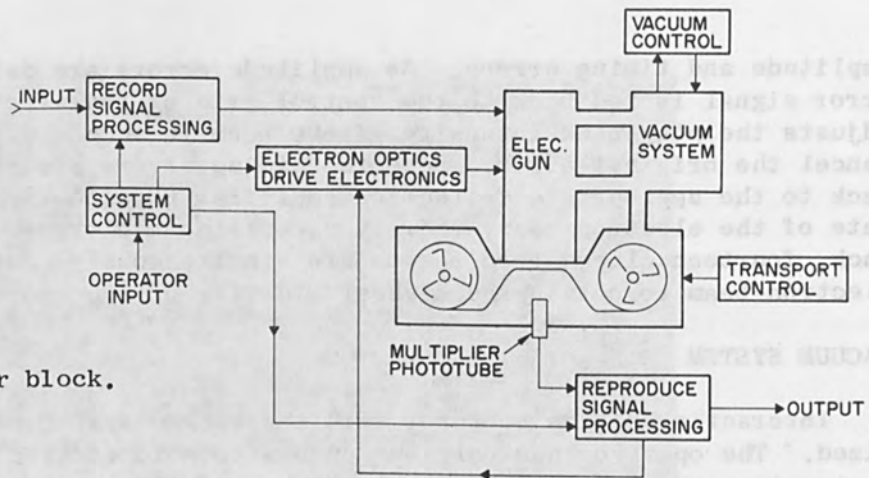


FIG. 7.--Recorder block.

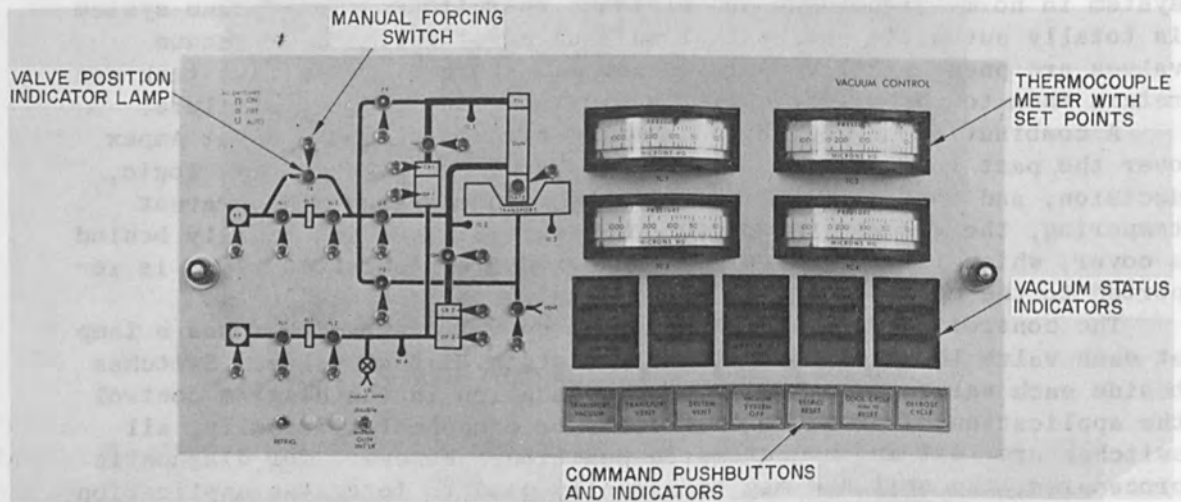
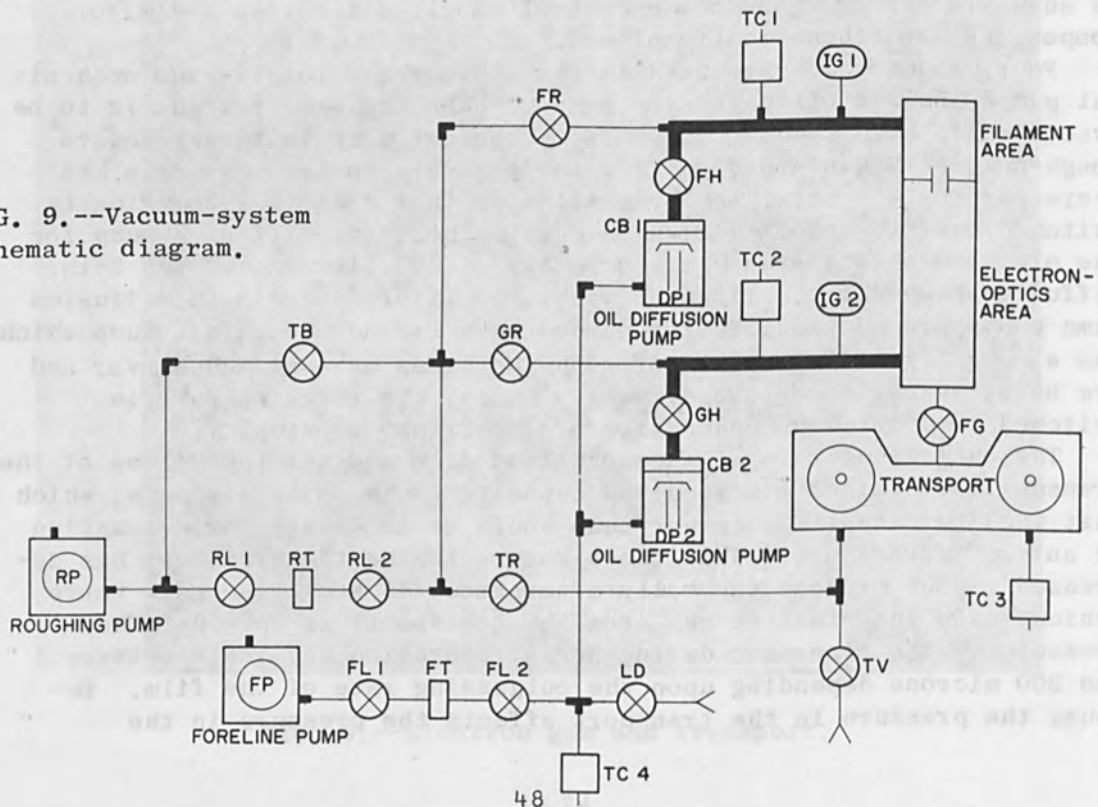


FIG. 8.--Vacuum-system control panel.

FIG. 9.--Vacuum-system schematic diagram.



electron-optics area of the electron gun through the open gate valve, the pressure in the electron-optics area ranges between 10^{-3} and 10^{-5} torr. The aperture between the cathode and electron-optics regions isolates these two areas from each other, allowing the former to be maintained below 10^{-6} torr. Such differential pumping permits a full reel of fresh film with its high outgassing rate to be used without first being preconditioned.

The electron-gun filament life is directly related to the pressure and contamination within the filament area. To obtain the necessary 75 to 100 hr. of operation, the pressure must be below 10^{-6} torr and the contamination as low as possible. By far the worst source of contamination is backstreaming from the vacuum pumps--the gradual migration of molecules of pump oil back through the vacuum plumbing towards the area being evacuated. To reduce the migration of oil from the diffusion pumps, thermo-electrically cooled, optically dense chevron baffles are placed between each diffusion pump and the area which that pump evacuates. The temperature of the baffles is maintained below the freezing point of the diffusion-pump oil, which is trapped and frozen to the baffles and which must be periodically defrosted during nonoperational periods. The defrosting cycle is initiated by the operator but is automatically controlled until completion by the vacuum-control electronics.

While the roughing pump is evacuating the transport, oil must be prevented from contaminating the transport and film. Therefore, a molecular sieve is used to trap the migrating oil. Because the quantity of gas flow above a few hundred microns of pressure prevents backstreaming, a trap bypass valve is used to pump around the trap until a pressure of 500 microns is reached. This decreases the time required to evacuate the transport from atmosphere to operating pressure. Once a pressure of 500 microns is reached, the bypass valve closes and the remainder of the pumping is done through the trap. A molecular-sieve trap is also placed between the foreline pump and the oil diffusion pumps. The absorbent material in the traps lasts about 3 months.

Figure 10 shows the vacuum system at the rear of the recorder. Except in the couplings to the mechanical pumps, copper pipe is used, joined by brazing techniques. Major components such as the diffusion pumps are coupled to the plumbing with quick-disconnect high-vacuum couplings. The mechanical-pump assembly (Fig. 11) is mounted on wheels to allow removal from the recorder frame for servicing. The mechanical pumps are connected to the plumbing through flexible hoses, to isolate pump-assembly vibration from the recorder main frame.

The final mechanical configuration of the vacuum system is the result of considerable experience at Ampex in designing, using, and maintaining vacuum systems for electron beam recording purposes. Layout and fabrication techniques have resulted in a reliable and easily maintained system.

ELECTRON GUN

The beam-forming and deflection components (Fig. 12) comprise a conventional triode structure with a directly heated hairpin tungsten cathode, which creates a 50- μ m-diameter spot at the center of the anode

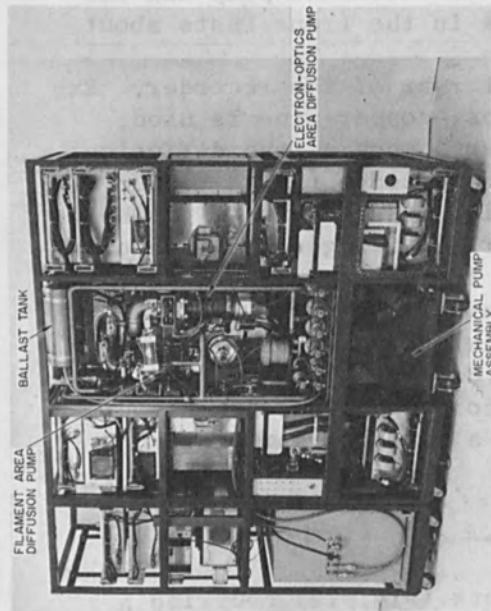


FIG. 10.--Recorder rear view.

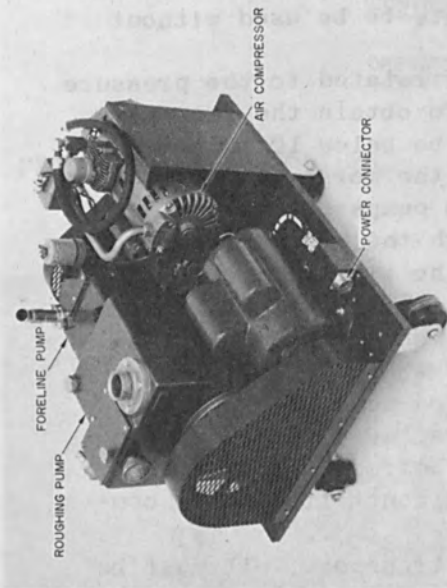


FIG. 11.--Mechanical-pump assembly.

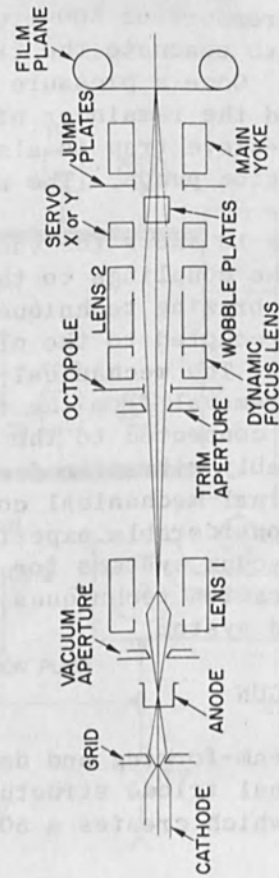


FIG. 12.--Electron-gun-beam-forming and deflection components.

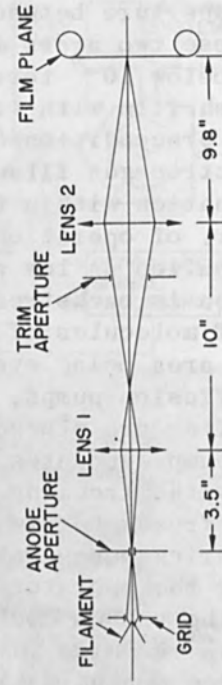


FIG. 13.--Electron-gun ray diagram.

aperture. The image of this spot serves as the object for Lens 1, which is a short-focal-length magnetic lens and reduces the object size by 8:1. The resulting image is relayed to the film plane by Lens 2, which is a long-focal-length magnetic lens. The two-lens system has advantages in that there is an electrical adjustment of spot size, the anode aperture can be large, and there is flexibility in placing the beam-forming and deflection components. The ray diagram, with some significant dimensions, is shown in Fig. 13.

Starting from the film plane, the deflection components are as follows:

(1) A main magnetic deflection yoke to produce the main scan across the film perpendicular to film motion.

(2) Electrostatic "jump" plates for deflection to compensate for the film motion during scan. These plates also create the rapid transition from one scan line to another at the end of each scan line.

(3) Electrostatic "wobble" plates which deflect the beam about half a spot diameter, perpendicular to the main scan, to create a signal that is used to servo the playback scan onto the recorded line.

(4) A magnetic servo yoke, of which one axis is used to servo the playback beam onto the recorded line, and the other to correct timing errors in the reproduced signal.

Because the film plane is flat and the point of focus of the electron beam describes a circular path, focus correction is necessary at the ends of the scan line. A small magnetic lens mounted near Lens 2 performs the required dynamic correction.

Deficiencies in the beam-forming and deflection components, together with the fact that the beam does not strike the film at right angles at the ends of the main scan, necessitates spot shape correction. Both static and dynamic correction are accomplished by an electrostatic octopole located just after the Lens 2 trim aperture.

PERFORMANCE

The following list defines some of the important parameters for analog recorders and describes the performance of the AER-1020 Electron Beam.

RECORDER. (1) Frequency Response. The AER-1020 specification is that the amplitude of a reproduced signal does not increase by more than 1 db nor decrease by more than 3 db as that signal is varied from 50 kHz to 30 MHz. The lower limit is determined by the amplifier which modulates the electron gun. The upper limit is set by the recorded wavelength approaching the diameter of the electron beam.

(2) Amplitude Distortion. Whenever a signal passes through a device which has a nonlinear transfer function, the shape of the signal is altered. This creates frequency components in the output that were not present in the input signal. Harmonic and intermodulation distortion are names given to the result of amplitude distortion. The parameter is measured as the ratio of the recorded signal to the amplitude of the unwanted frequency component. This ratio in the AER-1020 is 20 db. The largest contributor to amplitude distortion in the AER-1020 is the transfer function between the change in voltage applied to the electron gun to modulate the beam and the resulting change in beam current.

(3) Spurious Signals. The recorder itself can introduce unwanted signals into the playback frequency spectrum. Each recording technique has its own spurious signals. In the AER-1020 Recorder, the scanning rate introduces spurious signals that occur as sidebands about a recorded frequency. The ratio between the amplitude of a recorded signal and the amplitude of the spurious signal (or, if the spurious signal is not a product of a recorded signal, between the recorder's maximum recording level and the amplitude of the spurious signal) specified for the AER-1020 is 30 db.

(4) Signal-to-Noise Ratio. The signal-to-noise parameter describes the minimum level at which a signal may be detected and is measured as the ratio between the peak-to-peak value of a signal recorded at the recorder's maximum recording level and the rms value of the noise in the presence of that signal. The dominant source of noise in the AER-1020 is the noise generated at the photocathode of the multiplier phototube during readout. The amplitude of the noise is constant throughout the passband of the recorder. For the AER-1020, the specification for peak-to-peak signal to rms noise, measured over 30 MHz, is 30 db.

(5) Time-Base Error. If a reproduced signal on playback is compared to the signal source from which the recording was made, the deviation between the two signals in time is defined as the time-base error. The parameter is measured as the rms value of the time deviation between the two signals. In the AER-1020, timing errors occur because of the sideways motion of the film while it is moving forward and slight misregistration which occurs between the playback scan and the recorded track. The specification is 2.5×10^{-9} sec (rms).

SUMMARY

The design of a complex recorder that is reasonably simple to operate has led to the automation of much of the electronic portions of the recorder and of the vacuum system. The reduction of interaction of the operator with the vacuum system has enhanced the simplicity of operation. Reliability of all portions of the recorder has been a major objective. The electron gun has proved to be an easily adjustable, stable, and reliable gun. With the increasing need to extend recorded bandwidth beyond that achievable with magnetic techniques at present, electron-beam recording has stepped out of the laboratory and into the user's environment.

REFERENCES

1. E.V. Boblett and K.F. Wallace, Electron beam readout of silver-halide transparencies, Proc. 17th National Aerospace Electronics Conference, Dayton, Ohio, 10 May 1965.
2. B.V. Markevitch and E.W. Engberg, A high performance 5 MHz electron beam recorder reproducer, Second Annual Wideband Analog Recording Symposium, TR-68-201 Rome Air Development Center, Griffiss AFB, N.Y., TR-68-201, June 1968 (classified).
3. A.A. Tarnowsky and C.H. Evans, Photographic data recording by direct exposure with electrons, J. SMPTE 17: 765-768, 1962.

A 100-MHz MULTICHANNEL LASER RECORDER AND READOUT SYSTEM

H. W. PASS and L. R. TEEPLE JR.

Resalab, Inc., Los Angeles, Calif.

This article describes an advanced system which consists of a wide-bandwidth, multichannel laser recorder, an automatic data readout, and a digital signal-processing subsystem. The system consists of two six-channel laser recorders, each channel having a capability to record events with a risetime of less than 3.5 nsec over a 35- μ sec period. The recording is accomplished by scanning a modulated laser beam across photographic film, thereby permanently recording the 100-MHz video signal information of the transducer inputs. Digital identifiers, calibration, and reference signals are also recorded. The data readout and signal processing portions of the system include unique equipment to read out both oscilloscope and laser recorded formats. The complete readout system is van-mounted and is controlled by a digital computer. This computer controls the readout processes and normalizes and formats the output data. After suitable processing, data are read out into a magnetic tape for further processing in a CDC 6500 computer.

To record the nanosecond risetime pulses produced by sensors in an electromagnetic field simulating radiation from an atomic weapon detonation, a system capable of simultaneously recording twelve information channels of 100-MHz bandwidth was required. The mass of information recorded from 100 test pulses per day dictated a recording format compatible with automated reading techniques.

The basic requirements of the system were, in summary:

Bandwidth: 30 kHz to 100 MHz
Risetime: 3.5 nsec
Channels: 12, in two groups of six
Unfolding accuracy: 10%
Dynamic range: ± 40 db, bipolar
Time resolution: 1.8 nsec
Writing time: 35 μ sec
Readout: 200 6channel records per day

The choice of techniques to attain the desired results was not broad, generally limited to cathode-ray-tube or oscilloscope techniques, electron beam recording on film, or laser-beam recording on film.

The oscilloscope technique lacks the long writing capability relative to risetime; dynamic range is limited to about ± 20 db; and linearity of trace varies excessively, complicating normalization procedures.

Electron-beam recording attains a good dynamic range, but not the ± 40 db required; although linearity of trace is adequate over a 70 mm film width format, the duration of record requires a complex film transport; the simultaneous recording of six channels involves either a very large amount of machinery or a development program in multigun electron-beam generators.

The optimum choice of technique is thus the laser-beam recording sys-

mirrors, and camera--are mounted on a torsionally rigid closed-section structure isolated by vibration mounts from the supporting stand. Each wideband driver amplifier is placed directly over the modulator to be driven to preclude any possible cross talk from the high-level signals.

Since the system consists of two stands of six data channels each, a central control provides common functions, such as rotating mirror driver frequency, 10-MHz timing channel, and EMP firing delay and firing pulse. Rotating mirror position and phase are monitored on a dual-beam oscilloscope; mirrors are brought into rotational phase within 1° by changes in the phase of the driver pulse to one mirror motor.

The record is organized to facilitate automatic readout on a computer-controlled densitometer system (Fig. 3). At the time the rotating mirror is in position to write at the head of the track, a 32-level bipolar calibration signal consisting of a 4-MHz damped sine wave is injected into the entire rf signal system. Each record track carries at its head the 32 gray level calibration signal, which serves as a normalization standard for the data immediately following. Following the calibration signal, each track receives a binary coded decimal identification signal, including test number supplied by the local control panel, and the transducer identifier. The 10-MHz timing channel and the unmodulated laser channel furnish time and intensity correlation for the entire record.

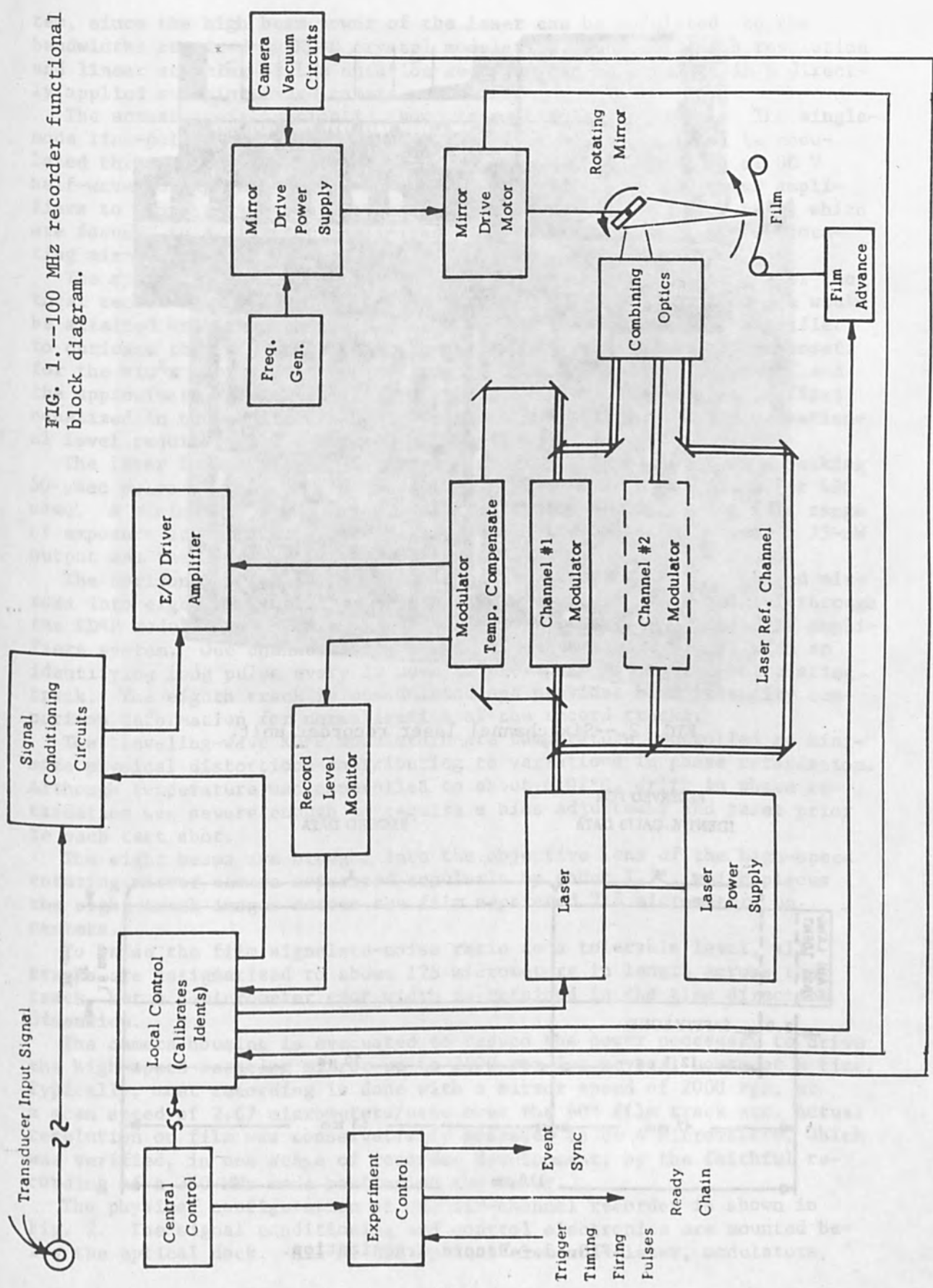
A typical record is shown in Fig. 4. The six tracks carry, first, the calibration signal, then a rather cryptically arranged set of BCD identifiers, after which (in the recording window) comes the analog record of the input pulses. The outside tracks are the laser intensity and timing tracks. In addition, a plain-language identifier is recorded on the film to provide a direct operator interface. Film is Eastman 7460 AHU microfilm, which is processed in a Prostar processor in the readout equipment trailer.

The processed film, in lengths to 200 ft, is automatically scanned, record by record, by computer-controlled microdensitometers. The analog data is converted to digital data, and the EMP data normalized to the calibration signal levels, variations in laser intensity, and variations in time base due to film shrinkage, if any. The data are formatted, blocked, and stored on magnetic tape, for further processing on the Hewlett-Packard 2116B computer in the readout equipment van, or on a CDC 6500 computer. Typically, a six-track record can be assessed in 5 min or less.

A typical record of a 40 mV. nanosecond risetime and 100 nsec duration pulse is shown in Fig. 5. The input pulse, recorded on a sampling oscilloscope, appears to carry less apparent noise than the unfolded output reconstruction in the CDC 6500 computer plotted by a CalComp plotter.

As an indication of the potential of the laser beam recorder in wide-band recording, we are now projecting utility in the 300-to 500-MHz range. The recording camera and optics, in developmental work, have recorded laser mode beating at 240 MHz at half camera speed; limiting resolution on this basis is about 600 MHz. Pre-amplifiers and power amplifiers appear to be feasible in the 300-to 500-MHz range at power levels required by the modulators. The modulation is the area of greatest concern at present in attainment of ultrawide bandwidth recording. However, recent techniques which shorten the required crystal lengths, coupled with reduction of laser-beam cross section, may well provide the necessary breakthrough.

FIG. 1.--100 MHz recorder functional block diagram.



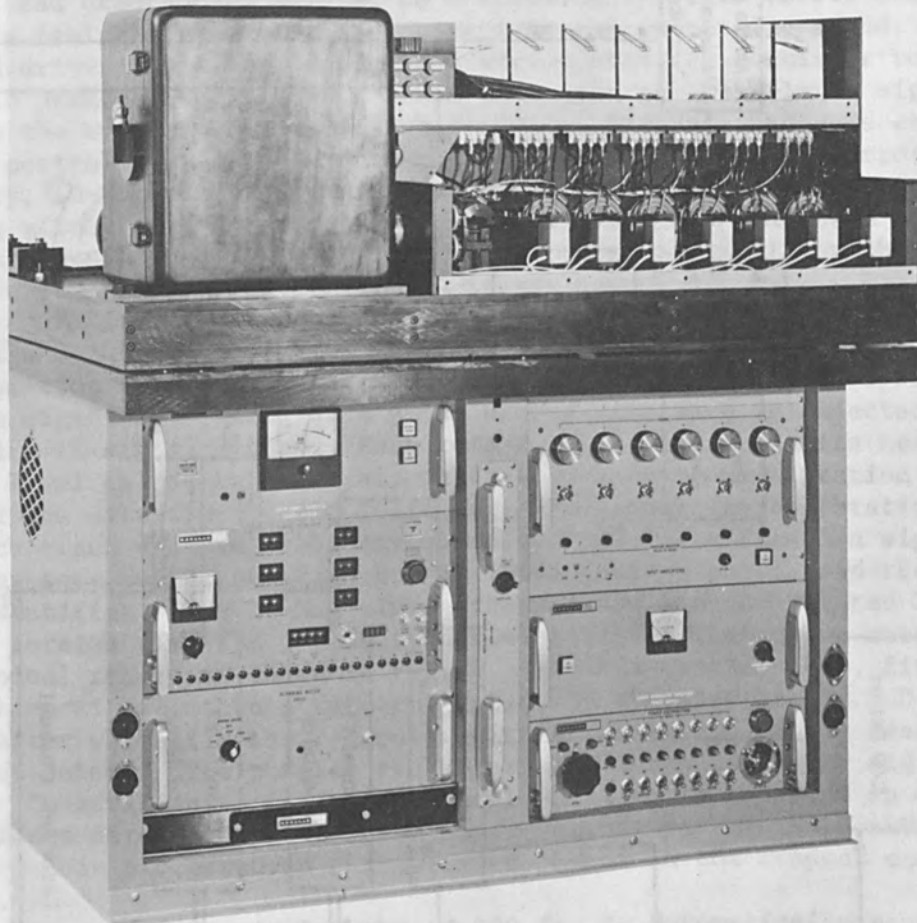


FIG. 2.--Six-channel laser recorder unit.

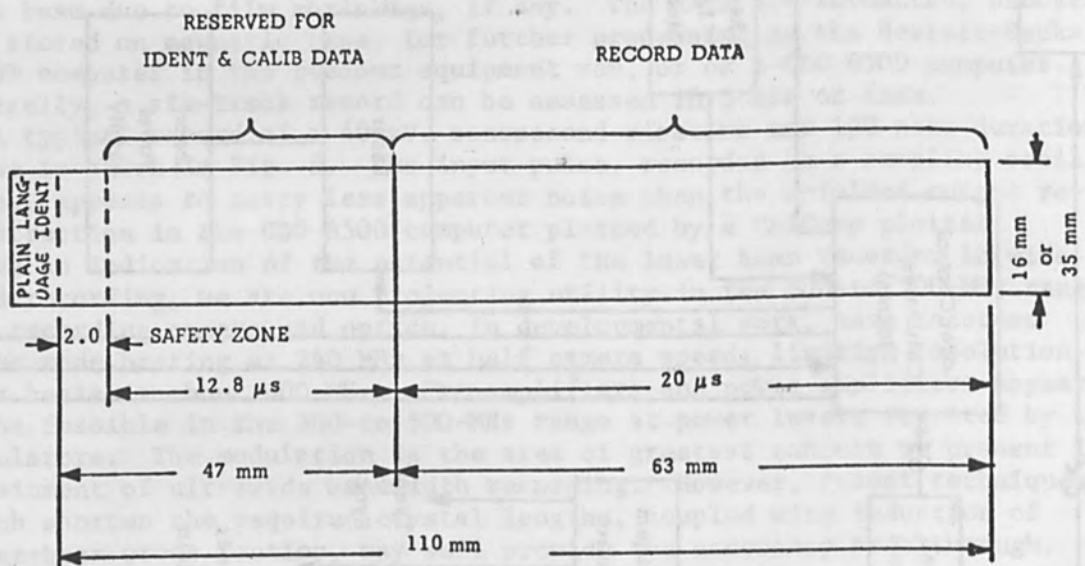


FIG. 3.--Record organization.

tem, since the high beam power of the laser can be modulated to the bandwidths required by KD*P crystal modulation, and ultra-high resolution and linear scanning of the duration required can be attained in a directly applied sweeping image camera.

The actual configuration is shown schematically in Fig. 1. The single-mode line-polarized 150-mW pulsed Argon laser beam (514.4 nm) is modulated through KD*P modulators and Glan analyzers. Modulators of 80 V half-wave voltage are driven by compression amplifiers and power amplifiers to convert ± 40 db electrical signals to modulated light beams which are focused to a diffraction-limited spot scanned by a high-speed rotating mirror along the length of a fine-grain film strip.

The system analysis, which derived a system transfer function for the total record-readout cycle, indicated that the ± 40 db dynamic range would be attained only through the use of a compression (nonlinear) amplifier, to optimize the gain at various levels of the input signal to compensate for the $\sin^2 x$ compression characteristic of the modulator response, and the approximately logarithmic film response. Thus, the signal is first equalized in the nonlinear amplifier and then amplified to the operational level required by the crystal modulator.

The laser is a nominal 1-W pulsed Argon laser, modified from a peaking 50- μ sec pulse to one putting out a level 150-mW beam at 514.5 nm for 400 μ sec. A minimum of 5 mW per channel was required to achieve a full range of exposure at 1.5 nsec exposure time. With transmission losses, a 75-mW output was the lowest tolerable power level.

The horizontally polarized beam is split through dielectric coated mirrors into eight beams of equal intensity. Six beams are modulated through the KD*P modulators and Glan-Air Prism analyzers by the wideband rf amplifiers system. One channel carries a 10-MHz square-wave signal with an identifying long pulse every 10 μ sec to provide a timing and correlating track. The eighth track is unmodulated and provides beam intensity comparison information for normalization of the record tracks.

The traveling-wave KD*P modulators are temperature controlled to minimize physical distortions contributing to variations in phase retardation. Although temperature was controlled to about 0.02°C, drift in phase retardation was severe enough to require a bias adjustment and reset prior to each test shot.

The eight beams are brought into the objective lens of the high-speed rotating mirror camera separated angularly by about 1.7°, which places the eight track images across the film separated 218 micrometers on centers.

To raise the film signal-to-noise ratio to a tolerable level, all tracks are astigmatized to about 125 micrometers in length across the track, but a 4-micrometer spot width is retained in the time direction dimension.

The camera housing is evacuated to reduce the power necessary to drive the high-speed rotating mirror up to 2500 rps for several hours at a time. Typically, most recording is done with a mirror speed of 2000 rps, at a scan speed of 2.67 micrometers/nsec over the 60° film track arc. Actual resolution on film was conservatively assessed to be 4 micrometers, which was verified, in one stage of recorder development, by the faithful recording of a 360-MHz mode beating of the laser.

The physical configuration of one six-channel recorder is shown in Fig. 2. The signal conditioning and control electronics are mounted below the optical deck. All of the optical elements--laser, modulators,

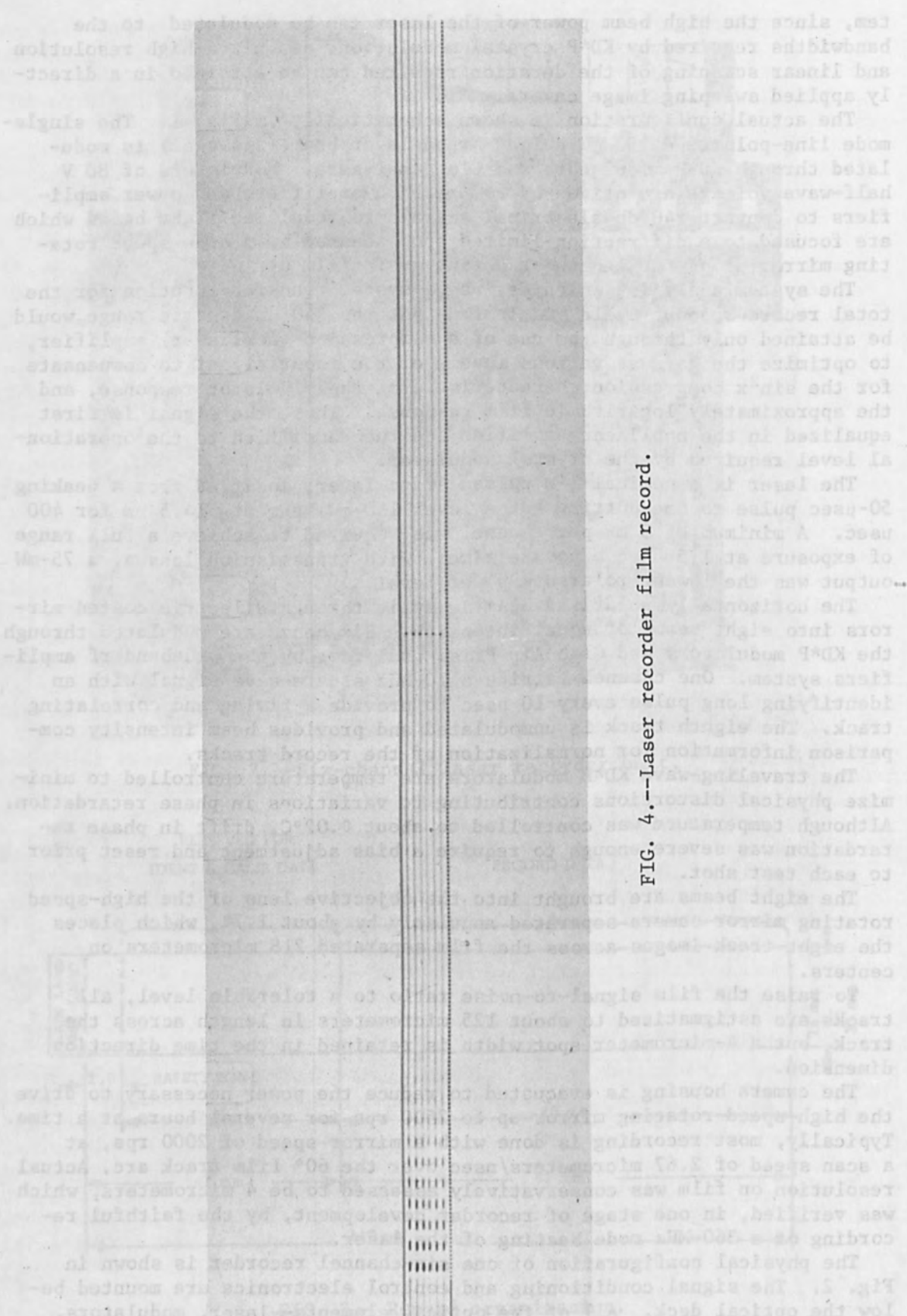


FIG. 4.--Laser recorder film record.

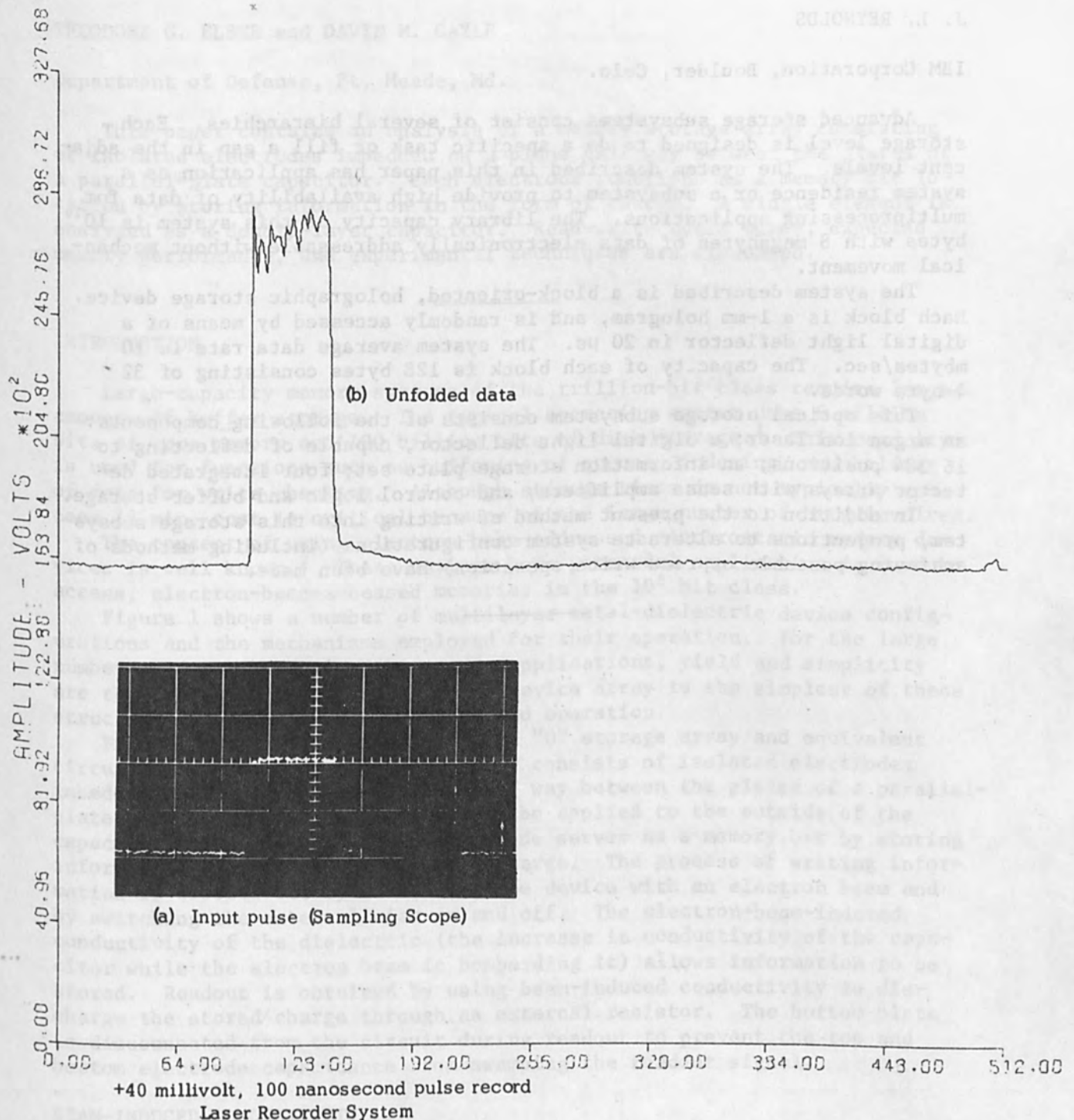


FIG. 5.--Input pulse and plot of unfolded data.

AN OPTICAL STORAGE SUBSYSTEM

J. L. REYNOLDS

IBM Corporation, Boulder, Colo.

Advanced storage subsystems consist of several hierarchies. Each storage level is designed to do a specific task or fill a gap in the adjacent levels. The system described in this paper has application as a system residence or a subsystem to provide high availability of data for multiprocessing applications. The library capacity of this system is 10^{10} bytes with 8 megabytes of data electronically addressable without mechanical movement.

The system described is a block-oriented, holographic storage device. Each block is a 1-mm hologram, and is randomly accessed by means of a digital light deflector in $20 \mu\text{s}$. The system average data rate is 10 mbytes/sec. The capacity of each block is 128 bytes consisting of 32 4-byte words.

This optical storage subsystem consists of the following components: an argon ion laser; a digital light deflector; capable of deflecting to 16 384 positions; an information storage plate set; four integrated detector arrays with sense amplifiers; and control logic and buffer storage.

In addition to the present method of writing into this storage subsystem, projections to alternate system configurations (including methods of achieving postable or read-write operation) have been made.

ANALYSIS OF AN IMBEDDED ELEMENT STORAGE ARRAY

THEODORE G. ELSER and DAVID M. GAYLE

Department of Defense, Ft. Meade, Md.

This paper contains an analysis of a memory storage array consisting of isolated electrodes imbedded on a plane half way between the plates of a parallel-plate capacitor. Each electrode functions as a memory bit location by storing information in the form of charge. A single element is analyzed as a double-layer capacitor. Read-write cycle times, expected memory performance, and experimental techniques are discussed.

INTRODUCTION

Large-capacity memory systems of the trillion-bit class require large amounts of buffer storage. The typical operating system uses 6 million bits of core memory and 100 billion bits of disk storage.¹ This capacity is used for functions such as buffering of queues, indexing, and holding of data for write checking. Although storage times do not typically exceed 15 min, cost is critical because of the large number of bits involved.

The concept of using electron-beam-addressed electrostatic memory devices is well known.² These devices have potential application in random-access, electron-beam-accessed memories in the 10^8 bit class.

Figure 1 shows a number of multilayer metal-dielectric device configurations and the mechanisms employed for their operation. For the large number of devices required by memory applications, yield and simplicity are the crucial issue. The type "0" device array is the simplest of these structures in terms of construction and operation.

Figure 2 shows a portion of a type "0" storage array and equivalent circuit of a single device. The array consists of isolated electrodes imbedded in dielectric on a plane half way between the plates of a parallel-plate capacitor. External biases can be applied to the outside of the capacitor only. Each imbedded electrode serves as a memory bit by storing information in the form of electric charge. The process of writing information is carried out by bombarding the device with an electron beam and by switching the external bias on and off. The electron-beam-induced conductivity of the dielectric (the increase in conductivity of the capacitor while the electron beam is bombarding it) allows information to be stored. Readout is obtained by using beam-induced conductivity to discharge the stored charge through an external resistor. The bottom plate is disconnected from the circuit during readout to prevent the top and bottom electrode capacitance from swamping the readout signal.

BEAM-INDUCED CONDUCTIVITY

Electron-beam-induced conductivity is caused by the increase in the number of carriers created when low-energy bound electrons are raised into the conduction band of a material by an electron beam. Because it is directly related to the operation of this memory scheme, capacitors of aluminum oxide and silicon monoxide were fabricated with aluminum electrodes. The dielectric thickness varied from 0.25 to 0.5 micron.

Type	Diagram	Method	
		Write	Read
O		EBIC	EBIC
A		EBIC	SEC
B		EBIC or SEC	SEC
OA		EBIC	SEC
OB		EBIC or SEC	SEC

FIG. 1.--Electrostatic storage device structures.

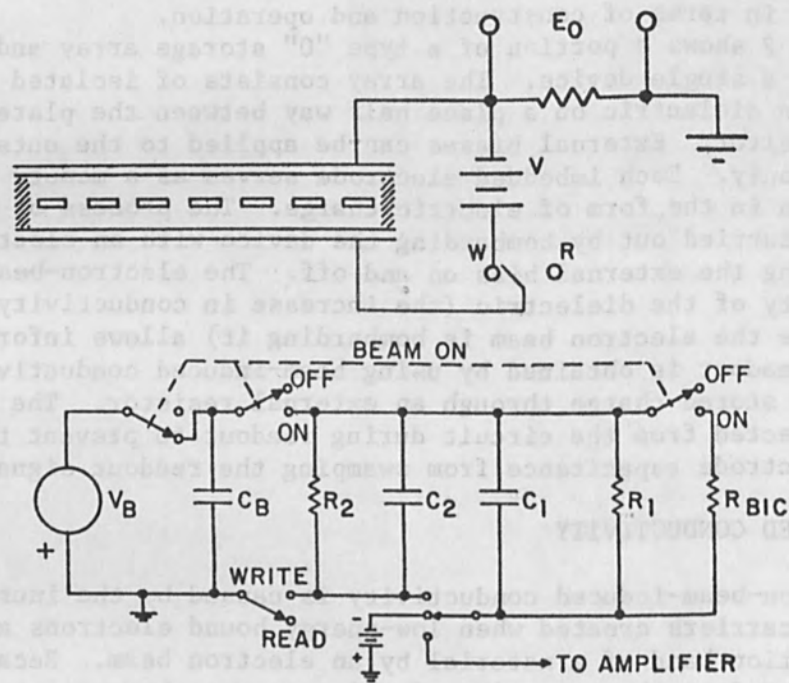


FIG. 2.--Type "0" device: top, array of electrodes embedded in a parallel-plate capacitor; below, equivalent circuit.

The capacitors were bombarded by an electron beam current I_b of 10^{-8} to 10^{-7} A focused to a 5- to 10-micron spot. Since all the beam current absorbed by either plate of the capacitor must drain to ground, the incident current can be measured by monitoring V_B across R_B (Fig. 3). The electron beam was pulsed on and off at a low frequency allowing the zero-beam (value of V_B) voltage to be continuously observed on an oscilloscope.

Measurement of the circulating current in the loop containing R_A will determine the induced conductivity of the capacitor. The voltage produced by the battery divides differently between the resistor and capacitor as the resistance of the capacitor changes. The absorbed beam current, which is not part of this circulating current, will always flow to ground in the same direction regardless of the polarity of the battery. By measuring I_+ with the battery voltage in one direction and then measuring I_- with the battery polarity reversed, the quantity $(I_+ - I_-)/2 = \Delta I$ gives the measured value of the circulating current without calculating the absorbed beam current.

The procedure is to increase the battery bias V in steps of 1.5 V from 0 to 7.5 V and then repeat from 0 to -7.5 V, measuring $V_A - V_B$ at each step. Since $V_A - V_B$ varies linearly with V , the gain calculation can be made at any bias and then normalized to unit field. The total gain G_a is given by

$$G_a = \frac{\Delta I}{I_b}$$

Then g , the percentage gain per unit field, is given by

$$g = \frac{G_a}{V/d}$$

This process was repeated for incident beam energies V_b ranging from 5 to 30 kV, so that gain can be plotted as a function of V_b .

It should be noted that the incident beam causes secondary electrons to be emitted from the surface. These electrons are attracted or repelled from the top electrode depending on its polarity. The secondaries that are attracted back will be measured as part of the beam current as they flow to ground. To avoid this error, a plate mounted above the specimen was set at +22 V to collect all the secondaries at each step.

Figure 3 shows how the BIC gain per unit field varies with incident beam energy. By normalizing the beam voltage to the square root of the capacitor thickness, the curves for samples of different thicknesses can be averaged. To convert the bottom scale to kilovolts, multiply by \sqrt{d} . The fact that the peaks for the two materials occur at nearly the same position is of no real significance. The factor of greatest importance is the difference in height of the two peaks. This shows that aluminum oxide has twice the conductance of silicon monoxide when exposed to equal incident beams, so that it is more desirable for this application. These results are consistent with data reported by other authors.^{3,4}

DEVICE OPERATION

The voltage on the electrodes during a typical write and read cycle is represented in Fig. 4. The voltage on the bit with respect to ground is plotted as a function of time as charge is stored on the element. In

The capacitor was powered by an electron beam current I_b of 10^{-7} to 10^{-6} A focused to a 2- to 10 micron spot. Since all the beam current is absorbed by either plate of the capacitor, the fact that the beam current can be measured by monitoring the voltage across the capacitor is not surprising. The electron beam was pulsed on and off at a low frequency allowing the zero-beam (value of V_b) voltage to be accurately observed on an oscilloscope. Measurements were made at various beam currents and the results are shown in Figure 3. The gain G_a is given by $G_a = \frac{V_A}{V_B}$ and the percentage gain per unit field is given by $\frac{G_a}{V/d}$. The procedure is to increase the battery bias V in steps of 1.5 V from 0 to 7.5 V and then repeat the above procedure for each step. Since V_A is a linear function of V , the gain G_a can be made as any bias and the normalized gain $G_a/V/d$ is given by $\frac{G_a}{V/d}$.

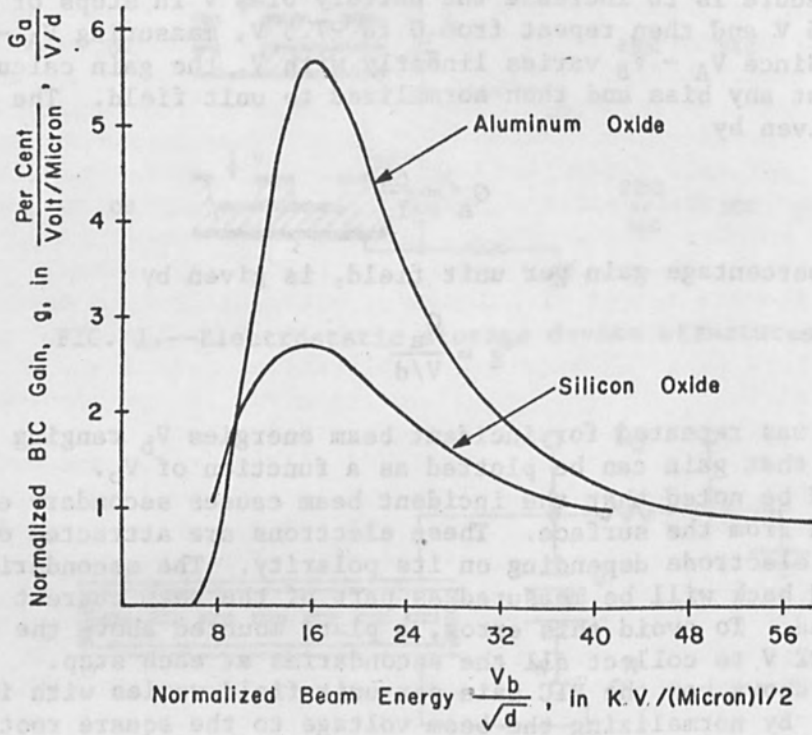
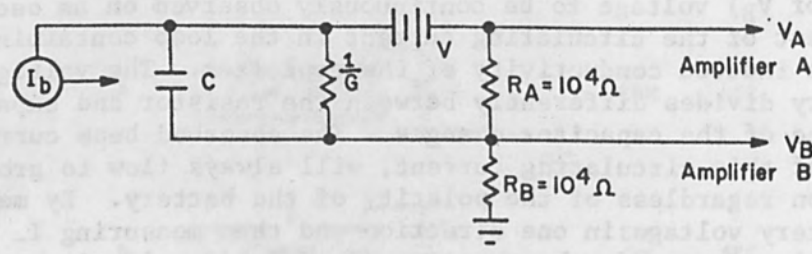


FIG. 3.--Beam-induced conductivity: top, circuit for measuring gain; below, conductivity as a function of induced beam energy.

the proposed scheme, the element always remains negative with respect to ground, as shown in the diagram.

Let us assume we have all uncharged bits at $t = 0$. The first step is to write a "ZERO" into each bit location by grounding the top and bottom electrodes of the capacitor and using the beam to bombard the bit location. A certain amount of charge will deposit on the center element. The beam is on during the time period from t_1 to t_2 , the element charges to a voltage of $-fI_b/G_1$, where fI_b is the amount of beam current stopping at the element and G_1 is the conductance of the upper layer with the beam on. The increased conductance induced by the beam causes some of the charge to leak off simultaneously with the storage. Equilibrium between storage and leakage occurs when the element has attained the voltage $-fI_b/G_1$. This level should be reached quickly, i.e., at the induced conductivity time constant which is on the order of a microsecond. If the beam is turned off at time t_2 , the voltage on the element begins to decay toward zero owing to leakage through the dark conductance at the long time constant τ_0 .

If a "ONE" state is to be written, a battery of total voltage V must be placed across the capacitor. The top electrode is made negative with respect to the bottom electrode. To eliminate blanking of the beam, the proposed scheme is to allow the beam to scan along a row of elements while the battery is switched on as the beam passes over a bit location where a "ONE" is to be written.

If at a time t_3 the battery is switched on, then a voltage of $-V/2$ is added to the center electrode. The beam is then switched on at t_4 in order to write the "ONE." Because of beam-induced conductivity, the upper layer is effectively shorted (represented by the time constant τ) and the imbedded electrode will charge up to the voltage on the upper plate, $-V$. Since beam electrons are also deposited on the element, the newly written "ONE" state will attain a voltage of $-[V + (fI_b/G_1)]$. Once the beam goes off, the state will begin to decay according to the dark-conductivity time constant τ_0 . Once the battery is switched off, a voltage of $-V/2$ is subtracted from the element and the decaying "ONE" state with initial voltage of $-[(V/2) + (fI_b/G_1)]$ remains. Since the "ZERO" has a voltage of $-fI_b/G_1$, the excess stored charge in a "ONE" state is equivalent to the voltage $-V/2$. Decay at t_5 is due to the dark-conductance time constant τ_0 .

With the battery off at time t_6 , the "ONE" decays toward an equilibrium voltage of zero. The total storage time is equal to the period required for it to decay to the voltage $-fI_b/G_1$ because at that point the "ONE" becomes indistinguishable from a "ZERO" bit upon readout. This may be of the order of one time constant, depending on the dark conductance.

The bit is read at time t_7 . It is assumed that the time period between t_5 and t_7 is short in comparison with τ_0 , so that sufficient charge remains on the element to be detected upon readout. During the readout process, the upper electrode of the capacitor is tied to an amplifier and the lower electrode is disconnected or permitted to float. If this plate were grounded, the capacitance of all the elements in the array would add in parallel. The result would be a long settling time after reading out each bit. With a floating lower electrode, the beam is permitted to scan the array of elements. Conductivity is induced between the imbedded electrode and the upper plate. Deposition of beam electrons on to the element during readout restores each bit to the "ZERO" state or

leaves it with a voltage $-fI_b/G_1$. Consequently if a "ZERO" has been stored, no excess charge will flow out through the amplifier. However, if "ONE" has been stored, excess charge represented by a voltage of $[(-V/2)\exp-(t-t_5)/\tau_0]$ flows through the amplifier giving rise to a pulse. The readout is destructive because all bits are left in the "ZERO" state. In the time after t_8 , the voltage on the bit will decay toward zero with the time constant τ_0 .

MEMORY PERFORMANCE

If we assume that a memory array is constructed of 3×3 -micron bits on 7 micron centers with alumina dielectric separation layers 5000 Å thick, the bit capacitance is given by $C = K \epsilon_0 A/\ell = 1.4 \times 10^{-15}$ farads, where $K = 8.6$. For this array at $V = 20$ V the beam-induced conductivity gain from Fig. 3 at $V_b = 12$ kV is given by

$$G_a = 0.056 V/d = 2.24$$

Since $G_a = I/I_b$ and $I_b = 5 \times 10^{-8}$ A, the current flowing through the dielectric when the beam is on is 1.12×10^{-7} A, which results in a dielectric conductance $G_m = 1.12 \times 10^{-8}$ mhos or a resistance of 8.9×10^7 ohms. Since this resistance is associated with the device during readout, the RC time constant of the device is 1.2×10^{-7} sec. If $V = 20$ V, the readout charge $q = 2.8 \times 10^{-14}$ coul. If we assume that current crowding reduces the amount of current that can flow in a time constant by 50 per cent, the readout current is given by $I_r = (1/2)dq/dt = 1.2 \times 10^{-7}$ A.

The noise current due to the altered dielectric conductance G_m at a bandwidth $B = 8.3$ MHz is given by

$$I_{nm} = (4KTG_m B)^{1/2}$$

Therefore I_{nm} , the noise current generated at room temperature by the dielectric conductance G_m during readout, is 39 pA. The noise associated with an electron beam can be represented by the equation

$$I_{nB} = (0.644 4KT_c G_B B)^{1/2}$$

For a cathode temperature $T_c = 3200^\circ\text{K}$ and a beam conductance, $G_B = 4.2 \times 10^{-12}$ mhos, the noise current for the same bandwidth is 2.0 pA. The remaining system noise originates at the load resistor and is represented by the sum of the thermal and shot noise,

$$I_{n\ell} = (4KT_G L B)^{1/2} + (2eI_0 B)^{1/2}$$

where e = the charge of an electron

T = the temperature of the load resistor

G_L = the load resistor conductance

I_0 = the total current in the load resistor

Then $I_0 = I_b + I_{nm} + I_r = 1.6 \times 10^{-7}$ A

and $I_{n\ell} = 3.6 \times 10^{-7} \sqrt{1/R_L} + 6.5 \times 10^{-10}$ A

The total noise current into an amplifier, assuming negligible leakage, is

$$I_{n0} = I_{nm} + I_{nB} = 41.8 \text{ pA}$$

The signal-to-noise ratio S/N for $R_L = 10^6 \Omega$ is given by

$$S/N = I_r / (I_{n0} + I_{n\ell}) \approx 100 \approx 40 \text{ db}$$

In practice, I_r will degrade immediately after writing by a factor of e^{-t/τ_0} because of the dark-conductance leakage, which limits the useful storage time to about 10 min at $S/N = 25 \text{ db}$. The ratio S/N is further affected by the fact that the readout and beam currents are combined, but this can be corrected by signal processing. The question is, how does BIC proceed? To our knowledge, no detailed measurements of BIC have been made at high frequencies. Such measurements would be necessary to evaluate the true read-write speed and expected S/N of an array.

In this example, the array has a packing density of $1.2 \times 10^7 \text{ bits/in.}^2$ as compared to $2 \times 10^6 \text{ bits/in.}^2$ for magnetic tape. Packing densities of 10^8 to 10^9 bits/in.^2 and $S/N = 32 \text{ db}$ represent design goals for this type of memory. Unfortunately, there are few device structures capable of achieving these goals. In any case, there is a definite need for performing a realistic detailed analysis of the device and systems structures of any proposed computer memory before development work is initiated.

REFERENCES

1. R. B. Gentile and R. W. Grove, Mass storage utility considerations for shared storage applications, presented at 1971 Intermag Conference, Denver, Colorado, to be published in IEEE Trans. Magnetics.
2. L. N. Heynick, Novel, electron-beam-addressable, alterable-storage devices, 1968 Government Microcircuit Applications Conf.
3. F. Ansbacher and W. Ehrenberg, Electron bombardment conductivity of dielectric films, Proc. Phys. Soc. A64, 1951.
4. L. Pensak, Conductivity induced by electron bombardment in thin insulating films, Phys. Rev. 75: 472, 1949.

EQUIPMENT APPLICATIONS FOR MATERIAL TRANSFER RECORDING

M. L. LEVENE and B. W. SIRYJ

Advanced Technology Laboratories, Government and Commercial Systems, RCA, Camden, N. J.

Material transfer recording is a technique now being developed which uses a focused laser beam to transfer "ink" from a substrate to a recording medium. The recording is immediately fully formed and available for readout. The more significant application advantages include quiet non-impact recording, real-time recording, high resolution, image permanence, and lack of chemical processing. Recent experiments have demonstrated increased writing effectiveness (up to 6000 in./sec) and wider availability of useful transfer materials. This paper updates the reported performance data and presents several proposed printing and recording systems based upon the material-transfer technique. Alphanumeric printers associated with communications systems and with computer printout are discussed, and comments are offered on the prospects for growth into toned image graphic recording.

INTRODUCTION

As first reported by Braudy,¹ the material-transfer process uses a focused laser beam to transfer "ink" from a substrate onto a recording medium. No other processing is required as the image has already been formed, developed, and fixed by the transfer process. Braudy's early work with 7- and 20-mW argon lasers and a variety of transferable materials achieved a fine line width at low speeds. In 1970, along with discussion of proposed physical models for the transfer phenomenon, we reported² that the use of a much more powerful Nd³⁺:YAG (22-w) laser permitted the transfer of carbon material from commonly available polyethylene-backed typewriter ribbon at speeds up to 1450 in./sec. Continued investigations have utilized 5-w argon lasers in conjunction with higher scanning speeds and more efficient transfer materials. We can now describe the achievement of transfer rates up to 6000 in./sec. The advance from 1450 to 6000 in./sec has established a sound basis for practical applications in printing and recording equipment.

The material transfer process has significant advantages: quiet, nonimpact operation, real-time recording, high resolution, image permanence, and absence of chemical processing. Protection from ambient light is not required; special vacuum environment is not necessary. These features can be of great importance in such applications as facsimile recorders and alphanumeric printers for communications and computer printout terminals. Prior publications have mentioned not only the forward-direction process for laser-scanned material transfer recording, but also reverse transfer and transfer across gaps in both directions.^{1,2} An "etching" process which may lead to interesting microfabrication techniques has also been described.² In this paper, we concentrate on reporting experimental advances in forward transfer onto paper and clear film, and on discussing application opportunities in alphanumeric printer and facsimile recorder equipment.

PERFORMANCE ACHIEVED

Figure 1 shows the basic process by which transferable material, bonded to a substrate, is transferred onto a recording medium (such as paper or Mylar). In this arrangement, a laser beam is focused onto a transferable material which, upon having received at least a threshold energy characteristic of the particular transferable material, vaporizes and redeposits itself on the recording medium.

Earlier experiments, performed with a Nd^{+3}YAG laser, yielded a considerable amount of guidance and direction pertaining to the general field of material transfer recording. From those experiments, the following conclusions were drawn:

- (1) In order to obtain material transfer at high speeds, the energy density of a focused laser beam has to be as high as practical.
- (2) The absorption coefficient of the transferable material should be as high as possible at the wavelength of the laser used.
- (3) The transferable material itself or its binder has to vaporize at a relatively low temperature.

With these objectives in mind, a new experimental test setup has been developed (Fig. 2). A 5-watt argon laser is now the power source. High reflectivity dielectric mirrors are used wherever possible to maintain a high over-all laser power efficiency. A beam expander is used to fill the focusing lens. A flying-spot scan has been accomplished by directing the focused cone of light coaxially onto a single-faced rotating mirror.

Since the angle between the axis of rotation and the mirror face is 55° , the central ray of the focusing cone, when rotating, describes the surface of a cone (Fig. 3a). The base of the cone is a circle traced by the focused spot. This method of beam deflection is termed a "conical scan." Another commonly used method of beam deflection is the circular scan, in which the central ray of the focusing cone is perpendicular to the plane of scan (Fig. 3b). The advantage of a conical scan as compared to a circular scan is that it is a flat-field scan and therefore does not require the recording surface to be curved or cupped as is a common requirement in standard circular scanning systems.

The rotor assembly which carries the single-faced mirror is supported on air bearings and is driven by an air turbine. At a radius of 3.25 in., the flying spot may be scanned up to 30 000 in./sec.

Both the recording medium and the transfer materials can be held onto the platen with vacuum. Since standard bond paper is the most frequently used recording medium, its porosity has been used to advantage. By placing the transfer material (usually a transferable material deposited on Mylar) directly in contact with the paper, both are not only held together but are also conformed to the platen by the same vacuum. It should be noted that vacuum is not needed to promote transfer. It has been used only because it is a most convenient method of material hold-down. As an alternate means to conform the materials, a quartz plate 0.125-in. thick has also been used as a "paper weight." A disadvantage associated with using quartz is the additional loss of laser power by reflection. The material-holding platen is attached to a carriage, which in turn is supported on translating air bearings. The drive for the carriage is an adjustable air piston-damper combination.

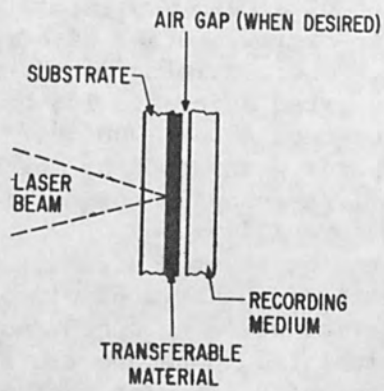


FIG. 1.--Basic arrangement of recording material.

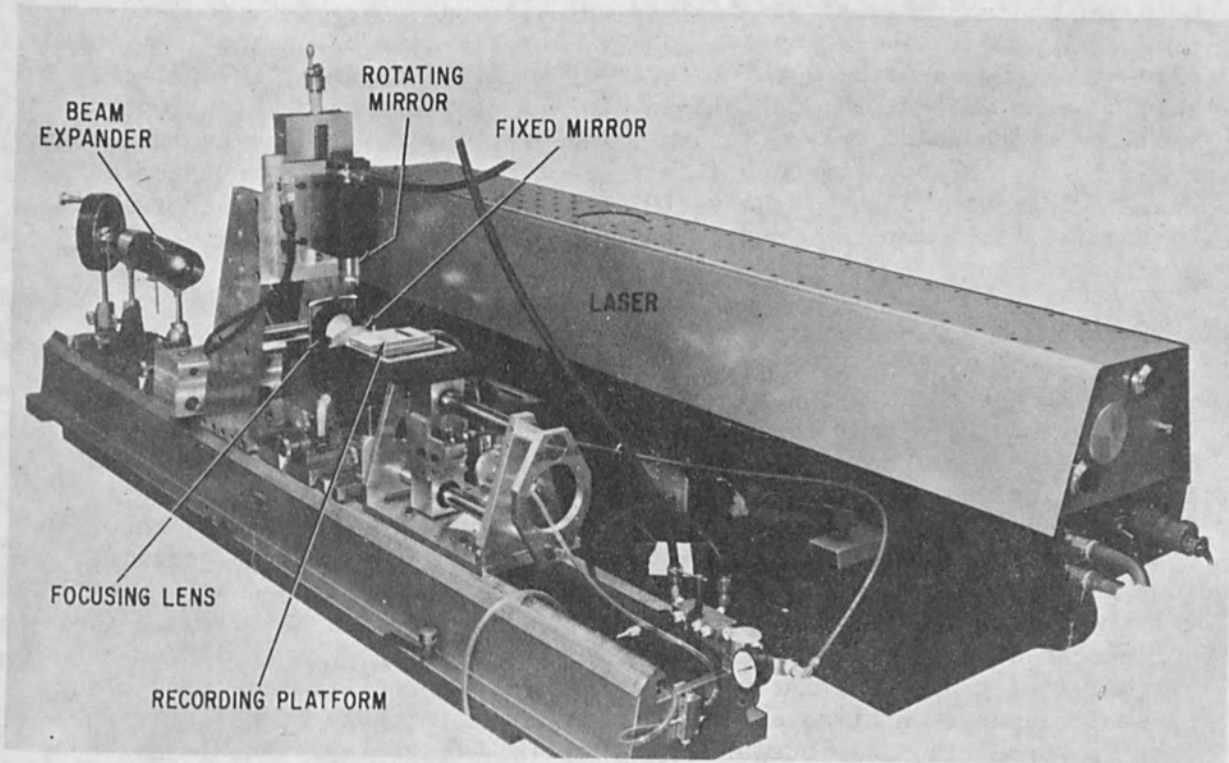


FIG. 2.--Apparatus for material-transfer experiments.

Thus far, we have been able to obtain best transfer, up to speeds of 6000 in./sec, with a material prepared by S. E. Harrison of RCA's Sarnoff Research Center in Princeton, N. J. Representative test results using this material are shown in Fig. 4. Other materials such as polyethylene-backed typewriter ribbon, common marking-pen dyes, and Du Pont's Latyl dyes have also been transferred successfully; however, none of these has yet achieved a rate higher than about 2000 in./sec. Figure 4 also presents an example of character generation by the material transfer process. A light-reflecting stencil was used in conjunction with the conical scan to generate the words "Material Transfer."

With an F/8 system, the calculated diffraction-limited spot diameter is 10 microns and the depth of focus is 64 microns. The energy density required to transfer material based on speed, power at the focal point, and line width is now calculated to be about 0.1 joule/cm^2 . Since the line width enters into the calculation of the energy density, one must not interpret energy density as a constant value, but rather as a specific value associated with a specific power and a specific focal setting. (For a further discussion of power versus line width, see a paper by Carlson and Ives.³) The very practical way to obtain optimum focus is to keep the power constant and periodically increase the speed while traversing back and forth through focus. Eventually, there will be only a very narrow range of focus through which material will transfer at all. It is interesting to note that the thickness of the transferable material plays a vital role in determining the maximum obtainable speed. The thinner the material, the higher the speed at which the material transfers. It is to be expected that best results will be obtained if the transferable material bonded to substrate is just thick enough to produce good contrast. The most likely explanation is that all else being equal, it takes more energy to vaporize a thick layer of material than a thin one. It should be noted that the calculated minimum spot diameter which controls the line width holds only for normal incident angles; in the conical scan, the tilt of the focusing cone with respect to the recording surface actually widens the line by the ratio of 1.7 to 1. Thus, more power should be required in a conical scan to produce the same energy density than in a circular scan.

APPLICATION OPPORTUNITIES

1. ALPHANUMERIC PRINTERS. The alphanumeric printers in most common use today employ either mechanical impact or electrostatic printing. Some varieties of photosensitive and electrochemical printers are also in use. The material transfer recording process offers most of their advantages and suffers few restrictions. It requires no special recording paper, does not require a "light-tight" or vacuum environment, provides good resolution, permits a variety of ordinary recording media, and offers relative insensitivity to variations in temperature and humidity in the ambient environment.

Material transfer printers may be expected to utilize electronic and optical elements in arrangements quite similar to those of the film recorders which also make use of laser scanning (Fig. 5a). The laser beam would be (1) modulated by an electro-optical modulator, (2) optically expanded, and (3) suitably focused to a small spot. The focal cone would be deflected by a mechanical scanning mirror. To appreciate how the

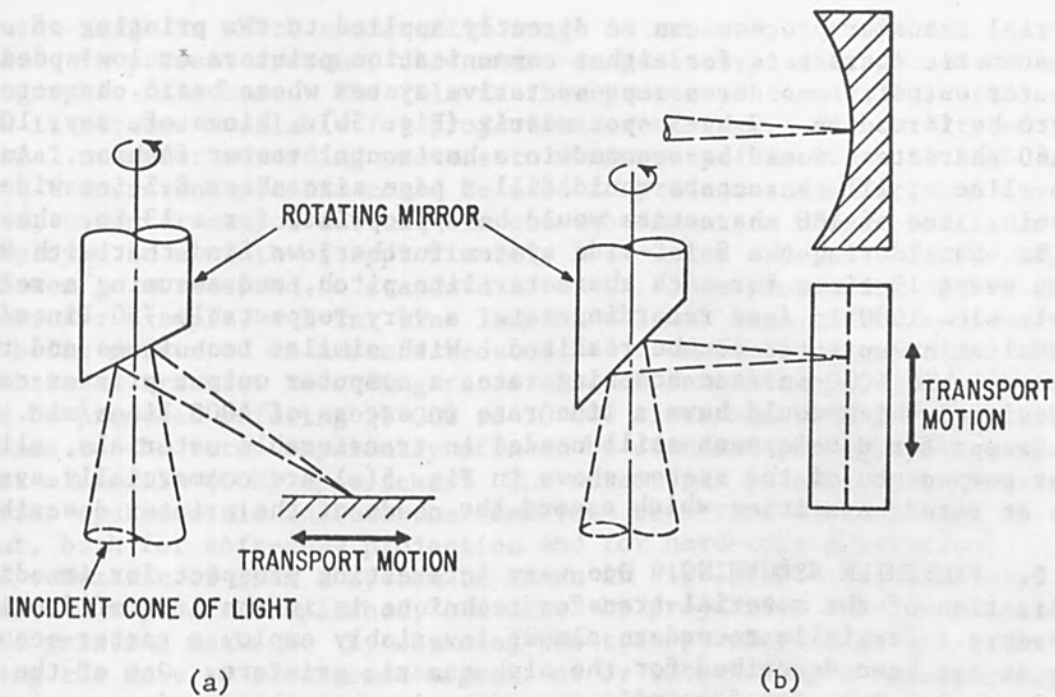
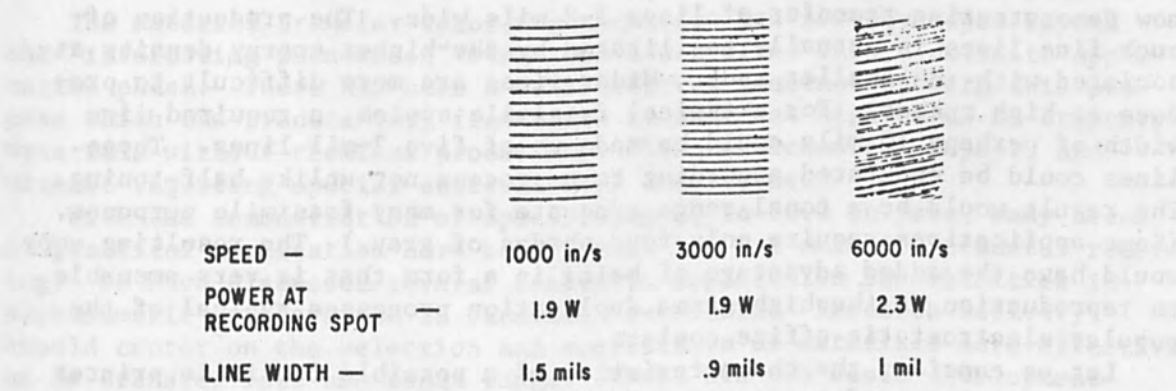


FIG. 3.--Scan configurations: (a) conical scan, (b) circular scan.



MATERIAL TRANSFER

MATERIAL TRANSFER*

*ENLARGED 2:1 TO SHOW LINE STRUCTURE

FIG. 4.--Material-transfer test results.

material transfer process can be directly applied to the printing of alphanumeric characters for either communication printers or low-speed computer output, consider a representative system whose basic characters are to be formed in a 7-by-5 spot matrix (Fig. 5b). Lines of, say, 100 to 160 characters would be scanned in a horizontal raster fashion. An 8-in. line of 111 characters would fill a page size sheet 8.5-in. wide. An 11.5-in. line of 160 characters would be appropriate for a 13-in. sheet width. Considering the 8-in.-wide system further, we find that with 8 in. being swept 10 times for each character line pitch, and assuming a relatively slow 1000 in./sec recording rate, a very respectable 750-lines/min communications printer can be realized. With similar techniques and the now-available 6000-in./sec scanning rate, a computer output printer could be designed which would have a line rate in excess of 4000 lines/min.

Except for development still needed in transferable materials, all other components of the system shown in Fig. 5(a) are commercially available at rated capacities which exceed the needs of the printer described.

2. FACSIMILE RECORDING. One very interesting prospect for immediate application of the material transfer technique is in the area of facsimile recorders. Facsimile recorders almost invariably employ a raster scan such as has been described for the alphanumeric printers. One of the usual requirements for facsimile recorders is that they produce an image with some degree of dynamic range. We have not yet looked for materials with wide tonal range; our primary goal has been to increase the speed of transfer. But it may not be necessary to wait for such materials before applications in facsimile recorders can be realized, since we are now demonstrating transfer of lines 1-2 mils wide. The production of such fine lines is actually facilitated by the higher energy density associated with the smaller spot. Wider lines are more difficult to produce at high speeds. For a typical facsimile system, a required line width of perhaps 10 mils could be made up of five 2-mil lines. These lines could be modulated according to a process not unlike half-toning. The result would be a tonal range adequate for many facsimile purposes. (Some applications require only four shades of gray.) The resulting copy would have the added advantage of being in a form that is very amenable to reproduction in the high-gamma duplication processes typical of the popular electrostatic office copiers.

Let us consider the characteristics of a possible facsimile printer using material-transfer recording. Assume, as an upper speed for the present, a 6000-in./sec scan and 2-mil scan line width. Also, assume the picture to be an 8 x 10-in. image divided at the transmission station into 1000 adjacent scan lines (8 in. long, 10 mils wide). Assuming, further, a 50-percent scanner duty cycle, we may then scan 375 2-mil lines/sec, or 75 10-mil equivalent lines/sec. Our system will require suitable buffers to store the transmitted line and organize its five-line equivalent. The five-by-five "dot" array which substitutes for each transmitted "dot" should result in a tonal range of about eight or nine $\sqrt{2}$ levels of gray. The 8 x 10-in. image can be printed in 13.4 sec. Present systems may not require such rapid rates, but material transfer recording now offers this high-speed facsimile printing, as well as all lower speeds appropriate to any given system.

3. A VERY HIGH-SPEED, MICROIMAGE-INTERMEDIATE COMPUTER OUTPUT PRINTER. There is some interest in a form of output peripheral for

computer usage in which a microfilm image is created at very high line rates.⁴ In present systems, this micro-image is typically placed on a photographic film base. The film is then processed chemically, after which it becomes available for projection or storage. The ability of the material transfer recording process to write very fine lines at high rates onto a transparent plastic could be used to produce a similar, but improved, computer output device. In one embodiment, a clear plastic could be employed in a width of approximately 1 to 2 in. The actual size might be chosen to correspond to standard 35-mm or 75-mm projection optics. Assume, for example, a 1-in. line length, a 1-mil line width, and characters being generated on a scale reduced 9:1 from final output copy. With the material transfer recording rates already demonstrated, a system could be produced offering 20 000 to 30 000 lines/min. This output corresponds to the rates apparently offered by standard photographic computer output microfilm (COM) approaches. The advantages gained by the material transfer system would include the immediate real-time availability of the output, both for soft-copy projection and for hard-copy generation.

A schematic of such a system is shown in Fig. 5(c). The hard-copy generation may be accomplished "off line" by projection onto an electrostatic printing machine. By scanning the transparency image and reconverting the data to electronic signal, or by interposing a magnetic-tape buffer to store original input data, the alphanumeric material-transfer printer described in Sec. 1 above could also serve the hard-copy function.

CONCLUSIONS

The material transfer recording technique has now developed beyond the "interesting phenomenon" stage and has evolved into a definite application phase. There has been a well-deserved fascination with this process which can produce very fine lines recorded at high rates on ordinary materials without chemical processing, without mechanical impact, and without requiring special environmental conditions.

With the demonstration of speeds ranging to 6000 in./sec, many areas of practical application have been identified for material transfer recording. We have discussed several realistic application possibilities in alphanumeric printers and in facsimile recorders. Research activity should center on the selection and acquisition of materials more effective as to transfer rate and tonal range. There are two basic development goals:

- (1) increased transfer rate to challenge high-speed recording now accomplished only by "photographic" technology; and
- (2) reduction in required laser power at the already useful rates attained (as in communication and facsimile applications) to permit compact, inexpensive, and reliable equipment.

REFERENCES

1. R. S. Braudy, Laser writing, Proc. IEEE 57: 1771, 1969.
2. M. L. Levene, R. D. Scott, and B. W. Siryj, Material transfer recording, Appl. Optics 9: 2260-2265, 1970.
3. C. O. Carlson and H. D. Ives, Some considerations in the design of a laser thermal microimage recorder, SIDAR, Proc. First Symp. Image Display and Recording 1, 1969.

4. F. J. Lavoie, COM unsnarls the computer-output jam, Machine Design March 4, 1971; pp. 68-74.

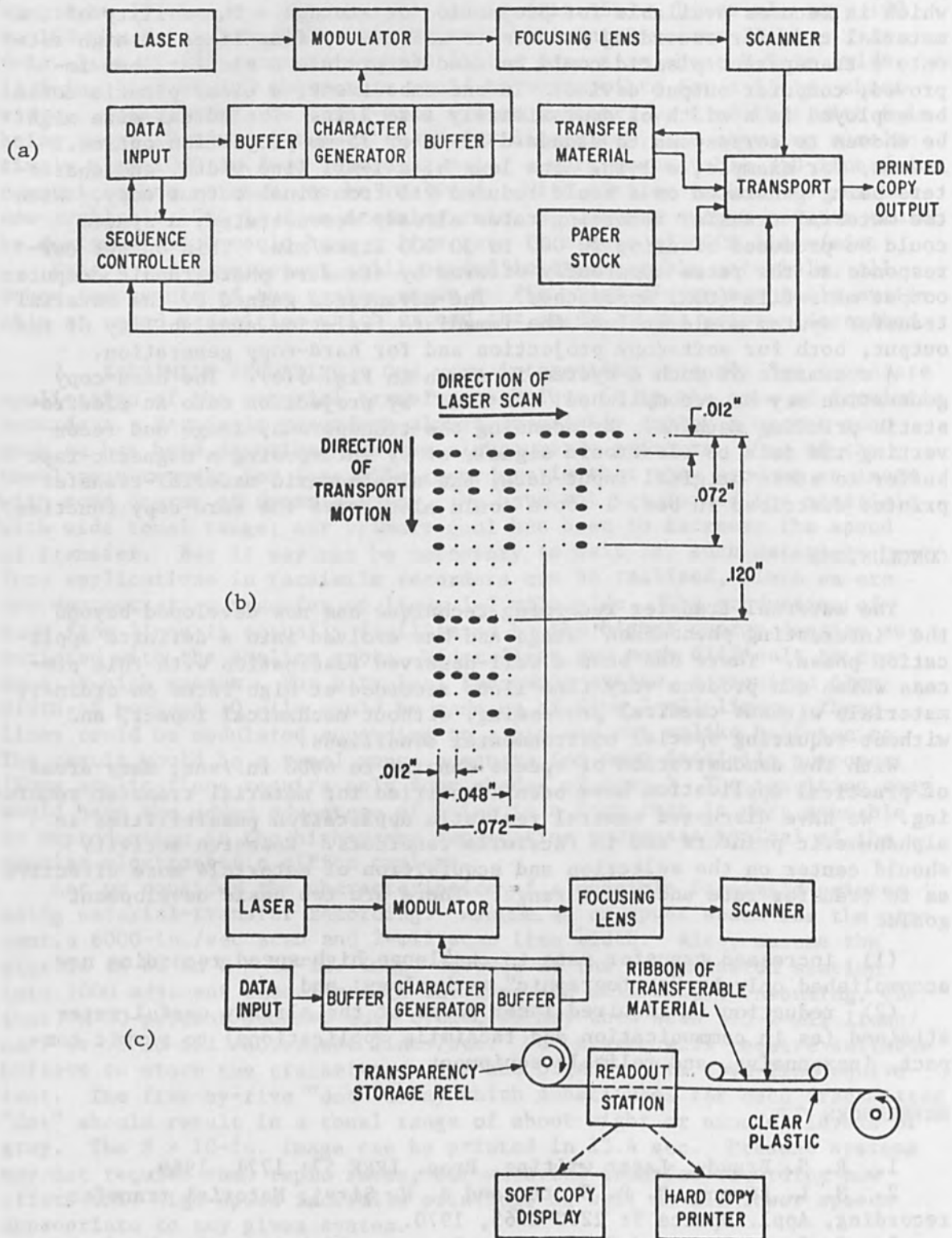


FIG. 5--(a) Alphanumeric printer; (b) character configuration; (c) high-speed computer output printer.

SESSION ON ANALYSIS

THE APPLICATION OF RADIOCHROMIC DYE FILM DOSIMETRY TO MEDIUM-Z ABSORBERS*

HARVEY EISEN** and MARVIN ROSENSTEIN†

National Bureau of Standards, Gaithersburg, Md., and University of Maryland, College Park, Md.

and

JOSEPH SILVERMAN

University of Maryland, College Park, Md.

INTRODUCTION

Radiochromic dye film dosimetry was employed to measure depth-dose distributions produced by plane-parallel electron beams in absorbers ranging in atomic number from 13 to 50. Data were obtained for aluminum, copper, and tin absorbers for incident beam angles of 0, 30, and 60° to the surface normal. All work was done in vacuum with 2-MeV electrons and in broad-beam geometrical configuration. The data are compared with computer calculations generated by means of the ETRAN program.¹

EXPERIMENTAL PROCEDURE

A detailed discussion of the experimental irradiation and dosimetry techniques is to be found in the work of Rosenstein et al.^{2,3} The radiochromic dye film utilized was a solid solution of hexahydroxyethyl pararosaniline dye cyanide in nylon.⁴ Thin layers (0.04 mm thick) were interposed between layers of the absorbing medium. The precise thickness of film samples was measured to normalize their response. The stack was assembled in an experiment ladder which also contained a monitor assembly for incident charge collection (Fig. 1). During exposure, the ladder was moved at a constant speed through a scanned 2-MeV electron beam in a vacuum chamber. An optical densitometer with appropriate filters was used to measure the pre- and post-irradiation absorbance of the film at 601 nm. The absorbance readings were converted to film dose through a previously determined calibration factor. Dose to the absorbing medium was obtained by application of an appropriate stopping power ratio. Division of the dose by the independently measured electron fluence yielded dose per unit fluence. Thus,

$$D_F = \frac{kA}{Ct}$$

$$\text{and } \frac{D_M}{\phi} = \frac{D_F}{\phi} \bar{S}$$

* This work was supported in part by the Division of Isotopes Development, U.S.A.E.C., and conducted in part at the National Bureau of Standards.

** Permanent address: Harry Diamond Laboratories, Washington, D.C.

† Permanent address: Bureau of Radiological Health, USPHS, Rockville, Md.

where D_F = film dose, MeV/g
 D_M = dose to the absorbing medium, MeV/g
 Φ = incident electron fluence, electrons/cm²
 k = 6.24×10^{13} MeV/g-Mrad
 A = absorbance change due to irradiation, optical density units (ODU)
 C = calibration factor, ODU/Mrad-mm
 t = film thickness, mm
 \bar{S} = ratio of the mass collision stopping power of the absorbing medium to that of the film at a mean electron energy value

An investigation was made to determine the error introduced as a result of evaluating the stopping power ratio by this simple approximation. Three ways of computing the stopping power ratio were compared: (1) evaluating the ratio at the mean electron energy of 1.0 MeV and using that at all depths in the absorber; (2) using an empirical expression relating the variation of mean energy of the spectrum with depth into the absorbers;⁵ and (3) using a more exact calculation involving an integral over the electron spectrum at each depth times the stopping power function.⁶ The difference between these methods of calculating the stopping power for any absorber is less than ± 3 per cent over 60 per cent of the depth-dose distribution.⁷ As a result, the simple procedure, method (1), was used for evaluation of the stopping power ratios. The ratio of the stopping power of the various absorbers used to that of the film was as follows: aluminum, 0.787; copper, 0.692; tin, 0.607.

RESULTS AND DISCUSSION

Experimental data and ETRAN calculations of a few cases are presented in the form of depth-dose profiles in Figs. 2 through 5. They illustrate the general results obtained for variations in absorber atomic number and angle of beam incidence. At least two sets of experimental data were taken for each set of conditions. The reproducibility of the results is ± 5 per cent. Agreement with theory is also ± 5 per cent.

Figure 2 shows the depth-dose distribution data for copper with the beam making an angle of 30° with the surface normal. The histogram is the computer code prediction. The present data are lower than the calculation but agree in the total fraction of incident electron energy deposited (area under the curve) within 8 per cent and in absolute value at any point on the distribution curve within 10 per cent.

Figure 3 shows the depth-dose distribution data for tin in comparison with the calculation for 60° beam incidence. The two are in excellent agreement.

In Fig. 4, the mean values of the measured depth-dose distributions at normal beam incidence are compared for the three different absorbers. The abscissa represents the ratio of the depth X in the absorber to the continuous-slowing-down-approximation range r_0 , i.e., the total path length.⁸ The intercept on the abscissa, which is the ratio of the maximum range obtained from the experimental curve to the theoretical path length, is observed to decrease with increasing atomic number. This observation is in accordance with expectations because of the angular scattering processes which produce deviations from a straight-line path. These processes are known to increase with Z . The maximum value of the energy deposition increases with Z and occurs at lower fractions of the path length.

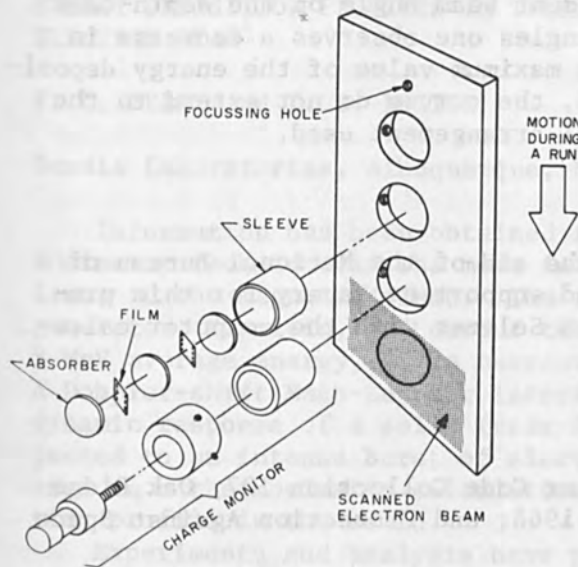


FIG. 1.--Experiment ladder containing absorber-film assembly and incident fluence monitor.

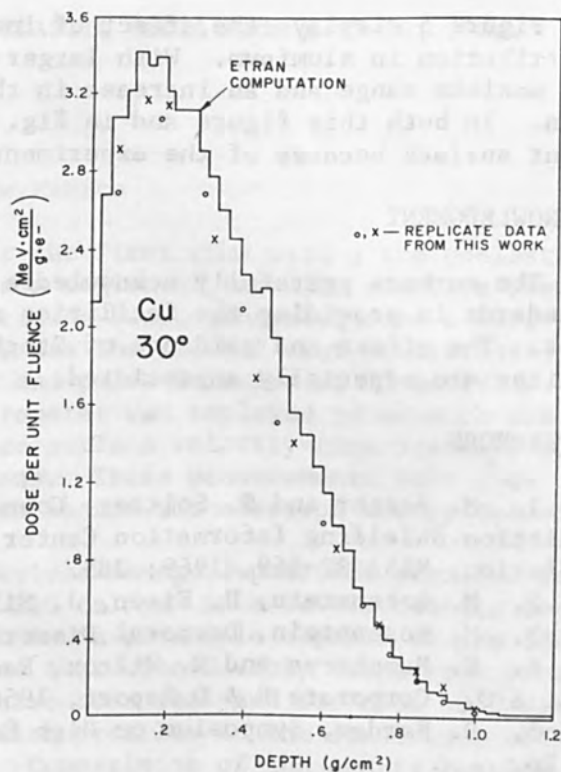


FIG. 2.--Comparison of present depth-dose data to theoretical computation for 2-MeV electrons incident at 30° to surface normal on copper slabs.

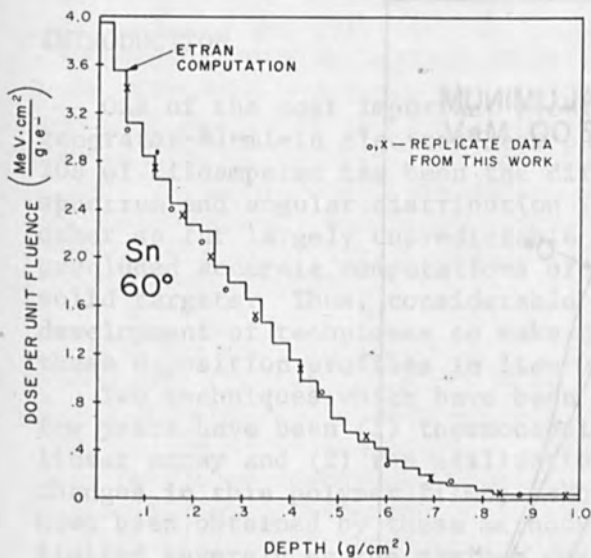


FIG. 3.--Comparison of present depth-dose data to theoretical computation for 2-MeV electrons incident at 60° to surface normal on tin slabs.

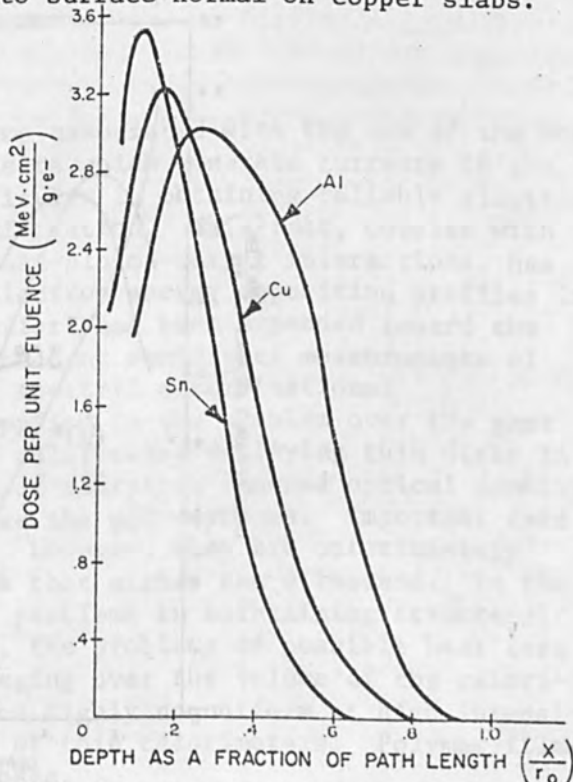


FIG. 4.--Measured depth-dose profiles for 2-MeV electrons in Al, Cu, and Sn slabs at normal incidence.

Figure 5 displays the effect of incident beam angle on the depth-dose distribution in aluminum. With larger angles one observes a decrease in the maximum range and an increase in the maximum value of the energy deposition. In both this figure and in Fig. 4, the curves do not extend to the front surface because of the experimental arrangement used.

ACKNOWLEDGMENT

The authors gratefully acknowledge the aid of the National Bureau of Standards in providing the facilities and support necessary for this project. The effort and guidance of Stephen Seltzer with the computer calculations are especially appreciated.

REFERENCES

1. M. Berger and S. Seltzer, Computer Code Collection 107, Oak Ridge Radiation Shielding Information Center, 1968; and Protection Against Space Radiation, NASA SP-169, 1969; 285.
2. M. Rosenstein, H. Eisen, J. Silverman, J. Appl. Phys. (in press).
3. M. Rosenstein, Doctoral Dissertation, University of Maryland, 1971.
4. K. Humpherys and R. Wilcox, Radiochromic Dosimetry Materials Study, E.G. & G. Corporate R & D Report, 1968.
5. D. Harder, Symposium on High Energy Electrons, Springer, 1965; p. 26.
6. M. Berger and S. Seltzer, Annals N. Y. Acad. Sci. 161: 8, 1969.
7. H. Eisen, M. Rosenstein, J. Silverman, J. Appl. Rad. and Isotopes (in press).
8. M. Berger and S. Seltzer, NASA SP-3012, 1964.

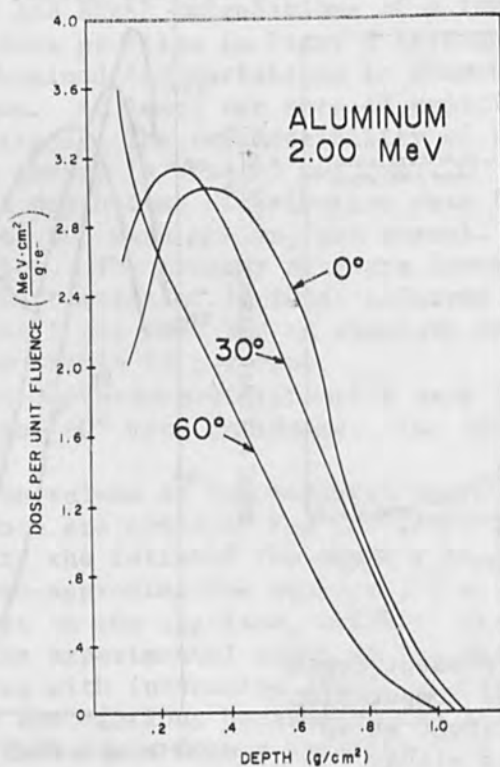


FIG. 5.--Measured depth-dose profiles in aluminum slabs for 2 MeV electrons at 0°, 30°, and 60° to surface normal.

ENERGY DEPOSITION PROFILES IN THERMOELASTIC MEDIA FROM A 45-kA, 3-MeV ELECTRON BEAM*

F. C. PERRY and L. D. BUXTON

Sandia Laboratories, Albuquerque, New Mexico

Information has been obtained for the first time with a thermoelastic dosimetry technique in the most intense region of the REBA electron beam, i.e., in the magnetic pinch. The electron beam, generated from a Marx generator, Blumlein, and output tube, has the nominal characteristics: 3 MeV average energy, 45 kA current, and pulse duration of 70 ns FWHM. A Doppler-shift Mach-Zehnder interferometer was employed to measure the dynamic response of a solid (rear free surface velocity-time history) subjected to an intense burst of electrons. These measurements were then used in a thermoelastic calculation to obtain the electron energy deposition profile in the solid.

Experiments and analysis have provided energy deposition profiles for beam intensities up to approximately 120 cal/cm^2 in a brittle single crystal, x-cut quartz. A quartz specimen is in principle capable of providing information for electron-beam fluences that considerably exceed the present maximum fluence of REBA. Data have also been analyzed for AISI 4340 steel hardened to RC-54, and energy-deposition profiles in the steel were obtained for fluences up to about 50 cal/cm^2 . Comparisons of the quartz results in the magnetic-pinch region and in a portion downstream from the pinch have suggested that the electron angular distribution varies with axial position and contains electrons with larger angles of incidence in the pinch region.

INTRODUCTION

One of the most important problems associated with the use of the Marx-generator-Blumlein electron-beam pulsers which generate currents in the 10s of kiloamperes has been the difficulty in obtaining reliable electron spectrum and angular distribution information. This fact, coupled with other so far largely unpredictable beam-plasma-target interactions, has precluded accurate computations of electron energy deposition profiles in solid targets. Thus, considerable effort has been expended toward the development of techniques to make direct or semidirect measurements of these deposition profiles in lieu of spectral determinations.

Two techniques which have been applied to the problem over the past few years have been (1) thermocouple calorimetry employing thin disks in a linear array and (2) the utilization of radiation induced optical density changes in thin polymer films, such as the polystyrenes. Important data have been obtained by these methods. However, they are unfortunately limited severely by the maximum doses that either can withstand. In the case of thin calorimeters, there are problems in maintaining structural integrity at high dose levels. Also, the problems of possible heat loss mechanisms and the necessity of averaging over the volume of the calorimeter (electron beams generally become highly nonuniform at high intensities) have reduced the effectiveness of thin calorimeters. Polymer films have been even less useful at high doses.

*This work was supported by the U.S. Atomic Energy Commission.

The use of stress pulses for the purpose of obtaining information about the energy deposition of pulsed charged particle beams is relatively recent. White^{1,2} in 1963 employed electron-beam pulses 2 μ s long to confirm some theoretical relationships involving the generation of thermoelastic stress. In 1967, Graham et al.³ demonstrated the feasibility of obtaining dosimetry information by measuring the stress pulses generated by a 6-kA, 1.5-MeV electron beam whose pulse duration was approximately 40 ns. In the experiments of White and Graham, stress measurements were performed with a piezoelectric transducer.

More recently, Schallhorn et al.⁴ have employed a Michelson interferometer to measure the thermoelastic response of solids subjected to a 25-ns, 10-kA, 2-MeV electron pulse. Constant volume heating was assumed in their analysis and energy deposition profiles were obtained for a variety of absorbers. Perry⁵ in 1970 also used a Michelson interferometer to measure the thermoelastic response of aluminum and copper to a 40-ns, 6-kA, 1.5-MeV electron beam. In that experiment, a more realistic thermoelastic analysis was employed in the data reduction. It provided for the finite heating rate, which was shown to be important for materials with high atomic numbers.

This paper presents some results of a continuing investigation of thermoelastic response of solids to a pulsed electron beam with the nominal characteristics:⁷ 45 kA current, 3 MeV electron average energy, and 70 ns FWHM pulse duration. Energy deposition profiles have been obtained for the first time in the most intense region of this beam, i.e., in the first magnetic pinch. The solids discussed in the present report are alpha quartz and AISA 4340 steel hardened to RC-54. These absorbers were chosen because they remain elastic at relatively high pressures (high beam fluences). It was of interest to determine the applicability of both a brittle crystal and a metal for thermoelastic dosimetry at high energy levels. The advantage of using a brittle crystal is a high Hugoniot elastic limit; the disadvantages are the relatively low electrical conductivity and the fact that brittle crystals are generally destroyed by the relief (tensile) waves. The corresponding advantages and disadvantages of a metal are the exact opposite. The technique used in these measurements was different from that of previous investigations, since free-surface velocity-time histories were measured directly with a Doppler-shift Mach-Zehnder interferometer.^{8,9} Direct velocity measurement has a considerable advantage over the previous displacement interferometric technique for thermoelastic dosimetry, as will be explained later.

THEORY

The theory of thermoelastic response of polycrystalline metals has been previously elucidated.^{5,6} In Ref. 6 a model was presented for the one-dimensional thermoelastic response of homogeneous isotropic metals to pulsed relativistic electron-beam absorption. The same analytic formalism will be adopted in the present paper. The justification for applying the same model in the case of alpha quartz, which is not a metal and is also an isotropic, is the following. Key¹⁰ showed that the basic stress-energy relationship holds for an isotropic elastic solids, but that the scalar Grüneisen parameter must be generalized to a Grüneisen tensor. For a crystal of specified symmetry (alpha quartz has the trigonal structure) and for response measurements performed along the axes of symmetry, the Grüneisen tensor is in diagonal form, where each diagonal element corresponds to the Grüneisen parameter component for that direction of symmetry. The Grüneisen parameter

for x-cut quartz is well known,¹⁰ and has been verified by the electron-beam technique.¹¹ Second, an assumption in the following analysis is that all of the electron energy is transferred to the lattice, i.e., effects of charge trapping and potential buildup are considered to be negligible. This assumption appears to be justified in the case of quartz by the outcome of the present experiment, where there was no evidence of range foreshortening as has been observed for low-conductivity polymers.¹¹⁻¹⁵

The one-dimensional thermoelastic behavior is described by the partial differential equation

$$\sigma_{tt} - a^2\sigma_{xx} = \rho\Gamma E_{tt} \quad (1)$$

where σ is the stress component in the direction perpendicular to the target surface, a is the dilational wave speed, ρ is the density, Γ is the Grüneisen parameter, E is the energy deposition per unit mass, and the subscripts x , t denote partial differentiation with respect to the position and time coordinates.

The appropriate solution to the above equation, which also satisfies momentum conservation $\rho V_t = -\sigma_x$ for energy supplied at a constant rate during τ_0 , is given by

$$V(L, t) = \frac{\Gamma}{a^2\tau_0} \int_0^{at} [E(L - u) - E(L + a\tau_0 - u)] du \quad (2)$$

This solution can also be written

$$E(L - at) - E(L - at + a_{\tau_0}) = \frac{a_{\tau_0}}{\Gamma} V_t(L, t) \quad (3)$$

Equations (2) or (3) can be used to convert the free-surface velocity-time histories to energy-deposition profiles. As can be noted from Ref. 5, the utilization of displacement-time histories requires either a double integration or double differentiation to obtain $E(x)$; thus the method of direct velocity determination has the advantage of eliminating the introduction of errors due to finite-difference differentiation.

EXPERIMENTAL TECHNIQUE

The velocity-interferometer-electron-beam technique has been described elsewhere; however, for the sake of clarity, a brief description is given here. Figure 1 shows a diagram of the interferometer, electron-beam generator, and beam drifting system. The generator itself, called REBA, consists of a Marx capacitor bank, Blumlein, and output tube, all of whose characteristics have been adequately described. Upon emission through a thin (0.0114 cm) titanium window, the beam was drifted into an aluminum cone in which the pressure could be altered to control the propagation. Fairly reproducible beam behavior was achieved for drift pressures from about 5 torr to atmospheric pressure. In the pressure range of 0.25 to 1 torr, the beam diverged and produced very low intensities. In the range 0.05 to 0.20 torr, the beam drifted in a tightly pinched configuration in an erratic and irreproducible manner. Below a pressure of about 0.05 torr, the beam blew up immediately in the drift region because of negative-space-charge

repulsion. Hence, considerable work with the beam has been performed under atmospheric drifting conditions, including this experiment.

In order to obtain a range of beam intensities, the target was affixed to the end of a hollow cylinder (Fig. 1) which could be moved along the axis of the drift cone. At atmospheric pressure, the electron beam self-focused (pinched) under the influence of its own azimuthal magnetic field at a position about 6.3 cm downstream from the anode. The cylinder-target assembly was placed at the pinch position for maximum intensity and, for continuously lower intensities, was positioned downstream from the pinch where the beam tends to diverge. An equilibrated steel calorimeter was used to determine the total beam energy density along the axis of the drift cone. These measurements were performed over the range of 20 cal/cm² (downstream of the pinch) to about 120 cal/cm² (in the pinch).

Also shown in Fig. 1 is a schematic of the Doppler-shift Mach-Zehnder interferometer employed to measure the material response. The target, in the shape of a disk, constituted one mirror of the interferometer. The mirror on the downstream face of the quartz targets was a thin layer of vapor-deposited gold. In the case of the steel targets, the mirror was provided by lapping and polishing the downstream faces.

The light source for the interferometer was a 1-mW HeNe laser, whose beam was directed through a hole in mirror A of Fig. 1 and was focused by the lens B through the hollow cylinder onto the target rear surface. The laser beam was then reflected back through the lens B, and mirror A directed the beam to the splitter C. Light which traversed the delay leg CDEF was combined with the reference beam which passed directly from C to splitter F to produce interference fringes. The combined reference and delayed light beams were then directed by means of two mirrors out of the radiation cell into an rf shielded photomultiplier of approximately 0.5 ns risetime. Two mirrors, D and E, were mounted on translation stages so that the length of the delay leg was continuously variable from approximately 0 to 20 m.

In Fig. 2 are shown typical results of interference fringes caused by the electron-beam-induced free-surface motion for targets of quartz and steel. The two traces correspond to electron fluences of approximately 120 and 40 cal/cm² for (a) and (b), respectively. The quartz target was considerably thicker (1.27 cm) than the steel target (0.635 cm). Oscillograph (a) shows a large initial negative excursion due to noise generated from the electron burst, whereas trace (b) was delayed by 0.3 ms to compensate for the transit time of the induced stress wave through the unheated portion of the target.

In general, the onset of fringes corresponds to the arrival at the back surface of a compression wave. The first cusp indicates a reversal in the direction of fringe motion, i.e., velocity. The reversal is then followed by a set of rapid fringes, corresponding to the sudden release of the free surface. After release of the free surface, a tensile wave normally follows, as is evident for steel. The interpretation of the wildly irregular behavior for the fringes following release in the case of quartz is that the target disintegrates in tension, an interpretation which can be rapidly verified by post-shot examination.

The reduction of data of the type shown in Fig. 2 to velocity-time histories was obtained by using the relationship⁸

$$V(t) = \frac{\lambda}{2\tau} N(t) \quad (4)$$

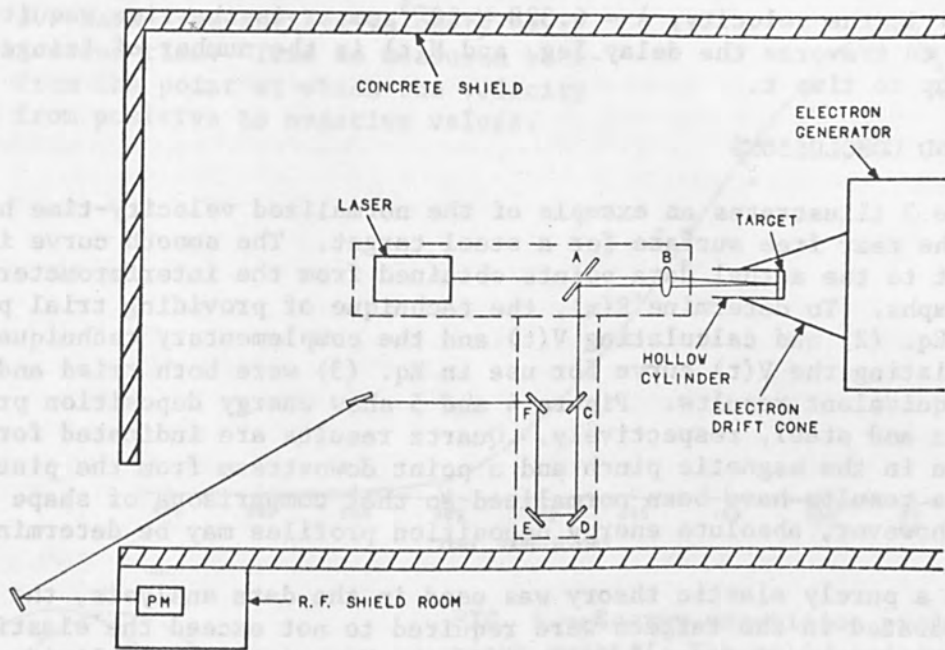
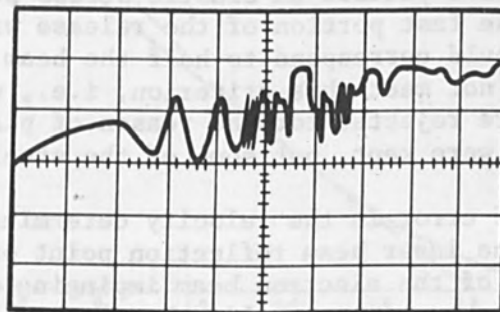
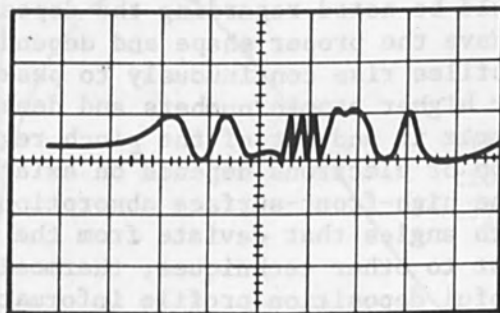


FIG. 1.--Experimental arrangement.



(a)



(b)

FIG. 2.--Oscillographs of interference fringes for (a) quartz (500 ns/div) and (b) steel (100 ns/div). The electron energy fluences for the shots shown in (a) and (b) were about 120 and 40 cal/cm², respectively.

where $V(t)$ is the velocity, $\lambda = 6.328 \times 10^{-5}$ cm, τ is the time required for light to traverse the delay leg, and $N(t)$ is the number of fringes detected up to time t .

RESULTS AND CONCLUSIONS

Figure 3 illustrates an example of the normalized velocity-time history of the rear free surface for a steel target. The smooth curve is a "best" fit to the actual data points obtained from the interferometer oscillographs. To determine $E(x)$, the technique of providing trial profiles in Eq. (2) and calculating $V(t)$ and the complementary technique of differentiating the $V(t)$ curve for use in Eq. (3) were both tried and yielded equivalent results. Figure 4 and 5 show energy deposition profiles for quartz and steel, respectively. Quartz results are indicated for both a position in the magnetic pinch and a point downstream from the pinch. All of the results have been normalized so that comparisons of shape can be made; however, absolute energy deposition profiles may be determined also.

Since a purely elastic theory was used in the data analysis, the pressures generated in the targets were required to not exceed the elastic limits. Using the reported¹⁶ values for the Hugoniot elastic limits of the materials, it was possible to estimate the maximum allowable dose levels. Because of machine dose irreproducibility and uncertainties in the elastic limit for a given target, the criterion used to determine whether an individual shot yielded an elastic stress pulse was the length of time measured for the fast portion of the release wave. For the model employed, this time should correspond to half the beam deposition time, 35 ns. Data which did not meet this criterion, i.e., with release times greater than 35 ns, were rejected for the reason of plastic deformation. All of the quartz data were kept, but some of the steel data at the highest doses were rejected.

The major source of error in the velocity determination was a possible misalignment between the laser beam reflection point on the target rear surface and the center of the electron beam impinging on the target front surface. Such a misalignment was usually the result of electron beam wander, an inherent problem of repeatability. Another factor which may have contributed to a spread in the data was a nonrepeatable aspect of the energy spectrum of the beam.

Several points should be noted regarding the deposition profiles. First, they appear to have the proper shape and dependence upon atomic number. All of the profiles rise continuously to peaks within the solid, and are more narrow for higher atomic numbers and densities. A comparison of the profiles for quartz in and out of the pinch region suggests that the angular distribution of electrons depends on axial position. In the pinch region itself, the high-front-surface absorption indicates a greater number of electrons with angles that deviate from the axial direction.

Finally, in contrast to other techniques, thermoelastic dosimetry has been shown to yield useful deposition profile information in the high intensity pinch region of the electron beam. Continuous profiles can be obtained at all dose levels as long as the absorbing medium remains elastic. There are no problems associated with heat loss or volume averaging as in the case of thin calorimeters. In principle, brittle crystal thermoelastic absorbers should be capable of providing dosimetry information at dose levels several times those encountered at present.

FIG. 3.--Back-free-surface velocity of steel versus time. Time is measured backward from the point at which the velocity goes from positive to negative values.

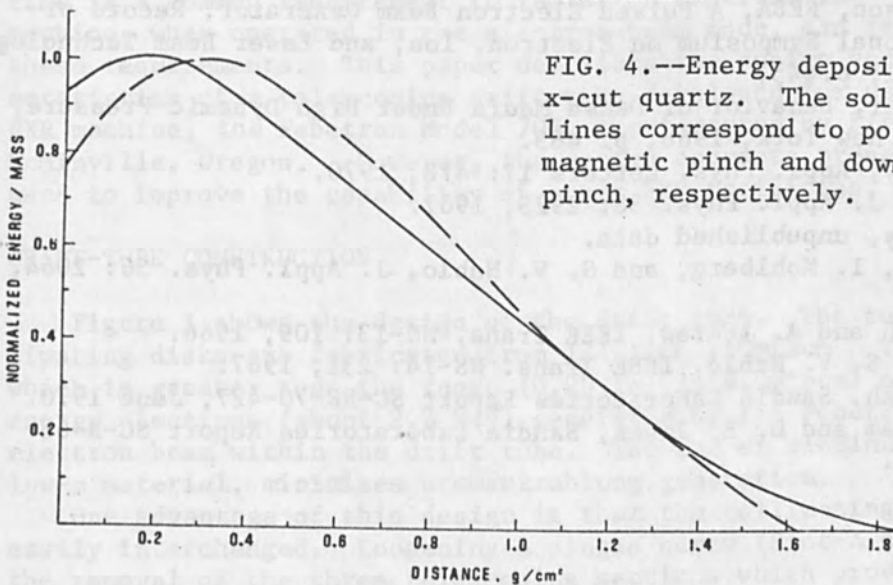
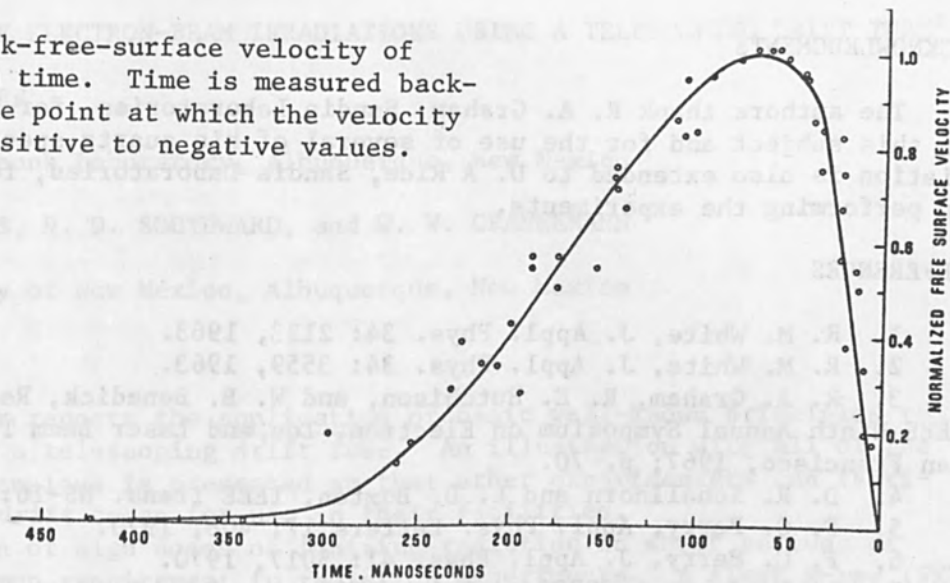


FIG. 4.--Energy deposition profiles in x-cut quartz. The solid and dashed lines correspond to positions in the magnetic pinch and downstream of the pinch, respectively.

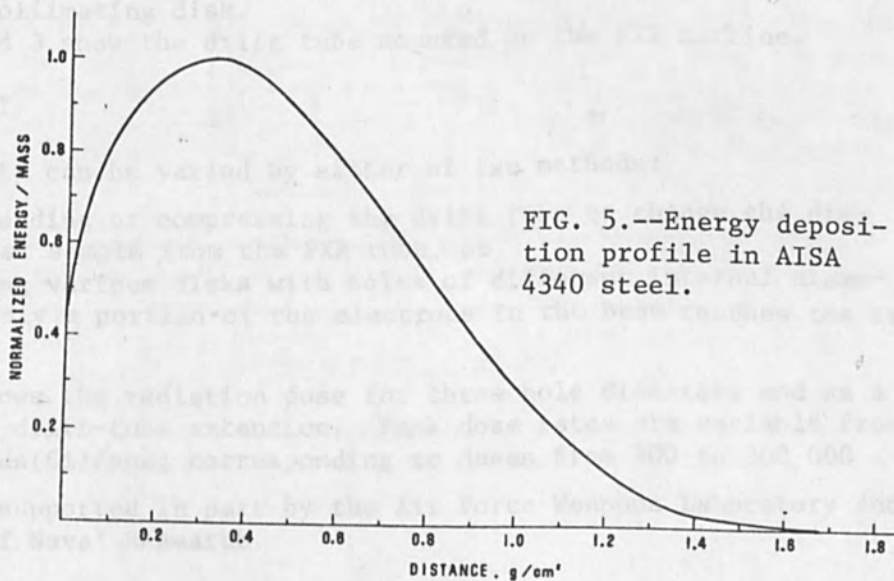


FIG. 5.--Energy deposition profile in AISA 4340 steel.

ACKNOWLEDGMENTS

The authors thank R. A. Graham, Sandia Laboratories, for his interest in this subject and for the use of several of his quartz specimens. Appreciation is also extended to D. A Rice, Sandia Laboratories, for assistance in performing the experiments.

REFERENCES

1. R. M. White, J. Appl. Phys. 34: 2123, 1963.
2. R. M. White, J. Appl. Phys. 34: 3559, 1963.
3. R. A. Graham, R. E. Hutchison, and W. B. Benedick, Record of the IEEE Ninth Annual Symposium on Electron, Ion, and Laser Beam Technology, San Francisco, 1967; p. 70.
4. D. R. Schallhorn and L. D. Buxton, IEEE Trans. NS-16: 242, 1969.
5. F. C. Perry, Appl. Phys. Letters 17: 408, 1970.
6. F. C. Perry, J. Appl. Phys. 41: 5017, 1970.
7. D. L. Johnson, REBA, A Pulsed Electron Beam Generator, Record of the 11th International Symposium on Electron, Ion, and Laser Beam Technology, San Francisco, 1971; p.445.
8. L. M. Barker, Behavior of Dense Media Under High Dynamic Pressure, Gordon and Breach, New York, 1968; p. 483.
9. F. C. Perry, Appl. Phys. Letters 17: 478, 1970.
10. S. W. Key, J. Appl. Phys. 38: 2923, 1967.
11. F. C. Perry, unpublished data.
12. H. Lackner, I. Kohlberg, and S. V. Nablo, J. Appl. Phys. 36: 2064, 1965.
13. J. E. Rauch and A. Andrew, IEEE Trans. NS-13: 109, 1966.
14. J. Dow and S. V. Nablo, IEEE Trans. NS-14: 231, 1967.
15. L. A. Harrah, Sandia Laboratories Report SC-RR-70-427, June 1970.
16. R. A. Graham and O. E. Jones, Sandia Laboratories Report SC-R-68-1857, October 1968.

HIGH-DOSE-RATE ELECTRON-BEAM IRRADIATIONS USING A TELESCOPING DRIFT TUBE*

C. L. SCHROEDER

Air Force Weapons Laboratory, Albuquerque, New Mexico

D. H. PHILLIPS, H. D. SOUTHWARD, and W. W. GRANNEMANN

The University of New Mexico, Albuquerque, New Mexico

INTRODUCTION

This paper reports the application of basic well-known principles to the design of a telescoping drift tube. An illustration with all of the necessary dimensions is presented so that other experimenters can fabricate similar drift tubes for use in their facilities.

Deposition of high doses of ionizing radiation in short periods of time is a common requirement in radiation experiments. A flash x-ray (FXR) machine, when operated in the electron-beam mode, can be used to satisfy these requirements. This paper describes the design and operational characteristics of a telescoping drift tube developed for use with a 2.3-MeV FXR machine, the Febetron Model 705, manufactured by Field Emission Corp., McMinnville, Oregon. However, the design concepts presented here can be used to improve the capability of other FXR facilities.

DRIFT-TUBE CONSTRUCTION

Figure 1 shows the design of the drift tube. The tube walls and collimating disks are fabricated from 1/4-inch aluminum. This thickness, which is greater than the range (0.20 in. in aluminum) of the highest-energy electrons (about 2.2 MeV) generated by the Febetron, contains the electron beam within the drift tube. The use of aluminum, which is a low-z material, minimizes bremsstrahlung generation.

One advantage of this design is that the collimating disks can be easily interchanged. Loosening a single screw (Slot-A setscrew) allows the removal of the three telescoping sections which provides front-end access to the collimating disk.

Figures 2 and 3 show the drift tube mounted on the FXR machine.

RADIATION OUTPUT

The dose rate can be varied by either of two methods:

- (1) by extending or compressing the drift tube to change the distance of the test sample from the FXR tube, or
- (2) by using various disks with holes of different internal diameters, so that only a portion of the electrons in the beam reaches the test sample.

Figure 4 shows the radiation dose for three hole diameters and as a function of the drift-tube extension. Peak dose rates are variable from 10^{10} to 10^{13} rads(Si)/sec, corresponding to doses from 300 to 300 000

*This work supported in part by the Air Force Weapons Laboratory and by the Office of Naval Research.

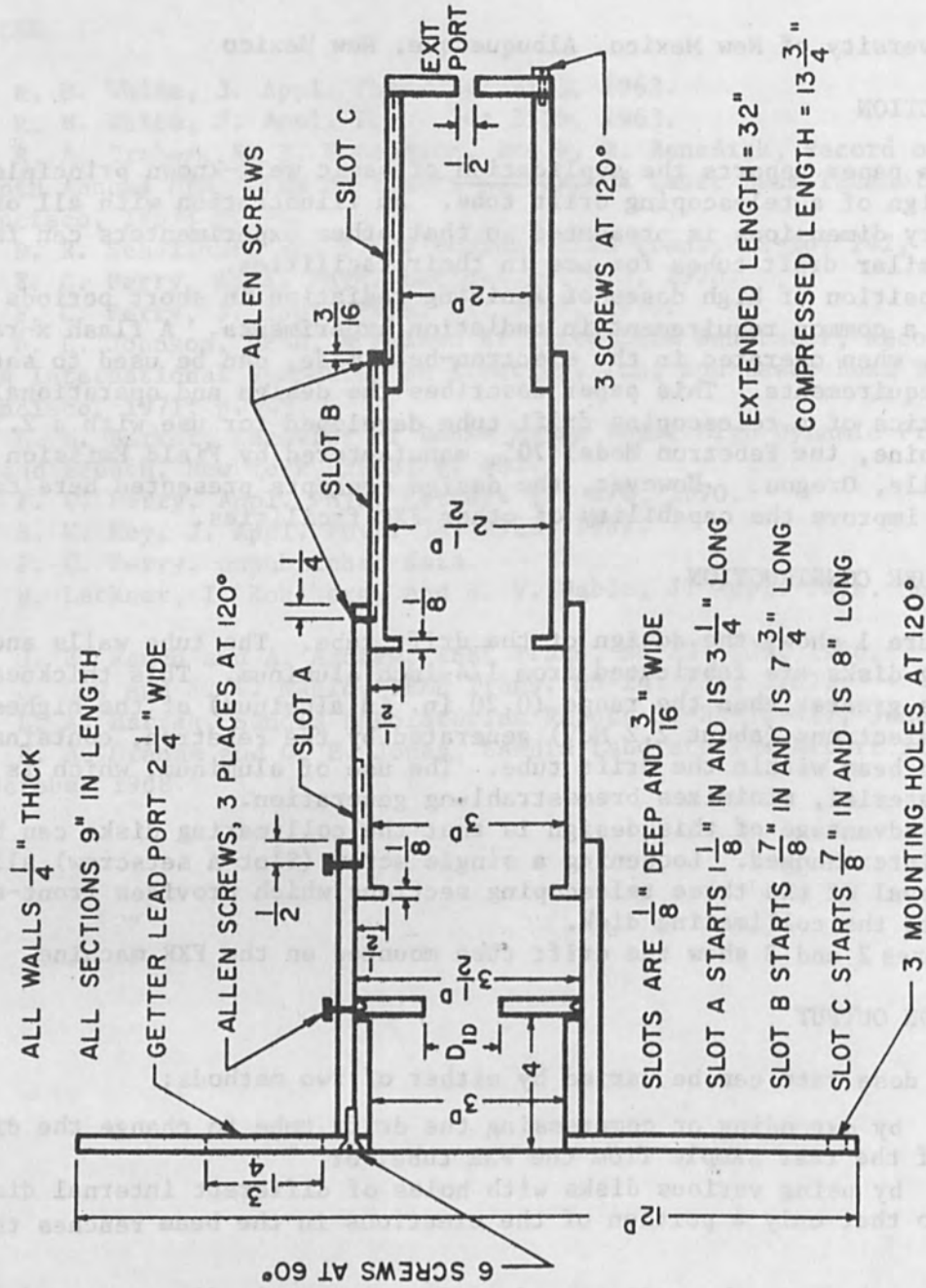


FIG. 1.--Construction details of telescoping drift tube; dimensions in inches. $D_{ID} = 1.5, 0.5, \text{ or } 0.25$ in.

rads(Si) per pulse. The radiation dose was measured 1 in. from the exit port of the drift tube because test samples are normally placed at that position.

Cobalt glass chips (manufactured by Bausch and Lomb, Rochester, New York) were used for dosimetry. These chips are made from a glass impregnated with a cobalt compound which darkens when irradiated. The amount of darkening is proportional to the absorbed radiation dose. The optical density of the cobalt glass chips is measured both before and after irradiation using filtered light with a wavelength of about 3600 Å. The dose is then read from a calibration curve of change in optical density versus dose.

Cobalt glass is usable from about 2 kilorads to 1 megarad at high dose rates. Its absolute accuracy is comparable to that of thermoluminescent dosimeters (TLDs)--about 20 per cent.

APPLICATIONS

The use of a drift tube satisfies one operational requirement of the Febetron--most of the electrons are returned to the FXR machine via the walls of the drift tube. Containing the electron beam in the drift tube structure

- (1) simplifies the design of collimation shields for the test fixture; and
- (2) reduces the amount of beam energy that ionizes air and produces electromagnetic interference (EMI).

This drift tube is most useful for radiation-effects experiments in which the experimenter needs to vary the test-sample dose or dose rate without changing the operating conditions such as charging voltage, magnet current, etc., of the FXR machine.

Most experimental applications of electron beams require the consideration of dose-depth profiles in the test sample. Although this drift tube does not employ techniques like diffusers, scattering foils, etc., which degrade the electron energy spectrum, the electron beam contains some short-range, low-energy electrons. The two major sources of low-energy electrons emanating from the exit port are

- (1) the FXR machine, which inherently produces low-energy electrons on the leading and trailing edges of the radiation pulse, when the pulser output voltage is low; and
- (2) secondary emission from the collimating disk and the drift-tube walls, which contributes to the low-energy portion of the total electron energy spectrum.

Applications requiring a high-energy electron beam with no low-energy electrons can be satisfied by using the deflection-tube design concepts described in a related paper.¹

REFERENCE

1. D. H. Phillips, H. D. Southward, and W. W. Grannemann, Removing the spectrum dependence from electron-beam dosimetry measurements by using a magnetic electron deflection tube (next paper in this Record).

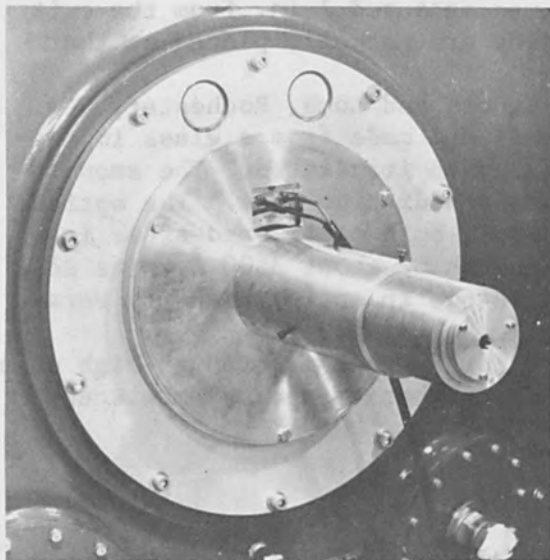


FIG. 2.--Fully compressed telescoping drift tube mounted on Febetron.

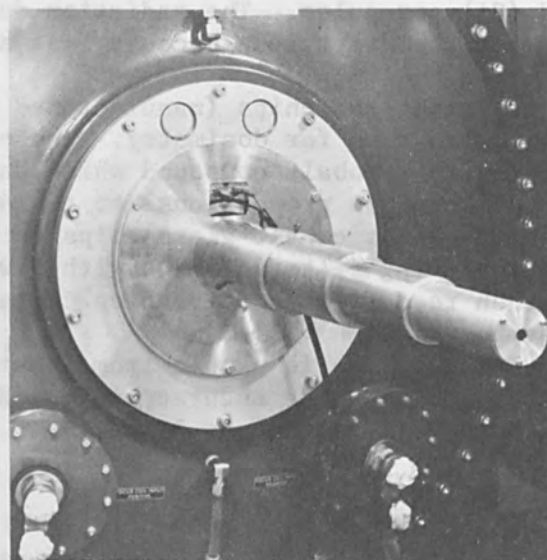


FIG. 3.--Fully expanded telescope drift tube mounted on Febetron.

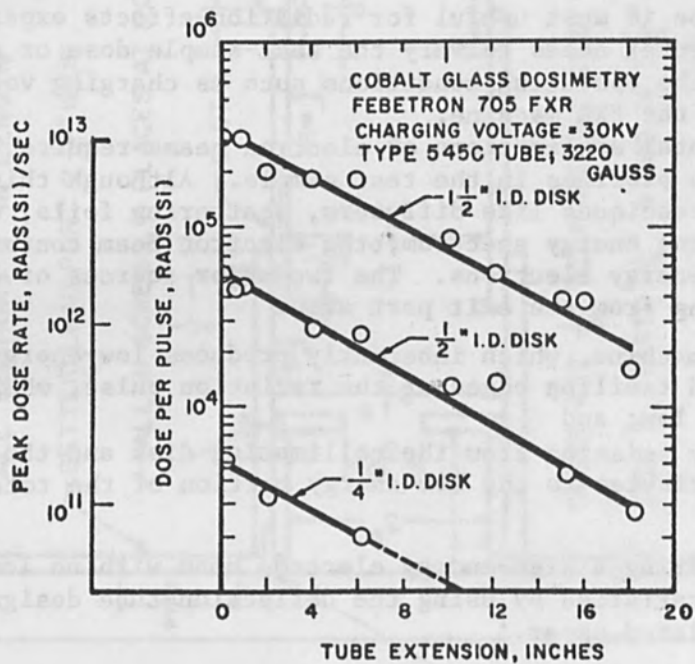


FIG. 4.--Radiation output as a function of drift tube extension. Fully compressed, zero length. Fully expanded, 18.25 in.

REMOVING THE SPECTRUM DEPENDENCE FROM ELECTRON-BEAM DOSIMETRY MEASUREMENTS BY USING A MAGNETIC ELECTRON DEFLECTION TUBE*

D. H. PHILLIPS, W. W. GRANNEMANN, and H. D. SOUTHWARD

The University of New Mexico, Albuquerque, New Mexico

The low-energy portion of a flash x-ray machine electron spectrum is undesirable in that irradiation of test samples using low-energy electron beams complicates dosimetry calculations. This paper describes the application of well-known basic principles in the design of a deflection tube which uses a 400-gauss magnet to deflect all low-energy ($E < 0.5$ MeV) electrons out of the horizontal electron beam. The remaining high-energy electrons can be used to irradiate test samples. If an electron beam contains no electrons with energies below 0.5 MeV, the absorbed dose in silicon semiconductor devices is (1) directly proportional to electron fluence, and (2) independent of the electron energy spectrum. For $0.5 < E < 3$ MeV electrons,

$$\gamma(\text{rads}(\text{Si})) = 2.6 \times 10^{-8} \phi \text{ (electrons/cm}^2\text{)}$$

$$\dot{\gamma}(\text{rads}(\text{Si})/\text{sec}) = 2.6 \times 10^{-8} \dot{\phi} \text{ (electrons/cm}^2\text{-sec)}$$

In this paper we present (1) the radiation output characteristics of the deflection tube and Febetron 705 flash x-ray (FXR) machine, (2) results of electron-beam dosimetry calculations, (3) optimum Faraday cup electron flux sensitivity, and (4) optimum Faraday cup dose-rate sensitivity for electron-beam transient radiation effects on electronics (TREE) experiments.

INTRODUCTION

Many flash x-ray machines are designed to operate in either the bremsstrahlung x-ray mode or the electron-beam mode. The FXR machine at The University of New Mexico is a Febetron 705. The pulser is charged to some desired voltage and multiplies the voltage by a factor of 65 to 70. The pulser charging voltage may be adjusted continuously from 9 to 35 kV, resulting in an output voltage (voltage delivered to the radiation tube) of 600 kV to 2.3 MV. In the electron-beam mode, the maximum electron energy is about 2.1 MeV.

REVIEW OF BASIC ELECTRON-BEAM DOSIMETRY PRINCIPLES

Irradiation of test samples using low-energy electron beams requires the dose to be calculated according to Attix and Roesch¹ as

$$\gamma = \frac{1}{100\rho} \int_0^{E_M} S(E)\Phi'(E) dE \quad (1)$$

where a unity buildup factor has been assumed. In the above equation,

*This work supported by the Office of Naval Research.

- γ = dose (rads)
 ρ = density of absorber, or test sample (g/cm^3)
 $S(E)$ = $-dE/dX$, the stopping power
 $\Phi'(E)$ = the spectral concentration of particle fluence with respect to energy (e.g., electrons/ $\text{cm}^2\text{-MeV}$)
 E = electron energy
 E_M = the maximum electron energy in the electron beam (e.g., 2.1 MeV for the Febetron).

Appendix A outlines the solution of the Bethe equation which allows calculation of the stopping power. The results are plotted in Fig. 1 for aluminum, silicon, and SiO_2 . These value of stopping power have been used to calculate the ratio of dose to electron fluence according to

$$\frac{\gamma}{\Phi} = \left(- \frac{dE}{dX} \right) \left(\frac{1}{100\rho} \right) \quad (2)$$

The solutions of Eq. (2) are plotted in Fig. 2. The value of γ/Φ depends strongly on E for $E < 0.5$ MeV. However, the value of γ/Φ is roughly constant for $E > 0.5$ MeV.

Irradiation of test samples using low-energy electron beams complicates the dosimetry calculations. Figures 1 and 2 show that the determination of absorbed dose for test samples requires a detailed knowledge of the electron energy spectrum if the spectrum contains electrons having energies $E < 0.5$ MeV. If the spectrum contains low-energy electrons, the solution of Eq. (1) frequently requires numerical integration. In practice, it usually is not practical to determine the electron spectrum accurately enough to perform adequate dosimetry calculations using Eq. (1).

As illustrated by Fig. 1, the stopping power is nearly constant for electrons having energies in the range from 0.5 to 3 MeV. The importance of this "constant $S(E)$ " range lies in the possibility of modifying the electron energy spectrum in a manner so that a knowledge of the spectrum is not needed to measure or calculate the dose--only the electron fluence must be measured.

REMOVAL OF LOW-ENERGY ELECTRONS

The electron beam produced by a FXR machine contains low-energy electrons which can be removed from the beam by magnetic deflection. Figures 3 and 4 show the configuration of a deflection tube designed for this purpose. A 400-gauss magnet is used to deflect all low-energy ($E < 0.5$ MeV) electrons out of the horizontal electron beam. (Construction details of the deflection tube and deflection dynamics calculations are given in a technical report published by the Bureau of Engineering Research, The University of New Mexico, Albuquerque, and available from the authors.) The remaining high-energy electron spectrum can be used to irradiate test samples with more uniform dose-depth profiles in the test sample.

The deflection dynamics of electrons in air, with this deflection tube, are discussed in a related paper.² Figure 5 shows the results of calculations which relate the magnetic flux density, B_{MAX} , at the center of the deflection volume, to the minimum electron energy remaining in the horizontal electron beam. Although the deflection tube was not designed for perfect beam collimation, it is assumed that electrons deflected through an angle of 5° or more do not pass through the center exit port.

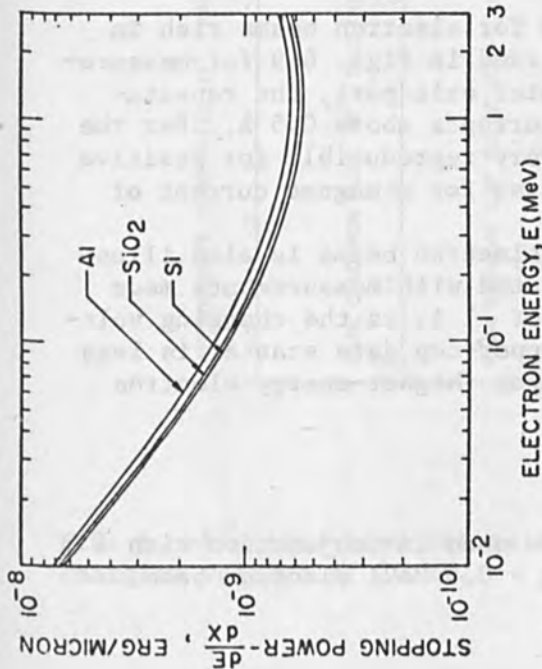


FIG. 1.--Stopping power vs electron energy.

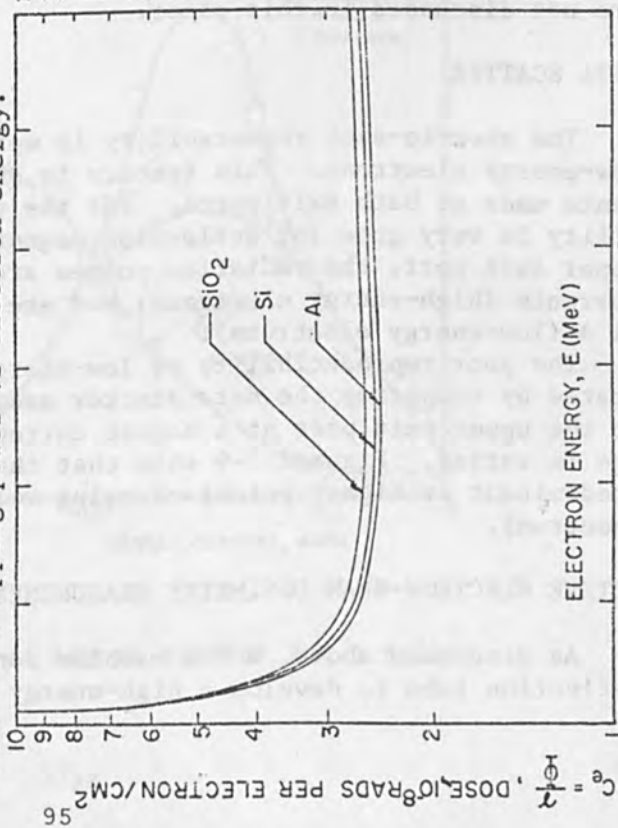


FIG. 2.--Ratio of dose to electron fluence as a function of electron energy.

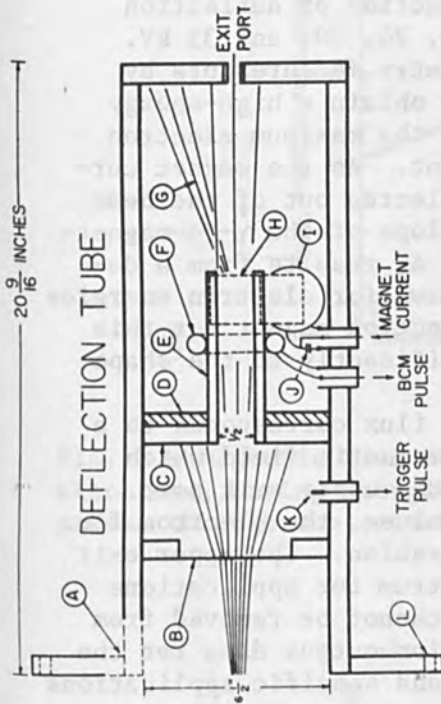


FIG. 3.--Magnetic electron deflection tube. (A) Opening for getter leads. (B) Aluminum diffuser, 4 mils thick. (C) Aluminum collimation shield. (D) Mu-metal magnetic shield to minimize interaction of electron beam with FXR machine focusing magnet. (E) Electron guide section (a short drift tube). (F) Beam current monitor coil. (G) Low-energy electrons are deflected out of horizontal electron beam. (H) Deflection magnet coil. (I) Deflection magnet coil. (J) Capacitor which insures constant magnet coil voltage during radiation pulse in presence of noise. (K) Charge-collection monitor, used to trigger oscilloscopes or other instrumentation. (L) Holes through mounting flange for mounting deflection tube to FXR machine.

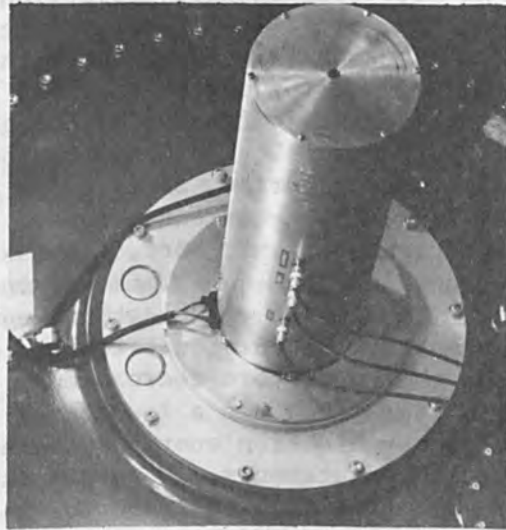


FIG. 4.--Magnetic electron deflection tube, shown mounted on Febetron 705 flash x-ray machine.

DOSE RATE

The deflection tube is intended for electron-beam experiments. When used with the Febetron, high-energy electron dose rates in silicon are variable from 2×10^8 to 3×10^{10} rads(Si)/sec. This range of dose rates may be obtained by changing the pulser charging voltage from 20 to 35 kV, thereby eliminating the need for a change in experimental configuration.

The range of dose rates can be decreased from the values given above by increasing the distance from the deflection tube to the test sample.

Figures 6-9 show the radiation output as a function of deflection magnet current for pulser charging voltages of 20, 25, 30, and 35 kV. The spectrum dependence can be removed from dosimetry measurements by use of the center exit port, with $I_{MAG} = \pm 1$ A, to obtain a high-energy spectrum of electrons. For the center exit port, the maximum electron flux is measured for zero deflection-magnet current. As the magnet current is increased, lower energy electrons are deflected out of the beam and the electron flux decreases. The change of slope of the γ -vs-magnet-current curves, for magnet currents from 0.7 to 1 A, results from a decreasing electron differential energy spectrum curve for electron energies from 0.3 to 0.5 MeV. Core saturation of the deflection magnet for this range of magnet current contributes almost insignificantly to the shape of the γ -vs-magnet-current curves.

For the upper exit port, the maximum electron flux corresponds to a magnet current of -1 A. This current produces a magnetic field which deflects the low-energy electrons upward, toward the upper exit port. As the magnet current tends to zero or positive values, the electron flux through the upper port decreases in a monotonic fashion. The upper exit port is used to obtain a low-energy electron spectrum for applications in which the electron energy spectrum dependence cannot be removed from dosimetry measurements. Consequently, the radiation-output data for the upper exit port is given here for reference only and specific applications are not discussed in this paper.

DATA SCATTER

The shot-to-shot repeatability is worse for electron beams rich in low-energy electrons. This feature is observed in Figs. 6-9 for measurements made at both exit ports. For the center exit port, the repeatability is very good for deflection-magnet currents above 0.5 A. For the upper exit port, the radiation pulses are very reproducible for positive currents (high-energy electrons) but are worse for a magnet current of -1 A (low-energy electrons).

The poor reproducibility of low-energy electron beams is also illustrated by comparing the data scatter associated with measurements made at the upper exit port at a magnet current of -1 A, as the charging voltage is varied. Figures 6-9 show that the upper-cup data scatter is less predominant at higher pulser-charging voltages (higher-energy electron spectrum).

ACTIVE ELECTRON-BEAM DOSIMETRY MEASUREMENTS

As discussed above, a FXR machine can be used in conjunction with a deflection tube to develop a high-energy ($E > 0.5$ MeV) electron beam.

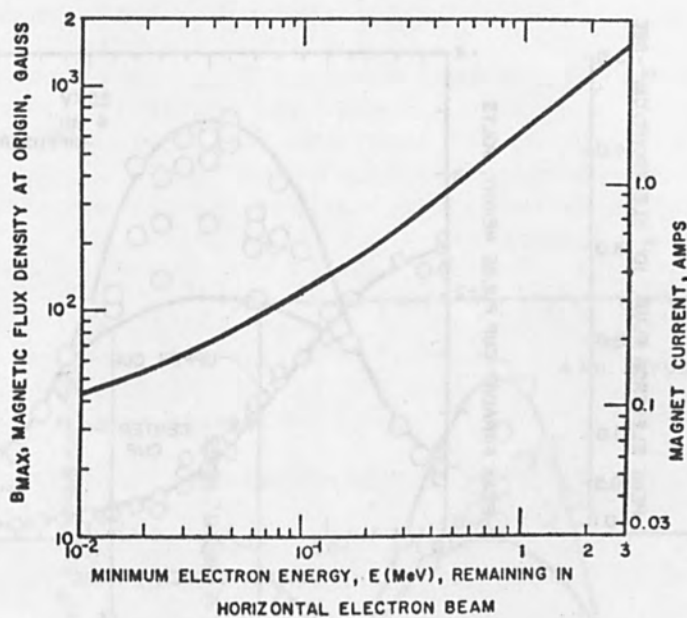


FIG. 5.--Magnetic flux density and magnet current required to deflect electrons, having energies below E, out of the horizontal beam which passes through the center exit port.

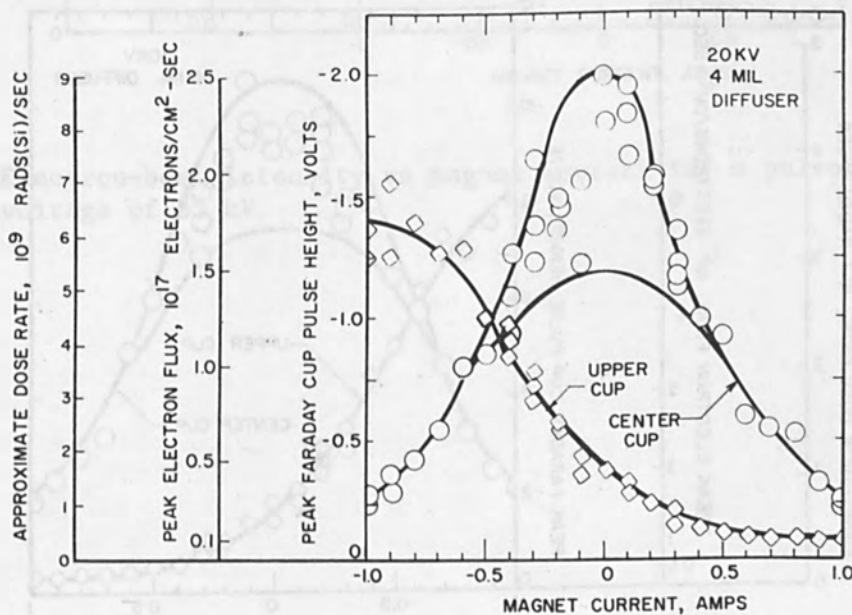


FIG. 6.--Electron-beam intensity vs magnet current for a pulser charging voltage of 20 kV.

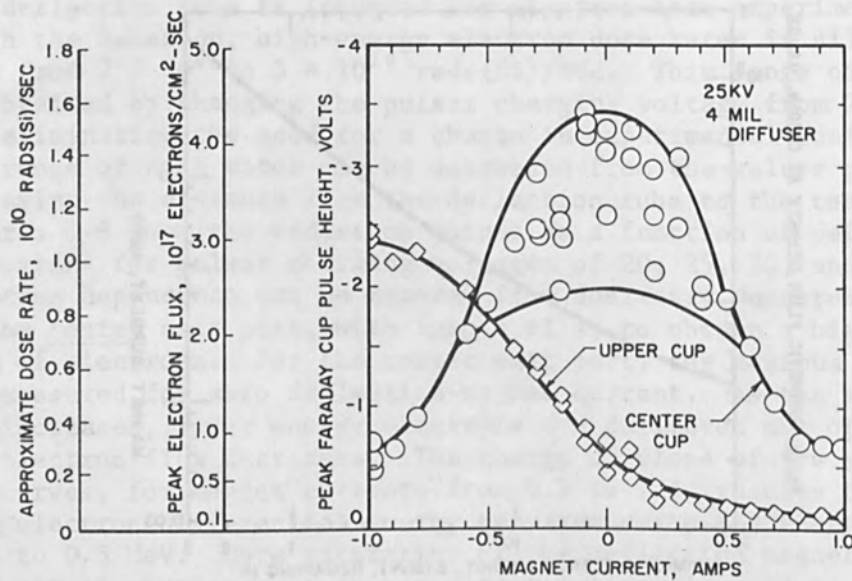


FIG. 7.--Electron-beam intensity vs magnet current for a pulser charging voltage of 25 kV.

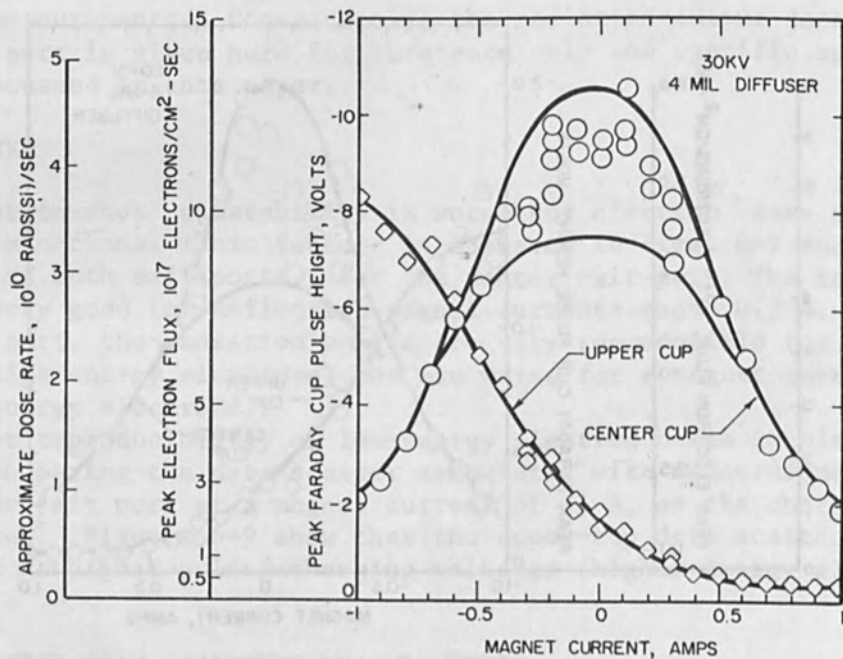


FIG. 8.--Electron-beam intensity vs magnet current for a pulser charging voltage of 30 kV.

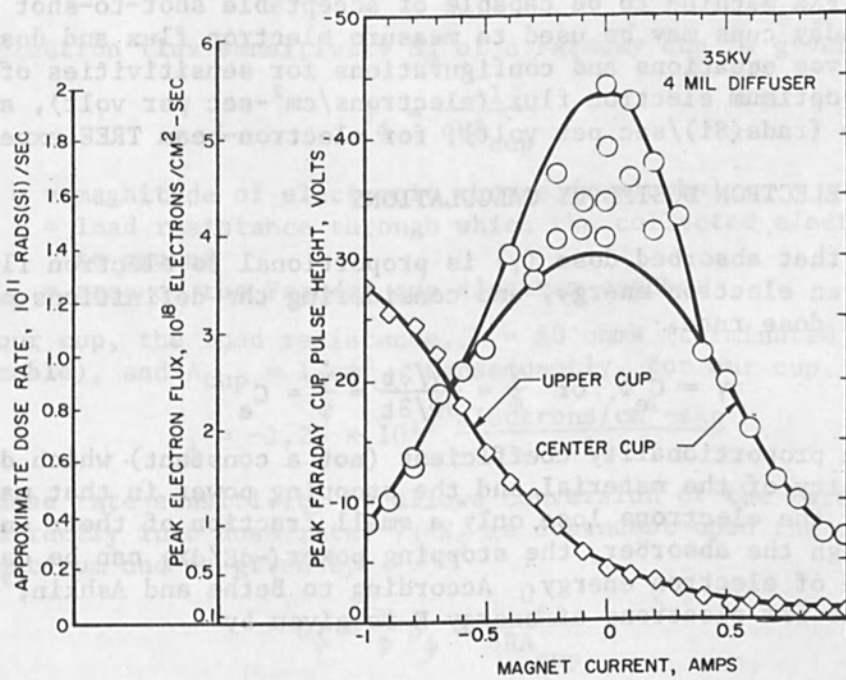


FIG. 9.--Electron-beam intensity vs magnet current for a pulser charging voltage of 35 kV.

If the electron beam contains no electrons with energies below 0.5 MeV, the absorbed dose is directly proportional to electron fluence,

$$\text{or } \left. \begin{aligned} \gamma &= 2.6 \times 10^{-8} \phi \\ \dot{\gamma} &= 2.6 \times 10^{-8} \dot{\phi} \end{aligned} \right\} 0.5 < E < 3 \text{ MeV} \quad (3)$$

where

$$\begin{aligned} \phi &= \text{electron fluence (electrons/cm}^2\text{)} \\ \dot{\phi} &= \text{electron flux (electrons/cm}^2\text{-sec)} \\ \dot{\gamma} &= \text{dose rate in (rads/sec)} \end{aligned}$$

Assuming the FXR machine to be capable of acceptable shot-to-shot repeatability, Faraday cups may be used to measure electron flux and dose rate. Appendix B gives equations and configurations for sensitivities of the Faraday cup, optimum electron flux (electrons/cm²-sec per volt), and optimum dose rate (rads(Si)/sec per volt), for electron-beam TREE experiments.

APPENDIX A: ELECTRON DOSIMETRY CALCULATIONS

Assuming that absorbed dose (γ) is proportional to electron fluence (ϕ) for a given electron energy, and considering the definitions of electron flux and dose rate,

$$\gamma = C_e \phi \quad \text{or} \quad \frac{\gamma}{\phi} = \frac{\partial \gamma / \partial t}{\partial \phi / \partial t} = \frac{\dot{\gamma}}{\dot{\phi}} = C_e \quad (A-1)$$

where C_e is a proportionality coefficient (not a constant) which depends upon the density of the material and the stopping power in that material. Assuming that the electrons lose only a small fraction of their energy in passing through the absorber, the stopping power ($-dE/dX$) can be calculated as a function of electron energy. According to Bethe and Ashkin,³ the stopping power for electrons of energy E is given by

$$\begin{aligned} -\frac{dE}{dX} &= \frac{2\pi e^4 NZ}{m_0 v^2} \left\{ \ln \left[\frac{m_0 v^2 E}{2I^2 (1 - \beta^2)} \right] - \left(2\sqrt{1 - \beta^2} - 1 + \beta^2 \right) \ln 2 \right. \\ &\quad \left. + (1 - \beta^2) + \frac{1}{8} \left[1 - \sqrt{1 - \beta^2} \right]^2 \right\} \text{ ergs/cm} \quad (A-2) \end{aligned}$$

where N = number of absorbing atoms (cm⁻³)
 Z = atomic number of absorbing medium
 E = kinetic energy of electron (ergs)
 I = average ionization energy of absorber (ergs)
 e = electron charge (esu)
 m_0 = electron rest mass (g)
 v = velocity of electron (cm/sec)
 c = velocity of light (cm/sec)
 β = v/c

Collision energy loss results from an interaction with orbital electrons and hence should be proportional to electron density, $N_e = NZ$, as is the case. For compounds, such as SiO₂, the average values of N , Z , and I for the compound must be used.

Equation (A-2) neglects energy loss due to bremsstrahlung generation. Bremsstrahlung production accounts for less than 5 per cent of the energy lost in low-Z materials for electron energies ($E \leq 2.1$ MeV) which can be generated by the Febetron.

Average ionization energy I has been the subject of extensive theoretical investigation, but values are probably best obtained from experiment. In the solution of Eq. (A-2), we have used values of I obtained by interpolation and extrapolation of data obtained by Bakker and Segre.⁴ Solutions of Eq. (A-2) are plotted in Fig. 2 for aluminum, silicon, and SiO₂.

APPENDIX B: OPTIMUM FARADAY CUP SENSITIVITIES FOR TREE EXPERIMENTS

The electron flux sensitivity S_ϕ of a Faraday cup is given by

$$S_\phi = \frac{-1}{qRA_{\text{cup}}} \quad (\text{B-1})$$

where q = magnitude of electronic charge (coulombs)
 R = load resistance through which the collected electrons flow to ground

A_{cup} = area of the Faraday cup electron catcher

For our cup, the load resistance, $R = 50$ ohms (terminated 50-ohm coaxial cable), and $A_{\text{cup}} = 1$ cm². Consequently, for our cup,

$$S_\phi = -1.25 \times 10^{17} \frac{\text{electrons/cm}^2\text{-sec}}{\text{volt}} \quad (\text{B-2})$$

The dose rate sensitivity S_γ^* allows conversion of the Faraday cup voltage directly into dose rate, $\dot{\gamma}$; S_γ^* is dependent upon the electron energy spectrum and is given by

$$S_\gamma^* = \frac{\gamma}{\phi} S_\phi = \frac{C_e}{qRA_{\text{cup}}} \quad (\text{B-3})$$

If the electron beam contains only high-energy electrons ($0.5 < E < 2.1$ MeV), the values of γ/ϕ and S_γ^* are independent of the electron energy spectrum. This condition can be achieved by using the deflection tube to remove all low-energy electrons from the horizontal electron beam which passes through the center exit port. The value of the dose rate sensitivity is then

$$S_\gamma^* = -3.12 \times 10^9 \frac{\text{rads(Si)/sec}}{\text{volt}} \quad (\text{B-4})$$

For TREE experiments, this dose rate sensitivity lies in the optimum range of $10^9 < S_\gamma^* < 10^{10}$ rads(Si)/(sec-V). Smaller values of S_γ^* could lead to cable crosstalk (lower signal-to-noise ratios) because of the large Faraday cup signals. Larger values of S_γ^* would result in lower Faraday cup signals which, if too low, could lead to measurement difficulty in the presence of noise. The Faraday cup voltage sensitivity can be varied at will by changing the area of the Faraday cup.

REFERENCES

1. F. H. Attix and W. C. Roesch, Radiation Dosimetry, Academic Press, New York, 1968; 2d ed. vol. 1, p. 34.

2. D. H. Phillips, W. W. Grannemann, and D. E. Dunham, Magnetic electron deflection tube, IEEE Trans. NS-18: 804-805, 1971.
3. H. A. Bethe and J. A. Ashkin, Experimental Nuclear Physics (E. Segrè, ed.), Wiley, New York, 1953; vol. 1.
4. C. J. Bakker and E. Segrè, Physics Review, 811, 489, 1951.

BIBLIOGRAPHY

- D. R. Alexander, J. S. Nichols, and A. H. Hoffland, Active measurements in the electron beam on the AFWL 2-MeV Field Emission flash x-ray machine, presented at the Instrumentation for Nuclear Weapon Effects Simulation Symposium on March 6, 1970; in AFSWC-TR-70-5, vol. 3, pp. 47-63, March 1970.
- J. L. Andrews and J. E. Tarka, Recent developments in transient radiation effects testing, *ibid.*, pp. 65-97.
- H. A. Bethe, Handbuch der Physik, Springer, Berlin, 1933; vol. 24, p. 273.
- R. E. Lapp and H. L. Andrews, Nuclear Radiation Physics, Prentice-Hall, Englewood Cliffs, N. J., 1963; p. 154.
- J. P. Mitchell and D. K. Wilson, Surface effects of radiation on semiconductor devices, Bell Syst. Tech. J. 44: pp. 1-80, 1967.
- J. E. Rauch, The determination of megavolt electron spectra from dose deposition profiles, presented at the IEEE Annual Conference on Nuclear and Space Radiation Effects, University of Montana, Missoula, Montana, July 18, 1968.

CONCENTRATION PROFILES AND ENHANCED DIFFUSION IN ION IMPLANTED SILICON STUDIED BY RADIOACTIVATION ANALYSIS

KENJI GAMO, MASAYA IWAKI, KOHZOH MASUDA, and SUSUMU NAMBA

Electrical Engineering, Osaka University, Toyonaka, Osaka, Japan

SHINJI ISHIHARA and ITSURO KIMURA

Research Reactor Institute, Kyoto University, Kumatori, Sennan-Gun, Osaka, Japan

Concentration profiles of ion-implanted antimony and indium are measured by means of radioactivation analysis. Indium is implanted in single-crystal silicon and amorphous silicon produced by nitrogen implantation and the effect of crystalline phase on impurity distribution is investigated. The effect of enhanced diffusion is also investigated. Concentration profiles of room-temperature ion-implanted indium are in agreement with those predicted by LSS theory. Antimony and indium show enhanced diffusion during heat treatment after room temperature implantation but in the case of indium enhanced diffusion occurs only in the lower concentration region than about 1×10^{19} In/cm³. The diffusion coefficient and profiles are obtained by solving the diffusion equation.

INTRODUCTION

Recently ion implantation has received considerable interest as a low-temperature, nonequilibrium doping method for semiconductor materials. It is of primary importance to dope impurity atoms with a desired concentration profile for semiconductor device design and fabrication. Ion-implantation techniques offer a simple controllable method for achieving impurity-concentration profiles not obtainable through the usual thermal techniques.

The concentration profiles of ion-implanted impurities are determined mainly by two factors, the collision of the projectile with target atoms and the enhanced diffusion during heat treatment after ion implantation or during high-temperature ion implantation. The collision phenomena are different from those in a single crystal and amorphous target. Channeling, for example, occurs in the single-crystal target. Therefore the profiles in single-crystal silicon and in amorphous silicon may be different.

Lindhard et al. developed general theory on average range and range straggling in amorphous target materials (LSS theory¹). Gibbons et al. carried out numerical calculation of average range and range straggling in several semiconductor materials according to LSS theory.² Recently Brice calculated these values in silicon target according to extended LSS theory developed by him.³

In this report the concentration profiles of ion-implanted antimony and indium into silicon are measured by radioactivation analysis and the results are compared with theoretical calculations. The effect of the crystalline phase on ion-implanted impurity distribution is also investigated. Enhanced diffusion during heat treatment after room temperature implantation is also measured and discussed.

the same region. This fact indicates that this tail is caused by channeling or interstitial diffusion. The behaviors of interstitial impurities of column 3 elements in silicon crystals has not been well investigated. No observations have been reported on the motion of interstitial indium in silicon crystals. It has been observed that aluminum interstitials in silicon crystals do not move at room temperature. Aluminum interstitials show the annealing stage at about 200°C.⁸ In light of this fact, channeling seems to be more a probable mechanism for the formation of the tail region of the indium concentration profile.

Enhanced diffusion of ion-implanted impurity in silicon was observed for antimony and indium during heat treatment after room-temperature ion implantation. The results are shown in Figs. 4 and 5. Figure 4 shows the concentration profiles of 20-KeV ion-implanted antimony before and after heat treatment at 700° for 20 min. From these results it is clear that the diffusion of antimony is markedly enhanced. The normal thermal diffusion coefficient of antimony in silicon crystals is extrapolated to be about 1×10^{-20} cm²/sec⁹. With this diffusion coefficient no observable diffusion occurs during heat treatment at 700°C for 20 min. The concentration profiles of 45-KeV indium before and after heat treatment at 900°C for 20 min after room-temperature ion implantation are shown in Fig. 5. In this case enhanced diffusion does not occur in the concentration region higher than about 1×10^{19} /cm³.

It was observed that outdiffusion of antimony does not occur during heat treatment at 800°C for 20 min. For the measurement of outdiffusion, samples were sealed in vacuum in a quartz tube after the neutron activation and then annealed. The intensity of γ ray emitted from an unidentified isotope evaporated from silicon samples was about 2 per cent of that of implanted antimony left in the silicon samples and the γ ray of antimony evaporated from silicon was completely masked by that of the unidentified isotope. Implanted indium also seems not to show outdiffusion within the experimental error of about 20 per cent during heat treatment at 900°C for 20 min.

The concentration profiles and the diffusion coefficient of ion implanted antimony and indium were obtained as follows by solving the diffusion equation. The diffusion of ion-implanted impurity is assumed to be expressed as

$$\frac{\partial N(x,t)}{\partial t} = D \frac{\partial^2 N(x,t)}{\partial x^2} \quad (1)$$

where $N(x,t)$ is the concentration of ion-implanted impurities, D is the diffusion coefficient, x is a distance, and t is time. For antimony Eq. (1) is solved under the condition

$$Q = \int_0^{\infty} N(x,T) dx \quad (2)$$

where Q is the total dose and T is the duration of the heat treatment. This condition means that evaporation from the surface does not occur. The initial concentration profile is assumed to be given by LSS theory:

$$N(x,0) = (Q/\sqrt{2\pi\sigma^2}) \exp [-(x - \bar{R}_p)^2/2\sigma^2] \quad (3)$$

EXPERIMENTAL PROCEDURES

Silicon crystals used were of about 5Ω cm boron doped p type and about 0.01Ω cm antimony doped n type. Antimony doped silicon was used only for room-temperature indium-ion implantation. The amorphous layer was formed by bombarding 45-KeV nitrogen molecular ions with a dose of about $5 \times 10^{15}/\text{cm}^2$.

Ion implantation was carried out at room temperature. The incident direction of the ion beam was tilted at about 8° to the 111 axis in order to reduce the effect of channeling. After the ion implantation the radioactivation of antimony and indium was carried out by means of (n, γ) nuclear reaction by exposure to a neutron flux of 2.8×10^{13} neutrons/ cm^2 sec. (Kyoto University reactor was used for the activation.) After the activation the samples were sectioned by anodization and dissolution of the anodic oxide in hydrofluoric acid solution. Details of anodization method used in the present experiment are described elsewhere.⁴ The thickness removed by anodization was determined by a multiple interference microscope or by the amount of radioisotope ^{122}Sb for antimony doped samples. Half-life determination and γ -ray spectral analysis by using a NaI well-type scintillator and a 100-channel pulse height analyzer were used for identification of the isotope $^{116\text{m}}\text{In}$ and ^{122}Sb .

RESULTS AND DISCUSSION

The concentration profiles of room-temperature ion-implanted indium in single-crystal silicon are shown in Fig. 1. The profiles seem to be slightly asymmetric, falling off sharply in the region from the peak to the surface and a tail in the deeper region. This characteristic may be caused by channeling along the high-order crystal axis or by rapid interstitial diffusion.⁵ This tail has been often found for the ion-implanted impurities in silicon.^{6,7} Marsh et al. observed a nearly exponential tail for bismuth implanted in silicon and suggests that this tail is formed from channeled particles.⁶

Theoretical values of the average projected range and the projected standard deviation can be obtained by LSS theory. These values are calculated by Johnson and Gibbons² in first-order approximation and by Brice³ in second-order approximation. Both Johnson and Brice assumed in applying the LSS theory that the ion-concentration profile is Gaussian. The experimental values and the theoretical values of the average projected range and the projected standard deviation are compared in Fig. 2. The experimental values of the projected standard deviation were determined as $0.47w$, where w is the half width at a tenth of the maximum concentration. As can be seen from Fig. 2, the experimental values and the calculated (by Brice³) are in agreement with each other.

The effect of crystalline phase on ion-implanted impurity distribution is shown in Fig. 3. The 45 KeV indium ion was implanted at room temperature in amorphous silicon produced by bombardment with 45 KeV nitrogen molecular ion at room temperature and in single-crystal silicon along the direction tilted at about 8° to the 111 axis. From the results shown in Fig. 3 it is clear that the concentration profiles for single-crystal silicon implanted along a random direction and for amorphous silicon are similar to each other except in the tail region. The concentration profile for single-crystal silicon shows the tail where the concentration decreases gradually, whereas that for amorphous silicon does not show the tail, falling off sharply in

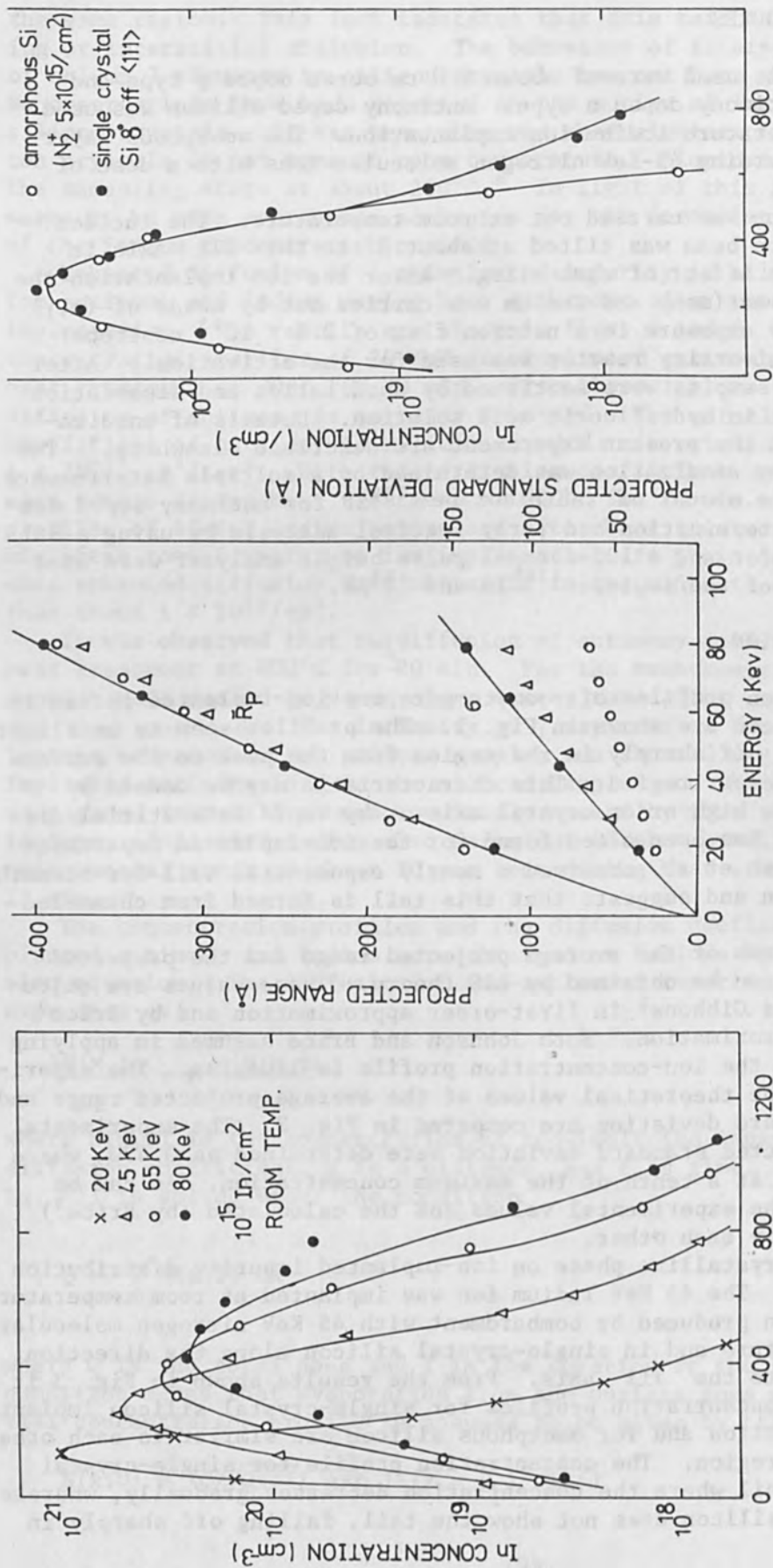


FIG. 1.--Concentration profiles of indium implanted in silicon single crystals in random direction at room temperature.

FIG. 2.--Average projected range and standard deviation of ion-implanted indium in silicon: ● experimental average projected range and its standard deviation; ○ calculated values by Johnson et al²; Δ calculated values by Brice.³

FIG. 3.--Comparison of concentration profiles of indium implanted in amorphous silicon and in single-crystal silicon along the direction tilted at about 8° to the <111> axis.

The solution of Eq. (1) is

$$N(x, T) = \frac{Q}{\sqrt{2\pi(\sigma^2 + 2DT)}} \left\{ \exp\left[-\frac{(x - \bar{R}_p)^2}{2\sigma^2 + 4DT}\right] + \exp\left[-\frac{(x + \bar{R}_p)^2}{2\sigma^2 + 4DT}\right] \right\} \quad (4)$$

where \bar{R}_p is the average projected range and σ is the projected standard deviation of range. The diffusion coefficient is assumed to be independent of a distance x in Eq. (3). The average projected range and the projected standard deviation are estimated to be about 114 Å and 35 Å according to the results given by Brice.³ The solid curve shown in Fig. 4 indicates the results of the calculation by using these values and diffusion coefficients of 1.1×10^{-15} cm²/sec. The experimental values of the average projected range and the projected standard deviation could not be determined. These values were not important in estimating the diffusion coefficient. The values of 114 Å and $\sigma = 60$ Å gave the diffusion coefficient of 0.97×10^{-15} cm²/sec and the same concentration profile as that indicated in Fig. 4.

For indium the diffusion coefficient seems to depend on a distance x from the result shown in Fig. 5. If the diffusion coefficient is assumed to be D_1 for $0 \leq x \leq l + \bar{R}_p$ and D_2 for $x \geq l + \bar{R}_p$ the diffusion equation is expressed as

$$D_1 \frac{\partial^2 N_1(x, t)}{\partial x^2} = \frac{\partial N_1(x, t)}{\partial t} \quad 0 \leq x \leq (l + \bar{R}_p)$$

$$D_2 \frac{\partial^2 N_2(x, t)}{\partial x^2} = \frac{\partial N_2(x, t)}{\partial t} \quad x \geq (l + \bar{R}_p) \quad (5)$$

The initial condition and boundary condition are assumed to be given by

$$N(x, 0) = \frac{Q}{\sqrt{2\pi\sigma^2}} \exp\left[-\frac{(x - \bar{R}_p)^2}{2\sigma^2}\right]$$

$$N_1[(l + \bar{R}_p), t] = N_2[(l + \bar{R}_p), t] \quad (6)$$

$$D_1 \frac{\partial N_1[(l + \bar{R}_p), t]}{\partial x} = D_2 \frac{\partial N_2[(l + \bar{R}_p), t]}{\partial x}$$

As shown in Fig. 5 the concentration near the surface is low and it seems to be a good approximation to assume that the diffusion takes place in an infinite body instead of a semi-infinite body. The solution of Eq. (5) is given by

$$N_1(x, T) = \frac{Q}{\sqrt{2\pi(2D_1T + \sigma^2)}} \left\{ \exp\left[-\frac{(x - \bar{R}_p)^2}{4D_1T + 2\sigma^2}\right] \left(1 - \frac{1}{2} \operatorname{erfc} \frac{2lD_1T - (x - \bar{R}_p - l)\sigma^2}{2\sqrt{D_1T}\sigma^2(2D_1T + \sigma^2)} \right) \right. \\ + \frac{2a}{a+1} \exp\left[-\frac{[ax - a\bar{R}_p + l(1-a)]^2}{4D_2T + 2\sigma^2}\right] \left(1 - \frac{1}{2} \operatorname{erfc} \frac{a\sigma^2(x - \bar{R}_p - l) - 2D_2T}{2\sqrt{D_2T}\sigma^2(2D_2T + \sigma^2)} \right) \\ \left. + \frac{1-a}{a+1} \exp\left[-\frac{(x - \bar{R}_p - 2l)^2}{4D_1T + 2\sigma^2}\right] \left(1 - \frac{1}{2} \operatorname{erfc} \frac{2lD_1T + (x - \bar{R}_p - l)\sigma^2}{2\sqrt{D_1T}\sigma^2(2D_1T + \sigma^2)} \right) \right\} \quad (7a)$$

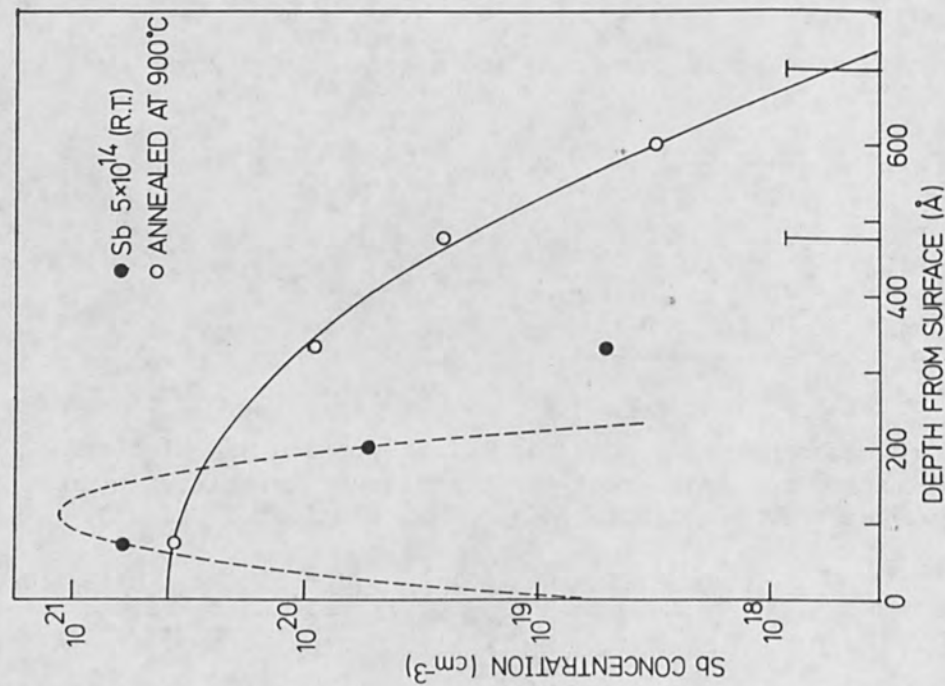


FIG. 4.--Concentration profiles of 20-keV room-temperature ion-implanted antimony with a dose of about 5×10^{14} ion/cm². Concentration in 4th removed layer of unannealed sample and in 5th removed layer of an annealed sample were within concentration corresponding to natural counts indicated by bars. Solid line indicates result of calculation of Eq.(4).

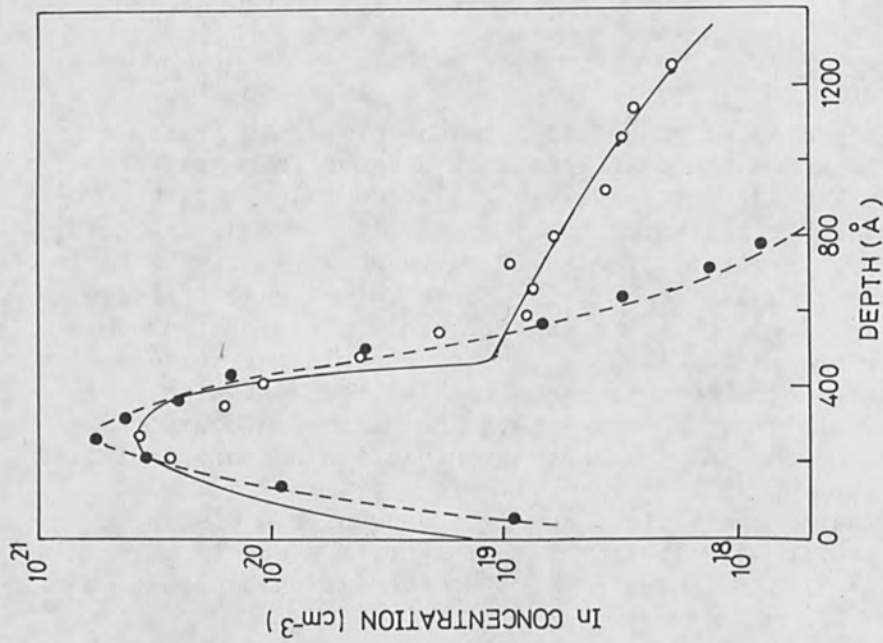


FIG. 5.--Concentration profiles of 45-keV room-temperature ion-implanted indium with a dose of about 1×10^{15} ion/cm². ● and ○ indicate the results obtained respectively before and after heat treatment at 900°C for 20 min. Solid line indicates result of calculation of Eq.(7).

$$\begin{aligned}
N_2(x, T) = & \frac{Q}{\sqrt{2\pi(2D_2T + \sigma^2)}} \left\{ \exp\left[-\frac{(x - \bar{R}_p)^2}{4D_2T + 2\sigma^2}\right] \left(1 - \frac{1}{2} \operatorname{erfc} \frac{(x - \bar{R}_p - \ell)\sigma^2 - 2D_2T\ell}{2\sqrt{D_2T}\sigma^2(2D_2T + \sigma^2)} \right) \right. \\
& + \frac{a-1}{a+1} \exp\left[-\frac{(x - \bar{R}_p - 2\ell)^2}{4D_2T + 2\sigma^2}\right] \left(1 - \frac{1}{2} \operatorname{erfc} \frac{2\ell D_2T + (x - \bar{R}_p - \ell)\sigma^2}{2\sqrt{D_2T}\sigma^2(2D_2T + \sigma^2)} \right) \\
& \left. + \frac{2}{1+a} \exp\left[-\frac{[x - \bar{R}_p - \ell(1-a)]^2}{4D_2T + 2\sigma^2 a^2}\right] \left(1 - \frac{1}{2} \operatorname{erfc} \frac{2\ell D_2T - a\sigma^2(x - \bar{R}_p - \ell)}{2\sqrt{D_1T}\sigma^2(2D_1T + \sigma^2)} \right) \right\} \quad (7b)
\end{aligned}$$

where $a^2 = D_2/D_1$. The solid line shown in Fig. 5 indicates the result of the calculation of Eq. (7) for values of $D_1 = 1.5 \times 10^{-16} \text{ cm}^2/\text{sec}$, $D_2 = 1.5 \times 10^{-14} \text{ cm}^2/\text{sec}$, $\ell = 200 \text{ \AA}$, $\sigma = 87 \text{ \AA}$, and $\bar{R}_p = 270 \text{ \AA}$. Diffusion coefficient obtained in the high concentration region (D_1) is in agreement with the normal thermal diffusion coefficient,⁷ whereas that in the low concentration region is enhanced by 10^2 over the normal thermal diffusion coefficient.

Precipitation may give the probable explanation for the fact that the diffusion is not enhanced in the high-concentration region. The solubility of indium in silicon is about $5 \times 10^{17}/\text{cm}^3$ ¹⁰ or $1 \times 10^{18}/\text{cm}^3$.¹¹ Backenstoss¹⁰ found that the resistivity becomes almost independent of the concentration of indium at a concentration higher than $5 \times 10^{17}/\text{cm}^3$ and observed precipitation of indium at this concentration region by autoradiography. The concentration of $1 \times 10^{19}/\text{cm}^2$ seems to be higher than the maximum solubility. For ion-implanted antimony it was observed that antimony is soluble over the maximum normal solubility.¹²

The probable explanation of the observed impurity-concentration profiles can be made by radiation-enhanced diffusion on the basis of a vacancy mechanism. According to this diffusion mechanism the enhanced diffusion occurs by excess vacancies produced by ion implantation and is more remarkable for the high dose rate implantation because more excess vacancies are produced. This is observed for high-temperature ion-implanted antimony.⁴ Vacancies are produced mainly within the average projected range¹³ and can be thought to diffuse faster than the ion-implanted impurities. The diffusion length of a vacancy has been reported to be about 0.3μ ¹⁴ or 3μ .¹⁵ The distance of diffusion of antimony was short enough in the present experiment compared with the diffusion length of a vacancy. Therefore vacancies distribute uniformly within the distance of the diffusion of antimony and consequently the diffusion coefficient is approximately independent of a distance x in the present experiment. In case of indium it was found by Hall effect and backscattering measurements that most In atoms occupy interstitial and random sites. Therefore interstitial diffusion also seems to be possible.

CONCLUSION

The following can be concluded from the measurement of the concentration profiles of ion-implanted antimony and indium.

1. Measured values of the average projected range and the projected standard deviation of 20- to 80-KeV indium are in agreement with the calculated values according to LSS theory.
2. The concentration profile of ion-implanted indium in silicon single-crystals along random direction is different from that in amorphous silicon. The tail is not observed in amorphous silicon.
3. Enhanced diffusion occurs for room-temperature ion-implanted antimony and indium during heat treatment. For indium this occurs in the concentration region lower than $1 \times 10^{19}/\text{cm}^3$.

ACKNOWLEDGMENT

The authors wish to express their thanks to Messrs. K. Kawasaki and S. Horibata for their help in performing the experiments.

REFERENCES

1. J. Lindhard, M. Scharff, and H. E. Schiott, Kgl. Danske Videnskab. Selskab. Mat. Fys. Medd. 33 (No. 14): 1963.
2. W. S. Johnson and J. F. Gibbons, Projected Range Statistics in Semiconductors, Stanford University Bookstore, 1970.
3. D. K. Brice, Proc. Intern. Conf. on Ion Implantation, Thousand Oaks, 1970 (to be published); and private communication.
4. K. Gamo, K. Masuda, S. Namba, S. Ishihara, and I. Kimura, Appl. Phys. Letters 17: 391, 1970.
5. J. A. Davies, L. Eriksson, and J. L. Whitton, Can. J. Phys. 46: 573, 1968.
6. O. J. Marsh, R. Baron, and G. A. Shifring, Appl. Phys. Letters 13: 199, 1968.
7. B. L. Crowder, J. Electrochem. Soc. 117: 363, 1970.
8. G. D. Watkins, IEEE Trans. on Nucl. Sci. 16: 13, 1969.
9. B. I. Boltaks, Diffusion in Semiconductors, Infosearch Limited, London, 1963.
10. G. Backenstoss, Phys. Rev. 108: 1416, 1957.
11. S. Fischler, J. Appl. Phys. 33: 1615, 1962.
12. J. W. Mayer, O. J. Marsh, G. A. Shifrin, and R. Baron, Can. J. Phys. 45: 4073, 1967.
13. B. L. Crowder and R. S. Title, Proc. Intern. Conf. on Ion Implantation, Thousand Oaks, 1970 (to be published).
14. H. Strack, J. Appl. Phys. 34: 2405, 1963.
15. P. Baruch, C. Constantin, J. C. Pfister, and R. Saintesprit, Discussions Faraday Soc. 31: 76, 1961.

LOW-ENERGY ELECTRON-BEAM EQUIPMENT FOR MICROELECTRONIC DEVICE EVALUATION

J. P. FLEMMING* and H. AHMED

Standard Telecommunications Laboratory, Harlow, and Cambridge University, Cambridge, England

INTRODUCTION

Electron-probe methods have been devised for the examination and testing of semiconductor device arrays and integrated circuits. For example, the scanning electron microscope has been used to examine integrated circuit patterns by means of the contrast obtained from the potential distribution over the surface.¹ However, this method usually requires electrical connections to be made to the circuit so that bias voltages may be applied. Some contrast can also be seen without bias voltages but the results are difficult to interpret.² Furthermore, in this method the electron probe is incident on the specimen at high energy with the possible consequence of specimen damage. By using an electron-probe method with a retarding field in front of the specimen it is possible to examine the semiconductor array quantitatively without having to make electrical contact with the contact pads of the devices and with only very-low-energy electrons incident on the specimen. We describe in this paper scanning-electron-beam equipment that has been built to examine a large specimen area, and which operates primarily in the retarding-field mode.

DESIGN

It was required to produce a spot of approximately 10 μm in diameter with a beam current of 10^{-7} A and to scan the probe over an area of about 2 in. in diameter. The accelerating voltage used could vary from 500 V to 10 kV but, near the specimen, the beam enters the retarding field region, decelerates, and only a fraction of the beam current reaches the specimen. Figures 1 and 2 are simplified diagrams of the electron-optical system of the instrument. The design was kept flexible enough to allow both a wide range of electron-optical conditions to be investigated and electronic measurement techniques to be set up and calibrated. Component parts were constructed on a modular basis so as to allow them to be interchanged or replaced. The geometrical parameters of the electron gun could be adjusted so that a satisfactory electron beam could be formed over the range of accelerating voltages between 500 V and 10 kV. Both the gun and the specimen were arranged to operate at voltages around earth, which allowed for more convenience in the connection of electronic circuits at the measurement point. A mesh in front of the specimen was held at a high potential and formed a boundary of the retarding field region. The mesh-specimen spacing could be changed and it was possible to align the mesh to be parallel to the plane of the specimen.

DETAILS OF CONSTRUCTION

A. GUN. The gun design was based on the conventional tungsten hair-pin filament and Wehnelt grid assembly. It was designed so that the anode-

*Now at Western Electric Engineering Research Center, Princeton, N. J.

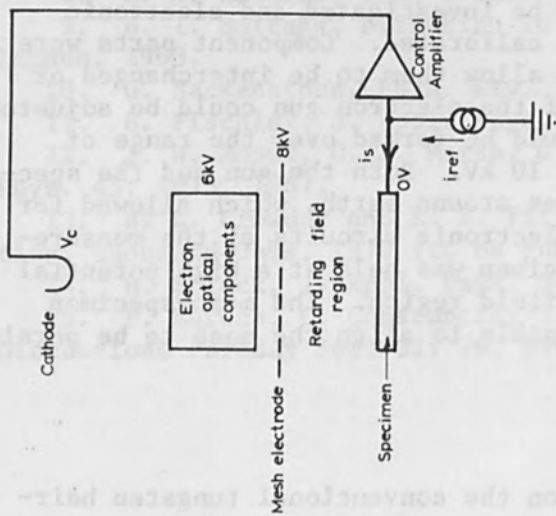


FIG. 1.--Simplified diagram of electron-optical system.

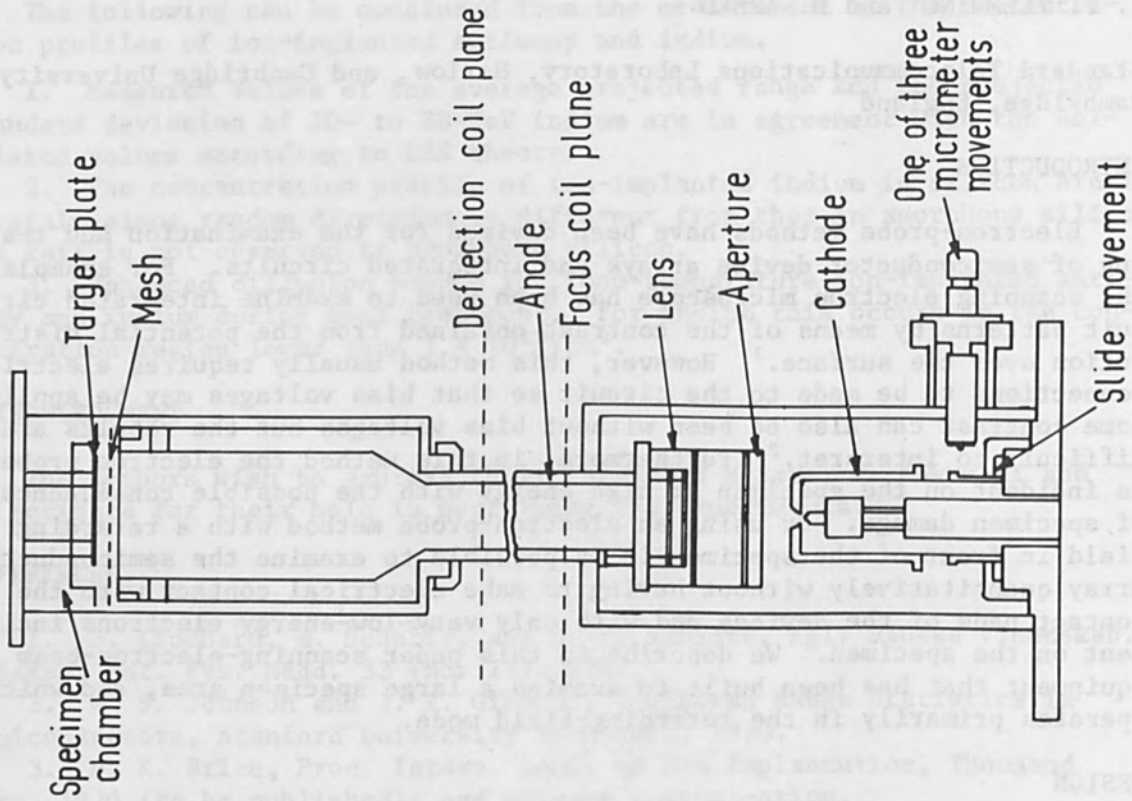


FIG. 2.--Equipment configuration.

grid spacing could be varied from contact to about 1 cm. The alignment at all accelerating voltages could be corrected by moving the filament-grid assembly using micrometer adjustments external to vacuum system. The gun assembly is shown in Fig. 3.

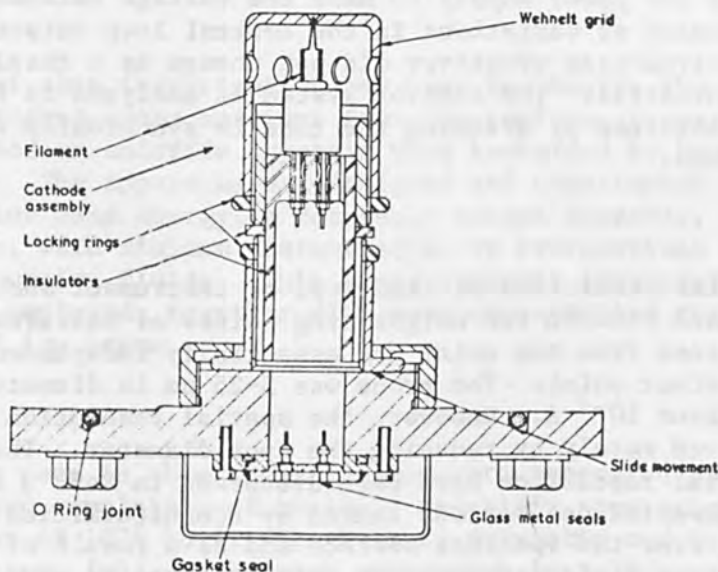


FIG. 3.--Gun assembly.

B. FOCUSING SYSTEM. The beam emerging from the aperture placed approximately at the gun crossover entered a three-element Einzel lens which was mechanically aligned during assembly. The demagnified spot entered a tube coated on the inside with a conducting film. A focus coil (including astigmatism and deflection defocusing correction coils) and a set of scan coils were placed around this tube.

C. SCANNING SYSTEM. The deflection half-angle used for the scanning system was about 10° depending on the length of the anode drift space. This allowed a region 2.5 in. in diameter to be scanned. The scan coils were driven from solid-state linear-current amplifiers. Inputs were supplied from a horizontal scan generator which produced a sawtooth signal with scan times variable from 1 ms to 2 sec and a digital frame scan generator which was switched at the completion of each line scan. The number of lines per frame could be varied and a fixed line scan could be placed at any position within the frame. The size and position of the frame within the total scanned area could be adjusted by dc shift and magnification controls.

D. TARGET AND RETARDING FIELD REGION. The final anode was insulated from the mesh electrode which was placed parallel to and within a few millimeters of the specimen. The mesh potential was brought into the system by an extrahigh-tension (eht) lead through the side of the column and could be adjusted. Until the beam passed through the mesh, the trajectory of the electrons was not affected by the potential distribution on the surface of the specimen.

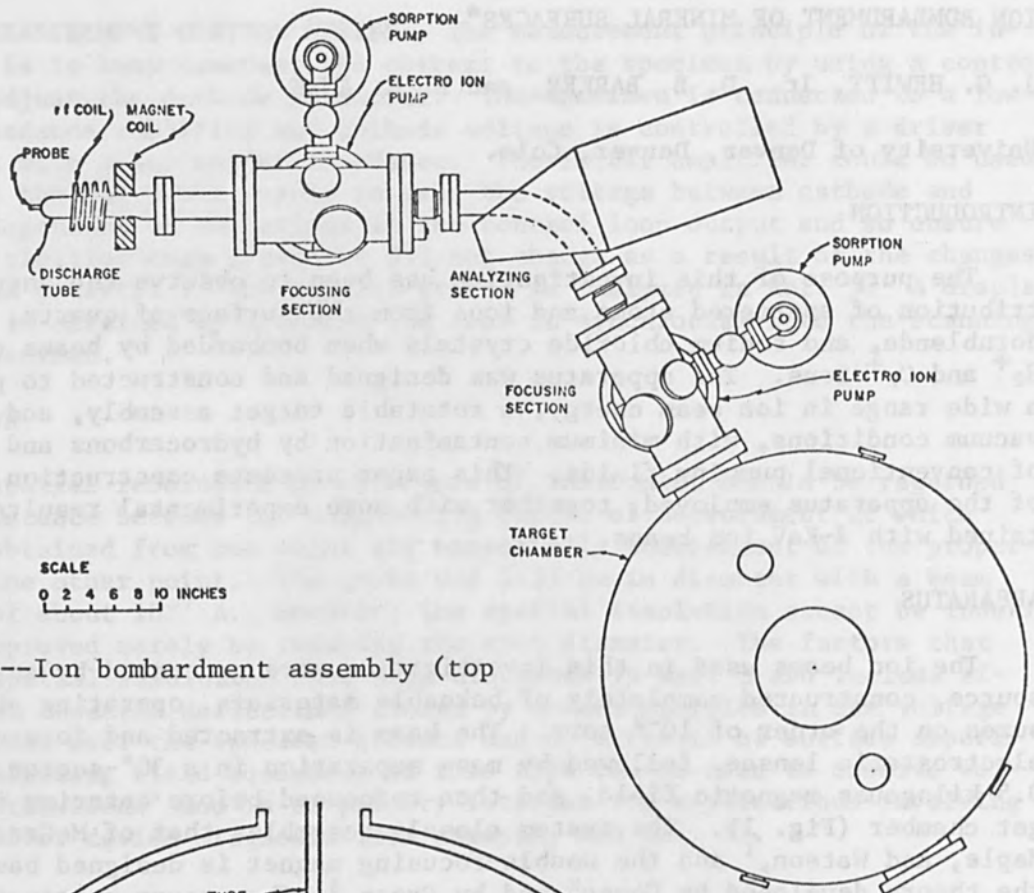


FIG. 1.--Ion bombardment assembly (top view).

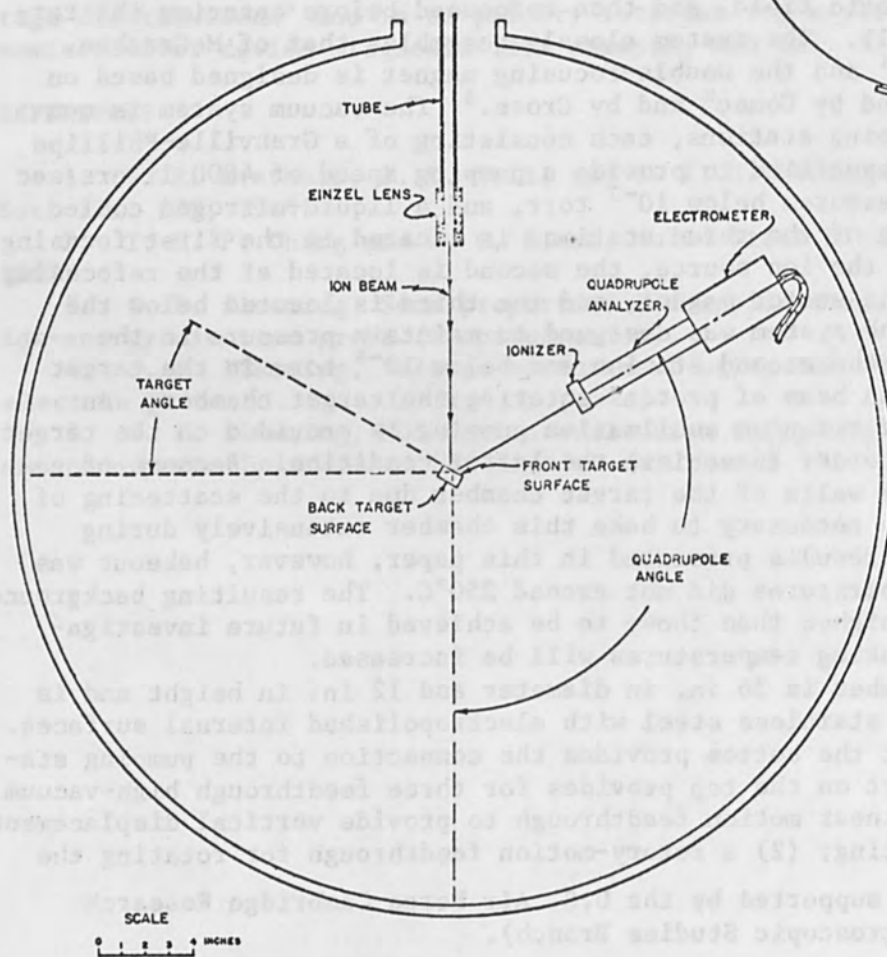


FIG. 2.--Target chamber arrangement.

target; (3) an electrical feedthrough for a Faraday cup detector and other connections. An additional 10-in. port on the bottom provides motion feedthrough for an rf quadrupole mass filter, equipped with ionizer and electrometer, that can be rotated nearly 180° with respect to the ion beam. Figure 2 displays the target chamber arrangement and defines the angular coordinates.

TARGET PREPARATION AND BOMBARDMENT

Quartz targets were prepared from natural crystals by cutting 3/4-in. cubes and lapping the surfaces to a $15\text{-}\mu$ in. finish. One face was perpendicular to each of the X, Y, and Z directions. For the work reported here, the planes perpendicular to the X direction were exposed to the beam.

A sodium chloride target was prepared from a single-crystal infrared window about 1/4 in. thick with a surface area of approximately $3/4$ in.² The bombarded surface had been polished for optical use. Hornblende is a mineral containing calcium, sodium, potassium, iron, aluminum, magnesium, silicon, oxygen, and possibly hydrogen and fluorine. The crystal employed had been cleaved on the $\langle 110 \rangle$ axis and polished. The sanidine sample was cleaved on the $\langle 001 \rangle$ axis. This mineral has the chemical composition KAlSi_3O_8 . Both hornblende and sanidine targets were thin wafers having irregular areas of about 3/4 in. linear dimension. After extensive bombardment, the target surfaces all showed visible damage due to sputtering. The surfaces were observed to glow under bombardment; extensive spectroscopic information was obtained for the case of quartz, but is not reported here. The luminescence showed that the beam was focused to a spot less than 1/4 in. in diameter. The spot would move about slightly on the central area, indicating the presence of a net surface change configuration. However, in these studies, no extensive effort was made to neutralize the surface during exposure. Consequently, the actual beam energy is less than the indicated values. The target chamber pressure was maintained at about 10^{-9} torr during bakeout and, for these measurements, rose to about 2×10^{-8} torr with the ion source operating but with the beam blocked. With the beam directed onto the target surface, the target chamber pressure rose somewhat higher owing to additional deabsorption from the target and from the chamber walls. Residual gas analysis showed that this pressure increase was due to a broad spectrum of background gases. The sputtered and scattered species were detected by comparing the magnitude of certain mass peaks with the beam on to those obtained with the beam blocked. Incident beam currents were on the order of several microamperes, while the collected currents representing scattered ions were of the order of 10^{-12} A. In order to reduce the level of interference due to the entry of residual gas species not coming directly from the bombarded surface, the mass analyzer (a Spectrascan Model 750) was modified to restrict entry into the ionizer to molecules arriving within a 10° cone.

EXPERIMENTAL RESULTS

Figures 3(a) and 3(b) show typical scans of the ions arriving at the quadrupole analyzer when O_2^+ beams of 7 KeV are directed onto the quartz and hornblende surfaces, respectively. For these data, the ionizer was not operating. It is seen that mass peaks 23 and 39 are dominant for both minerals, which correspond to sodium and potassium. The quartz data

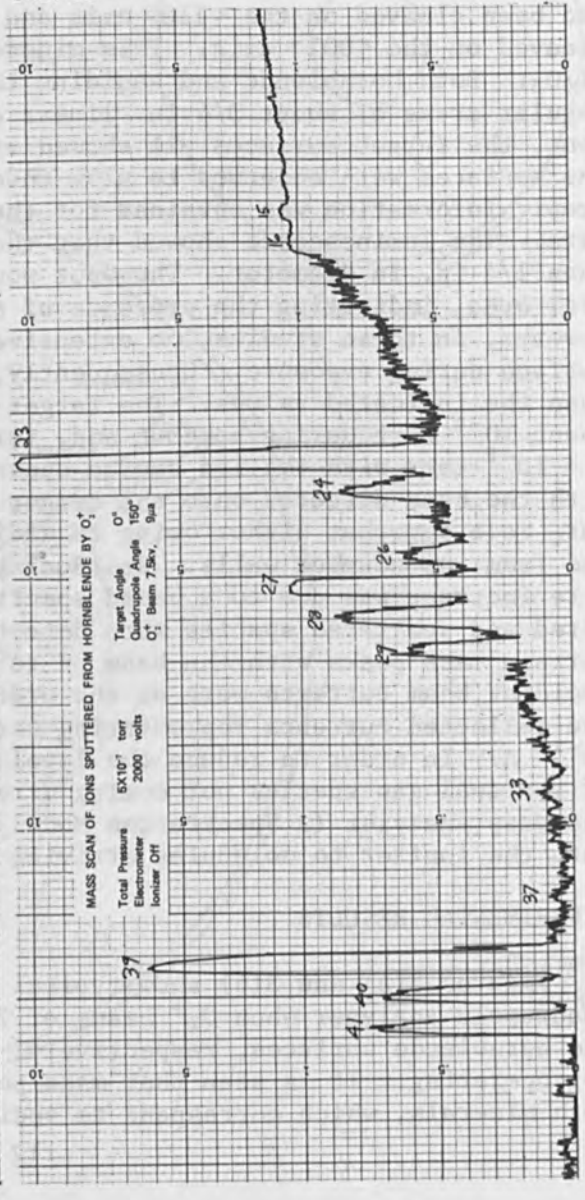
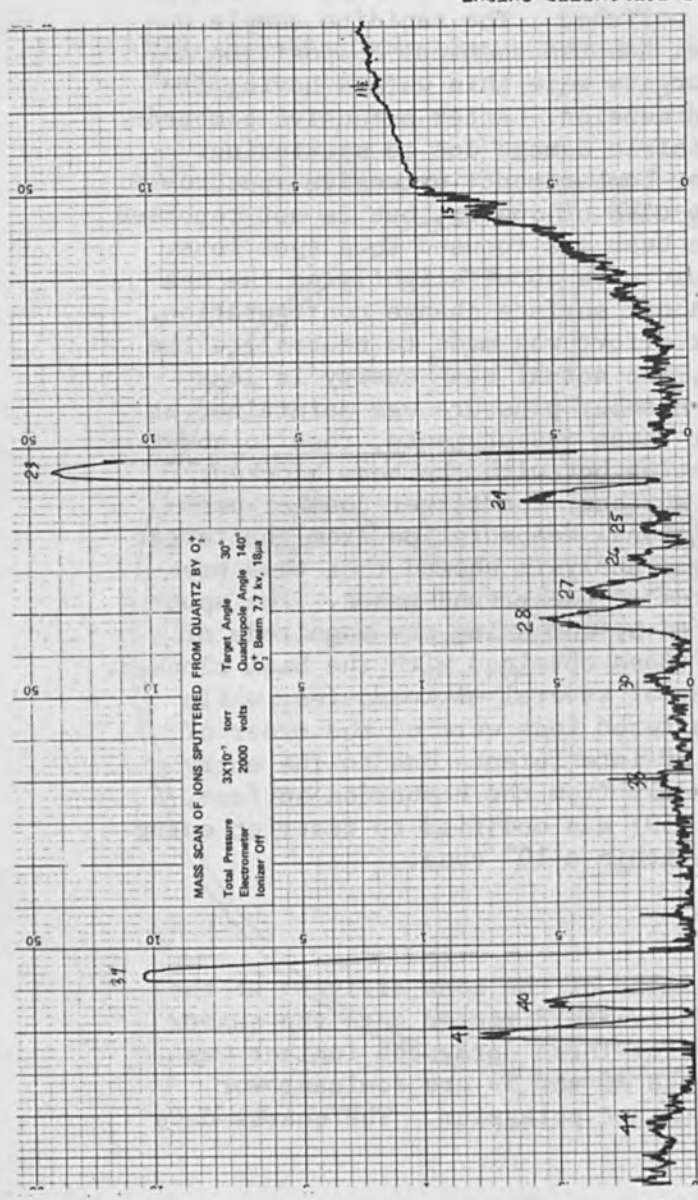


FIG. 3.--Mass scan of ions sputtered from (a) quartz (top) and (b) hornblende by O_2^+ .

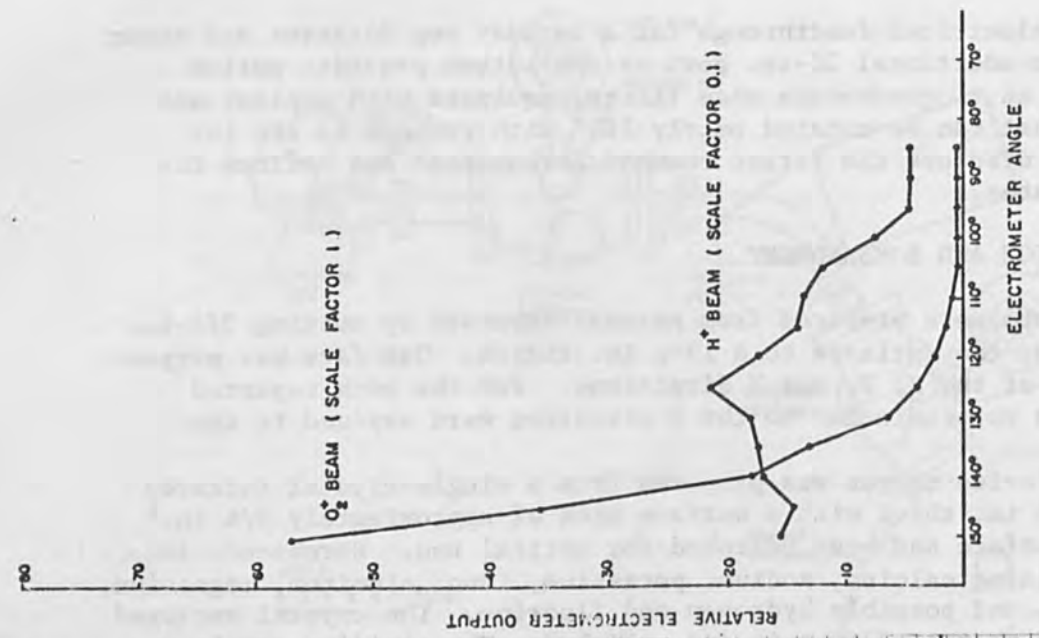


FIG. 4.--Total positive collection vs angle: H^+ and O_2^+ beams (Sanidine target). Electrometer, 2000 V; H^+ beam 7.8 KV, 4 µA; target angle 0° ; ionizer off; O_2^+ beam 7.7 KV, 16 µA.

suggest that these elements are a result of resputtering, from the chamber walls, residues from previous experiments with salt crystals. Since hornblende contains both these masses the two peaks represent both direct sputtering and resputtering effects. The major differences between the traces are the mass 27 and 29 peaks observed in the hornblende. Mass 29 is not observed in the case of quartz. The large increase (about 4×) in the mass 27 peak occurring in hornblende corresponds to ^{27}Al . The small mass 44 peak observed in the quartz scan, but absent from the hornblende scan, probably corresponds to SiO .

Figure 4 for sanidine compares the total positive ion current collected as a function of the collector angle for H^+ beams with that observed for O_2^+ beams. The latter beam causes more total ionized particle current than H^+ , as anticipated. The total current is much more sharply peaked in the backscattered direction for the O_2^+ beam than for H^+ . In this case, as in all other observed cases of O_2^+ bombarding minerals, no O_2^+ or O^+ ions could be detected, and a definite increase of neutral O was observed. This observation indicates that O_2^+ ions readily undergo either surface neutralization or reaction, or both.

Figure 5 shows the total positive ion current collected as a function of angle for O_2^+ ions incident normally on hornblende, salt, and sanidine. A remarkably strong peak is observed at 110° in the case of hornblende; the angle dependence for the other two cases is one of monotonic behavior. A similar maximum was observed when the target angle was increased to 30° , the maximum occurring again at an angle of 20° from the target surface plane. To investigate further the effect of the angle of beam incidence, series of data were obtained with hornblende, varying the target angle. As seen in Fig. 6, the relative maximum always occurs at the same angle. In addition, the quadrupole mass analyzer could resolve ion peaks at angles above and below the relative maximum, but not at the maximum. This finding suggests that the scattered and sputtered ions at this angle have higher energies.

ACKNOWLEDGMENT

The authors are indebted to Dr. Peter Dybwad of the U. S. Air Force Cambridge Research Laboratories for helpful discussions and for the sanidine and hornblende samples employed in this study.

REFERENCES

1. G. M. McCracken, J. H. C. Maple, and H. H. H. Watson, Rev. Sci. Instr. 37: 860, 1966.
2. M. Comac, Rev. Sci. Instr. 22: 197, 1951.
3. W. G. Cross, Rev. Sci. Instr. 22: 717, 1951.

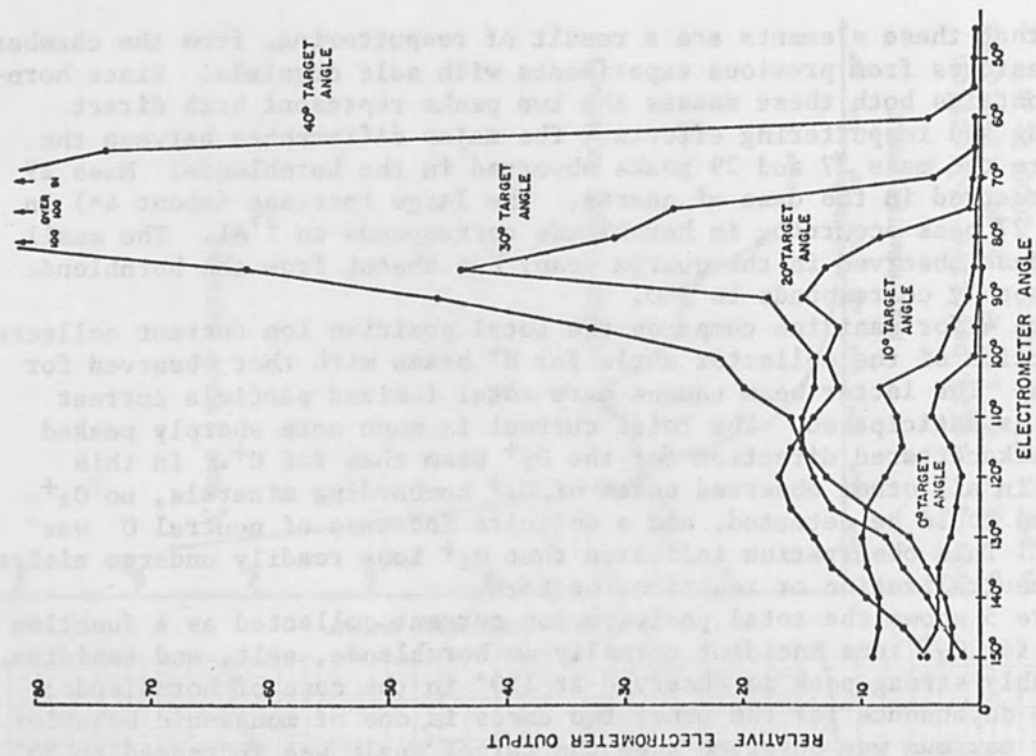


FIG. 6.--Total positive-ion collection vs angle: O_2^+ beam (Hornblende target); electrometer, 1200 V; ionizer off; O_2^+ beam 7.5 KV, 10 μA .

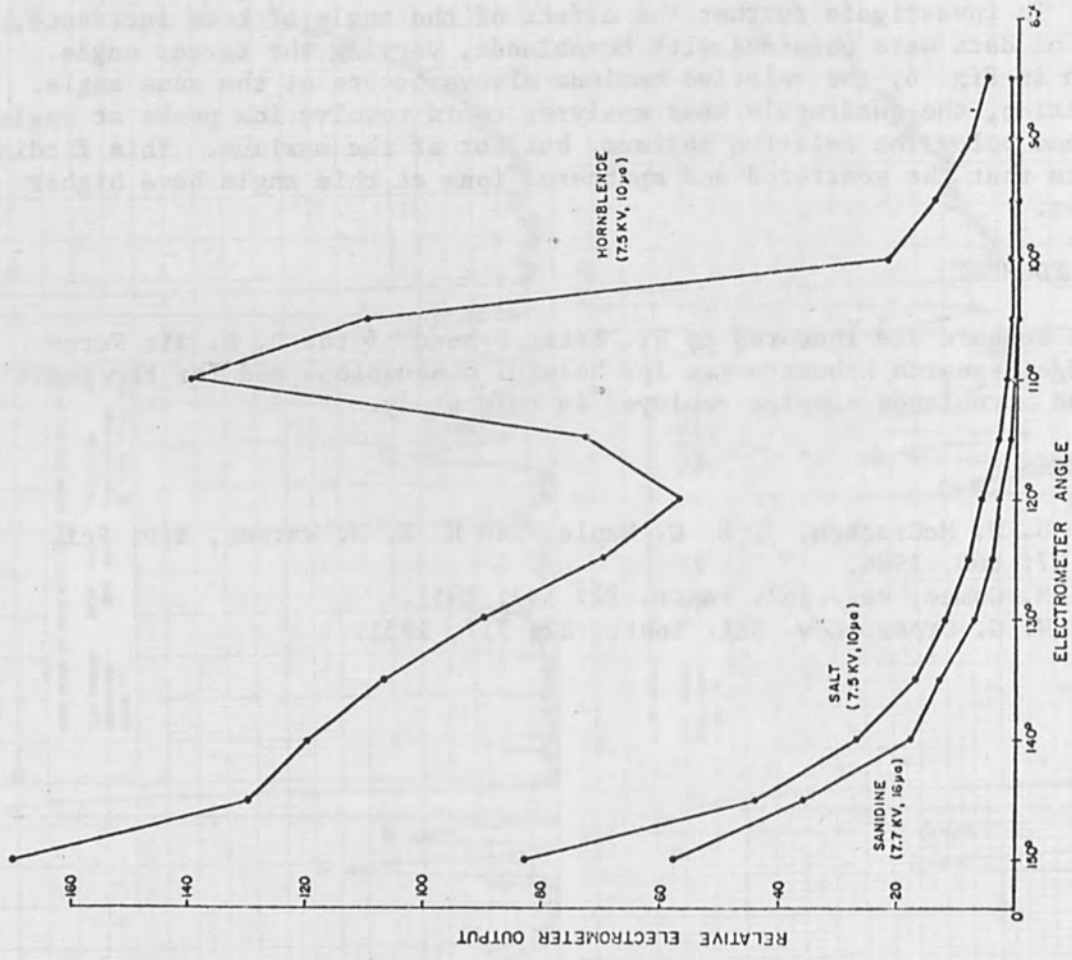


FIG. 5.--Total positive ion collection vs angle: O_2^+ beams (various targets). Electrometer, 2000 V; ionizer off; target angle 0°.

SPECTROSCOPIC STUDIES OF THE EMISSION FROM PLASMAS GENERATED BY AN INTENSE ELECTRON BEAM*

G. A. CARLSON

Sandia Laboratories, Albuquerque, N. M.

INTRODUCTION

A high-temperature materials research program is being established at Sandia Laboratories using a Nereus pulsed electron-beam generator as an energy source. The present study was undertaken to develop spectroscopic techniques which might be useful in this research program. An additional goal of this study was to identify the species responsible for the intense light emission observed when pulsed electron beams are transmitted through a gas.

EXPERIMENTAL METHOD

A Nereus pulsed electron beam machine developed at Sandia Laboratories¹ was used in these studies. The machine's output is a 30-nsec half-width electron beam with a peak energy of 250-300 keV and a peak current of 60-80 kA. The beam emits from a 1-in.-diam. planar brass field-emission cathode with cross-hatched surface and passes through a 1-mil aluminum transmission anode (0.25-cm anode-cathode spacing) into a 23-cm-diam., 35-cm-long Lucite drift tube. When the drift tube is filled with the appropriate pressure of gas, the electron beam propagates axially until it strikes a target placed near the end.

The experimental arrangement used to collect spectral data is shown in Fig. 1. The electron beam is perpendicular to the plane of the paper. Except as noted below, the Lucite drift tube is covered with opaque black paper. Time-integrated photographs of the light emission were obtained through a wide aperture in the drift tube covering using a 4 × 5 view camera. Time-integrated, spatially resolved spectra of the light emitted by the beam-generated plasma were obtained by allowing the light which exited through a 0.1-cm-wide, 35-cm-long slit in the drift tube covering to pass through a transmission grating (Bausch and Lomb, 600 grooves/mm, 5700 Å first-order blaze wavelength) directly into a 4 × 5 view camera which was focused on the slit. The camera and grating were located about 250 cm from the drift tube. The dispersion of the "spectrograph" was approximately 106 Å/mm, and the highest resolution observed was approximately 5 Å. Spectral information was obtained from 3500 Å, the Lucite drift tube cutoff, to 6300 Å, the cutoff of the Kodak Ektapan cut film (ASA 100) used to record the spectra.

Time-resolved, spatially fixed spectra were recorded with a TRW Model 1D image-converter camera in the streaking mode with a spectrographic attachment (spectral range about 3800-6200 Å). The camera was positioned 50 cm from the drift tube. The collector lens used was slightly defocused, so that light emitted from a 1-cm-diam. spot approximately 3-4 cm axial distance from the anode was collected. The camera was triggered by a signal from the Marx generator approximately 0.2-0.4 μsec prior to electron-beam generation.

Mercury lamp calibration lines were added to the time-integrated and streak spectra prior to each shot. The calibration was only accurate to

*This work was supported by the U.S. Atomic Energy Commission.

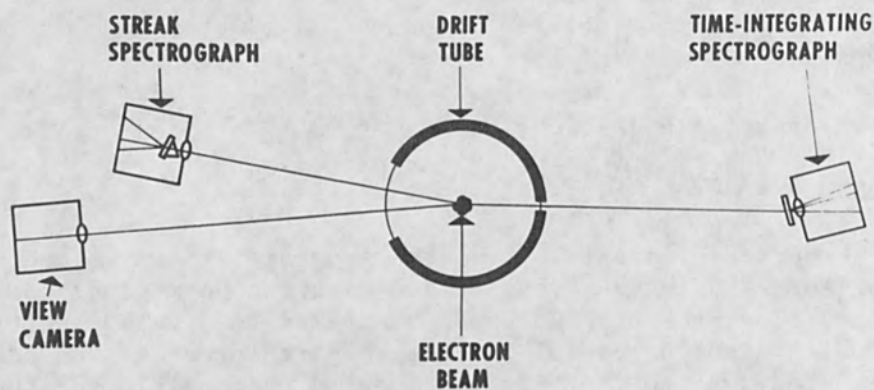


FIG. 1.--Experimental arrangement used for the collection of spectroscopic data.

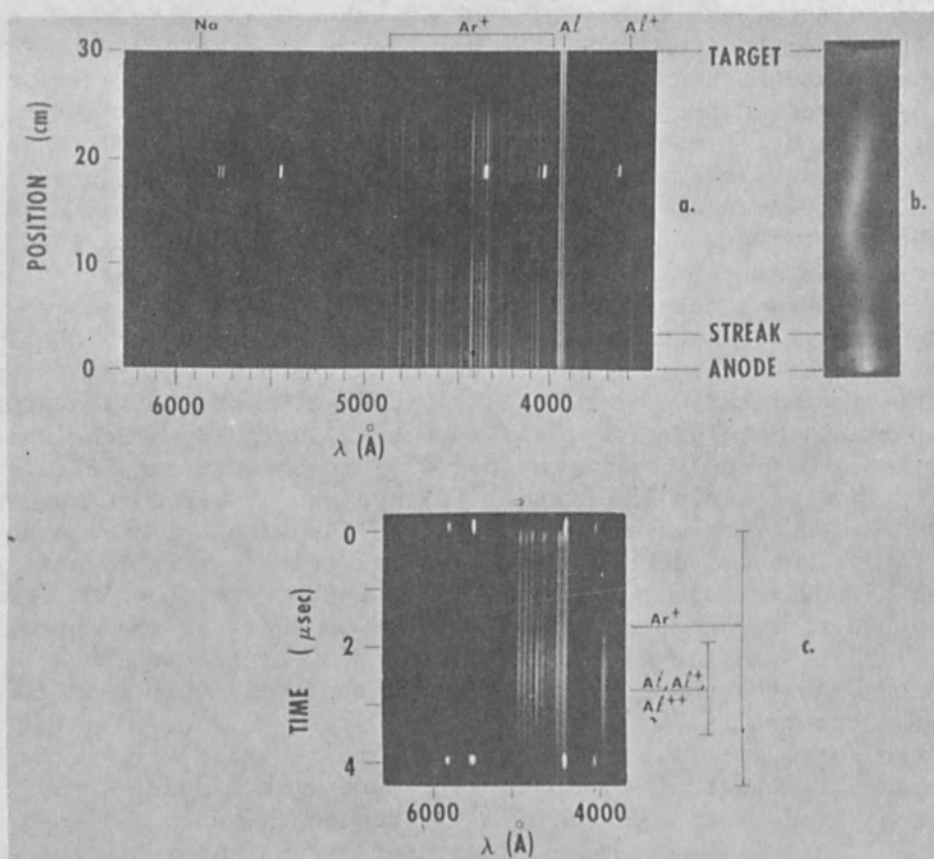


FIG. 2.--Data from 0.5-Torr Ar experiment: (a) time-integrated beam spectrum; (b) time-integrated beam photograph; (c) time-resolved beam spectrum.

$\pm 5-10 \text{ \AA}$ for the time-integrated spectra because the mercury lamp was not placed exactly in the same position as the slit in the drift-tube wall. However, several easily identified lines which were observed in almost all experiments served as an adequate internal calibration.

Gases used in these experiments were commercial grades of O_2 , N_2 , He, Ar, and room air. The desired pressure of gas was introduced into the drift tube after the system had been flushed several times, and after the drift tube had been evacuated with a mechanical pump to 0.02-0.03 Torr. To achieve from 0.1- to 2-Torr test gas pressure, a flow system was established with a variable leak input near the anode and a mechanical pump exhausting through the drift tube end plate. For 10 Torr, a static pressure was introduced. Pressures were measured with a calibrated 0-20 Torr Wallace and Tiernan gage. Accuracy of the pressure measurements was approximately ± 0.05 Torr.

EXPERIMENTAL RESULTS

Light emission resulting from electron-beam passage through various gases was studied at pressures of 0.1, 0.5, 2, and 10 Torr. Over this pressure range, the electron-beam propagation characteristics varied markedly. At 0.1 Torr, the beam tended to pinch initially and then blow up. No damage was observed at the target location 30 cm from the anode. At 0.5 and 2 Torr, the beam drifted in a controlled manner and caused relatively severe damage to aluminum targets. At 10 Torr, beam behavior varied, depending on the drift gas used. Helium was the only gas in which target damage was observed at 10 Torr.

Most of the spectral data to be presented were taken at a pressure of 0.5 Torr, not only because the controlled drifting beam has important practical applications, but also because the most varied data were observed at this pressure. Data recorded at other pressures will also be discussed, however.

The spectra show that the observed light emission may originate from several sources: vaporization from the surface of the brass field-emission cathode (Cu, Zn, Pb); vaporization of the transmission anode (Al); excitation of the drift gas; target vaporization (Al); and impurities (Na, Ca). With certain drift gases (O_2 and air), emission was also observed from chemical reaction products (AlO).

In general, analysis of the spectra is limited to identification of the species responsible for the emission and does not include the specific transitions or wavelengths observed. References to the lines and bands commonly observed in emission from various atoms, ions,^{2,3,4} and molecules⁵ may be found elsewhere. The relative intensities of the various lines observed for a given species in this study were generally the same as given in the above compilations. Emission from all sources other than the drift gas will be referred to as "debris" emission. For reference, lines commonly observed as debris emission are listed in Table I.

1. ARGON. Figure 2 shows emission observed in 0.5-Torr Ar. Except for minor debris emission, the time-integrated, spatially resolved spectrum (Fig. 2a) is attributable exclusively to Ar^+ . The spatial variation in the Ar^+ emission is similar to that seen in the integrated beam light picture (Fig. 2b), if one recalls that the narrow slit through which the spectrum was recorded discriminates against any light emission which is

TABLE I.--Debris lines commonly observed in emission with Nereus pulsed electron beam.

Wavelength(Å)	Species	Source
6362	Zn	Cathode
6243	Al ⁺	Anode, target
6231	Al ⁺	
5889, 96	Na	Contaminant
5782	Cu	Cathode
5722	Al ⁺⁺	Anode, target
5700	Cu	
5696	Al ⁺⁺	
5593	Al ⁺	
5336	AlO	Chemical reaction
5218	Cu	
5153	Cu	
5105	Cu	
5079	AlO	
4842	AlO	
4810	Zn	
4722	Zn	
4680	Zn	
4666	Al ⁺	
4648	AlO	
4529	Al ⁺⁺	
4512	Al ⁺⁺	
4479	Al ⁺⁺	
4470	AlO	
4226	Ca	Contaminant
4150	Al ⁺⁺	
4062	Cu	
4057	Pb	Cathode
4022	Cu	
3968	Ca ⁺	Contaminant
3961	Al	Anode, target
3944	Al	
3933	Ca ⁺	
3587	Al	

not on axis. The streak spectrum (Fig. 2c) of light emitted approximately 3-4 cm from the anode shows that the Ar^+ emission is bright near $t = 0$ (probably during beam passage), maintains a relatively constant though reduced intensity for the next 2 μsec , appears to intensify as the aluminum anode debris passes through the field of view around 2-3 μsec , and finally disappears somewhat after 4 μsec .

Similar spectra were observed at 0.1-Torr Ar. At 2-Torr Ar, more complex axial intensity variations of the Ar^+ emission were observed. Experiments at 10-Torr Ar showed no emission attributable to the drift gas about half the time, and showed Ar^+ emission near the anode only the remainder of the time. The time-history of the Ar^+ emission was essentially independent of pressure from 0.1 to 10 Torr.

2. HELIUM. The spectra from 0.5-Torr He (Fig. 3) are dominated by debris emission. Only a few lines of He^+ and He are observed. The streak spectrum shows very intense Al, Al^+ , Al^{++} lines beginning at $t = 1.5 \mu\text{sec}$, and also shows the beginning of emission from Cu and Zn at $t = 5 \mu\text{sec}$.

Helium was not tested at 0.1 or 2 Torr. At 10 Torr, the neutral He lines were somewhat brighter than at 0.5 Torr, but the 4686 Å He^+ line was absent. The intensity of debris emission was considerably reduced. The streak spectrum showed emission from He lasted for several μsec , the intensity decaying at a uniform rate.

3. OXYGEN. In Fig. 4, the light emission observed in 0.5-Torr O_2 shows a relatively similar behavior to Ar. The lines showing a distinct spatial variation are all due to O^+ . No other oxygen emission (e.g., O, O_2 , O_2^+) was observed under any conditions. Some AlO emission is observed near 5000 Å, indicating that a chemical reaction has occurred between the Al anode or target debris and the drift gas. The streak spectrum shows O^+ emission persists for 3-4 μsec . Emission from Al is again observed, beginning around 2 μsec .

At 0.1-Torr O_2 , similar time-integrated spectra were observed. Experiments at 2- and 10-Torr O_2 illustrated the significant role that chemical reactions may play in the light emission observed. Figure 5 shows an experiment at 2-Torr O_2 . Although the electron beam did propagate through the drift tube and damage the aluminum target, no emission attributable to O_2 is observed. The very intense light emission observed is almost exclusively due to AlO, formed from the reaction of aluminum from the anode and to a lesser extent from the target with the O_2 drift gas. Experiments at 10-Torr O_2 were similar, except that O^+ radiation was observed very close (1-2 cm) to the anode. No streak spectra were recorded for O_2 at 0.1, 2 or 10 Torr.

4. NITROGEN, AIR. In comparison with the results discussed thus far, the spectra from air and N_2 , which were nearly identical, display some unique characteristics. Figure 6 shows the light emission recorded with 0.5-Torr N_2 . The emission lines which are quite bright in the first 6 cm from the anode in Fig. 6(a) are due to N^+ and N^{++} (the N^{++} lines are somewhat shorter). Contrasted to the marked spatial variation of N^+ and N^{++} , molecular band systems of N_2^+ (first negative, 3914, 4278 Å) and N_2 (second positive, 3755, 3804, 3998, 4059 Å) are observed which show almost no spatial variation.

The streak spectrum shows that significant differences are also found in the time history of emission from the various species. Both N_2^+ and N_2

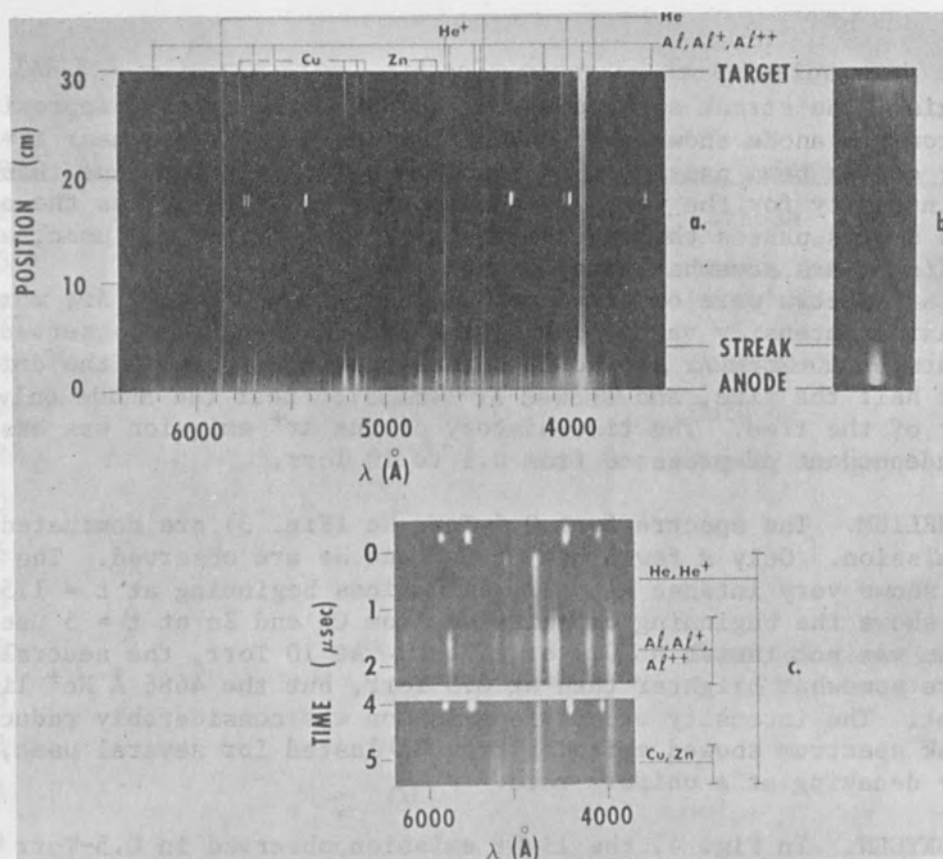


FIG. 3.--Data from 0.5-Torr He experiment: (a) time-integrated beam spectrum; (b) time-integrated beam photograph; (c) time-resolved beam spectrum.

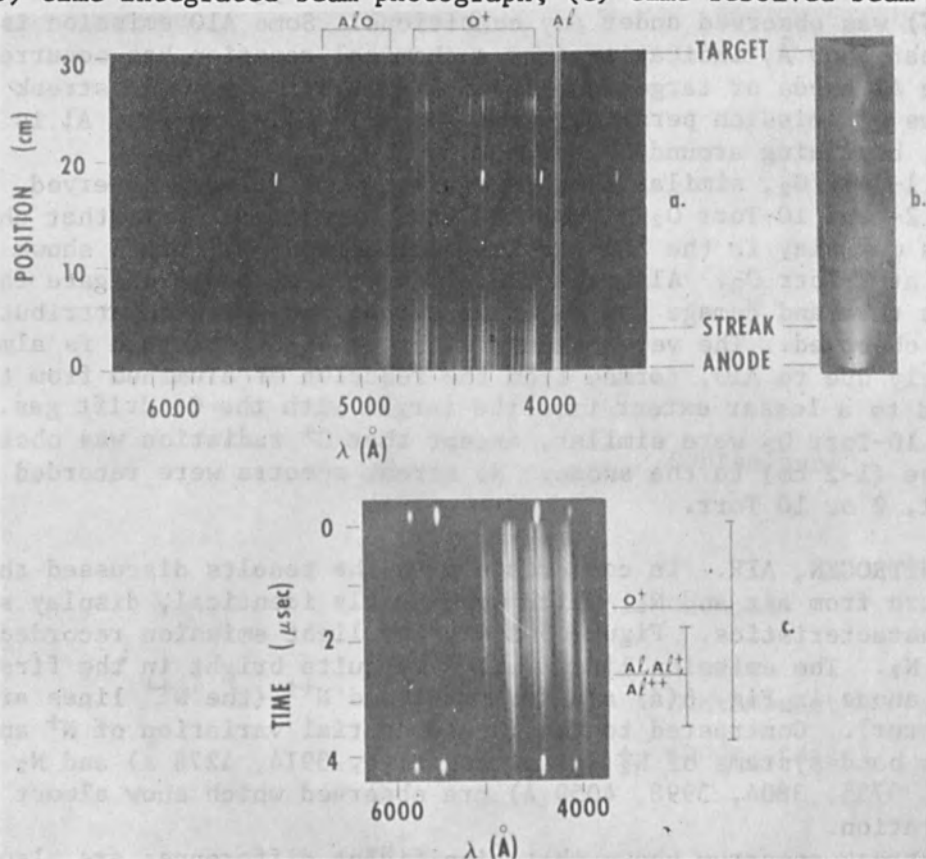


FIG. 4.--Data from 0.5-Torr O₂ experiment: (a) time-integrated beam spectrum; (b) time-integrated beam photograph; (c) time-resolved beam spectrum.

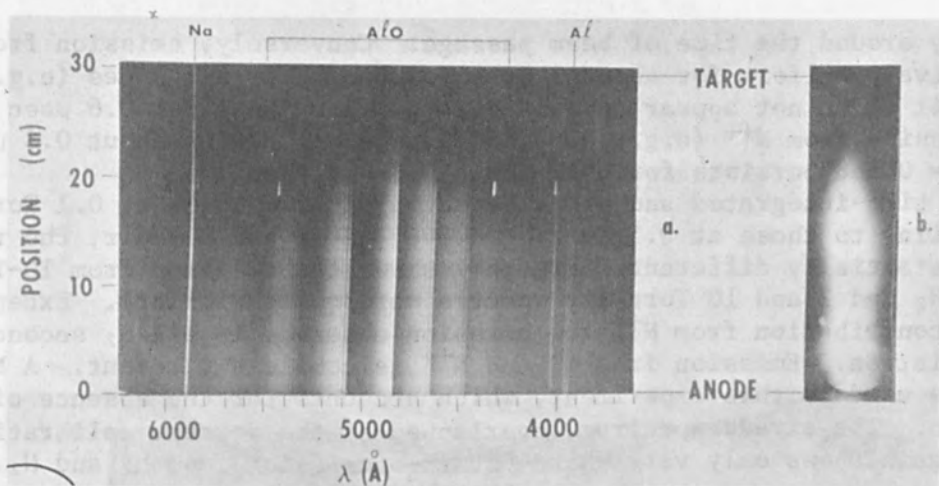


FIG. 5.--Data from 2.0-Torr O_2 experiment: (a) time-integrated beam spectrum; (b) time-integrated beam photograph.

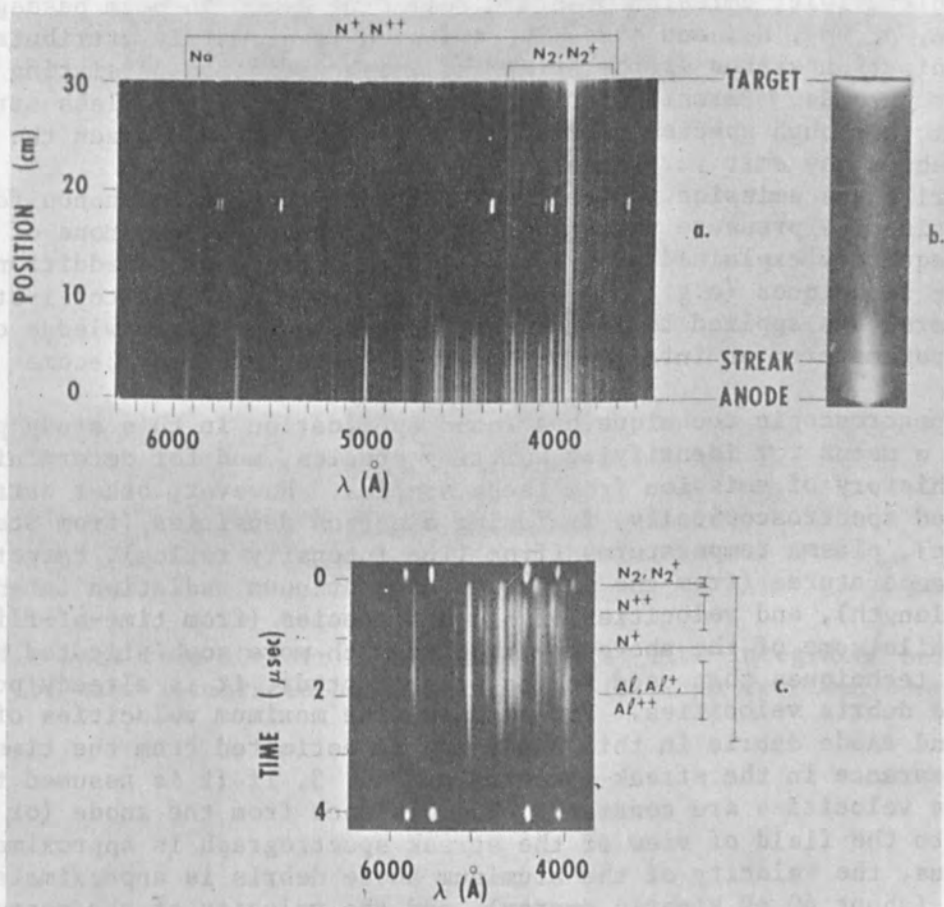


FIG. 6.--Data from 0.5-Torr N_2 experiment: (a) time-integrated beam spectrum; (b) time-integrated beam photograph; (c) time-resolved beam spectrum.

emit only around the time of beam passage. Conversely, emission from N^+ is relatively uniform for about 2 μsec , although certain lines (e.g., 4041, 4241 \AA) do not appear to emit strongly for the first 0.6 μsec or so. Emission from N^{++} (e.g., 4097, 4379, 4867 \AA) begins about 0.3 μsec after $t = 0$ and persists for only about 0.5-0.7 μsec .

Both time-integrated and streak spectra of air and N_2 at 0.1 Torr were similar to those at 0.5 Torr. However, at 2 and 10 Torr, the results were substantially different. Figure 7 shows the emission from 10-Torr N_2 (2-Torr N_2 and 2 and 10 Torr air spectra were quite similar). Except for a minor contribution from N_2^+ , the emission observed is all N_2 second positive radiation. Emission from N^+ and N^{++} is completely absent. A Mylar anode was used in this experiment, which accounts for the absence of Al radiation. The streak spectrum, overlapped by the mercury calibration lines, again shows only very short-duration emission from N_2^+ and N_2 .

DISCUSSION

Spectroscopic techniques have been demonstrated in this study which have allowed an identification of the species responsible for the visible and near-ultraviolet emission observed following electron beam passage through He, Ar, O_2 , N_2 , and air. The emission is primarily attributable to low ionization states of the drift gas, with radiation persisting for a few microseconds. Emission from other sources is observed less strongly in general, although species formed by chemical reaction between the drift gas and debris may emit very intensely.

The drift gas emission typically exhibits marked spatial nonuniformities, distinctive pressure variations, and long decay times, none of which can be adequately explained at present. It is hoped that as additional diagnostic techniques (e.g., net-current monitors, segmented total-stopping calorimeters) are applied to Nereus, giving more complete knowledge of the beam parameters, an interpretation of these features may become possible.

The spectroscopic technique has found application in this study primarily as a means for identifying emitting species, and for determining the time history of emission from these species. However, other data may be obtained spectroscopically, including electron densities (from Stark broadening), plasma temperatures (from line intensity ratios), target surface temperatures (from the variation of continuum radiation intensity with wavelength), and velocities of blowoff species (from time-of-flight data). While some of the above may require much more sophisticated spectroscopic techniques than used in the present study, it is already possible to measure debris velocities. For example, the maximum velocities of the cathode and anode debris in this study may be estimated from the time of their appearance in the streak spectrum of Fig. 3, if it is assumed that the debris velocities are constant. The distance from the anode (or cathode) to the field of view of the streak spectrograph is approximately 3 cm. Thus, the velocity of the aluminum anode debris is approximately 2 $\text{cm}/\mu\text{sec}$ (about 40 eV kinetic energy), and the velocity of the copper and zinc cathode debris is approximately 0.6 $\text{cm}/\mu\text{sec}$ (about 12 eV kinetic energy).

The authors would like to thank T. M. Kasper for his help in setting up the streak camera, and J. A. Walker for his help in setting up the target. J. V. Walker, and J. C. Kelly for many helpful discussions during the course of this work.

The data presented here are the first results of a program to develop a microbeam test system that can be used to test large microcircuit arrays. The system is described in detail in a separate report.

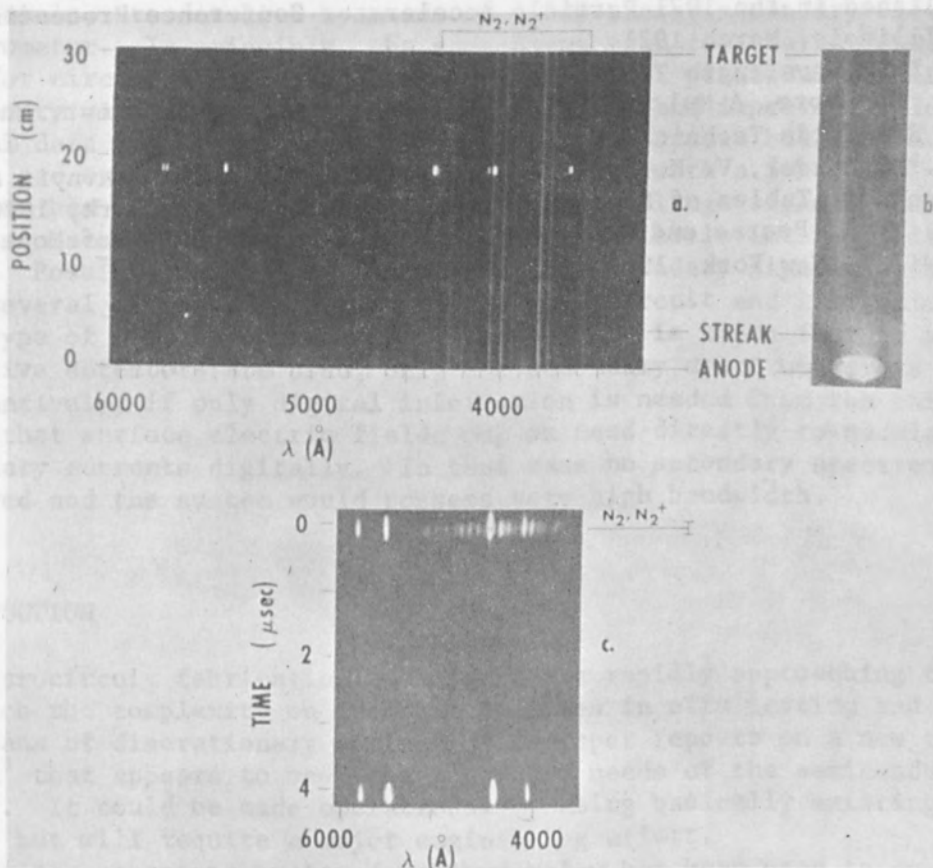


FIG. 7.--Data from 10-Torr N_2 experiment: (a) time-integrated beam spectrum; (b) time-integrated beam photograph; (c) time-resolved beam spectrum.

EXPERIMENTAL APPARATUS

The preprototype system is shown in Fig. 1. A single electron gun consisting of a hair-pin cathode, a control grid, electrostatic focusing, and electrostatic deflection projects a 5-10 μ A electron beam into a 1-cm spot on a microcircuit target. The primary beam striking the target results in the emission of low-energy secondary electrons (SEs) with energies primarily in the 1-10 eV range, and a low level of X rays. The low-energy SEs are collected by a coaxial-cylindrical type electrostatic energy analyzer (Fig. 2). The spectrometer is at about 50 volts above ground. Since the target is approximately at ground potential, the collected electron energy is about 50 eV.

ACKNOWLEDGMENTS

The author would like to thank T. M. Kerley for his help in conducting these experiments and D. A. McArthur for his help in setting up the streak spectrographic apparatus. Thanks are also due to D. A. McArthur, L. S. Nelson, J. V. Walker, and J. G. Kelly for many helpful discussions during the course of this work.

REFERENCES

1. K. R. Prestwich, Nereus, a 250 kV, 80 kA electron beam generator, to be published in the 1971 Particle Accelerator Conference Proceedings, Chicago, Illinois, March 1971.
2. M.I.T. Wavelength Tables, Wiley, New York, 1956.
3. C. E. Moore, A Multiplet Table of Astrophysical Interest, National Bureau of Standards Technical Note 36, 1959.
4. A. N. Zaidel, V. K. Prokofev, S. M. Raiskii, V. A. Slavnyi, and E. Y. Schreider, Tables of Spectral Lines, IFI/Plenum, New York, 1970.
5. R. W. B. Pearse and A. G. Gaydon, The Identification of Molecular Spectra, Wiley, New York, 1963.

ELECTRON MICROBEAM TESTING FOR LARGE MICROCIRCUIT ARRAYS

C. K. CRAWFORD and P. E. KUDIRKA

Particle Optics Laboratory, Massachusetts Institute of Technology,
Cambridge, Mass.

A testing scheme is proposed in which test signals are injected directly into unencapsulated-unwired microcircuit arrays via high-voltage, low-current electron beams. Surface potentials, used both automatically to feedback-stabilize incoming voltage signals and to measure output circuit levels, are detected by means of a low-energy secondary-electron spectrometer. In principle, the same beams used for testing could be used for circuit fabrication, which would permit practical in situ discretionary wiring, greater design flexibility, and improved yield. Experimental data are presented for a pre-prototype system built at M.I.T. Target pad stabilization is better than 100 mV with a 5-kV, 10^{-6} -A beam. The beam has been used both to inject analog voltage signals into an isolated contact, and to read out analog voltage levels into a digital voltmeter. Possible methods of separating the secondary signals resulting from several microbeams bombarding the same circuit and limitations on this type of testing system are discussed. It is shown that if phase-sensitive detectors are used, only one secondary spectrometer is required. Alternatively, if only digital information is needed from the chip, it is shown that surface electric fields may be used directly to modulate the secondary currents digitally. In that case no secondary spectrometer is required and the system would possess very high bandwidth.

INTRODUCTION

Microcircuit fabrication techniques are rapidly approaching the stage at which the complexity on one chip requires in situ testing and a practical means of discretionary wiring. This paper reports on a new testing scheme¹ that appears to meet the long-term needs of the semiconductor industry. It could be made operational by using basically existing technologies, but will require a major engineering effort.

The pre-prototype system described below has been used to demonstrate signal injection and signal readout with a single large-diameter beam. No experimental work has yet been done with small beams or multibeam systems, although calculations show that such systems would work well.

EXPERIMENTAL APPARATUS

The pre-prototype system is shown in Fig. 1. A simple electron gun consisting of a hairpin cathode, a control grid, electrostatic focusing, and electrostatic deflection projects a 5-kV, 10^{-6} -A electron beam into a 1-mm spot on a mockup-microcircuit target. The primary beam striking the target results in the emission of low-energy secondary electrons (along with reflected primaries, Auger electrons, impact desorbed neutrals, ions, and a few soft X rays). The low-energy secondaries are drawn into a coaxial-cylinder type electrostatic energy spectrometer (Fig. 2). The spectrometer is at about 60 V above ground. Since the target is approximately at ground potential, the selected electron energy is about 60 eV.

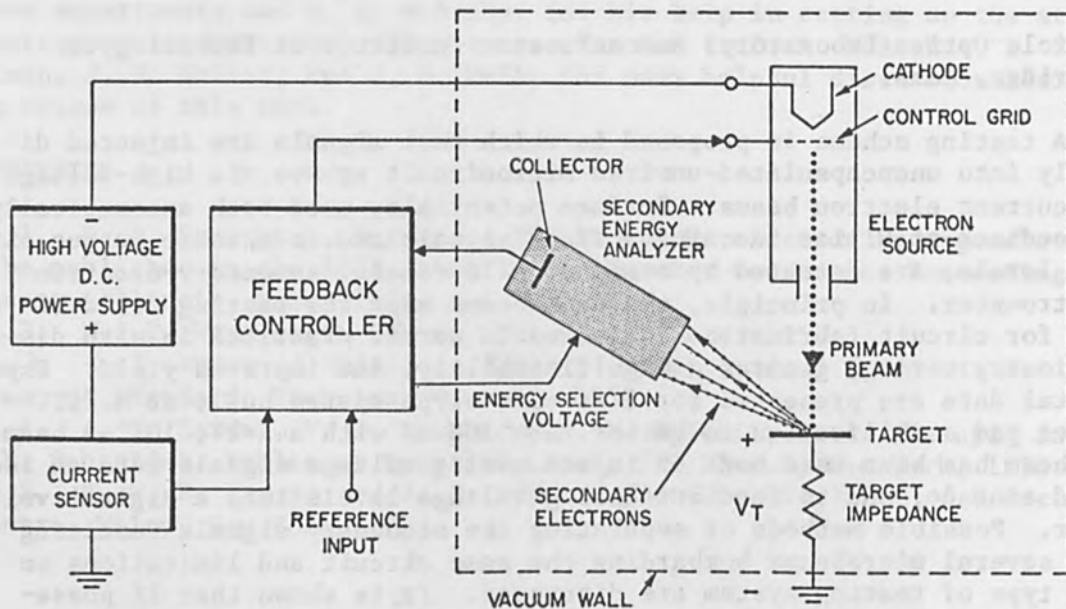


FIG. 1.--Experimental arrangement used to test the electron beam feedback stabilization concept. Output of the secondary energy analyzer is used either to control the primary current and thus stabilize target potential, or to control the energy selection voltage and thus force the spectrometer to track the target potential.

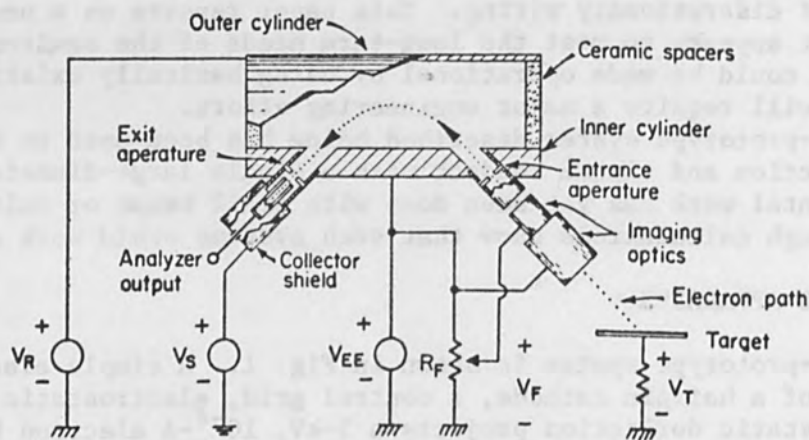


FIG. 2.--Axial-cylinder electron spectrometer used to sense target potential by means of the low-energy secondary electron distribution.

As the spectrometer has a resolution of approximately 50, the minimum energy difference resolvable is a little over 1 V.

Each particle upon leaving the target surface gains an energy equal to the spectrometer aperture potential minus the target potential as it moves into the spectrometer. The energy measured by the spectrometer is this amount plus the electron initial energy. A typical initial energy distribution is shown dotted in Fig. 3. Here the apparent energy with respect to ground (the electron kinetic energy in a field-free region of zero space potential) has been used as the abscissa. The effect of finite spectrometer resolution (solid line in Fig. 3) is to spread the curve out and lower its peak amplitude; the infinite resolution curve is convolved with the spectrometer transmission function. The target potential relative to ground shows up directly as the distance between the origin and the zero emitted kinetic-energy point.

OPERATING MODES

The gun and spectrometer shown in Fig. 1 may now be used in several ways:

(1) The gun alone may be used to inject currents directly into a microcircuit. If the input impedances of a large number of circuits on the chip are all the same (as for example the inputs of a large number of gates) current injection is equivalent to voltage injection. Such operation is stable enough for the injection of digital information.

(2) While injecting a primary beam, the secondary spectrometer can be swept through energy and a quite accurate measurement can be made of the target potential. An alternate procedure, setting the spectrometer energy constant and spatially sweeping the primary beam, is a well-known method for obtaining voltage contrast in scanning electron microscopes.³

(3) The spectrometer output may be fed to a feedback controller which controls the primary beam current. In this way the target potential may be stabilized to any value within the operating limits of the primary beam; and high accuracy analog voltage information may be injected into a circuit even in the face of a time-varying input impedance.

(4) With a fixed primary beam current, the output of the spectrometer can be used to feedback-control the energy selected by the spectrometer. In this way the spectrometer can be made to track the target potential, and the voltage level at any arbitrary target point may be read out directly.

The experimental work described here has been most concerned with modes (3) and (4). For operation in either of these feedback modes, an operating point is chosen about halfway up the low-energy side of the low-energy electron distribution. The current at this point is continuously monitored by the spectrometer. If the target potential changes positively, this current increases; if the target changes negatively, the current decreases. Note that an operating point can be chosen on the high-energy side of the low-energy distribution (where the sign of the changes would be reversed). Experimentally, points chosen here do not work as well, probably because the slope is not as steep.

Mode (3) has an additional small problem that does not occur in mode (4). The spectrometer output is not only a function of the target potential, but is also linearly proportional to primary beam current. This ratio can then be compared with the reference value, and the difference amplified and used to set the gun control grid.

Because the feedback loop is highly nonlinear, due to the shape of the secondary distribution, it is difficult to treat analytically; however, a computer simulation was made which approximately agrees with the results.

RESULTS

System performance was monitored by comparing two digital voltmeters. One voltmeter was connected to the controller reference input, with an operational amplifier used to take out various offsets and calibration constants. The second voltmeter, equipped with a high-impedance input, was connected between the target and ground.

The system holds target potentials to within about 100 mV or about 1 per cent of full range; regulation is limited mainly by two factors. First, the electronic circuits used in these initial experiments are full of noise and drift. Second, the secondary emission yield δ is not constant but varies with time as a result of contamination of the target pad by cracking of residual organics under primary-electron bombardment. These experiments were all done in a 10^{-7} -torr vacuum system in which the organic background was quite high. In a production microbeam tester in which higher accuracy is required, either good vacuum must be provided, or testing must be accomplished quickly before contamination layers have time to build up. In the present system contamination was always present; thus the solid curve in Fig. 3 really represents the secondary yield of a contamination layer rather than the underlying stainless steel.

Regulation was observed over a range in target potential of about 0.1 to 10 V and a range in target impedance from 10^6 to $10^7 \Omega$. For voltages at the low end of the voltage range and for high target impedances the performance is limited by noise. For low impedances, the performance is limited by the available primary-beam current. The primary current was arbitrarily temperature limited in the gun to a value of about 1.3×10^{-6} A because this is the approximate limiting value that is experienced when small-diameter beams are used.

Operation in the potential sensing mode is checked by connecting one digital voltmeter to the energy analyzer selection voltage (via another appropriate calibration network) and adjusting the feedback loop to make the spectrometer track the target. The second voltmeter is connected to the target as before. Performance in this mode is comparable to the previous in terms of sensitivity and frequency response; actually operation is easier since the feedback loop is simpler and there aren't fewer ways for the system to become unstable.

The frequency response is limited at present by the poor electronics to about 10 Hz. With better electronics a gun-spectrometer combination could inject signals in the megacycle range. For high-frequency response, it would be desirable to add an electron multiplier to the spectrometer output.

The secondary yield δ at 5 kV is of the order of 0.5; most of the electrons are in the low-energy part of the distribution. Since primary beam currents of 10^{-6} A result in peak secondary currents of only about 4×10^{-9} A, it is clear that the optics imaging the emitted secondaries into the spectrometer are not very efficient. No serious attempt has been made to make this design efficient. Considerable improvement is possible.⁴

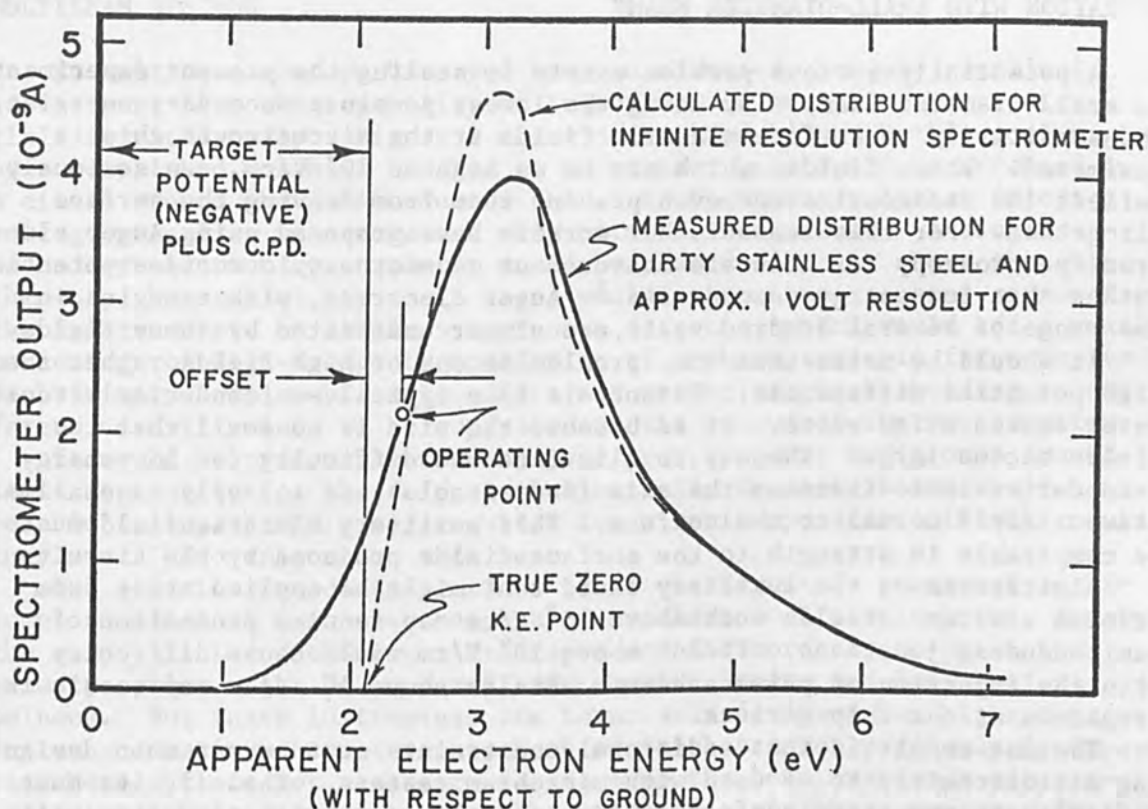


FIG. 3.--Electron spectrometer output as a function of electron kinetic energy referenced to a field-free region of zero space potential. Note that poor spectrometer resolution does not preclude accurate measurement of the target potential.

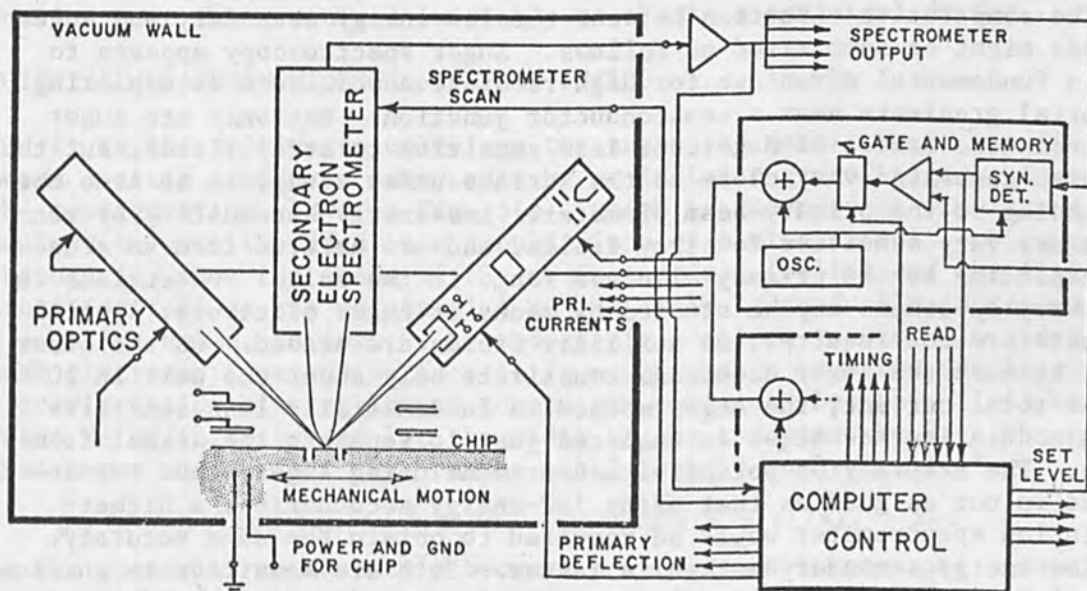


FIG. 4.--Proposed multibeam system using several electron guns and a single electron spectrometer. Synchronous detectors are used to separate the secondary currents due to each primary beam. (The divide-by-primary-current function is provided inside the computer control.) Geometry is not to scale.

OPERATION WITH SMALL-DIAMETER BEAMS

A potentially serious problem exists in scaling the present experiments to small-diameter beams. By using the lowest possible secondary energies, the sensitivity to surface electric fields at the microcircuit chip is maximized. These fields, which may be as high as 10^4 V/cm, can seriously deflect the secondaries and even prevent them from leaving the surface altogether. For this reason other workers have proposed using Auger electron spectroscopy for accurate measurement of microscopic surface potential rather than low-energy secondaries.⁵ Auger electrons, with energies in the range of several hundred volts, are almost unaffected by these fields.

It should be noted that the problem is one of high fields rather than high potential differences. Potentials in a typical semiconductor circuit never exceed a few volts. It is because the size is so small that the fields become large. The way to alleviate the difficulty for low-energy secondaries is to increase the size (undesirable), or to apply an auxiliary drawout field normal to the surface. This auxiliary electric field must be comparable in strength to the surface fields produced by the circuit.

Limitations on the auxiliary field that might be applied arise from several sources. Fields much above 10^3 V/cm may require protection of semiconductor junctions. Fields above 10^4 V/cm would cause difficulty with the injection of primary beams. Fields above 10 V/cm may result in breakdown at the chip surface.

The net result is that additional constraints must be met when designing microcircuitry to be used with microbeam testers. The circuits must not generate excessive surface fields, and they must withstand the auxiliary field used to collect secondaries. Probably all semiconductor junctions will have to be shielded by an insulated overlying metal layer. These constraints are not unreasonable when one considers the major changes that will be required in the microcircuitry anyway to take advantage of microbeam testing and the magnitude of the advantages which accrue.

The comparative situation between the low-energy secondary and Auger methods might be summarized as follows. Auger spectroscopy appears to have a fundamental advantage for high-resolution work such as exploring potential gradients near a semiconductor junction. Not only are Auger electrons two orders of magnitude less sensitive to stray fields, but they are also generated very close to the surface under study, in an area corresponding to the primary-beam diameter. Low-energy secondaries by contrast are very sensitive to stray fields, and are emitted from an area corresponding to the primary electron range in the solid. Potentials in arbitrary specimens may be studied by means of Auger electrons; special circuits are not required; no auxiliary fields are needed. On the other hand, because the Auger electrons constitute only about one part in 10^3 of the total current, the Auger method is fundamentally less sensitive and a modulation technique is required just to separate the signal from noise. The accuracy of potential measurement using Augers thus far obtained is not as good as that using low-energy secondaries; a higher-resolution spectrometer would be required to obtain the same accuracy. The low-energy secondary method is faster. Both are sensitive to surface contamination.

In short, the Auger method is better suited as an analytical technique, whereas the secondary method is more suitable for high-volume production testing.

MULTIBEAM SYSTEMS

No multibeam systems have yet been constructed, but any practical tester must have the capability of injecting and measuring many potentials simultaneously. Figure 4 shows one method by which this goal might be accomplished. A half a dozen or so primary guns would be arranged in a circle around the semiconductor chip. Each gun would either inject a voltage signal or interrogate a chip potential as needed. A single secondary-electron spectrometer would be placed directly above the chip; the chip, because of its small size, would approximate a point source for the spectrometer. A simple synchronous detector, which would add a small percentage of high-frequency modulation of a characteristic frequency to each primary beam, would allow different potentials corresponding to different circuit points to be separated at the output of the spectrometer.

It would be presumably necessary to provide power and ground connections separately for the chip as realistically designed beams would not be able to inject the power required for circuit operation; if they could they would also inject too much heat.

The question immediately arises as to whether it is practical to attempt to place so much electron optics so close to a single point, namely the chip. It is. Scanning microscopes and microprobes, to which the primary optics might be compared, use massive lenses and long optical columns. But these instruments are invariably designed for highest resolution and maximum beam current, both of which are not particularly important here. It is not necessary to use even the best available electrostatic systems⁶ in order to meet the needs of a microbeam tester. In this laboratory a small electrostatic optical system has been designed (for another purpose) that has an over-all outside diameter of 1.5 cm, an objective lens⁷ with a working distance of about 1 cm, and a spherical aberration coefficient of only a few centimeters. With a reasonably bright electron source such guns would produce about 10^{-6} A in a 1- μ m spot--a smaller spot than required initially to obtain a practical device.

POTENTIAL MEASUREMENT USING SURFACE FIELDS

It is instructive to calculate the shape and magnitude of the field above a strip conductor surrounded by an infinite ground plane. Consider the configuration shown in Fig. 5(a), which is intended to simulate a flat conducting wire imbedded in a ground plane of a microcircuit. Figures 5(b) through (f) show the shape of the equipotentials (solid) and the field lines (dotted) as the potential ϕ on the strip is gradually increased from a negative value, through 0, to moderately positive values. In order to draw electrons from the surface it is necessary to have the auxiliary electric field pointing inward toward the surface. Let this field have value E_0 at infinity and let the width of the conductor be $2a$. The potential above the surface here can be easily solved analytically:⁸

$$\phi = (\phi_0/\pi) \{ \text{arc tan}[(x + a)/z] - \text{arc tan}[(x - a)/z] \} + E_0 z \quad (1)$$

As the potential on the strip becomes positive, an interesting situation occurs. The field in the center of the strip still points in (drawing out electrons), whereas at the edge of the strip the emission of electrons is retarded. As the potential is made more positive, a critical potential is reached where the field in the center of the strip is zero. The value of the potential at this point is

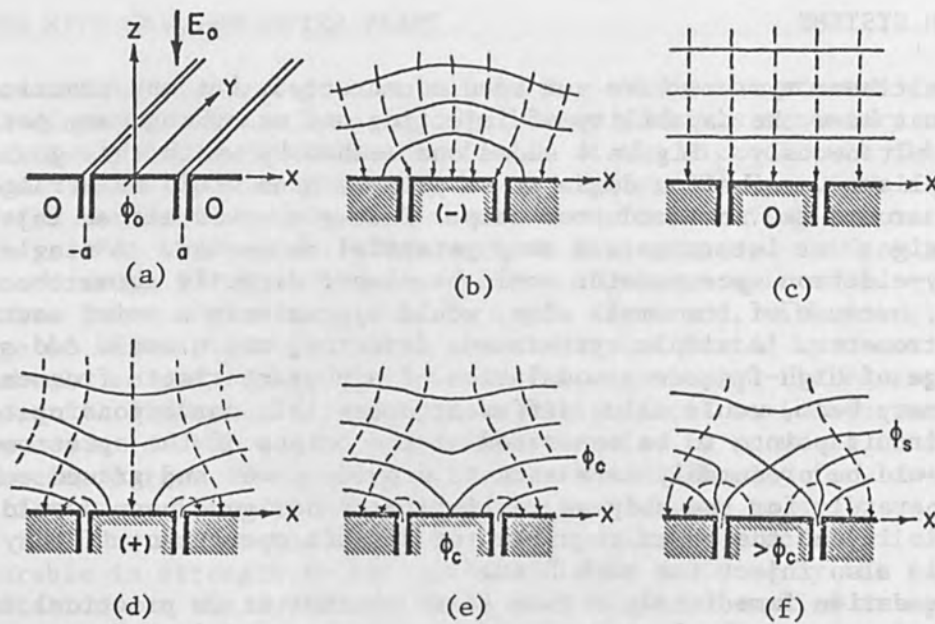


FIG. 5.--Equipotential and field lines in the neighborhood of a narrow flat strip imbedded in an infinite conducting plane.

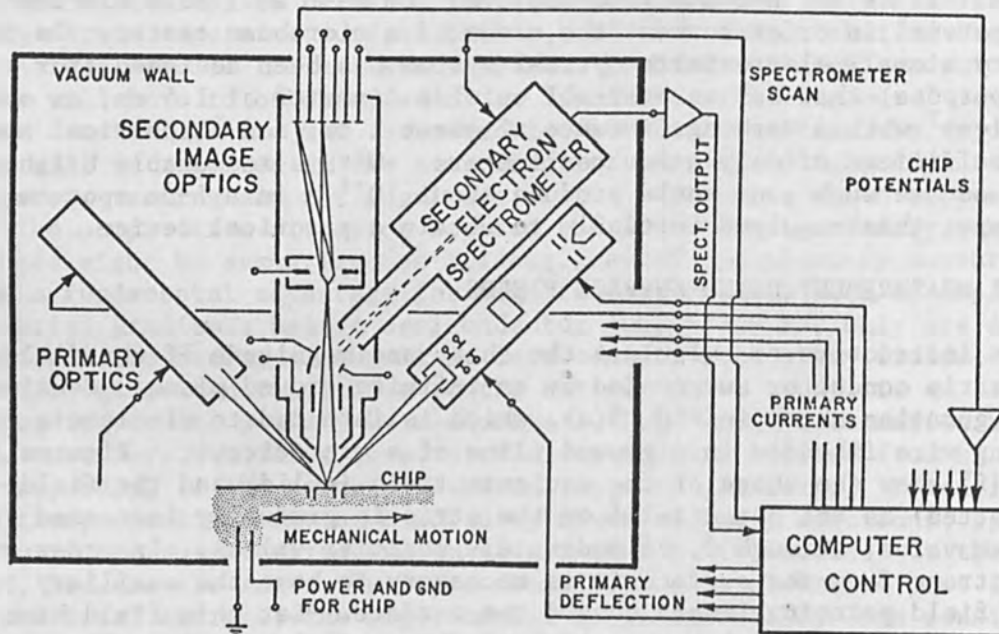


FIG. 6.--Proposed binary microcircuit tester using surface fields to modulate secondary electron emission. Image optics similar to that of an emission microscope would be used to project each secondary signal onto a separate collector. An auxiliary electron spectrometer would allow analog information to be obtained from any single arbitrary point. Electron multipliers could be inserted if required for higher speed; ultimate speed limitations would be very high.

$$\phi_0 = \phi_c = \frac{\pi}{2} aE_0 \quad (2)$$

Further increase results in a saddle point (potential ϕ_s) launching itself off into space above the strip. When this occurs a trap potential surrounds the strip which prevents the escape of all electrons with initial energies less than $e\phi_t$, where

$$\phi_t = \phi_0 - \phi_s = \phi_0 [1 - (2/\pi) \arctan(a/z_s)] \quad (3)$$

Here z_s is the z coordinate of the saddle point above the surface and is obtained by solving the transcendental equation

$$\arctan(a/z_s) = (\pi/2)^2 (aE_0/\phi_0) [(z_s/a)^2 + 1] \quad (4)$$

An instructive and easily solved case occurs when $z_s = a$, at which point $\phi_t = \phi_0/2$. When $z_s = 0$, $\phi_t = 0$; as z_s goes to infinity, ϕ_t goes to ϕ_0 , its maximum value.

It is now seen that for low-energy secondaries with initial kinetic energies of only 2-3 eV, and chip potentials which vary in the same range, one can use the chip potentials to turn secondary emission on or off in a binary way. It is only necessary to provide a suitable ground plane on either side of each conductor and supply an appropriate draw-out field. Whereas previously the largest possible draw-out field was desired for maximum spectrometer transmission, one now sees that the field should not exceed

$$E_0 = \frac{(2/\pi)^2 \phi_0 \arctan(a/z_s)}{a[(z_s/a)^2 + 1]} \quad (5)$$

where z_s is chosen to be small compared to the distance between two wires (to prevent interactions).

A configuration suitable for taking advantage of this effect is shown in Fig. 6. Test points in the circuit would either emit or not emit low-energy secondaries under primary interrogation, depending upon a low or high logic level. Note that an energy spectrometer is no longer required (but energy selection would improve the ratio of signal to noise). The image optical system for handling the secondary electrons would be similar to that of an emission microscope; this class of instruments has been well studied. An array of collectors in an image plane responds to the secondary signals from each circuit point. Calculations show that the microscope optics could easily have sufficient resolution (limited primarily by chromatic aberration, which results from the initial secondary energies), that back scattered primaries would not be a major problem, and that there is room for all this equipment near a chip. Collectors corresponding to input points on the chip could be used to check proper signal injection for guns operating in mode (1).

As a final embellishment, one might include a set of deflection plates and a secondary spectrometer to allow analog measurements to be made at a single arbitrary point in the circuit.

CONCLUSIONS

Instruments of this type might be combined advantageously with the electron-beam fabrication technology now being vigorously developed by many workers, and should provide a major boost to the semiconductor processing industry. In principle the same primary beams could be used both

for fabrication and testing. In such a case, discretionary wiring could be used to overcome the yield problems associated with very large arrays as well as greatly to reduce setup costs. It should be possible to fabricate, test, and encapsulate circuits completely in an ultra-high-vacuum environment, all with processes that are particularly amenable to computer control.

REFERENCES

1. C. K. Crawford, M.I.T. Particle Optics Laboratory Tech. Rep. 2, Feb. 1968; P. E. Kudirka, Thesis, M.I.T. (June 1970); and C. K. Crawford and P. E. Kudirka, Bull. Am. Phys. Soc. 16: 187, 1971.
2. V. V. Zashkvara, M. I. Korsunskii, and O. S. Kosmachev, Sov. Phys.-Tech. Phys. (Engl. Trans.) 11: 96, 1966; H. Z. Sar-El, Rev. Sci. Instr. 38: 1210, 1967; and H. Hafner, J. A. Simpson, and C. E. Kuyatt, Rev. Sci. Instr. 39: 33, 1968.
3. O. C. Wells and C. G. Bremer, J. Sci. Instr. 1: 902, 1968.
4. A. J. Lichtenberg, Phase-Space Dynamics of Particles, Wiley, New York, 1969.
5. N. C. MacDonald, Scanning Electron Microscopy/1970, ITT Res. Inst., Chicago, 1970, p. 481; N. C. MacDonald, Appl. Phys. Lett. 16: 76, 1970.
6. A. V. Crewe et al. Rev. Sci. Instr. 39: 576, 1968; J. Appl. Phys. 39: 5861, 1968.
7. A. Septier, CERN 60-39.
8. P. M. Morse and H. Feshbach, Methods of Theoretical Physics, McGraw-Hill, New York, 1953; also see comment by O. C. Wells, Scanning Electron Microscopy/1970, ITT Res. Inst., Chicago, 1970.
9. P. Grivet, Electron Optics, Pergamon Press, New York, 1965.

SESSION ON BEAM PHYSICS

ELECTRON-BEAM DEFLECTION IN TRAVELING-WAVE OSCILLOSCOPES*

JAMES R. ANDREWS and N. S. NAHMAN

National Bureau of Standards, Boulder, Colo.

A generalized electron-beam deflection theory is presented that is applicable to fast- or slow-wave deflection structures in traveling-wave oscilloscopes. The theory includes the deflection structure circuit properties and the electron beam dynamics. The results of experiments on two traveling-wave deflectors are presented: (1) a fast-wave rectangular transmission line, and (2) a slow-wave serrated rectangular transmission line. The theoretical and experimental results were correlated in the frequency and time domains. The rise times of the experimental traveling-wave oscilloscopes were in the range of 95 to 211 picoseconds (ps).

INTRODUCTION

A pulse instrumentation system¹ consists of three basic parts: (1) the pulse generator, (2) the interconnecting transmission line and connectors, and (3) the detector. To date, the most useful instrument for pulse detection has been the oscilloscope. For extremely fast pulse measurements in the subnanosecond ($< 10^{-9}$ s) region, there are two types of oscilloscopes: the sampling oscilloscope, and the direct-deflection, traveling-wave oscilloscope. The state of the art in sampling oscilloscopes is at present in the region of 20 to 30 ps (10^{-12} s) 10-90-percent transition times. The major disadvantage of the sampling oscilloscope is that it requires a repetitive waveform. For the measurement of single subnanosecond transients, the only instrument available is the traveling-wave cathode-ray-tube oscilloscope (TWCRT). The state of the art in TWCRTs is at present in the region of 70-ps transition times.

This paper is concerned with the traveling-wave oscilloscope. A generalized set of TWCRT deflection equations are presented² and, from them, the deflection system transfer function $H(j\omega)$ can be obtained. $H(j\omega)$ is defined as the complex ratio of the electron beam displacement to signal voltage applied to the deflection structure. Although many TWCRTs have been described, none has been rigorously analyzed to determine $H(j\omega)$. It is desirable to know $H(j\omega)$ as this removes one unknown from the pulse measurement system. If $H(j\omega)$ and the transmission-line transfer function are known, then for a given pulse input, it is possible to compare the predicted and the observed waveforms.

If a relatively simple fast-wave structure is used for the traveling-wave deflector, it is possible to build a TWCRT with a transfer function that is very predictable and based only upon fundamental measurements of length and dc voltage. An actual experimental fast-wave TWCRT is described which has a calculated deflection rise time of 211 ps.

To obtain further reductions in the risetime while maintaining the same deflection sensitivity, one must use slow-wave transmission-line deflection structures. In this paper, a TWCRT using a rectangular transmission line with a serrated inner conductor as a deflection structure

*Contribution of the National Bureau of Standards. Not subject to copyright.

is described. An experimental TWCRT with a calculated 10-90-percent deflection transition time of 95 ps has been constructed with this slow-wave deflector.

THEORY

In TWCRT deflection system (Fig. 1), the deflection plates are considered to be a transmission line of impedance Z_0 and phase velocity v_p . Electrons enter from the left and travel towards the screen with an axial velocity v_z .

An insight into the operation of a TWCRT can be obtained by performing a time-domain analysis of the step response of a simple, fast, forward-wave deflection structure.³ For this case, the transmission-line deflector's impedance and phase velocity are independent of frequency. In addition, to ensure that only forward traveling waves are present, we set Z_0 equal to the load impedance Z_L and the generator impedance Z_G .

Assume that the generator switch is closed at $t = t_0$. The electric field applied across the deflectors has a wavefront that moves toward the right with a velocity v_p . The E-field forward-moving wavefront affects various electrons differently depending on their location relative to the deflection plates at $t = t_0$. Consider electron e_1 which has not yet entered the deflection region at $t = t_0$. When it enters the deflection region it simply sees a steady dc field between the plates. It undergoes a simple dc deflection and arrives at the screen after a time of flight of $\tau_{dp} + \tau_{ds}$, where τ_{dp} and τ_{ds} are the electron transit times through the deflection region and drift space, respectively. The other limiting case is for an electron e_3 lying within the deflection region such that its position at $t = t_0$ is given by

$$z_3 = v_z (\tau_{dp} - \tau_w) \quad (1)$$

Here, τ_w is the electromagnetic wave transit time through the deflection region. Because the electromagnetic wave is usually traveling faster than the electrons, it eventually catches up with the electrons. In the case of electron e_3 , the electron just leaves the deflection region at the same instant that the wave overtakes it, time $t_0 + \tau_w$. Thus the net deflection is zero for electron e_3 and all the electrons preceding it.

From these two cases, then, the transition time can be deduced. The spot displacement at the screen starts from the 0-percent level at time $t_0 + \tau_w + \tau_{ds}$ and goes to the 100-percent level after time $t_0 + \tau_{dp} + \tau_{ds}$. Thus the 0-100-percent transition time is

$$\tau_t = \tau_{dp} - \tau_w = \sigma \tau_{dp} \quad (2)$$

where σ is defined as a slipping factor

$$\sigma \equiv (v_p - v_z) / v_p \quad (3)$$

The step response is shown in Fig. 2. The actual shape of the transition is discussed later.

A detailed analysis of TWCRT deflection must include many factors. It must allow for both forward and reverse (reflected) traveling electromagnetic waves. Magnetic deflection of the electron beam due to currents flowing in the deflection plates must be included in addition to the beam deflection caused by voltages on the plates. The analysis should consider

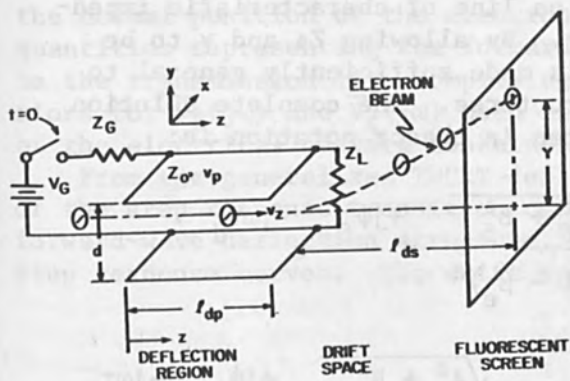


FIG. 1.--TWCRT deflection system.

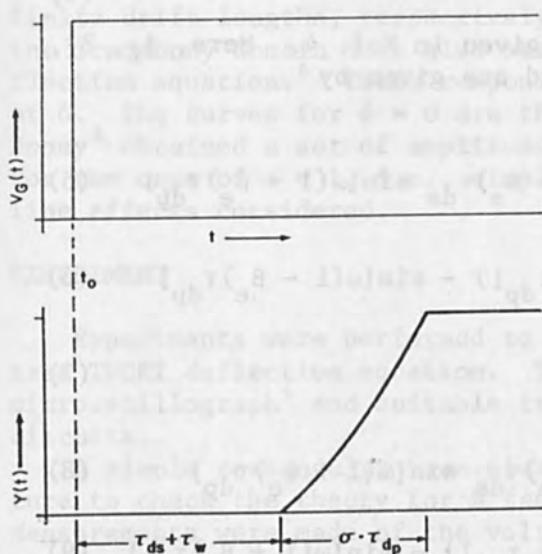


FIG. 2.--Step response to fast-wave TWCRT.

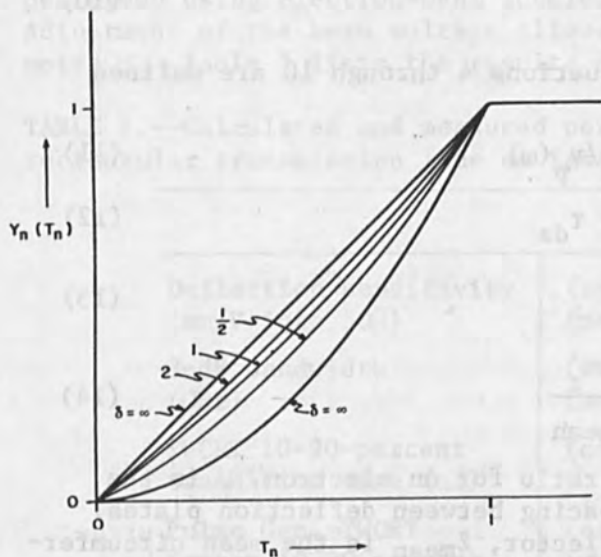


FIG. 3.--Normalized step response of simple forward traveling-wave CRT deflection system; δ is drift space parameter.

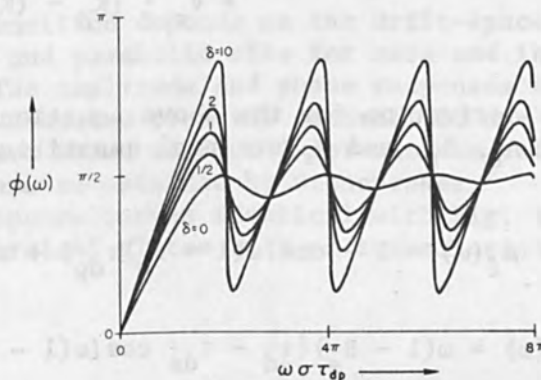
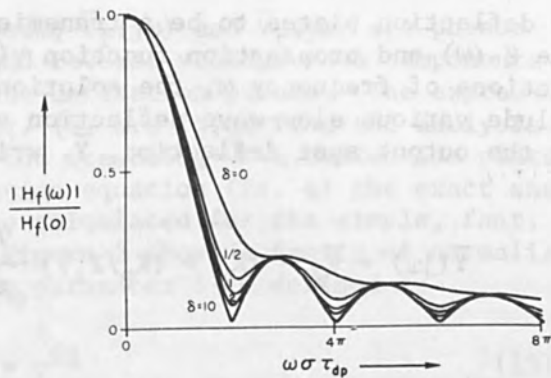


FIG. 4.--Amplitude and phase responses vs frequency for simple forward traveling-wave CRT deflection structure.

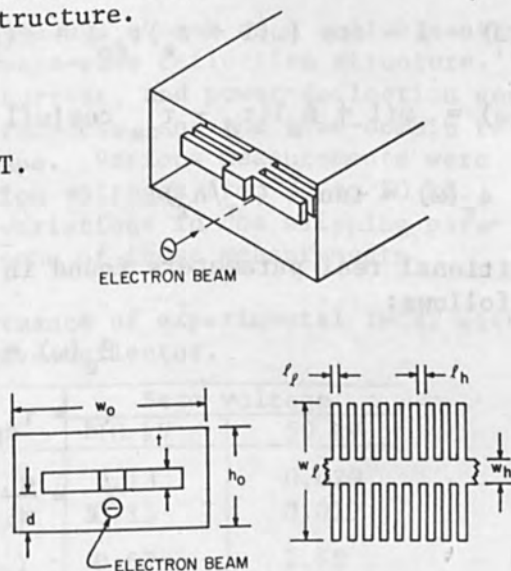


FIG. 5.--Serrated rectangular transmission-line slow-wave deflection structure.

the deflection plates to be a transmission line of characteristic impedance $Z_0(\omega)$ and propagation function $\gamma(\omega)$. By allowing Z_0 and γ to be functions of frequency ω , the solution is made sufficiently general to include various slow-wave deflection structures. The complete solution for the output spot deflection, \bar{Y} , written in phasor notation is:

$$\begin{aligned} \bar{Y}(j\omega) = & \bar{V}_f \cdot [K_E + (K_B/Z_0)] \frac{\sqrt{A_f^2 + B_f^2}}{\omega^2(1 - \beta_e)^2} e^{+j\phi_f} e^{-j\omega\tau_d} \\ & + \bar{V}_r \cdot [K_E - (K_B/Z_0)] \frac{\sqrt{A_r^2 + B_r^2}}{\omega^2(1 + \beta_e)^2} e^{+j\phi_r} e^{-j\omega\tau_d} \end{aligned} \quad (4)$$

The derivation for the above equation is given in Ref. 4. Here, A_f , B_f , ϕ_f , A_r , B_r , and ϕ_r are real quantities and are given by

$$A_f(\omega) = 1 - \cos[\omega(1 - \beta_e)\tau_{dp}] + \omega(1 - \beta_e)\tau_{ds} \sin[\omega(1 - \beta_e)\tau_{dp}] \quad (5)$$

$$B_f(\omega) = \omega(1 - \beta_e)\{\tau_d - \tau_{ds} \cos[\omega(1 - \beta_e)\tau_{dp}]\} - \sin[\omega(1 - \beta_e)\tau_{dp}] \quad (6)$$

$$\phi_f(\omega) = \tan^{-1} (B_f/A_f) \quad (7)$$

$$A_r(\omega) = 1 - \cos[\omega(1 + \beta_e)\tau_{dp}] + \omega(1 + \beta_e)\tau_{ds} \sin[\omega(1 + \beta_e)\tau_{dp}] \quad (8)$$

$$B_r(\omega) = \omega(1 + \beta_e)\{\tau_d - \tau_{ds} \cos[\omega(1 + \beta_e)\tau_{dp}]\} - \sin[\omega(1 + \beta_e)\tau_{dp}] \quad (9)$$

$$\phi_r(\omega) = \tan^{-1} (B_r/A_r) \quad (10)$$

Additional real parameters found in equations 4 through 10 are defined as follows:

$$\beta_e(\omega) = v_z/v_p(\omega) \quad (11)$$

$$\tau_d = \tau_{dp} + \tau_{ds} \quad (12)$$

$$K_E = \frac{e}{m_0} \frac{1}{d} \quad (13)$$

and

$$K_B = \frac{-e}{m_0} \frac{\mu v_z}{\ell_{\text{mean}}} \quad (14)$$

The factor e/m_0 is the charge-to-mass ratio for an electron, μ is the magnetic permeability, and d is the spacing between deflection plates. In a rectangular transmission-line deflector, ℓ_{mean} is the mean circumference of the H-field lines around the center conductor which pass through

the normal position of the electron beam; $\bar{V}_f(j\omega)$ and $\bar{V}_r(j\omega)$ are phasor quantities representing the forward and reverse voltage-wave components on the transmission line comprising the deflection plates. The expressions for $\bar{V}_f(j\omega)$ and $\bar{V}_r(j\omega)$ used in Eq. (4) are found from the analysis of the electrical network containing the traveling-wave deflection plates.

From the generalized TWCRT deflection equation (Eq. 4) the exact shape of the step response transition can be calculated for the simple, fast, forward-wave deflection structure.⁵ Figure 3 shows a family of normalized step response curves. The drift space parameter δ is defined as

$$\delta \equiv \frac{\tau_{ds}}{\tau_{dp}} = \frac{l_{ds}}{l_{dp}} \quad (15)$$

The shape of the 0- to 100-percent transition depends on the drift-space parameter. It is bounded by a linear and parabolic rise for zero and infinite drift lengths, respectively. The amplitude and phase responses in the frequency domain have also been calculated from the generalized deflection equation.⁶ These responses are shown in Fig. 4 for various values of δ . The curves for $\delta = 0$ are the same as obtained by Stonebraker.⁷ Honey⁸ obtained a set of amplitude response curves identical with Fig. 4(a) for the case of $\sigma = 1$, i.e., simple parallel plates with no transmission-line effects considered.

EXPERIMENT

Experiments were performed to demonstrate the utility of the generalized TWCRT deflection equation. The work was done using a modified Lee microscillograph⁹ and suitable trigger, unblanking, and time-base¹⁰ circuits.

A simple rectangular transmission line was chosen as a suitable structure to check the theory for a fast forward-wave deflection structure.¹¹ Measurements were made of the voltage, current, and power-deflection sensitivities, the amplitude-vs-frequency response, and the time-domain response to a fast pulse of known wave shape. Various measurements were performed using electron-beam acceleration voltages from 10 to 50 kV. Adjustment of the beam voltage allowed variations in the slipping parameter σ . Table I lists the results of some of these measurements.

TABLE I.--Calculated and measured performance of experimental TWCRT with rectangular transmission line as fast-wave deflector.

		Beam voltage	
		10 kV	50 kV
Deflection sensitivity (mm/V into 50 Ω)	(calc.)	0.13	0.020
	(meas.)	0.13	0.019
3-dB bandwidth (GHz)	(calc.)	0.57	1.68
	(meas.)	0.58	1.48
TWCRT 10-90-percent transition time (ns)	(calc.)	0.608	0.211
Pulse Gen.-TWCRT System 10-90-percent transition time (ns)	(calc.)	0.65	0.29
	(meas.)	0.65	0.30

A slow-wave deflection structure was also operated.¹² The slow-wave configuration was a rectangular transmission line of the same over-all dimensions as that used in the fast-wave study. The center conductor was serrated as shown in Fig. 5. The calculated deflection step response of this structure is shown in Fig. 6. The 10-90-percent deflection transition time is 95 ps. Owing to inability to obtain a sharp beam focus through this deflector it was not possible to make precise measurements. Measurements of the TWCRT response to a high-speed pulse of known wave-shape did give agreement between calculated and measured values of 10-90-percent transition time to within ± 22 per cent. For example, the calculated generator/TWCRT system transition time was 183 ps, whereas the measured value was between 0.14 and 0.22 ns.

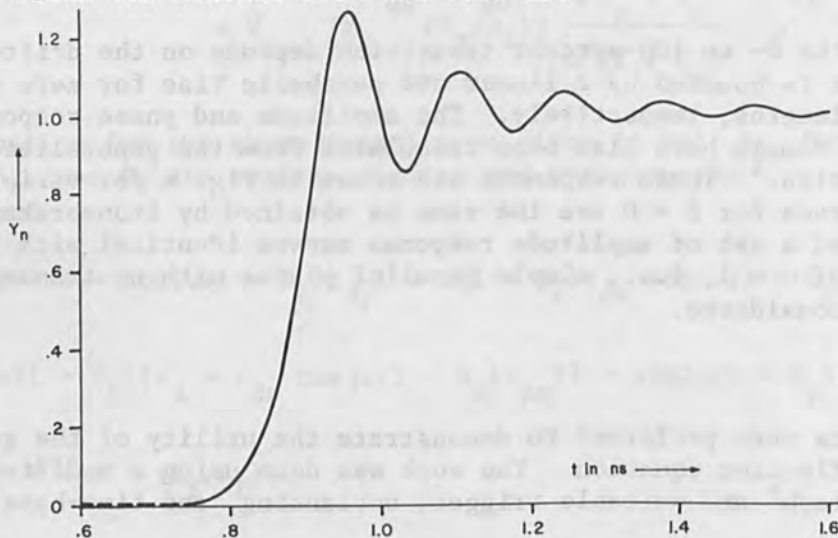


FIG. 6.--Calculated deflection step response of slow-wave TWCRT for 50-kV beam voltage.

REFERENCES

1. N. S. Nahman, Measurement of baseband pulse rise times of less than 10^{-9} second, Proc. IEEE 55: 855-864, 1967.
2. J. R. Andrews, Deflection Theory of Traveling Wave Oscilloscopes, Ph.D. Dissertation, Electrical Engineering Dept., Univ. of Kansas, Lawrence, Kansas, April 1970.
3. Ibid., Sec. 3.2.
4. Ibid., Sec. 3.3.
5. Ibid., Sec. 3.5.
6. Ibid., Sec. 3.4.
7. D. M. Stonebraker, Analysis and design of an oscilloscope deflection system with a calculable transfer function, J. Res. NBS, 72C: No. 2, April-June 1968.
8. R. C. Honey, A traveling-wave electron deflection system, IRE Trans. MTT-2: 2-9, 1954.
9. G. M. Lee, A three-beam oscillograph for recording at frequencies up to 10,000 megacycles, Proc. IRE (Waves and Electrons), pp. 121W-127W, Mar. 1946.
10. J. R. Andrews, Horizontal-time-base sweep generator for a traveling-wave oscilloscope, to be published.
11. Ref. 2, Chap. 4.
12. Ibid., Chaps. 6 and 7.

A NEW TYPE OF TRAVELING-WAVE DEFLECTION SYSTEM

T. TAKAGI and I. YAMADA

Kyoto University (Dept. of Electronics), Kyoto, Japan

The analysis of the meander lines type of traveling-wave deflection system shows that the deficiency in the dispersion characteristic is due to the interaction of the electromagnetic field on a section of a finger with that on the other fingers. Insertion of a shielding plate between two neighboring sections of the fingers reduces the mutual interactions. The meander line with the shielding plate is called the trough-type of traveling-wave deflection system. The analysis shows that uniform characteristics of the dispersion and the admittance with respect to the frequency are expected in the trough type of traveling-wave deflection system. Loading by dielectric material of the space among electrodes serves to decrease the phase velocity and to increase the deflection sensitivity. In the experimental CRT in which the trough type of traveling-wave deflection system is used, a uniform sensitivity is confirmed experimentally in the frequency range from dc to above 4 GHz and the deflection of 6 mm by 10-mW input is measured.

INTRODUCTION

Traveling-wave deflection systems are commonly used to obtain a uniform characteristic of the deflection of the beam in a wide frequency range. These systems are basically designed to match the phase velocity of the signal along the tube axis to the electron-beam velocity. Several types of traveling-wave deflection systems have been proposed,¹ and recently some of them have been put into practical service. However, to the knowledge of the authors, until now the analysis of deflection characteristics has been done either by equivalent circuit approximation or, in the case of narrow frequency bandwidth, by considering only the low frequency range. These analyses give good approximations for special conditions, but since neither the periodic structure nor the size of the system are considered, they cannot describe all the characteristics of the traveling-wave deflection system over wide frequency ranges.

The authors analyzed the meander type of traveling-wave deflection system by using the Fletcher's method and showed that the deficiency in the dispersion characteristics is due to the interaction of the electromagnetic field on a finger of the structure with that on other fingers.² A new system based on the meander type of traveling-wave deflection system has been proposed. Improvement of the frequency characteristics can be expected when a shielding plate is inserted between the fingers to reduce mutual interactions.³ The structure of the meander line with the shielding plate is periodic and one section of the structure is like the structure of a trough line. The meander line with the shielding plate is thus called the trough-type of traveling-wave deflection system.

In general it seems practically impossible to realize a phase velocity of the traveling wave slower than about one-tenth of the light velocity. The slow-wave circuits as a traveling-wave deflection system are required to have a phase velocity as slow as possible and a high impedance for the

fundamental mode in order to deflect the electron beam efficiently. Loading of the circuit by the dielectric material decreases phase velocity and thus increases the deflection sensitivity.⁴

The electromagnetic fields and admittance function of the traveling wave deflection system are obtained by Fletcher's method,⁵ and the dispersion equation is derived under the given boundary conditions in terms of an admittance function. These results are used to derive the theoretical characteristics of propagation, which are in turn applied to determine the deflection characteristics of this new type of deflection system. The displacements of electron beams which are deflected by the interaction of the electric field in the fundamental mode are calculated and used also to derive the frequency characteristic of deflection.

Finally, experimental verification of the theory by means of experimental cathode-ray tubes is given.

THEORETICAL ANALYSIS

The new type of traveling-wave deflection system and the meander type are shown in Fig. 1. The electric fields on the deflection system are expressed by the sum of the space harmonics satisfying the boundary conditions of the system. The field equations, with the field components E_y and E_z are expressed as a function of θ and z as follows:

$$E_y = -j \sum_{n=-\infty}^{\infty} E_n \frac{\cosh[(\theta + 2n\pi)(y_2 - y)/L]}{\sinh[(\theta + 2n\pi)y_2/L]} e^{-j[(\theta + 2n\pi)/L]z} \quad (1)$$

$$E_z = \sum_{n=-\infty}^{\infty} E_n \frac{\sinh[(\theta + 2n\pi)(y_2 - y)/L]}{\sinh[(\theta + 2n\pi)y_2/L]} e^{-j[(\theta + 2n\pi)/L]z} \quad (2)$$

where for the meander type E_n is defined as

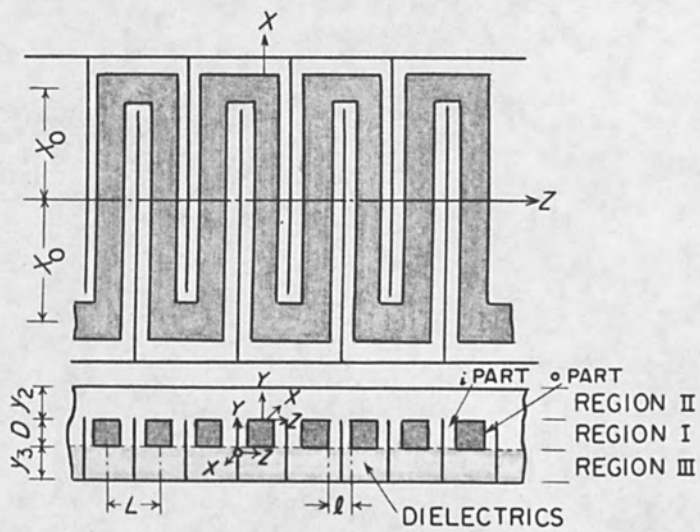
$$E_n = j(-1)^n \frac{2A_0}{L} \sin \frac{\theta}{2} \frac{\sin[(\theta + 2n\pi)\ell/2L]}{[(\theta + 2n\pi)\ell/2L]} \quad (3)$$

and for the trough type,

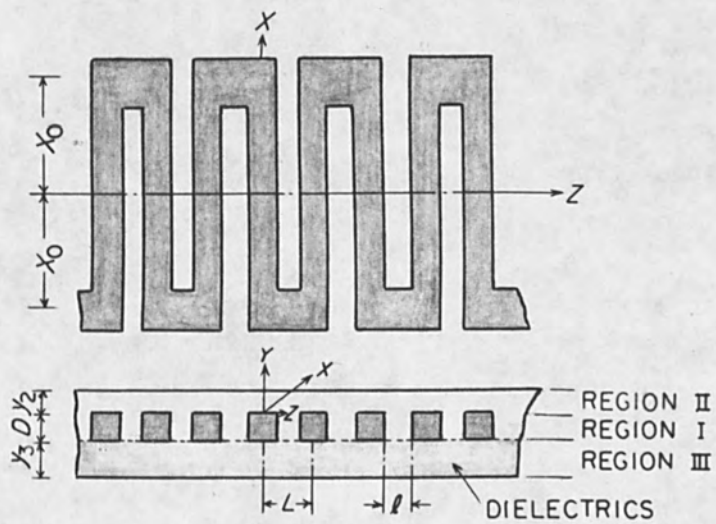
$$E_n = -j(-1)^n \frac{2A_0}{L} \sin \left(\frac{\theta + 2n\pi}{4L} \ell - \frac{\theta}{2} \right) \frac{\sin[(\theta + 2n\pi)]}{[(\theta + 2n\pi)]} \quad (4)$$

Here A_0 is a constant and θ is the phase parameter relating to the frequency by the dispersion equation presented later.

To obtain the dispersion equation, we apply the matching conditions, as follows:



(a)



(b)

FIG. 1.--Two types of traveling-wave deflection systems: (a) trough type, (b) meander type.

$$\tan^2 \frac{\theta_0}{2} = \frac{Y(\theta_0)}{Y(\theta_0 + \pi)} \tan \phi_{10} \tan \phi_{20} \quad (5)$$

$$\tan^2 \frac{\theta_0}{2} = \frac{Y(\theta_0)}{Y(\theta_0 + \pi)} \cot \phi_{10} \cot \phi_{20} \quad (6)$$

where

$$\phi_{10} = \phi_0 \sqrt{\varepsilon(\theta_0 + \pi)} \quad \phi_{20} = \phi_0 \sqrt{\varepsilon(\theta_0)} \quad \phi_0 = \frac{2\pi}{c} f x_0 \quad (7)$$

and θ_0 is equal to $(\theta + \pi)$ considering the boundary conditions of currents at $\pm X_0$. The admittance function $Y(\theta)$ and the effective dielectric constant $\varepsilon(\theta)$ that was developed by Chen:⁶

$$Y(\theta) = \sqrt{\varepsilon_0/\mu_0} (\theta_1 + \theta_2 + \sqrt{\varepsilon_3} \theta_3) \quad (8)$$

$$\varepsilon(\theta) = \frac{\theta_1 + \theta_2 + \varepsilon_3 \theta_3}{\theta_1 + \theta_2 + \theta_3} \quad (9)$$

For the meander type

$$\theta_1 = 4 \frac{D}{\ell} \sin^2 \frac{\theta}{2}$$

$$\theta_3 = 2 \frac{L - \ell}{L} \sin \frac{\theta}{2} \sum_{-\infty}^{\infty} (-1)^n \coth \left(\frac{\theta + 2n\pi}{L} y_2 \right) \frac{\sin \left(\frac{\theta + 2n\pi}{2L} \ell \right) \sin \left(\frac{\theta + 2n\pi}{2L} (L - \ell) \right)}{\left(\frac{\theta + 2n\pi}{2L} \ell \right) \left(\frac{\theta + 2n\pi}{2L} (L - \ell) \right)}$$

For the trough type

$$\theta_1 = 4 \frac{D}{\ell} ; \quad \theta_2 = 16 \frac{\ell}{L} \sum_{-\infty}^{\infty} (-1)^n \coth \left(\frac{\theta + 2n\pi}{L} y_2 \right) \frac{\sin \left(\frac{\theta + 2n\pi}{4L} \ell \right)}{\left(\frac{\theta + 2n\pi}{L} \ell \right)^2} \cdot \sin \left(\frac{\theta + 2n\pi}{4L} \ell - \frac{\ell}{2} \right) \sin \left(\frac{\theta + 2n\pi}{4L} - \frac{\theta}{2} \right) \sin \left(\frac{\theta + 2n\pi}{2L} \ell - \frac{\theta}{2} \right) ;$$

$$\theta_3 = 8 \frac{\ell}{L} \sum_0^{\infty} \coth \left(\frac{(2n+1)}{L} y_3 \right) \frac{\sin \left(\frac{2n+1}{L} \pi \ell \right)}{\left(\frac{2n+1}{L} \pi \ell \right)^2}$$

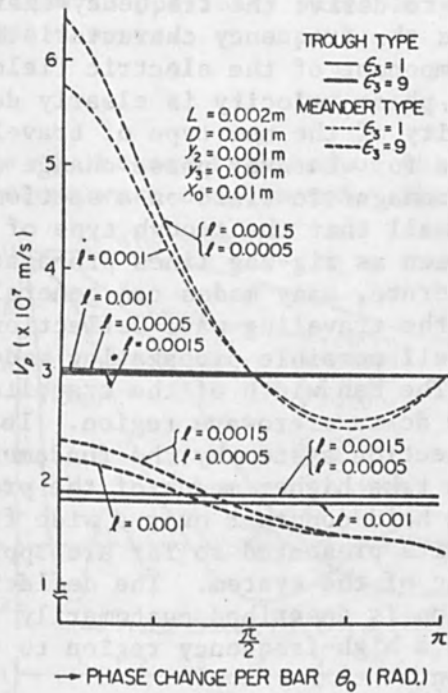


FIG. 2.--Phase velocity.

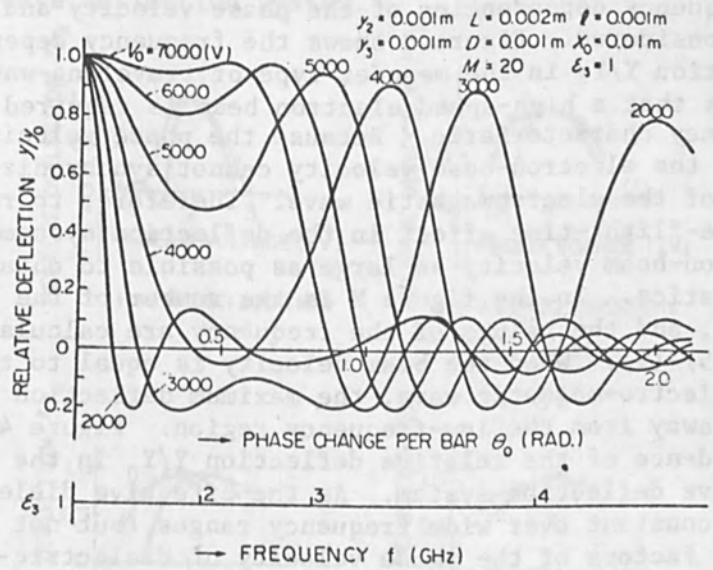


FIG. 3.--Frequency characteristics of relative deflection in meander type of traveling-wave deflection system.

These equations are used to derive the frequency characteristics of phase velocity. Figure 2 shows the frequency characteristic of the phase velocity for a fundamental component of the electric field. The effect of dielectric material on the phase velocity is clearly demonstrated in the figure. The phase velocity of the new type of traveling-wave deflection system is almost constant for whatever phase change of θ_0 , since the mutual interaction of the electromagnetic field on a section of finger with that on other fingers is so small that the trough type of traveling-wave deflection system may be seen as zig-zag lines propagating TEM waves.

In any periodic structure, many modes can generally propagate at a given frequency. Since the traveling-wave deflection system discussed here has a periodicity, all possible propagating modes of the wave must be taken into account. The bandwidth of the traveling-wave deflection system should cover from dc to microwave region. It is therefore necessary to operate the deflection system by the fundamental mode of the propagating wave. If we take higher modes of the propagating wave, the phase velocity cannot be held constant over a wide frequency range.

The theoretical results presented so far are applied to the study of deflection characteristic of the system. The deflection characteristic in a high-frequency region is described customarily in terms of the ratio of the displacement Y in a high-frequency region to the displacement Y_0 in a low-frequency region.

We obtain the displacement of an electron beam deflected by the interaction of the electric field E_y and E_z in the fundamental modes of the field equations (1) and (2). The displacement is obtained by a computer calculation of the electron orbit, which yields not only the displacement of the electron beam but also the frequency dependence of the deflection, because the frequency dependencies of the phase velocity and of the field intensity are considered. Figure 3 shows the frequency dependence of the relative deflection Y/Y_0 in the meander type of traveling-wave deflection system and shows that a high-speed electron beam is required to obtain a wideband frequency characteristic. Because the phase velocity changes with frequency, the electron-beam velocity cannot synchronize with the phase velocity of the electromagnetic wave. Therefore, to reduce the electron's finite-flight-time effect in the deflection system, we have to make the electron-beam velocity as large as possible to obtain a wideband characteristics. In the figure M is the number of the fingers of deflection system, and the values of the frequency are calculated by the relation of Eqs.(5)-(9). When the beam velocity is equal to the phase velocity of the electro-magnetic wave, the maximum deflection is obtained at a frequency away from the low-frequency region. Figure 4 shows the frequency dependence of the relative deflection Y/Y_0 in the trough type of traveling-wave deflection system. As the effective dielectric constant $\epsilon(\theta)$ is almost constant over wide frequency ranges (but not for the meander type), slow factors of the phase velocity of dielectric-loaded deflection systems do not change with frequency. Therefore, relations between the relative deflection and frequency for various dielectric constants can be shown by the same curves as shown in the figure. There is a most suitable accelerating voltage synchronizing with phase velocity for the trough type. In the deflection system shown in Fig. 4, with load dielectrics of $\epsilon_3 = 1$, this voltage is 2600 V. For larger dielectric constants, the beam accelerating voltage decreases. Even if the most suitable accelerating voltage is applied, we cannot expect to have $Y = Y_0$ because the energy

needed to deflect the beam is partially taken away from the fundamental wave by the space-harmonic waves.

EXPERIMENTAL RESULTS

Experimental models of the new type and of the meander type of traveling-wave deflection systems were constructed. The cross section of the

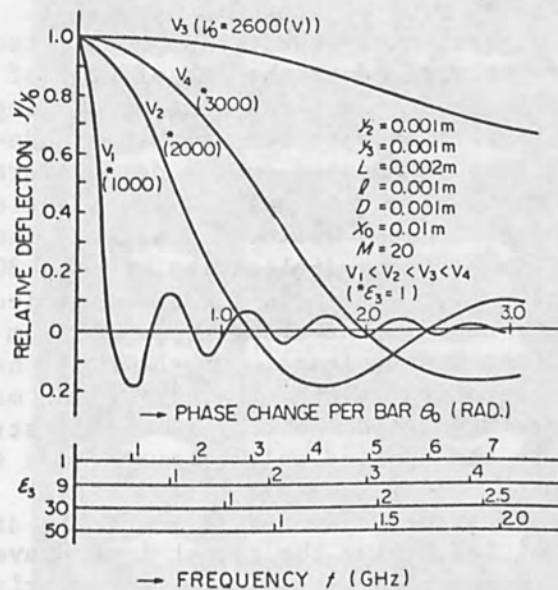


FIG. 4.--Frequency characteristics of relative deflection in meander type of traveling-wave deflection system.

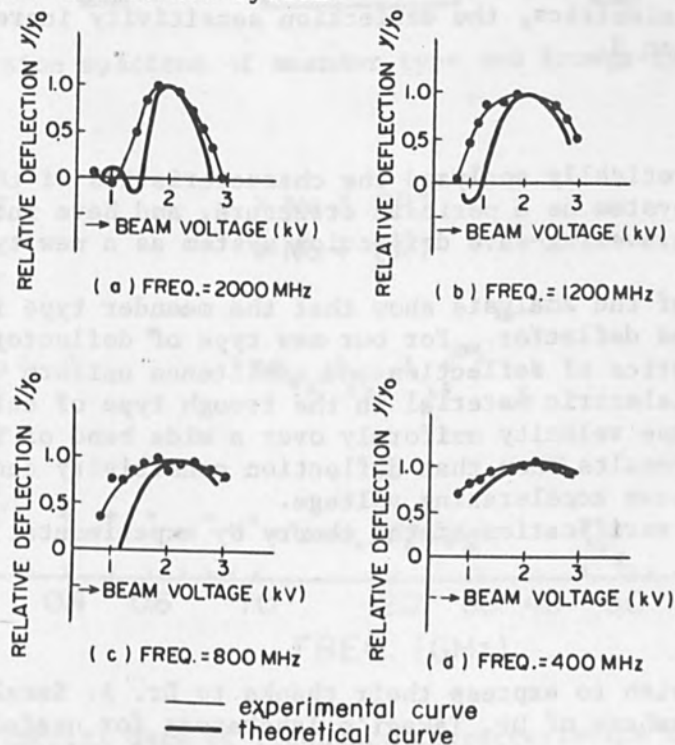


FIG. 5.--Comparison between experimental and theoretical results of inversion system.

fingers of deflection systems is circular, to ease construction of the test tubes.

The inversion spectrum proposed by Hollman⁷ has been studied in order to clarify the relationship between the accelerating voltage and sensitivity. The inversion spectrum is also used to show the frequency dependence of the phase velocity of the deflection system. Figure 5 shows the comparison of the theoretical and the experimental results of the inversion spectrum of the trough type of traveling-wave CRT. Agreement between theoretical and experimental results is good. Discrepancies at lower beam voltages are attributed to the end effects of the field distribution and the shape effects of the cross section of fingers.

Figure 6 shows the inversion spectrum of the cathode-ray tube in which an ac voltage of 60 Hz is superimposed on the dc accelerating voltage, with the electron velocity changing periodically. A deflecting voltage of 60 Hz is also supplied to the horizontal deflection plate. The trough type of the deflection system is loaded by dielectrics of $\epsilon_3 = 30$, whereas the meander type of the deflection system is loaded by dielectrics of $\epsilon_3 = 6$. We can see in the figure that in the trough type maximum values of deflection are obtained at a constant voltage. On the other hand, in the meander type, the beam accelerating voltage that gives the maximum deflection changes with frequency. The reason is that to obtain strong interaction the beam velocity due to the applied voltage must equal the phase velocity of the wave, which depends on frequency.

Figure 7 shows the frequency characteristic of the displacement measured in the experimental CRT having the trough-type traveling-wave deflection system. No. 3 CRT is loaded with dielectric materials ($\epsilon_3 = 30$) and No. 1 CRT is not loaded. Displacement is measured at 10 mW input. Uniform deflection is obtained in the frequency range from dc to above 4 GHz. By loading the dielectrics, the deflection sensitivity increases by a factor of more than 3.

CONCLUSION

We have theoretically analyzed the characteristics of the traveling-wave deflection system as a periodic structure, and have introduced the through-type of traveling-wave deflection system as a new type of wide-band deflector.

The results of the analysis show that the meander type is not practical as a wide-band deflector. For our new type of deflector, analysis shows characteristics of deflection and admittance uniform with frequency. Loading of the dielectric material in the trough type of deflection system decreases the phase velocity uniformly over a wide band of frequency. This analytical results show that deflection sensitivity can be improved by use of a low beam accelerating voltage.

Experimental verification of the theory by experimental cathode ray tubes is given.

ACKNOWLEDGMENT

The authors wish to express their thanks to Dr. A. Sasaki, Dr. T. Tsuda, and the members of Dr. Takagi's laboratory for useful discussions and suggestions on the present work.

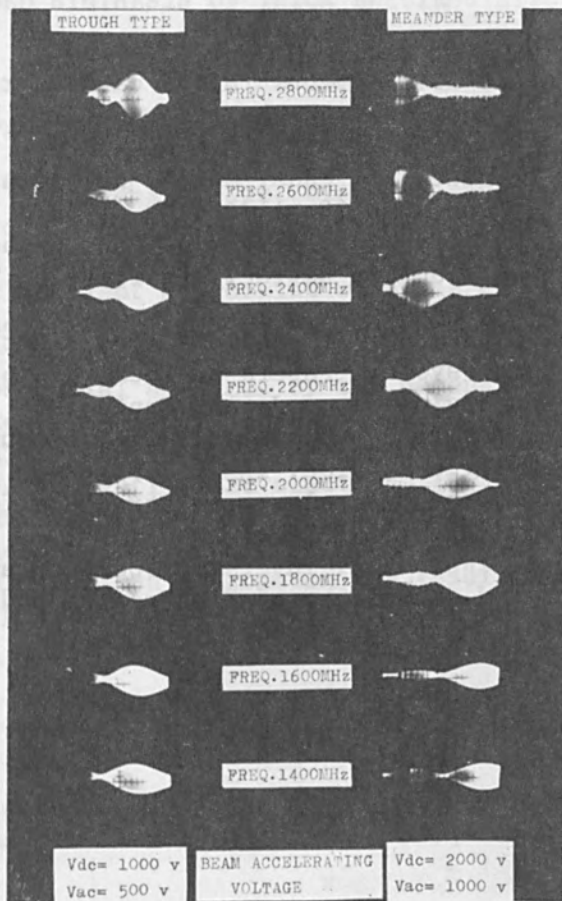


FIG. 6.--Inversion spectrum of meander type and trough-type deflection systems.

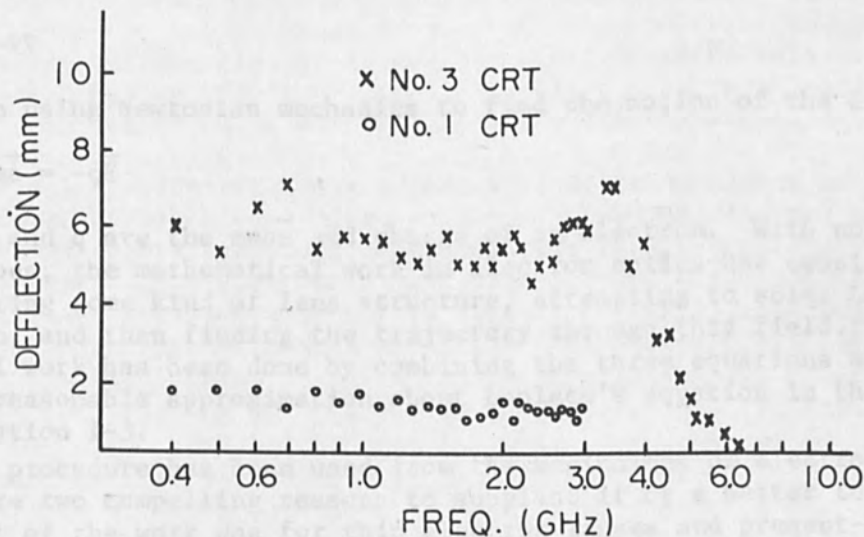


FIG. 7.--Experimental data of frequency characteristics of deflection in trough type of traveling-wave cathode-ray tubes.

REFERENCES

1. J. E. Day, Recent developments in the cathode ray oscilloscope, Advances in Electronics and Electron Physics, Academic Press, 1958; vol. 10, p. 246.
2. K. Owaki, S. Terahata, T. Hada, and T. Nakamura, The traveling-wave cathode-ray tube, Proc. IRE 38: 1172-1180, 1950.
3. T. Nakamura and I. Yamada, Ultra wide band cathode-ray tube, Papers of Tech. Group on Electron Device, Institute of Television Engineers of Japan, Jan. 1965 (in Japanese).
4. T. Takagi and I. Yamada, An analysis of dielectrically loaded traveling-wave deflection system, Papers of Tech. Group on Electron Device, Institute of Television Engineers of Japan, Sept. 1968 (in Japanese).
5. R. C. Fletcher, A broad band interdigital circuit for use in traveling-wave-type amplifiers, Proc. IRE 40: 951-958, 1952.
6. F. S. Chen, The comb-type slow-wave structure for TWM applications, Bell Syst. Tech. J. 43: 1035-1065, 1964.
7. H. Maeda and H. Ishibashi, Inversion spectrography on traveling-wave cathode-ray tubes, J. Institute of Electronics and Communication Engineers of Japan 39: 38-42, May, 1964.

J. R. ASHLEY

University of Colorado, Colorado Springs, Colo.

The synthesis of space-charge-free electron lenses can be approached by first assuming solutions for Laplace's equation in terms of cylindrical harmonics. The hybrid computer can quickly generate these assumed solutions and their gradient by working with the differential equations obtained from product separation of variables. The gradient is used in the integration for the trajectory to determine if the lens is useful. If it is, either equipotential surfaces or the potentials along a desired surface are generated with the computer to guide the physical realization of the lens. Certain cases in which space charge cannot be neglected are solved by truncation of rectilinear electron flow. Poisson's equation is solved in the computer to serve as a Cauchy boundary condition to Laplace's equation outside the electron beam. The hybrid computing technique and the experimental verification of some of the results in cathode-ray-tube electron lenses is presented.

1. INTRODUCTION

In the cryptic language of vector calculus, electron optics appears to be a quite simple matter of solving Laplace's equation for the electrostatic potential V ,

$$\nabla^2 V = 0 \quad (1)$$

doing a simple differentiation to find the electrostatic field,

$$\vec{E} = -\nabla V \quad (2)$$

and then using Newtonian mechanics to find the motion of the electron.

$$\vec{f} = m\vec{a} = -q\vec{E} \quad (3)$$

Here, m and q are the mass and charge of an electron. With notably few exceptions, the mathematical work in electron optics has consisted of postulating some kind of lens structure, attempting to solve Laplace's equation, and then finding the trajectory through this field. The most fruitful work has been done by combining the three equations above with a fairly reasonable approximation about Laplace's equation in the paraxial-ray equation 1-3.

This procedure has been used from the beginnings of electron optics. There are two compelling reasons to supplant it by a better technique: (1) Most of the work was for thin electron lenses and present-day requirements are for thick lenses. (2) A wide variety of computing equipment is now available to make possible different mathematical techniques. Kirstein et al. give a good account of the use of digital computers for the case of space-charge flow in a magnetic field.⁴ For the most part, the partial differential equations of their methods are solved by finite

difference methods; the approach is one of analysis rather than synthesis.

In the case of low-density space charge in purely electrostatic fields (e.g., in cathode-ray tubes) a better approach is to change the order of attack on the problem:⁵

(1) Assume a scalar potential function $V(r,z)$ known to be a solution of Laplace's equation.

(2) Differentiate this function analytically to find the electrostatic field.

(3) Use a computer to find the trajectory of an electron in this field. (Often this is a set of trajectories to define the lens aberration.)

(4) Evaluate the trajectories. If they are not useful, the detailed information from the computer usually gives a great deal of insight into improving the assumption of Step 1.

(5) Once satisfactory trajectories are found, evaluate $V(r,z)$ at the lens boundary (e.g., a CRT bulb) and use various electrodes and resistive coatings to synthesize the boundary potential.

Instead of solving a boundary-value problem and differentiating (numerically) to find forces on an electron, we thus use separation-of-variable solutions; the desirability of using a small number of cylindrical harmonics is usually compatible with minimizing aberrations in thick lenses.⁶ Obviously, this method would be impractical without modern computing equipment; furthermore, the separation of variables means relatively simple ordinary differential equations and hybrid computation.

2. SOLUTIONS FOR LAPLACE'S EQUATION

The space-charge-free electrostatic electron lens is based on the solutions of Laplace's equation in axisymmetric cylindrical coordinates. Following Courant and Hilbert,⁷ we can use an assumed sum to separate variables and obtain

$$V(r,z) = \frac{1}{2} Tz^2 + C_1z - \frac{Tr^2}{4} + C_2 \quad (4)$$

where T is a separation constant, C_1 and C_2 are arbitrary constants, and the condition for axial symmetry has been employed. Rudenberg employed Eq. (4) with $C_2 = C_1 = 0$ in a true synthesis procedure and obtained aberration-free lenses with hyperbolic electrode shapes.⁸ These electrodes have limited utility so we must add other terms (and possibly aberration) to obtain more useful electrode shapes. Addition of cylindrical harmonics⁹ yields a total potential function of the form

$$V(r,z) = \frac{1}{2} Tz^2 + C_1z - \frac{Tr^2}{4} + C_2 + \sum_{n=1}^N A_n \sin(n\pi z/L) I_0(n\pi r/L) \quad (5)$$

where $I_0(n\pi r/L)$ is a Bessel function. This potential allows net acceleration and periodic places where

$$\partial V/\partial r = 0 \quad (6)$$

for the location of flat electrode surfaces (such as a CRT screen) per-

pendicular to the lens axis. Obviously, there are sufficient parameters to adjust. Fortunately, N is usually less than three and the computation of trajectories is not too difficult.

3. ASSIGNMENT OF COMPUTING TASKS

These methods allow a wide variety of computing equipment to be used. It is possible to solve the whole problem on anything from a medium-sized iterative analog computer (about 60 amplifiers and 10 multipliers) to a terminal on a time-shared digital computing system.

The first step, the assumption of a potential function, is the most demanding. The iterative analog (or analog portion of a hybrid) computer is the most useful tool, since it can handle the two independent variables by time sequencing. Examples of the iterative analog output are shown in Figs. 1 and 2.

The integration of the force equations to find electron trajectories can be done in several ways. If the potential function has been completely implemented on the iterative analog computer, the information regarding the partial derivatives for the gradient is available. With some additional multipliers and summers, the electric field can be obtained. Four integrators can be used to find trajectories in an iterative fashion. The two z integrators are first operated for a small increment (about 1/50th of the total length of the lens) and placed in HOLD; then the two r integrators are operated through a similar small increment and placed in HOLD. The integrators generating the field information are operated from the start of the lens to the position of the electron along the trajectory where comparators cause these integrators to HOLD the value of electrostatic field at this position. Now the trajectory integrators are incremented to advance the computation another step. Since velocity information for the electron and potential information for the field are both available, an energy check along the trajectory detects the growth of error and shows when error is excessive.

This method of analog generation of the electrostatic-field components has been implemented for one or two terms and found to work quite well. The disadvantage is that the essentially parallel nature requires typically 4 integrators and 4 multipliers per cylindrical-harmonic term. Since the trajectory integrators are in a HOLD mode while the field computations are being performed, it is far more satisfactory to use the digital portion of a hybrid computer for this task.

When the electrostatic-field information is generated in the digital computer, it is much simpler to use the readily available series solutions for Bessel's equation than to integrate this equation directly.

Once the digital computer is used for evaluating the potential function and the electrostatic field, very little additional programming effort is required for the numeric integration of the trajectory equations. Not much memory is required because of the nature of the problem formulation and the whole procedure is well suited for solution with a terminal of a time-shared digital computer. Considering the rapidly increasing availability of these terminals, it is worth enduring their slow input-output to get solutions that would be easier to visualize (because they are easy to plot) from a hybrid computer.

The organization of the hybrid form of this computation is shown in Fig. 3. The patching of the analog portion for asynchronous logic is shown in Fig. 4. In this figure, the servo set pots could be replaced

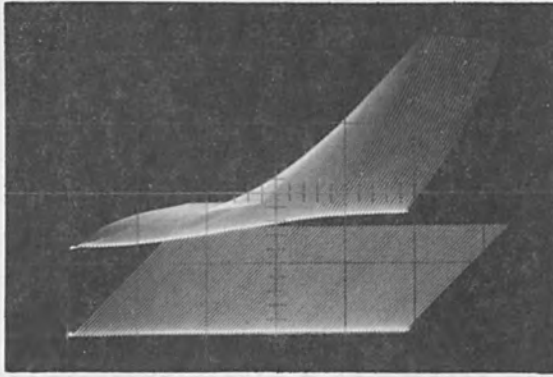


FIG. 1.--Potential in electrostatic lens.

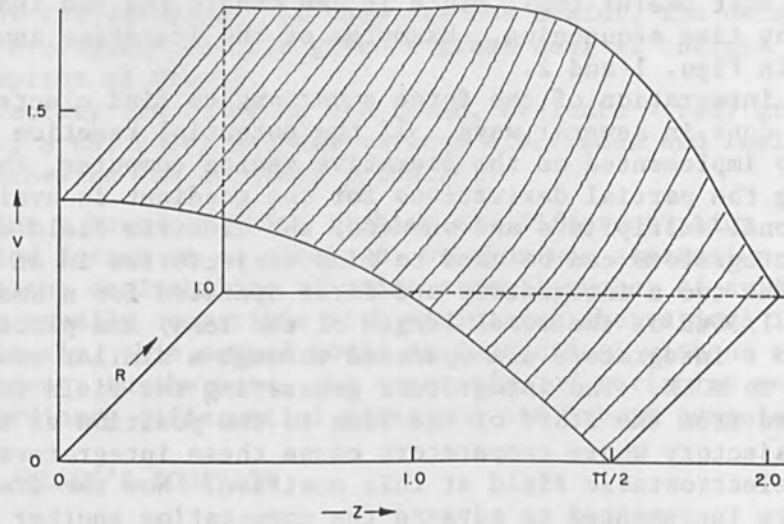


FIG. 2.--Potential in periodic electrostatic lens.

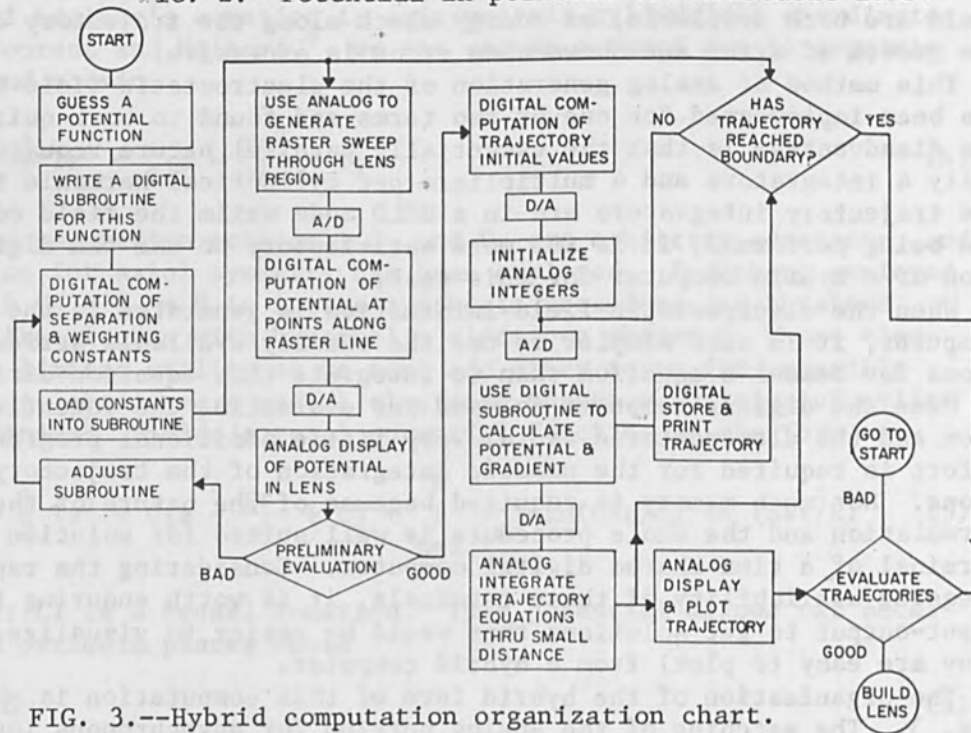


FIG. 3.--Hybrid computation organization chart.

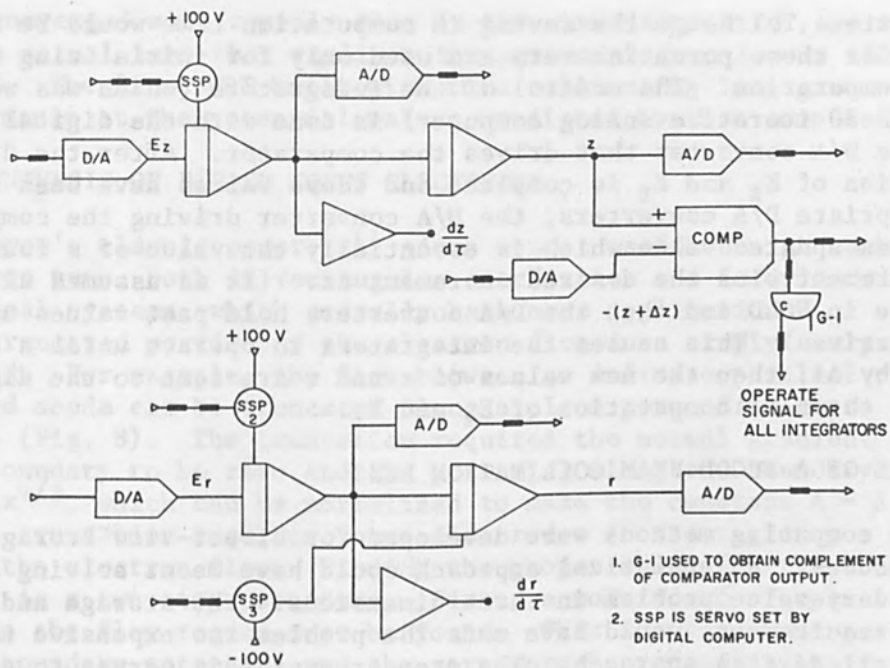


FIG. 4.--Analog integration of trajectory equations.

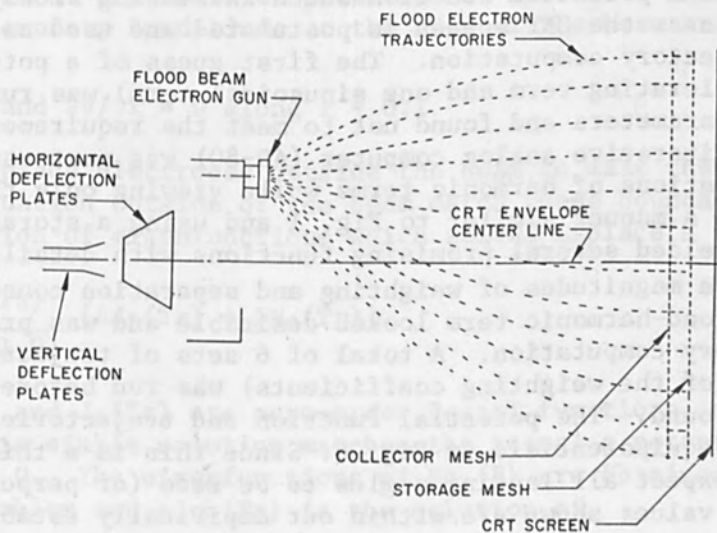


FIG. 5.--Flood-beam requirements for direct-view storage CRT.

by D/A converters, although the saving in computation time would be negligible because these potentiometers are used only for initializing the trajectory computation. The control of the integrators (which was worked out for an AD-80 iterative analog computer) is done with the digital computer via the D/A converter that drives the comparator. After the digital computation of E_z and E_r is complete and these values have been sent to the appropriate D/A converters, the D/A converter driving the comparator is sent an updated value which is essentially the value of z found on the last increment plus the desired increment Δz . (It is assumed all integrators are in HOLD and that the D/A converters hold past values until new values arrive.) This causes the integrators to operate until z is incremented by Δz ; then the new values of z and r are sent to the digital computer for the next computation of E_z and E_r .

4. SYNTHESIS OF A FLOOD-BEAM COLLIMATION LENS

The above computing methods were developed for direct-view storage cathode-ray tubes. An analytical approach would have meant solving a complex boundary-value problem in three dimensions. The storage and solution-time requirements would have made the problem too expensive to solve by an all-digital approach. The present synthesis serves to solve a three-dimensional problem with mostly two-dimensional computation.

In this example (Fig. 5), the flood beam of a direct-view storage CRT supplies the actual viewing electrons and must deliver a constant current density to the collector mesh. For uniform erasure properties, the electrons must arrive at the screen on a trajectory normal to the screen (collimated). Moreover, the flood electron gun must be placed off the axis of symmetry.

We separate the flood-beam problem and consider it in terms of its own axis of symmetry. A potential function which increases slowly at first and then rapidly near the CRT screen is postulated and used as the first guess in the trajectory computation. The first guess of a potential function (an accelerating term and one sinusoidal term) was run through some 10 sets of parameters and found not to meet the requirements of this application. An iterative analog computer (AD-80) was next used to explore many combinations of harmonic terms while viewing only the potential function (in a manner similar to Fig. 1 and using a storage CRT.) This procedure yielded several promising functions with details about signs and relative magnitudes of weighting and separation constants. The addition of a second-harmonic term looked desirable and was programmed into the trajectory computation. A total of 6 sets of trajectories (for different values of the weighting coefficients) was run before a satisfactory set was found. The potential function and trajectories are given along with a few equipotentials in Fig. 6. Since this is a thick electron lens, we cannot expect all landing angles to be zero (or perpendicular to the screen): the values shown are within our empirically established goal of $\pm 3^\circ$.

The traversal of the various major and minor loops of Fig. 3 some 25 times by means of three different computing installations does not mean that the cost of finding this lens was excessive. The actual computing charges totaled less than the cost of two experimental CRTs and the support engineering was also less expensive. The trajectory information gained from the computer were so much more useful than the "yes or no" type of answer from an experimental CRT that the final stages of the pro-

cess converged more rapidly than in the experimental CRT approach.

The actual lens that realizes the potential function is illustrated in Fig. 7. The first CRT built with this collimating lens gave excellent performance at the potential values predicted by this computation method.

5. SYNTHESIS OF PIERCE FOCUS ELECTRODES

Pierce's classic paper ^{1,11} gives a most useful design technique for electron guns, both in rectangular coordinates and in cylindrical and spherical systems, which actually have more applications.

A truncated portion of the electron flow in a simply analyzed system is used. For example, the flow between an infinite parallel plane cathode and anode can be truncated along a plane perpendicular to the electrodes (Fig. 8). The truncation requires the normal gradient along the flow boundary to be zero and the potential along the boundary to be given by $V_x = Ax^{4/3}$, which can be normalized to make the constant $A = 1$.

The truncation requires focus electrodes in the region $y > 0$ to replace the electron flow. Finding the proper shape for the focus electrodes is a two-step procedure. First, a solution for Laplace's equation outside the flow region must be found. This solution must match the known boundary potential and the zero normal gradient along $y = 0$. Second, equipotential contours are selected from this solution and used as the focus electrodes.

The computer solution for rectangular coordinates yields excellent agreement with a solution Pierce obtained by conformal transformation.¹⁰ The more important case of a cylindrical beam emitted from a flat cathode is solved below.

With the center of the beam at $r = 0$, it is convenient to normalize the beam radius to 0.1 times the cathode-to-anode spacing and assume the anode operates at a normalized potential of 1.0. For these dimensions, the Cauchy boundary conditions at the edge of the beam are

$$V = z^{4/3} \text{ and } \partial V / \partial r = 0 \text{ along } r = 0.1 \quad (7)$$

and we must place electrodes outside the beam to make the solution of Laplace's equation outside of the beam match these boundary conditions. One combination of eigenfunctions which solves Laplace's equation is

$$V = \frac{\sinh(Tz)}{\sinh(1.0)} [AJ_0(Tr) + BN_0(Tr)] \quad (8)$$

where $N_0(Tr)$ and $J_0(Tr)$ are zero-order Bessel functions. Along the flow boundary, this simple solution matches the actual z potential to within 5% for $T = 1.0$. The eigenfunctions of Eq.(8) are obtained from separation of variables and $\sinh(Tz)$ is the solution of

$$\frac{d^2 F_z}{dz^2} - T^2 F_z = 0 \quad (9)$$

and the Bessel functions are solutions of

$$\frac{d^2 F_r}{dr^2} + \frac{1}{r} \frac{dF_r}{dr} + T^2 F_r = 0 \quad (10)$$

$$V = 66 + 11.25 Z - 38.19 \sin(TZ) I_0(TR) + 4.775 \sin(2TZ) I_0(2TR)$$

WHERE $T = .393$ AND $V=0$ AT FLOOD GUN CATHODE

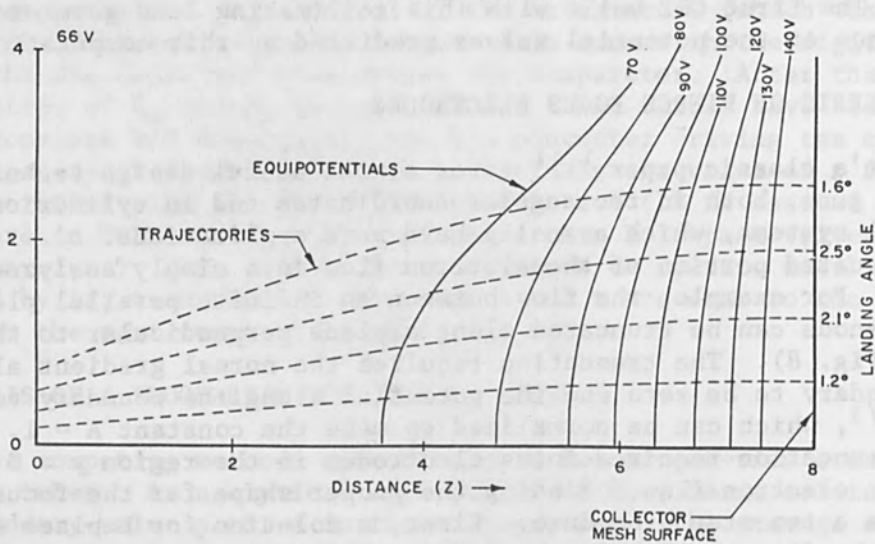


FIG. 6.--Computed trajectories and potentials.

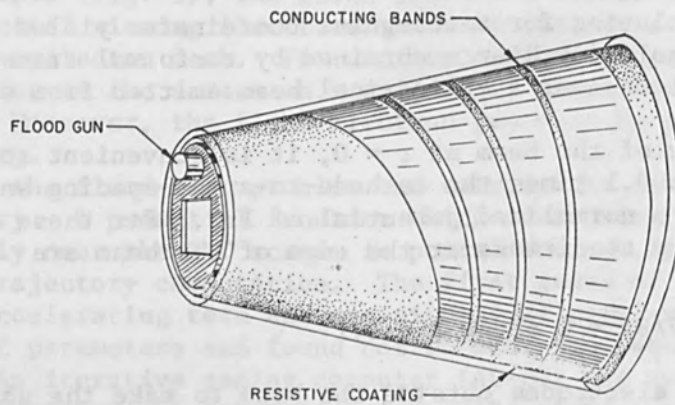


FIG. 7.--Realization of lens for collimating flood beam.

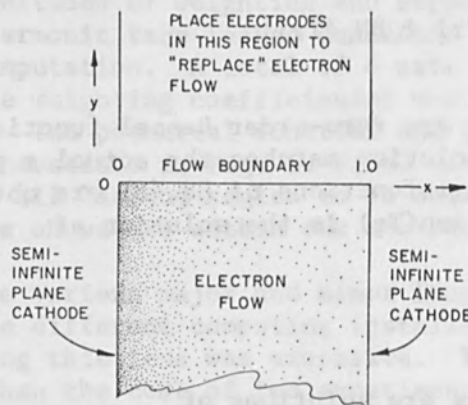


FIG. 8.--Truncation of electron flow between parallel-plane cathode and anode.

and the $T = 1.0$ was obtained by a simple approximation of boundary conditions. Following our original reasoning that it is a worthwhile approximation to violate the idea that T must be constant,¹⁰ we solve Eq. (9) for $T^2(z)$ and then use it in Eq. (10) to find the potential moving away from the flow boundary. That is, we determine T^2 along the beam edge by

$$T^2(z) = \frac{dF}{dz} / F_z = \frac{4}{9} z^{-2/3} / z^{4/3} = 4/9z^2 \quad (11)$$

and use it in the solution of Eq. (10) starting from $r = 0.1$ with initial conditions

$$F_r = z^{4/3} \text{ and } dF_r/dr = 0 \quad (12)$$

The computer solution consists of three parts: (1) finding $T^2(z)$; (2) extending the solution in the r direction; and (3) picking out equipotential contours. For analog computation, z and z^2 are generated by two successive integrations of a constant. The z is sent to a diode function generator to give the $z^{4/3}$ required here. In operation, these two z integrators are operated in small increments ($\Delta z \approx 0.05$) and placed in HOLD while the r integrators are operated to carry the solution away from the beam boundary.

During the (complementary) time while the z integrators are in HOLD, another group of two integrators is used to solve the Bessel equation, Eq. (10), with the initial conditions of Eq. (12). Note how naturally the use of complementary integrator control allows the use of two independent variables and the solutions of two ordinary differential equations to be combined into a good approximate solution of a partial differential equation.

The analog computer patching to mechanize this solution is a simple adaptation of the rectangular coordinate solution.¹⁰ Each solution in the r direction requires 200 ms and the total time the z integrators operate is 2 s. The z integrators are operating on a "pulsed" basis, and the total computation time is the sum of 2 s for the z integrators and the number of 200-ms solutions in the r direction. The total computing time thus depends on the fineness of the quantization in the z direction. In contrast to other computing methods, increasing the fineness of the z quantization does not require additional equipment or memory space.

The set of Pierce focus electrodes generated by this computational technique is shown in Fig. 9. The shapes are in good agreement with a solution obtained by Radley for the same problem.¹² This method is much simpler from a computational standpoint than either the one used by Radley or those described by Kirstein et al.⁴ Finally, this procedure is much more satisfying than fishing the shapes out of an electrolytic tank.

6. CONCLUDING REMARKS

By reversing the sequence of attack on Laplace's equation, several synthesis methods for electron lenses have been developed that rely on the mathematical technique of separation of variables rather than finite differences and exhibit great computational stability. The methods can be used on a wide variety of analog, digital, or hybrid computing equipment and have a particular advantage in being easy to implement on the

time-shared digital computer terminals which are becoming widely available in the U.S.A.

REFERENCES

1. J. R. Pierce, Theory and Design of Electron Beams, Van Nostrand, New York, 1954.
2. K. R. Spangenberg, Vacuum Tubes, McGraw-Hill, New York, 1948.
3. W. W. Harman, Fundamentals of Electronic Motion, McGraw-Hill, New York, 1953.
4. P. T. Kirstein, G. Kino, and W. Waters, Space-Charge Flow, McGraw-Hill, New York, 1968.
5. J. R. Ashley, Computer-aided design of the flood beam system for a direct view storage CRT, 1969 International Electron Devices Meeting, Oct. 1969, Washington, D.C.
6. F. Gray, Electrostatic electron optics, Bell Syst. Tech. J. 18: 1-31, 1939.
7. R. Courant and D. Hilbert, Methods of Mathematical Physics, Interscience, New York, 1962; vol. 2.
8. R. Rudenberg, Electron lenses with hyperbolic shapes, J. Franklin Inst. 1948.
9. S. Ramo, J. R. Whinnery, and T. Van Duzer, Fields and Waves in Communication Electronics, Wiley, New York, 1965.
10. J. R. Ashley, Iterative integration of Laplace's equation within axially symmetric boundaries, Simulation, Aug. 1967.
11. J. R. Pierce, Rectilinear electron flow in beams, J. Appl. Phys., Aug. 1940.
12. D. E. Radley, The theory of the Pierce type electron gun, J. Electronics and Control, Feb. 1958.

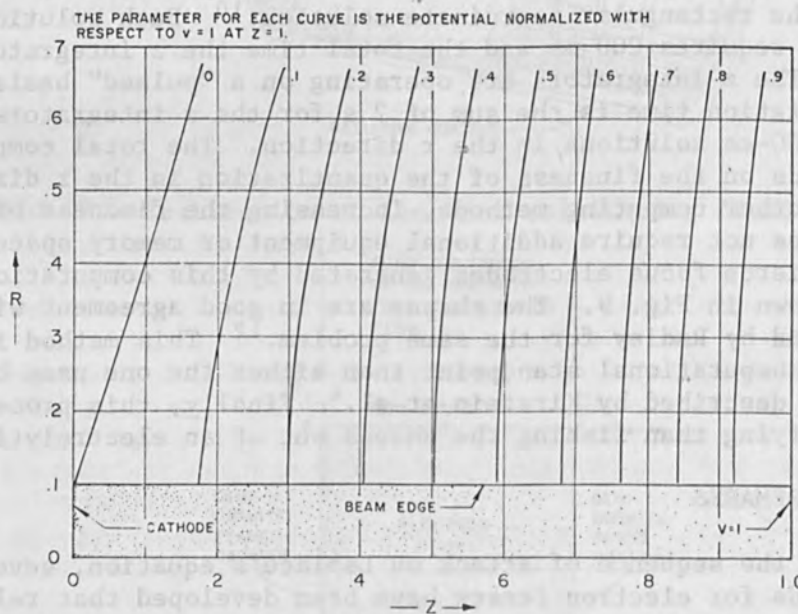


FIG. 9.--Pierce focus electrodes for cylindrical beam.

DIGITAL-COMPUTER SOLUTION OF LAPLACE'S EQUATION INCLUDING DIELECTRIC INTERFACES AND SMALL FLOATING ELECTRODES*

J. E. BOERS

Sandia Laboratories, Albuquerque, New Mexico

A digital computer program has been written for the general solution of Laplace's equation $\nabla^2 V = 0$ and the plotting of equipotential and equipotential lines. The program simulates any rectangular or axisymmetric configuration of dielectrics and small floating electrodes. The potentials are simulated on a large matrix of up to 201×201 points. It is written in the CDC 6600 Fortran IV programming language, but can easily be translated into any other Fortran dialect. Solutions with errors of less than 5 per cent are obtainable in less than 10 min on the CDC 6600. A description of the various techniques employed on the discrete matrix and some typical problems that have been solved during the design of high-voltage generators are presented.

SIMULATION METHOD

The method employed is basic, iterative relaxation of a rectangular array of points, laid out in squares. The simulation is carried out on a matrix of up to 201×201 points, all or any portion of which may be employed for a particular problem. All electrode and dielectric surfaces must lie on matrix points; i.e., no partial matrix increments may be employed. Laplace's equation, expressed in difference form, is solved iteratively at all points within the electrode configuration. The difference equations employed are derived below.

A flow chart for the program is shown in Fig. 1. Initializing the matrix consists of setting potentials on electrodes and putting linear voltage distributions between electrodes. The relaxation procedure consists of alternately relaxing the coarse matrix (all the odd numbered points) and the fine matrix (consisting of all matrix points). This procedure was improved by Richard Kouzes at the Naval Research Laboratory,¹ who added the over-relaxation to the computation of each matrix point,

$$V_{n+1} = (V_{\text{new}} - V_n)\beta + V_n \quad (1)$$

where β is the over-relaxation constant, V_n is the value from the n^{th} pass, and V_{new} the value computed by the procedures described below. The value of β is initially about 1.8 and is reduced to 1 as convergence is approached.

Equipotential and equipotential plots are then available as output from the program. Over-all and expanded plots of any areas of interest may be obtained from the program. In addition, it is possible to save sufficient data to produce blowups, with greater accuracy, by re-solving a section of the plot on a finer mesh. Printout of the above data furnishes immediate, quantitative values of potentials or fields.

The difference equations employed are derived from Laplace's equation expressed in axisymmetric coordinates,

*This work is supported by the U.S. Atomic Energy Commission.

$$\frac{\partial^2 V}{\partial z^2} + \frac{\partial^2 V}{\partial r^2} + \frac{1}{r} \frac{\partial V}{\partial r} = 0 \quad (2)$$

Rectangular coordinates are obtained by letting r become large. The difference equations for a uniform dielectric region are well known:

$$V_{i,j} = \frac{V_{i+1,j} + V_{i,j+1} + V_{i-1,j} + V_{i,j-1} + (V_{i,j+1} - V_{i,j-1})\Delta r}{4 + 8r_j} \quad (3)$$

for the general point, and

$$V_{i,j} = \frac{1}{6} (4 V_{i,j+1} + V_{i-1,j} + V_{i+1,j}) \quad (4)$$

for points on the axis, where an array of squares ($\Delta z = \Delta r$) is employed and i, j, r_j , and Δr are described in Fig. 2.

Dielectric interfaces which are parallel, perpendicular, and at $\pm 45^\circ$ to the axis are handled in the following manner. Equation (2) could probably be solved exactly for a dielectric interface passing through a matrix point, but the expression would be unwieldy at best. Solutions for dielectric interfaces parallel or $\pm 45^\circ$ to the axis of symmetry are obtained fairly easily and are employed in the program.

For the case of a dielectric surface parallel to the axis of symmetry, Eq. (2) becomes in difference form

$$\begin{aligned} \epsilon_{12} \frac{V_{i+1,j} - 2V_{i,j} + V_{i-1,j}}{(\Delta z)^2} + \frac{\epsilon_2 (V_{i,j+1} - V_{i,j}) - \epsilon_1 (V_{i,j} - V_{i,j-1})}{(\Delta r)^2} \\ + \frac{1}{2} \left(\frac{\epsilon_2 (V_{i,j+1} - V_{i,j})}{\Delta r (r_j + \frac{\Delta r}{2})} + \frac{\epsilon_1 (V_{i,j} - V_{i,j-1})}{\Delta r (r_j - \frac{\Delta r}{2})} \right) = 0 \end{aligned} \quad (5)$$

where ϵ_2 is the dielectric constant above (away from the axis), the point i, j , ϵ_1 is the dielectric constant below (nearer the axis), and the point i, j , and ϵ_{12} is undefined. This equation can be solved for $V_{i,j}$, assuming a square matrix; e.g., $\Delta z = \Delta r$,

$$V_{i,j} = \frac{\epsilon_1 V_{i,j-1} + \epsilon_2 V_{i,j+1} + \epsilon_{12} (V_{i+1,j} + V_{i-1,j}) + \frac{\Delta r}{2r_j} \left(\frac{\epsilon_2 V_{i,j+1}}{1 + \frac{\Delta r}{2r_j}} - \frac{\epsilon_1 V_{i,j-1}}{1 - \frac{\Delta r}{2r_j}} \right)}{2\epsilon_{12} + \epsilon_1 + \epsilon_2 + \frac{\Delta r}{2r_j} \left(\frac{\epsilon_2}{1 + \frac{\Delta r}{2r_j}} - \frac{\epsilon_1}{1 - \frac{\Delta r}{2r_j}} \right)} \quad (6)$$

For a dielectric surface at 45° to the axis, Eq. (4) becomes

$$\begin{aligned} \frac{\epsilon_2 (V_{i-1,j} - V_{i,j}) - \epsilon_1 (V_{i,j} - V_{i+1,j})}{\Delta z^2} \\ + \frac{\epsilon_2 (V_{i,j+1} - V_{i,j}) - \epsilon_1 (V_{i,j} - V_{i,j-1})}{(\Delta r)^2} \end{aligned} \quad (\text{continued})$$

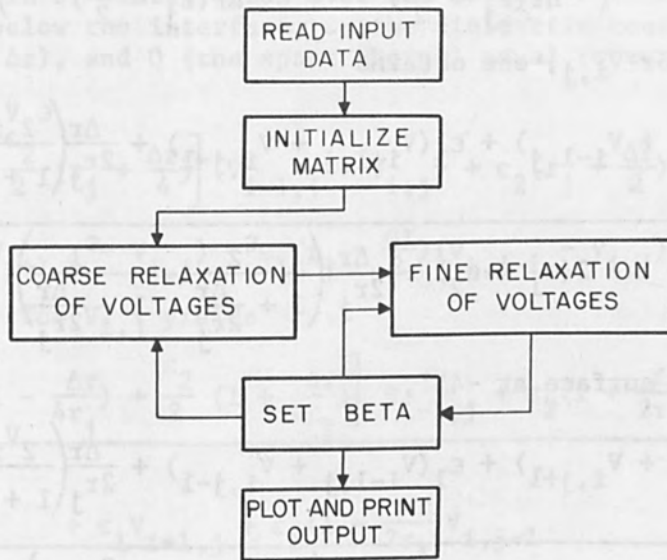


FIG. 1.--Basic flow chart for Laplace solution program.

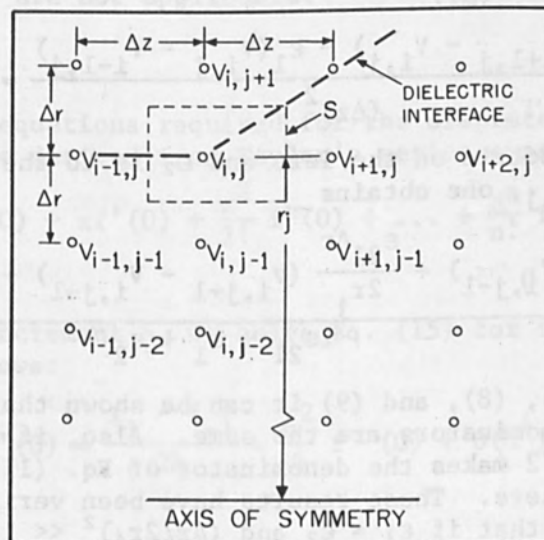


FIG. 2.--Definition of matrix terms and quantities.

$$+ \frac{1}{2} \left(\frac{\epsilon_2 (V_{i,j+1} - V_{i,j})}{\Delta r (r_j + \frac{\Delta r}{2})} + \frac{\epsilon_1 (V_{i,j} - V_{i,j-1})}{\Delta r (r_j - \frac{\Delta r}{2})} \right) = 0 \quad (7)$$

Again, solving for $V_{i,j}$, one obtains

$$V_{i,j} = \frac{\epsilon_2 (V_{i,j+1} + V_{i-1,j}) + \epsilon_1 (V_{i+1,j} + V_{i,j-1}) + \frac{\Delta r}{2r_j} \left(\frac{\epsilon_2 V_{i,j+1}}{1 + \frac{\Delta r}{2r_j}} - \frac{\epsilon_1 V_{i,j-1}}{1 - \frac{\Delta r}{2r_j}} \right)}{2(\epsilon_1 + \epsilon_2) + \frac{\Delta r}{2r_j} \left(\frac{\epsilon_2}{1 + \frac{\Delta r}{2r_j}} - \frac{\epsilon_1}{1 - \frac{\Delta r}{2r_j}} \right)} \quad (8)$$

Similarly, for a surface at -45° ,

$$V_{i,j} = \frac{\epsilon_2 (V_{i+1,j} + V_{i,j+1}) + \epsilon_1 (V_{i-1,j} + V_{i,j-1}) + \frac{\Delta r}{2r_j} \left(\frac{2V_{i,j+1}}{1 + \frac{\Delta r}{2r_j}} - \frac{\epsilon_1 V_{i,j-1}}{1 - \frac{\Delta r}{2r_j}} \right)}{2(\epsilon_1 + \epsilon_2) + \frac{\Delta r}{2r_j} \left(\frac{\epsilon_2}{1 + \frac{\Delta r}{2r_j}} - \frac{\epsilon_1}{1 - \frac{\Delta r}{2r_j}} \right)} \quad (9)$$

For surfaces perpendicular to the axis of symmetry, the difference equation becomes

$$\epsilon_{21} \left(\frac{V_{i,j+1} - 2V_{i,j} + V_{i,j-1}}{(\Delta r)^2} + \frac{1}{2r_j} \frac{V_{i,j+1} - V_{i,j-1}}{\Delta r} \right) + \frac{\epsilon_2 (V_{i+1,j} - V_{i,j}) - \epsilon_1 (V_{i,j} - V_{i-1,j})}{(\Delta z)^2} = 0 \quad (10)$$

where ϵ_1 is the dielectric on the left and ϵ_2 is to the right. Solving this equation for $V_{i,j}$, one obtains

$$V_{i,j} = \frac{\epsilon_{21} (V_{i,j+1} + V_{i,j-1}) + \frac{\epsilon_{21} \Delta r}{2r_j} (V_{i,j+1} - V_{i,j-1}) + \epsilon_2 V_{i+1,j} + \epsilon_1 V_{i-1,j}}{2\epsilon_{21} + \epsilon_1 + \epsilon_2} \quad (11)$$

In comparing Eqs. (6), (8), and (9) it can be shown that if $\epsilon_{12} = 1/2(\epsilon_1 + \epsilon_2)$, the denominators are the same. Also, if $(\Delta r/2r_j)^2 \ll 1$, then $\epsilon_{21} = (\epsilon_1 + \epsilon_2)/2$ makes the denominator of Eq. (11) approximately equivalent to the others. These results have been verified on the computer. It can also be shown that if $\epsilon_1 = \epsilon_2$ and $(\Delta r/2r_j)^2 \ll 1$, these equations reduce to Eq. (3).

Other dielectric interfaces are solved by a technique developed by Dorny,² who employs Gauss' flux theorem

$$- \int_S \epsilon \nabla_n dS = Q \quad (12)$$

for a closed surface S , where V_n is the gradient of V in the direction of the outward normal to S , ϵ is the dielectric constant, and Q is the total charge enclosed in S . Integration over the surface S in Fig. 2 with ϵ_1 the dielectric below the interface, ϵ_2 the dielectric constant above the interface ($\Delta r = \Delta z$), and Q (the space charge) equal to zero, leads to the following:

$$\left[\frac{\epsilon_1}{2} \left(r_j - \frac{\Delta r}{4} \right) + \frac{\epsilon_2}{2} \left(r_j + \frac{\Delta r}{4} \right) \right] (V_{i-1,j} - V_{i,j}) + \epsilon_2 \left(r_j + \frac{\Delta r}{2} \right) (V_{i,j+1} - V_{i,j}) + \epsilon_1 r_j (V_{i+1,j} - V_{i,j}) + \epsilon_1 \left(r_j - \frac{\Delta r}{2} \right) (V_{i,j-1} - V_{i,j}) = 0 \quad (13)$$

Solving Eq. (13) for $V_{i,j}$ yields

$$V_{i,j} = \frac{\left[\frac{\epsilon_1}{2} \left(1 - \frac{\Delta r}{4r_j} \right) + \frac{\epsilon_2}{2} \left(1 + \frac{\Delta r}{4r_j} \right) \right] V_{i-1,j} + \epsilon_2 \left(1 + \frac{\Delta r}{2r_j} \right) V_{i,j+1} + \epsilon_1 V_{i+1,j} + \epsilon_1 \left(1 - \frac{r}{2r_j} \right) V_{i,j-1}}{\epsilon_1 \left(\frac{3}{2} - \frac{5\Delta r}{8r_j} \right) + \epsilon_2 \left(\frac{5}{2} + \frac{5\Delta r}{8r_j} \right)} \quad (14)$$

and similar solutions for other dielectric shapes can be easily derived by inspection, as Dorny asserts.²

The solutions in Eqs. (6), (8), (9), and (11) are used where applicable, since they have been found slightly more accurate than the solutions found from Dorny's method. Dorny's solutions are used at interface points where the above equations are not applicable.

ACCURACY OF PROGRAM

The difference equations required for the discrete simulation on the digital computer are derived from Taylor's series expansion about zero:

$$f(x) = f(0) + xf'(0) + \frac{x^2}{2!} f''(0) + \dots + \frac{x^n}{n!} f^{(n)}(0) \quad (15)$$

$$0 < \alpha < 1$$

Assuming a matrix increment h , we solve Eq. (15) for the first and second derivatives as follows:

$$f'(0) = \frac{f_1 - f_{-1}}{2h} - \frac{h^2}{6} f'''(0) + O(h^4) \quad (16)$$

and

$$f'''(0) = \frac{f_1 - 2f_0 + f_{-1}}{h^2} - \frac{h^2}{12} f^{iv}(0) + O(h^4), \quad (17)$$

where $f_1 = f(h)$, $f_0 = f(0)$, and $f_{-1} = f(-h)$. If only the first term on the right-hand side of either equation is employed, the error is seen to be the order of h^2 .

Results from the computer have indicated that the error in one-dimensional cases is indeed the order of h^2 . In two dimensions (as we have here), the error seems to be proportional to h , generally one-half to one-third of h . This gives an error of less than 1 per cent for most interesting cases. Results for cases where the exact solutions are known have generally been within 0.5 per cent when a 50×50 matrix is employed.

COMPUTER PROGRAM

The iterative procedure consists of applying the difference equations at appropriate points within the area to be analyzed. The matrix consists of a two-dimensional array as shown in Fig. 2. The first subscript (usually i) begins at the left edge of the matrix and increases axially in the $+z$ direction. The second subscript (usually j) begins at the axis and increases radially. The relaxation operations are generally carried out starting at the left side of the matrix and passing up each column in sequence across the matrix.

This method of computing the potentials requires a knowledge of the locations of electrodes and dielectric interfaces relative to the radial columns. This information is obtained by supplying as input data matrices which specify the j coordinates of electrodes and dielectric interfaces. Computations are carried out in each column i from the first matrix $j(i,1)$ to $j(i,2)$, then from $j(i,3)$ to $j(i,4)$, up to 7 pairs of matrices. The axis may be included in the computations by specifying appropriate values of $j(i,1)$ as zero. Any finite or infinite offset from the axis may also be specified.

Dielectric surfaces at 45° or less to the axis are specified by setting the upper limit of one of these matrix pairs equal to the lower limit of the next pair; e.g., $j(i,2) = j(i,3)$. Surfaces perpendicular or at steep angles to the axis are treated separately.

Floating electrodes are treated as special dielectrics and are specified by separate pairs of matrices in the input data. These are given an initial relative dielectric constant of 101.0 in the input data. This value is automatically increased by the program up to a final value of 100,000 in three steps. The initial relatively low dielectric constant permits the electrode to "float" to the local potential value; then as the dielectric constant is increased the equipotentials inside the electrode are pushed out until the dielectric becomes a unipotential body.

Subroutines are available at the end of a run to plot equipotentials, compute and plot equipotential lines, and to save data for more accurate blow-ups of small areas of the original plot.

If equipotential plots are desired, up to 24 equipotentials to be plotted are specified in the input data. In addition to an over-all plot, expanded plots of sections of the matrix can be obtained by specifying the desired sections in the input data.

The equipotential plots are obtained in a similar manner, but the field values plotted are determined automatically by the program since it is generally impossible to know the values desired ahead of time. The values and plots must be interpreted fairly carefully, since there are discontinuities in the field at dielectric and electrode boundaries.

Data may be saved by the blowup subroutine to permit analysis of small sections of a larger plot. This routine saves the boundary data for the section to be expanded and interpolates for the intermediate values. The data so saved can be used by the main program to re-solve the problem and either improve the accuracy or include more details.

SAMPLE PLOTS

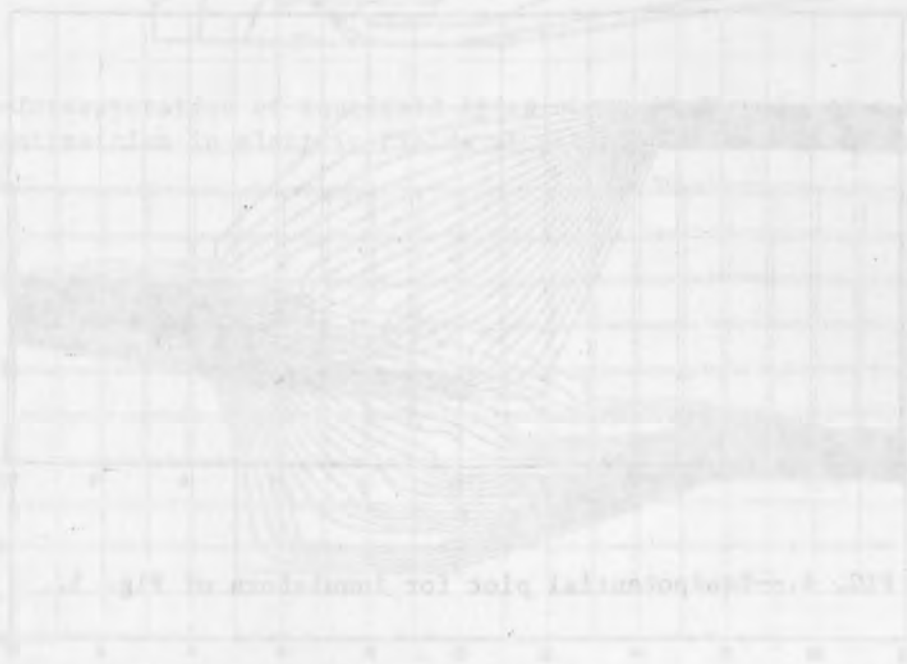
A proposed design for the insulators of a high-voltage diode is shown in Fig. 3. To the left is a coaxial transmission line with transformer oil insulation; to the right is the diode vacuum. The insulators are polymethyl methacrylate with metallic grading rings between the insulators. The complete equipotential plot for this configuration is shown in Fig. 4. Equipotentials are plotted at 5-percent intervals. Note that the 25; 50; and 75-percent lines lie on or very near the metallic rings, indicating nearly perfect grading across the insulators. It should also be noted that the equipotentials come out of the insulators near the pointed edge so that the hold-off capability would most likely be poor.

Figures 5 and 6 are plots of the equifield lines. Figure 5 is the raw plot from the computer and Fig. 6 is the interpretation of the lines accounting for discontinuities at dielectric and metallic surfaces.

An improved version of the insulator section is shown in Fig. 7, where a fifth insulator has been added and the grading rings extended past the tip of the insulators. Note that the peak field in the oil has also been reduced by smoothing the bend in the cylinder.

REFERENCES

1. R. Kouzes, private communication.
2. C. N. Dorny, Proc. IEEE 57: 856-858, 1969.



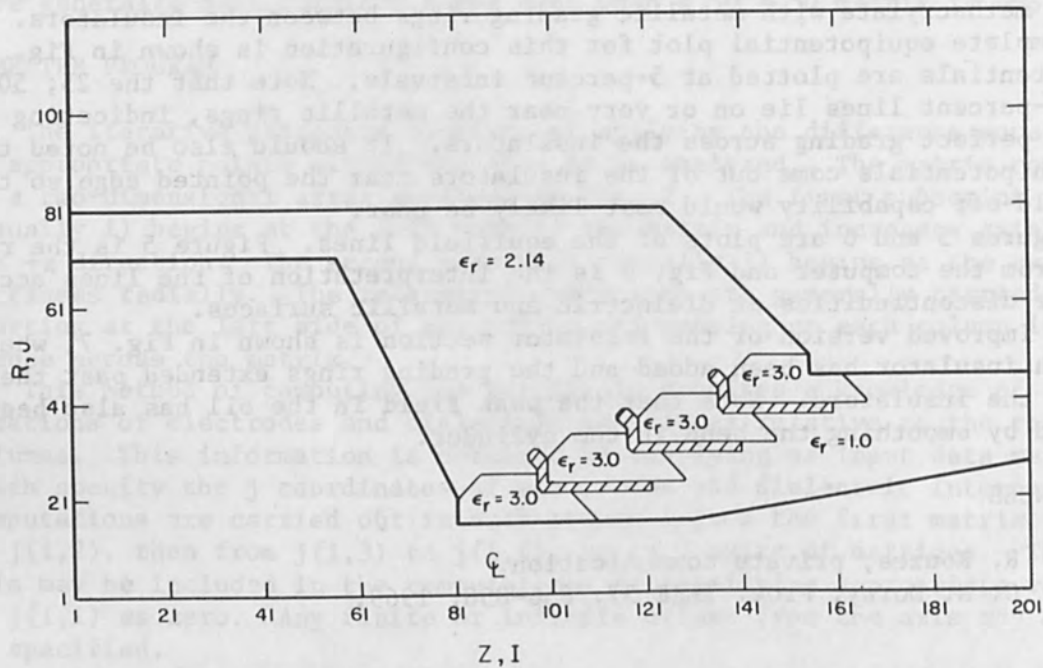


FIG. 3.--Initial proposed insulator design for low-inductance, high-voltage diode.

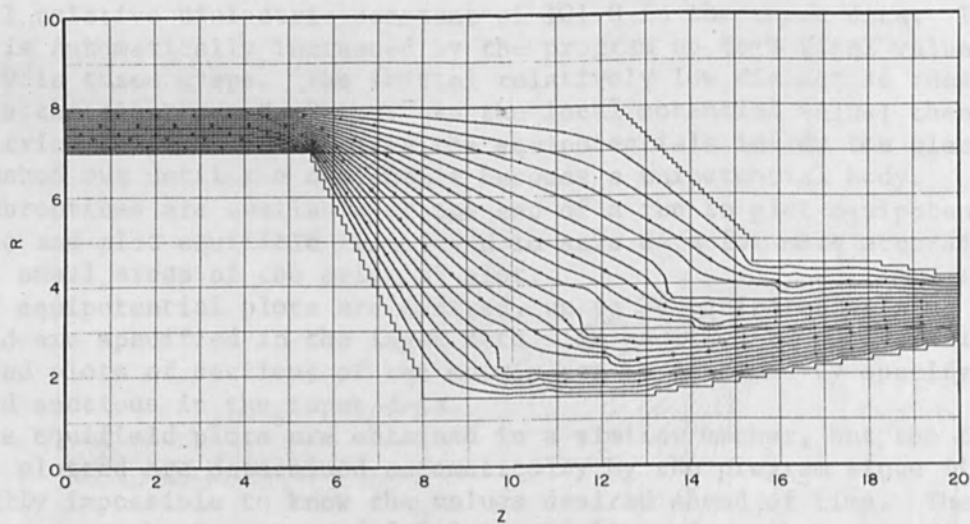


FIG. 4.--Equipotential plot for insulators of Fig. 3.

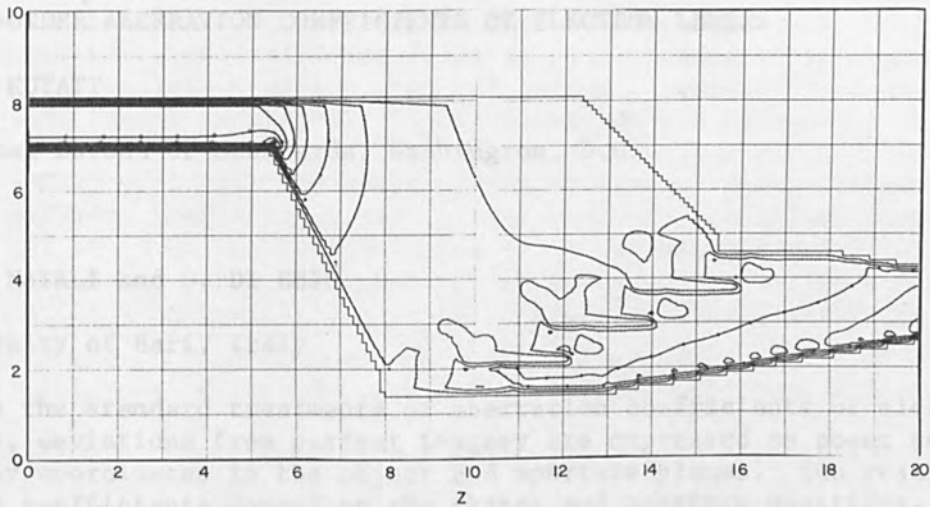


FIG. 5.--Equifield plot for insulators of Fig. 3.

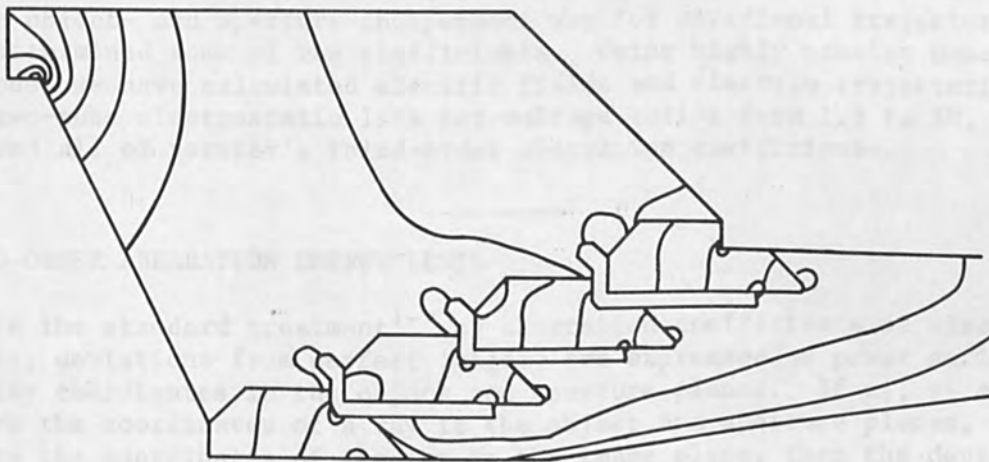


FIG. 6.--Interpretation of equipotential lines shown in Fig. 5, accounting for discontinuities in electric fields at dielectric boundaries and electrodes.

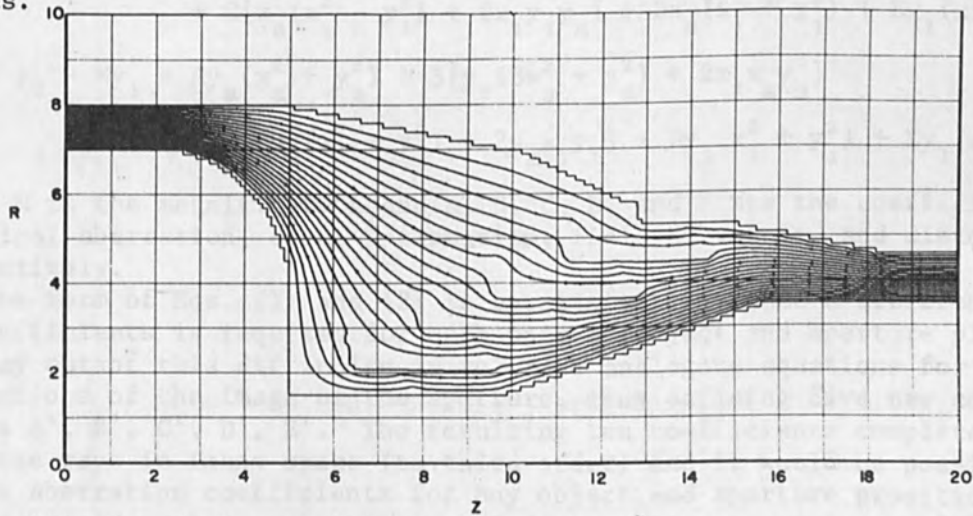


FIG. 7.--Equipotential plot of improved insulator design.

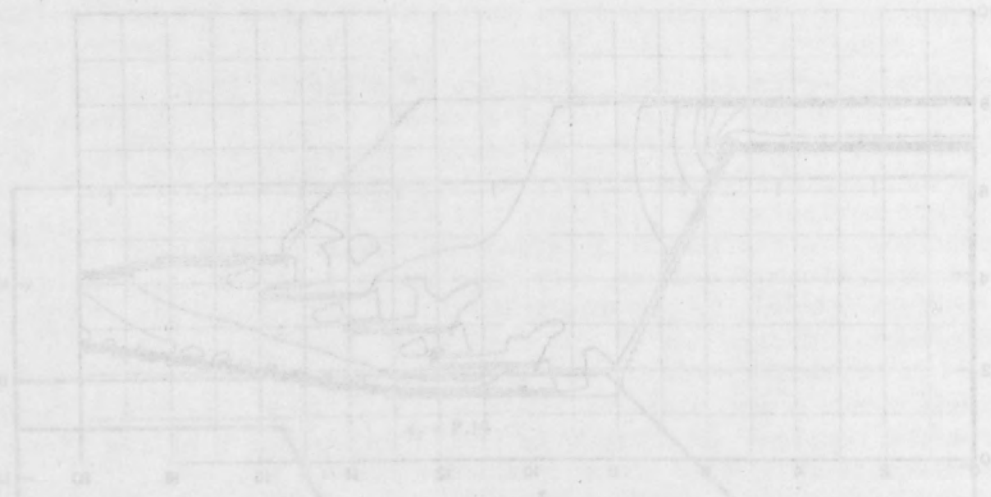


FIG. 2--Equalized plot for insulators of Fig. 1.

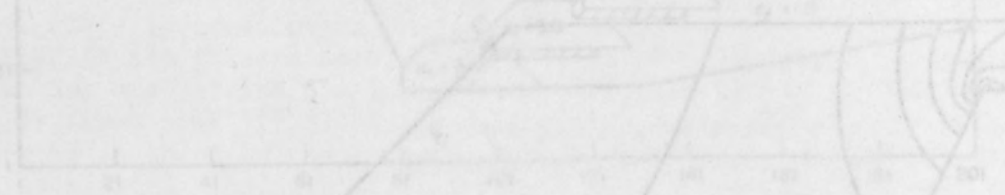


FIG. 3--Equalized plot for insulators of Fig. 2.



FIG. 4--Equalized plot for insulators of Fig. 3.

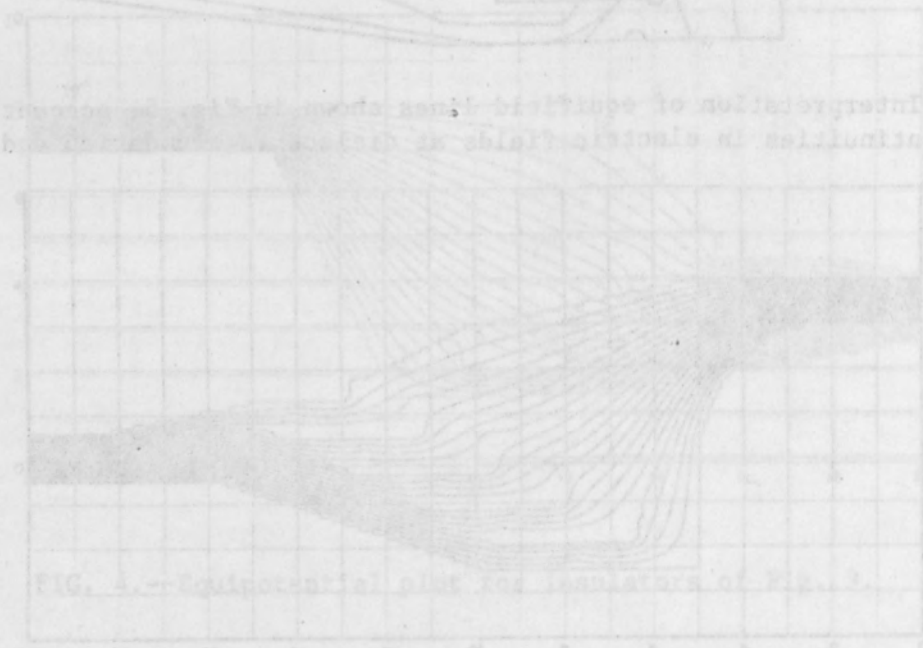


FIG. 5--Integration of electric field lines in electric field at insulator and also for discontinuities in electric field at insulator.

THIRD-ORDER ABERRATION COEFFICIENTS OF ELECTRON LENSES

C. E. KUYATT

National Bureau of Standards, Washington, D.C.

and

S. V. NATALI and D. Di CHIO

University of Bari, Italy

In the standard treatments of aberration coefficients of electron lenses, deviations from perfect imagery are expressed as power series of the ray coordinates in the object and aperture planes. The resulting aberration coefficients depend on the object and aperture positions, and a complete description of the aberrations of a lens would, in principle, require a doubly infinite set of aberration coefficients.

Verster has formulated the third-order aberrations of electron lenses in an object- and aperture-independent way for meridional trajectories and has determined some of the coefficients. Using highly precise numerical methods, we have calculated electric fields and electron trajectories in the two-tube electrostatic lens for voltage ratios from 1.5 to 50, and have derived all of Verster's third-order aberration coefficients.

THIRD-ORDER ABERRATION COEFFICIENTS

In the standard treatment¹⁻³ of aberration coefficients of electron lenses, deviations from perfect imagery are expressed as power series of the ray coordinates in the object and aperture planes. If x_1, y_1 and x_a, y_a are the coordinates of a ray in the object and aperture planes, and x_2, y_2 are the coordinates of the ray in the image plane, then the deviations from the first-order image point are given by³

$$\Delta x_2 = x_2 - Mx_1 = Ax_a(x_a^2 + y_a^2) + B[x_1(3x_a^2 + y_a^2) + 2y_1x_ay_a] + C[x_a(x_1^2 - y_1^2) + 2x_1y_1y_a] + Dx_a(x_1^2 + y_1^2) + Ex_1(x_1^2 + y_1^2) \quad (1)$$

$$\Delta y_2 = y_2 - My_1 = Ay_a(x_a^2 + y_a^2) + B[y_1(3x_a^2 + y_a^2) + 2x_1x_ay_a] + C[-y_a(x_1^2 - y_1^2) + 2x_1x_1y_1] + Dy_a(x_1^2 + y_1^2) + Ey_1(x_1^2 + y_1^2) \quad (2)$$

where M is the magnification and $A, B, C, D,$ and E are the coefficients of spherical aberration, coma, astigmatism, field curvature, and distortion, respectively.

The form of Eqs. (1) and (2) is unsatisfactory since a different set of coefficients is required for each pair of object and aperture planes. One way out of this difficulty is to write analogous equations for the aberrations of the image of the aperture, thus defining five new coefficients A', B', C', D', E' . The resulting ten coefficients completely define the rays in image space (to third order) and it would be possible to derive aberration coefficients for any object and aperture position. Such a procedure has never been carried out. In some treatments⁴⁻⁷ the

aberrations are given as a power series in the position and direction of the ray in the object plane. This is still unsatisfactory, since a different set of coefficients is needed for each object position.

Ideally, one should use aberration coefficients that depend only on the lens and that are independent of the location of the object and the aperture. Verster⁴ has described such a method for rays in meridional planes (planes containing the lens axis). The incident and emerging rays are taken to be the asymptotes to the actual rays. The incident ray is given by its position r_1 and slope r_1' at the first focal plane, and the emerging ray by its position r_2 and slope r_2' at the second focal plane. Then to third order

$$r_2' = -(r_1/f_2) + m_{13}r_1'^3 + m_{14}r_1'^2(r_1/f_2) + m_{15}r_1'(r_1/f_2)^2 + m_{16}(r_1/f_2)^3 \quad (3)$$

$$(r_2/f_1) = r_1' + m_{23}r_1'^3 + m_{24}r_1'^2(r_1/f_2) + m_{25}r_1'(r_1/f_2)^2 + m_{26}(r_1/f_2)^3 \quad (4)$$

where f_1 and f_2 are the focal lengths and the m_{ij} are dimensionless coefficients.

Hawkes⁵⁻⁷ has carried out a more general treatment not restricted to meridional rays. The following treatment for electrostatic lenses is based on Hawkes' formulation.

Let the incident asymptotic ray be defined by its direction cosines α_1, γ_1 and its coordinates x_1, y_1 at the first focal plane, and the emerging asymptotic ray by its direction cosines α_2, γ_2 and its coordinates x, y_2 at the second focal plane. With the help of the dimensionless quantities $X_1 = x_1/f_2$ and $Y_1 = y_1/f_2$, the coordinates are grouped as system invariants:

$$r = X_1^2 + Y_1^2 \quad s = \alpha_1^2 + \gamma_1^2$$

$$u = X_1\alpha_1 + Y_1\gamma_1 \quad v = X_1\gamma_1 - Y_1\alpha_1$$

The coefficient of v vanishes for electrostatic lenses.

Hawkes derives the third-order properties from a characteristic function which is second order in r, s, u :

$$(r \ s \ u) \begin{pmatrix} F_{11} & F_{12} & F_{13} \\ 0 & F_{22} & F_{23} \\ 0 & 0 & F_{33} \end{pmatrix} \begin{pmatrix} r \\ s \\ u \end{pmatrix}$$

Here we have deviated from Hawkes' treatment by defining the F 's as dimensionless quantities. From this characteristic function there results:

$$X_2 = \alpha_1 + 4F_{11}X_1r + 2F_{12}X_1s + 2F_{13}X_1u + F_{13}\alpha_1r + (F_{23} - \frac{1}{2})\alpha_1s + 2F_{33}\alpha_1u \quad (5)$$

$$\alpha_2 = -X_1 + (F_{13} - \frac{1}{2})X_1r + F_{23}X_1s + 2F_{33}X_1u + 2F_{12}\alpha_1r + 4F_{22}\alpha_1s + 2F_{23}\alpha_1u \quad (6)$$

where $X_2 = x_2/f_1$. The corresponding equations for Y_2 and γ_2 are obtained by replacing X_1 and α_1 with Y_1 and γ_1 .

To get Verster's equations, put $Y_1 = 0$. Then $r = X_1^2, s = \alpha_1, u = X_1\alpha_1$, and

$$X_2 = \alpha_1 + 4F_{11}X_1^3 + 3F_{13}X_1^2\alpha_1 + (2F_{12} + 2F_{33})X_1\alpha_1^2 + (F_{23} - \frac{1}{2})\alpha_1^3 \quad (7)$$

$$\alpha_2 = -X_1 + (F_{13} - \frac{1}{2})X_1^3 + (2F_{12} + 2F_{33})X_1^2\alpha_1 + 3F_{23}X_1\alpha_1^2 + 4F_{22}\alpha_1^3 \quad (8)$$

Therefore, Verster's coefficients are related to the F 's by

$$\begin{aligned} m_{16} &= F_{13} - \frac{1}{2} & m_{26} &= 4F_{11} \\ m_{15} &= 2F_{12} + 2F_{33} & m_{25} &= 3F_{13} \\ m_{14} &= 3F_{23} & m_{24} &= 2F_{12} + 2F_{33} \\ m_{13} &= 4F_{22} & m_{23} &= F_{23} - \frac{1}{2} \end{aligned} \quad (9)$$

and the relationships between these coefficients derived by Verster follow immediately:

$$\begin{aligned} m_{14} &= 3m_{23} + 1.5 \\ m_{24} &= m_{15} \\ m_{25} &= 3m_{16} + 1.5 \end{aligned} \quad (10)$$

CALCULATION OF COEFFICIENTS

Verster has determined four of the m_{ij} with an automatic trajectory plotter connected to an electrolytic tank.

Using highly precise numerical methods⁸ we have calculated electric fields and electron trajectories in the two-tube electrostatic lens for voltage ratios from 1.5 to 50. For voltage ratios of 2, 5, 10, 20, and 40 a large number of trajectories were calculated and fit to Eqs. (3) and (4), yielding values for all of the coefficients m_{ij} . The results are given in Table I and II, together with the values given by Verster. Agreement with the values of Verster is very good for m_{13} , fairly good for m_{23} and m_{26} , but very poor for m_{16} .

Since we have determined all of the m 's independently it is possible to check the relationships given in Eq. (10). Table III gives the results. In almost all cases the relationships are verified to within a few per cent.

Ramberg⁹ has found that for the two-tube lens, m_{13}/f_1^2 and m_{26}/f_2^2 should be approximately equal and change slowly with V_2/V_1 . Table IV gives values of these quantities calculated from our results, together with values obtained by Verster. Ramberg's relation is well satisfied by the weakest lenses.

El-Kareh³ has calculated the spherical aberration coefficients for two-tube lenses. These coefficients, C_{S1} and C_{S2} , are related to the m 's by:

$$C_{S1} = -f_2 m_{13} \quad C_{S2} = -f_1 m_{26}$$

Table V compares our results with those of El-Kareh. The agreement is reasonably good.

TABLE I.--Aberration coefficients in expansion of r_2' .

V_2/V_1	Present Results				Verster	
	m_{13}	m_{14}	m_{15}	m_{16}	m_{13}	m_{16}
2	-285	-1029	-1240	-502		
5	-7.34	-31.6	-47.0	-23.6	-7.32	-9.18
10	-1.44	-6.77	-12.0	-7.06	-1.58	-1.48
20	-.460	-2.23	-4.27	-3.44	-0.480	-0.40
40	-.186	-.722	-2.03	-2.29	-0.186	-0.23

TABLE II.--Aberration coefficients in expansion of r_2 .

V_2/V_1	Present Results				Verster	
	m_{23}	m_{24}	m_{25}	m_{26}	m_{23}	m_{26}
2	-364	-1270	-1480	-575		
5	-11.0	-47	-69	-34.7	-9.21	-36.8
10	-2.71	-11.4	-19.6	-12.2	-3.37	-15.7
20	-1.16	-5.29	-8.05	-7.27	-1.52	-9.68
40	-.65	-2.19	-3.03	-6.52	-0.90	-7.34

TABLE III.--Test of relations among the m 's.

V_2/V_1	$-3m_{23}$	$-m_{14}+1.5$	$-3m_{16}$	$-m_{25}+1.5$	m_{15}	m_{24}
2	1093	1030	1508	1491	-1240	-1270
5	33.1	33.1	70.2	70.7	-47.0	-47.1
10	8.14	8.27	21.2	21.1	-12.0	-11.4
20	3.49	3.73	10.33	9.55	-4.27	-5.29
40	1.95	2.22	6.86	4.53	-2.03	-2.19

TABLE IV.--Test of Ramberg relation for m_{13} , m_{26} .

V_2/V_1	$-m_{13}/f_1^2$		$-m_{26}/f_2^2$	
	Present Results	Verster	Present Results	Verster
2	2.37		2.39	
5	2.39	2.40	2.26	2.40
10	2.27	2.39	1.92	2.38
20	2.23	2.34	1.75	2.35
40	2.09	2.10	1.83	2.08

TABLE V.--Comparison of spherical aberration coefficients.

V_2/V_1	C_{s1}		C_{s2}	
	Present Results	El-Kareh	Present Results	El-Kareh
2	4430	4119	6320	5807
5	28.8	26.3	61.0	56.3
10	3.64	3.50	9.76	10.06
20	.936	.92	3.31	3.52
40	.352	.375	1.95	1.86

CONCLUSIONS

We have obtained, for the first time, a complete set of third-order aberration coefficients for the two-tube electrostatic lens. It is now possible to calculate the position and slope to third order of the exit trajectory which corresponds to any incident meridional ray.

From the equations derived by Verster⁴ it is possible to calculate the more usual coefficients of spherical aberration, coma, curvature of field, and distortion for any position of the object and aperture. Calculation of these coefficients will be the subject of a future paper.

REFERENCES

1. W. Glaser, *Grundlagen der Elektronenoptik*, Springer, Vienna, 1952.
2. P. Grivet, *Electron Optics*, Pergamon Press, Oxford, 1965.
3. A. B. El-Kareh and J. C. J. El-Kareh, *Electron Beams, Lenses, and Optics*, Academic Press, New York, 1970; vol. 2.
4. J. L. Verster, *Philips Res. Repts.* 18: 465, 1963.
5. P. W. Hawkes, *Optik* 27: 287, 1968.
6. P. W. Hawkes, *Optik* 31: 213, 1970.
7. P. W. Hawkes, *Quadrupoles in Electron Lens Design*, Academic Press, New York, 1970.
8. S. V. Natali, D. Di Chio, and C. E. Kuyatt, in preparation.
9. E. G. Ramberg, *J. Appl. Phys.* 13: 582, 1942.

TABLE V. Comparison of experimental and theoretical results.

Order	Experimental results		Theoretical results	
	α	β	α	β
1	0.00	0.00	0.00	0.00
2	0.10	0.10	0.10	0.10
3	0.20	0.20	0.20	0.20
4	0.30	0.30	0.30	0.30
5	0.40	0.40	0.40	0.40
6	0.50	0.50	0.50	0.50
7	0.60	0.60	0.60	0.60
8	0.70	0.70	0.70	0.70
9	0.80	0.80	0.80	0.80
10	0.90	0.90	0.90	0.90

The values of α and β are given in the table.

CONCLUSIONS

We have calculated, for the first time, a complete set of third-order aberration coefficients for the two-tube electrostatic lens. It is now possible to calculate the position and slope to third order of the exit trajectory which corresponds to any incident meridional ray. From the equations derived by Verker, it is possible to calculate the more usual coefficients of spherical aberration, coma, curvature of field, and distortion for any position of the object and aperture. Calculations of these coefficients will be the subject of a future paper.

REFERENCES

1. W. Glaser, *Grundlagen der Mikroskopentechnik*, Springer, Vienna, 1957.
2. P. Grivet, *Electron Optics*, Pergamon Press, Oxford, 1957.
3. A. B. Ehrlich and J. C. P. de Winter, *Electron Optics*, and *Optics*, Academic Press, New York, 1959, vol. 1.
4. J. L. Katzberg, *Kolloid Zeits.* 184, 482, 1962.
5. P. W. Hawkes, *Optik* 37, 197, 1968.
6. P. W. Hawkes, *Optik* 31, 213, 1970.
7. P. W. Hawkes, *Quadrupoles in Electron Lens Design*, Academic Press, New York, 1970.
8. S. V. Natali, D. Di Chio, and G. E. Kuyatt, in preparation.
9. E. C. Ramberg, *J. Appl. Phys.* 33, 1942, 1962.

0.4	0.2	0.1	0.05
0.5	0.3	0.15	0.075
0.6	0.4	0.2	0.1
0.7	0.5	0.25	0.125
0.8	0.6	0.3	0.15
0.9	0.7	0.35	0.175
1.0	0.8	0.4	0.2
1.1	0.9	0.45	0.225
1.2	1.0	0.5	0.25

E × B MASS SEPARATOR DESIGN*

R. L. SELIGER

Hughes Research Laboratories, Malibu, Calif.

The equations of motion are developed and solved for ion trajectories inside an E × B-type mass separator. Curves are presented which illustrate the focusing of the undeflected ion beam, the trajectories along which ions of different mass species disperse inside the separator channel, and the exit slopes of mass species leaving the separator, as functions of a separator strength parameter. For strong separators, beam focusing is significant and is shown to be nonaxisymmetric when the electric and magnetic fields are uniform and orthogonal. A method of correcting the astigmatism by tilting the magnetic polepieces is presented.

INTRODUCTION

During recent years the E × B (Wein) velocity filter has been used as an alternative to the sector magnet as the mass separation element in ion implantation systems.^{1,2} The purpose of the E × B mass separator is to provide separation of one species of ion out of a beam consisting of a mixture of ions with different axial velocities v_z . The E × B mass separator and its dispersion of an ion beam are shown in Fig. 1. Since the axial velocity v_z for an ion is related to its charge e , mass m , and potential V_0 by $v_z = \sqrt{2eV_0/m}$, velocity differences between particles to be separated may be caused by differences in charge-to-mass ratio $\eta_m = e/m$, potential V_0 , or both. By suitable adjustment of the separator's electric and magnetic field strengths E_0 and B_0 , deflection forces are set up inside the device which just cancel for ions with axial velocity equal to E_0/B_0 . Such ions emerge from the separator undeflected, whereas ions with velocities other than E_0/B_0 are deflected and become dispersed in space.

Along with spatial dispersion, the forces inside E × B separators also cause focusing of the beam. In past separator designs, this focusing is not axisymmetric and astigmatism is introduced into the undeflected beam. Typically, an entering beam with circular cross section gives rise to an emerging undeflected beam with an elliptical shape. Since the focusing forces inside the E × B channel can be varied by shaping the magnetic pole pieces and electrostatic plates, a configuration was sought which produces axisymmetric or stigmatic focusing.

A stigmatic configuration suitable for fabrication was found by analysis. For this stigmatic E × B mass separator design, extensive calculations have been made of (1) the axisymmetric focusing of the undeflected beam as a function of the separator design parameters, (2) the trajectories along which ions of different masses disperse inside the separator channel, and (3) the exit slopes of dispersed mass species as a function of the beam energy and the separator parameters, length, and field strengths.

*This work was partially supported by the U.S. Naval Air System Command

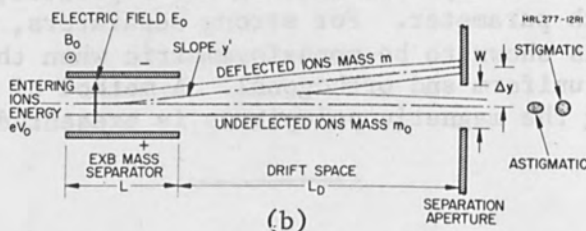
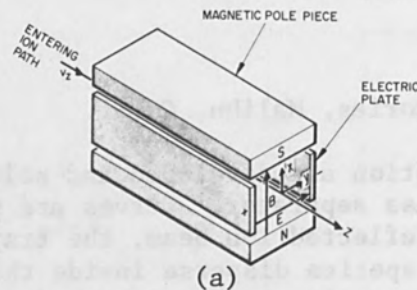
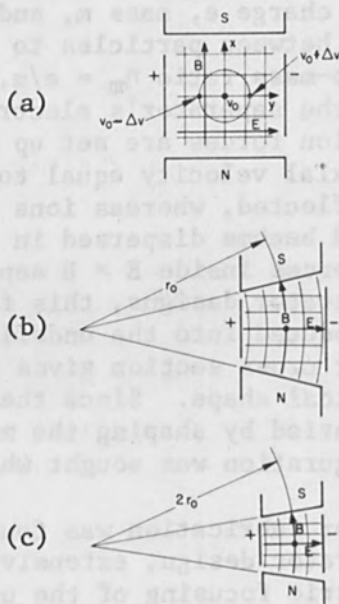


FIG. 1.--E x B velocity analyzer mass separator: (a) field configuration, (b) beam separation.



Fields	Equations of Motion	Focusing x - direction y - direction
$E_x = 0$ $E_y = E_0$ $B_x = B_0$ $B_y = 0$	$\ddot{x} = 0$ $\ddot{y} = -\eta^2 B_0^2 y$ $\eta = \frac{e}{m}$	No Yes
$E_x = 0$ $E_y = E_0$ $B_x = B_0 (1 - y/r_0)$ $B_y = -B_0 x/r_0$ $r_0 = 2V_0/E_0$	$\ddot{x} = -\eta^2 B_0^2 x$ $\ddot{y} = 0$	Yes No
$E_x = 0$ $E_y = E_0$ $B_x = B_0 (1 - y/2r_0)$ $B_y = -B_0 \frac{x}{2r_0}$	$\ddot{x} = -1/2 \eta^2 B_0^2 x$ $\ddot{y} = -1/2 \eta^2 B_0^2 y$	Yes Yes

FIG. 2.--E x B mass separator cross-section configurations: (a) rectangular, (b) tilted polepieces; (c) partially tilted polepieces.

STIGMATIC SEPARATOR DESIGN

The equations of motion for each of the three separator configurations presented in Fig. 2 are derived by substituting the given expressions for the electric and magnetic field components E_x , E_y , B_x , and B_y into the general differential equations

$$m\ddot{x} = eE_x + e\dot{z}B_y \quad (1a)$$

$$m\ddot{y} = eE_y - e\dot{z}B_x \quad (1b)$$

$$m\ddot{z} = e\dot{y}B_x - e\dot{x}B_y \quad (1c)$$

and retaining up to first-order (linear) terms in x and y . Equations (1) refer to the left coordinate system shown in Fig. 2(a). These equations govern the ion trajectories inside ($0 \leq z \leq L$) the separator channel where it is assumed that the effects of space charge can be neglected and that the fields have no components or variations in the z direction. The width of the fringe field regions at the entrance and exit of the separator channel can be made small, compared with separator length, by using shorting rings.

The linearization of Eqs. (1) is analogous to that employed in the derivation of the paraxial-ray equation. Such treatments govern ion trajectories that remain near the principal beam direction (z). In our analysis, the paraxial approximation is supported by the following conditions: (1) transverse ion velocities inside the separator \dot{x} and \dot{y} remain small, compared with the axial velocity v_0 , i.e.,

$$\dot{x}/v_0 \ll 1 \quad \text{and} \quad \dot{y}/v_0 \ll 1 \quad (2)$$

and, (2) the transverse displacements inside the channel x and y remain small, i.e.,

$$x/r_0 \ll 1 \quad \text{and} \quad y/r_0 \ll 1 \quad (3)$$

The natural length scale to which transverse displacements are compared, r_0 , is the cyclotron radius $v_0/\eta_0 B_0$ of a particle of velocity v_0 and charge-to-mass ratio η_0 in a magnetic field B_0 . A second expression for r_0 , found by invoking the balance condition $E_0 = v_0 B_0$, is $r_0 = 2V_0/E_0$. The inequalities given in Eqs. (2) and (3) thus allow the linear equations for x and y given in Fig. 2 to be derived from Eq. (1). The linearized equation for the z direction,

$$\ddot{z} = \eta_0 \dot{y} B_0 \quad (4)$$

follows similarly from Eq. (1) and applies to all three cross-section configurations.

A consideration of two separator cross-section configurations (Figs. 2b and 2c), in addition to the usual rectangular orthogonal field configuration (Fig. 2a), was a result of the nonaxisymmetric focusing produced by the configuration of Fig. 2(a). In a lens, an entering ray is bent in proportion to its distance from the lens axis. In terms of the equations of motion for ions, this condition means that the fields must produce a transverse restoring force that is linear in the off-axis directions. Astigmatism occurs when the restoring force is not axisymmetric, i.e., not the same for the x - and y -directions. The first channel configuration considered (Fig. 2a) is rectangular and produces uniform orthogonal fields

(to first order in x and y). The equations of motion for this case show that there is focusing in the y direction due to the restoring force term $-\eta^2 B_0^2 y$ but there is no focusing in the x direction. An entering beam of circular cross section would therefore emerge with an elliptical shape. A physical understanding of the cause of the y -axis focusing in the configuration of Fig. 2(a) has led to the subsequent separator configurations. Referring to Fig. 2(a), consider a round parallel beam at the beginning of the separator channel. If ions on the z axis with velocity $v_0 = \sqrt{2e/mV_0}$ move straight along the z axis, then ions located to the right, at positive y , are at the higher potential $V_0 + E_0 y$ and hence have a higher axial velocity $v_0 + \Delta v$. Such ions experience a larger magnetic force $B_0(v_0 + \Delta v)$ than electric force $E_0 (= B_0 v_0)$; the resultant force drives the ions back toward the z -axis. On the other hand, ions lying to the left of the z axis move at a reduced velocity $v_0 - \Delta v$ and are deflected toward the z axis by the larger electric force. The net effect is a focusing in the y direction. The variation in the magnetic force from $(v_0 - \Delta v)B_0$ to $(v_0 + \Delta v)B_0$ across the beam can be compensated for by having the magnetic field vary with y . The y -axis focusing can be eliminated completely by tilting the pole pieces as shown in Fig. 2(b). However, along with the desired y variation of B_x produced by the tilted polepieces, the condition $\text{curl } \underline{B} = 0$ requires that an x variation be introduced into B_y ; the precise expression is $B_y = -B_0 x/r_0$. Unfortunately, this B_y term causes a linear restoring force in the x equation which produces x direction focusing. Apparently, tilting the pole pieces has "moved" all of the focusing from the y direction to the x direction. A compromise between the first two configurations, which produces equal focusing in the x and y directions, is obtained by tilting the polepieces only half as much as in Fig. 2(b). Whereas an entering beam of circular cross section would emerge elliptical from separators designed with the first two configurations, the beam cross section does not change shape in a separator with the cross section shown in Fig. 2(c). In this latter design axisymmetric focusing is present and astigmatism is removed.

The amounts of focusing and dispersion produced by a separator with stigmatic cross section (Fig. 2c) will now be determined as a function of the fields E_0 and B_0 and the separator length L . It will be shown that separators can be designed with very weak focusing power but adequate dispersion to be suitable for practical application. For such separators, r_0 is large enough (over 1 m) to make tilting the polepieces unnecessary. The astigmatism produced by the rectangular configuration of Fig. 2(a) would be negligible. A separator will also be discussed that has high dispersion for which the focal strength is significant and the stigmatic design of Fig. 2(c) eliminates the pronounced astigmatism that would occur for a separator with rectangular configuration.

FOCUSING

The amount of focusing of the undeflected ion beam as it passes through the stigmatic $E \times B$ separator is found by solving the linearized equations of motion. The equations for x and y are given in Fig. 2(c); the z equation is Eq. (4). For an ion initially located at $(x_0, y_0, 0)$ with velocity $\dot{x}_0, \dot{y}_0, v_0 [1 + (y_0/r_0)]$, the solutions to the equations of motion are

$$x = x_0 \cos \theta + r_0 \sqrt{2} (\dot{x}_0/v_0) \sin \theta \quad (5a)$$

$$y = y_0 \cos \theta + r_0 \sqrt{2} (\dot{y}_0/v_0) \sin \theta \quad (5b)$$

$$z = \theta r_0 \sqrt{2} \left[1 + (y_0/r_0) \frac{\sin \theta}{\theta} - (\dot{y}_0/v_0) \left(\frac{\cos \theta - 1}{\theta} \right) \right] \quad (5c)$$

where $\theta = \eta_0 B_0 t / \sqrt{2}$. From Eqs. (5a) and (5b), it is seen that the beam radius undergoes sinusoidal oscillations inside the separator channel as a function of θ . For example, an initially parallel beam ($\dot{x}_0 = \dot{y}_0 = 0$) crosses over at $\theta = \pi/2$. Under the assumptions in Eqs. (2) and (3), it follows from Eq. (5c) that

$$z \sim \theta r_0 \sqrt{2} \quad (6)$$

At the end of the channel the final value of θ is $\theta_L = L/\sqrt{2} r_0$. The variable θ_L is a good measure of the focusing and dispersive "strengths" of an $E \times B$ mass separator. Additional insight into the focusing properties of the stigmatic separator is obtained by expressing its transfer matrix³ as a function of θ_L . This matrix expresses the linear relationships between the position and slope of an ion trajectory at $z = L$ and the initial position and slope. For the stigmatic separator the same matrix applies to both the x - and y -directions. The matrix elements are determined (using the x -direction) from Eq. (5a) and the equation for the slope x'

$$x' = - (x_0/\sqrt{2}r_0) \sin \theta + x'_0 \cos \theta \quad (7)$$

where $x' = \frac{dx}{dz} = \frac{dx}{d\theta} \frac{d\theta}{dz}$; $x'_0 = \dot{x}_0/v_0$

and the approximate Eq. (6) may be used for the determination of $d\theta/dz$. With $\theta = \theta_L$, Eqs. (5a) and (7) can be written as

$$\begin{pmatrix} x_L \\ x'_L \end{pmatrix} = \begin{pmatrix} \cos \theta_L & r_0 \sqrt{2} \sin \theta_L \\ -\frac{\sin \theta_L}{r_0 \sqrt{2}} & \cos \theta_L \end{pmatrix} \begin{pmatrix} x_0 \\ x'_0 \end{pmatrix} \quad (8)$$

It is enlightening to factor the transfer matrix in Eq. (8) into the product of three matrices⁴

$$\begin{pmatrix} 1 & \ell \\ 0 & 1 \end{pmatrix} \begin{pmatrix} 1 & 0 \\ -\frac{1}{f} & 1 \end{pmatrix} \begin{pmatrix} 1 & \ell \\ 0 & 1 \end{pmatrix}$$

where $\ell = \frac{1 - \cos \theta_L}{\sin \theta_L} r_0 \sqrt{2}$ (9)

and $f = \frac{r_0 \sqrt{2}}{\sin \theta_L}$ (10)

The product expansion shows that the stigmatic separator is optically equivalent to a convergent thin lens of focal length f located between two equal drift regions of lengths ℓ . The dependence of ℓ and f on θ_L , L and r_0 is illustrated in Fig. 3. For small values of θ_L , say $\theta_L < 0.5$, Eqs. (9) and (10) reduce to

$$\ell \sim L/2 \quad \text{and} \quad f \sim 2r_0^2/L$$

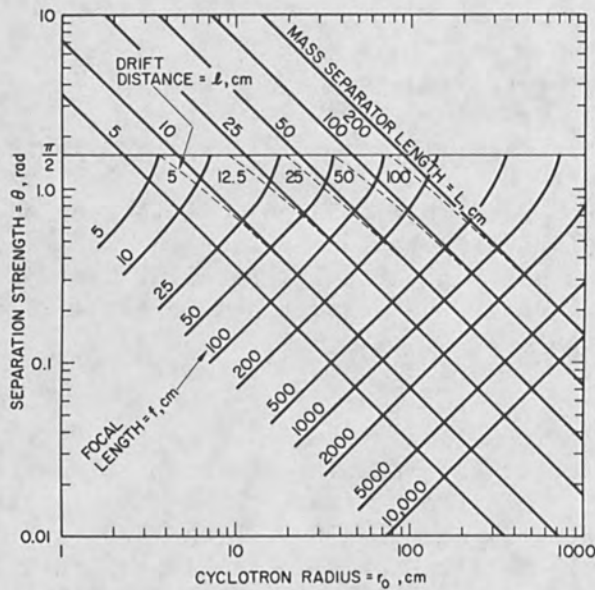


FIG. 3.--Stigmatic E x B mass separator length, focal length, and drift distance as function of its separation strength and cyclotron radius.

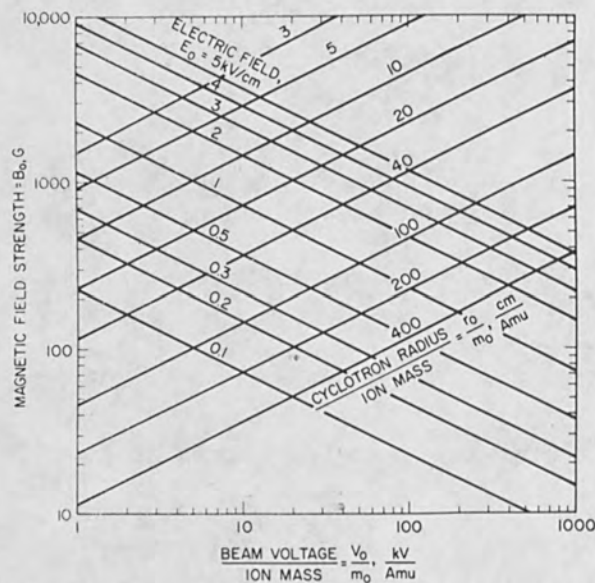


FIG. 4.--Illustration of the E x B balance condition $E_0 = B_0 v_0$, $v_0 = \sqrt{2e/m_0 v_0}$.

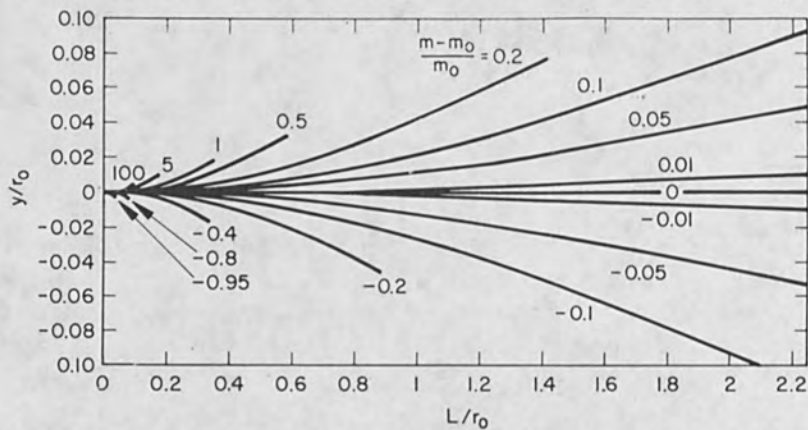


FIG. 5.--Dispersion of mass species inside E x B mass separator.

A typical weak separator design which is adequate for ion implantation system applications has a separator length $L = 15$ cm, a strength $\theta_L = 0.1$, and a cyclotron radius $r_0 = 100$ cm. The focal length of this separator is then seen to be very long ($f = 13$ m) and the drift distance ℓ is half the separator length 7.5 cm. The balance equation $E_0 = B_0 v_0$ is illustrated in Fig. 4. For the above separator, it is seen that in order to obtain the cyclotron radius of 100 cm for a boron beam, the following are required: $V_0 = 100$ kV, $m_0 \sim 10$, $B_0 \sim 1500$ G, and $E_0 \sim 2$ kV/cm.

A strong separator, e.g., with $\theta_L = 1.0$ and length $L = 60$ cm, has a cyclotron radius $r_0 = (L/\sqrt{2} \theta_L) = 42$ cm. For $V_0 = 100$ kV, it then follows that $E_0 = 2V_0/r_0 = 5$ kV/cm. Then, from Fig. 4, the magnetic field required for boron ($m_0 = 10$) is found to be about 3500 G. The focal length of this separator is about 70 cm (Fig. 3). From Eq. (10), it follows that an entering parallel beam ($\dot{x} = \dot{y} = 0$) would reduce in diameter by a factor $\cos \theta$ (0.54) for $\theta = \theta_L = 1.0$ at the exit of this strong separator. The astigmatism produced if a separator of this strength ($\theta_L = 1.0$) is not of the stigmatic design therefore will be appreciable.

It should be noted that $E \times B$ separators currently in use can operate at the field strengths required for $\theta_L = 1.0$. (For example, a modified version of the 60-cm Colutron $E \times B$ separator now in use at Hughes Research Laboratories can supply magnetic fields as large as 12 kG and electric fields of 10 kV/cm.)

DISPERSION

The most critical factor in the performance of a mass separator is dispersion--the ability to isolate ions of one mass species from a beam comprising many mass species. After passing through an $E \times B$ separator, ions of mass different from that of the desired species emerge deflected from the z -axis, i.e., dispersed in space. This situation is illustrated in Fig. 1(b), where the desired ions (mass m_0) are undeflected and ions with mass m emerge as a deflected beam with slope y' . After traversing a drift region of length L_D , the distance between the centers of the undeflected and deflected beam centers is

$$\Delta y = y' [(L/2) + L_D] \quad (11)$$

If the beam diameters are smaller than Δy , an aperture can be used to isolate the desired beam with particle mass m_0 . Clearly, the smaller the beam diameters are in the aperture plane, the smaller the required separation Δy . The beam diameters are determined by the diameter and slope of the ion beam at the entrance to the separator and by the focusing produced by the separator. The entrance conditions depend on the beam forming system upstream of the separator. The focusing was analyzed above for the stigmatic separator design (Fig. 2c) as a function of the field strengths E_0 and B_0 and the separator length L . The dispersion produced by the stigmatic separator design will now be determined.

To determine the exit slope y' of the center of a deflected beam, one must calculate the trajectory of a particle of mass m initially located on the z axis and moving in the z direction. The analysis will be carried out employing the linearized equations of motion. The assumptions in Eqs. (2) and (3) are maintained with v_0 replaced by $v_m = (2eV_0/m)^{1/2}$ in Eq. (3). Since there is no initial velocity or forces in the x direction on this particle, it remains in the z -plane. The equations of motion for the y and z directions are

$$\ddot{y} = \eta_m \{E_0 - \dot{z} B_0 [1 - (y/2r_0)]\} \quad (12)$$

$$\ddot{z} = \eta_m \dot{y} B_0 \quad (13)$$

When Eq. (13) is integrated once, one obtains

$$\dot{z} = v_m + \eta_m B_0 y = kv_0 [1 + (ky/r_0)] \quad (14)$$

where in view of the initial conditions, $\dot{z}_0 = v_m$ and $k^2 = m_0/m$. The substitution of \dot{z} from Eq. (14) into Eq. (12) then gives

$$\ddot{y} + k^3 [k - (1/2)] \eta_0^2 B_0^2 y = k_0^2 \eta_0^2 B_0^2 r_0 (1 - k) \quad (15)$$

The solutions to eqs. (14) and (15) are

$$\frac{y}{r_0} = \frac{k^2 \eta_0^2 B_0^2 (1 - k)}{\omega_m^2} \begin{cases} (1 - \cos \omega_m t), & k > 1/2 \\ (1 - \cosh \omega_m t), & k < 1/2 \end{cases} \quad (16)$$

$$\frac{z}{r_0} = \frac{k \eta_0 B_0}{\omega_m} \begin{cases} \omega_m t + \frac{k^3 \eta_0^2 B_0^2 (1 - k)}{\omega_m^2} (\omega_m t - \sin \omega_m t), & k > 1/2 \\ \omega_m t + \frac{k^3 \eta_0^2 B_0^2 (1 - k)}{\omega_m^2} (\omega_m t - \sinh \omega_m t), & k < 1/2 \end{cases} \quad (17)$$

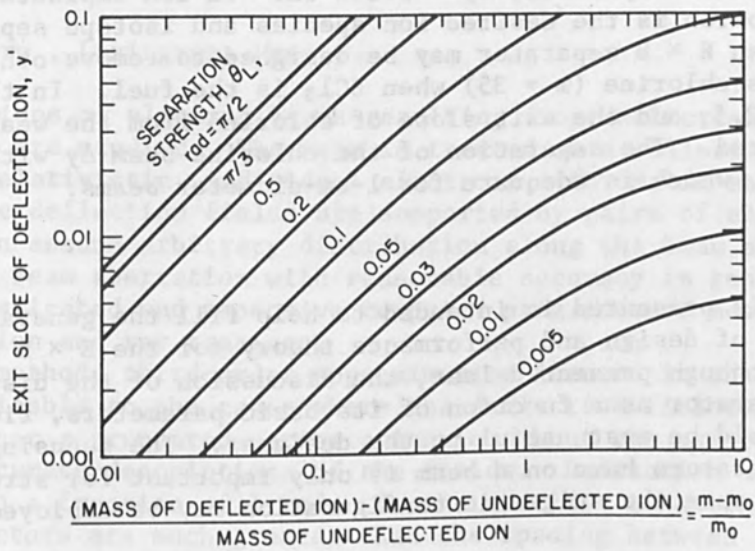
$$\text{where } \omega_m = k^{3/2} \eta_0 B_0 \begin{cases} (k - 1/2)^{1/2}, & k > 1/2 \\ (1/2 - k)^{1/2}, & k < 1/2 \end{cases} \quad (18)$$

For $k = 1/2$, the solutions are

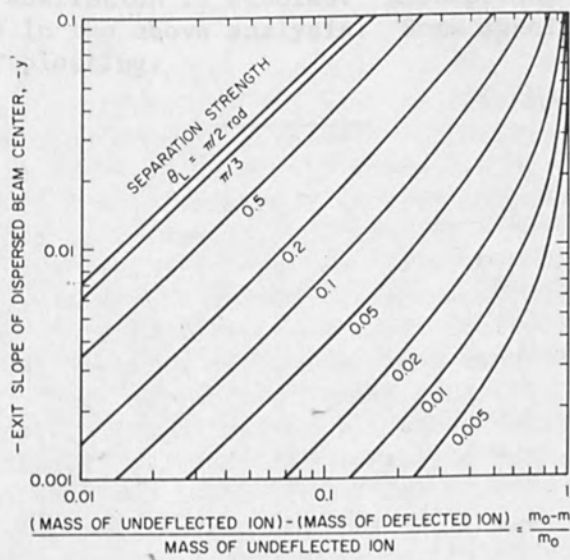
$$y = (\eta_0 B_0 t)^2 (r_0/16) \quad \text{and} \quad z = (1/2) v_0 [t + (\eta_0^2 B_0^2 t^3/96)] \quad (19)$$

By means of Eqs. (16) and (17), the dispersion of ion species inside the separator channel is illustrated in Fig. 5. Because of the approximations $y/r_0 \ll 1$ and $\dot{y}/v_m \ll 1$, and the linear analysis employed, the solutions are only shown in their regions of validity (i.e., $y/r_0 \leq 0.1$, $\dot{y}/v_m \leq 0.1$). The dispersion, or spreading of mass species, occurring in the strong separator $\theta_L = 1.0$ where $L/r_0 = \sqrt{2}$ $\theta_L = 1.4$ is seen to be dramatically larger than in the weak separator $\theta_L = 0.1$, where $L/r_0 = 0.14$.

The exit slope ($dy/dz = \dot{y}/\dot{z}$) of ions of mass m is plotted as a function of $(m - m_0)/m_0$ and separator strength $\theta_L (= L/\sqrt{2} r_0)$ in Fig. 6. The positive exit slopes for mass species with $m > m_0$ are presented in Fig. 6(a); the negative exit slopes of mass species with $m < m_0$, in Fig. 6(b). These curves tell a designer what separation strength is required for specific applications. Alternatively, the curves can be used to evaluate the performance of a given separator design in an application. As an example of the latter, the performance of the two separators considered above ($\theta_L = 1.0$ and $\theta_L = 0.1$) is evaluated for the case of separating the boron isotopes, i.e., mass 11 ($= m$) from mass 10 ($= m_0$) at energy 100 keV. With $(m - m_0)/m_0 = 0.1$, it can be seen from Fig. 6(a) that for the strong separator, the exit slope of the $m = 11$ species is about 0.06 rad. The separation between the isotopes Δy at a distance $L_D = 30$ cm from the strong separator ($\theta_L = 1.0$, $L = 60$ cm), is then found from Eq. (4) to be 3.6 cm. For the weak separator ($\theta_L = 0.1$, $L = 15$ cm), the exit slope is about 0.0065 rad and the separation Δy (again with $L_D = 30$ cm) is 0.244 cm. If the diameters of the mass 10 and mass 11 ion beams are 1 cm at the



(a)



(b)

FIG. 6.--Exit slope of ion species dispersed by $E \times B$ mass separator:
 (a) $m > m_0$; (b) $m < m_0$.

separation aperture plane, then the strong separator for which $\Delta y = 3.6$ cm is capable of separating mass 10 from mass 11 but the weak separator produces insufficient dispersion, $\Delta y = 0.244$ cm. In ion implantation applications where boron is the desired ion species and isotope separation is not required, an $E \times B$ separator may be designed to remove other mass species such as chlorine ($m = 35$) when BCl_3 is the fuel. In this case $(m - m_0)/m_0 = 2.5$, and the exit slope of chlorine from the weak separator is about 0.06 rad. The separation of the chlorine beam Δy with $L_D = 30$ cm is then 2.3 cm, which is adequate for 1-cm-diameter beams.

CONCLUSIONS

The analysis presented is intended to help fill the general void in the literature of design and performance theory for the $E \times B$ type of mass separator. Although presented last, the discussion of the dispersion produced by a separator as a function of its basic parameters, field strengths, and length should be most useful to the designer. The focusing effect that $E \times B$ separators have on a beam is only important for strong separators, in which case the stigmatic configuration may be employed.

REFERENCES

1. L. Wahlin, Nucl. Instr. and Methods 27: 55, 1964.
2. R. G. Wilson and D. M. Jamba, Nucl. Instr. and Methods 85: 1, 1970.
3. See, for example, A. Galejs and P. H. Rose, Optics of electrostatic accelerator tubes, in Focusing of Charged Particles, Academic Press, New York, 1967; vol. II, p. 310.
4. H. A. Enge, Deflecting magnets, loc. cit., p. 211.

ABERRATION ANALYSIS OF ELECTROSTATIC SMALL ANGLE DEFLECTION

C. C. T. WANG

Micro-Bit Corp., Lexington, Mass.

Aberrations of electron beams resulting from deflection by electrostatic means are studied. The beam is treated as a collection of noninteracting, nonrelativistic, individual electrons. Chromatic aberration is ignored. The deflection fields are supported by pairs of electrodes and therefore can assume arbitrary distribution along the beam axis direction. To calculate beam aberration with reasonable accuracy in general cases, rather sophisticated and expensive computer programs are necessary to perform relaxation and ray tracings.

In this method, third-order approximation is used in the analysis. This is applicable to the cases where the deflection fields are spatially smooth, so that a truncated-series expansion about the axis provides sufficiently accurate descriptions of the fields. Deflection angles are restricted to a fraction of 1 rad. In the specific cases where the length of the deflectors are much greater than the spacing between the electrodes, the field distributions may be closely approximated by simple empirical functions. This procedure permits analytical and/or simple computer-aided calculation of aberration coefficients.

The natures of the aberrations are discussed in some detail and methods to minimize these aberrations are suggested. Electrostatic and magnetic deflections are compared from different viewpoints. It was found that, with electrostatic deflection, anastigmatic conditions cannot be achieved without external corrections.

Finally, the change in current density distribution within the spot due to deflection aberration is studied. Assumptions used here are consistent with those in the above analysis. Some specific cases are illustrated by computer plotting.

ABERRATION ANALYSIS OF ELECTROSTATIC SMALL ANGLE DIFFRACTION
C. G. T. VAN...
Microfilm Corp...
Calculations of electron beam aberrations from the deflection by electric
static means are studied. The beam is treated as a collection of noninter-
acting, nonrelativistic, individual first-order particles. Aberration is
ignored. The deflection fields are supported by pairs of electrodes and
therefore can assume arbitrary distribution along the beam axis direction.
To calculate beam aberration with reasonable accuracy in general cases,
rather sophisticated and expensive computer programs are necessary to per-
form relaxation and ray tracing. A computer program has been designed to per-
form this method. In this method, the electron beam is treated as a collection
of particles. In the case where the deflection fields are spatially
smooth, so that a truncated Fourier expansion of the axis provides an
adequately accurate description of the fields, the deflection angles are
restricted to a fraction of a wavelength. In cases where the length
of the deflector is much greater than the spacing between the electrodes,
the field distributions may be closely approximated by simple empirical
functions. This procedure permits analytical and/or simple computer-aided
calculation of aberration coefficients. The nature of the aberrations and methods
to minimize these aberrations are suggested. Electrostatic and magnetic
deflection are compared. The results are compared with those obtained
with electrostatic deflection, analytical conditions cannot be achieved
without external correction. For a range of deflection angles, θ ,
Finally, the change in current density distribution within the spot
due to deflection aberration is studied. Assumptions used here are con-
sistent with those in the above analysis. Some specific cases are illus-
trated by computer plotting.

DOUBLE-DEFLECTION ABERRATIONS IN A SCANNING ELECTRON MICROSCOPE

K. AMBOSS and E. D. WOLF

Hughes Research Laboratories, Malibu, Calif.

INTRODUCTION

The scanning electron microscope (SEM) is designed primarily as a diagnostic tool but has been recently found useful in the electron-beam fabrication of microelectronic devices. Large-area scan fields are required in this application to reduce the number of mechanical step-and-repeat operations necessary to cover the entire wafer. Deflection aberrations limit the area over which an electron beam of a given diameter can be scanned and consequently limit the area over which a circuit pattern can be exposed with a given minimum device size. Deflection aberrations have been discussed in detail for high-resolution cathode-ray tubes. Apparently this type of information is unavailable for the SEM except for some limited data by Chang and Stewart.¹ Deflection aberrations must be known accurately as a function of position within the deflection field to permit generation of appropriate dynamic corrections and hence the use of a larger scan field more suitable for circuit fabrication.

This paper describes an experimental study of these aberrations on a Stereoscan Mark IIa SEM (Cambridge Scientific Instruments, Cambridge, England). A qualitative analysis of the origin of the aberrations and of their relative magnitudes by a synthesis of the aberration figures by means of a digital computer is given.

II. MEASUREMENT OF THE ABERRATIONS

The electron optical design of the final demagnification stage in the SEM is a compromise that reflects the need to keep the working distance of the final lens short in order to minimize its spherical aberration, and at the same time permit scanning of a relative large area. Figure 1 shows schematically the arrangement that is generally adopted to overcome the difficulty of placing deflection coils between the lens and the specimen plane. Two sets of deflection coils are placed ahead of the lens. The first pair D_1 deflects the beam off axis; the second pair D_2 reverses the sense of the deflection and returns the beam to the axis at the center of the lens with a finite slope which it retains on passage through the lens. In the instrument studied, a stigmator is placed between the deflection coils to cancel out a static axial astigmatism of unknown origin.

Computer-controlled² electron-beam microrecordings were made in Kodak HRP emulsions and were examined at high magnification in an optical microscope as well as in the SEM. The computer-generated patterns consisted of a square matrix of discrete beam locations which was "sized" by means of the SEM magnification controls and the gain digital-to-analog converters to cover a square of 2 mm on a side. The computer program variables were point spacing, number of points per field, and exposure time per beam location. After exposure and development, the emulsion plate revealed the electron-beam density cross section of the aberrated beam spot as a function of position within the square scan field. The linearity of the scan field was also available from the position of the recorded microspots (i.e., deflection coil and/or deflection amplifier linearity, etc.).

The primary beam acceleration voltage was 10 kV and the beam current was about 5×10^{-10} A as measured in a Faraday cup. Two types of apertures were used: a conventional 600- μm -diam knife-edge final aperture and a specially fabricated 1-mm-diam annular aperture with a 60- μm -wide ring opening centered at a radius of 500 μm . A working distance of 10 mm was used exclusively throughout this study.

Care was taken in the experiments to minimize light exposure of the silver halide emulsion by the hot tungsten filament of the SEM. This effect was appreciable when the specimen was left in any one position too long; i.e., the electron exposed dot pattern was "lost" in the background caused by the diffracted light spot on the plate. SEM analysis of the deflection aberrations was possible because the secondary-electron yield from the silver deposits was high. However, the emulsion film soon deteriorated under intense electron beam bombardment; therefore, all analyses were performed at 1000 \times optical magnification with transmitted-light photography.

Figure 2 shows aberration patterns in the plane of best central focus which were observed when the SEM beam was scanned over a square of side 2 mm using the 600- μm -diam final aperture. This aperture size is larger than the 200 μm used in routine operation. Considerable simplification in the aberration pattern results from the use of an annular aperture since blocking out the central portion of the aperture reduces the aberration pattern to relatively simple Lissajous figures. The technique of using an annular stop to analyze aberrations has been described elsewhere.³⁻⁶

Figure 3 shows the aberration pattern which was obtained by replacing the 600- μm -diam final aperture with the 1-mm-diam annular stop. Similar patterns were obtained under slightly different focus conditions. Field distortions (scan-field linearity) cannot be measured accurately using the annular stop because there is substantial uncertainty in the location of the beam center in such large, irregularly shaped beam profiles. However, other experiments² suggest that field distortion at least for a 0.5 mm square field are less than about 0.1 μm .

Deflection hysteresis is another deflection defect which was measured in this particular instrument and was found to cause a relative positional error of 0.4 μm between two adjacent beam locations (on axis) when exposed using opposite directions of approach in a 2 mm square scan field (at 1 cm working distance). This error must be eliminated either by unidirectional addressing of field location or by redesign of the deflection coils.

III. ANALYSIS OF THE ABERRATIONS BY SYNTHESIS ON A DIGITAL COMPUTER

A theoretical treatment of the aberrations of systems with superimposed focusing and deflection could be based on the techniques developed by Sturrock⁷ for the analysis of the effect of asymmetries in magnetic electron lenses. Here only a qualitative assessment of the observed aberrations is given.

As Fig. 1 shows, the deflection scheme may be thought of producing an aberrated virtual object at a distance r'_0 from the axis for the final lens to image at a distance r_0 from the axis. Because the lens is highly demagnifying r'_0 is large and the aberrations associated with off-axis objects in round lenses must be large. To these must be added the aberrations of the double-deflection system and possibly also the off-axis aberrations produced by the stigmator which is located between the pairs of deflection coils.

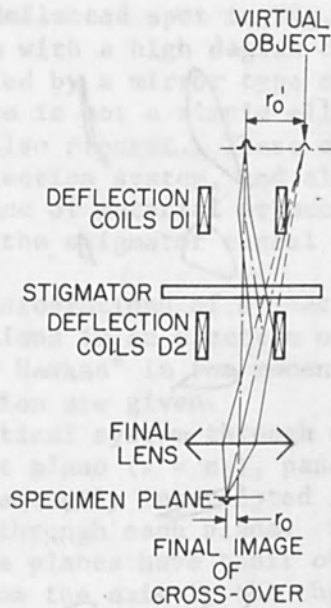


FIG. 1.--Schematic arrangement of final demagnification stage in scanning electron microscope.

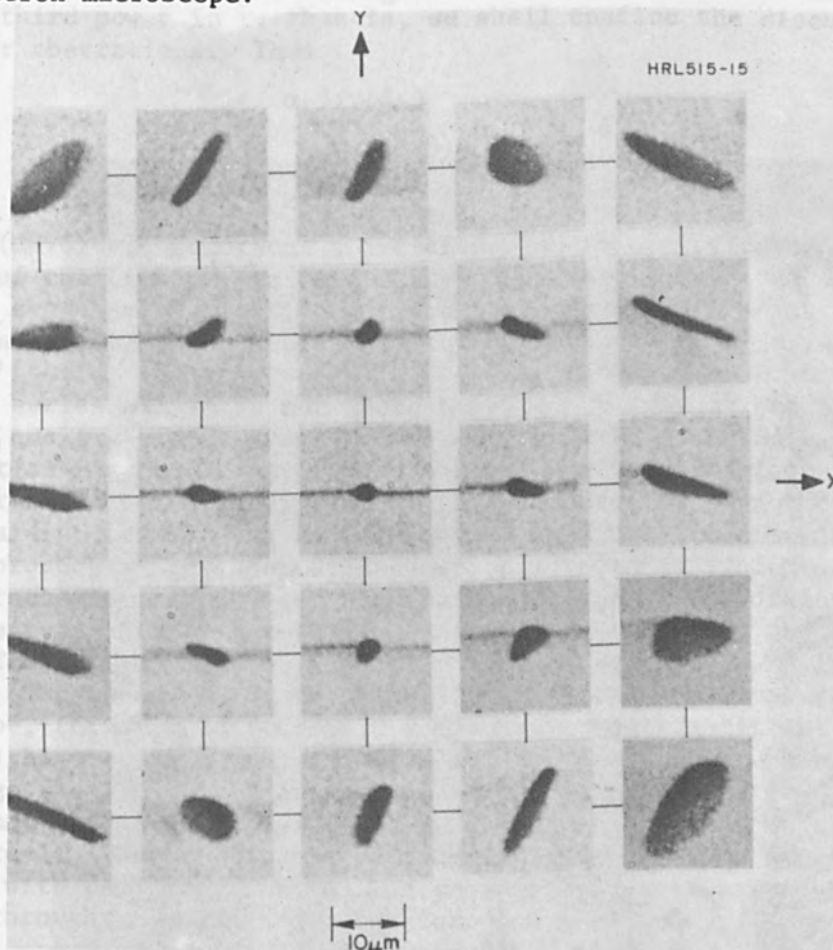


FIG. 2.--Deflection aberrations over a 2 x 2-mm scan field observed in plane of best central focus with 600- μ m aperture.

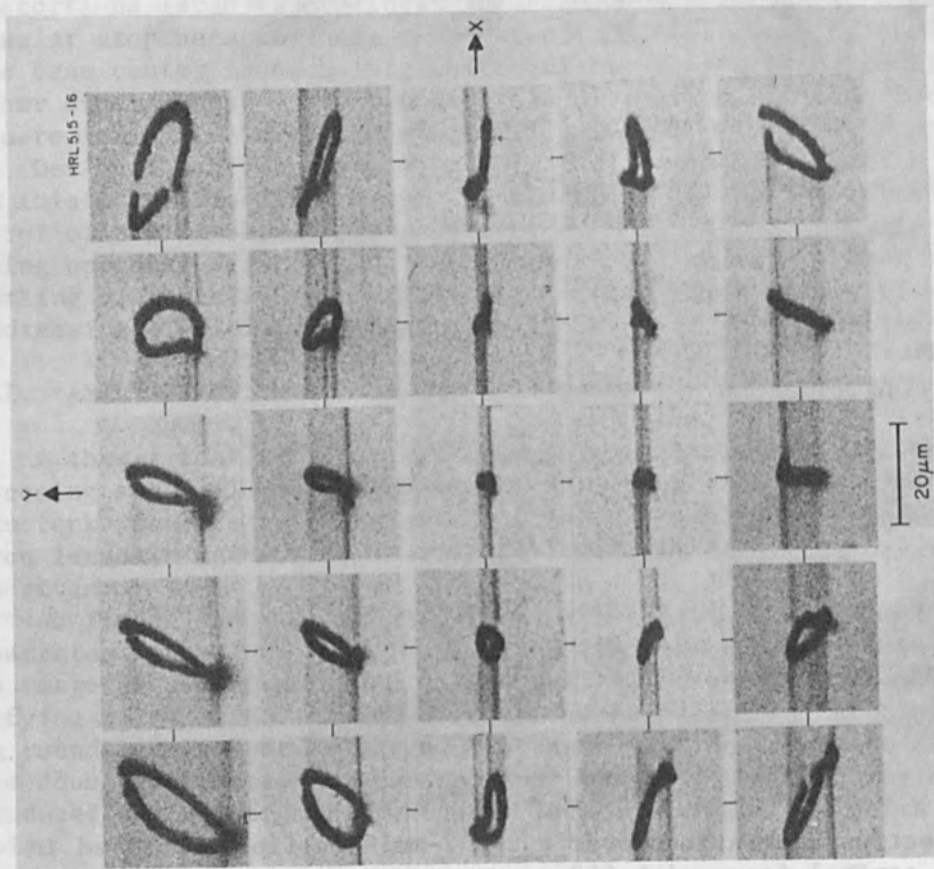


FIG. 3.--Deflection aberrations of Fig. 2 observed with 1000- μm annular aperture.

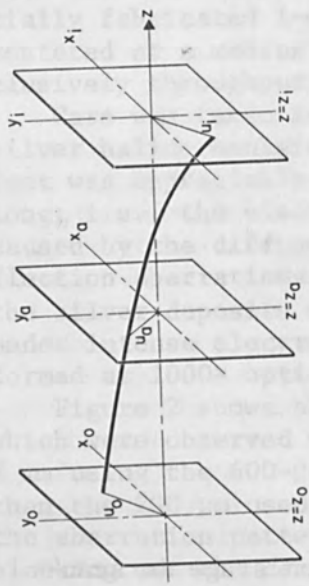


FIG. 4.--Ray diagram showing notation used in text.

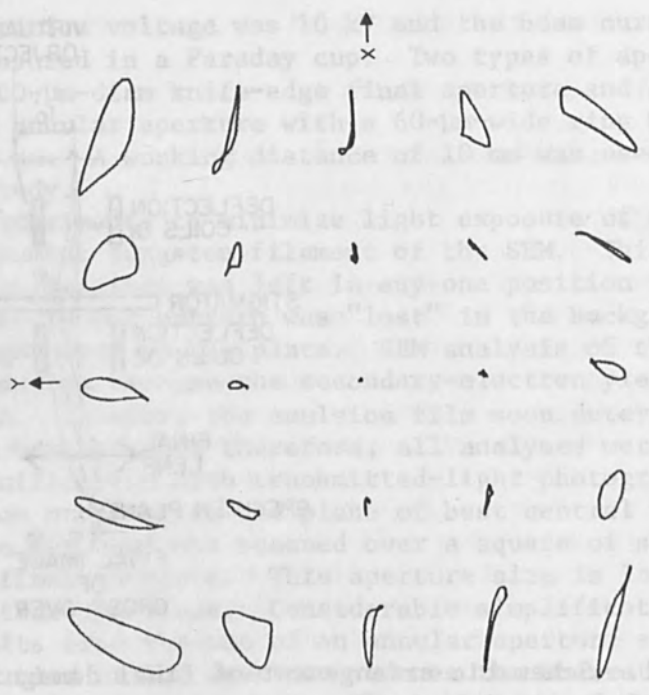


FIG. 5.--Synthesis of aberration pattern of Fig. 3 from terms listed in Eq. (5).

The elongation of the deflected spot in Fig. 3 shows the dominant aberration to be an astigmatism with a high degree of four-fold symmetry. The pattern is, however, modified by a mirror type of symmetry about the y axis. Also, each aberration figure is not a simple ellipse or circle and hence coma-like aberrations are also present. These aberrations are produced by the round lens, by the deflection system, and also by machining errors and misalignments. The existence of material or machining defects is evidenced by the necessity of having the stigmator cancel out fields of two-fold symmetry.

It is possible from considerations of symmetry to deduce the nature of the imagery and the aberrations in an electron optical system. The technique has been described by Hawkes⁸ in the recent literature and here only the results of its application are given.

Consider an electron optical system through which a ray passes (Fig. 4). The ray starts in the object plane ($z = z_0$), passes through the aperture plane ($z = z_a$), and is subsequently intercepted in the image plane ($z = z_i$). A ray axis passes normally through each plane. Sets of complex coordinates (u, \bar{u} where $u = re^{i\theta}$) in the planes have their origins on the axis. The displacements of the ray from the axis in the three planes are u_0, u_a, u_i . Let u_i be given by a function $F(u_0, \bar{u}_0, u_a, \bar{u}_a)$ and let us approximate this function by writing u_i as a power series in $u_0, \bar{u}_0, u_a, \bar{u}_a$. Since in electron optics the distances r_0 and r_a are small, we shall include only terms up to the third power in r ; that is, we shall confine the discussion to the third-order aberrations. Thus

$$u_i = \sum_{\alpha, \beta, \gamma, \delta \leq 0}^{(\alpha\beta\gamma\delta)} u_0^\alpha \bar{u}_0^\beta u_a^\gamma \bar{u}_a^\delta$$

where the $(\alpha\beta\gamma\delta)$ are numerical coefficients which can be calculated from a knowledge of the fields. In this study they are given values which are found by a systematic comparison of the patterns shown in Fig. 2 with the figures traced out by the series (1) for various values of u_0, \bar{u}_0 with r_a fixed.

In the series all terms not containing r_a are distortions that do not affect the quality of the image and hence cannot be measured by a study of the aberration figures. They fall outside the scope of this paper, although their importance in the generation of precise patterns cannot be neglected. Of the remaining terms those containing the aperture contribution in the form $u_a \bar{u}_a$ produce a displacement proportional to the r_a^2 which gives rise to the characteristic appearance of the coma figure. By working with an annular aperture this effect is eliminated. The remaining aberrations are listed in Table I, which also gives the type of symmetry associated with the terms. The terms marked rotationally symmetric can also arise in systems of two-, three-, and four-fold symmetry. The terms linear in u_a other than (0010) have a defocusing effect which is generally known as curvature of the image field. The relationship between various coefficients, if any exist, cannot be inferred from Table I. It can be shown that the defocusing terms are real. The aberrations of two-fold and four-fold symmetry can be associated with deflection as well as passage by an off axis pencil of electrons through an energized stigmator.

TABLE I.--Aperture-dependent aberrations and their associated symmetry.

Term	Name	Symmetry
(0010) u_a	Defocusing	Rotational
(0001) \bar{u}_a	Axial Astigmatism	2-Fold
(0020) u_a^2	Axial Coma	Mirror Symm.
(0002) \bar{u}_a^2	Axial Anticoma	3-Fold
(1010) $u_o u_a$	Defocusing	Mirror
(0110) $\bar{u}_o u_a$	Defocusing	Mirror
(1001) $u_o \bar{u}_a$	Astigmatism	Mirror
(0101) $\bar{u}_o \bar{u}_a$	Astigmatism	Mirror
(0030) u_a^3	Rosette	4-Fold
(0003) \bar{u}_a^3	Star	4-Fold
(0021) $u_a^2 \bar{u}_a$	Spherical Aberr.	Rotational
(0012) $u_a \bar{u}_a^2$	Astigmatism	2-Fold
(2001) $u_o^2 \bar{u}_a$	Astigmatism	Rotational
(0210) $\bar{u}_o^2 u_a$	Defocusing	2-Fold
(0120) $\bar{u}_o u_a^2$	Coma	Rotational
(1002) $u_o \bar{u}_a^2$	Anticoma	2-Fold
(2010) $u_o^2 u_a$	Defocusing	2-Fold
(0201) $\bar{u}_o^2 \bar{u}_a$	Astigmatism	2- 4-Fold
(1020) $u_o u_a^2$	Coma	2-Fold
(0102) $\bar{u}_o \bar{u}_a^2$	Anticoma	2- 4-Fold
(1110) $u_o \bar{u}_o u_a$	Defocusing	Rotational
(1101) $u_o \bar{u}_o \bar{u}_a$	Astigmatism	2-Fold

The deflection aberrations for simultaneous deflection in two perpendicular directions, neglecting distortion, are usually⁹ written in the form

$$\Delta x = (A_4 X_S^2 + B_5 Y_S^2) x_a + (A_6 + B_6) X_S Y_S y_a + A_7 X_S x_a^2 + A_8 X_S y_a^2 + 2B_8 Y_S x_a y_a \quad (2a)$$

and

$$\Delta y = (B_4 Y_S^2 + A_5 X_S^2) y_a + (A_6 + B_6) X_S Y_S x_a + B_7 Y_S y_a^2 + B_8 Y_S x_a^2 + 2A_8 X_S x_a y_a \quad (2b)$$

where X_S and Y_S are deflections in two perpendicular directions and x_a , y_a are the coordinates of an electron in the aperture.

By writing these quantities in complex form

$$\left. \begin{aligned} X_S + iY_S &= u_0 = r_0 e^{i\theta_0} \\ X_S - iY_S &= \bar{u}_0 = r_0 e^{-i\theta_0} \\ x_a + iy_a &= u_a = r_a e^{i\theta_a} \\ x_a - iy_a &= \bar{u}_a = r_a e^{-i\theta_a} \end{aligned} \right\} \quad (3)$$

Eqs. (2) can be cast into the form of Table I to give

$$\begin{aligned}
 \Delta u_i &= 2[(A_4 - A_5) - (B_4 - B_5)]u_0\bar{u}_0\bar{u}_a \\
 &+ [(A_4 - A_5) + (B_4 - B_5) + (A_6 + B_6)]u_0^2\bar{u}_a \\
 &+ [(A_4 - A_5) + (B_4 - B_5) - (A_6 + B_6)]\bar{u}_0^2\bar{u}_a \\
 &+ 2[(A_4 + A_5) + (B_4 + B_5)]u_0\bar{u}_0u_a \\
 &+ [(A_4 + A_5) - (B_4 + B_5)]u_0^2u_a \\
 &+ [(A_4 + A_5) - (B_4 + B_5)]\bar{u}_0^2u_a \\
 &+ [(A_7 - B_7)]u_0u_a^2 \\
 &+ [(A_7 - B_7) - 2(A_8 - B_8)]u_0\bar{u}_a^2 \\
 &+ [A_8 + B_8]\bar{u}_0u_a^2 \\
 &+ [A_8 + B_8]\bar{u}_0\bar{u}_a^2 \\
 &= (1101)u_0\bar{u}_0\bar{u}_a + (2001)u_0^2\bar{u}_a + (0201)\bar{u}_0^2\bar{u}_a \\
 &+ (1110)u_0\bar{u}_0u_a + (2010)u_0^2u_a + (0210)\bar{u}_0^2u_a \\
 &+ (1020)u_0u_a^2 + (1002)u_0\bar{u}_a^2 + (0120)\bar{u}_0u_a^2 \\
 &+ (0102)\bar{u}_0\bar{u}_a^2
 \end{aligned} \tag{4}$$

A relationship between some of the coefficients in Table I is now apparent. It is also seen that terms generally associated with rotational symmetry are present.

The result of modeling the aberrations is shown in Fig. 5 and can be compared with Fig. 3. The figure is composed of coefficients

$$\begin{aligned}
 &(0010)u_a \\
 &(0002)\bar{u}_a^2 \\
 &(1010)u_0u_a \\
 &(0110)\bar{u}_0u_a \\
 &(1001)u_0\bar{u}_a \\
 &(0101)\bar{u}_0\bar{u}_a \\
 &(2001)u_0^2\bar{u}_a \\
 &(0210)\bar{u}_0^2u_a \\
 &(0120)\bar{u}_0u_a^2 \\
 &(1002)u_0\bar{u}_a^2 \\
 &(2010)u_0^2u_a \\
 &(0201)\bar{u}_0^2\bar{u}_a \\
 &(0102)\bar{u}_0\bar{u}_a^2 \\
 &(1110)u_0\bar{u}_0u_a \\
 &(1101)u_0\bar{u}_0\bar{u}_a
 \end{aligned} \tag{5}$$

in varying ratios. The synthesis was halted after the main features of the observed pattern had been reproduced. The astigmatism term (2001) in this list is composed of a contribution from Eq. (4) where it appears in

a relationship with (0201) and an independent contribution from the anisotropic astigmatism of the round lens.

The contribution to the aberration figures of the various coefficients is demonstrated in Figs. 6 through 8 by a successive elimination of the various terms. Elimination of the coma-type terms gives the aberration pattern shown in Fig. 6. Elimination of the astigmatism associated with the lens, the term (2001), produces the pattern shown in Fig. 7. Elimination of the defocusing associated with the terms of mirror symmetry (1010) and (0110) and of the mirror type astigmatisms (1001) and (0101) gives Fig. 8 which shows the remaining astigmatism produced by a set of not quite identical x and y deflection coils.

A reduction in the size of the annular stop from 1000 μm to 200 μm changes the pattern of Fig. 5 into that shown in Fig. 9. The contribution of the coma-like terms has all but disappeared, although a considerable degree of astigmatism remains. A 200- μm aperture produces reasonable exposure times for submicron configurations when used in a computer-controlled pattern generating SEM.² Because the astigmatism decreases linearly with aperture radius, a stop of impractical proportions would be required to reduce the astigmatism to satisfactory proportions. Dynamic focus and astigmatism correction are therefore required.

SUMMARY

The origin of the deflection aberrations in a scanning electron microscope has been investigated. The study shows that both the final lens and deflection coils combine to produce an unacceptably large amount of astigmatism within a scan field 2 mm square, when submicron pattern elements are required. The coma-like aberrations are of manageable proportion. The astigmatism cannot be reduced to a satisfactory level solely by a reduction in aperture size without incurring unacceptably long exposure times; dynamic control of astigmatism and curvature of field have to be used. Some attempt has been made to evaluate the distortion the system produces. It appears that there are field distortions but their magnitude is small compared with the deflection aberrations.

An anomalous astigmatism and defocusing has been observed. Its origin is not known although the defect can theoretically be produced by a tilt of the specimen plane or transverse misalignment of the coils or defining aperture with respect to the lens axis.

The location of the stigmator between the deflection coils can produce off-axis aberrations. No experiments to separate the effect it produces from those of the deflection coils have been carried out.

Deflection hysteresis is another deflection defect which in this particular instrument caused a total relative positional error of 0.4 μm between two adjacent elements when exposed using opposite direction of approach in a 2 mm square scan field (at 1 cm working distance). This error is too large for submicron device fabrication and must be eliminated either by unidirectional addressing of field locations or by redesign of the deflection coils.

REFERENCES

1. T. H. P. Chang and A. D. C. Stewart, Rec. 10th Symp. Electron, Ion, and Laser Beam Technology, San Francisco Press, 1969; p. 97.
2. F. S. Ozdemir, E. D. Wolf, and C. R. Buckley, Rec. 11th Symp. Electron, Ion, and Laser Beam Technology, San Francisco Press, 1971.

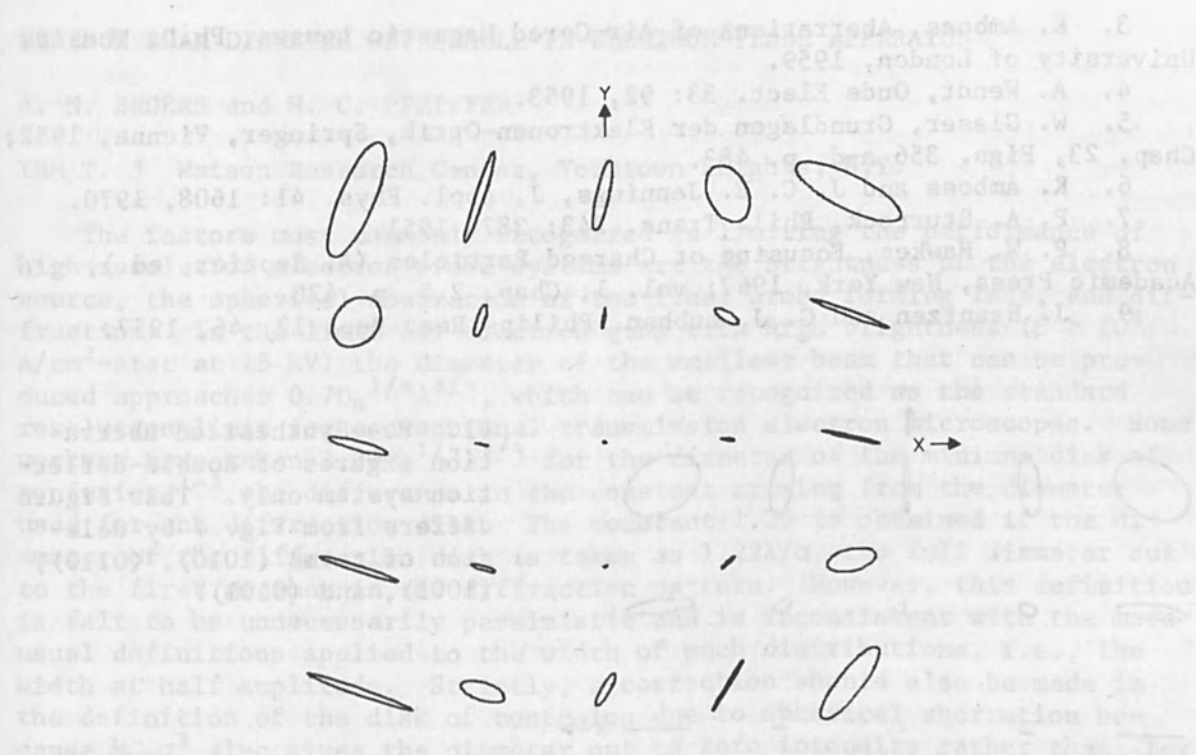


FIG. 6.--Synthesis of aberration pattern without contribution of coma-like terms (0002), (0120), (1002), and (0102).

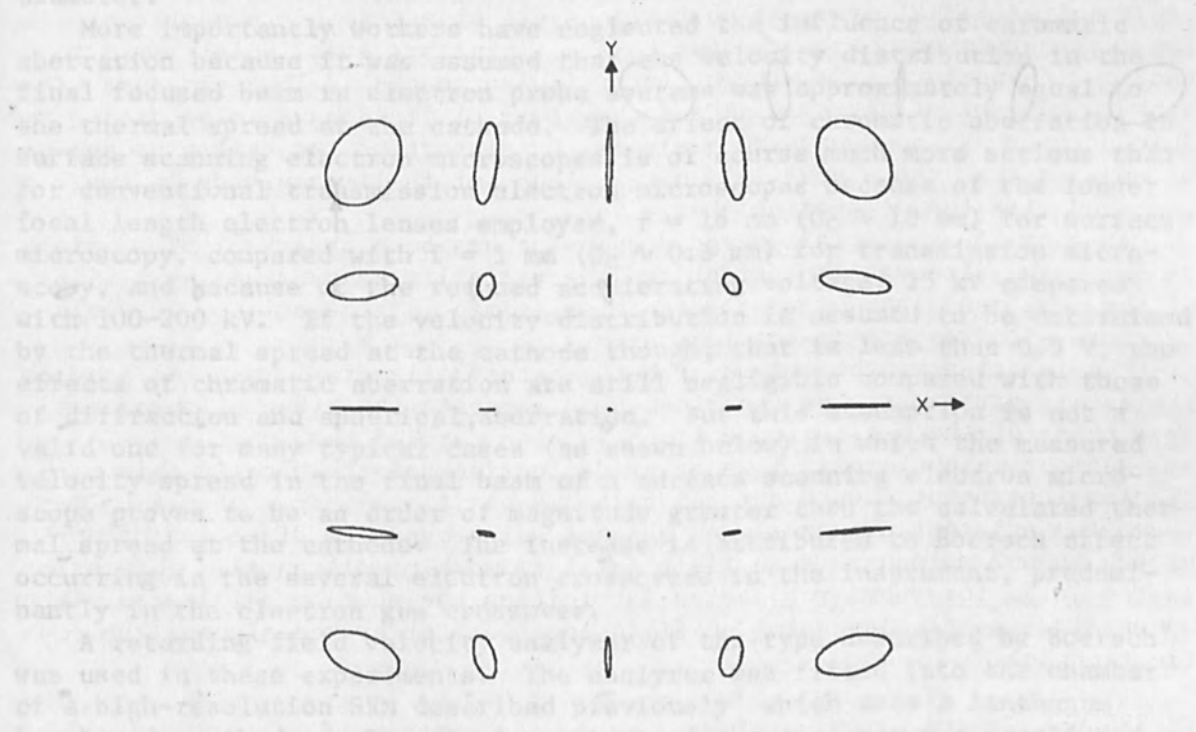


FIG. 7.--Synthesized aberration figures after deletion of anisotropic astigmatism contribution (0201) of round lens and of coma contribution.

3. K. Amboss, Aberrations of Air-Cored Magnetic Lenses, Ph.D. Thesis, University of London, 1959.
4. A. Wendt, *Onde Elect.* 33: 92, 1953.
5. W. Glaser, *Grundlagen der Elektronen-Optik*, Springer, Vienna, 1952; Chap. 23, Figs. 356 a-d, p. 483.
6. K. Amboss and J. C. E. Jennings, *J. Appl. Phys.* 41: 1608, 1970.
7. P. A. Sturrock, *Phil. Trans.* 243: 387, 1951.
8. P. W. Hawkes, *Focusing of Charged Particles* (A. Septier, ed.), Academic Press, New York, 1967; vol. 1, Chap. 2.5, p. 420.
9. J. Haantzen and G. J. Lubben, *Philips Res. Rep.* 12: 46, 1957.

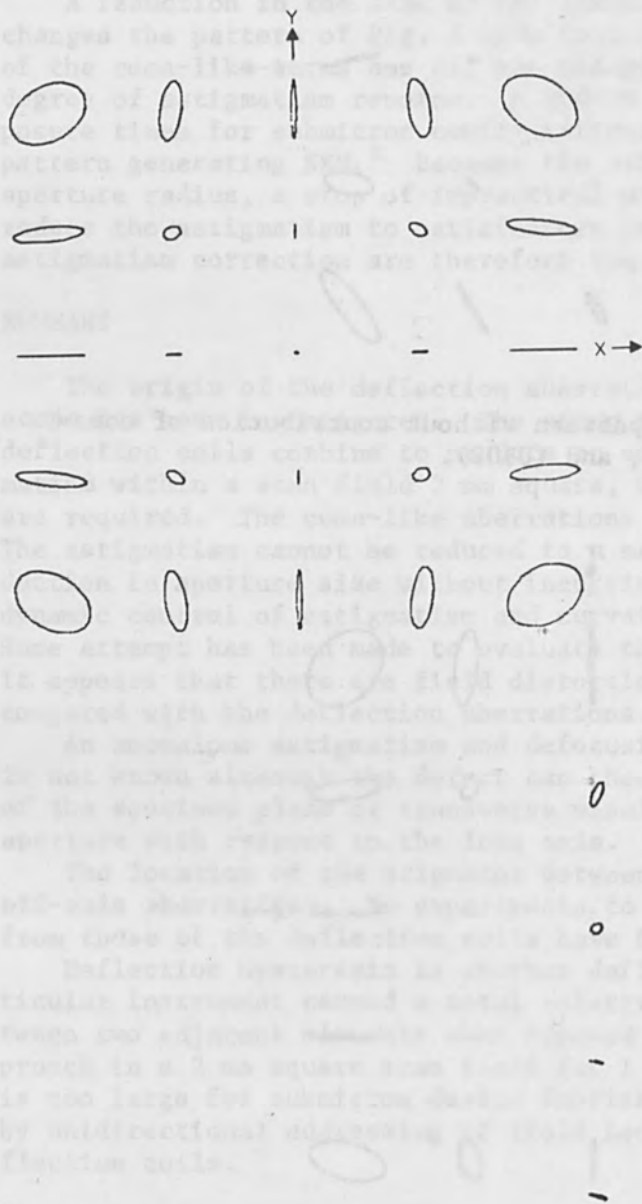


FIG. 8.--Synthesized aberration figures of double-deflection system only. This figure differs from Fig. 7 by deletion of terms (1010), (0110), (1001), and (0101).

FIG. 9.--Aberration pattern with same coefficients as in Fig. 5 but with aperture radii reduced by a factor of 5.

MINIMUM BEAM DIAMETER OBTAINABLE IN ELECTRON-PROBE APPARATUS

A. N. BROERS and H. C. PFEIFFER

IBM T. J. Watson Research Center, Yorktown Heights, N.Y.

The factors most commonly recognized as limiting the performance of high-resolution electron probe systems are the brightness of the electron source, the spherical aberration of the final probe forming lens, and diffraction. In the limit for electron guns with high brightness ($\beta > 10^6$ A/cm²-ster at 15 kV) the diameter of the smallest beam that can be produced approaches $0.7C_S^{1/4}\lambda^{3/4}$, which can be recognized as the standard resolution limit for conventional transmission electron microscopes. Some workers have taken $1.29C_S^{1/4}\lambda^{3/4}$ for the diameter of the minimum disk of confusion,¹⁻³ the difference in the constant arising from the diameter used for the diffraction disk. The constant 1.29 is obtained if the diameter of the diffraction disk is taken as $1.22\lambda/\alpha$, the full diameter out to the first minimum in the diffraction pattern. However, this definition is felt to be unnecessarily pessimistic and is inconsistent with the more usual definitions applied to the width of such distributions, i.e., the width at half amplitude. Strictly, a correction should also be made in the definition of the disk of confusion due to spherical aberration because $\frac{1}{2}C_S\alpha^3$ also gives the diameter out to zero intensity rather than, for example, out to half intensity. The result of this correction, however, is relatively unimportant because it is equivalent to a change in C_S , and C_S is raised to the 1/4 power in the expression for the minimum beam diameter.

More importantly workers have neglected the influence of chromatic aberration because it was assumed that the velocity distribution in the final focused beam in electron probe systems was approximately equal to the thermal spread at the cathode. The effect of chromatic aberration in surface scanning electron microscopes is of course much more serious than for conventional transmission electron microscopes because of the longer focal length electron lenses employed, $f = 16$ mm ($C_C \sim 10$ mm) for surface microscopy, compared with $f = 1$ mm ($C_C \sim 0.6$ mm) for transmission microscopy, and because of the reduced accelerating voltage, 25 kV compared with 100-200 kV. If the velocity distribution is assumed to be determined by the thermal spread at the cathode though, that is less than 0.5 V, the effects of chromatic aberration are still negligible compared with those of diffraction and spherical aberration. But this assumption is not a valid one for many typical cases (as shown below) in which the measured velocity spread in the final beam of a surface scanning electron microscope proves to be an order of magnitude greater than the calculated thermal spread at the cathode. The increase is attributed to Boersch effect occurring in the several electron crossovers in the instrument, predominantly in the electron gun crossover.

A retarding-field velocity analyzer of the type described by Boersch⁴ was used in these experiments. The analyzer was fitted into the chamber of a high-resolution SEM described previously³ which uses a lanthanum hexaboride cathode.⁵ The final aperture of the analyzer was prealigned with respect to the electron beam by using the instrument in the scanning microscopy mode, and the first electrode, which contained a 100- μ m aperture, was laterally positioned with micrometers from outside the vacuum chamber. The resolution of the analyzer was checked by verifying that

the measured value was close to the thermal spread at the cathode when the electron gun was operated at relatively low brightness (about 10^3 A/cm²-ster) and with a small crossover. H. C. Pfeiffer has shown that the velocity spread ΔE is proportional to βr_0 , where β is the electron brightness and r_0 is the radius of the beam crossover. A velocity spread of 0.38 V was measured with the LaB₆ rod cathode⁵ operating with 5.0 A in the heater coil and no electron bombardment, and with the autobias adjusted so that the total current from the cathode was 3.5 μ A.

The radius of the tips of the particular cathodes used varied between 10 and 20 μ m. This is typical for LaB₆ cathodes made from sintered material where no particular attention has been paid to cathode tip preparation. Sharper cathodes produce smaller crossovers, reducing the velocity distribution, as mentioned above, and higher maximum brightness because the higher field at the cathode surface is more effective in suppressing space-charge divergence of the beam as it leaves the cathode. The measured brightness of one of the cathodes with a tip 12 μ m in radius was 9×10^5 A/cm²-ster at 13.6 kV with 5.3 A in the heater coil and 10 W of electron bombardment power. At approximately this brightness and with 400 μ A of total gun current the velocity spread in the final beam was measured to be between 3 and 5 V, depending on the particular cathode used. If the total gun current and therefore the crossover diameter was reduced in the electron gun the velocity spread was reduced, e.g., for 100 μ A total current ΔE was between 1.8 and 2.5 V, but because the cathodes were relatively blunt the brightness was reduced under these conditions. With a velocity spread of 3 V the diameter of the disk of confusion due to the chromatic aberration of the final lens is 40 \AA at 30 kV. This is to be compared with a value for $C_s^{1/4} \lambda^{3/4}$ of about 20 \AA . Under these typical operating conditions, therefore, chromatic aberration, rather than spherical aberration and diffraction, limits the performance of the instrument. When a crossover limiting aperture 20 μ m in diameter was placed in the plane of the gun anode with the 12- μ m radius tip cathode, a velocity spread of 2.9 V was measured, compared with 3.1 V without the aperture for the same operating conditions. The similarity in the two values for ΔE indicates, as expected, that the gun crossover was not significantly larger than 20 μ m and that the aperture was not reducing the effective size of the crossover by an appreciable amount. With tungsten hairpin cathodes, where the crossover is larger, such an aperture can reduce the velocity spread increase considerably. Most SEMs are operated with tungsten hairpin cathodes, and with these cathodes ΔE is higher for given brightness than for the pointed LaB₆ cathodes because, to obtain optimum brightness hairpin cathodes have to be well immersed in the gun accelerating field in order to concentrate the field at the cathode surface and prevent space-charge divergence of the beam, which means using larger total beam currents (i.e., above 200 μ A) and larger crossovers; ΔE can be as high as 5 V at a brightness of 10^5 A/cm²-ster (15 kV). Such a chromatic spread produces a disk of confusion with a diameter of 50-60 \AA , once again showing that chromatic aberration is the dominant aberration limiting the minimum beam diameter even for this relatively low brightness where the probe diameter is larger.

The degree of Boersch effect occurring in the electron beam subsequent to the gun crossover was estimated by measuring the spread in the final beam over a range of three orders of magnitude in final beam current, that is from 10^{-12} to 10^{-9} A. The gun operating conditions were held constant and the beam current altered by adjusting the strength of the condenser lenses. The velocity spread in the final beam varied from 2.1 V for a

final beam current of 10^{-12} A to 2.4 V at 10^{-9} A. This change is insignificant compared with the over-all velocity spread, indicating that Boersch effect in the beam subsequent to the gun crossover is not important.

We conclude that under many operating conditions where high brightness is needed, the velocity spread produced by Boersch effect in the crossover of standard triode-type electron microscope guns is so large that chromatic aberration, rather than spherical aberration and diffraction, limits the minimum beam diameter produced in a surface scanning electron microscope. The velocity spread is reduced if a pointed LaB_6 cathode is used rather than a tungsten hairpin cathode, but results with an LaB_6 cathode with a tip radius of $12 \mu\text{m}$ show that chromatic aberration is still the dominant aberration. Sharper cathodes will produce higher brightness and lower velocity spread.

The diameter of the disk of confusion due to diffraction has been taken by some workers to be larger than is consistent with the definitions for the over-all beam diameter. Such an error can lead to the use of final lens apertures larger than optimum.

REFERENCES

1. K. C. A. Smith, Ph.D. Dissertation, Cambridge University, 1959.
2. C. W. Oatley, W. C. Nixon, and R. F. W. Pease, *Advan. Electronics and Electron Phys.* 21: 181, 1965.
3. A. N. Broers, *Rev. Sci. Instr.* 40: 1040, 1969.
4. H. Boersch, *Z. Phys.* 139: 115, 1954.
5. A. N. Broers, *J. Sci. Instr. (J. Phys. E)* 2: 273, 1969.

The electron gun was designed to operate at a voltage of 15 kV and a current of 100 mA. The gun consists of a cathode, a grid, and an anode. The cathode is a tungsten filament which is heated to a temperature of 2500°C. The grid is a cylindrical mesh which is placed at a distance of 1 cm from the cathode. The anode is a cylindrical rod which is placed at a distance of 2 cm from the grid. The gun is operated at a voltage of 15 kV and a current of 100 mA. The electron beam is focused by a series of lenses. The first lens is a spherical lens which is placed at a distance of 10 cm from the anode. The second lens is a cylindrical lens which is placed at a distance of 20 cm from the first lens. The third lens is a spherical lens which is placed at a distance of 30 cm from the second lens. The electron beam is focused to a spot diameter of 10 μm at a distance of 100 cm from the gun. The electron beam is used for the study of the photoelectric effect. The photoelectric effect is the emission of electrons from a metal surface when it is illuminated by light of a frequency greater than a certain value. The photoelectric effect is studied by measuring the current of electrons emitted from a metal surface as a function of the frequency of the incident light. The photoelectric effect is one of the most important phenomena in quantum mechanics. It is the only phenomenon which cannot be explained by classical physics. The photoelectric effect is explained by the quantum theory of light. According to the quantum theory of light, light consists of particles called photons. Each photon has a certain amount of energy which is proportional to its frequency. When a photon strikes a metal surface, it can transfer its energy to an electron in the metal. If the energy of the photon is greater than the work function of the metal, the electron will be emitted from the metal surface. The work function is the minimum energy which is required to remove an electron from the metal surface. The photoelectric effect is studied by measuring the current of electrons emitted from a metal surface as a function of the frequency of the incident light. The photoelectric effect is one of the most important phenomena in quantum mechanics. It is the only phenomenon which cannot be explained by classical physics. The photoelectric effect is explained by the quantum theory of light. According to the quantum theory of light, light consists of particles called photons. Each photon has a certain amount of energy which is proportional to its frequency. When a photon strikes a metal surface, it can transfer its energy to an electron in the metal. If the energy of the photon is greater than the work function of the metal, the electron will be emitted from the metal surface. The work function is the minimum energy which is required to remove an electron from the metal surface. The photoelectric effect is studied by measuring the current of electrons emitted from a metal surface as a function of the frequency of the incident light.

A COMPUTER ANALYSIS OF THE SPHERICAL ABERRATION OF THREE ELECTROSTATIC IMMERSION LENSES

D. L. FRASER, Jr., W. J. MEYERS, and T. G. ELSER

Department of Defense, Fort Meade, Md.

This paper contains a theoretical computer analysis of three electrostatic, axially symmetric immersion lenses. The focal properties of a flat-plate lens, a Crewe lens, and a hyperbolic lens are calculated. The focal properties of the flat-plate lens are shown to agree with published experimental and theoretical values. Further, the spherical aberration for finite object distances of three lenses is presented as a function of the lens configuration and object distance. The immersion lens designed by Butler for the Crewe gun is found to have the lowest spherical aberration coefficient of the three under the restrictions noted.

INTRODUCTION

A computer analysis of electrostatic immersion lenses was undertaken to aid in the design of a high-resolution electron beam that utilizes a field-emission source. The primary aim of this analysis was to investigate the possibility of reducing the aberrations of the lens by shaping the lens plates. Of all third-order aberrations that can cause a lens of this type to distort an image, only spherical aberration is possible for a point source located on the optical axis. Special emphasis was placed on the shape designed by Butler¹ for the Crewe gun² because of its use with a field emission source to obtain a 100-Å-diam electron beam. The following is an attempt to investigate the general properties of the spherical-aberration coefficient for several finite object distances as a function of the lens-plate separation and hole diameter.

LENS CONFIGURATION

The three lenses discussed in this paper are shown in Fig. 1. The flat-plate lens is used as a standard to evaluate the performance of the Crewe and hyperbolic lenses. We define for the three lenses the plate separation A , the plate hole diameter D , and the object and image distances P and Q , respectively. Further, because the principal focal planes are not at the center of the lens for this type of lens, it is necessary to use the thick-lens equation³ to determine the image and object points correctly.

The first shaped lens to be considered is the aforementioned Crewe lens shown in Fig. 1(b).^{2,4} Butler, who did the original calculations for this lens, found that spherical aberration could be significantly reduced by forcing the axial potential distribution to be a simple cubic polynomial. The exact shape that was used in this analysis was determined by a curve fitting program and can be expressed by

$$r(z) = 2.05964z - 0.12164z^2 + 0.01418z^3 \quad (1)$$

Note that this shape is rotationally symmetric as well as being symmetric about the geometric center of the lens.

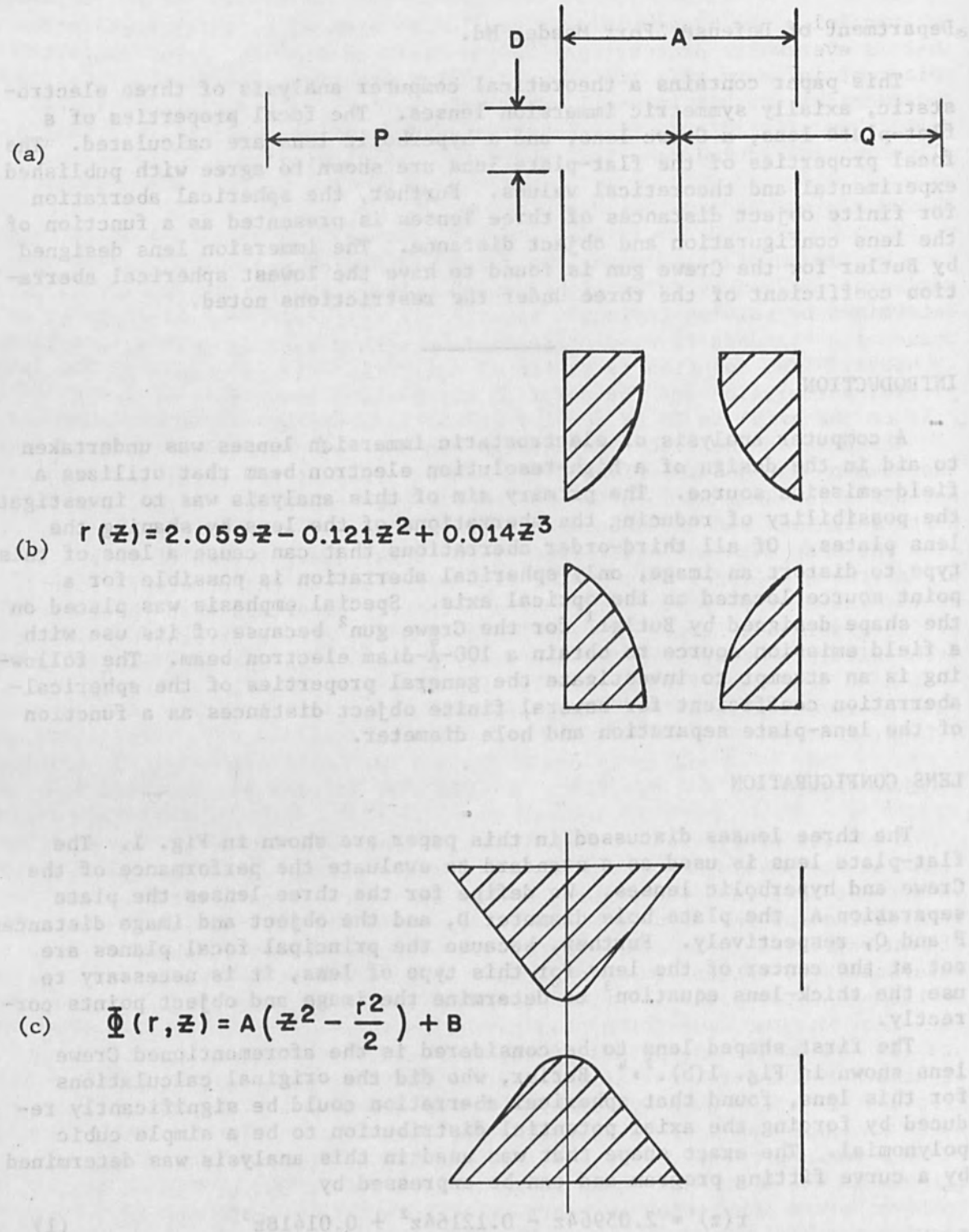


FIG. 1.--Flat-plate, Crewe, and hyperbolic lens shapes.

The second shaped lens to be considered (Fig. 1c) is an adaptation of Rüdénberg's symmetrical hyperbolic einzel lens.⁵ The potential distribution for such a lens is of the form

$$\phi(r,z) = A[z^2 - (r^2/2)] + B \quad (2)$$

In principle, the hyperboloid of revolution creates a radial field E_r that is everywhere proportional to the distance from the axis. For an object at infinity this field would reduce spherical aberration to zero and therefore result in small spherical aberrations for finite objects. Using this principle Septier constructed and tested three einzel lenses all of which reduced spherical aberration by varying amounts.⁶

METHOD AND ACCURACY OF THE CALCULATIONS

The method of calculating the focal properties and the spherical aberration of the lenses is straightforward. The potential distributions are determined by solving Laplace's equation in cylindrical coordinates by means of a standard five point relaxation method such as that described by Weber.⁷ The solution is continued until the voltage change from the preceding iteration (at the point at which the voltage is varying the most on the grid) is 10 μ V for 1 V on the lens plate.

The path of the electrons through the lens was calculated by using the Hamming method⁸ solution of the second order differential equation of motion.⁹ The Hamming solution was chosen over the Euler, Milne, and Runge-Kutta solutions because it combines the smallest per step truncation error with the best solution stability. This latter quantity, which is a measure of the difference between the true solution and the numerical solution as the integration proceeds, becomes extremely important when the range of integration is large. A detailed discussion of the errors that result from calculations of both the potential and electron has been published.¹⁰ It can be concluded from the evaluation of these errors that the lens parameters calculated from the paraxial rays are accurate to at least 0.5 per cent.

FOCAL PROPERTIES

The focal properties of each lens were determined from the path of a paraxial ray passing from left to right and a path of a second ray passing from right to left. The principal plane position is calculated by the intersection of the incoming paraxial ray with the extrapolated exit path of the ray. The four focal lengths are then measured from where the ray intersects the optical axis to either the geometrical center of the lens or the principal plane locations as shown in Fig. 2. It is important to note that the two restrictions on this four-focal-length representation are (1) that the focal points of the lens must lie outside the region of significant potential variation³ and (2) that the principal planes are crossed. As was proven by El-Kareh,¹¹ for all weak electrostatic lenses the principal planes are always crossed.

The focal properties (f_0 , f_i , F_0 , and F_i) of the flat-plate lens were calculated for a voltage ratio range of from 1.5 to 30 for lenses with a ratio of plate separation to aperture diameter A/D from 0.5 to 10.0. The results for $A/D = 3$ are shown in Fig. 2(b) and are representative of the results for other values. Note that the image changes from virtual to real at a voltage ratio of about 6.

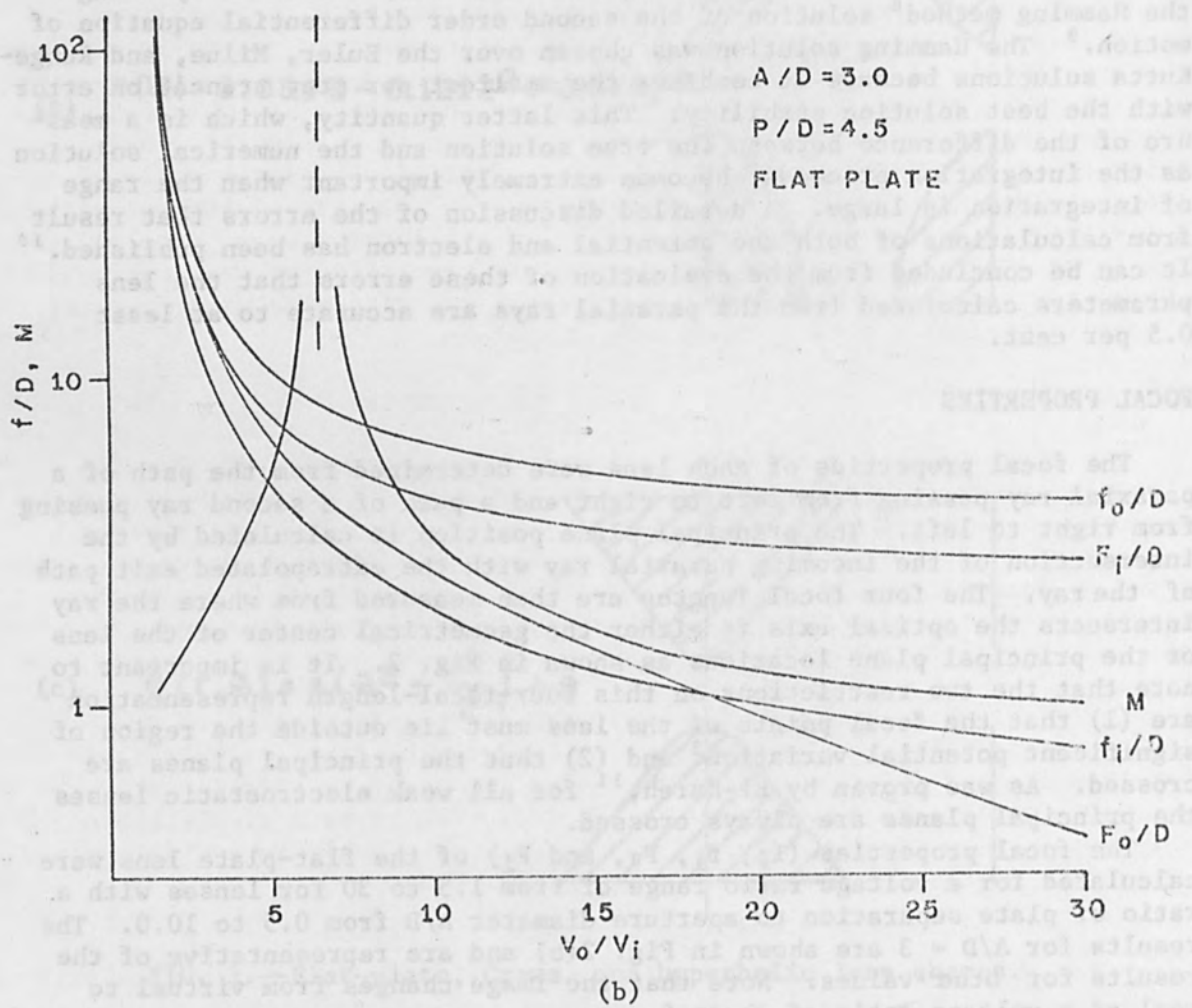
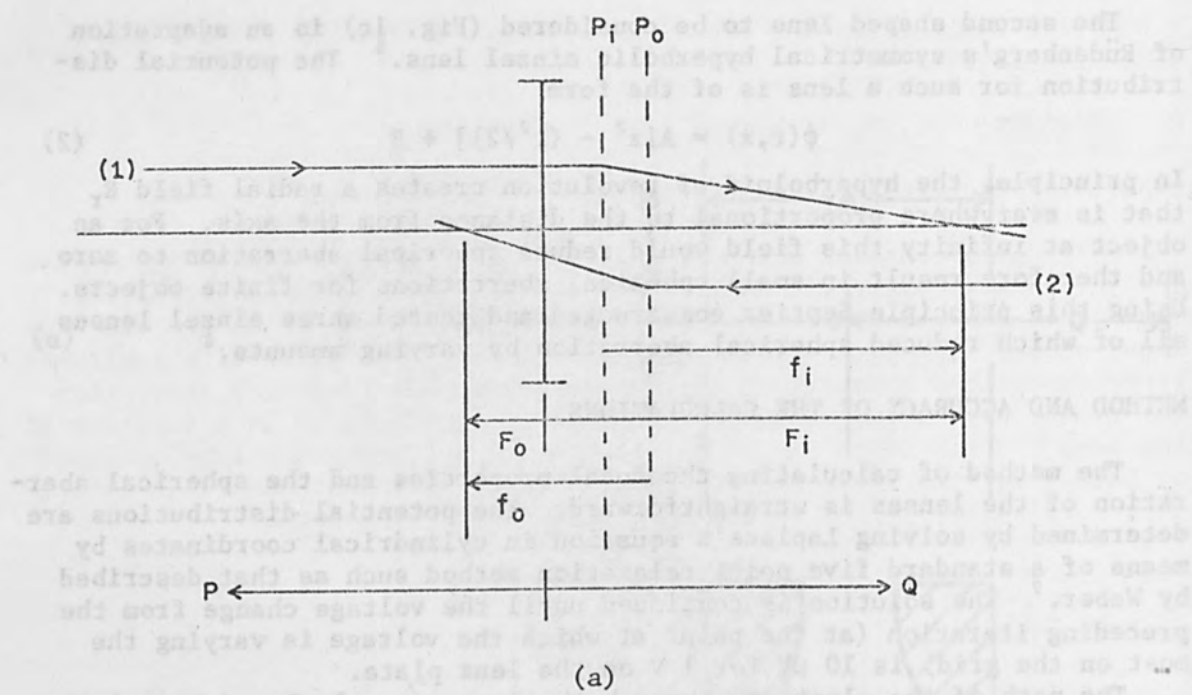


FIG. 2.--(a) Focal property definitions; (b) typical flat-plate focal properties.

Comparing our results with the calculated values of Read¹² and the experimental values of Spangenberg,³ it appears that our calculations are in general higher than Spangenberg's and lower than Read's. Specifically, for $A/D = 3$ and at a voltage ratio of 6, our focal parameters are 3 to 4 per cent closer to Spangenberg's values than are Read's values. This comparison is necessarily vague because the exact location of both principal planes is very critical. As was pointed out by Read,¹² the data presented by Spangenberg for $A/D = 1$ shows that the principal planes are not crossed. This fact is inconsistent with a theoretical analysis of weak electrostatic lenses, and therefore the absolute values of these focal lengths are suspect. Our own preliminary experimental results indicate that our measured values are within 5 per cent of our calculated results.

SPHERICAL ABERRATION

The spherical aberration coefficient C_{S0} referred back to the object side was calculated with the object at a finite distance from the center of the lens. Our specific application requires that the electron optics system be capable of addressing a large number of locations in a rapid, random manner. This restriction means that the beam energy must be kept as low as possible, resulting in the use of the immersion lens primarily in the decelerating mode. Therefore, the calculations for the lens properties were made with the highest voltage on the object side of the lens. It is important to note that C_{S0} for an immersion lens in the decelerating mode is larger than that of the accelerating mode, but the relationship between C_{S0} and its physical configuration is identical.¹²

The value of C_{S0} is calculated by passing rays through the lens at various departure angles α_0 from the source and then measuring the disk formed at the image plane. Specifically, the first ray with a departure angle of 0.1 mrad is used to define the gaussian image plane by the intersection of this ray with the optical axis. Then rays leaving the source at angles of from 1 to 50 mrad are calculated with the radius of the disk formed at the gaussian image plane denoted by Δr (Fig. 3a). The spherical aberration coefficient is then calculated from

$$\Delta r = MC_{S0}\alpha_0^3 \quad (3)$$

where $M = -f_0/(P - F_0)$ is the linear magnification. The variance of the calculated values of C_{S0} with the object divergence angle is shown in Fig. 3(b). The small variation in C_{S0} as a function of α_0 is an indication of the accuracy of the potential calculation, the accuracy of the ray trace solution, and the justification for the assumption that only the axial potential is needed for small excursions of the electrons from the axis.

The effect on C_{S0} of changing P/D , the object distance normalized with respect to the hole diameter for a fixed lens configuration, is shown in Fig. 4(a). Note that C_{S0}/D increases with increasing P/D . If one fixes the object distance and increases the plate separation for a fixed hole diameter, then the spherical aberration should decrease. This trend is shown in Fig. 4(b) for a flat-plate lens at four voltage ratios. It is clear that C_{S0} decreases with increasing A/D and that this decrease is greater for the lower voltage ratios. These two graphs indicate that when possible, one should reduce P/D while increasing A/D to reduce the spherical aberration coefficient.

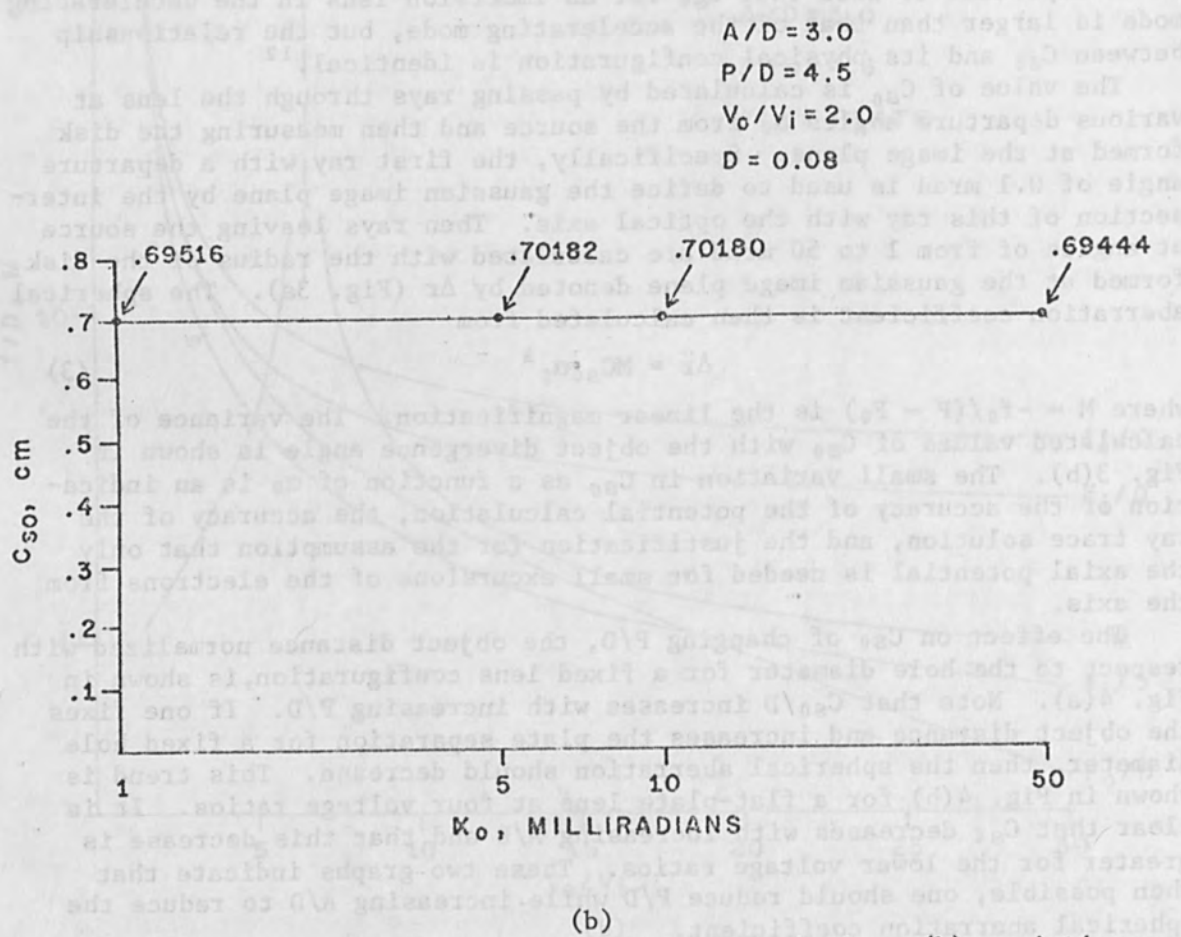
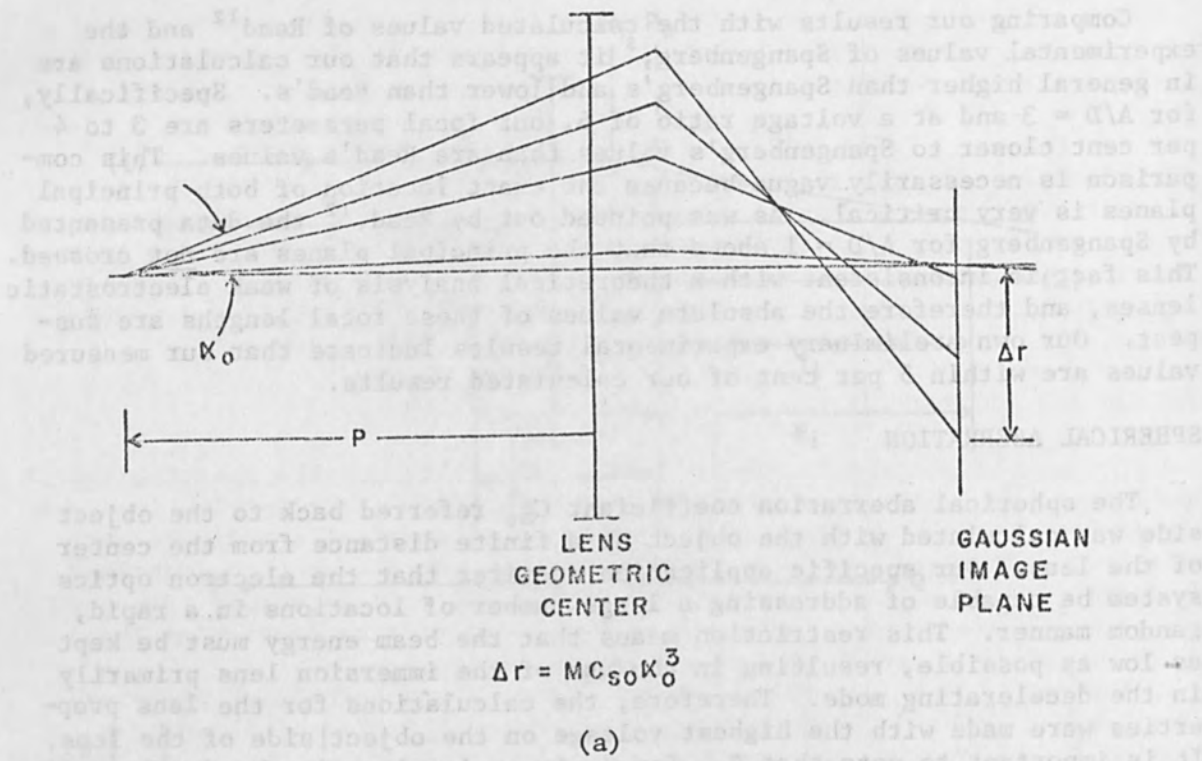
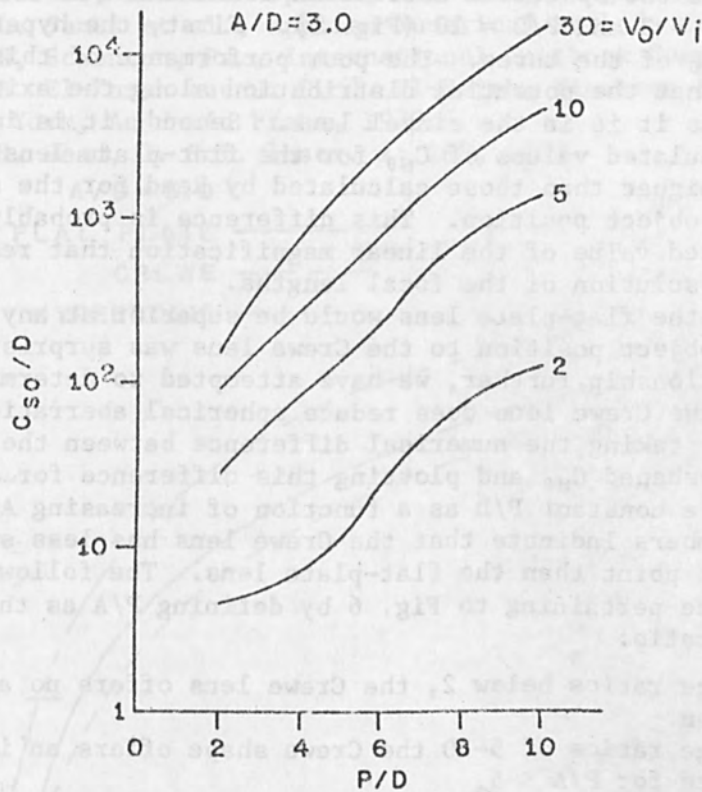
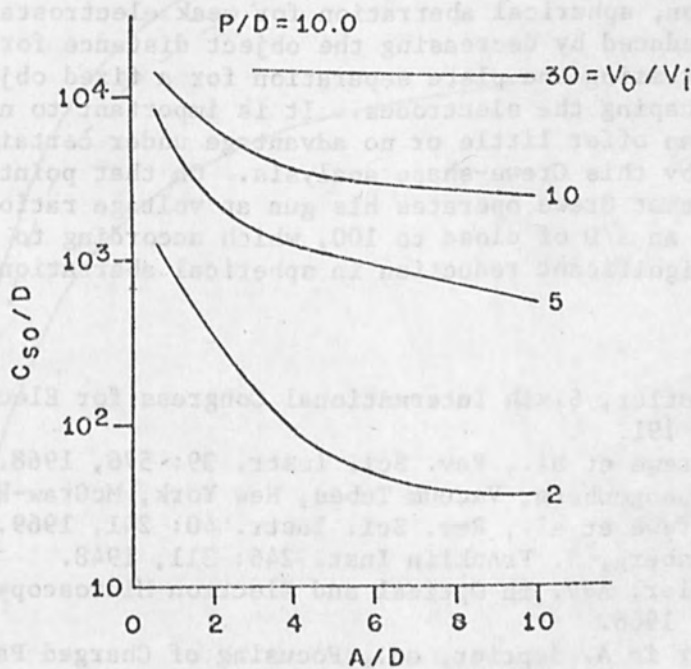


FIG. 3.--(a) Method of spherical-aberration calculation; (b) variation in spherical-aberration coefficient.



(a)



(b)

FIG. 4.--Effect of spherical aberration on increasing (a) normalized object distance, (b) normalized plate separation.

Next we compare the spherical aberration coefficient of the three lens shapes at $A/D = 3$ and $P/D = 10$ (Fig. 5). First, the hyperbolic lens has the highest C_{S0} of the three. The poor performance of this lens is due to the fact that the potential distribution along the axis is not exactly the same as it is in the einzel lens. Second, it is important to note that the calculated values of C_{S0} for the flat-plate lens are between 3 and 4 per cent higher than those calculated by Read for the same lens configuration and object position. This difference is probably due to the slightly reduced value of the linear magnification that resulted from the more accurate solution of the focal lengths.

The fact that the flat-plate lens would be superior at any voltage ratio and/or any object position to the Crewe lens was surprising. Exploring this relationship further, we have attempted to determine the regions in which the Crewe lens does reduce spherical aberration. Figure 6 was constructed by taking the numerical difference between the flat-plate C_{S0} and the Crewe-shaped C_{S0} and plotting this difference for constant voltage ratios at a constant P/D as a function of increasing A/D . Therefore, positive numbers indicate that the Crewe lens has less spherical aberration at that point than the flat-plate lens. The following observations can be made pertaining to Fig. 6 by defining P/A as the object to plate separation ratio:

- (1) For voltage ratios below 2, the Crewe lens offers no advantage at any object position.
- (2) For voltage ratios of 5-10 the Crewe shape offers an improvement over the flat plate for $P/A < 5$.
- (3) For voltage ratios above 10, the Crewe lens offers a significant reduction in spherical aberration when P/A is kept below 3.5.
- (4) The flat-plate lens is superior for all $P/A > 5$.

In conclusion, spherical aberration for weak electrostatic immersion lenses can be reduced by decreasing the object distance for a fixed plate separation, increasing the plate separation for a fixed object distance, and carefully shaping the electrodes. It is important to note that electrode shaping can offer little or no advantage under certain conditions, as can be seen by this Crewe-shape analysis. On that point it is interesting to note that Crewe operates his gun at voltage ratios of 10-20, at $P/A \approx 1$, and at an A/D of close to 100, which according to this analysis would offer a significant reduction in spherical aberration.

REFERENCES

1. J. W. Butler, Sixth International Congress for Electron Microscopy, Kyoto, 1966; p. 191.
2. A. V. Crewe et al., Rev. Sci. Instr. 39: 576, 1968.
3. K. R. Spangenberg, Vacuum Tubes, New York, McGraw-Hill, 1948.
4. A. V. Crewe et al., Rev. Sci. Instr. 40: 241, 1969.
5. R. Rüdénberg, J. Franklin Inst. 246: 311, 1948.
6. A. Septier, Adv. in Optical and Electron Microscopy, New York, Academic Press, 1966.
7. C. Weber in A. Septier, ed., Focusing of Charged Particles, New York, Academic Press, 1967; p. 45.
8. R. W. Hamming, Numerical Methods for Scientists and Engineers, New York, McGraw-Hill, 1962.

9. P. Grivet, *Electron Optics*, New York, Pergamon Press, 1965.
10. M. L. James et al., *Applied Numerical Methods for Digital Computation with FORTRAN*, Scranton, Pa., International Textbook Company, 1967.
11. A. B. El-Kareh and J. C. J. El-Kareh, *Electron Beams, Lenses, and Optics*, New York, Academic Press, 1970.
12. F. H. Read, *J. Sci. Instr.* 2: 165, 1969.

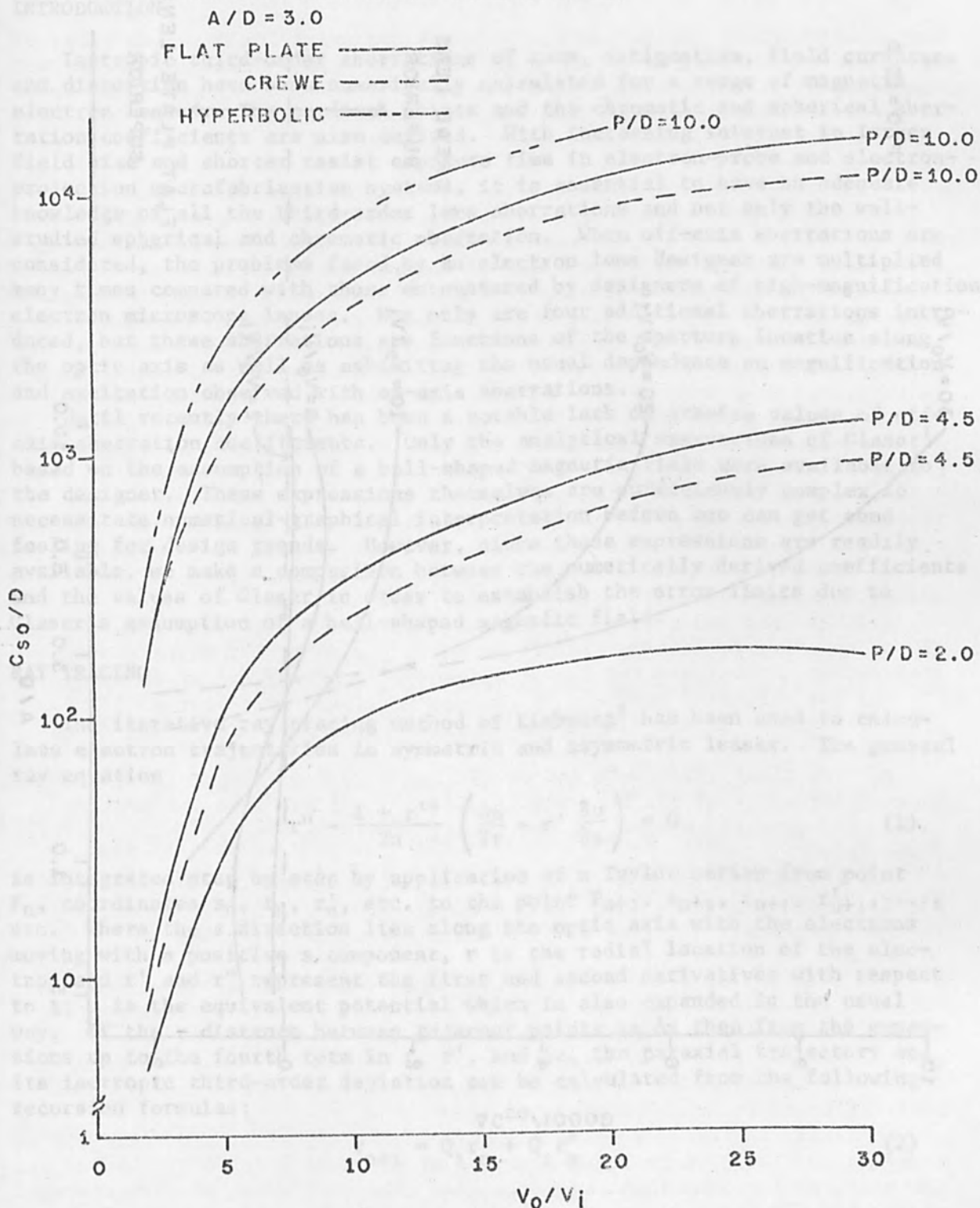


FIG. 5.--Effect of spherical aberration on increasing lens strength for three lens shapes.

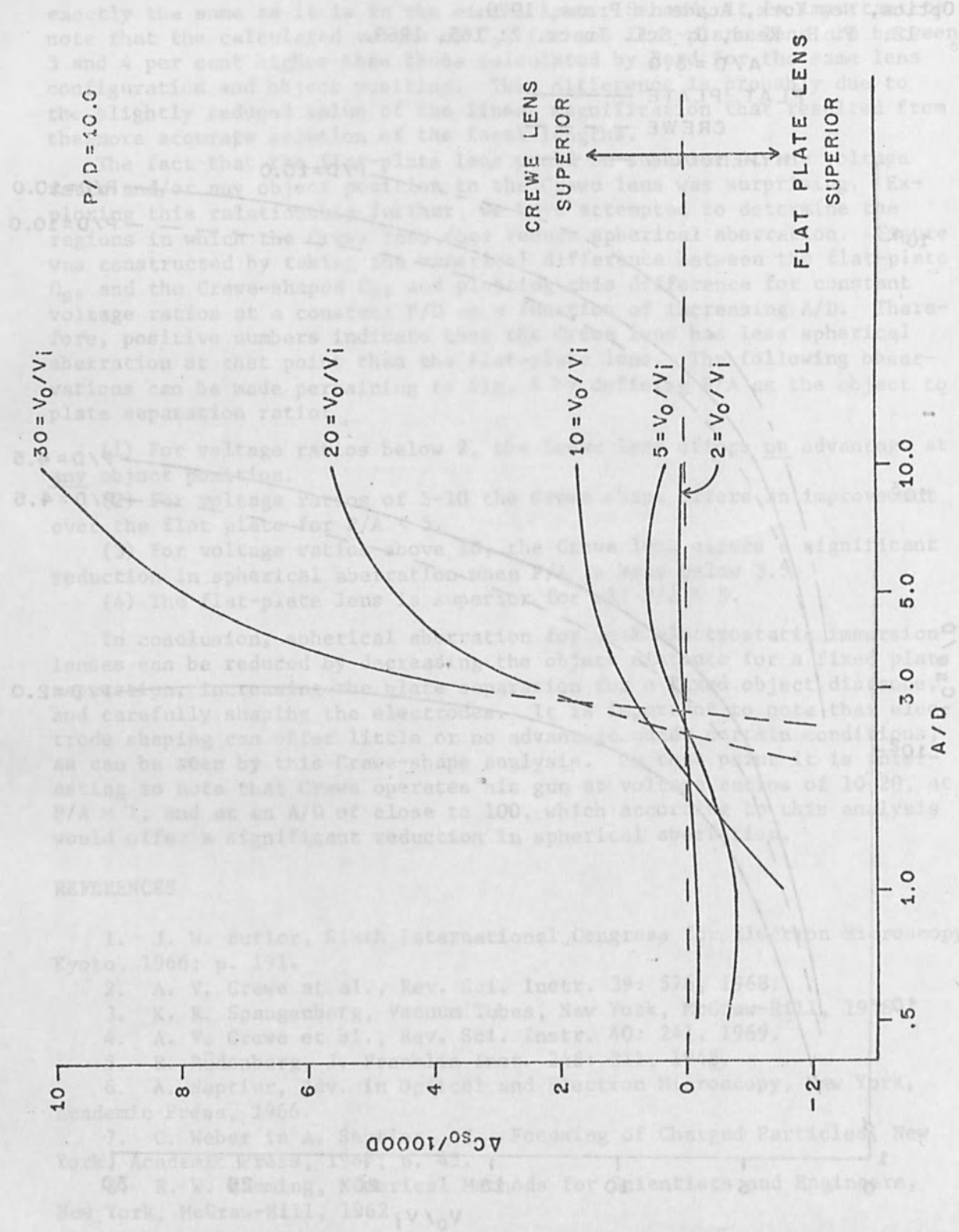


FIG. 6.--Comparison of spherical aberration for flat-plate lens with that of Crewe lens.

REFERENCES

1. J. V. Butler, *1966 International Congress on Electron Microscopy*, Kyoto, 1966; p. 171.
2. A. V. Crewe et al., *Rev. Sci. Instr.* 39: 51 (1968).
3. K. K. Spangenberg, *Vacuum Tubes*, New York, McGraw-Hill, 1948.
4. A. V. Crewe et al., *Rev. Sci. Instr.* 40: 2 (1969).
5. G. Weber in A. V. Crewe et al., *Proceedings of Charged Particle Optics*, New York, Academic Press, 1966.
6. R. W. Whiting, *Electron Optics*, New York, McGraw-Hill, 1962.

THIRD-ORDER ABERRATIONS OF MAGNETIC ELECTRON LENSES

M. B. HERITAGE

IBM Research Center, Yorktown Heights, N.Y.

INTRODUCTION

Isotropic third-order aberrations of coma, astigmatism, field curvature and distortion have been numerically calculated for a range of magnetic electron lenses. The cardinal points and the chromatic and spherical aberration coefficients are also derived. With increasing interest in larger field size and shorter resist exposure time in electron-probe and electron-projection microfabrication systems, it is essential to have an adequate knowledge of all the third-order lens aberrations and not only the well-studied spherical and chromatic aberration. When off-axis aberrations are considered, the problems faced by an electron lens designer are multiplied many times compared with those encountered by designers of high-magnification electron microscope lenses. Not only are four additional aberrations introduced, but these aberrations are functions of the aperture location along the optic axis as well as exhibiting the usual dependence on magnification and excitation observed with on-axis aberrations.

Until recently there has been a notable lack of precise values of off-axis aberration coefficients. Only the analytical expressions of Glaser¹ based on the assumption of a bell-shaped magnetic field were available to the designer. These expressions themselves are sufficiently complex to necessitate numerical-graphical interpretation before one can get some feeling for design trends. However, since these expressions are readily available, we make a comparison between the numerically derived coefficients and the values of Glaser in order to establish the error limits due to Glaser's assumption of a bell-shaped magnetic field.

RAY TRACING

The iterative ray tracing method of Liebmann² has been used to calculate electron trajectories in symmetric and asymmetric lenses. The general ray equation

$$r'' - \frac{1 + r'^2}{2u} \left(\frac{\partial u}{\partial r} - r' \frac{\partial u}{\partial z} \right) = 0 \quad (1)$$

is integrated step by step by application of a Taylor series from point P_n , coordinates z_n , r_n , r'_n , etc. to the point P_{n+1} , z_{n+1} , r_{n+1} , r'_{n+1} , ..., etc. Where the z direction lies along the optic axis with the electrons moving with a positive z component, r is the radial location of the electron and r' and r'' represent the first and second derivatives with respect to z ; u is the equivalent potential which is also expanded in the usual way. If the z distance between adjacent points is Δz then from the expansions up to the fourth term in r , r' , and Δz , the paraxial trajectory and its isotropic third-order deviation can be calculated from the following recursion formulas:

$$r_{n+1} = Q_1 r_n + Q_2 r'_n \quad (2)$$

$$r'_{n+1} = Q_3 r'_n + Q_4 r_n \quad (3)$$

$$\Delta r_{n+1} = Q_1 \Delta r_n + Q_2 \Delta r'_n \quad (4)$$

$$\Delta r'_{n+1} = Q_3 \Delta r' + Q_4 \Delta r_n + Q_5 \quad (5)$$

The coefficients Q_1 to Q_4 are functions of the axial field and Δz only; Q_5 is the coefficient which expresses the third-order radial deviation from the paraxial meridional trajectory and is a function of r_n and r'_n as well as the axial field and its first and second derivatives.

FIELD CALCULATION

The field data is derived from a program incorporating a general subroutine due to Cooley³ which solves either Poisson's or Laplace's equations by Stone's⁴ method. In Stone's method modifications are made to the matrix, formed by the difference equations generated by the application of Laplace's equation to a potential net, so that the matrix can be factorized without increasing the number of nonzero elements in each row of the factors. The solution of the modified set of equations can thus be obtained efficiently. An iterative procedure is used so that the solution provided by the modified equations converges to that of the original set to a point of some predetermined accuracy. The subroutine due to Cooley makes no demand on either the boundary conditions or the coordinate system. The boundary conditions set by the author for asymmetric lenses are illustrated in Fig. 1. AH is the optic axis of an asymmetric ($R_1 \neq R_2$) round lens of gap to bore ratio S/D. The approximate boundary conditions for the computation of the scalar magnetic potentials within the lens are defined along ABCDEFGH. The assumptions made in defining this boundary are:

(a) The lens polepieces have infinite permeability. This sets BCD and EFG at magnetic potentials of $1/2$ and $-1/2$, respectively, where the potential difference between the two polepieces is arbitrarily set to unity.

(b) The potential gradient in the gap is linear at a radius of 1.5 times the radius of the larger bore R_1 . Thus the potential along DE is given by $\Phi = z/S$.

(c) The field throughout the whole lens bore has dropped to zero beyond an axial distance of $6R_1$ into the larger bore and $6R_2$ into the smaller bore. The potentials along AB and GH are therefore $\Phi = 1/2$ and $\Phi = -1/2$, respectively.

For a symmetric lens ($R_1 = R_2$) a plane of symmetry is generated at $z = 0$. The boundary is then defined along ABCD'O. Similar assumptions to the above apply with the addition that the potential along O'O is set to zero.

The accuracy of the program working with these boundary conditions was verified experimentally. For a given test lens, the theoretical maximum axial field strength differed from the measured by 1 per cent and the theoretical half-width of the axial field differed from the measured by 3 per cent. The former error is some measure of the lens iron loss which has been neglected in the boundary conditions.

Typically the field program computes scalar magnetic potentials for an array of 50×200 points to an accuracy of at least 5 in 10^6 in 25 sec of CPU time, at the same time requiring less than 800K bytes of core storage of the IBM 360 Model 91.

THIRD-ORDER ABERRATION COEFFICIENTS

The isotropic aberration coefficients presented in this paper are defined in the usual manner in which the radial deviation from a meridional paraxial ray is given by:

$$\Delta r/R = S\alpha^3 + 3C\alpha^2(r/R) + (2A + F)\alpha(r/R)^2 + D(r/R)^3 \quad (6)$$

where S, C, A, F, and D are respectively the dimensionless third-order aberration coefficients of spherical aberration, coma, astigmatism, field curvature, and distortion, and α is the angle between the paraxial ray and the principal ray at a point in the Gaussian image plane a radial distance r from the optic axis; R is the mean radius of the lens bore as defined in Fig. 1.

Four meridional rays and their third-order deviations are traced through the lens by means of Eqs. (2), (3), (4), and (5). One of the meridional rays enters the lens parallel to the optic axis and passes through the focal point. This ray is used to determine the focal length and cardinal points. It is noted Eq. (6) shows that tracing of meridional rays alone does not permit the coefficients of astigmatism and field curvature to be separated. However, Glaser shows that the application of Petzval's theorem leads to the relationship

$$F - A = 2k^2 \int_{z_0}^{z_i} B_z^2(z) dz \quad (7)$$

where k^2 is a dimensionless constant expressing the strength of the lens excitation

$$k^2 = 0.022 B_{z(\max)}^2 R^2/V \quad (8)$$

and $B_z(z)$ is the axial magnetic field normalized to its maximum value $B_{z(\max)}$, and V is the beam voltage.

Thus from Eqs. (6) and (7) all five of the aberration coefficients can be determined from the four trajectories. The aperture dependence of the coefficients is determined by noting the radii of the trajectories at a predetermined number of aperture locations. The determination of the coefficients as a function of aperture location thus demands an insignificant amount of extra storage and time.

Typically the ray-tracing program generates the focal length and cardinal points, the five isotropic aberration coefficients, and the chromatic aberration coefficient for thirty aperture locations and for thirty values of excitation in under 10 sec of CPU time on the IBM 360 Model 91 with less than 500K bytes of core storage.

The ray-tracing and aberration-coefficient program was tested for error by entering a bell-shaped magnetic field as initial data, in place of the more accurate values derived from the solution of Laplace's equation, and the resulting coefficients were compared with the analytic expressions of Glaser.¹ An agreement of better than 0.5 per cent was found for the aberration coefficients. The error in the focal length and cardinal points was virtually insignificant.

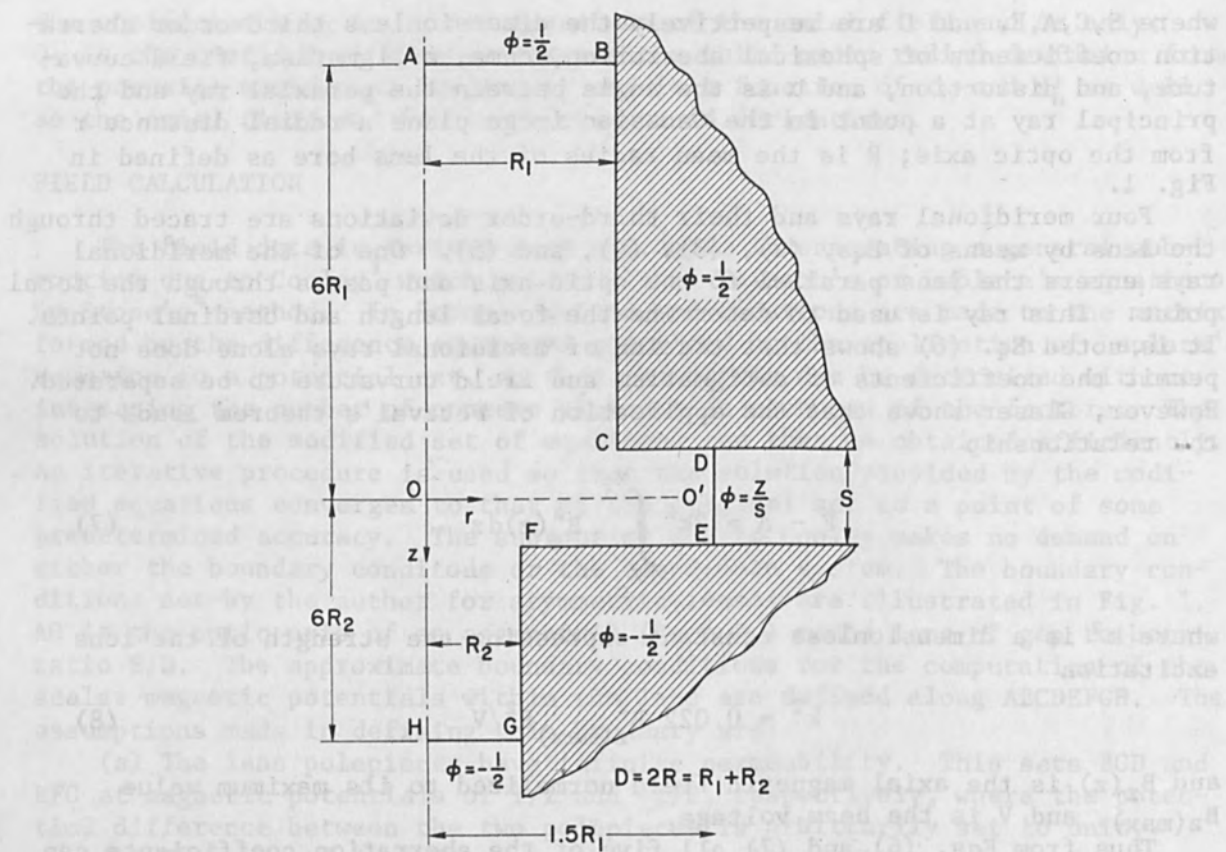


FIG. 1.--An r - z cross section of polepieces of asymmetric round magnetic electron lens, showing approximate boundary conditions used in computation of lens field.

RESULTS

Figures 2-5 are typical of the output of the ray-tracing program. The values of the off-axis aberration coefficients of coma, astigmatism, field curvature, and distortion within the focal plane of a symmetric lens ($ASM = 1.0$) of gap-to-bore ratio $S/D = 0.1$ is given for a range of aperture locations and excitations. The aperture locations (ZAP) along the optic axis are given in units normalized to the mean bore radius R . The electrons are taken to be traveling in a positive z direction with the center of the gap being the origin (Fig. 1); KSQ is the excitation parameter k^2 defined in Eq. (8).

The importance of the location of the aperture is clearly seen in Fig. 5, which shows that an aperture plane lying between 0.0 and -0.5 yields a lens that is virtually free from isotropic distortion over the whole range of excitation. In the same way lenses that are free from either coma or astigmatism can be designed. However, field curvature is positive for all aperture locations.

The ray-tracing program can be used to generate comparisons between lenses of different configurations. In such comparisons it is convenient to normalize the off-axis distance r in Eq. (6) to the focal length rather than the mean bore radius R . By this means one can compare the variation of aberration coefficients with polepiece configuration for lenses of equal focal length. Figures 6-8 show the chromatic-aberration, spherical-aberration, and field-curvature coefficients defined in this way for symmetric lenses of gap-to-bore ratio $S/D = 0.1, 0.5, 1.0,$ and 1.5 with the aperture location held at $ZAP = 0.0$. It is in making the comparisons between lenses of different configurations that the real design problems arise. At first glance it would seem that Fig. 7 shows that a large gap-to-bore ratio is advantageous in designing a probe lens since this configuration has a lower spherical aberration constant for a given focal length. However, as Mulvey⁵ has shown, if the spherical aberration is normalized to the working distance rather than the focal length then the situation is reversed. Since the working distance is a design parameter fixed prior to the design of the lens rather than the focal length, the smaller gap-to-bore ratios are preferred in probe lenses. Thus, design decisions must be made in terms of the parameters which are fixed externally to the lens. Universal design curves are therefore difficult to generate. The same argument applies to Figs. 6 and 8; moreover, for Fig. 8 the problem is further compounded by the location of the aperture. Although it is true that a lens of large S/D gives a larger field-curvature coefficient for a given focal length over the whole range of lens excitation, the possibility cannot be precluded that another aperture location exists where the reverse is true.

COMPARISON WITH THE APPROPRIATE GLASER VALUES

The programs discussed in this work generate the exact lens data at very little cost and offer distinct advantages when lenses with asymmetric and shaped polepieces are being considered. However, the Glaser¹ expressions for the approximate off-axis aberrations of symmetric lenses are readily available. Unfortunately the errors introduced by the Glaser approximation of the lens field by a bell-shaped magnetic field are uncertain and the expressions themselves are sufficiently cumbersome to require numerical graphical interpretation. It is useful then to understand the error limits of the Glaser expressions by testing them against the coefficients

Figures 2-3 are typical of the output of the ray-tracing program. The values of the off-axis aberrations (distortion, coma, astigmatism, field curvature, and distortion) within the focal plane of a symmetric lens (ASM S/D=0.1) of aperture diameter 1.0 are shown in Figures 2 and 3. The values are given in units of millimeters. The aperture diameter (S/D) is the ratio of the aperture to the focal length of the lens. The values of the aberrations are given in millimeters. The values of the aberrations are given in millimeters. The values of the aberrations are given in millimeters.

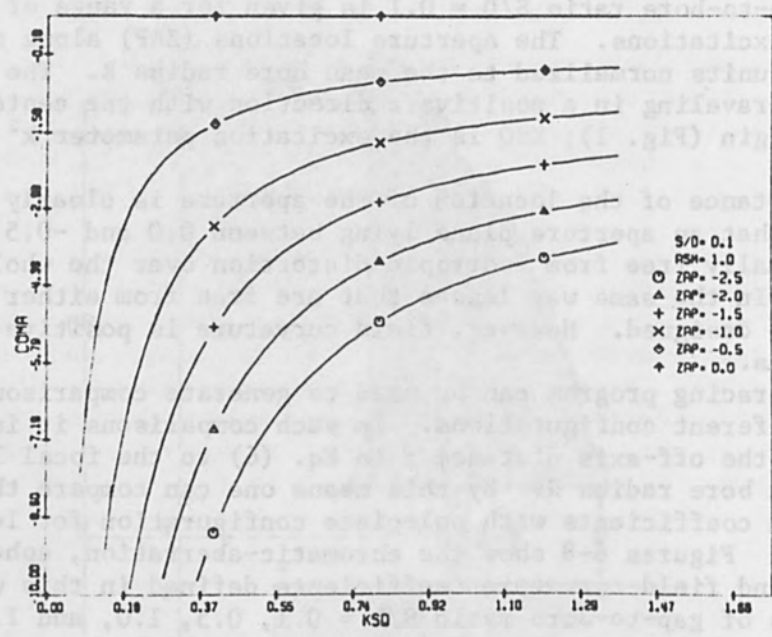


FIG. 2.

The program described in this paper is a ray-tracing program for the design of lenses. It is a computer program that calculates the aberrations of a lens. The program is written in Fortran and runs on a mainframe computer. The program is designed to calculate the aberrations of a lens for a given set of parameters. The parameters are the aperture diameter, the focal length, and the refractive index of the lens material. The program calculates the aberrations of the lens for a given set of parameters. The aberrations are the coma, the astigmatism, the field curvature, and the distortion. The program is designed to calculate the aberrations of a lens for a given set of parameters. The parameters are the aperture diameter, the focal length, and the refractive index of the lens material. The program calculates the aberrations of the lens for a given set of parameters. The aberrations are the coma, the astigmatism, the field curvature, and the distortion.

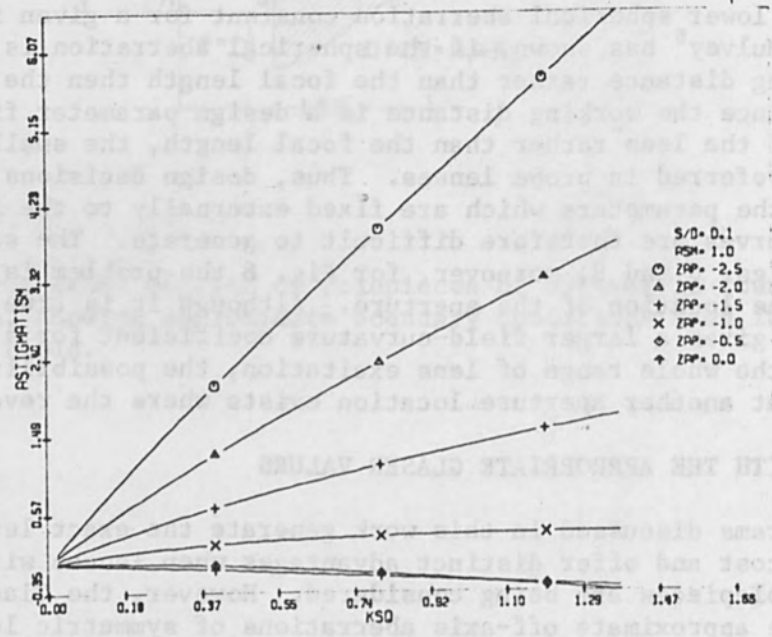


FIG. 3.

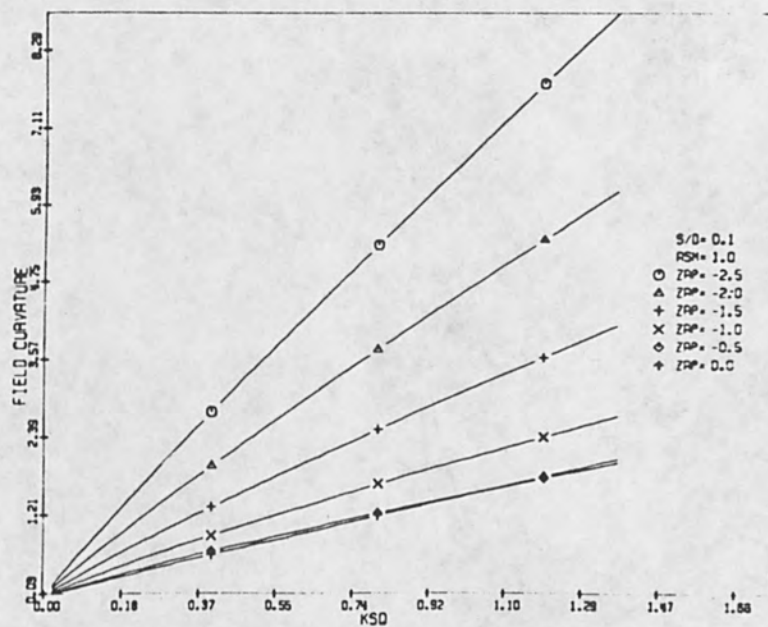
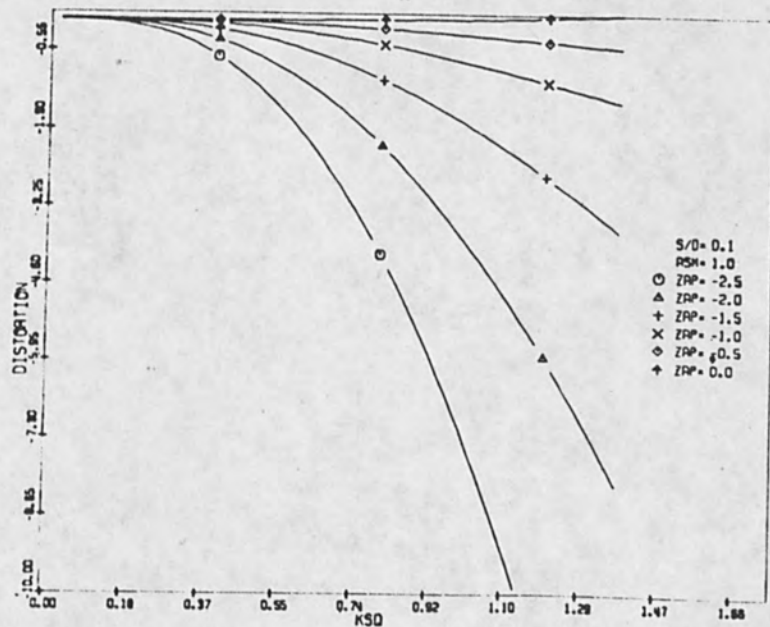


FIG. 4



FIGS. 2-5.--Aberration coefficients of coma, astigmatism, field curvature, and distortion as defined by Eq. (6), shown as functions of lens-excitation parameter k^2 (KSD) and position of aperture along optic axis (ZAP) for symmetric (ASM = 1.0) magnetic lens of gap-to-bore ratio $S/D = 0.1$.

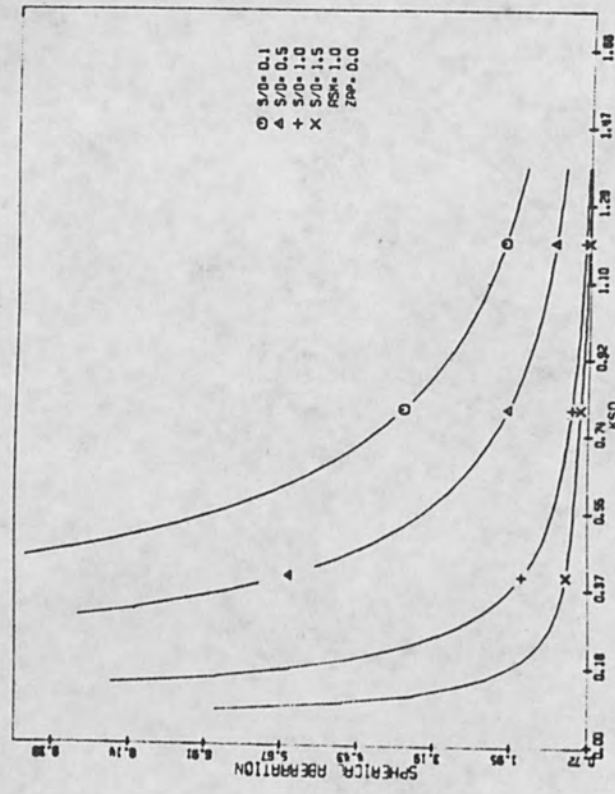
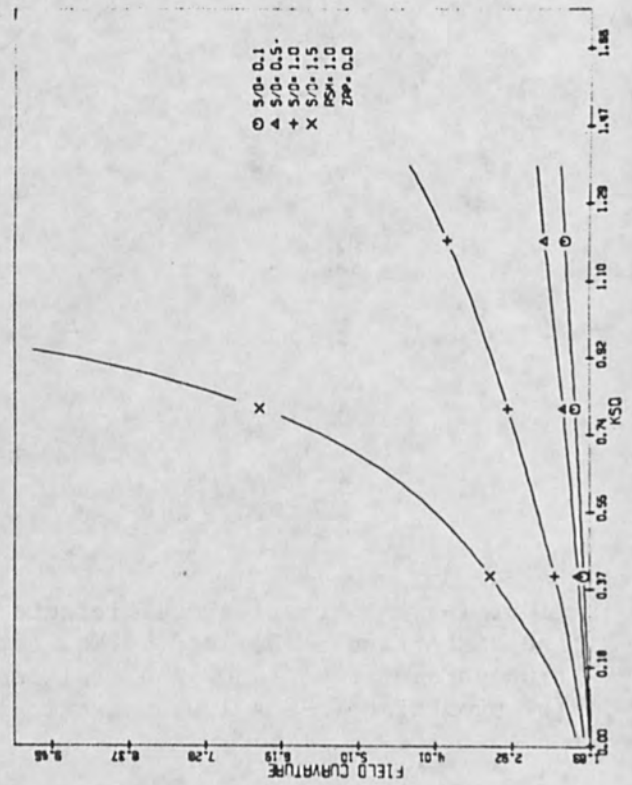
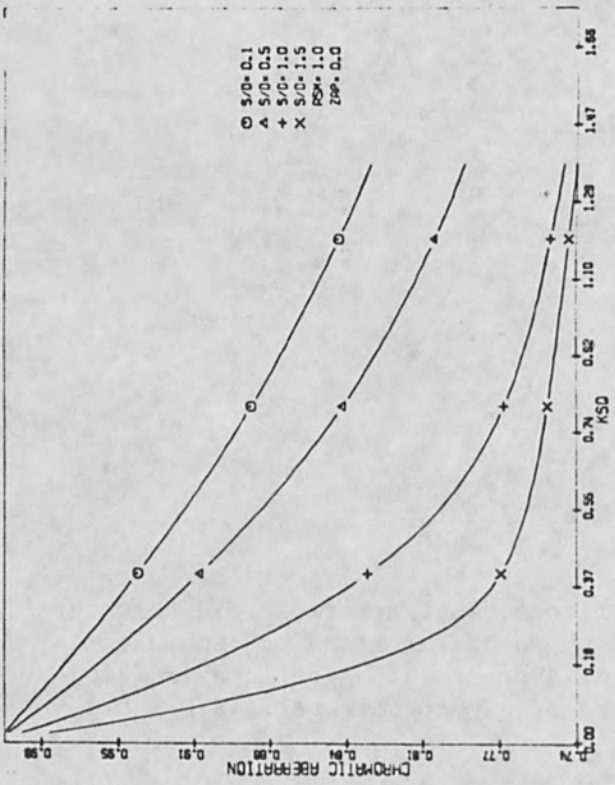


FIG. 6 -8.--Variation of chromatic-aberration, spherical-aberration, and field-curvature coefficients as function of polepiece configuration (S/D) and lens excitation (KSO) for lenses of equal focal length. Aperture location along optic axis is origin ZAP = 0.0.

derived using the more accurate field computation described earlier. In Table I the five isotropic third-order aberrations for the lens $S/D = 1.0$, $k^2 = 1.0$ are compared with the appropriate Glaser values taking the bellfield halfwidth equal to $1.1R$. It is seen that the Glaser values are

TABLE I.--Comparison of computed aberration coefficients with appropriate Glaser values.

Ap.	$S/D = 1.0$		$k^2(\text{Liebmann}) = 1.0$					
	Coma		Astig.		F. Curv.		Dist.	
	Heritage	Glaser	Heritage	Glaser	Heritage	Glaser	Heritage	Glaser
-2.4	-1.361	-0.864	1.286	0.513	4.212	3.324	-4.475	-2.948
-2.2	-1.202	-0.773	0.849	0.280	3.775	3.090	-3.432	-2.378
-2.0	-1.043	-0.679	0.466	0.069	3.393	2.880	-2.599	-1.896
-1.8	-0.884	-0.585	0.138	-0.117	3.064	2.694	-1.946	-1.495
-1.6	-0.725	-0.488	-0.136	-0.278	2.790	2.533	-1.447	-1.163
-1.4	-0.565	-0.389	-0.357	-0.413	2.570	2.398	-1.075	-0.890
-1.2	-0.405	-0.286	-0.523	-0.521	2.403	2.290	-0.800	-0.666
-1.0	-0.242	-0.177	-0.636	-0.599	2.291	2.212	-0.594	-0.477
-0.8	-0.074	-0.060	-0.693	-0.642	2.234	2.169	-0.426	-0.306
-0.6	0.106	0.070	-0.686	-0.640	2.240	2.171	-0.262	-0.129
-0.4	0.310	0.224	-0.595	-0.570	2.332	2.242	-0.045	0.104
-0.2	0.560	0.421	-0.362	-0.373	2.565	2.438	0.348	0.522
-0.0	0.901	0.705	0.173	0.131	3.100	2.942	1.294	1.584

S.A. (Heritage) = 0.933

S.A. (Glaser) = 0.645

$d(\text{Glaser}) = 1.1R$

surprisingly good. For the most part the error is less than 40 per cent and often it is much smaller. The errors can be as large as 200-300 per cent or more for aperture positions $ZAP < -2.0$ or at coefficient zeroes. Within these limits, however, the Glaser values give a good idea of general trends and it is particularly useful to note that the Glaser predictions of the aperture positions at which particular aberrations vanish are fairly accurate.

SUMMARY

Highly precise numerical methods of field calculation and ray tracing have been presented. Only a fraction of the data these programs have generated can be given here. Indeed, it is the problem of a surfeit of data and the wide choice of design parameters that leads one to suggest that the best wide-field lenses can be designed only when numerical optimization methods are used. It has also been shown that the position of the aperture plane is most important in reducing some of the off-axis aberrations. The usefulness of the expressions of Glaser based on the bellfield assumption is also reaffirmed.

REFERENCES

1. W. Glaser, Grundlagen der Elektronenoptik, Springer-Verlag, 1952.
2. G. Liebmann, Proc. Phys. Soc. B62: 753, 1949.
3. J. W. Cooley, IBM Watson Research Center, Yorktown Heights, N.Y.; personal communication.
4. H. L. Stone, SIAM J. Numer. Anal. 5: 530, 1968.
5. T. Mulvey, J. Sci. Inst. 36: 350, 1959.



surprisingly good. For the most part the error is less than 40 per cent and often it is much smaller. The error can be as large as 200-300 per cent or more for aperture positions $NAR = 2.0$ or at coefficient errors. Within these limits, however, the Glaser values give a good idea of general trends and it is particularly useful to note that the Glaser predictions of the aperture positions at which particular aberrations vanish are fairly accurate.

Highly precise numerical methods of field calculation and ray tracing have been presented. Only a fraction of the data these programs have generated can be given here. Indeed, it is the problem of a certain amount of data and the wide choice of design parameters that leads one to suggest that the best wide-field lenses can be designed only when numerical optimization methods are used. It has also been shown that the position of the aperture plane is most important in reducing some of the off-axis aberrations. The inclusion of the expressions of Glaser based on the bell-shaped assumption is also well justified.

ANALYTICAL SOLUTION OF THE AXIAL POTENTIAL FOR A THREE-ELEMENT ELECTRO-STATIC LENS

H. G. PARKS

General Electric Research & Development Center, Schenectady, N.Y.

I. INTRODUCTION

Lenses of the three-element variety have a well-established position in electron optics. Generally these lenses are formed by applying potentials to three axially aligned apertures or cylinders (Fig. 1). These lenses are often operated with the outer electrodes tied to anode potential and the center element to the cathode, with one of these potentials at ground. In this mode of operation the optical properties of the lens depend only on the lens dimensions and not on the operating voltage. Another mode of operation is to connect the center element to some potential other than cathode potential. In this case the optical properties are functions of the ratio of central to outer electrode potential as well as the lens dimensions, and thus can be controlled by varying the center-element potential.

Despite the widespread use of three-element electron lenses, data for their optical properties are fairly scarce, particularly for the three-cylinder lens. Moreover, most of the available data seem to be for the einzel connection and not for the more flexible case when the center-element potential is variable. What follows is a first step in alleviating the shortage of optical data for the three-cylinder lens. An expression for the axial potential of the lens is derived. A particularly interesting and quite unusual feature of this solution is that the axial potential for both symmetrical and asymmetrical electrode configurations can be defined. Because of the potential application to lens analysis, some optical properties and literature comparisons are presented and discussed.

II. AXIAL POTENTIAL OF A THREE-CYLINDER LENS

With rotational symmetry, Laplace's equation is

$$\nabla^2\Phi = \frac{1}{r} \frac{\partial}{\partial r} \left(r \frac{\partial\Phi}{\partial r} \right) + \frac{\partial^2\Phi}{\partial z^2} = 0 \quad (1)$$

Bertram¹ has shown that a general solution of (1) is given by

$$\Phi(r, z) = \int_{-\infty}^{+\infty} f(\mu) e^{j\mu z} I_0(\mu r) d\mu + C \quad (2)$$

where C is an arbitrary constant and $I_0(\mu r)$ is the modified Bessel function of first kind and zero order, defined by the series

$$I_0(\mu r) = \sum_{k=0}^{\infty} \frac{1}{(k!)^2} \left(\frac{\mu r}{2} \right)^{2k} \quad (3)$$

To determine the potential distribution for the lens considered here, we must evaluate the function $f(\mu)$ and the constant C in (2) from our

knowledge of the potential variation along the boundary formed by the lens cylinders. Along the boundary (i.e., at $r = R$) the potential is a function of z only:

$$\Phi(R, z) = g(z) + C \quad (4)$$

Thus from (2) we see that the function $g(z)$ in (4) is given by

$$g(z) = \int_{-\infty}^{+\infty} f(\mu) e^{j\mu z} I_0(\mu R) d\mu \quad (5)$$

Interpreting (5) as the Fourier inversion integral

$$g(z) = \frac{1}{2\pi} \int_{-\infty}^{+\infty} G(\mu) e^{j\mu z} d\mu \quad (6)$$

we can define $f(\mu)$ as

$$f(\mu) = \frac{G(\mu)}{2\pi I_0(\mu R)} \quad (7)$$

where $G(\mu)$ is the Fourier integral of the variational component of the boundary potential $\Phi(R, z)$ and is given by

$$G(\mu) = \int_{-\infty}^{+\infty} g(z) e^{-j\mu z} dz \quad (8)$$

The constant C is determined from $\Phi(R, z)$ in such a way that the condition of absolute integrability

$$\int_{-\infty}^{+\infty} |g(z)| dz = \int_{-\infty}^{+\infty} |\Phi(R, z) - C| dz < \infty \quad (9)$$

required for the existence of (6) and (8) is satisfied.

Let us now consider the boundary potential $\Phi(R, z)$. We do not in fact know this potential exactly, but we can approximate it and obtain a mathematical solution of the axial potential that allows calculation of the electron-optical properties of the lens with a high degree of accuracy. For purposes of analysis we therefore assume that the outer cylinder electrodes of the lens extend to infinity. In terms of the boundary potential, this assumption means that $\Phi(R, z) = V_1$ is maintained along these cylinders. Furthermore, we assume that $\Phi(R, z)$ varies linearly from V_1 to V_2 in the gaps S_1 and S_2 between the outer and inner cylinders of the lens. The resulting boundary potential (Fig. 2) may at first sight seem to be a gross approximation for the lens boundary potential. However, this type of approximation is quite familiar in the field of electron optics and not unfounded, as is verified by its successful application in the analysis of other types of lenses.^{2,3} With $\Phi(R, z)$ defined in this manner, we can now evaluate the function $g(z)$ and the constant C in (4). Referring to Fig. 2 we see that selecting $C = V_1$ defines $g(z)$ by (4), as shown in Fig. 3, such that the condition of absolute integrability (9) is satisfied. Mathematically $g(z)$ can be expressed as

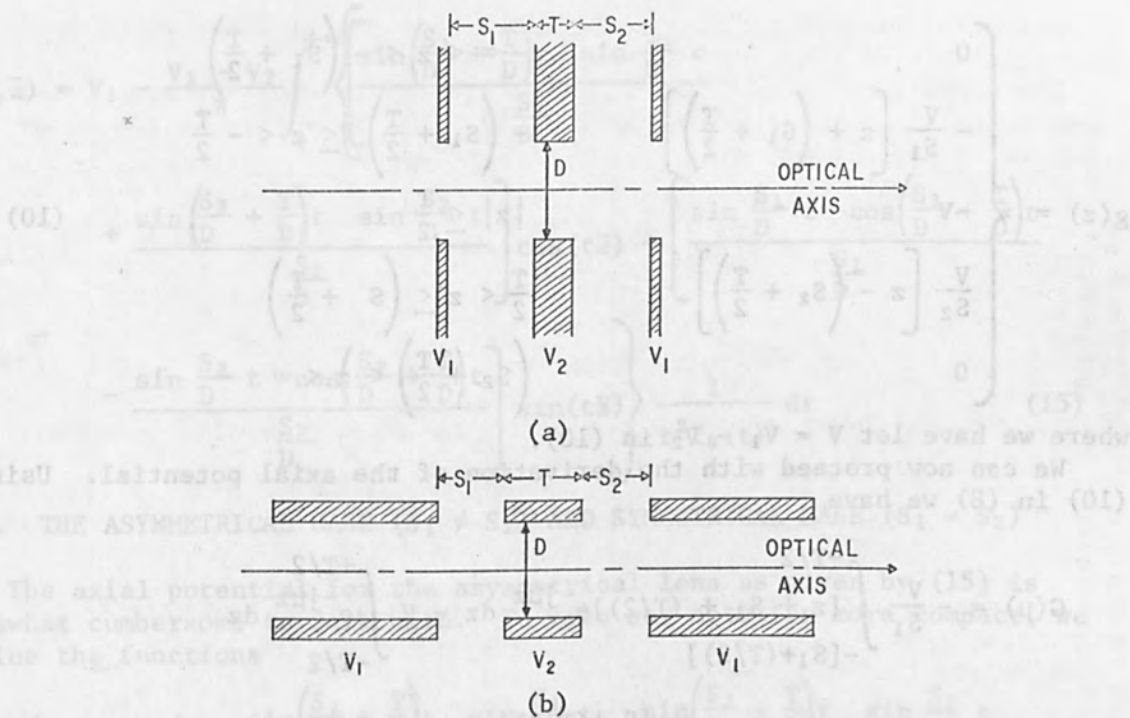


FIG. 1.--(a) Three-aperture lens; (b) three-cylinder lens.

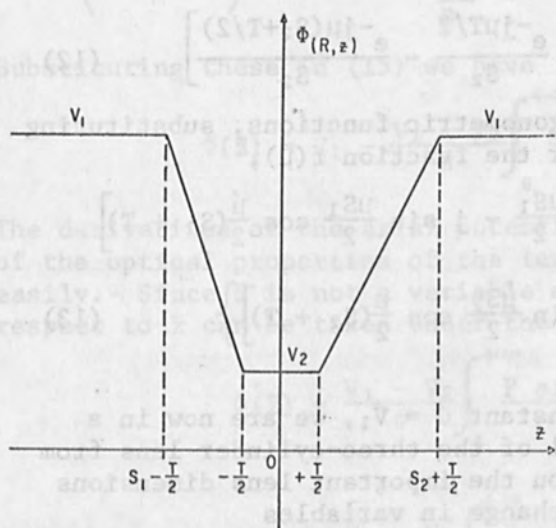


FIG. 2.--Assumed boundary potential for the three-cylinder lens.

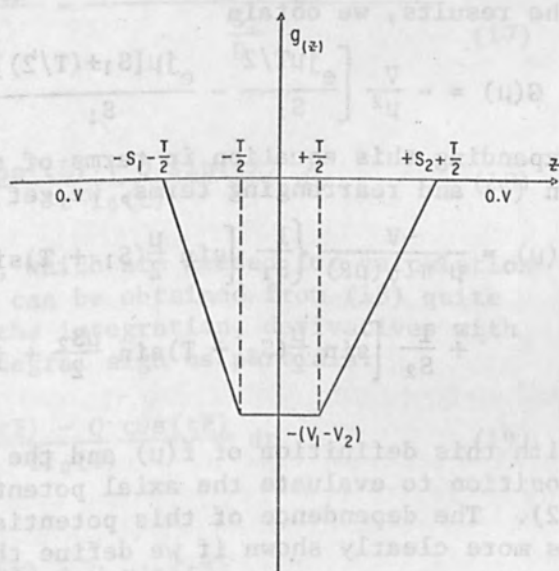


FIG. 3.--Variational component of the lens boundary potential.

$$g(z) = \begin{cases} 0 & -\infty < z < -\left(S_1 + \frac{T}{2}\right) \\ -\frac{V}{S_1} \left[z + \left(S_1 + \frac{T}{2}\right) \right] & -\left(S_1 + \frac{T}{2}\right) \leq z < -\frac{T}{2} \\ -V & |z| \leq \frac{T}{2} \\ \frac{V}{S_2} \left[z - \left(S_2 + \frac{T}{2}\right) \right] & \frac{T}{2} < z \leq \left(S_2 + \frac{T}{2}\right) \\ 0 & \left(S_2 + \frac{T}{2}\right) < z < \infty \end{cases} \quad (10)$$

where we have let $V = V_1 - V_2$ in (10).

We can now proceed with the derivation of the axial potential. Using (10) in (8) we have

$$G(\mu) = -\frac{V}{S_1} \int_{-[S_1+(T/2)]}^{-T/2} [z + S_1 + (T/2)] e^{-j\mu z} dz - V \int_{-T/2}^{+T/2} e^{-j\mu z} dz + \frac{V}{S_2} \int_{T/2}^{[S_2+(T/2)]} [z - [(S_2 + (T/2))]] e^{-j\mu z} dz \quad (11)$$

The integrals in this equation are straightforward and easily evaluated. Performing these integrations between the indicated limits and simplifying the results, we obtain

$$G(\mu) = -\frac{V}{\mu^2} \left[\frac{e^{j\mu T/2}}{S_1} - \frac{e^{j\mu[S_1+(T/2)]}}{S_1} + \frac{e^{-j\mu T/2}}{S_2} - \frac{e^{-j\mu(S_2+T/2)}}{S_2} \right] \quad (12)$$

Expanding this equation in terms of trigonometric functions, substituting in (7) and rearranging terms, we get for the function $f(\mu)$,

$$f(\mu) = \frac{-V}{\mu^2 \pi I_0(\mu R)} \left\{ \frac{1}{S_1} \left[\sin \frac{\mu}{2}(S_1 + T) \sin \frac{\mu S_1}{2} - j \sin \frac{\mu S_1}{2} \cos \frac{\mu}{2}(S_1 + T) \right] + \frac{1}{S_2} \left[\sin \frac{\mu}{2}(S_2 + T) \sin \frac{\mu S_2}{2} + j \sin \frac{\mu S_2}{2} \cos \frac{\mu}{2}(S_2 + T) \right] \right\} \quad (13)$$

With this definition of $f(\mu)$ and the constant $C = V_1$, we are now in a position to evaluate the axial potential of the three-cylinder lens from (2). The dependence of this potential on the important lens dimensions is more clearly shown if we define the change in variables

$$\mu = \frac{t}{R}, \quad d\mu = \frac{dt}{R}, \quad \bar{z} = \frac{z}{R} \quad (14)$$

Thus using (13) and (14) in (2), noting that $D = 2R$, and rearranging terms, we finally obtain the axial potential for the three-cylinder lens as

$$\begin{aligned} \Phi(0, \bar{z}) = V_1 - \frac{V_1 - V_2}{\pi} \int_0^{+\infty} & \left\{ \frac{\sin\left(\frac{S_1}{D} + \frac{T}{D}\right)t \sin \frac{S_1}{D} t}{\frac{S_1}{D}} \right. \\ & + \left. \frac{\sin\left(\frac{S_2}{D} + \frac{T}{D}\right)t \sin \frac{S_2}{D} t}{\frac{S_2}{D}} \right\} \cos(t\bar{z}) + \left[\frac{\sin \frac{S_1}{D} t \cos\left(\frac{S_1}{D} + \frac{T}{D}\right)t}{\frac{S_1}{D}} \right. \\ & \left. - \frac{\sin \frac{S_2}{D} t \cos\left(\frac{S_2}{D} + \frac{T}{D}\right)t}{\frac{S_2}{D}} \right] \sin(t\bar{z}) \Bigg\} \frac{1}{t^2 I_0(t)} dt \end{aligned} \quad (15)$$

III. THE ASYMMETRICAL CASE ($S_1 \neq S_2$) AND SYMMETRICAL CASE ($S_1 = S_2$)

The axial potential for the asymmetrical lens as given by (15) is somewhat cumbersome to work with. To make our notation more compact, we define the functions

$$P = P\left(\frac{S_1}{D}, \frac{S_2}{D}, \frac{T}{D}, t\right) = \frac{\sin\left(\frac{S_1}{D} + \frac{T}{D}\right)t \sin \frac{S_1}{D} t}{\frac{S_1}{D}} + \frac{\sin\left(\frac{S_2}{D} + \frac{T}{D}\right)t \sin \frac{S_2}{D} t}{\frac{S_2}{D}} \quad (16)$$

and

$$Q = Q\left(\frac{S_1}{D}, \frac{S_2}{D}, \frac{T}{D}, t\right) = \frac{\sin \frac{S_1}{D} t \cos\left(\frac{S_1}{D} + \frac{T}{D}\right)t}{\frac{S_1}{D}} - \frac{\sin \frac{S_2}{D} t \cos\left(\frac{S_2}{D} + \frac{T}{D}\right)t}{\frac{S_2}{D}} \quad (17)$$

Substituting these in (15) we have

$$\Phi(\bar{z}) = V_1 - \frac{V_1 - V_2}{\pi} \int_0^{+\infty} \frac{P \cos(t\bar{z}) + Q \sin(t\bar{z})}{t^2 I_0(t)} dt \quad (18)$$

The derivatives of the axial potential, which are needed for calculation of the optical properties of the lens, can be obtained from (18) quite easily. Since \bar{z} is not a variable of the integration, derivatives with respect to \bar{z} can be taken under the integral sign as partials:

$$\Phi'(\bar{z}) = \frac{V_1 - V_2}{\pi} \int_0^{+\infty} \frac{P \sin(t\bar{z}) - Q \cos(t\bar{z})}{t I_0(t)} dt \quad (19)$$

$$\text{and} \quad \Phi''(\bar{z}) = \frac{V_1 - V_2}{\pi} \int_0^{+\infty} \frac{P \cos(t\bar{z}) + Q \sin(t\bar{z})}{I_0(t)} dt \quad (20)$$

for the first and second derivatives of the axial potential, respectively.

As an example of the asymmetrical lens potentials, results for the case $S_1/D = 0.3125$, $S_2/D = 0.625$, $T/D = 0.25$ are given here. The axial potential and its first and second derivatives for the case $V_2/V_1 = 0$, with V_1 normalized to 1, are plotted in Fig. 4. We note the shifting of

the potential minimum to the weaker-field side of the lens, which is characteristic of this type of asymmetrical lens.

The symmetrical lens potential is a special case of the more general asymmetrical lens potential given in (18). For $S_1 = S_2 = S$, the equations for P and Q given by (16) and (17) reduce to

$$P_s = P\left(\frac{S}{D}, \frac{T}{D}, t\right) = \frac{2 \sin\left(\frac{S}{D} + \frac{T}{D}\right)t \sin \frac{S}{D} t}{\frac{S}{D}} \quad (21)$$

$$Q_s = Q\left(\frac{S}{D}, \frac{T}{D}, t\right) = 0 \quad (22)$$

and in view of these equations and (18), the axial potential becomes

$$\Phi(\bar{z}) = V_1 - \frac{V_1 - V_2}{\pi} \int_0^{+\infty} \frac{P_s \cos(t\bar{z})}{t^2 I_0(t)} dt \quad (23)$$

The vanishing of the function Q under the condition of symmetry is not a surprising result. The condition of symmetry along the z axis of the lens is reflected in the potential as

$$\Phi(\bar{z}) = \Phi(-\bar{z}) \quad (24)$$

Since Q is the coefficient of the $\sin(t\bar{z})$ in the general potential (18), we see from (24) that it is only reasonable that it vanishes for the symmetrical case. The derivatives of the axial potential are obtained from (23) as

$$\Phi'(\bar{z}) = \frac{V_1 - V_2}{\pi} \int_0^{+\infty} \frac{P_s \sin(t\bar{z})}{t I_0(t)} dt \quad (25)$$

$$\Phi''(\bar{z}) = \frac{V_1 - V_2}{\pi} \int_0^{+\infty} \frac{P_s \cos(t\bar{z})}{I_0(t)} dt \quad (26)$$

The axial potential and its derivatives for the case $S/D = 0.625$, $T/C = 0.25$ with V_1 normalized to 1, and $V_2/V_1 = 0$, are shown in Fig. 5. We note the even symmetry exhibited by $\Phi(\bar{z})$ and $\Phi''(\bar{z})$ and the odd symmetry of $\Phi'(\bar{z})$.

IV. CALCULATION OF OPTICAL PROPERTIES AND LITERATURE COMPARISONS

Two programs have been written in GE Time-Sharing Fortran to evaluate the optical properties of three cylinder lenses. One of these programs uses the general potential equation and its derivatives, equations (18), (19), and (20), respectively, and can thus be used for asymmetrical lenses. The other program takes advantage of the simpler equations for the symmetrical case (21), (22), and (23) and the even and odd symmetry properties of these in the evaluation of the potential and its derivatives. In both of these programs the axial potential and derivatives are numerically integrated via a modified form of Simpson's rule.⁴ These values are then used in conjunction with Liebmann's ray tracing technique⁵ to determine the trajectories of paraxial rays that enter the lens parallel to the

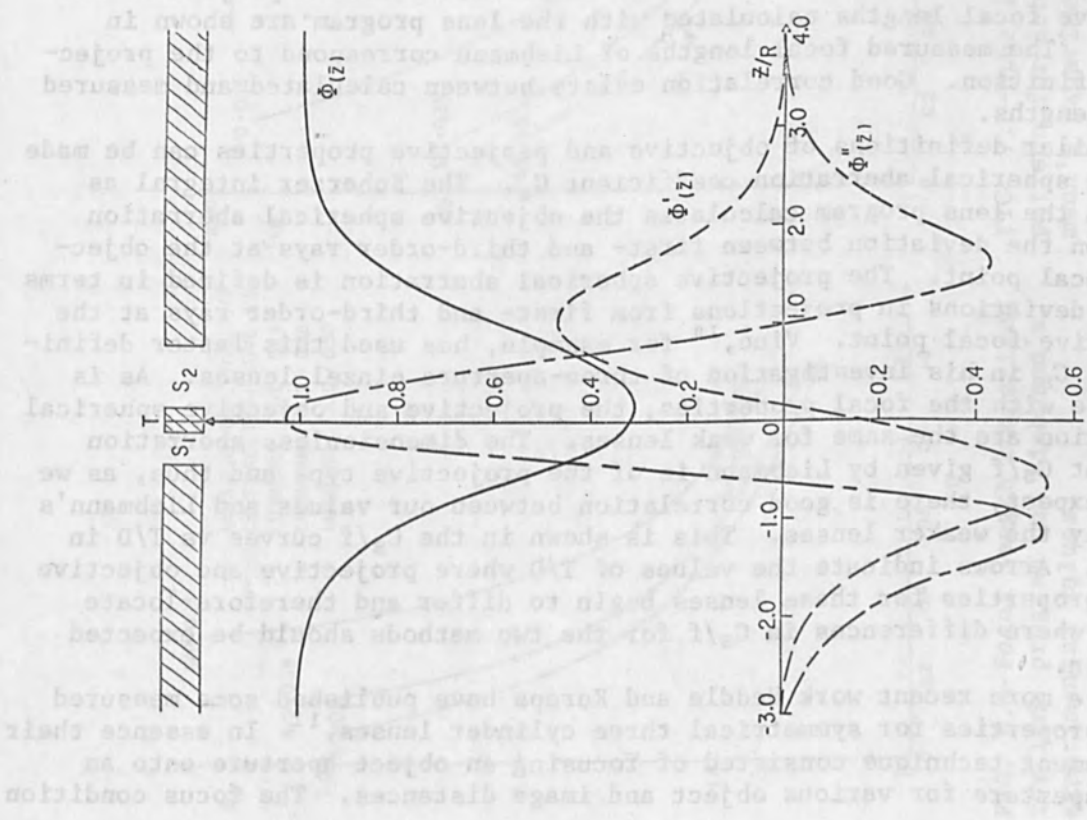


FIG. 4.--Axial potential and derivatives for the asymmetric lens $S_1/D = 0.3125$, $S_2/D = 0.625$, $T/D = 0.25$.

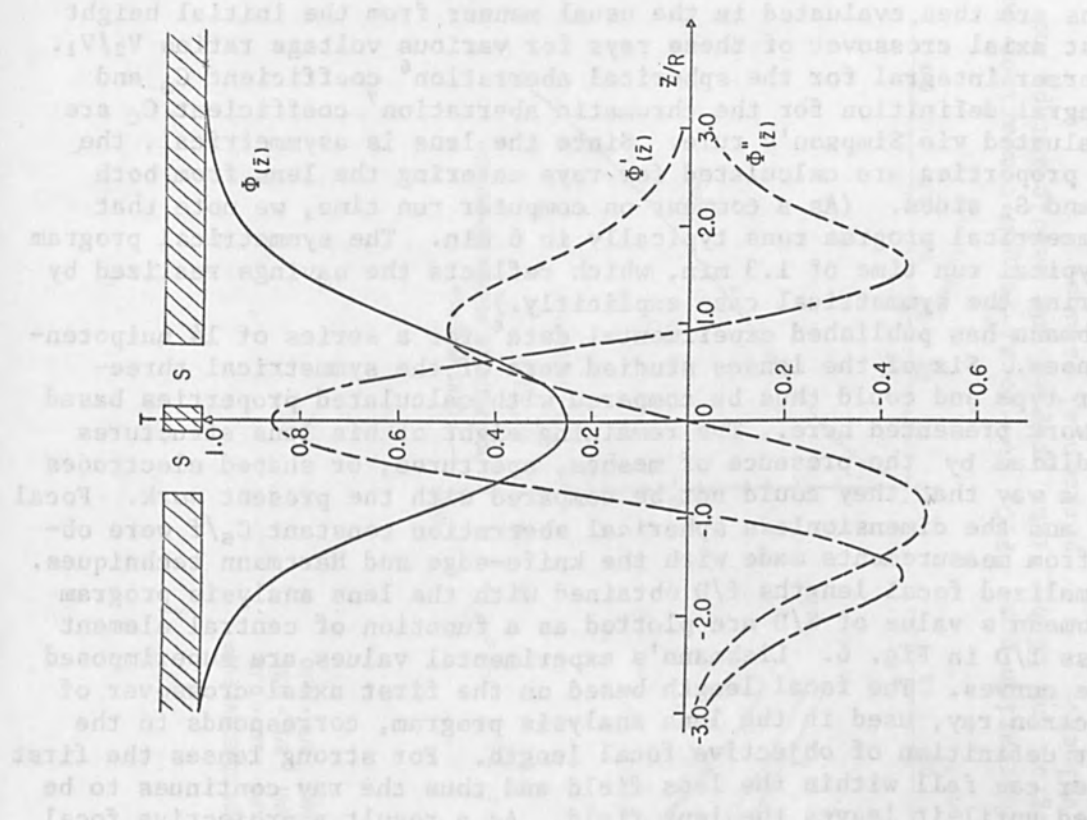


FIG. 5.--Axial potential and derivatives for the symmetrical lens $S/D = 0.625$, $T/D = 0.25$.

optical axis. The focal lengths, midfocal lengths, and principal-plane locations are then evaluated in the usual manner from the initial height and first axial crossover of these rays for various voltage ratios V_2/V_1 . The Scherzer integral for the spherical aberration⁶ coefficient C_S and the integral definition for the chromatic aberration⁷ coefficient C_C are also evaluated via Simpson's rule. Since the lens is asymmetrical, the optical properties are calculated for rays entering the lens from both the S_1 and S_2 sides. (As a comment on computer run time, we note that the asymmetrical program runs typically in 6 min. The symmetrical program has a typical run time of 1.3 min, which reflects the savings realized by considering the symmetrical case explicitly.)

Liebmann has published experimental data⁸ for a series of 14 unipotential lenses. Six of the lenses studied were of the symmetrical three-cylinder type and could thus be compared with calculated properties based on the work presented here. The remaining eight of his lens structures were modified by the presence of meshes, apertures, or shaped electrodes in such a way that they could not be compared with the present work. Focal lengths and the dimensionless spherical aberration constant C_S/f were obtained from measurements made with the knife-edge and Hartmann techniques.

Normalized focal lengths f/D obtained with the lens analysis program for Liebmann's value of S/D are plotted as a function of central element thickness T/D in Fig. 6. Liebmann's experimental values are superimposed on these curves. The focal length based on the first axial crossover of the electron ray, used in the lens analysis program, corresponds to the familiar definition of objective focal length. For strong lenses the first crossover can fall within the lens field and thus the ray continues to be refracted until it leaves the lens field. As a result a projective focal length is also defined, based on straight-line projections of the ray after it has passed through the lens.⁹ The differences between projective and objective focal lengths calculated with the lens program are shown in Fig. 6. The measured focal lengths of Liebmann correspond to the projective definition. Good correlation exists between calculated and measured focal lengths.

Similar definitions of objective and projective properties can be made for the spherical aberration coefficient C_S . The Scherzer integral as used in the lens program calculates the objective spherical aberration based on the deviation between first- and third-order rays at the objective focal point. The projective spherical aberration is defined in terms of the deviations in projections from first- and third-order rays at the projective focal point. Vine,¹⁰ for example, has used this latter definition of C_S in his investigation of three-aperture einzel lenses. As is the case with the focal properties, the projective and objective spherical aberration are the same for weak lenses. The dimensionless aberration constant C_S/f given by Liebmann is of the projective type and thus, as we might expect, there is good correlation between our values and Liebmann's for only the weaker lenses. This is shown in the C_S/f curves vs T/D in Fig. 7. Arrows indicate the values of T/D where projective and objective focal properties for these lenses begin to differ and therefore locate points where differences in C_S/f for the two methods should be expected to begin.

In a more recent work Heddle and Kurepa have published some measured focal properties for symmetrical three cylinder lenses.¹¹ In essence their measurement technique consisted of focusing an object aperture onto an image aperture for various object and image distances. The focus condition

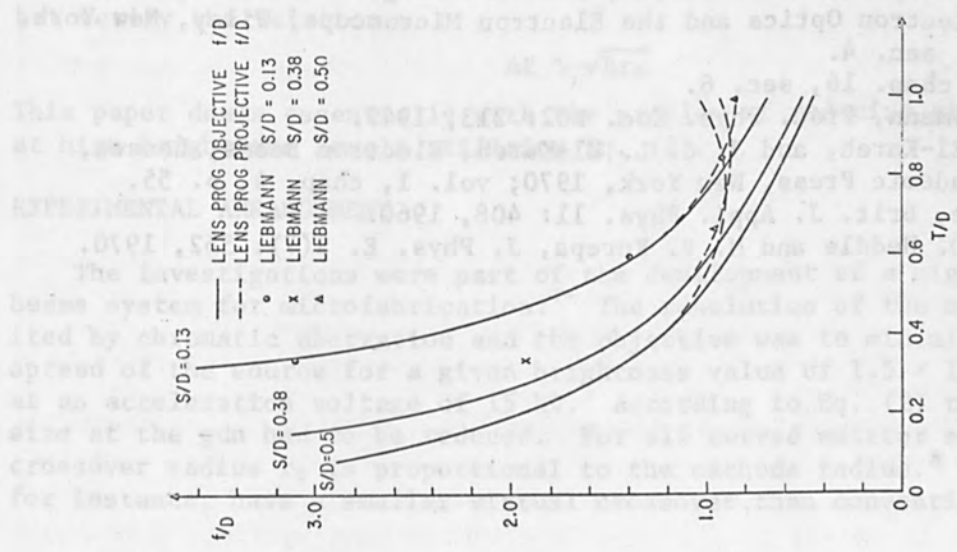


FIG. 6.--Focal length comparison for lens program and Liebmann's experimental values.

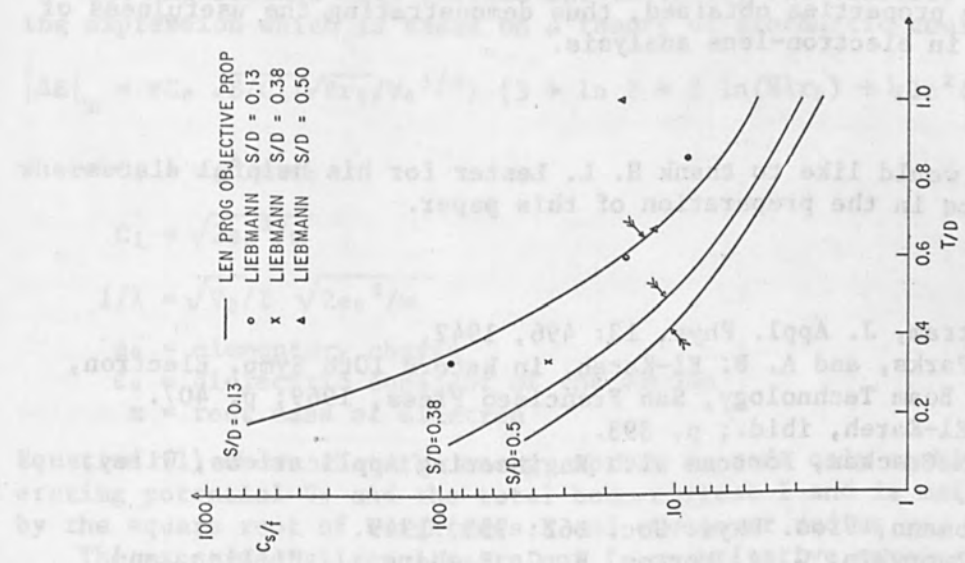


FIG. 7.--Spherical aberration comparison for lens program and Liebmann's experimental values.

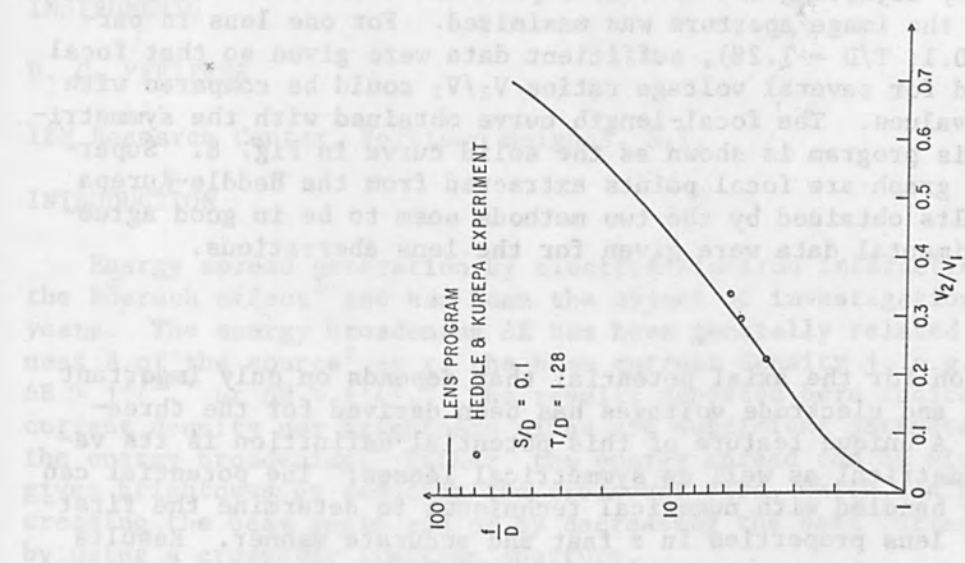


FIG. 8.--Focal-length comparison for lens program and Heddle-Kurepa experimental values.

was determined by adjusting the electrode potentials so that the current passing through the image aperture was maximized. For one lens in particular ($S/D = 0.1$; $T/D = 1.28$), sufficient data were given so that focal lengths obtained for several voltage ratios V_2/V_1 could be compared with our calculated values. The focal-length curve obtained with the symmetrical lens analysis program is shown as the solid curve in Fig. 8. Superimposed on this graph are focal points extracted from the Heddle-Kurepa data. The results obtained by the two methods seem to be in good agreement. No experimental data were given for the lens aberrations.

V. CONCLUSION

An expression for the axial potential that depends on only important lens dimensions and electrode voltages has been derived for the three-cylinder lens. A unique feature of this potential definition is its validity for asymmetrical as well as symmetrical lenses. The potential can be conveniently handled with numerical techniques to determine the first- and third-order lens properties in a fast and accurate manner. Results and literature comparisons presented verify the low computer run time and accuracy of the properties obtained, thus demonstrating the usefulness of this potential in electron-lens analysis.

ACKNOWLEDGMENT

The author would like to thank H. L. Lester for his helpful discussions and advice in the preparation of this paper.

REFERENCES

1. S. Bertram, *J. Appl. Phys.* 13: 496, 1942.
2. H. G. Parks, and A. B. El-Kareh, in *Record 10th Symp. Electron, Ion, and Laser Beam Technology*, San Francisco Press, 1969; p. 407.
3. A. B. El-Kareh, *ibid.*; p. 393.
4. D. D. McCracken, *Fortran with Engineering Applications*, Wiley, New York, 1969.
5. G. Liebmann, *Proc. Phys. Soc.* B62: 753, 1949.
6. V. K. Zworykin, G. A. Morton, E. G. Ramberg, J. Hillier, and A. W. Vance, *Electron Optics and the Electron Microscope*, Wiley, New York, 1945; chap. 16, sec. 4.
7. *Ibid.*; chap. 16, sec. 6.
8. G. Liebmann, *Proc. Phys. Soc.* B62: 213, 1949.
9. A. B. El-Kareh, and J. C. L. El-Kareh, *Electron Beams, Lenses, and Optics*, Academic Press, New York, 1970; vol. 1, chap. 4, p. 55.
10. J. Vine, *Brit. J. Appl. Phys.* 11: 408, 1960.
11. D. W. O. Heddle and M. V. Kurepa, *J. Phys. E.* 3(7): 552, 1970.

EXPERIMENTAL INVESTIGATION OF ENERGY BROADENING IN ELECTRON OPTICAL INSTRUMENTS

H. C. PFEIFFER

IBM Research Center, Yorktown Heights, N.Y.

INTRODUCTION

Energy spread generation by electron-electron interaction is known as the Boersch effect¹ and has been the object of investigations for many years. The energy broadening ΔE has been generally related to the brightness B of the source² or to the beam current density j , e.g., $\Delta E \sim j$,^{1,3} $\Delta E \sim j^{1/2}$,⁴ or $\Delta E \sim j^{1/3}$.⁵ The results reported here indicate that neither current density nor brightness alone are sufficient parameters to describe the energy broadening. Rather, the energy spread can be minimized for a given brightness by reducing the crossover size, which can be done by increasing the beam angle and/or by decreasing the beam current or simply by using a crossover limiting aperture.

The experiments were carried out to verify the validity of the following expression which is based on a theory of stochastic coulomb interaction:⁶

$$|\Delta E|_m = \pi C_0 \sqrt{8/C_1} (\sqrt{Br_0}/V_0^{1/4}) [3 + \ln 2 + 2 \ln(8\lambda r_0) + \frac{1}{4} \ln^2(8\lambda r_0)]^{1/2} \quad (1)$$

where $C_0 = e_0^2/4\pi\epsilon_0$

$$C_1 = \sqrt{2e_0^3/m}$$

$$1/\lambda = \sqrt{V_0/I} \sqrt{2e_0^3/m}$$

e_0 = elementary charge

ϵ_0 = dielectric constant of the vacuum

m = rest mass of electron

Equation (1) shows that the energy spread depends only weakly on the accelerating potential V_0 and the total beam current I and is mainly affected by the square root of brightness B and crossover radius r_0 .

The experimental results are not in quantitative agreement with (1) but verify the relation

$$\Delta E \sim \sqrt{Br_0} \quad (2)$$

This paper deals essentially with the problem of reducing the energy spread at high brightness levels utilizing Eq. (2).

EXPERIMENTAL ARRANGEMENT

The investigations were part of the development of a high current square beams system for microfabrication.⁷ The resolution of the system was limited by chromatic aberration and the objective was to minimize the energy spread of the source for a given brightness value of 1.5×10^5 A/cm²-str at an acceleration voltage of 15 kV. According to Eq. (2) the crossover size at the gun had to be reduced. For all curved emitter surfaces, the crossover radius r_0 is proportional to the cathode radius.⁸ Point cathodes, for instance, have a smaller virtual crossover than conventional tungsten

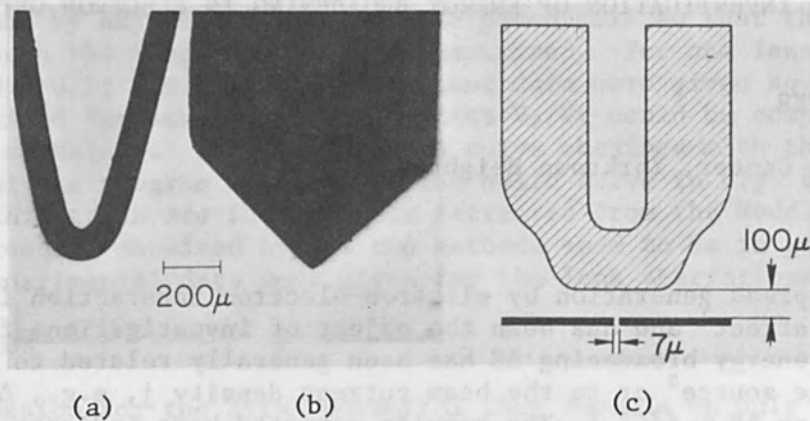


FIG. 1.--Emitter structures: (a) tungsten hairpin emitter (50 x); (b) LaB_6 rod emitter (50 x); (c) aperture-limited LaB_6 emitter.

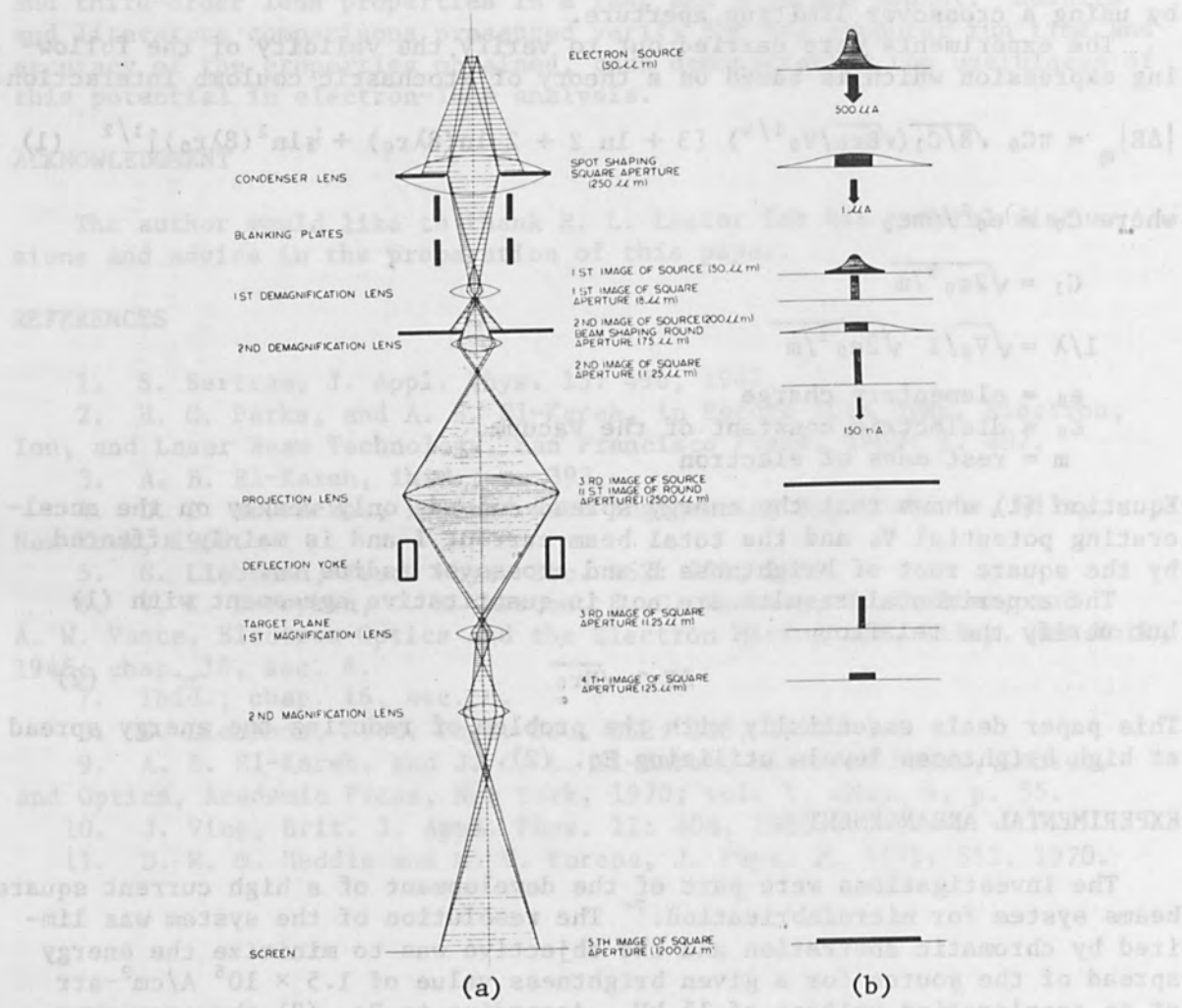


FIG. 2.--Imaging concept: (a) beam configuration; (b) intensity distribution in image planes.

hairpins.⁹ A pointed LaB₆ emitter¹⁰ has therefore been compared with a tungsten hairpin in a conventional triode gun. Gun No. 3 has a positive grid as a beam limiting aperture and was specially developed as a low energy spread source.¹¹ Figure 1 shows the three emitter structures.

Three basic parameters have been analyzed:

- (a) energy spread ΔE [eV]*
- (b) crossover size r_0 [cm]
- (c) brightness B [A/cm²-str]

All measurements have been carried out on a modular system for microfabrication (Fig. 2).

(a) The energy spread was measured with a retarding potential analyzer¹ that replaced the condenser lens for measurements of the energy broadening at the gun. In order to determine the total energy spread contributing to the chromatic aberration of the projection lens the analyzer was located at the target area. The resolution of the analyzer (< 0.1 eV) had been checked at very low brightness ($< 10^3$ A/cm²-str), where the energy distribution is almost Maxwellian and the width is determined by the temperature of the emitter rather than by Boersch effect.

(b) The size of the gun crossover was measured by imaging the virtual crossover with the condenser lens 1:1 into the target plane (demagnification stages and the projection lens removed). The image was scanned across a test target or calibrated by means of the magnification and viewing stages.

(c) The brightness was determined by measuring spot size, spot current, and beam semi-angle at the target plane with the original set up shown in Fig. 2. Figure 3 shows an oscillograph for spot size and resolution determination. The upper beam trace represent, the integral current signal while the beam is sweeping across a 5- μ m wire. The wire diameter is used for calibration purposes. The lower trace displays the intensity distribution of the square beam. In alternating sequence the beam was scanned perpendicular to this direction to avoid astigmatic beam shape.

RESULTS

Figure 4 shows the relation between energy spread and brightness on a double logarithmic scale for the three different guns. The tungsten hairpin has the highest level of energy spread, as expected--about four times higher than the aperture-limited LaB₆ gun. The gun with the pointed LaB₆ rod emitter has an energy spread up to three times lower than the hairpin gun. The curves demonstrate that there is no fixed relation between energy spread and brightness. However, the measurements verify the relation $\Delta E \sim \sqrt{Br_0}$. This is obvious for the aperture limited gun, where $\Delta E \sim \sqrt{B}$ and $r_0 = \text{constant}$ by definition. For the pointed gun, the crossover radius increases rapidly with brightness. In order to obtain the minimum crossover for a given brightness, the emitter temperature remained always at the upper limit determined by the required life time (2950°K for the tungsten hairpin; approximately 1900°K for the LaB₆ emitters) and the brightness was altered by changing the bias voltage. The emission was strictly space-charge limited and brightness never became independent of emission current. The crossover of the hairpin gun reaches a minimum size and is

* ΔE is in all cases defined for the 1- to (1/e)-range of the distribution which contains approximately 63 per cent of the total current.

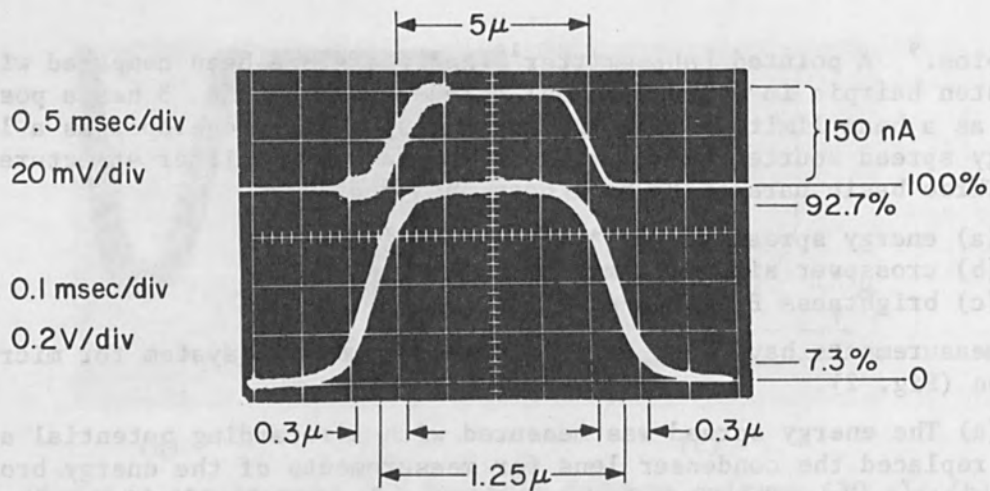


FIG. 3.--Spot-size distribution. Upper trace: scan signal across 5- μ m wire; lower trace: first derivative of signal ramp at upper beam trace (bright line).

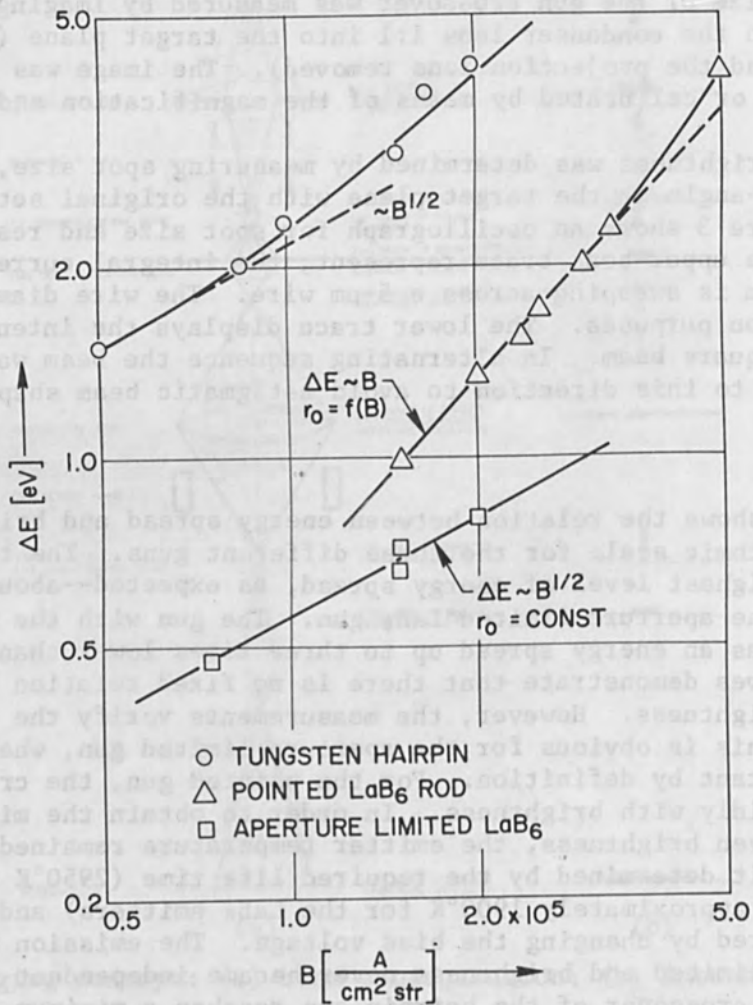


FIG. 4.--Gun energy spread vs gun brightness.

almost constant at lower brightness values and increases slowly at higher brightness.

Figure 5 proves that the hairpin gun and the pointed LaB₆ gun also follow Eq. (2) independently. The different slopes can be explained by the fact that the logarithmic term in Eq. (1) that shows a weak current dependence has been totally neglected so far. However, the emission current of the two guns is high and differs by more than an order of magnitude (see Table I). In this case the logarithmic term varies about 30 per cent, which corresponds to the slope difference in Fig. 5.

TABLE I.--Energy spread and gun data at a brightness of 1.5×10^5 A/cm²-str and an accelerating voltage of 15 kV.

Gun Type	B (A/cm ² -str)	r ₀ (μ)	I _E (μA)	j _{cross} (A/cm ²)	ΔE _{Gun} (eV)	$\frac{\Delta E_{\text{Gun}}}{\sqrt{Br_0}}$	ΔE _{syst} (eV)	ΔE _{tot} (eV)
Tungsten hairpin	1.5×10^5	30	300	10	3.0	1.4	3.5	4.5
Pointed LaB ₆ rod		4.5	25	30	0.95	1.2	2.2	2.4
Aperture-limited LaB ₆		3.5	2.7	6.5	0.65	1.0	1.6	1.85

In addition to the thermal energy spread ΔE_{th} and the energy broadening at the gun crossover ΔE_{1.cross} which are combined in ΔE_{gun}, an energy broadening ΔE_{syst} due to interactions at the column crossovers contributes to the total energy spread:

$$\begin{aligned}
 (\Delta E_{\text{gun}})^2 &= (\Delta E_{\text{th}})^2 + (\Delta E_{1.\text{cross}})^2 \\
 (\Delta E_{\text{tot}})^2 &= (\Delta E_{\text{gun}})^2 + (\Delta E_{\text{syst}})^2
 \end{aligned}
 \tag{3}$$

Figures 6 and 7 show the drastic increase in energy spread due to ΔE_{syst}. The curve for ΔE_{tot} in Fig. 6 has the same slope as ΔE_{gun} ($\sim \sqrt{B}$) which is to be expected if ΔE_{syst} follows Eq. (2) and all column crossovers remain constant with brightness.

Figure 7 confirms $\Delta E_{\text{syst}} \sim \sqrt{Br_n}$ because the imaging concept provides that all column crossovers r_n are independent of brightness.

Table I gives a comparison of the parameters for all three guns at the required systems brightness of 1.5×10^5 A/cm²-str. The crossover radius varies by about one order of magnitude; the emission current I_E varies by more than two orders of magnitude. There is obviously no fixed relation between current density of the gun crossover j_{cross} and ΔE_{gun} as well as between brightness and ΔE.

Finally, Fig. 8 shows the systems performance for the three different guns. The edge resolution was measured by means of scanning techniques as shown in Fig. 3. The system was designed for an optimum resolution of 0.25 μm and a target current of 150 nA in a square spot of 1.25 μm. The total aberrations--except chromatic aberration--have been kept below 0.2 μm and an energy spread of about 1 eV was tolerable. Only the aperture-limited LaB₆ gun provides the necessary low energy spread to meet the specifications but is restricted to a very narrow range of operation. The pointed LaB₆ gun has substantially lower energy spread than the tungsten hairpin gun at $1-2 \times 10^5$ A/cm²-str and offers the additional advantage of very high potential brightness values. However, the chromatic aberration of the system increases rapidly with increasing brightness.

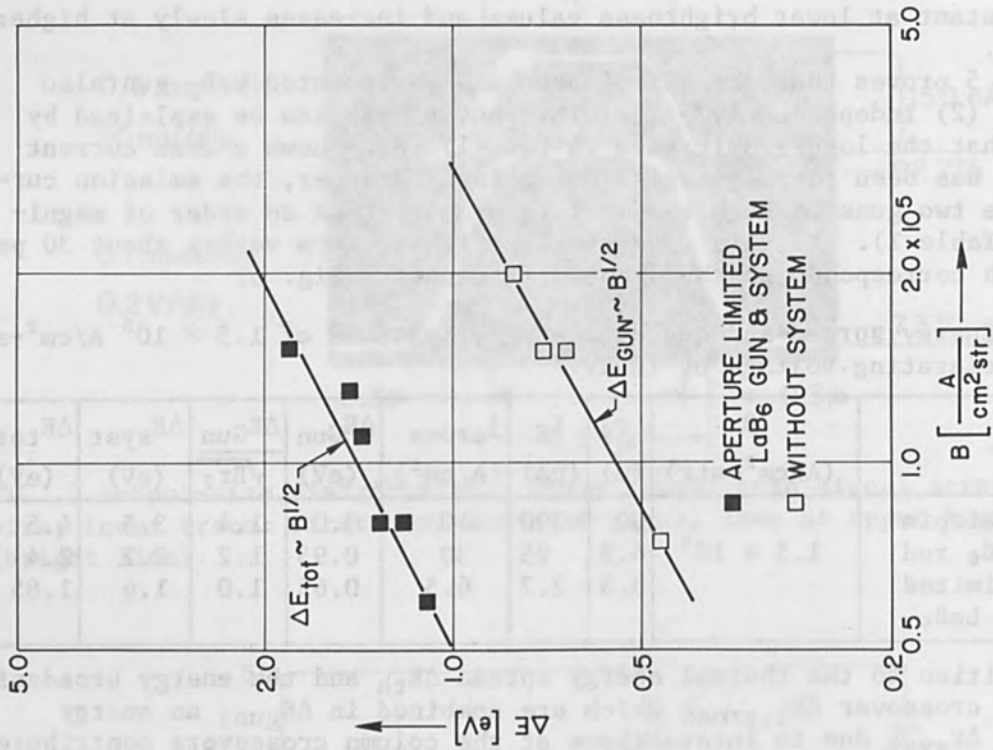


FIG. 6.--Energy spread ΔE_{tot} , ΔE_{gun} vs brightness.

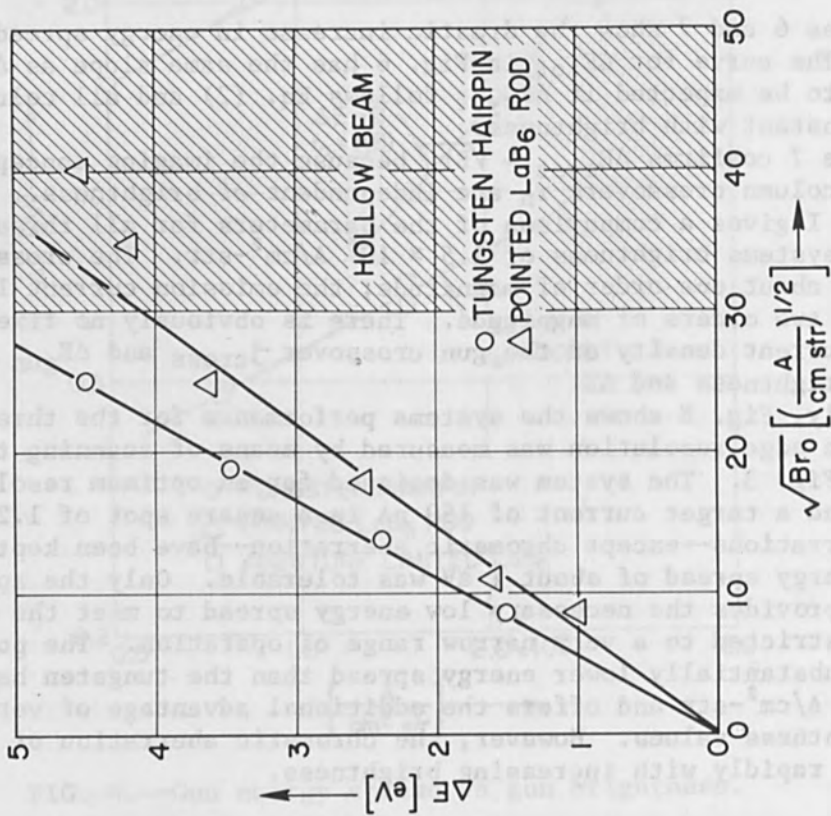


FIG. 5.-- $\Delta E \sim \sqrt{Br_0}$.

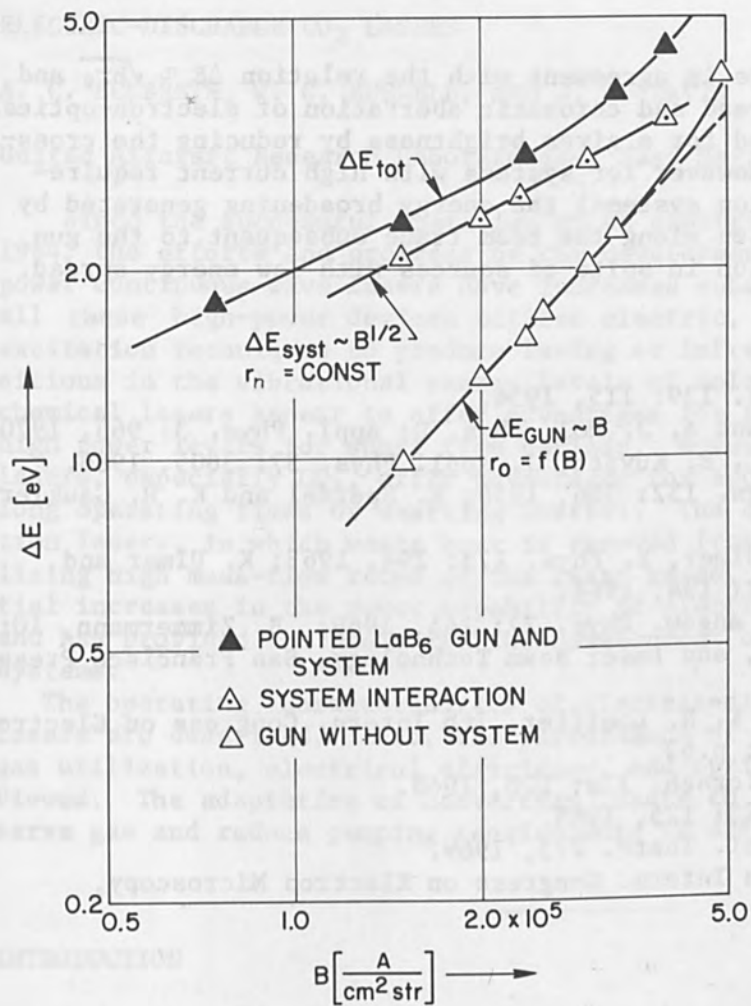


FIG. 7.-- $(\Delta E_{tot})^2 = (\Delta E_{gun})^2 + (\Delta E_{syst})^2$ vs brightness.

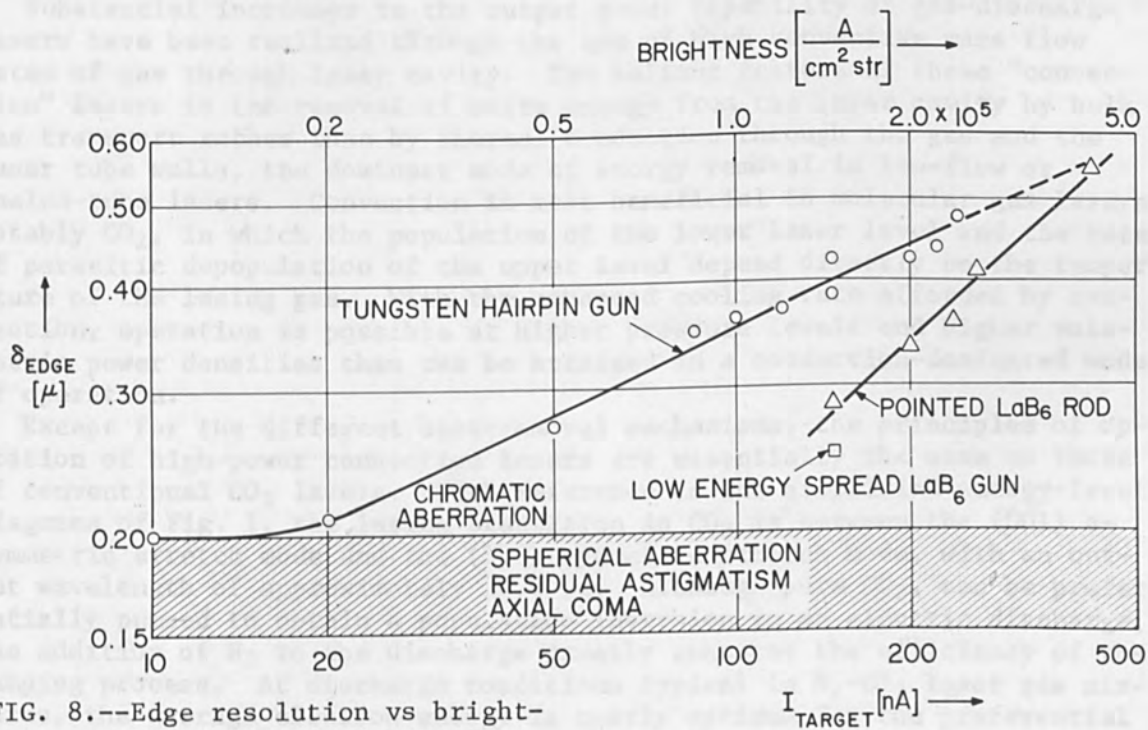


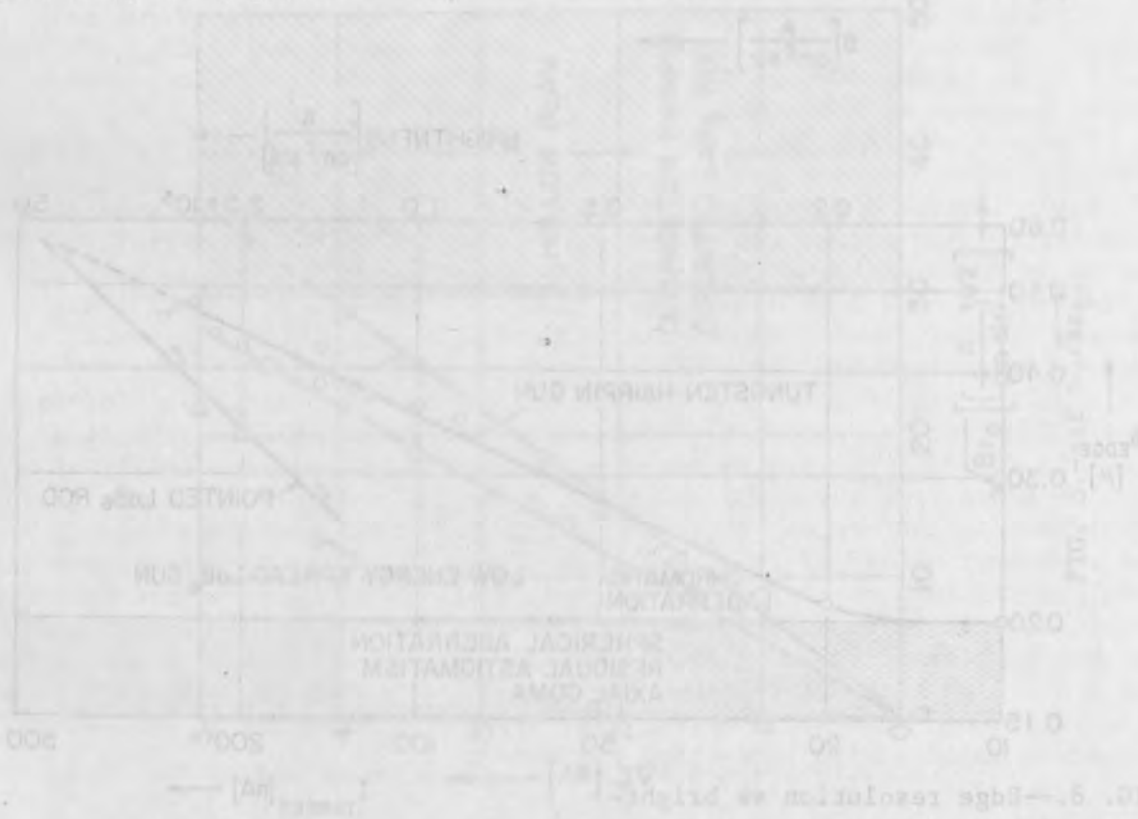
FIG. 8.--Edge resolution vs brightness and beam current at target.

CONCLUSION

The reported results are in agreement with the relation $\Delta E \sim \sqrt{Br_0}$ and demonstrate that energy spread and chromatic aberration of electron-optical instruments can be minimized for a given brightness by reducing the cross-over size of the source. However for systems with high current requirements (e.g., microfabrication systems) the energy broadening generated by electron-electron interaction along the beam trace subsequent to the gun represents a basic limitation in spite of sources with low energy spread.

REFERENCES

1. H. Boersch, Z. Phys. 139: 115, 1954.
2. W. H. J. Anderson and A. J. Mol, Phys. D: Appl. Phys. 3: 965, 1970.
3. J. H. Simpson and C. E. Kuyatt, J. Appl. Phys. 37: 3805, 1966.
4. W. Dietrich, Z. Phys. 152: 306, 1958; R. Speidel and K. H. Gaukler, Z. Phys. 208: 419, 1968.
5. D. Hartwig and K. Ulmer, Z. Phys. 173: 294, 1963; K. Ulmer and B. Zimmermann, Z. Phys. 182: 194, 1964.
6. K. H. Loeffler, Z. angew. Phys. 27: 145, 1969; B. Zimmermann, 10th Symposium on Electron, Ion, and Laser Beam Technology, San Francisco Press, 1969: p.297.
7. H. C. Pfeiffer and K. H. Loeffler, 7th Intern. Congress on Electron Microscopy, Grenoble, 1970; p.63.
8. R. Lauer, Z. Naturforsch. 23a: 100, 1968.
9. R. Speidel, Optik 23: 125, 1965.
10. A. N. Broers, J. Sci. Instr. 273, 1969.
11. K. H. Loeffler, 7th Intern. Congress on Electron Microscopy, Grenoble, 1970; p.77.



SESSION ON LASER TECHNOLOGY

ELECTRIC-DISCHARGE CO₂ LASERS

A. C. ECKBRETH, W. G. BURWELL, AND J. W. DAVIS

United Aircraft Research Laboratories, East Hartford, Conn.

Since the successful operation of an electric-discharge CO₂ laser in 1964, the efforts and progress on the development of efficient, high-power continuous-wave lasers have increased substantially. Practically all these high-power devices utilize electric, gas-dynamic, or chemical excitation techniques to produce lasing at infrared wavelengths from transitions in the vibrational energy levels of molecules. Gas-dynamic and chemical lasers appear to offer advantages for applications requiring very high power levels for short time periods. However, electric-discharge lasers, especially CO₂, offer advantages for applications that require long operating times or exacting control. The development of CO₂ convection lasers, in which waste heat is removed from the laser cavity by utilizing high mass-flow rates of the laser gases, has resulted in substantial increases in the power capability of electric-discharge CO₂ lasers and has provided the basis for the development of compact high-power laser systems.

The operating characteristics of electric-discharge CO₂ convection lasers are described. Also, the performance of these lasers in terms of gas utilization, electrical efficiency, and optical beam quality is reviewed. The adaptation of convection lasers to a closed-gas cycle to conserve gas and reduce pumping requirements is also discussed.

INTRODUCTION

Substantial increases in the output power capability of gas-discharge lasers have been realized through the use of high convective mass flow rates of gas through laser cavity. The salient feature of these "convection" lasers is the removal of waste energy from the laser cavity by bulk gas transport rather than by thermal conduction through the gas and the laser tube walls, the dominant mode of energy removal in low-flow or sealed-tube lasers. Convection is most beneficial in molecular gas lasers, notably CO₂, in which the population of the lower laser level and the rate of parasitic depopulation of the upper level depend directly on the temperature of the lasing gas. With the enhanced cooling rate afforded by convection, operation is possible at higher pressure levels and higher volumetric power densities than can be attained in a conduction-dominated mode of operation.

Except for the different heat-removal mechanisms, the principles of operation of high-power convection lasers are essentially the same as those of conventional CO₂ lasers. With reference to the simplified energy-level diagrams of Fig. 1, the lasing transition in CO₂ is between the (001) asymmetric stretch mode and the (100) symmetric stretch mode, with an output wavelength of approximately 10.6 μm . Although pure CO₂ can be preferentially pumped to obtain a population inversion in an electric discharge, the addition of N₂ to the discharge greatly enhances the efficiency of the pumping process. At discharge conditions typical in N₂-CO₂ laser gas mixtures, the average electron energy is nearly optimum for the preferential

excitation of the vibrational levels of N_2 by direct electron impact.^{1,2} The upper laser level (001) of CO_2 is in turn pumped by the near-resonant transfer of energy from the $v = 1$ level of N_2 . A third gaseous constituent, He, is used in CO_2 lasers to promote the relaxation of the lower laser level (100) by increasing the rate of relaxation from the (010) bending-mode level to the (000) ground-state level, the rate-limiting step in the depopulation process. Furthermore, the addition of helium increases the heat capacity (because of an increase in operating pressure) and the thermal conductivity of the gas mixture, and thereby has the added beneficial effect of lowering the gas temperature. The enhanced thermal conductivity of the mixture, in turn, leads to more uniform and stable operation of the discharges at high electrical power levels.

The operation of electric-discharge CO_2 lasers at multikilowatt cw power levels was first demonstrated^{3,4} with conventional slow-flow lasers, with reported³ power levels up to 8800 W with the folded-tube configuration shown in Fig. 2. However, the laser tubes employed in these important early demonstrations were inordinately long, over 200 m for the 8800-W power level. The great lengths required were a direct result of the limitation in the rate of waste heat removal by the thermal conduction process, a process that restricts power scaling to a length dependence rather than a more general volume dependence. In practical conventional CO_2 lasers, the output power per unit length is typically in the range from 50 to 100 W/m, almost independent of tube diameter.

ELECTRIC-DISCHARGE MIXING LASERS

The beneficial effect of employing gas-convection cooling to achieve high output powers was first demonstrated with a mixing laser,⁵ in a configuration substantially different from Patel's⁶ original CO_2 laser. In the high-flow mixing laser (Fig. 3), N_2 is excited in a discharge tube external to the laser cavity and the excited N_2 flows into a laser channel of rectangular cross section. Cold CO_2 is injected into the excited N_2 flow uniformly along the width of the channel. The optical axis is aligned along the width of the channel and optical power is extracted transverse to the flow. Mixing lasers of circular cross section and the employment of fast-flow techniques and with the optical and flow axes aligned have also been investigated.^{7,8} Upon mixing, vibrational energy is transferred from the excited N_2 to the CO_2 , and a population inversion is obtained in the CO_2 . The mixing laser is feasible because of the very slow relaxation of excited N_2 , so that transport of the excited N_2 from the discharge to the laser cavity can be readily accomplished with a negligible loss in the stored vibrational energy.

Theoretically,² if the electric discharge can be operated at conditions which provide E/N (electrical field/neutral density) values in the range between 10^{-16} to 10^{-15} V-cm², large fractions of the electrical input power can be deposited in the vibrational levels of N_2 , thus providing a very strong and efficient laser pump. This theoretical result is shown in Fig. 4, where it can be seen that 90% of the electrical power should be deposited into $v = 1-8$ levels of nitrogen at a value of E/N of 2×10^{-16} V-cm². Without any auxiliary means of ionization, typical discharges in high flow lasers have been found to operate in the range from 2 to 4×10^{-16} V-cm, indicating that from 60-90 per cent of the power should be deposited in the appropriate vibrational levels. The data in Fig. 5,

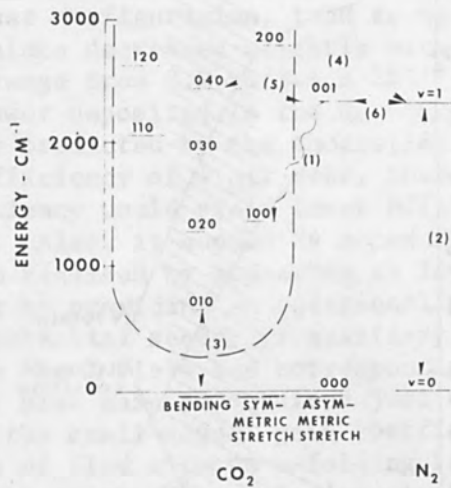


FIG. 1.--Energy transfer processes in CO₂ lasers.

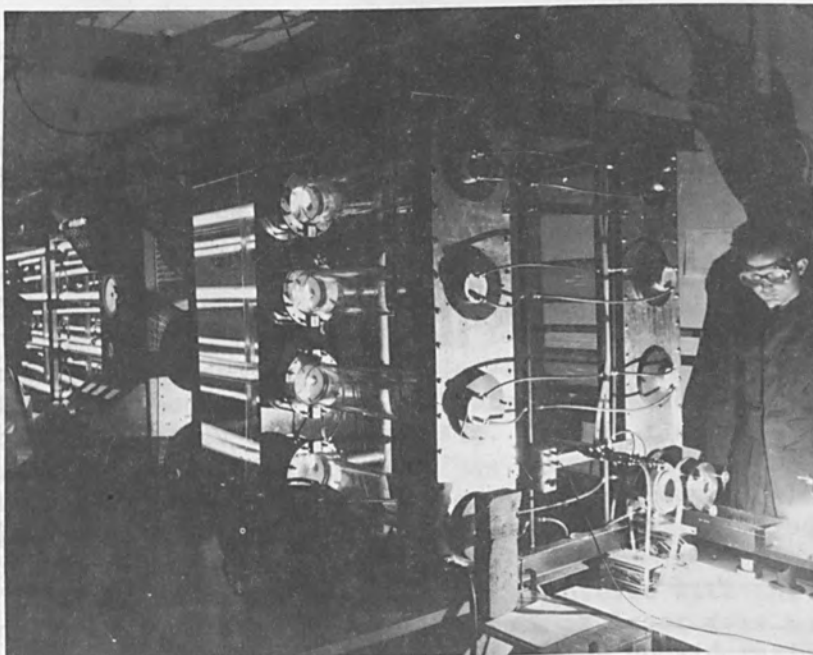


FIG. 2.--Raytheon high-power folded-tube conventional laser.

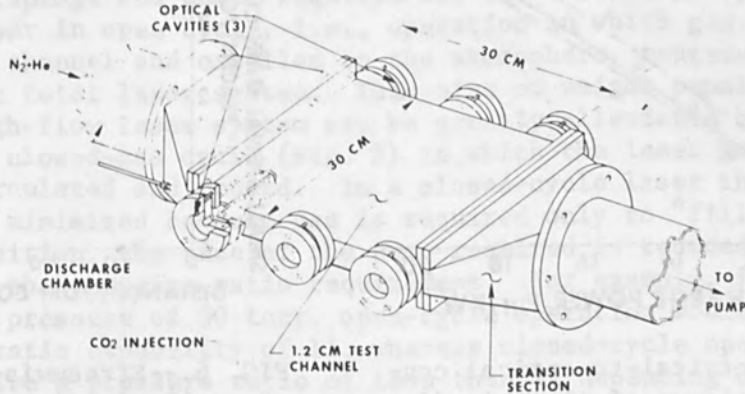


FIG. 3.--Electric-discharge mixing laser.

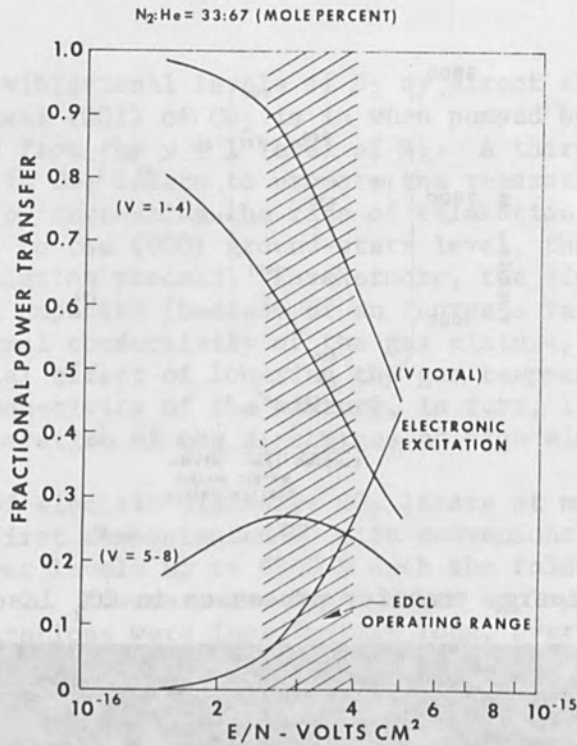


FIG. 4.--Fractional power transfer in N_2 -He electric discharge.

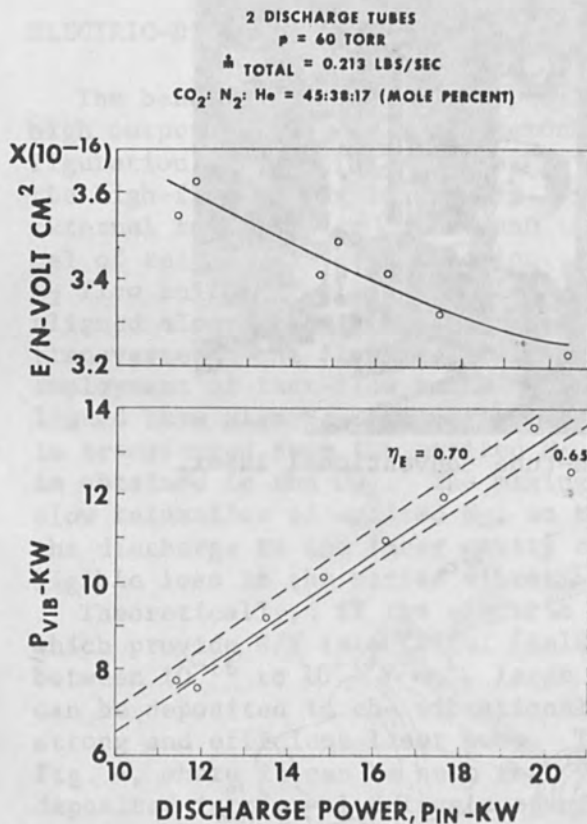


FIG. 5.--Electrical-to-optical conversion efficiency of electric-discharge laser.

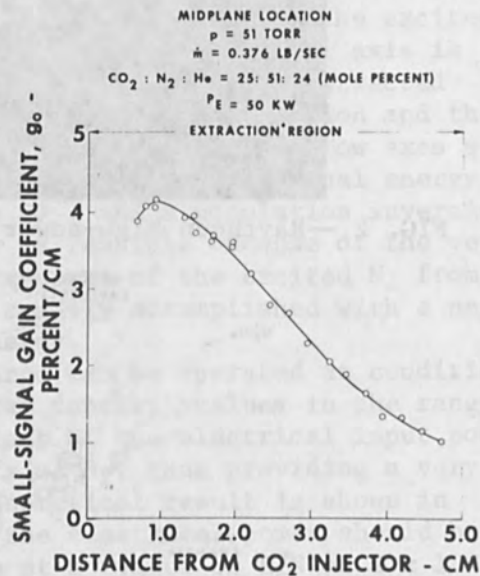


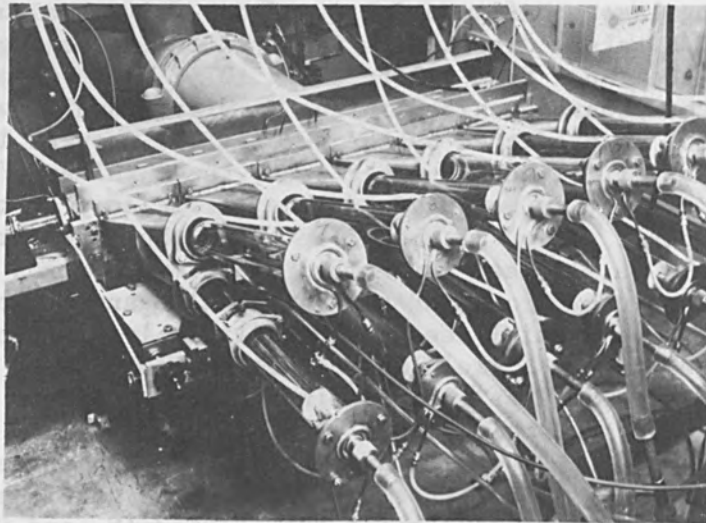
FIG. 6.--Streamwise distribution of small-signal gain coefficient in electric-discharge mixing laser.

taken with a mixing laser configuration, tend to verify the theory. As noted in Fig. 5, E/N values decreased slightly with increasing power, but were generally in the range from 3.2 to 3.6×10^{-16} V-cm². The corresponding fraction of power deposited in the N₂ vibrational levels was between 0.65 and 0.70, as predicted by the theoretical results in Fig. 4. With a laser quantum efficiency of 4 per cent, these values of vibrational excitation efficiency would yield laser efficiency in the range from 26 to 29 per cent. Also, it should be noted that further increases in efficiency should be realized by operating at lower values of E/N. Control of E/N is possible by providing an additional means of ionization (e.g., low ionization potential seeds, rf auxiliary ionization, etc.), in the discharge to reduce the E field and correspondingly, E/N.

In the mixing laser peak gain is obtained just downstream of the N₂-CO₂ mixing region, and the small-signal gain coefficient then decays spatially in the direction of flow with an e-folding length approximately equal to $\frac{v}{p} (p\tau)_u$, where v is the flow velocity, p the static pressure, and $(p\tau)_u$ the collisional decay constant for the grouped (N₂ and CO₂) upper laser level. A typical distribution of the small-signal gain is shown in Fig. 6. Operation at pressures up to 100 torr has been achieved with flow velocities in the range from 100 to 200 m/sec. Peak small-signal gains of 6 %/c have been measured at a pressure of approximately 40 torr.

In the high-flow mixing laser, power is extracted transverse to the flow direction by either oscillator or amplifier optics in the vicinity of the peak-gain region. With a mixing laser having a flow channel 1 m wide by 2 cm high (Fig. 7), a cw output power of over 11 kW has been obtained with hole-couple oscillator optics. In this laser 12 separate discharge tubes, each 45 cm long, were employed for excitation; and the conversion efficiency from the electric-discharge power to optical power was 13.5 per cent at the 11-kW level. In operation at lower power levels, efficiencies up to 18 per cent have been achieved. In yet another mixing laser investigation,⁹ 1.2 kW was obtained from a channel 1.27 cm high by 20 cm wide employing amplifier optics as shown in Fig. 8. The electrical to optical conversion efficiency was 9 per cent. This investigation also demonstrated the efficacy of using the mixing laser as an efficient pulse amplifier provided the characteristics of the flow are carefully tailored to the properties of the optical pulse train.

Although impressive performance has been achieved with the high-flow mixing laser, further development of this type of laser does not seem warranted at this time. This position is based on consideration of the ultimate requirements for high-flow laser systems. From a systems standpoint the gas tankage and pumps required for the continuous operation of a high-flow laser in open cycle, i.e., operation in which gas is pumped from the laser channel and expelled to the atmosphere, represent a large fraction of the total laser system. This size or weight penalty associated with a high-flow laser system can be greatly alleviated by operating the laser in a closed-gas cycle (Fig. 9) in which the laser gases are continuously recirculated and reused. In a closed-cycle laser the gas tankage problem is minimized because gas is required only to "fill" the laser system. In addition, the size of the pump required is reduced, because of a reduction in the pressure-ratio requirement. For example, for a laser operating at a pressure of 50 torr, open-cycle operation would require a pump pressure-ratio capability of 15, whereas closed-cycle operation would typically require a pressure ratio of less than 2, depending on the pressure losses in the gas-circulating system. Hence, substantial weight sav-



Electric-discharge mixing laser, 11 kW.

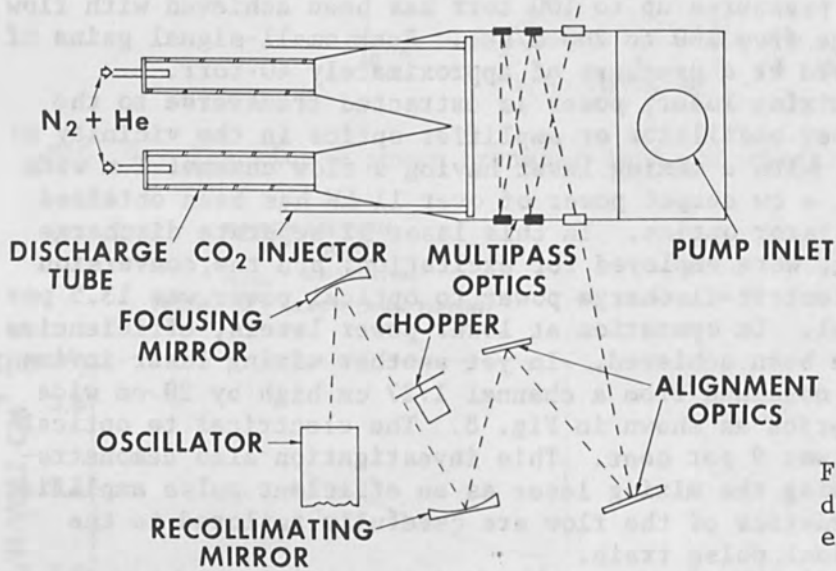


FIG. 8.--Electric-discharge mixing laser amplifier, 1 kW.

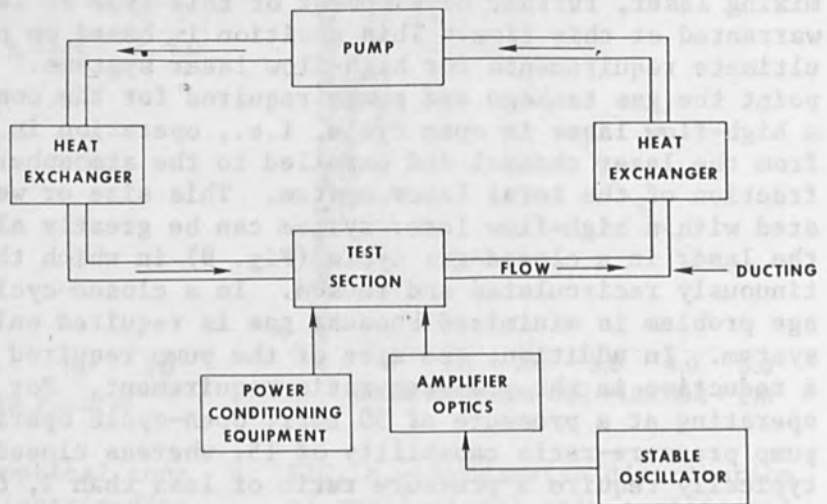


FIG. 9.--Closed-cycle laser system schematic.

ings are realized in a closed-cycle system because, for a given volumetric pumping capacity, pump weight and size are almost directly proportional to pressure ratio. It should be noted that with the mixing laser, systems analysis reveals that the benefits derived from the closed-cycle operation are in large part offset by the penalties associated with the required gas separator to remove CO_2 from the N_2 and He. Thus, the mixing laser cannot be readily adapted for use in an efficient and compact closed-cycle system.

PREMIXED ELECTRIC-DISCHARGE CONVECTION LASERS

High-flow lasers in which the gaseous constituents are premixed are better suited than the mixing laser for adaptation in a closed gas cycle. Therefore, more recent work, mostly within the last three years, has concentrated on the development of high-flow premixed lasers. Although numerous laser configurations have been suggested and tested, in general these lasers can be categorized into three types in accordance with the relative orientation of the directions of flow, electric discharge, and optical extraction. Schematics of these three different types of electric-discharge convection lasers are depicted in Fig. 10 as (1) the coaxial,^{8,10} in which the direction of the discharge, flow, and optical extraction are coaxial within an essentially cylindrical laser tube; (2) the cross-beam,^{11,12} in which the discharge is maintained in the direction of flow in a channel of rectangular cross section, and power is extracted normal to the flow direction; and (3) the cross flow,^{13,14} in which the discharge is maintained across the flow in a channel of rectangular cross section, and power is extracted normal to the flow direction. Cross-flow lasers have been operated with the discharge maintained both across the height¹³ and across the width of the laser channel.¹⁴ With some lasers of this type, magnetic fields,¹⁴ preionization,¹⁵ and aerodynamic techniques have been employed to stabilize the discharge against the drag forces of the flowing gas.

In these convection lasers, the gas temperature increases in the direction of flow, and there is a maximum length L_m , dictated by the calorimetry of the flowing gas and a critical temperature T_m , beyond which efficient lasing action cannot be maintained. The effect of gas temperature on the population of the important vibrational levels of CO_2 is illustrated in Fig. 11. Here it has been assumed that the population of the upper laser level (001) is held constant by laser pumping action and that the populations of all other levels are in thermal equilibrium at the translational temperature of the gas. The gain of the medium is directly proportional to the difference in population between the upper and lower laser levels, depicted as $(N_{001} - N_{100})$ in Fig. 11. For the conditions assumed in Fig. 11, note that the population inversion is completely destroyed at temperatures above 700°K. In a practical laser T_m is nominally about 500–600°K.

Scaling the convection lasers to higher power levels is based on increasing the mass flow of gas under conditions of constant specific power (optical output power/mass flow), which implies a constant exit temperature. For a laser system with fixed volumetric pumping capacity, and assuming constant efficiency of excitation, the output power is directly proportional to pressure. However, under this constant-specific-power condition, the small-signal gain varies inversely with pressure and with the length L_m of the discharge in the direction of flow. Hence, for a

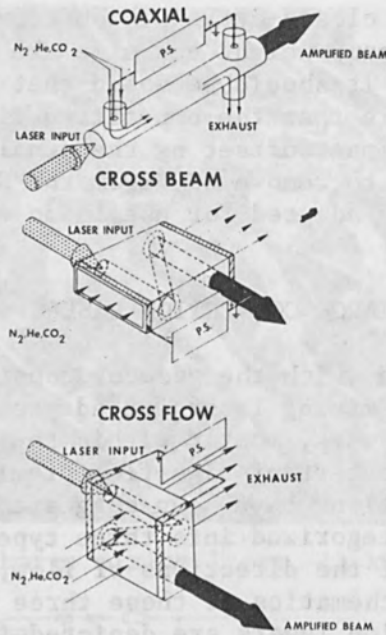


FIG. 10.--Electric-discharge convection laser configurations.

ASSUMPTIONS:

1. 001 LEVEL MAINTAINED AT FRACTIONAL POPULATION OF 0.03 BY PUMPING
2. ALL LEVELS EXCEPT 001 IN THERMAL EQUILIBRIUM AT TRANSLATIONAL TEMPERATURE OF THE GAS

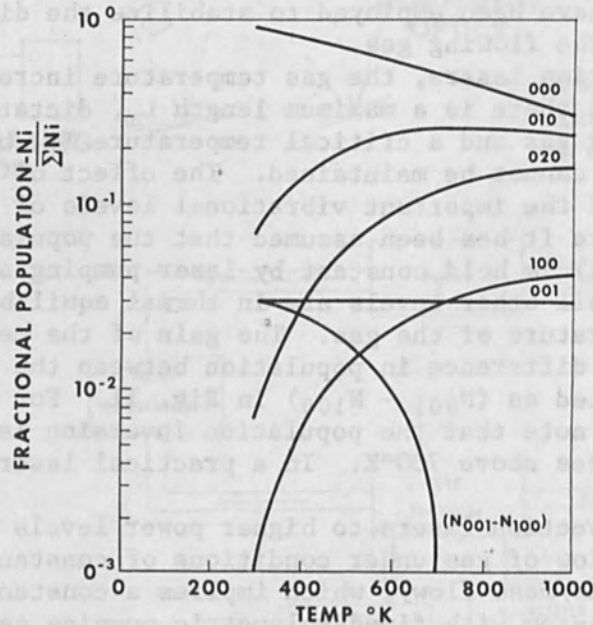


FIG. 11.--Fractional population in CO₂ lasers as function of gas translational temperature.

given cross-sectional area, the small-signal gain of cross-flow lasers is usually somewhat higher than that of the coaxial and cross-beam types, with nominal respective values of 2-4 %/cm compared to 0.5-2 %/cm.

Of the three types of convection lasers, the coaxial laser has been operated most extensively. Although it has been used as a power amplifier, its cylindrical configuration is best suited for use as a laser oscillator. The data shown in Fig. 12 were obtained with a small coaxial laser but illustrate the important operating characteristics of all types of convection lasers. These data were obtained by fitting a 60-cm-long coaxial laser with fully reflecting water-cooled copper mirrors to form an optical cavity with a very high Q. With a cavity of this type over 90 per cent of the available optical power in the active medium is absorbed by the mirrors (and measured calorimetrically), thus providing an excellent technique of measuring the optical power generated. The data were obtained for a variety of mass-flow rates with two different electrode configurations. Both the optical cavity power and the discharge power are normalized to mass flow; and, as shown in Fig. 12, the data for a given electrode configuration all fall on a generalized curve. At low values of discharge specific power conversion efficiencies over 30 per cent were obtained, but the efficiency falls off with increasing power, corresponding to increasing gas temperature. Optical specific powers up to 60 kW per lb/sec were obtained at an efficiency of approximately 20 per cent. Further reductions in optical specific power and efficiency would accrue with beam-power extraction from the cavity. Also, in accordance with the data shown in Fig. 12, trade-offs between efficiency and specific power can be made to optimize the design of a laser system.

The cross-beam laser appears to be the best configuration for generating high output power levels in an efficient and compact laser system. It is most suitable for use as a power amplifier. Recently, Hill¹¹ has reported the achievement of 19.1 kW of continuous optical power in a single-mode beam from this type of laser (Fig. 13). The circulating capacity of the system is 28 000 cfm. The power amplifier utilized 17 passes in a 5.6 x 76 x 100-cm laser channel, and it was driven by a single-mode oscillator with a power level of approximately 120 W. Efficiencies up to 24 per cent have been reported. These results represent a significant milestone in the development of high-power CO₂ lasers and quite vividly demonstrate the beneficial effects of gas convection on laser performance.

Impressive performance has also been demonstrated by Sylvania¹³ with the gas-transport laser and at United Aircraft¹⁴ with a cross-field laser. The Sylvania laser is shown in Fig. 14. It also utilizes a closed-cycle system. Although it uses approximately 3000 cfm to produce 1.1 kW of optical power, it operates with very little pressure loss in the flow system. This low pressure loss is quite significant because it reduces the required size of the pump and the associated power requirements. Sylvania quotes an over-all efficiency of 10 per cent, taking into account the power required for the pump as well as that for the laser discharge.

The United Aircraft cross-field laser (Fig. 15) utilizes a transverse magnetic field to stabilize a single discharge maintained across the width of the flow channel. The discharge configuration is cylindrical in shape and can be well matched to a Gaussian mode of an optical cavity. The strength of the required magnetic field is directly proportional to flow velocity and pressure. Although this laser has only been operated at power levels of approximately 500 W, it does develop very high gain, up to 5 %/cm, because of the relatively small discharge volume. Also, similar to the

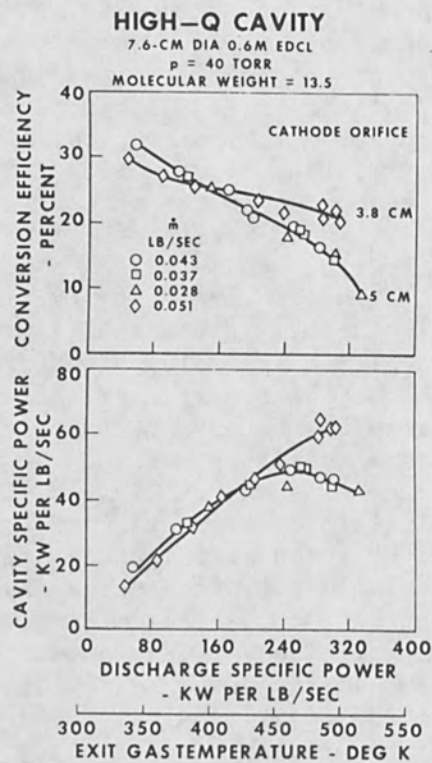


FIG. 12.--Open-cycle performance of coaxial electric-discharge convection laser.

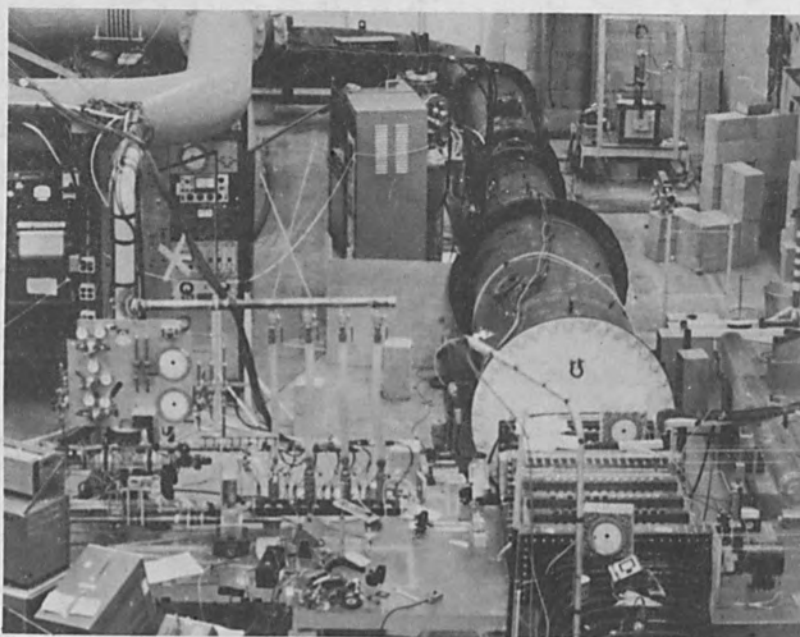


FIG. 13.--Electric Aerodynamic laser system, 19 kW.

HIGH-POWER VISIBLE LASERS...
 Sylvania Laser...
 Control Laser...
 Sylvania Laser...
 Control Laser...
 Sylvania Laser...
 Control Laser...

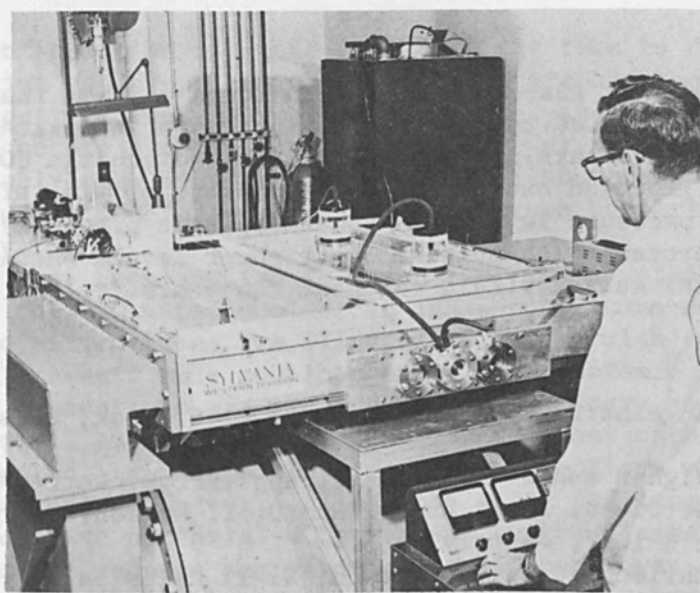


FIG. 14.--Sylvania gas transport laser, 1 kW.

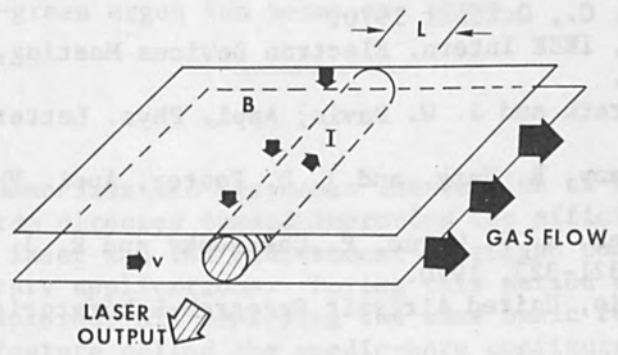


FIG. 15.--Cross-field laser schematic.

Sylvania laser, it has low pressure losses, so that relatively simple, single-stage pumps can be used to circulate the gas. The operating characteristics of both of these lasers indicate that only modified "window fans" will be required for the circulation of gas in future closed-cycle convective lasers.

SUMMARY

The employment of gas-convection techniques to cool the laser medium more effectively has led to substantial increases in optical output power and decreases in the physical size of electric-discharge CO₂ lasers. Furthermore, with improved excitation techniques to provide efficient operation at higher pressure levels (up to atmospheric pressure), extremely compact laser systems with multikilowatt power levels should be available on the commercial market within the next few years.

REFERENCES

1. A. G. Engelhardt, A. V. Phelps and C. G. Risk, Phys. Review 135: 1566, 1964.
2. W. L. Nighan and J. H. Bennett, Appl. Phys. Letters 14: 240, 1969.
3. T. A. Horrigan, R. I. Rudko, and D. T. Wilson, Raytheon Research Division Report S-1037, January 1968.
4. J. J. Ehrlich, G. J. Hutcheson, W. T. Hales, and T. G. Roberts, IEEE Conf. Laser Engineering and Applications, Washington, D. C., June 1967.
5. C. O. Brown, Appl. Phys. Letters 17: 388-391, 1970.
6. C. K. N. Patel, Phys. Rev. Letters 13:6.7, 1964.
7. T. A. Cool and J. A. Shirley, Appl. Phys. Letters 14: 70, 1969.
8. T. F. Deutsch, F. A. Horrigan, and R. I. Rudko, Appl. Phys. Letter 15: 88, 1969.
9. A. C. Eckbreth, J. W. Davis, and E. A. Pinsley, Appl. Phys. Letters 18:73, 1971.
10. C. O. Brown and J. W. Davis, IEEE Intern. Electron Devices Meeting, Washington, D. C., October 1970.
11. A. E. Hill, IEEE Intern. Electron Devices Meeting, Washington, D. C. October 1970.
12. A. C. Eckbreth and J. W. Davis, Appl. Phys. Letters, to be published.
13. W. B. Tiffany, R. Targ, and J. D. Foster, Appl. Phys. Letters 15: 91-93, 1969.
14. C. J. Buczek, R. J. Wayne, P. Chenausky and R. J. Freiberg, Appl. Phys. Letters 16: 321-323, 1970.
15. R. H. Bullis, United Aircraft Research Laboratories, private communication.

HIGH-POWER VISIBLE LASERS FEATURING AN EXTERNALLY CHARGED PLASMA-DISCHARGE BORE FOR STABLE, LONG-LIFE OPERATION*

DAVID E. FLINCHBAUGH

Control Laser-Orlando, Inc., Orlando, Fla.

A unique configuration of noble-gas ion laser tube is discussed. The plasma-tube design employs a current-conducting graphite bore. The system incorporates electrical and optical improvements, such as the ability for self-start, to operate cleanly with minimal bore or electrode erosion, and to perform reliably over long periods of time without the need for gas refill. A thermally stable ceramic-glass structure supports the optical resonator cavity.

This concept has been applied to argon-ion laser systems ranging from 5 mW air-cooled to 22 W water-cooled, in TEM₀₀ continuous-wave operation. Sealed-off fused silica tubes are illustrated, along with recent designs including an all-ceramic tube envelope and a metal-ceramic type. Electrical feedthrough connections are provided for the primary anode, the secondary anode (bore), and the directly heated dispenser cathode. The bore consists of oriented, finned, pyrolytic graphite sections which form a continuous electrical conductor. All points along the length of the bore are held at a positive potential with respect to the plasma discharge. This repelling field reduces positive-ion bombardment, gas cleanup, and material transport to a minimum. Optically contacted vacuum seals are used at the Brewster end windows to avoid introducing contaminants from adhesives.

Primary goals of the present effort are to exploit this configuration for optimum efficiency and rugged, compact packaging. Performance data for tubes with bore lengths from 3 to 140 cm are presented. Laser output power is plotted against discharge current at fixed argon fill pressures for two tube sizes. Discharge voltage versus operating time for 1000 hr is shown for a small 1-W laser tube. Examples of drilling and cutting refractory materials (such as stainless steel, tantalum, and asbestos firebrick) with blue-green argon ion beams are shown.

BACKGROUND

This paper summarizes and discusses the results of a 3-yr gas-ion laser development program directed toward improving the efficiency of operation of this class of laser and the achievement of rugged compact designs for specialized military applications. During this period a variety of laser tube sizes was explored, all employing the same basic features and having a unique design feature called the anodic-bore configuration. This design, along with the use of optical contacting techniques, has permitted the construction of very clean-running high-power and low-power ion laser tubes with long lifetimes in a sealed-off condition. Thus they require no maintenance other than providing power, proper cooling, and a reasonably stable mechanical and thermal environment to maintain optical alignment.

*Portions of this work were sponsored under WPAFB Contract No. F33615-68-C-1397, as reported in AFAL-TR-70-211, August 1970.

APPROACH

Figure 1 illustrates the basic approach we have taken to the construction of ion laser systems. The power supply provides well-regulated dc to the plasma tube. Experiments with SCR controls have led to the use of a simple and very reliable transistor amplifier circuit to achieve voltage adjustment. The solenoid winding around the tube to produce an axial magnetic field is conventional, with a dc supply to power it. The cathode consists of a directly heated dispenser-type barium-impregnated tungsten helix, and the primary anode is also of a hollow configuration made as a molybdenum cylinder. The most unusual feature is the use of the bore as a secondary anode, connected via a bias resistor (the idler resistor) to the primary anode. When the tube draws current, the small potential drop across this resistor maintains a voltage differential of about 10-15 V between the primary and secondary anode and also between the cathode and the cathode end of the secondary anode. This voltage usually adjusts itself to a symmetrical value at each end. The mirrors at each end form the optical resonant cavity. The resonator is mechanically stabilized by the use of a material with a very low coefficient of expansion, the Owens-Illinois CER-VIT ceramic glass, as the mirror support structure, which yields a dimensionally stable optical resonator cavity in the face of small temperature fluctuations during operation of the laser.

RESULTS

Table I illustrates power output in a single transverse mode (TEM_{00}) for all laser output lines as a function of discharge current. It also

TABLE I.--Power output of anodic-bore plasma tube with argon at 240 microns as measured with a Coherent Radiation Model 201 power meter. Magnetic field intensity is 1 kG. Anode to cathode potential is 250 V. Single line data with a Littrow prism.

Discharge current (A)	Power output in TEM_{00} mode (W)		
	All lines	4880 Å	5145 Å
7.0	0.025	0.019	0
9.5	0.100	0.075	0
12.0	1.220	0.175	0
14.5	0.470	0.325	0.035
17.0	1.10	0.515	0.15
19.5	1.55	0.760	0.53
22.0	2.65	1.12	0.92
25.0	4.25	1.67	1.50
27.0	5.30	1.95	2.00
29.5	7.00	2.40	2.50
32.0	8.75	3.00	3.19
34.5	9.80	3.50	3.35
37.0	11.00	3.80	3.75

shows the division of output power in the primary lasing wavelengths of the argon laser system as selected by a Littrow-mounted prism forming one end of the laser cavity. Powers up to 11 W are shown. Figure 2 shows a logarithmic plot of power output versus discharge current comparing our

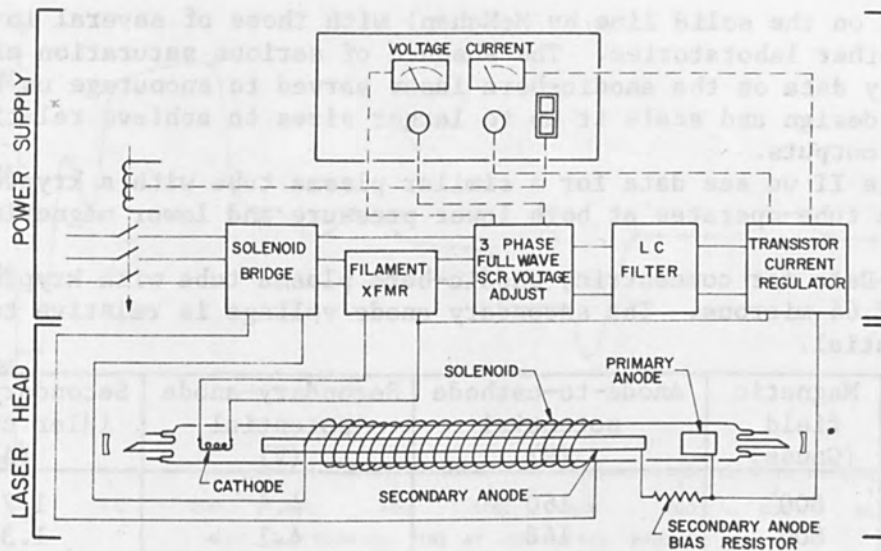


FIG. 1.--Anodic-bore laser system.

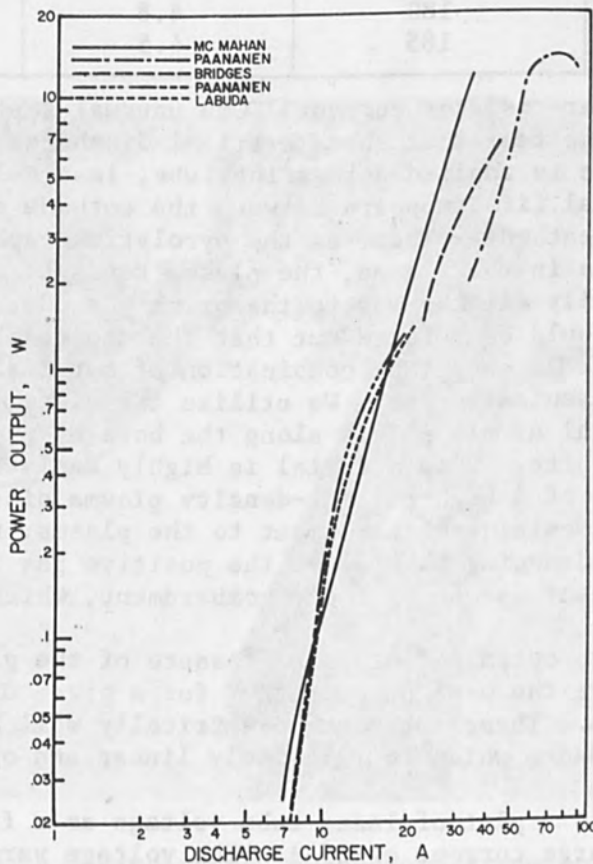


FIG. 2.--Comparison of argon laser power data. TEM₀₀ mode output power is compared with published data of others. Data are for 70-cm-long discharge bore 4 mm in diameter. Comparison data probably for laser action in more than one transverse mode.

data (shown on the solid line by McMahan) with those of several investigators at other laboratories. The absence of serious saturation effects in the early data on the anodic-bore laser served to encourage us to exploit this design and scale it up to larger sizes to achieve relatively high power outputs.

In Table II we see data for a similar plasma tube with a krypton gas fill. This tube operates at both lower pressure and lower magnetic field;

TABLE II.--Data for concentric, anodic-bore plasma tube with krypton at pressure of 64 microns. The secondary anode voltage is relative to a full anode potential.

Discharge current (A)	Magnetic field (Gauss)	Anode-to-cathode potential (V)	Secondary-anode potential (V)	Secondary-anode idler current (A)
10	800	160	4.4	1.77
15	800	168	4.1	1.36
20	800	170	3.7	1.23
25	800	175	2.6	.86
30	800	180	2.8	.94
10	500	175	6.2	2.01
15	500	175	5.4	1.80
20	500	180	5.0	1.66
25	500	180	4.8	1.60
30	500	185	4.5	1.50

Note the value of idler-resistor current. One unusual feature of the anodic-bore tube is the fact that the electrical discharge, once a voltage sufficient to light it is applied across the tube, is a self-initiating one. A large potential first appears between the cathode end of the secondary anode and the cathode. Then, as the pyrolytic graphite bore warms and changes resistance in the plasma, the plasma tends to creep along the bore and travels finally all the way to the primary anode. Thus the tube lights itself. It should be pointed out that the choice of pyrolytic graphite here provides an excellent combination of material properties in an electrical and mechanical sense. We utilize the electrical resistivity to tailor the potential at all points along the bore by proper machining of the pyrolytic graphite. This material is highly resistant to the usual deteriorating effects of a high-current-density plasma discharge. Being charged electrically positive with respect to the plasma, the bore is protected from the most damaging particles, the positive gas ions, and does not suffer a significant amount of ionic bombardment, which makes for unusually long life.

It is important to optimize both the pressure of the gas fill and the magnetic field to give the best power output for a given discharge current or range of operation. These tubes are electrically well behaved and exhibit a dynamic impedance which is relatively linear and of the order of 0.5-1 Ω .

Shown in Fig. 3 is a plot of laser tube voltage as a function of running time at a discharge current of 25 A. The voltage varies about 12 V over a period of 1000 hr. These small voltage changes occur from the fact that the tube is operating at slightly different pressures at different times. There is normally a small difference in pressure between cold (off)

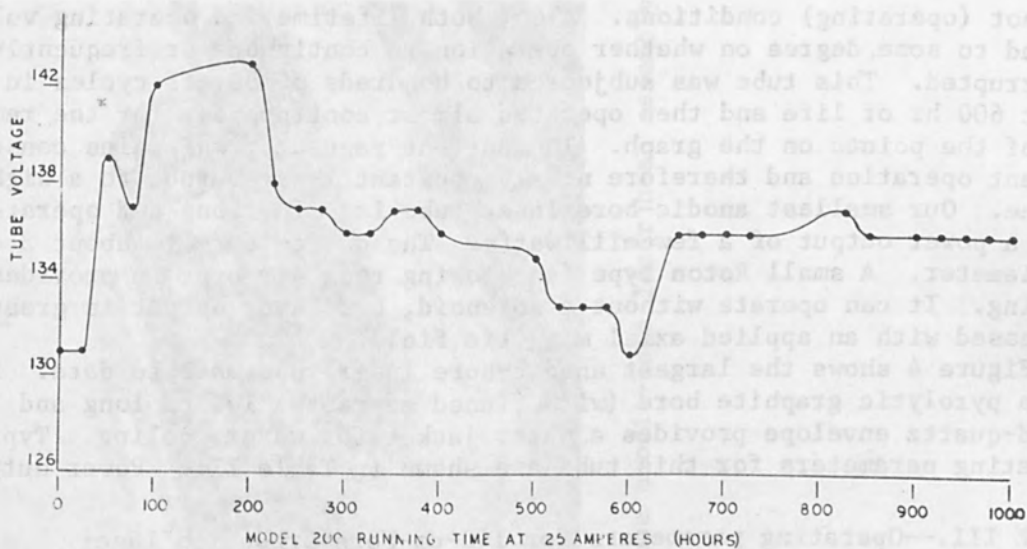


FIG. 3.--Laser-tube voltage vs operating time.

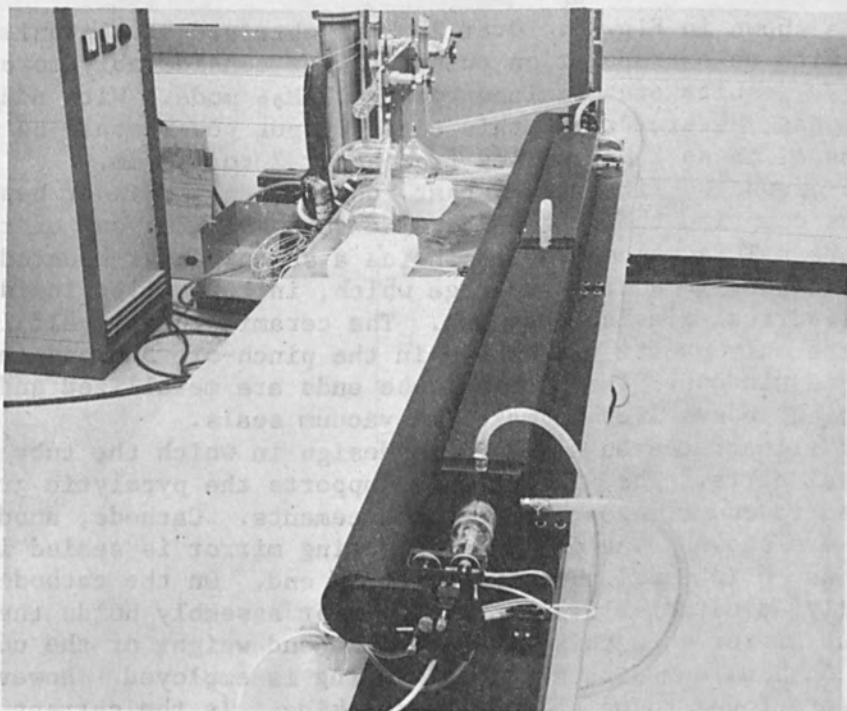


FIG. 4.--High-power 140-cm bore argon ion laser.

and hot (operating) conditions. Also, both lifetime and operating voltage depend to some degree on whether operation is continuous or frequently interrupted. This tube was subjected to hundreds of on-off cycles in the first 600 hr of life and then operated almost continuously for the remainder of the points on the graph. The current regulator maintains constant-current operation and therefore nearly constant laser output to a high degree. Our smallest anodic-bore laser tube is 9 in. long and operates with a power output of a few milliwatts. The quartz bore is about 3 cm in diameter. A small Roton type fan blowing room air over it provides cooling. It can operate without a solenoid, but laser output is greatly increased with an applied axial magnetic field.

Figure 4 shows the largest anodic-bore laser tube made to date. It has a pyrolytic graphite bore (with finned segments) 140 cm long and the fused-quartz envelope provides a water jacket for water cooling. Typical operating parameters for this tube are shown in Table III. Power output

TABLE III.--Operating parameters for 140-cm-bore argon ion laser.

Voltage (V)	592	585
Current (A)	41.0	33.5
Power (W)	18.5	9.0
Pressure (microns)	106	140
Solenoid current (A)	8.0	7.5
Idler current (A)	3.0	2.8
Ballast resistor (Ω)	---	90
Filament current (A)	78 (at 1075°C)	84

vs current is shown in Fig. 5. Over 22 W is obtained at approximately 54 A, along with an extrapolation potential for considerably more power output. These results are obtained for the TEM₀₀ mode. With additional transverse modes, several times this total output power would be obtained. The bore size of these tubes varies from about 2 to 4.5 mm.

Figure 6 shows the first attempt at ruggedizing the laser head package. Metal flanges comprise the ends of ceramic tube sticking out of the solenoid enclosure. This assembly fits inside a set of Invar-mounted mirror assemblies enclosed in a rib-like cage which, in turn, fits inside the polished cylindrical aluminum housing. The ceramic tube itself is aluminum oxide, and the only quartz pieces are in the pinch-off arm and in the Brewster angle windows. The alumina tube ends are metallized and brazed to the metal end assemblies to make the vacuum seals.

Figure 7 illustrates an all-ceramic design in which the tube has no external metal parts. The alumina tube supports the pyrolytic graphite and is sealed to end flanges with ceramic cements. Cathode, anode, and bore pieces are shown. The maximum reflecting mirror is sealed in place and aligned as an integral part of the anode end. On the cathode end flange a fully adjustable Invar mounted mirror assembly holds the long-radius output mirror. In this way both size and weight of the unit are decreased. An aluminum wire solenoid winding is employed. However, alumina tubes were found to be subject to cracking. In the current version the ceramic and pyrolytic graphite and all electrode elements are enclosed in a stainless-steel vacuum jacket which is mechanically extremely rugged. This tube is now being tested.

As a follow-up to our presentation at the previous Symposium, we show three photographs illustrating the material-cutting capabilities of our

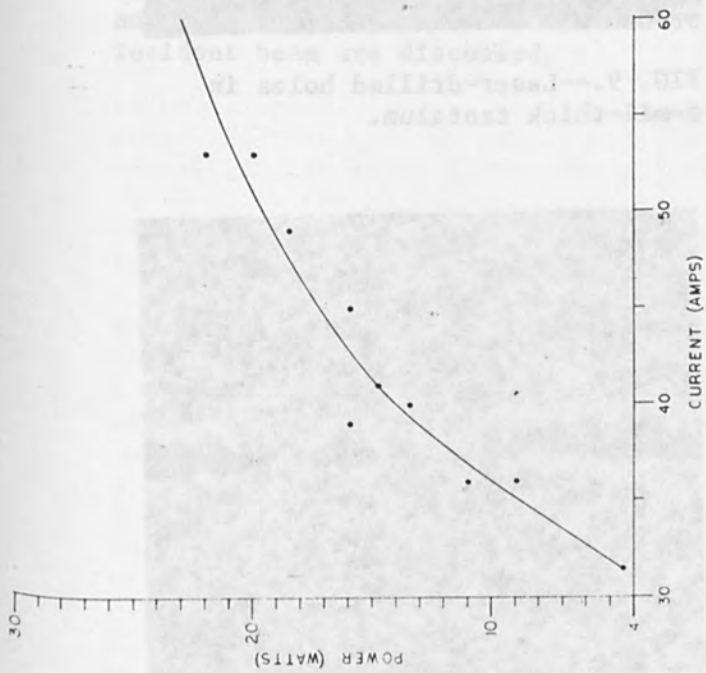


FIG. 5.--High-power argon ion laser output vs discharge current.

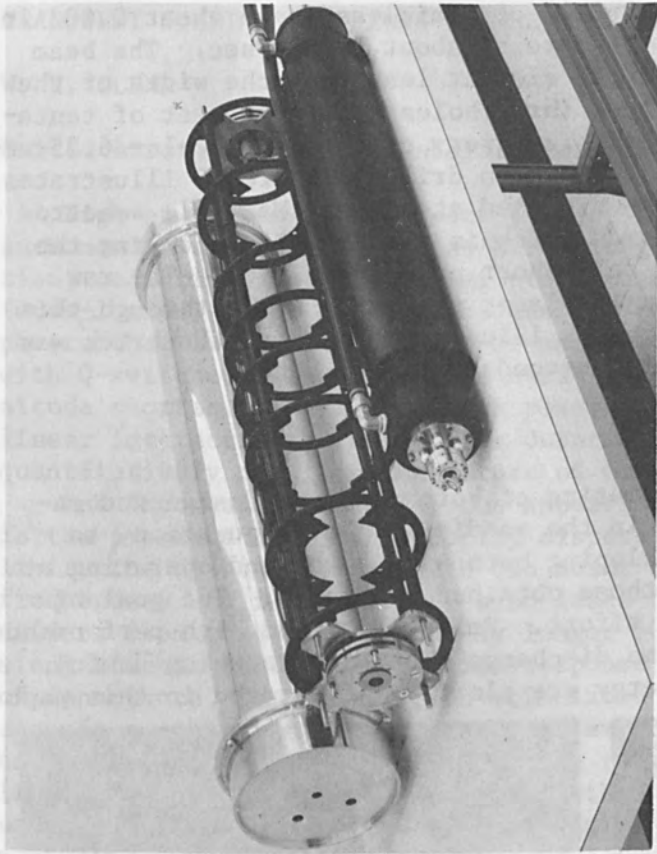


FIG. 6.--Ceramic tube anodic-bore laser head assembly.

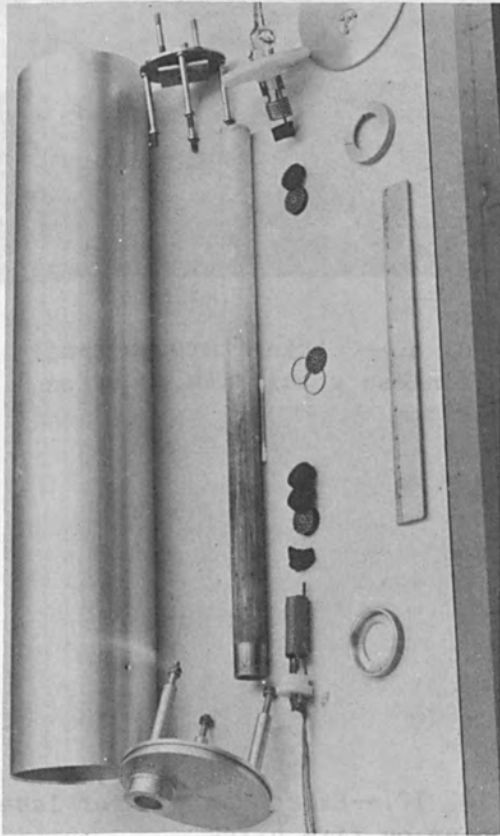


FIG. 7.--Compact alumina plasma tube.

6-W argon laser. Figure 8 shows a piece of stainless-steel sheet 0.002 in. thick in which a slit was cut at the rate of about 0.3 mm/sec. The beam was focused with an inexpensive single element lens, and the width of the cut averages 0.16 mm. Figure 9 shows three holes cut in a sheet of tantalum 0.005 in. thick. The center hole is a very clean and circular 6.25- μ m-diam hole which took approximately 90 sec to drill. Figure 10 illustrates the power of an unfocused 20-W beam directed at a Johns Manville asbestos ceramic fire brick. This tan-colored brick is effective in blocking the penetrating power of the beam for only short periods of time. The raw 2-mm beam approximately 10 ft from the laser gradually burns through this material. Penetration of about 1 mm is illustrated here as the brick was moved manually in the beam every few seconds across a bench.

CONCLUSIONS

We have demonstrated an ideal mating of both a unique design and material, namely pyrolytic graphite in the anodic-bore configuration, to produce ion lasers capable of developing both high power and operating at efficiencies at least as high as those obtained by others. The goal of ruggedization requires additional effort. Reliability and high performance in a sealed off, low-volume, plasma discharge tube for producing useful ranges of visible laser output energy are clearly illustrated in this paper.



FIG. 8.--Cutting through 2-mil stainless steel with an argon laser.



FIG. 9.--Laser-drilled holes in 5-mil-thick tantalum.

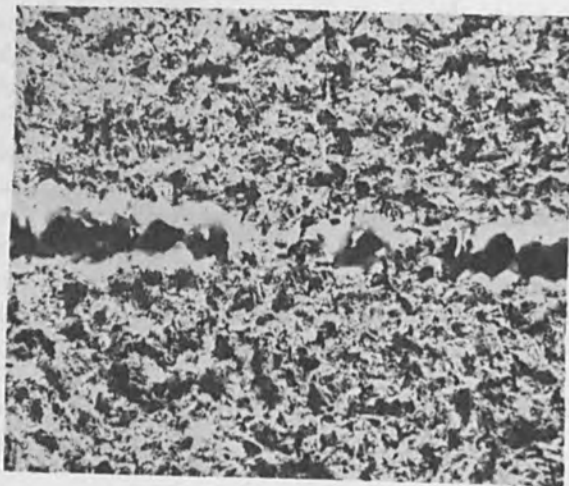


FIG. 10.--Effect of 20 W of laser power on fire brick.

TRANSIENT NONLINEAR EFFECTS IN THE PROPAGATION OF HIGH-POWER LASER BEAMS

W. H. GLENN

United Aircraft Research Laboratories, East Hartford, Conn.

High-power Q-switched laser pulses have been used extensively to study such nonlinear interactions as harmonic generation, parametric amplification, and stimulated scattering processes. Work on pulse-regenerative (mode-locked) laser oscillators has led to the production of pulses having powers that are several orders of magnitude higher than those obtainable with Q-switched pulses and time durations that are several orders of magnitude shorter. The higher peak power increases the strength of the nonlinear interactions; the shorter duration of the pulses qualitatively and quantitatively modifies the nature of many of these interactions.

One important reason for the appearance of transient nonlinear effects is the presence of group-velocity dispersion in the nonlinear medium, which limits the distance over which two beams of short pulses having different frequencies can interact. It also leads to distortion of the pulses that differs from that experienced by longer pulses. Another source of transient effects is the finite time response of the nonlinearity, which is of importance, for example, in stimulated Raman scattering. The scattering depends on the buildup of a material excitation (phonon) and this buildup has a time constant determined by the reciprocal of the spontaneous Raman line width. If pulse durations less than this characteristic time are used, the scattering process is strongly modified. Similar considerations modify the thresholds for self focusing of intense beams by electrostriction or the molecular Kerr effect. Another class of transient effects occurs when the duration of the exciting pulse is shorter than the phase memory time for a resonant nonlinearity. This condition leads to such effects as self-induced transparency.

This paper reviews some recent experimental and analytical investigations of these transient effects. Their effect on the beam propagation and on the generation of radiation at frequencies other than that of the incident beam are discussed.

TRANSMISSION CHARACTERISTICS IN THE PRESENCE OF HIGH-POWER LASER BEAMS
 The beam had the cross-section of a Gaussian beam and the wavelength was 632.8 nm. The beam diameter at the waist was 0.5 mm and the waist length was 0.5 mm. The distance between the waist and the interaction point was 0.5 m. The interaction point was a thin layer of a dielectric material with a thickness of 0.1 mm. The dielectric constant of the material was 1.5. The refractive index of the material was 1.5. The permittivity of the material was 2.25. The permeability of the material was 1. The conductivity of the material was 0. The loss tangent of the material was 0. The dielectric loss of the material was 0. The dielectric constant of the material was 1.5. The refractive index of the material was 1.5. The permittivity of the material was 2.25. The permeability of the material was 1. The conductivity of the material was 0. The loss tangent of the material was 0. The dielectric loss of the material was 0.

The diagram shows the interaction of a laser beam with a dielectric layer. The laser beam is incident on the dielectric layer from the left. The reflected beam is shown to the left of the dielectric layer. The transmitted beam is shown to the right of the dielectric layer. The dielectric layer has a thickness of 0.1 mm. The laser beam has a wavelength of 632.8 nm. The dielectric constant of the material is 1.5. The refractive index of the material is 1.5. The permittivity of the material is 2.25. The permeability of the material is 1. The conductivity of the material is 0. The loss tangent of the material is 0. The dielectric loss of the material is 0.

The diagram shows the effect of a 20 W laser beam on a dielectric layer. The laser beam is incident on the dielectric layer from the left. The reflected beam is shown to the left of the dielectric layer. The transmitted beam is shown to the right of the dielectric layer. The dielectric layer has a thickness of 0.1 mm. The laser beam has a wavelength of 632.8 nm. The dielectric constant of the material is 1.5. The refractive index of the material is 1.5. The permittivity of the material is 2.25. The permeability of the material is 1. The conductivity of the material is 0. The loss tangent of the material is 0. The dielectric loss of the material is 0.

DEVELOPMENT OF HIGH-POWER ND: GLASS LASER SYSTEMS*

J. M. McMAHON and J. L. EMMETT

Naval Research Laboratory, Washington, D.C.

Design of high power Nd: glass laser systems requires the simultaneous optimization of both oscillator and amplifier operating parameters. Thus we require a detailed understanding of the relevant laser physics, laser materials parameters, cavity design, flashlamp excitation parameters, and driving-circuit design.

INTRODUCTION

The development of high-energy short-pulse laser systems has been stimulated primarily by the desire to use them for rapid heating of high-density plasmas. Solid-state laser systems capable of producing kilojoule pulses of subnanosecond duration are large, complex, and costly. It is not sufficient just to achieve operation at this level for a few shots before the system degrades. The laser is expected to produce hundreds to thousands of shots on a reliable reproducible basis.

In this paper we discuss some aspects of developing high-power solid-state laser systems using Nd^{3+} as the active ion. Parameters and design philosophy of laser oscillators, amplifiers, and pumping systems are discussed from the point of view of realizing predictable, reproducible operation with useful system lifetimes.

OSCILLATOR OPTIMIZATION

For purposes of discussion we may treat the laser oscillator as a "black box" device that emits a single pulse of a desired duration and of some desired energy content. The chief distinction among various oscillators is in the desired pulsewidth.

For pulses longer than 10^{-8} sec, Pockels cell or rotating mirror Q-switched lasers are used. The theory of such devices is well known, as is their optimization. Examination of the results of Wagner and Lengyel shows that the minimum pulsewidth occurs when the ratio of loss to small-signal gain is about 0.28. The pulsewidth is approximately $9.2t_1/\alpha$, where t_1 is the single-pass transit time and α is the gain coefficient.¹ From the analysis of Wagner and Lengyel we also find that in this case the inversion remaining at the end of the pulse is only 4 per cent of the initial inversion; i.e. almost all of the energy is extracted from the rod. Figure 1 shows the shape of the curve for pulsewidth as a function of the ratio of gain to loss. Figure 2 shows Wagner and Lengyel's result for the ratio of final inversion to initial inversion as a function of the same parameter. From these two results we can see that a natural operating point exists which will result in operation which is quite stable both with respect to pulsewidth and pulse energy.

For pulses with a duration from 1 to 10 nsec two techniques are used. The first method is to use an optical shutter to "chop" out a short seg-

*This work was funded by the Advanced Research Projects Agency under ARPA Order 660.

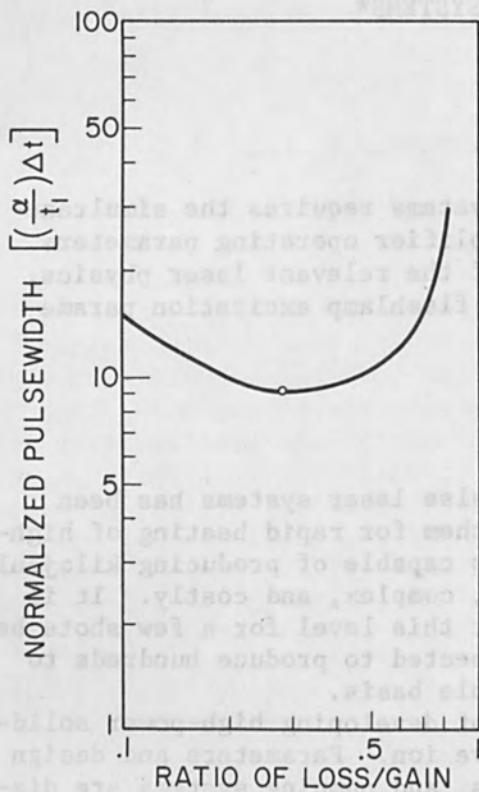


FIG. 1.--Relation between normalized pulsewidth and loss-gain ratio for Q-switched oscillators.

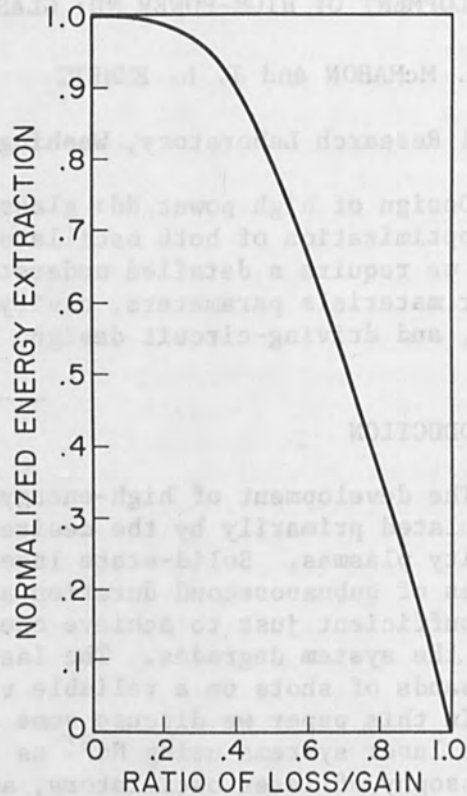


FIG. 2.--Relation between energy extraction efficiency (initial inversion-final inversion) and loss-gain ratio for Q-switched oscillators.

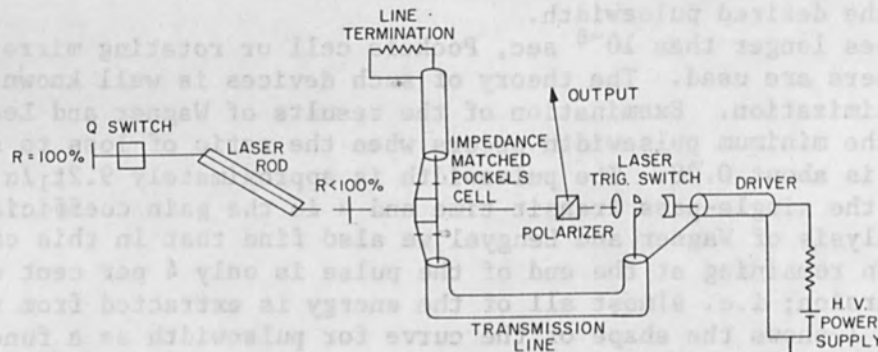


FIG. 3.--Typical arrangement for Q-switched oscillator with "pulse chopper."

ment from a longer pulse.² A typical arrangement is shown in Figure 3. The second method is to use a pulse-transmission mode-switched oscillator.³ In the PTM oscillator an optical switch is used to maintain the resonant cavity at a low Q until the desired inversion has been attained. It is then switched to a high-Q condition to allow the power density in the cavity to build up. At a predetermined level the switch is fired again and the cavity charge is "dumped" via the polarizer.

For pulsewidths of 10^{-9} sec or less the only useful technique employs a mode-locked oscillator followed by a shutter which gates out a single pulse from the mode-locked pulse train.⁴ One aspect of this approach that is not fully appreciated is that there is enough flexibility in the design of these systems to optimize separately both the width of an individual pulse and the envelope of the pulse train. The pulsewidth of a single pulse will depend on the available bandwidth and can be adjusted using transmission etalon(s) in the cavity.⁵ Figure 4 shows typical results for a saturable absorber-mode locked and Q-switched YAIG system. With no etalon the pulsewidth as determined from two photon fluorescence was 20 psec. When tilted etalons of different thicknesses were inserted in the cavity and adjusted so that a transmission maximum coincided with the peak fluorescence of the 1.06- μ m line, stable operation was obtained at pulsewidths up to 1.25 nsec.

An analysis similar to that of Wagner and Lengyel can be used to insure that the duration of the mode locked train is a minimum. This results in stable operation with all of the output energy in a minimum number of pulses. Pulse trains with more than 40 per cent of the total energy in the strongest pulse have been observed in our laboratory. Somewhat longer lower peak power pulse trains such as that shown in Fig. 5 are more optimal from the standpoints of avoiding a mirror damage and allowing time to turn on the Pockels cell switch.

The current state of the art with regard to fast optical switches is quite encouraging. The Pockels cell is pulsed by discharging a length of cable charged to the desired voltage through the cell by a laser triggered switch. As has been shown by Alcock and by Guenther et al., high pressure gaps can be made to close very rapidly with a small jitter.^{6,7} The Pockels cell can also be constructed as a portion of a transmission line with a characteristic impedance equal to that of the driver. The extinction ratio of such a switch is typically 300:1 to 1000:1 and is limited only by the optical quality of the modulator crystal. Table I summarizes the properties of such switches.

TABLE I.--Present state of the art of impedance-matched Pockel cell shutter and laser-triggered spark-gap combination: typical shutter performance.

Material	KD*P
$V\lambda/2$ (kV)	10
Delay of laser switch	≥ 10 nsec
Risetime	≈ 300 psec
Contrast ratio	$> 300:1$

AMPLIFIER OPTIMIZATION

PHYSICS OF SATURABLE AMPLIFIERS. The successful achievement of kilojoule subnanosecond pulses with high reliability depends on the simultaneous optimization of a number of disparate characteristics of laser am-

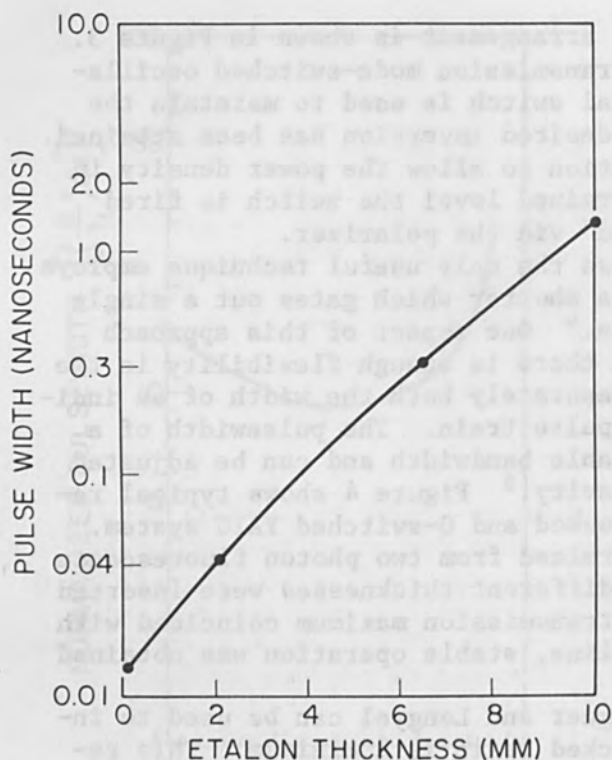


FIG. 4.--Pulse-width vs transmission mode selector thickness for mode-locked Nd: YAlG.

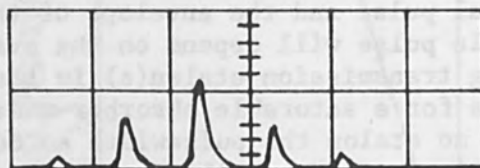


FIG. 5.--Mode-locked pulse train from Nd: YAlG laser with about 40 per cent of energy in strongest pulse. Total energy, 90 millijoules in a 5-mm-diam. beam; width of each pulse measured to about 350 psec.)

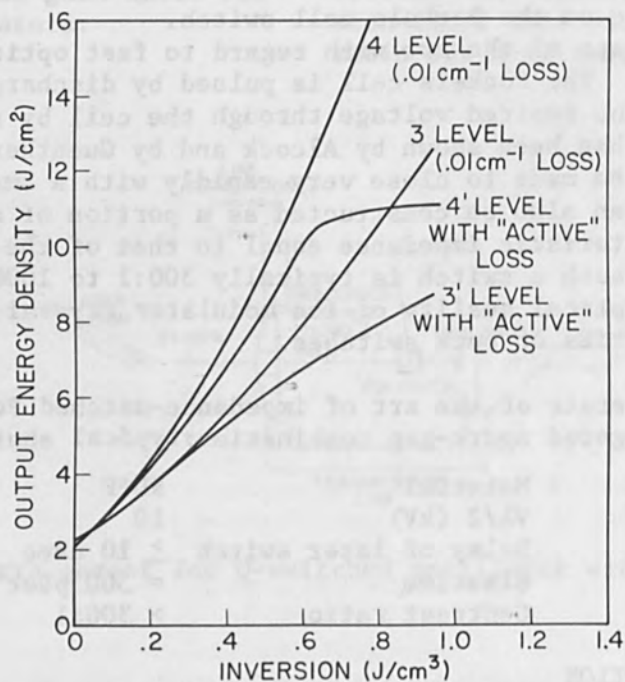


FIG. 6.--Output energy density vs inversion for amplifier 32 cm long of Owens-Illinois ED-2 laser glass. Four-level case is appropriate for pulses longer than lower-level relaxation time T_L ; three level case is appropriate for pulses shorter than T_L . "Active losses" are scaled from the references noted in the text.

plifiers. As the duration of a pulse into an amplifier is changed, the detailed characteristics of the amplification process will also change. For pulses long in duration compared to the upper-state cross relaxation time T_2 and the lower-level lifetime T_L , neodymium is effectively a four-level system. If the pulsewidth is short compared to the lower-level lifetime but longer than T_2 , the laser is effectively a three-level laser where the lower level is initially empty but fills during the passage of the pulse. Figure 6 shows the results of a typical calculation for these two conditions for Owens-Illinois ED-2 laser glass. Also shown are the same results for cases where a pump-dependent loss instead of a constant loss was assumed. The pump-dependent loss used in the calculation was similar to previously measured characteristics of laser glasses.⁸⁻¹¹

The exact values of T_L and T_2 for neodymium in glass are not known with great precision. Duston's measurement of T_L as in the range of 5 to 20 nsec for Owens-Illinois ED-2 is consistent with some measurements on pulse broadening at high intensity done in our laboratory and reported previously.^{12,13} The recent result of DuMarchin et al. reporting T_L to be in excess of 100 nsec for Soveril MG915 glass¹⁴ seems to be at variance with other reported results on similar types of glass.¹²

The value of T_2 for any laser glass has not been directly measured, but the experiments that have been done indicate that T_2 is less than 10^{-9} sec.^{12,15} The results of many workers on mode-locked neodymium glass lasers may well indicate that T_2 is longer than the inverse of the bandwidth (about 10^{-13} sec) since the results of photon correlation experiments show a very narrow spike with rather broad wings.^{16,17} The cause of this behavior is not clear at present but leads one to suspect that a pulsewidth greater than 10^{-12} sec is necessary to achieve linear amplification.

AMPLIFIER CHAIN CONFIGURATION. Neodymium laser glass with a high damage threshold and excellent optical quality is both expensive and essentially unobtainable in very large pieces ($V > 2000 \text{ cm}^3$). It is additionally desirable to maximize the pumping efficiency without degrading the beam quality.

The above considerations make it very desirable for most of the input energy to go to amplifiers operated at or above the saturation flux but well below the damage threshold of the glass. One choice of operating points is used by the Compagnie Générale d'Electricité in their laser systems such as the VD 640. This system in the configuration shown produces a 500-joule, 30-nsec pulse. The oscillator produces a 3-joule pulse which two preamplifiers raise to 50 joules over 8 cm^2 . The following three amplifiers have successively larger cross-sectional areas by a factor of two and are run with an input level of 0.7-0.8 of the saturation flux. The output flux is 1.3-1.6 times the 10-J/cm^2 saturation flux. The over-all efficiency is relatively good in that the total pump energy required for the 500 joule output is 100-120 kJ.

Since damage threshold for the glass is 40 J/cm^2 and the peak energy density at the output of any stage is less than 20 J/cm^2 , no degradation is observed over many hundreds of shots.

The French design does not necessarily represent the optimum choice but illustrates many qualities that a good system must have to perform reliably. The factor of two scaling from stage to stage allows the extraction of 35-40 per cent of the total stored energy and there is a wide enough margin between the operating level and the damage threshold to allow for mistakes in aligning the device without causing immediate disaster.

DISKS VS ROD AMPLIFIERS. Slab or disc laser amplifiers have been considered for applications where a large aperture is required and/or a high repetition rate is necessary. What follows is not concerned with high-prf slab devices, but rather with the comparison of the relative suitability of faced pump-slab amplifiers and solid-rod amplifiers for high-peak-power applications.

Several considerations limit the utility of large solid-rod amplifiers. The attainable inversion is limited by the ratio of surface area to volume, since one must pump through the cylindrical surfaces. This limitation translates into another on useful operational flux density in the beam since the flux density at which the gain approaches zero is approximately proportional to N/γ and varies as R^{-1} due to the ratio of surface area to volume.

Since rods are cooled at the interface between the rod surface and the coolant, a definite time is required between shots that is proportional to the radius if an acceptably low thermal distortion and birefringence is to be maintained. For the VD 640 this interval is 8 min.

For a disk amplifier these constraints are significantly eased at the cost of a somewhat lower pump coupling efficiency due to the openness of the structure. Figure 7 shows a plan view of one such device, the one under construction at NRL. Similar devices have been built and operated at the Lawrence Livermore Laboratory and the University of Rochester. The disks are generally placed at Brewster's angle to the beam in a zig-zag fashion to minimize beam walk off.

Since the length of such a device increases with the aperture size, the surface area to volume ratio remains constant as the device is scaled up.

The cooling problem is different for a disk system in that the ratio of surface area to volume is much larger than for a rod system. The predominant distortions will be nearly normal to the beam path and for this reason will be more tolerable.

The materials problem is significantly eased from the standpoint of availability if not price since the relatively small volumes of glass are needed per disk. However fabrication costs are very high, as all the many surfaces must be very carefully finished.

DAMAGE THRESHOLDS OF LASER MATERIALS. At the present time selected samples of most available laser glasses have demonstrated damage thresholds in excess of 30 J/cm^2 for a 30-nsec pulse. These values appear to be sufficient for systems available at present, since surface damage to beam-handling optics is more generally the problem.

The real present needs in this area are for research into the nature of surfaces and the development of polishing techniques that will allow routine operation at high levels. In addition, determination of the mechanisms and thresholds of self-focusing in laser glasses would be of significant value. It has been reported that Soveril MG915 damages owing to self-trapping at about 14 J/cm^2 and the Owens-Illinois ED-2 between 20 and 28 J/cm^2 with a pulse of a few nanoseconds long.^{18,19} If this large difference is correct it is quite interesting as it holds out the possibility of developing base glass formulations with even higher thresholds.

LASER PUMPING SYSTEMS

At the present time all high-energy Nd:glass laser systems are pumped

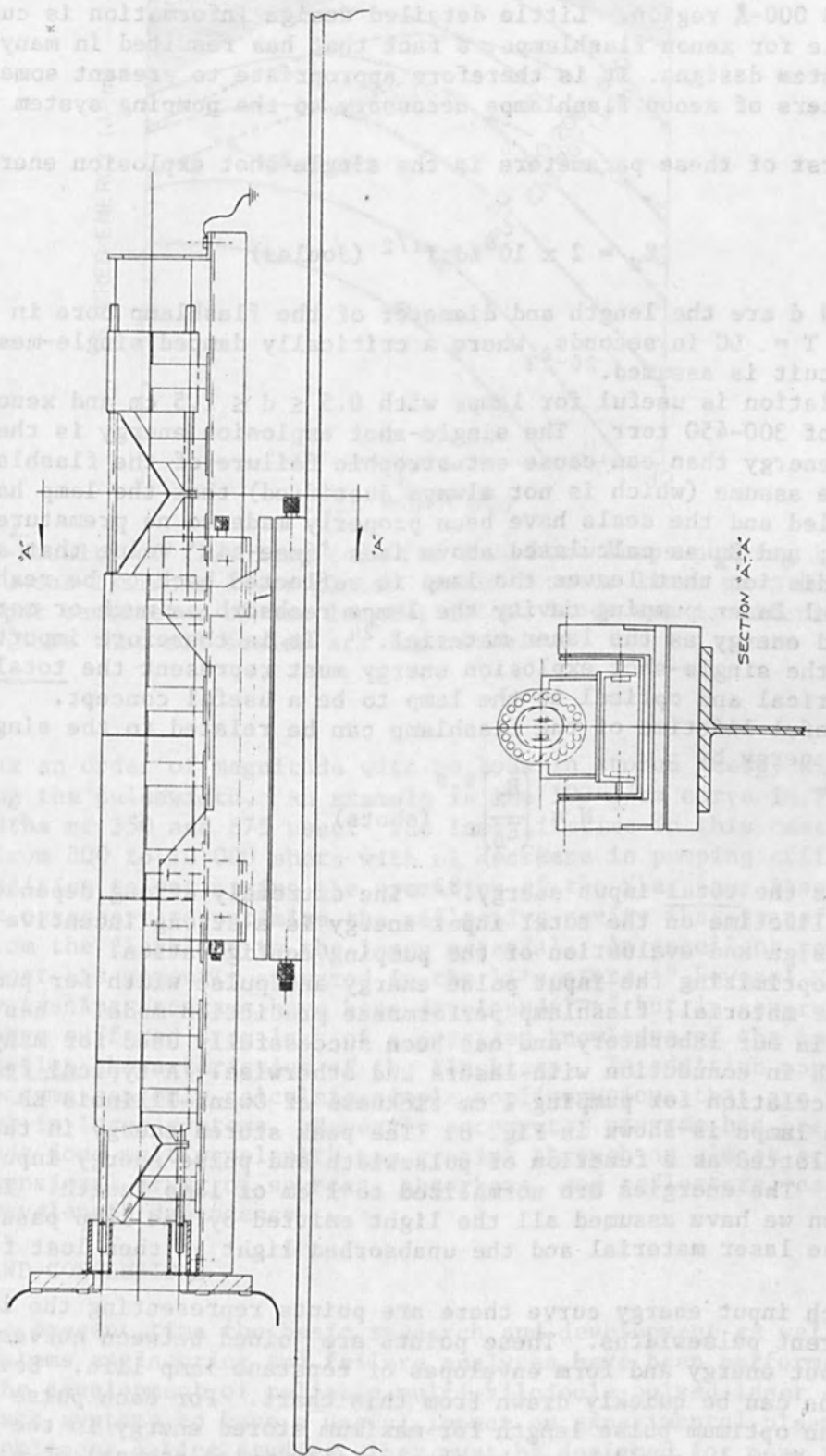


FIG. 7.--Plan view of NRL disk laser amplifier. Eleven elliptical disks are at Brewster's angle and twenty-two linear flashlamps pump device with up to 180 kilojoules from capacitor bank.

with xenon flashlamps. The lamp is a relatively efficient device as it converts 50-60 per cent of the electrical input energy into radiation in the 2000-10 000-Å region. Little detailed design information is currently available for xenon flashlamps, a fact that has resulted in many poor pumping system designs. It is therefore appropriate to present some of the parameters of xenon flashlamps necessary to the pumping system design problem.

The first of these parameters is the single-shot explosion energy E_x given by

$$E_x = 2 \times 10^4 \ell d T^{1/2} \text{ (Joules)}$$

where ℓ and d are the length and diameter of the flashlamp bore in centimeters and $T = LC$ in seconds, where a critically damped single-mesh discharge circuit is assumed.²⁰⁻²³

This relation is useful for lamps with $0.5 \leq d \leq 1.5$ cm and xenon fill pressures of 300-450 torr. The single-shot explosion energy is the minimum input energy that can cause catastrophic failure of the flashlamp envelope. We assume (which is not always justified) that the lamp has been well annealed and the seals have been properly made so no premature failures occur; and E_x as calculated above is a 'free-air' value that assumes that no radiation that leaves the lamp is reflected back to be reabsorbed. In an actual laser pumping cavity the lamps reabsorb as much or more of the emitted energy as the laser material.²⁴ It is therefore important to note that the single-shot explosion energy must represent the total input both electrical and optical to the lamp to be a useful concept.

The useful lifetime of the flashlamp can be related to the single shot explosion energy by

$$N \approx \left(\frac{E_x}{E_0} \right)^{8.8} \text{ (shots)}$$

where E_0 is the total input energy.²³ The extremely strong dependence of flashlamp lifetime on the total input energy is a strong incentive for careful design and evaluation of the pumping configuration.

As to optimizing the input pulse energy and pulse width for pumping a given laser material, flashlamp performance prediction model²⁵ has been developed in our laboratory and has been successfully used for many problems, both in connection with lasers and otherwise. A typical result of such a calculation for pumping 1 cm thickness of Owens-Illinois ED-2 with 1-cm: diam lamps is shown in Fig. 8. The peak stored energy in the laser glass is plotted as a function of pulsewidth and pulse energy input to the flashlamp. The energies are normalized to 1 cm of lamp length. In this calculation we have assumed all the light emitted by the lamp passes once through the laser material and the unabsorbed light is then lost from the system.

On each input energy curve there are points representing the lifetime for different pulsewidths. These points are joined between curves of different input energy and form envelopes of constant lamp life. Several conclusions can be quickly drawn from this chart. For each pulse energy there is an optimum pulse length for maximum stored energy in the laser material. This pulsewidth can be shorter (low pulse energy) or significantly longer (high pulse energy) than the fluorescent lifetime. It is also of significance to note that lamp lifetime can often be extended by

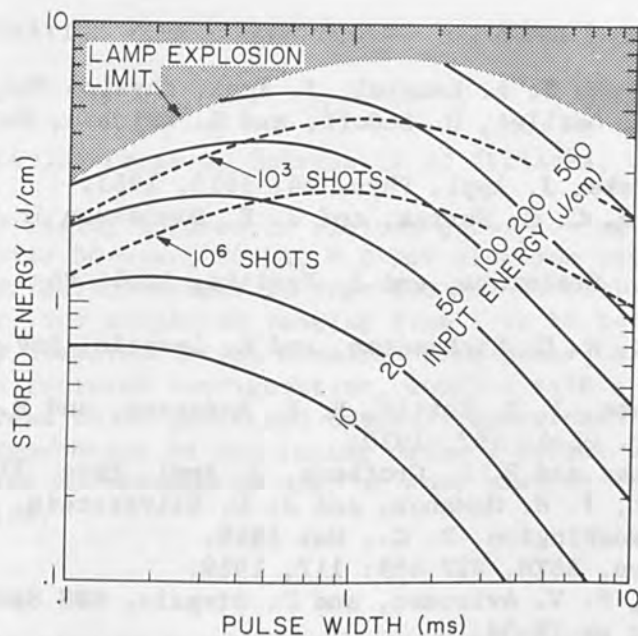


FIG. 8.--Results of flashlamp code for 1-cm bore lamps pumping 1 cm thickness of Owens-Illinois laser glass. Solid contour lines give input energy to lamp per centimeter of arc length; dotted lines are isolifetime contours. (Note that all scales are logarithmic.)

as much as an order of magnitude with no loss in stored energy simply by increasing the pulsewidth. An example is the 100-J/cm curve in Fig. 8 at pulse widths of 350 and 675 μ sec. The lamp lifetime in this case increases from 800 to 10 000 shots with no decrease in pumping efficiency.

In addition to optimizing the operation of the flashlamp itself it is of course necessary to optimize the reflective cavity that transfers the energy from the flashlamp to the laser material. An excellent review of this subject has recently appeared in the literature.²⁶ Several Monte Carlo ray tracing programs have been developed²⁶⁻²⁸ but in general the results have suffered from lack of a detailed knowledge of the emission and absorption characteristics of the flashlamp. In addition most of these programs can only calculate simple configurations that are usually not useful in large systems. Recently a computer program has been developed²⁸ that does multiwavelength ray tracing through an almost arbitrary three-dimensional array of sources, absorbers, and reflectors, each with its own wavelength dependence.

SUMMARY AND CONCLUSIONS

At the present time the basic research and development as well as much of the systems engineering and failure analyses have been performed to support the development of reliable multi-kilojoule pulsed laser systems.

For such systems to have a useful impact on experimental plasma physics and nonlinear optics studies, they must be designed for many reproducible operations, not for for a few shots. Component failure mechanisms and levels are well enough understood to make such operation feasible at the present time.

REFERENCES

1. W. G. Wagner and B. A. Lengyel, *J. Appl. Physics* 34: 2040, 1963.
2. M. Michon, H. Guillet, D. LeGoff, and S. Raynaud, *Rev. Sci. Instr.* 40: 263, 1969.
3. A. A. Vuylsteke, *J. Appl. Phys.* 34: 1615, 1963.
4. A. J. DeMaria, C. M. Ferras, and G. E. Danielson Jr., *Appl. Phys. Letters*. 8: 22, 1966.
5. G. Kachen, L. Steinmetz, and J. Kysilka, *Appl. Phys. Letters* 13: 229, 1968.
6. A. J. Alcock, M. C. Richardson, and K. Leopole, *Rev. Sci. Instr.* 41: 7, 1970.
7. A. H. Guenther, J. R. Bettis, R. E. Anderson, and R. V. Wick, *IEEE J. Quant. Electr.* QE-6: 492, 1970.
8. P. V. Avizones and R. L. Grotbeck, *J. Appl. Phys.* 37: 687, 1966.
9. J. L. Emmett, J. M. McMahon, and J. D. Silverstein, paper 10-10, CLEA Meeting, IEEE, Washington, D. C., May 1969.
10. J. M. McMahon, ASTM, STP 469: 117, 1969.
11. C. R. Jones, P. V. Avizones, and P. Sivgals, NBS Special Publication No. 341, 1970; pp.28-36.
12. D. K. Duston, Thesis, Rensselaer Polytechnic Institute, May 1969; also presented as postdeadline paper 10-9 at CLEA Meeting, Washington, D. C., May 1969.
13. J. M. McMahon, ASTM Symposium on Damage in Laser Glass, NBS Special Technical Publications No. 341, 1970.
14. R. Dumanchin, J. C. Farcy, M. Michon, and P. Vincent. *IEEE J. Quant. Electr.* QE-7: 53-58, 1971.
15. J. H. Boyden and G. L. Clark, *IEEE J. Quant. Electr.* QE-2: 42, 1966.
16. S. L. Shapiro and M. A. Duguay, *Phys. Lett.* 28A: 698, 1969.
17. R. C. Eckardt and C. H. Lee, *Appl. Phys. Lett.* 15: 425, 1969.
18. J. Davit, ASTM STP 469: 100, 1969, and NBS Special Publication No. 341, 1970.
19. J. Davit, private communication.
20. I. S. Marshak, *Appl. Opt.* 2: 793, 1963.
21. I. S. Marshak, *Impulsngye istochniki sveta (Pulsed Light Sources)*, Gosenergoizdat, Moscow-Leningrad, 1963. (Naval Research Laboratory Translation 1210, AD 704-944.)
22. H. E. Edgerton, H. H. Goncz, and P. W. Jameson, in *Proc. 6th Intern. Congress High Speed Photography*, H. O. Tjeck Willink and Zoon, Haarlem, 1963.
23. Technical Bull. 1, ILC, Inc., Sunnyvale, Calif.
24. J. L. Emmett, A. L. Schawlow, and E. H. Weinberg, *J. Appl. Phys.* 35: 2601, 1964.
25. J. B. Trenholme and J. L. Emmett, in *Proc. 9th Intern. Congress High Speed Photography*, SMPTE, New York, 1970.
26. Yu, A. Kalinin and A. A. Mak, *Soviet J. Opt. Tech.* 37: 129, 1970.
27. D. R. Skinner and J. Tregellas-Williams, *Aust. J. Phys.* 19: 1, 1966.
28. E. J. Seppi, Institute for Defense Analysis Paper P-655, Arlington, Va., December 1970.
29. The computer program has been developed by Systems, Science and Software, Inc., La Jolla, Calif., under contract to Naval Research Laboratory, Washington, D. C.

GAS LASER EXCITATION WITH A RELATIVISTIC ELECTRON BEAM

GEORGE H. MILEY*

Nuclear Engineering Program, University of Illinois, Urbana, Ill.

Studies of lasing induced in various gases during the propagation of a relativistic 50-nsec, 30-kA, 0.5-MeV electron beam are described. A spiked, superradiant output is reported for several lines in neon, argon, and air, for pressures ranging from 1 to 10 torr. The laser power is small compared to the electron-beam power, but it is suggested that an improved configuration, coupled with a magnetic guide field, might lead to an increased output. Measurements of the timing and pressure dependence of the lasing offer a unique opportunity to study excitation mechanisms as well as some aspects of the electron-beam propagation.

INTRODUCTION

The present studies were initiated to investigate the possibility of population inversion during the propagation of a high-current relativistic electron beam through a low-pressure gas. The beam was generated using a vacuum diode driven by Cornell University's Marx generator--folded Blumlein system.¹ A 50-nsec, 30-kA pulse of 0.5-MeV electrons was employed throughout. Such a beam will propagate through a variety of gases provided an appropriate pressure is maintained (usually a fraction to tens of torr) and a drift tube (here a 5.5-in.-diameter Lucite tube lined with a copper screen mesh) is employed.²

Several laser pumping studies³⁻⁵ have employed Blumlein or similar devices to obtain large pulsed currents; however, these techniques introduce the current transversely to the laser cavity. In contrast, in the present case, the electron beam propagates over distances of several meters while the optical cavity is oriented along the axis of propagation. Bolotovskiy and Tsytovich⁶ have suggested that such a situation might lead to an efficient Cerenkov laser; however, the present work is concerned with possible atomic or ionic lasing in the gas through which the beam propagates. Neon and argon are mainly discussed here, but obviously numerous other gases could be considered.

EXPERIMENTAL APPARATUS

As shown in Fig. 1, the electron beam enters the guide tube through a thin tantalum membrane which serves as the anode of the vacuum diode¹ and also allows a pressure differential between the diode and the guide tube. A gradual 20° bend in the guide tube permits the final 4-ft section to be used as a line-of-sight optical cavity. The end of the guide tube is reduced in diameter and placed in a 1-kG magnetic field

*This work was performed while the author was a visiting member of the Department of Applied Physics, Cornell University, Ithaca, N.Y. Support by the Office of Naval Research (ONR Contract No. N00014-67A-0077-002) and the Cornell Laboratory of Plasma Studies is gratefully acknowledged.

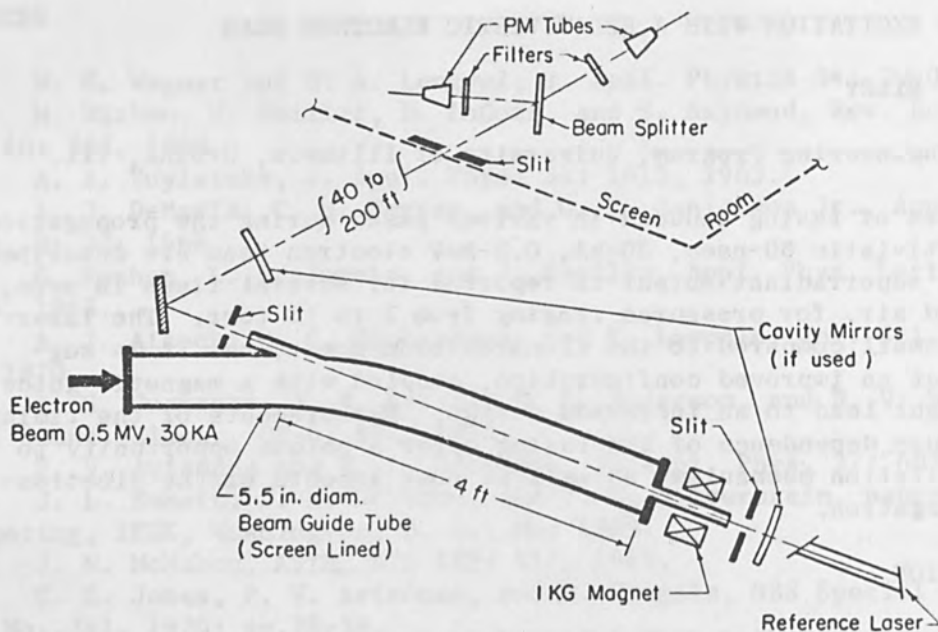


FIG. 1.--Experimental arrangement.

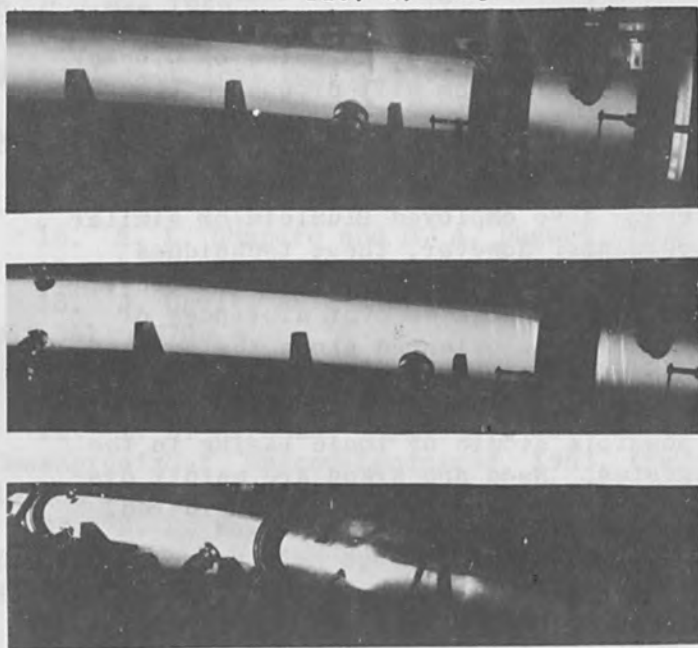


FIG. 2.--Electron beam propagation through curved guide tube. Upper photograph, for neon at 0.3 torr, shows slight feathering and bright or pinched region in curved section. Beam originates from diode section at left. Reduced-diameter optical window section begins at far right. Bright spark in the background is from Marx generator switch. Beam becomes more uniform at higher pressures (cf. middle photo for 1 torr). However, above 10 torr, as seen in lower picture, beam does not penetrate entire tube length.

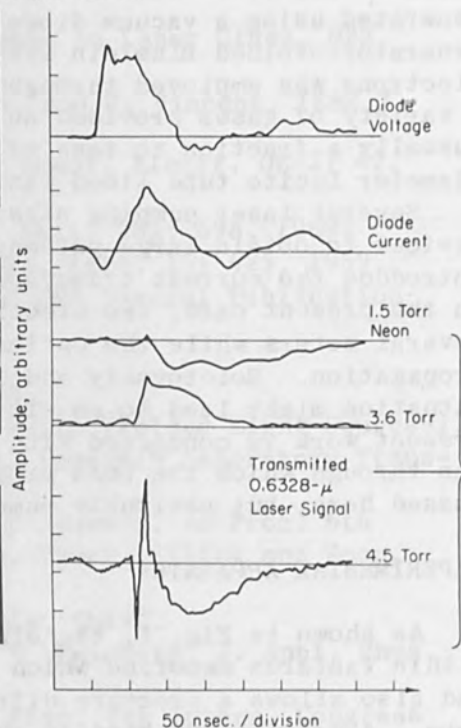


FIG. 3.--Current-voltage traces and 6328-Å gain measurements for several neon pressures.

in order to stop the electron beam and thus prevent damage to the optical window. (Such precautions are not necessary for the other window since it does not lie in the direction of propagation.)

Open-shutter photographs such as shown in Fig. 2, combined with streak photographs of the beam front, indicate that the slight curvature of the guide tube does not seriously affect beam propagation. A slight distortion is discernible at lower pressures (upper photo, Fig. 2), but a consistent, uniform beam is obtained over a pressure range nearly as large as previously observed for straight tubes.²

This basic configuration makes several types of experiments possible. In one, a conventional (reference) laser is directed through the windows to permit measurement of gain or absorption at select wavelengths. In other experiments the reference laser was removed and mirrors were placed just outside the windows to create an optical cavity. Finally, superradiance and spectral studies were carried out with both the mirrors and the reference laser removed.

All detectors and associated apparatus were placed in a screen room to reduce electrical pickup. Background measurements made with helium at low pressure (below 0.5 torr) and also air in the guide tube verified that fluctuations of the reference laser, detector and cable pickup, etc., during the pulse were negligible compared to the signals of interest here. The apparatus used in most experiments comprised a beam splitter, interference filters, and two photomultipliers as indicated. The electronics consisted of high-frequency amplifiers, the output signals being recorded with Tektronix 556 oscilloscopes. This system allowed a time resolution better than 3 nsec.

Some spectra were also recorded with a high-aperture transmission spectrograph and image-converter camera in place of the photomultipliers.

To test beam divergence, additional mirrors were employed to lengthen the distance to the detector from a normal 40 to over 200 ft.

Typical electron-beam voltage and current traces, shown in Fig. 3, were monitored by a resistive toroidal shunt and a voltage divider located on the vacuum diode.¹ As seen, the pulses were slightly longer than 50 nsec with the current peak trailing the voltage rise. Some details, e.g. the second (small) pulse, are due to a slight mismatch between the line and diode impedances, which varied somewhat when different diodes were employed. However, fairly reproducible V-I characteristics were obtained within any series of runs; hence only a single set of "representative" curves is shown in the following figures for each type of experiment.

Gases were introduced through a preset needle valve. In some instances, where it was desired to converse gas, the pump was turned off and the tube was filled just prior to the pulse. In either case, some air was always present, but generally with a partial pressure below 50 microns.

NEON STUDIES

Fairly extensive studies of lasing within the visible neon spectrum were performed with the use of gain measurements, cavity techniques, and spectroscopic recordings.

A. GAIN MEASUREMENTS AT 6328 Å. Figure 3 shows typical scope traces with a 6328-Å (red) reference laser, as indicated in Fig. 1. At low pressures, illustrated here by the 1.5-torr trace, there was a marked absorption (up to 30%), beginning roughly at the time of peak current and lasting about 100 nsec beyond the primary current-voltage pulse. (For neon at these pressures, the beam propagation velocity is about 0.5c. Thus, although the current-voltage traces were measured at the diode, the electron beam passes the reference laser beam less than 10 nsec later.) As the pressure is increased, the absorption decreases and gradually shifts to a gain as illustrated for 3.6 torr. Further increases in pressure result in spiked absorption-gain regions followed again by a longer term absorption as shown in Fig. 2 for 4.5 torr. A plot of the fractional peak gain, i.e., the increase in peak signal ΔI , normalized by the reference laser output I , is shown as function of pressure in Fig. 4. (Except for a narrow range of pressures between 3.5 to 4 torr, absorptive regions occurred simultaneously with the gain.) The gain decreased markedly above 5 torr, but photographs indicated that the electron beam itself maintained excellent propagation characteristics up to about 10 torr.

B. CAVITY MEASUREMENTS AT 6328 Å. Dielectric mirrors with maximum reflectivity were placed as indicated in Fig. 1 to form an optical cavity, and the output was recorded for a pressure of 3.9 torr where a maximum gain had been observed. The output trace, shown in Fig. 5, appears to consist of a series of three or more overlapping spikes followed by a final, smaller spike which occurs roughly at the second voltage pulse. The peak output is estimated to be of order of 10 W/cm^2 . In the hope of increasing the output, several runs with He/Ne mixtures were attempted, but as shown in Fig. 5, smaller outputs similar in shape to the pure Ne case were obtained.

To study the effect of the mirrors, they were removed one at a time, with the results indicated in Table I. The ineffectiveness of the mirrors is reasonable if it is assumed that the gas is superradiant and if it is further noted that the electron-beam duration in the cavity is so short that the output light cannot undergo a sufficient number of passes for effective buildup of the cavity energy density. Note, however, that the energy density must have increased somewhat with both, or even one mirror present. Otherwise, placing a mirror between the filter detector and the tube would drastically reduce the output.

In a further check of the superradiant character of the output, the distance to the detector was increased from 40 to 200 ft. A decrease of less than 10 per cent in signal was observed. (A 1-cm^2 collimator was placed in front of the detector so that the active detection area essentially matched that of the output window on the guide tube.)

C. GREEN AND RED SUPERRADIANCE. Since several investigators^{4,7,8} have reported a strong superradiant green line at 5401 Å in neon, the beam-splitter and filter arrangement of Fig. 1 was used to detect this line simultaneously with the red (6328-Å) line. No cavity mirrors were used; the output from the guide tube window was recorded directly. A typical result at lower pressures is shown in Fig. 6. The green line is considerably more spiked than the red, and it precedes the latter by roughly 50 nsec. The peak of the green line generally fell between the current and voltage pulse peaks. (The fact that the red line lags the

TABLE I.--Cavity experiments with neon at 3.9 torr.

Detector Output (mV)

Experiment No.	3/15*	3/21**
Mirrors		
Both	160	1500
One†	100	1500
None	80	1400

* Using a pair of 2-m and 1-m mirrors with 99.5% reflectivity at 6328 Å.

**Using an output (detector side) mirror of 85% reflectivity. The larger outputs recorded in this experiment are due to use of a more sensitive photomultiplier. To help insure that no stray wavelengths were passing the filter, the plane mirror inside the cavity was replaced by a 6328-Å dielectric mirror.

† In both cases the mirror on the detector side of the cavity was retained. Thus it effectively blocked the beam and should have caused a reduced output unless, as suggested in the text, the energy density in the "cavity" simultaneously increased.

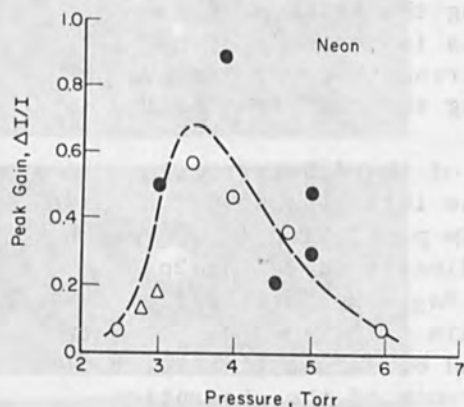


FIG. 4.--Fractional gain at 6328 Å vs neon pressure. (Data point shapes indicate measurements taken at different times; hence alignment and other differences are expected.)

FIG. 6.--Comparison of time traces for 5401- and 6328-Å outputs from neon.

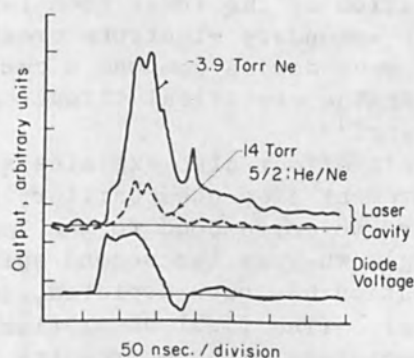
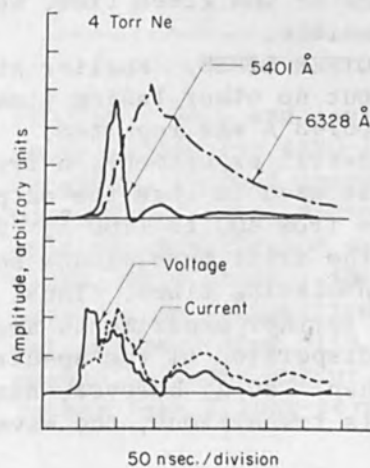


FIG. 5.--Output traces for Ne and He-Ne with 6328-Å optical cavity.



current pulse more than in the preceding measurements is attributed to an increased impedance mismatch.) As shown in Fig. 7, the amplitude of the green line increases at higher pressures, whereas the red-line output continues to decrease. Although other studies⁷ indicate that the maximum green output might occur near 30 torr, beam propagation becomes erratic above about 9 torr, which is thought to account for the fall-off shown in Fig. 7.

Although the red line is one of the best-known lasing lines, the above represents the first observation of superradiant output at this wavelength. In fact, oscillations on it have been thought to be impossible in pure neon (as opposed to He/Ne mixtures) because of the relative cross sections involved. This argument, however, breaks down in the present case of excitation by electrons of very high energy.

The timing of the red and green outputs suggests the following simplified view of the mechanism. The electron beam causes direct excitation of both the 3s (upper red level) and 2p (lower red level, upper green level, cf. Fig. 8), but the 2p population initially exceeds the 3s value so that only the green line appears. However, the 2p lifetimes are of order of 20 nsec, as opposed to about 200 nsec for the upper red state (3s₂),^{10,11} Because of its short lifetime, the 2p population is quickly depleted, and once it drops below the 3s value, red lasing commences. The decay of the red line is then roughly governed by the 3s₂ lifetime. The decay actually appears to be slightly faster than this would predict, possibly because of back-excitation of the lower neon levels following the buildup of low-energy secondary electrons created as the gas is ionized. (Actually these secondaries compose a current which streams back to diode, thus closing the electrical circuit and preventing the beam from self-pinching.^{1,2})

This effect also explains some features of the 4.5-torr gain measurement presented earlier in Fig. 3. The initial absorption spike appears to correspond to the large initial 2p population (i.e., green lasing), whereas the second spike (gain) indicates where the 2p population has been depleted, inverting the 3s₂ - 2p₄ states (red lasing). (The final absorption region in this trace does not seem to be consistent with the results in Figs. 5 and 6, and its interpretation is not clear.) Note that the initial appearance of the absorption spike at higher pressures is generally consistent with the pressure dependence of the green line, which makes the foregoing explanation more plausible.

D. OTHER LINES. Earlier studies of neon generally found the green line^{4,7} but no other lasing lines; or in one case,⁸ superradiance at 5944 and 6143 Å was reported.

In several experiments a transmission spectrograph-image converter camera was used to scan the output beam for additional lasing lines in the range from 400 to 7500 Å. The spectrograph was located over 100 ft from the drift tube window so that the divergence would discriminate against nonlasing lines. Thus, while the lines observed may be superradiant, further experiments are required to ascertain it fully.

The dispersion of the spectrograph prevented an absolute resolution better than ± 10 Å; however, assuming that the lines observed originate from 2p-1s transitions, the wavelength assignments of Tables II and III

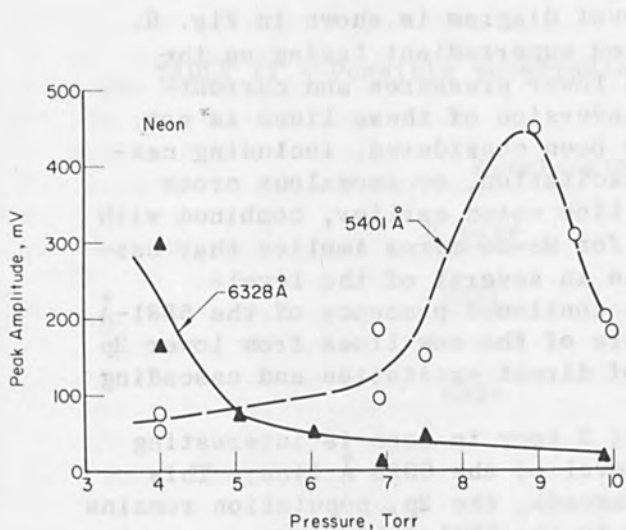


FIG. 7.--Pressure variation of 5401- and 6328-Å output from neon.

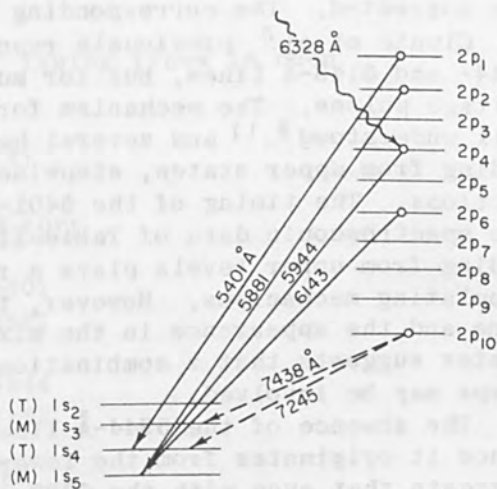


FIG. 8.--Level diagram for 2p-1s transitions observed in neon.

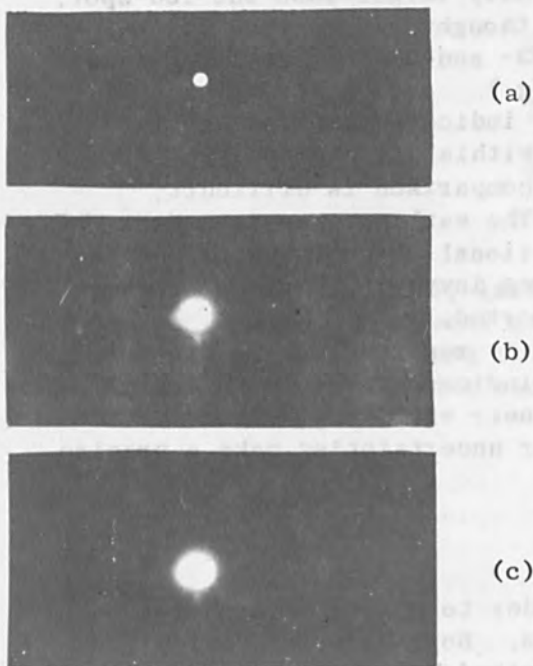


FIG. 9.--Spot size comparisons. Open-shutter photographs of the output beam for (a) 4-torr neon with a 6328-Å interference filter in front of the camera; (b) 9-torr neon with a 5401-Å interference filter; (c) 9-torr neon, no filters.

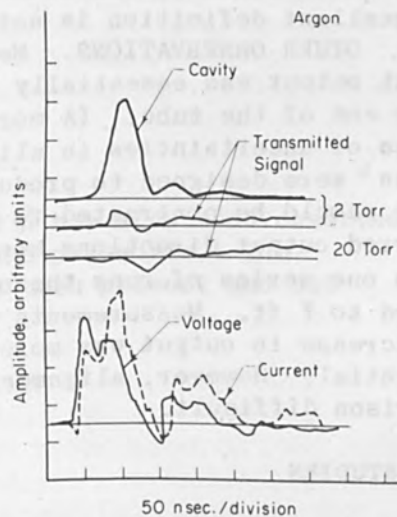


FIG. 10.--Gain and cavity measurements for 4880-Å line in argon. (Pulsed argon with microsecond pulse width was used in transmission experiments. Thus gradual increase observed in transmitted signal is associated with slow change in laser output, rather than a long-term gain.)

are suggested. The corresponding level diagram is shown in Fig. 8.

Clunie et al.⁸ previously reported superradiant lasing on the 5944- and 6143-Å lines, but for much lower pressures and current-voltage pulses. The mechanism for inversion of these lines is not well understood^{8,11} and several have been considered, including cascading from upper states, stepwise excitation, or anomalous cross sections. The timing of the 5401-Å line noted earlier, combined with the spectroscopic data of Table III for He-Ne mixes implies that cascading from upper levels plays a role in several of the level-populating mechanisms. However, the continued presence of the 5881-Å line and the appearance in the mixture of the new lines from lower 2p states suggests that a combination of direct excitation and cascading steps may be involved.

The absence of the 5944-Å line at 3 torr in neon is interesting since it originates from the lower level of the 6328-Å line. This suggests that even with the 6328-Å cascade, the 2p₄ population remains well below the 2p₂ value which leads to the 5881-Å line.

E. SPOT SIZE. Several spot-size measurements were made in which the optical output (no mirrors or reference laser) was directed into an open shutter camera (f/5.8, d = ∞) placed 11 ft from the output window. As seen in Fig. 9, the 6328-Å spot size, obtained with an interference filter in front of the camera, was found to be approximately half the total-beam spot size (no filter). The 5401-Å spot was also slightly smaller than the total beam, but considerably larger than the red spot. (As suggested earlier, the total beam is thought to comprise several superradiant lines in addition to the 0.63- and 0.54-μ lines, so that its excellent definition is not surprising.)

F. OTHER OBSERVATIONS. Measurements indicate that the superradiant output was essentially the same, within a factor of two, from either end of the tube. (A more precise comparison is difficult because of uncertainties in alignment.) The earlier experiments by Shipman⁴ were designed to produce a directional output; the present result should be contrasted to pulsed tubes involving electrodes where preferred output directions have been reported.⁸

In one series of runs the optical-cavity region (Fig. 1) was increased to 7 ft. Measurements with neon indicated that the corresponding increase in output was more nearly linear with length than exponential. However, alignment and other uncertainties make a precise comparison difficult.

ARGON STUDIES

Studies of argon were initiated in order to obtain information on the production of excited ions in the beam. Both gain and cavity experiments similar to those already described for neon were repeated for argon. A pulsed argon-ion laser was used as the reference laser in the gain studies. Its output was predominantly at 4880 and 5145 Å, although 4658-, 4765-, and 5287-Å lines were also present. The results of measurements are illustrated in Fig. 10 where a filter was used to isolate the 4880-Å line. The transmitted signal trace for 2 torr is characteristic of those obtained between 0.5 and 3 torr where a spiked (about 30-nsec) gain was observed near the end of the diode voltage pulse but slightly preceding the peak current. (The rather complex

TABLE II.--Possible superradiant lasing lines in neon.

Wavelength (Å)	
3 torr	10 torr
5881	5401 5881
6328	5944 6143

TABLE III.--Possible superradiant lasing lines in 9:1 He-Ne mixtures.

Wavelength (Å)		
4 torr	10 torr	16 torr*
5881	5881	5881
7245	7245	
7438	7438	

*As indicated in Fig. 5, lasing at 6328 Å has also been observed in He/Ne at slightly different gas ratios and pressures. The output was relatively weak so it might have been present and not recorded in the spectroscopic studies.

current-voltage traces in Fig. 10 are again due to a poor diode impedance match.) Peak gains as high as 14 per cent were observed. At higher pressure, e.g., at 20 torr as shown in Fig. 10, no gain was observed but a sharp absorption occurred at 30 to 40 nsec after the diode current peak. Beam propagation was found to be possible at much higher pressures in argon than in neon; the measurements were made up to 80 torr.

When a set of 4880-Å mirrors were placed around the guide tube to form a cavity (Fig. 1) a sharp output was observed as indicated in Fig. 10. As expected, it coincided with the time during which gain was observed. As in the case of neon, the mirrors were found to be of little value for increasing the output, and divergence measurements with the mirrors removed indicated a superradiant condition. Peak powers approaching 1 kW were observed. Spectroscopic studies indicate that in addition to the standard ion lines, a strong output occurs on several lines in the 4200- to 4600-Å region, but a positive identification has not been made. These lines persist at high pressures where the 4880-Å line is extinguished.

MIXTURES INCLUDING AIR

Some experiments were attempted with various mixtures, including He-Ne, Ne-O₂, Ne-He-Ar, Ne-Ar, and Ar-N₂. The main objective was either to obtain selective collisional transfer into an upper lasing state or to depopulate the lower state. Both short and long (afterglow) time scales were investigated. Although some changes in output were observed, no definitive enhancement or afterglow lasing was found. The study of pressures and mix ratios was not exhaustive and further studies are required to confirm that optimal conditions do not exist.

It was observed that a very strong output is emitted from air above a few torr pressure. The lines seem to lie chiefly in the 3800- to 4400-Å range, but time was too short to permit their resolution. Several experiments with pure N₂ indicate that the strongest lines originate from it, although the well-known superradiant 3371-Å line^{3,4} did not dominate as might have been anticipated.

DISCUSSION AND COMMENTS

These results demonstrate that a superradiant output is obtained on a variety of lines when a relativistic electron beam propagates through a gas. The excellent collimation of the output observed here is generally consistent with the coherence brightening theory of superradiance developed by Dicke¹² and in particular with his postulation of an "end-fire" mode.

The rather low output powers (tens to hundreds of watts) compared to the electron beam power may seem to be disappointing at first. To be sure, neither the configuration used at present nor the gas selection are optimal. For example, simply enlarging the windows and lengthening the optical-cavity region would increase the output proportionately. Another technique that would enhance the efficiency of coupling between gas and electron beam would be to add a strong magnetic guide field (tens of kilogauss). It has been shown¹³ that such a

field reduces the propagation velocity and results in greater energy deposition in the gas. Both effects should be beneficial, which (together with longer tube lengths) should lead to a more effective use of mirrors to build up cavity energy densities. One remaining difficulty is that the relatively large electron energy results in the excitation of many levels, as opposed to a selective excitation of a single line. This problem could be avoided if an appropriate gas or mixture of gases could be found such that cascading or transfer reactions ultimately channel the excitation into one or a few levels. However, attempts to do so with well-known mixtures were unsuccessful, possibly owing to the highly nonequilibrium energy distributions (beam plus secondaries) involved; an improved understanding of this feature may lead to a proper selection of mixtures and conditions.

The ultimate efficiency for laser pumping with relativistic electron beams remains in doubt, but the present studies demonstrate that interesting and new basic information related to both excitation mechanisms and electron-beam propagation can be obtained. Also the short duration and high energy of the beam suggest that it can be used to obtain inversion on some lines that would not be possible otherwise. Even in the present rather limited study several new superradiant lines were observed in neon.

ACKNOWLEDGMENTS

J. Glancy assisted in many of the experiments. The help and continued encouragement of the EB facility staff, especially M. Ury, M. Andrews, M. Friedman, and J. Nation, was invaluable. Discussions with J. Nation, H. Fleischmann, J. Guyot, and R. McFarlane were most illuminating, and R. McFarlane arranged several equipment loans. The support of N. Rostoker, S. Linke, and P. Auer made the author's visit and the experiment possible.

REFERENCES

1. J. J. Clark, M. Ury, M. L. Andrews, D. A. Hammer, and S. Linke, in Record 10th Symp. Electron, Ion, and Laser Beam Technology, San Francisco Press, 1969; p. 117.
2. M. L. Andrews, H. Davitian, D. A. Hammer, H. H. Fleischmann, J. Nation, and N. Rostoker, *Appl. Phys. Letters* 16: 98, 1970.
3. J. D. Shipman and A. C. Kobb, *IEEE J. Quant. Elect.* QE-2: 298, 1966.
4. J. D. Shipman Jr., *Appl. Phys. Letters* 10: 3, 1967.
5. R. Hodgson, *Phys. Rev. Letters* 25: 494, 1970.
6. V. N. Tsytovich, On the Possibilities for Using High-Current Relativistic Beams in Plasma Physics, AEC-TR-7061, 1969.
7. D. A. Leonard, R. A. Neal, and E. T. Gerry, *Appl. Phys. Letters* 7: 175, 1965.
8. D. M. Clunie, R. S. A. Thorn, and K. E. Trezie, *Phys. Letters* 14: 28, 1965.
9. C. G. B. Garrett, *Gas Lasers*, McGraw Hill, New York, 1967; p. 64.

10. T. Hausch and P. Toschek, Phys. Letters 20: 273, 1966.
 11. W. R. Bennett Jr., and P. J. Kindlmann, Phys. Rev. 149: 38, 1966.
 12. R. H. Dicke, in 3^e Conf. Intern. d'Electronique Quantique, Dunod, Paris, and Columbia U. Press, New York, 1964; p. 35.
 13. M. Andrews, J. Bzura, H. H. Fleischmann, and N. Rostoker, Effects of a Magnetic Guide Field on the Propagation of Intense Relativistic Electron Beams, Lab. of Plasma Studies Report 18, Cornell Univ., Ithaca, N. Y., July 1969.

However, the present study is concerned with the propagation of intense relativistic electron beams in a magnetic guide field. The present study is concerned with the propagation of intense relativistic electron beams in a magnetic guide field. The present study is concerned with the propagation of intense relativistic electron beams in a magnetic guide field. The present study is concerned with the propagation of intense relativistic electron beams in a magnetic guide field.

Even in the present study several new phenomena were observed in beam propagation.

ACKNOWLEDGMENTS

The author wishes to express his appreciation to the following persons for their assistance in the preparation of this report: J. Glancy assisted in designing the experimental apparatus; the detailed construction of the apparatus was done by J. Glancy, J. Bzura, and J. Rostoker; the author is indebted to J. Bzura and J. Rostoker for their assistance in the construction of the apparatus; and to J. Rostoker for his helpful discussions and the experimental assistance.

REFERENCES

1. J. Bzura, J. Rostoker, and N. Rostoker, Phys. Rev. Lett. 19: 1025, 1967.
 2. M. Andrews, J. Bzura, D. A. Hammer, J. Rostoker, and N. Rostoker, Phys. Rev. Lett. 19: 1025, 1967.
 3. M. Andrews, J. Bzura, D. A. Hammer, J. Rostoker, and N. Rostoker, Phys. Rev. Lett. 19: 1025, 1967.
 4. J. Bzura, J. Rostoker, and N. Rostoker, Phys. Rev. Lett. 19: 1025, 1967.
 5. J. Bzura, J. Rostoker, and N. Rostoker, Phys. Rev. Lett. 19: 1025, 1967.
 6. J. Bzura, J. Rostoker, and N. Rostoker, Phys. Rev. Lett. 19: 1025, 1967.
 7. J. Bzura, J. Rostoker, and N. Rostoker, Phys. Rev. Lett. 19: 1025, 1967.
 8. J. Bzura, J. Rostoker, and N. Rostoker, Phys. Rev. Lett. 19: 1025, 1967.
 9. J. Bzura, J. Rostoker, and N. Rostoker, Phys. Rev. Lett. 19: 1025, 1967.
 10. J. Bzura, J. Rostoker, and N. Rostoker, Phys. Rev. Lett. 19: 1025, 1967.
 11. J. Bzura, J. Rostoker, and N. Rostoker, Phys. Rev. Lett. 19: 1025, 1967.
 12. J. Bzura, J. Rostoker, and N. Rostoker, Phys. Rev. Lett. 19: 1025, 1967.
 13. J. Bzura, J. Rostoker, and N. Rostoker, Phys. Rev. Lett. 19: 1025, 1967.
 14. J. Bzura, J. Rostoker, and N. Rostoker, Phys. Rev. Lett. 19: 1025, 1967.
 15. J. Bzura, J. Rostoker, and N. Rostoker, Phys. Rev. Lett. 19: 1025, 1967.
 16. J. Bzura, J. Rostoker, and N. Rostoker, Phys. Rev. Lett. 19: 1025, 1967.
 17. J. Bzura, J. Rostoker, and N. Rostoker, Phys. Rev. Lett. 19: 1025, 1967.
 18. J. Bzura, J. Rostoker, and N. Rostoker, Phys. Rev. Lett. 19: 1025, 1967.
 19. J. Bzura, J. Rostoker, and N. Rostoker, Phys. Rev. Lett. 19: 1025, 1967.
 20. J. Bzura, J. Rostoker, and N. Rostoker, Phys. Rev. Lett. 19: 1025, 1967.

INTERNAL Q-SWITCHING AND LONG TIME DELAY PHENOMENA IN ELECTRON BEAM EXCITED GaAs LASERS

SUSUMU NAMBA, AKIO MASUYAMA, MITSUO KAWABE, and KOHZOH MASUDA

Electrical Engineering, Osaka University, Toyonaka, Osaka, Japan

Internal Q-switching and long-time-delay phenomena were observed in electron-beam-excited p-type and n-type GaAs lasers above the transition temperature. The same phenomena observed in homostructure diode lasers have been explained by the double-acceptor type of trapping model, but the phenomena observed in single heterostructure diode lasers have been explained by a hole injection model.

The fact that the phenomena are observed as a bulk effect in the electron-beam-excited GaAs lasers without p-n junction suggests that the phenomena cannot be explained by the hole-injection model. The fact that both p and n-type GaAs show the same phenomena suggests that both type of GaAs have the same optical absorbing trapping centers.

INTRODUCTION

A long time delay of the stimulated emission from the beginning of an exciting pulse and an internal Q-switching (IQS) generated at the termination of the exciting pulse have been observed in several types of GaAs lasers such as stripe-geometry type GaAs diode lasers,¹⁻⁴ GaAs-Ga_xAl_{1-x}As single-heterostructure lasers,⁵ and electron-beam (EB) excited GaAs lasers.^{6,7}

The long time delay, of the order of several hundred nanoseconds, was observed above a certain temperature that is the transition temperature T_t , and explained by the assumption of a suitable number of optical reabsorption centers in the material.⁸ Below T_t , the time delay was only about 10^{-9} sec and was explained as the time required to fill the carrier traps and build up the population inversion in the active region.^{9,10}

Recently the IQS was observed in samples with the long time delay. To explain the two phenomena observed in the same sample the double-acceptor type of trapping model²⁻⁴ was proposed as an improvement of the optical reabsorption model. On the other hand, the same phenomena were observed in single heterostructure diode lasers and explained as related to a hole-injection phenomenon.⁵ It is clear that there is no common explanation for the phenomena at present.

In this paper, the same phenomena observed in the EB excited p-type and n-type GaAs lasers without p-n junction are reported, and discussed in comparison with the abovementioned models.

EXPERIMENTAL PROCEDURE

1. EXPERIMENTAL APPARATUS. The cleaved faces of the GaAs samples were bombarded by an EB pulse whose acceleration voltage was from 25 to 30 kV, with an EB density of about 1 A/cm^2 . The repetition rate was 40 pps. The excitation pulse width was variable from about 50 nsec to several microseconds. The samples were mounted on a copper heat sink cooled by liquid nitrogen or by liquid helium. The heat-sink temperature

above the liquid-nitrogen temperature was controlled by a heater around the heat sink. The laser light was detected by an RCA-7102 photomultiplier through a grating monochromator, or an EG&G SGD-100 silicon photodiode. The output laser light and the input EB current signals were observed by an oscilloscope.

2. SAMPLES. The physical properties of the GaAs samples such as the carrier type, doped impurities, carrier densities, cavity faces, and cleaved faces are summarized in Table 1.

Table 1. Carrier densities, cavity lengths, cavity faces, and cleaved faces used in this experiment.

GaAs sample	(A)	(B)	(C)
Type	p-type	n-type	n-type
Impurity	zinc	tellurium	tin
Carrier density (cm^{-3})	7.6×10^{18}	$1.7-2.0 \times 10^{18}$	9.6×10^{17}
Cavity length(mm)	0.30-0.40 mm	0.59 mm	0.45 mm
Cavity face	<111>	<100>	<100>
Cleaved face	<110>	<110>	<110>

A laser cavity of the Fabry-Perot type was formed by the mechanically polished surfaces, which were perpendicular to the <110> cleaved faces. The cleaved <110> faces were bombarded by the electron beam.

3. EXPERIMENTAL RESULTS. The spectrum of the IQS light for the Sn-doped sample (C) is shown in Fig. 1. The half-width of the IQS spectra is about 15 Å, which is similar to normal stimulated emission of EB lasers. The light intensity of the IQS emission was of the same order of magnitude as the normal EB laser emission.

The typical output of the IQS in the Zn-doped sample (A) for various input pulse widths is shown in Fig. 2. The upper traces are the output responses and the lower traces are the input current pulses, where the sweeping time is 0.2 $\mu\text{sec}/\text{div}$. The pulse width of the IQS light was observed to be about 10 nsec, which depended on the decay time of the EB excitation pulse. The intensity of the IQS light did not change with increasing the exciting pulse width from about 10^{-8} to 10^{-6} sec. However, below about 10^{-6} sec the light intensity decreased gradually. The spectrum peaks of the IQS light shifted toward the long wavelength with increase in the width of the excitation pulse. These peaks are considered to be the heating effect during the excitation.⁷

The relation of the normalized input current density J/J_{TH} to the time delay of the stimulated emission for the sample (A) is shown in Fig. 3, where J is the EB current density and J_{TH} is the threshold current density. Figure 3(a) shows the relation below T_t . At 42°K the threshold current density is 0.22 A/cm² at 25 kV acceleration voltage and the time delay of several nanoseconds decreases with increasing the J/J_{TH} . Figure 3(b)

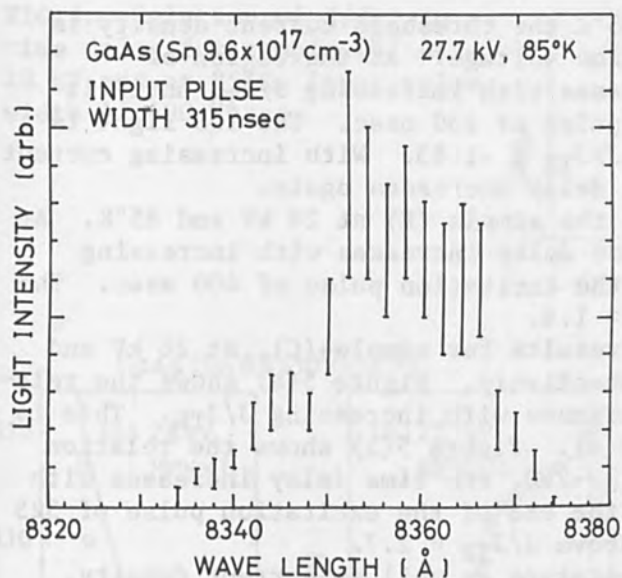


FIG. 1.--Spectrum of the internal Q-switching (IQS) for sample (C) at 27.7 kV and at 85°K. Light peaks occurred at vertical straight line during 1 sec. Repetition rate is 40 pps.

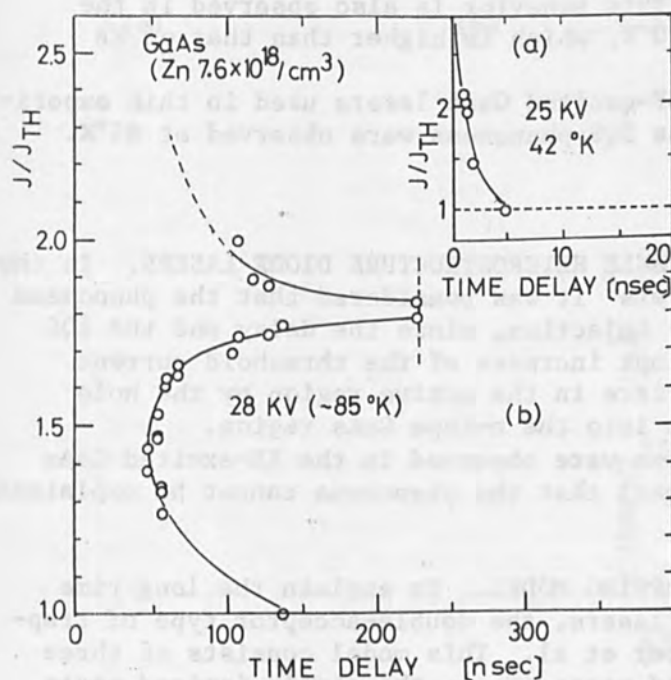


FIG. 3.--(a) Relation of normalized input current density J/J_{TH} to time delay for sample (A). Relation below transition temperature T_t . Threshold current density J_{TH} is about 0.22 A/cm² at 25 kV and 42°K. (b) Relation above T_t . Input pulse width is 230 nsec. J_{TH} is about 1.0 A/cm² at 28 kV and 85°K.

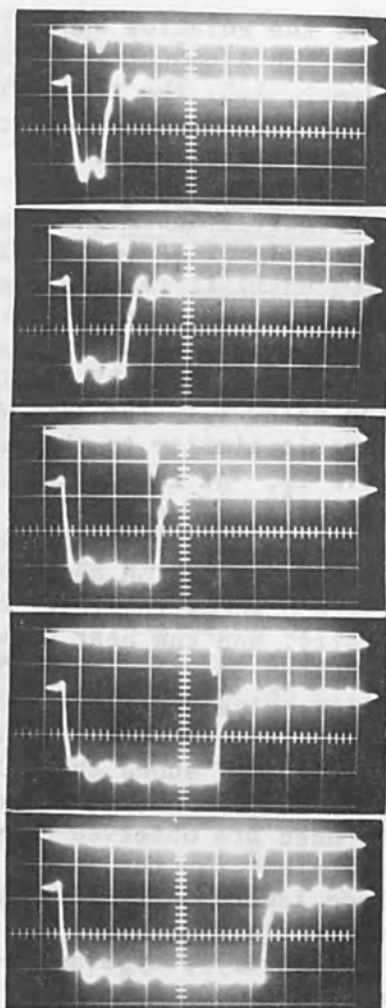


FIG. 2.--Typical output of IQS in p-type EB GaAs laser for various input pulse widths at 28 kV and at liquid-nitrogen heat-sink temperature. Upper and lower traces are light emissions of IQS and current pulses, respectively. (Horizontal scale, 0.2 μs/div.)

shows the relation above T_t . At 85°K the threshold current density is about 1.0 A/cm² at 28 kV acceleration voltage. At the region of $J/J_{TH} \geq \sim 1.5$, the time delay increases with increasing J/J_{TH} until it reaches the end of the excitation pulse of 230 nsec. The IQS light is observed in the region of $\sim 1.78 \leq J/J_{TH} \leq \sim 1.83$. With increasing current density above this value, the time delay decreases again.

Figure 4 shows the results for the sample (B) at 28 kV and 85°K. At the region of $J/J_{TH} \geq \sim 1.2$, the time delay increases with increasing J/J_{TH} until it reaches the end of the excitation pulse of 400 nsec. The IQS light is observed above $J/J_{TH} \approx 1.4$.

Figures 5(a) and (b) show the results for sample (C), at 28 kV and 19°K, and at 27.7 kV and 85°K, respectively. Figure 5(a) shows the relation below T_t . The time delay decreases with increasing J/J_{TH} . This is a result similar to that of Fig. 3(a). Figure 5(b) shows the relation above T_t . At the region of $J/J_{TH} \geq \sim 2.0$, the time delay increases with increasing J/J_{TH} until it reaches the end of the excitation pulse of 325 nsec. The IQS light is observed above $J/J_{TH} \approx 2.7$.

The IQS region depends on temperature as well as current density. Figure 6 shows the relations among the IQS region, the exciting current density, and the heat sink temperature. The IQS phenomenon is observed in region II. In region I the stimulated emission occurs during the exciting pulse and in region III only spontaneous emission is observed. Similar results are observed in the diode lasers.^{2,6,11}

Figure 7 shows the relation of the time delay to the heat-sink temperature. As shown in these figures, the time delays from 60 nsec to 100 nsec are observed above T_t which is, for example, 62°K at 25 kV, and 0.27 A/cm² for the sample (A). This behavior is also observed in the diode lasers, but T_t is about 120°K, which is higher than that of EB excited lasers.⁶

In every p-type and n-type EB-excited GaAs lasers used in this experiment, the long time delay and the IQS phenomena were observed at 85°K.

DISCUSSION

1. HOLE INJECTION IN THE SINGLE HETEROSTRUCTURE DIODE LASERS. In the single heterostructure diode lasers⁵ it was considered that the phenomena seemed to be related to the hole injection, since the delay and the IQS were observed just after the abrupt increase of the threshold current which is due to the loss of carriers in the active region by the hole injection from the active region into the n-type GaAs region.

The results that the phenomena were observed in the EB-excited GaAs lasers without p-n junction suggest that the phenomena cannot be explained by the hole-injection model.

2. DOUBLE ACCEPTOR TYPE TRAPPING MODEL. To explain the long time delay and the IQS in GaAs diode lasers, the double-acceptor type of trapping model³ was proposed by Ripper et al. This model consists of three states: the nonelectron-captured state (T_{R1}), the singly ionized state (T_{R2}), and the double-ionized state (T_{R3}). When an electron is captured by a trapping center whose energy level E_1 is close to the valence band, the singly ionized trap makes an optical absorbing level whose energy level E_2 is close to the conduction band and the energy difference $E_2 - E_1$ is close to the energy of the laser light. The density of T_{R2}

FIG. 4.--Relation of J/J_{TH} to time delay for sample (B) at 28 kV and at 85°K. Input pulse width is 400 nsec.

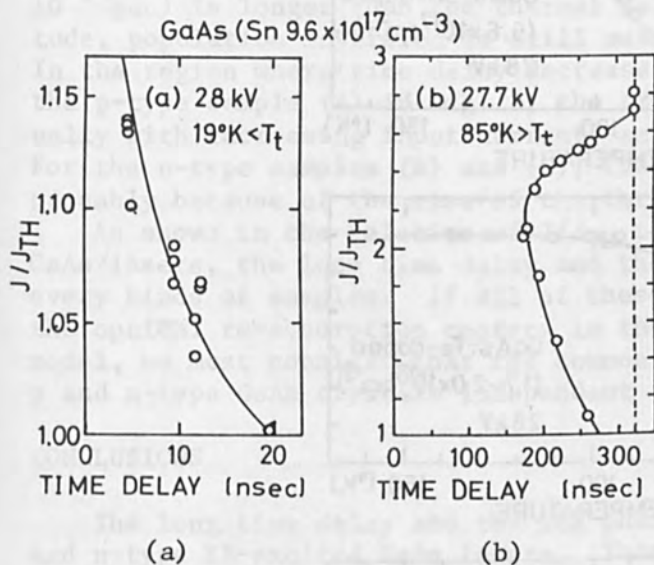
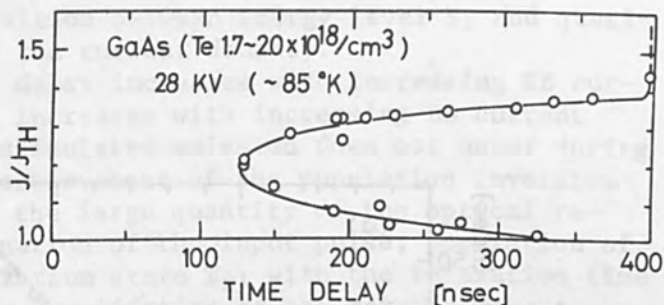


FIG. 5.--(a) Relation of J/J_{TH} to time delay for sample (C) below T_t . (b) Relation of J/J_{TH} to time delay for the sample (C) at 27.7 kV and at 85°K. Input pulse width is 325 nsec.

GaAs (Te $1.7-2.0 \times 10^{18}/\text{cm}^3$)
27.6 kV, (Pulse Width 720 nsec)

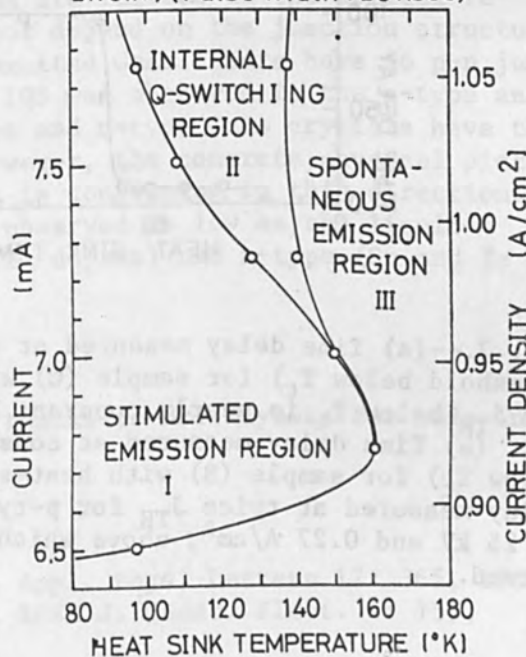


FIG. 6.--Relation of input EB current density to heat-sink temperature for sample (B), which shows the IQS region II. Input pulse width is 720 nsec.

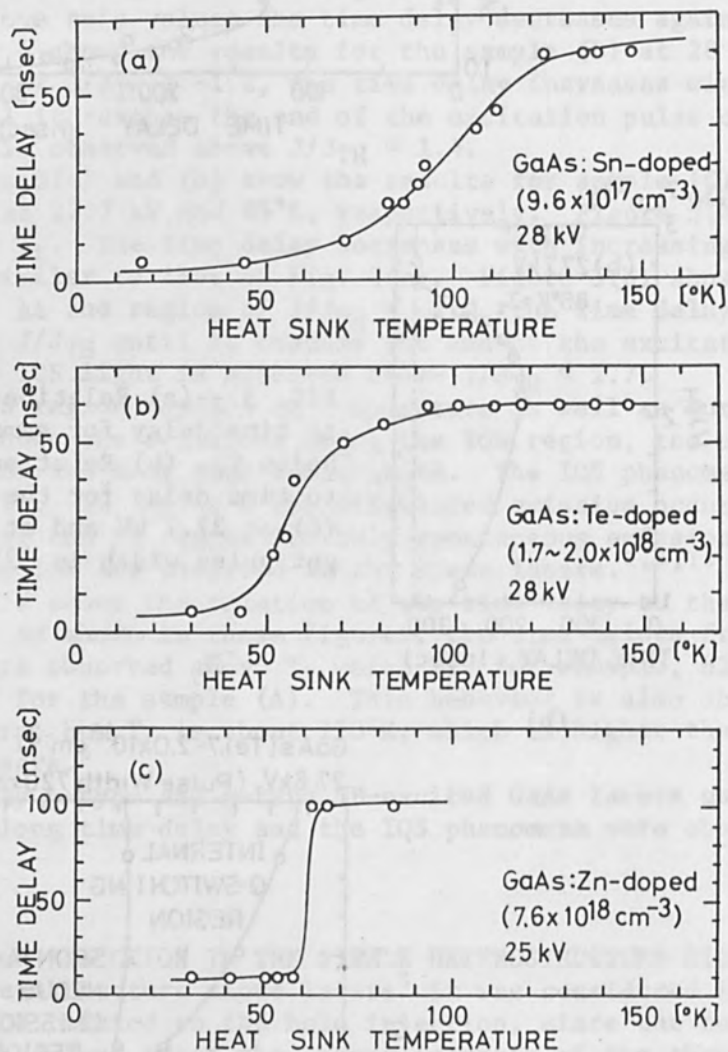


FIG. 7.--(a) Time delay measured at constant current density (at twice threshold below T_t) for sample (C) with heat-sink temperature at 28 kV. The J_{TH} below T_t is nearly constant but abrupt increase of J_{TH} occurs at T_t . (b) Time delay measured at constant current density (at 1.3 times J_{TH} below T_t) for sample (B) with heat-sink temperature at 28 kV. (c) Time delay measured at twice J_{TH} for p-type sample (A). The T_t is about 62°K at 25 kV and 0.27 A/cm², above which about 100 nsec time delay is observed.

is controlled by the relative position between energy level E_1 and quasi-Fermi level E_F , which depends on the current density.

In the region where the time delay increases with increasing EB current density, the density of T_{r2} increases with increasing EB current density. In the IQS region the stimulated emission does not occur during the excitation, in spite of the achievement of the population inversion in the active region, because of the large quantity of the optical re-absorbing centers. At the termination of the input pulse, population of T_{r2} returns to the thermal equilibrium state T_{r1} with the relaxation time of the order of 10^{-11} sec. Since the lifetime of the carrier (about 10^{-9} sec) is longer than the thermal relaxation time by orders of magnitude, population inversion is still maintained and oscillation occurs. In the region where time delay decreases with increasing J/J_{TH} , again for the p-type sample (A) in Fig. 3, the trapping centers are saturated gradually with increasing input current, and the time delay decreases again. For the n-type samples (B) and (C), the last region was not observed, probably because of the rise of the threshold by the heating effect.

As shown in the relation of J/J_{TH} to the time delay for p and n-type GaAs lasers, the long time delay and the IQS phenomena are observed in every kinds of samples. If all of these results could be explained by the optical re-absorption centers in the double-acceptor type of trapping model, we must consider that the common optical trapping centers exist in p and n-type GaAs crystals independent of the sorts of impurities.

CONCLUSIONS

The long time delay and the IQS phenomena are observed in the p-type and n-type EB-excited GaAs lasers. These are the same phenomena as those of the GaAs diode lasers.

It is considered that the phenomena are related to the optical re-absorbing centers in the bulk and do not depend on the junction structure and a hole injection, because the EB-excited GaAs lasers have no p-n junction structure. The results that the IQS was observed in the p-type and n-type samples suggest that both p-type and n-type GaAs crystals have the same optical re-absorbing centers. However, the concrete physical picture of the centers is not clear yet. Work is continuing in this direction.

The transition temperature T_t was observed as low as the liquid-nitrogen temperature in every p-type (Zn dopant) and n-type (Sn and Te dopants) GaAs single crystals.

ACKNOWLEDGMENT

The authors wish to express their thanks to Mr. Miyaoka for help in the experimental work.

REFERENCES

1. J. E. Ripper and J. C. Dymont, Appl. Phys. Letters 12: 365, 1968.
2. J. C. Dymont and J. E. Ripper, IEEE J. Quant. Elect. 4: 155, 1968.
3. J. E. Ripper, IEEE J. Quant. Elect. 5: 391, 1969.
4. J. E. Ripper and J. C. Dymont, IEEE J. Quant. Elect. 5: 396, 1969.

5. E. A. Ulmer Jr. and I. Hayashi, IEEE J. Quant. Elect. 6: 297, 1970.
6. M. Kawabe, A. Masuyama, K. Masuda, and S. Namba, Japan J. Appl. Phys. 9: 850, 1970.
7. A. Masuyama, M. Kawabe, K. Masuda, and S. Namba, Suppl. Japan J. Appl. Phys. 40: 161, 1971. (Proc. 2nd conf. on Solid-State Devices, Tokyo, 1970)
8. G. E. Fenner, Solid-State Electron 10: 753, 1967.
9. K. Konnerth and C. Lanza, Appl. Phys. Letters 4: 120, 1964.
10. K. Konnerth, IEEE Trans. Electron Device 12: 506, 1965.
11. Y. Unno, M. Yamamoto, and S. Iida, Japan J. Appl. Phys. 9: 1181, 1970.

CONCLUSIONS

The long time delay and the lps phenomena are observed in the p-type and n-type EB-excited GaAs lasers. These are the same phenomena as those of the GaAs diode lasers.

It is considered that the phenomena are related to the optical re-absorption centers in the bulk and do not depend on the junction structure and a hole injection, because the EB-excited GaAs lasers have a p-n junction structure. The results that the lps was observed in the p-type and n-type samples suggest that both p-type and n-type GaAs crystals have the same optical re-absorption centers. However, the concrete physical picture of the centers is not clear yet. Work is continuing in this direction.

The transition temperature T_0 was observed as low as the liquid-nitrogen temperature in every p-type (2n dopant) and n-type (2n and 2p dopants) GaAs single crystals.

ACKNOWLEDGMENT

The authors wish to express their thanks to Mr. M. Nishikawa for his helpful discussions during the course of this work.

REFERENCES

1. J. E. Ripper and J. C. Dymant, Appl. Phys. Letters 13: 355, 1968.
2. J. E. Ripper and J. C. Dymant, IEEE J. Quant. Elect. 4: 155, 1968.
3. J. E. Ripper, IEEE J. Quant. Elect. 5: 391, 1969.
4. J. E. Ripper and J. C. Dymant, IEEE J. Quant. Elect. 5: 386, 1969.

PUMPING AND ENHANCEMENT OF GAS LASERS VIA ION BEAMS*

G. H. MILEY, J. T. VERDEYEN, T. GANLEY, J. GUYOT, and P. THIESS

Nuclear Engineering Program and Gaseous Electronics Laboratory,
University of Illinois, Urbana, Ill.

The possible use of high-energy ions produced by nuclear reactions to pump gas lasers or alternately to enhance the output of electrically pumped lasers is discussed. Results from optical emission and also metastable level densities for helium, neon, and He-Ne mixtures are reviewed. Results demonstrating the enhancement of the output from an operating CO₂ laser are presented.

INTRODUCTION

The possibility of efficient coupling of lasers and nuclear reactors or radioisotopes has generated an interest in the use of high-energy ion beams to pump lasers. To avoid radiation-damage problems, gas lasers are generally thought of in this connection. The status and history of this area were reviewed by the authors¹ in 1970, and more recently by Thom and Schneider;² hence only a few key points will be noted here.

Nuclear radiation can be used in two ways: to pump the laser directly, or alternately to enhance operation of a laser by use of an electric discharge or other means as the main pump. The feasibility of direct pumping has yet to be proved unequivocally, although three encouraging results have been reported. Andriakhin et al.³ recently reported possible lasing in Hg at 6150 Å when a Hg-He³ mixture was irradiated with a neutron flux of 5×10^{16} n/cm²-sec from a pulsed neutron source. Earlier studies at Northrop Corp. Laboratories indicated large outputs from Ne-O₂ and also from argon under bombardment by fission fragments from a uranium coating at neutron fluxes of a similar magnitude. Finally, studies described later in this paper have lead Guyot⁴ to suggest that a small (less than 4%/meter) gain may occur on several neon lines during bombardment by alpha particles and lithium ions from a boron coating under high neutron fluxes.

The possibility of using high-energy ion bombardment to enhance the output of an electrically pumped laser has been demonstrated quite conclusively. Andriaklin et al.⁵ found increases of a factor of 2 or 3 when a low-pressure CO₂ laser was irradiated by a 3-MeV proton beam from an accelerator. Allario and Schneider⁶ found an increase of a few per cent when He³ was substituted for He⁴ in a CO₂ laser irradiated by neutrons from a low-power reactor. Ganley et al.⁷ recently reported large increases in output from a low-pressure CO₂ laser with neutron irradiation of a boron coating to provide alpha and lithium ion bombardment. Additional results from the latter study are presented here.

*This work supported by grant AT(11-1) 2007 from the Research Division of the U.S. Atomic Energy Commission.

METASTABLE MEASUREMENTS IN He, Ne, AND He-Ne

Calculations^{1,2} have indicated that lasing should be possible in He-Ne using direct pumping techniques based on neutron fluxes available in the Illinois TRIGA reactor. He-Ne is considered an attractive system because the well-known He-Ne collisional transfer mechanism selectively excites the upper neon lasing levels. (This is an important feature, since high-energy ions, with energies so much larger than atomic energy levels, tend to create a distributed rather than selective excitation.) In addition, the average energy of the thermalized electron distribution created in the irradiated gas is thought to be relatively low and should not back-populate lower lasing levels as severely as in an electrical discharge.

After some preliminary experiments with actual laser tubes, it was decided that a more informative investigation would involve measurement of metastable level densities in He and Ne during irradiation of a boron-coated tube placed next to the core of the Illinois TRIGA reactor (Fig. 1). This study involved passing light through the tube under irradiation and measuring the resulting absorption at a select wavelength. Details of the technique are reported elsewhere,^{4,5} along with results for the He(2^3S), He(2^1S), Ne($1s_2$), and Ne($1s_3$) densities in the respective unmixed gases. The helium metastable densities in He-Ne mixtures are vital to the determination of possible inversion. However, these densities were too low in the mixture to be measured directly with the present technique. Thus a simple calculational model^{4,8} which agrees quite well with unmixed gas measurements has been used to predict the mixture densities shown in Fig. 2. This suggests that inversion of the 1.15- and 3.39- μ m lines in the 9:1 He-Ne mixture should be possible with available neutron fluxes below 10^{16} n/cm²-sec. For example, a 5% gain/pass on the 1.15- μ line requires a He(2^3S) density of 4×10^{10} atm/cm³; and according to Fig. 1, this is just achieved at a flux of 10^{16} n/cm²-sec. Attempts to verify this prediction by gain measurements seem to indicate a small gain (less than 4 %/meter), but the measurement technique is not sensitive enough for an unequivocal proof.

SPECTROSCOPIC STUDIES

The development of nuclear-radiation pumping requires a better understanding of the radiation-induced plasma. This plasma is distinguished by being highly nonequilibrium;^{9,10} the high-energy primary ions and associated δ rays are superimposed on a background of thermalized electrons and ions. Also, the average energy of the latter may be much lower than is commonly encountered in gaseous discharges, in which the electron swarm is heated by an electric field. These differences can be expected to lead to unique excited state distributions, which may in turn allow lasing on new lines, or alternately prevent it on well-known lasing transitions.

Spectroscopic studies of the emission from a radiation-induced plasma have been undertaken to obtain basic information. Alpha particle bombardment is achieved using a 500 mCi Po-210 coating on the inner walls of a cylindrical plasma chamber 1.5 in. in diameter and 12 in. long. A current of about 10^7 5-MeV He⁺⁺ ions/cm²-sec is obtained.

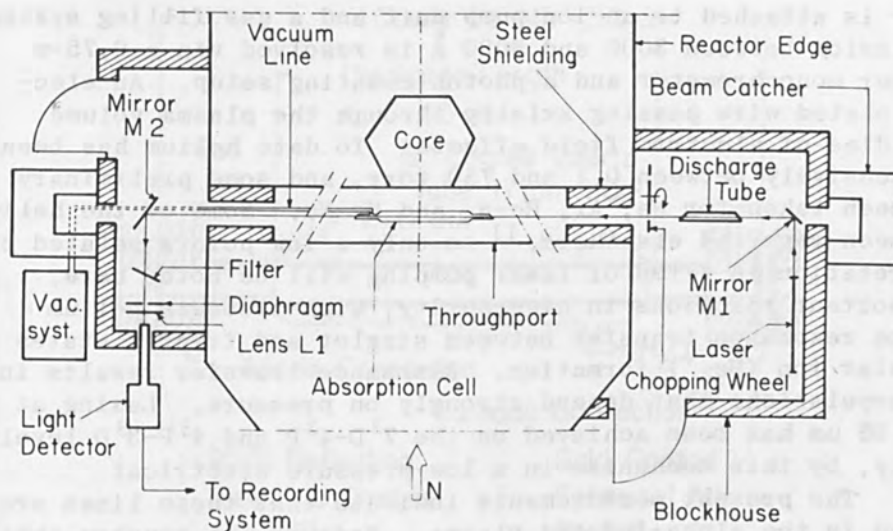


FIG. 1.--Sketch of arrangement used for metastable density measurements. Light from discharge tube is chopped so that phase sensitive detection can be used to reduce background.

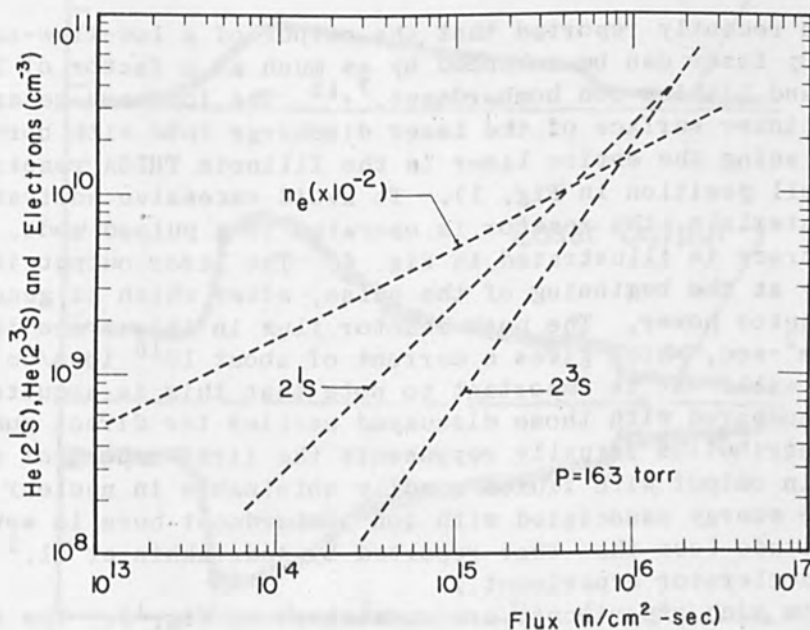


FIG. 2.--Calculated metastable densities for 9:1 He-Ne. Model used has been checked against measurements in unmixed gases. Pressure of 163 torr is thought to be near optimum for gain. Lower pressures reduce energy deposited by ions, i.e., reduce metastable densities. Higher pressures involved excessive line broadening.

The chamber is attached to an ion pump unit and a gas filling system. Optical emission between 3000 and 8000 Å is resolved via a 0.75-m Czerny-Turner monochromator and a photon counting setup. An electrically isolated wire passing axially through the plasma volume permits studies of electric field effects. To date helium has been studied extensively between 0.1 and 750 torr, and some preliminary data have been taken for Ne, Ar, He-N₂ and He-Ne. Some of the helium data have been reported elsewhere,¹¹ so only a few points related to its interpretation in terms of laser pumping will be noted here.

Two important reactions in high-purity, high-pressure helium appear to be resonance transfer between singlet and triplet states and also molecular ion (He₂⁺) formation. Resonance transfer results in large n³S populations that depend strongly on pressure. Lasing at both 2.06 and 1.96 μm has been achieved on the 7³D-4³P and 4³P-3³D levels, respectively, by this mechanism in a low-pressure electrical discharge. The present measurements indicate that these lines are not inverted in the alpha-induced plasma. However, it appears that an inversion of other triplet states (e.g., 5³S-4³P) may be achieved by the addition of small amounts (less than 0.01%) of N₂ impurity. The role of N₂ is not entirely clear. One possible explanation is that it collisionally deexcites the triplet metastable, thus preventing possible back-excitation into lower laser levels. It simultaneously provides for more effective thermalization of subexcitation electrons (below 15 eV) that might enter into the back-reaction.

ENHANCEMENT OF CO₂ LASER OPERATION

The authors recently reported that the output of a low-flow-rate, low-pressure CO₂ laser can be enhanced by as much as a factor of 2 or more by alpha and lithium ion bombardment.^{7,13} The ions are generated by coating the inner surface of the laser discharge tube with boron (Fig. 3) and placing the entire laser in the Illinois TRIGA reactor (at the gain cell position in Fig. 1). To avoid excessive activation of the laser materials, the reactor is operated in a pulsed mode. A typical scope trace is illustrated in Fig. 4. The laser output is seen to rise sharply at the beginning of the pulse, after which it generally follows the reactor power. The peak reactor flux in this trace is about 10¹¹ n/cm²-sec, which gives a current of about 10¹⁰ ions/cm²-sec from the boron wall. It is important to note that this is a quite moderate flux compared with those discussed earlier for direct pumping. The present contribution actually represents the first report of such large changes in output with fluxes readily obtainable in nuclear reactors. (The energy associated with ion bombardment here is several orders of magnitude less than that reported by Andriakhin et al.⁵ for their proton accelerator experiment.)

Results from such experiments are summarized in Fig. 5. The curves in (a) correspond to the case in which the laser is operating at steady state prior to the reactor pulse, whereas in (b) the laser current is swept from 0 to 70 mA during the reactor pulse so that gas is "cold" to start with. In case (a), the sudden drop in voltage (due to radiation-induced conductivity) during the pulse allows the gas to cool somewhat. This in turn helps depopulate the lower lasing state which, combined with improved pumping, probably accounts for the enhanced output. Note

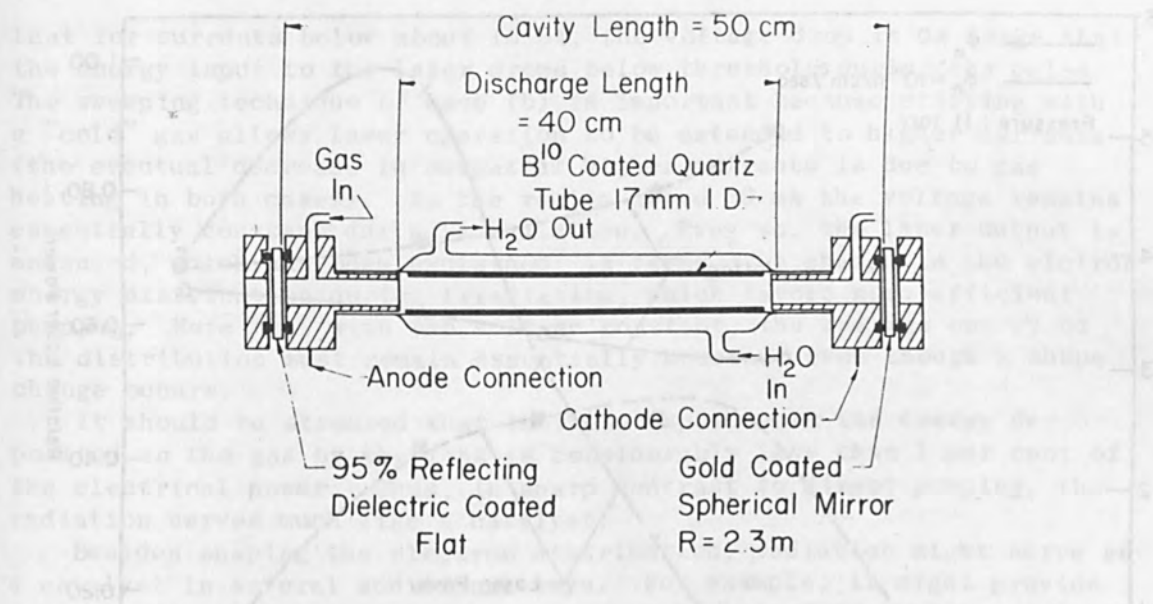


FIG. 3.--Details of boron-lined low-pressure CO₂ laser used in radiation enhancement experiments.

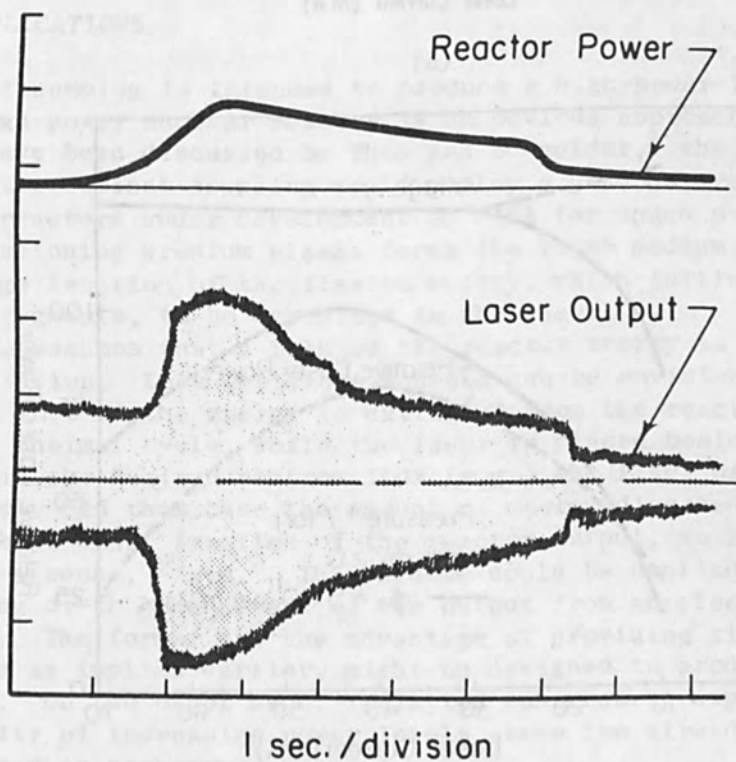
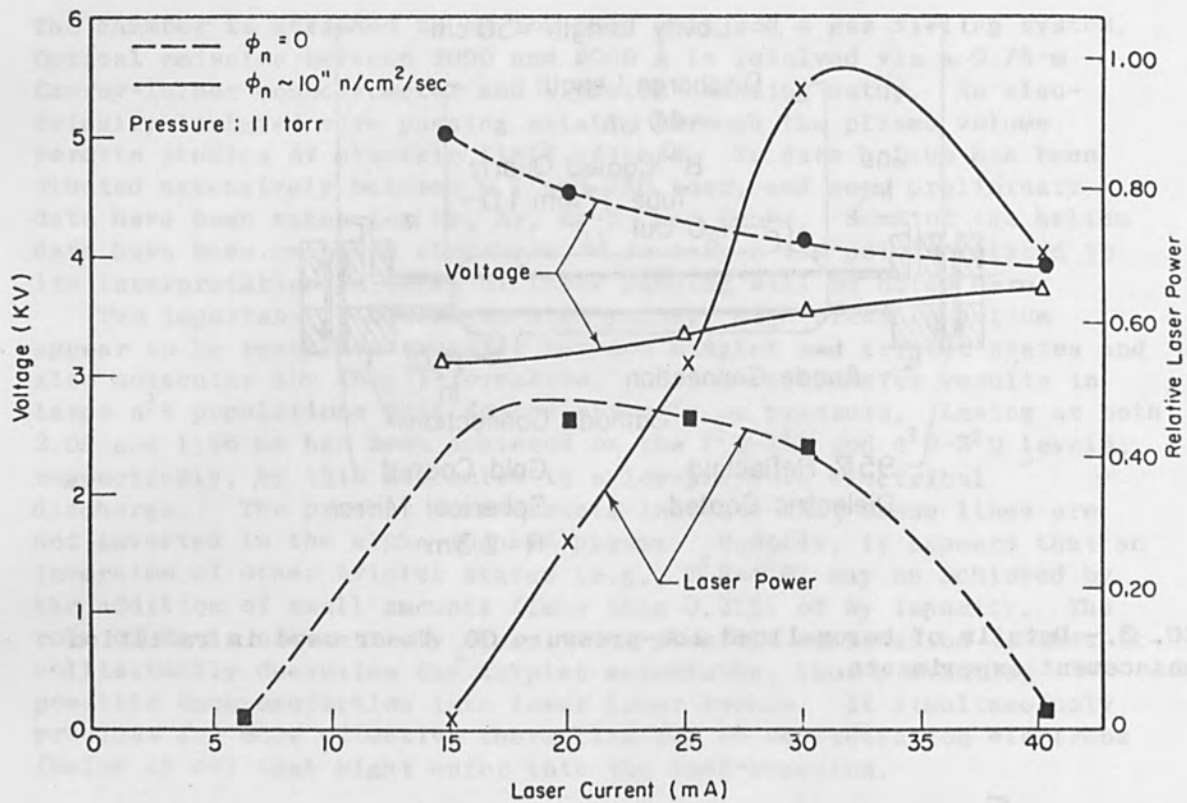
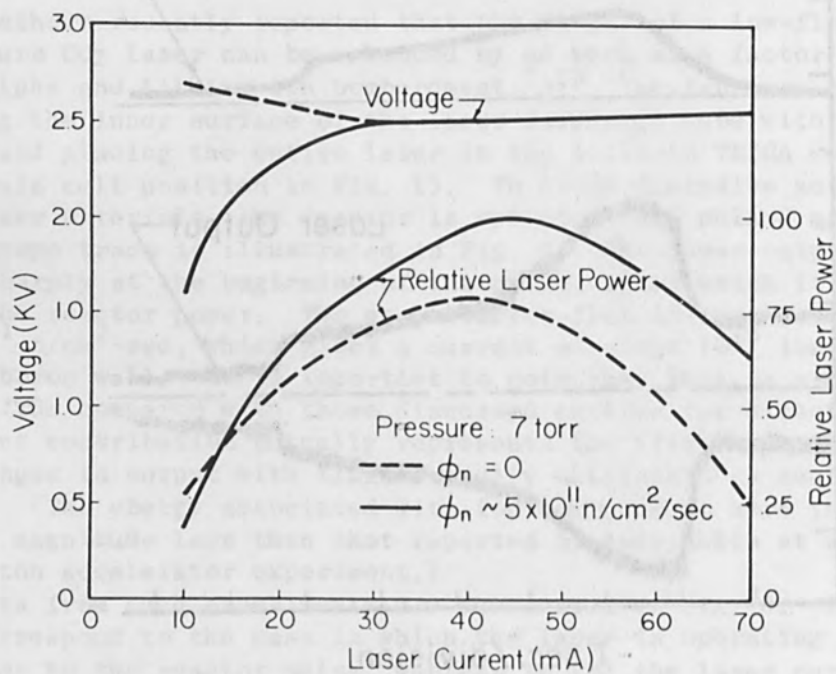


FIG. 4.--Reproduction of scope trace showing enhanced output from operating CO₂ laser. Laser output appears as broad band because it is chopped via ac operation. Reactor trace corresponds to \$1.00 pulse with peak flux of about 10^{11} n/cm²-sec.



(a)



(b)

FIG. 5.--(a) Voltage-current and laser output characteristics with laser is operating at steady state prior to the nuclear reactor pulse. (Cf. Fig. 4; points shown here represent peak values during pulse.)

(b) Results when laser current is swept from 0 to 70 mA during reactor pulse.

that for currents below about 15 mA, the voltage drop is so large that the energy input to the laser drops below threshold during the pulse. The sweeping technique of case (b) is important because starting with a "cold" gas allows laser operation to be extended to higher currents (the eventual decrease in output at higher currents is due to gas heating in both cases). In the region above 30 mA the voltage remains essentially constant during irradiation. Even so, the laser output is enhanced, which has been explained⁷ in terms of a change in the electron energy distribution during irradiation, which favors more efficient pumping. Note that with the voltage constant, the average energy of the distribution must remain essentially constant even though a shape change occurs.

It should be stressed that in these experiments the energy deposited in the gas by the ions is considerably less than 1 per cent of the electrical power. Thus, in sharp contrast to direct pumping, the radiation serves much like a catalyst.

Besides shaping the electron distribution, radiation might serve as a catalyst in several additional ways. For example, it might provide preionization and more uniform characteristics in pulsed high-pressure lasers. Recent experiments by the authors using a TEA Laser have indeed indicated larger outputs might be obtained in this fashion. (After additional experiments, these results will be published in the near future.)

POSSIBLE APPLICATIONS

If direct pumping is intended to produce a high-power laser, coupling to a high-power nuclear reactor is an obvious approach. Several approaches have been discussed by Thom and Schneider,² who point out that the most efficient coupling would employ a gaseous uranium core (similar to reactors under development by NASA for space propulsion) where the fissioning uranium plasma forms the laser medium. This allows a large fraction of the fission energy, which initially resides in fission fragments, to be deposited in the laser.

The above assumes that a bulk of the reactor energy is desired as coherent radiation. Less ambitious schemes can be envisioned if it is assumed that most of the energy is extracted from the reactor via a conventional thermal cycle, while the laser is placed beside or in the core to obtain the desired neutron flux (e.g., the laser of Fig. 3 could be used). In this case the amount of energy diverted to the laser would be a small fraction of the reactor output, so laser pumping would be, in a sense, "free." This scheme could be applied to either direct pumping or to enhancement of the output from an electrically pumped laser. The former has the advantage of providing simple direct coupling, and as implied earlier, might be designed to produce unique output lines. On the other hand, radiation enhancement appears to have the possibility of increasing power levels above the already large values obtained in high-power systems.

Radiation pumping/enhancement can also be conceivable for small mobile devices if future development makes it possible to use the lower particle currents obtainable from a radioisotope.

Although the ultimate goal of this work is to develop efficient laser-nuclear power source coupling, much of the basic data needed can

be acquired by ion accelerator experiments. Our choice of reactor/
Po-210 experiments was governed by availability, and symposium partici-
pants interested in accelerators may want to consider research along
these lines also.

REFERENCES

1. J. C. Guyot, G. H. Miley, J. T. Verdeyen, and T. Ganley, On laser pumping via nuclear radiations, in Proc. Symp. Uranium Plasmas and Their Technological Application, U. of Florida, Gainesville, Jan. 1970. (In press, NASA SP236.)
2. K. Thom and R. T. Schneider, Nuclear Pumped Gas Lasers, 9th Aerospace Sciences Meeting, New York, January 1971, AIAA paper no. 71-110.
3. V. M. Andriakhin et al., ZHETF, Pis. Red. 12: 83, July 1970.
4. J. C. Guyot, Measurement of Atomic Metastable Densities in Noble Gas Plasmas Created by Nuclear Reactions, Ph.D. Thesis, N. E. Program, U. of Illinois, Urbana, 1971.
5. V. M. Andriakhin et al., JETP Letters 8: 214, 1968.
6. F. Allario and R. T. Schneider, Enhancement of laser output by nuclear reactions, in Proc. Symp. Uranium Plasmas and Their Technological Application, U. of Florida, Gainesville, Jan. 1970. (In press, NASA SP236.)
7. T. Ganley, J. T. Verdeyen, and G. H. Miley (In press, Appl. Phys. Letters.)
8. J. C. Guyot, G. H. Miley, and J. T. Verdeyen, submitted, J. Appl. Phys.
9. P. E. Thiess and G. H. Miley, Calculations of ionization-excitation source rates in gaseous media irradiated by fission fragments and alpha particles, in Proc. Symp. Uranium Plasmas and Their Technological Applications, University of Florida, Gainesville, Jan. 1970. (In press, NASA SP236.)
10. D. B. Rees, C. B. Leffert, and D. J. Rose, J. Appl. Phys. 40: 1884, 1969.
11. P. E. Thiess and G. H. Miley, Optical emission from noble gas plasmas created by alpha particles, Trans. Am. Nucl. Soc. 14: 1971.
12. C. K. N. Patel, W. R. Bennett Jr., W. L. Faust, and R. A. McFarlane, Phys. Rev. Letters 9: 102, 1962.
13. T. Ganley, J. T. Verdeyen, and G. H. Miley, Effect of nuclear radiation on operating characteristics of a CO₂ laser, Trans. Am. Nucl. Soc. 14: 1971.

A BEAM PROFILE ANALYZER FOR HIGH-POWER LASER BEAMS

T. V. GEORGE

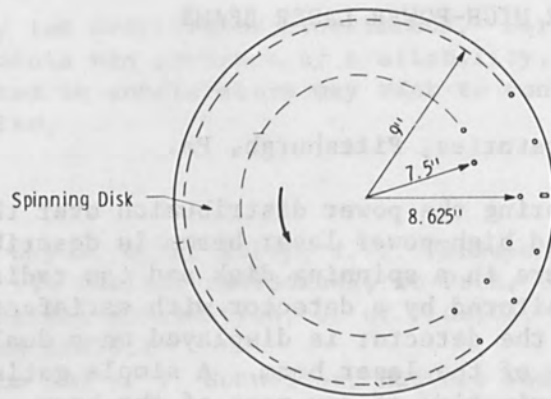
Westinghouse Research Laboratories, Pittsburgh, Pa.

An instrument for measuring the power distribution over the cross section of focused or unfocused high-power laser beams is described. The beam is scanned by a fine aperture in a spinning disk and the radiation emerging through the aperture is monitored by a detector with satisfactory time resolution. The output of the detector is displayed on a dual-beam oscilloscope to give the profile of the laser beam. A simple gating and displaying circuit permits examination of any part of the beam. Beam profile data on a 200-W cw CO₂ laser is presented.

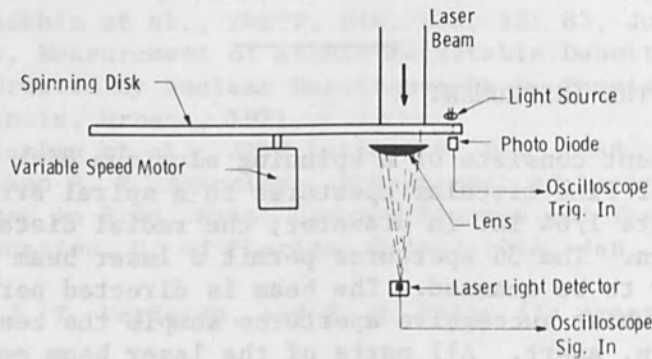
DESCRIPTION OF THE INSTRUMENT

The instrument consists of a spinning aluminum disk 9 in. in diameter with a series of fine circular apertures in a spiral arrangement (Fig. 1). The apertures are 1/64 in. in diameter; the radial distance is changed in steps of 1/32 in. The 36 apertures permit a laser beam as large as 1-1/8 in. in diameter to be scanned. The beam is directed perpendicular to the spinning disk, whose successive apertures sample the beam in nearly linear segments 1/32 in. apart. All parts of the laser beam emerging through the apertures are collected by a lens and focused at a gold-doped germanium detector with a risetime less than 100 ns. The output of the detector is displayed directly on an oscilloscope.

In order to obtain a series of trigger pulses to initiate the horizontal sweep of the oscilloscope in synchronism with beam sampling, an equal number of equally spaced holes are located near the rim of the disk. Light from an incandescent bulb is chopped by these holes and a photodetector is used to obtain the trigger pulses. The hole corresponding to the scanning aperture farthest from the center is larger than the rest to yield a larger trigger pulse. If the oscilloscope trigger level is set for this largest pulse and the sweep duration is made equal to the period of revolution of the spinning disk, the oscillogram will show a series of pulses corresponding to the power density distribution over each linear segment scanned by the sampling apertures (Fig. 2). The linear segments are separated from each other by 1/32 in. Thus the oscillogram is a display of a spatially resolved power-density profile. The speed of rotation of the spinning disk can be adjusted so that a desired integral number of pulses is displayed per unit length of the oscillogram. In Fig. 2, 4 pulses/cm was obtained, so that the horizontal scale is $4 \times (1/32)$ or 1/8 in. per cm. However, if the oscilloscope trigger is set low so that it will be triggered by every trigger pulse and if the sweep rate is increased by a factor equal to the total number of sampling apertures, the oscillogram will show a large number of superimposed traces (Fig. 3). This overlapping set of traces gives quantitative information on the power density distribution over the entire beam cross section; however, if this information is to be extracted, the traces must be separately displayed.



Top View of the Disk



Side View

FIG. 1.--Laser beam power density analyzer.

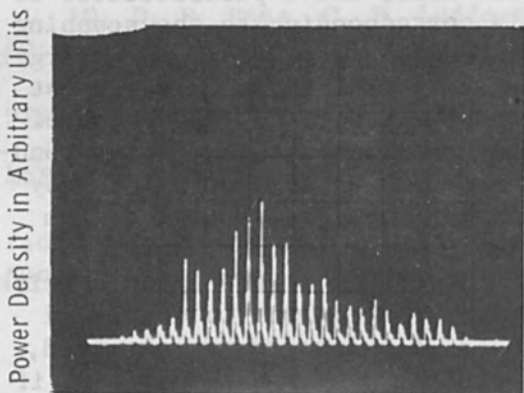


FIG. 2.--Power density distribution across unfocused laser beam.

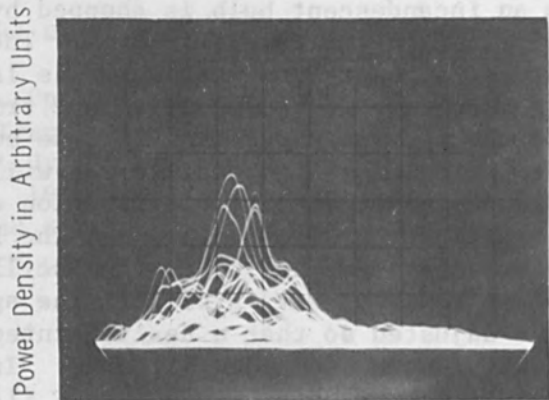


FIG. 3.--Spatially resolved power density sampled by apertures in spinning disk.

IMPROVED OSCILLOSCOPE DISPLAY SYSTEM

To unravel the overlapping traces shown in Fig. 3 the pulses are displayed on successively shifted base lines and the undesired traces are selectively blanked. A Tektronix 555 dual-beam oscilloscope is used for this purpose. The signal from the gold-doped germanium detector is displayed on the upper channel using a standard plug-in unit (such as Type L) to obtain an oscillogram similar to Fig. 2. For the lower channel, a differential amplifier plug-in unit (such as Type CA) is used. The signal is fed into the 'A' input, and the sawtooth output from the upper channel sweep is fed into the 'B' input. The lower channel is operated as in Fig. 3. In Fig. 4 the upper photo shows the oscillogram of the two sets of traces. The lower traces give a three dimensional presentation of the power density, with each of the traces portraying the power density as sampled by the respective scanning aperture. The irregular shapes of these traces are believed to arise from the superposition of a number of modes. The top trace gives the variation of power density in a direction normal to the scanning direction of the apertures. The absolute value of power density can be obtained by normalizing the volume under the set of lower traces against the total power measured by a calorimeter. The instrument is also capable of yielding quantitative information on temporal variations in the power density distribution of a laser beam.

If the number of traces on the lower channel display is too large and confusing, the trigger into this channel can be selectively gated on, permitting the display of only the traces needed for the measurement. In Fig. 4, the lower photograph shows the oscillogram displaying six out of thirteen traces, as shown in the upper photograph. The upper channel is intensity modulated for easy identification of the traces displayed on the lower channel. The block diagram is shown in Fig. 5 and the various circuits are shown in Fig. 6. The delayed trigger output pulse of the Tektronix 555 scope is fed into a monostable multivibrator, the output of which is connected to a gating circuit and the baseline brightening circuit of the upper channel. The gating circuit passes the trigger pulses into the lower channel only in the presence of an output pulse from the multivibrator and the upper channel baseline is brightened during that time. By suitably delaying the pulse and varying the pulse width, any number of pulses seen on the upper channel can be selectively displayed on the lower channel, which permits easy measurement of power density over any linear segment of the laser beam scanned by the spinning device.

To investigate the power density distribution of a focused laser beam by means of the same spinning disk, the optical system shown schematically in Fig. 7 is used. The laser beam is focused by a concave mirror of long focal length at point P. A plane mirror and a concave mirror of shorter focal length are then used to magnify the image of P at the spinning disk with sufficient magnification to obtain satisfactory spatial resolution. The results of the investigations carried out on a home-built carbon dioxide laser are shown in Fig. 8. The pressure of the $\text{CO}_2:\text{N}_2:\text{He}$ gas mixture is varied from 20 to 40 torr, with the discharge current kept constant at 125 mA. The oscillograms show better distribution of power density at higher pressures. From the magnification factor of the optical system and the focal length of the first concave mirror, the observed spatial distribution of power density can be transformed into power per unit solid angle. For example, for a distance between two successive line segments of $1/32$ in. the spacing between two adjacent pulses on the upper channel is 0.3 mrad.

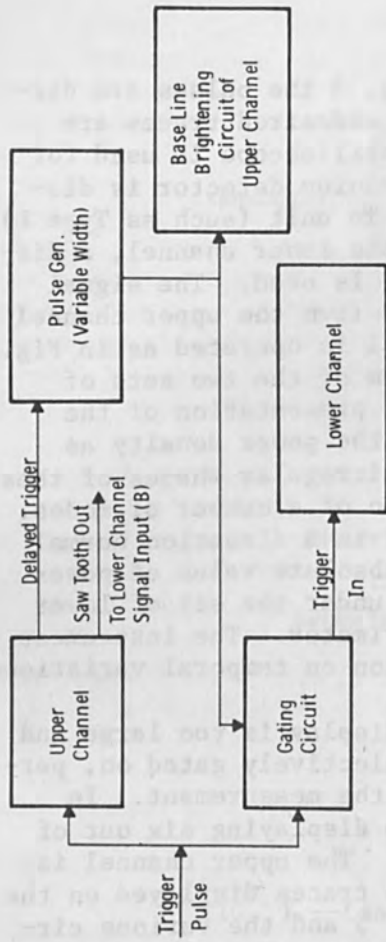


FIG. 5.--Block diagram of circuitry used in display systems.

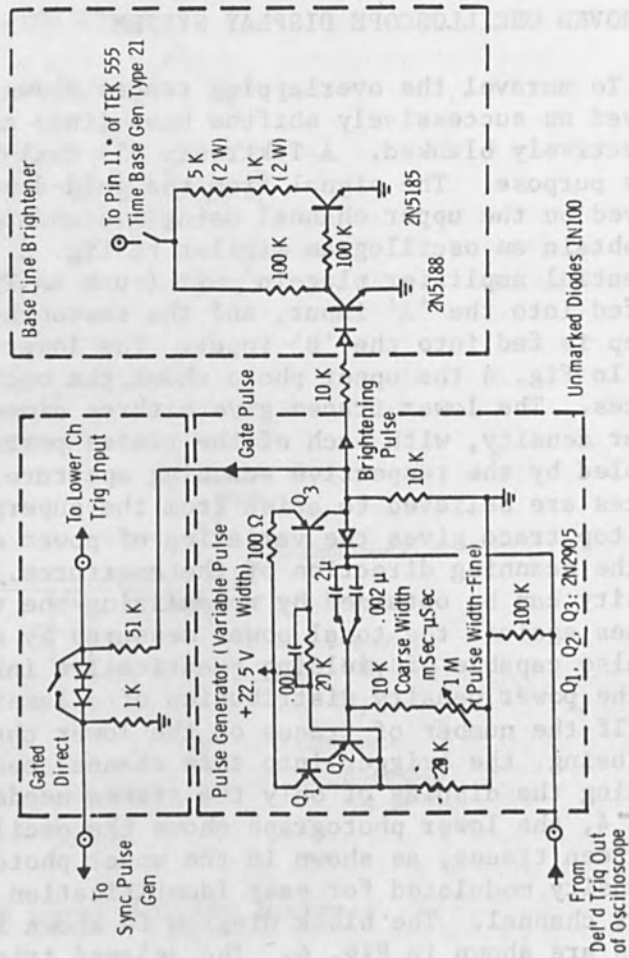


FIG. 6.--Gating circuit diagrams.

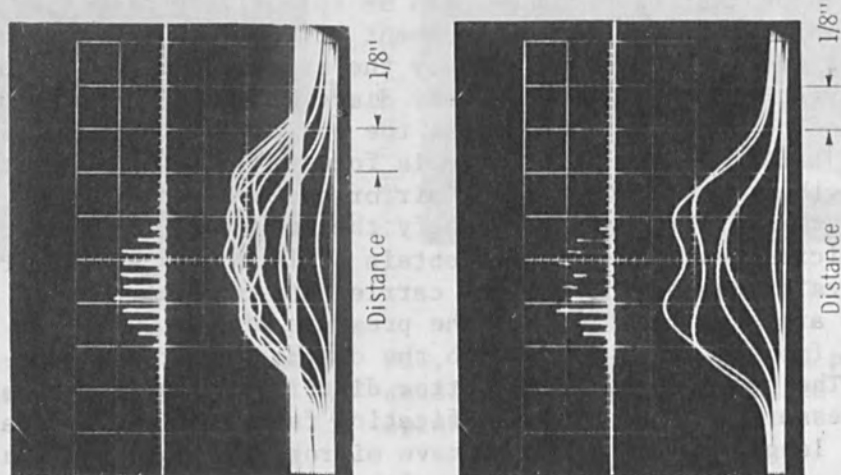


FIG. 4.--Power density variation shown on successively displaced base lines.

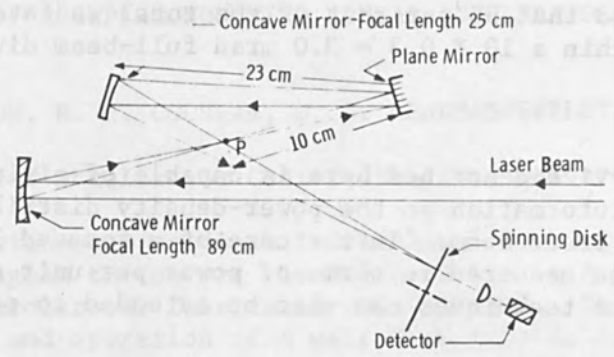


FIG. 7.--Optical arrangement for investigations of power density variation of focused laser beam.

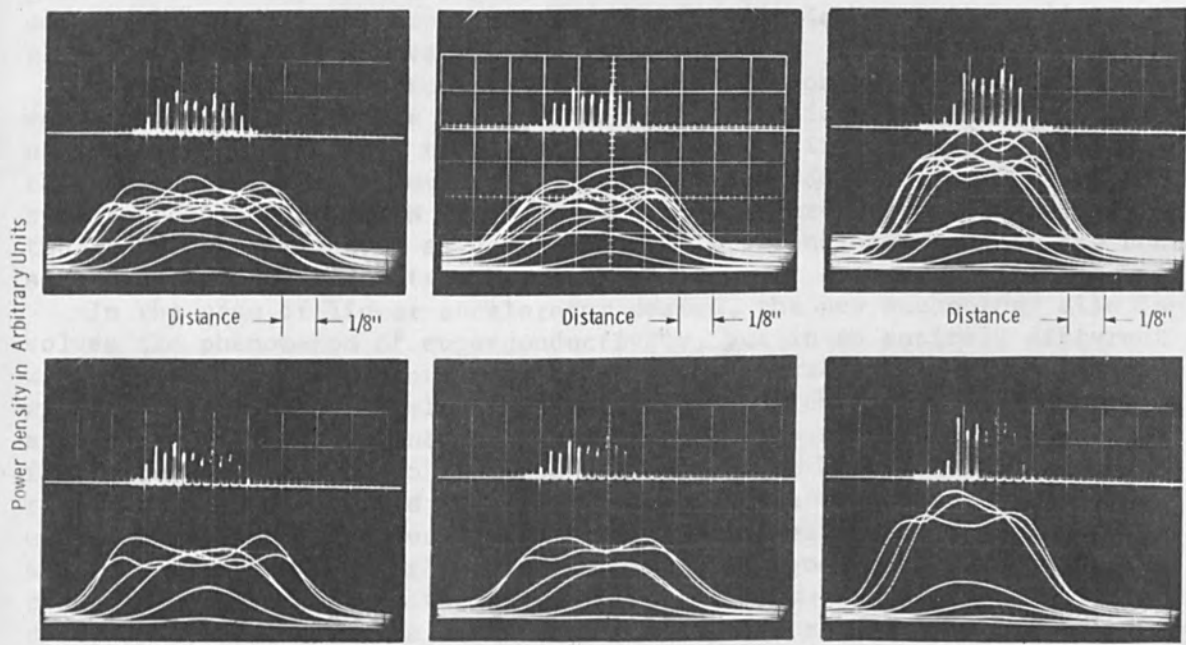


FIG. 8.--Variation of power density profile of focused laser beam for various pressures of CO_2 : N_2 : He mixture and constant discharge current (125 mA). Left to right: 20 Torr, 125 W; 30 Torr, 215 W; 40 Torr, 280 W.

Thus it can be concluded that 95 per cent of the total radiated power from the laser beam lies within a $10 \times 0.3 = 3.0$ mrad full-beam divergence angle.

CONCLUSION

The experimental device described here is capable of giving time-resolved quantitative information on the power-density distribution across a focused or unfocused laser beam. In the case of a focused laser beam, the power density can be measured in terms of power per unit solid angle of beam divergence. The techniques can also be extended to pulsed lasers.

ACKNOWLEDGMENT

A similar technique for measuring the power-density distribution of an electron beam using a perforated spinning disk was previously developed by Drs. B. W. Schumacher and J. Fink of Westinghouse Research Laboratories (unpublished). The author also acknowledges the able assistance of Mr. James Nee in the instrumentation and data acquisition.



SESSION ON FABRICATION TECHNOLOGY

FABRICATION OF A SUPERCONDUCTING LINEAR ACCELERATOR BY ELECTRON-BEAM WELDING*

A. E. JOHNSTON, R. R. COCHRAN, W. B. HERRMANNSFELDT, and G. P. FRITZKE

Stanford Linear Accelerator Center, Stanford University, Stanford, Calif.

The electron-beam welding of columbium (niobium) is being studied as part of a program to convert the Stanford Linear Accelerator to a superconducting accelerator fabricated from niobium. This paper describes the construction and operation of a welder to provide test parts for this program.

The Stanford Linear Accelerator Center has as its principal instrument a two-mile linear electron accelerator. This machine is capable of accelerating electrons to an energy above 2×10^{10} eV. The maximum beam power is over 600 kW. The chief limitations of this instrument are the maximum energy and the low duty cycle (about 0.0005). The long-term productivity of the laboratory would be greatly enhanced if both the energy and the duty cycle could be increased. Accordingly, a study program¹ is under way with the goal of converting the accelerator to a superconducting accelerator capable of achieving energies of about 10^{11} eV and also a substantial improvement in the duty cycle.

High-energy accelerator design and construction has throughout the world advanced to a point at which further significant gains in operating parameters must use "new technology" or be prohibitively expensive. Thus the two newest accelerators to be approved, the NAL 200- to 500-GeV proton synchrotron² and the CERN 300-GeV proton synchrotron,³ both project further increases in energy as coming from "new technology," namely the construction of superconducting magnets.

In the case of linear-accelerator design, the new technology also involves the phenomenon of superconductivity, but in an entirely different way. A linear accelerator consists of an accelerating structure excited with rf power to create electric fields on which charged particles can be accelerated. In a conventional accelerator, this structure is generally fabricated from copper to get good efficiency; perhaps 10 per cent of the rf power can be converted to beam power. Substantial improvements in efficiency depend on reducing the resistive losses in the structure itself. Unlike the case of dc resistivity, which goes to zero at superconducting temperatures, the rf resistance remains finite although it does decrease somewhat as a function of temperature. Of the superconducting metals only two, lead and niobium, have been found to have improvement factors large enough to be considered seriously for this application. The improvement factor, defined as the ratio of room-temperature copper resistivity to the resistivity of the superconducting material, must be of the order of 10^6 to make it possible to reach significantly higher fields and still keep the losses low enough to make the refrigeration system economically feasible. The poor structural properties of lead and its tendency to be easily oxidized leave niobium as the best known material for a superconducting accelerator structure.

All successful laboratory tests indicate that the accelerating structure surface must be very smooth and very clean to achieve the required improvement factors. At present, the process used to achieve these

*Work supported by the U. S. Atomic Energy Commission.

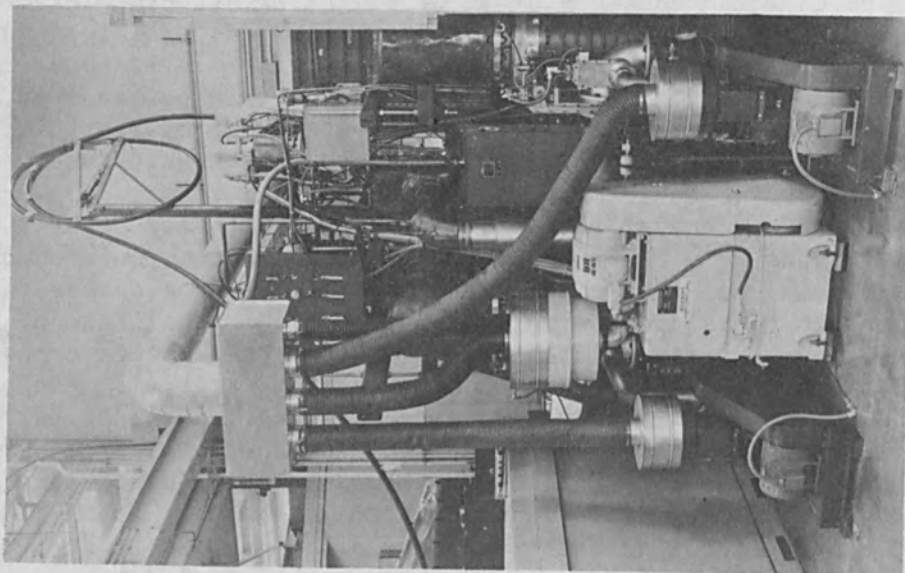


FIG. 1.--Exterior of welder showing vacuum pumps and humidity controlled enclosure.

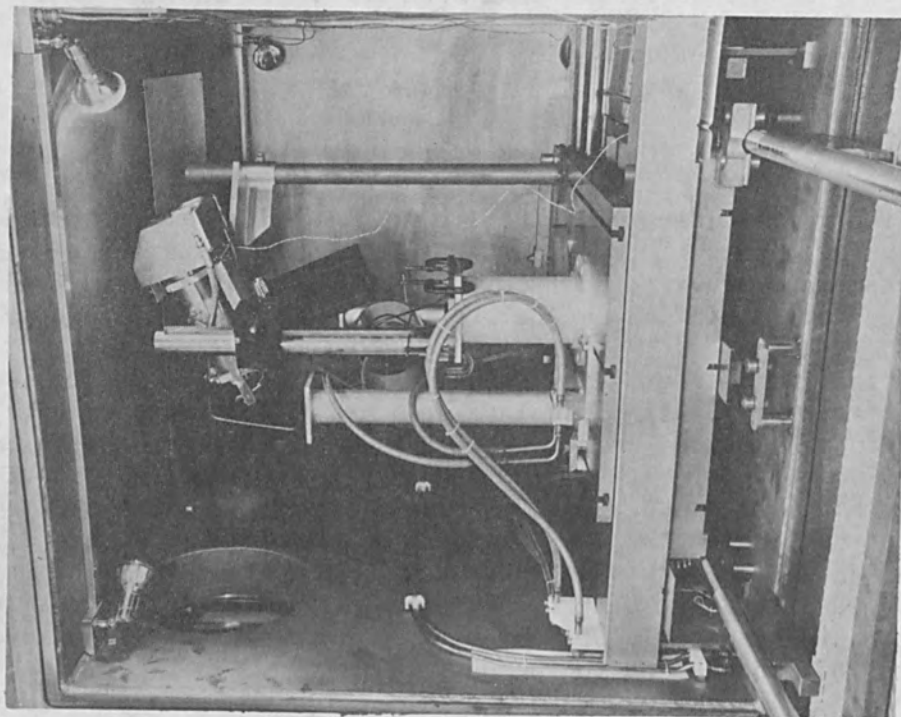


FIG. 2.--Interior of weld chamber. Rotary fixture with cryopanel for welding accelerating structure mounted on X-Y table.

surface properties involves chemical etching and vacuum firing of the parts at about 1900°C. Needless to say, the niobium itself must be very pure.

In addition to surface properties, the structure must be dimensionally accurate and stable. The welds must have the same properties as the rest of the surface and must be such that dimensional changes (if any) produced by the weld are consistent from weld to weld. Since the structure operates immersed in superfluid liquid helium, all joints must be absolutely tight.

To prevent contamination of the pure niobium by the welding process, the welding chamber and vacuum system are operated at a pressure of about 10^{-6} torr. In addition, cryopanel, which are copper shields, cooled by liquid nitrogen, would be used in the vicinity of critical joints to reduce the possibility of contamination further. These panels are designed for each critical set up. When used, they lower the pressure locally (and often in the whole chamber) by at least one order of magnitude.

The electron gun and optical assembly plus all the electronics are parts from a salvaged 25-kW Hamilton-Standard welder (Fig. 1). The vacuum chamber, which was designed and fabricated at SLAC, is 60 in. wide, 64 in. high and 108 in. long. The full-size doors at either end can be removed to add chamber sections if additional length is required. The chamber walls are bare carbon steel. Some concern had been expressed about wall contamination or rust. However, after 7 months of operation, there is no sign of rust, and the vacuums achieved speak for themselves.

The chamber design generally follows that of an equivalent Hamilton-Standard chamber. The principal differences, aside from the vacuum system, are in the frame and some of the details. Square and rectangular tubing was used to reinforce the walls and simultaneously support the chamber and the diffusion pumps. Instead of laminating the leaded X-ray glass for the windows, a piece of plate 3/4 in. thick glass was used to take the vacuum load and to make the seal. The lead glass was then placed over the window out of the vacuum. This method reduces the cost of the window and allows easy removal of X-ray glass for annealing out radiation browning.

The vacuum system consists of two CVC 20-in. diffusion pumps with refrigerated cold caps, backed up with two 50-cfm mechanical pumps. A 300-cfm Stokes Microvac mechanical pump is provided for roughing the chamber and for additional backing for the diffusion pumps. The pumps are isolated from the chamber by 20-in. vacuum valves. For most welds (without cryopanel), this system pumps the chamber down to 10^{-6} torr in about 30 min. During one typical pump down, the chamber base pressure was 5×10^{-7} torr and after cooling down the cryopanel, the pressure was 6×10^{-8} torr. Cooling down and warming up the cryopanel usually takes longer than pumping down and letting up the chamber vacuum.

Parts are positioned by an X-Y table of about 1200 lb capacity. The table drive is mounted under the operator's platform and coupled to the vacuum feedthrough shafts by elastomeric couplings. These couplings have effectively isolated drive vibration from the welding chamber. The X-Y table can be run out on tracks to facilitate making setups outside the chamber. Entrance to the chamber is from a pressure- and humidity-controlled enclosure that helps keep gross contamination under control.

Rotary welds are made on a powered spindle similar to that on a Hardinge lathe, so that Hardinge collets and chucks may be used directly. The spindle housing is provided with tapped holes to facilitate adding a

tail stock or other special fixture as required. The dc drive motor is sealed in a vacuum-tight housing and drives the spindle or other fixture by roller chain and sprockets. The rotary fixture is shown on the X-Y Table in Fig. 2.

Figure 3 shows the design of a short test accelerator structure called Leapfrog. It is a traveling-wave structure which means, from a practical point of view, that it has a return path (a rectangular waveguide) for the rf power that provides a location for various tuning and monitoring devices as well as a place for a power input. The return loop is attached to the accelerating structure through special "coupler" cavities at each end. Each cavity must be welded at the inner and outer diameters. (A typical cavity is shown in Fig. 5.)

The cavities are coldformed in the shape of cups or, in special cases, by machining out of solid bar stock. The accelerator structure (Fig. 3) is not circularly symmetrical. The structure is welded in a specially designed and fabricated rotary fixture which can be split apart down the center after the ends are welded on. Figure 2 also shows this fixture.

The rectangular waveguide, which has many joints, is welded in a fixture that can be rotated so that successive welds can be done around a joint without opening the chamber (Fig. 4). Rotation is achieved by pushing a plunger against the chamber wall with the X-Y table. The plunger in turn pushes an arm that is connected to a shaft through a one-way roller clutch. Detents are provided every 90° and a pointer tells the operator when he is near a detent. This fixture saves at least 3 out of 4 possible pumpdowns. It is also possible to have both the rectangular waveguide and the cavity welds done during the same pumpdown, saving considerable time.

WELDING EXPERIENCE

Surface-quality requirements call for all cavity joints to be welded both on the inside and outside. The inside weld is a cosmetic weld and is to be as smooth as possible, with no regard to strength. It also serves the purpose of preventing spatter on the inside of the cavity from an external weld. Outside welds are usually done at higher power to develop strength in the joints.

Typically, cosmetic welds are done at about 2 ips, 120 kV, and a beam current of 6 mA with a defocus of about 15 per cent. The latter parameter is at present set by focusing to the smallest beam spot visually, then changing the focus controls by a predetermined amount. Eventually, a flying wire scanner is to be mounted on a small elevator, which will provide a more accurate and convenient way of measuring and setting beam focus. A circle generator is often used that sweeps the beam in a circle up to 0.060 in. in diameter or an ellipse as narrow as 0.010 × 0.125 in. Strength welds are typically made at 120 kV, 8 mA, a defocus of 5 per cent and about 2 ips. Needless to say, these are not the only parameters that are used and some of the others are noted on Figs. 6 through 10.

Although there is a flood lamp in each upper corner of the chamber and lamps associated with the operator's telescope, one of the biggest problems is in seeing the workpiece. Most of the round parts are so shiny that light and images bounce any way except up the telescope, so that the operator sees either a glare or two or three joints instead of the one that is actually there. A quartz-halogen lamp mounted at the lower end of the rotary fixture provides good viewing of internal welds. However, no arrangement of lamps has been satisfactory for external welds. Rectangular and flat parts do not usually present a problem.

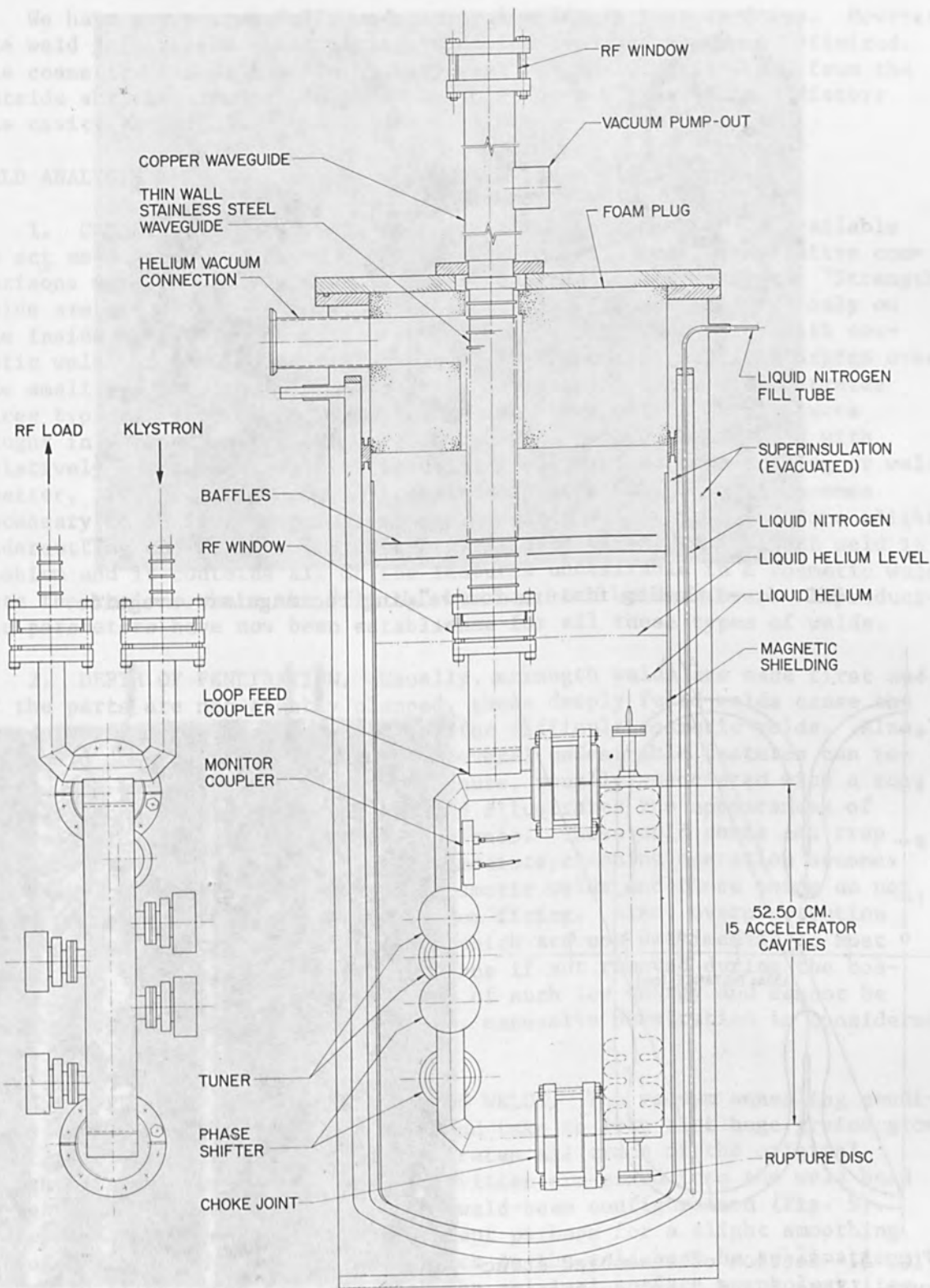


FIG. 3.--"Leapfrog" superconducting accelerator test showing liquid He dewar and accelerator structure.

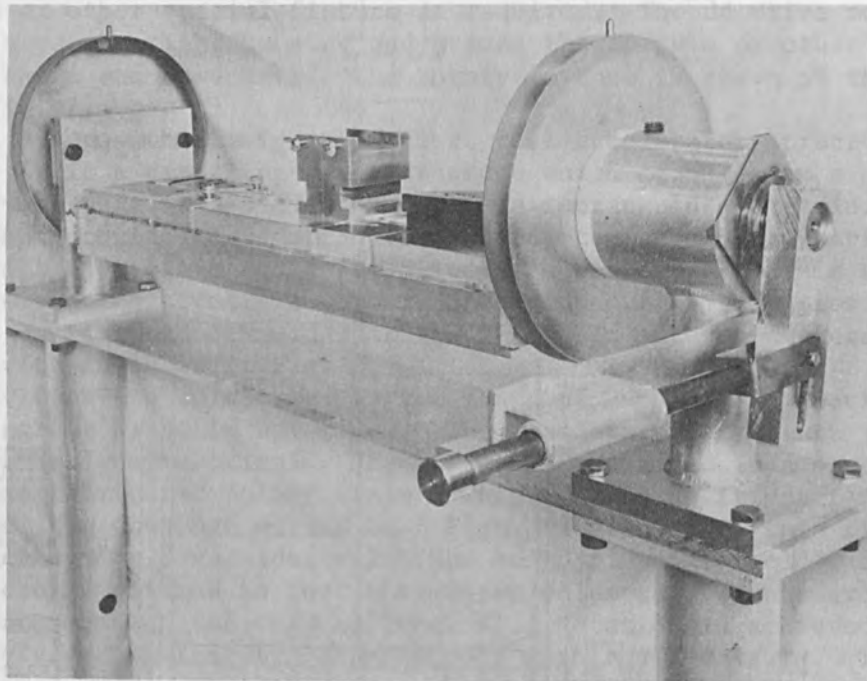


FIG. 4.--Indexing fixture for welding rectangular waveguide.

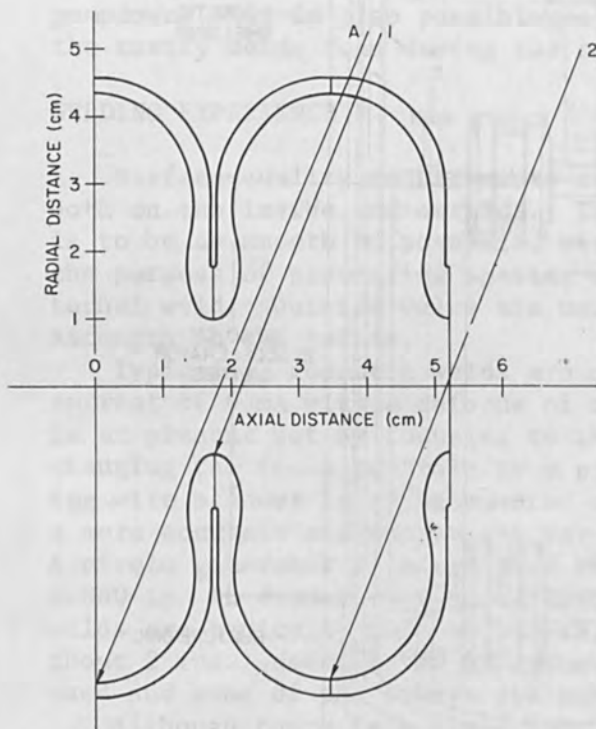


FIG. 5.--Section of assembled structure. Lines 1 and 2 are successive beam paths to weld the structure from half-cavity shells. Line A is the path required if the structure is to be assembled from full cavity sections.

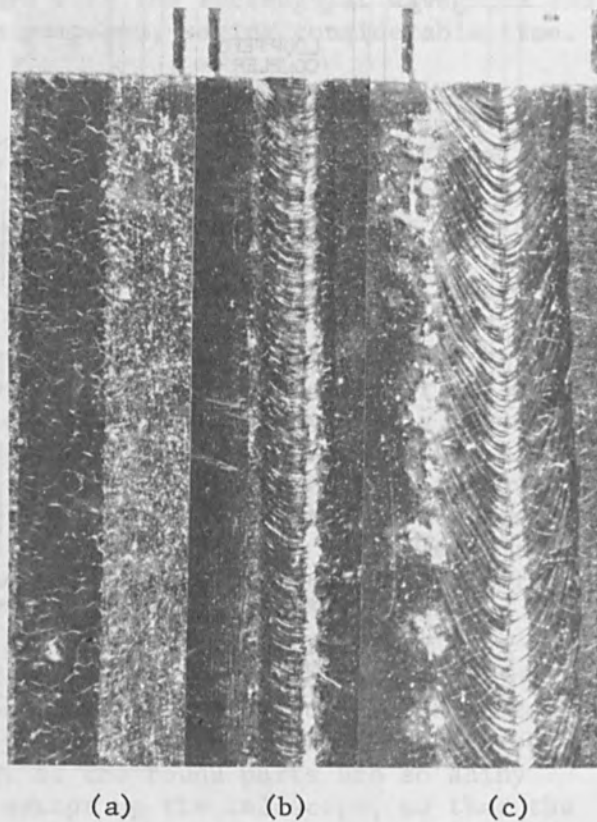


FIG. 6.-- (a) Cosmetic, (b) strength, and (c) "typical" electron beam welds in niobium (10 x).

We have now successfully made several welds in test cavities. However, the weld joining the small diameters of the cups has not been optimized. The cosmetic weld at the tip is very weak and the strength weld from the outside shrinks, tending to pull the joint open at the tip and distort the cavity shape.

WELD ANALYSIS

1. COSMETIC WELDS. Since no quantitative information is available to act as a guide for the smoothness of a cosmetic weld, qualitative comparisons were the only kinds of comparisons that could be made. "Strength" welds are made from the outside and cosmetic welds are required only on the inside surfaces, but some depth of fusion must take place with cosmetic welds or else there will be insufficient molten metal to bridge over the small gap between two components. As examples, Fig. 6 illustrates three typical electron-beam seam welds and shows all of the features sought in various welds. Figure 6(a) shows a good cosmetic weld with relatively smooth surface, little weld ripple, and no undercutting or weld spatter. Figure 6(b) shows a strength weld in which, when it becomes necessary to achieve deep fusion, a pronounced weld ripple and some slight undercutting can be seen. Figure 6(c) illustrates a "typical" EB weld in niobium and it contains all of the features undesirable in a cosmetic weld. Note the regions where the "fit up" has not been bridged over. Reproducible parameters have now been established for all these types of welds.

2. DEPTH OF PENETRATION. Usually, strength welds are made first and, if the parts are not tightly clamped, these deeply fused welds cause the inside surfaces to gap open and make for difficult cosmetic welds. Also, when weld penetration is excessive, several undesirable features can result. One is the formation of cold shuts, usually associated with a too-sharply focused beam. Figures 7 and 8 illustrates the appearances of typical cold shuts in two different planes. These cold shuts can trap acid and other impurities if an intermediate cleaning operation becomes necessary between the strength and cosmetic welds and these voids do not close up in the high-temperature vacuum firing. Also, overpenetration produces some "micro dingle berries" which are not detrimental to most welds, but cause microwave perturbations if not removed during the cosmetic pass. Since cosmetic welds are of such low energy and cannot be expected to remove the dingle berries, excessive penetration is considered to be highly undesirable.

3. EFFECTS OF VACUUM ANNEALING ON WELDS. The vacuum annealing conditions are at such high temperatures and take so long that huge grains grow after recrystallization, which obliterates all trace of the original wrought grains. However, enough impurities are mixed into the weld bead to leave some traces of the original weld-beam configuration (Fig. 9). There is no outer surface change, except perhaps for a slight smoothing action of the high spots of the ripples in the weld bead by sublimation. Figure 10 illustrates the fact that the original surface morphology (for instance, a weld bead) seems to be completely oblivious to the subsequent growth of new grains.

Another interesting factor for which we had great hopes was investigated with negative results. We had hoped that the unfused weld joint, from an underpenetrated strength weld, would diffuse together under the



FIG. 7.--Cold shuts in electron-beam welded niobium. Weld is at top and parent metal at bottom; weld direction to right (50 x).

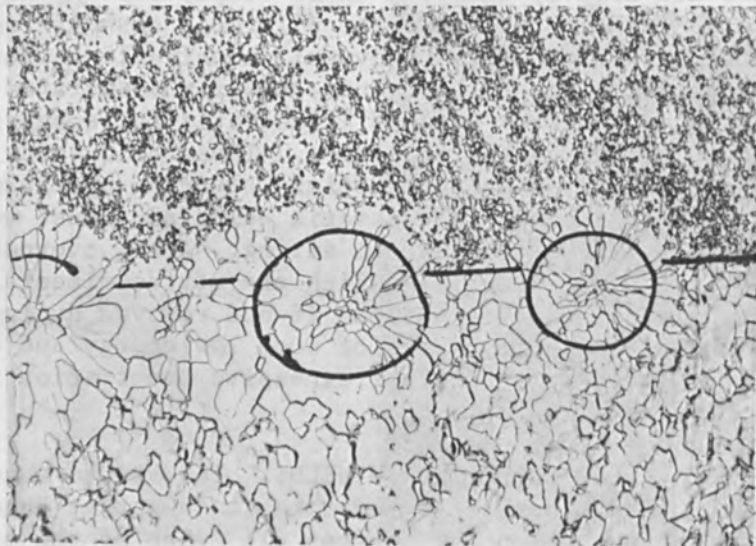


FIG. 8.--Cold shuts in electron-beam welded niobium. Looking vertically into weld seam; weld direction to right (50 x).



FIG. 9.--Electron-beam weld in niobium after vacuum annealing at 2000°C for 20 hr (50 x).

INTRODUCTION

In the deposition of thin films, the grain structure of the film is determined by various parameters such as the substrate temperature, the rate of deposition, the nature of the substrate, and the nature of the film-forming material. The grain structure of the film is important because it affects the physical and chemical properties of the film. This paper reports on the grain structure of thin films deposited on various substrates at different temperatures and rates of deposition.



FIG. 10.--Recrystallized grain boundary (triple point) among weld-bead ripples (100 x).

Work supported by Naval Air Systems Command, Washington, D. C.

combined annealing conditions and shrinkage stresses in the weld. Stress relief in pure niobium probably takes place fast enough to prevent this factor from being operative at high temperatures. We have tried to vacuum-anneal specimens immediately after welding to minimize surface contamination, but with no good results. Chemical cleaning is, of course, another approach, but we felt the high probability of surface contamination by the cleaning chemicals and the difficulty of removing chemicals from the capillary joint would prevent a good diffusion bond.

REFERENCES

1. P. B. Wilson, R. B. Neal, G. A. Loew, H. A. Hogg, W. B. Herrmannsfeldt, R. H. Helm, and M. A. Allen, Superconducting accelerator research and development at SLAC, Particle Accelerators 1: 223, 1970.
2. Design Report, National Accelerator Laboratory, University Research Association (1968).
3. Edoardo Amaldi, The 300-DeV accelerator in the European programme for high energy physics, Proc. Sixth Intern. Conf. High Energy Accelerators, CEAL-2000 (1967).

THE INFLUENCE OF ION KINETIC ENERGY ON THE SURFACE REACTIVITY OF ION-BEAM-DEPOSITED Cu*

W. B. SHEPHERD

Boeing Scientific Research Laboratory, Seattle, Wash.

Results are reported of an experiment that demonstrates the ability of particle kinetic energy to alter the reaction rates, at a substrate, between ionically deposited metal and gases introduced into the deposition chamber. Measurement of the rate of mass collection on a substrate exposed to a monoenergetic beam of Cu ions in the presence of O₂, H₂S, or H₂O gaseous ambients showed that with O₂ and H₂S ambients, the rate of gas collection by the ionically deposited film was energy dependent. No gas absorption was observed when the deposition energy was below approximately 20 eV. Above this threshold, a general increase in absorption rate up to a saturation value sufficient to form CuO or CuS was observed. The absorptions differed in detail for the two gases. No absorption of H₂O could be measured up to ion energies of 1 keV. Since the reactions between Cu and O₂ or H₂S are exothermic, whereas that between Cu and H₂O is endothermic, these results demonstrate the ability of the ions to supply the activation energy for an otherwise energetically favorable reaction. Measurements to determine the relationship between the formation parameters of the films and their composition and electrical properties are discussed.

INTRODUCTION

In the deposition of elemental and compound thin films, adjustments of the film's physical, chemical, and electrical properties are achieved through variation of substrate temperature, vacuum-system ambients, and source parameters. The range of variation in the film characteristics is limited by the allowable adjustments of these parameters. In particular, the substrate material or the composition of deposits on the substrate usually impose restrictions on the range of temperatures that may be employed, either because of material instability at higher temperatures or because of mismatch between the temperature coefficient of expansion of the various materials used for thin-film devices. Techniques that augment or supplant variation of the substrate temperature offer the possibility of increasing the degree of control that can be maintained over thin film properties and of introducing previously unavailable films to thin-film technology.

This paper describes experiments with low-energy beams of Cu⁺ ions that demonstrate the role of particle kinetic energy in promoting the formation of various compounds between the Cu ions and gaseous components residing on a substrate surface. The present work is intended to establish the degree to which particle kinetic energy can affect such reactions and to elucidate the basic mechanisms of the process, so that materials systems of practical interest may be identified and exploited.

*Work sponsored by Naval Air Systems Command, Washington, D. C.

APPROACH

The ion gun (Fig. 1) is a relatively simple structure primarily intended for formation and control of highly uniform beams of singly charged condensible ions with kinetic energies in the range from 0 to 1 keV. Ions are extracted from a low-voltage arc along the axis of the source cylinder at the left. The arc is struck in the vapor of the beam material between an electron emitting filament and the vapor-source crucible. Typical arcs draw 2 A at 15 V and can deliver up to 50 μ A of beam current at the target. Details of this source are given elsewhere.¹ Ions are extracted to the right and bent electrostatically to separate the vapor from the ion stream. The ion beam is focused to the target, placed as shown. In the present operation a defocused beam 0.2-0.3 cm in diameter is used with a current density uniform to ± 5 per cent over the target area. Typical beam currents are 2 to 5 μ A in the energy range from 10 to 500 eV. The energy distribution width of the present beam is less than 10 eV at FWHM. Guns of this type have been operated with a wide variety of high and low vapor pressure metals and a few compounds such as SiO₂.

The basic measurement in the present work with Cu is made by collecting the ions on the surface of a 10-MHz quartz-crystal microbalance that has been coated with Cu by ion deposition at low energy from the gun. The rate of mass increase or decrease is proportional to the rate of frequency change of the oscillator and is continuously monitored with the microbalance. The mass collection data are correlated with measurements made on the deposits with a calibrated electron microprobe, thus providing a calibration of the mass sensitivity of the crystal. The depositions are conducted in a double-oil-diffusion-pumped chamber with LN₂ trapping. The base pressure during measurements is in the 10⁻⁹-torr range. Reactive deposition is studied by admitting various gases to the chamber during deposition and noting the effect on the mass collection rate at the crystal microbalance. In the work with Cu ions reported here two extremes of the gas pressure are examined. Data are presented for the cases $R_p \ll 1$ and $R_p \geq 10$ where R_p is the ratio of the rate of impingement of gas atoms on the target to the rate of impingement of ions.

As an example of typical reactive deposition data, Fig. 2 shows the general behavior of the mass collection rate as a function of gas pressure, or R_p , for the deposition of Cr in O₂. Although Cr oxidizes at all ion energies it does illustrate several important features of reactive ionic deposition that are shared by most of the metal-gas systems studied so far. The ordinate is the mass sputtering yield S_m defined by:

$$S_m = - \frac{\text{rate of change of the target mass} - \text{rate of arrival of ion mass}}{\text{rate of arrival of ion mass}}$$

With this definition, an increase in mass collection results in a decrease in S_m . If the rate of accumulation (or loss) of beam material is independently known, then the rate of collection (or loss) of a second known species can be deduced from measurements of S_m .

In general, with active metals deposited in O₂, S_m vs R_p plots show an increase in the rate of mass collection at the target in the range $R_p \approx 1$ to ≈ 10 . This increase in mass collection tends to saturate above $R_p = 10$ and is attributed primarily to collection of O₂ as a reacted species in the deposit. In the case of Cr deposition in O₂ at 10 eV we find saturation at an oxygen/chromium ratio equivalent to the composition of CrO₃. As will be discussed for the case of Cu deposition in O₂, S_m also

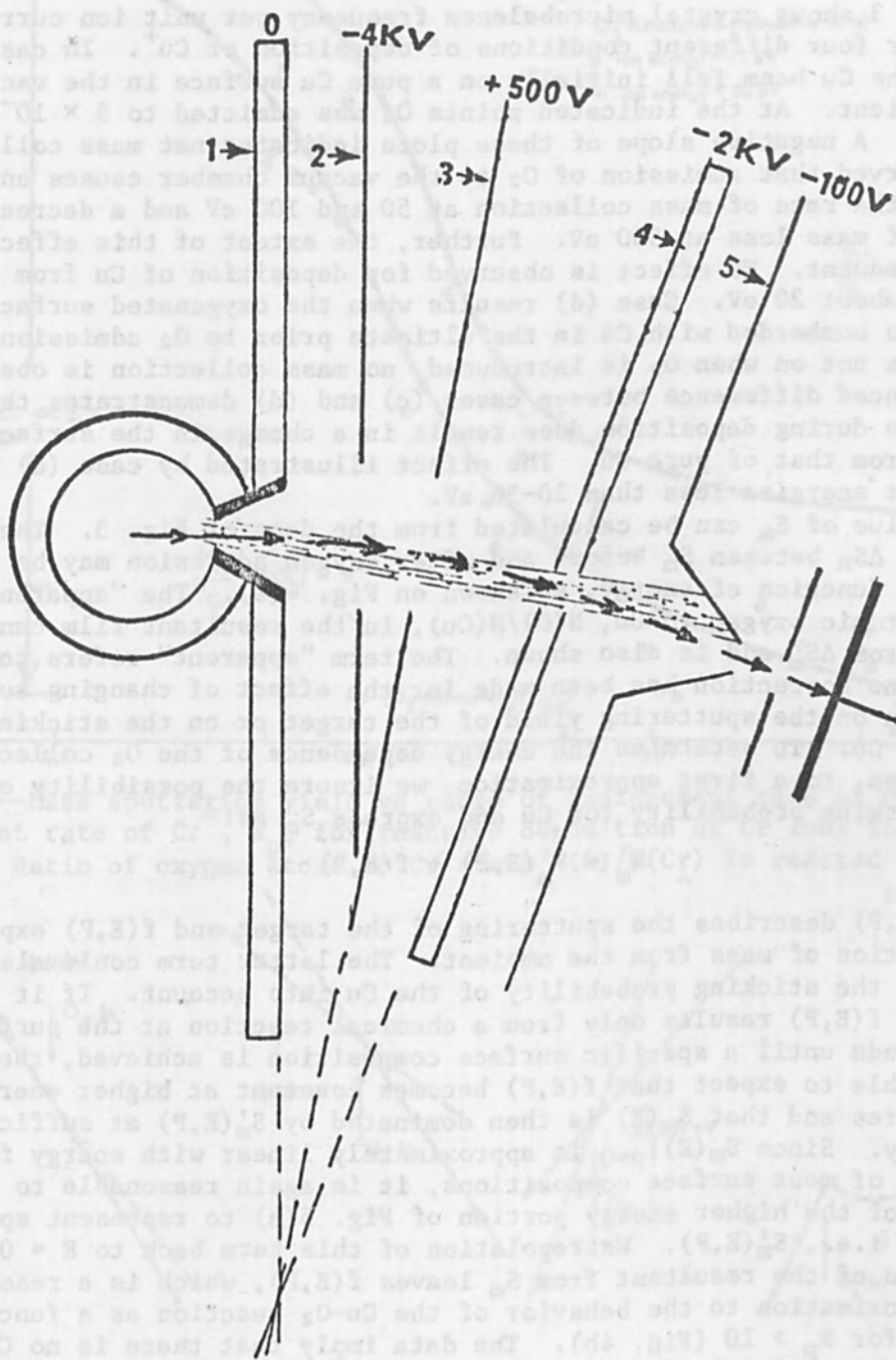


FIG. 1.--Ion gun for deposition of low-energy condensible ions; typical operating voltages are shown.

exhibits changes attributable to a reduction in the sputtering yield for the beam on the reacted surface.

Figure 3 shows crystal microbalance frequency per unit ion current vs time for four different conditions of deposition of Cu^+ . In cases a, b, and c the Cu beam fell initially on a pure Cu surface in the vacuum system ambient. At the indicated points O_2 was admitted to 5×10^{-5} torr ($R_p > 10$). A negative slope of these plots indicates net mass collection. It is observed that admission of O_2 to the vacuum chamber causes an increase in the rate of mass collection at 50 and 100 eV and a decrease in the rate of mass loss at 500 eV. Further, the extent of this effect is energy dependent. No effect is observed for deposition of Cu from thermal energy to about 20 eV. Case (d) results when the oxygenated surface of case (c) is bombarded with Cu in the ultimate prior to O_2 admission. If the beam is not on when O_2 is introduced, no mass collection is observed. The pronounced difference between cases (c) and (d) demonstrates that oxygenation during deposition does result in a change in the surface composition from that of pure Cu. The effect illustrated by case (d) is not observed at energies less than 20-30 eV.

The value of S_m can be calculated from the data of Fig. 3. Then the difference ΔS_m between S_m before and after oxygen admission may be determined as a function of energy, as shown on Fig. 4(a). The "apparent" ratio of atomic oxygen to Cu, $N(\text{O})/N(\text{Cu})$, in the resultant film can be inferred from ΔS_m and is also shown. The term "apparent" refers to the fact that no correction has been made for the effect of changing surface composition on the sputtering yield of the target or on the sticking probability of Cu. To determine the energy dependence of the O_2 collection in the films, to a first approximation, we ignore the possibility of change in the sticking probability for Cu and express S_m as:

$$S_m = S_m^i(E,P) + f(E,P)$$

where $S_m^i(E,P)$ describes the sputtering of the target and $f(E,P)$ expresses the absorption of mass from the ambient. The latter term could also take changes in the sticking probability of the Cu into account. If it is assumed that $f(E,P)$ results only from a chemical reaction at the surface that proceeds until a specific surface composition is achieved, then it is reasonable to expect that $f(E,P)$ becomes constant at higher energies and pressures and that $S_m(E)$ is then dominated by $S_m^i(E,P)$ at sufficiently high energy. Since $S_m(E)|_{P=0}$ is approximately linear with energy for sputtering of most surface compositions, it is again reasonable to take the slope of the higher energy portion of Fig. 5(a) to represent sputtering alone, i.e., $S_m^i(E,P)$. Extrapolation of this term back to $E = 0$ and subtraction of the resultant from S_m leaves $f(E,P)$, which is a reasonable first approximation to the behavior of the Cu- O_2 reaction as a function of energy for $R_p > 10$ (Fig. 4b). The data imply that there is no Cu- O_2 reaction at energies below about 20 eV and that the reaction is essentially complete at about 150 eV. Further, if there is no change in the rate of Cu collection in the presence of O_2 , then the terminal composition of the films for energies at 150 eV or above is evidently equivalent to CuO .

To determine the chemical and physical properties of the oxygenated, ion-beam deposited Cu films, a number of measurements have been made that compare films formed at selected energies both in the ultimate and at 5×10^{-5} torr. The techniques used have been measurement of conductivity vs electric field and temperature, electron microscopy and diffraction,

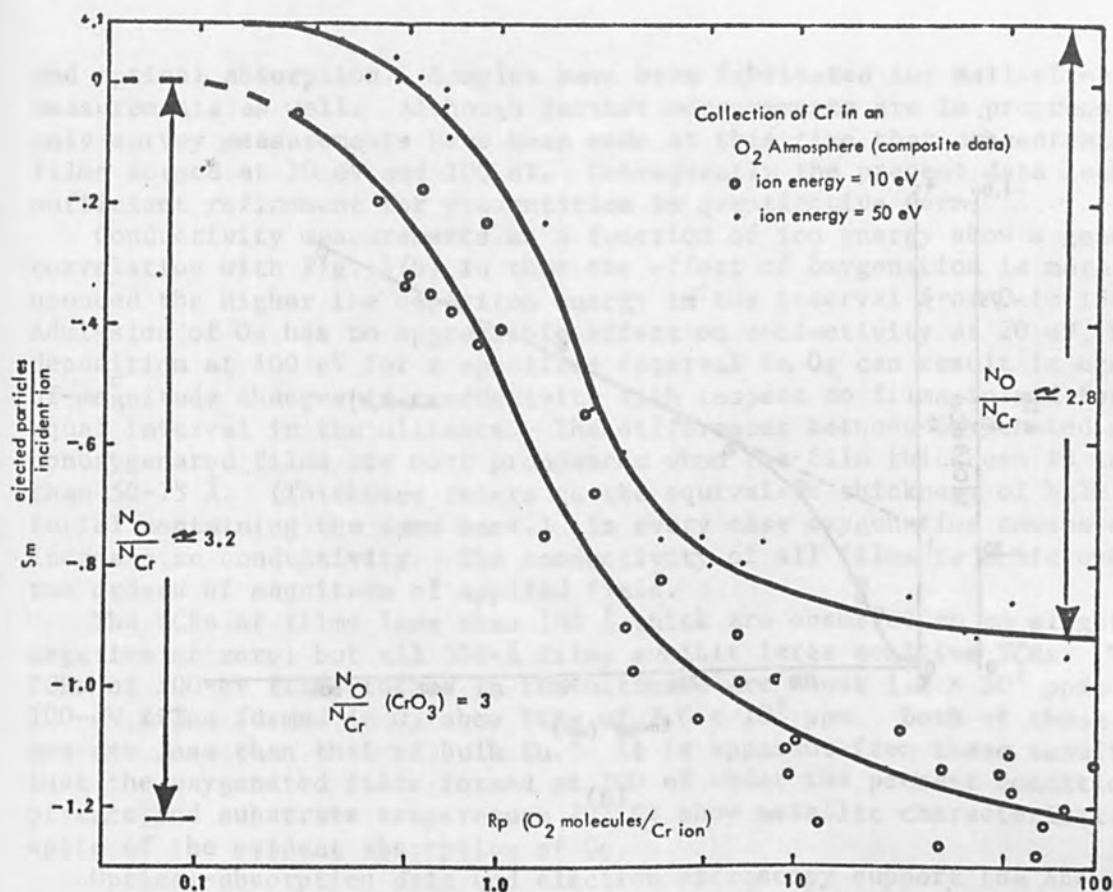


FIG. 2.--Mass sputtering yield vs ratio of impingement rate of O_2 to impingement rate of Cr^+ , R_p , for reactive deposition of Cr ions in O_2 ambient. Ratio of oxygen atoms to Cr atoms $N(O)/N(Cr)$ in reacted films is indicated.

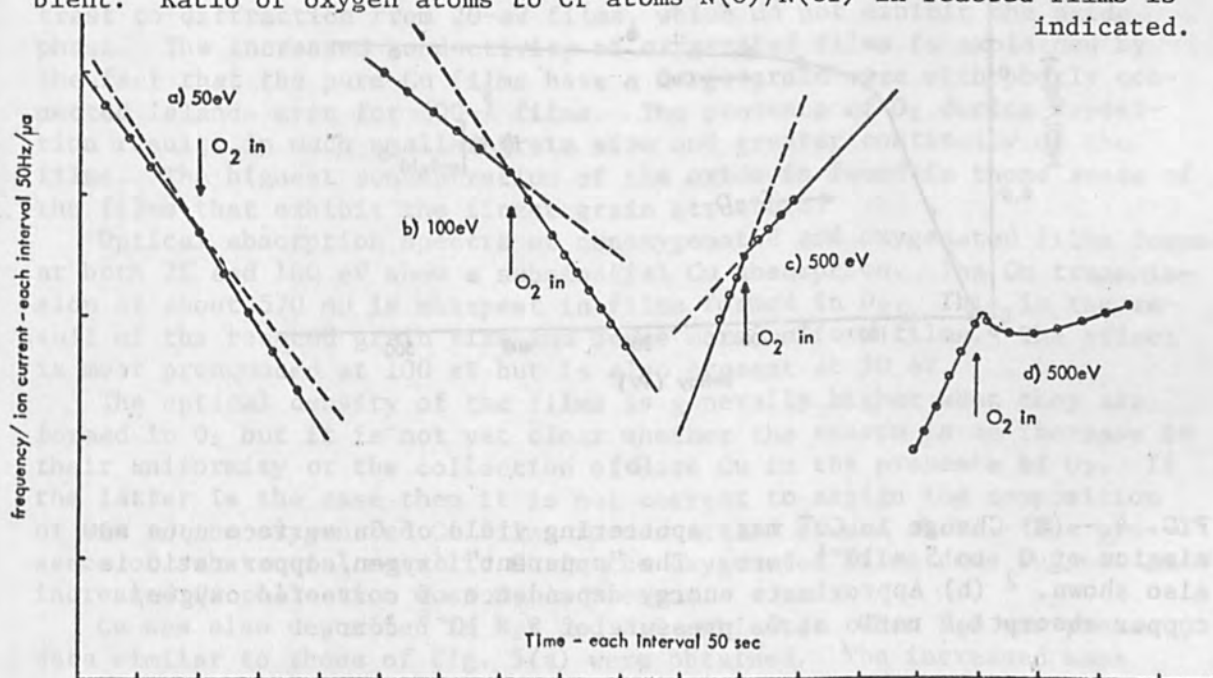
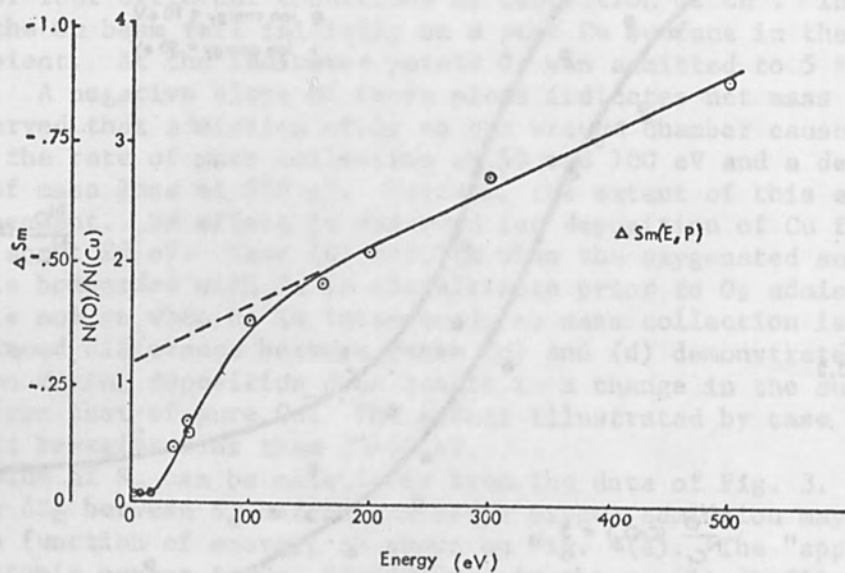
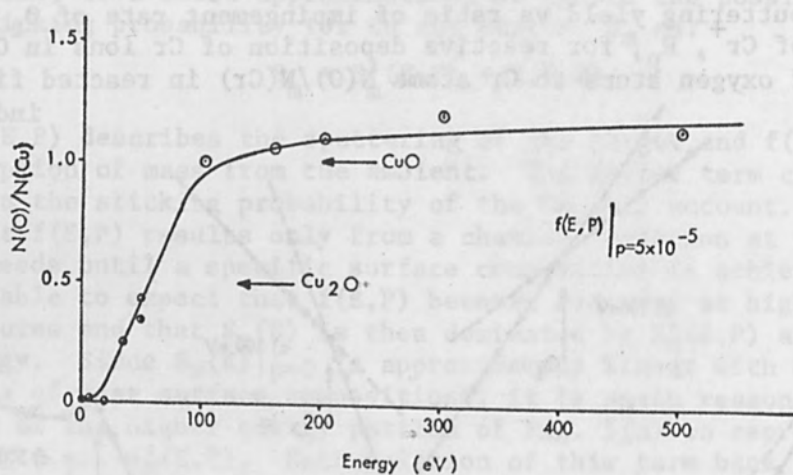


FIG. 3.--Crystal microbalance frequency per microampers of Cu ion current. Deposition starts in 10^{-9} torr O_2 followed by admission of 10^{-5} -torr O_2 as indicated. Cases (a), (b), (c) have pure Cu substrates. Substrate of case (d) is result of oxygenation of case (c).



(a)



(b)

FIG. 4.--(a) Change in Cu^+ mass sputtering yield of Cu surface upon admission of O_2 to 5×10^{-5} torr. The "apparent" oxygen/copper ratio is also shown. (b) Approximate energy dependence of corrected oxygen/copper absorption ratio at O_2 pressure of 5×10^{-5} torr.

and optical absorption. Samples have been fabricated for Hall effect measurements as well. Although further measurements are in progress, only survey measurements have been made at this time that concentrate on films formed at 20 eV and 100 eV. Consequently the present data lack sufficient refinement for presentation in quantitative form.

Conductivity measurements as a function of ion energy show a general correlation with Fig. 4(b) in that the effect of oxygenation is more pronounced the higher the deposition energy in the interval from 0 to 150 eV. Admission of O_2 has no appreciable effect on conductivity at 20 eV, but deposition at 100 eV for a specified interval in O_2 can result in orders-of-magnitude changes in conductivity with respect to films formed for an equal interval in the ultimate. The differences between oxygenated and nonoxygenated films are most pronounced when the film thickness is less than 50-75 Å. (Thickness refers to the equivalent thickness of bulk material containing the same mass.) In every case oxygenation causes an increase in conductivity. The conductivity of all films is ohmic over two orders of magnitude of applied field.

The TCRs of films less than 100 Å thick are observed to be slightly negative or zero; but all 300-Å films exhibit large positive TCRs. The TCRs of 100-eV films formed in the ultimate are about 1.2×10^3 ppm; 100-eV films formed in O_2 show TCRs of 2.0×10^3 ppm. Both of these values are less than that of bulk Cu.² It is apparent from these results that the oxygenated films formed at 100 eV under the present conditions of rate and substrate temperature (25°C) show metallic characteristics in spite of the evident absorption of O_2 .

Optical-absorption data and electron microscopy support the above. Electron diffraction of 100-eV films formed in O_2 shows the presence of Cu crystallites mixed with crystallites of a copper oxide; the distinction between CuO and Cu_2O has not been completed. This result is in contrast to diffraction from 20-eV films, which do not exhibit the oxide phase. The increased conductivity of oxygenated films is explained by the fact that the pure Cu films have a large grain size with poorly connected islands even for 300-Å films. The presence of O_2 during deposition results in much smaller grain size and greater continuity of the films. The highest concentration of the oxide is found in those areas of the films that exhibit the finest grain structure.

Optical absorption spectra of nonoxygenated and oxygenated films formed at both 20 and 100 eV show a substantial Cu absorption. The Cu transmission at about 570 m μ is sharpest in films formed in O_2 . This is the result of the reduced grain size and hence more uniform films. The effect is most pronounced at 100 eV but is also present at 20 eV.

The optical density of the films is generally higher when they are formed in O_2 but it is not yet clear whether the reason is an increase in their uniformity or the collection of more Cu in the presence of O_2 . If the latter is the case then it is not correct to assign the composition of CuO to the oxygenated Cu films formed at 150 eV and above. The presence of substantial metallic Cu in the oxygenated films does suggest an increased Cu collection when O_2 is present.

Cu was also deposited in H_2S and H_2O ambients. When H_2S was present, data similar to those of Fig. 5(a) were obtained. The increased mass absorption was not observed until the ion energy exceeded 20 eV and saturation of the effect required energies above 500 eV. There was no change in the mass collection in the presence of H_2O vapor for ion energies from thermal to 1 keV.

The formation of the oxides of Cu from O₂ and the sulfides of Cu from H₂S are endothermic,³ whereas oxide formation from H₂O is exothermic. Thus, the ion beam is evidently capable of supplying the activation energy for formation of these compounds but it is not effective in supplying the heat of formation for an exothermic reaction.

CONCLUSIONS

The kinetic energy of Cu ions is capable of promoting the reactions between Cu and O₂ and Cu and H₂S at the surface of a room temperature substrate. Measurements of the resultant film properties for oxygenated Cu show that films formed at room temperature and a deposition rate of 5-10 Å/min in O₂ contain an oxide phase but complete oxidation has not occurred at ion energies up to 100 eV. The presence of the O₂ is observed to decrease the grain size and increase the uniformity of the films. In spite of the absorption of O₂, optical and electrical properties of the oxygenated films retain metallic characteristics.

In view of the data of Fig. 3 and the results of deposition in H₂S and H₂O, it is felt that the ion beam is capable of significantly affecting the chemical composition of the reactively deposited films. Increase of the deposition energy, variation of the film deposition rate, and adjustment of the O₂ pressure is expected to lead to more fully oxidized Cu films. Investigation of these variables is being continued.

ACKNOWLEDGMENTS

The author wishes to express his appreciation of the support and stimulating technical exchange provided by A. R. Wolter and R. A. Mickelsen and of the experimental assistance of D. Watkins.

REFERENCES

1. A. R. Wolter, Proc. Fourth Microelectronics Symp. 2A-1, 1965.
2. Handbook of Chemistry and Physics, Chemical Rubber Company, Cleveland, Ohio, 49th ed. 1968-69; pp. F-140.
3. Ibid. pp. D-38.

RESPONSE OF THE POSITIVE ELECTRON RESIST ELVACITE 2041 TO KILOVOLT ELECTRON BEAM EXPOSURE

E. D. WOLF, F. S. OZDEMIR, W. E. PERKINS, and P. J. COANE

Hughes Research Laboratories, Malibu, Calif.

Electron beam energy-dissipation profiles were measured in a commercially available polymethyl methacrylate polymer. Profiles were obtained in both thick ($\geq 3 \mu\text{m}$) and thin ($\leq 0.4 \mu\text{m}$) films on silicon using a line charge density of q_ℓ , where $3 \times 10^{-10} \text{ C/cm} \leq q_\ell \leq 3 \times 10^{-8} \text{ C/cm}$, and primary electron beam acceleration voltages of 5, 10, 15, and 20 kV. Profile information in the thin resist films is useful for submicron device fabrication. A minimum linewidth of 450 \AA was obtained. The electron beam exposure as well as the analysis was done in a computer-controlled scanning electron microscope (SEM).

INTRODUCTION

High-resolution electron beam device fabrication depends in part on proper exposure of suitable electron beam resists which serve as primary process masks for deposition and removal of material from the device surface. This paper describes measurements of the electron beam energy-dissipation profile in a positive electron resist commercially available under the name DuPont Elvacite 2041 which we have been using for electron-beam device fabrication.^{1,2} This very high molecular weight polymethyl methacrylate (PMM) exhibits most, if not all, of the properties of a specially synthesized polymethyl methacrylate polymer for electron beam exposure reported by Haller et al.³ and Hatzakis⁴ (e.g., acid and base etch resistant, $\sim 10^{-5} \text{ C/cm}^2$ sensitivity at 10 to 15 kV). Furthermore, we have found this resist useful as a mask for ion beam sputtering as well as for ion implantation doping.¹

EXPERIMENTAL PROCEDURE AND RESULTS

The resist was exposed under computer control in the same instrument as was used for these profile measurements.⁵ Energy dissipation profiles vs exposure were obtained by a cleaving technique similar to that described by Hatzakis.⁶ Silicon substrates were used as received with "native" oxide or with a few thousand angstroms of a thermally grown oxide. In general, better adhesion of the resist was obtained with the thicker oxide. The wafers were spin coated with the PMM using methyl isobutyl ketone as the solvent.

Both interferometry (Fig. 1) and scanning electron microscopy were used to measure the resist thickness. Several different weight-percent solutions were used. Figure 1 shows the resist thickness for a 4.5 wt-% solution as a function of the number of applications of the resist to the wafer.

Computer-generated patterns of five sets of ten lines each (Fig. 2) were used to expose the specimens. Several of these patterns were placed on the wafer in such a manner as to insure a high probability of intersecting a line set when the wafer was cleaved. Computer program variables

FIG. 2.--Computer-generated resist exposure pattern.

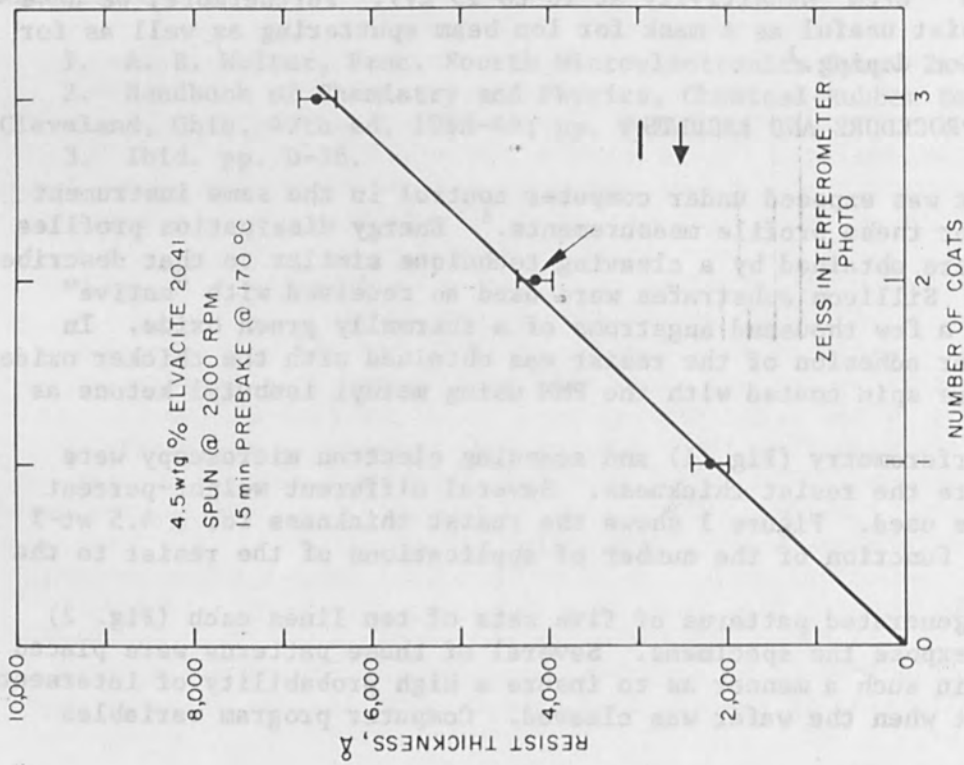
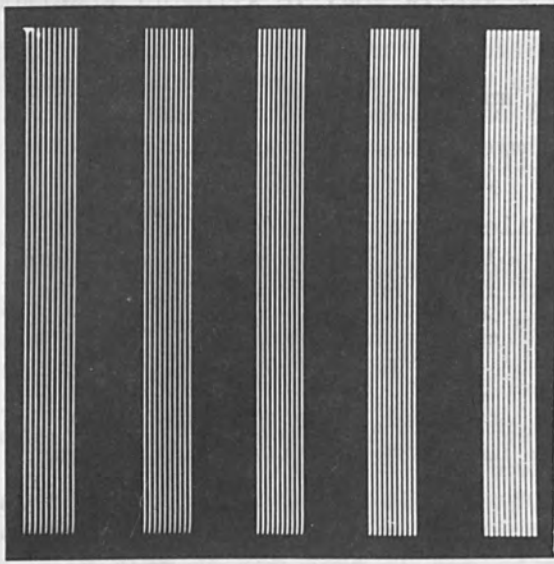


FIG. 1.--Resist thickness vs number of coats.

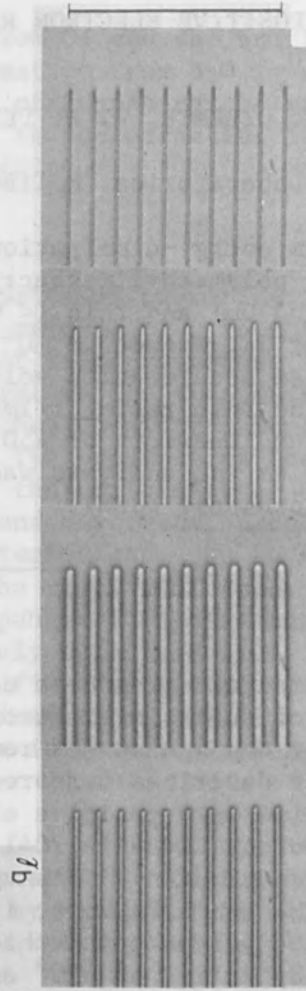


FIG. 3.--1000 × optical photographs (originally) of exposure series at primary beam acceleration voltage of (left to right) 5, 10, 15, and 20 kV; $q_0 = 1 \times 10^{-8}$ C/cm. (Vertical scale indication is 45 μm.)

were line spacing, number of lines, spacing of adjacent beam locations along each line, and beam on time per location.

Optical photos at 1000 \times (Fig. 3) revealed that for a given charge q_0 deposited per unit length along the line, the 10-kV exposure produced the widest line in thick resist after development in a 1:3 mixture of methyl isobutyl ketone and 2-propanol. This was a consistent result observed throughout these experiments. Here q_0 was defined as 1×10^{-8} C/cm along the scan path, that is, a line-charge density. This definition was adopted because generally d_B , the beam diameter, is not known accurately, and the diameter of the energy dissipation profile is greater than d_B and varies as a function of distance from the resist surface (see Fig. 5).

A better view of the exposed beam track was obtained by cleaving the wafer and observing the edge-on-view of the resist edge in the SEM (Fig. 4), with q_0 the variable in this series of exposures. Note that the volume of resist affected increases with q_0 , i.e., the greater the charge (dose) deposited, the greater the effect. This "critical" energy dissipation volume is that amount of polymer converted to a lower weight-average molecular weight by bond scission and thus removed during development because of its increased solubility. Results may vary slightly from laboratory to laboratory because different thickness of metal overlayers may be used to prevent beam charging of the resist, and different procedures for development may exist. However, for a given set of conditions, this critical energy dissipation profile should be proportional to the amount of energy deposited in the resist. The dashed line is a 12-kV profile from the work of Hatzakis⁶ at slightly higher q_0 . No quantitative comparison was possible for the reasons stated previously; however, the trend is as expected. Small artifacts were found occasionally in the bottom of the profile and were probably evidence for the onset of cracking in the resist. This tendency was prominent in thick resist (≥ 3 μ m), but essentially non-existent for thin resists (≤ 4000 \AA).

Rather than concentrating our experiments on profiles in thick resists, the effect of the silicon substrate on the exposure of thin resist layers was examined. This is a more important question to answer for reproducible submicron device fabrication.

Figure 5 shows profiles obtained in thin resist using a 10-kV primary beam accelerating voltage. The family of curves resulting from the data in Fig. 5 combined with similar data for 5, 15, and 20 kV exposures (not shown here) is presented in Fig. 6.

A series of exposures were made in very thin resist (~ 1000 \AA) using a much reduced line-charge density in order to confine the developed profile very closely to the incident electron beam path (Fig. 7). The minimum linewidth obtained at the resist/silicon dioxide interface was about 450 \AA . The profiles widened to about 1000 \AA at the higher line-charge density of $0.3q_0$. The beam diameter was estimated to be between 100 and 200 \AA for this series of exposures. These profiles were originally photographed at 120 000 magnification.

DISCUSSION AND EXAMPLES OF SUBMICRON DEVICE CONFIGURATIONS

Several trends are immediately evident in Fig. 6. First, the 10 kV "anomaly" is present, i.e., maximum linewidth for a given q_0 . An effective center of origin for backscattered electrons progresses deeper into the substrate with increasing primary beam acceleration voltage as expected from range-energy curves for kilovolt electrons. This effect is manifest in all the curves.

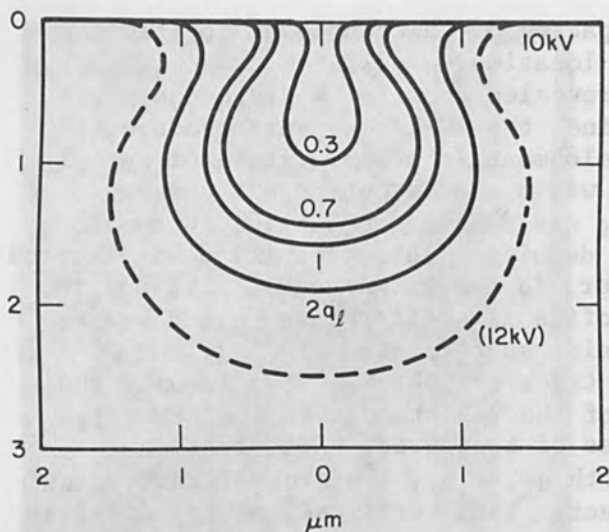


FIG. 4.--Energy dissipation profiles in thick Elvacite 2041 for various values of q_l . Dashed profile is from data of Hatzakis⁶ for IBM polymer.

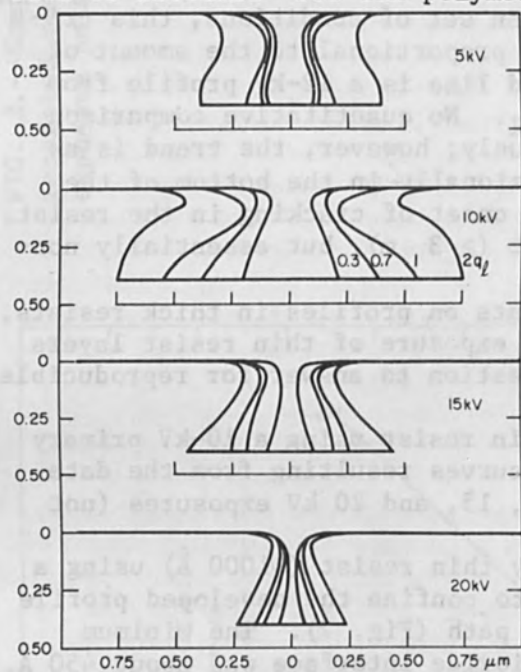


FIG. 6.--Family of profiles for exposures at 5, 10, 15, and 20 kV.

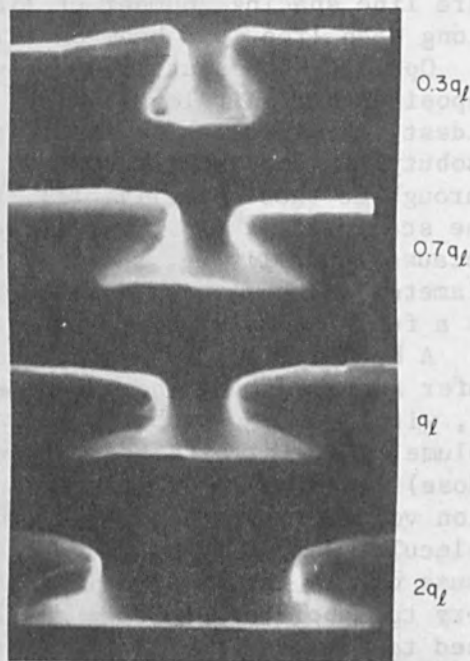


FIG. 5.--Energy dissipation profiles in thin (4000 Å) resist film.

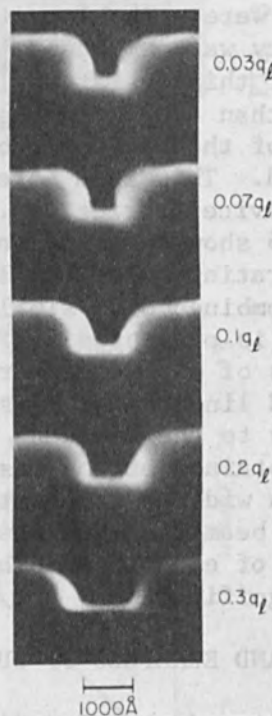


FIG. 7.--Energy dissipation profiles in very thin (1000 Å) resist films. Minimum linewidth is about 450 Å.

The 10-kV anomaly is not really anomalous when electron energy dissipation in solids is considered in more detail. For an electron beam with near zero energy the range is very short and all the energy is lost within a few hundred angstroms of the surface. When electrons with higher energy are used more energy is dissipated in the resist layer, producing a wider line, but after progressing through some maximum linewidth (perhaps at about 10 kV), the energy dissipated is distributed deeper into the substrate with less effect on the resist layer. Thus, the present data are qualitatively correct in exhibiting a maximum in linewidth vs primary electron beam acceleration voltage.

The data presented in Fig. 6 are for essentially noninteracting exposures, i.e., little or no contribution from adjacent exposures. The latitude for proper device exposures is reduced substantially as the linewidth and line spacing are decreased. For example, the Δq or "window" for proper exposure of a line 2800 Å wide is about $\pm 0.08 q$, where q is the optimum exposure (C/cm); Δq is three to four times less critical for linewidths greater than 1 μm when the linewidth and line separation are the same and a 10-kV exposure is used.

Analytical solutions are being sought for the energy dissipation of kilovolt electrons in layered structures such as the resist/silicon (oxide) structure, where boundary conditions in the Rutherford scattering have to satisfy discontinuities in both the atomic number and density of the thin layers. The information available in Fig. 6 has already been applied to the electron-beam fabrication of devices with submicron elements.

Surface-wave acoustic transducers (SWAT) have been fabricated on lithium niobate to form multiple-tap L-band surface-wave acoustic delay lines.^{2,7} Figure 8 shows part of a 10-electrode pair transducer with a center frequency of 1.1 GHz. Slightly higher frequency SWATs are shown in Fig. 9. Still higher frequency transducers have been fabricated by Broers and Hatzakis.⁸

As a demonstration of combined electron and ion beam technology, an ion-implanted junction field-effect transistor has been fabricated and reported.^{1,7} In Fig. 10 are two composite scanning electron micrographs which show the microstructure of the device. In the top half of each micrograph, the source and drain metallization stripes are displayed using the secondary electron emissive mode. In the lower half of each micrograph, the higher rate of recombination of electron-hole pairs generated by a 3-kV electron beam in the ion-implanted regions ($n \sim 10^{20}/\text{cm}^3$ and some residue damage is also present) was shadowed onto the underlying epitaxy p-n junction. The significant features in this interdigital structure are the ion implanted extensions of the source (and drain) regions, each of which is about 0.4 μm wide. These regions were ion implanted through a gold contact mask which was defined on the device surface prior to metallization by means of electron-beam exposure of PMM and ion beam sputtering to remove a thin gold film from the areas that were then implanted with 70-keV phosphorus ions.

CONCLUSIONS

Energy dissipation profiles in both thick and thin films of Elvacite 2041 have been measured. Near-optimum exposure of a film 1000 Å thick has produced a minimum linewidth in this film of about 450 Å. Functional devices with submicron elements have been fabricated using this polymethyl methacrylate as a positive electron resist for pattern definition.

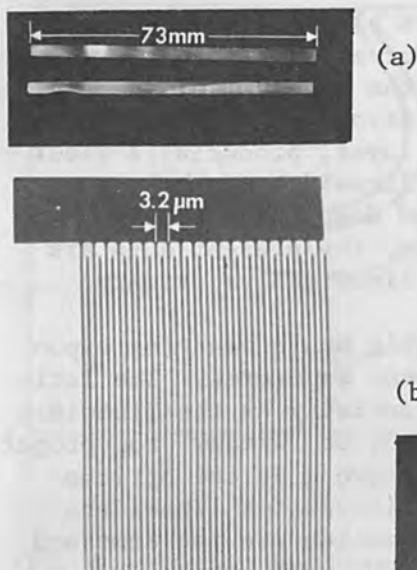


FIG. 8.--(a) 3 in. long LiNbO_3 crystals with three 1.1 GHz aluminum surface wave acoustic transducers spaced 6 μsec apart. (b) Typical transducer (originally 1000 \times , photographed using transmitted light).

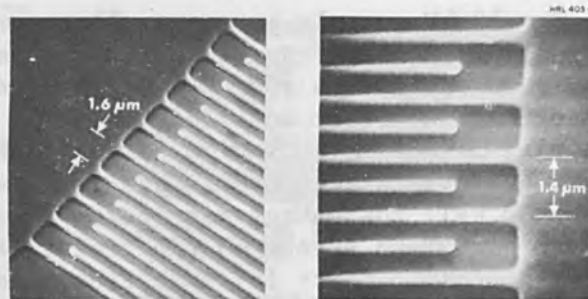


FIG. 9.--Higher-frequency surface-wave acoustic transducers (Al on LiNbO_3)

(b)

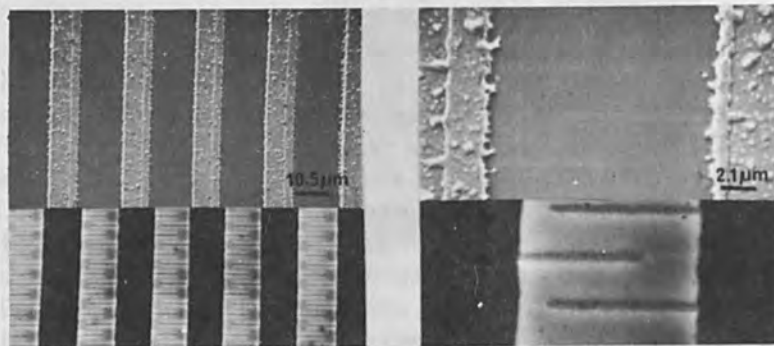


FIG. 10.--Top half of each composite is secondary electron emission scanning electron micrograph. Bottom half of each shows continuation of same area, but as electron-beam induced current displays showing ion implanted regions about 0.4 μm in width. (Wolf et al.¹)

ACKNOWLEDGMENT

The authors acknowledge several helpful discussions with Prof. T. E. Everhart.

REFERENCES

1. E. D. Wolf, L. O. Bauer, R. W. Bower, H. L. Garvin, and C. R. Buckey, *IEEE Trans. ED-17*: 446, 1970.
2. H. M. Gerard, R. D. Weglein, and E. D. Wolf, L-band acoustic surface-wave tapped delay line, *IEEE 1970 International Microwave Symposium*, Newport Beach, Calif. (11-14 May 1970).
3. I. Haller, M. Hatzakis, and R. Srinivasan, *IBM J.*, 251, May 1968.
4. M. Hatzakis, *J. Electrochem. Soc.* 116: 1033, 1969.
5. F. S. Ozdemir, E. D. Wolf, and C. R. Buckey, *Computer-controlled scanning electron microscope for high resolution microelectronics pattern fabrication*, *Rec. 11th Symp. Electron, Ion, and Laser Beam Technology*, San Francisco Press, 1971.
6. M. Hatzakis, *J. Appl. Phys. Letters* 18: 7, 1971.
7. E. D. Wolf, W. E. Perkins, and P. J. Coane, *Proc. Cambridge Stereoscan Colloquium* 3: 99, 1970. (Kent Cambridge Scientific, Inc., Morton Grove, Ill.)
8. A. N. Broers and M. Hatzakis, *Microwave J.* 13: 97, 1970.

ELECTRON-BEAM TECHNIQUES FOR FABRICATING FINE METAL LINES

M. HATZAKIS and A. N. BROERS

IBM Research Center, Yorktown Heights, N.Y.

I. INTRODUCTION

The use of poly-methyl methacrylate (PMM), an electron-sensitive resist developed at IBM for the fabrication of submicron transistors and other devices has been reported previously.^{1-4,6} It has been shown⁴ that metallic structures with line widths down to 1000 Å can be fabricated using the lift-off metallization technique with methacrylate resist with an electron beam apparatus capable of minimum probe sizes of 30 Å. The lift-off technique is illustrated in Fig. 1. This paper demonstrates limits in fabricated line resolution and presents methods that allow the fabrication of metal lines 600 Å wide.

II. RESOLUTION LIMITS IN THICK RESIST LAYERS

Electron-beam penetration profiles on resist layers⁵ indicate that electron scattering in the resist is the major factor limiting resolution in relatively thick resist layers. Figure 2 is a composite photomicrograph of the cross sections of two lines exposed in thick resist at 12 kV. The outer profile is the cross section of the line exposed at a charge density twice that of the inner line. This lateral spreading, which also depends on the exposure density, determines how closely two lines can be spaced in a thick resist layer before the resist wall between the two lines collapses. Figure 3 shows the dependence of lateral spreading on the accelerating potential of the electron beam. It is fairly obvious that for thick resist layers, such as used in metallization with the lift-off technique for transistor fabrication, a higher accelerating voltage would yield higher resolution due to deeper penetration in the resist layer and less lateral spreading. The minimum center-to-center spacing of lines exposed at 25 kV as a function of resist layer thickness is shown in Fig. 4. The thickness of metallization that can be continually achieved by evaporation through the resist is also indicated in Fig. 4. Note that the values shown in these curves represent resolution that can be achieved on a routine basis. Higher resolution can be realized if special care is exercised during the resist development process.

The exposure charge density is also a critical factor in line resolution; the values used for the curves on Fig. 4 vary from 1.3×10^{-8} coul/cm of line length for the 8000-Å resist layer to 1.2×10^{-9} coul/cm for the 1000-Å layer. Development time is fairly constant at approximately 1 min in a solution of 1 part of methyl isobutyl ketone to 3 parts of isopropyl alcohol at 70°F.

The effects of line proximity to resolution can be seen in Fig. 5, which is a composite scanning micrograph of two sections of lines exposed on methacrylate resist, on the same sample, at 15 kV. The same charge density of 4×10^{-9} coul/cm was used for both exposures and the beam size was below 200 Å, yet the line width for the closely spaced lines is 30 per cent larger than the widely spaced lines. This indicates an adjacency effect similar to that observed in high resolution line exposure of photographic emulsions with light. In the case of electron-beam exposure of

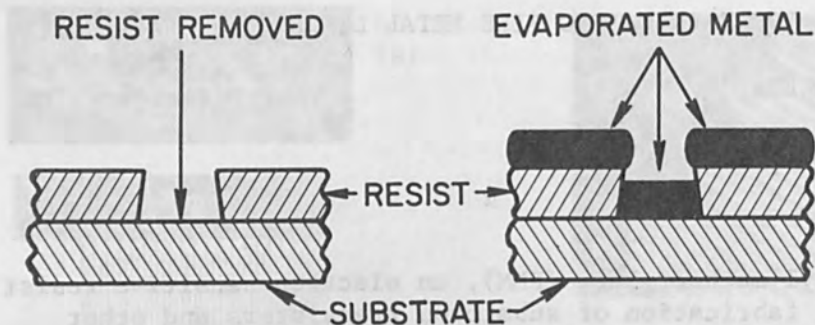


FIG. 1.--Metallization by lift-off technique used with PMM electron resist.

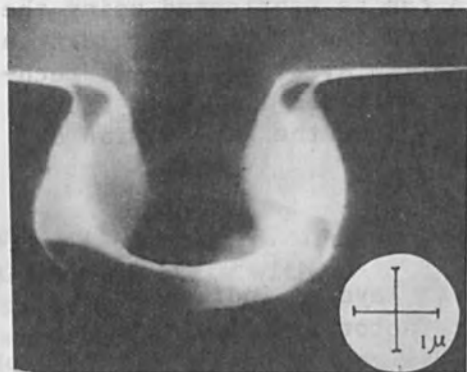


FIG. 2.--Composite photomicrograph of cross sections of two lines exposed in thick resist at 12 kV.

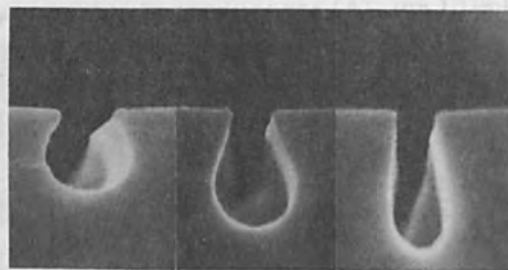


FIG. 3.--Composite photomicrograph of the cross sections of three lines exposed at 10^{-4} coul/cm² varying beam accelerating voltages (left to right: 10, 15, 25 kV).

FIG. 4.--Graphs of minimum line center-to-center spacing vs resist and metal layer thickness at 25 kV.

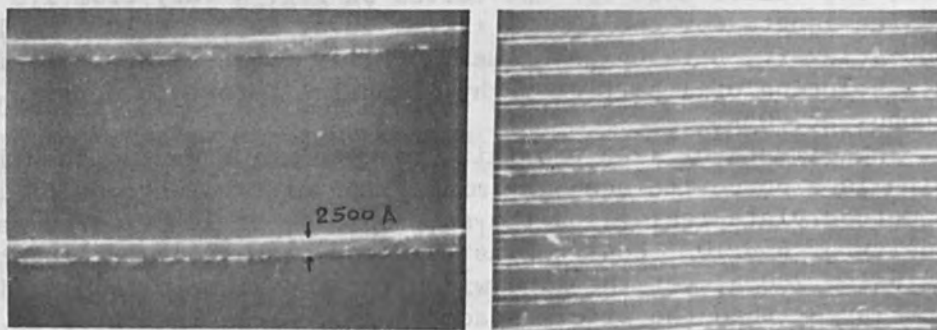
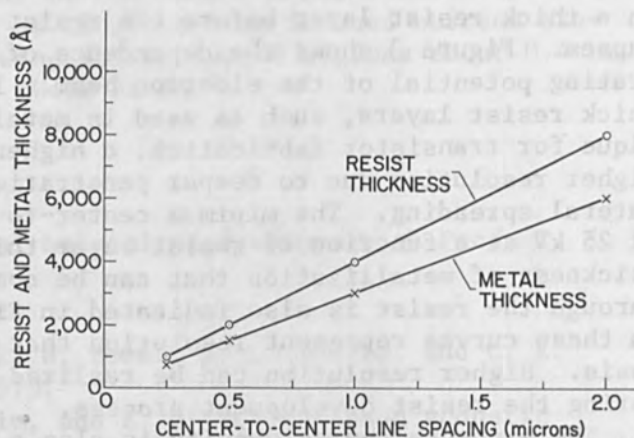


FIG. 5.--Composite photomicrograph of lines exposed at 15 kV, indicating the proximity effect.

resists the effect is caused by lateral beam scattering in the resist which increases the exposure density of neighboring lines.

Figure 6 shows the height-to-width ratio that can be achieved at 25 kV if some care is exercised during development by accurate control of the development time. The resist layer thickness in this case is 3 μm ; the line width at the top is about 1 μm and the line spacing, 4 μm . If this pattern is used for metal evaporation, a height-to-width ratio of 2:1 in the final metal lines can be easily achieved. Figure 7 is a cross section of three resist lines after metal evaporation and before lift-off. Note that there is some tapering in the metal line width which continues as the metal thickness is increased. This tapering is caused by the fact that some metal settles at the edges of the resist lines and as the evaporation continues the resist line width at the top is effectively decreased.

III. RESOLUTION LIMITS FOR THIN RESIST LAYERS

In the exposure of very thin resist layers of below 2000 \AA , beam scattering in the resist is minimized since the beam penetration range even at 15 kV is much larger than the resist thickness. The minimum isolated linewidth that can be achieved in this case is determined by beam scattering on the substrate surface. High-energy electrons are backscattered from the substrate surface in all directions including directions almost parallel to the substrate surface. These electrons cause lateral exposure of the resist layer, which widens the line exposed by the primary beam. Obviously the atomic number of the substrate is also a factor in this case, since backscattering increases with atomic number. The limit of resolution obtained to date is illustrated in Fig. 8, which shows gold-aluminum wires 600 \AA wide and approximately 800 \AA thick on an oxidized silicon substrate. The wires were fabricated with a 25-kV accelerating potential and a resist layer 1000 \AA thick.

IV. RESIST SENSITIVITY

Sensitivity experiments were performed on thick resist layers (8000 \AA) to establish the dependence of sensitivity on beam accelerating voltage. Rasters of nonresolved lines 0.010×0.010 in. were exposed on the resist with the charge density varied through multiple exposure of the same area. The resist samples were then developed in a solution of 1 part of methylisobutyl-ketone and 3 parts isopropanol, which will be referred to as "standard developer," for 2 min at 70°F. After development the percentage of area where the resist was removed was measured for each exposure (Fig. 9). Note that the minimum charge density required for full raster development at 25 kV is twice that at 6 kV, since at 6 kV almost all of the electron energy is lost in the resist layer due to the shorter penetration range. Unfortunately the resolution is poorer at low accelerating voltages, as Fig. 3 clearly shows. Moreover, the electron-beam system brightness, which determines the maximum beam current that can be obtained for a given beam spot size, is four times higher at 25 kV than at 6 kV. At high charge densities of 10^{-3} coul/cm² and above the resist becomes insoluble again due to the fact that at these exposures crosslinking dominates so that overexposed resist cannot be removed by any known solvent.

The sensitivity of PMM resist can be improved by at least an order of magnitude through a modification in the developing process, as long as removal of part of the unexposed resist can be tolerated. In this modified

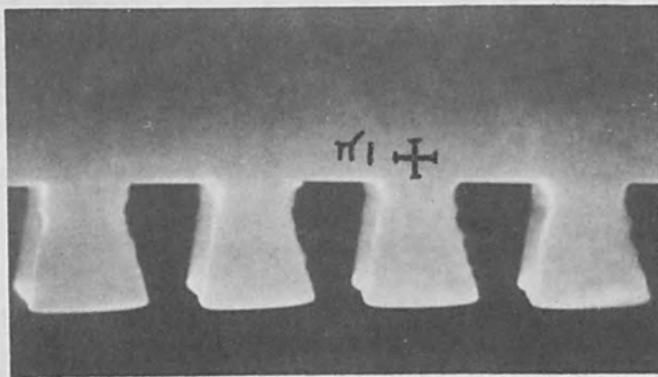


FIG. 6.--Cross section of closely spaced lines exposed on thick resist layer at 25 kV. 1 μ m thick. (Before lift-off.)

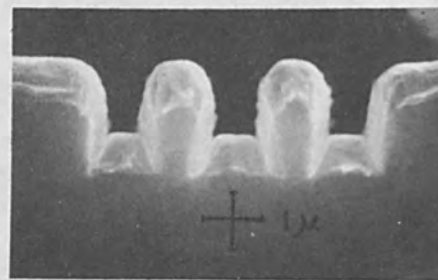


FIG. 7.--Cross section of three lines exposed on thick resist, developed and metallized with aluminum (Before lift-off.)

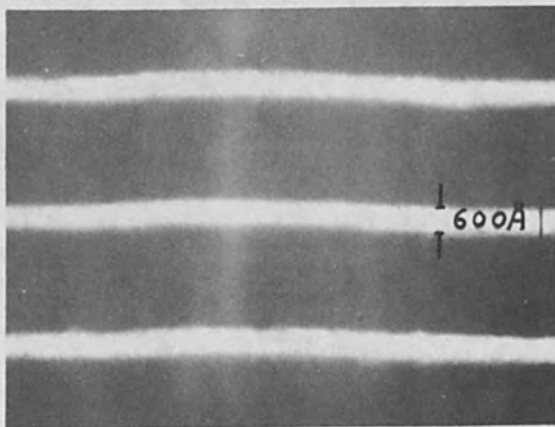


FIG. 8.--Photomicrograph of very thin gold-aluminum lines fabricated by lift-off technique at 25 kV.

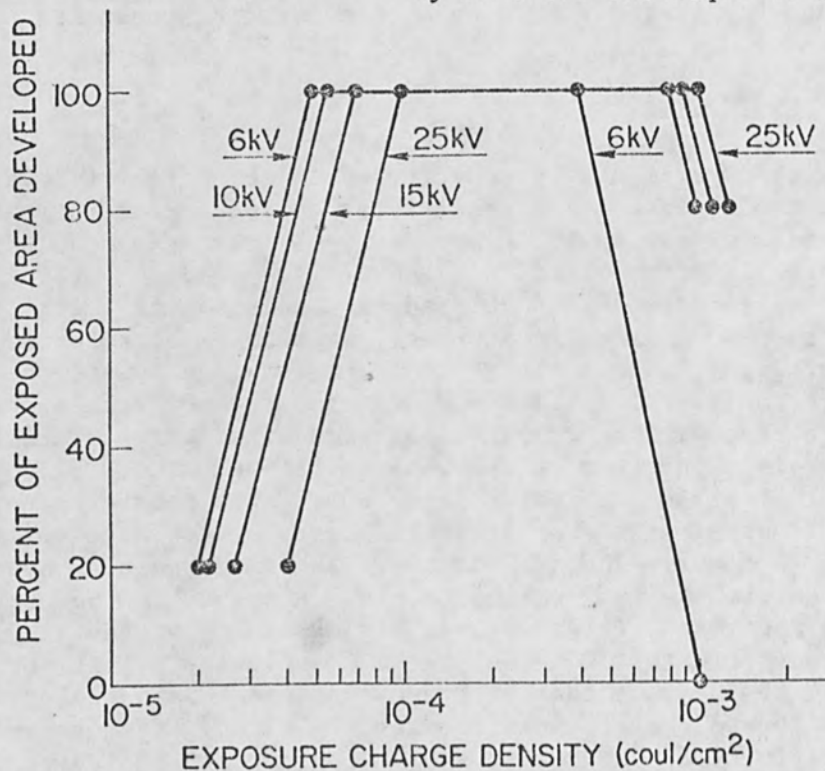


FIG. 9.--PMM resist sensitivity vs electron-beam accelerating voltage. Resist layer thickness is 8000 Å, developed in standard developer for 2 min at 70°F.

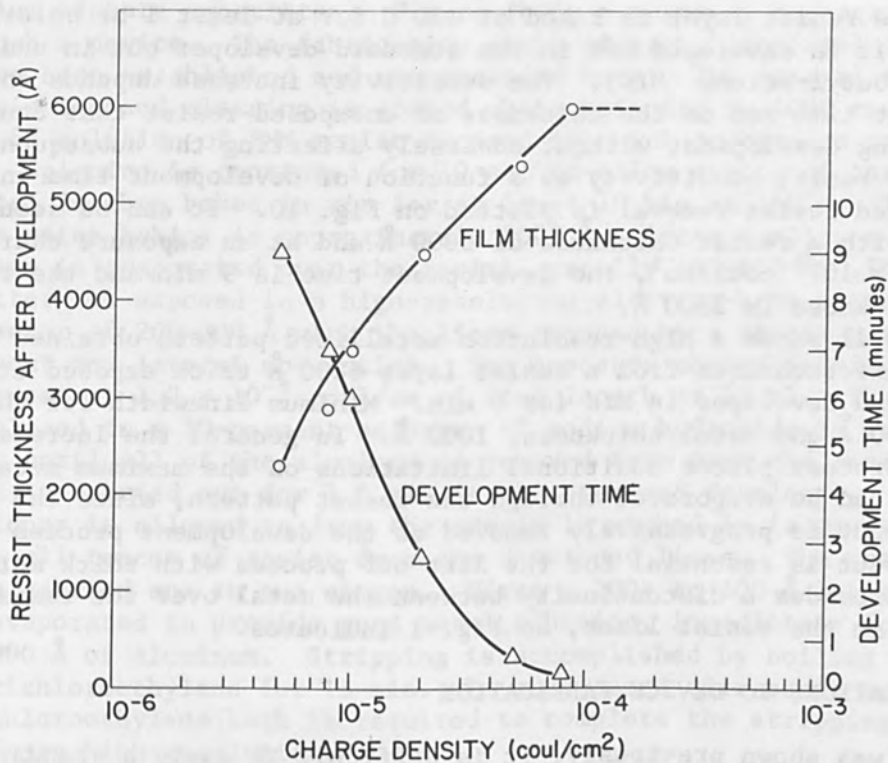


FIG. 10.--Resist sensitivity vs development time and rate of unexposed resist removal. Initial resist thickness is 6000 Å, exposed at 15 kV and developed in methyl-isobutyl-ketone at 70°F.

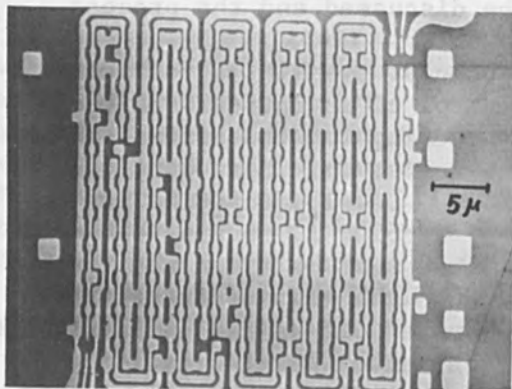


FIG. 11.--High-resolution metalized pattern obtained by lift-off technique from resist layer 6000 Å thick exposed at 5×10^{-6} coul/cm² and developed in MIK for 9 min.

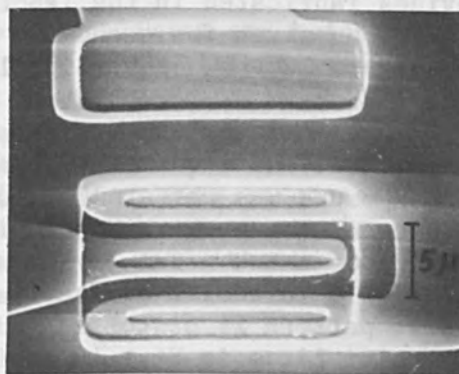


FIG. 12.--Scanning micrograph of working 1-μm transistor fabricated by electron-beam exposure of PMM resist.

process the resist layer is baked at 170°C for at least 1 hr before exposure, and it is developed not in the standard developer but in undiluted methyl-isobutyl-ketone (MIK). The sensitivity increase depends on the development time and on the thickness of unexposed resist that can be removed during development without adversely affecting the subsequent process. The resist sensitivity as a function of development time and rate of unexposed resist removal is plotted on Fig. 10. It can be seen that, starting with a resist thickness of 6000 Å and at an exposure charge density of 5×10^{-6} coul/cm², the development time is 9 min and the remaining resist thickness is 2300 Å.

Figure 11 shows a high-resolution metallized pattern obtained through the lift-off technique from a resist layer 6000 Å thick exposed at 5×10^{-6} coul/cm² and developed in MIK for 9 min. Minimum linewidth for this pattern is 200 Å and metal thickness, 1000 Å. In general the increased sensitivity process places additional limitations on the maximum metal thickness than can be evaporated through the resist pattern, since the resist line undercut is progressively removed as the development process continues. This undercut is essential for the lift-off process with thick metal layers since it provides a discontinuity between the metal over the resist and the metal in the resist lines, as Fig. 1 indicates.

V. APPLICATIONS TO DEVICE FABRICATION

As it was shown previously, it is difficult to apply a standardized process for the fabrication of fine metal structures through electron-beam exposure of PMM resist. The number of variables in the process, i.e., resist thickness, exposure charge density, development time and temperature, beam accelerating potential, etc., is too large and the choice of conditions depends on the application requirements such as desired metal thickness, line proximity, linewidth, etc. For this reason some of the devices fabricated in the laboratory will be discussed and the process conditions given for each.

Figure 12 shows a working 1- μ m silicon bipolar transistor fabricated with the electron-beam system, under the control of an optical scanner, through all processing steps including SiO₂ etching for the diffusion steps. For the final metallization step the resist thickness was 1 μ m and the exposure was set at 10^{-4} coul/cm² at 15 kV. Development time was one minute and the evaporated aluminum thickness was 6000 Å. During the evaporation of thick metal layers such as this, care must be taken not to exceed 100°C in resist surface temperature because the edge undercut in the resist pattern is distorted and eventually rounded off as the cross section of resist lines in Fig. 13 indicate. Note that after heating at 135°C for 5 min the pattern is so grossly distorted that metallization could not be successfully lifted off at any metal thickness. Figure 14 shows a magnetic head where permalloy was plated through the resist. A side view of the 1- μ m gap is shown in Fig. 15. Note that when plating is used the resist thickness can be smaller than the metal thickness since no metal settles on top of the resist. This method of metallization is recommended for thick metal layers, if plating is possible.

The high-resolution feature of the process makes it particularly suited to the fabrication of acoustic surface-wave transducers. In this case line spacing (and not metal thickness) is most important, since the line spacing determines the operating frequency of the device. For a frequency of 3.5 GHz, a center-to-center spacing of adjacent lines of 0.5 μ m is required

for lithium niobate substrates. Figure 16 is a scanning micrograph of one end of such a device. The fabrication steps of such high-resolution devices have been established and are included here. The crystal substrate after polishing and cleaning is coated while spinning at 4000 rpm by 2-3 drops of 5% solution of PMM resist dropped in quick succession onto its surface. Spinning is continued for 10 sec to allow drying of the resist. The crystal is then baked in air for at least 10 min at 160°C. The resist thickness after baking is approximately 2000 Å. After cooling a thin layer of aluminum is evaporated over the resist, usually 400-600 Å. The transducer pattern is exposed in a high-resolution electron-beam system with a spot diameter of 200-300 Å with the lines exposed by a single pass of the beam without any lateral modulation. The exposure charge density for this device is set at 1.2×10^{-9} coul/cm of line length at 15 kV. The sample is then placed in a 10-percent solution of sodium hydroxide in water for 30 sec or until all of the aluminum is removed from over the resist. Development is carried out for 1.5 min in the standard developer. Before the developer is allowed to dry, the sample is washed in isopropyl alcohol to remove all traces of resist from the developed lines. The metal evaporation is carried out in two stages. First a 200- to 400-Å layer of chromium is evaporated to provide good metal adhesion, immediately followed by 800-1000 Å of aluminum. Stripping is accomplished by boiling the crystal in trichloroethylene for 15 min. In many cases ultrasonic agitation in a trichloroethylene bath is required to complete the stripping of structures of very high resolution.

Figure 17 shows a lower frequency acoustic surface wave device exposed in the optical scanner control system for focused wave operation. The resist thickness for this device was 6000 Å and the metal thickness 3000 Å. Exposure charge density was set at 8×10^{-5} coul/cm² at 15 kV.

VI. CONCLUSIONS

The above are general guidelines on resolution limits and height-to-width ratios for metallized structures made through the lift-off technique with PMM electron resist. It was shown that with proper choice of substrate, resist thickness and electron beam accelerating potential linewidths down to 600 Å can be realized and for thick metal structures a height-to-width ratio of 2:1 can be achieved. The process parameters can be accurately determined only for the particular application requirements so that some experimentation is always necessary to optimize the process.

REFERENCES

1. I. Haller, M. Hatzakis, and R. Srinivasan, IBM J. Res. Develop. 12: 251, 1968.
2. M. Hatzakis, J. Electronchem. Soc. 116(No. 7): 1969.
3. R. F. M. Thornley, M. Hatzakis, and V. A. Dhaka, IEEE Trans. ED-17 (No. 11): 1970.
4. M. Hatzakis and A. N. Broers, Rec. 10th Symp. Electron, Ion, and Laser Beam Technology, San Francisco Press, 1969.
5. M. Hatzakis, Appl. Phys. Letters 8(No. 1): 1971.
6. A. N. Broers and M. Hatzakis, Septieme Congres Intern. de Microscopie Electronique, Grenoble, 1970.
7. L. T. Romankiw, I. M. Croll, and M. Hatzakis, IEEE Trans. MAG-6 (No. 3): 1970.

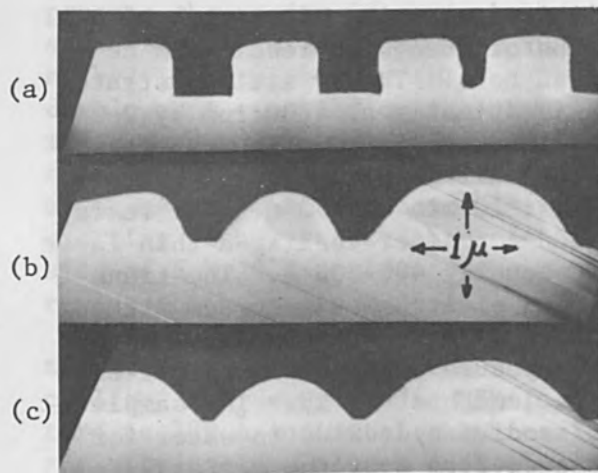


FIG. 13.--Cross section of lines exposed in PMM resist 5000 Å thick before and after heating, indicating pattern distortion with heating: (A) before heating; (B) after heating at 135°C, 5 min; (C) after heating at 135°C, 10 min.



FIG. 15.--Scanning electron micrograph of one end of 1- μ m gap indicating plating over original resist thickness.

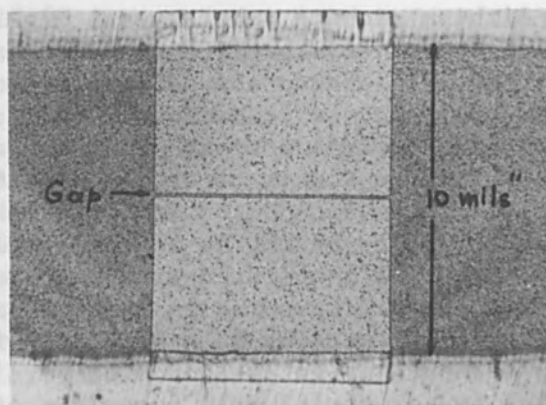


FIG. 14.--Optical micrograph of complete 1- μ m-gap magnetic head.

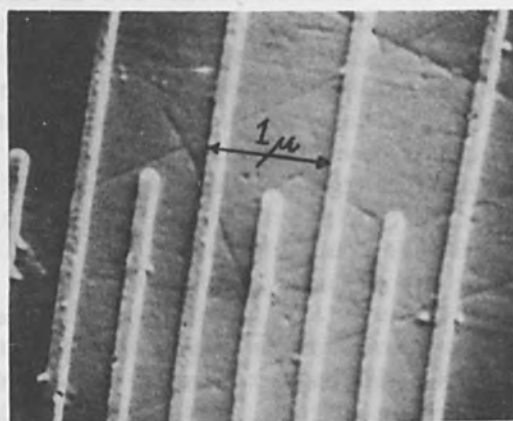


FIG. 16.--Scanning electron micrograph of one end of the 3.5-GHz acoustic surface-wave transducer.

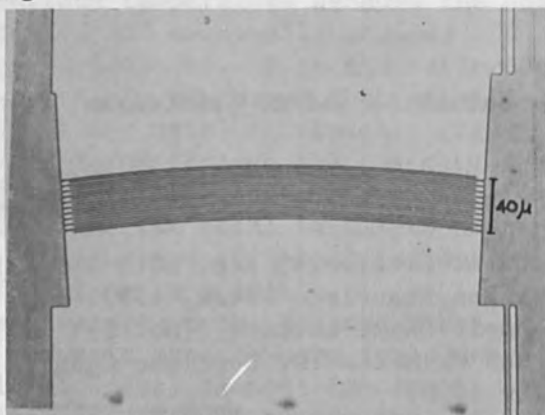


FIG. 17.--Curved transducer for focused-wave operation.

ELECTRON SCATTERING AND THE SENSITIVITY OF POSITIVE ELECTRON RESIST

C. H. TING

IBM Components Division, Hopewell Junction, N.Y.

The positive electron resist poly-methyl-methacrylate (PMMA) has been used extensively in electron-beam fabrication of microcircuits. The sensitivity of this electron resist was determined here by measuring the solubility rate of the exposed as well as the unexposed region. A 15-kV electron-beam system was used to expose the resist at various charge densities, and methyl-isobutyl-ketone at 21°C was used as a developer. The resist thickness as a function of developing time was measured by the optical interference technique. It was found that the solubility rate not only changes with exposure density but also with the distance from the surface at any given exposure. This nonlinear behavior at a given exposure is due to the fact that the energy loss of electrons in a solid is not uniform. The differential solubility S , defined as the difference in solubility between the exposed region and the unexposed region, was found to change when the exposure density was raised to the power of 1.3. From this empirical relationship and the well-known depth-dissipation function for electrons in solids, the thickness-vs-time curves can be calculated for any exposure density and resist thickness. The calculated results agree very well with experimental findings.

INTRODUCTION

Electron-beam technology, with its capability of being easily automated and of producing extremely small and accurate dimensions, has attractive applications in microelectronics. Due to its simplicity and high resolution capability, poly-methyl-methacrylate (PMMA), a positive electron resist, has been used extensively in electron beam fabrication of microcircuits.^{1,2} The sensitivity of this resist was reported to be 5×10^{-5} coul/cm².^{3,4} However, higher sensitivity can be used if one uses a developing solution which attacks not only the exposed area but also the unexposed area. The resist sensitivity is, therefore, not only a function of the resist thickness before and after developing. In this study, resist thickness and developing time were measured as functions of exposure density. The resist sensitivity was expressed quantitatively in terms of the solubility of the exposed and unexposed areas. The effect of electron scattering in solids was also taken into consideration.

EXPERIMENTAL PROCEDURE

Silicon wafers with 5000-Å thermal SiO₂ were coated with various concentrations of PMMA dissolved in methyl-isobutyl-ketone (MIBK). The coated wafers were baked at 165°C for at least 1 hr. The exposing electron beam, operating at 15 kV, was scanned in a raster mode over an area approximately 1 × 1 mm. The spot size and the number of scan lines were adjusted for significant overlapping so that no line details could be observed. The exposure density Q is given by

$$Q = It/A \text{ (coul/cm}^2\text{)} \quad (1)$$

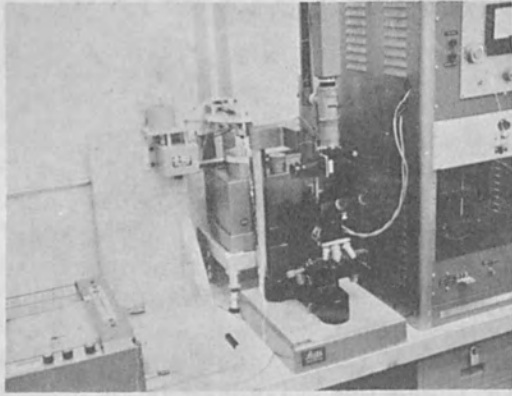


FIG. 1.--Microspectrophotometer setup.

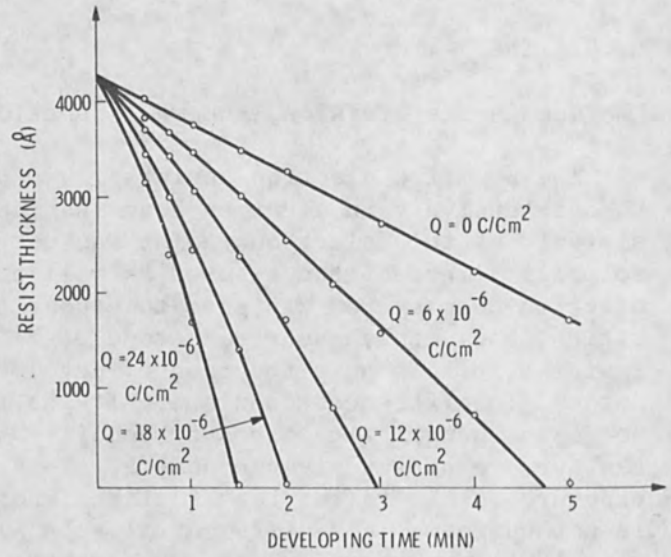


FIG. 2.--Resist thickness vs development time (starting thickness, 4190 Å).

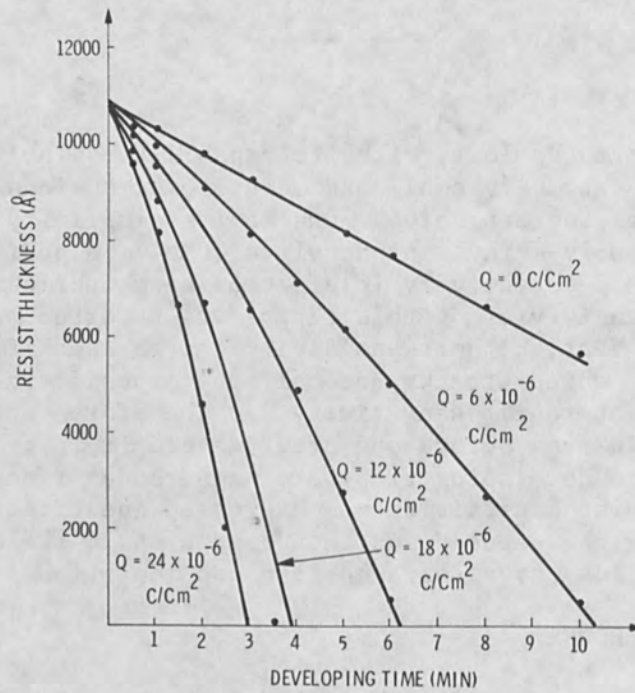


FIG. 3.--Resist thickness vs developing time (starting thickness, 10900 Å).

where I is the beam current measured by a Faraday cup, t is the time for the raster scan, and A is the scanned area measured after developing the resist.

The exposed samples were developed in MIBK with moderate agitation. The developing solution was kept constant at 21°C. After the desired developing time, the samples were quickly dried by surface blowing of freon gas. The resist thickness of the exposed as well as the unexposed area was measured with a microspectrophotometer, an instrument which combines a monochromator with a Leitz Ortholux microscope. The monochromator prism was rotated by an external motor synchronized with the x axis of a recorder. Light from the monochromator entered horizontally from the side of the microscope and was focused on the sample surface under it. The light reflected from the sample was detected by a photomultiplier tube which drove the y axis of the recorder. The reflected light intensity was measured as a function of wavelength from 4500 to 6500 Å. The structure of the reflectance curve was calibrated with respect to the film thickness so that a thickness variation of less than 100 Å could be readily determined. Figure 1 shows the microspectrophotometer setup.

With the microspectrophotometer, the resist thickness was determined as a function of developing time. In Fig. 2, the measured resist thickness of the unexposed region as well as regions exposed with four different densities was plotted as a function of developing time. It can be seen that the thickness of the unexposed resist decreases linearly with developing time, giving a constant solubility rate of 520 Å/min. The solubility rate of the exposed region increased rapidly with the exposure density; therefore, the required developing time decreased rapidly as the exposure was increased. Figure 3 shows similar results obtained from a thicker resist film.

The data from the various resist thicknesses shown in Figs. 2 and 3 are plotted together in Fig. 4 as the thickness of removed layer against developing time. The fact that the measurement from two different resist thicknesses yields such excellent agreement indicates that, for sensitivity measurements, the role of backscattered electrons from the resist and silicon dioxide interface is negligible. Therefore, once the proper developing time for a given exposure is determined for the thick resist, the required developing time for thinner resist can be obtained directly from the curves shown in Fig. 4.

An interesting point shown in Fig. 4 is that the thickness of the exposed regions does not decrease linearly with time. The solubility rate, which is given by the slope of the thickness-vs-time curves, increases with the distance from surface. Evidently energy dissipation of electrons in solids is not uniform but follows a well-known depth-dissipation curve which has a peak at approximately 0.4 of the penetration range. The depth-dissipation curve can be described empirically by the function⁶

$$\alpha = 0.76 + 5.44(Z/R) - 11.64(Z/R)^2 + 5.64(Z/R)^3 \quad (2)$$

where R is the penetration range and Z is the distance from surface. Equation (2) is plotted as the function of the normalized distance Z/R in Fig. 5. For a 15-kV electron beam, the penetration range in PMMA can be assumed to be the same as in polystyrene, which is 5 μm.⁷

The solubility rate S can be expressed as

$$S = S_0 + S' \quad (3)$$

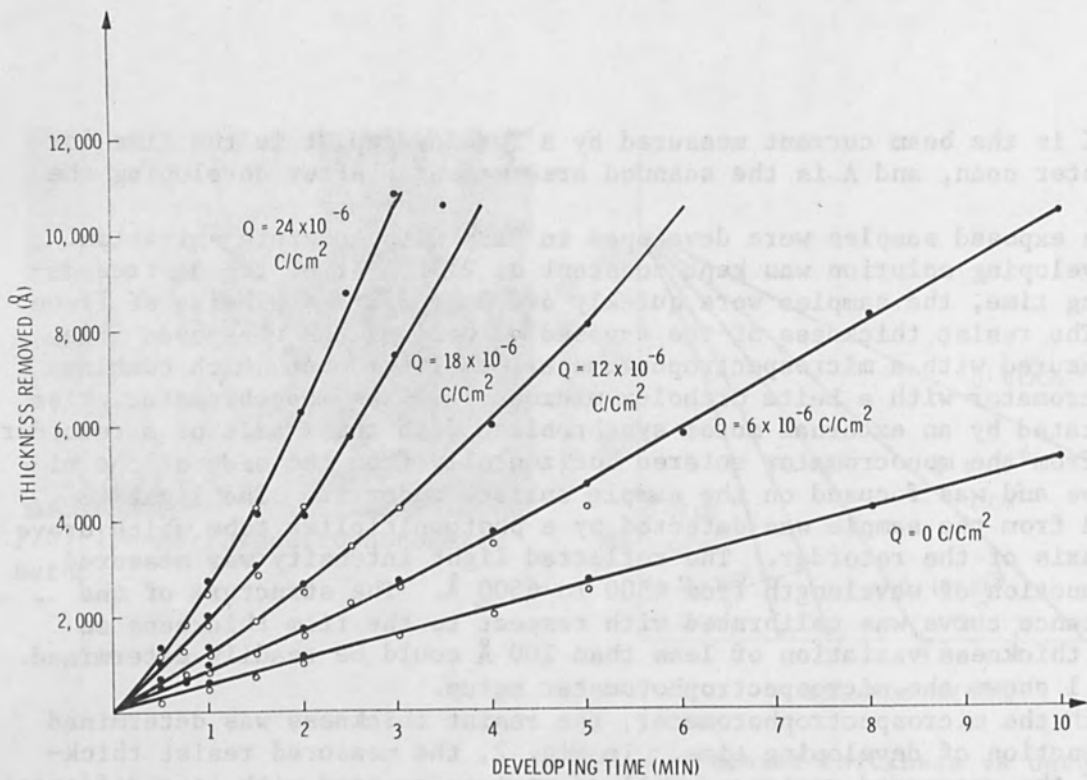


FIG. 4.--Removed resist thickness vs developing time (composite of Figs. 2 and 3).

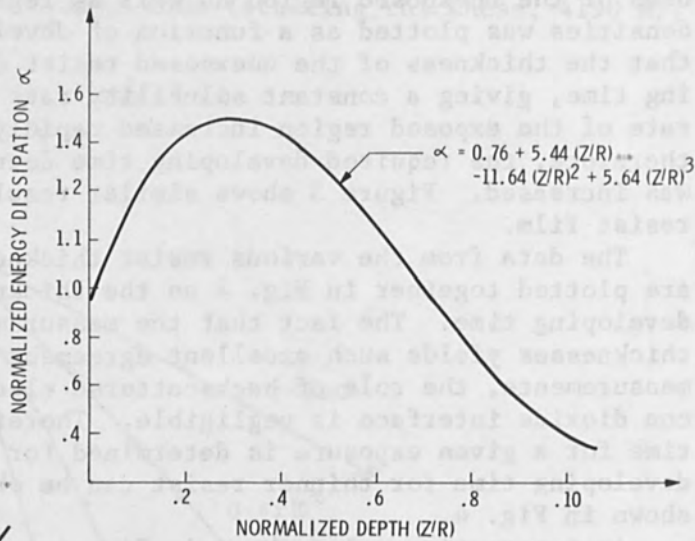


FIG. 5.--Normalized depth-dissipation function.

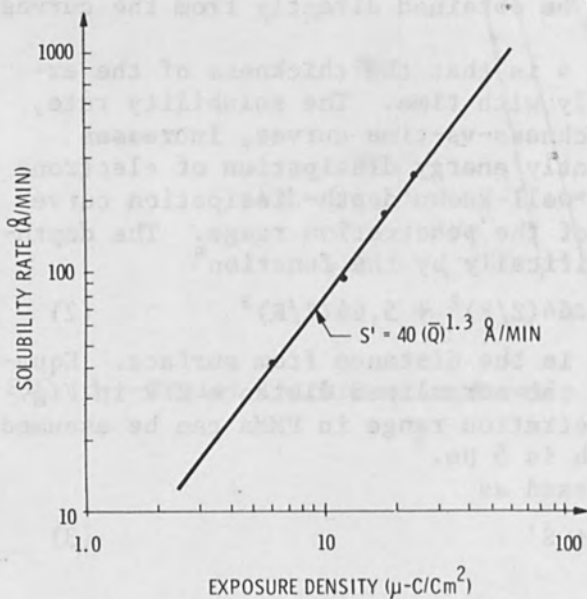


FIG. 6.--Beam-induced solubility vs exposed density.

where S_0 is the solubility rate of the unexposed resist and S' is the increase in solubility rate due to electron-beam exposure. The values of S can be obtained by evaluating the slopes of the thickness-vs-time curves of Fig. 4. Since the energy dissipation factor α is a function of depth, the effective exposure density \bar{Q} at any depth can be defined as

$$\bar{Q} = \alpha Q \quad (4)$$

For a comparison of the solubility rate for different exposure densities, the value of α must also be taken into consideration. For PMMA exposed with a 15-kV electron beam, the value of α is approximately unity at $Z = 2500 \text{ \AA}$. The values of S' at 2500 \AA for four different exposures are plotted as functions of \bar{Q} in Fig. 6. Since a straight line gives a good fit for the experimental points shown in Fig. 6, the increase in solubility can be expressed as

$$S' = K\bar{Q}^n \quad (5)$$

where the values of K and n can be obtained from the intercept and the slope of the straight line shown. In our case, we get

$$S' = 40\bar{Q}^{1.3} \text{ \AA/min} \quad (6)$$

where \bar{Q} is given in the units of microcoul/cm.

The resist thickness-vs-developing time curves can now be calculated from Eq. (6), since

$$\frac{dZ}{dt} = S = S' + S_0 = 40(\alpha Q)^{1.3} + 520$$

Therefore,

$$\int_0^Z \frac{dZ}{40[Q(0.76 + 5.44(Z/R) - 11.64(Z/R)^2 + 5.64(Z/R)^3)]^{1.3} + 520} = \int_0^t dt \quad (7)$$

Numerical integration of this expression provides the results shown in Fig. 7, where, for comparison, the experimentally measured points are also shown. It is clearly demonstrated that excellent agreement is obtained between the calculated and measured values.

CONCLUSION

By measuring the resist thickness as a function of developing time for various exposure densities it was shown that the developing time of the resist film is a function of both resist thickness and exposure density. We have demonstrated experimentally that at a given exposure, once the developing time for the thick film is determined, the required time for thinner films can be obtained directly from the thickness-vs-time curves. A linear interpretation is not sufficient, however, since the solubility rate of the exposed region is not uniform but increases with distance from the surface. This nonlinearity can be explained by the fact that electron scattering in solids yields an energy dissipation curve which has a peak below the resist surface. It was established experimentally that the solubility rate of PMMA resist changes when the exposure density is raised to the power of 1.3. From this empirical formula, one can calculate the thickness-vs-time curves for any exposure density and resist thickness. The calculated results agree very well with the measured results.

REFERENCES

1. M. Hatzakis, J. Electrochem. Soc. 116: 1033, 1969.
2. M. Hatzakis, S. Magdo, and C. H. Ting, Proc. 4th Intern. Conf. Electron and Ion Beam Science and Technology, 1970; p. 524.
3. I. Haller, M. Hatzakis, and R. Srinivasan, IBM J. Res. and Develop. 12: 251, 1968.
4. H. Y. Ku and L. C. Scala, J. Electrochem. Soc. 116: 980, 1969.
5. M. Hatzakis and A. Broers, Rec. 10th Symp. Electron, Ion, and Laser Beam Technology, San Francisco Press, 1969; p. 107.
6. P. Hoff and T. E. Everhart, *ibid.*, p. 454.
7. W. Ehrenberg and D. E. N. King, Proc. Phys. Soc. 81: 751, 1963.

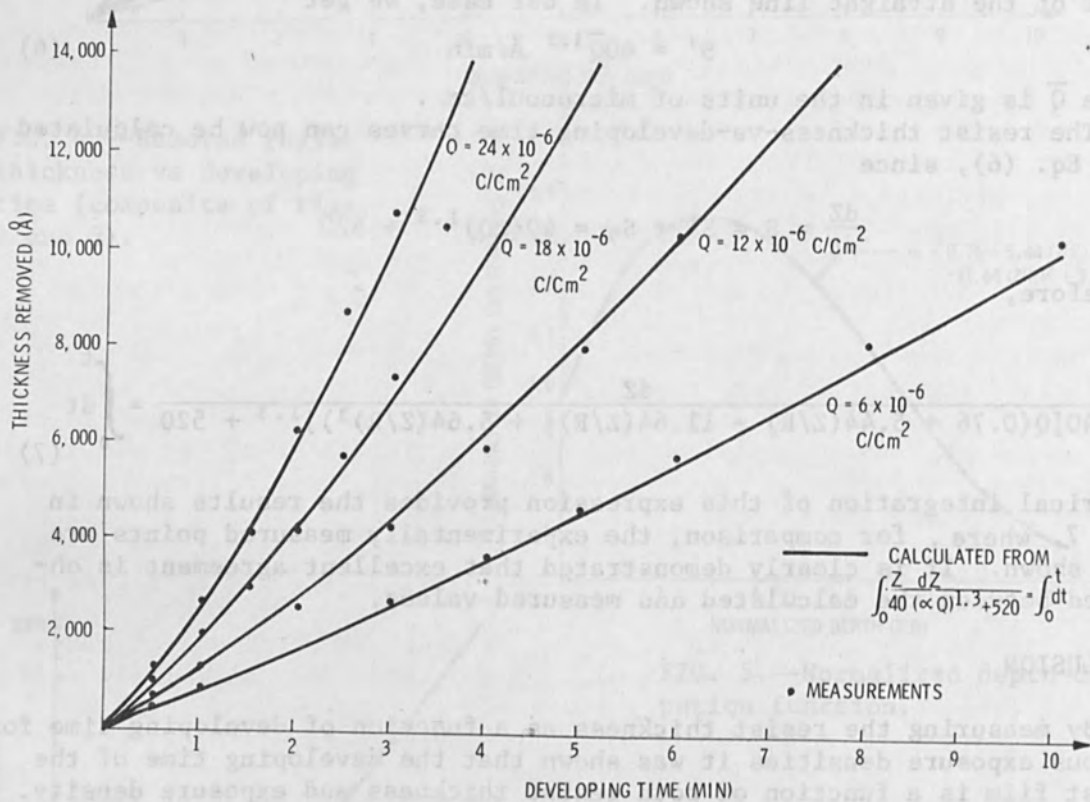


FIG. 7.--Comparison of calculated resist removal rate with experimental findings.

ION IMPLANTATION SYSTEM FOR DEVICE PRODUCTION*

R. G. WILSON and G. A. SHIFRIN

Hughes Research Laboratories, Malibu, Calif.

A device and circuit production implantation system has been placed in operation in a MOS integrated circuit manufacturing environment. This system was developed to convert the process of ion implantation doping of MOSFET devices and integrated circuits from a proved laboratory technique to a reliable and economical manufacturing process. The system was designed with consideration for reliability, safety, ease of maintenance, and economy of manufacturing processes. A target chamber was developed which allows a variable number of various sized wafers (e.g., 45 2-in. wafers) to be implanted in each pumpdown. The target chamber and beam transport and handling system were designed to be compatible, to have a short vacuum cycle time, and to be operated easily by a production worker at a rate of more than 200 2-in. wafers per day (at a dose of 10^{14} ions/cm²). The vacuum pumpdown and implantation cycle is largely under automatic control. Manufacturing techniques are being developed to be compatible with present planar MOS technology. The ion energy can be varied from 20 to 120 keV (boron or phosphorus, etc.). The dose range capability is 2.5×10^{11} to 2×10^{15} /cm². Boron current to the target can be varied from about 0.1 to 20 μ A and can be rastered (scanned) uniformly over an area 10×10 cm. The pressure during implantation is less than 2×10^{-6} torr and pumpdown between sample batches is less than 10 min.

BACKGROUND

A research program in ion implantation doping of semiconductor materials begun in 1965 has grown into advanced device and system development in certain areas and (beginning in 1969) a production implantation system and a manufacturing technique development program. A joint program with the U.S. Air Force Manufacturing Technology Branch was launched on 1 January 1970 to convert ion implantation doping from a proved laboratory technique to a reliable and economical manufacturing process.

SYSTEM SPECIFICATIONS AND PERFORMANCE ACHIEVEMENTS

The production implantation system was designed with consideration for reliability, safety, ease of maintenance, economy of manufacturing processes, and compatibility with present planar MOS technology. A target chamber was developed which allows a variable number of various sizes of wafers (e.g., 45 2-in. wafers) to be implanted in each pumpdown. The target chamber and beam transport system were designed to be compatible, to have a short vacuum cycle time, and to be operated easily by a production worker at a rate of over 200 2-in. wafers/day (at a dose of 10^{14} boron ions/cm²), after initial setup by a trained operator. The vacuum pumpdown and implantation cycle are largely under automatic control.

*Partially supported by the Air Force Aeronautical Systems Division, Manufacturing Technology Branch.

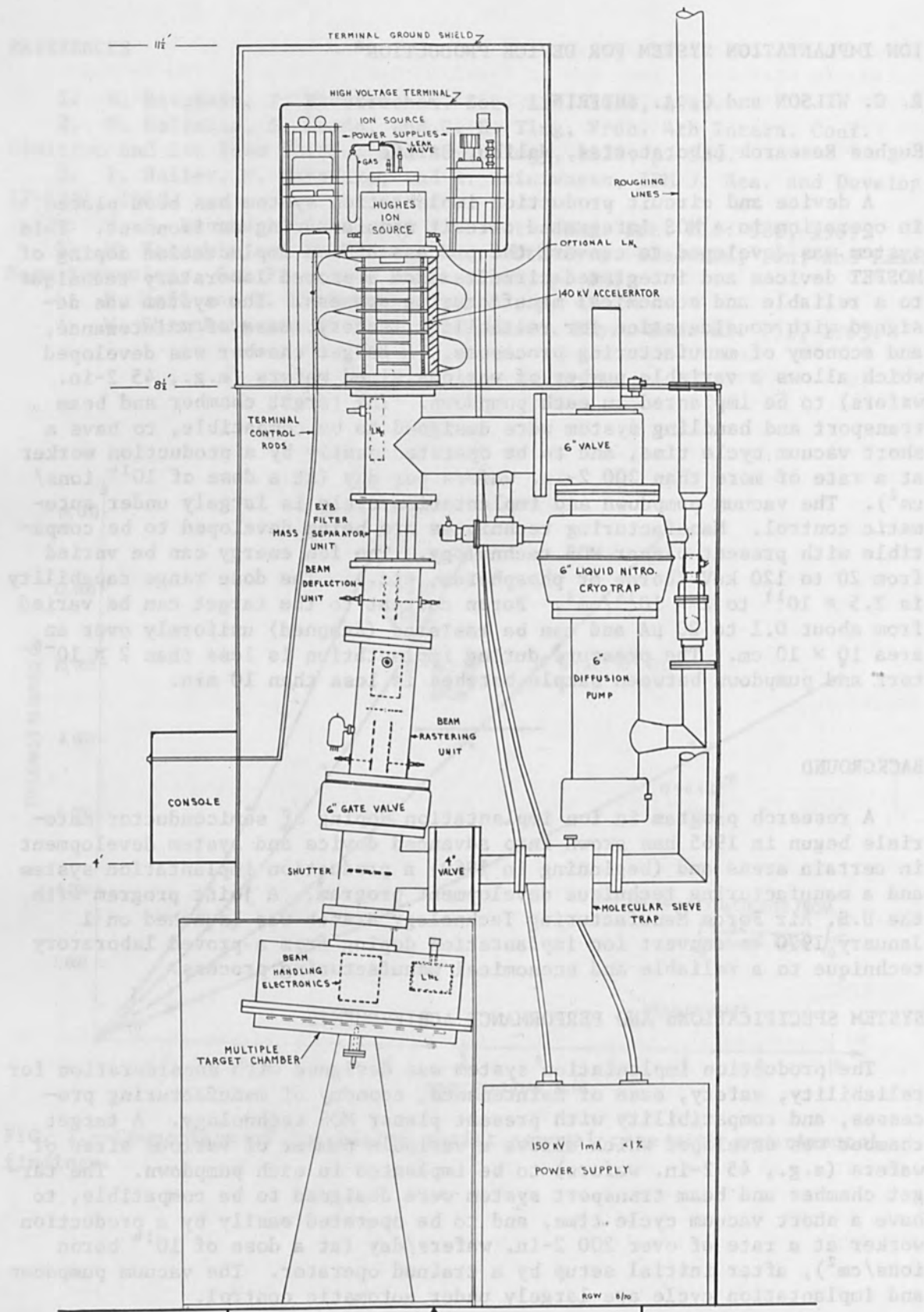


FIG. 1.--Schematic layout of complete system.

This ion implantation system was designed to produce a mass-separated boron ion beam in the energy range of approximately 20 to 120 kV, and to raster scan it uniformly over an area of approximately 100 cm², through which can be passed targets (for example MOS integrated circuits) that receive a predetermined dose in the range from 2×10^{11} to 10^{15} ions/cm². The ion current is reduced at lower energies but this is conveniently compatible with the lower ion dose which the lower-energy applications require, e.g., for CMOS threshold control.

A 150-kV maximum voltage ion accelerator oriented with the beam axis nearly vertical (Fig. 1) provides the required boron ion energy and allows the wafers to be processed on a horizontal and easily exchangeable wheel or tray. A minimum of floor space is required by this configuration; and the high-voltage portion of the system is located at ceiling height, out of the way of personnel during operation. A cage runs from the top of the system to the ceiling to protect personnel from the high-voltage portion of the system.

The performance specifications and achievements of this system are listed in Table I.

SYSTEM DESCRIPTION

A general schematic layout of the total system is shown in Fig. 1. Two similar but independent vacuum systems pump the two different sections of the implantation system, the target chamber and the beam line. The target chamber is evacuated every time a tray of wafers is implanted (several to a dozen times in one shift, depending on the required dose). Since the ion source, accelerator, and beam line should never be exposed to atmospheric pressure for optimum operation, this portion of the system is kept at high vacuum at all times. A fast, large-capacity vacuum system is provided for the target chamber in order to prevent the pumpdown time from becoming a limiting factor for low-dose implantation requirements. The lines to both mechanical pumps are 3 in. in diameter. The vacuum systems each include a 6-in. oil diffusion pump covered by Granville-Phillips liquid nitrogen traps and 6-in.-high vacuum angle valves. The two vacuum systems are isolated by a 6-in. gate valve in the beam line. Each system is independently vented to dry nitrogen. Three traps and a reservoir must be filled with liquid nitrogen as part of the regular operation of the production system, in addition to the two diffusion pump traps - a trap within the target chamber, one in the beam line, and one at the source. A reservoir is located near the high voltage terminal at the highest point in the liquid system. Liquid nitrogen is supplied to the system from a 110-liter storage dewar. The Granville-Phillips traps are filled manually through solenoid valves at the beginning of each shift. The other traps are automatically kept full by a pneumatic level-control system that senses the level of the nitrogen in the reservoir. The automatic system supplies LN₂ across high voltage to the accumulation dewar and the trap at the source.

The vacuum environment in the target chamber is improved by the presence of a large-area (2-ft²) liquid nitrogen cryowall. Hydrocarbons, e.g., oil vapors from the vacuum systems (oil diffusion and mechanical roughing pumps) are of special concern. Both roughing lines are provided with molecular sieve traps to lessen the chance of oil vapor entering the target chamber during roughing. A 5° bend is provided in about the center of the beam line to prevent any particles of corrosion or energetic neutral particles from striking the target surface.

TABLE I.--Performance specifications and achievements.

	Specification	Achievement
Target chamber pressure	$< 2 \times 10^{-6}$ torr	Achieved $< 10^{-7}$ torr with no beam; under implantation condition, mid to high 10^{-7} torr in target chamber, mid 10^{-6} torr in beam line
Target chamber environment	LN ₂ surfaces in chamber LN ₂ trapped diffusion pump Molecular sieve-trapped roughing lines	Done Done Done
Target chamber pumpdown time	< 10 min to 2×10^{-6} torr after 2-min exposure to atmospheric pressure	~ 5 to 6 min with partial tray of test wafers - same after ~ 10 hr of continuous operation and a half a dozen cycles
Ion species	Boron (others possible, e.g., P)	Done
Ion energy	20 to 125 keV	20 to 120 keV
Dose range capability	2.5×10^{11} to 2×10^{15} ions/cm ²	Done
Typical B ⁺ current at target	0.1 to 20 μ A	Achieved ($> 20 \mu$ A observed; $\sim 40\%$ of beam is B ⁺)
Time to dope one 2-in. wafer	~ 2 min for $\sim 10^{14}$ /cm ² ~ 0.2 min for 10^{12} /cm ²	0.5 to 1.1 min achieved Can be lower
Number of samples and batch time	~ 45 2-in. wafers; ~ 15 3-in. wafers ≤ 2 hr/batch (for 10^{14} dose)	Achieved Achieved (< 1 hr observed)
Dose control (absolute)	$\pm 10\%$ of nominal	$\pm 8\%$ achieved (the experimental error in dose measurement)
Dose reproducibility (relative)	$\pm 5\%$ among wafers in batch	
Dose uniformity	Objective: $\pm 2\%$ over 2-in. wafer	$\pm 4\%$ achieved to date (improvement being sought)
Beam scan area at target (maximum wafer size)	3.5 in.	Achieved
Floor space required	50 ft ² (plus some access)	Achieved
Electron flooding at target	Energy and current variable. Compatible with circuit being doped. Interlocked with vacuum and ion beam.	Achieved
Beam target alignment	Nominally normal - no special alignment	Done
Automation	Manual start up by trained technician - routine operation by untrained operator. Automatic dose control, pumpdown, sample sequencing, overrides to allow manual operation, troubleshooting, and check out.	Done
Maintenance	Easy fuel gas and ion source change. Easy startup. Good tolerance levels on beam-line components.	Done

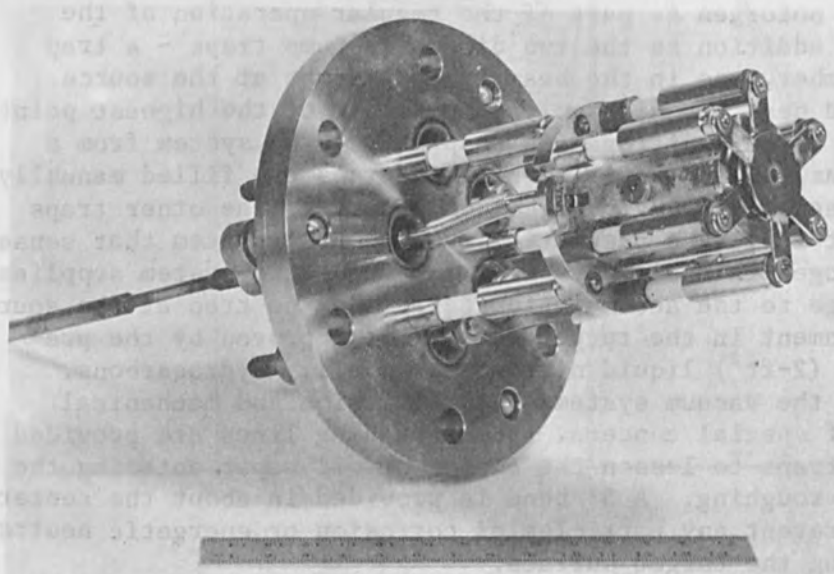


FIG. 2.--Ion source.

A cold-cathode electron bombardment ion source (Fig. 2), demonstrated to be reliable for producing a boron ion beam of more than 10 μ A for many months was selected for use in this production system. One such ion source has been operated for about 3 yr in an implantation system with cleanings every 3 or 4 mo. The boron ions are derived from the flow of BCl_3 gas through a controlled leak valve between the source and a lecture bottle. The BCl_3 bottle is replaced about twice per year. Other gases could just as well be substituted to produce other ions, e.g., PF_5 for phosphorus, H_2S for sulphur, etc.; or a multiple-feed system with valving could be used to provide a selection of ions.

The ion source discharge chamber is mounted on a small flange (Fig. 2) which mates to a flange on the top of the ion source housing. A magnet is wound on the outside of this housing and a lens is mounted inside the source housing.

The LN_2 at the ion source provides extra vacuum pumping at the ion source exit, where high pressure causes scattering of the ions from the beam and causes charge-exchange collisions which result in sputtering of electrodes. The temperature of LN_2 is sufficient to condense BCl_3 and its byproducts.

Ions are extracted from an aperture in the source screen electrode. The screen and extraction electrodes have concentric apertures with diameters, shaped edges, and spacings all critical to the extraction optics designed by digital and analog computer programs. This high-perveance optics allows substantial ion current to be extracted with about 2 kV in this case. Power supplies are required for the anode, screen, magnet, and lens, and are driven by four Variacs mounted on the terminal housing base. These four Variacs are controlled by rods which terminate on the control panel on the front of the system cabinet. A fifth control rod is attached to the variable-leak valve in the ion source feed system. The controls terminate in six 16-turn Helipot duo dials, allowing about 1000 numbers of position location (10 turns) for one turn of each Variac. The magnet is not essential to the operation of the source in the high end of the pressure range. It is convenient to use it for lower ion currents (lower gas pressures), where it is important in obtaining maximum ion current.

Mass separation is performed with a simple, inexpensive, permanent magnet $E \times B$ velocity filter, shown in Fig. 3. Its active length is 6 in. (15 cm). It has a rectangular cross section with flanges at either end to couple to a 6-in. beam line. The shape of the electrostatic plates was determined from the results of studies using an electrolytic-tank analog computer. The design criterion was to create a large area of uniform electric field between the plates in the region of the beam to prevent beam aberration resulting from nonuniform electric fields and to eliminate the need for electrostatic shims. The magnetic field is provided by two Varian 8 liter/sec ion pump magnets fastened side by side and placed over the channel. The magnet polefaces are machined at an angle appropriate for 100-keV boron ions. Two electrical feedthroughs are required for the two electrodes. Approximately 10 kV can be applied between the electrodes.

Definition of the separated masses is provided by a slit, located further downstream in the beam raster scanner, requiring proper orientation of the sweeping plates. Essentially no ions pass through the mass-defining slit to reach the target wafers other than boron. The distance from the $E \times B$ separator to the target is the total dispersion defining length for what passes through the slit. Using

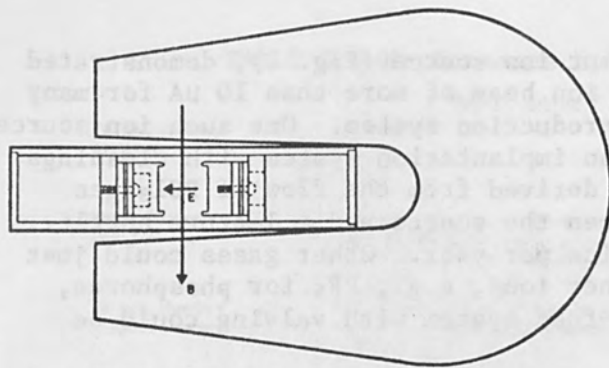
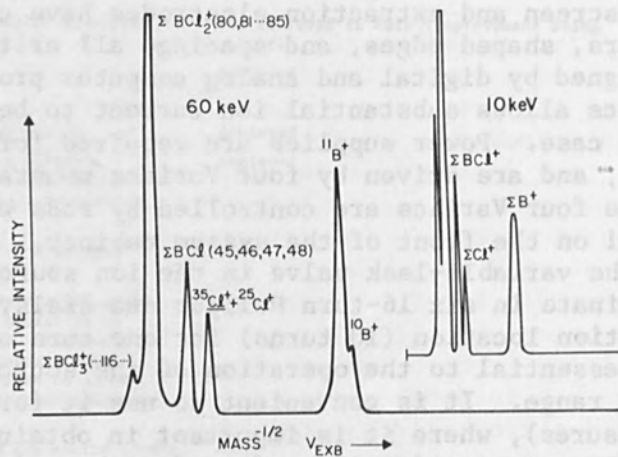
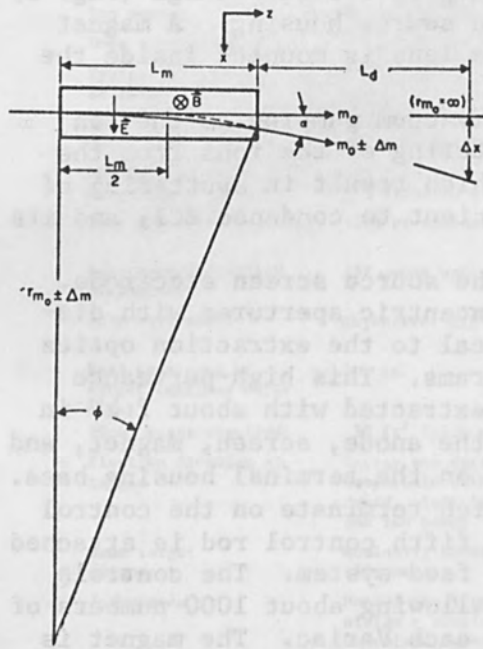
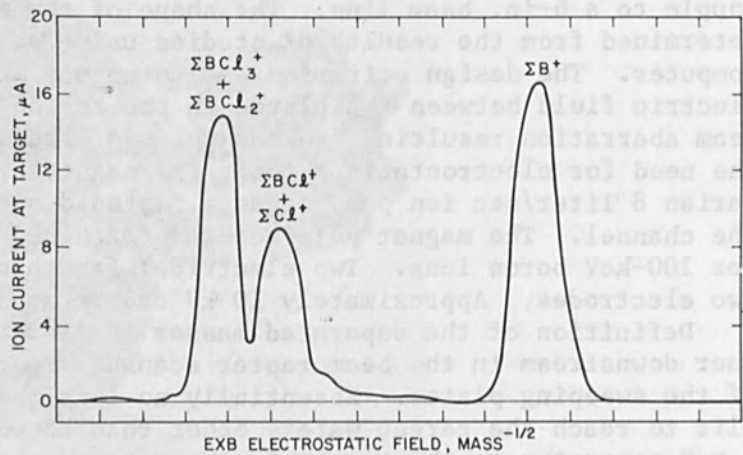


FIG. 3.--E x B mass separator.



(a)



(b)

FIG. 4.--Mass spectrum of a beam generated from BCl_3 : (a) Faraday cup, (b) 2-in. collector.

$$D = \frac{E}{2V_0} \left(\frac{L_m^2}{2} + L_m L_d \right) \left[1 - \left(\frac{m_0}{m} \right)^{1/2} \right]$$

where $E/2V_0 = 10^{-2}$ for 100 keV and the expression in the bracket is 0.114 for $m_0 = 11$ and $m = 14$ (N^+) and 0.439 for $m_0 = 11$ and $m = 35$ (Cl^+); $L_m = 15$ cm; L_d to slit = 25 cm; and L_d to target = 46 cm. Then

To the slit:	mass 14	0.54 cm = 0.21 in.
	mass 35	2.15 cm = 0.85 in.
To the target:	mass 14	0.88 cm = 0.35 in.
	mass 35	3.5 cm = 1.4 in.

For a 1-cm slit, the dispersion cutoff distance is 0.5 cm. Because the beam is about 1 cm in diameter, some N^+ would get through if it were present (none is observed), but no Cl^+ will get through. Good resolution mass spectra were measured with a Faraday cup illustrated in Fig. 4(a) for BCl_3 . The resolving power of the system is 15, and the ion spectrum from the source shows nothing within a factor of 2 in mass of boron; the two boron isotopes 10 and 11 are just resolved. The greatest current density measured in the Faraday cage was $40 \mu A/cm^2$. The total beam mass spectrum measured in a 0.5-in. cup collector is shown in Fig. 4(b).

A quartz plate at the location of these collectors was used for visual observation of the beam spot sizes and shapes. The spots were qualitatively round and appeared to be about 1 cm in diameter. The boron beam of 100 keV was allowed to strike a tantalum plate for several hours. Examination of this plate showed a burned spot with a ring structure. The spot diameter and shape could be studied more quantitatively. The spot is slightly elliptical. The major and minor diameters are 0.9 and 0.7 cm.

The target chamber is a hollow stainless-steel cylinder which is split into two portions to permit the insertion and removal of the wafer tray. The upper portion is permanently attached to the lower end of the beam line. The lower portion is translated by hydraulic cylinders and travels from a position in contact with the upper portion to one where it presents itself at a convenient height to the operator for easy loading and unloading operations. The necessary hydraulic actuation for these movements is performed automatically. The two portions are sealed with a large O-ring. The lower portion of the target chamber contains the wafer tray, its driving hub, and a reference signal device. The driving hub is attached to a rotary feedthrough, so that from outside the vacuum system the hub is driven by a stepping motor through a worm and worm gear combination with a ratio of 180:1. The stepping motor is driven electronically from the current integrator. A complete revolution requires 36 000 steps; thus, each step of the motor shifts the wafer tray by 0.01° .

The wafer tray is a light, perforated stainless-steel assembly, annular in shape, with two handles attached to its inner edge. Radial clamps enable the operator to hold or release the wafer tray from the hub as required. The inner and outer edges of the wafer tray are drilled with holes which retain special slips to hold the wafers on the tray. The wafers may be placed within the annular region of the tray (about 3.5 in. wide) as densely as their size and shape permits.

Proper operation of the production system is provided under the direct control of an automatic sequencer which is a flexible commercial programming switch advanced by a stepping motor. Each electrical function is

connected to a SPDT switch on the programming switch drum. In certain hold-mode situations, the last required switch closure requires actuation of a manual ADVANCE button. At appropriate times the final required closure occurs at a prescribed pressure in the system, signalled by a thermocouple sensor, or by the location of a shaft signalled by a limit switch.

Dose control is provided by a stepping motor (36 000 steps/revolution) that drives the target wheel under the control of the integrator which provides the driving pulses. The current to the integrator is not received directly from the target, where accurate measurements of current and hence dose are difficult to make in the presence of flooding electrons, heating (if employed), and the difficult task of suppressing secondary electrons over a 100-cm² area. Rather, integration is performed just above the target plane and just upstream from the source of flooding electrons and is done with carefully designed strip Faraday cages running parallel to the sides of the target area within the 100-cm² scan area.

By following calibration curves the operator is able to preset the dose on the front panel. The dose can be varied continuously from 2×10^{11} to 2×10^{15} ions/cm².

Raster alignment or positioning is provided by two orthogonal pairs of sensing wires at the periphery of the 100-cm² scan area. The signals from these wires are fed to a pair of zero-center null meters. Variable dc offset bias voltages can be applied to orthogonal sets of plates in the beam line to cause the sensing meters to null, thereby centering the raster.

Electrons of selectable energy from a dual-filament emitter are caused to flood the target area in a sufficiently uniform manner (by a potential distribution determined by the use of an electrolytic-tank analog computer) to prevent any insulating areas of the target wafers from becoming charged to a high positive potential by the incident ion beam.

GENERATION OF BEAMS OF CHARGED LIQUID PARTICLES

STEVEN B. SAMPLE, RAGHUPATHY BOLLINI, and DONALD A. DECKER

School of Electrical Engineering, Purdue University, Lafayette, Ind.

A process is described for generating collimated beams of monodisperse, charged liquid particles. The process utilizes the harmonic electrical spraying of liquids, wherein charged droplets are regularly emitted from an electrically stressed meniscus at a capillary tip. The emitted particles are extremely uniform in size and charge, and collinear in trajectory; thus, beams of such particles can be readily focused, accelerated, and deflected by purely electrical means. The diameter of the particles generated by the harmonic spraying process can at present be varied from 50 to 500 μm , with a corresponding variation in charge-to-mass ratio from 10^{-2} to 10^{-4} coul/kg. However, with improved techniques being studied at present, it should be possible to produce beams of uniform particles having diameters as low as 10 μm .

The original experiments with the harmonic spraying process were limited to water as the working fluid, but our current investigations show that this process can also be used to generate beams of molten metal particles in vacuum. Such beams could be employed for coating and abrading solid surfaces within microscopic tolerances without the need for masks or baffles. Thus these beams might find application in such diverse fields as integrated-circuit fabrication, micromachining and polishing, high-density information storage, and hypersonic erosion studies.

APPARATUS FOR SPRAYING WATER

A schematic of the experimental apparatus is shown in Fig. 1. A stainless-steel hypodermic needle, with the tip ground and polished flat, fits into a plastic syringe, which is in turn connected by a tube to a reservoir of liquid. Variations in liquid pressure head (measured from the needle tip to the top of the liquid in the reservoir) are obtained by adjusting the height of the reservoir. A grounded plate with a small hole in the middle is centered directly under the tip of the needle and about 2 or 3 cm below it. A small cup, located directly underneath the grounded plate, is used to collect the drops. The needle is connected to one side of a high-voltage ac-dc supply, which is capable of providing 0 to 75 kV dc at 1.5 mA and/or 0 to 15 kV peak ac from 20 Hz to 20 kHz. The grounded side of the supply is connected directly to the grounded plate, and is also connected through an electrometer to the collector cup.

The spraying process is observed through a small microscope (not shown) and is recorded with a conventional 16-mm movie camera focused through a long focal-length lens. The high-frequency (about 400 Hz) periodic spraying process is effectively slowed to about 1 Hz by setting the frequency of the stroboscope close to the spraying frequency. This technique permits direct measurement of the spraying frequency and also allows slow-motion movies to be taken at 16 frames/sec without any synchronization between the camera and the stroboscope.

The mass flow rate is measured by observing the rate of fall of the reservoir level through a small telescope. The mass of the emitted particles is then computed by dividing the mass flow rate by the frequency of droplet emission (as measured with the stroboscope). Similarly, the charge

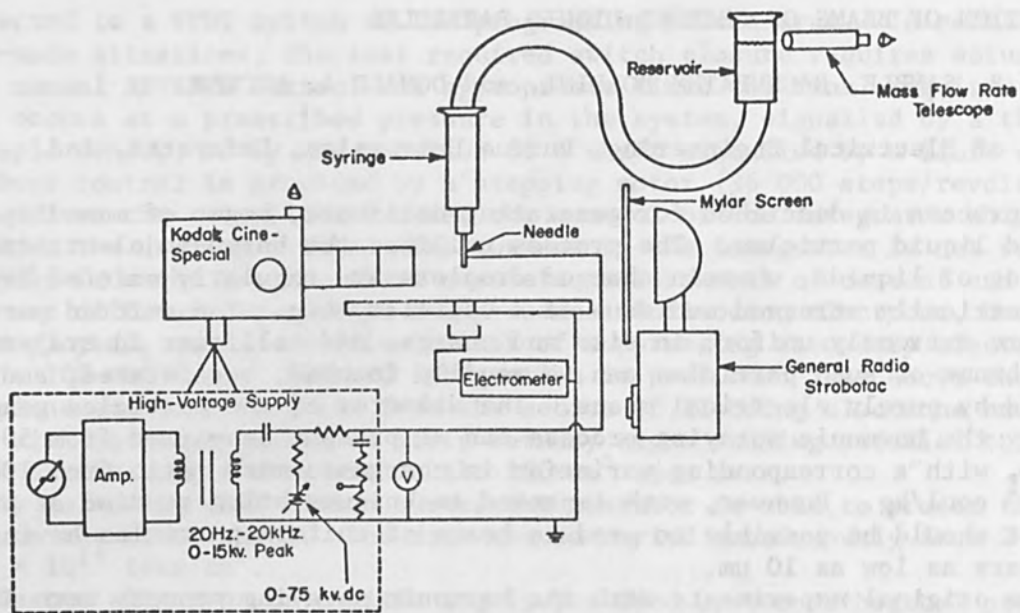


FIG. 1.--Experimental apparatus for studying the harmonic electrical spraying process.

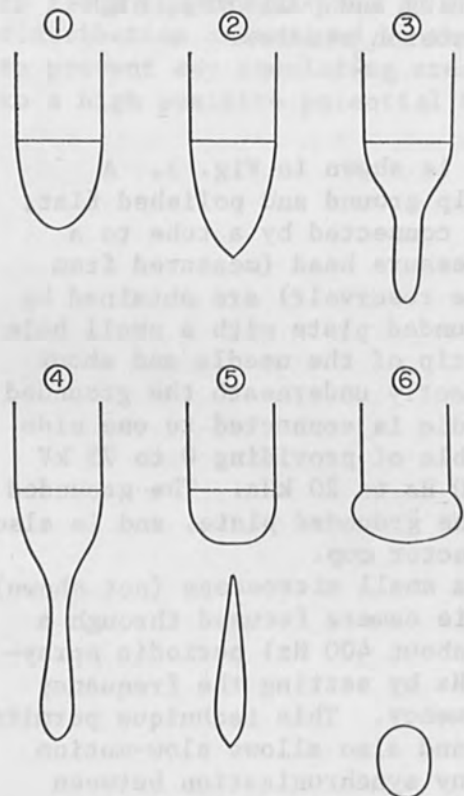


FIG. 2.--Six sequential stages in the formation of a drop at the needle tip during harmonic spraying.

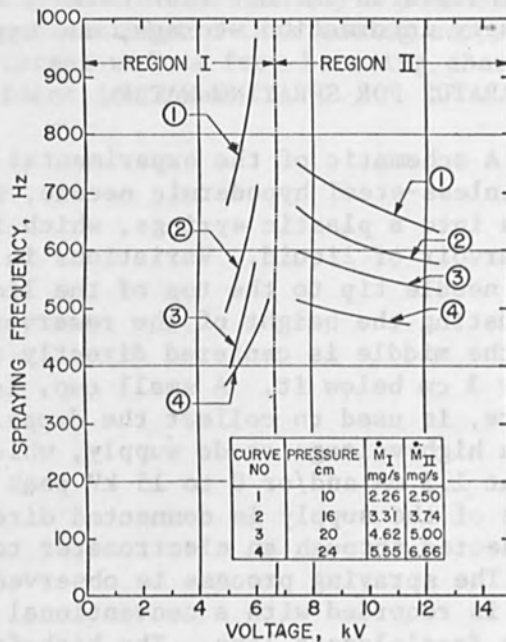


FIG. 3.--Harmonic spraying frequency vs applied dc voltage; needle OD, 0.41 mm; ID, 0.20 mm. Symbol M stands for mass flow rate.

on each drop is obtained by dividing the electrometer current by the frequency of emission.

EXPERIMENTAL RESULTS WITH WATER^{1,2}

The reservoir height is first adjusted so that, with no applied voltage, liquid just begins to drip from the needle. As the voltage is increased, the frequency of dripping increases, whereas the size of the individual drops decreases. The mass flow rate (i.e., the product of the dripping frequency and the mass of each drop) remains essentially constant. Finally, at about 4 to 6 kV, a point is reached at which the relatively low-frequency (about 10 Hz) dripping abruptly ceases, and harmonic spraying (at about 500 Hz) is observed. This transition is marked by a sharp increase in the frequency of droplet emission, and by a sharp decrease in the size of the meniscus, the mass flow rate, and the diameter of the emitted particles. Moreover, the droplets are no longer pulled off directly from the needle (as in the case of dripping), but rather are pulled out from the front surface of the electrically stressed meniscus (Fig. 2). As each drop separates from the meniscus it carries with it part of the surface charge that is induced on the meniscus by the high voltage. After separation, the meniscus relaxes back toward the needle; the process then repeats itself in a regular, periodic manner. The emitted particles are thus uniform in size and charge, and collinear in trajectory.

Figure 3 shows the behavior of the spraying frequency as a function of voltage, using the same needle with four different pressure heads. Figure 4 shows the variations in drop diameter as a function of voltage for three different needles and pressure heads. It can be seen from the figures that, for a given pressure head and needle size, a band of voltages exists over which no harmonic spraying occurs. For voltages within this forbidden band the spraying is very random and irregular. At voltages below the forbidden band (region I) the spraying frequency increases rapidly with increasing voltage; for voltages above the forbidden band (region II) the frequency decreases slowly with increasing voltage.

Figure 5 shows the dependence of drop diameter on the pressure head. It is evident from this figure that varying the pressure head is a very effective method for obtaining controlled particle diameters over a wide range. In particular, in the case of curve 1, the drop diameters vary over almost a 4:1 range, which represents a 64:1 range in drop masses. The frequency range for curve 1 is from 750 Hz for the 120- μm drops to 270 Hz for the 460- μm drops. The lower pressures in Fig. 5 are below the minimum levels necessary for zero-voltage dripping; thus, in order to achieve harmonic spraying for these pressures, it is usually necessary to begin spraying at higher pressures and then decrease the pressure to the desired level.

A crude model for the charge-to-mass ratio of the emitted particles can be developed as follows. In the process of being pulled from the meniscus, each droplet develops a sharp point at its forward tip (see Fig. 2). This pointed tip indicates that the front surface of the droplet is unstable. Therefore, just at the instant the drop is formed, the charge density over the front half of the drop is roughly equal to the charge density necessary to overcome the surface tension stress. On the other hand, since very few electric-field lines terminate on the back side of the drop, the charge density on the back surface at the instant of formation must be close to zero. Thus, the charge-to-mass ratio of each droplet should be roughly half the maximum possible charge-to-mass ratio for an isolated

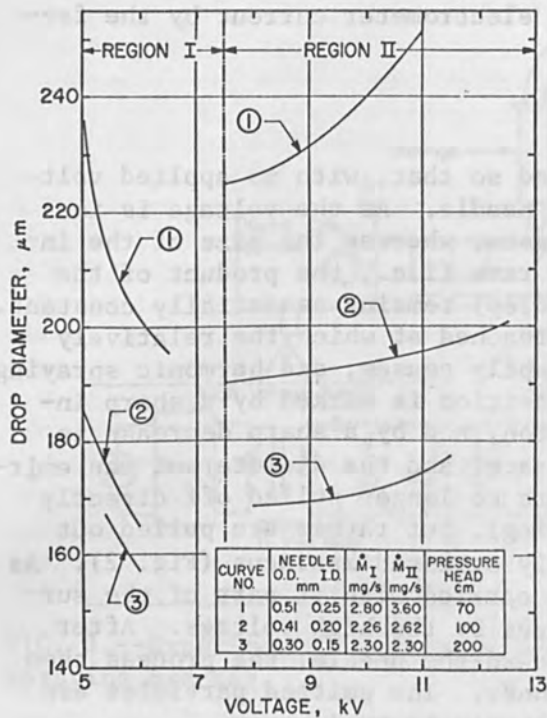


FIG. 4.--Emitted drop diameter vs applied dc voltage for three different needles and pressure heads.

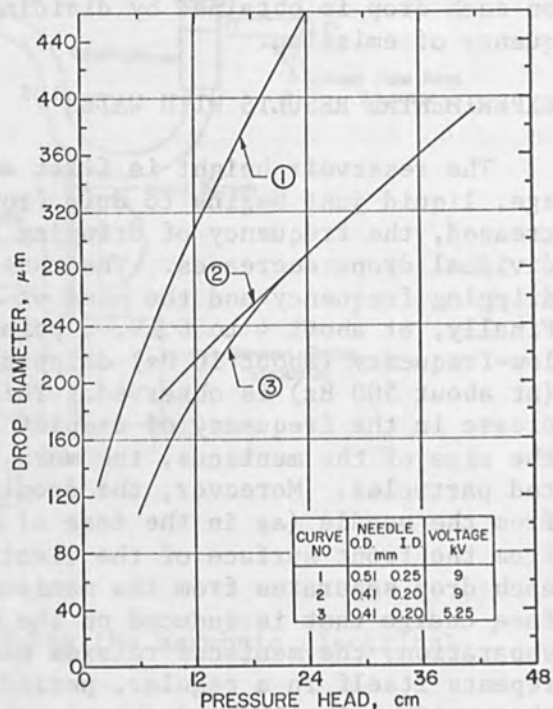


FIG. 5.--Emitted drop diameter vs pressure head for two different needles and dc voltages.

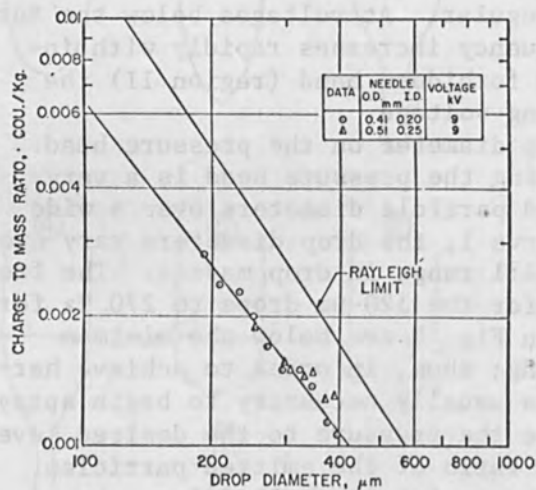


FIG. 6.--Charge-to-mass ratio vs emitted drop diameter. For small-needle data the pressure ranges from 8 to 42 cm; for the large-needle data, from 5 to 230 cm.

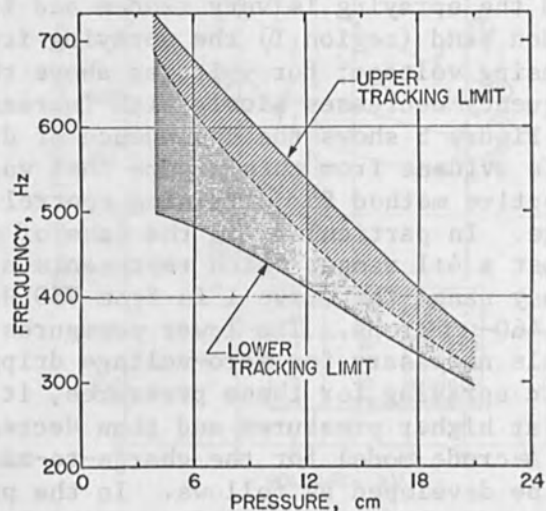


FIG. 7.--Tracking bandwidth of harmonic spraying process vs pressure head. Applied dc voltage, 8 kV; ac voltage, about 900 V rms; needle OD 0.51 mm; ID, 0.25 mm.

liquid drop of the same radius. This maximum charge-to-mass ratio, known as the Rayleigh limit,³ is given in mks units by:

$$\left(\frac{q}{m}\right)_{\max} = \frac{6(\epsilon\gamma)^{1/2}}{\rho r^{3/2}} \quad (1)$$

Figure 6 shows the behavior of the charge-to-mass ratio of the emitted particles as a function of particle diameter. It is interesting to note that the data for both needles agree very well with the model proposed above.

It was found that the addition of an ac voltage to the dc spraying potential can be used to improve the periodicity of the spraying process, and can also be used as a means for controlling the frequency of droplet emission. The ac frequency, of course, must be close to the natural harmonic spraying frequency. The exact amount of ac voltage necessary to control the process varies with the dc potential; however, good results are usually obtained with an ac peak voltage equal to about 20 per cent of the dc voltage. Figure 7 shows the behavior of the tracking bandwidth (i.e., the range of frequencies over which the spraying frequency tracks the ac voltage frequency) as a function of pressure, for a typical needle diameter and voltage. The solid curve inside the tracking region represents the natural spraying frequency (or natural characteristic frequency of the meniscus) as a function of pressure.

APPARATUS FOR SPRAYING METALS

A diagram of the apparatus used for spraying molten metals in vacuum is shown in Fig. 8. The vacuum chamber consists of a 2-ft section of 6-in.-ID glass pipe. The furnace is an aluminum tube 3 in. in diameter approximately 1 ft long with the heater wire strung vertically from stand-off insulators in a zig-zag fashion around the inside surface. Due to the substantial expansion of the wires upon heating, it became necessary to enclose the wire in glass tubing. The liquid reservoir is a 0.5-in. pyrex tube with the needle attached on the end. In order to shield the effects of the high-voltage connection to the needle, and thus keep the electric field as symmetrical as possible about the axis of spraying, the needle is inserted through a small hole in a 1.5-in.-diam copper disk. A small spring clamp around the hole electrically connects the needle to the disk, which in turn is connected to the high-voltage lead. The disk is connected to the sides of the oven by means of ceramic stand-off insulators.

The top of the reservoir is connected to a valve system for controlling the pressure on the liquid to be sprayed. Since some pressure (of the order of a few mm of Hg) is normally required in order to initiate dripping, it is necessary to close the glass shut-off valve before applying the high voltage in order to prevent the gas in the reservoir from ionizing and shorting out the high-voltage supply.

EXPERIMENTAL RESULTS WITH TIN

Since the furnace is made of aluminum and the reservoir is made of Pyrex, only metals which melt below 400°C can be sprayed. At first Wood's metal (eutectic alloy, melting point 80°C) was tried but it was difficult to obtain clean samples of this alloy and as a result it constantly clogged the needles. After various other metals were tried, it was found that tin

would give the best results. However, even with 30-mesh reagent grade tin, a careful cleaning process had to be developed before the molten metal would flow consistently through the small needles and thus allow stable, repeatable periodic dripping.

Originally experiments were carried out using stainless-steel needles mounted in chromeplated brass hubs. However, these needles clogged easily since the chrome had a tendency to flake off and contaminate the molten tin. At present, a system (i.e., hub, needle, and luer-lock) made entirely of stainless steel is giving satisfactory results.

Molten tin does not wet stainless steel and therefore the meniscus forming at the tip of the needle does not extend to the outer diameter of the needle. Even so, the actual drop size is still larger than the ID of the needle.

After reliable dripping and prevention of voltage breakdown problems were achieved, harmonic electrical spraying of tin was accomplished. With a 27-gage needle 3/4 in. long (410 μm OD and 200 μm ID) the drop diameter varied between 260 μm to 320 μm . The frequency varied between 60 and 160 Hz.

Most of the characteristics of the spraying process seem to be similar to that of water. For example, the spraying process can be locked with an ac voltage of the right frequency and amplitude (as described in water experiments). This permits the spraying frequency to be varied by varying the applied ac frequency.

At the present time, no reliable data for the charge-to-mass ratio for molten tin drops has been obtained. But if we assume that the results of the experiments using water apply (i.e., the charge-to-mass ratio is one-half the Rayleigh limit), one can expect the charge-to-mass ratio for a molten tin drop with a 300- μm diameter (density = 6.94 g/cm³ and surface tension = 612 dynes/cm) to be 5×10^{-4} coul/kg. At present large needles are being tried in order to overcome initial problems and achieve harmonic spraying, but from past experience with water, it is reasonable to conclude that with a needle of ID of 100 μm , drops of about 30 μm can be obtained by proper adjustment of the pressure and the charge-to-mass ratio for these drops should be of the order of 10^{-2} coul/kg.

APPLICATIONS

The broad range of potential applications of harmonic spraying stems from the fact that, in principle, any material which melts below the softening point of the spraying capillary, and which exhibits a conductivity greater than 10^{-8} mho/m, can be harmonically sprayed. In particular it should be possible to spray mixtures, solutions, and colloidal suspensions. Thus, a material which does not melt easily might be sprayed by being first suspended in a liquid vehicle, whereas a material with a very low conductivity might be sprayed after it has been lightly doped with an electrolyte.

Figure 9 illustrates one possible configuration for depositing harmonically sprayed particles in precise patterns without the use of masks. It should be pointed out that there is essentially no physical interaction between adjacent drops in the beam, and thus, provided the deflection amplifiers are sufficiently fast, the beam can be swept instantaneously from one point to another point some distance away without leaving any trace deposition in between.

In the area of engineering applications, some of the potential uses for harmonically sprayed particle beams are:

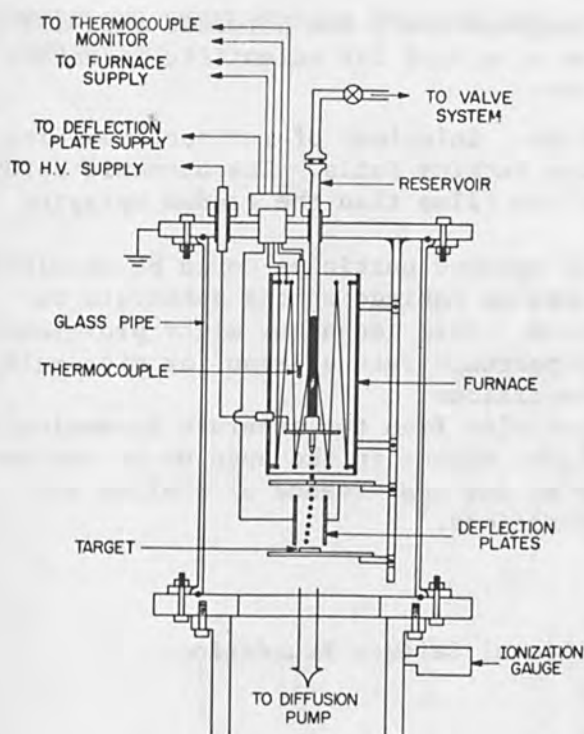


FIG. 8.--Apparatus for spraying molten metals in vacuum. Connectors 1, 2, and 3 are used for current measurements.

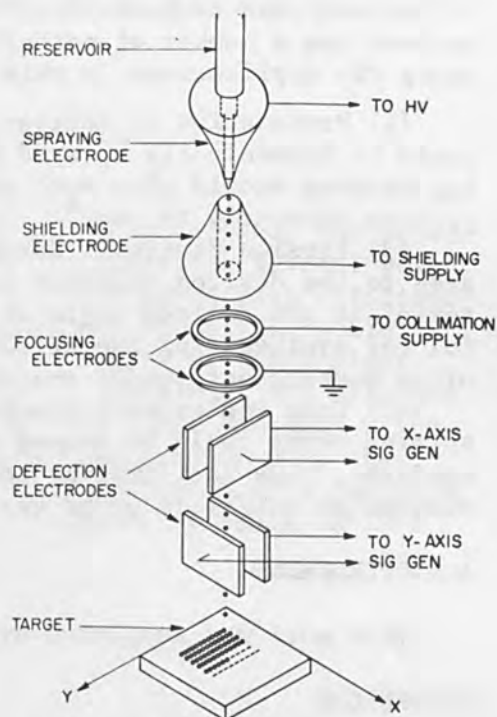


FIG. 9.--Possible configuration for depositing harmonically sprayed particles in precise patterns without masks.

(1) Integrated Circuits. Electrically focused and deflected beams could be used for metallization and deposition of dopants without the need for masks, thus saving several steps in the fabrication process. This application might be particularly useful for fabricating and modifying experimental circuits, and for very low-volume production runs.

(2) Hybrid Circuits. Deposition of thick- and thin-film resistors and interconnecting metallization. This application would compete with conventional printing techniques only in those cases where extremely close tolerances were required.

(3) High-Impact Film Deposition. In this application, the sprayed particles could be electrically accelerated to high velocities, thus generating high local temperatures and pressures at the instant of impact. This technique, which amounts to explosion bonding on a microscopic scale (without the bulk deformations that normally accompany macroscopic explosion bonds), might facilitate film deposition on those substrate materials (such as aluminum) that resist film deposition by more conventional techniques.

(4) Printing. Potentially useful where more precision is required than can be obtained using liquid-jet techniques.⁴ The process might also prove useful for generating precision printing plates, and for high-density information storage.

(5) Micro-Machining and Polishing. In this application, the grinding or polishing agent could be suspended in a liquid vehicle. A beam of particles sprayed from this mixture could be focused on a particular spot of the substrate, so that each particle struck the substrate obliquely and then bounced off again.

In addition to these engineering applications, the harmonic spraying process has a number of potential uses as a tool for scientific research. Among the applications in this area are:

(1) Preparation of Radioactive Films. Solutions of radioactive salts could be harmonically sprayed onto thin backing foils. The harmonic spraying process should give much more uniform films than the random spraying process currently in use.⁵

(3) Erosion Studies. Harmonically sprayed particles could be accelerated to the desired velocity and allowed to impinge on the substrate material at the desired angle of incidence. This technique might prove useful for synthesizing the effects of hypersonic rain erosion⁶ or micrometeorite bombardment⁷ under controlled conditions.

(3) Drop Coalescence Studies. Particles from two separate harmonically sprayed beams could be caused to collide, either in the open or on various surfaces, thus facilitating the study of the coalescence of similar and dissimilar materials under various conditions.⁸

ACKNOWLEDGMENT

This work was supported by the National Science Foundation.

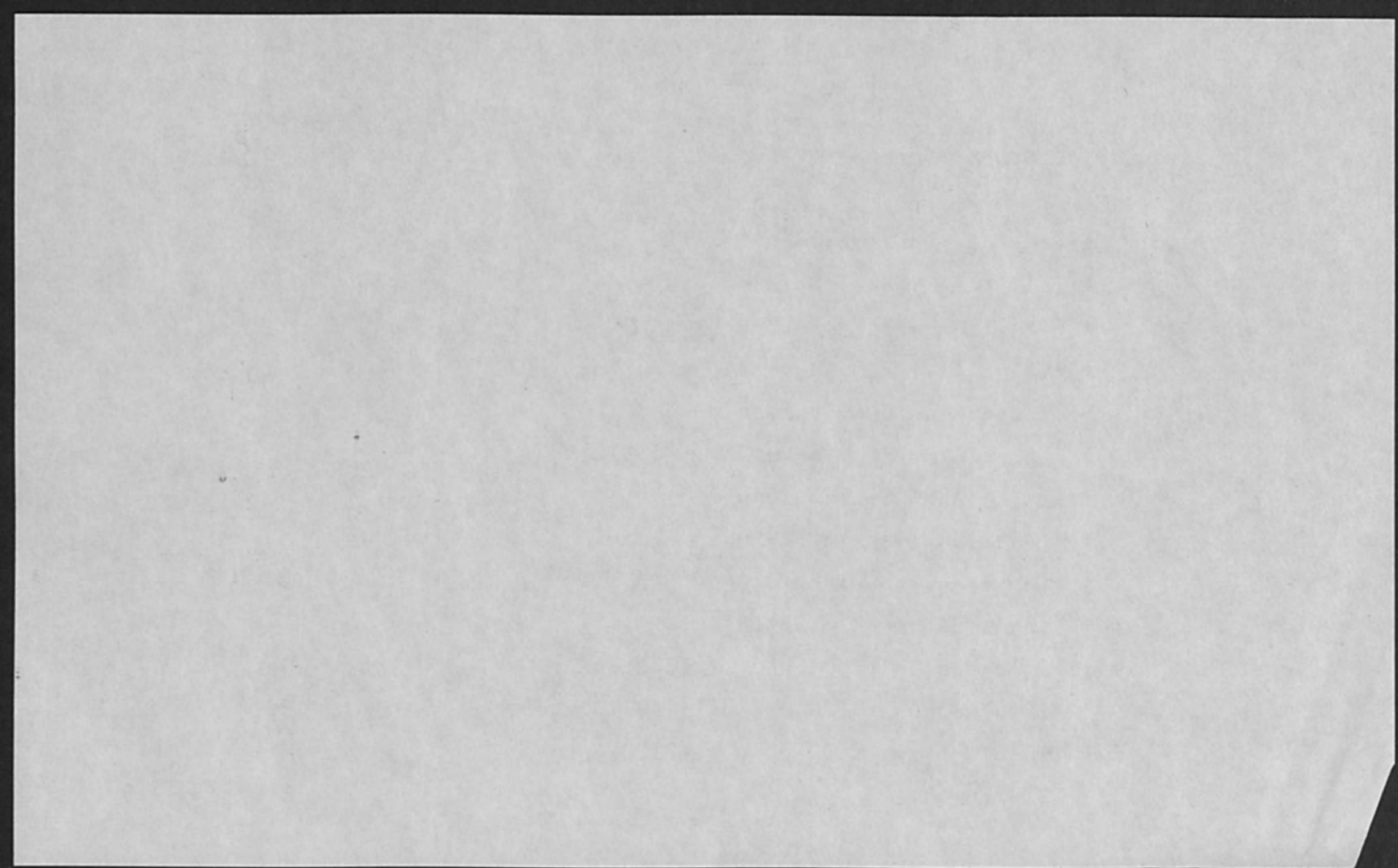
REFERENCES

1. S. B. Sample and B. Raghupathy, Proc. Nat. Elec. Conf. 25: 260, 1969.
2. B. Raghupathy and S. B. Sample, Rev. Sci. Instr. 41: 645, 1970.
3. Lord Rayleigh, Phil. Mag. 14: 184, 1882.
4. N. R. Lindblad and J. M. Schneider, J. Sci. Instr. 42: 635, 1965.
5. K. F. Lauer and V. Verdingh, Nucl. Instr. and Meth. 21: 161, 1963.
6. O. G. Engel, Symposium on erosion and cavitation, ASTM Special Technical Publication No. 307, 1961.
7. H. Shelton, C. D. Hendricks, and R. F. Weurker, J. Appl. Phys. 31: 1243, 1960.
8. J. M. Schneider, N. R. Lindblad, and C. D. Hendricks, J. Colloid. Sci. 20: 610, 1965.

ERRATUM

In the paper by K. Amboss and E.D. Wolf, "Double-deflection aberrations in a scanning electron microscope" (pp. 195-204), substitute the following equation for Eq. (4):

$$\begin{aligned}
 \Delta u_i &= \frac{1}{8}(A_4 + A_5 - B_4 - B_5)u_0^2u_a \\
 &+ \frac{1}{4}(A_4 + A_5 + B_4 + B_5)u_0\bar{u}_0u_a \\
 &+ \frac{1}{8}(A_4 + A_5 - B_4 - B_5)\bar{u}_0^2u_a \\
 &+ \frac{1}{8}(A_4 - A_5 + B_4 - B_5 + 2A_6 + 2B_6)u_0^2\bar{u}_a \\
 &+ \frac{1}{4}(A_4 - A_5 - B_4 + B_5)u_0\bar{u}_0\bar{u}_a \\
 &+ \frac{1}{8}(A_4 - A_5 + B_4 - B_5 - 2A_6 - 2B_6)\bar{u}_0^2\bar{u}_a \\
 &+ \frac{1}{8}(A_7 + A_8 - B_7 - B_8)u_0u_a^2 \\
 &+ \frac{1}{8}(A_7 - 3A_8 - B_7 + 3B_8)u_0\bar{u}_a^2 \\
 &+ \frac{1}{8}(A_7 + A_8 + B_7 + B_8)\bar{u}_0u_a^2 \\
 &+ \frac{1}{8}(A_7 - 3A_8 + B_7 - 3B_8)\bar{u}_0\bar{u}_a^2 \\
 &= (1101)u_0\bar{u}_0\bar{u}_a + (2001)u_0^2\bar{u}_a + (0201)\bar{u}_0^2\bar{u}_a \\
 &+ (1110)u_0\bar{u}_0u_a + (2010)u_0^2u_a + (0210)\bar{u}_0^2u_a \\
 &+ (1020)u_0u_a^2 + (1002)u_0\bar{u}_a^2 + (0120)\bar{u}_0u_a^2 \\
 &+ (0102)\bar{u}_0\bar{u}_a^2
 \end{aligned}
 \tag{4}$$



SESSION ON MOLECULAR LASER INTERACTIONS

CONTINUOUS SYNTHESIS OF POLYMER FUELS THROUGH HIGH-TEMPERATURE LASER BEAM INTERACTIONS

J. F. ASMUS

Institute for Defense Analyses, Arlington, Va.

Heating with focused laser radiation has been used to study the dynamics of high-temperature rapid-quench chemical reactions for several years. However, it is only with the development of the high-power high-efficiency CO₂ laser that such reactions become interesting for industrial-scale chemical processing. This paper reports on the results of bench plant production synthesis of typical industrial (e.g., acetylene) and military (e.g., diborane) fuels in an HTLR (High-Temperature Laser Reactor). The results are compared with equilibrium concentrations predicted by the JANAF Thermochemical Tables. An analysis of the economics of a GDL-HTLR by-product cycle modification to an H-oil coal processing plant is also discussed.

INTRODUCTION

In recent years the laser has found application in boring, trimming, and welding processes; nondestructive testing; military ranging and target designating systems; and optical instrumentation. However, although one of the earliest proposals for laser application¹ involved photocatalysis of chemical reactions, such use has not yet found practical implementation in commercial chemical production. It is not for lack of fundamental work: Buddenhagen et al.² reported ruby laser induced photopolymerization in 1962, followed by reports of multiphoton photopolymerization³ and photolysis.⁴ Multiphoton excitation is of particular significance in that it facilitates deep penetration of the exciting radiation. All the above involved the excitation of photochemical reactions. In contrast the work of Shultz and Sharkey⁵ utilized the brightness of a ruby laser to produce high-temperature chemical reactions in the pyrolysis of coal.

These and other pioneering efforts⁶ in laser-induced chemical reactions served to establish the feasibility of such laser excitation techniques. However, owing to performance limitations (efficiency, tunability, wavelength selection, average power), it was difficult to make a case for the laser as a replacement for more conventional techniques in chemical processing. More recently, Tiffany et al.⁷ demonstrated that monochromatic laser radiation did possess the unique capability of selectively exciting a particular isotopic molecular species. Unfortunately, the associated photochemical process led to a chain reaction so that isotope enrichment was not achieved. Mayer et al.⁸ were successful in this latter enrichment step by making use of the large isotopic splitting of the HF and DF vibrational lines and a high-performance HF chemical laser.

Thus, the groundwork has been laid for the development of practical laser photocatalysis techniques. However, the realization of a commercial laser photocatalysis must await either the emergence of a high-performance tunable laser technology that could find application in driving broad classes of chemical reactions or, if a chemical processing step of sufficiently unique importance and conventional difficulty were identified,

the development of the necessary chemistry for instituting a specific laser photocatalysis technique at a currently available laser wavelength. Implementation of laser photocatalysis thus may have to await further progress in the development of high-performance lasers.

Another possibility might be the development of a chemical process induced by CO₂ lasers. Present performance in terms of average power, efficiency, and wavelength selectivity may be suitable for practical chemical processing. Unfortunately, the absorption of a 10.6- μ m photon by a molecule amounts to an excitation energy of only 2.7 Kcal/mole, which is far below typical molecular bond energies (40-240 Kcal/mole). Thus, a 10.6- μ m photon is probably useful for photocatalysis only in weakly bound systems (viz., thermally unstable molecules). The work of Brunet and Voignier⁹ is notable in that a photodissociative reaction was demonstrated with the minimal excitation of 10.6- μ m photons. The inverse type of reaction, an ethylene iodine addition reaction, has also recently been demonstrated.¹⁰ Thus, infrared laser photocatalysis may find a limited utility in weakly bound systems.

HIGH-TEMPERATURE RAPID-QUENCH CHEMISTRY

The development of high-performance CO₂ lasers such as the GDL¹¹ suggests a role somewhat less ambitious than photocatalysis for the laser in chemical processing. Isotope separation, cell modification, etc. are engaging possibilities; moreover, even at the present state of the art, very significant high-temperature rapid-quench chemical reactions appear possible.

In some applications, lasers become merely "expensive blowtorches" in their ability to heat substances. There are certainly less expensive and more direct means of delivering raw calories of heat to an arbitrary region. The simile is also misleading in that blowtorches are quite limited in their ability to heat relative to the laser. For example neutron generation is quite feasible by means of laser heating, but unthinkable with a blowtorch.

Similarly, many chemical processes take place at temperatures in the range 4000-5000°K. Commercial chemical processing generally abandons the blowtorch in favor of electrical, electric-arc, or plasma-jet heating to achieve such temperatures. The severe limitations of such techniques can be illustrated by reviewing the high-temperature rapid-quench chemical reaction common to such processes.

At any given temperature a chemical mixture at equilibrium has a specific molecular composition. In general the concentrations of a specific molecular species changes with temperature. For a given atomic composition the molecular concentrations at various temperatures can be calculated from the temperature-dependent equilibrium constants for the appropriate reactions, as tabulated in the JANAF Thermochemical Tables.¹²

Let us consider the simple example of the heating of carbon in a hydrogen atmosphere at a pressure of 1 atm. According to the JANAF Tables the equilibrium constants for the important molecular species at elevated temperatures are those given in Table I. From these data we can calculate the partial pressures of the various species and in particular C₂H₂ (acetylene) which could be considered the product in this pyrolysis calculation.

These pressures are given in Table II for a fixed 1-atm H₂ background pressure. We see that with a constant hydrogen atmosphere the partial pressures of the various molecular species (based on 1 mole H₂) are very

TABLE I.--Equilibrium constants for carbon-hydrogen system at various temperatures.

TEMPERATURE (°K) JANAF DATA	2000	2500	3000	3500	4000
$K_p(H)$	-2.791	-1.601	-0.803	-0.231	0.200
$K_p(C_2H_2)$	-3.055	-1.906	-1.142	-0.597	-0.189
$K_p(C)$	-10.48	-6.75	-4.27	-2.50	-1.18
$K_p(C_2)$	-11.67	-7.37	-4.52	-2.50	-0.99
$K_p(C_3)$	-10.58	-6.52	-3.84	-1.95	-0.54

TABLE II.--Equilibrium pressures (atm) vs temperature for carbon-hydrogen system.

TEMPERATURE (°K) SPECIE	2000	2500	3000	3500	4000
H_2	1 ATM	1	1	1	1
$1/2H$	0.00081	0.0128	0.0787	0.294	0.792
C_2H_2	0.000882	0.0124	0.0721	0.253	0.648
$3/2C_3$	-	0.000005	0.00022	0.0168	0.434
C_2	-	-	0.00003	0.0032	0.098
$1/2C$	-	0.000001	0.00003	0.0016	0.033

TABLE III.--Breakdown of heat inputs (per mole) for carbon-hydrogen pyrolysis at various temperatures.

TEMPERATURE (°K) HEATS (KCAL/MOLE)	2000	2500	3000	3500	4000
ΔH_H	54.2	54.6	54.9	55.2	55.3
$\Delta H_{C_2H_2}$	52.7	52.5	52.4	52.3	52.3
ΔH_C	170.9	170.5	170.0	169.6	169.1
ΔH_{C_2}	197.3	196.0	194.9	193.8	192.7
ΔH_{C_3}	186.4	184.8	183.0	181.1	179.2
$(H_T^\circ - H_{700}^\circ) H_2$	9.85	14.04	18.40	22.90	27.57
$(H_T^\circ - H_{700}^\circ) C(s)$	7.07	10.03	13.04	16.09	19.17

TABLE IV.--Total heat inputs for carbon-hydrogen pyrolysis at various temperatures.

TEMPERATURE (°K) HEATS (KCAL)	2000	2500	3000	3500	4000
TOTAL $C_p(H_2)$	9.87	14.4	21.2	35.4	64.7
TOTAL $C_p(C(s))$	0.01	0.25	1.89	8.56	47.1
C_2H_2	0.04	0.42	3.78	13.2	33.9
H	0.08	1.35	8.65	32.5	87.5
C_3	----	----	0.03	2.0	51.8
C_2	----	----	----	0.6	18.9
C	----	----	0.01	0.5	11.2
GRAND TOTAL	10.00	16.42	35.56	92.8	315.1

sharp functions of temperature. By doubling the temperature from 2000 to 4000°K the pressure of acetylene increases by almost three orders of magnitude. This example illustrates the utility of high temperatures in producing new molecular compounds. Implicit in this calculation is the role played by the composition of the background atmosphere in determining the high-temperature product spectrum. Laser heating of chemical mixtures evidently has unique advantages.

First, it is possible to achieve almost complete freedom in selecting an optimum temperature by adjusting the laser power or focal system f -number--as against electrical heating, where material properties are a severe limitation. Also, in conventional high-temperature electric-arc furnaces, problems such as electrode fouling¹³ and life can be serious. Laser beam heating is of course free from such difficulties as no apparatus is required in the reaction region.

Second, unlike the situation for electric arc, corona,¹⁴ or electrical heating there is complete freedom in the pressure and composition of the background atmosphere with laser processing. The only requirement is that of maintaining transparency to the laser beam.

Finally, there is the question of quenching. The partial pressures tabulated in Table II are not in general preserved when the system is returned to ambient temperature. The high-temperature product concentration is frozen only if the quench is sufficiently rapid. In electric-arc chemical processing typical flow velocities are about 3×10^3 cm/sec out of the arc.¹³ Thus, for a dimension of 1 cm, the quench time is 0.3 ms. For more intense heating with focused laser radiation velocities of 10^4 cm/sec are easily obtained. For a typical focal spot of 0.3 mm the quench time is 0.3 μ sec--an improvement of three orders of magnitude. Thus, the chemical freezing in laser pyrolysis should be decidedly more efficient than other techniques.

Ultimately, the role of high-temperature laser pyrolysis in chemical processing will be dictated by economic considerations. Returning to the previous carbon-hydrogen example, the minimum cost of acetylene production can be determined by adding up the heats required to bring the various species up to the pyrolysis temperature. This heat input yields the acetylene partial pressures given in Table II. The heat inputs (per mole) are given in Table III, where the values are broken down into the heats of formation and the heat required to raise the source materials [H_2 and $C(\text{solid})$] from 700°K to the pyrolysis temperature.

Next, the heats given in Table III are multiplied by the partial pressures given in Table II to calculate the absolute total heat input (Table IV). With these data it is possible to calculate the energy input per mole of product (C_2H_2), the efficiency of energy utilization, and product cost. For the product cost a raw energy (electricity) cost of 0.5¢/kW-hr is assumed along with a laser conversion efficiency of 25 per cent. The results are given in Table V, from which several features emerge.

First, it is clear that there is an optimum pyrolysis temperature (3500°K). Second, 3500°K pyrolysis is considerably more efficient than even 2500°K pyrolysis. Finally, the proposed acetylene manufacturing process is not competitive at the calculated 15¢/lb as the industrial price¹⁵ is 5-9¢/lb at present. Further, the ideal numbers above are optimistic in that perfect quenching is assumed and no capital investment and raw material charges are included. Further, it should be pointed out that in the previous equilibrium calculations other important species such as CH_2 were neglected. Consequently, the above estimates represent the most optimistic

possibility for laser polymer synthesis. However, it may be possible to select temperatures and pressures where C_2H_2 dominates all other species.¹⁶

The above situation improves somewhat if the calculations are repeated for a background hydrogen pressure of 10 atm. Again taking a 25-percent laser efficiency leads to a product cost of 10¢/lb, which is marginally competitive. This should not be discouraging for two reasons. First, no provision has been included for recovering the waste heat (75 per cent of the heat input). Second, acetylene is quite an inexpensive product so that an economically more favorable reaction should be easy to find. These topics are treated in the next section.

BYPRODUCT CYCLE MODIFICATION TO AN H-OIL COAL PROCESSING PLANT

A present trend in many nations is the processing of coal into more useful fuels and chemicals. A coal utilization plant can convert 2000 lb of Illinois No. 6 coal into the product spectrum given in Table VI. A schematic diagram of such a processing plant based on the H-oil coal hydrogenation cycle (Cities Service Oil Co. refinery in Lake Charles, La.)¹⁷ is shown in Fig. 1.

To incorporate a GDL pyrolysis cycle into the coal plant the H-oil hydro plant must be modified so that the heat is utilized first to generate a supersonic N_2-CO_2 flow. The waste heat from the GDL is then returned to the hydro plant (Fig. 2).

The economics of the unmodified plant are given in Table VII. For this 30 000-ton/day capacity the return on investment is 7.7 per cent.

The potential return on investment increases when the by-product cycle of Fig. 2 is added. This cycle produces diborane (\$5/lb market value) through the high-temperature pyrolysis of sodium borate. As the electrical CO_2 laser's performance has been extensively studied and is well documented in the literature, it will form the basis for the following economic analysis.

Let the capacity of the steam power plant (Table VII) be increased to 3300 tons per day. For 50-percent efficiency in generating electricity and a 20-percent electric laser efficiency, 2.4×10^4 kW-hr/day of optical energy is available for the high-temperature pyrolysis. At 5 kW-hr/lb of diborane produced (based on the acetylene calculation) the byproduct production is 4.8×10^3 lb of diborane or $\$2.4 \times 10^4$ per day.

Assuming a \$40 000 000 investment in the byproduct cycle and an annual return of \$8 750 000 for the diborane credit indicates a return on investment of 8.7 per cent, an improvement of 13 per cent over the unmodified plant.

Unfortunately, the annual market for diborane is at present orders of magnitude below the output of this plant. However, the above example serves to illustrate the economic benefits possible with a favorable byproduct production spectrum.

EXPERIMENTS IN BENCH PLANT PRODUCTION OF ACETYLENE AND DIBORANE

In the preceding sections the maximum potential yield of acetylene through pyrolysis was calculated along with the economics of diborane production. A bench plant has been assembled to explore the practical aspects of high-temperature laser pyrolysis. It utilized a 1-kW electrical CO_2 laser (Korad model KG-1000) and a continuous-feed reaction chamber (Fig. 3).

Two sets of runs have been accomplished to date. In the first pulverized coal was fed into the reaction chamber in the presence of a hydrogen

TABLE V.--Cost and efficiency of acetylene manufacture utilizing laser pyrolysis.

YIELD	TEMPERATURE (°K)				
	2000	2500	3000	3500	4000
ΔH , KCAL/MOLE C_2H_2	1.1×10^4	1.3×10^3	493	367	486
KWH/MOLE C_2H_2	13	1.5	0.57	0.425	0.56
$\$/LB C_2H_2$ ($\eta_{LASER} = 25\%$)	4.52	0.52	0.20	0.15	0.20
UTILIZATION EFFICIENCY, % (INPUT ENERGY)	0.49	4.1	10.9	14.7	11.1

TABLE VI.--Product spectrum from coal processing cycle.

FEED	LB.
COAL	2000
HYDROGEN	190
	2190
PRODUCTS	
OIL	1020
FUEL GAS	297
NH_3	13
H_2S	66

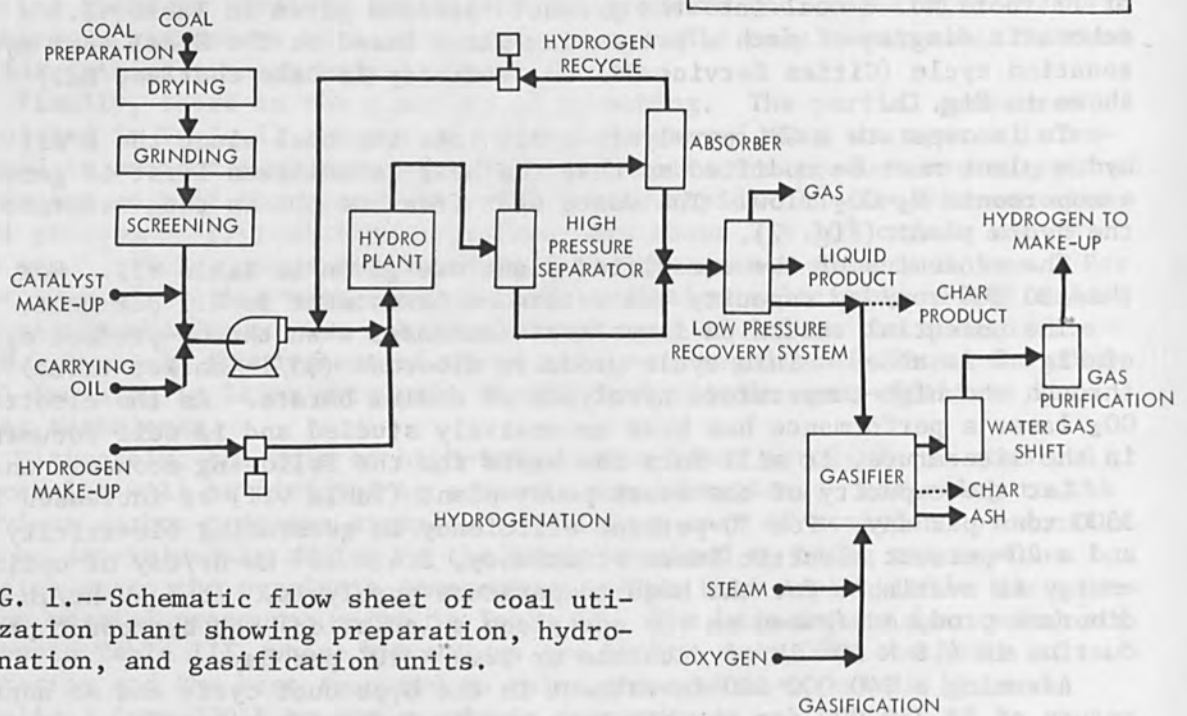


FIG. 1.--Schematic flow sheet of coal utilization plant showing preparation, hydrogenation, and gasification units.

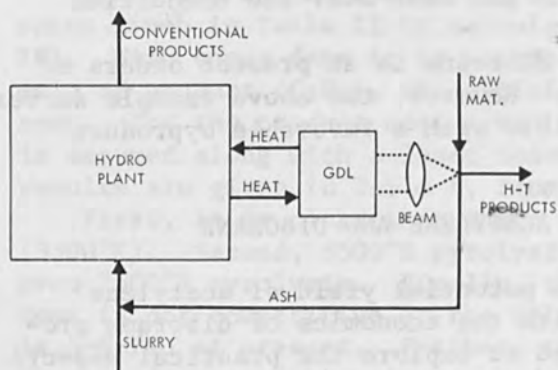


FIG. 2.--High-temperature GDL by-product modification to coal processing plant.

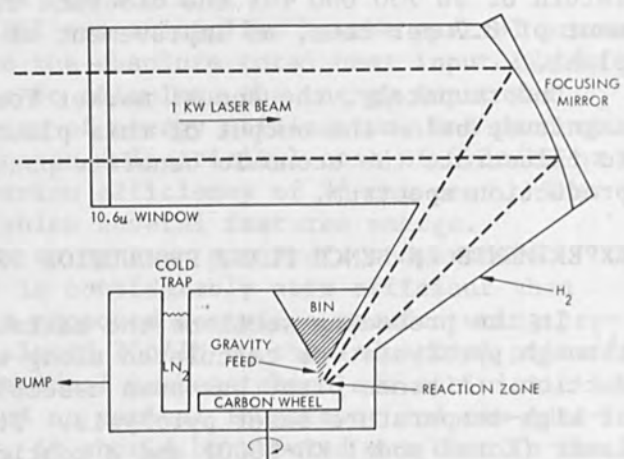


FIG. 3.--Bench plant laser pyrolysis apparatus.

atmosphere ($p \approx 0.1$ atm) to produce acetylene. Boron powder in a hydrogen atmosphere ($p \approx 0.5$ atm) yielded diborane. No diagnostics were employed to measure the fraction of the laser beam that intercepted the feed material; nor was the reaction temperature measured. However, the reaction products were identified by gas chromatography and IR spectroscopy. Product quantities were determined from the reaction chamber pressure rise upon bringing the cold trap up to ambient temperature. Typical pyrolysis runs lasted 1-10 min.

The average acetylene production for several 5-min runs at 1 kW laser output was 3.7 g. At 0.5¢/kW-hr total electrical input to the laser system, the energy cost for the pyrolysis was 25¢/lb. Due to the uncertain energy deposition and temperature it is difficult to compare this result with the previous calculations. The boron pyrolysis runs were somewhat less successful in that higher temperatures were evidently required for efficient diborane formation. The aberrations in the optical system prevented the attainment of the optimum temperature. The energy cost for the diborane that was produced was about \$10/lb.

CONCLUSION

It is clear from the analysis and the experimental data presented that only a marginal case can be made for the potential utility of laser-induced chemical processing with state-of-the-art technologies. However, there is reason to expect that higher chemical yields can be obtained than reported here; little attention was paid to maximizing the laser beam absorption or to optimizing the fuel feed rate.

Nor is it evident at present how the rapid-quench laser-induced reactions can best be applied from the rather cursory survey of this investigation. As the initial economic investment would be substantial for plants of the scale discussed, a rather comprehensive systems study is needed to determine the most advantageous exploratory routes to follow in commercial laser byproduct cycle development.

ACKNOWLEDGMENTS

The facilities employed in the bench plant pyrolysis were provided by Gulf General Atomic Inc., San Diego, Calif.

Drs. John Norman and Ulrich Merten of Gulf General Atomic Inc. are thanked for their considerable assistance and encouragement during the course of the work reported here.

REFERENCES

1. A. L. Schawlow, Bell Labs Rec. 38: 403, 1960.
2. D. A. Buddenhagen et al., Proc. Nat. Acad. Sci. 49: 303, 1962.
3. Y. H. Pao and P. M. Rentzepis, Appl. Phys. Letters 6: 93, 1963.
4. A. M. Prokhorov et al., Soviet Phys.-Dokl. 12: 783, 1968.
5. J. L. Shultz and A. G. Sharley, Carbon 5: 57, 1967.
6. For a bibliography see: A. F. Haught, Rev. Phys. Chem. A19: 343, 1968.
7. W. B. Tiffany et al., Science 157: 40, 1967.
8. S. W. Mayer et al., Isotope Separation with the Hydrogen Fluoride Laser, Paper IX-3, The Laser in Science and Technology, Seattle, Wash., 1970.

9. H. Brunet and F. Voignier, Comptes Rendus 266C: 1206, 1968.
10. U. Merten, Gulf General Atomic Internal Memorandum, January 16, 1969.
11. Industrial Research L3, July 1970.
12. JANAF Thermochemical Tables, Dow Chemical Co., Midland, Mich., 1964.
13. P. R. Ammann et al., Chem. Engg. Progress 60: 52, 1964.
14. S. J. Lawrence, *ibid.*, p. 45.
15. W. E. Lobo, *ibid.* 57: 35, 1961.
16. R. E. Duff and S. H. Bauer, The Equilibrium Composition of the C/H System at Elevated Temperatures, Los Alamos Scientific Laboratory, Report LA-2556, June 1961.
17. S. B. Alpert et al., Chemical Engg. Progress 60: 35, 1964.

TABLE VII.--Economics of unmodified coal processing plant (30 000 tons/day Illinois No. 6 coal to heavy synthetic crude).

INVESTMENT	
BATTERY LIMITS: HYDROGENATION, COAL FEED PREPARATION, COAL-OIL SEPARATION, HYDROGEN MANUFACTURE	\$110,000,000
OFF SITES: UTILITIES, STEAM, POWER, WATER	20,000,000
BUILDINGS AND GROUNDS	5,000,000
RAW MATERIALS AND PRODUCT STORAGE	5,000,000
	<u>\$140,000,000</u>
WORKING CAPITAL, ONE-MONTH RAW MATERIALS AND PRODUCTS	9,000,000
TOTAL INVESTMENT	\$149,000,000
REVENUE	
OIL, 87,600 BBL./DAY AT \$2.25/BBL.	\$ 65,040,000
GAS, 216 MMM BTU/DAY AT 50.50/MM BTU	35,640,000
	<u>\$100,680,000</u>
EXPENSES	
COAL: PROCESS 33,000 TON/DAY AT \$4/TON	\$ 43,500,000
BOILER, POWERHOUSE, HEATERS 3,000 TON/DAY	3,960,000
OXYGEN, 6,300 TON/DAY AT \$4.75/TON	9,880,000
CHEMICALS AND CATALYSTS	1,400,000
PROCESS LABOR, 54 MEN/SHIFT AT \$2.25/HR.	1,070,000
SUPERVISION, 50% OF LABOR	530,000
OVERHEAD 25% OF LABOR AND SUPERVISION	400,000
LOCAL TAXES AND INSURANCE, 2% OF B.L. INVESTMENT	2,200,000
MAINTENANCE, 4% OF B.L. INVESTMENT	4,400,000
MISCELLANEOUS UTILITIES CHARGE:	
LABOR, MAINTENANCE, TAXES, ETC.	1,300,000
	<u>\$ 68,640,000</u>
NET OPERATING INCOME	\$ 32,040,000
% ON INVESTMENT	21.5%
AMORTIZATION	
BATTERY LIMITS PLANT, 15 YR.	\$ 7,330,000
UTILITIES, 30 YR.	670,000
BUILDINGS, 50 YR.	100,000
STORAGE, 30 YR.	170,000
	<u>\$ 8,270,000</u>
PROFIT BEFORE TAXES	\$ 23,770,000
PROFIT BEFORE TAXES, % ON INVESTMENT	16.6%
FEDERAL INCOME TAX (52%)	\$ 12,360,000
PROFIT AFTER TAXES	\$ 11,410,000
RETURN ON TOTAL INVESTMENT	7.7%

LASER-INDUCED CHEMICAL REACTION: DECOMPOSITION OF VARIOUS COMPOUNDS AND REACTION OF DECOMPOSED FRAGMENTS WITH LOW HYDROCARBONS

PIL HYON KIM, KO TAKI, and SUSUMU NAMBA

The Institute of Physical and Chemical Research, Wako-shi, Saitama, Japan

Various copper metal salts of organic acid were decomposed by laser heating and conventional heating methods. The product distributions are reasonably explained by the expected reaction of the decarboxylated fragments. Generally the yield percentage of products is higher in laser decomposition than in thermal decomposition. However, in maleate and fumarate the product distribution is quite different in thermal and laser decomposition. The main product is acetylene in the laser decomposition, but ethylene in the thermal decomposition. This difference may be due to the fact that the simultaneous decarboxylation of two carboxyl groups occurs in the former, while the successive decarboxylation occurs in the latter.

By laser heating of the solid target in gaseous substrates, the products by the reaction of the decomposed fragments from the target with gaseous substrates were obtained. In the system of maleate and ethylene, the yield of C₄ compounds is relatively higher than that in maleate only. In the system of CuCN and hydrocarbons, CN and NC added products are obtained. In the system of CuO and hydrocarbons, however, oxygen added or inserted products are not detected, but the products from the decomposed hydrocarbon are detected. The reaction mechanism is discussed.

INTRODUCTION

In the laser-induced chemical reaction, the following four types of reaction have been studied: (1) photodissociation,¹ (2) reaction of the vapors produced by laser heating of the solids,² (3) breakdown of gases,³ and (4) heat decomposition.⁴ In a previous paper,⁵ the reaction of low hydrocarbons with carbon vapor produced by laser heating and the reaction caused by the breakdown of hydrocarbon gases have been reported. As the ruby laser lacks sufficient photon energy to dissociate compounds, any photochemistry by the ruby laser is restricted and some of reaction must be performed by multiphoton absorption processes. Therefore, the ruby laser may be most useful for pyrolysis.

In this paper, various compounds are decomposed by the ruby laser and the product distribution in laser heating (laser decomposition) is compared with that in conventional heating (thermal decomposition). Also, the reaction of low hydrocarbons with the decomposed fragments in laser decomposition is investigated.

Various copper and nickel carboxylic acid salts were decomposed, because these blue or green salts absorb the ruby laser beam efficiently and metal salts of carboxylic acid are known to be decomposed to produce organic radicals and ketons under decarboxylation.⁶ Since rapid heating and quenching are characteristic of laser heating, it is expected that the products in laser decomposition are different from those in thermal decomposition.

In a binary system, such as a metal compound and hydrocarbon, the metal compound is decomposed selectively by laser irradiation, because only the metal compound absorbs the laser beam. Therefore, the decomposed fragments can react with the hydrocarbon which is not decomposed. By this method, the reactions of hydrocarbons with organic fragments decomposed from carboxylic acid metal salts, with CN from metal cyanides, and with oxygen from metal oxides are investigated.

EXPERIMENTAL PROCEDURE

The ruby laser used was a normal laser, the output energy and pulse duration of which were about 3 J and 0.5 msec, respectively. In laser decomposition, the sample target in a 1-cm³ Pyrex cell was irradiated by the laser beam (Fig. 1). Metal cyanides and oxides were decomposed by

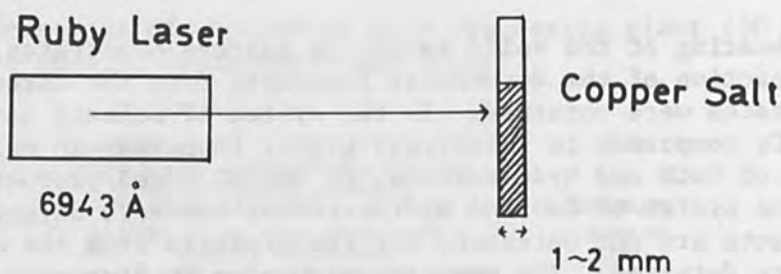


FIG. 1.--Experimental block diagram.

the focused laser beam by a lens of 10 cm focal length. All the targets were powder except the metal oxides. In the reaction of the hydrocarbon with the decomposed fragments, the metal compound was decomposed by laser irradiation in a 7-cm³ cell filled with the hydrocarbon (700-760 torr). After 2-7 pulse irradiations, the reaction products were analyzed by gas chromatography. Silica-gel, activated-charcoal, squalane, and polyethylene glycol columns were used in the analysis of hydrocarbons. Dioctyl phthalate and dinonyl phthalate were used in the analysis of cyanide and oxide compounds. Quantitative analysis was performed by the internal standard system.

The thermal decomposition of metal salts (about 0.1 g) was carried out in a metal bath for 30-60 sec at various temperatures. The decomposition temperature was checked by differential thermal analysis and thermal gravimetric analysis.

RESULTS AND DISCUSSION

A. DECOMPOSITION OF METAL SALTS. Various copper salts (acetate, propionate, n-butyrate, isobutyrate, acrylate, malonate, benzoate, phthalate, succinate, adipate, maleate, and fumarate) were decomposed by

both the thermal and laser decomposition methods. The results for several salts are shown in Table I. The decomposition of carboxylic acid produces

TABLE I.--Product yield from copper salts in thermal and laser decomposition based on CO₂ produced.

Substrate	Product	Yield (%)	
		Thermal decomp.* (at 400 °C)	Laser decomp. (6 pulses)
Copper acrylate	CH ₄	0.011	0.39
	C ₂ H ₆	0.0011	0
	C ₂ H ₄	6.7	15
	Butadiene	0.023	3.2
Copper succinate	CH ₄	0.05	0.37
	C ₂ H ₆	0.014	0.07
	C ₂ H ₄	2.3	14
	Propane	0	0.26
	C ₂ H ₂	0	1.7
Copper maleate	C ₂ H ₄	2.2	1.2
	C ₂ H ₂	trace	8 - 12
Copper fumarate	C ₂ H ₄	2.4 - 4.7	5.0
	C ₂ H ₂	trace	10 - 12

* The yield percents of CO₂ for salts used were 80 - 90 % in maleate and 45 - 50 % in fumarate.

carbon dioxide. The amount of carbon dioxide may be considered to represent the fraction of the decomposed copper salt. For convenience, the product yields may be represented as percentage of carbon dioxide. Generally the product distributions are almost the same in the two decomposition methods, but maleate and fumarate are exceptions; and the product yields are much higher in the laser decomposition.

In the laser decomposition on both copper maleate and fumarate, the gaseous products consisted of 10-15 per cent noncondensable gases at the temperature of liquid nitrogen, which are methane and carbon monoxide, but hydrogen was not detected. Of the condensable gases, 65 per cent consisted of carbon dioxide and the rest were hydrocarbon and water. The hydrocarbon consisted of acetylene, ethylene, and a small amount of C₃ and C₄ compounds as listed in Table II. Acetylene is the main product, but the yield is only about 10 per cent of the carbon dioxide (10⁻⁵-10⁻⁶ mol). The decomposition processes are considered to be as follows:

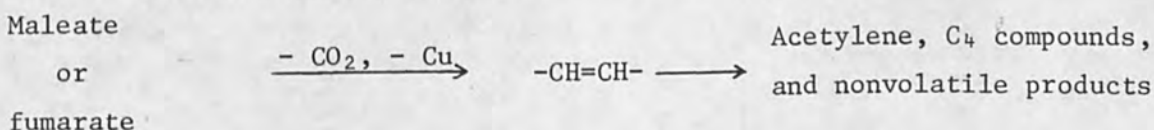


TABLE II.--Product yield from copper maleate and fumarate in laser decomposition based on CO₂ produced.

Product	Substrate	
	Maleate	Fumarate
Methane	0.5 %	2.2 %
Ethane	0.05	0.2
Ethylene	1.2	5.0
Acetylene	8 - 12	10 - 12

On the other hand, the thermal decomposition gave not acetylene but ethylene under 350°C. The high-temperature decomposition gave acetylene, but ethylene was still obtained in a high yield as listed in Table III.

TABLE III.--The ratio of acetylene to ethylene from copper maleate and fumarate in thermal decomposition at various temperatures.

Substrate	C ₂ H ₂ /C ₂ H ₄			
	350 °C	500 °C	570 °C	670 °C
Copper maleate	0.0015	0.22	-	1.3
Copper fumarate	0.009	0.12	0.15	-

- Detection was not carried out.

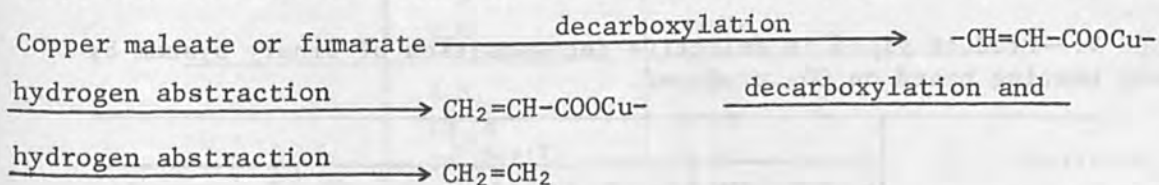
In the laser decomposition, the ethylene yield increased as the laser power was lowered by using a copper-sulfate-solution filter, but acetylene is still the main product as is shown in Table IV.

TABLE IV.--The ratio of acetylene to ethylene from copper maleate and fumarate in laser decomposition at various transmissions of laser beam through CuSO₄ solution filter.

Substrate	C ₂ H ₂ /C ₂ H ₄		
	100 % trans.	50 % trans.	25 % trans.
Copper maleate	6 - 10	5.8	4.9
Copper fumarate	2 - 2.4	2.0	1.3

From the above results, the difference between the laser and the thermal decomposition does not seem to depend only on the decomposition temperature. In the laser heating, the temperature rises very rapidly to decompose the salt in a moment and then two decarboxylations are brought about at the same time to produce a fragment (-CH=CH-). This fragment forms acetylene intramolecularly. Therefore, the formation of acetylene seems to depend on the heating rate.

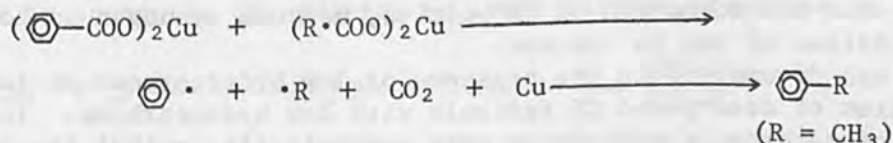
In the thermal decomposition, the formation mechanism of ethylene and acetylene is not clear because the secondary decomposition may occur at a high temperature. However, on the basis of data obtained by differential thermal analysis and thermal gravimetric analysis, the decomposition occurs over a wide temperature range in copper maleate (170-340°C) and fumarate (170-380°C). Therefore, it may be more or less presumed that the decarboxylation is brought about step by step, that the $-\text{CH}=\text{CH}-\text{COO}-\text{Cu}-$ thus obtained may abstract hydrogen to produce an acrylic compound, and that the secondary decarboxylation may give ethylene:



In fact, copper acrylate is decomposed to give ethylene in both the laser and thermal decomposition (Table I).

The difference between two types of decomposition may depend on whether or not the two decarboxylations occur at the same time. Moreover, it may also be decided by the property of the one-decarboxylated fragment. In fact, no difference was found in copper succinate (decomposition temperature range: 280-380°C). In this case, the decarboxylated fragment, $-\text{CH}_2-\text{CH}_2-\text{COOCu}-$, may form ethylene intramolecularly in the thermal decomposition.

The mechanism of decarboxylation in the laser decomposition may be supported by the following experimental fact. In the mixture of copper benzoate and acetate, the laser heating of the mixture gave toluene (about 1 per cent based on CO_2 produced). However, in the thermal decomposition at 400°C, toluene was not detected. The toluene may be formed by a recombination of the phenyl and alkyl radicals. Therefore, it is necessary for the decarboxylation of the two components to occur at the same time in a mixture of copper salts. The reaction mechanism may be considered to be as follows:



Each component is decomposed to produce R-R and biphenyl by both the laser and thermal decompositions. As each component is decomposed in a different temperature range (acetate: 125-300°C; benzoate: 220-450°C), it is hard to obtain the toluene in thermal heating. This experimental result may be explained by the rapid heating and quenching by the laser heating. This type of pyrolysis is only possible in the laser heating.

B. REACTION OF DECOMPOSED FRAGMENTS WITH LOW HYDROCARBONS. 1. Reaction of Low Hydrocarbons with Decomposed Fragments of Metal Salts. In a binary system, such as copper maleate and ethylene, the laser beam may decompose copper maleate only, and not ethylene, because the laser beam is absorbed on the copper maleate. If some fragments are produced in the decomposition of copper maleate, the reaction of fragments with ethylene will be possible. In the laser decomposition of copper maleate, the

-CH=CH- fragment seems to be produced as mentioned before. The fragment intramolecularly forms acetylene mainly, but a fraction reacts with ethylene to produce C₄ compounds. As the fragment may be also dimerized to produce C₄ compounds, determination of C₄ compounds was performed in the presence and in the absence of ethylene. The relative product yields in the binary system of copper maleate and hydrocarbon gases are listed in Table V. From the table, it is clear that the decomposed fragment reacts with hydrocarbon substrates. The reaction is only possible in laser heating.

TABLE V.--Product yield in selective decomposition of binary system by laser heating based on CO₂ produced.

Substrate	Yield %			
	C ₃ compounds	C ₄ compounds	C ₅ compounds	C ₆ compounds
Copper maleate and 760 Torr nitrogen	0.2	0.6	0.17	0
Copper maleate and 730 Torr ethylene	0.35	3.9	-	-
Copper maleate and 730 Torr propylene	-	-	0.45	-
Copper maleate and 730 Torr 1-butene	-	-	-	0.67

- Detection was not carried out.

2. Reaction of CN with Low Hydrocarbons. The formation of free CN radicals in gaseous state has been reported by many authors.⁷ But no work has been reported on the reaction of CN with hydrocarbons in gaseous state. In the laser decomposition of CuCN, Co(CN)₂, and AgCN, cyanogen was obtained as in the thermal decomposition. The above experimental fact may show the formation of CN species, because cyanogen is formed by the combination of two CN species.

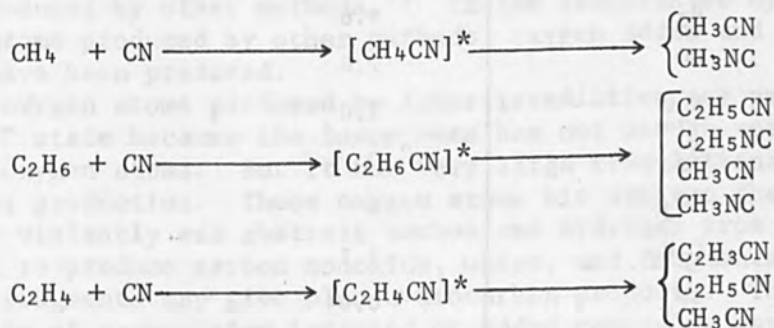
CuCN was decomposed in the presence of low hydrocarbons to investigate the reaction of decomposed CN radicals with low hydrocarbons. In the presence of methane, the products were acetonitrile, methyl isocyanide, and some hydrocarbons. In ethane, the products were methyl isocyanide, acetonitrile, propionitrile, ethyl isocyanide, and other hydrocarbons. And in ethylene, acrylonitrile and propionitrile were produced. The results are summarized in Table VI.

From the reaction products it may be considered that the formation process of nitrile and isocyanide is the combination of methyl and ethyl radical with CN species. The formation of alkyl radical may be brought about by the hydrogen abstraction from hydrocarbon. The most probable hydrogen abstractor may be considered to be CN species resulting in formation of hydrogen cyanide. But in this reaction the nitrile and isocyanide are obtained without the formation of hydrogen cyanide, and in the reaction with methane the formation of ethane (combination of methyl radical) is just trace only. From these results the reaction of methyl and ethyl radicals with CN species is not probable.

TABLE VI.--Product yield in reaction of CN with low hydrocarbons for 6 pulse irradiations.

Substrate (Hydrocarbon)	Product	Yield ($\times 10^{-6}$ mol)
CH ₄	C ₂ N ₂	0.20
	CH ₃ CN	0.007
	CH ₃ NC	0.03
	C ₂ H ₆	trace
C ₂ H ₆	C ₂ N ₂	0.20
	CH ₃ CN	0.03
	CH ₃ NC	0.03
	C ₂ H ₅ CN	0.003
	C ₂ H ₅ NC	0.006
	C ₂ H ₃ CN	0.02
	CH ₄	0.10
	C ₂ H ₄	0.40
	C ₂ H ₂	0.20
C ₂ H ₄	C ₂ N ₂	0.20
	C ₂ H ₃ CN	0.05
	CH ₄	0.02
	C ₂ H ₆	0.03
	C ₂ H ₂	0.60
	Vinylacetylene	trace
	Diacetylene	trace

The reaction process with hydrocarbon may be considered to be the decomposition of CN adducts to substrate. (Higher hydrocarbons may be decomposed by energetic CN addition to lower nitrile fragments.)



(In this case isocyanide was not detected.)

In the reaction of propane, butyronitrile and propyl isocyanide were not detected either. And in the reaction of cyclohexane, cyclohexyl cyanide was not detected. In these cases, energetic CN adduct may decompose to small fragments. But in the reaction of benzene, benzonitrile and phenyl isocyanide were produced in almost equivalent yield ($0.7\sim 2 \times 10^{-8}$ mol for 7 pulse irradiations). In this case, the formation of higher nitrile and isocyanide may be due to the stability of the benzene ring.

In order to examine the formation of hydrogen cyanide, several experiments were performed with copper cyanide prepared by various methods. The freshly prepared copper cyanide gave hydrogen cyanide in hydrogen but with aging of time of copper cyanide the yield of hydrogen cyanide decreased, and finally it did not give hydrogen cyanide after about a week. But the formation of cyanogen was not influenced by the aging of time of copper cyanide. No differences among these samples were found in x-ray diffraction pattern and emission spectrum excited by the laser irradiation, whereas copper cyanide heated at 100–200°C under vacuum gave hydrogen cyanide. The maximum yield of HCN was obtained at a heating temperature of about 170°C. The authors have no reasonable explanation for this experimental fact. From the result it seems unlikely that hydrogen cyanide may be formed by the reaction of hydrogen and CN radical. In the reaction of nitrogen atom with hydrocarbon, hydrogen cyanide is a main product, and the formation mechanism may not be considered to be the reaction of CN with hydrocarbon and hydrogen.⁸ Moreover, in the addition of ammonia⁹ the mechanism may be considered to be the reaction of CH with nitrogen because the increase of ammonia gives the increase of the yield of hydrogen cyanide.

3. Reactions of Oxygen Atoms with Low Hydrocarbons. In the laser decomposition of CuO and NiO, the yield of O₂ gas was about 3×10^{-7} mol for 5 pulse irradiations. The presence of oxygen atoms may be confirmed by the formation of oxygen molecules. The presence of oxygen atoms may be also supported by the experimental fact that the laser irradiation on CuO in the presence of low hydrocarbons gave carbon monoxide but did not give any oxygen molecule.

A CuO target in ethylene was irradiated by the focused laser beam. Hydrogen, carbon monoxide, and water were produced but oxygen and carbon dioxide were not found. The data are shown in Table VII. The product

TABLE VII.--The reaction products of oxygen atoms produced by 7 pulse irradiations on CuO with ethylene.

Product	Yield ($\times 10^{-6}$ mol)
H ₂	9.6
CO	7.0
H ₂ O	5.0
O ₂	0
CO ₂	0
C ₂ H ₂	1.7
CH ₄	0.04
C ₂ H ₆	0.10
C ₃ -Compounds	0.05
C ₄ -Compounds	0.2
Vinylacetylene	0.05
Diacetylene	0.10

yields in other low hydrocarbons are shown in Table VIII. As shown in both tables, any oxygen atom added or inserted compounds were not detected.

TABLE VIII.--Reaction products of oxygen atoms produced by 7 pulse irradiations on CuO with low hydrocarbons.

Product	Yield ($\times 10^{-6}$ mol)					
	Substrate					
	Methane	Ethane	Acetylene*	Propylene	1-Butene	Isobutylene
CH ₄	-	1.8	0.02	0.25	0.58	0.44
C ₂ H ₆	0.17	-	0.05	0.40	0.15	0.10
C ₂ H ₄	0.06	1.6	0.10	0.95	0.57	0.13
C ₂ H ₂	0.07	0.2	-	1.85	0.70	0.55
C ₃ H ₈	0	0.3	0	0.58	0.01	0.10
n-Butane	0	0	0	0	0.25	0.19
Isobutane	0	0	0	0	0.08	0.58
Vinylacetylene	0	-	0.10	0.04	-	-
Diacetylene	0	-	1.50	0.02	-	-
Benzene	0	-	0	0.06	-	-

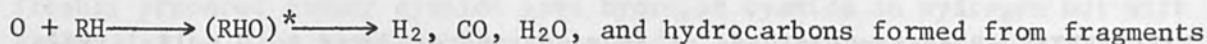
* Black polymerized product was observed, but its property was not examined.

- Detection was not performed.

The results were quite different from those in the reaction of oxygen atoms produced by other methods.¹⁰ In the reaction of hydrocarbons with oxygen atoms produced by other methods, oxygen added and inserted compounds have been produced.

The oxygen atoms produced by laser irradiation may probably be in the ground ³P state because the laser beam has not enough energy to produce excited oxygen atoms. But it has very large translational energy at the moment of production. These oxygen atoms hit against the hydrocarbon molecule violently and abstract carbon and hydrogen from the substrate molecule to produce carbon monoxide, water, and fragments. The combination of fragments may give also hydrocarbon products. Thus the rate of production of oxygen atom inserted or added compounds may be extremely small. The explanation may be supported by the fact that the laser irradiation on nickel plate in organic gases also gives the hydrocarbon products. In this case the high energetic nickel vapor collides with organic molecules. By the collision energy transfer from nickel atoms to organic molecules may take place to cause the decomposition of the organic molecules.

From the above results, the reaction processes may be considered to be as follows:



ACKNOWLEDGMENT

The authors wish to acknowledge the valuable assistance of Miss K. Motegi in carrying out this work.

REFERENCES

1. W. B. Tiffany, J. Chem. Phys. 48: 3019, 1968; I. Tanaka, Y. Mori, Y. Minagawa, and E. Okutsu, J. Phys. Chem. 72: 2684, 1968.
2. K. Taki, P. H. Kim, and S. Namba, Bull. Chem. Soc. Japan 42: 823, 1969; J. F. Verdick and A. W. H. Mau, Chem. Commun. 226, 1969; R. Schaeffer and R. K. Pearson, J. Amer. Chem. Soc. 91: 2153, 1969.
3. A. H. Adelman, J. Chem. Phys. 45: 3152, 1966; K. Taki, P. H. Kim, and S. Namba, Bull. Chem. Soc. Japan 42: 2377, 1969.
4. K. Taki, P. H. Kim, and S. Namba, Bull. Chem. Soc. Japan 43: 1450, 1970.
5. S. Namba, P. H. Kim, and K. Taki, Record 10th Symp. on Electron, Ion, and Laser Beam Tech. (L. Marton, ed.), San Francisco Press, 1969, p. 493.
6. E. Piers and R. K. Brown, Can. J. Chem. 40: 559, 1962.
7. J. U. White, J. Chem. Phys. 8: 79, 1940; *ibid.* 8: 459, 1940; -- A. Mele and H. Okabe, *ibid.* 51: 4798, 1969; D. R. Safrany and W. Jaster, J. Phys. Chem. 72: 3318, 1968.
8. Y. Titani and N. N. Lichtin, J. Phys. Chem. 72: 526, 1968; D. R. Safrany and W. Jaster, *ibid.* 72: 3323, 1968.
9. D. R. Safrany, R. R. Reeves, and P. Harteck, J. Amer. Chem. Soc. 86: 3160, 1964.
10. R. J. Cvetanović, Can. J. Chem. 36: 623, 1958; S. Sato and R. J. Cvetanović, *ibid.* 36: 1608, 1958; A. N. Hughes, M. D. Scheer, and R. Klein, J. Phys. Chem. 70: 798, 1966; J. T. Herron and R. E. Huie, *ibid.* 73: 3327, 1969.

LASER BEAM TECHNOLOGY FOR REMOTELY SENSING INVISIBLE MOLECULES IN THE POLLUTED ATMOSPHERE

TAKAO KOBAYASI and HUMIO INABA

Research Institute of Electrical Communication, Tohoku University, Sendai, Japan

This paper describes some experimental and theoretical studies on the new family of remote-sensing systems of invisible air pollutants by the application of the laser radar technique. Four schemes are compared extensively in terms of their respective functional capabilities and performances.

The Raman backscattering or laser-Raman scheme was demonstrated experimentally to detect specific pollutants in the atmosphere. By incorporating a UV pulsed nitrogen or a Q-switched ruby laser, many molecules including SO_2 , NO , CO_2 , H_2S , CH_4 , CO , and H_2CO in the polluted air as well as N_2 , O_2 , and H_2O in the ordinary air were identified separately by spectroscopic analysis. The combined scheme of fluorescence and resonance Raman backscattering was examined in the experiment by using a frequency-tunable dye laser pumped by a pulsed nitrogen laser.

Besides these two methods, we include in the analytical discussion the resonance scattering scheme for detecting metallic vapor pollutants and the absorption scheme for measuring average or total concentrations of atomic and molecular pollutants over the optical path. Theoretical expressions are derived for estimating scattering cross section, minimum detectable concentration, and range capability of these four schemes, and the comparisons are made.

1. INTRODUCTION

There are acute needs in electronic instrumentation for measuring directly parameters of our environmental air in three dimensions, over large volumes, and with enough resolution in time and space.¹ With such an ability of measurement, one can predict, confirm and effectively control air pollution.

Investigations of remote optical sensing have already been evaluated, including passive or active lang-path absorption spectroscopy² and correlation spectroscopy³ in various regions of the optical spectrum. With the advent of laser technology, attention has been given to its potential application to a variety of scientific measurements and controls. Among others, the laser radar technique makes it possible to realize the single-ended and range-resolved measurement of optical signals, backscattered from particulate matters existing in the atmosphere.⁴⁻⁶ It is this scheme of operation that can overcome the disadvantage of lack of range resolution in the remote optical sensing techniques that have been developed without lasers.

In this paper, the new family of laser-beam systems as an extension of conventional laser radar technique are discussed from the viewpoint of both qualitative and quantitative analyses of remote pollutants in the atmosphere. The experimental approach is also included, with respect to the two practically important schemes associated with Raman scattering and the combination of fluorescence and resonance Raman backscatterings. Finally, the comparison of detection sensitivity and systems analysis

is described for the four possible operating schemes for laser-radar applications to remote sensing of air pollutants.

2. CLASSIFICATION OF ACTIVE OPTICAL REMOTE SENSING METHODS

In this section we briefly review and discuss possible spectroscopic remote-sensing methods of polluted air employing an optical beam from active sources such as lasers and optical parametric oscillators, to provide the range-resolved measurement. Related techniques based on the passive method of long-path correlation spectroscopy³ in the infrared, visible, and ultraviolet regions are not covered, since these schemes lack the range resolution.

Three possible interactions of optical waves with the atmospheric constituents are summarized in Table I. Optical scattering is usually

TABLE I.--Comparison of optical interaction processes and their applications in active optical remote sensing methods.

Interaction	Process	Wavelength Laser : λ Detection: λ_r	Cross-section (cm^2/str)	Detectable Constituents
Scattering	Mie	$\lambda_r = \lambda$	10^{-26} to 10^{-8}	Particulate matter
	Rayleigh	$\lambda_r = \lambda$	10^{-26} (non-resonance) 10^{-23} (resonance)	Atomic vapor and Molecule
	Raman	$\lambda_r \neq \lambda$	10^{-29} (non-resonance) 10^{-26} (resonance)	Molecule (Atomic vapor)
Emission	Fluorescence	$\lambda_r = \lambda$	10^{-26} (quenched)	Atomic vapor and Molecule
		$\lambda_r \neq \lambda$	10^{-26} (quenched)	
Absorption		$\lambda_r = \lambda$	10^{-20}	Atomic vapor and Molecule

divided into three kinds of processes (called after Mie, Rayleigh, and Raman), depending on the species and the size of constituents compared with the wavelength. Although emission includes both the spontaneous and stimulated ones, the latter scheme seems to contribute nothing to observable scattered energy in the atmosphere. In the second to last column, typical values of interaction cross sections per one molecule of SO_2 are shown, except for the case of Mie scattering. These values are applicable to the optical wave in the region 3000-4000 Å.

The use of laser radar for air pollution detection has been so far mainly confined to the monitoring of Mie scattering at the transmitted wavelength by particulate matters existing in the atmosphere.⁴⁻⁶ Though the cross section of this scattering is usually very large for the particles whose diameter is close to or larger than the optical wavelength (yielding very high sensitivity for detecting particulate matter), the Mie scattering scheme does not lead to the quantitative analysis of molecular constituents in the atmosphere.

The Rayleigh scattering component for molecules is known to be in phase with the incident radiation. Because the central frequency of this

component is identical with the frequency of Mie component, the measurement of Rayleigh scattering does not customarily lead to specific analysis of molecular constituents in the atmosphere. However, if the incident light wavelength is tuned carefully to a particular absorption line of the investigated species, we obtain a large increase in the cross section of Rayleigh scattering by such a resonance interaction. Heitler⁷ has referred to this process as the resonance fluorescence in his well-known book, and recently, Huber⁸ called it resonant scattering in his theoretical analysis. To avoid confounding this terminology with the process involved in the fluorescence scheme, we use "resonance Rayleigh scattering" in a strict sense, or simply "resonance scattering."

The frequency of this scattering may coincide with that of fluorescence at the unshifted frequency in atoms and molecules, as discussed later. Consequently, the two components may also contribute to the backscattering at the laser wavelength, although the fluorescence backscattering is quenched appreciably at atmospheric pressure.

The laser radar scheme based on this resonance scattering process has been proposed by the present authors.^{9,10} Nakahara et al.¹¹ performed an experimental study of this type of scattering from SO₂ by utilizing the second-harmonic beam of a tuned dye laser at 3001 Å. The minimum detectable concentration of this resonance-scattering scheme laser radar is limited by the presence of an intense Mie component, and is estimated to be of the order of 10³ ppm for typical polluting molecules depending on the visual range of the atmosphere. Hence, we do not give further consideration to this type of laser radar for the detection of specific molecules in air.

Nevertheless, atomic vapors may possess quite large cross sections for the resonance scattering by the resonance radiation,¹² about 10⁸ to 10¹⁰ as large as that for molecules. Then, several atomic vapors in the atmosphere may be detected sensitively by using this resonance-scattering scheme, especially if very short laser pulses in the subnanosecond or picosecond range are used for the measurement, as proposed by the authors.¹⁰ This problem is discussed at the end of this paper.

The Raman scattering component from a specific molecule is shifted from the incident beam frequency by a proper amount corresponding to the internal vibration and rotation of the molecule. Figure 1 shows frequency shifts of the vibrational Raman spectrum of typical chemicals in polluted air. Molecules such as N₂, O₂, and H₂O present in the ordinary atmosphere are also indicated for the reference. All listed value of the Raman shifts refer to the central frequencies of the Q-branch of the Raman band. As these shifts are specific to each molecule, the measurement allows remote range-resolved detection of the variety of pollutant molecules.

The Raman scattering scheme or the laser-Raman radar scheme for chemical analysis of the polluted air has been proposed by the authors,¹³ and independently by some others.¹⁴ Raman backscatterings from dominant molecules such as N₂ and O₂ have already been observed by Leonard¹⁵ and Cooney;¹⁶ also the H₂O component in the atmosphere has been detected by Melfi et al.¹⁷ and Cooney.¹⁸ We have performed the spectral analysis of the Raman backscatters from CO₂ and SO₂ in polluted air and made an evaluation of their concentrations.^{19,20}

The cross sections for Raman scattering are three orders of magnitude smaller than Rayleigh cross sections. However, the Raman scheme provides a means of identifying and monitoring a number of molecules from a single location;

and it occurs regardless of the transmitting optical frequency. Although its frequency need not be matched to the proper resonance of matter to induce transitions of molecules and atoms, the resonance Raman effect is very attractive because the scattering cross sections it yields are so greatly enhanced that range or concentration limitation are overcome. The specific method based on the resonance Raman backscattering realized with the tunable laser source is discussed in the succeeding sections.

The second interaction principle described in Table I is the spontaneous emission process of photons, corresponding to the fluorescence or the fluorescence backscattering. This process differs from Rayleigh or resonance scattering because of time lag of re-emission and the frequency shift from the exciting light frequency. A detection scheme for molecular constituents with the laser radar technique with the help of this fluorescence backscattering has already been discussed by us^{9,10} and independently by Derr et al.,²¹ and is analyzed in this paper.

This scheme always requires the tuning of the laser frequency to match the molecular resonance. The re-emitted radiation measured at appropriate frequencies can be used to identify uniquely the molecular species responsible for the backscattering. However, it is to be remembered that the fluorescence is, in general, quenched in the atmosphere because of collisions with air molecules. Its intensity is apparently lowered by several orders of magnitude compared with the low-pressure case encountered in the laboratory or in the earth's upper atmosphere. Nevertheless, the cross section of quenched fluorescence is still larger, in general, than Rayleigh or Raman cross sections, depending on the nature of the transition.

For the atomic case, Bowman et al.²² observed sodium vapor layers between about 80 and 100 km in the upper atmosphere, using dye lasers tuned to one of the D lines of this atom. This method may be properly called fluorescence backscattering according to our classification, although part of scattered intensity could be ascribed to the resonance scattering component.

The third interaction scheme is the absorption process, which may also be utilized to measure remote pollutants. The laser-radar absorption spectroscopy has been proposed by Zaromb,²³ Kildal and Byer,²⁴ and investigators in Japan.^{11,25} Zaromb has reported that this method has very high sensitivity for detecting average densities, of the order of 0.15 ppm for NO₂ with a light absorption path of 6 km, or a scanning distance of 3 km. However, the absorption scheme lacks the range-resolution capability and permits only measurement of trace or total amount in the optical path concerned. This disadvantage may be partly overcome by the range-resolved method proposed by Igarashi et al.,²⁵ in which Mie scattering components between on- and off-absorption frequencies are compared simultaneously.

3. EXPERIMENTAL APPROACH

A. LASER-RAMAN RADAR SCHEME. Systems design considerations require the laser-Raman radar to consist of:

- (a) a high-power laser transmitter and collimating optics to transmit the laser pulse into the atmosphere;
- (b) receiving optics comprising a reflecting telescope to collect backscatters;

(c) a monochromator to discriminate the Raman-shifted component from unshifted Mie and Rayleigh components; and

(d) a photodetector and data-processing and display systems to convert the signal into a usable format.

Figure 2 shows the experimental system. As a first step, a Q-switched ruby laser with 5-10 MW peak power and 30-ns width at 6943 Å is used. Spectroscopic analyses of Raman backscattering from N₂ and O₂ molecules in the ordinary atmosphere²⁶ and SO₂ and CO₂ molecules in the polluted air were carried out with the ruby laser beam, as reported previously.^{19,20} A second instrument employed a N₂ pulsed laser delivering 10 MW of average power at 3371 Å and 20 kW peak power of 10-ns halfwidth and a repetition rate of 50 pps. This choice is based on the fact that, besides high-repetition rate operation, the Raman scattering intensities (which depend on the fourth power of the frequency) favor shorter wavelength. In order to reject the fluorescence originating from the N₂ laser tube, a filtering device utilizing a diffraction grating is placed between the laser and the collimating optics. The receiving optics is a 30-cm-diam, 150-cm focal-length reflection telescope with a rotatable mount. An f/8.5, 0.5-m single-grating monochromator was set as a spectral analyzer along with a rejection filter of 1×10^{-3} transmission at 3371 Å. For the detector, we employ a photomultiplier HTV R-374 (Hamamatsu TV Co.) with S-20 spectral response. The electronics is a boxcar integrator which is composed of a pulse gate or sampling circuitry with gate time variable from 0.1 to 10 ns, a CR integrator, and a time or range delay. An X-Y recorder was used to display the observed results. The output of the photomultiplier is also monitored by a 100-MHz oscilloscope.

The assembled laser-Raman radar system was successfully operated in preliminary field tests, at a range of about 30 m, which was limited by the experimental situation, to show the capability of analyzing spectroscopically various molecules existing in ordinary and polluted atmosphere. Figure 3 shows the result of the spectral measurement of Raman backscatters from the ordinary atmosphere. The Rayleigh and Mie components centered at the transmitted laser wavelength are also included in the figure. The vertical arrow indicates the expected central wavelength of the Q branch of vibrational-rotational Raman lines for each molecular species. It should be noted that the Raman spectra from the major components such as N₂ and O₂ as well as CO₂ and H₂O molecules are well identified. The spectral width of the Q branch of N₂ and O₂ is instrumental, and O and S branches are distributed on both sides of each Q branch.

Figure 4 is the Raman spectrum backscattered from an oil smoke plume. Fuel oil was burned in a burner to flow the oil smoke plume, which was so tenuous that it was barely visible to the eye, through a chimneytop into the atmosphere. The intensity peaks were observed at the Raman-shifted wavelengths corresponding to SO₂, CO₂, H₂CO, NO, CO, H₂S, CH₄, and also O₂, N₂, and H₂O molecules. The last three molecules offer convenient references for the laser-Raman radar. Intensity fluctuation in the range of 3760-3840 Å may be ascribed to fluorescence from particulate matters in the smoke plume.

Figure 5 also exhibits the spectrum of Raman backscatters from automobile exhaust gas. The exhaust gas of the automobile was sent into the atmosphere through a chimney. The Raman bands due to the presence of NO and CO are identified in addition to the ordinary atmospheric components. Also, intense fluorescence components are observed from 3700 to 3880 Å.

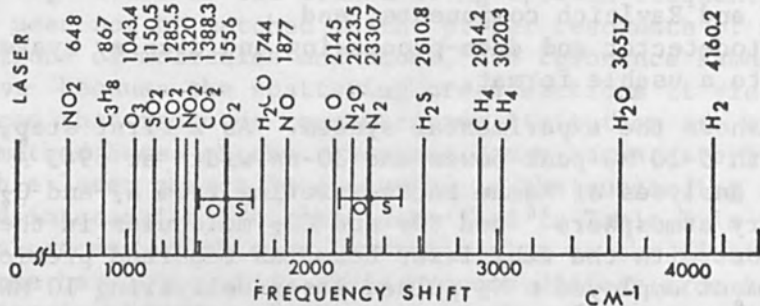


FIG. 1.--Frequency shifts of Q branch of vibrational-rotational Raman spectra of various species involved in polluted air as well as those present in ordinary atmosphere.

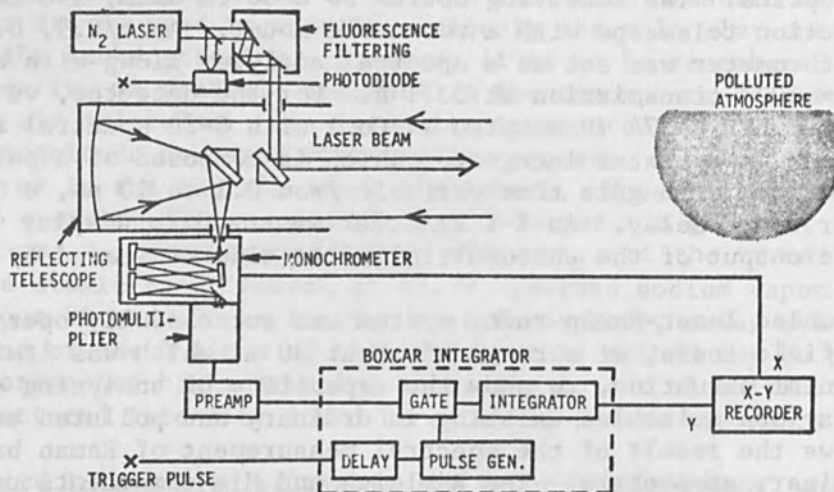


FIG. 2.--Schematic of laser-Raman radar system used in field experiments.

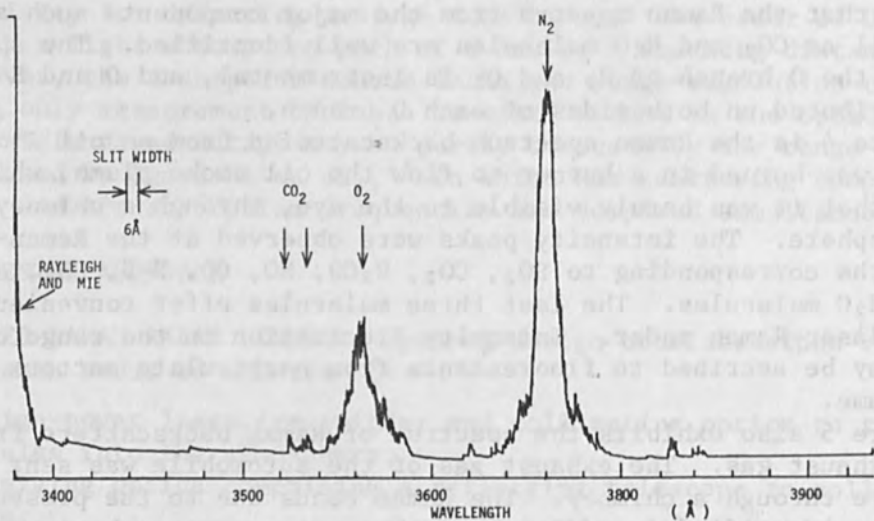


FIG. 3.--Spectral profile of Raman-shifted and unshifted backscatters from ordinary atmosphere.

The Raman components of NO_2 , H_2S , and H_2O molecules seemingly appeared, but some uncertainties remain owing to interference with the 0 band and also strong fluorescences.

The observation time required to make the complete scan for the interval of about 500 \AA was approximately 40 min. However, 10 sec was enough for the measurement of the central peak of the Raman band of a specific molecule. In the measurements shown in Figs. 4 and 5, a short-wavelength cut filter was employed in front of the monochromator to reject intense unshifted components. Decrease in intensity below 3600 \AA was mainly due to the transmission loss of the filter.

Although the calibration of absolute intensities of each Raman components and evaluation of the number density of each molecular species have not yet been performed, the unique capability of the laser-Raman radar in identifying and monitoring a number of molecular species in the mixed gases from a single location has been demonstrated by these experiments.

B. FLUORESCENCE BACKSCATTERING SCHEME. It is well known in physics that the interaction cross section increases greatly when the exciting frequency approaches a proper resonance of the internal motion of atoms and molecules. Such resonance spectroscopic schemes constitute a potential for application to the remote sensing of air pollution in conjunction with the laser radar technique. The resonance Raman scattering and fluorescence spectra in some heavy halogen gases have been observed and discussed by Holzer et al.,²⁷ who used five emission lines of an argon ion laser for the excitation. The authors refer to fluorescence as resonance fluorescence. However, this process is different from Heitler's resonance fluorescence,⁷ which involves the simultaneous interaction of two photons.

From the viewpoint of laser radar applications, it is of great interest to investigate these resonance effects with frequency tunable lasers in order to understand the precise characteristics of a variety of molecules and atoms in the atmosphere. By the use of the organic dye laser, we have studied provisionally some molecules including I_2 and NO_2 vapor which have rather intense absorption lines and bands in the visible region.

For this experiment, the frequency-tunable dye laser pumped by a nitrogen laser used previously in the laser-Raman radar experiments was incorporated. Several dyes were employed to realize lasing across the visible spectrum. The spectral width of rhodamine 6G dye was approximately 0.5 \AA when the laser cavity was composed of the combination of a plane mirror and a diffraction grating for the tuning. The pulse duration was 8 ns and the peak power was about 1 kW ($8 \mu\text{J}/\text{pulse}$) with a repetition rate of 50 pps. The dye laser beam was focused into a small double-pass quartz gas cell. The spectra were recorded with a JASCO CT-50D double monochromator and a boxcar integrator.

As an example of the detected resonance effects, the observed spectra of the I_2 molecule are compared in Fig. 6. A typical fluorescence spectrum is shown in Fig. 6(a) for the case of I_2 pressure of 0.3 torr. The molecule was excited by the dye laser beam at 5628 \AA which corresponds to the head of the (21-1) vibrational band of the ${}^3\Pi-1\Sigma$ electronic transition. Many Stokes overtone lines are observed, as is partly shown in the figure, up to about 8000 \AA , a limit set by the detector sensitivity. The fluorescence intensity was found to decrease with increasing I_2 or mixed foreign gas pressure. This quenching behavior is a crucial test for the evidence of fluorescence.

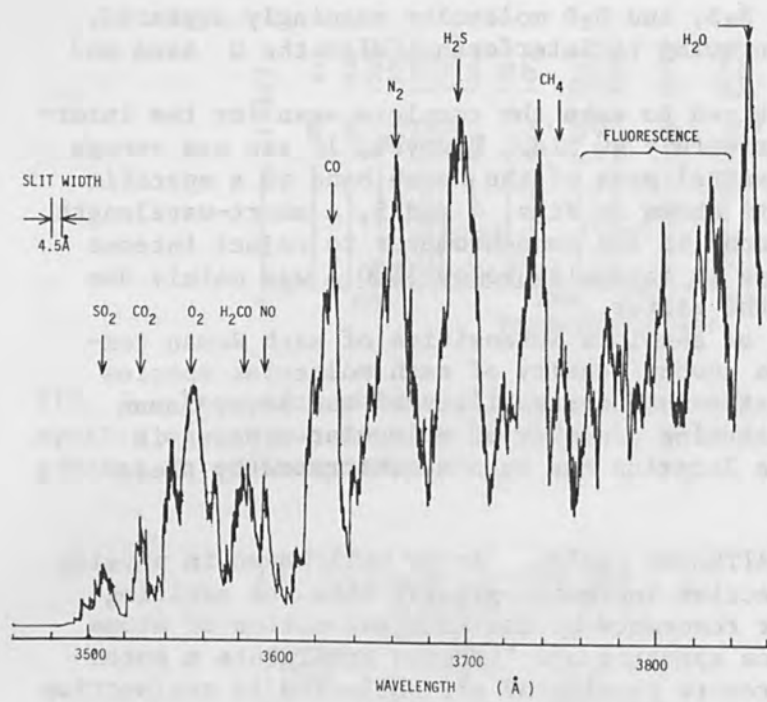


FIG. 4.--Spectral distribution of Raman-shifted components from various molecules in oil smoke plume analyzed by laser-Raman radar system.

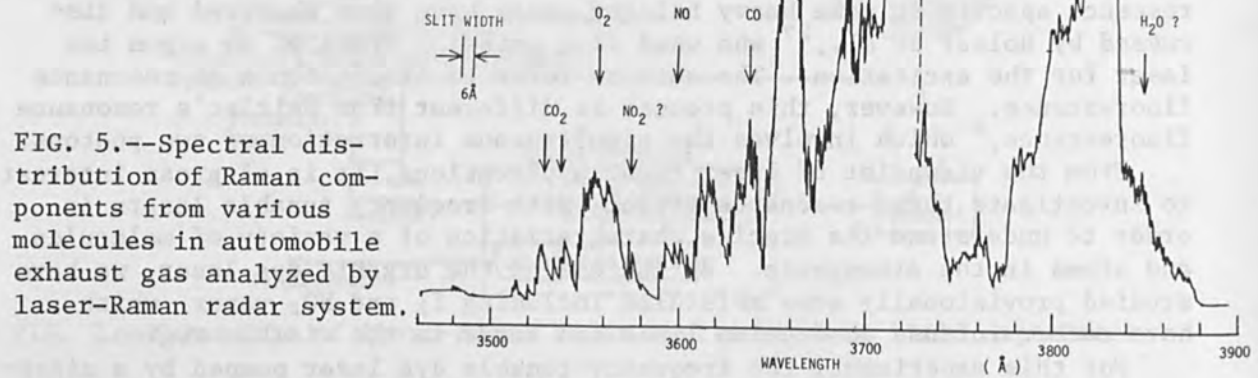


FIG. 5.--Spectral distribution of Raman components from various molecules in automobile exhaust gas analyzed by laser-Raman radar system.

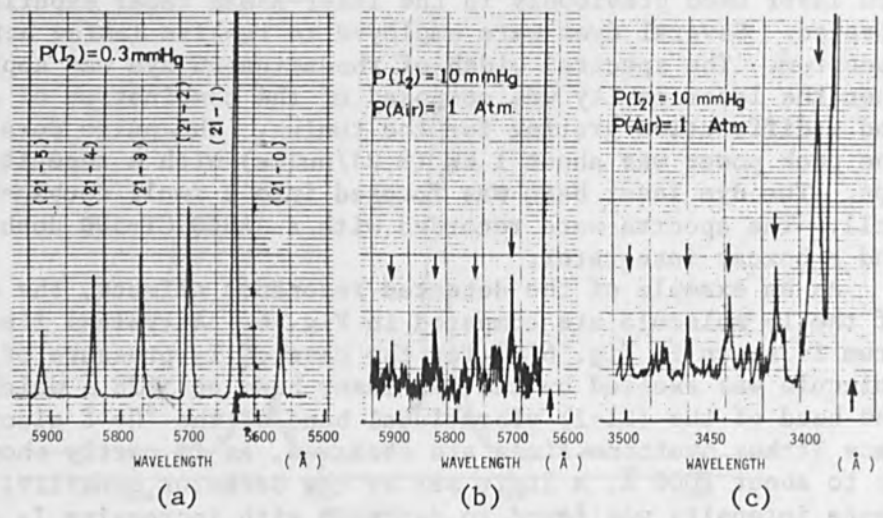


FIG. 6.--Comparison of observed spectra of I_2 molecule: (a) Fluorescence spectrum without quenching at a pressure of 0.3 torr excited at 5628 Å; (b)

combined spectra of fluorescence and resonance Raman scattering observed at I_2 pressure of 10 torr by mixing air at atmospheric pressure; (c) resonance-Raman scattering spectrum at I_2 pressure of 10 torr and air of 1 atm (excitation at 3371 Å).

Figure 6(b) shows the spectrum of I₂ fluorescence quenched by mixing air at 1 atm pressure. The observed emission lines indicated by vertical arrows may be produced by the combination of fluorescence and resonance Raman scattering. As the frequency shifts of these two components are almost the same, spectral analysis alone is insufficient to separate the two contributions. Polarization characteristics and pressure dependence may be useful to give necessary information. Also, the collisionally excited fluorescence lines were observed when the foreign gas pressure was increased.

Figure 6(c) represents the resonance Raman spectrum of the I₂ molecule when it was excited by a N₂ laser beam at 3371 Å. As indicated by Holzer et al.,²⁷ the resonance Raman effect is observed clearly with incident light energies higher than the dissociation limit of the excited state of I₂. However, this effect may be observed even below the convergence limit, if the series of intense fluorescence lines are quenched considerably by high-pressure foreign gases. The higher overtone pattern is also one of the characteristics of the resonance Raman effect.

Fluorescence and/or resonance Raman backscatterings may be thus applied simultaneously for the spectroscopic detection of molecular species in the atmosphere, because their frequency shifts avoid interference with intense Mie and Rayleigh components. Quantitative discussion of these resonance effects for optical remote-sensing techniques is given in the next section.

4. ANALYTICAL STUDY OF DETECTION SENSITIVITY

For the over-all evaluation of the extent of applicability of laser radar spectroscopy to the remote sensing of commonly encountered pollutants, the cross sections of the four optical schemes are theoretically analyzed and the detection capability is discussed in this section.

A. CROSS SECTIONS. (a) Absorption. The absorption cross section is usually given by¹²

$$\sigma_{\text{abs}} = (\pi e^2/mc^2)f_{12} \quad (1)$$

where e is the electron charge, m is the electron mass, c is the light velocity, and f_{12} is the oscillator strength of the transition between the energy levels 1 and 2. It is related to the spontaneous emission rate A_{21} by

$$f_{12} = (g_2\pi mc^3/2g_1\omega_0^2 e^2) A_{21} \quad (2)$$

$$A_{21} = (8\pi\omega_0^3/3hc^3) |\mu_{12}|^2 \quad (3)$$

where g_i is the degeneracy of the level i , ω_0 is the central angular frequency of the transition, h is the Planck's constant, and μ_{12} is the matrix element of the dipole moment.

(b) Fluorescence. Fluorescence can occur only when the frequency of the exciting radiation lies in an absorption line or band of the material. It is the spontaneous emission process which re-emits the photon after the absorption and is sometimes followed by the relaxation process from the higher level 2 to the lower levels m . Its cross section is determined by^{12,28}

$$d\sigma_{fl}/d\Omega = (\sigma_{abs}/4\pi)Qp_{2m} \quad (4)$$

where Ω is the solid angle, Q is the quenching factor, and p_{2m} is the fluorescence efficiency in the observed transition $2 \rightarrow m$. The quenching factor is given by the Stern-Volmer relation¹²

$$Q = 1/(1 + \sum_i a_i P_i) \quad (5)$$

where a_i is the factor characterizing the collision with the i -th molecule, and P_i is the partial pressure of the i -th molecule. The fluorescence efficiency may be related to the A coefficient by

$$P_{2m} = A_{2m}/\sum_n A_{2n} \quad (6)$$

where the summation is taken over all allowed transitions from the higher level 2.

Table II summarizes the cross sections of the three typical molecules under atmospheric pressure. Indicated are the values for maximum absorption and the integrated values over the fluorescence band along with the

TABLE II.--Cross sections of three typical molecules for absorption, fluorescence, and resonance scattering under atmospheric pressure.

Molecule	Transition	Wavelength λ	Lifetime τ_N	Quenching Factor Q	Cross-section		
					σ_{abs}	$(d\sigma_{fl}/d\Omega)_c$	$(d\sigma/d\Omega)_c$
SO ₂	A(¹ B ₁)-X(¹ A ₁)	2600-3400	$\sim 10^{-5}$ sec	$\sim 1 \times 10^{-6}$	2×10^{-19} cm ²	$\sim 1 \times 10^{-26}$ cm ² .str ⁻¹	1.5×10^{-23} cm ² .str ⁻¹
NO ₂	A(² B ₁)-X(² A ₁)	3520-5750	$\sim 10^{-5}$	3.8×10^{-6}	4.0×10^{-19}	1.2×10^{-25}	
I ₂	B ³ π_{ou}^+ -X ¹ Σ_g^+	4990-5900	$\sim 5 \times 10^{-7}$	$\sim 1 \times 10^{-3}$	$\sim 1 \times 10^{-17}$	$\sim 1 \times 10^{-21}$	

quenching factor Q . The resonance scattering cross section, which will be discussed in the next paragraph, is also shown for the case of SO₂ molecule¹¹ in the last column, for comparison.

(c) Resonance Scattering (Resonance Rayleigh Scattering). As mentioned before, this scattering occurs in the form of the two-photon interaction process, and may be called resonance Rayleigh scattering in a strict sense. According to Huber,⁸ the cross section of this process is given by

$$d\bar{\sigma}/d\Omega = (3/8\gamma_N) X\omega^4 \quad (7)$$

$$X = 2\pi|\mu_{12}|^4/3c^4h^2$$

where ω is the frequency of the incident light, and γ_N is the natural line width. Two limiting cases are considered to be of importance in the laser radar applications:

(1) natural broadening limit ($\gamma_N \gg \gamma_C, \gamma_D$):

$$\begin{aligned} (d\sigma/d\Omega)_N &= \bar{\sigma}(\omega_0)/\Delta\nu_N \quad \text{for } \Delta\nu \leq \Delta\nu_N \\ &= \bar{\sigma}(\omega_0)/\Delta\nu \quad \text{for } \Delta\nu > \Delta\nu_N \end{aligned} \quad (8)$$

(2) collision broadening limit ($\gamma_C \gg \gamma_D, \gamma_N$):

$$\begin{aligned} (d\sigma/d\Omega)_C &= \bar{\sigma}(\omega_0)/\Delta\nu_C \quad \text{for } \Delta\nu \leq \Delta\nu_C \\ &= \bar{\sigma}(\omega_0)/\Delta\nu \quad \text{for } \Delta\nu > \Delta\nu_C \end{aligned} \quad (9)$$

where $\Delta\nu$ is the spectral width of the incident light, $\Delta\nu_N = \gamma_N/\pi$ is the natural line width, and $\Delta\nu_C = \gamma_C/\pi$ is the collision-broadened line width.

In these analyses, elastic collisions are assumed. This assumption will be fulfilled if the pulse duration of the incident light τ is shorter than the mean collision time interval: $\tau < 1/\gamma_C$, where $1/\gamma_C$ will be of the order of 10^{-10} sec at atmospheric pressure. If the light pulse is wider than this limit, the interaction process is so incoherent that the nature of the scattering becomes similar to fluorescence owing to the collision quenching in the atmosphere. To realize this requirement, the subnanosecond (picosecond) pulses from the mode-locked dye laser²⁹ will be favorable for practical applications.

Table III shows the estimated cross sections of five atomic vapors for the resonance scattering process in both the cases of natural and

TABLE III.--Calculated cross sections of five atomic vapor pollutants for the resonance scattering and fluorescence processes.

Atom	Wavelength	Line width $\Delta\nu_C$	Quenching Cross-section $\sigma_Q^2(N_2)$	Quenching Factor Q	Cross-section		
					$(d\sigma/d\Omega)_N$ ($\Delta\nu < \Delta\nu_N$)	$(d\sigma/d\Omega)_C$ ($\Delta\nu < \Delta\nu_C$)	$(d\sigma_{fl}/d\Omega)_C$ ($\Delta\nu < \Delta\nu_C$)
	(\AA)	(Hz)	(cm^2)		(cm^2/str)	(cm^2/str)	(cm^2/str)
Na	5890	1.15×10^{10}	61×10^{-16}	1×10^{-3}	5.3×10^{-12}	4.6×10^{-15}	$\sim 3 \times 10^{-18}$
Hg	2537	8.7×10^9	0.247×10^{-16}	2.3×10^{-3}	1.4×10^{-12}	2.38×10^{-16}	3.60×10^{-19}
K	7665	$\sim 1 \times 10^{10}$			8.8×10^{-12}	$\sim 5 \times 10^{-15}$	
Cd	3261	$\sim 1 \times 10^{10}$			2.4×10^{-12}	$\sim 2 \times 10^{-17}$	
Cd	2288	$\sim 1 \times 10^{10}$			7.9×10^{-13}	$\sim 6 \times 10^{-15}$	
Pb	2833	$\sim 1 \times 10^{10}$			1.8×10^{-12}	$\sim 3 \times 10^{-15}$	

collision broadening. For comparison, the fluorescence cross sections taking into account the quenching effect are listed for Na and Hg atoms. The collision-broadened line width in air is calculated by reference to Mitchel and Zemansky.¹² The cross section for fluorescence is smaller by three orders of magnitude than that for resonance scattering, because of the quenching by the air molecules.

(d) Raman Scattering. The cross section for Raman scattering is generally expressed by³⁰

$$\frac{d\sigma_R}{d\Omega} = \frac{(\omega - \omega_{21})^4}{c^4} |\alpha_{12}|^2 \quad (10)$$

$$\alpha_{12} = \frac{1}{\hbar} \sum_r \left(\frac{\mu_{r2} \mu_{1r}}{\omega_{r1} - \omega + i\gamma_r} + \frac{\mu_{1r} \mu_{r2}}{\omega_{r2} + \omega + i\gamma_r} \right) \quad (10)$$

where ω_{21} is the Raman angular frequency-shift given by $\omega_{21} = (E_2 - E_1)/\hbar$, E_1 and E_2 are energies of the initial and final state, r denotes the intermediate state, and ω_r is the line width of the intermediate state r . It is generally known that the cross section increases as $(\omega - \omega_{21})^{-4}$, so that shorter wavelengths make for efficient excitation of the Raman scattering.

When the angular frequency of the incident light ω approaches the electronic transition frequency $\omega_{r1} = (E_r - E_1)/\hbar$, the first term in the scattering tensor α_{12} increases drastically. This phenomenon is called the resonance Raman effect, and a 10^6 increase in cross sections has been observed for complicated organic molecules in the liquid state.³¹ As far as we know, however, no reliable absolute measurement of these Raman cross sections of molecular gases such as found in the atmosphere has been reported. The relative value can be deduced from the knowledge of the Rayleigh cross section and the Raman to Rayleigh cross section ratio.³² For instance, the Raman cross section of N_2 molecule is $d\sigma_R/d\Omega = 5.2 \times 10^{-30} \text{ cm}^2/\text{str}$ at the excitation wavelength of 3371 Å, $3.0 \times 10^{-30} \text{ cm}^2/\text{str}$ at 3472 Å, and $1.3 \times 10^{-31} \text{ cm}^2/\text{str}$ at 6943 Å. The relative cross section of SO_2 and NO Raman band with respect to N_2 as the reference gas has been recently measured by Leonard.³³ By combining this measured value for SO_2 with the above cross sections of N_2 , the Raman cross section for SO_2 was calculated as shown in Table IV.

TABLE IV.--Comparison of detection sensitivity of SO_2 molecule by laser-Raman radar systems using photon-counting detection method. (Detection time, 100 sec; gate time, 66.7 ns; $K = 0.1$; $A_r = 600 \text{ cm}^2$.)

LASER	RUBY	Nd-YAG SHG	RUBY SHG	N_2 GAS	DYE-SHG
WAVELENGTH (Å)	6943	5320	3472	3371	3001
OUTPUT ENERGY (mJ)	300	30	50	0.8	0.1
REPETITION RATE (pps)	1	100	1	100	100
RAMAN WAVELENGTH (Å)	7546	5667	3617	3508	3108
RAMAN CROSS-SECTION (cm^2/str)	5×10^{-31}	1.6×10^{-30}	$\sim 1 \times 10^{-29}$	$\sim 1 \times 10^{-29}$	$\sim 1 \times 10^{-26}$
QUANTUM EFFIC. OF DETECTOR	7×10^{-3}	7×10^{-2}	1.5×10^{-1}	1.5×10^{-1}	1.5×10^{-1}
CLEAR SKY RADIANCE ($W/\text{Åcm}^2\text{str}$)	5×10^{-8}	2×10^{-7}	1×10^{-7}	9×10^{-8}	2×10^{-8}
N_{\min}/R^2 (ppm/ m^2) FOR NIGHT	1.6×10^{-2}	6.9×10^{-5}	4.7×10^{-4}	3.1×10^{-4}	2.8×10^{-6}
N_{\min}/R^2 (ppm/ m^2) FOR DAYTIME	9.6×10^{-2}	2.3×10^{-2}	1.4×10^{-2}	8.3×10^{-2}	3.1×10^{-4}

B. DETECTION SENSITIVITY AND SYSTEMS ANALYSIS. The received power $P_r(\omega_r)$ backscattered from the atmospheric constituents at a range R can be calculated from the generalized laser radar equation:

$$P_r(\omega_r, R) = P_0(\omega) \ell K T(\omega) T(\omega_r) A_r Y(R) N(R) (d\sigma/d\Omega) / R^2 \quad (11)$$

This equation takes the different frequencies ω and ω_r of the transmitted and received power into account. Here, $P_0(\omega)$ is the transmitted power of the laser pulse, ℓ is one half of the laser pulse length, K is the efficiency of the total system, $T(\omega)$ and $T(\omega_r)$ are the one-way atmospheric transmittances at the transmitted and received frequencies, respectively, A_r is the effective receiver aperture, $Y(R)$ is the geometrical factor that accounts for overlap of the transmitted and received beam paths, $N(R)$ is the concentration, and $(d\sigma/d\Omega)$ is the backscattering differential cross section of the pollutant concerned.

If the signal is very weak, as is commonly the case in laser radar operation, the photon counting method gives suitable performance in the detection. If an air column of length L is sampled by the gate in a time interval τ_g at the receiver, the number of photoelectrons converted from the received signal by the photodetector is

$$n_r(\omega_r) = \bar{n}_0(\omega) f \tau \eta(\omega_r) L K T(\omega) T(\omega_r) A_r Y(R) N(R) (d\sigma/d\Omega) / R^2 \quad (12)$$

where $\bar{n}_0(\omega)$ is the number of photons in a transmitted laser pulse, f is the pulse repetition rate, τ is the total observation time, and $\eta(\omega_r)$ is the quantum efficiency of the photocathode. We are generally interested in the region where $Y(R) = 1$, i.e., signal power is dominated by $1/R^2$ falloff.

The expected signal-to-noise ratio for the photon counting detection is determined by

$$S/N = n_r(\omega_r) / \sqrt{n_r(\omega_r) + 2n_b(\omega_r)} \quad (13)$$

where $n_b(\omega_r)$ is the number of photoelectrons produced by the background:

$$n_b(\omega_r) = B f \tau \tau_g \eta(\omega_r) K A_r \Omega_r \Delta\lambda \quad (14)$$

where B is the background radiance in the unit of photons/sec·cm²·str·Å, Ω_r is the solid angle of the field of view of the receiver, and $\Delta\lambda$ is the spectral width of the filtering device in the receiver.

By means of the above relations, we can discuss the fundamental capabilities and limitations of the laser remote-sensing schemes described in the preceding sections from the viewpoints of detection sensitivity and range performance.^{10,20}

(a) Laser-Raman Radar Scheme. For the systems analysis, some parameters and operational performances of typical laser oscillators in the visible and near UV region are shown in Table IV. In the last column, the second-harmonic wavelength of the dye laser is assumed to be tuned to the peak of the SO₂ absorption band so as to cause either the resonance Raman effect or fluorescence backscattering. The listed parameters for the lasers and optics are rather conservative so that they may be easily achieved by the present state of the art in laser engineering. The evaluation of the minimum detectable concentration N_{\min} of the SO₂ molecule, as a typical example of air pollutant, is also summarized. In this analysis, the detection time τ is taken to be 100 sec and the gated range depth L is 10 m.

In Fig. 7, N_{\min} vs range curves are shown for both night and daytime operations. For night observation, sensitivity is limited by shot noise; in daytime, it is limited by the background noise. The second-harmonic (SH) beam of Nd-YAG laser yields the best sensitivity in night operation, and the SH beam of ruby laser is suitable for the daytime operation owing to the background reduction realized by the small number of shots with high-energy output. In practice, the estimated values of N_{\min} may be decreased by an order of magnitude or more by increases in parameters such as the receiver aperture, laser output power, and background noise rejection. Because the range resolution of the Raman backscattering scheme depends on the laser pulse duration and the gate time, it can be improved considerably by use of a shorter laser-pulse transmitter and a high-speed detection system.

(b) Fluorescence and Resonance Raman Backscattering Schemes. By substituting the cross sections listed in Table II into Eqs. (12)-(14), we can derive the N_{\min} value for detecting SO_2 and NO_2 molecules by the fluorescence scheme under the shot-noise-limited condition. Figure 8 shows the results for output energy $W_0 = P_0(2\ell/c) = 1$ mJ from the frequency-tuned laser transmitter. In practice, since we anticipate that the resonance Raman component is superposed on the fluorescence backscattering as described, both contributions should be included additively in the systems analysis. For comparison, the nonresonance Raman curve is also shown in Fig. 8. It is evident that an improvement in sensitivity of about three orders of magnitude in the fluorescence and resonance Raman backscattering schemes is achieved.

For the operation of this scheme, it is not difficult to separate the intense frequency-unshifted components from the shifted Raman or fluorescence components if a double monochromator or a combination of a single monochromator and rejection filters is employed.¹³

Since the quenching time of fluorescence is very short, of the order of 10^{-10} sec at atmospheric pressure, there is no serious problem in the range resolution for this scheme. If the fluorescence spectra are distributed broadly, the detection sensitivity is reduced due to the increase in background noise. Optical correlation techniques may be useful for discriminating such noise components and interference effects by the presence of other pollutants.

(c) Resonance Scattering Scheme. As discussed in Sec. 2, the resonance scattering or resonance Rayleigh scattering scheme is expected to be very sensitive to the detection of metallic vapor pollutants. Figure 9 shows N_{\min} vs range relation for Na, Hg, Cd, K, and Pb atoms in the atmosphere. As the detection sensitivity is excellent, these measurements can be performed with a single A-scope observation. Also shown in the figure is the N_{\min} vs range curve of Na and Hg for the fluorescence backscattering at the same frequency as with the laser beam. In both scattering schemes, the N_{\min} values are usually limited by intense Mie backscatter at the same frequency. Because the Mie backscattering intensity depends on the atmospheric visibility V ,²³ open circles and squares in the figure correspond to the smallest value of the minimum detectable concentration for $V = 1$ and 10 km. Within a distance shorter than the range corresponding to each marked point, the minimum detectable concentration thus becomes constant, independent of the range.

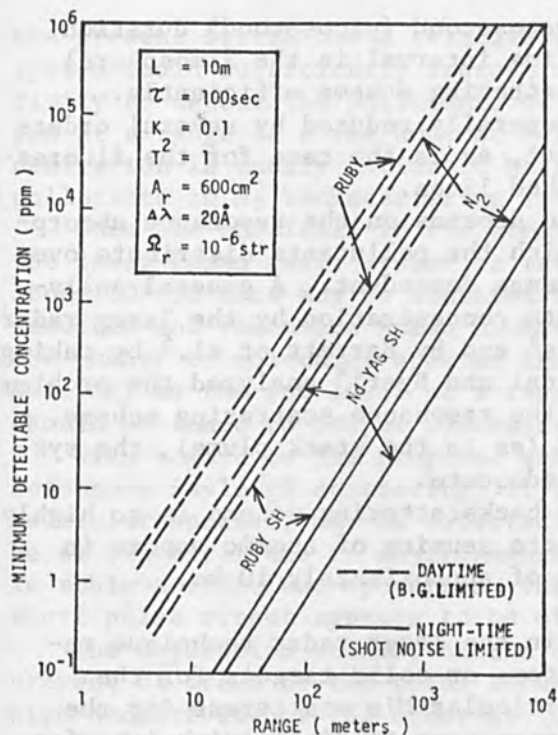


FIG. 7.--Comparison of minimum detectable concentrations of laser-Raman radar systems. System sensitivities were calculated using typical parameters listed in Table IV.

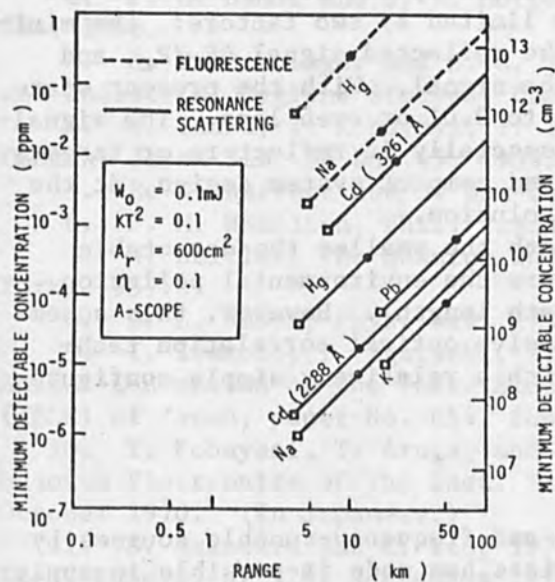


FIG. 9.--Minimum detectable concentration vs range for resonance-scattering scheme laser-radar for detections of metallic vapor pollutants.

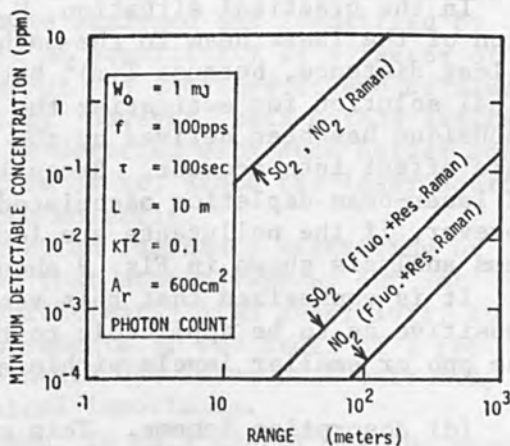


FIG. 8.--Minimum detectable concentration vs range for laser radar with fluorescence and resonance Raman backscattering schemes.

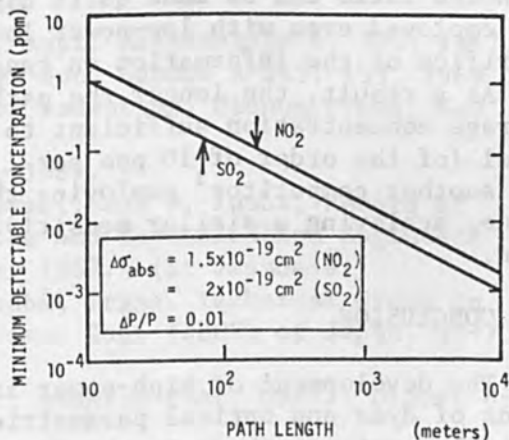


FIG. 10.--Minimum detectable concentration of SO_2 and NO_2 as function of path length for absorption scheme laser-radar.

Mode-locked dye laser pulses of subnanosecond (picosecond) duration (i.e., shorter than the mean collision time interval in the atmosphere) are required to realize the resonance scattering scheme efficiently. Otherwise the detection sensitivity is generally reduced by several orders of magnitude owing to the quenching effect, as is the case for the fluorescence backscattering scheme shown by dashed lines.

In the practical situation, N_{\min} also depends on the resonance absorption of the laser beam in the path in which the pollutants distribute over a long distance, because $T(\omega)^2$ becomes range dependent. A general analytical solution for estimating the absolute concentration by the laser radar technique has been derived by the authors⁴ and by Barrett et al.⁵ by taking this effect into account. Recently, Kildal and Byer^{2,4} analyzed the problem of laser-beam depletion associated with the resonance scattering scheme. However, if the pollutants are localized (as in the stack plume), the systems analysis shown in Fig. 9 should be adequate.

It is emphasized that this resonance backscattering scheme is so highly sensitive as to be applicable to the remote sensing of atomic vapors in the ppb or smaller levels within a range of approximately 10 km.

(d) Absorption Scheme. This scheme in the laser radar technique requires reflecting targets such as reflectors or solid targets for the average concentration measurement, or particular Mie scatterers for the range-resolved measurement. It is also necessary to distinguish interference effects from other pollutants in this method. For this purpose, the two-frequency differential method measuring on- and off-absorption or the correlation technique with a broadband laser beam is necessary.

As an example, minimum detectable concentrations of SO_2 and NO_2 as a function of path length for this absorption scheme are shown in Fig. 10. In the evaluation of N_{\min} over the path length, the difference in the cross sections between maximum and minimum absorption frequencies is utilized. The detection sensitivity may be limited by two factors: the minimum value of the relative variation of the reflected signal $\Delta P_r/P_r$, and the signal-to-noise ratio in detecting the signal. With the present state of art of electronics, $\Delta P_r/P_r$ may be set to 0.01 or even less. The signal-to-noise ratio can be made quite high, especially if reflectors or targets are employed even with low-power lasers and compact system design, at the sacrifice of the information on range resolution.

As a result, the longer the path length the smaller the detectable average concentration sufficient to measure the environmental pollution level (of the order of 10 ppb per 1 km path length). However, this scheme has another competitor³ employing the passive optical correlation technique, achieving a similar sensitivity with a relatively simple configuration.

5. CONCLUSION

The development of high-power lasers and frequency-tunable sources by means of dyes and optical parametric devices has made it possible to apply optical sensing methods in the detection of molecular and atomic constituents of the atmosphere. The four schemes of remote air pollution detection techniques have been discussed, and their basic techniques, capabilities, and limitations have been compared.

Experiment shows that the laser-Raman radar technique allows instantaneous identification of a variety of molecules in the atmosphere. Although

the present system has a relatively short range capability, a well-designed system could sufficiently improve (without great difficulty) the sensitivity to detect the pollutants of medium level concentration such as few ppm at a range of a few hundred meters. In the Raman scheme, absolute concentration is easily estimated by relating the backscattering for specific pollutants to N_2 backscattering intensity existing in the same location.

Once the chemicals in the atmosphere are analyzed and identified by the laser-Raman radar system, a refinement of sensitivity by a factor of about 10^3 or more may be achieved by means of the combined scheme of fluorescence and resonance Raman backscattering. However, this method limits the number of molecular species that can be detected with such better sensitivity as the ppb level at a range of 1 km or so, since the laser source should be tuned to proper resonances of the molecule.

With regard to the proposed scheme based on resonance scattering or resonance Rayleigh scattering, it is shown that atomic vapors, but not molecular species, may be detected with sufficiently high sensitivity to be of practical use in environmental measurements of the order of 1 ppb. To achieve efficient operation, the mode-locked dye laser with extremely short pulse output appears to be of practical importance.

The absorption scheme, on the other hand, is only useful for the measurement of trace or the total amount of pollutants in the optical path, with high sensitivity of the order of 10 ppb level per 1 km. The lack of range resolution may be partly overcome by some techniques such as incorporating many solid targets at different distances, or measuring Mie echoes at the two frequencies of on- and off-absorption as a function of range.

REFERENCES

1. A. E. O'Keeffe, IEEE Trans. GE-8: 145, 1970.
2. P. L. Hanst and J. A. Morreal, J. Air Pollution Control Assoc. 18: 754, 1968.
3. A. R. Barringer and B. C. Newbury, Ninth Conference, Air Pollution and Industrial Hygiene Studies, Pasadena, Calif., February 1968.
4. H. Inaba, T. Kobayasi, T. Ichimura, M. Morihisa, and H. Ito, Electron, Commun. Japan 51B: 36 and 45, 1968.
5. E. W. Barrett and O. Ben-Dov, J. Appl. Meteorology 6: 500, 1967.
6. P. M. Hamilton, Phil. Trans. Roy. Soc. London A-265: 153, 1969.
7. W. Heitler, The Quantum Theory of Radiation, Plenum Press, New York, 1957.
8. D. L. Huber, Phys. Rev. 178: 93, 1969.
9. I. Iwamoto, T. Igarashi, T. Kobayasi, and H. Inaba, Record of Annual Convention of the Inst. Electronics and Communication Engineers (IECE) of Japan, paper No. 654, September 1969. (In Japanese.)
10. T. Kobayasi, T. Aruga, and H. Inaba, Trans. Technical Group on Quantum Electronics of the Inst. Elec. Comm. Eng. (IECE) of Japan, QE-70-26, October 1970. (In Japanese.)
11. S. Nakahara and K. Ito, 1970 Int. Quantum Elec. Conf., Digest of Tech. Papers, p. 226, September 1970.
12. A. C. G. Mitchel and M. W. Zemansky, Resonance Radiation and Excited Atoms, Macmillan, New York, 1934.
13. H. Inaba and T. Kobayasi, Nature 224: 170, 1969.
14. T. Hirschfeld, S. Klainer, and R. Burton, Proc. Electro-optical Systems Design Symposium, p. 418, September 1969.

15. D. A. Leonard, *Nature* 216: 142, 1967.
16. J. A. Cooney, *Appl. Phys. Letters* 12: 40, 1968.
17. S. H. Melfi, J. K. Lawrence, and M. P. McCormic, *Appl. Phys. Letters* 15: 295, 1969.
18. J. A. Cooney, *J. Appl. Meteorology* 9: 182, 1970.
19. T. Kobayasi and H. Inaba, *Appl. Phys. Letters* 17: 139, 1970.
20. T. Kobayasi and H. Inaba, *Proc. IEEE* 58: 1568, 1970.
21. V. E. Derr and C. G. Little, *Appl. Opt.* 9: 1976, 1970.
22. M. R. Bowman, A. J. Givson, and M. C. W. Sandford, *Nature* 221: 456, 1969.
23. S. Zaromb, *Proc. Electro-optical Systems Design Symposium*, p. 609, September 1969.
24. H. Kildal and R. L. Byer, private communication.
25. H. Inomata and T. Igarashi, *Trans. Technical Group on Quantum Electronics of the Inst. Elec. Comm. Eng. (IECE) of Japan QE-70-36*, December 1970. (In Japanese.)
26. T. Kobayasi and H. Inaba, *Opto-electron.* 2: 45, 1970.
27. W. Holzer, W. F. Murphy, and H. J. Bernstein, *J. Chem. Phys.* 52: 399, 1970.
28. P. Pringsheim, *Fluorescence and Phosphorescence*, Interscience, New York, 1949.
29. D. J. Bradley and F. O. Neill, *Opto-electron.* 1: 69, 1969.
30. G. Placzek, *Handbuch der Radiologie*, Akademische Verlagsgesellschaft, 1934; vol. VI(2), p. 209.
31. J. Berlinger, in H. A. Szymanski, ed., *Raman Spectroscopy, Theory and Practice*, Plenum Press, 1967; p. 168.
32. E. J. Stransbury, M. F. Crawford, and H. L. Welsh, *Can. J. Phys.* 31: 954, 1953.
33. D. A. Leonard, *J. Appl. Phys.* 41: 4238, 1970.

LASER-INDUCED DEGRADATION OF INORGANIC SYSTEMS

N. E. VANDERBORGH, W. T. RISTAU, and S. COLOFF

Department of Chemistry, University of New Mexico, Albuquerque, N.M.

INTRODUCTION

Laser-induced degradation offers a rapid, reproducible method for the characterization of materials exhibiting low vapor pressures at usual temperatures. Several workers have shown that the product distribution resulting from the quenching of a laser plasma, monitored with a gas chromatograph, is characteristic for a wide variety of materials.¹⁻⁴

Some materials, typically amorphous, transparent solids, show low absorptivity of laser radiation. In these cases, the sample may be loaded with inert materials, typically powdered carbon, to absorb laser radiation more effectively.^{1,2} Previous experiments have shown that this loading can markedly effect product distributions.⁵ We have explored these effects more fully. Degradations effected upon organic molecules of high molecular weight are complicated in that large fragments result in addition to gases of low molecular weight such as acetylene, ethane, etc., which one would predict from the quenching process. This should not be the case when inorganic systems are degraded. We report here results obtained for degradations of nitrates, sulfates, thiosulfates, and oxalates.

Thermodynamic considerations allow a prediction of product distributions. Therefore, free-energy calculations were performed to determine the distribution with the lowest free energy. These calculations might also be quite useful in estimating temperatures reached during the laser thermal event.

APPROACH

Two types of experimental approach were used. Degradations were effected within a pyrolysis chamber connected on line to a Perkin-Elmer Model 800 gas liquid chromatograph. These studies were made with a Hughes Model HM-20 ruby laser (6943 nm) operating in the normal pulsed mode (Fig. 1).^{4,5} Other experiments were performed within the vacuum chamber of a time-of-flight mass spectrometer. The experimental arrangement is shown in Fig. 2. A 10-W continuous CO₂ laser, interrupted by a mechanical shutter, was focused through a KBr window into the ion-source compartment of a Bendix Model 12-101 TOF mass spectrometer. Also passing through the shutter was the beam from an alignment laser which fell upon a photodiode; the output from this device was recorded along with outputs from two separate m/e channels. Studies of this type have been reported by several workers, including Lincoln⁶ and Vastola.⁷

Many of the gaseous products are not detectable with a flame ionization detector. The gas chromatograph was modified to include a beta-induced luminescence detector at a tee at the end of the chromatographic column. Either or both detectors could be used to record the products from any specific laser degradation event. Unfortunately, neither of these detectors shows a response for nitrogen gas.

Reagent-grade chemicals were used as received. Carbon loading was effected by mixing Darco (R)(G-60), nominally 5 per cent by weight, with the compound of interest, grinding carefully and then loading 40-40 mg

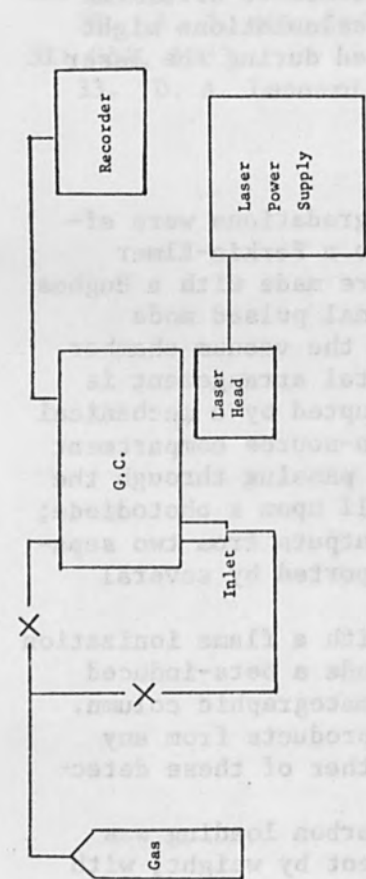


FIG. 1.--Schematic representation of laser-gas chromatographic apparatus.

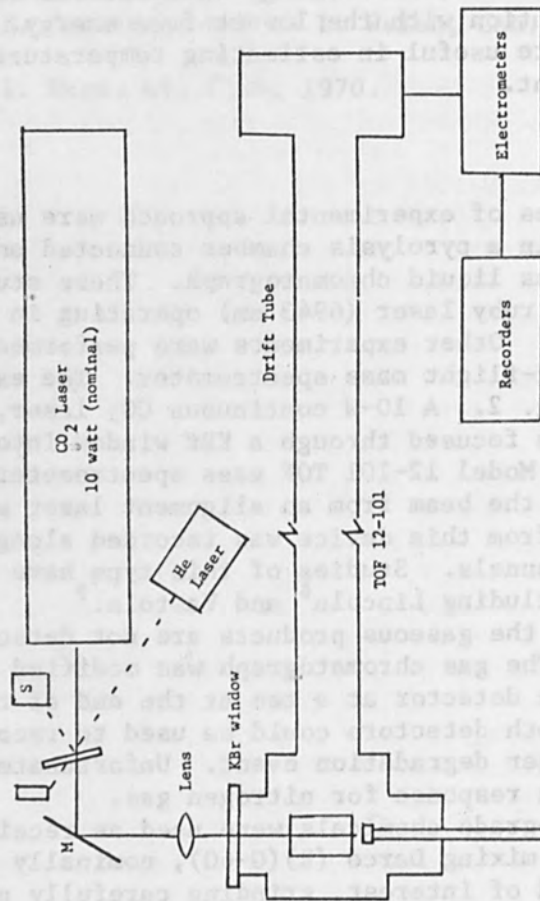


FIG. 2.--Representation of laser-TOF mass spectral instrumentation. Laser: CO₂, 0-10 W, continuous wave. TOF : Bendix Model 12-101, operated at 5×10^{-5} torr (during pyrolysis).

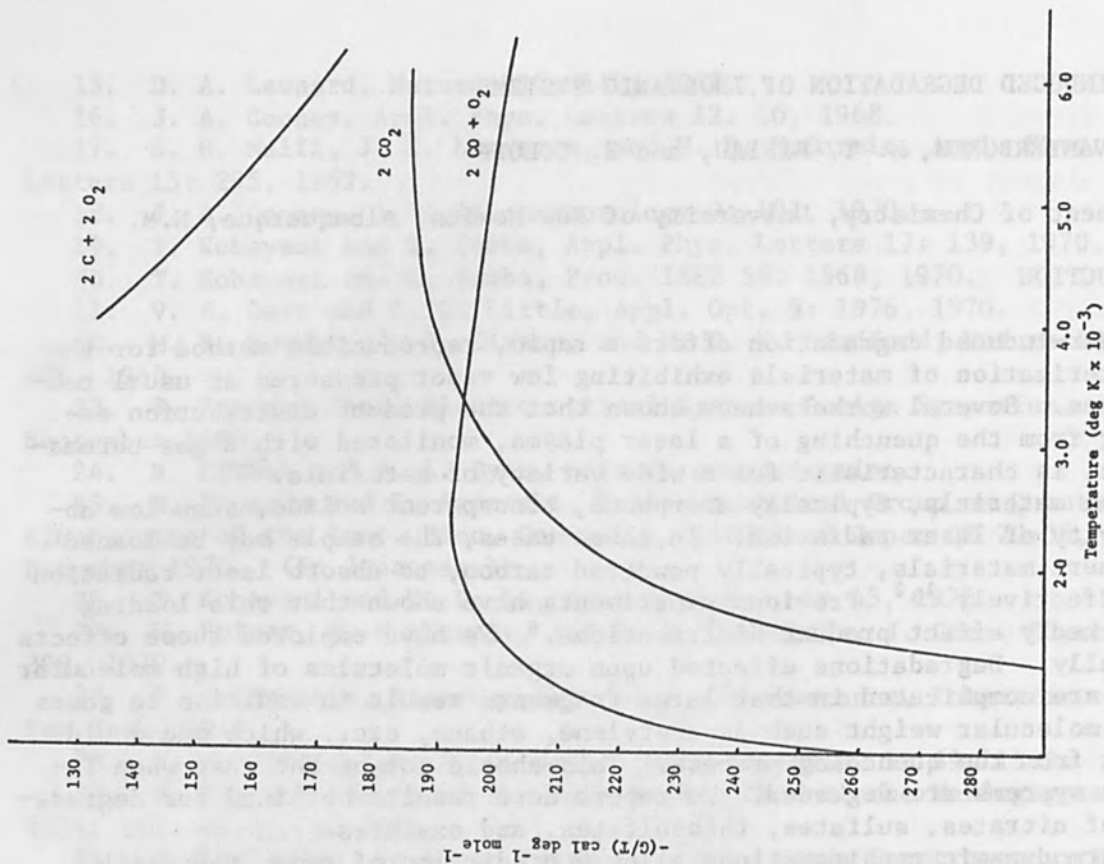


FIG. 3.--Standard free energies for distributions resulting from sodium oxalate.

into the pyrolysis assembly. Typically 3-4 mg of sample was consumed in any experiment.

The prediction of products resulting from a degradation process is not entirely straightforward. For instance, for silver sulfate, several possible product distributions are possible:



Here we represent the process as two distinct steps, laser heating resulting in pumping matter into the plume followed by quenching, into one of five possible product distributions. Experimentally we find that each event leaves behind a silver mirror (on the walls of the degradation chamber) and thus leads to the elimination of the first two distributions.

Standard free energy changes in a chemical process are given by

$$\Delta G_R^\circ = \sum (\Delta G_F^\circ)_{\text{products}} - \sum (\Delta G_F^\circ)_{\text{plasma}} \quad (2)$$

where ΔG_F° refers to the change in free energy corresponding to a chemical substance in its standard state from that of the elements in their standard state. Higher stability is shown by larger negative free energies of formation. It is not necessary to reference these changes back to normal standard states if our task is only to determine stabilities. For instance we compare the relative stability of the following:



We consider some temperature reached during cooling of the plasma when stable chemical bonds first form. Since only relative stabilities need be considered, we assign the free energy of the plasma an arbitrary zero value and then calculate the total free energies for the different product distributions. The distribution with the lowest free energy is the most stable. Moreover, for two distributions with closely similar energies, we can predict the probability of finding each distribution using an equation of functional form given by the Boltzmann relationship.

It is then necessary to determine free energies as a function of temperature. Free-energy functions, $(G-H)/T$, are readily available over the temperature range of 0 to 6000°K and standard enthalpies are also available. From these values, estimations for energies over the temperature range of 500 to 6000°K were determined. Such computations are shown in Figs. 3-5 plotted as (G/T) , cal/mole-K, vs temperature.

RESULTS

Silver nitrate, barium, silver and mercury(I) sulfates, barium thiosulfate, and sodium oxalate were degraded using the pulsed ruby laser-gas chromatograph apparatus. Results are shown in Table I. Silver nitrate

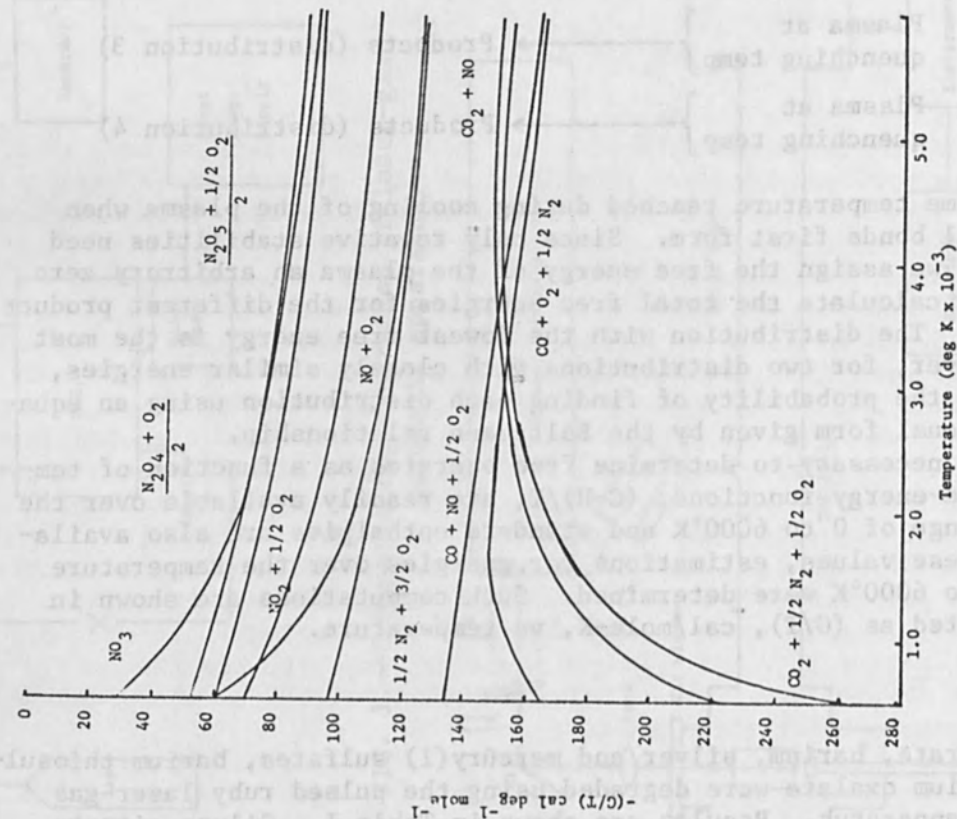


FIG. 4.--Standard free energies for distributions resulting from silver nitrate and carbon-loaded silver nitrate.

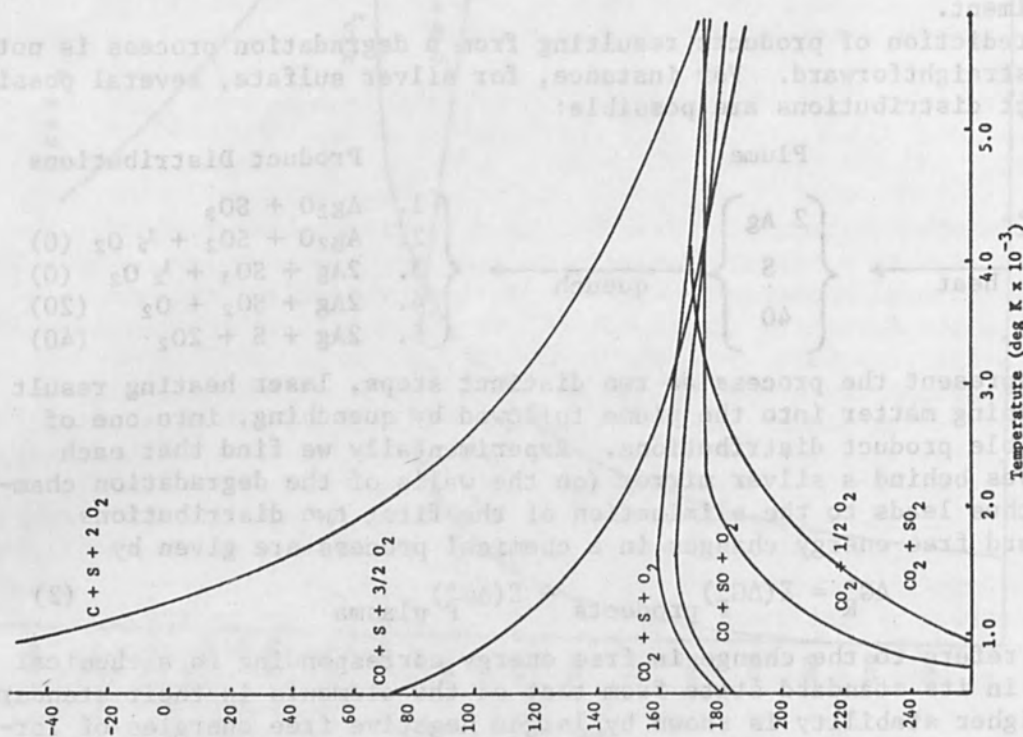


FIG. 5.--Standard free energies for distributions resulting from carbon-loaded sulfate systems.

TABLE I.--Comparison of predicted and determined product distributions from thermally quenched plasma.

System (a)	Predicted products (b)	T (c)	Observed products (d)
AgNO ₃	N ₂ (0.20) (e), O ₂ (0.70), NO (0.10)	4000	O ₂ +NO (0.99), NO ₂ (T), Ag
AgNO ₃ +C	N ₂ (0.20), O ₂ (0.30), CO ₂ (0.25) CO (0.25), NO (T)	3300	CO+O ₂ (0.80), CO ₂ (0.20), Ag
AgNO ₃ +C	N ₂ (0.10), CO+O ₂ (0.80), CO ₂ (0.10)	3500	
BaSO ₄	O ₂ (0.50), SO ₂ (0.50)	3500	O ₂ (0.50), SO ₂ (0.50)
Ag ₂ SO ₄	O ₂ (0.50), SO ₂ (0.50)	4000	O ₂ (0.50), SO ₂ (0.50), Ag
Hg ₂ SO ₄	O ₂ (0.66), SO ₂ (0.33), S	4500	O ₂ (0.50), SO ₂ (0.50)
Ag ₂ SO ₄ +C	CO+O ₂ (0.50), CO ₂ (0.25), SO ₂ (0.25)	3800	CO+O ₂ (0.85), CO ₂ (0.15), SO ₂ (T), Ag, S
	CO+O ₂ (0.90), CO ₂ (0.05), SO ₂ (0.05)	4100	
BaS ₂ O ₃	O ₂ (0.05), SO ₂ (0.95)	4000	O ₂ (0.05), SO ₂ (0.95), S
	O ₂ (0.15), SO ₂ (0.85)	4400	
BaS ₂ O ₃ +C	(see SO ₄ +C, above)		CO+O ₂ (0.90), CO ₂ (0.10), S
Na ₂ C ₂ O ₄	CO+O ₂ (0.50), CO ₂ (0.50)	3500	CO+O ₂ (0.92), CO ₂ (0.08)
	CO+O ₂ (0.80), CO ₂ (0.20)	3700	
	CO+O ₂ (0.99)	4000	
Na ₂ C ₂ O ₄ +C			CO+O ₂ (0.98), CO ₂ (0.02)

(a) Carbon-loaded systems, 5% C, by weight.

(b) Numbers in parentheses show mole fractions with estimated accuracy of $\pm 10\%$.

(c) Temperature (deg K) at which predicted distribution was calculated.

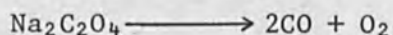
(d) Numbers in parenthesis show mole fractions with relative standard deviation of $\pm 2.0\%$.

(e) Nitrogen cannot be detected with the experimental apparatus used.

yields a residual silver mirror and a mixture of NO and O₂. It is probable that N₂ also is included in this distribution but neither of the detectors used in this study could verify the presence of N₂. The sulfates show a mixture of SO₂ and O₂; barium thiosulphate shows predominately SO₂ with a small amount of O₂, and sodium oxalate shows a mixture of CO and O₂ (these gases are not separable with the columns used) and carbon dioxide.

Carbon loading on these systems affects the product distributions to a remarkable degree. In the case of nitrate, sulfate, and thiosulfate systems, we note a shift from oxides of nitrogen and sulfur to oxides of carbon.

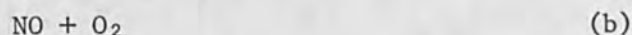
These results can be predicted to some degree from free-energy considerations. Degradations of sodium oxalate yields a product distribution of a mixture of CO + O₂ with a small amount of CO₂, approximately 0.08 mole fraction. Free-energy calculations were done on two different product distributions:



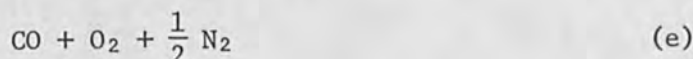
Results are shown in Fig. 3. Here we see that the first distribution should predominate up to a temperature of 3300°K; at higher temperatures,

the second distribution, resulting in a mixture of CO and O₂, is more probable. The determined distribution shows a small amount of CO₂ and indicates the products formed at a temperature near 3500°K.

Free-energy computations of possible product distributions resulting from degradations of silver nitrate are shown in Fig. 4. For systems with no carbon present, higher nitrogen oxides (NO₃, N₂O₄, N₂O₅, etc.) are clearly unfavorable distributions; we should expect to find one of the following distributions:



Experiment results show predominately O₂ + NO with a trace (less than 0.1%) of NO₂. The most favorable distribution, up to a temperature of 5500°K, is (a), containing N₂. Since the detection system is not responsive to this molecule, we cannot distinguish between distributions (a) and (b). Adding carbon to the system results in distributions of lower free energy:



Up to a temperature of 3100°K, distributions (d) and (g) are most favorable; at higher temperatures, distribution (6) predominates. Experimentally, we find a mixture containing CO + O₂ + CO₂. We would not expect to find CO₂ at temperatures in excess of 3700°K. The inability to determine nitrogen precludes the estimation of a lower temperature. However, the reason for finding a distribution richer in carbon oxides is quite clear.

Degradations on sulfate systems yields a equimolar mixture of SO₂ and O₂. Free-energy predictions show this is the expected result up to a temperature in excess of 4000°K. Carbon loading the sulfate system results in a mixture containing CO, O₂, and CO₂ with no sulfur oxides. Free-energy predictions (Fig. 4), show significant amounts of SO₂ in the distribution up to a temperature of 3800°K.

Degradations conducted within the time of flight mass spectrometer (TOF) yielded additional information concerning both the pyrolysis and quenching processes. These experiments differ from those reported up to now in two ways. A cw, low power, 10-W CO₂ laser was used and the degradations were performed within the mass spectrometer, i.e., at pressures of 10⁻⁵ torr instead of within a flowing stream of helium gas at pressures of about 10³ torr.

Two experimental approaches were used with the TOF instrumentation. The first simply used the CO₂ laser radiation to vaporize the sample. Again, the effects of carbon loading were investigated. Table II shows results obtained for BaSO₄ and BaS₂O₃. These spectra, run with an ionizing voltage of 100 V and under continuous illumination, show general agreement

TABLE II.--Time of flight mass spectral investigations of pure and carbon-loaded BaSO₄ and BaS₂O₃. (Experimental conditions: Ionizing voltage = 100 V, Bendix Model 12-101; TOF mass spectra; spectra normalized to read 100 for the most intense peak, laser intensity = 7.0 W; T = trace.)

Compound	Fragments	m/e	Background ^(a)	Pure ^(b)	5% Carbon loaded ^(c)
BaSO ₄	Ba	137	0	0	0
	S	32	(d)	(d)	(d)
	SO	48	0	21	11
	SO ₂	64	0	21	14
	SO ₃	80	0	35	11
	SO ₄	96	0	0	0
	Ar	40	46	39	39
	C	12	0	0	16
	CO	28	(e)	(e)	(e)
	CO ₂	44	0	0	100
BaS ₂ O ₃	Ba	137	0	0	0
	S	32	(d)	(d)	(d)
	SO	48	0	33	T
	SO ₂	64	0	100	16
	SO ₃	80	67	100	50
	S ₂ O ₃	112	0	T	T
	Ar	40	82	50	50
	C	12	0	0	0
	CO	28	(e)	(e)	(e)
	CO ₂	44	0	0	1

(a) Background spectra with no irradiation.

(b) Spectra of pure material.

(c) Similar spectra with carbon loaded sample.

(d) Impossible to monitor due to O₂ interference.

(e) Impossible to monitor due to N₂ interference.

with results obtained from the ruby laser experiments. BaSO₄ degradations yield a mixture of SO, SO₂, and SO₃. (Product distributions are quite altered by the secondary degradation process, the electron beam within the ion source.) Addition of carbon to the sample markedly changes the product distribution to yield, predominantly, CO₂, with a corresponding decrease in the intensity of the peaks resulting from sulfur oxides.

Other experiments made use of the time-resolution features of the TOF. The laser beam was interrupted with a mechanical shutter, which allowed for reproducible pyrolysis times. Rather long exposure times were necessary to deposit sufficient energy into the material to record a measurable trace. Figure 6 shows the time-resolved spectra monitoring peaks at m/e 44 (CO₂⁺) and 64 (SO₂⁺) resulting from the degradation of carbon-loaded BaSO₄. The uppermost trace records the irradiation profile, switching the beam on at the right-hand side and switching it off 0.99 sec later. (Time moves from right to left on the trace.) This figure leads to several observations.

The data show a representation of products resulting from the surface as the temperature of the material is increased. Initially, the material is at ambient temperature and heats up during the exposure period. Considerations of velocities and mean free paths expected under irradiation conditions of temperature and pressure lead to the conclusion that the transit time (from the BaSO₄ to the ion source) is less than the repetition time of

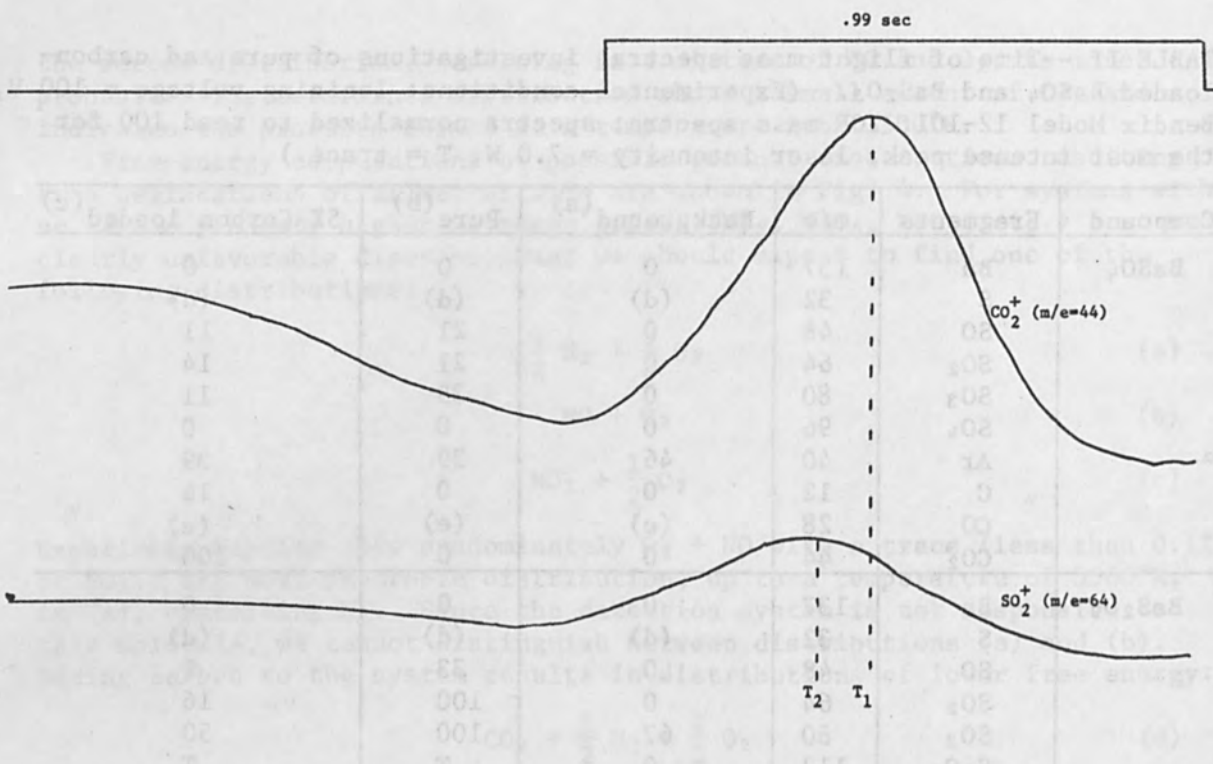


FIG. 6.--Time-resolved TOF spectrum with analog output monitoring m/e values of 44 and 64. (Sample: Carbon-loaded BaSO_4 , laser intensity 7 W.)

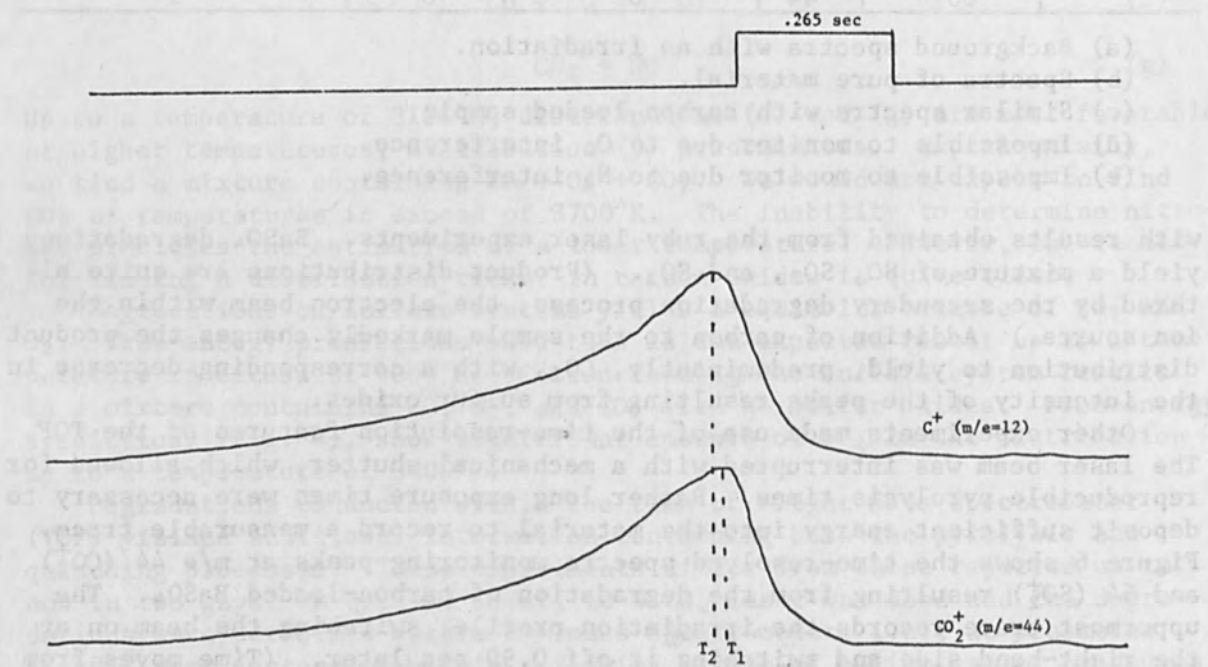


FIG. 7.--Time-resolved TOF spectrum with analog output monitoring m/e values of 12 and 44. (Sample: Carbon-loaded BaSO_4 , laser intensity 7 W.)

the instrument and that small differences in velocity resulting from differences in mass of CO_2 and SO_2 cannot be detected. As can be seen, after a time of approximately 0.1 sec, CO_2 is detected by the instrument, followed by SO_2 . Both of these peaks reach a maximum and then fall off to approximately background while the beam is still on. After the thermal event, during the cooling cycle, another CO_2 peak occurs as well as a long, flat peak due to SO_2 .

These results cannot be explained in the same manner as that given for the pulsed ruby laser-GC data. Here we must consider heating the solid sample, a mixture of BaSO_4 and carbon, with a continuous thermal flux of much lower energy than obtained by the pulsed ruby source. This lower flux does not provide sufficient energy to pump the chemical species into a plasma. Free-energy considerations must include heats of vaporization, values difficult to obtain. However, the data do indicate that CO_2 is formed initially and then the rate of production of CO_2 decreases and other chemical species predominate during the latter part of the thermal event.

We need now to find the fragments of lower molecular weight produced during the pyrolysis event. This knowledge would be helpful in predicting ultimate temperatures and, incidentally, verifying the conclusions drawn above. One would predict that both CO ($m/e = 28$) and O_2 ($m/e = 32$) would be possible products. Background nitrogen and oxygen interfere with measurements at both these m/e positions. Figure 7 shows a thermal pulse, now of 0.265-sec duration, on the same system. Here both m/e 44 (CO_2^+) and m/e 12 (C^+) are monitored. The peak of 44 slightly precedes that of m/e of 12. Certainly the majority of the carbon peak results from the second degradation process, ion bombardment of CO_2 . However, if this were the only source of m/e 12, the 12 peak and 44 peak should have identical shapes. The profiles are similar but the data indicate that C ($m/e = 12$) slightly lags the CO_2 peak and that not all of the peak $m/e = 12$ results from ionic bombardment of CO_2 . The process that produces C^+ is most probably pumping unreacted carbon into the ion source. Thus, we conclude that the disappearance of CO_2 (Fig. 6) results in $\text{CO} + \text{O}_2$ with surface temperatures of approximately 3800°K, quite similar to those found with the ruby laser experiments.

CONCLUSIONS

These experiments show that carbon loading should affect product distributions resulting from the quenching of plasmas containing inorganic ions. A quenching route to a lower total free energy is offered and can be predicted from thermodynamics.

Quenching temperatures for all pulsed laser systems studied indicate that the product distribution results in the temperature range of 3600-3900°K. Degradation of various metallic sulfates show that the metal ion is not a factor in determining the product distribution; all show an equimolar mixture of O_2 and SO_2 as predominate products. Carbon loading changes the product distribution, predominantly to oxides of carbon.

Time of flight mass spectral studies show agreement with the conclusions reached using pulsed laser radiation. There, from carbon loaded sulfate systems, CO_2 is produced at the surface of the material. Comparison of the product distributions resulting from a ruby laser and from a CO_2 laser, indicates similar degradation and quenching processes.

ACKNOWLEDGMENT

The authors would like to express their appreciation to the U.S. Air Force Weapons Laboratory (Kirtland AFB, Albuquerque, N.M.), where the mass spectral experiments were performed.

REFERENCES

1. B. T. Guran, R. J. O'Brien, and D. H. Anderson, *Anal. Chem.* 42: 115, 1970.
2. O. F. Folmer and L. U. Azarraga, *Advances in chromatography-1969*, in A. Zlatkis (ed.), Preston Technical Abstracts.
3. R. H. Wiley and P. Veeraga, *J. Phys. Chem.* 72: 2417, 1968.
4. W. T. Ristau and N. E. Vanderborgh, *Anal. Chem.* 42: 1848, 1970.
5. W. T. Ristau and N. E. Vanderborgh, *Anal. Chem.* 43: 702, 1971.
6. K. A. Lincoln and D. Werner, Time-resolved mass spectrometry applied to laser-induced vaporization, paper presented at 15th Annual Conference on Mass Spectrometry and Applied Topics, Denver, Colo., May 1967.
7. F. J. Vastola, A. J. Pirone and B. E. Knox, The production of vapor species in a mass spectrometer ionization chamber, paper presented at 14th Annual Conference on Mass Spectrometry and Allied Topics, Dallas, Texas, 1966.
8. JANAF Thermochemical Tables, Institute for Applied Technology, National Bureau of Standards PB 168-370, 1965.

LASER-GENERATED ACOUSTIC WAVES IN LIQUIDS

LYNN HUTCHESON, OYVIND ROTH, and FRANK S. BARNES

University of Colorado, Boulder, Colo.

A study of the acoustic waves generated by a laser has been conducted by means of a small Q-switched ruby in variable concentrations of Prussian blue dye. Theories for the generation of acoustic waves by heat impulses have been developed by Gournay¹ and Hu² for the case of plane and spherical waves. The experimental results show a transition from plane to spherical approximations for the peak amplitude of the pressure wave with variations in dye concentration and focusing configuration. There is also some evidence for dye saturation and its effect on the shape of the acoustic waves. Techniques for measuring these acoustic pulses and preventing confusion by surface phenomena is also briefly described.

I. INTRODUCTION

There are several mechanisms by which a portion of the energy delivered by an optical pulse to a liquid may be converted into an elastic wave: thermal expansion, electrostriction, boiling, and dielectric breakdown.³⁻⁸ The present experiments are primarily limited to the range of parameters in which the principal mechanism for the generation of acoustic waves is thermal expansion.

Theories for magnitude and shape of these elastic waves have been developed in the plane wave case by Gournay¹ and in the spherical case by Hu.² In general, our results are in agreement with these theories over a limited range of parameters. When we account for changes in configuration with power density as a result of dye saturation, our results are brought into agreement with these linear theories. We also find generated wave shapes at both high and low power densities that seem to lie outside the present theory.

Both the linear theories are derived from Newton's second law, which may be written in the form²

$$\frac{D(\rho\vec{v})}{Dt} = \vec{F} - \nabla p + \text{loss terms due to viscosity} \quad (1)$$

where D/Dt is the total derivative, ρ is the density, \vec{v} is the velocity, \vec{F} is the driving force, and ∇p is the pressure gradient. For our problems the driving force \vec{F} is given by the thermal expansion and may be written as

$$\vec{F} = -B \nabla(\beta\theta) \quad (2)$$

where B is the adiabatic bulk modulus of the medium, β is the volume thermal expansion coefficient and θ is the excess temperature. Additionally, it is assumed that displacements μ are small so that to first order

$$p = -B \nabla \cdot \vec{\mu} \quad (3)$$

With these approximations, Eq. (1) can be rewritten as

$$\rho \frac{\partial^2 \vec{\mu}}{\partial t^2} = B \nabla(\beta\theta) + B \nabla(\nabla \cdot \vec{\mu}) \quad (4)$$

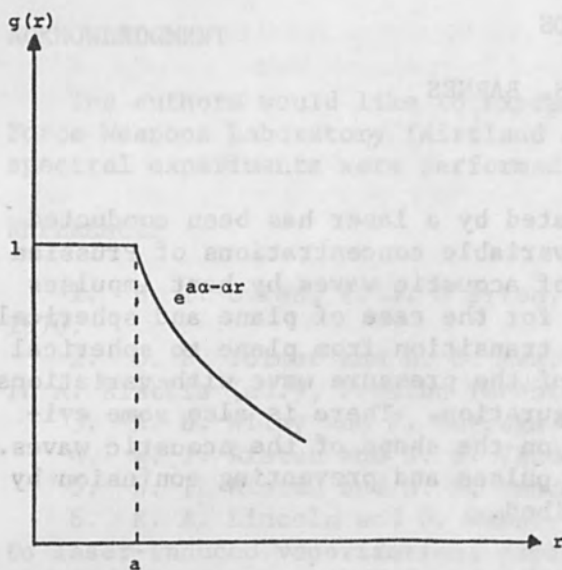


FIG. 1.--Normalized space distribution of laser intensity or temperature near focus.

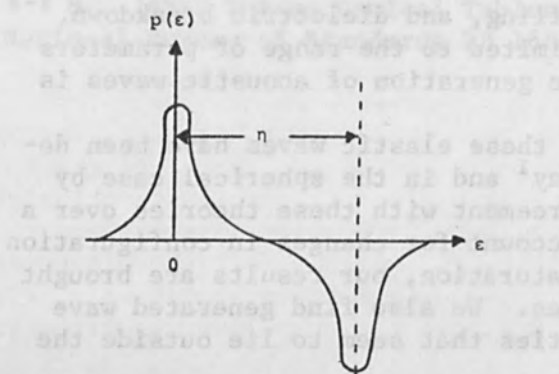


FIG. 3.--Pressure wave at any point as a function of normalized reduced time.

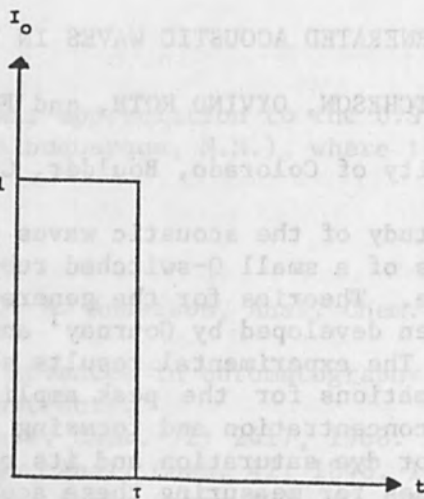


FIG. 2.--Normalized time distribution of laser intensity at any point in space.

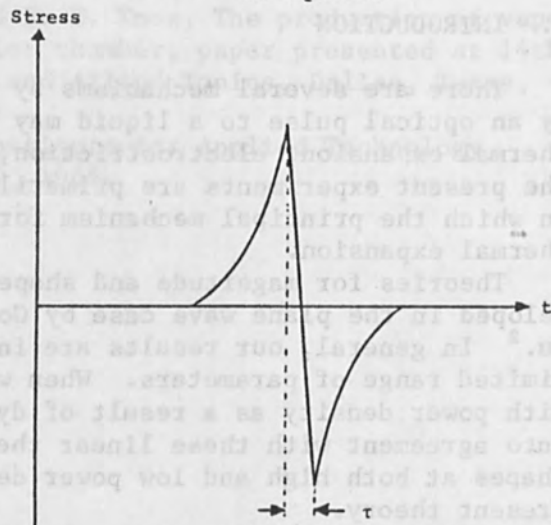


FIG. 4.--Computed stress in water as a function of time, free surface.

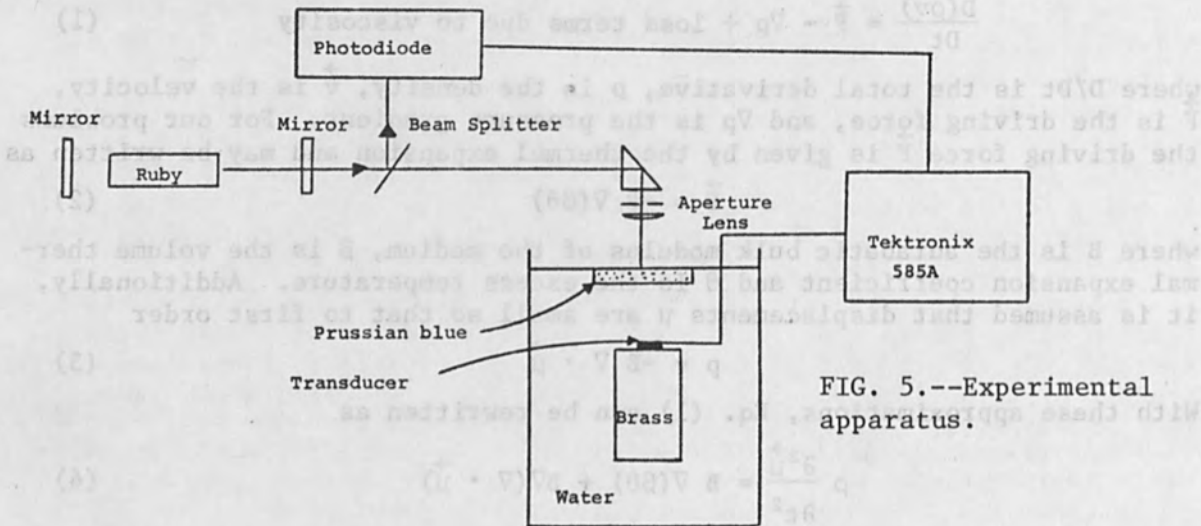


FIG. 5.--Experimental apparatus.

In the spherical coordinates with the initial conditions shown in Figs. 1 and 2, the wave shape shown in Fig. 3 can be obtained as a solution for the pressure wave as a function of normalized time at a radius r from the absorbing sphere. The parameters η and μ are defined by $\eta = \alpha\tau$ and $\epsilon = \alpha c [t - (r/c)]$ where c is the velocity of sound. The expression for the peak pressure is given by

$$P_{\max} = \frac{3c\beta P\alpha}{8\pi\sigma J r} \frac{[\alpha a]^2/2 + \alpha a + 1}{(\alpha a)^3 + 3(\alpha a)^2 + 6\alpha a + 6} \quad (5)$$

where P is the power in the pulse, J is the joule calorie conversion factor, and σ is the specific heat. Inspection of the terms in Eq. (5) shows that

$$P_{\max} \sim \frac{E}{\tau} \frac{1}{r} \quad (6)$$

where E is the pulse energy and τ is the pulse length.

In the plane-wave case¹ it is assumed that the power is absorbed in the medium as

$$I(x) = I_0 e^{-\alpha x} \quad (7)$$

and that we have a square pulse in time of length τ . With appropriate approximations and the assumption of a free surface at the incentive light boundary the pressure-vs-time wave shape is shown in Fig. 4. The peak pressure is given by

$$P_{\max} = \frac{c\beta I_0}{2J\sigma} (1 - e^{-\alpha c\tau}) \quad (8)$$

II. EXPERIMENTAL RESULTS

A. APPARATUS. The apparatus for the experimental part of this study consisted of a Q-switched ruby laser and its power supply, a photodiode, container with the absorbing liquid, ultrasonic transducer, and a Tektronix 585A oscilloscope. A laser calorimeter was also used intermittently to check laser output.

To generate the ultrasonic pulses, laser pulses were directed into a Prussian blue dye dissolved in water. An ultrasonic transducer was positioned in the ultrasonic field for the purpose of displaying the ultrasonic pulses on the scope. This transducer was a piezoceramic transducer (Clevite PZT-5) located at a known distance below the surface. Figure 5 shows the experimental setup.

The ruby laser delivered 5-15 MW in the Q-switched mode. The ruby rod was 3.5 in. long and 3/8 in. in diameter. The system was operated as a Q-switched laser by means of a 99.9-percent dielectric reflective mirror at 400 Hz, which yielded a very stable output with single-pulse action with a pulse width of 50 nsec.

B. MEASUREMENTS. The laser beam was focused onto the Prussian blue solution by means of a focusing lens. The illuminated area on the solution was circular in shape and had a radius of about 1 mm. For low absorption, the pulse has a rather unsymmetric shape--only a tensile stress pulse and virtually no compressible stress pulse. As α was increased, the pressure pulse rapidly built up to the point where P_{\max} became equal to P_{\min} . Beyond an intensity of 20-40 MW/cm², depending on the absorption coefficient of the medium, the pulse became much longer. These comparisons are shown in

FIG. 6.--Acoustic pulses generated by irradiating Prussian Blue with Q-switched ruby laser. (P = laser power, a = diameter of laser beam, α = optical absorption of Prussian Blue.)

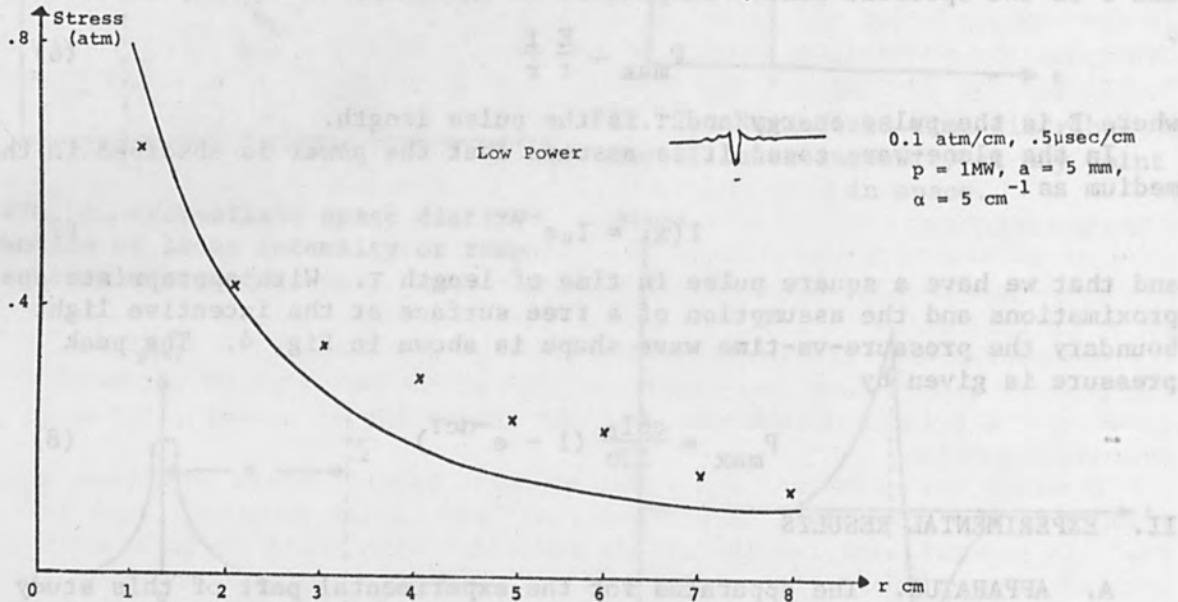
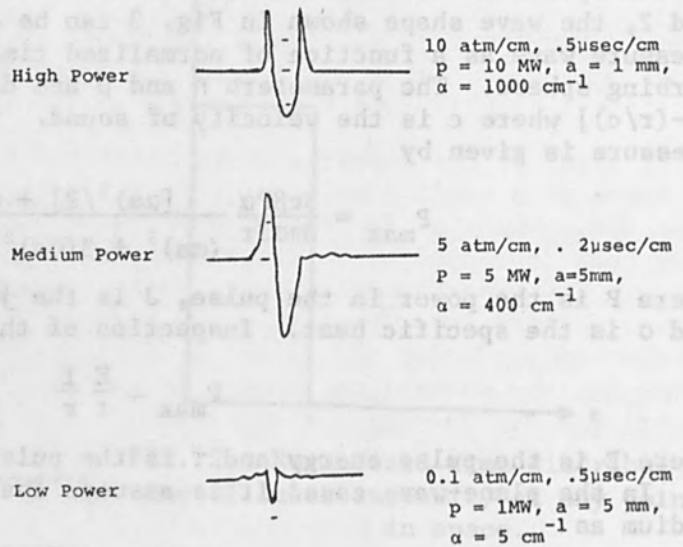


FIG. 7.--Experimental and theoretical behavior of peak stress vs radius of observation. ($P = 1 \text{ MW}$, $\tau = 100 \text{ nsec}$, $a = 1 \text{ mm}$, $\alpha = 20 \text{ cm}^{-1}$.)

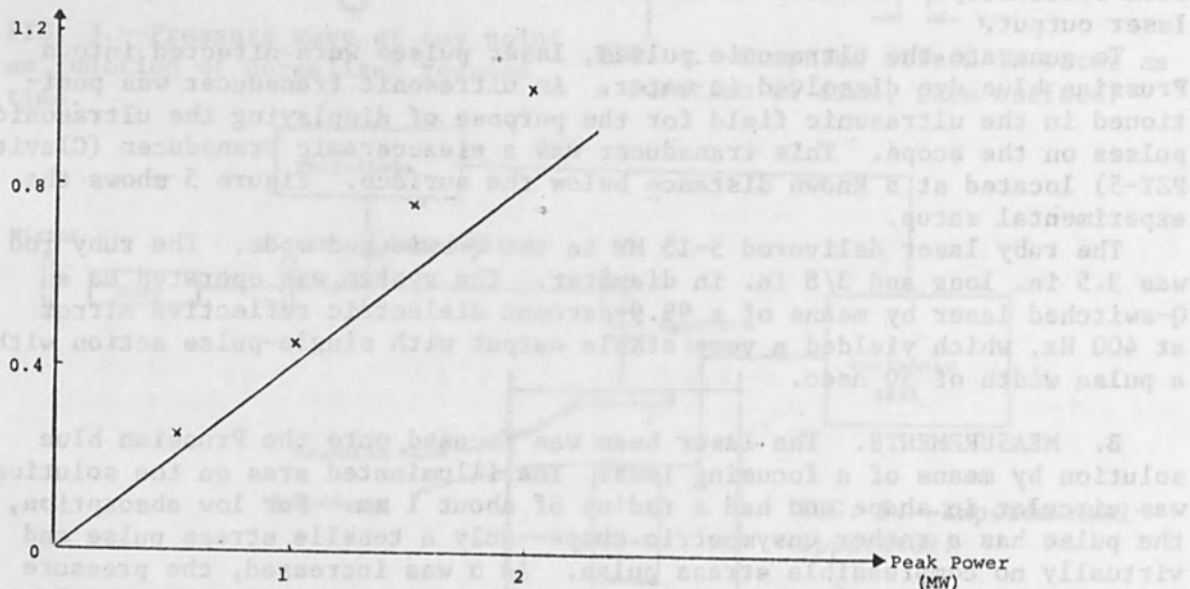


FIG. 8.--Theoretical and experimental behavior of peak pressure vs peak power. ($P = 1 \text{ MW}$, $\tau = 100 \text{ nsec}$, $a = 1 \text{ mm}$, $\alpha = 20 \text{ cm}^{-1}$.)

Fig. 6. The first pulse shape is not explained by the linear theories. In the midpower range we have good qualitative agreement, and in the high-power ranges again theory and experiment diverge.

We believe new theory needs to be developed to explain both the high- and low-power wave shapes. Such a theory will have to take into account the saturation of the dye absorption coefficient which will be discussed later.

The expression for P_{\max} in the spherical case was given by Eq. (5) and it showed that the stress amplitude is proportional to $1/r$. To check this variation a transducer was positioned at a 0° angle with respect to the axis of incoming light. Power was adjusted to 1 MW and the spot radius was 1 mm. Laser pulses were radiated into the medium and the generated acoustic pulses recorded on Polaroid film were picked up by the transducer at radii up to 8 cm. The same experiment was repeated with the transducer at an angle of 60° with respect to the laser impact point. These results were virtually the same as at 0° except for a very slight deviation in amplitude. Figure 7 shows the obtained results under 0° angle which are compared with theory. Except for a finite offset due to absolute stress units, the result is in agreement with theory. The physical reason for the $1/r$ dependence of the peak stress is the fact that the acoustic intensity is proportional to $1/r^2$ and that pressure is proportional to the square root of the acoustic intensity.

The maximum stress was measured as a function of laser peak power. The laser pulses were radiated into a solution of $\alpha = 20 \text{ cm}^{-1}$ and radius of impact of 1 mm and the radius of observation was 2 cm. To vary the power, the laser beam was radiated through an iris that pinched off more or less of the beam. Figure 8 shows the measured and theoretical relationship between maximum stress and laser power. The linear dependence appears to hold up to power densities of 150 MW/cm^2 .

The maximum stress as a function of α (absorption coefficient) was also measured. Here we set the power of the laser at 1 MW and varied α from 20 to 1200 cm^{-1} . The theoretical and experimental behavior for the maximum stress dependence on α are shown in Figs. 9 and 10. As can be seen from Eq. (5) the theoretical stress curve is proportional to the factor

$$\alpha \frac{[(\alpha a)^2/2] + \alpha a + 1}{(\alpha a)^3 + 3(\alpha a)^2 + 6\alpha a + 6} \quad (9)$$

Theoretical and experimental results are in close agreement for small α .

As the value of α increases the radiating configuration changes from one that approximated by a sphere to one which is better approximated by a thin disk. The limiting value for the peak stress wave changes from that given by Eq. (5) to that for a disk which is given by the plane wave expression in Eq. (8), with an appropriate modification for diffraction by the finite size of the spot. This change takes place at different α for different power densities, indicating that saturation increases the optical excited volume. The value of incident power governs the cutoff point; the new level is probably caused by diffraction-limited plane waves rather than spherical waves. Figure 10 shows the same sort of thing for $a = 5 \text{ mm}$.

The maximum stress was measured as a function spot radius a . Parameters chosen for this experiment were $P = 2 \text{ MW}$, $\alpha = 50 \text{ cm}^{-1}$, and $r = 2 \text{ cm}$. The spot radius a was changed by moving the focusing lens with respect to the absorbing medium. Resulting relationship between the generated peak stresses and spot radii from 0.3 to 1.5 mm is shown in Fig. 11 together with the theoretical curve. For this curve stress is proportional to

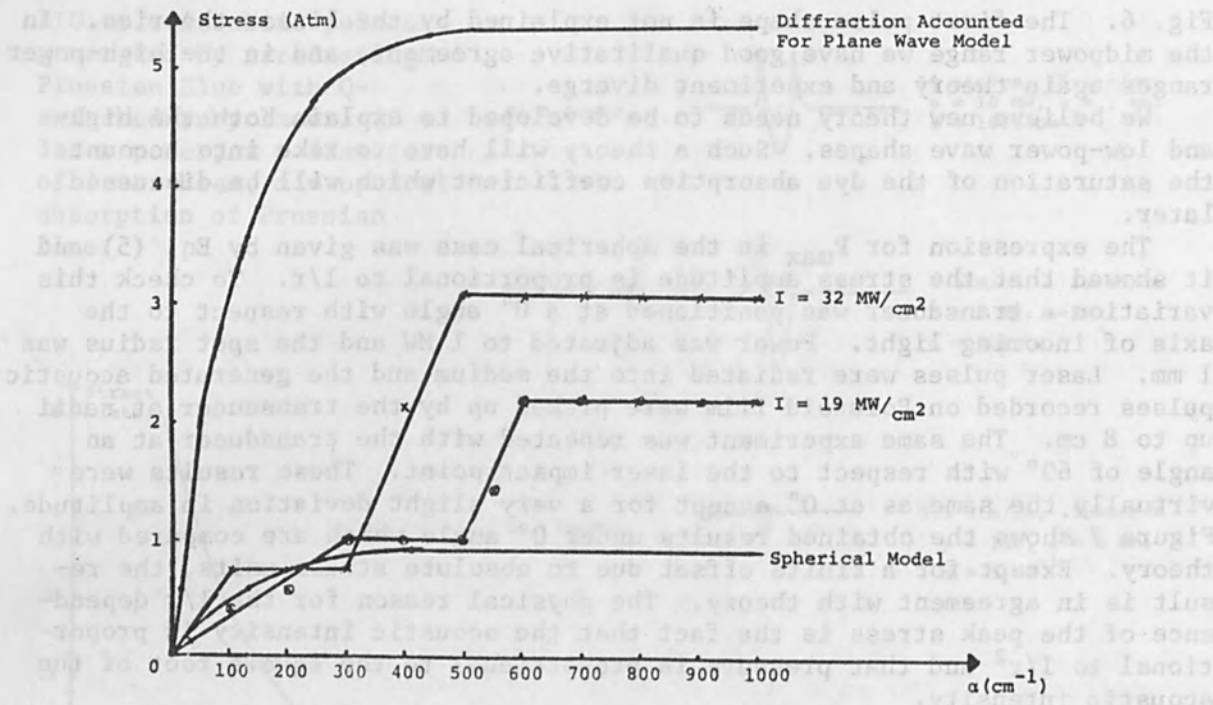


FIG. 9.--Theoretical and experimental peak stress vs absorption coefficient. ($r = 2$ cm, $\tau = 50$ nsec, $a = 1$ mm.)

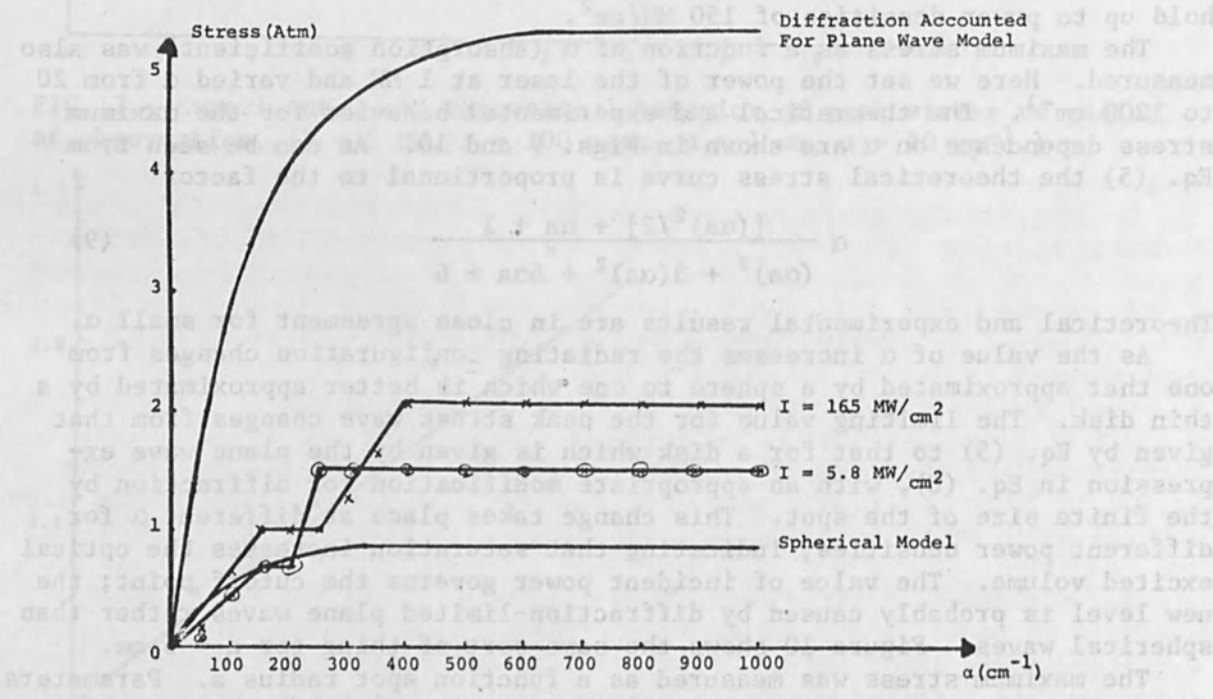


FIG. 10.--Theoretical and experimental peak stress vs absorption coefficient. ($r = 2$ cm, $\tau = 50$ nsec, $a = 5$ mm.)

$$\frac{[(\alpha a)^2/2] + \alpha a + 1}{(\alpha a)^3 + 3(\alpha a)^2 + 6\alpha a + 6} \quad (10)$$

For intensities below 150 MW/cm², there is a fairly good agreement between the predicted and experimental result. For higher intensities we see that the behavior contradicts the theory since the peak stress decreases with increasing intensity. It is reasonable to believe that at these high intensities, several effects occur that lower the conversion efficiency of optic to elastic energy. Boiling seems to be at least part of the reason. Furthermore, it is reasonable to believe that some of the linear relationships upon which theory is based do not hold at high intensities.

The effect of changing α as the input intensity is varied was also observed. Figure 12 shows how α varied as a function of input intensity for two different values of dye concentration. This experiment was made by comparing the peak light intensity at the input and output of a thin section of dye solution in a plane wave situation where

$$I(x) = I_0 e^{-\alpha \ell} \quad \text{or} \quad \alpha = \frac{1}{\ell} \ln \frac{I_i}{I_0} \quad (11)$$

where ℓ is the thickness of the dye solution, I_i is the input intensity, and I_0 is the output intensity. Here ℓ was chosen as 0.25 cm for both cases.

The last four figures indicate that the linear theory presented before is limited by the spot radius a , the absorption coefficient α , and the power input density I_i . When α is low spherical waves are generated because the beam penetrates a distance into the medium that is of the same order as the spot radius. Therefore it was surprising to observe spherical waves up to an absorption coefficient of $\alpha \approx 300 \text{ cm}^{-1}$. Such a high value of α and a spot radius of 1 mm would indicate a disk-like absorption configuration, leading to plane waves. However, time measurements indicated that a certain bleaching took place in the medium, thus causing the laser beam to penetrate farther into the medium than indicated by the value of α . In essence, the effective α was lower than expected. Figure 12 does in fact show that the effective α is low. This left us with a disk-like absorption of the electromagnetic energy, which generates plane waves, but since a spot radius of 1 mm was used, we obtained a small radiation aperture for the ultrasonic pulses and therefore wide-angle radiation.

From Fig. 12 a few reasonable calculations can be made relating the effective α to the expected α . Let $\alpha_e = (1/x)\alpha_0$ where α_0 is the expected and α_e is the effective values. Figure 12 shows curves for two values of α_0 (25 cm^{-1} and 10 cm^{-1}). For example, x was calculated for $I_i = 32 \text{ MW/cm}^2$ since this is a value for power density used for one of the curves in Fig. 9. For $\alpha_0 = 25 \text{ cm}^{-1}$, $x = 2.2$; for $\alpha_0 = 10 \text{ cm}^{-1}$, $x = 2.1$. These values are in quite good agreement with each other. Therefore, it can be assumed that x is constant for constant power density. From Fig. 9 the switch over from spherical waves to plane waves occurs at $\alpha = 300 \text{ cm}^{-1}$ for $I_i = 32 \text{ MW/cm}^2$. Therefore, our effective α_e is 136 cm^{-1} . This is certainly part of the reason for observing spherical waves at such high α , but not the only reason.

In conclusion we have shown that dye saturation must be taken into account in predicting the peak stress generated by typical Q-switched laser pulses and that further theoretical work will be required to describe the variety of wave shapes we observe.

REFERENCES

1. L. S. Gournay, J. Acoustical Soc. Am. 40: 1322, 1966.
2. C. L. Hu, *ibid.* 46: 728, 1969.
3. R. H. Cole, Underwater Explosion, Princeton University Press, Princeton, 1948.
4. U. S. Office of Naval Research, Underwater Explosion Research, U.S. Office of Naval Research, Washington, D. C., 1950.
5. E. Gamire, F. Pandarese, and C. H. Townes, Phys. Rev. Letters 11: 160, 1963.
6. H. Chiao, C. Townes, and N. Stoichef, *ibid.* 12: 592, 1964.
7. R. G. Brewer and K. E. Riechoff, *ibid.* 13: 334-336, 1964.
8. E. F. Carome, C. E. Moeller, and N. A. Clark, J. Acoustical Soc. Am. 40: 1462-1466, 1966.

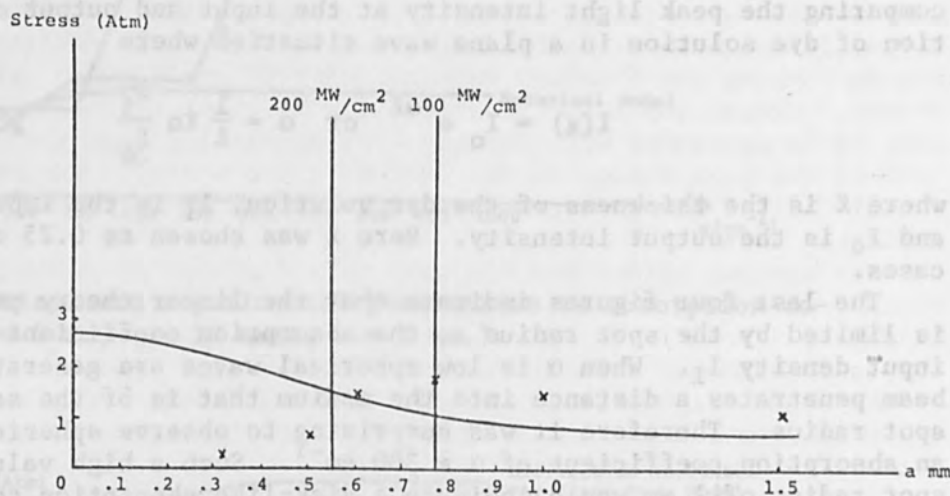


FIG. 11.--Theoretical and experimental behavior of peak stress vs radius a . ($P = 2 \text{ MW}$, $\tau = 50 \text{ nsec}$, $\alpha = 50 \text{ cm}^{-1}$, $r = 2 \text{ cm}$.)

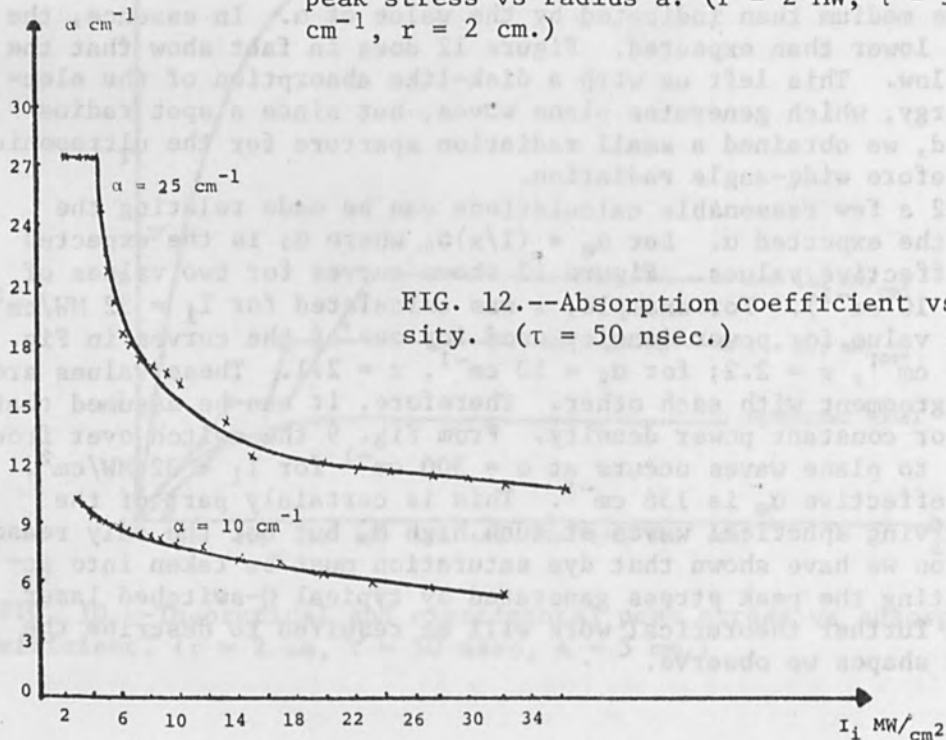


FIG. 12.--Absorption coefficient vs input intensity. ($\tau = 50 \text{ nsec}$.)

DEVELOPMENT AND APPLICATION OF A 1-MV, 1-MA MYLAR DIELECTRIC PULSED ELECTRON ACCELERATOR AND CONCEPTS FOR HIGHER ENERGY MODULAR GENERATOR SYSTEMS*

G. YONAS, I. SMITH, P. SPENCE, S. PUTNAM, and P. CHAMPNEY

Physics International Company, San Leandro, Calif.

INTRODUCTION

Pulsed relativistic electron beams have been used over the last five years for applications to the following:

- (1) pulsed bremsstrahlung generation
- (2) ion acceleration
- (3) high energy density equation-of-state studies
- (4) plasma heating

In each of these areas it has become apparent that requirements for higher output currents from pulsed electron-beam generators necessitate a modularization of machine components and the combination of the outputs from these separate generators. This modular approach has already been employed in the generators themselves, as illustrated in this paper. However, the next order-of-magnitude increase in output current will require the transport and combination of beams from separate generators. The objective of this paper is to illustrate these two types of modularization and recombination. The first section describes the manner in which eight separate Mylar dielectric Blumleins have been combined to obtain 1.0 MA of output current from a single diode. The following section presents alternative schemes for beam transport and combination of beams from several such diodes. Each of these techniques is described in terms of its advantages and limitations.

PULSER DESCRIPTION

The pulsed electron accelerator constructed for these experiments is shown in Fig. 1. Design output levels for this machine (SNARK) were peak voltage and current levels of 1 MV and 1 MA. Since the maximum linear current density from a Mylar stripline into a matched load is 330 kA/m (at the peak operational stress of 1.5 MV/cm) it was decided to use two modules, each containing two parallel lines with copper electrodes 1.35 m wide, in order to operate at more conservative electric field levels. Each module could therefore safely provide 500 kA at operating fields of 0.85 MV/cm. Another factor in the design of the pulser was the desire to limit the absolute voltage on a single Blumlein to a value ≤ 500 kV (on the basis of previous experiments with high voltage Mylar striplines.) Thus in order to achieve the output voltage of 1 MV, two additional lines were placed in series with the above two parallel lines in each module (Fig. 2). Each Blumlein has an impedance of 1.1Ω , giving a module impedance for the series-parallel combination of 1.1Ω . The over-all generator impedance is therefore 0.55Ω from the two modules connected in parallel. In order to achieve the design goal for a $1-\Omega$ tube, each Blumlein must be pulsed charged to 400 kV.

The lines are immersed in a copper sulphate solution to avoid flashover problems at the edges of the copper sheets which compose the Blumleins.

*Work supported in part by U.S. Defense Atomic Support Agency.

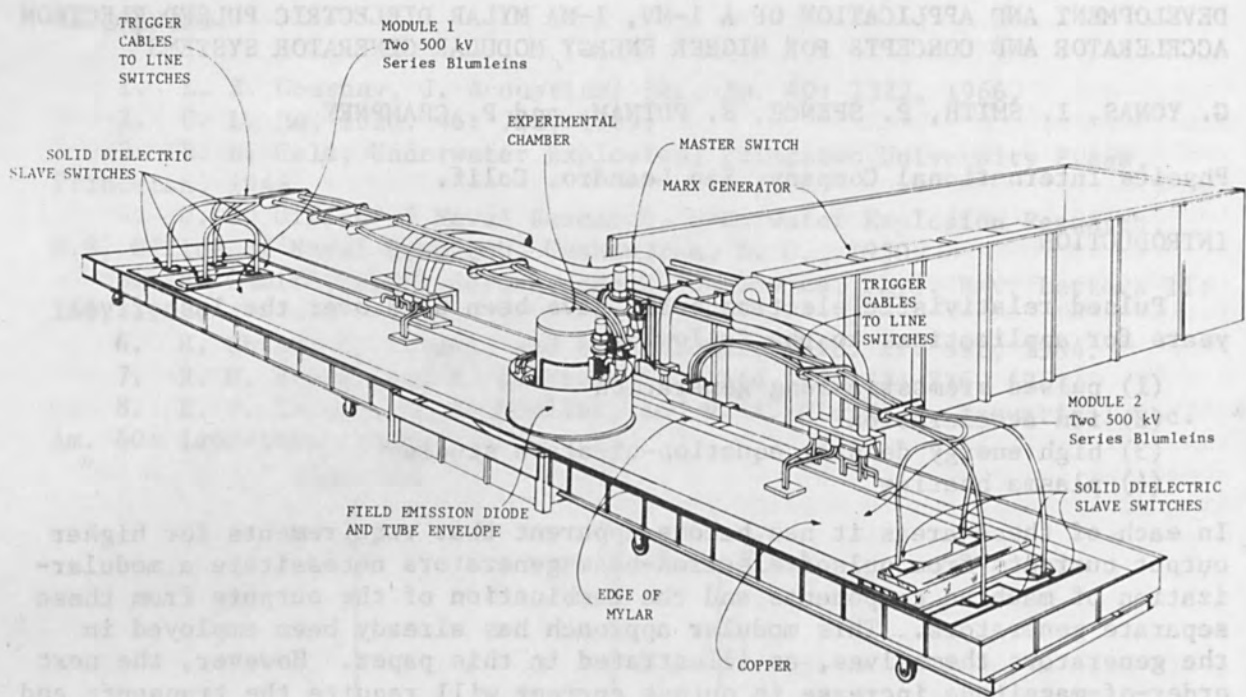


FIG. 1.--SNARK layout. 1-MV, 50-nsec pulsed electron accelerator.

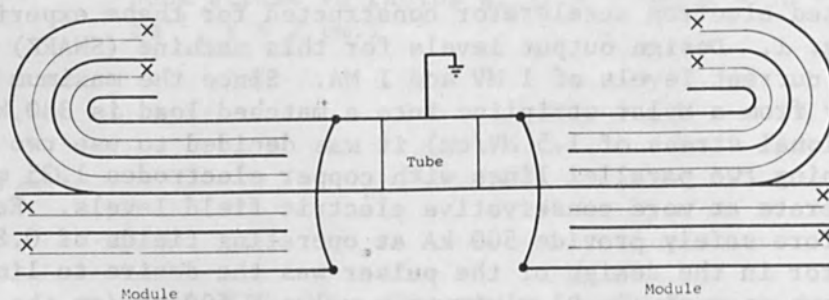


FIG. 2.--Schematic of SNARK.

The resistive solution is allowed to form a thin tapered layer leading from the edge of the sheet by attaching a wire bead to the edge of the copper. This layer acts like a resistor in series with the edge of the line to reduce the electric fields. The lines are assembled dry and then impregnated with CuSO_4 solution while under vacuum. This process considerably eases assembly and minimizes the possibility of bubble formation during operation.

The lines are pulse-charged from a separate Marx tank containing 72 0.5- μF capacitors wired in six stages. Charging cables lead from the Marx to the lines and each line is fired by means of a triggered slave switch. A self-firing master switch sends synchronized trigger pulses to the slave switches. These switches were originally replaceable stabbed polyethylene cards and provided current risetime in the 10^{14} -A/sec range through multichanneling in each of the eight switches. However, this method required an inconvenient process of switch card changing between shots, and the cards have been replaced by recently developed gas switches.² These 7.0-nH triggered rail-type switches have operated over a range of from 80 to 450 kV at currents up to 0.9 MA and have shown reproducible multichanneling for a large number of shots without maintenance.

The tube configuration is shown schematically in Fig. 3. A single, 1.5 m-diam cast epoxy insulator 15 cm wide is designed to permit operation at 1 MV. The anode plate is recessed into the insulator so as to hold the gap between the anode and the cathode plate to a minimum. Cleaning and oiling the cathode plate between shots assures that this gap can withstand over 500 kV/cm without emission. The anode plate and test volume together with the associated vacuum system are removed from the tube between shots to allow access to the cathode surface and insulator.

The postulated output of SNARK operating at the maximum charging voltage can be deduced as outlined in Fig. 4. The major energy losses occur during transfer of energy from the Marx generator into the Mylar itself, where there is a 40-percent energy loss due largely to the parallel copper sulphate resistive line edges. There is an additional energy loss of 20 per cent due to series damping resistance in the Marx. Such large losses are not inevitable, but are accepted as the price for minimizing the possibility of line damage. A further 25-percent loss occurs due to use of a safety factor with a self-fire master switch (self-fire at 85-percent peak Marx output), but this could be reduced by use of a triggered master switch fired closer to peak Marx output. Additional energy loss occurs in the transfer of energy from the charged striplines into the electron beam; the primary loss processes being impedance mismatch (between line and load) and impedance collapse. With these transfer losses, and a Blumlein pulse charge of 400 kV, 65 kJ is stored in the line and it is reasonable to expect an electron beam output in the range of 50 kJ.

The maximum measured output of the generator to date has been 56 ± 5 kJ when the lines were connected to a 0.55- Ω resistive load. Diagnostic traces from this shot and a similar 40 ± 4 -kJ shot are shown in Fig. 5. On the higher shot, the line was charged to slightly over 400 kV and an edge breakdown in the Mylar near one side of the tube occurred after the main discharge pulse. Since the operating fields were well below that thought to be maximum, the reason for the failure is not known. Because of this type of failure, it may be necessary to add two additional series Blumleins to each module to achieve the 1-MV 1-MA output reliably. However, further work will be needed to identify the cause of this failure.

The pulser has reliably produced electron beam output levels of 25 kJ when the load used is a single field emission diode. Output diagnostics

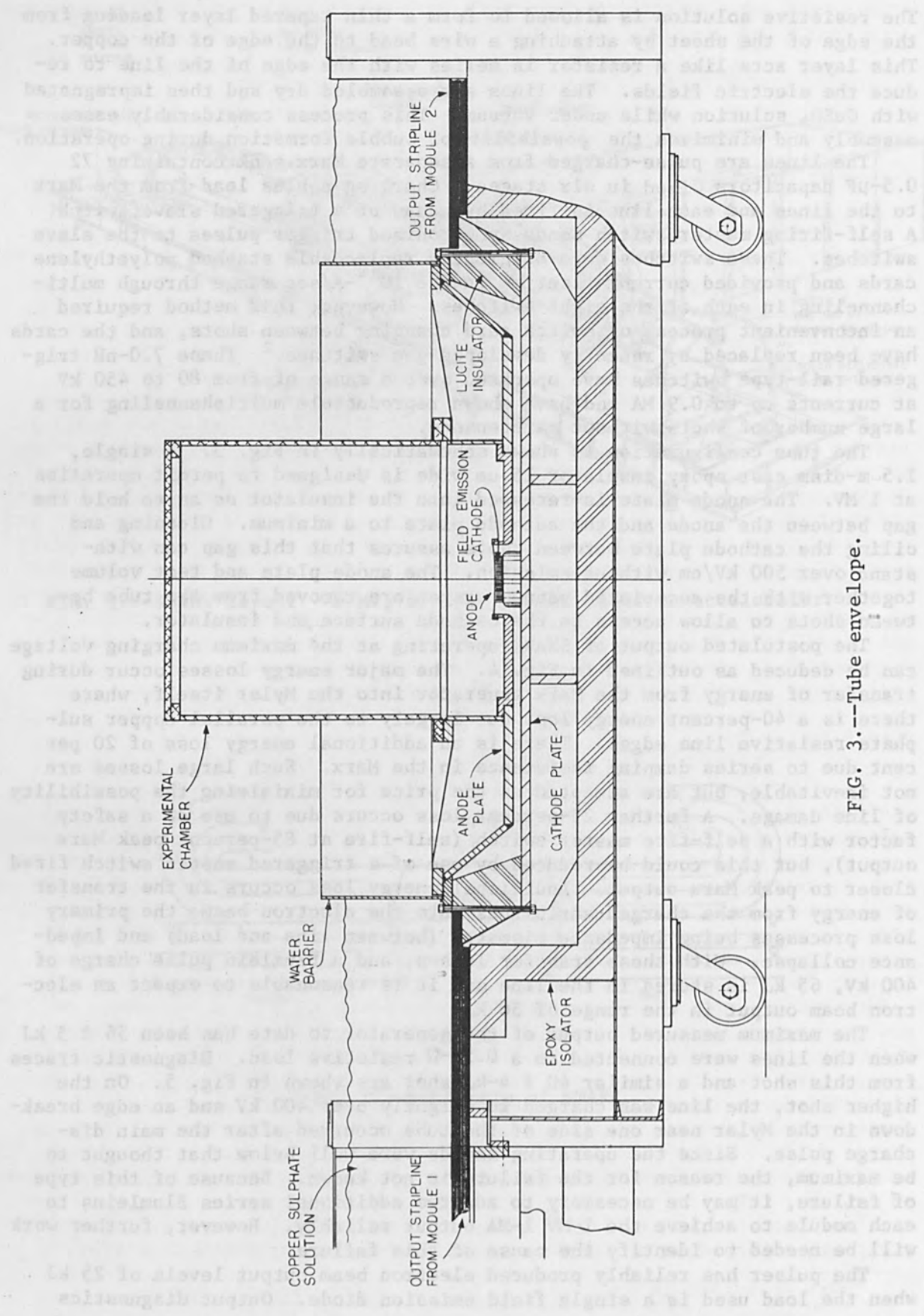


FIG. 3.--Tube envelope.

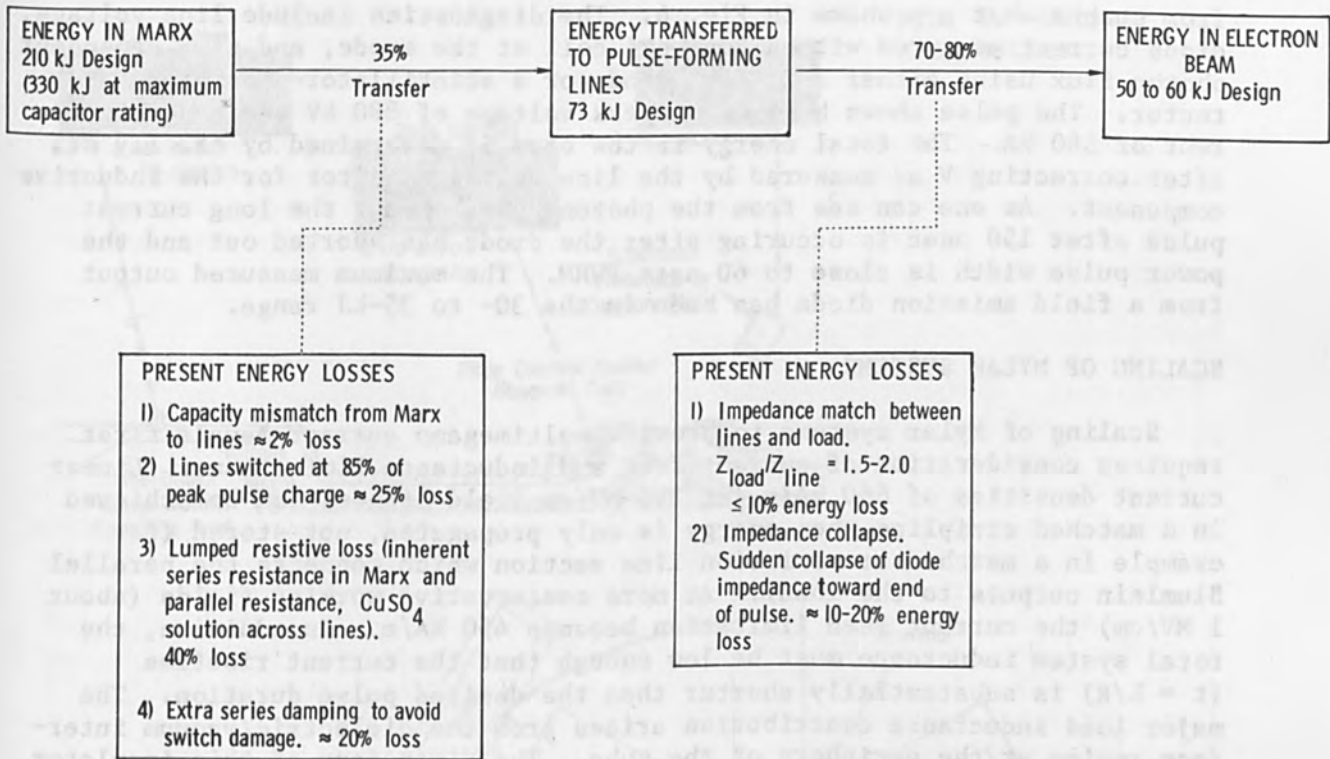


FIG. 4.--Energy output considerations--50 kJ SNARK.

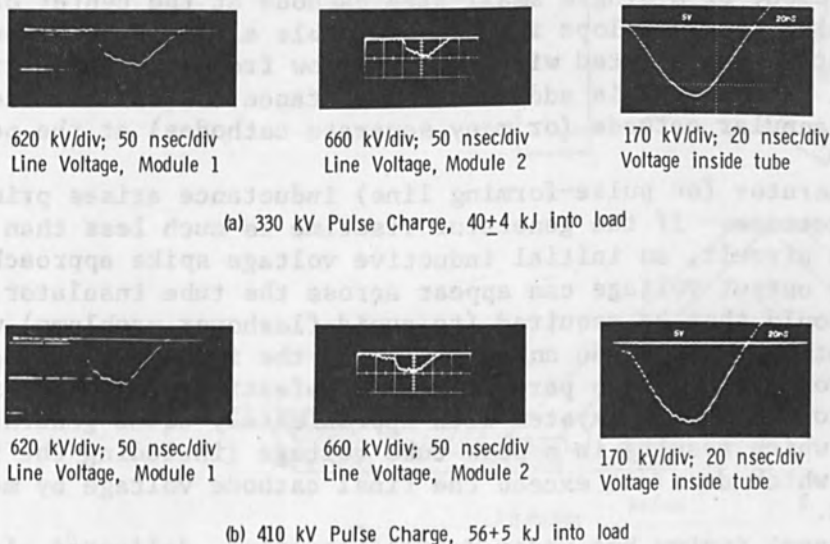


FIG. 5.--Output into $0.55\text{-}\Omega$ resistive load.

from such a shot are shown in Fig. 6. The diagnostics include line voltage, diode current measured with a Rogowski coil at the anode, and time dependent photon flux using either a Compton diode or a scintillator-photodiode detector. The pulse shown here has a peak voltage of 880 kV and a peak current of 580 kA. The total energy in the beam is determined by the $\int IV dt$, after correcting V as measured by the line voltage monitor for the inductive component. As one can see from the photon pulse shape, the long current pulse after 150 nsec is occurring after the diode has shorted out and the power pulse width is close to 60 nsec FWHM. The maximum measured output from a field emission diode has been in the 30- to 35-kJ range.

SCALING OF MYLAR SYSTEMS

Scaling of Mylar systems to provide multimegamp current levels first requires consideration of current feed and inductance limitations. Linear current densities of 660 kA/m (at 1.5-MV/cm field stress) can be achieved in a matched stripline when energy is only propagated, not stored (for example in a matched transmission line section which connects the parallel Blumlein outputs to the load). At more conservative working fields (about 1 MV/cm) the current feed limitation becomes 450 kA/m. In addition, the total system inductance must be low enough that the current risetime ($t = L/R$) is substantially shorter than the desired pulse duration. The major load inductance contribution arises from the dielectric/vacuum interface region at the periphery of the tube. The dimensions of this insulator region are governed by the voltage holdoff characteristics of the insulator (at present 15 x 15 cm for the oiled epoxy insulator used on SNARK at 1 MV). Inductance estimates for an annular dielectric/vacuum interface are then about $4.5/R$ -nH, where R is the radius (in meters) of the annular insulator. Additional inductance is added by the spacing of the anode and high voltage plates internal to the insulator envelope (about 2 cm at 1 MV). For this reason placement of a single small-area cathode at the center of the above large-diameter tube envelope is not a workable alternative because of the large inductance associated with current flow from the tube periphery to the central cathode. This additional inductance can be minimized by placement of an annular cathode (or many separate cathodes) at the periphery of the tube.

The generator (or pulse-forming line) inductance arises primarily from switch inductance. If the generator risetime is much less than the risetime of the tube circuit, an initial inductive voltage spike approaching twice the matched output voltage can appear across the tube insulator. A thicker insulator would then be required (to avoid flashover problems) which would increase both the amplitude and duration of the inductive voltage spike. This solution is therefore partially self-defeating. A more workable approach is to operate the system with approximately equal generator and load risetimes, which results in a peak tube voltage (including the inductive component) which does not exceed the final cathode voltage by more than 14 per cent.¹

The present system has under normal operation, delivered close to 1 MA to the 1.5-m-diam tube fed from two sides. The circumference of the tube, 4.7 m, is sufficiently large to feed a total of 2 MA from parallel Blumlein combinations, if two additional identical modules are added at right angles to the existing modules. If multiple cathodes are placed adjacent to the insulator, the tube inductance would be an acceptable 8 nH, giving a pulse risetime (for equal generator and load risetimes) of about 16 nsec.

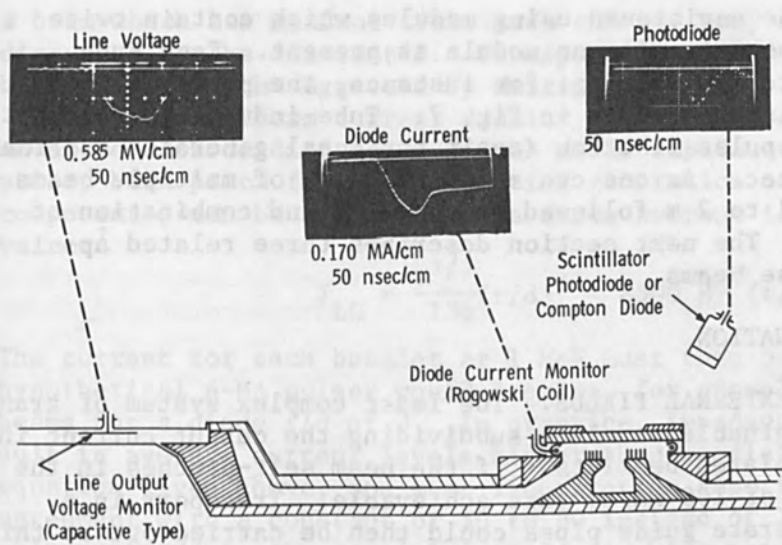


FIG. 6.--Output diagnostics.

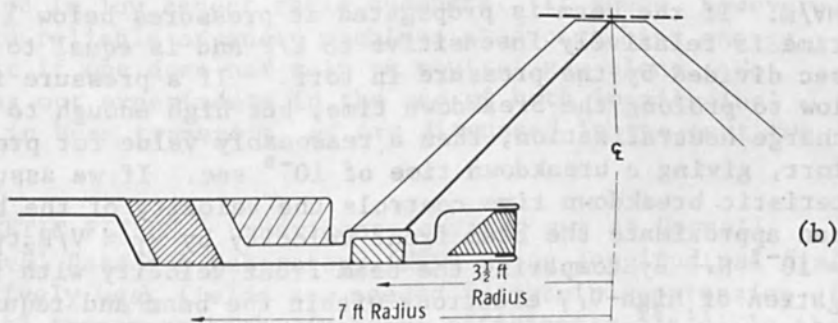
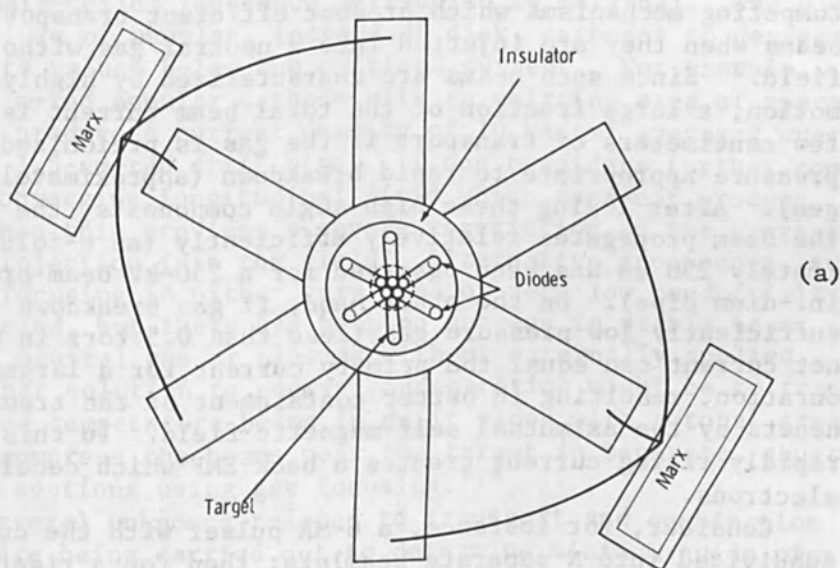


FIG. 7.--1 MV, 6 MA pulser: (a) circular array; (b) cross-sectional view of tube.



Further scaling can be envisioned using modules which contain twice the number of Blumleins as exist in one module at present. Each such module could deliver up to 1 MA giving, for instance, the possibility of producing a 6-MA 1-MV pulser as shown in Fig. 7. Tube inductance is about 5 nH, which would give a pulse risetime (again for equal generator and load risetimes) of about 30 nsec. As one can see, transport of multiple beams over distances of about 1 to 2 m followed by focusing and combination of these beams is required. The next section describes three related approaches to handling these beams.

BEAM TRANSPORT AND COMBINATION

NEUTRAL GAS WITHOUT EXTERNAL FIELDS. The least complex system of transport and combination imaginable involves subdividing the output current into separate magnetically isolated beamlets. If the beam self-pinches in the diode, current densities of 100 kA/cm² are achievable. Transport in a thin-walled array of separate guide pipes could then be carried out at this current density. It has been known for some time, however, that there are competing mechanisms which prevent efficient transport of pinched high v/γ beams when they are injected into a neutral gas without externally applied field.³ Since such beams are characterized by highly nonparaxial electron motion, a large fraction of the total beam current is lost over the first few centimeters of transport if the gas is preionized or if it is at a pressure appropriate to rapid breakdown (approximately 0.75 torr in nitrogen). After losing these high-angle components, the remaining portion of the beam propagates relatively efficiently (an e-folding distance of approximately 250 cm has been observed for a 250-kV beam propagating in a 1.25-in.-diam pipe). On the other hand, if gas breakdown is delayed by use of sufficiently low pressure gas (less than 0.5 torr in nitrogen), then the net current can equal the primary current for a larger fraction of the pulse duration, resulting in better containment of the transverse energy components by the aximuthal self-magnetic field. In this case, however, the rapidly rising current creates a back EMF which decelerates the energetic electrons.

Consider, for instance, a 6-MA pulser with the current of the machine subdivided into N separate beamlets; then for a risetime of 20 nsec, we get E_z (V/m) = 10^{-7} dI/dt (A/sec) = $10^{-7} \times (6 \times 10^6)/N \times (1/20 \times 10^{-9}) = (30/N)$ MV/m. If the beam is propagated at pressures below 1 torr, the breakdown time is relatively insensitive to E/P and is equal to approximately 10^{-9} sec divided by the pressure in torr.⁴ If a pressure is chosen sufficiently low to prolong the breakdown time, but high enough to give collisional charge neutralization, then a reasonable value for pressure would be 0.1 torr, giving a breakdown time of 10^{-8} sec. If we assume that the characteristic breakdown time controls the velocity of the beam front, then we can approximate the beam front velocity by $v_f \approx V/E_z t_B$. This gives $\beta_f = 10^{-2} N$. By comparing the beam front velocity with the velocity of propagation of high- v/γ electrons within the beam and requiring negligible erosion over distances of roughly 2 m, we see that at least thirty separate beams are required. In addition, there is some question as to the allowable pipe diameter for efficient transport of the self-pinched beam. Previous experience⁵ indicates that the low-pressure beam behavior is subject to even greater losses than from erosion alone when the beam is contained within a relatively small-diameter conducting pipe. As a result, one is not able to closely pack the transported beams over a small output area. By creating

a beam which has minimal transverse energy, many of the problems previously discussed can be eliminated. Transport of such a "cold" beam has, in fact, been the approach suggested by Martin.⁶

Assuming uniform current density from a disk cathode of radius r , for an anode-cathode distance d and no diode impedance collapse during the pulse, beam pinch (and the resulting generation of large transverse energy components) can be avoided if the diode current is less than the critical value:⁷

$$I_{LC} = \frac{v^{3/2}}{136}(r/d)^2 < 8500 \beta\gamma (r/d)$$

The current for each beamlet at 1 MeV must then be less than 85 000 A. The hypothetical 6-MA pulser would require, for example, 90 separate 65 000-A beams for a diode r/d of 3. In practice, impedance collapse phenomena result in average current levels higher than predicted by the Langmuir-Childs equation given above, and most laboratories report better average impedance agreement with a constant of 50 to 80 instead of 136. This implies maximum values of r/d in the range 1.3 to 2, at which point the assumption of $r/d \gg 1$ in the Langmuir-Childs impedance derivation is marginal. One possible solution is the use of annular, instead of disk, cathodes to decrease the emission current to values below the critical current. For example, if $d = 0.5$ cm, a 1.5-cm-rad annular cathode with an emitting area of approximately 3.5 cm² would produce a current density of 10 kA/cm² averaged over the area (7 cm²) of a 1.5-cm-rad drift pipe. If one considers further compression by using a converging longitudinal field which does not produce electron mirroring, then this provides a severe restriction on the average angle of the beam at injection into the field. Alternative approaches, such as using geometrical focusing in either very high or very low conductivity gases have been suggested, but there has been no success in stable beam combination in either neutral gas or plasmas without externally applied fields to date. Another solution to energy concentration might be to transport the low transverse temperature beams in drift pipes with a total area of about 600 cm² and compress the beams near the target in separate, short, low pressure, conical sections using gas focusing.^{8,9}

As one can see, several unknowns related to transport and combination remain. Experiments are being carried out to determine minimum guide pipe diameters for efficient transport of relatively low transverse energy beams, and on beam combination in low aspect ratio chambers. It seems, however, that more flexible and reliable advanced machines producing high energy densities can be built if one does not rely on neutral gas alone. We are therefore carrying out experiments in the use of both longitudinal and azimuthal fields in beam transport, as are discussed in the next two subsections.

LONGITUDINAL MAGNETIC FIELDS. Experiments carried out at Cornell University and the Naval Research Laboratory (NRL) using longitudinal fields have shown that relatively weak fields are needed to obtain suppression of diode self pinch and to transport high- v/γ beams efficiently.^{10,11} In these experiments, the diode is extended on a stalk into the region of uniform field within a solenoid and the target is similarly immersed at the other end of the solenoid in a region of uniform field. In both the NRL and Cornell experiments, there has been no attempt at preionization and it is found that transport of beams with $v/\gamma > 10$ over 1-m distances is typically 85 per cent efficient. The results at NRL indicate that the field required to prevent self pinch in the diode is given by

$$\frac{B_{\text{ext}}}{B_{\text{diode}}} > (v/\gamma)(r/2d)$$

If one assumes 100-percent diamagnetism and magnetic pressure balance as suggested by Hammer,¹² then the field required for efficient transport is given by $B_{\text{ext}} = k \sqrt{J}$, where

$$k = \sqrt{680\pi \langle \beta_{\perp}^2 \rangle / \langle \beta_{\parallel} \rangle} \gamma$$

Thus a current density of 50 to 100 kA/cm² would require an external field of from 15 to 21 kG (if $\langle \beta_{\parallel} \rangle = 0.7$). If the transport length is 2 m, the total beam cross-sectional area is 100 cm², and the total current is 6 MA, then the field energy in the transport region is 40 kJ. With six separate beams of 16.5 cm cross-sectional area each, and assuming a Child's law impedance, the diodes have an anode-cathode gap of 2 mm. Such a configuration probably would be impractical because of hydrodynamic response of the anode and/or cathode resulting in rapid impedance collapse. One solution to the problem of anode motion is to increase the anode-cathode distance, but to utilize plasma in the diode to reduce the effective impedance. Work carried out at both NRL and Maxwell Laboratories has indicated that a Child's law impedance can be used in the case of large prepulse if the effective anode-cathode distance is given by a Debye length in the prepulse plasma.¹³ In this way impedances of 1 Ω can be achieved with a 2-in.-diam cathode and anode-cathode distances of the order of 1 cm. With such a diode one expects that the effect of anode/cathode motion on diode impedance will be greatly reduced. Use then of longitudinal fields with a diode operating under prepulse conditions does remain as one way of achieving beam extraction and transport at current densities of about 50 kA/cm².

Another way to use a longitudinal-field transport system would be to propagate beams with a lower current density and compress them at the target in a magnetic mirror. If the transported beam area is increased to 1000 cm² at a current density of 6 kA/cm², the required field drops by a factor of three and the total energy in the field remains constant. The advantage gained here is that the individual cathode radii can be increased to 6.9 cm with a corresponding anode-cathode distance of 0.6 cm assuming Child's law impedance behavior. However, the requirement for 10-fold compression at the target is equivalent to requiring that the beam transverse energy at injection into the drift region be less than 10 per cent of the total energy. Whether such a beam can be produced in a field of reasonable magnitude is still open to question.

Even with a suitably efficient means of transport the longitudinal-field configuration has two disadvantages. First, the stalk required to extend the cathode into the uniform field region of the solenoid provides an additional inductance to the diode. For instance, a reasonable inductance for such a single 1-MV 1-MA diode configuration would be 10 nH. With six such stalks at the periphery of a large-diameter single tube, the total tube inductance is increased by about 2 nH and the pulse risetime would be increased by about 12 nsec. Second, packing the separate solenoids close together at the target location and compressing or mixing their outputs presents problems. Even if a single mirror field is used as the final transport stage for several beams, the separate beams do not mix. The longitudinal field maintains the identity of each beam and any nonreproducibility in the diodes is preserved at the output. Diagnosing the output during an actual shot would in itself be difficult and would greatly hamper any application.

Stallings¹⁴ is studying a unique beam generation and transport configuration that does not require beam compression or mixing. The beam is generated from a single ring cathode at the periphery of the diode and this annular beam is transported between two converging cones so that the total beam area is held constant (Fig. 8). In this way, there is no beam compression and current densities of tens of kA/cm² can be achieved over 100 cm² without possible consequences of mirroring. The fields required to suppress the self-pinch are minimized by the annular configuration. The obvious problem with such a scheme in future multimegampere machines is related to the requirements for uniform emission over what is essentially an edge cathode as much as 20 ft in length. The advantage of such a system is its obvious simplicity and the modèst energy potentially needed to generate the fields. For instance, a 6-MA 100-cm² hollow-beam guide system would require field energy of only about 20 kJ in the transport region even for $|\vec{B}_z| = |\vec{B}_\theta|$ in the diode.

LINEAR PINCH (B_θ). The injection of one or more high v/γ beams into a linear pinch device for either transport or beam mixing and compression has been recently studied. Roberts and Bennett¹⁵ first investigated the beam/pinch interaction by injecting a low- v/γ beam (3.5 MV, 30 kA) into a 50-kA pinch for the purpose of determining feasibility of this technique to achieve higher current densities ("super-pinch"). Benford and Ecker extended the application of this technique to transport and control of high- v/γ beams.^{16,17} The potential advantages of this technique over the use of a longitudinal field relate to (a) the total energy required for transport, (b) the fact that the field in the transport region does not penetrate the diode, thus permitting diode pinch and higher current densities with large cathodes, and (c) that a pinch device can be used to mix several beams so as to minimize the requirements of separate diode reproducibility.

Of the three techniques, least is known about the limitations of the pinch device, as work to date has concentrated on study of beams in the 200-kA range and only preliminary beam combination or compression studies have been carried out. This technique, however, has already demonstrated efficient transport at current densities of about 20 kA/cm² and energy flux control by containment of the beam within the collapsing pinch current sheet. The pinch has also been shown to redirect a beam injected slightly off the axis and has the possibility of providing power concentration through the attraction of several peripheral beams to a central intense pinch.

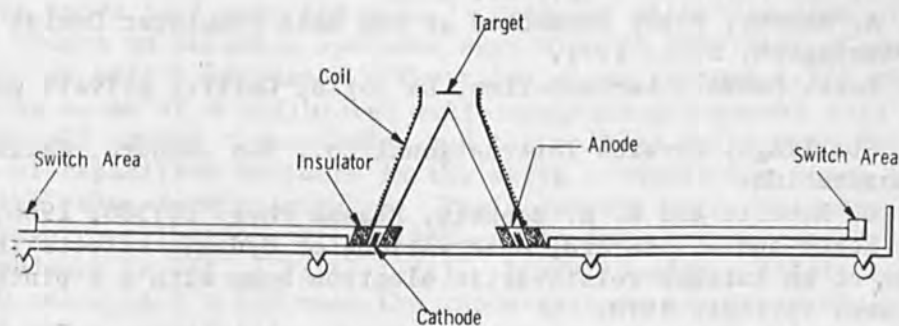


FIG. 8.--Conical B_z beam generation and transport approach.

CONCLUSION

Most of the fundamental problems associated with a modular multimegampere pulsed electron-beam accelerator have been solved; the principal remaining unanswered questions concern transport and combination of high-intensity electron beams. The major developments in generator technology have been primarily associated with providing synchronized low-inductance switches and diodes. Beam-handling techniques have until recently been limited to beams propagating in their self-fields in initially neutral gas, but are now generally directed toward propagation in pre-ionized gases with externally applied fields. Of the approaches under consideration, the application of longitudinal fields to strip, low-transverse-energy beams and use of linear pinch devices to contain high-transverse-temperature beams appear to be the most promising. Experiments in progress at present should determine the feasibility of eventually constructing pulsers providing sub-MeV beams in the megajoule range.

REFERENCES

1. S. Shope, G. Yonas, I. Smith, R. Ward, P. Spence, and B. Ecker, Development and Application of Mylar Striplines, DASA 2482, January 1970.
2. P. Champney, A Low-Inductance Triggered Multichannel Gas Switch, PIIR-23-70, Physics International Co., San Leandro, Calif., October 1970.
3. G. Yonas, P. Spence, and B. Ecker, Current neutralization in high v/γ relativistic electron streams, Bull. Am. Phys. Soc. 14:1070, 1969.
4. G. Yonas and P. Spence, Experimental investigation of high- v/γ beam transport, in L. Marton (ed.), Rec. 10th Symp. Electron, Ion, and Laser Beam Technology, San Francisco Press, 1969.
5. G. Yonas et al., Dynamic Effects of High v/γ Beam Plasma Interactions, DASA 2426, August 1969.
6. J. C. Martin, Paper presented at the DASA Simulator Design Conference, Washington, D.C., 1971.
7. F. Friedlander, R. Hectel, and J. Jory, TR-1 under DASA 01-68-C-0025, January 1968.
8. G. Yonas and P. Spence, Experimental Investigation of High v/γ Electron Beam Transport, DASA 2175, October 1968.
9. J. C. Martin, AWRE, Aldermaston, England, private communication.
10. L. Levine and I. Vitkovitsky, Propagation of large current relativistic electron beams, Bull. Am. Phys. Soc. 15:1401, 1970.
11. J. Bzura and S. Linke, Electron beam energy transport in magnetic fields, Bull. Am. Phys. Soc. 15:1452, 1970.
12. D. A. Hammer, Paper presented at the DASA Simulator Design Conference, Washington, D.C., 1971.
13. A. Kolb, Maxwell Laboratories, La Jolla, Calif., private communication.
14. C. Stallings, Physics International Co., San Leandro, Calif., private communication.
15. T. G. Roberts and W. H. Bennett, Plasma Phys. 10:380, 1968.
16. B. Ecker and J. Benford, Observations of dynamic effects in the interaction of an intense relativistic electron beam with a z-pinch, Bull. Am. Phys. Soc. 15:1401, 1970.
17. J. Benford and B. Ecker, Transport of intense relativistic electron beams in a z-pinch, submitted for publication to Phys. Rev. Letters.

INTENSE BEAM GENERATION AT MEGAMPERE CURRENTS AND BEAM TRANSPORT IN PULSED EXTERNAL MAGNETIC FIELD CONFIGURATIONS*

B. ECKER, J. BENFORD, C. STALLINGS, S. PUTNAM, and P. SPENCE

Physics International Company, San Leandro, Calif.

INTRODUCTION

Utilization of the energy available from low-impedance, fast-pulse generators (such as the 1- Ω , 60-nsec FWHM, \leq 1-MV generator SNARK¹) requires development of low-impedance field-emission diodes with impedance lifetimes above 100 nsec and of beam-transport and energy-density control techniques. Further scaling of generator systems to multimegampere current levels will involve generation of many separate electron beams or one large annular beam. Here again, utilization of the energy from such configurations will necessitate beam transport and concentration at a target location. Presented here are results of specific experiments related to electron-beam generation from single and double diodes and to electron-beam transport in both longitudinal and azimuthal external magnetic field configurations. Most of the work was performed with two Mylar dielectric pulsed electron-beam generators, the 1.1- Ω , 350-kA PIML generator and the 1- Ω , 1-MV, 1-MA SNARK generator.

DIODE STUDIES

When operated at or near impedance-matched conditions, high-current, low-impedance ($< 1\text{-}\Omega$) field-emission diodes at high applied voltages (typically 0.1 to 1.0 MV) yield pulsed currents high enough to produce substantial magnetic self-interaction, of self-pinching. This feature is not included in the relativistic Child-Langmuir treatment of space-charge-limited flow in a planar diode; thus the relationships between diode voltage, current, and configuration in the low-impedance, high- v/γ regime have required elucidation. With planar, cylindrically symmetric, annular cathodes opposite a stretched-foil anode in the SNARK or PIML Mylar strip-line machines, we have measured the dependence of diode impedance on cathode radii r_{in} and r_{out} , anode-cathode distance d , and applied voltage $V_0(t)$. Annular cathodes ($r_{in} > 0$) were used for two reasons: first, to explore diode behavior at fixed outer radius but variable total area; and second, to extend impedance lifetimes by preventing the early-time anode-cathode shorting that results when the pinched beam vaporizes, ionizes, and generally explodes the anode foil near the axis.² Cathodes with role pins or sharp circular ridges as emission surfaces were used to determine if surface structure can affect impedance. The total diode current $I_0(t)$ was time-resolved by means of a calibrated self-integrating Rogowski coil in the cylindrical wall around the cathode, and the voltage $V_0(t)$ was time-resolved by means of capacitive dividers in the strip transmission lines that constitute the pulse-forming network. Their outputs were corrected for inductive voltage contributions (flux linkages in the monitor circuit). The diode impedance is $Z(t) \equiv V_0(t)/I_0(t)$. Diode impedance lifetime was typically 110 nsec; at $t \approx 110$ nsec the anode-cathode gap would short, as mentioned above, manifesting a sudden current surge and voltage drop.

*This work was supported in part by DASA Contracts No. DASA 70-C-0063 and 71-C-0052.

Past experience has shown that the impedance lifetime can be extended arbitrarily by an increase in the anode-cathode distance and a simultaneous increase in the cathode size to avoid the corresponding increase in impedance. In what follows we are concerned with diode behavior prior to this collapse of impedance.

The data obtained to date give strong support for the parapotential model of the high-aspect-ratio, high-current diode developed by De Packh,³ Friedlander et al.,⁴ and Creedon.⁵ This picture rests on the possibility that there is a class of electron trajectories in the diode that are force-free. This possibility is based on the following arguments. In beam pinch, electrons emitted near the cathode outer edge (at $r = r_{out}$) move to a much smaller radius as they traverse the anode-cathode gap. Such an accumulation of charge near the axis must depress the axial electric field at the cathode at interior radii, so that electron emission is predominantly from the cathode periphery. The instantaneous equipotentials of the applied field are as in Fig. 1(a). The electric force is of course perpendicular to the equipotentials. An electron moving radially inward along a single equipotential also experiences a magnetic force (due to the azimuthal magnetic field B_θ) that is also perpendicular to the equipotential and opposes the electric force. These two forces are equal and opposite when the electron velocity divided by the speed of light is $\beta = E/B_\theta$; in such a case no net force acts on the electron, and its motion is force-free as well as parapotential. (This is akin to the situation in a magnetron, with the magnetic field acting as an insulator in the interelectrode space.) The assumption of steady-state ($\partial I_0/\partial t = 0$), parapotential, force-free flow provides partial information on the spatial dependence of the current density, charge density, and fields. The added requirements of Ampere's law and Poisson's equation result in the fundamental equation of the flow,³

$$\nabla^2 V = 2r^{-2} dI^2/d^2V \quad (1)$$

where r is the radius in cylindrical coordinates, $V = V(r, z)$ is the potential, and $I = I(r, z)$ is the total current flowing within radius r through the plane $z = \text{constant}$. Solutions to Eq. (1) indicate that a "bias current" must flow in the axial direction inside the parapotential flow in order that the conditions for the flow be satisfied. The bias current, arbitrary except for a lower limit, is included in the current I in Eq. (1); analytically it is a parameter whose physical origin is outside the theory as it now stands. De Packh has shown that the minimum allowable bias current corresponds to electron parapotential flow along all equipotentials, including those grazing along the anode. Higher bias currents constrain the flow to lower-lying equipotentials, raising the impedance of the diode.

A simple picture due to Creedon⁵ that facilitates application of this analysis to high-aspect-ratio planar diodes is shown in Fig. 1(b). The equipotentials of Fig. 1(a) are idealized into conical surfaces over most of the interelectrode region. Near the cathode edge, electrons are assumed already to populate the various equipotentials, and near the axis, where Fig. 1(b) is unphysical, the flow is presumably orthopotential but is not considered to affect the parapotential flow in most of the diode volume. Creedon treats the "grazing" case mentioned above and finds the voltage-current characteristics shown by the smooth curve in Fig. 2, for which

$$I_0 = 8500 (r_{out}/d) \gamma_0 \ln[\gamma_0 + (\gamma_0^2 - 1)^{1/2}] \quad (\text{mks})$$

where $\gamma_0 = 1 + (eV_0/mc^2)$.

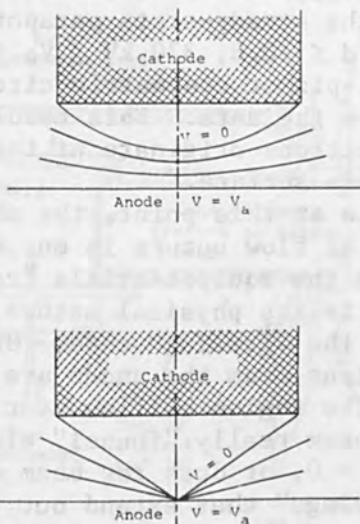
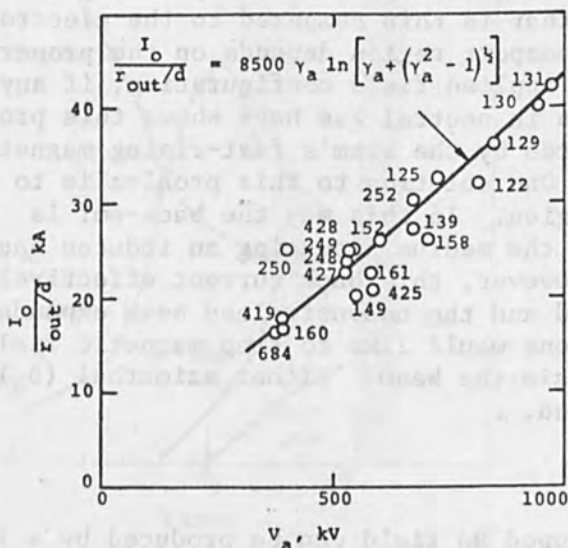


FIG. 1.--Equipotentials due to hypothetical steady-state voltage applied across diode. (a) Physical schematic: electric field is suppressed over most of cathode surface due to beam pinch; (b) idealized configuration for parapotential flow calculations.



Pulse no.	$\frac{r_{out}}{d}$	Cathode		anode	gen.	
		type*	r_{out}			r_{in}
122	19.8	R.P.	5.9	3.3	2-mil Ta	Snark
125	16.9	R.P.	5.9	3.3	2-mil Ta	Snark
129	16.9	R.P.	5.9	3.3	2-mil Ta	Snark
130	18.3	R.P.	5.9	3.3	2-mil Ta	Snark
131	19.8	R.P.	5.9	3.3	3-mil Ta	Snark
139	18.3	R.P.	5.9		2-mil Ta	Snark
149	15.9	C.R.	5.6	2.7	2-mil Ta	Snark
152	14.0	C.R.	4.9	3.7	2-mil Ta	Snark
158	12.3	C.R.	5.6	4.6	2-mil Ta	Snark
160	12.3	C.R.	5.6	4.6	2-mil Ta	Snark
161	15.9	C.R.	5.6	3.7	2-mil Ta	Snark
248	20.4	C.R.	7.2	4.6	2-mil Ta	Snark
249	20.8	R.P.	7.3	3.9	2-mil Ta	Snark
250	20.4	C.R.	7.2	4.6	2-mil Ta	Snark
252	20.8	R.P.	7.3	3.9	2-mil Ta	Snark
419	22.4	R.P.	7.3	3.9	2-mil Ta	Snark
425	22.4	R.P.	7.3	3.9	2-mil Ta	Snark
427	22.4	R.P.	7.3	3.9	1/2-mil Al	Snark
428	20.8	R.P.	7.3	3.9	1/2-mil Al	Snark
684	7.3	R.P.	1.8	0	1-mil Al	PIML

* R.P. = Roll-pin, C.R. = Concentric ridge

FIG. 2.--Comparison of current-voltage characteristics as predicted by steady-state parapotential analysis with measured values. For this comparison data are restricted to $\partial I_0/\partial t = 0$: $I_0 \equiv [I_0(t)]_{max} = I_0(t_m)$, $V_0 \equiv V_0(t_m)$; each experimental point (I_0, V_0) comes from single beam pulse.

Our diode measurements for $\partial I_0/\partial t = 0$ ($I_0 = I_0^{\max}$) are also shown in the figure. They agree with the steady-state parapotential calculations over the ranges of $7.26 \leq r_{\text{out}}/d \leq 20.8$, $370 \text{ kV} \leq V_0 \leq 970 \text{ kV}$. The type of cathode surface used (roll-pin or concentric circular ridge) does not appear to be discernible from the data. This result gives added support to the view that the beam electrons originate at the cathode periphery, rather than from the planar cathode surface.

If, as seems reasonable at this point, the above is interpreted to mean that "grazing" parapotential flow occurs in our diodes, we must then ask how electrons come to populate the equipotentials "correctly," whether there is a real bias current, what is its physical nature, and why does it have the value that corresponds to the "grazing" case? One possibility for the bias current is that positive ions from the anode are accelerated toward the cathode along the axis. The region of flow near the axis has not been physically modelled; does the beam really "funnel" along the equipotentials down to small spot when $\partial I_0/\partial t = 0$, or does the beam current density vs radius at the anode plane have "wings" that extend out to the cathode radius? The results of recent mappings of the time-resolved radial structure of the current density at the anode show that all electrons are not swept into the pinch, and that broad "wings" in the current distribution extend well outside the pinched core. The analytical and experimental clarification of these points is important at this point in the understanding of very high current diodes.

BEAM TRANSPORT STUDIES

High-current electron beams are injected into a transport region simply by a choice of an anode thickness that is thin compared to the electron range. Beam propagation in the transport region depends on the properties of the fill gas and the externally applied field configuration, if any. Studies of intense beam propagation in neutral gas have shown this process to be lossy.⁶ The back-emf generated by the beam's fast-rising magnetic field decelerates beam electrons. One solution to this problem is to pre-ionize the gas in the transport region. In this way the back-emf is shorted out by the conductivity of the medium producing an induced back current of secondary electrons. However, this back current effectively neutralizes the self-magnetic field and the unconstrained beam expands quickly to the walls.⁷ Therefore one would like to trap magnetic fields in the background plasma to constrain the beam. Either azimuthal (B_θ) or longitudinal (B_z) fields can be used.

B_θ SYSTEMS

A conducting plasma with a trapped B_θ field can be produced by a linear pinch. With this configuration the anode of the beam-generating diode and the cathode of the z-pinch are the same thin foil so that the beam enters the pinch directly (Fig. 3). Thus the beam and pinch current are parallel and the pinch magnetic field acts to constrain the beam. The beam is transported along the collapsing plasma column, strikes the pinch anode plate, and produces the X rays by which transport efficiency is measured.

By this technique, a series of experiments have been performed with the pinch tube varying from 2 to 4 in. in radius and from 1 to 2 ft in length.⁸ Beams with peak currents of 120 kA, 140 kA, and 160 kA with corresponding mean energies of 750 keV, 625 keV, and 500 keV were injected into a collapsing pinch discharge. Transport of these beams was complete, as evidenced

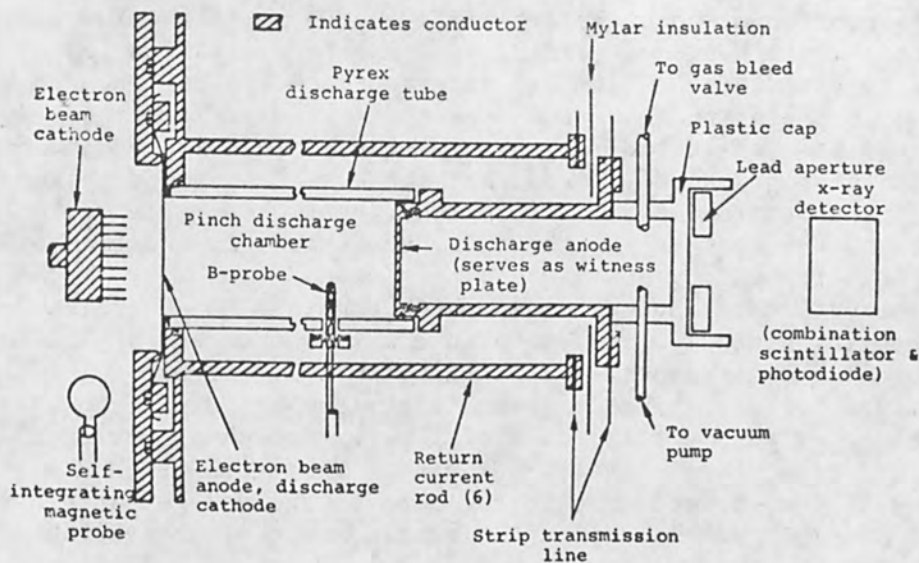


FIG. 3.--Experimental configuration of z-pinch apparatus and beam-generating diode.

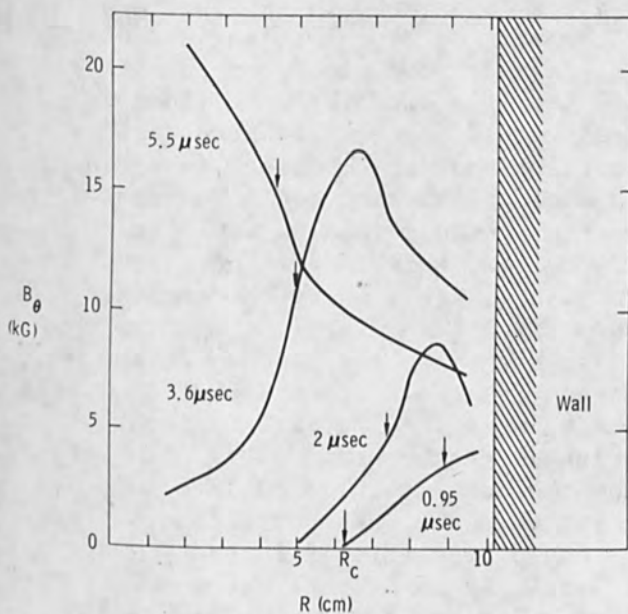


FIG. 4.--Magnetic field profiles at times of beam injection: R_c is beam cathode radius; arrows indicate damage radii of transported beams.

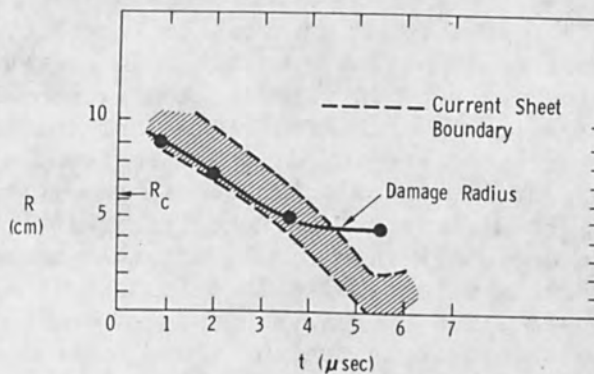


FIG. 5.--Diode damage on inside of current sheet during collapse.

by the preservation of both the amplitude and shape of the X-ray signal produced in the pinch anode. Virtually complete neutralization of the self-magnetic field of the beam was inferred from the low induced voltage across the pinch electrodes. (The appearance of any net current due to the beam must produce an $L \, dI/dt$ voltage drop.) The size of the damage patterns at the pinch anode showed that the beam propagated inside the collapsing pinch current sheet. This configuration permits variation of the fluence of the beam at the target by variations in the time of beam injection into the pinch.

Recent experiments have extended this technique to 300-kA, 600-kV SNARK beams. An 8-in. pinch 1.5 ft long with a maximum current of 750 kA was used to obtain beam transport and fluence control. Figure 4 shows magnetic field profiles for four times of beam injection. Figure 5 shows that diode damage again occurred on the inside of the current sheet during collapse. Transport efficiency was above 90 per cent. Variation of the injection time from 0.95 to 5.6 μ sec changed the area of the damage pattern from 250 cm^2 to 50 cm^2 , showing the extensive fluence control available with this technique.

The results of the above experiments may be understood as follows. Current neutralization quenches the self-field of the injected beam. The electrons of the beam are therefore decoupled from each other. Beam electrons follow single-particle orbits and, are deflected at the inner edge of the current sheet by its magnetic field. They fill the inside of the current sheet as if they were inside a perfectly reflecting tube. In Fig. 6, a typical field profile for a linear pinch is shown. In region 1 beam electrons execute periodic orbits about the axis of the pinch as just described. Region 1 is that radius interval in which the pinch current is insufficient to turn a beam electron back into the diode. For a linearly rising field profile, this critical current would be the Alfvén current $I_A = 17\,000 \beta_{||} \gamma$. For field profiles more like that of the pinch (such as considered by Hammer and Rostoker⁹), the enclosed current could be greater. (Note that pinch current enclosed by the beam channel is always of the order of the Alfvén critical current.) However, this is not the only mode of transport possible. In region 2 of Fig. 1(b), where the enclosed pinch current is greater than I_A and $\partial B_{\theta}/\partial r > 0$, beam electrons undergo a ∇B drift type of trajectory that turns them back into the diode. On the other hand, region 3, where enclosed current is greater than I_A but $\partial B_{\theta}/\partial r < 0$, should transport beam current because the ∇B drift is in the right direction. Evidence for this conclusion can be seen in Fig. 5, where injection at late time (such that much of the beam is injected into $\partial B/\partial r < 0$ regions) allows transport and yet the beam does not expand. Observation of the existence of region 2 would be difficult in that damage to the anode in regions 1 and 3 would essentially obliterate any annulus undamaged by the beam itself. Reversal of the pinch current (antiparallel to beam) would cause transport to be possible only in region 2. However, reversal of the pinch current has only been attempted for collapsing pinch profiles where only region 1 received injected electrons. In this case, the beam was expelled quickly to the wall, in agreement with this argument.

Since the beam current is neutralized by a background conducting plasma, the only condition for propagation of very high current beams is that the magnetic field of the pinch must be sufficiently strong to turn back the beam particles before they reach the discharge tube wall. For particle energies of about 1 MeV or less, this condition is easily achieved. However, since the construction of high-current machines demands large cathode

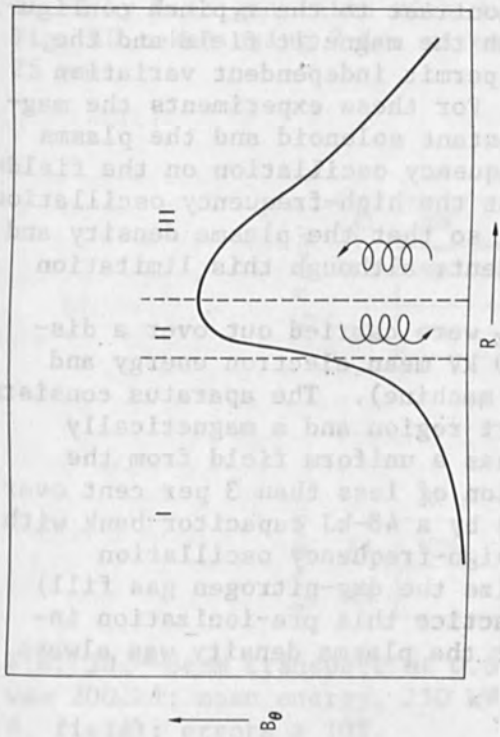


FIG. 6.--Typical field profile for collapsing linear pinch current sheet. Beam electron drift is shown for regions II and III.

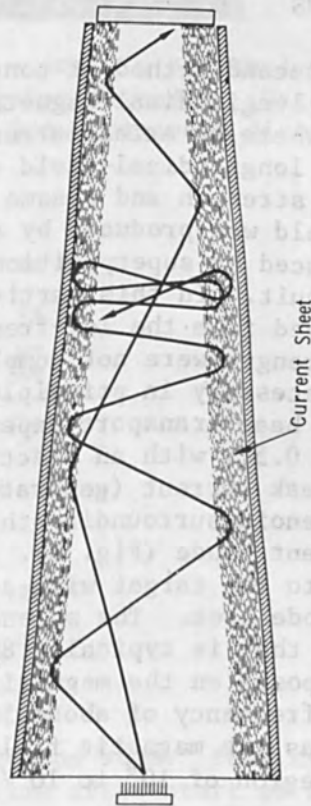


FIG. 8.--Transmission and reflection of beam electrons in tapered z-pinch with sharp current sheet.

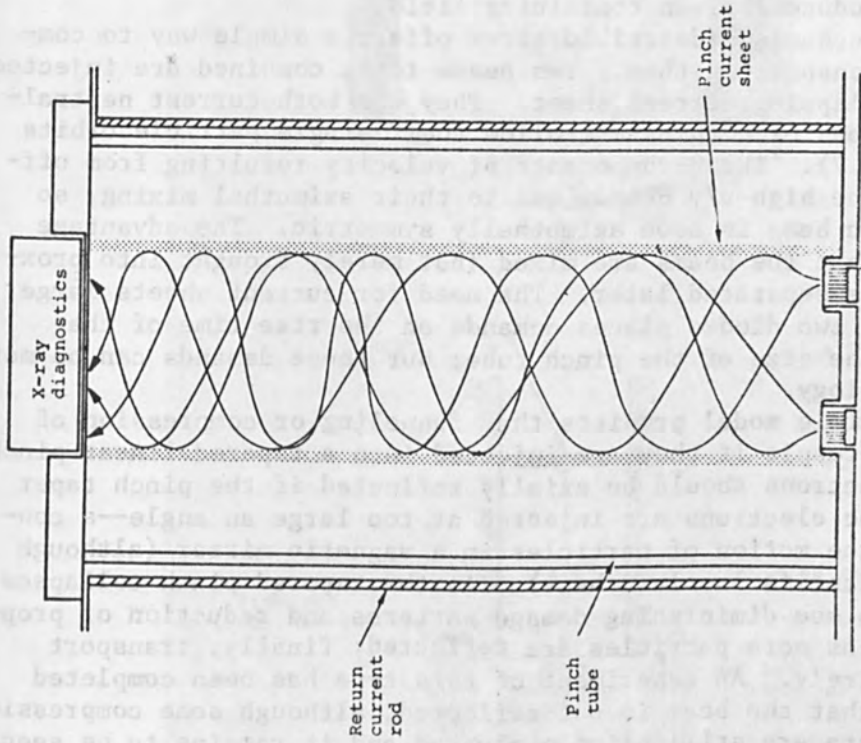


FIG. 7.--Beam combination in z-pinch.

areas, the pinch diameter must increase as well, which implies a larger pinch current to produce a given containing field.

The transport mechanisms described above offers a simple way to combine beams while transporting them. Two beams to be combined are injected inside a single collapsing current sheet. They are both current neutralized and the electrons of both beams follow their single particle orbits to the target (Fig. 7). The θ -components of velocity resulting from off-axis injection of the high- v/γ beams lead to their azimuthal mixing, so that the combination beam is soon azimuthally symmetric. The advantage of this scheme is that the beams are mixed (not merely brought into proximity) and cannot be separated later. The need for current sheets large enough to encompass two diodes places demands on the rise time of the pinch bank and on the size of the pinch tube; but these demands can be met with present technology.

The single-particle model predicts that funneling or compression of beam electrons can result if they are injected into a tapered linear pinch (Fig. 8). Beam electrons should be axially reflected if the pinch taper is too severe or the electrons are injected at too large an angle--a condition similar to the motion of particles in a magnetic mirror (although no adiabatic invariant is involved here). As the tapered pinch collapses one might expect to see diminishing damage patterns and reduction of propagation efficiency as more particles are reflected; finally, transport should cut off entirely. An experiment of this type has been completed and the result is that the beam is not reflected, although some compression does occur. The data are still being evaluated and it remains to be seen whether this finding is compatible with the single-particle model described here.

B_z SYSTEMS

The second method of containing beams in a background plasma is the use of a longitudinal magnetic field. In contrast to the z-pinch configuration (where an axial current provides both the magnetic field and the plasma), longitudinal-field configurations permit independent variation of field strength and plasma properties.¹⁰ For these experiments the magnetic field was produced by a long-time-constant solenoid and the plasma was produced by superposition of a high-frequency oscillation on the field-coil circuit. In this particular experiment the high-frequency oscillation was derived from the low-frequency circuit, so that the plasma density and field strength were not completely independent, although this limitation is not necessary in principle.

Most beam-transport experiments with B_z were carried out over a distance of 0.5 m with an electron beam of 250 kV mean electron energy and 200 kA peak current (generated by the PIML machine). The apparatus consists of a solenoid surrounding the beam transport region and a magnetically transparent diode (Fig. 9). The solenoid has a uniform field from the cathode to the target with a radial variation of less than 3 per cent over the cathode area. The solenoids are driven by a 48-kJ capacitor bank with a period that is typically 800 μ sec. The high-frequency oscillation (superimposed on the magnetic field to ionize the dry-nitrogen gas fill) is at a frequency of about 500 kHz. In practice this pre-ionization increased as the magnetic field increased but the plasma density was always in the region of 10^8 to $10^9/\text{cm}^3$.

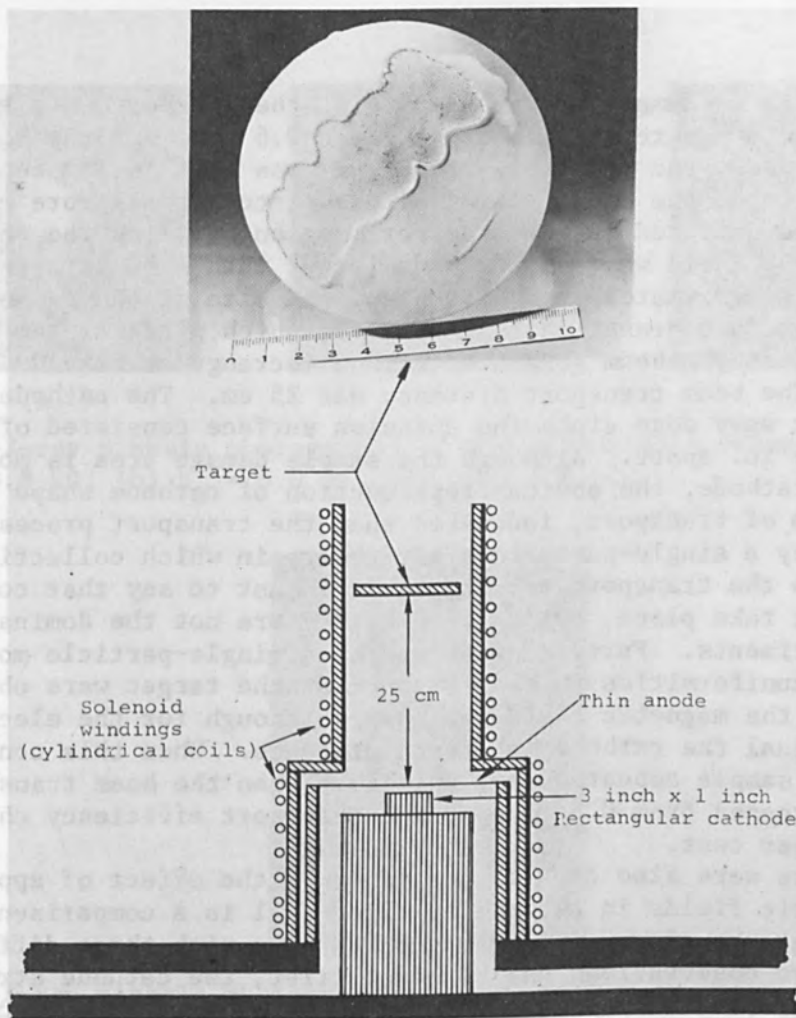


FIG. 9.--Solenoid transport system and damage crater in polythylene produced by beam generated with 3 × 1-in. rectangular cathode. (Data in Fig. 10 taken using 3-in. circular cathode.) Beam transport distance, 25 cm.

		Pressure (millitorr)		
		200	600	1000
B_z (k gauss)	4.1	65%	92%	93%
	8.25	92%	98%	60%
	13.7	69%	72%	75%

$t = 240 \mu\text{sec}$

		Pressure (millitorr)		
		200	600	1000
B_z (k gauss)	8.4	100%	98%	93%
	14.0		100%	

FIG. 10.--Beam transport at 0.5 m for PIML electron beam. Peak current was 200 kA; mean energy, 250 kV; $t = 150 \mu\text{s}$ (time after start of applied B_z field); errors $\pm 10\%$.

Figure 10 is a summary of the results of these experiments for the PIML beam. When the pressure in the solenoid was 0.6 torr and the magnetic field was not used, the transport efficiency was 42 ± 10 per cent. Without the magnetic field, the diode region pinched into a small core and the beam then spread and diffused in the transport region, filling the entire drift tube. When a B_z field was used (fields larger than 4 kG were tested) the beam retained approximately the same shape and size as the cathode. This result is shown most dramatically in Fig. 9, which pictures the damage pattern produced by a beam generated with a rectangular cathode (about 3×1 in.). The beam transport distance was 25 cm. The cathode itself had a somewhat wavy edge since the emission surface consisted of 1/16-in.-diam rods 0.25 in. apart. Although the sample damage area is more irregular than the cathode, the obvious reproduction of cathode shape and area, even after 1 m of transport, indicated that the transport process can be approximated by a single-particle orbit theory in which collective effects are ignored in the transport region. That is not to say that collective effects do not take place, but only that they are not the dominant processes in these experiments. Further evidence for a single-particle model was that local nonuniformities in beam fluence at the target were obviously present until the magnetic field was lowered enough for the electron gyro diameter to equal the cathode inter-rod distance. When this condition was satisfied the sample appeared very uniform. When the beam transport distance was increased from 0.5 to 1 m, the transport efficiency changed by less than 10 per cent.

Experiments were also carried out to study the effect of applied longitudinal magnetic fields in the diode. Figure 11 is a comparison of x-ray pinhole photographs of a 3-in.-diam. rod cathode with three different field strengths. Two observations can be made: first, the cathode structure is discernible in even the lowest external field; and second, the current density appears higher near the cathode center at all field levels studied. Because of the first observation, the second one cannot be explained by the assumption of beam self-pinch, since the latter characteristically does not preserve cathode surface structure. To explain the observed effects, we propose an explanation of diode behavior when B_z is of the same order as B_0^{\max} . The magnetic field in the diode is the sum of the applied uniform axial field and the azimuthal self-field, which increases with radius. The net field, therefore, is helical, and the pitch decreases as radius increases. With the assumption that the electrons in some sense follow the field lines, the electron axial velocity is a decreasing function of radius and the time spent in the diode by an electron is an increasing function of radius. The space-charge-limited current density would therefore decrease with increasing radius for a given anode-cathode voltage. To test this hypothesis, a hollow-core multirod cathode with a 3-in. OD and a 1-in. hollow-core diameter was tested. If the beam were pinching due to its own self-field, the highest current density would be at the central axis; but if the above arguments apply, then the current density would be zero over the hollow core. This type of behavior is evident in Fig. 12, which is an x-ray pinhole photograph taken with this hollow cathode. The self-field of the beam at the edge of the cathode was 10 kG and the longitudinal magnetic field was 11.8 kG. This result supports the model presented above.

Since the current density is highest at the innermost cathode emitters, the diode impedance should not be sensitively dependent upon cathode area (when the latter is above a certain critical value). Figure 13 shows

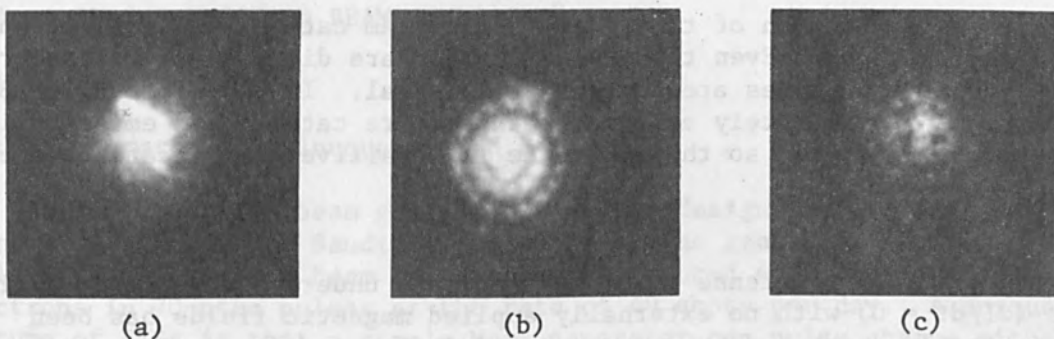


FIG. 11.--X-ray pinhole photographs of anode with 3-in.-diam rod cathode. (a) $B_z = 3.8$ kG, (b) $B_z = 6.0$ kG, (c) $B_z = 7.9$ kG.

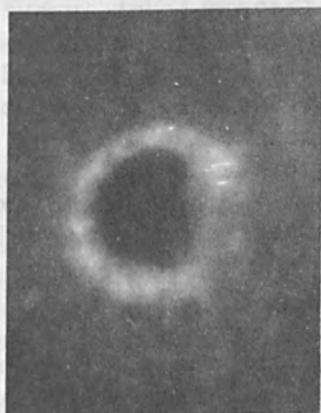


FIG. 12.--X-ray pinhole photograph of anode with 3-in.-diam hollow cathode and 1-in.-diam hole in center. $B_z = 11.8$ kG and $B_{\theta}^{\max} = 10$ kG.

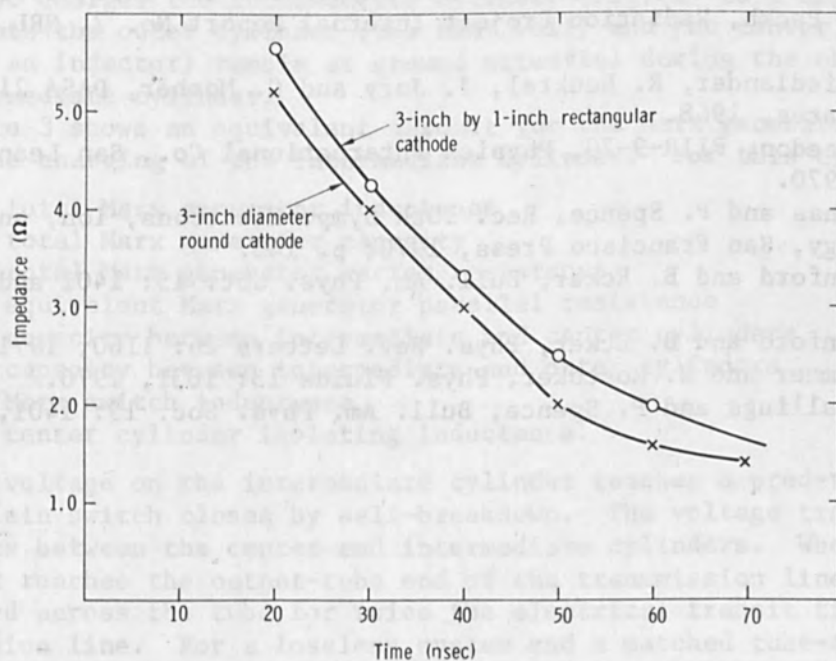


FIG. 13.--Impedance as function of time for two cathodes.

impedance as a function of time for a 3-in.-diam cathode and a 3×1 -in. rectangular cathode. Even though their areas are different by a factor of 2.3, their impedances are approximately equal. In the limit $B_z \gg B_0$, the field is approximately axial over the entire cathode and emission is approximately uniform, so the impedance is sensitive to the cathode area.

CONCLUSIONS

The behavior of intense beams in the diode under steady-state conditions ($dI/dt = 0$) with no externally applied magnetic fields has been satisfactorily described by a parapotential flow model. Applying a B_z field to the diode inhibits self-pinch of the beam. However, the current density is still highest at the innermost cathode radius, presumably because of space-charge effects associated with the twisted field lines.

Propagation of intense electron beams in sufficiently conductive plasma is consistent with single-particle motion in the externally applied magnetic fields. In both linear-pinch and solenoid-field configurations this effect gives high transport efficiency. The z-pinch also allows control of beam fluence, beam combination, and a degree of beam compression, whereas the solenoid system maintains the shape and size of the cathode over the distances that have been tested. No evidence is found for pressure balance effects due to the beam in solenoid systems over these distances.

REFERENCES

1. G. Yonas, I. Smith, P. Spence, S. Putnam, and P. Champney, Development and application of a 1-MV, 1-MA mylar dielectric pulsed electron accelerator and concepts for higher energy modular generator systems, Rec. 11th Symp. Electron, Ion, and Laser Beam Technology, San Francisco Press, May 1971.
2. G. Loda and P. Spence, Bull. Am. Phys. Soc. 15: 1401, 1970.
3. D. De Packh, Radiation Project Internal Report No. 7, NRL, April 1968.
4. F. Friedlander, R. Hecktel, J. Jory and C. Mosher, DASA 2173, Varian Associates, 1968.
5. J. Creedon, PIIR-9-70, Physics International Co., San Leandro, Calif., May 1970.
6. G. Yonas and P. Spence, Rec. 10th Symp. Electrons, Ion, and Laser Beam Technology, San Francisco Press, 1970; p. 143.
7. J. Benford and B. Ecker, Bull. Am. Phys. Soc. 15: 1401 and 1448, 1970.
8. J. Benford and B. Ecker, Phys. Rev. Letters 26: 1160, 1971.
9. D. Hammer and N. Rostoker, Phys. Fluids 13: 1831, 1970.
10. C. Stallings and P. Spence, Bull. Am. Phys. Soc. 15: 1401, 1970.

REBA, A PULSED ELECTRON BEAM GENERATOR*

D. L. JOHNSON

Sandia Laboratories, Albuquerque, N.M.

A pulsed electron beam generator has been designed and constructed and is now in operation at Sandia Laboratories. The generator, called REBA (Relativistic Electron Beam Accelerator), produced 45-kA beams of 3-MeV electrons in 70-nsec pulses at the rate of 40 shots per day. A unique feature of REBA is that a single Marx generator can pulse charge either of two Blumlein transmission lines and thus provides two independent sources of electrons for experiments. The design considerations of the Marx generator, the Blumlein transmission lines, and the output tube are discussed. Preliminary electron beam measurements are also presented.

INTRODUCTION

Before discussing the design and output characteristics of REBA, shown in Fig. 1, we discuss briefly the operation of an electron-beam generator of this type to demonstrate the operation of REBA.

Figure 2 diagrams a simplified pulsed electron-beam generator utilizing a Blumlein transmission line¹ as the high-speed energy store. It consists of a Marx generator, a Blumlein transmission line, and an output tube. Energy is transferred from the Marx generator to the Blumlein transmission line which in turn serves as a fast-discharge, low-inductance energy source for the output tube. Transformer oil is used as the insulating dielectric.

The Marx generator consists of a bank of capacitors charged in parallel and discharged in series by means of spark-gap switches.² The Marx generator pulse charges the intermediate cylinder (Fig. 2) to a negative potential. Both the outer cylinder (the tank wall) and the center cylinder (through an inductor) remain at ground potential during the charging of the intermediate cylinder.

Figure 3 shows an equivalent circuit for the Marx generator and Blumleins during the charging of the intermediate cylinder. For this circuit

- L_m = total Marx generator inductance
- C_m = total Marx generator capacity
- R_s = total Marx generator series resistance
- R_p = equivalent Marx generator parallel resistance
- C_1 = capacity between intermediate and center cylinders
- C_2 = capacity between intermediate and outer cylinders
- L_1 = Marx switch inductance
- L_2 = center cylinder isolating inductance.

When the voltage on the intermediate cylinder reaches a predetermined value, the Blumlein switch closes by self-breakdown. The voltage transient created propagates between the center and intermediate cylinders. When the voltage transient reaches the output-tube end of the transmission line, a voltage is created across the tube for twice the electrical transit time of the transmission line. For a lossless system and a matched tube-to-Blumlein impedance, the tube voltage is equal to the charging voltage applied to the intermediate cylinder.

*This work is supported by the U.S. Atomic Energy Commission.

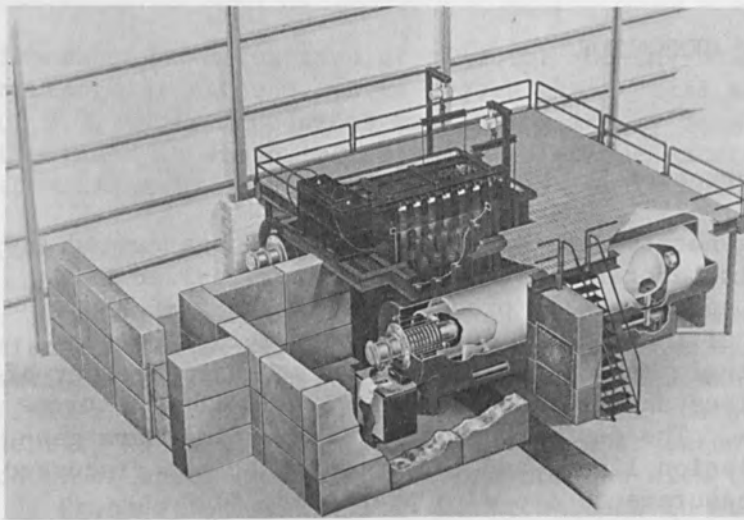


FIG. 1.--Artist's drawing of REBA.

FIG. 2.--Simplified Blumlein machine.

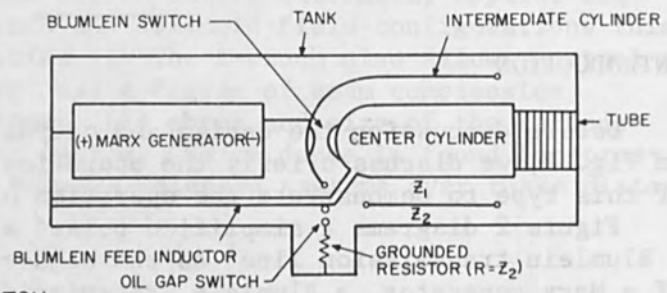
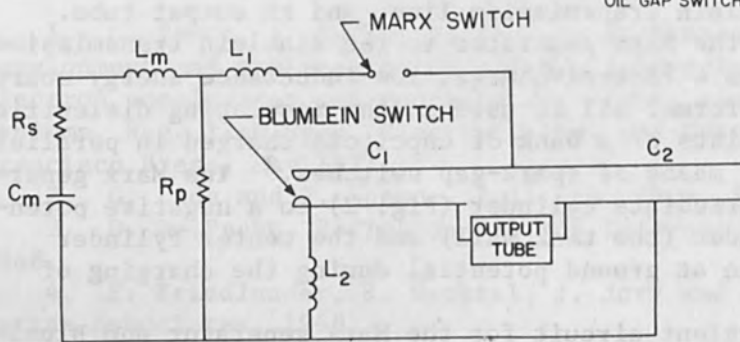
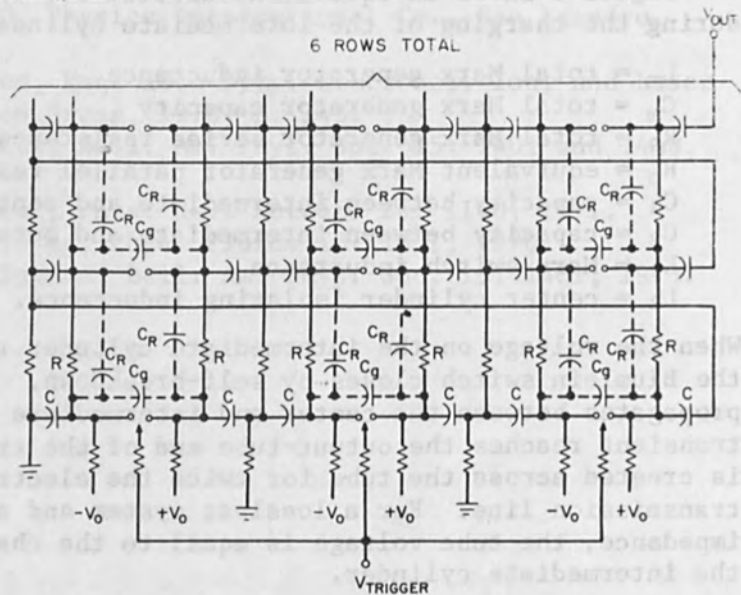


FIG. 3.--Equivalent Marx-Blumlein charging circuit.

FIG. 4.--Marx generator circuit.



The output tube is an evacuated, insulating chamber with a space-charge-limited cathode and a "thick target" anode for bremsstrahlung production, or an anode thin enough to allow electrons to pass through it with minimal loss if electron experiments are to be performed. In that case the electrons emerge from the tube into a drift chamber where they are drifted or focused.

MARX GENERATOR

The Marx generator used in REBA is housed in a tank 10 ft wide, 13 ft long, and 12 ft high. It consists of 38 0.5- μ f, 100-kV BICC capacitors with 19 gas spark gap switches, stores 95 kJ at full voltage (100 kV), and has an output capacity of 13.1 nf and an inductance of 24 μ H. Figure 4 shows a schematic diagram of the generator; Fig. 5 is a photograph of the assembled generator. The resistors interconnecting the capacitors are made of polyvinyl chloride tubing filled with a copper sulfate solution. The ground resistors are each 10 k Ω and the charging resistors are each 1.2 k Ω . The Marx generator is dc-charged with a variable ± 125 kV, 30 mA power supply that can be operated manually or automatically. The Marx generator may be connected to either of the two Blumleins by means of a hydraulically operated switch.

The spark gap shown in Fig. 6 is used in switching the Marx generator from a parallel to a series configuration. Tests were performed to determine a suitable spark-gap material.³ A tungsten-copper-nickel alloy, commonly called heavy metal (89% W, 7% Cu, 4% Ni), was selected for its resistance to arc erosion. The electrode shape was by means of an electrolytic tank plotter. The shape selected gave a uniform electric field over a 1.5-in.-diam circle at the end of the electrode. The fill gas used is a mixture of 70 per cent dry nitrogen and 21 per cent dry oxygen.

Figure 7 is an oscillograph of the Blumlein charge voltage under normal conditions. The voltage rises rapidly until the oil gap in the Marx switch breaks down and then continues to rise until the Blumlein switch breaks down. Figure 8 is an oscillograph of the Blumlein charge voltage in the case where the Blumlein switch did not break down on the first charging cycle.

BLUMLEIN TRANSMISSION LINE

Figure 9 is a side view of one of the two Blumlein transmission lines. The impedances and capacities are 7.5 Ω , 4.9 nf for the outer line and 10.1 Ω , 3.15 nf for the inner line. The transmission line will generate a 73-nsec pulse across the output tube. The return line corresponds to L_2 in Fig. 3 and is 3.2 μ H.

The Blumlein switch initiates the voltage transient in the Blumleins and affects the risetime of the voltage pulse across the output tube. Using formulas developed by Martin,⁴ the switch risetime can be determined:

$$\tau_R = \frac{5}{Z^{1/3} E^{4/3}}$$

$$\tau_L = \frac{L}{Z}$$

where τ_R = risetime due to the resistive phase of the breakdown (nsec)
 τ_L = risetime due to the inductive phase of the breakdown (nsec)

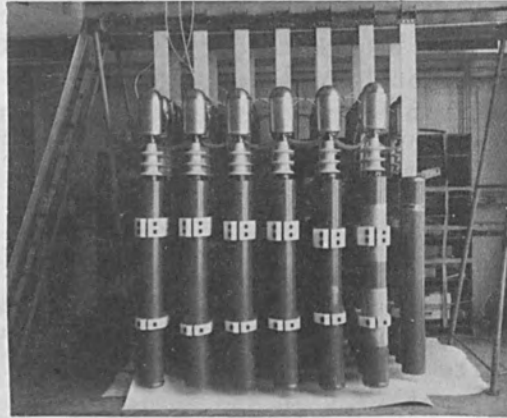


FIG. 5.--Assembled REBA Marx generator.

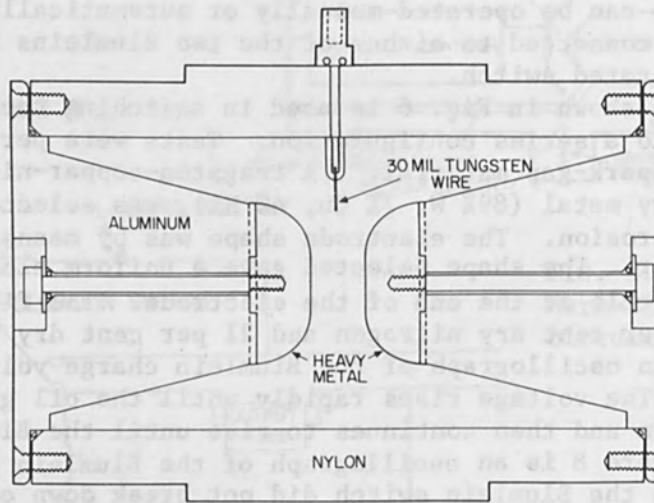


FIG. 6.--REBA triggered spark gap.

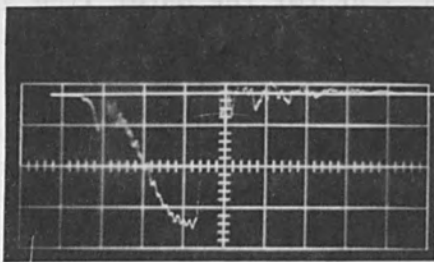


FIG. 7.--Blumlein charging voltage (normal): sweep, 0.5 μ sec/div.; vertical, 0.7 MV/div.

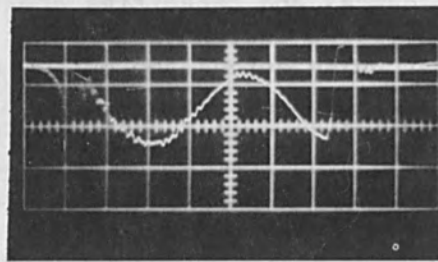


FIG. 8.--Blumlein charging voltage (ring over): sweep, 0.5 μ sec/div.; vertical, 0.7 MV/div.

E = electric field strength in the switch (0.36 MV/cm)
 Z = impedance of the inner transmission line (10.1 Ω)
 L = inductance of the spark channel (150 nH)
 $\tau_R \approx 10$ nsec
 $\tau_L \approx 15$ nsec
 $\tau_{TOTAL} = \tau_R + \tau_L = 25$ nsec.

This time constant, together with the time constant associated with the output tube, determines the risetime of the output voltage pulse.

A computer program developed by Boers⁵ was used to analyze the voltage gradients in the Blumleins. Figure 10 is an equipotential plot of the switch end of the inner transmission line. The electric field near enhancement points was kept below 0.65 MV/in.; the breakdown level for the type of oil used in REBA is 0.91 MV/in. for 1- μ sec pulses.

High-density polyethylene truncated cones are used to support the Blumleins. High density polyethylene is used because of its high pulsed breakdown voltage, mechanical strength, and dielectric strength are similar to that of the insulating oil.

OUTPUT TUBE

The tube used in REBA is shown in Fig. 11. The tube envelope consists of eighteen Lucite insulators, 24 in. in diameter, alternated with aluminum grading rings.⁶ Each Lucite insulator is 1.75 in. thick and the aluminum grading rings are 0.25 in. thick. The grading rings provide a more uniform voltage gradient across the insulator surfaces and capacitively grade the pulsed voltage. At pressures within the tube of typically 10^{-5} torr, the insulator rings can withstand an electric field of 180 kV/in. before surface breakdown occurs. For a 4-MV pulse on the tube, the stress on the insulators is 127 kV/in. This reduced level should extend the life of the tube and increase the maintenance intervals.

The cathode shank and hemispherical cathode tip are made of 303 stainless steel and the anodes are 4-mil-thick titanium foil. The cathode-anode separation is typically 2.75 in., which gives a tube impedance of 65 to 75 Ω and an inductance of 800 nH. Typical voltage and current waveforms are shown in Fig. 12 and 13, respectively.

Closer cathode-anode spacings give lower impedances and hence increase the current output. However, care must be taken to minimize the prepulse voltage (i.e., any voltage appearing across the tube prior to the main pulse). This goal is met by a series of oil spark gaps between the inner line and output tube. These spark gaps isolate the tube for prepulse of 300 kV but will break down as the main voltage pulse arrives at the tube. For this arrangement, currents of 90 kA at 2.5 MV have been achieved using a plasma⁷ cathode at a 1-in. cathode-anode spacing.

Table I gives a listing of typical operating levels for REBA. Repeatability for the values listed is within ± 10 per cent.

TABLE I. REBA operating parameters.

Cathode diameter (in.)	Blumlein charge voltage (MV)	Tube voltage (MV)	Tube current (kA)	Tube impedance (Ω)
3	2.20	2.5	90	28
3	2.30	3.4	40	85
4	2.00	2.75	49	56

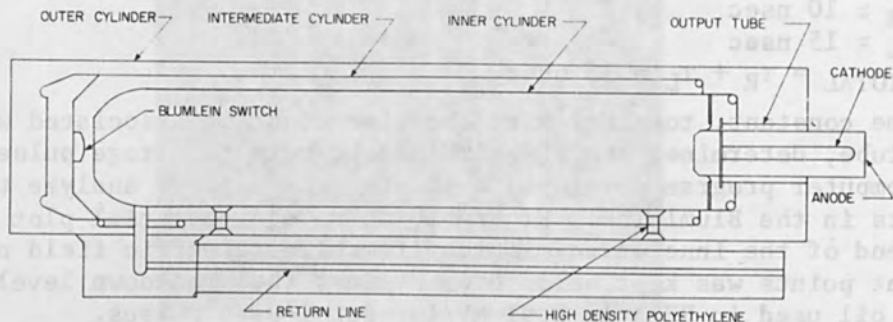


FIG. 9.--Cross section of REBA Blumlein.

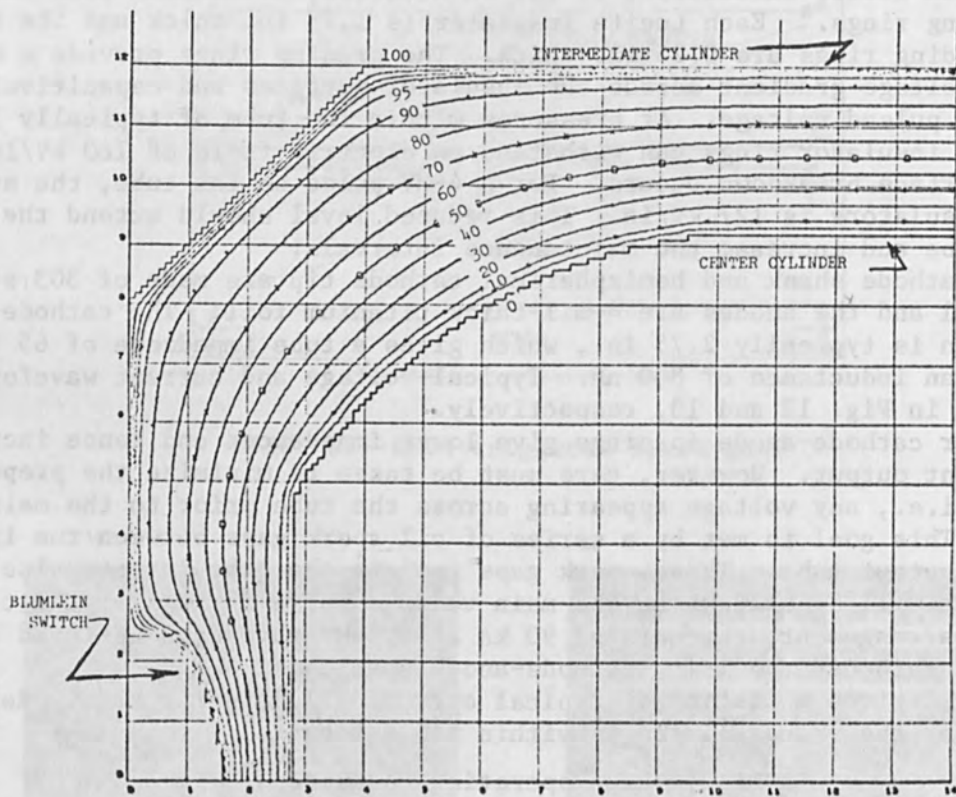


FIG. 10.--Equipotential plot of the Blumlein switch region. (Numbers shown are percentage of applied voltage between intermediate and center cylinders.)

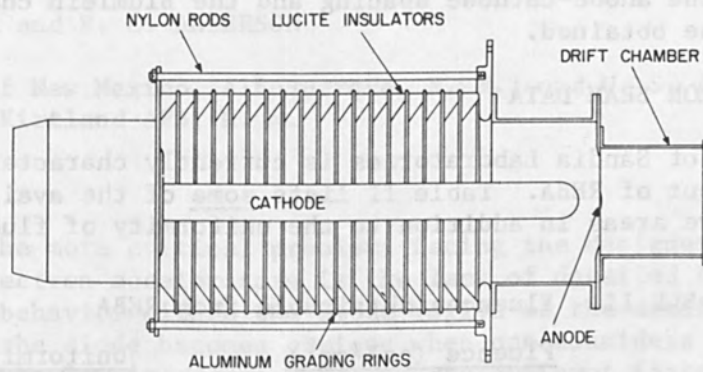


FIG. 11.--REBA output tube.

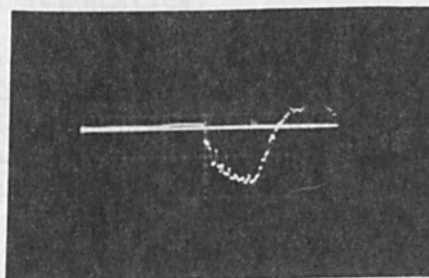


FIG. 12.--Typical output voltage waveform: 50 nsec/div., 2.7 MV/div.

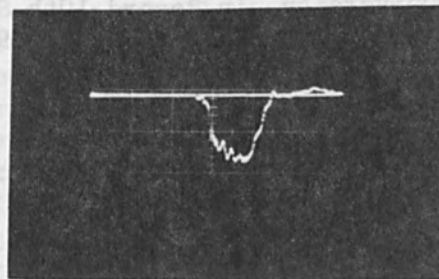


FIG. 13.--Typical output current waveform: 50 nsec/div., 27 kA/div.

These values should not be taken as the only operating levels available; by varying the anode-cathode spacing and the Blumlein charge other levels can be obtained.

PRELIMINARY ELECTRON BEAM DATA

Division 5226 of Sandia Laboratories is currently characterizing the electron-beam output of REBA. Table II lists some of the available fluences and effective areas in addition to the uniformity of fluence over the areas.

TABLE II. Fluences obtainable from REBA.

<u>Area (cm²)</u>	<u>Fluence (cal/cm²)</u>	<u>Uniformity</u>
2	200	---
20	30	25%
100	15	50%

Generally the higher the fluence desired, the smaller the effective area becomes for a given uniformity. The values listed in Table II are meant only as an indication of what can be obtained.

REFERENCES

1. H. Aslin, D. Sloan, et al., Feasibility Analysis of Advanced Power Concentrators, Kirtland AFB, N.M., AFWL-TR-66-119, 1967; vol. 1, p. 8.
2. K. R. Prestwich and D. L. Johnson, Development of an 18-megavolt Marx generator, Proc. 1969 Particle Accelerator Conference, 1969; p. 64.
3. Ibid.
4. J. C. Martin, AWRE, private communication.
5. J. E. Boers, Digital computer solution of Laplace's equation including dielectric interfaces and small floating electrodes, in Record 11th Symp. Electron, Ion, and Laser Beam Technology, San Francisco Press, 1971.
6. I. D. Smith, Pulse breakdown of insulator surfaces in a poor vacuum, Proc. Intern. Symp. Insulation of High Voltages in Vacuum, 1964; pp. 261-280.
7. J. J. Clark et al., High-current relativistic electron beam accelerators at Cornell University, in Record 10th Symp. Electron, Ion, and Laser Beam Technology, San Francisco Press, 1969; p. 117.

THE BEHAVIOR OF LOW-IMPEDANCE, FIELD EMISSION DIODES*

R. K. PARKER and R. E. ANDERSON

University of New Mexico, Albuquerque, N. M.; and U. S. Air Force Weapons Laboratory, Kirtland AFB, N. M.

INTRODUCTION

One of the more critical problems facing the designer of pulsed, low-impedance electron accelerators is the lack of detailed information concerning the behavior within the diode region of the accelerator. The importance of the diode becomes obvious when one considers that the time response of the low-impedance diode is the dominant factor limiting the ability of the accelerator to convert stored energy to electron-beam kinetic energy. Furthermore, the quality of the emitted electron beam depends strongly on the diode behavior.

An investigation of the physics underlying the behavior of low-impedance diodes is greatly simplified if the pulsed power system satisfies two important criteria. First, the pulsed power system must generate a "clean," undistorted, output pulse. Second, the system must incorporate accurate and reliable electrical diagnostics.

ACCELERATOR DESCRIPTION

The pulsed power system designed and constructed for the U. S. Air Force Weapons Laboratory by Field Emission Corp. in 1963 meets the criteria listed above. Although the system was originally developed as an exploding bridge wire device, it has since been modified for use as a low-impedance electron accelerator. The required modifications consisted of reversing the system polarity and installing an electron-beam tube to replace the exploding wire transducer chamber. With these exceptions, the system remains as described in the literature.¹⁻³

The basic design concept for this system is the paralleling of fifteen synchronized 320-kV Marx surge generators into a common matched-impedance transmission line. This approach was taken to minimize the system inductance; a low system inductance is necessary for a fast-risetime, low-impedance source. A cross-sectional view of the system in its original exploding wire configuration is shown in Fig. 1. The electrical energy is stored in the fifteen 70- Ω pulsers (E) which are connected in parallel to the 4.7- Ω coaxial transmission line (I and J). Each pulser consists of a stack of 25 energy storage modules which form a modified Marx surge circuit. The energy storage modules are LC lumped constant storage lines fabricated from high-dielectric-constant ceramic storage elements. At the maximum charging voltage of 32 kV, each pulser delivers a 4600-A trapezoidally shaped current pulse at 320 kV into a matched 70- Ω resistive load. The pulse length is 50 nsec (FWHM) and has a rise time of approximately 4 nsec between the 10 and 90-percent points. The output pulses are transmitted to the common coaxial line by 70- Ω coaxial directive switches (F). When discharged into a matched 4.7- Ω resistive load, the system produces a 70 000-A current pulse at 320 kV. The output pulse has an 8-nsec

*This work constitutes partial fulfillment of the requirements for the Ph.D. degree in Nuclear Engineering at the University of New Mexico.

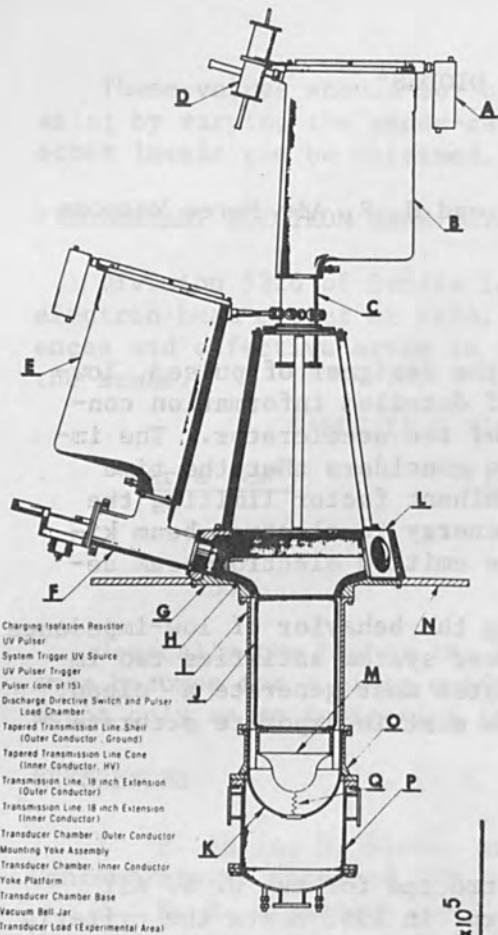


FIG. 1.--System cross section.

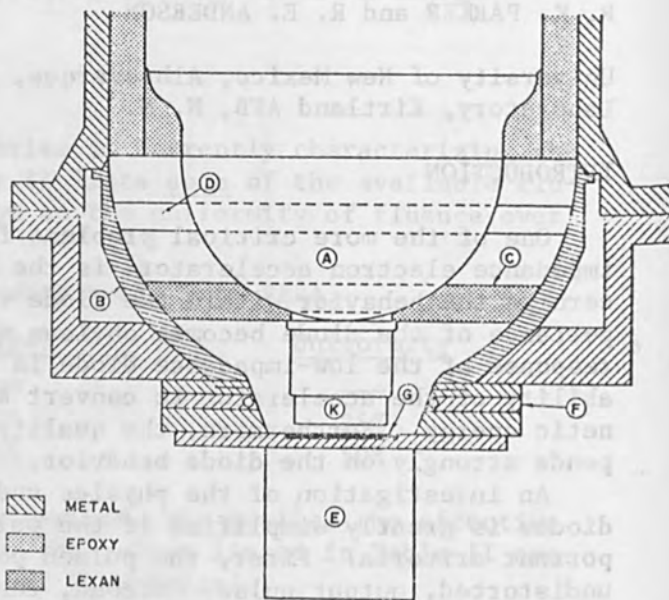


FIG. 2.--Tube cross section.

- A Charging Isolation Resistor
- B UV Pulser
- C System Trigger UV Source
- D UV Pulser Trigger
- E Pulser (one of 15)
- F Discharge Directive Switch and Pulser Load Chamber
- G Tapered Transmission Line Sheath (Outer Conductor - Ground)
- H Tapered Transmission Line Cone (Inner Conductor - HV)
- I Transmission Line - 18 inch Extension (Outer Conductor)
- J Transmission Line - 18 inch Extension (Inner Conductor)
- K Transducer Chamber - Outer Conductor
- L Mounting Yoke Assembly
- M Transducer Chamber - Inner Conductor
- N Yoke Platform
- O Transducer Chamber Base
- P Vacuum Bell Jar
- Q Transducer Load (Experimental Area)

FIG. 3.--Response of a 2-in.-diam cathode with 0.113 in. diode spacing.

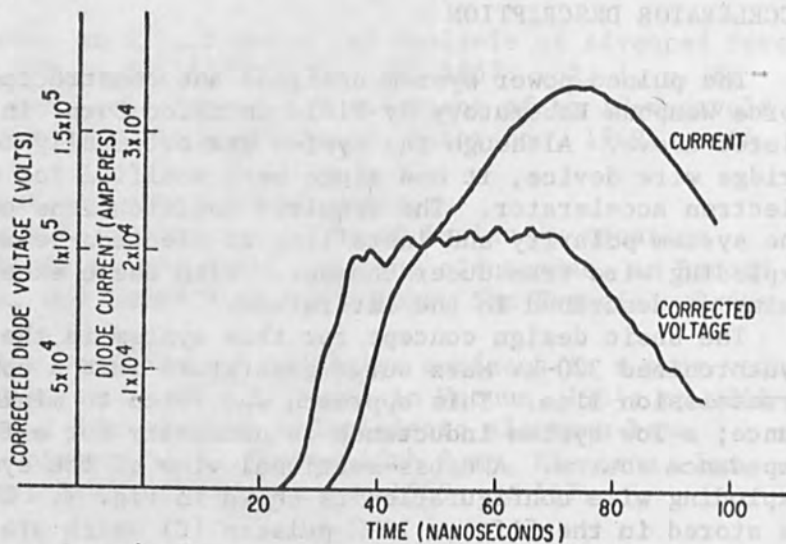
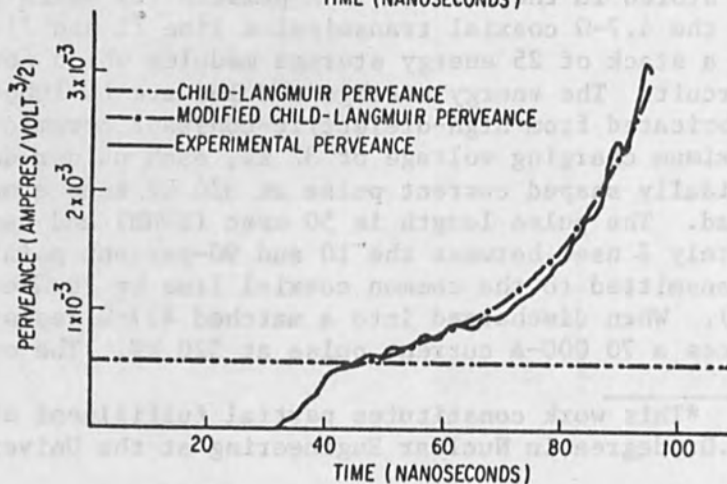


FIG. 4.--Diode perveance for 2-in.-diam cathode with 0.113 in. diode spacing.



risetime and a 50-nsec (FWHM) duration. The energy content of the output pulse is approximately 1 kJ.

If the rise time of the combined output pulse is to be 8 nsec, the firing time span of the fifteen pulsers must be approximately 4 nsec. To achieve this degree of synchronization, a combination of ultraviolet light spark gap illumination and overvoltage of a trigger electrode is required.³ When the UV pulser (B) is fired, the energy from the pulser is discharged through the spark gap in the UV trigger source (C) and then flows to ground through a multi-output pulse-splitting transformer. The individual voltage pulses from the transformer are applied to the trigger electrodes, which are positioned between the electrodes of the top spark gap in each pulser. The application of the trigger pulses is delayed 15 nsec relative to the UV illumination of the top gaps. For normal operation, the pulsers are charged to within 10 per cent of self-fire for a given pressure. Since the Marx erection time is a sensitive function of the percentage self-fire voltage, any variation in the correlation between the pulser pressure and the charging voltage results in variations in the delay between the trigger input and the pulser output.

To operate the pulsed power system as a low-impedance electron accelerator, the transducer chamber (P and Q) of the exploding-wire configuration must be replaced by an electron-beam tube designed for this purpose (Fig. 2). The basic hemispherical configuration of the exploding-wire chamber underwent several modifications. An inner hemisphere (A) 4-3/8-in. in radius was chosen to minimize the tube inductance. The outer hemisphere remained at its original 6-3/8-in. radius. To avoid the surface flash-over problem at the epoxy-vacuum interface, a lexan disk was inserted at (C). The region above the disk could then be filled with an insulating gas and the diode region below evacuated. The basic electrical diagnostics for the diode are a capacitive voltage divider (D), a Faraday cup-calorimeter current monitor (E), and a set of four magnetic pickup loops (F) which respond to the time derivative of the current. The diode is formed by the cylindrical graphite cathode (K) and the graphite sensing disk (G) of the Faraday cup, which is located on the anode plane. For applications other than the diode study, the Faraday cup is replaced by an assembly which stretches a thin aluminized Mylar film across the anode plane.

The diodes used during this study may be described as planar with a broad area "cold" cathode. The cathodes were 1.5- and 2-in-diam graphite cylinders with machined faces. The anode-cathode spacing varied from approximately 0.1 to 0.3 in. No special effort was made to smooth the cathode face or to round the cathode edge.

BASIC DIODE PHYSICS

The phenomena within the diode region of a low-impedance electron accelerator are quite complex. Instead of a detailed description, the approach taken during this preliminary diode study was to evaluate the response of the diode in an attempt to determine the electron emission characteristics and the effects of space charge on the flow of diode current.

Prior to the application of the voltage pulse, the cathode surface is at room temperature. Early in the pulse, the macroscopic voltage gradient in the diode region is in the range of 10^5 to 10^6 V/cm. While these conditions exist, the only plausible mechanism for the emission of the observed current levels is field emission. As time progresses and the diode

current increases, the situation becomes more complex; but the first few nanoseconds of diode response should be characterized by strict field-emission behavior.

An expression descriptive of the field emission current must take the microscopic condition of the cathode surface into consideration. Any surface roughness distorts the macroscopic field at the cathode, causing a local field enhancement. In general, the value of the local field at the irregularity can be taken as βF , where β is the field-enhancement factor and F is the macroscopic voltage gradient (V/cm). Under the present circumstances, when the cathode surface is bound to have some roughness, the field-emission equation must be modified to include the effects of the microscopic field variations. The natural logarithm of the appropriate form of the field emission equation is⁴

$$\ln (I/F^2) = \ln K_1 + \ln A + 2 \ln \beta - K_2/\beta F \quad (1)$$

where I is the field emission current (A), A is the cathode area (cm²), and K_1 and K_2 are constants characteristic of the cathode material. For graphite, K_1 and K_2 are 5.08×10^{-7} and 6.93×10^8 respectively. If the current is emitted from the cathode by field emission, a plot of $\ln(I/F^2)$ vs $1/F$ should be a straight line with an intercept on the logarithmic axis of $\ln K_1 + \ln A + 2 \ln \beta$ and a slope of $-K_2/\beta$.

Within a few nanoseconds after the application of the voltage pulse, the diode current increases very rapidly. The increasing number of electrons in the diode region constitutes a space charge that exerts a retarding field at the cathode. The number of electrons in the diode region, and hence the retarding component of the field at the cathode, increases with increasing current. As a result, the behavior of the diode should correspond at some point in time to space-charge-limited flow.

The space-charge relation appropriate to the planar-diode configuration used during this study can be quickly derived from the infinite planar diode described by the Child-Langmuir space-charge law:

$$I = jA = \frac{2.335 \times 10^{-6} V^{3/2} A}{X^2} \quad (2)$$

where j is the current density (A/cm²), A is the cathode area (cm²), V is the diode voltage (V), and X is the anode-cathode spacing (cm). The diode perveance is then

$$P \equiv \frac{I}{V^{3/2}} = \frac{2.335 \times 10^{-6} A}{X^2} \quad (3)$$

The significance and usefulness of the perveance is that it represents an upper limit to the electron flow in a diode imposed by space-charge effects. The limit is determined by the geometrical shape of the diode but is independent of the size of the diode and the magnitude of the applied voltage.

EXPERIMENTAL DATA

The intent of this preliminary diode study was to determine the characteristics of the electron emission process and the effects of space charge on the current flow. The analytical approach was very carefully to resolve the time variation of the diode voltage and current on a common time base. The measured voltage was corrected to remove the inductive component and leave only the resistive voltage developed across the diode.

The corrected voltage and measured current signals were then used to develop the field-emission and perveance plots. Finally, the time response of the diode was interpreted from an evaluation of these plots.

The diode data have been categorized according to (1) cathode type, (2) cathode diameter, (3) anode-cathode spacing, (4) tube pressure, and (5) system charging voltage. Specification of the system charging voltage provides a measure of the magnitude of the voltage pulse applied to the diode since the applied voltage cannot be predicted prior to the discharge of the system. If the accelerator were "ideal," i.e., no losses or impedance mismatches, the voltage developed across the load would be given by the following expression:

$$V_L(t) = 25 V_{ch} \frac{R(t)}{R(t) + 4.7} \quad (4)$$

where V_L and V_{ch} are respectively the voltage across the load and the charging voltage in volts and $R(t)$ is the diode resistance in ohms. Since the diode resistance as a function of time is not known until after the diode response is measured, Eq. (4) cannot be used to predict the applied voltage. The results of the diode experiments were therefore categorized by charging voltage. When the system was terminated by a constant-resistance load, the actual load voltage was found to be approximately 20 per cent lower than the "ideal" values predicted by Eq. (4). The difference between these values is attributed to the losses and slight impedance mismatches in the real system.

Before investigating the variation in diode behavior as a function of the parameters listed above, consider the response of the diode formed by a 2-in.-diam graphite cathode positioned at a distance of 0.113 in. from the anode to the voltage pulse produced by the accelerator after it has been charged to 14 kV. The tube pressure for this experiment was 2×10^{-5} torr. The corrected voltage and current traces are shown in Fig. 3. The zero point for the relative time base in these data plots is correlated to the discharge of the UV pulser. Note that the voltage is applied at 23 nsec and a measurable current began to flow at 32 nsec. Figures 4 and 5 are the diode-perveance and field-emission plots derived from the corrected voltage and current data.

To begin the diode analysis, consider the results of the field emission plot. For the time interval from 32 to 35 nsec, the data points fall on a straight line. This correlation confirms the field emission character of the initial emission from the cathode surface. However, at a point between 35 and 36 nsec a rapid transition takes place. From the slope of the field-emission line, the field enhancement factor was found to be 877. Similarly, the logarithmic intercept yielded an emission area of 9.4×10^{-7} cm².

The values of β and A must be interpreted with care. If a single surface irregularity were the emission source, these values could be used directly to determine the approximate configuration of the source. However, for a broad area cathode the existence of many emission sites must be anticipated. Under these circumstances, Tomaschke et al.⁵ have shown that the field emission plot retains its linear character. The field enhancement factor derived from the plot is now weighted toward the larger enhancement factors of the set. Similarly, the derived emission area is not the total emission area but rather a qualitative measure of the magnitude of the actual emission area.

The enhancement factor calculated from the field-emission plot should be considered as the product of an enhancement factor β_1 , associated with the microscopic projections on the cathode and a local enhancement β_2 , related to the macroscopic effects of the cathode edge. For a radius of curvature of the cathode edge of approximately 9×10^{-2} mm and an anode-cathode spacing of 2.87 mm, the edge effects should account for a factor of 4 in the measured value of β .⁶ The microscopic enhancement factor would then be reduced to about 220. Such a value for the enhancement factor indicates that the current is emitted from microprojections or whiskers on the cathode surface. Based on calculations by Alpert et al.⁶ and by Charbonnier,⁷ the ratio of the microprojection height to base radius could vary from 500 to 25 depending on the projection configuration.

In a later paper, Charbonnier⁸ reviews the processes associated with the initiation of vacuum breakdown. According to the field-emission hypothesis, a stable field-emission current should be drawn from the whiskers at low diode voltages. As the gap voltage is increased, a sharp transition from stable emission to breakdown occurs at a well-defined value of the cathode field. For steady fields, breakdown occurs at from 5 to 8×10^7 V/cm. Under pulsed conditions, the critical voltage gradient should be essentially independent of pulse duration for pulses longer than a microsecond but can increase substantially when the pulse duration is in the nanosecond range. To determine whether the breakdown process is initiated at the anode or cathode, Charbonnier⁷ derived a critical value for the field enhancement factor which depends on the duration of the applied voltage pulse. For pulses in the nanosecond range, the critical enhancement factor is rather low. The probability of cathode-initiated breakdown is therefore quite high.

Recent work by Mesyats et al.⁹ has shown that the application of pulsed fields in excess of the critical value results in the explosion of the emitting whiskers. The expansion velocity of the cathode flare formed by the projection explosion was observed to be constant in time and independent of the applied voltage. For the several metals investigated, the expansion velocities varied from 1 to 2×10^6 cm/sec.

If one applies the field-emission hypothesis for vacuum breakdown, the discontinuity in the field-emission plot can be interpreted as the explosion of the emitting microprojections. The macroscopic field at that point in time was 3.33×10^5 V/cm. From the measured value of the enhancement factor, the corresponding microscopic voltage gradient was 2.9×10^8 V/cm. As expected, the observed value for the critical field was significantly higher than the steady-field values listed above.

Having used the field emission plot to interpret the first 12 nsec, of diode behavior, let us now consider the perveance plot shown in Fig. 4. The experimental perveance exhibits a distinct change in slope when it reaches the theoretical Child-Langmuir value. The rapid current increase observed at this time has been related to the production and expansion of cathode flares, but the Child-Langmuir perveance is determined by the physical diode configuration. The tendency of the diode to respond at the theoretical limit must therefore be interpreted as indicating that the plasma emission surface formed by the rapid merger of many cathode flares has effectively spread over the cathode surface, but has not yet moved significantly into the diode region.

If the flare expansion velocity is constant, the "virtual" cathode formed by the flare plasma then moves toward the anode at a constant rate. With this assumption, the Child-Langmuir perveance expression can be modified to take the form

$$P = \frac{2.335 \times 10^{-6} A}{(X - vt)^2} \quad (5)$$

where v is the cathode flare expansion velocity (cm/sec) and t is the expansion time (sec). To fit the modified perveance expression to the experimental data, we set $t = 0$ at the instant the "knee" occurred in the perveance plot. The modified perveance curve shown in Fig. 4 results from an assumed expansion velocity of 3.1×10^6 cm/sec. The validity of the proposed model is established by the strong correlation between the theoretical curve and the experimental data.

With the validity of the analytical approach established, the variation in diode behavior as a function of several macroscopic parameters can be evaluated. A decrease in the cathode diameter should result in a decrease in the diode perveance but should have no effect on the field-emission characteristics of the diode. In contrast, an increase in the amplitude of the applied voltage pulse should affect the field-emission characteristics but not the diode perveance. An increase in the diode spacing should affect both the diode perveance and the field-emission characteristics. Finally, the diode response was found to be essentially independent of tube pressure over the range 2×10^{-5} to 5×10^{-3} torr.

With these considerations in mind, the cathode diameter was reduced from 2 to 1.5 in. and the diode spacing increased from 0.113 to 0.176 in. The response of this diode configuration was then evaluated for accelerator charging voltages of 14, 20, and 26 kV. In each of these cases, the stable field emission lasted for about 10 nsec. The observed field-emission characteristics were very similar to those described for the previous diode.

By definition, the perveance of a diode should be independent of the applied voltage. The perveance for these three events (Fig. 6) demonstrates the validity of that concept for these diodes. The relative shift of these curves on the common time base is not a function of the diode behavior but rather is related to the erection time of the Marx circuits of the accelerator. In contrast to the perveance curve in Fig. 4, the knee on these curves occurred well above the theoretical Child-Langmuir value. This discrepancy can be explained if the flare density on the cathode surface is assumed to be sufficiently low so that the flares move a significant distance into the anode-cathode region before the merger occurs. In this case, the perveance knee would correspond to a decreased diode spacing. Following the knee, the remainder of the perveance curve matched the behavior predicted by Eq. (5). The velocities for the 14, 20, and 26 kV experiments were 3.2, 3.5, and 3.9×10^6 cm/sec, respectively.

An increase in the diode spacing to 0.292 in. resulted in the diode response shown in Fig. 7. The accelerator charging voltage was again set at 14.0 kV. The effects of the increased diode spacing can be interpreted from the perveance and field-emission plots shown in Figs. 8 and 9, respectively. Although the perveance curve has lost its characteristic shape, i.e., no sharp discontinuity at the Child-Langmuir limit, the field-emission plot has retained the linear relationship indicative of stable field emission. In contrast to the diode behavior at decreased diode spacing, the interval for stable field emission extended well into the duration of the pulse. An analysis of the data yielded an enhancement factor of 1620 and an emission area of 7.7×10^{-5} cm².

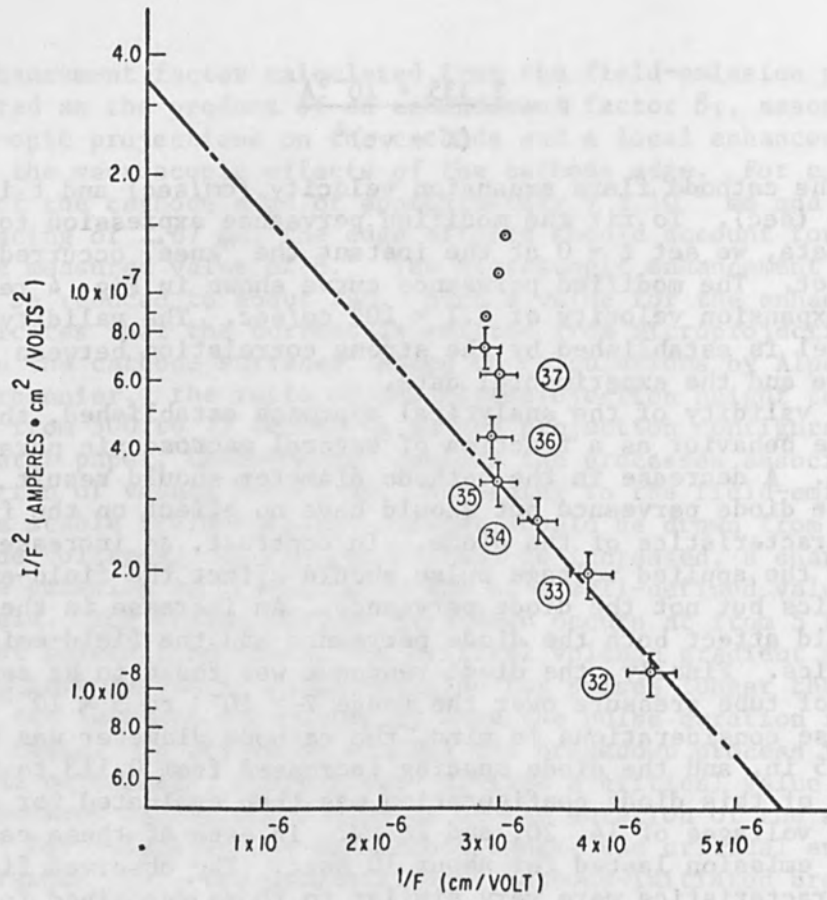


FIG. 5.--Field emission plot for 2-in.-diam cathode with 0.113-in. diode spacing.

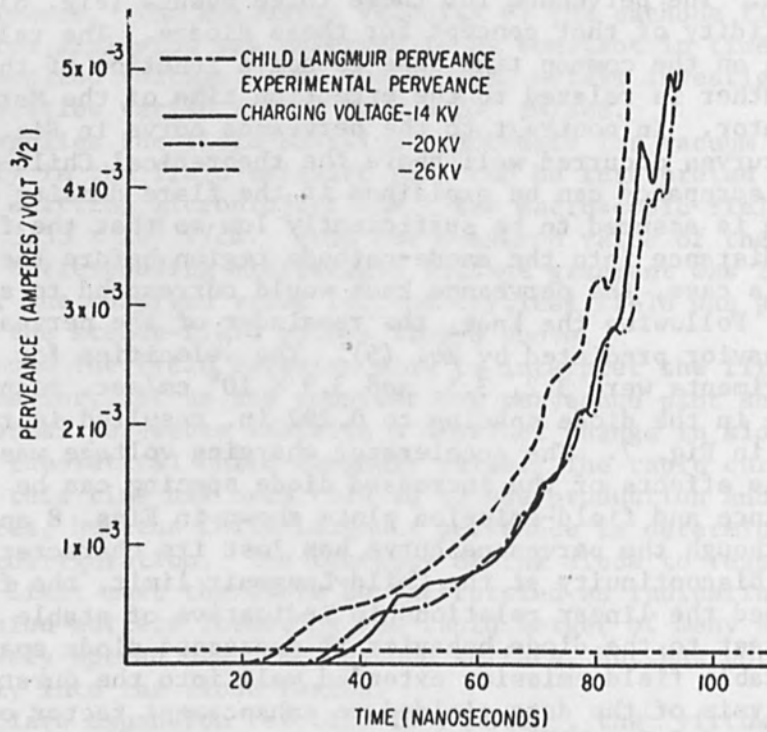


FIG. 6.--Perveance of 1.5-in.-diam cathode with 0.176-in. diode spacing.

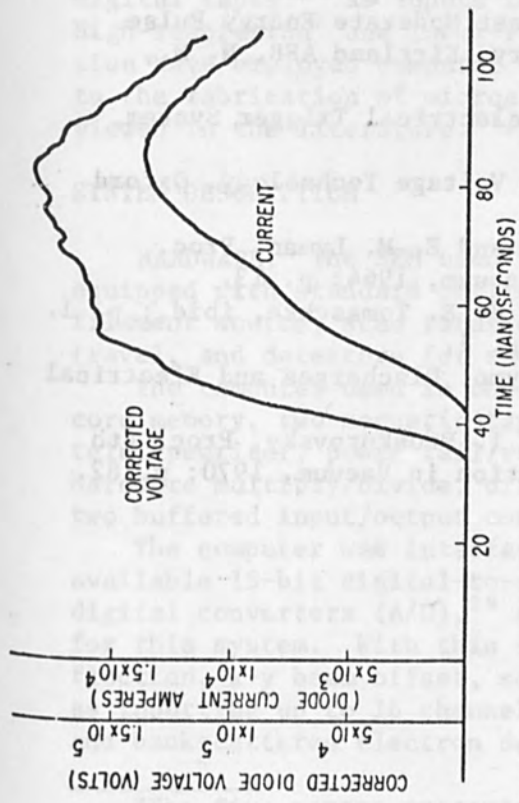


FIG. 7.--Response of a 1.5-in.-diam cathode with 0.292-in. diode spacing.

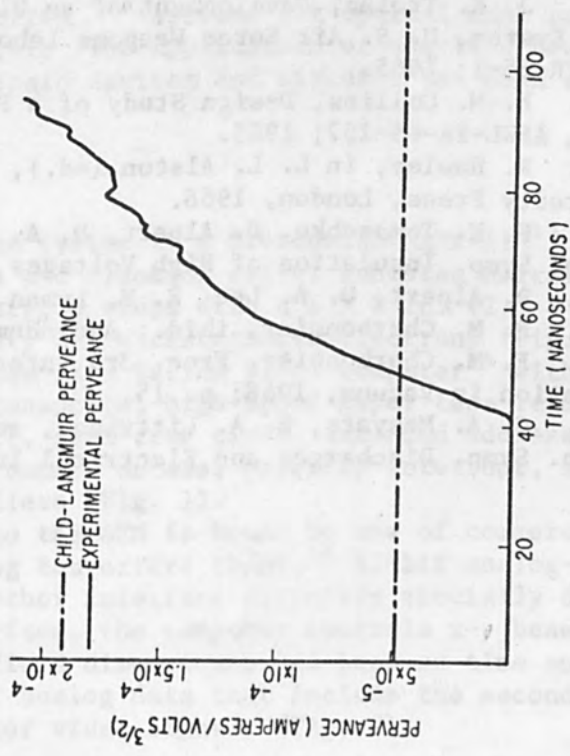


FIG. 8.--Diode perveance for 1.5-in.-diam cathode with 0.292-in. diode spacing.

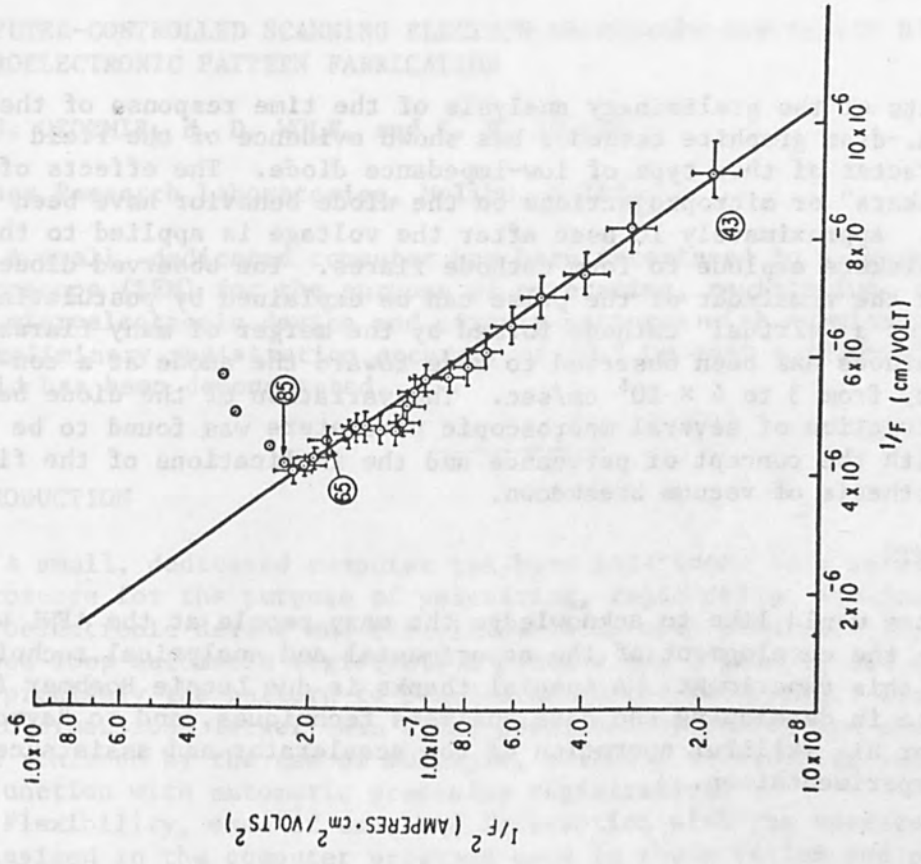


FIG. 9.--Field emission plot for 1.5-in.-diam cathode with 0.292-in. diode spacing.

CONCLUSIONS

The results of the preliminary analysis of the time response of the 1.5- and 2-in.-diam graphite cathodes has shown evidence of the field emission character of this type of low-impedance diode. The effects of cathode "whiskers" or microprojections on the diode behavior have been demonstrated. Approximately 10 nsec after the voltage is applied to the diode, the whiskers explode to form cathode flares. The observed diode perveance for the remainder of the pulse can be explained by postulating the movement of a "virtual" cathode formed by the merger of many flares. The plasma cathode has been observed to move toward the anode at a constant velocity from 3 to 4×10^6 cm/sec. The variation of the diode behavior as a function of several macroscopic parameters was found to be consistent with the concept of perveance and the implications of the field emission hypothesis of vacuum breakdown.

ACKNOWLEDGMENTS

The authors would like to acknowledge the many people at the AFWL who cooperated in the development of the experimental and analytical techniques required for this experiment. A special thanks is due Leonie Boehmer for her assistance in developing the data analysis techniques, and to Raymond Hollenbeck for his skillful operation of the accelerator and assistance during the experimentation.

REFERENCES

1. J. K. Trolan, F. M. Charbonnier, F. M. Collins, and A. H. Guenther, *Exploding Wires*, Plenum Press, New York, 1964; vol. 3, p. 361.
2. J. K. Trolan, *Development of an Ultrafast Moderate Energy Pulse Power System*, U. S. Air Force Weapons Laboratory, Kirtland AFB, N. M., AFWL-TR-65-1; 1965.
3. F. M. Collins, *Design Study of a Photoelectrical Trigger System*, *ibid.*, AFWL-TR-65-157; 1965.
4. R. Hawley, in L. L. Alston (ed.), *High Voltage Technology*, Oxford University Press, London, 1968.
5. H. E. Tomaschke, D. Alpert, D. A. Lee, and E. M. Lyman, *Proc. Intern. Symp. Insulation of High Voltages in Vacuum*, 1964; p. 13.
6. D. Alpert, D. A. Lee, E. M. Lyman, and H. E. Tomaschke, *ibid.*; p. 1.
7. F. M. Charbonnier, *ibid.*; Addendum 1, p. 1.
8. F. M. Charbonnier, *Proc. 3rd Intern. Symp. Discharges and Electrical Insulation in Vacuum*, 1968; p. 15.
9. G. A. Mesyats, E. A. Littvinov, and D. I. Proskurovsky, *Proc. 4th Intern. Symp. Discharges and Electrical Insulation in Vacuum*, 1970; p. 82.

SESSION ON COMPUTER-CONTROLLED MICROFABRICATION*

COMPUTER-CONTROLLED SCANNING ELECTRON MICROSCOPE SYSTEM FOR HIGH RESOLUTION MICROELECTRONIC PATTERN FABRICATION

F. S. OZDEMIR, E. D. WOLF, and C. R. BUCKEY

Hughes Research Laboratories, Malibu, Calif.

A small, dedicated computer has been interfaced to a scanning electron microscope (SEM) for the purpose of generating, registering, and fabricating microelectronic device and circuit patterns with submicron dimensions. A preliminary registration accuracy of $\pm 0.1 \mu\text{m}$ over a $(950\text{-}\mu\text{m})^2$ pattern field has been demonstrated.

INTRODUCTION

A small, dedicated computer has been interfaced to a scanning electron microscope for the purpose of generating, registering, and fabricating microelectronic device and circuit patterns with submicron dimensions. A closed-loop automatic registration process was developed and used to register precisely the pattern to benchmarks on the substrate. Single-pattern field dimensions larger than those permitted by deflection aberrations¹ were achieved by the use of multiple, slightly overlapping scan fields in conjunction with automatic precision registration.

Flexibility, ease of use, and interaction with the operator have been emphasized in the computer programs used in registration and pattern writing.

Prior techniques have utilized SEMs with flying-spot scanners²⁻⁵ or digital tapes^{6,7} as inputs for high-resolution direct device fabrication. High-resolution² and lower-resolution⁷⁻¹⁰ systems for optical mask generation have employed computer control. The application of electron beams to the fabrication of microelectronic devices and circuits has been reviewed in the literature.^{11,12}

SYSTEM DESCRIPTION

HARDWARE. The SEM used in the system is a Stereoscan MARK IIA¹³ equipped with standard deflection and blanking coils, tungsten hairpin filament source, scan rotation unit, a stage with a 1×2 in. (2.5×5 cm) travel, and detectors for secondary and backscattered electrons (Fig. 1).

The computer used in the system is a Varian 620/i computer¹⁴ with 8K core memory, two magnetic-tape transports, high-speed paper-tape reader, teletypewriter, power fail/restart, real-time clock, extended addressing, hardware multiply/divide, direct memory access, priority interrupt, and two buffered input/output controllers (Fig. 1).

The computer was interfaced to the SEM in house by use of commercially available 15-bit digital-to-analog converters (D/A),¹⁵ 12-bit analog-to-digital converters (A/D),¹⁵ and other interface circuitry specially designed for this system. With this interface, the computer controls x-y beam deflection, x-y beam offset, scan-field dimensions, and beam on time as well as inputting up to 16 channels of analog data that include the secondary and backscattered electron detector video signals (Fig. 2).

*The five papers presented in this session (pp. 463-512) are scheduled to appear as a group in IEEE Transactions on Electron Devices.

COMPUTER-CONTROLLED SCANNING ELECTRON MICROSCOPE SYSTEM FOR HIGH RESOLUTION MICROELECTRONIC PATTERN FABRICATION

It is necessary to use a scanning electron microscope (SEM) for the purpose of monitoring, registering and analyzing the microstructure of the patterned surface. A specially designed computer has been developed for a scanning electron microscope (SEM) for the purpose of monitoring, registering and analyzing the microstructure of the patterned surface. A preliminary experimental accuracy of 0.5% (over a 0.50-um) pattern field has been demonstrated.

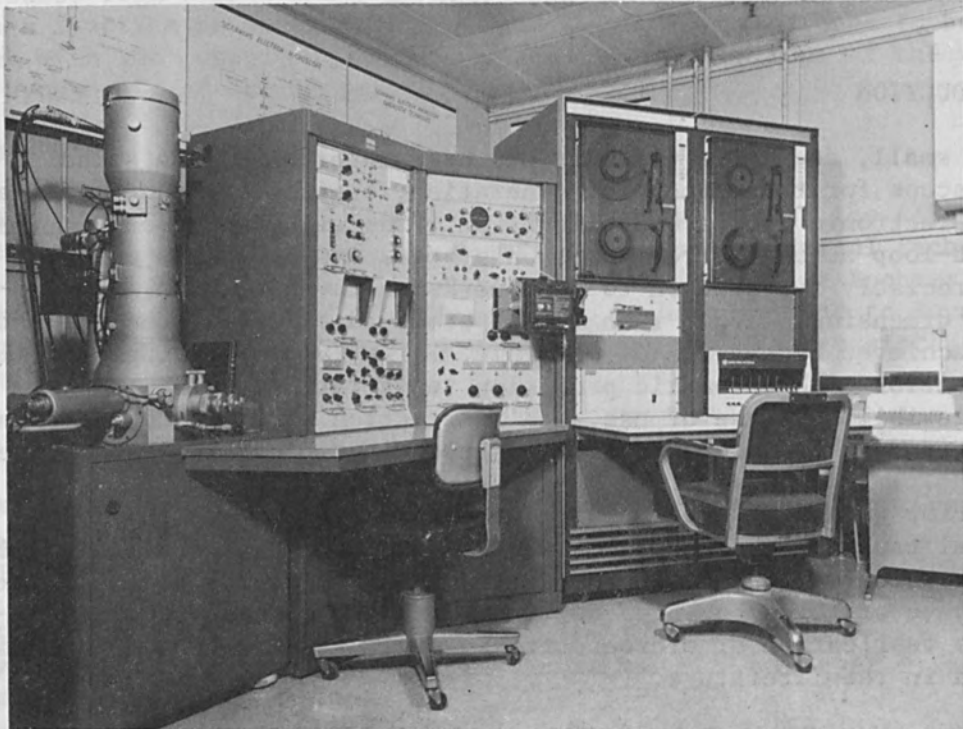


FIG. 1.--Electron beam microfabrication system.

The computer was interfaced to the SEM to house by use of commercially available 12-bit digital-to-analog converters (D/A), 12-bit analog-to-digital converters (A/D), and other interface circuitry specially designed for this system. With this interface, the computer controls x-y beam deflection, x-y beam offset, scan-field dimensions, and beam on time as well as interfacing up to 16 channels of timing data that include the secondary and backscattered electron detector slow signals (Fig. 2).

The five papers presented in this session (pp. 463-513) are scheduled to appear as a group in IRM Transactions on Electron Devices.

SOFTWARE. The Varian 620/i computer has its own Master Operating System (MOS)¹⁴ resident on magnetic tape and in approximately 1K of the core memory. Software programs for registration and pattern writing were developed within the framework of this operating system. Software flexibility and interaction with the user are emphasized in the registration and pattern-writing programs. The programs are composed of small, independent sections which facilitate corrections and alterations and also permit rearrangement of these sections to compose new pattern programs. User-program interaction during fabrication of the pattern permits a given program to generate more than one fixed pattern. The programs are constructed to accept process parameters from user prior to registration and pattern writing, to issue diagnostic messages, to respond to optional directives during fabrication, and to issue messages after completing certain portions of the process.

REGISTRATION AND PATTERN WRITING. The process of fabricating patterns on a wafer begins with the writing of the initial benchmarks on the wafer. The silicon wafer is first coated with a thin layer of an electron resist, polymethyl methacrylate.¹⁶ After mounting the wafer on the stage and placing the stage in the SEM, the scan axis is aligned to the wafer edge and the misalignment between the wafer edge and stage axis is determined. This latter error is compensated for in subsequent mechanical stepping. The initial set of benchmarks consists of a series of row and circuit benchmarks (Fig. 3). The row benchmarks are single lines with a cross bar at the center. The circuit benchmarks consist of five elements indicated as solid squares in Fig. 3. Both the row and circuit benchmarks are written using a $(500\text{-}\mu\text{m})^2$ scan field. After exposure the wafer is developed in methyl isobutyl detone diluted with three volumes of 2-propanol and gold benchmarks are formed on the silicon wafer by means of the electron resist liftoff technique.¹⁷ The wafer is recoated and placed in the SEM.

Misalignment between wafer axis and stage axis is determined by means of the first-row benchmark in the first and last rows. This error is compensated for in subsequent mechanical stepping. The scan axis is aligned to the row benchmark. The stage is then mechanically stepped to the location of subcell 1 (Fig. 3). The scan field is registered to the three benchmark elements falling within the scan field. The portion of the pattern falling within this subcell is written and the stage is moved to subcell 2, where the process is repeated. After writing all the 1 and 2 subcells in a given row, the stage is moved back to the row benchmark and the above process repeated for all 3 and 4 subcells in that row. Then a new row is started. After the last time a given row benchmark or a circuit benchmark element is used, it is destroyed and a new row benchmark or a circuit benchmark element is written next to it. The new element is one of the elements indicated as empty squares in Fig. 3. The wafer is then removed from the SEM and processed. Figure 3 has been drawn for a hypothetical, four-step device fabrication process. Thus, at each step fresh sets of row and circuit benchmarks are available.

The alignment of the scan axis to a row benchmark is now described in detail to explain how certain portions of the registration programs operate. Figure 4 shows a row benchmark which is misaligned by an amount $\Delta\theta$. The program performs an alignment scan at one end of the scan field, collecting and storing the secondary electron signal that has been converted by the A/D. The data are then digitally smoothed and the location of bar is determined. A similar process is carried out at the other end of the bar.

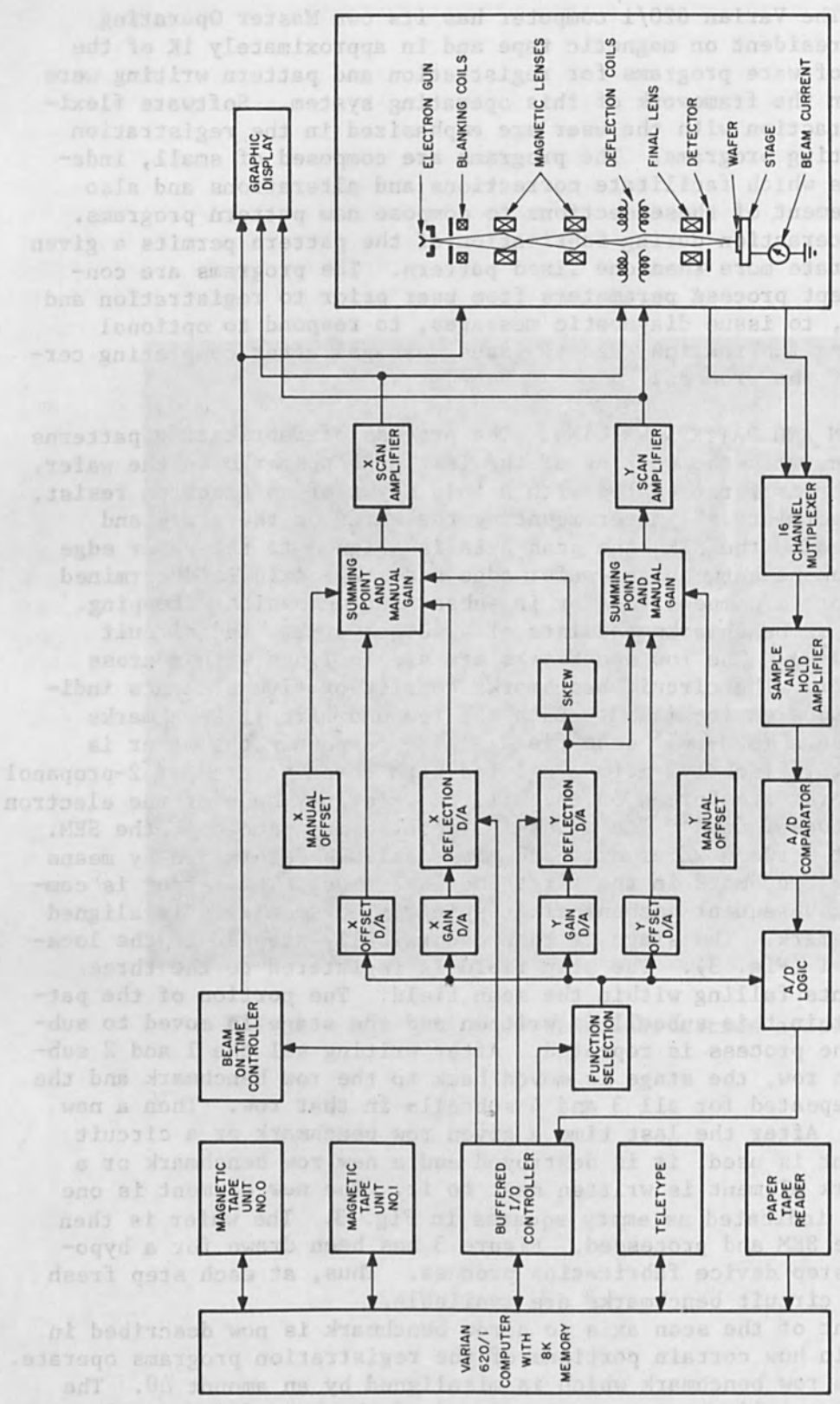


FIG. 2.--Computer-SEM interface.

The difference in the x coordinates of the bar as determined by the two scans is the error signal used in aligning the scan field. Alignment to within $\pm 0.01^\circ$ is routinely achieved.

The software programs intended for interaction with the user, perform the registration, and write the patterns do not fit into the 8K core memory. Therefore they were divided into four sections and stored on magnetic tape (Fig. 5). A small, resident program, upon being executed, loads the next program from magnetic tape in such a way that the previous program is overlaid by the new program. The first program inputs process parameters from the user and/or interacts with the user to perform the scan axis alignment to the row benchmark. It then exits to the resident program which in turn loads in the registration program. Upon successfully registering the scan field to the circuit benchmark elements, the resident program is used again to load the pattern-writing program. After completing the pattern writing, this program is overlaid by the registration and benchmark writing program which repeats the registration process and then writes new benchmarks and destroys old ones. Before exiting to the resident program, this program can rewind the magnetic tape and skip the first program if instructed to do so. This cyclic process continues until it is interrupted by the appropriate command.

RESULTS

A simple test pattern was devised to demonstrate precision automatic registration of a pattern composed of four overlapping scan fields. The pattern is basically a series of concentric squares covering four scan fields and is shown in Fig. 6 as photographed from a CRT screen. Five of the squares make up pattern 1 and the other five make up pattern 2. Figure 6(a) shows pattern 1 in subcell 1; Fig. 6(b) shows pattern 2 in subcell 1. Figure 6(c) is a composite of patterns 1 and 2 in subcell 1. Figure 6(d) shows the full composite pattern. Comparison of Fig. 6(d) with Fig. 3 reveals that the rectangular notches in two of the squares are needed to avoid the region reserved for benchmark elements. Programming a circuit pattern around these areas leads to no significant difficulty.

Results obtained on a silicon wafer using pattern 1 are shown in Figs. 7 through 10. Figure 7 shows optical photographs of the exposed and developed polymethyl methacrylate on the silicon wafer. Figure 7(a) is an overview, and Figs. 7(b) and 7(c) are 500x and 1000x photographs of two areas where the scan fields and patterns overlap. Figure 8(a) shows an overview of the pattern in gold on the silicon wafer after the metal evaporation and liftoff.¹⁷ Figures 8(b) through 8(d) show three different magnifications of an area where the patterns from two adjacent subcells overlap. The overlap area shown in Fig. 9 differs from that shown in Fig. 8 and is in the region of the "notches." Linewidth in the nonoverlap regions is approximately 1.0 μm and registrational accuracy is within $\pm 0.1 \mu\text{m}$. Figure 10 is a pattern obtained from another exposure. Here the total charge deposit per unit length was less than that used for the pattern in Figs. 8 and 9, which results in a narrower gold line. Linewidth in the nonoverlap regions is approximately 0.3 μm and registrational accuracy is well within $\pm 0.1 \mu\text{m}$. Figures 8 through 10 are scanning electron microphotographs. It should be noted that the circuit benchmark, as well as the overlap region, are located at the periphery of the scan field where deflection aberrations are greatest.

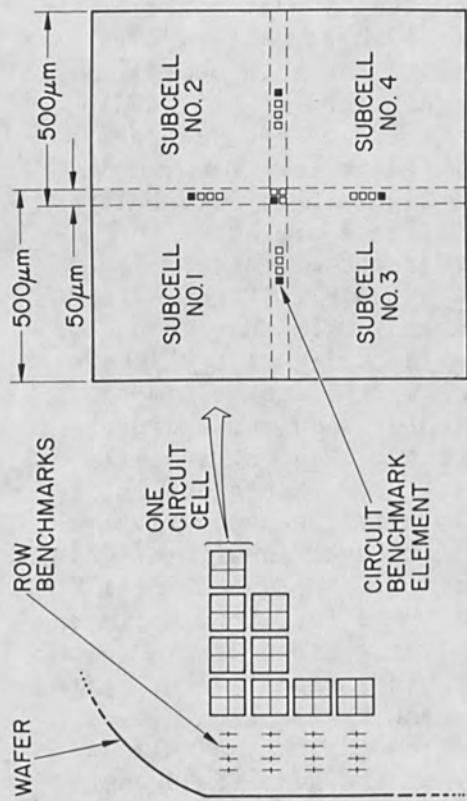


FIG. 3.--Row and circuit benchmarks and pattern field on wafer.

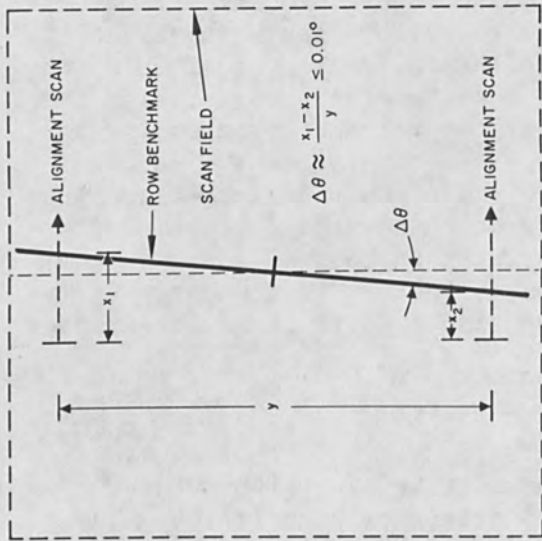


FIG. 4.--Rotational alignment of scan field to row benchmarks.

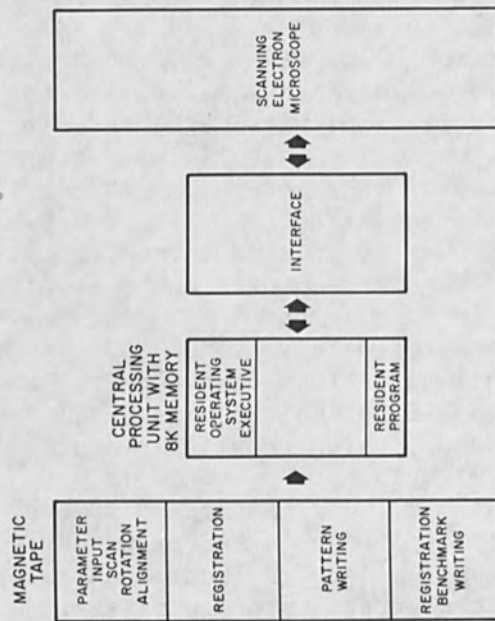


FIG. 5.--Magnetic tape and core memory usage during registration and pattern writing.

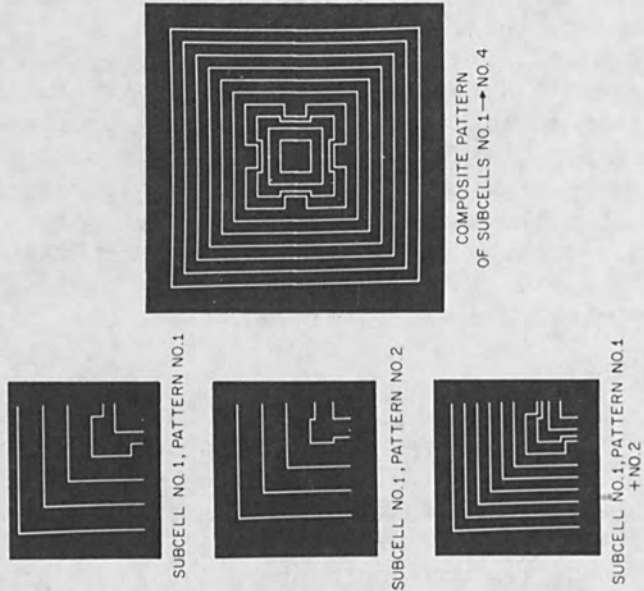


FIG. 6.--CRT display of test pattern.

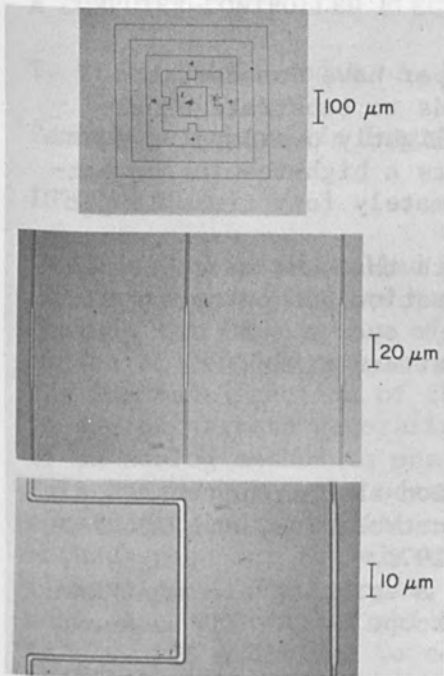


FIG. 7.--Exposed and developed resist on silicon wafer.

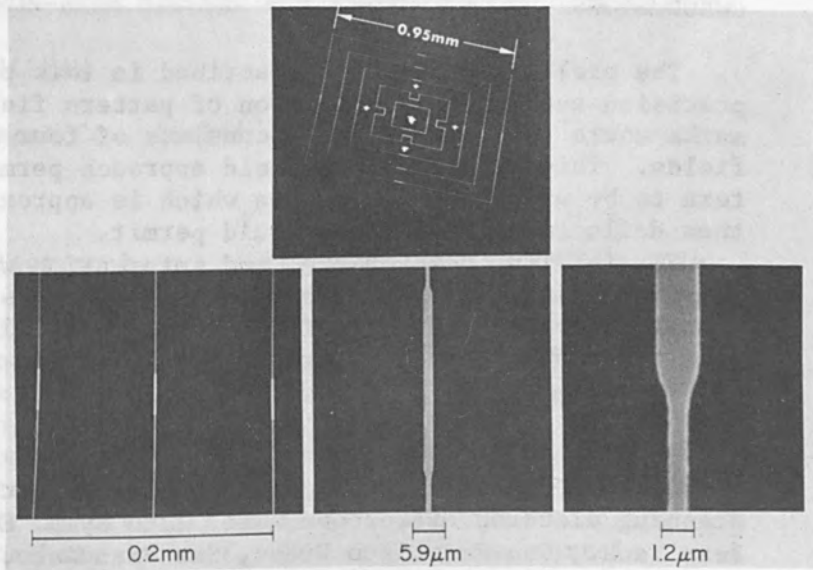


FIG. 8.--Gold pattern on silicon wafer.

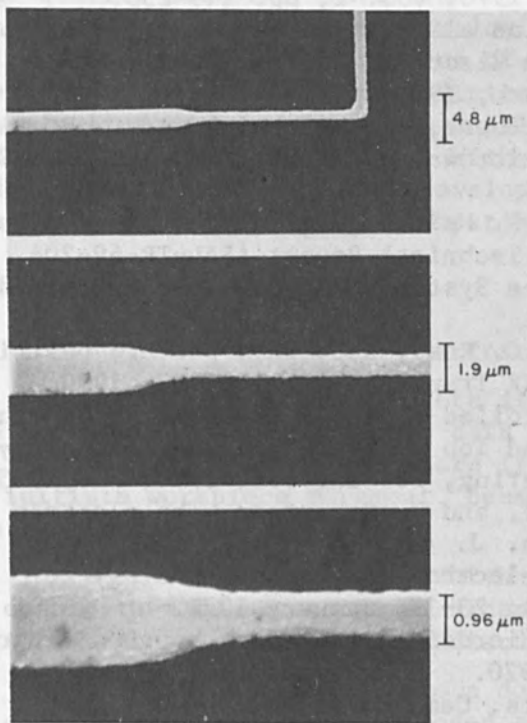


FIG. 9.--Detail of broad line pattern on silicon wafer.

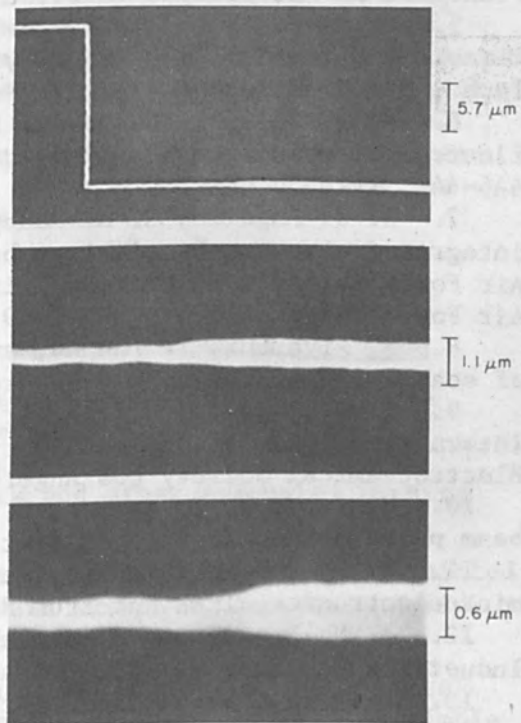


FIG. 10.--Detail of narrow line pattern on silicon wafer.

CONCLUSIONS

The preliminary results described in this paper have demonstrated precision automatic registration of pattern fields to substrate benchmarks where the pattern field consists of four slightly overlapping scan fields. This multiple-scan-field approach permits a high-resolution pattern to be written over an area which is approximately four times larger than deflection aberrations would permit.

Flexibility, ease of use, and interaction with the user have been emphasized in the computer programs used in registration and pattern writing.

A preliminary registration accuracy of $\pm 0.1 \mu\text{m}$ over a $(950 \mu\text{m})^2$ pattern field has been demonstrated for submicron pattern dimensions.

REFERENCES

1. E. D. Wolf and K. Amboss, Double-deflection aberrations in a scanning electron microscope, Rec. 11th Symp. Electron, Ion, and Laser Beam Tech., San Francisco Press, San Francisco, 1971.
2. T. H. P. Chang, Device fabrication using a scanning electron beam system, Proc. 4th Annual Scanning Electron Microscope Symp., IIT Research Institute, Chicago, 1971; pp. 417-424.
3. A. N. Broers, Electron beam fabrication, Program of the Topical Meeting on the Use of Optics in Microelectronics, Optical Soc. Am., Las Vegas, Nev., 1971; pp. TA1-1-4.
4. A. N. Broer and M. Hatzakias, The scanning electron microscope in the fabrication of microminiature electronic components, Seventh International Congress on Electron Microscopy, Grenoble, France, Société Française de Microscopie Électronique, 1970; vol. 1, pp. 249-250.
5. T. H. P. Chang, A high resolution electron-beam system for microcircuit fabrication, Rec. 10th Symp. on Electron, Ion, and Laser Beam Tech., San Francisco Press, San Francisco, 1969; pp. 97-106.
6. E. D. Wolf, L. O. Bauer, R. W. Bower, H. L. Garvin, and C. R. Buckley, Electron beam and ion beam fabricated microwave switch, IEE Trans. ED-17: 446-449, 1970.
7. S. J. Angello, R. M. Handy, P. R. Malmberg, et al., Maximum density integrated circuits by electron beams, Technical Report AFAL-TR-69-204, Air Force Avionics Laboratory, Air Force Systems Command, Wright-Patterson Air Force Base, Ohio, August 1969.
8. S. Miyauchi, T. Tanaka, and J. C. Russ, Automatic pattern positioning of scanning electron beam exposure, IEEE Trans. ED-17: 450-457, 1970.
9. J. P. Beasley, A computer controlled electron mask maker, Fourth International Conference on Electron and Ion Beam Science and Technology, Electrochemical Society Los Angeles Meeting, Los Angeles, 1970; p. 515-523.
10. W. Samaroo, J. Raamot, P. Parry, and G. Robertson, The electron beam pattern generator, Bell Syst. Tech. J. 49: 2077-2093, 1970.
11. G. Brewer, The application of electron ion beam technology to microelectronics, IEEE Spectrum 8(No.1): 23-37, January 1971.
12. A. N. Broers and M. Hatzakis, Microcircuits made through microscopes, Industrial Research 12: 56-58, March 1970.
13. Cambridge Scientific Instruments, Cambridge, England.
14. Varian Data Machines, Irvine, Calif.
15. Astrodata, Anaheim, Calif.
16. E.D. Wolf, F.S. Ozdemir, and W.E. Perkins, in this Record.
17. M. Hatzakias, J. Electrochem. Soc. 110: 1033-1037, 1969.

A COMPUTER-CONTROLLED ELECTRON-BEAM MACHINE FOR MICRO-CIRCUIT FABRICATION

T. H. P. CHANG* and B. A. WALLMAN

Cambridge Scientific Instrument Co., Cambridge, England

INTRODUCTION

A computer-controlled electron-beam machine automated for the fabrication of microcircuits has been developed. Its potential applications include the fabrication of high-definition photo-masks and direct fabrication of devices on semiconductor wafer.

The main function of the electron beam in microcircuit fabrication is one of pattern generation, which can be analog or digital. An example of an analog method is one based on the flying-spot scanning system.^{1,2} This approach has the advantage of being relatively simple and cheap to construct, and in addition it is directly compatible with the scanning methods used for the electron-beam machine. However, it has certain limitations. For example, the system requires a high-quality optical mask, the artwork for which must be prepared by a precision machine. It is also not practical to consider a system with a definition of more than 2000-3000 lines over the pattern area, owing to resolution limitations of the cathode-ray tube used in the scanner. However, this technique has been very successful for the fabrication of discrete devices (particularly for generating curved configurations) and has proved to be a very valuable research and development tool.

The digital technique has the fundamental advantage of not requiring high-quality artwork. Furthermore, the system may be made to operate at a much higher speed than the analog system, as the electron beam need only be deflected over the areas of the pattern requiring exposure. As the pattern is specified in a digital form, the complexity of the pattern is only limited by the storage available, which can easily be expanded according to the requirement. With the increasing emphasis on computer-aided design in microcircuit development, the digital approach has the advantage of being directly compatible with such facilities.

COMPUTER-CONTROLLED FUNCTIONS

The computer system must perform two primary functions:

- (1) pattern generation, where it is used as a large-capacity data storage device with high-speed data retrieval; and
- (2) repeating patterns, where it is used as a program controller to initiate workpiece movement, beam shifts, and other essential machine control functions.

There are several ways in which microcircuit patterns may be specified to enable them to be stored as binary numbers within a computer. A few of the most useful methods are discussed below.

- (a) Divide the pattern into a dot matrix and store the coordinates of each dot that has to be exposed to form the pattern. This is a simple system but would require an unacceptably large amount of storage to define

*Now at IBM Research Center, Yorktown Heights, N.Y.

the pattern. If we assume that a resolution of 1 part in 4000 is required for both x and y axes of a square field, and that 25 per cent of this area is to be exposed, then 4×10^6 dots have to be specified. This is clearly impractical, because it would require an unacceptably large store. In addition, this method would be slow (in the range of a few hundred kilohertz) because it is store-cycle time limited. However, this method may have some limited application where small areas of irregular shape have to be exposed that cannot be conveniently specified by other means.

(b) Divide the pattern into a series of lines and specify the coordinates of the start and end of each line. This procedure would reduce the amount of storage in the computer as compared with method (a) but the total storage required could still be unacceptably large.

(c) Cover the entire pattern area with a conventional television type of raster scan and store in the computer the positions along each scan line where the electron beam has to be turned either on or off. This method would allow the storage of pattern data to be reduced to a manageable level and would have the added advantage that any hysteresis effect in the deflection system from both electrical and thermal sources would be minimized. However, the main disadvantage of this approach is that the electron beam has to scan over the entire field, including areas where no pattern exposure is needed, which is uneconomical for high-speed operation.

(d) Synthesize the pattern by basic shapes and hold in the computer store the equations and coordinates that describe the shapes. This method has the advantage of greatly reducing the amount of storage necessary to hold the pattern information. Its main disadvantages are that the operating speed would be relatively slow because of the need to compute each exposure position. In addition this method can only be used with well-defined geometrical shapes.

(e) Divide the patterns into their constituent rectangles and specify each rectangle by the coordinates of the two diagonally opposite corners. This method requires the computer solely to store and unpack groups of four words which specify each rectangle and does not require its use for computation. The computer storage required to hold the pattern information depends of course on the complexity of the pattern. It has been estimated that for fairly complex circuits in preparation at present, the pattern may contain 10^4 corners, although the average at the moment is less than 10^4 . Taking 10^4 as a guide, that corresponds to 2000 rectangles, which implies that a store of 8K would be needed, which can be readily achieved. Moreover, as this method does not require the electron beam to scan over areas where no pattern exposure is needed, it is more compatible with the requirement of high-speed operation. One restriction of this method is that the shape of the pattern should have straight sides parallel to the x and y axes. As most microcircuit patterns to date are of this type, this is not considered a serious restraint. Even nonrectangular shapes can be handled by this method if they are subdivided into a composite of small rectangles.

From the above analysis, it has been concluded that method (e) offers the best solution as to both speed and storage requirements and is therefore being adopted for the electron-beam machine described here. Important extensions that have been incorporated include the ability to define certain other straight-sided shapes such as triangles, parallelograms, etc. The system has been designed with sufficient flexibility so that it can be easily modified to accept pattern data based on the other methods described previously, too.

Ideally, we should like to deflect the electron beam over the entire mask or wafer area, say, 50×50 mm or 100×100 mm, so that patterns may be exposed without a change in the position of the workpiece. Limitations in the field of coverage make that impracticable; therefore, the pattern must be divided into fields and subfields and the workpiece covered by a combination of mechanical and electrical shifts. The computer controls the build-up of patterns over the whole workpiece in the manner shown in Fig. 1, as summarized below:

(1) The basic pattern is to be defined by a 12-bit matrix (4096×4096 picture points). Should the pattern require a higher resolution than can be achieved with a single 12-bit matrix field, then the pattern can be generated as a composite of subfields each defined by a 12-bit matrix.

(2) A subfield is located by a high-stability dc beam shift. The maximum number of subfields that can be used depends on circuit complexity and over-all stability of the deflection system. Typically the number is 4×4 , and as each contains a 12-bit matrix, a maximum of 14-bit (approximately $16\,000 \times 16\,000$ picture points) field can be defined. Such a composite of subfields results in a complete field (or chip) and requires continuity across the boundary of the subfields. However, the same technique can be used to expose a group of patterns in each subfield that are separate.

(3) Each complete field is accessed by a mechanical workstage movement, which allows the pattern to be repeated over the entire workpiece surface. The pattern to be exposed at each field location need not be identical and field locations may be skipped if required.

The computer-control facility can be extended to include various automation features such as (a) registration of successive patterns, (b) pattern-size calibration, (c) fault detecting, (d) focusing, etc. In automating these features, it is generally necessary for the control unit to perform certain mathematical computations (e.g., addition, subtraction, and averaging of several numbers), which can be readily achieved by using suitable software in the computer. However, in cases where the control is best achieved by using special logic hardware, the computer can be used to initiate the operation of such hardware in a programmed manner.

GENERAL DESCRIPTION OF THE AUTOMATED ELECTRON-BEAM MACHINE³

The system (Figs. 2 and 3) is intended to operate primarily as a microfabrication machine but facilities are incorporated to allow the system to be used also as a scanning microscope for inspection and general monitoring purposes.

The automation system is based on a small general-purpose computer, the PDP-11/20. Pattern data are synthesized as a series of rectangles and read into the computer either via a high-speed paper-tape reader or if necessary manually via a teletypewriter. The computer is programmed to accept and store the pattern information and to transfer it to the interface control unit in blocks of four words which define each rectangle. The computer is also coupled to the cathode-ray-tube displays which enable the pattern to be verified and the exposure process to be continuously monitored.

The interface control unit receives the digital information from the computer and converts it into the analog signals to control the position

of the beam and worktable and to perform other essential functions on command from the computer. The unit may be divided into two parts. The main part is a system of registers that hold and define the operating conditions of the electron-beam machine. The subsidiary part is the data-flow elements that enable the computer to set and read the registers. To fulfill the pattern-generation function, four registers are used to enable the interface unit to accept and hold the blocks of four-word outputs from the computer. This information is converted into the appropriate analog signals that drive the deflection system to produce a bidirectional scan of the electron beam to fill in the rectangle. The digital-to-analog converters used are 12-bit, high-speed, high-stability devices, capable of working as hybrid multipliers over a limited analog range. The hybrid multiplication facilities allow a fine magnification control to be applied. The incrementing frequency of the clock source is manually selected with a range of pulse repetition frequencies up to several megahertz. To enable the computer to position the beam in a dot or line manner, the normal type of rectangle scan described above is modified. In this mode of operation the beam is switched on for a predetermined time after each set of dot or line coordinates have been loaded into the relevant registers. This facility may be used to expose very small areas of irregular shape, as previously discussed. Additional program-addressable registers are provided within the interface control unit to control the operation of the static deflection of the beam for subfield location, to instruct the workstage control system, and to control various other automatic routines such as automatic registration.

The electron-optical column is developed from a high-resolution scanning electron microscope, the Stereoscan II A, with various modifications to convert it to a suitable fabrication machine. The original column has a tungsten hairpin electron gun followed by three magnetic lenses. Modifications that have been incorporated are:

- (a) a new electron gun using a lanthanum hexaboride cathode⁴ to improve both brightness and stability;
- (b) a new deflection coil assembly to enable continuous scanning, static beam shift, and fine beam alignment to be performed; the complete assembly can be rotated mechanically on its own axis by a control outside the vacuum;
- (c) a new collector system based on channel multipliers to achieve good collection efficiency in conjunction with a large flat specimen;
- (d) a new worktable capable of 50×50 -mm movement in x and y direction controlled by stepping motors; fine controls for rotation and height of the workpiece are also provided; and
- (e) a new work-chamber arrangement to enable working distance to be varied from 1 to 20 cm.

The column (Fig. 4) can be operated at accelerating voltages from 1 to 30 kV and beam current in the final probe can be varied from 10^{-12} to 10^{-5} A. When used as a scanning electron microscope the column has a resolving power of about 100 Å.

An analog pattern-generation facility using a flying-spot scanner has also been developed and is integrated into the system by coupling the scan amplifiers of the scanner to the interface control unit, as shown in Fig. 2.

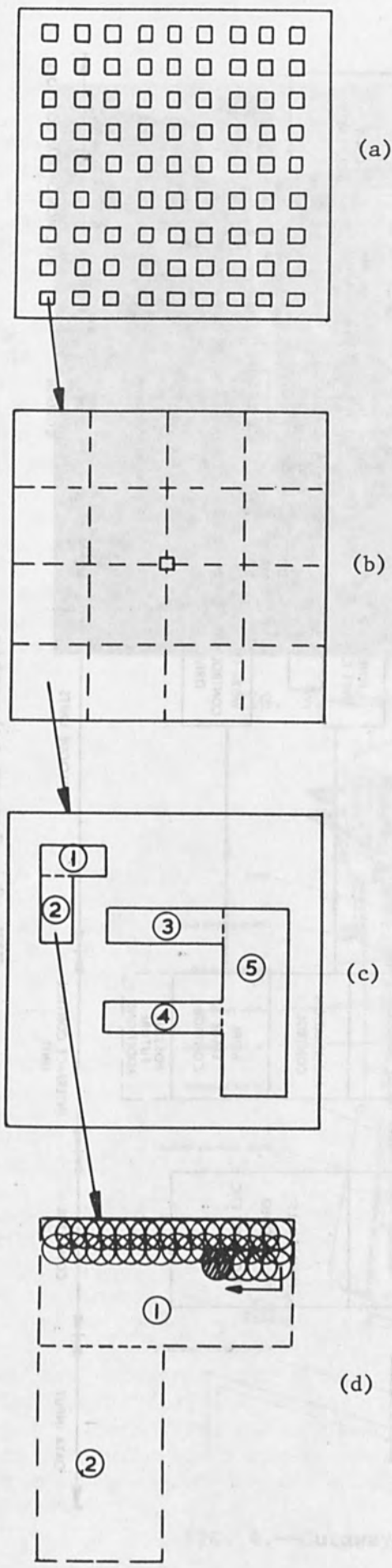


FIG. 1.-- Build-up of pattern. (a) Mask or wafer: divided into series of fields each accessed by mechanical movement of work stage. (b) Field or chip: divided into subfields each accessed by high-stability dc shifts of electron beam; registration mark if used would situate in center of field as shown. (c) Subfield: defined by 4096×4096 exposure points and pattern to be divided into rectangles. (d) Pattern rectangles: to be covered by high-speed digital scanning of electron beam.

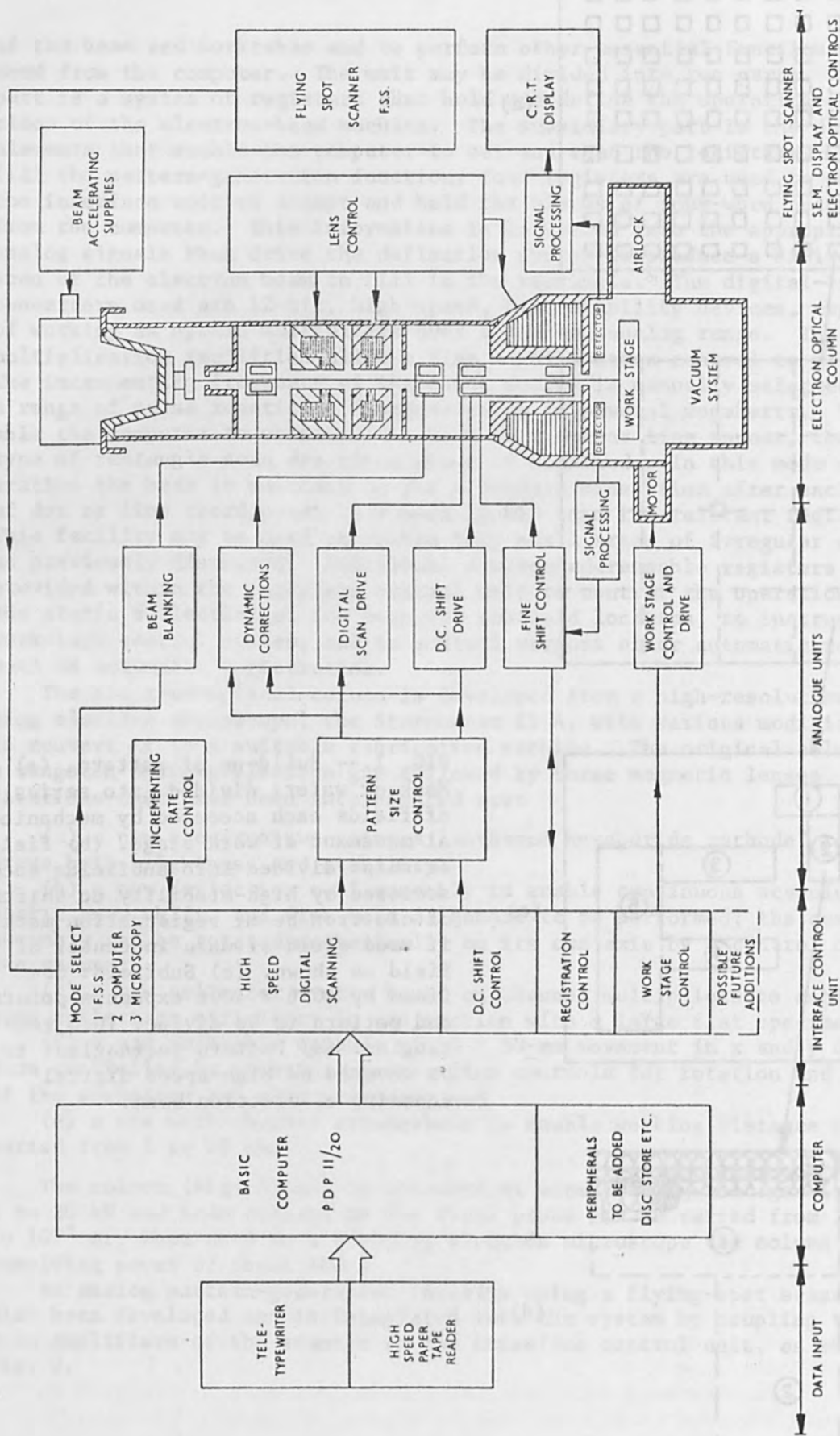


FIG. 2.--System schematic.

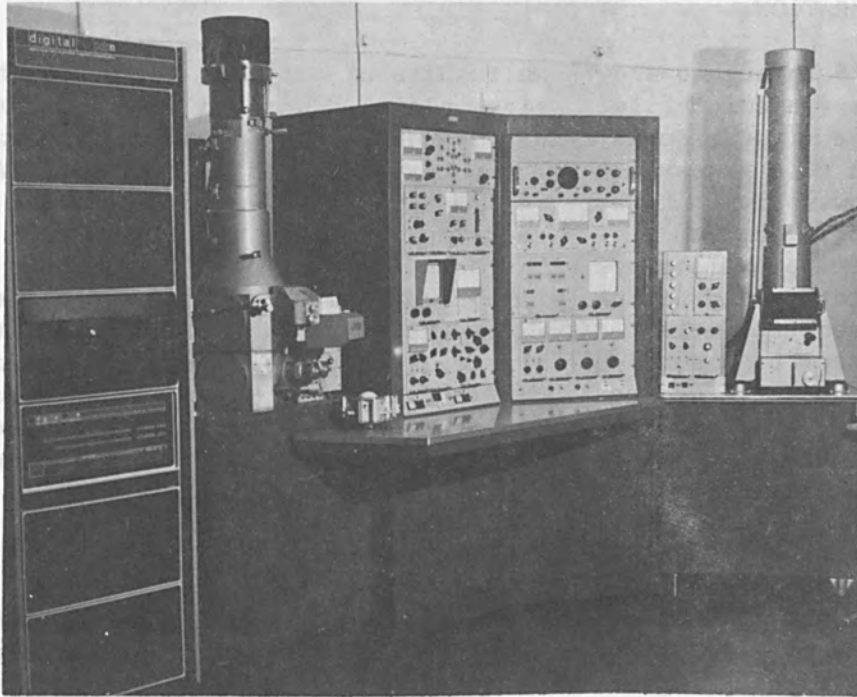


FIG. 3.--Over-all system.

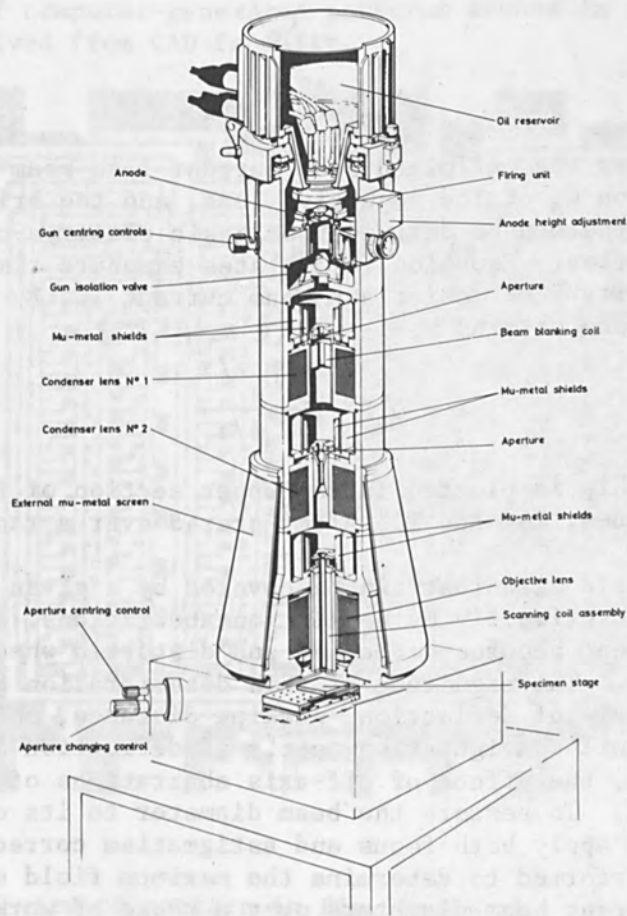


FIG. 4.--Cutaway drawing of column.

PATTERN GENERATION

Figures 5 through 8 show some results of patterns etched on chromium photo plates (chromium film on glass plate) generated under computer control. The first example (Figs. 5 and 6) shows a pattern generated using a data tape prepared by a computer-aided design facility, CAMP. Figure 5 shows part of an array of patterns produced by automatic mechanical step and repeat and Fig. 6 shows one of these patterns with a minimum linewidth of approximately $2 \mu\text{m}$. The second example (Figs. 7 and 8) shows a pattern based on data synthesized manually from a published photograph of a computer memory circuit. The original pattern is built up from the repeat of a small pattern cell; only the rectangles inside this cell pattern need be synthesized. The computer is programmed automatically to step and repeat the cell pattern electrically to form the entire pattern. Figure 8 shows details of this pattern with minimum linewidth of approximately $1 \mu\text{m}$.

RESOLUTION, EXPOSURE SPEED, AND FIELD SIZE

The exposure speed and field of coverage are both related to the electron-beam diameter used and hence to the resolution. The relationship between exposure speed and beam diameter can be calculated from the following two equations:

$$I = 1.15B \frac{d^{8/3}}{C_s^{2/3}} \quad (1)$$

$$t = \frac{AS}{I} \quad (2)$$

Equation (1) relates the optimized beam current I to beam diameter d , the spherical aberration C_s of the objective lens, and the brightness B of the electron gun, and can be derived from basic electron-optical principles of beam formation. Equation (2) relates exposure time t for a given area A to sensitivity S of resist and beam current I . By combining Eqs. (1) and (2), one obtains

$$t = 0.87 \frac{AS}{B} \frac{C_s^{2/3}}{d^{8/3}} \quad (3)$$

This relationship is plotted in the upper section of Fig. 9 for two gun brightness values, 10^5 and 10^6 A/cm²-sterad over a range of C_s and S values.

The maximum field size that can be covered by a given electron-beam diameter is limited primarily by deflection aberrations. It is well known that an electron beam becomes defocused and distorted when deflected from its axial position. The magnitude of this deterioration depends on several factors such as angle of deflection, working distance, solid angle of the beam, deflection-coil configuration, etc. If deflection is applied before the objective lens, the effect of off-axis aberrations of the lens must also be considered. To restore the beam diameter to its original value, it is necessary to apply both focus and astigmatism corrections. Experiments have been performed to determine the maximum field size that can be achieved for different beam diameters over a range of working distances

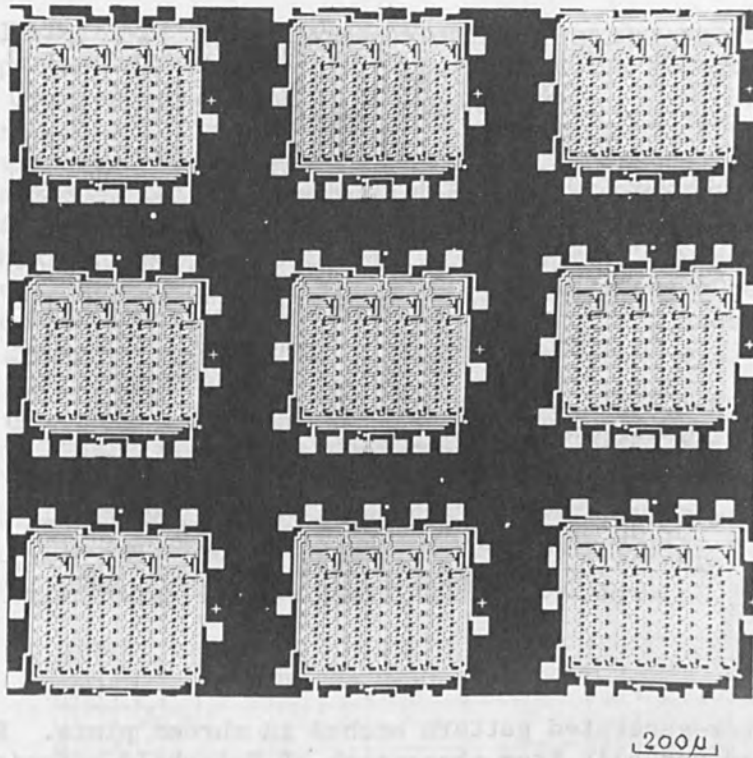


FIG. 5.--Array of computer-generated patterns etched in chrome plate. Pattern data derived from CAD facility.

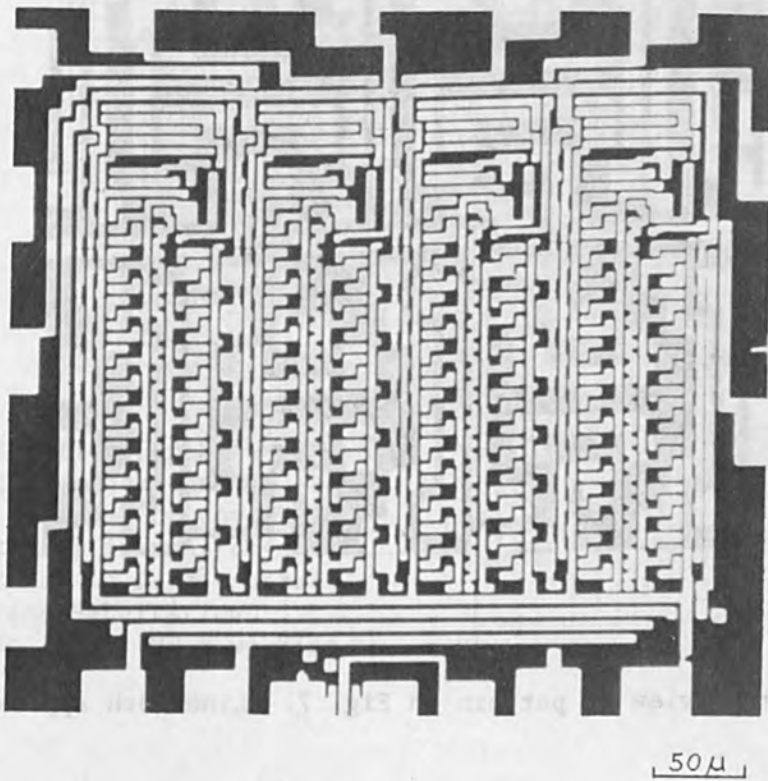
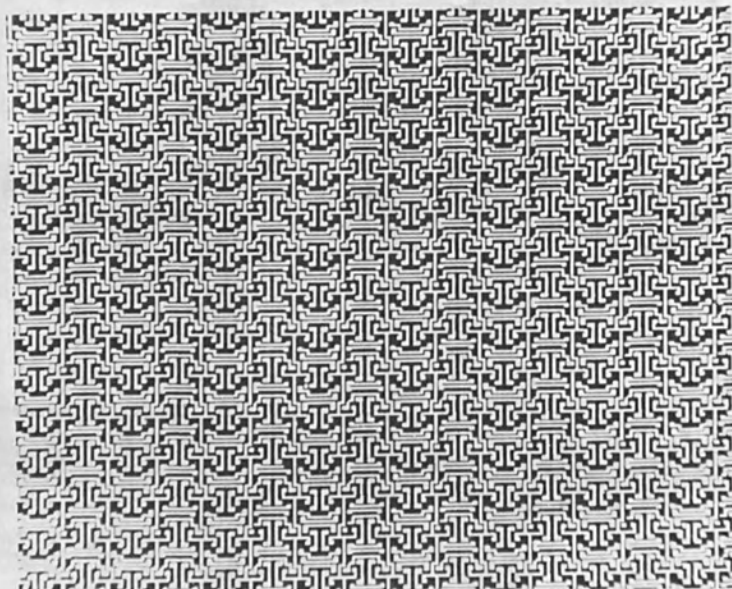
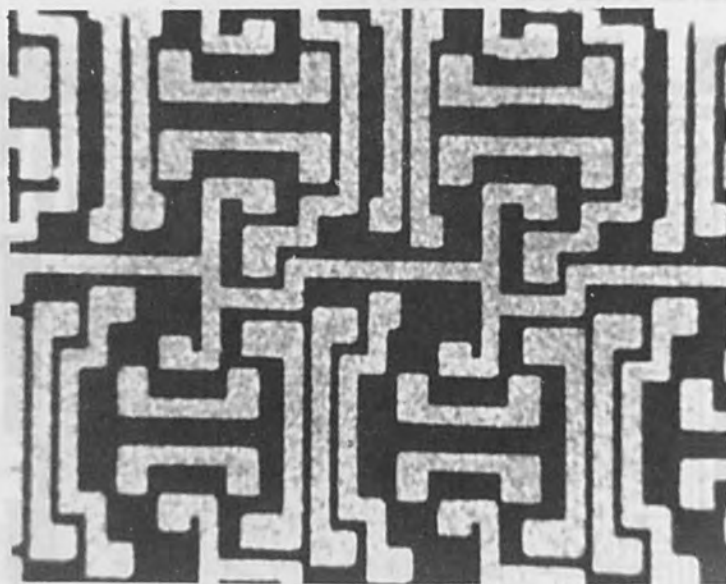


FIG. 6.--Enlarged view of pattern in Fig. 5 showing linewidths of approximately 2 μm .



100 μ

FIG. 7.--Computer-generated pattern etched in chrome plate. Pattern data synthesized manually from photograph of Fairchild circuit.



5 μ

FIG. 8.--Enlarged view of pattern in Fig. 7. Linewidth approximately 1.5 μ m.

with the application of both focus and astigmatism corrections. These results are plotted against beam diameter in the lower section of Fig. 9.

Figure 9 relates both exposure speed and field size to beam diameter. Since C_s increases with working distance, the trade-off between exposure speed and field size can be established. The relationship between C_s and working distance depends on individual lens design; it is possible to optimize the design of a lens for a given working distance to get a C_s of about four times that working distance. The table summarizes the trade-off between exposure speed and field size for a 0.5- μ m-diameter beam, probably the most suitable beam size for pattern generation for present-day micro-

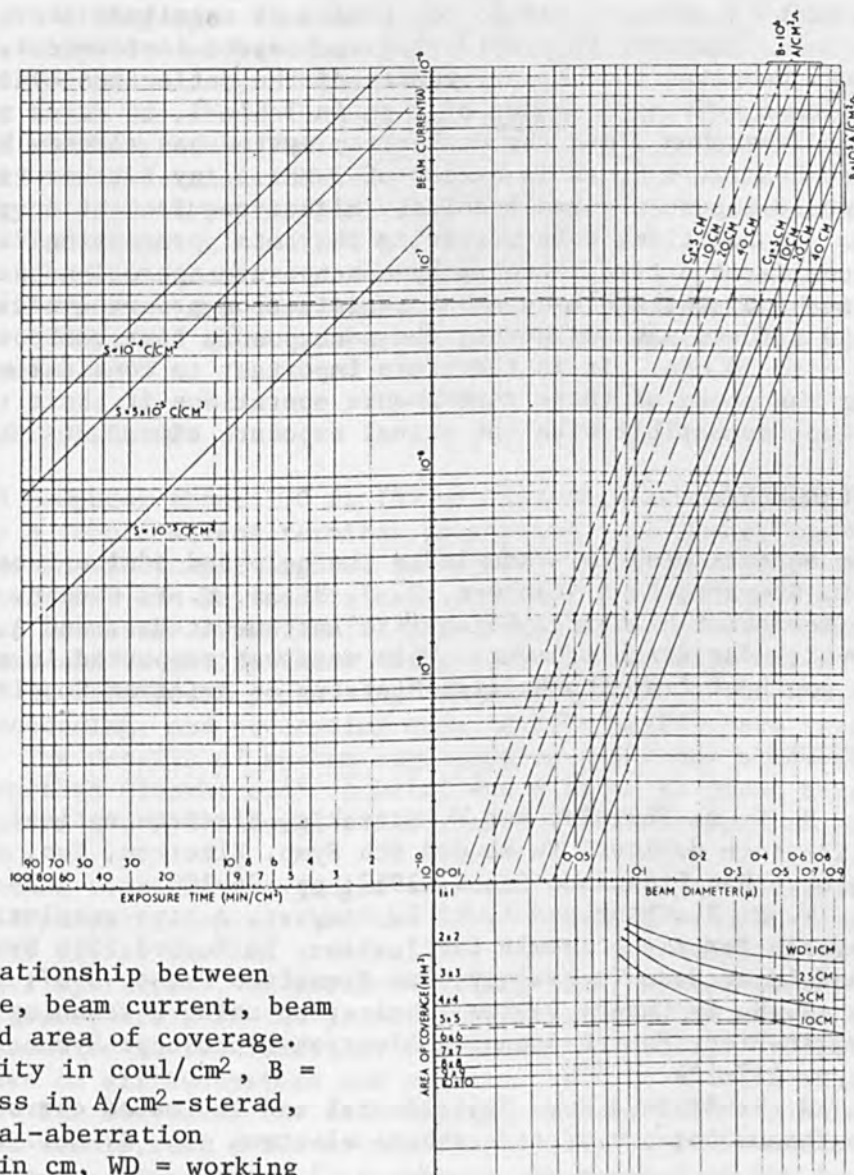


FIG. 9.--Relationship between exposure time, beam current, beam diameter, and area of coverage. S = resistivity in coul/cm², B = gun brightness in A/cm²-sterad, C_s = spherical-aberration coefficient in cm, WD = working distance.

circuits, where linewidths down to 2 μm are present. In the table, the pattern area is assumed to take up 25 per cent of the field area; gun brightness is 5×10^5 A/cm²-sterad; resist sensitivity is 1×10^{-4} coul/cm .

Working distance (cm)	1	2	5	10
Field size (mm \times mm)	2.5 \times 2.5	3 \times 3	4 \times 4	5 \times 5
Exposure time (sec)	2	6	14	35

The exposure speed can be increased with improvement in gun brightness and resist sensitivity and experiments have already shown that gun brightness⁶ of 5×10^6 A/cm²-sterad and resist sensitivity⁷ better than 1×10^{-5} coulomb/cm² could be achieved, which would indicate a possible improvement in speed of one to two orders of magnitude above the values in Table I. However, in considering such speed improvement, some attention must be given to the performance of the deflection system. For example, for a working distance of 1 cm in Table I, to cover the 2.5 \times 2.5-mm field in less than 2 sec the deflection system has already had to increment the beam at a speed in excess of 3 MHz. Any further increase of speed would impose a correspondingly higher requirement on the deflection system. In addition, when assessing the total processing time, one must also consider the time taken up by nonexposure operations such as setting up of machine, worktable movement registration process, etc. Typically, for a 50 \times 50-mm mask or wafer, the nonexposure time can total approximately 5 to 10 min. It is therefore important to consider means of improving the speed of these nonexposure operations if their total time is to be kept compatible with the actual exposure time.

ACKNOWLEDGMENT

The authors wish to acknowledge the help and advice received from A. D. G. Stewart, P. A. Charmen, D. J. Hills, M. F. Cousin, J. Sommers, and R. Newman of Cambridge Scientific Instrument Co., and A. C. Prior of the Royal Radar Establishment. This work was supported in part by a research contract from the British Ministry of Aviation Supplies.

REFERENCES

1. R. F. M. Thornley and M. Hatzakis, Electron optical fabrication of solid-state devices, in Record 9th Symp. Electron, Ion, and Laser Beam Technology, San Francisco Press, 1967; pp. 94-100.
2. T. H. P. Chang and A. D. G. Stewart, A high resolution electron beam system for microcircuit fabrication, in Record 10th Symp. Electron, Ion, and Laser Beam Technology, San Francisco Press, 1967; pp. 97-106.
3. T. H. P. Chang, Device fabrication using a scanning electron beam system, in Proc. Fourth Scanning Electron Microscope Symposium (IITRI), 1971; pp. 417-424.
4. A. N. Broers, Some experimental and estimated characteristics of the lanthanum hexaboride rod cathode electron gun, J. Sci. Inst. 2(2): 1969.
5. A computer-aided mask production facility at Royal Radar Establishment, Worcs., England.
6. A. N. Broers, Factors affecting resolution in the SEM, in Proc. 3rd Scanning Electron Microscope Symp. (IITRI), 1970.
7. M. Hatzakis and A. N. Broers, High resolution electron beam fabrication, Record 10th Symp. Electron, Ion, and Laser Beam Technology, San Francisco Press, 1969; p. 107.

COMPUTER-CONTROLLED RESIST EXPOSURE IN THE SCANNING ELECTRON MICROSCOPE*

R. F. HERZOG, J. S. GREENEICH, T. E. EVERHART, and T. VAN DUZER

University of California, Berkeley, Calif.

In modern microelectronics, complicated structures with very small dimensions must be fabricated on active-device materials. This task has been traditionally accomplished by photolithographic techniques, but electron-beam exposure of resist materials has recently been explored.¹⁻³ Submicron electron devices have been fabricated in several laboratories, often featuring a flying-spot scanner to generate the pattern being exposed.⁴⁻⁷ Paper tape drives have been used for repetitive patterns,⁸ and computer control of the electron beam has been reported also.^{1,9} The electron resist which has shown the highest resolution to date appears to be poly-(methyl methacrylate) (PMM). We have used this material in a resist form for microelectronic device fabrication, and in bulk form to determine energy dissipation profiles; the exposure is performed with a computer-controlled scanning electron microscope (CCSEM). In this paper, we describe the electron beam system briefly, discuss the processes involved in resist exposure and development, describe our exposure procedures using the CCSEM, and show results of fabricated devices and energy dissipation studies.

THE COMPUTER-CONTROLLED SEM

An IBM 1800 computer about 170 ft (55 m) distant has been interfaced with the SEM by a remote-access terminal consisting of a 16-key keyboard, various switches and indicator lights, and a message storage CRT. The remote access terminal can be used to call programs stored on a disk file at the computer, to change experimental parameters as a series of experiments progresses, and to verify these changes via the message CRT. The system (Fig. 1) is capable of processing images produced by the SEM, and of directing, recording, and processing quantitative solid-state experiments as well. The details of system organization and these other applications are described elsewhere.¹⁰ A brief description is given here of system organization and operational procedures for resist-exposure experiments.

A remote-access terminal was judged essential because of the distance between the multipurpose computer and the SEM. Ideally, a CCSEM user should be able to sit at the SEM terminal and direct the computer to perform a variety of operations, to perform calculations related to the experiment in progress, etc. In the present installation, the master control program cannot be called remotely, but a limited monitor or EXECUTIVE gives full access to all subsystems and performs certain housekeeping chores as well. The subsystem for each experiment consists of a MAIN module, a CHANGE module, and a LOG module (Fig. 2). The MAIN module performs the experiment. Experimental parameters are entered at the terminal through the CHANGE module, which also calculates quantities needed from these parameters, and automatically enters these new values in the MAIN module. The LOG module displays experimental parameters as they are

*Work supported by NIH Grant GM-17523-01 and by contract DA-ARO-D-31-124-70-G60.

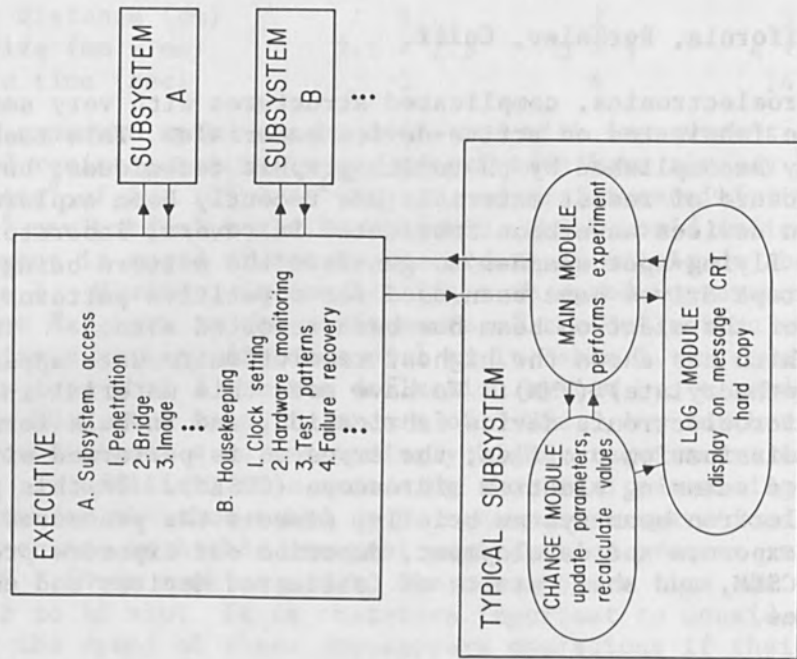


FIG. 2.--Computer software organization is chosen to facilitate program writing and debugging.

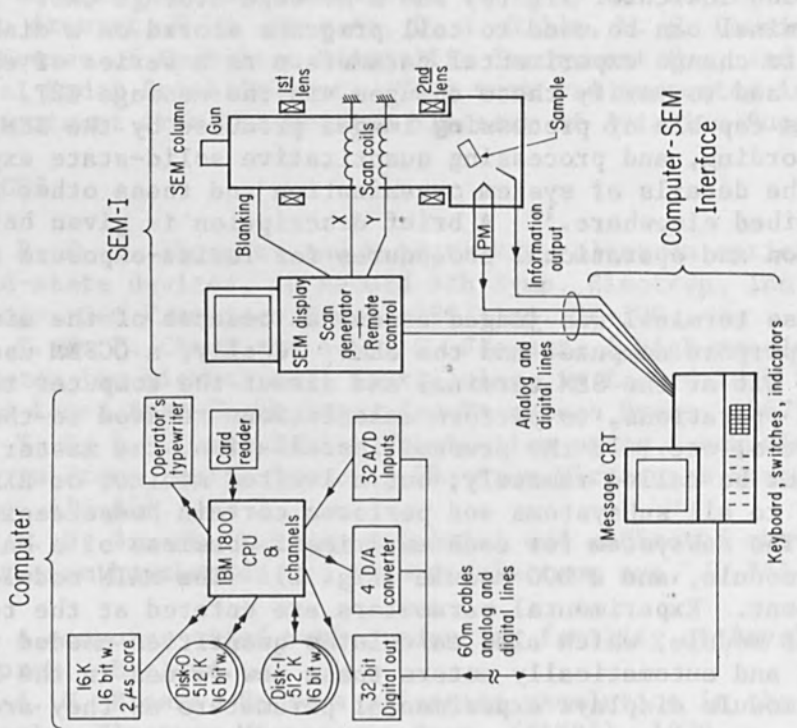


FIG. 1.--Computer-controlled scanning electron microscope shows how interface at microscope allows operator to interact with both SEM and computer.

entered, can display the entire set of experimental parameters on the MESSAGE CRT, and can provide hard copy at the computer.

The subroutines have been written in machine language for efficiency and speed; parallel operations of the CPU and the data channels are used. Each subroutine governs one operation. Typical operations are: scan a line and record a given analog signal into an array during the scan, display an array using intensity modulation on the display CRT, display an array using Y modulation on the display CRT, scan a predetermined pattern for resist exposure, etc. The EXECUTIVE and the modules are programmed in FORTRAN, the unique high-level language of this computer. EXECUTIVE is stored on the disk and read in and out of the core memory as any other program. Only the manufacturer's resident package and the interrupt routines are kept in the core memory permanently. This modular organization facilitates program development and debugging of programs.

To expose a resist pattern, the operator mounts the sample in the SEM, focuses the beam correctly, and measures the beam current and voltage. These and other measured or specified parameters are entered into the computer by calling the CHANGE module (two key strokes), naming the parameter which is to be entered (two key strokes), and entering the data via the keyboard. After each keystroke operation is completed, the computer responds to the operator via the MESSAGE CRT. For example, after the data are recorded in the computer, they are displayed on the MESSAGE CRT for verification. When verified, the next parameter needed is automatically requested, etc. One can enter or leave any module, such as the CHANGE module, at any time.

RESIST EXPOSURE AND DEVELOPMENT

Having a computer-controlled electron beam provides flexibility in exposing a given pattern to the desired charge density at a given beam voltage. Choice of beam voltage and charge density for proper exposure depends on the resist material used and influences the resolution which can be obtained. Development of the resist is also critical; and both exposure and development must be reproducible. For certain devices, registration of successive steps can be a serious problem. First, we describe how the electron beam affects the PPM resist and give certain criteria for choosing developers of the exposed resist. Next we describe a successful exposure procedure for a superconducting bridge, and finally we discuss experiments carried out on a commercial plastic which provide new information on electron-beam dissipation profiles in solids.

POLY-(METHYL METHACRYLATE) AS A POSITIVE RESIST. When an organic polymer is subjected to ionizing radiation, energy is absorbed and the polymer undergoes chemical change affecting both its physical and chemical properties. For resist purposes it is the change in chemical properties which is of interest. Chemical changes involve two possible events.¹¹ One event is polymer cross-linking, in which adjacent polymer chains chemically crossconnect to form a complex three-dimensional structure which has a higher average molecular weight than the original polymer chains. The second is random-chain scission of the polymer--that is, chemical bonds are broken by the electron radiation, causing polymer degradation to lower average molecular weight. In general, both processes occur to different degrees in the same polymer. In PMM, random-chain

scission processes dominate cross-linking events under moderate (less than 10^{-3} coul/cm²) doses of kilovolt electron-beam radiation. A typical distribution of molecular weights of an irradiated region of PMM is shown schematically in Fig. 3 (solid line).¹² The surrounding regions, which were not subjected to radiation, exhibit the original distribution of molecular weights (broken line).

The classification of a resist as positive- or negative-acting depends on what happens to the irradiated region during development. Positive resists are characterized by the removal of the irradiated region during development; in negative resists, the irradiated region remains during development while the surrounding regions are removed. Electron-beam-sensitive resists are developed by the method of fractional solution.^{3,12} For a given polymer, organic solvents at a given temperature dissolve polymer chains of molecular weight below some particular value. For PMM, for which the average molecular weight decreases under radiation, a solvent is used that removes the polymer chains of lower weight while leaving the surrounding chains of higher molecular weight. Thus it is a positive resist.

SENSITIVITY OF PMM. An important aspect of electron-beam-sensitive resists is the sensitivity which, for a chosen developer (or class of developers), indicates the required incident charge density yielding successful development of the irradiated pattern. The smaller the required charge density, the smaller the required time of exposure. Brewer¹ points out that since electron-beam sources have been developed to a high degree, improvement in exposure times will probably come as a result of improvements in the sensitivity of resists, so that understanding the factors influencing it is of importance. The two important factors are the influence of the developing solution and the interaction of the electron beam with the resist. The chemical properties of the resist manifest themselves in an expression relating the incident charge density to the energy absorbed by the polymer when it undergoes degradation.

Without investigating the actual chemical changes occurring in a polymer of the degrading type, a relationship between the incident charge density, the number of chemical events caused by energy absorption from the kilovolt electron beam, and the resulting number average molecular weight of the fragmented polymers can be developed. It is assumed that the polymer degrades by random-chain scission of the bonds between monomers, and that the energy loss in the resist film as a function of penetration depth is linear. This last approximation is reasonable since the average atomic number for PMM is low (3.6) and hence the amount of energy absorbed by a 3000-Å PMM film is only a few per cent of the incident energy. It is assumed that all the energy absorbed causes scissions between monomers. The desired expression can be shown to be¹³

$$\rho = \frac{100q\rho_r A_0 (\bar{M}_n - \bar{M}_f)}{EG(s)\bar{M}_n \bar{M}_f} \quad (1)$$

where ρ is the charge density (coul/cm²), q is the electronic charge (1.6×10^{-19} coul), ρ_r is the density of the PMM resist film (g/cm³), A_0 is Avogadro's number, \bar{M}_n is the number average gram molecular weight of the original polymer, \bar{M}_f is the number average gram molecular weight of the fragment polymers, E is the energy loss per centimeter for the electron

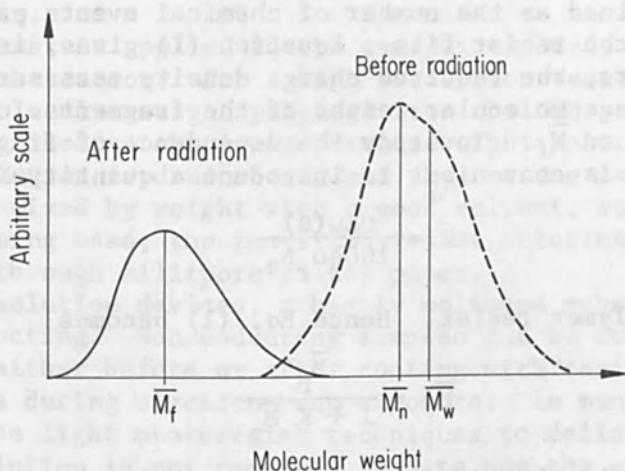


FIG. 3.--Typical distribution of molecular weights for poly-(methyl methacrylate) (PMM) shows how electron radiation reduces most probable molecular weight M_n ("number average molecular weight") by scission, producing distribution about M_f (number average molecular weight after bombardment).

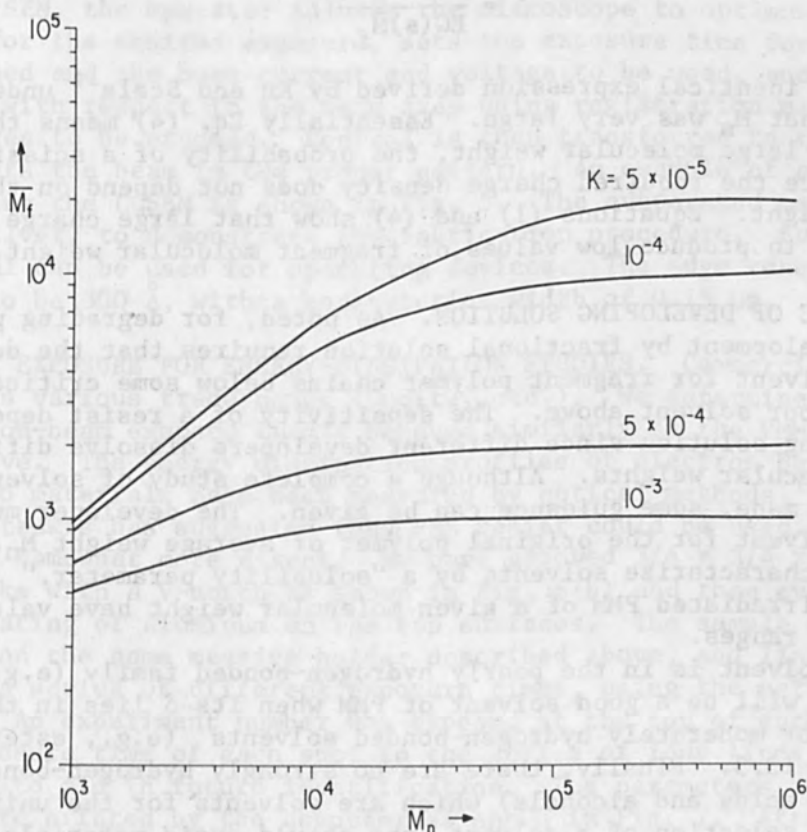


FIG. 4.--Plots of \bar{M}_f vs \bar{M}_n with K as parameter; K is proportional to charge density required for exposure of PMM.

traversing the resist film, and $G(s)$ is the radiation chemical yield for scission events defined as the number of chemical events per 100 eV of energy absorbed by the resist film. Equation (1) gives, in terms of polymer resist parameters, the required charge density necessary to produce \bar{M}_f , the number average molecular weight of the fragments. Let us consider the influence of \bar{M}_n on \bar{M}_f . To study the dependence of fragmentation on beam parameters, it is convenient to introduce a quantity K , where

$$K = \frac{\rho EG(s)}{100q\rho_r A_0} \quad (2)$$

for a particular polymer resist. Hence Eq. (1) becomes

$$\bar{M}_f = \frac{\bar{M}_n}{1 + K \bar{M}_n} \quad (3)$$

In Fig. 4, \bar{M}_f vs \bar{M}_n is plotted for several typical values of K . (For PMM, a typical value is $K \approx 1.3 \times 10^{-4}$.) The important feature of Fig. 4 is that for a particular K , \bar{M}_f tends toward a constant for large values (greater than 5×10^5) of \bar{M}_n . Thus by appropriate choice of original polymer molecular weight, the influence of \bar{M}_n on \bar{M}_f can be eliminated. For $\bar{M}_n/\bar{M}_f \gg 1$, Eq. (1) becomes

$$\rho = \frac{100q_r A_0}{EG(s)\bar{M}_f} \quad (4)$$

which is the identical expression derived by Ku and Scala¹² under the assumption that \bar{M}_n was very large. Essentially Eq. (4) means that, for molecules of large molecular weight, the probability of a scission at a bond and hence the required charge density does not depend on that large molecular weight. Equations (1) and (4) show that large charge densities are required to produce low values of fragment molecular weight.

INFLUENCE OF DEVELOPING SOLUTION. As noted, for degrading polymer resists, development by fractional solution requires that the developer be a good solvent for fragment polymer chains below some critical weight \bar{M}_{fc} , and a poor solvent above. The sensitivity of a resist depends upon the developing solution since different developers dissolve different fragment molecular weights. Although a complete study of solvents has not yet been made, some guidance can be given. The developer must not be a good solvent for the original polymer of average weight \bar{M}_n . The handbooks¹⁴ characterize solvents by a "solubility parameter." Good solvents for unirradiated PMM of a given molecular weight have values of δ in specified ranges.

If the solvent is in the poorly hydrogen-bonded family (e.g., hydrocarbons), it will be a good solvent of PMM when its δ lies in the range 8.9-12.7. For moderately hydrogen-bonded solvents (e.g., esters), the range is 8.5-13.3. Finally, there are no strongly hydrogen-bonded solvents (e.g., acids and alcohols) which are solvents for the unirradiated PMM. In the selection of a solvent, one should avoid materials with values of δ in the above-mentioned ranges. The question of how poor a solvent for the original PMM is a good developer for the fragmented polymer chains must be answered experimentally. For example, we have found that ethyl alcohol at room temperature gives excellent results for

incident charge densities of 5×10^{-5} coul/cm² in a beam at 10 kV with a silicon substrate.

The resist must be applied to the sample, exposed, developed, and then used for microfabrication. For a high-resolution resist, it is desirable to remove low-molecular-weight polymers from the PMM. Hence, a poor solvent is used to dissolve the low-molecular-weight molecules in the PMM powder. The solution is drained off and the residue is allowed to dry. This residue is mixed by weight with a good solvent, such as trichlorethylene. Before being used, the resulting resist solution is centrifuged and force-filtered through millipore filter paper.

For high-resolution devices, a highly polished substrate is required, preferably conducting. Nonconducting samples can be coated with a thin layer of metal either before or after coating with resist to eliminate charging effects during electron-beam exposure. In many cases it is advantageous to use light photoresist techniques to delineate large areas where high resolution is not required, and to use the electron beam to provide only the high-resolution exposure. The sample is coated with resist by flooding of the substrate with the PMM solution, spinning at high speed to produce a uniform coating, and then baking at 160°C to harden the resist.

The prepared sample is placed on a massive holder for mechanical stability, equipped with a Faraday cup for beam-current measurements, and a screen for focusing, astigmatism correction, etc. After placing the sample in the SEM, the operator adjusts the microscope to optimum operating condition for the desired exposure, sets the exposure time for the area to be scanned and the beam current and voltage to be used, and registers the device with respect to the beam axes using registration marks away from the area to be exposed. Control is then transferred to the computer, which directs the beam in the proper pattern. An example of a bridge fabricated using the CCSEM is shown in Fig. 5. The evaporated metal used here was silver, to demonstrate the fabrication procedure. Superconducting material can be used for operating devices. The edge resolution is estimated to be 300 Å, with a constriction width of 0.15 μm.

PLASTIC EXPOSURE FOR ENERGY-DISSIPATION STUDIES. Commercially available PMM has various trade names (Lucite, etc.). We determined quickly that electron-beam exposed Lucite behaved similarly to the PMM resist described above. The energy dissipation profiles of electron beams penetrating into materials have been measured by optical methods,^{15,16} and recently Hatzakis has suggested that PMM resist could be used.¹⁷ Our approach is somewhat more direct. We have grooved $3/4 \times 3/4 \times 1/8$ -in. Lucite blocks with a V-notch as shown in Fig. 6(b) and then evaporated a 100 Å coating of aluminum on the top surfaces. The sample was mounted in the SEM on the same massive holder described above, and lines were exposed with a series of different exposure times, using the pattern of Fig. 6(a). An experiment number was exposed at the top of each pattern, and the exposure time of each spot in the series of four lines was written by the beam to aid in future identification. The parameters of each experiment were printed by the computer as shown in Fig. 7. After exposure, the aluminum film was removed by a 25-percent NaOH solution; then the sample was rinsed in distilled water. A high-resolution light microscope revealed some patterns before development. Nomarski interference optics proved much more sensitive than conventional. The sample was developed in 95-percent ethyl alcohol with ultrasonic vibration for 30 sec and

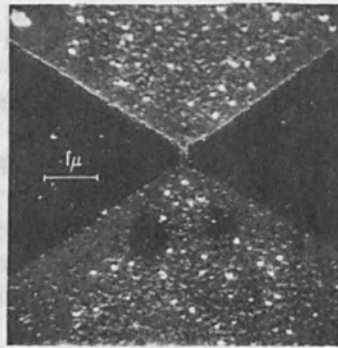


FIG. 5.--Scanning electron micrograph of bridge structure fabricated with CCSEM used to expose thin PMM resist on silicon substrate.

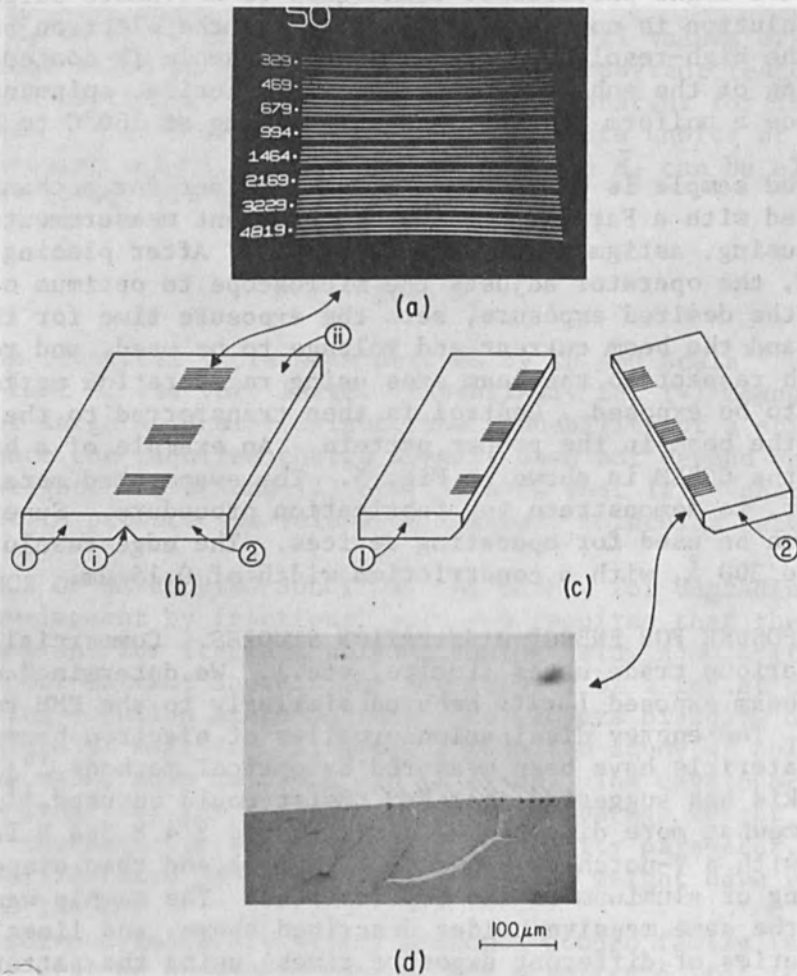


FIG. 6.--Electron-beam exposure of bult plastic samples is useful in determining energy-dissipation profiles: (a) Typical exposure pattern in CCSEM, showing experiment number (5)), dwell time per spot of electron beam for each set of four lines (329, 469, ...), and increasing intensity of each line; (b) schematic representation of plastic sample, showing notch (i) and surface covered with 100 Å of aluminum (ii), as well as position of patterns; (c) plastic block after cleaving; (d) edge view of twice-developed plastic block.

APRIL 15, 1971 HERZOG HIGH VOLT.

EXPOSURE NUMBER 72
TIME IS 23 48 16
X DENSITY (POINTS) 2048.00
Y DENSITY (POINTS) 64.00
GEOMETRIC LAW REASON 1.50
TIME/SPOT : MICRO-S 499.00
POINTS IN A LINE 1600.00
EXPOSURE TIME SEC 154.65
TMAX/SPOT : MICRO-S 7704.00

DX = 16 DY = 512 IT = 91

APERT 400. IBEAM. 0.381E-09 VBEAM. 29500.
LENS1 4498. LENS2 9276. SMAG 2.

TIME FOR GROUPS IN MICRO SECOND / POINT

1 499.
2 724.
3 1059.
4 1564.
5 2319.
6 3454.
7 5154.
8 7704.

FIG. 7.--Printout from computer of parameters used in plastic block exposure. X DENSITY is number of points in line if each were exposed, 0 X DENSITY, 4096. Y DENSITY is number of horizontal lines in pattern if each were exposed, 0 Y DENSITY, 1024. GEOMETRIC LAW REASON is approximate factor by which given exposure time is multiplied to get next exposure time. TIME/SPOT is minimum dwell TIME/SPOT on given line. This time is multiplied by GEOMETRIC LAW REASON factor 1.5 to obtain TIME/SPOT for set 2, by 1.5^2 to obtain TIME/SPOT for set 3, etc. POINTS IN A LINE sets line length, once X DENSITY is known. EXPOSURE TIME is calculated by computer so that total time is known to operator before exposure starts. TMAX/SPOT is maximum time/spot for given exposure, also calculated by computer. DX and DY are increments for D/A converters, and IT is timing interval: time/spot is $[5 * IT + 44]$ μ s. APERT, IBEAM, etc. are SEM parameters useful in reducing data.

squirted with the same alcohol for 15 sec, and this sequence was immediately repeated two more times. The sample was then blown dry. Next, the sample was cleaved over a sharp blade inserted in the notch; one half was again developed as above and the other half was not. Both halves were then mounted on specimen stubs, coated with an estimated 100 Å of evaporated gold while rotating, and subsequently examined in a scanning electron microscope. It was found that the gold-coated Lucite was stable under bombardment by 3-keV electrons, and this voltage was used for all examinations. A low-magnification micrograph of the twice-developed half is shown in Fig. 6(d), for a typical cleaved sample. Profiles of the developed sample were obtained by viewing the sample along the groove and perpendicular to the cleaved surface, as shown in Figs. 8 and 9. Since four profiles could be seen for each exposure, a good check on reproducibility was available for numerical evaluation of these results (to be reported later). It was discovered that the samples developed only once from the top surface of the Lucite before cleaving did not always exhibit the same contour as those developed for a second time after cleaving. In addition, a certain amount of debris often remained in the deeper once-developed grooves.

The profiles of grooves that have been fully developed are believed to represent surfaces of constant-energy dissipation. The reasoning is as follows: a dissipation function $g(\vec{r})$ represents the mean energy dissipation per unit volume as a function of vector position \vec{r} from the point of beam entry. Some critical energy dissipation g_{crit} is required to degrade the PMM for a given developer. While g_{crit} will be a function of the developer chosen, it should be a constant for a given developer and development time. The profiles shown here are two-dimensional projections of $g(\vec{r})$ produced by scanning the exposing beam along the line. As expected, profiles vary with beam voltage, as shown in Fig. 10. Development after cleavage seems essential to produce equi-energy dissipation contours and to remove all undeveloped PMM. Numerical reduction of these contours to mathematical expressions useful for future electron device fabrication and analysis by electron beam techniques is in progress, and will be reported in a later paper.

CONCLUSION

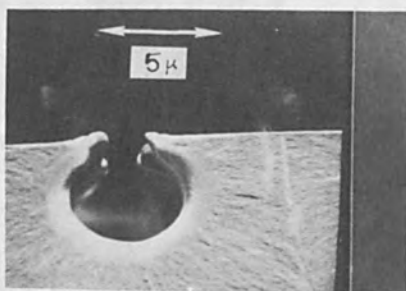
The CCSEM has enabled us to expose a variety of patterns useful for electron device fabrication and electron energy dissipation studies. An improved understanding of PMM exposure and development processes has enabled us to use developers and solvents other than those previously reported, and to devise a simple technique for writing information with high resolution on a common, commercially available plastic.

ACKNOWLEDGMENTS

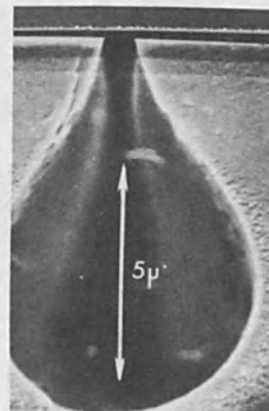
The authors would like to thank many colleagues for valuable discussions, especially Professors C. W. Turner and M. H. Graham, and to thank T. Scott and G. Tietz for valuable assistance in developing and recording the profiles given in Figs. 8-10. Appreciation is also due to the Physical Electronics Group at the Stanford Research Institute for helpful suggestions.



FIG. 8.--Scanning electron micrograph of exposed lines and numbers on plastic block sample.



(a)



(b)

FIG. 9.--Scanning electron micrographs of cleaved Lucite samples, typical of those from which profiles are obtained: (a) beam voltage = 14.86 kV; (b) beam voltage = 29.5 kV.

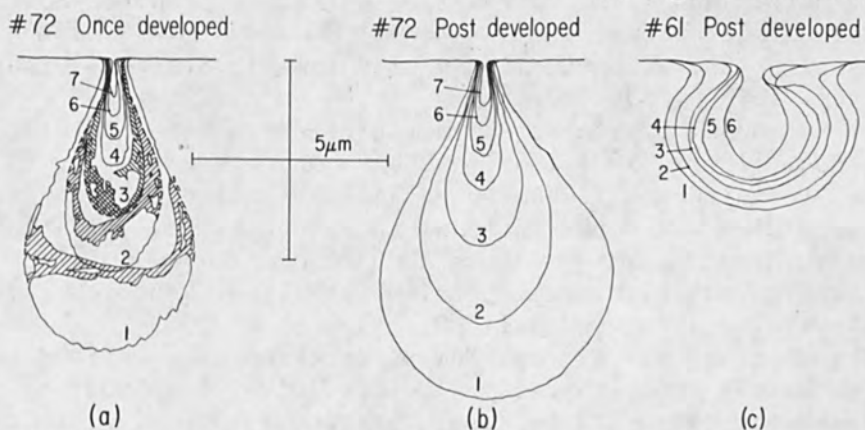


FIG. 10.--Tracings of equi-energy dissipation profiles obtained from series of exposures: (a) Sample 72, half developed from top only, beam voltage = 29.5 kV. (b) Sample 72, half developed as (a), and also after cleaving. Note that profiles are significantly different, and that debris present in 72 (a) is absent in 72 (b). (c) Sample 61, developed before and after cleaving, beam voltage = 14.86 kV.

REFERENCES

1. G. R. Brewer, The application of electron/ion beam technology to microelectronics, IEEE Spectrum 8(No. 1): 23-37, 1971.
2. R. F. M. Thornley and T. Sun, Electron beam exposure of photoresists, J. Electrochem Soc. 112: 1965.
3. I. Haller, M. Hatzakis, and R. Srinivasan, High resolution positive resists for electron-beam exposure, IBM J. Res. Dev. 12: 251-256, 1968. See also M. Hatzakis, J. Electrochem Soc. 116: 1033, 1969.
4. R. F. M. Thornley and M. Hatzakis, Electron optical fabrication of solid state devices, Rec. 9th Symp. on Electron, Ion, and Laser Beam Tech, S.F.Press, 1967; pp. 94-100. See also R. F. M. Thornley, M. Hatzakis, and V. A. Dhalea, Electron-optical masking of semiconductor structure, IEEE Trans. ED-17: 961-964, 1970.
5. M. Hatzakis and A. N. Broers, High resolution electron beam fabrication, Rec. 10th Symp. on Electron, Ion, and Laser Beam Tech, S.F.Press 1969; p. 107.
6. A. N. Broers, E. G. Lean, and M. Hatzakis, 1.75 GHz acoustic-surface-wave transducer fabricated by an electron beam, Appl. Phys. Lett. 15: 98-101, 1969.
7. T. H. P. Chang and A. D. G. Stewart, A high resolution electron beam system for microcircuit fabrication, Rec. 10th Symp. on Electron, Ion, and Laser Beam Tech, S.F.Press, 1969; pp. 97-105.
8. E. D. Wolf, W. E. Perkins, and P. J. Coane, Device fabrication with the stereoscan, Proc. 3rd Annual Stereoscan Colloquium, Kent Cambridge Sci. Inc., 1970; pp. 99-107.
9. S. Miyauchi, K. Tanaka, and J. C. Ross, Automatic pattern positioning of scanning electron beam exposure, IEEE Trans. ED-17: 450-457, 1970.
10. R. F. Herzog and T. E. Everhart, A versatile computer-controlled scanning electron microscope, accepted for publication, Rev. Sci. Instr.
11. A. Chapiro, Radiation Chemistry of Polymeric Systems, Wiley, New York, 1962; vol. 15, pp. 339-380.
12. H. Y. Ku and L. C. Scala, Polymeric electron beam resists, J. of Electrochem. Soc. 116: 7, 980, 1969.
13. J. S. Greeneich and T. Van Duzer, A Fabrication Procedure for Superconducting Thin-Film Constrictions, to be published. Also in J. S. Greeneich, M. S. Thesis, University of California, Berkeley.
14. J. Brandrup and E. H. Immergut (eds.), Polymer Handbook, Interscience Publishers, New York, 1966; pp. 341-368.
15. W. Ehrenberg and J. Franks, The penetration of electrons into luminescent material, Proc. Phys. Soc. 13, 66: 1057-1066, 1953.
16. W. Ehrenberg and D. E. N. King, The penetration of electrons into luminescent materials, Proc. Phys. Soc. 81: 751, 1963.
17. M. Hatzakis, New method of observing electron penetration profiles in solids, Appl. Phys. Lett. 18: 7-10, 1971.

PAPER TAPE-CONTROLLED ELECTRON PROBE RESIST EXPOSURE AND DIRECT METALLIC DEPOSITION

C. DIX, J. P. BALLANTYNE, and W. C. NIXON

University of Cambridge, Cambridge, England

Computer-aided design techniques are now used extensively for the production of masks in the microelectronic industries. In these methods the microcircuit patterns are broken down into simpler component parts, such as rectangles, whose coordinates are punched onto paper tape.

A logic system has been developed to control an electron probe from coordinates read in on paper tape. Successive rectangles specified on the tape are scanned by the probe on the specimen, exposing an electron-sensitive material. A microcircuit pattern is thus built up from these basic rectangular elements. The use of an electron probe allows the generation of patterns with submicron dimensions within a reasonable time.

The system outlined above has been used to produce microcircuit patterns using two techniques. In one, electron-sensitive resist is used to define a pattern etched in underlying material; in the other, metallic patterns are deposited directly by the decomposition of a metallic compound.

INTRODUCTION

The dimensions of the components in integrated circuits have been getting steadily smaller since the advent of microelectronics. At the present time these dimensions are approaching the optical limit, and there are some applications, such as microwave transistors, where line widths of 0.5 micron or less could be useful.

While individual structures have been getting smaller, the number of devices per chip has increased, so that the production of the original artwork for one of today's highly complex circuits consumes a large number of man-hours, despite the extensive use of computer-aided design (CAD).

Electron-beam pattern generation can be useful in producing submicron structures directly from the digital information which results from present CAD techniques.

INITIAL APPROACH

The early electron-beam-produced patterns were made by means of a flying spot scanner. This system requires a high-definition master which would be prepared by the photoreduction of an artwork drawing similar to that used for making microcircuit masks.

The flying-spot scanner also suffers from a limited resolution (at present about 2000 lines) although higher definition CRTs may be developed in the future. In addition, the whole area of the master must be scanned irrespective of the content of the pattern. Speed-up techniques can reduce the time wasted on unexposed areas.

COMPUTER METHODS

The use of a computer coupled to a scanning electron microscope (SEM) for controlling the electron probe offers many advantages over the flying-spot scanner. These systems have digital-to-analog converters (DAC) to interface between the computer and the SEM. Therefore, the limit of resolution within a given area of the specimen is determined by the number of bits the DAC can handle, and by the over-all stability of the electron beam system. Theoretically, this stability could be very high and certainly better than that achieved by the flying-spot scanner.

In these systems the electron beam scans only the areas to be exposed. Thus, time is not wasted by scanning blank areas. Also the computer can be used to perform other functions, such as processing of the data and alignment.

The sensitive materials, such as photoresists or electron-sensitive resists, can be exposed very rapidly by the electron beam. Therefore, fast access of the pattern information is required. For this reason a large part of the computer's store would be used purely for the pattern data.

SIMPLIFIED DIGITAL CONTROL SYSTEM

The basic requirement of a digital pattern generator is not a computer but a pair of digital-to-analog converters (DACs), one each for the X and Y scan directions. These DACs, coupled to a pair of counters fed from a suitable information reader, form the basis of a simple digital control system. The system built at Cambridge University uses a paper-tape reader to input the data to a special purpose logic system which is the pattern generator.

In a simplified system the shape of the data fed in is important as no data processing is possible. It was therefore decided that the format of the data should be one of the standard ones used for the computer-aided design of integrated circuits. This would mean that existing data tapes or tapes made by existing computer programs could be used to drive the pattern generator.

One widely used CAD system produces a tape to steer the cutting knife of an automated coordinatorgraph. This produces the artwork, which (after stripping off the unwanted areas by hand) is then photographically reduced in the conventional manner. This is a very flexible method which allows any shape of pattern to be drawn. However, owing to the fact that the knife only cuts around the edges of the design, it is not directly compatible with electron-beam pattern generation.

The most promising system looked at was that of the David Mann Co. Pattern Generator. This system exposes rectangles of variable size at appropriate positions onto a photographic plate to build up the desired circuit pattern. The plate produced is 10 times the final size of the circuit. A set of such plates is reduced in a step-and-repeat camera to produce the mask set for that particular circuit.

This was the system adopted for the pattern generator described in this paper. The difference in this system is that the electron probe scans out a raster of a variable size for each rectangle. Also, the pattern can be written directly onto the mask plate or silicon slice at any dimensions determined by the gain settings of the scan amplifiers.

INPUT FORMAT

The circuit pattern is divided into component rectangles. Each rectangle is specified by four coordinates (Fig. 1). The point (X, Y) is the center of the rectangle and can be any point within the total working field defined by the DACs. In the Mann system these coordinates are expressed in twelve bits (i.e., up to a value of 4095). However, for experimental purposes it was thought that ten bits (1023) would be sufficient, thus allowing comparatively inexpensive DACs to be used.

The width W and height H of the rectangle are expressed in eight-bit numbers (up to 255) as in the Mann system. The extra coordinate, the angle of rotation of the rectangle, was omitted as it was thought to be nonessential.

The four coordinates are punched in a condensed code, requiring only eight columns of holes on paper tape. Two columns are required for each coordinate. The beginning of each block of data (one rectangle) is coded. If the block were punched, for instance in BCD (Binary Coded Decimal), 14 hole positions would be required for the numerical data plus extras for the start code and X, Y, W, and H characters if included. Therefore, by using the condensed code, the time required to read each block is approximately halved.

OPERATION OF THE PATTERN GENERATOR

Figure 2 shows a simplified block diagram of the pattern generator. The four coordinates of a rectangle are read from the tape by the tape reader and are loaded into the appropriate buffer stores. Because the centerpoint of the rectangle is specified, it is necessary to subtract half the values of W and H from X and Y, respectively. This gives a corner point of the rectangle from which the scanning of the electron probe will start. The subtraction is done by the circuits $X - (W/2)$ and $Y - (H/2)$. The two counters are at zero so that the coordinates of the corner point are fed to the DACs, and the electron probe is moved to the corresponding point on the workpiece.

The electron beam is then switched on by the beam-control circuit. For simplification the means by which this function is initiated is not shown in Fig. 2. The clock generator pulses the X counter increasing its value from zero by one on each pulse. This value is added to the $X - (W/2)$ coordinate, which steps the probe on the workpiece so as to build up a line scan.

The X scan continues until the value of the X counter equals the stored value of W, as detected by a comparator which switches off the probe, resets the X counter, and clocks the Y counter one position. The probe is switched on again and the X scan restarted. Thus the electron probe scans out a raster corresponding to the size of the rectangle, the scan ending when both the X and Y counters equal their respective values of W and H. When this happens the whole system is reset and the next block of data is read in.

One extra facility which was built into the system enables the probe always to scan lines in the longer direction of any rectangle. Figure 1 shows how the scan is built up for the two rectangles A and B, A being longer in the X direction and B being longer in the Y direction.

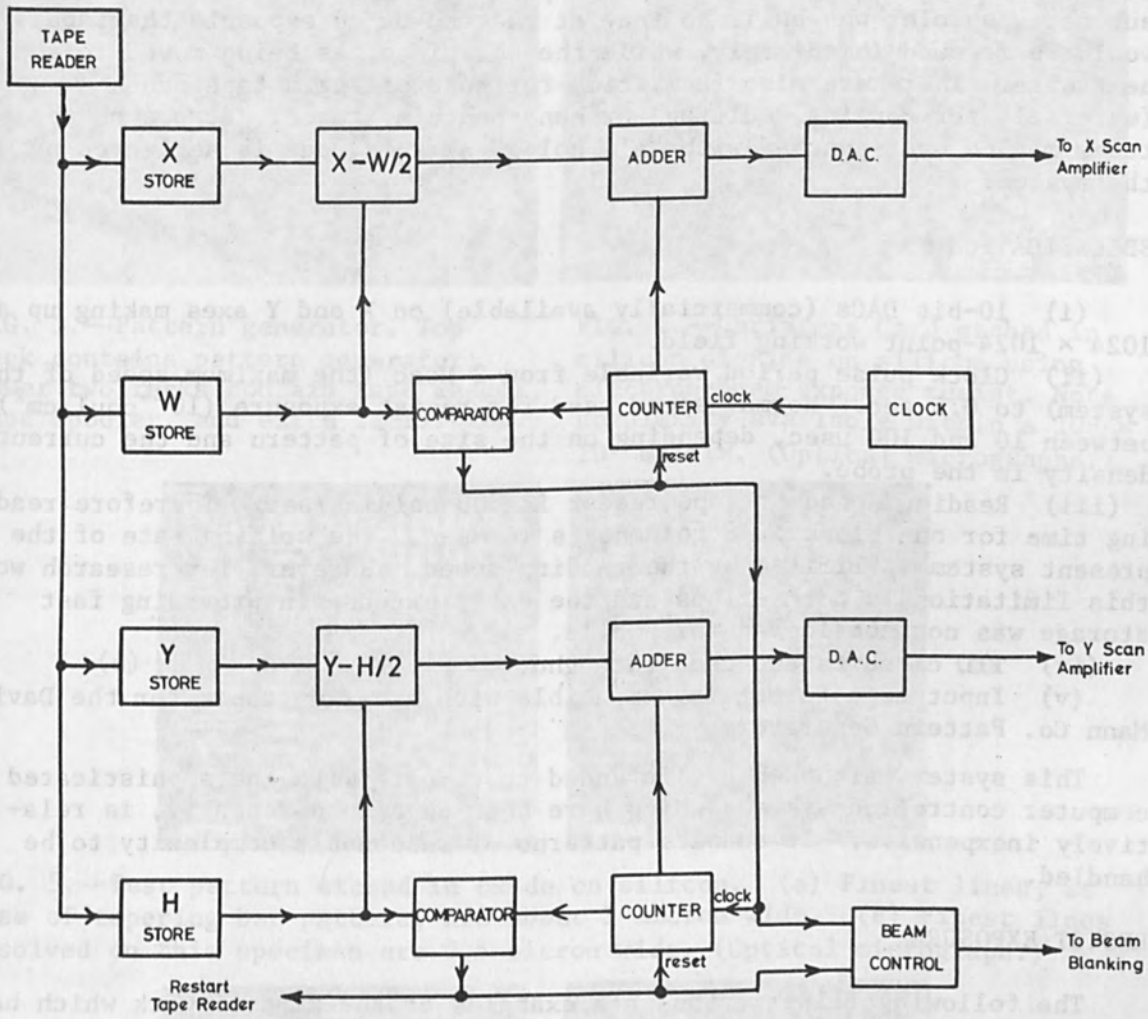


FIG. 2.--Simplified block diagram of the pattern generator.

THE FINISHED CONTROL SYSTEM

Figure 3 shows the completed system. The top rack contains the pattern generator described above. The unit at the right end is the clock generator which has thumbwheel switches to set up the clock pulse period (and thus the exposure).

The lower sections contain the tape reader and an automatic spooler. Since there is no storage for the pattern information, it is necessary to rewind and rerun the tape for each pattern exposed. Therefore the automatic spooler was built so that at the end of an exposure the tape would be rewound immediately, while the workpiece was being moved to the next site. There are also facilities for controlling a tape punch (external) for copying, editing, or hand-punching tapes. Errors on the tapes may be over-punched with "all holes" as this code is neglected by the system.

SPECIFICATION

(i) 10-bit DACs (commercially available) on X and Y axes making up a 1024×1024 -point working field.

(ii) Clock pulse period variable from 2 μ sec (the maximum speed of the system) to 0.5 sec. Normal speed used for resist exposure (10^{-4} coul/cm²) between 10 and 100 μ sec, depending on the size of pattern and the current density in the probe.

(iii) Reading speed of tape reader is 500 columns/sec. Therefore reading time for one block of 8 columns is 16 msec. The writing rate of the present system is limited by the reading speed. However, for research work this limitation is not serious and the extra expense in providing fast storage was not considered worthwhile.

(iv) TTL circuits are used throughout.

(v) Input tape format is compatible with steering tapes for the David Mann Co. Pattern Generator.

This system, although not intended to compete with the sophisticated computer controlled systems which have been developed recently, is relatively inexpensive. It enables patterns of reasonable complexity to be handled.

RESIST EXPOSURE

The following illustrations are examples of the kind of work which has been done with the pattern generator to date. The patterns in Fig. 4, 5, and 6 were produced by exposing electron-sensitive resist on oxidized silicon slices, and in all cases the oxide (approximately 1100 Å thick) has been etched. All micrographs, except Figs. 6(b), 7(a), and 7(b), were taken with an optical microscope owing to the difficulty in obtaining sufficient contrast in the SEM used for the resist exposures.

Figure 4 is an example of the complexity which can be achieved using 10-bit DACs. The distance between the corner marks is 1.5 mm. The distortion is due to the optical microscope.

Figure 5(a) shows a resolution test pattern which is approximately 400 microns square. The finest lines at the base of the tapered bar pattern are just over one micron wide. There is a fault in the SEM, thought to be hysteresis in the scanning section, which prevents the rectangles from joining up.

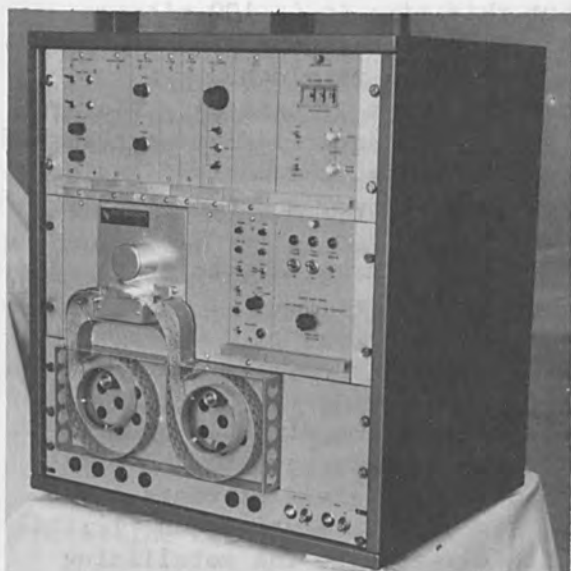


FIG. 3.--Pattern generator. Top rack contains pattern generator; lower two racks contain tape reader, tape spooler, and extra facilities.



FIG. 4.--Christmas Card etched in silicon dioxide on silicon using electron-beam-exposed resist. Note complexity available within a $10^3 \times 10^3$ matrix. (Optical micrographs.)

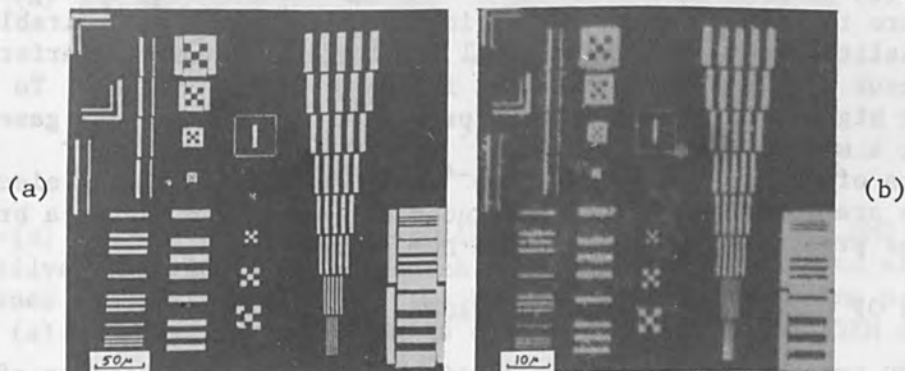


FIG. 5.--Test pattern etched in oxide on silicon. (a) Finest lines, at base of tapering bar pattern, are about 1 micron wide. (b) Finest lines resolved on this specimen are 0.5 micron wide. (Optical micrograph.)

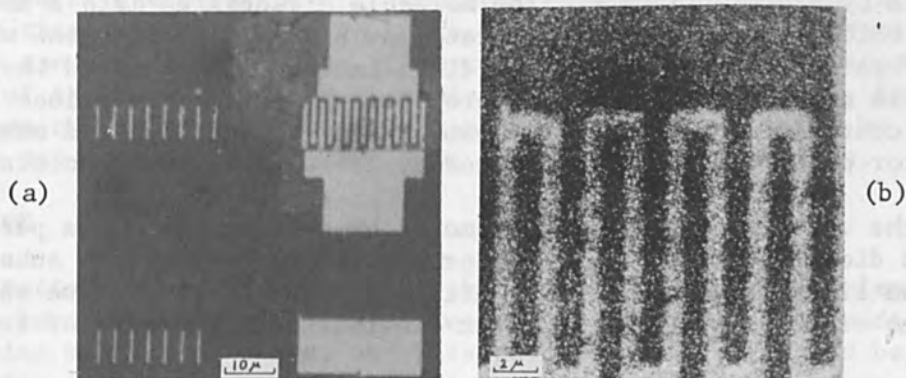


FIG. 6.--(a) Part of composite mask for a transistor etched into oxide on silicon. (Optical micrographs.) (b) SEM micrograph of section of metalizing pattern. Fingers are 1 micron wide and 2 microns apart.

Figure 5(b) is of the same pattern but this time it is 100 microns square. The finest lines resolved in this case, the second group up from the base of the tapered bar pattern, are 0.5 micron in width.

Figure 6(a) is of a composite mask pattern for a transistor. The area seen in the micrograph is approximately 90 microns square. The sections of the mask are, from the bottom right moving clockwise, the base diffusion area, the emitter diffusion areas, the contact windows, and the metallization areas.

Figure 6(b) shows a section of the metallizing area as seen in the SEM. The fingers are 1 micron wide and 2 microns apart.

DIRECT METALLIC DEPOSITION

The selective deposition of conducting metal films directly onto a substrate, by electron decomposition, offers a new approach to the metallizing of microcircuits and the formation of microstorage elements. When Direct Metallic Deposition (DMD) is used, the high resolution and flexibility of electron-beam methods can be applied directly to the metallizing stage of fabrication.

Conducting metal films, directly deposited from tetrabutyltin,¹ stannous chloride,² tungsten hexycarbonyl,³ and silver chloride⁴ have been reported. Most of this work involved the production of large-area films using a flood beam of low-energy electrons. Methods such as these allow easy measurement of film properties. However, when high resolution metal patterns are required, the use of a fine electron probe is desirable.

The quality of the deposited metal films can vary when interfering reactions occur with the residual gases in the specimen chamber. To ensure consistent high quality, the partial pressures of the residual gases should be kept at a minimum.

Results of DMD in high vacuum (10^{-8} Torr) using a scanning electron microscope are described in the remainder of this paper, after a brief review of the principles underlying the DMD process.

PRINCIPLES OF DIRECT METALLIC DEPOSITION

The DMD process relies on the ability of an electron beam to effect molecular dissociation of a metal compound. Consider the case of a thin film of a metal compound on a substrate. When a beam of electrons strikes the thin film, molecules in the compound may be excited into a dissociative state by electron impact. The molecule dissociates into a metallic component which remains on the substrate and a volatile component which leaves. When a sufficient number of dissociations has occurred the remaining film may exhibit conducting properties. Resistance values can be varied by controlling the electron-beam exposure. The size and shape of the resistor pattern will be determined by the exposure pattern scanned by the beam.

When the unexposed material is removed by solvent action, a pattern of controlled dimensions and electrical properties is left on the substrate. The minimum line widths that can be attained with this technique should be of the same order as those obtained in electron-beam exposure of resist materials.

DMD OF SILVER FROM SILVER CHLORIDE

Thin films of silver chloride were prepared by evaporation onto an oxidized silicon substrate. The films were exposed to an electron probe in a vacuum of 10^{-8} Torr. Following exposure, the unexposed compound was removed in a solution of ammonia.

When resistance values were required, the films were annealed after exposure, and after the solvent treatment. Annealing and resistance monitoring were conducted with the specimen in vacuum. Ohmic resistance values obtained range from $1\Omega/\text{square}$ to $1\text{ k}\Omega/\text{square}$. Values as high as $300\text{ k}\Omega/\text{square}$ have been obtained, but these values are generally unstable and decrease considerably during annealing.

The metallizing pattern shown in Fig. 7(a) was generated in silver chloride using the pattern generator described above. The exposure selected for this pattern generates a sheet resistance value of about $10\Omega/\text{square}$. The edge definition in Fig. 7(b) is less than 1 micron. Submicron line widths have been obtained in films 1 micron thick.

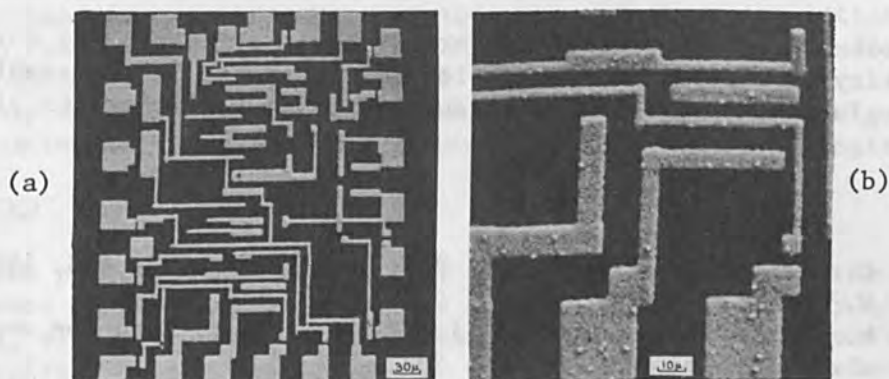


FIG. 7.--(a) SEM micrograph of metallizing pattern formed by DMD in thin film of silver chloride 1 micron thick. Substrate is oxidized silicon. Finest lines are 3 microns wide. (b) Detail of the metallizing pattern shown in (a). The edge definition is on the order of $0.5\ \mu$. (SEM micrograph.)

SENSITIVITY

At present, the exposure required to produce conducting films in silver chloride is of the order of 10^{-2} coul/cm² when 30-kV electrons are used. However, this figure applies to a process where very little chemical amplification can be employed. The film-preparation technique causes severe fogging of the thin film when a developing step is attempted. Experiments have shown that with improved films the amplification offered by a developing step may considerably enhance the speed of the DMD process.

DISCUSSION

The pattern generator described above contains the basic elements for electron-beam control. A total system consisting of an intermediate SEM, a precision mechanical stage, and this pattern generator would be about one-quarter the cost of a full computer-controlled system. A system of intermediate cost and complexity could include a fast-data store and simple data processing.

A logic system based on a higher number of bits is also possible. However, such an expansion will be limited by the over-all stability of the electron-beam positioning system. For example, if a minimum line width of $0.5 \mu\text{m}$ is to be produced by 5 line scans, the required step length is $0.10 \mu\text{m}$. A 10-bit system provides this step length over a field $100 \mu\text{m} \times 100 \mu\text{m}$. A 15-bit system can provide the same step length over an area $3.2 \times 3.2 \text{ mm}$. However, the stability required in the positioning electronics is of the order of 3 parts in 10^5 . For a dynamic system this is a very stringent stability requirement.

The resist exposure and DMD, described previously, were carried out in two quite different systems. Multiple processing on a single chip would be best carried out in one system, where the geometrical parameters characteristic of the electron-beam system, specimen stage, step-and-repeat drive, and pattern generator remain constant from one process to another. The system must achieve a vacuum level adequate for both resist exposure and direct metallic deposition.

ACKNOWLEDGMENTS

This work has been supported in part by equipment purchases through the generosity of the Wolfson Foundation and the Royal Radar Establishment, Malvern, England. We also wish to thank Dr. P. J. W. Rayner for aid in circuit design.

REFERENCES

1. A. G. Baker and W. C. Morris, Rev. Sci. Instr. 32: 458, 1961.
2. R. W. Christy, J. Appl. Phys. 33: 1884, 1962.
3. J. M. Hlavin and A. Fotland, 1st Intern. Conf. Electron and Ion Beam Science and Technology, 1965; p. 231.
4. J. R. Banbury, Ph.D. Dissertation, Cambridge University, 1970.

ELECTRON IMAGE PROJECTION SYSTEMS FOR MICROCIRCUIT LITHOGRAPHY

W. R. LIVESAY and R. B. FRITZ

Radiant Energy Systems, Inc., Newbury Park, Calif.

INTRODUCTION

The limitation of conventional photolithographic techniques, when applied to the fabrication of high-density, high-resolution microcircuits, has prompted considerable research in electron-beam lithography to replace the optical techniques. Virtually all electron-beam systems constructed to date utilize a single electron beam that serially scans out the desired patterns on a mask or wafer. Although this technique is valuable for mask fabrication and prototype circuit development, it is much too slow to be of value for the production exposure of devices themselves.

This paper describes an electron-image projection system which exposes all points on the entire pattern simultaneously. The system uses the electron-image converter-tube technique to convert a mask pattern to an electron image and then projects the entire electron image onto a silicon wafer coated with an electron resist. Performance characteristics of a laboratory system (Fig. 1) are presented and design changes dictated by an evaluation of the system are discussed.

BACKGROUND

At the present state of the art, the photolithographic step in the manufacture of an integrated circuit is most commonly done by contact printing, either from an emulsion mask or a chrome mask. The abrasion that results from the contact of the mask with the silicon wafer causes defects both in the photoresist surface of the wafer and in the mask. An obvious solution to the problem is to project the image rather than contact-printing it. However, optical projection systems introduce a new set of problems. The area that can be projected with high resolution is very limited (less than 1 cm in diameter for usable 1- μ m line widths) and the depth of field is extremely shallow (less than 4 μ m at that resolution).¹

DESCRIPTION OF AN ELECTRON PROJECTION SYSTEM

The electron projection system dispenses with the optical system entirely and employs instead a patterned electron beam. The scheme for producing the patterned electron beam and focusing it on the resist-coated silicon wafer target is shown in Fig. 2. The electron beam is produced by a photocathode surface excited by an ultraviolet (UV) source. The photocathode consists of a thin layer of palladium, which is deposited over a titanium dioxide mask of the same pattern as that to be exposed on the silicon wafer. Where UV light passes through the titanium dioxide mask, the palladium emits photoelectrons at energies of a few tenths of an electron volt. A uniform electric field of 10 kV/cm then accelerates the electrons from the cathode to the silicon target through an axial magnetic field of approximately 1000 gauss, which is generated by the focus coils. This arrangement causes electrons coming from a given cathode point emitted at any angle to be focused at a corresponding point on the

wafer. The result is a 1:1 projection of the entire pattern on the silicon wafer. The electron-beam resist (polymethyl-methacrylate) is developed in a solvent which removes the depolymerized pattern. The remaining wafer-processing steps follow conventional practice.

The patterned photocathode is the electron optical equivalent of the photo mask in the optical process, but since the electron-beam system uses projection rather than contact printing, there is no mask wear and no danger of wafer damage. The mask in the electron-beam system has an unlimited lifetime. If the emission of the palladium layer drops too low, the metal can be stripped away and a new layer can be deposited by evaporation. In addition to eliminating defects caused by contact of the mask with the wafer, the electron-beam process has several other advantages:

- (1) The achievable resolution is approximately five times better than in optical techniques.
- (2) The depth of field is 14 times that of an optical projection system.
- (3) The achievable image diameter is limited only by the size of the focus coils. Present equipment accommodates wafers up to 2.5 in. (6.25 cm) in diameter.
- (4) The electron beam can be magnetically deflected, so that the pattern position may be adjusted electronically rather than mechanically.

PHOTOCATHODE LIFE

One of the earliest concerns in deciding whether the electron-image-projection technique was commercially feasible was cathode life. How many exposures could be made before the cathode emission dropped to a level below which exposures were intolerably long?

Early studies indicated that photocathode degradation was due primarily to outgassing of the electron resist and substrate under electron bombardment. Cathodes which were operated in a clean environment (that is, an ion-pumped system, baked and operating at a pressure of 10^{-7} torr or below) exhibited unlimited life. However, when the electron-resist-coated wafer was introduced into the system, the emission levels dropped sharply after only a few exposures. Monitoring of the system by a quadropole mass analyzer revealed that the principal contaminants produced by the electron bombardment of the electron resist were water and oxygen. Accordingly, the prototype electron projection system was designed in such a manner as to provide the maximum possible vacuum conductance in the region of the photocathode, to reduce cathode fatigue from subsequent ionization and ion bombardment from these contaminants.

When cathode emission drops to an unusably low value, several rejuvenation techniques are available. Another very thin layer (about 20 Å) of palladium may be evaporated on top of the original. This process may be repeated up to three times. After that, the palladium can be stripped off with a hot nitric acid solution and a new palladium layer evaporated on. The palladium may be stripped from the titanium dioxide mask as many times as desired without damaging the mask. Another rejuvenation technique is to bake the photocathode in the vacuum to drive off adsorbed surface films. The baking can be done with the UV source being used for exposure or, more quickly, with an infrared heat lamp.

In the life-test data on the prototype system (Fig. 3), curve A shows the emission vs number of exposures for a fresh cathode, that is, a cathode which was put in the system immediately after the palladium film had been

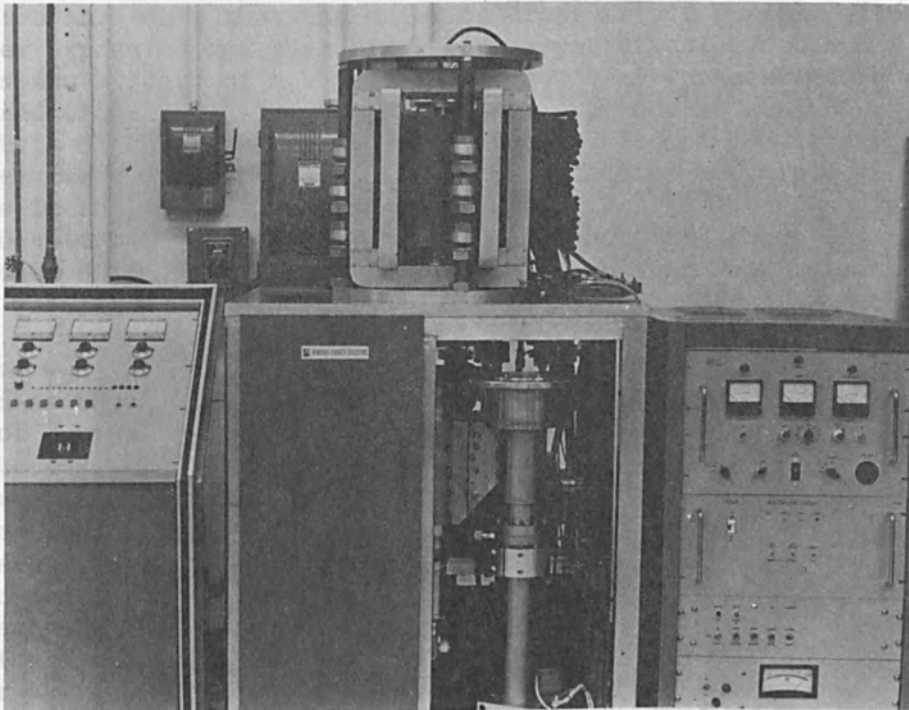


FIG. 1.--Research model electron projection system.

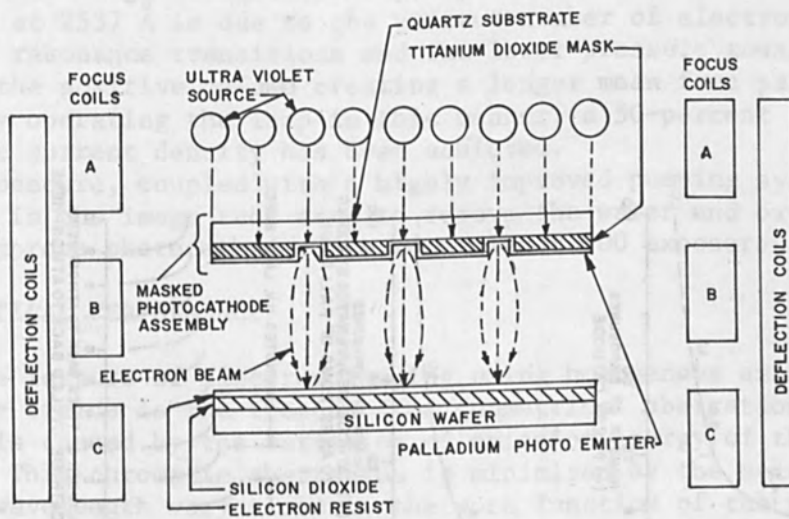


FIG. 2.--Principles of electron pattern projection.

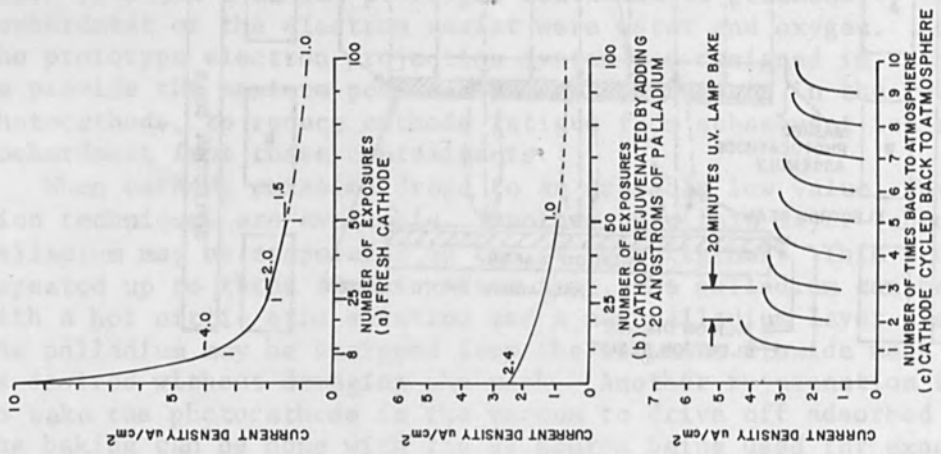


FIG. 3.--Cathode life test results.

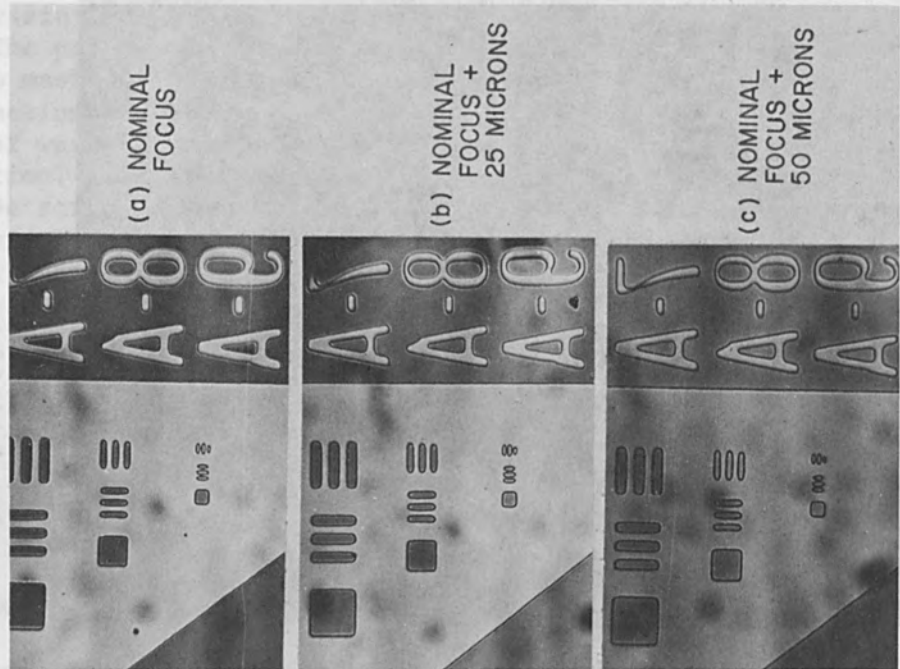


FIG. 4.--Resolution patterns illustrating depth of field. Narrowest lines are 1.2 μm .

evaporated on. Note that the emission drops rather sharply after the first few exposures and then levels out asymptotically. Curve B shows the emission history of a photocathode that has been renewed by evaporating an additional 20-Å layer of palladium over the initial 40-Å layer.

In both of the above tests, each exposure was of 10-sec duration and the wafers were cycled in and out at the rate of one every 4 min. The pressure in the image tube was approximately 2×10^{-5} torr during exposure. Development was normal after 50 exposures and there was no visible degradation of image quality. The measured current density after 50 exposures was $1.5 \mu\text{A}/\text{cm}^2$ for a fresh cathode and $1.0 \mu\text{A}/\text{cm}^2$ for the rejuvenated cathode. Ten-sec exposures have been made with current densities as low as $0.3 \mu\text{A}/\text{cm}^2$. These exposures yielded acceptable results and are regarded as the lowest limit of useful emission from a cathode. Extrapolation of curves A and B out to 100 exposures shows them to be still well above the lower emission limit.

Curve C shows the emission history of a cathode exposed to air several times and then baked to restore its emission. The bake was done simply by exposing the cathode to the normal UV excitation and monitoring the emission current while baking. Approximately 20 min of baking was required after each exposure to air to bring the cathode back up to its peak emission. The excitation source in all cases was a low-pressure mercury-arc lamp formed in the shape of a pancake spiral operating at normal voltage. Operating in this manner, the lamp produces over 90 per cent of its output at 2537 Å, which is the wavelength desired to match the work function of the palladium photoemitter.

By increasing the voltage drop across the electrodes of a low-pressure mercury-arc lamp, an increase in total output illumination can be achieved at the expense of radiant output efficiency at 2537 Å. However, by cooling the outer envelope of the mercury bulb, one may decrease the pressure and still maintain a high efficiency output of 2537-Å radiation. The increase in emission at 2537 Å is due to the greater number of electrons available for causing resonance transitions and the lower pressure towards the outer portion of the positive column creating a longer mean free path for 2537-Å photons. By operating the lamp in this manner, a 50-percent increase in photocathode current density has been achieved.

This procedure, coupled with a highly improved pumping system using cryo-panels in the image tube area to remove the water and oxygen, is expected to improve photocathode life to at least 500 exposures.

ELECTRON-OPTICAL PERFORMANCE

A unique feature of electron imaging using homogenous axial electric and magnetic fields is the freedom from geometrical aberrations. The only aberration is caused by the variation of emission energy of the photoelectrons. This chromatic aberration is minimized by the selection of an excitation wavelength very close to the work function of the photoemitter. Since geometric aberrations are absent, there is no loss of resolution from center to edge of the pattern being projected. However, the magnetic and electric fields must be uniform over the image format projected if high resolution is to be achieved from edge to edge. In the present system, the uniformity of the magnetic and electric fields is better than 1 part in 10^4 over a 2.5-in. (6.25-cm) diameter. Resolution patterns containing bar targets with lines less than $1 \mu\text{m}$ wide have been exposed over a 2-in. (5-cm) diameter field.

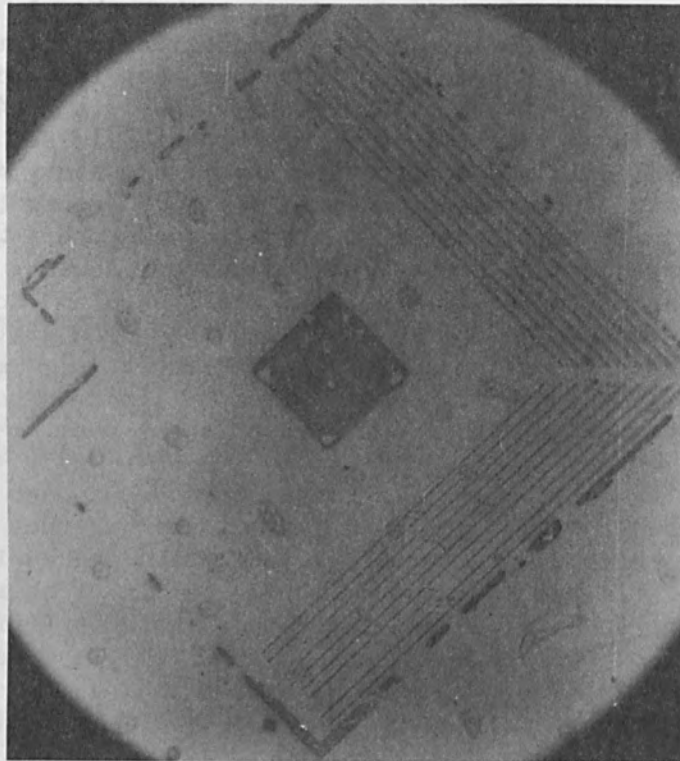


FIG. 5.--Example of 0.5- μ m on 2.5- μ m centers printed on resist by electron projection system.

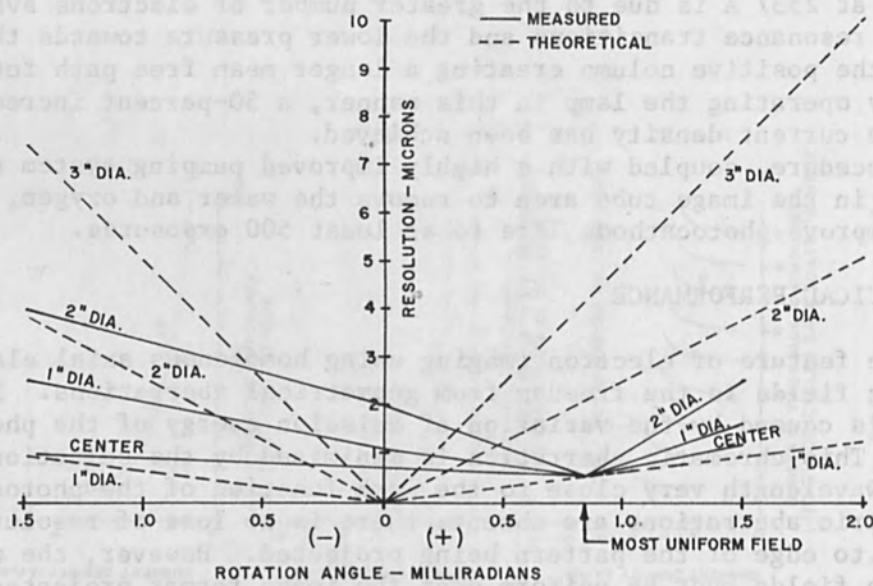


FIG. 6.--Defocusing due to magnetic rotation.

The ultimate resolution of the system is calculated to be approximately $0.2\ \mu\text{m}$ based on an electron emission energy of $0.1\ \text{eV}$. This result has been confirmed by tests in which $0.5\text{-}\mu\text{m}$ lines have been reproduced with approximately $0.2\text{-}\mu\text{m}$ edge definition (Fig. 5). The photocathode mask which was used to project this image was fabricated on a scanning electron microscope.

Defocusing caused by the alignment deflection system is negligible. No line broadening is detectable in a $1\text{-}\mu\text{m}$ line when the pattern is deflected to its maximum, $0.010\ \text{in.}$ ($0.25\ \text{mm}$).

Depth of field of the system is calculated to be $\pm 25\ \mu\text{m}$ for $1\text{-}\mu\text{m}$ resolution. In actual practice, it appears to be somewhat better. Figure 4 shows three exposures: (1) at nominal focal distance, (2) at the nominal focal distance $+25\ \mu\text{m}$, and (3) at nominal $+50\ \mu\text{m}$. The line width of the smallest pattern is $1.2\ \mu\text{m}$. The line broadening of the $1.2\text{-}\mu\text{m}$ lines is not discernible at $25\ \mu\text{m}$ and becomes barely noticeable at $50\ \mu\text{m}$ out of focus.

AUTOMATIC ALIGNMENT

The first prototype system used electron-beam induced conductivity (EBIC) in the wafer oxide layer as a detection mechanism for pattern alignment errors.² Although this technique produces acceptable alignment performance, the EBIC markers are difficult to produce reliably and require several extra processing steps that are undesirable in the production of integrated circuits. The system now in use has two 0.010-in. (0.25-mm) diameter holes as markers in the wafer and detects the primary beam current reaching the rear side of the wafer through these holes from alignment marks in the photocathode. The holes can be produced either by a laser or an air abrasive drill.

The alignment mark is so designed that it produces the maximum amplitude signal when it is centered about the wafer hole. A computer-controlled scan pattern first locates the hole and then scans successively smaller patterns, recalculating the center each time until an optimum alignment is attained. The total alignment time is approximately $1\ \text{sec}$, and the system detects and corrects alignment errors as small as $0.2\ \mu\text{m}$. In this technique, the size of the hole is not critical; nor is it important whether it grows or shrinks during the processing steps, so long as it changes uniformly.

IMAGE ROTATION

The first system achieved image rotation for alignment by an alteration in the uniformity of the magnetic focusing field in such a manner as to cause an angular shift in the projected pattern. The total rotation achievable by this technique is approximately $\pm 1.5\ \text{mrad}$. However, since the axial magnetic field is caused to increase or decrease radially during rotation, the image focus deteriorates as a function of the rotation angle and of the distance from the center of the image. Results of resolution measurements at several rotation angles are shown in Fig. 6.

From Figure 6, it is clear that magnetic rotation has unacceptable defocusing characteristics for patterns having line widths below $4\ \mu\text{m}$ over a wafer $2\ \text{in.}$ ($5\ \text{cm}$) in diameter. Even with $4\text{-}\mu\text{m}$ configuration, the rotation angle is limited to less than $\pm 1.5\ \text{mrad}$, which allows a very small

tolerance on mechanical wafer placement accuracy; and, for wafers 3 in. (7.5 cm) in diameter, magnetic rotation is clearly out of the question.

It was necessary, therefore, to use instead a hybrid alignment system which utilizes magnetic deflection for X and Y corrections but uses a proprietary mechanical system for angular corrections. This mechanical system is somewhat unique in that it uses no bearings and can be accurately moved in increments of 1 mrad with a total excursion of ± 10 mrad. Use of a mechanical rotation system eliminates the need for the center focus coil and greatly simplifies the focus coil power supply. Eliminating the center focus coil also greatly simplifies the automatic wafer-handling system and permits a much more efficient vacuum system in the region of the photocathode.

REFERENCES

1. R. E. Tibbets, OSA Topical Meeting on Optics in Microelectronics.
2. T. W. O'Keefe, IEEE Trans. ED-17: 465-469, 1970.
3. T. W. O'Keefe and J. Vine, Adv. Electronics & Electron Physics, Academic Press, New York, 1969; vol. 28A, p. 47.

SESSION ON RELATIVISTIC ELECTRON BEAMS

NRL RELATIVISTIC ELECTRON BEAM PROGRAM

J. BLOCK, J. BURTON, J. M. FRAME, D. HAMMER, A. C. KOLB,* L. S. LEVINE, W. H. LUPTON, W. F. OLIPHANT, J. D. SHIPMAN JR., and I. M. VITKOVITSKY

Plasma Physics Division, Naval Research Laboratory, Washington, D. C.

Two large electron beam generators, Gamble I and Gamble II, have been designed and constructed at NRL. They are used for studies of the propagation of intense pulsed relativistic electron beams and the interactions of such beams with matter. Typical parameters of the electron beams produced are: beam energy, 1 MeV; beam current, 1 MA; pulse duration, 40 nsec. Gamble I is designed to produce beams of up to 20 kJ of kinetic energy; Gamble II, up to 60 kJ. The propagation of very high current relativistic electron beams ($v/\gamma \approx 10$) over distances of 1 m, has been studied as a function of drift-tube gas pressure and applied axial magnetic field.

INTRODUCTION

The purpose of this paper is to provide a general introduction to the NRL relativistic electron beam program, and to report on some recent results on diode development and beam drifting. The program is only 4 years old, but related research at NRL existed long before that, including experimental¹ and theoretical² studies of electron-beam dynamics and an active program of high-voltage technology in connection with exploding-wire research.³ A major effort to produce and study intense relativistic beams was initiated in 1967 with the construction of a 40- Ω oil Blumlein line and a 7- Ω water Blumlein generator.⁴

Gamble I was designed and built at NRL in 1968;⁵ Gamble II became operational in June 1970.^{6,7} Electron-beam propagation was studied concurrently in collaboration with the Cornell University Laboratory for Plasma Studies.⁸

Among the applications of the NRL programs are studies of the effects of intense energy deposition on materials, the generation of microwave radiation, and the utilization of relativistic electron beams for controlled thermonuclear fusion.⁸

GAMBLE I AND GAMBLE II ELECTRON BEAM GENERATORS

Gamble I and Gamble II are each capable of producing well over 10^4 J of 1-MeV electrons in a 50-nsec pulse. The two generators are similar and differ from one another principally in size. What follows refers mainly to the design and behavior of Gamble II, with specific reference to Gamble I only where significant differences exist.

Both generators are charged coaxial transmission lines, designed to produce a 1-MV pulse across a field-emission diode for 50 nsec. They both utilize high-resistivity water as the dielectric. Water was chosen as the dielectric not only because it is convenient, inexpensive, and self-healing after a breakdown, but primarily because of its very high dielectric constant (80 as compared to 2 or 3 for oil or Mylar), which implies that a very high density of energy storage is possible and that

*Present address: Maxwell Laboratories, Inc., San Diego, Calif.

the pulse-forming line can be shortened. The reason water is not used more extensively as a dielectric is that its breakdown properties are highly time dependent. Even if one uses demineralized high-resistivity (say, $\rho > 1 \text{ M}\Omega\text{-cm}$) water, its practical utility as an energy-storage dielectric is limited to systems in which voltages are maintained for no more than a fraction of a microsecond. Fortunately, extensive studies of the nature of electrical breakdown in water have been conducted by J. C. Martin and his co-workers at AWRE Aldermaston in England.¹⁰ Their work has not only shown the nature of breakdown, but has provided empirical formulas relating the breakdown field strengths to the electrode polarity and area, and the time for which the field appears at the electrode surfaces.¹¹ These relationships were used extensively in the design of Gamble I and Gamble II.

To the rear of the coaxial line of Gamble II (Fig. 1) is the Marx generator, which was designed and built by Physics International Co. It is composed of 120 stages, each of which consists of a single capacitor of $0.5 \mu\text{F}$ rated at 85 kV. The stages are charged in parallel and erected by switching them in series, with every third switch being triggered. The total stored energy in the bank is 228 kJ at full charging voltage; its output capacitance is 4.1 nF.

The Marx generator erects and charges a coaxial water transfer capacitor section of 7.4 nF to a voltage of up to 6.0 MV. The transfer or intermediate storage section is designed to withstand the high voltage for the relatively long charging time of 1.2 μsec . It is used to reduce the more stringent requirements on rapid Marx discharge time which would be needed if the Marx directly charged the pulse-forming section. The intermediate storage section and the remainder of the water line are separated from the oil-filled Marx generator tank by a pair of polyurethane diaphragms 1 in. thick that must support any pressure differentials between the oil and water sections and withstand large voltages during Marx erection and discharge.

The intermediate storage section is, in turn, discharged into the pulse-forming line through an overvoltaged water switch. This gap, as well as a similar one at the output of the pulse-forming line, has been designed according to the water breakdown formulas mentioned above. The electrodes are so designed that breakdown along streamers from the negative electrode occurs at a voltage level only slightly lower than that along streamers from the positive electrode. This condition results in a minimum gap spacing and therefore minimum switch inductance. The switch and other parts of the generator were designed with the help of electrolytic-field plotting tanks and an electrostatic potential plotting computer code,¹² to ensure that the electric fields were kept sufficiently below breakdown values throughout the system.

For statistical reproducibility, each of the two switches must be adjusted to fire at between 80 and 90 per cent of peak voltage, a condition that imposes a significant loss in energy transfer through the system. For this reason, and because of the need for precise time synchronization of the beam generator for some applications, effort has been devoted to the development of command triggered water switches; a preliminary design of a switch being for the output of the pulse-forming line is shown in Fig. 2.¹³ A positive trigger signal derived from the intermediate-storage and pulse-forming sections make the use of gas switching impractical there; the required gap spacing to prevent breakdown would make the switch so inductive as to degrade significantly the risetime of the generator

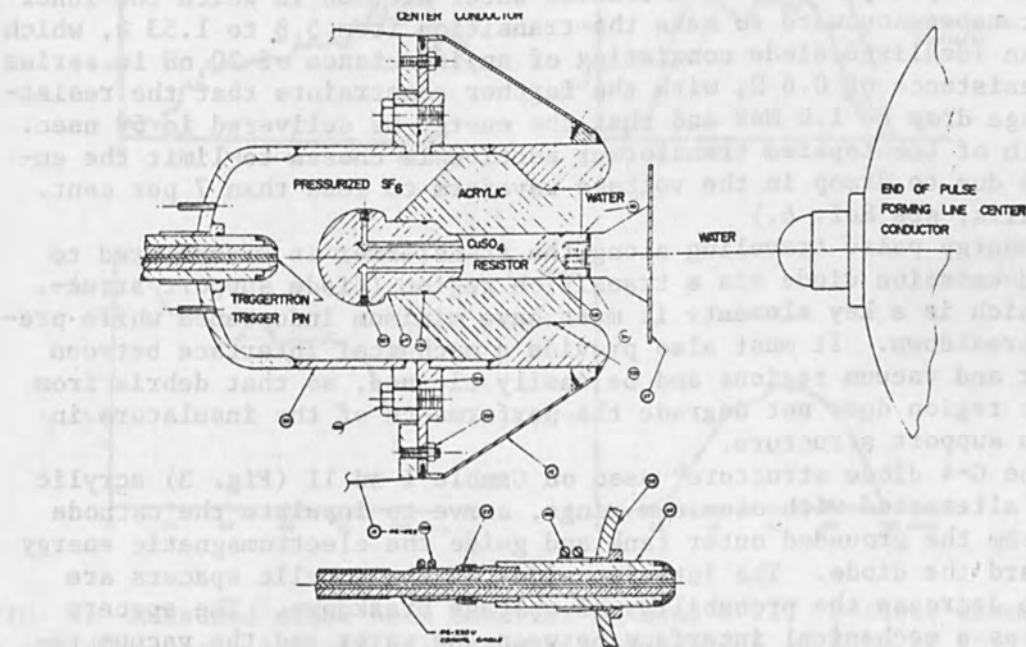
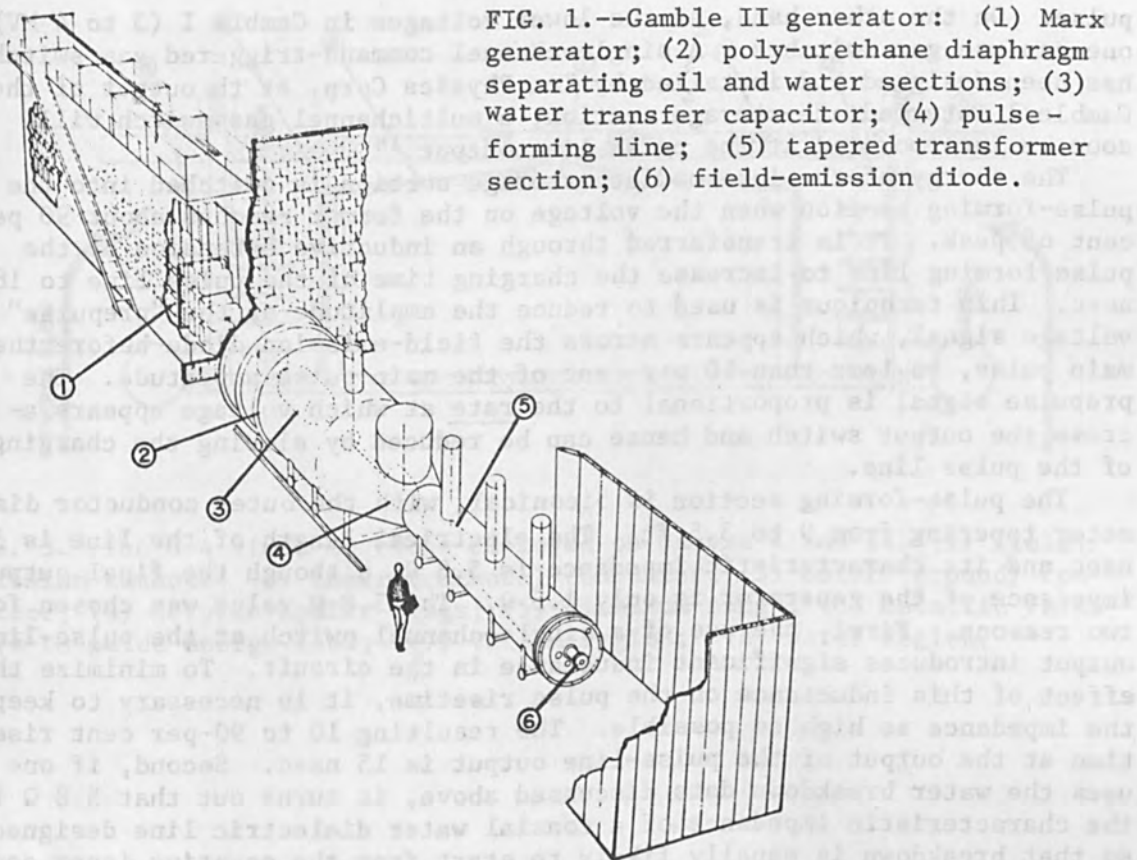


FIG. 2.---Triggered water switch for pulse forming line of Gamble II.

pulse. On the other hand, at the lower voltages in Gamble I (3 to 4 MV) one can use gas switches. A single-channel command-triggered gas switch has been designed and installed by Ion Physics Corp. at the output of the Gamble I intermediate-storage section; a multichannel gas switch will soon be incorporated at the pulse line output.¹⁴

The energy of the intermediate-storage section is switched into the pulse-forming section when the voltage on the former reaches about 90 per cent of peak. It is transferred through an inductive extension of the pulse-forming line to increase the charging time of the pulse line to 180 nsec. This technique is used to reduce the amplitude of the "prepulse" voltage signal, which appears across the field-emission diode before the main pulse, to less than 10 per cent of the main pulse amplitude. The prepulse signal is proportional to the rate at which voltage appears across the output switch and hence can be reduced by slowing the charging of the pulse line.

The pulse-forming section is biconical, with the outer conductor diameter tapering from 9 to 3.5 ft. The electrical length of the line is 50 nsec and its characteristic impedance is 5.8Ω , although the final output impedance of the generator is only 1.5Ω . The $5.8\text{-}\Omega$ value was chosen for two reasons. First, the use of a single-channel switch at the pulse-line output introduces significant inductance in the circuit. To minimize the effect of this inductance on the pulse risetime, it is necessary to keep the impedance as high as possible. The resulting 10 to 90-per cent risetime at the output of the pulse-line output is 15 nsec. Second, if one uses the water breakdown data discussed above, it turns out that 5.8Ω is the characteristic impedance of a coaxial water dielectric line designed so that breakdown is equally likely to start from the negative inner conductor and the positive outer one; such a line can store or transmit the most electrical energy for a given outer diameter, since either higher or lower impedance lines will break down at lower fields.

The final generator output impedance is obtained by propagating the pulse-line output pulse along a coaxial water section in which the inner conductor tapers outward to make the transition from 5.8 to 1.53Ω , which matches an idealized diode consisting of an inductance of 20 nH in series with a resistance of 0.6Ω , with the further constraints that the resistive voltage drop be 1.0 MeV and that the energy be delivered in 50 nsec. The length of the tapered transformer section is chosen to limit the energy loss due to droop in the voltage waveform to less than 7 per cent. (For details, see Ref. 6.)

The energy pulse traveling along the transformer is transmitted to the field-emission diode via a transition region (diode support structure), which is a key element: it must have minimum inductance while preventing breakdown. It must also provide a mechanical interface between the water and vacuum regions and be easily cleaned, so that debris from the diode region does not degrade the performance of the insulators in the diode support structure.

In the G-4 diode structure⁶ used on Gamble I and II (Fig. 3) acrylic spacers, alternated with aluminum rings, serve to insulate the cathode region from the grounded outer tank and guide the electromagnetic energy flow toward the diode. The interior sides of the acrylic spacers are angled to decrease the probability of voltage breakdown. The spacers also act as a mechanical interface between the water and the vacuum region of the diode. Great care must be exercised in the design of this region to minimize voltage flashover. Metallic falsework is introduced

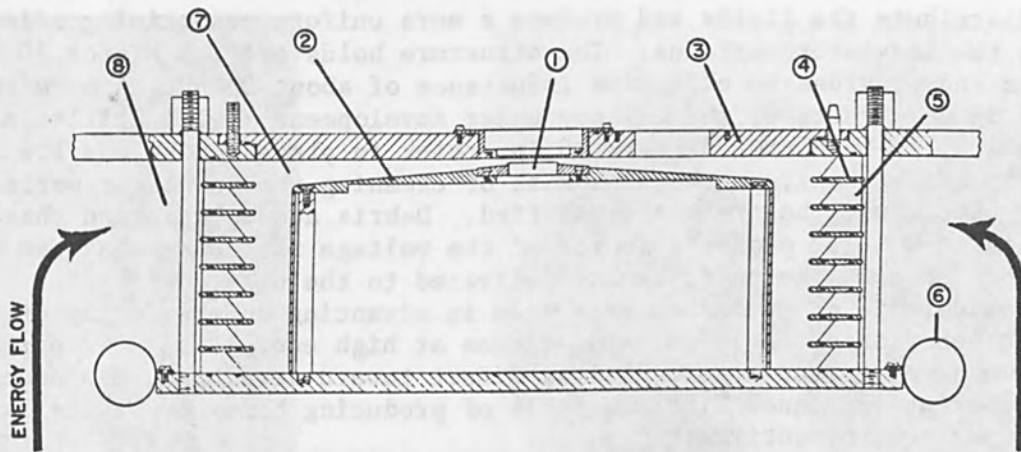


FIG. 3.--The G-4 diode envelope employed on Gamble I and II: (1) field-emission cathode; (2) inner (cathode) conductor; (3) outer (ground) conductor; (4) acrylic spacer rings; (5) aluminum rings; (6) metallic false-work to guide energy flow; (7) vacuum region; (8) water region.

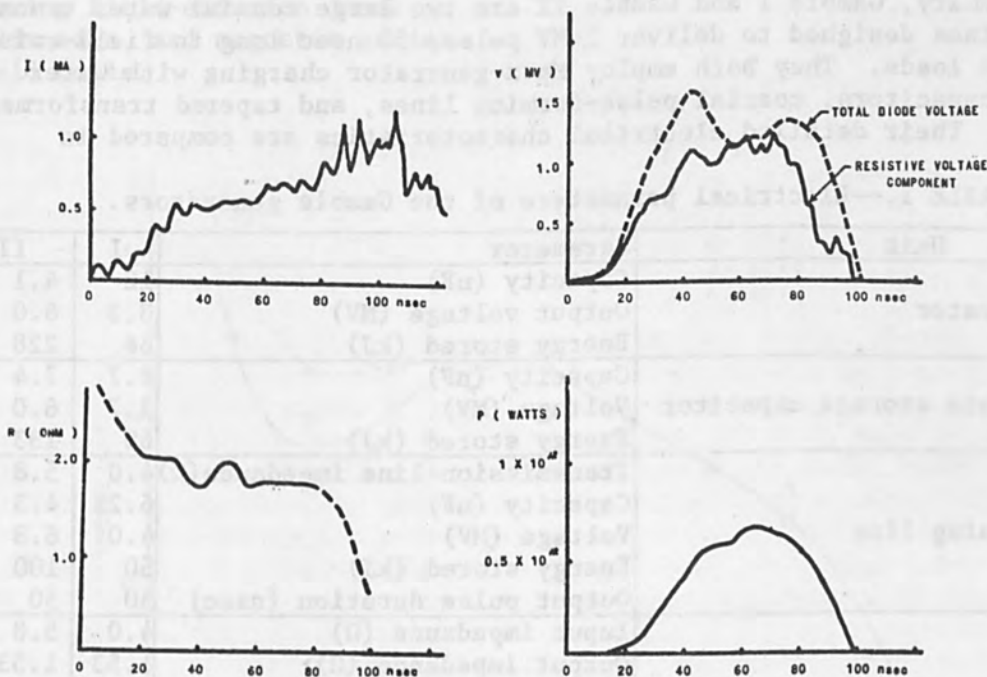


FIG. 4.--Measured diode beam behavior on Gamble II. Cathode diameter, 4 cm; diode gap, 6.5 mm; background pressure, 2×10^{-4} torr; applied axial magnetic field, 8 kG. Total beam energy, 28 kJ.

to redistribute the fields and produce a more uniform potential gradient across the insulator surfaces. The structure holds off 1.5 MV for 70 to 80 nsec and provides an effective inductance of about 30 nH. A more advanced diode structure, the G-5 now under development¹⁵ will utilize a single acrylic insulator plate 2.25 in. thick in place of the acrylic and aluminum spacer ring, so that the task of cleaning the insulator surfaces between shots will be greatly simplified. Debris accumulating on these surfaces is a major probable source of the voltage flashover that can appreciably shorten the energy pulse delivered to the beam.

Considerable progress has been made in advancing understanding of the dynamic behavior of field-emission diodes at high energies.¹⁶ In particular, we have devoted a good deal of effort toward developing reproducible, constant-impedance diodes capable of producing beams of several kilojoules per square centimeter.

Diode current and voltage are monitored with standard magnetic-loop probes and capacitive voltage dividers. Typical Gamble II diode current and voltage traces are shown in Fig. 4, as are the calculated power and impedance as functions of time. For beam-propagation studies, the anode is typically a sheet of 1/4-mil aluminized Mylar. The drifting beam is typically propagated in a 4-in. Plexiglass drift tube lined with an aluminum mesh return conductor and filled with air at a pressure of between 0.1 and 5 torr. The diode itself is maintained at a pressure of 0.5×10^{-3} torr. An external axial magnetic field (up to 10 kG) is generally applied over the entire diode and drift-tube region. The magnetic-field pulse is sufficiently slow to permit the field to penetrate the entire diode. The configuration of the front end of one of the generators, with the diode and drift tube, is shown schematically in Fig. 5.

In summary, Gamble I and Gamble II are two large coaxial water transmission lines designed to deliver 1-MV pulses 50 nsec long to field-emission diode loads. They both employ Marx-generator charging with water transfer capacitors, coaxial pulse-forming lines, and tapered transformer sections. Their detailed electrical characteristics are compared in Table I.

TABLE I.--Electrical parameters of the Gamble generators.

Unit	Parameter	I	II
Marx generator	Capacity (nF)	12	4.1
	Output voltage (MV)	3.3	6.0
	Energy stored (kJ)	66	228
Intermediate storage capacitor	Capacity (nF)	8.7	7.4
	Voltage (MV)	3.7	6.0
	Energy stored (kJ)	60	133
Pulse-forming line	Transmission-line impedance (Ω)	4.0	5.8
	Capacity (nF)	6.25	4.3
	Voltage (MV)	4.0	6.8
	Energy stored (kJ)	50	100
	Output pulse duration (nsec)	50	50
Coaxial transformer	Input impedance (Ω)	4.0	5.8
	Output impedance (Ω)	1.53	1.53
	Output voltage (MV)	1.0	1.0
	Design load (Ω and nH)	1;20	0.6;20
	Energy delivered to load (kJ)	32	60

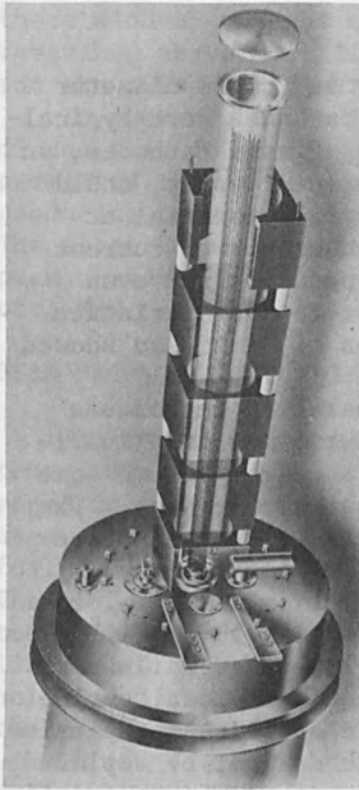


FIG. 5.--Front end of relativistic electron-beam generator, showing field-emission diode, drift tube, and magnetic guide field coils.

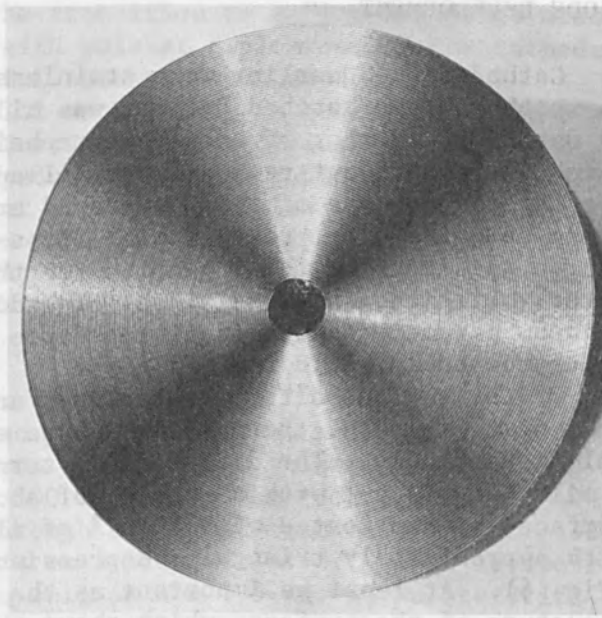


FIG. 6.--New cathode of spiral-grooved variety.

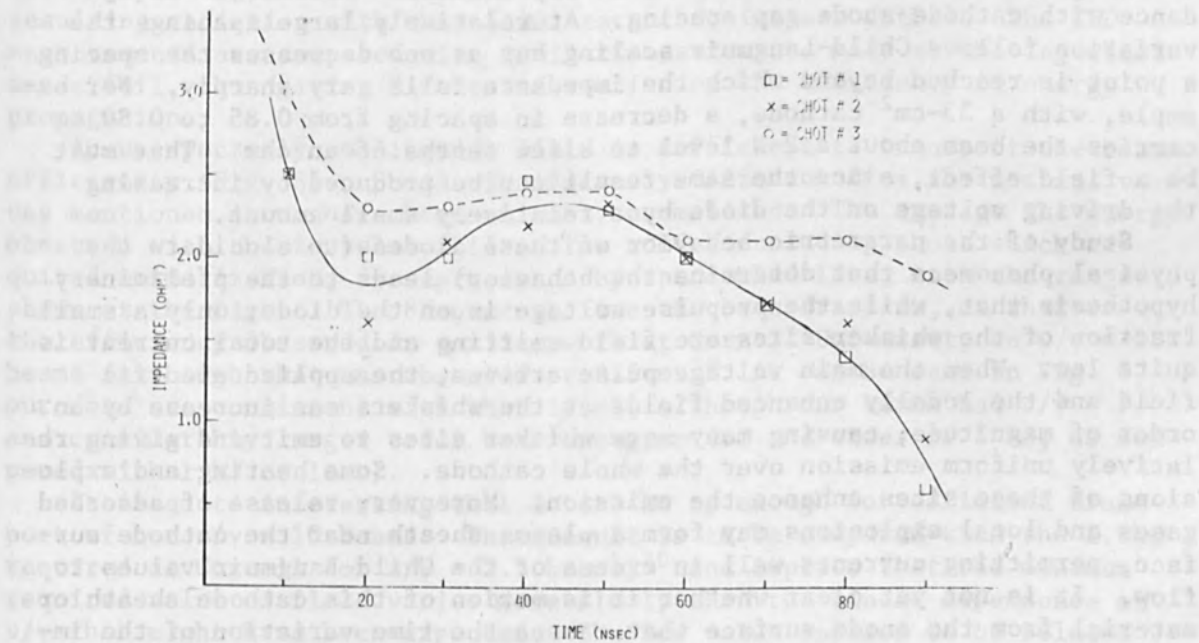


FIG. 7.--Impedance variation with spiral-grooved cathode. Shots 1 and 2 are 25-kJ beams; shot 3 is 18-kJ beam with carbon anode.

DIODE DEVELOPMENT

Cathodes used earlier were stainless-steel disks 4-7 cm in diameter on which a cross-hatched pattern was milled. These cathodes were typically used for a number of shots before being replaced. Plasma cathodes, in which the milled-out regions were filled with a plastic or epoxy, could not be used because of the very rapid erosion of the fill material at these energies. The results with cross-hatched cathodes showed current and voltage reproducibility no better than 15 or 20 per cent and even worse variations in pulse width. In addition to shot-to-shot variation in beam parameters, the diode impedance as a function of time also showed an unacceptably rapid falloff.¹⁷

Of the various alternate cathodes and diode-preparation techniques that were explored, the one that shows most promise utilizes a cylindrical disk cathode. The disk face is turned flat and a spiral groove some 4 mils deep is cut with a spacing of about 10 mils between grooves. The surface is then coated with 1000 Å of aluminum, leaving a fresh surface with approximately triangular depressions separated by flat regions (Fig. 6). At least as important as the disk configuration is the microstructure of the surface, which shows whisker densities of 10^5 to 10^6 cm⁻² on fresh cathodes. After a shot in which the diode impedance falls very rapidly to a low value, many whisker sites show evidence of local explosions, as reported in other studies.¹⁸ Such evidence of whisker explosion is lacking in normal shots. In either case, the cathode must be replaced after each shot for maximum reproducibility.

If the cathode is constructed as described above, and if the surface is refinished after each shot, reproducibilities in current and voltage waveforms better than ± 5 per cent can be achieved, when external magnetic fields are employed, and this scatter is probably as much due to lack of reproducibility in the generator output waveform as in the diode behavior. Moreover, the time-varying impedance now shows a fairly gradual decrease (Fig. 7). A remaining problem is the very nonlinear variation of impedance with cathode-anode gap spacing. At relatively large spacings the variation follows Child-Langmuir scaling but as one decreases the spacing a point is reached beyond which the impedance falls very sharply. For example, with a 33-cm² cathode, a decrease in spacing from 0.85 to 0.80 cm carries the beam about a 2- Ω level to a few tenths of an ohm. That must be a field effect, since the same result can be produced by increasing the driving voltage on the diode by a relatively small amount.

Study of the parametric behavior of these diodes (to elucidate the physical phenomena that determine the behavior) leads to the preliminary hypothesis that, while the prepulse voltage is on the diode, only a small fraction of the whisker sites are field emitting and the total current is quite low. When the main voltage pulse arrives, the applied electric field and the locally enhanced fields at the whiskers can increase by an order of magnitude, causing many more whisker sites to emit and giving relatively uniform emission over the whole cathode. Some heating and explosions of these sites enhance the emission. Moreover, release of adsorbed gases and local explosions may form a plasma sheath near the cathode surface, permitting currents well in excess of the Child-Langmuir values to flow. It is not yet clear whether it is motion of this cathode sheath or material from the anode surface that causes the time variation of the impedance. The amount of gas adsorbed or absorbed on the anode surface is found to be very important in determining the impedance characteristics of

these diodes. On the other hand, the transition to a "low-impedance mode" described above most likely starts with whisker explosions on the cathode and the subsequent jetting of material across to the anode.

In summary, there is clearly still much about the behavior of these diodes that is poorly understood. However, semi-empirical studies have permitted the development of low-impedance diodes capable of reproducibly producing beams of more than 30 kJ at current densities of 20 to 40 kA/cm². The electron beams that have been produced in these experiments have had peak currents well in excess of 1 MA, with electron energies of the order of 1 MeV.

BEAM PROPAGATION STUDIES

Preliminary experiments have been performed on the propagation of intense relativistic electron beams from the Gamble I generator in applied magnetic guide fields.¹⁸ Nominally 600-kV and 300-kA (peak) beams of 40-nsec duration (fwhm) are injected through a 1/4-mil aluminized Mylar anode foil into a drift tube containing air at a pressure of $0.2-0.4 \times 10^{-3}$ torr. The anode and cathode structures, as well as the 4.5-in.-ID Lucite drift tube are placed within a 6-in.-ID solenoid 120 cm long. The drift tube is lined with wire screen to provide a return conductor for the beam. The solenoid is pulsed from a 640- μ F capacitor bank; the resulting risetime of the magnetic field in the coil is about 8 msec. All metal structures within the field, including the stainless-steel cross-hatched cathode, are fully permeated by the field. The magnitude of the applied field is varied from 0 to 10 kG. Diagnostics consists of radiation dosimetry, carbon-block calorimetry, pin-hole radiography, and the use of magnetic pick-up loops within the drift tube. The efficiency of beam energy propagation is monitored in two ways. Absolute measurements of propagated energy are made by means of a carbon-block calorimeter placed at various distances down the tube. As a check, relative radiation dosimetry measurements are made by placing a thin tantalum foil in the beam path and monitoring the resulting radiation with thermoluminescent dosimeters (TLDs). The TLD measurements are compared with similar measurements made at the injection anode foil, thus giving direct information on the efficiency of energy propagation.

An unexpectedly small guide field is sufficient to transport the beam efficiently (Fig. 8). Shots significantly different from the nominal values mentioned above have been suitably normalized. The average TLD energy observed with the tantalum foil at the anode, including shots which required normalization, is represented by the dashed line, with the range shown at the right. The 85-percent line has been drawn in, as that is the efficiency observed in earlier work at Cornell University on $v/\gamma = 2.5$ beams (although that was observed at 2.5 m.²⁰ As can be seen in Fig. 8, our data are consistent with that level, although our beams had $v/\gamma = 7$ and considerably larger total beam energies (of the order of 5 kJ, as compared with 1 kJ or less).

It is quite interesting that 2 to 3 kG is enough for efficient transport of our $v/\gamma = 10$ beams. This result is to be compared with the 1.6kG required at Cornell for $v/\gamma = 2.5$ beams,²⁰ and implies that the minimum required value of field varies more slowly than the linear dependence on v/γ that might have been expected. The low value appears to be related to a balance of perpendicular particle pressure in the drifting beam with magnetic pressure. A simple particle model of beam electrons spiraling

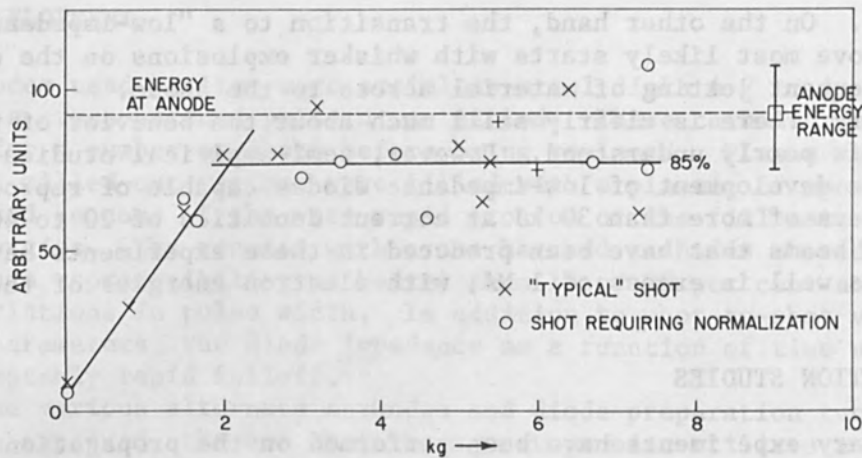


FIG. 8.--Beam propagation efficiency as function of applied magnetic field 1 m along drift tube.

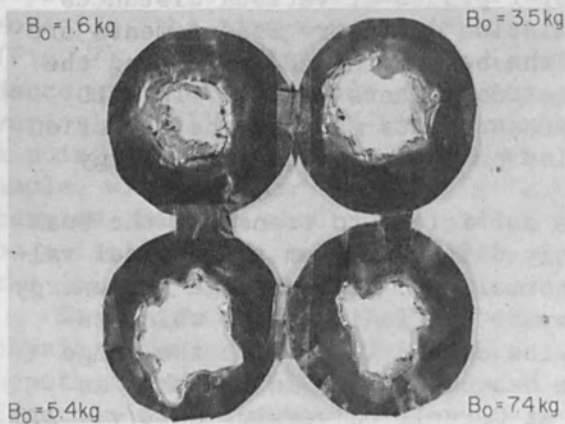


FIG. 9.--Tantalum foil damage as function of magnetic field 1 m along drift tube.

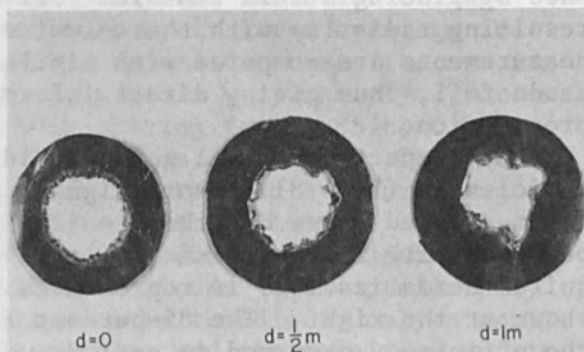


FIG. 10.--Tantalum foil damage as function of distance down drift tube, at $B_z = 5.4$ kG.

along field lines leads to the relationship²¹

$$B_0^2 / \mu_0 = nW_1$$

where B_0 is the applied axial field, n is the beam electron density, and W_1 is the component of beam electron kinetic energy due to transverse motion. This is the perpendicular pressure balance equation for the electron beam in the guide field. For a 300-kA beam and a 20-cm² cathode, $n = 3 \times 10^{12}/\text{cm}^3$; at 2 kG, we would be allowed perpendicular energy per particle W_1 of only 80 keV, which is most likely an underestimate, given what we know of beam pinching in the cathode-anode gap.

The above calculation is overly pessimistic for several reasons. First, since the cathode is 5 cm in diameter and the drift tube is 10 cm, there is considerable room for beam expansion before the beam hits the walls. There is, indeed, evidence of just such beam expansion to achieve pressure balance. If the effective beam area were to double, the allowed perpendicular energy per particle would be 160 keV, or more than 25 per cent of the total kinetic energy. Second, in relatively small, high- v/γ beams such as we have here, a large fraction of the perpendicular energy can be introduced by pinching within the diode itself. However, if one applies an axial guide field to the cathode-anode gap, experiments have shown²² that complete control of the diode pinch can be obtained if

$$\frac{B_0}{B_s} > \frac{v}{v} \frac{r}{2d}$$

where B_s is the maximum self field of the beam, r is the cathode radius, and d is the gap spacing. In the present set of experiments, the required applied field is about 5 kG, but between zero and this field, there is a gradual variation between total pinch and total control of pinch. Thus, as the external magnetic field is increased, not only is the confining magnetic pressure increased, but the perpendicular beam pressure due to diode pinching is decreased. This effect, together with actual expansion of the beam in the drift tube, appears to be sufficient to explain the observed propagation.

Two points relevant to this argument are illustrated in Fig. 9. It shows the damage done to the tantalum foils placed 1.05 m from the diode at four different values of magnetic field. We note that the lower the field value, the more diffuse is the boundary of damage on the tantalum. In fact, at the highest field value, 7.4 kG, this boundary is very narrow. Also, it is clear that the highest field shot has the smallest damage area. Both of these results are completely verified in the pinhole radiographs.

Also seen in Fig. 9 is evidence of a flute instability on the beam as seen by the damage patterns on the foils from the shots at higher magnetic fields. This effect is observed on the tantalum foils and the pinhole radiographs on every shot above about 4 kG, although neither the exact pattern nor the number of lobes is reproducible. Figure 10 shows a series of three shots, one with the tantalum converter at the anode, one 0.5 m from the anode, and one at the usual position (1 m from the anode). If we assume that the linear regime of this instability extends at least as far as the 1-m point, these foils seem to indicate an e-fold length for flute amplitude of about 0.5 m. For a beam velocity of 2×10^8 m/sec, this im-

plies an e-folding time of 2-3 nsec. A second observation from Fig. 10 is that the higher azimuthal modes (of order 14) seem to dominate at the 0.5-m point, whereas lower mode numbers (of order 6 or 8) dominate at the 1-m point.

If one calculates the flute instability growth time, assuming a sharp beam boundary separating the beam and its self-generated plasma from the neutral gas, one obtains²³:

$$t = L\sqrt{M/Np_1}$$

where N is the mode number, L is the characteristic length of the magnetic field inhomogeneity, M is the total mass density of the plasma, p_1 is the perpendicular plasma pressure, and t is the growth time. We assume a field inhomogeneity of 20 per cent occurring over a length scale of 30 cm based on the nature of the magnet coils we have used. We also assume the pressure is predominantly that of the beam transverse kinetic motion, taken to be 200 keV. It is somewhat harder to estimate the mass density. There is much evidence that background ionization in a drift region builds up relatively slowly until the large induced electric fields due to the rising magnetic field of the beam front can cause avalanche breakdown.²⁴ Once breakdown occurs, the plasma mass density is much too high for this instability to grow on the time scale of our experiments. However, before avalanche breakdown occurs, in the first nanosecond or two after the beam front passes a point in the drift tube, the plasma density is mainly beam electrons and the few ions that are present. For ion number densities small compared to the beam density ($n_i < 10^{-2} n_b$), the growth time can easily be of the order of 10 nsec divided by the square root of the azimuthal mode number. It is also consistent with the higher order modes dominating at shorter distances. These modes tend to grow first, but saturate when their amplitude becomes comparable with wavelength. The lower modes thus eventually dominate as is observed.

In summary, we suggest that the fluting instability occurs very early in time and, as soon as the background plasma builds up and avalanche breakdown occurs along the path taken by the beam front, the flutes are frozen in by the plasma mass. The result is a very clean flute pattern, with sharp boundaries surrounding a relatively uniform beam.

CONCLUSIONS

We have described the design parameters and operating conditions of two large electron-beam generators, Gamble I and Gamble II. These machines are capable of producing 20 and 60 kJ of 1-MeV electrons, respectively, in pulses of 50 nsec or less. They are being used for fundamental beam studies and applications. We have described some recent developments in field-emission diode design, which permit good reproducibility and impedance characteristics even at high beam energies. We also have discussed recent work on beam propagation in axial magnetic fields done with Gamble I.

It is a pleasure to acknowledge the continued support of the Defense Atomic Support Agency for this research.

REFERENCES

1. D. C. dePackh, The NRL Sozotron Project, Progress Report. Naval Research Laboratory, Washington, D.C., 1966.
2. D. C. dePackh and P. B. Ulrich, J. Electronics and Control 10: 139, 1961.
3. I. M. Vitkovitsky, P. P. Bey, W. R. Faust, R. Fulper Jr., G. E. Leavitt, and J. D. Shipman Jr., W. G. Chace and H. K. Moore (eds.), Proc. 2nd Conf. on Exploding Wires, Plenum Press, New York, 1962; p. 87.
4. J. J. Condon, in L. Marton (ed.), Record 10th Symp. Electron, Ion, and Laser Beam Technology, San Francisco Press, San Francisco, 1969; p. 131.
5. W. F. Oliphant and I. M. Vitkovitsky, Production of intense relativistic electron beams, Bull. Amer. Phys. Soc. 15:1401, 1970.
6. J. D. Shipman Jr., Proc. Fourth Symp. on Eng. Probs. of Fusion Research, Washington, D.C., April, 1971. (To be published.)
7. J. D. Shipman Jr., Final Electrical Design Report of the Gamble II Pulse Generator, MR-2212, Naval Research Laboratory, Washington, D.C., 1971.
8. J. J. Clark, M. Ury, M. L. Andrews, D. A. Hammer, and S. Linke, in L. Marton (ed.), Rec. 10th Symp. Electron, Ion, and Laser Beam Technology, San Francisco Press, San Francisco, 1969; p. 117.
9. L. S. Levine and T. M. Vitkovitsky, Proc. Fourth Symp. on Eng. Probs. of Fusion Research, Washington, D.C., April, 1971. (To be published.)
10. Much of the original data concerning dielectric breakdown, as well as a variety of other information concerning the design, construction and operation of pulsed power generators, was developed by J. C. Martin and his co-workers at AWRE Aldermaston, England.
11. Based on experimental data obtained by J. C. Martin and co-workers, we can derive expressions for breakdown due to streamers from the positive electrode of a water dielectric system, $F_+ t^{1/3} = 0.287A^{-0.0902}$ and for breakdown due to streamers from the negative electrode, $F_- t^{1/3}/\alpha = 0.579A^{-0.0920}$, where $F_{+,-}$ is the electric field (MV/cm) on the surface of the electrode corresponding to breakdown due to streamers from the positive or negative electrode, t is the effective time in microseconds and is defined as the time that the surface field exceeds 63 per cent of the breakdown value, A is the effective area (cm^2) and is defined as the area over which the electric field is more than 90 per cent of the breakdown field, and $\alpha = 1 + 0.12 [(F_{\text{max}}/F_{\text{mean}}) - 1]^{1/2}$.
12. J. E. Boers, Digital computer simulation of high current, relativistic and field emission electron tubes, in Rec. 11th Symp. Electron, Ion, and Laser Beam Technology, San Francisco Press, San Francisco, 1971;
13. J. D. Shipman Jr., Triggered water switch development for Gamble II, Proc. DASA Simulator Design Symposium, Washington, D.C., January, 1971. (To be published.)
14. H. Milde (private communication.)
15. J. D. Shipman Jr., A new electron beam envelope for Gamble I and II, Proc. DASA Simulator Design Symposium, Washington, D.C., January 1971. (To be published.)
16. J. J. Clark and S. Linke, IEEE Trans. ED-18:322, 1971.
17. I. M. Vitkovitsky, Proc. 6th Symp. Fusion Technology; Commission of the European Communities, Luxembourg, 1970; p. 59.
18. I. Brodie, J. Appl. Phys. 35:2324, 1964.

19. L. S. Levine and I. M. Vitkovitsky, Propagation of large current relativistic electron beams, Bull. Amer. Phys. Soc. 15: 1401, 1970; D. A. Hammer, J. L. Block, L. S. Levine, and I. M. Vitkovitsky, Propagation of intense relativistic electron beams in applied axial magnetic guide fields, Bull. Amer. Phys. Soc. 16:595, 1971.

20. J. Bzura and S. Linke, Electron beam energy transport in magnetic fields, Bull. Amer. Phys. Soc. 15:1452, 1970.

21. Suppose we assume that all beam electrons are spiraling down the drift tube along magnetic field lines with the same velocity v_{\perp} perpendicular to the applied field. Then all the beam electrons will have Larmor radii, R_L given by (MKS units) $R_L = v_{\perp} \gamma m / e B_0$, where B_0 is the magnitude of the applied field and γ is the usual relativistic factor. If the beam is uniform out to a sharp boundary, there is a net motion of electrons around the beam only near the boundary. This looks like a single turn solenoid, which results in a diamagnetic field B_d given approximately by $B_d = \mu_0 n e v_{\perp} R_L = \mu_0 n v_{\perp}^2 \gamma m / B_0$, where n is the beam electron number density. However, beam electrons would no longer be confined at the boundary when $B_d > B_0$. To find the limit, take these two fields equal, and the result is $B_0^2 / 2 \mu_0 = \gamma m v_{\perp}^2 / 2 = n W_{\perp}$, where W_{\perp} is the perpendicular kinetic energy of an electron.

22. D. Hammer, F. Oliphant, I. Vitkovitsky, and V. Fargo, Interaction of Accelerating High Current Electron Beams with External Magnetic Fields, 1970. (Submitted for publication.)

23. C. L. Longmire, Elementary Plasma Physics; Wiley-Interscience, New York, 1963; p.246.

DIGITAL COMPUTER SIMULATION OF HIGH-CURRENT,
RELATIVISTIC, AND FIELD EMISSION ELECTRON TUBES*

J. E. BOERS

Sandia Laboratories, Albuquerque, N.M.

A digital computer program for the simulation of very-high-energy electron beams has been written. The program is similar to a program reported earlier¹ but has been modified to handle much more complex cathode shapes and electron flows. The program includes space-charge effects through the solution of Poisson's equation and magnetic effects (both applied and induced) through the relativistic trajectory equations. Computations of the induced field permit cycloiding electron flows within the tube.

The program employs relaxation techniques while alternately computing electric fields and trajectories. Execution time is generally less than 10 min on a CDC 6600 digital computer. Either space-charge-limited or field-emission cathodes may be simulated. Results obtained with the program are presented and compared with experimental results.

ANALYSIS

Poisson's equation in axially symmetric, cylindrical coordinates (r, θ, z) is

$$\frac{1}{r} \frac{\partial}{\partial r} r \frac{\partial V}{\partial r} + \frac{\partial^2 V}{\partial z^2} = - \frac{\rho}{\epsilon_0} \quad (1)$$

where derivatives with respect to θ are eliminated in view of the axial symmetry. Assuming a matrix of squares $(\Delta z = \Delta r)$, this equation can be expanded in difference form

$$\begin{aligned} & \frac{V_{i,j+1} - 2V_{i,j} + V_{i,j-1}}{(\Delta r)^2} + \frac{1}{r_j} \frac{V_{i,j+1} - V_{i,j-1}}{2(\Delta r)} \\ & + \frac{V_{i+1,j} - 2V_{i,j} + V_{i-1,j}}{(\Delta r)^2} = - \frac{\rho}{\epsilon_0} \end{aligned} \quad (2)$$

where (i, j) , Δr , Δz , and r_j are as defined in Fig. 1. Solving for $V_{i,j}$, one obtains

$$\begin{aligned} V_{i,j} = & \frac{1}{4} (V_{i,j+1} + V_{i,j-1} + V_{i+1,j} + V_{i-1,j}) \\ & + \frac{\Delta r}{8r_j} (V_{i,j+1} - V_{i,j-1}) + \rho_{i,j} \end{aligned} \quad (3)$$

*This work is supported by the U.S. Atomic Energy Commission.

where $\rho_{i,j} = \rho(\Delta r) / 4\epsilon$. On the axis of symmetry

$$V_{i,j} = \frac{1}{6} (4V_{i,j+1} + V_{i+1,j} + V_{i-1,j}) + \frac{2}{3} \rho_{i,j} \quad (4)$$

Equations (3) and (4) are solved iteratively at all points within the electrode configuration. An effective over-relaxation is obtained by solving these equations initially on only the odd numbered points of the matrix. Convergence on this coarse matrix is faster in two respects: the time per pass is less than one-fourth that required when all points are employed, and the number of passes through the matrix required to reach convergence is significantly reduced. The use of more complex over-relaxation techniques would probably save very little time and would create more complexity in the program.

The axisymmetric relativistic trajectories are derived from the relativistic Lagrangian for an electron

$$L = eV - e(\vec{A} \cdot \vec{v}) - m_0 c^2 \sqrt{1 - \left(\frac{v}{c}\right)^2} \quad (5)$$

where \vec{v} is the velocity, \vec{A} the magnetic vector potential, m_0 the rest mass, e the electronic charge, and c the velocity of light. Expanding Eq. (5) with the Lagrange equation, it can be shown that the θ equation in axisymmetric coordinate becomes

$$\frac{m_0 r^2 \ddot{\theta}}{\sqrt{1 - \beta^2}} = e(rA_{\theta} - r_0 A_{\theta_0}) \quad (6)$$

where $\beta = v/c$ and $A_{\theta_0} = A_{\theta}(r_0, z_0)$, with r_0, z_0 being the point at which $\dot{\theta} = 0$, i.e., the cathode. Employing Eq. (6) in the remaining Lagrange expansions, we see that

$$\ddot{r} \left(\frac{1 + \frac{\dot{r}^2}{\delta^2 \gamma}}{\delta} \right) = \dot{r} \frac{\lambda}{\delta} - \ddot{z} \frac{\dot{r}\dot{z}}{\delta^3 \gamma} + \eta \frac{\partial V}{\partial r} + \eta \dot{z} B_{\theta} + \eta^2 \delta \alpha \left(\frac{r_0 A_{\theta_0}}{r^2} + \frac{\partial A_{\theta}}{\partial r} \right) \quad (7)$$

$$\text{and } \ddot{z} \left(\frac{1 + \frac{\dot{z}^2}{\delta^2 \gamma}}{\delta} \right) = \dot{z} \frac{\lambda}{\delta} - \ddot{r} \frac{\dot{r}\dot{z}}{\delta^3 \gamma} + \eta \frac{\partial V}{\partial z} - \eta \dot{r} B_{\theta} + \eta^2 \delta \alpha \frac{\partial A_{\theta}}{\partial z} \quad (8)$$

where

$$\alpha = A_{\theta} - \frac{r_0}{r} A_{\theta_0} \quad (9)$$

$$\gamma = c^2 + \eta^2 \alpha^2 \quad (10)$$

$$\delta = \sqrt{1 - \beta^2} \quad (11)$$

$$\text{and } \lambda = \eta^2 \alpha (c^2 - \dot{z}^2 - \dot{r}^2) \frac{\frac{\partial A_\theta}{\partial z} \dot{z} + \left(\frac{r_0}{r^2} A_{\theta 0} + \frac{\partial A_\theta}{\partial r} \right) \dot{r}}{\delta^2 \gamma^2} \quad (12)$$

These equations are nonlinear with respect to r and z , and exact solutions would be difficult, if not impossible, to obtain.

The trajectories as computed by the computer will be a sequence of points $r_1, r_2, \dots, r_{k-1}, r_k, r_{k+1}, \dots$ and $z_1, z_2, \dots, z_{k-1}, z_k, z_{k+1}, \dots$. At any given point (e.g., r_k, z_k) that point and all previous points are known and the next point r_{k+1}, z_{k+1} must be computed. If \dot{r} and \dot{z} can be approximated by

$$\dot{r} = \frac{r_k - r_{k-1}}{\Delta t} \quad (13)$$

rather than the more exact expression

$$\dot{r} = \frac{r_{k+1} - r_{k-1}}{2\Delta t} \quad (14)$$

then all the terms in Eqs. (7) and (8) are already known except the acceleration terms \ddot{r} and \ddot{z} . Since these equations are linear functions of \ddot{r} and \ddot{z} , they can be solved exactly to obtain r_{k+1} and z_{k+1} . If these values can then be fed back, via Eq. (14), more exact values can be obtained.

The induced circumferential magnetic flux density B_θ , can be defined as

$$B_\theta = \frac{u_0}{r} \int_0^r r J_z dr \quad (15)$$

where J_z is the axial component of current density and u_0 is the permeability of free space. The θ -component of the magnetic vector potential can be defined as

$$A_\theta = \frac{1}{r} \int_0^r r B_z(r) dr, \quad (16)$$

where $B_z(r)$ is the total axial magnetic field; A_θ will be zero if there is no applied magnetic field.

Some of the higher-order effects, such as the induced axial magnetic field due to radial motion of the electron, are neglected. Effects beyond those considered above do not seem to be significant even at megavolt levels.

THE SIMULATION METHOD

The method employed is basic iterative relaxation. The potentials and trajectories are alternately computed until they reproduce themselves from one cycle to the next.

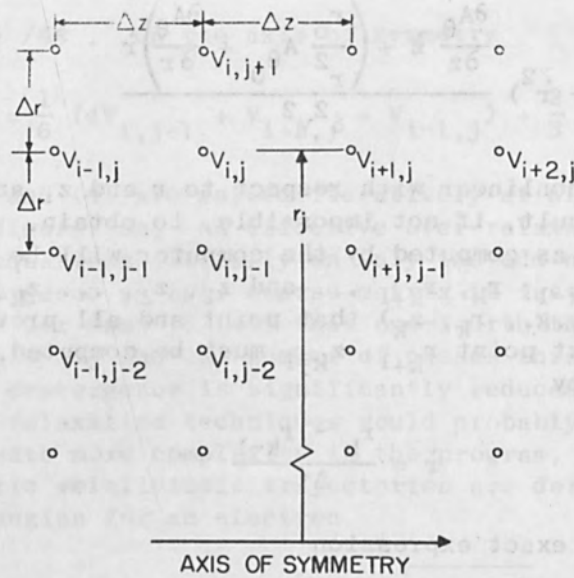


FIG. 1.--Definitions of matrix terms.

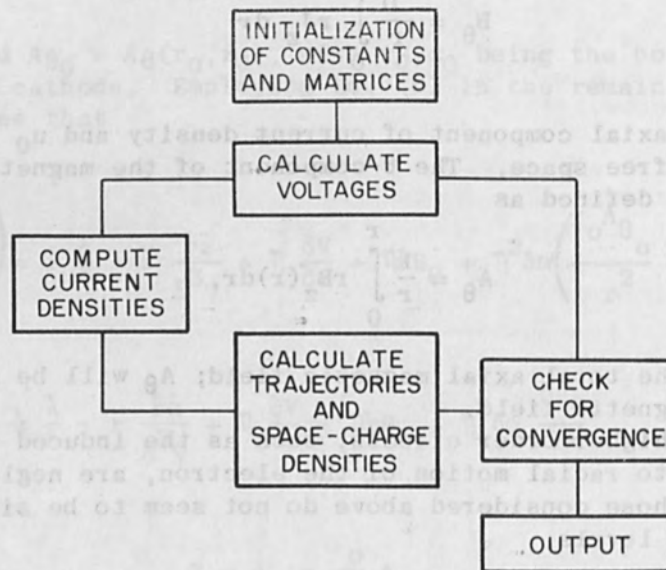


FIG. 2.--General flow chart for tube program.

The voltages, space-charge densities, z-directed current, and induced magnetic fields are all simulated on 121 X 91 matrices. The voltages are computed by relaxation using the space-charge densities from the space-charge-density matrix. The space-charge-density matrix and the z-directed current matrix are computed from the trajectories. The induced azimuthal magnetic-field matrix is computed from the z component of the current matrix.

A general flow chart for the program is shown in Fig. 2. Initialization consists of presetting many of the matrices with either an initial guess for the values to be used or presetting many constants involved in the computations. Linear potentials are set between the cathode and anode and approximate space-charge and current-density distributions are laid out.

The procedure for relaxing the potentials on the V matrix is quite straightforward. The first subscript (usually I) begins at the left edge of the matrix and increases axially in the +z direction. The second subscript (usually J) begins at the axis and increases radially. The relaxation operations are carried out starting at the left edge of the matrix and passing up each column in sequence across the matrix.

This method of computing the fields requires a knowledge of the locations of electrodes relative to the radial columns. This information is obtained by supplying as input data matrices which specify the J coordinates of the electrodes. Computations are carried out from either the axis or the cathode to the anode coordinate, and may be resumed (in the same column) on the far side of an electrode by specifying the lower and upper limits of such areas.

The cathode current densities are then computed by employing either Child's law for space-charge-limited current or the Fowler-Nordheim law for field-emission current. It is also possible to force a specified current density along the cathode. One of these three methods is selected in the input data.

The layout of trajectory starting points along the cathode is specified in the input data. There must be at least one trajectory starting point for each matrix square along the cathode. Additional trajectories can be added if more detail is desired.

The trajectories are then computed from the cathode to the anode. The program automatically computes the self-induced magnetic forces and an applied axial magnetic field may also be included. The space-charge density distribution is computed at the same time since it is computed directly from the trajectories.

Convergence of the program is determined by comparing the new beam border with that of the previous cycle. This border has been found very sensitive to changes within the beam and furnishes a simple and quick check on the program's progress.

The program then returns to the potential relaxation if the convergence requirement is not met. If convergence has been reached, the results are printed and sufficient data can be saved to permit a restart with the same (or modified) design or to permit plotting of the results by a plotting program. The program itself can produce a plot of the trajectories and cathode current density distribution if desired.

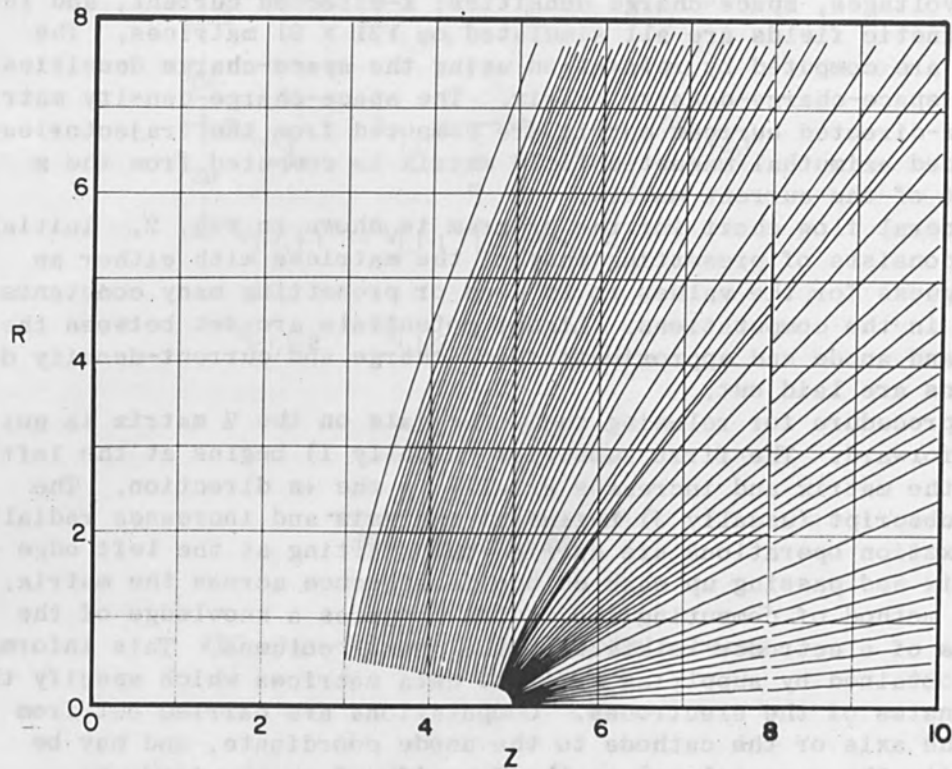


FIG. 3.--Trajectories from a 1- μ m radius field-emission needle.

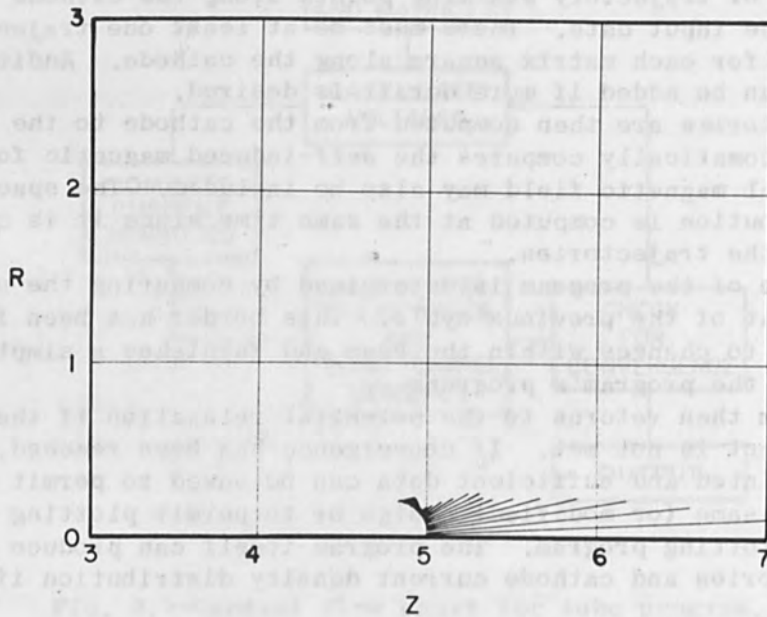


FIG. 4.--Relative current densities for 1- μ m needle.

RESULTS

Results obtained for low and moderate energy tubes have been excellent. The results for a field-emission case are shown in Figs. 3 and 4. Here a sharp needle with a tip radius of $1\ \mu\text{m}$ is employed. Figure 3 shows the trajectories for this configuration. The length of the lines in Fig. 4 are proportional to the current density at corresponding points along the cathode. Most of the current is seen to be coming from a very small area on the tip. The density along the shank is down by several orders of magnitude. The bulk of the current falls within a 0.2-mm-diameter spot on the anode.

The current computed by the digital program is 0.7 A with a peak current density of $2 \times 10^{10}\ \text{A/m}^2$, which compares with a current of 0.4 A and a peak current of $10^{11}\ \text{A/m}^2$ according to the theory of Dyke for such a needle. Since the field-emission equations are exponential, a small error in either the equations or Dyke's computations could easily account for the discrepancies.

At higher energies some problems with instabilities have been encountered. It is not clear whether these instabilities are physical or computational. Several under-relaxations have been built into the program in an attempt to stabilize the results. The most significant are the under-relaxations of the space-charge densities, induced magnetic field, and cathode shank current.

Figure 5 shows the trajectories for a 3-MV, 45-kA diode as employed in the REBA³ electron-beam machine at Sandia Laboratories. This is a fully converged solution but was obtained only by very careful adjustment of the various under-relaxation factors. A solution that fluctuates 6 or 7 per cent about the stable solution can be obtained fairly easily. The current and beam diameter obtained here are in excellent agreement with the experimental device.³

ACKNOWLEDGMENTS

The author would like to acknowledge valuable discussions of the program with Dr. J. Freeman of Sandia Laboratories, Dr. J. Uglum (formerly of Ion Physics Corporation), Dr. J. Creedon of Physics International, and Captain C. Rogers of the Air Force Weapons Laboratory.

REFERENCES

1. J. R. Boers, Digital computer analysis of electron flows, Proc. 1965 Conf. Electron and Laser Beams, Penn. State Univ., 1965; pp. 445-470.
2. W. P. Dyke, Field emission: A newly practical electron source, IRE Trans. MIL-4: 38-45, 1960.
3. D. L. Johnson, REBA: A pulsed electron beam generator, Rec. 11th Symposium on Electron, Ion, and Laser Beam Technology, University of Colorado, San Francisco Press, San Francisco, 1971; p. 000.

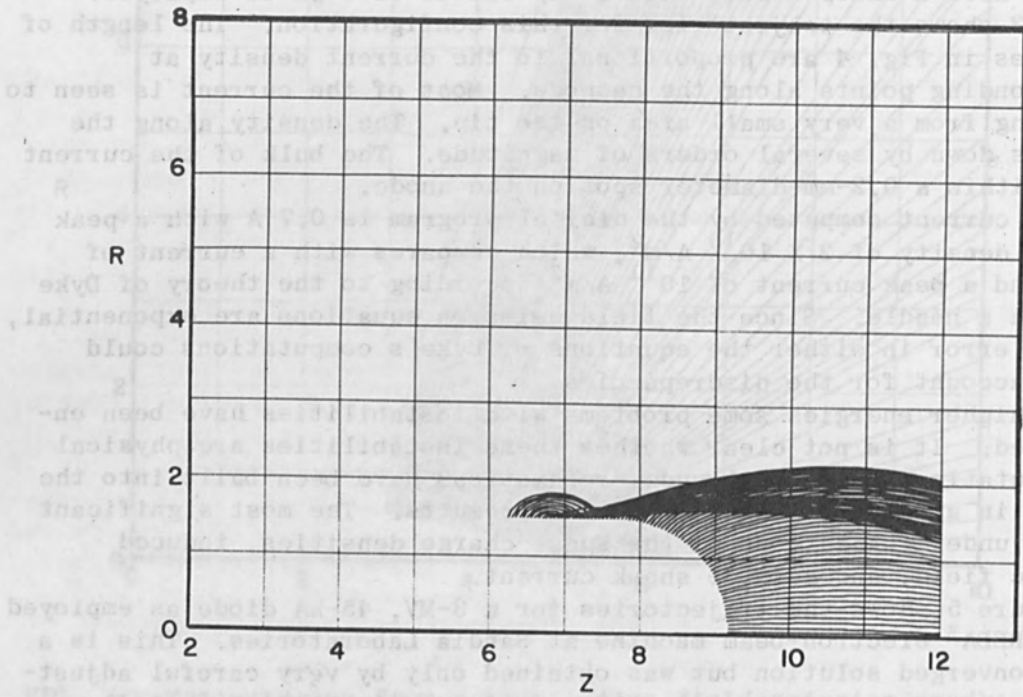


FIG. 5.--Trajectories for 45-kA, 3-MV diode.

ACKNOWLEDGMENTS

The author would like to acknowledge valuable discussions of the program with Dr. J. Freeman of Sandia Laboratories, Dr. J. Uglow (formerly of Los Alamos Corporation), Dr. J. Chisdon of Physics International, and Captain G. Rogers of the Air Force Weapons Laboratory.

REFERENCES

1. J. R. Soars, Digital computer analysis of electron flow, Proc. 1965 Conf. Electron and Laser Beams, Penn. State Univ., 1965; pp. 442-470.
2. W. P. Dyke, Field emission: A newly practical electron source, IRE Trans., MIL-4, 38-43, 1960.
3. D. L. Johnson, HERF: A pulsed electron beam generator, 15th Symposium on Electron Ion, and Laser Beam Technology, University of Colorado, See Proceedings Press, See Proceedings 1971, p. 100.

COMPUTATIONAL STUDIES OF RELATIVISTIC ELECTRON BEAMS

JAY P. BORIS and ROSWELL LEE

Naval Research Laboratory (Plasma Physics Division), Washington, D.C.

INTRODUCTION

This paper presents numerical calculations of relativistic electron-beam and electron-ring phenomena. In these calculations the fully coupled set of Maxwell-Lorentz equations are solved for a large number of charged particles accelerated by their self-consistent and external electric and magnetic fields. In this formulation electromagnetic retardation effects are retained so that beam-related radiation effects are properly modelled. Thus the method, though applicable to quasistationary phenomena, is used most efficiently in the study of rapid dynamic phenomena such as the onset of the electron return current when a relativistic electron beam penetrates undisturbed plasma. These calculations were performed to support and augment the experimental programs in relativistic electron beams carried on jointly by the Naval Research Laboratory and Cornell University and the experimental and theoretical programs (culminating in construction of an electron-ring accelerator) carried on by the University of Maryland and NRL.

The CYLRAD code¹ was developed to solve the fully relativistic Maxwell-Lorentz equations in cylindrical r - z coordinates. Two- and three-dimensional computations on such complex problems would have been impractical on the small, slow computers of a few years ago, the problem of finding efficient, accurate, numerical models for solving these equations has only recently become more than an academic exercise. But the larger and faster computers available at present make these calculations possible today, and the soaring costs of high-technology plasma experiments make them necessary.

The next section describes the CYLRAD algorithm briefly. As the method has been treated in detail in Ref. 1, only a short description of the techniques will be given centering on those aspects of the code pertinent to the calculations presented here.

In the next section, we discuss our electron-beam calculations and how we plan to extend them. We report results on the expansion of infinitely long homogeneous relativistic beams with and without a magnetic guide field. The dynamics of beams with v/γ both greater than and less than unity have been studied and compared with analytical theory. We also consider the onset of inductively generated electron return currents in an inhomogeneous configuration where a strong electron beam propagates into a quiescent neutral background plasma.

In the last section our preliminary results for partially neutralized relativistic electron rings are presented. We display the outwardly displaced equilibrium of the ring due to the induced magnetic fields of the ring current. This displacement is compared with several theoretical predictions, the Ott, Sudan, Lawson solution agreeing most closely with the observed results. Oscillations about this equilibrium of both electrons and ions are noted and explained. These azimuthally symmetric oscillations appear capable of undergoing a resonance in a

wide variety of circumstances which could drive the radial motions of the trapped ions to such large amplitude that the $1/\gamma$ charge-neutralizing effect on the ring stability would be lost. The ring may become so diffuse, if these resonances are not suppressed, that coherent acceleration of the ions in an electron-ring accelerator will be greatly hindered.

THE CYLRAD CODE

CYLRAD is an optimized, highly flexible computer program for performing radiation, beam, and plasma simulations in cylindrical coordinates with dielectrics and realistic boundary conditions. The physical system is r - z cylindrical with azimuthally symmetric rings as the elementary charges. The methods developed for CYLRAD, however, generalize quite readily to other coordinates and to three dimensions. A detailed description of the mathematical foundations and numerical techniques used in CYLRAD has been given previously.¹ The ideas employed in CYLRAD that are not new are taken primarily from papers by Buneman² and by Boris and Roberts.³ Reference 1 contains a fairly complete bibliography.

Although all θ variations are neglected in CYLRAD $\partial/\partial\theta \equiv 0$, all three components of the electric and magnetic fields are advanced forward step by step in time on a two-dimensional spatial mesh using the evolvant Maxwell equations,

$$\frac{\partial \underline{E}}{\partial t} = c \nabla \times \underline{B} - 4\pi \underline{J} \quad (1a)$$

$$\frac{\partial \underline{B}}{\partial t} = -c \nabla \times \underline{E}. \quad (1b)$$

The algorithm for integrating these equations is fully reversible and ensures that the constitutive Maxwell equations,

$$\nabla \cdot \underline{E} = 4\pi\rho \quad (2a)$$

$$\nabla \cdot \underline{B} = 0 \quad (2b)$$

are satisfied to computer round-off accuracy at each timestep. Here \underline{E} and \underline{B} are the vector and magnetic fields respectively, \underline{J} and ρ are the current and charge densities, and c is the velocity of light. Azimuthal symmetry implies simple boundary conditions on \underline{E} , \underline{B} , \underline{J} , and ρ at axis. Perfectly conducting metallic boundary conditions are applied at a finite radius r_{\max} and periodic boundary conditions are applied in z with a replication length of z_{\max} .

The relativistic Newton's equation is solved for each particle using the Lorentz force,

$$\frac{d\underline{P}}{dt} = \frac{q\underline{E}}{m_0} + \frac{q\underline{V}}{m_0 c} \times \underline{B} \quad (3a)$$

where \underline{E} and \underline{B} are evaluated at the particle position. Here q and m are the particle charge and rest mass and the velocity \underline{V} is related to \underline{P} by

$$\underline{V} \equiv \underline{P} / \sqrt{1 + (P^2/c^2)} \quad (3b)$$

The rest mass has been extracted from \underline{P} in this definition. The CYLRAD algorithm contains an accurate, single-pass integration of these particle equations which gives correct particle trajectories in the simple limits of spatially constant \underline{E} and \underline{B} fields. Furthermore, because the integration is second order and special account is taken of the cylindrical geometry, particles can be integrated right through the axis without loss of accuracy. The CYLRAD algorithm has several other advantages, besides cylindrical geometry, over schemes used elsewhere.^{2,4-6} These advantages are described in detail in Ref. 1.

Figures 1 and 2 show the important features of the CYLRAD calculation. Figure 1 shows the "time line" for CYLRAD, the time at which each of the various physical quantities is specified. Here we show a case where three full radiation steps are taken for each particle timestep, that is

$$\delta t_{\text{particle}} = 3\delta t_{\text{radiation}}$$

To achieve a second-order accurate time integration, a fully centered "leapfrog" algorithm is used. In the lower half of the figure \underline{V} and \underline{X} for each particle can be seen to be specified at times differing by half a particle timestep. Assuming that $\underline{V}_{-3/2}$ and \underline{X} are known, \underline{V} can be integrated forward to $\underline{V}_{+3/2}$ using the forces all evaluated at the centered time $t = 0\delta t_{\text{radiation}}$:

$$\underline{V}_{3/2} = \underline{V}_{-3/2} + \delta t_{\text{particle}} \cdot \left. \frac{d\underline{V}}{dt} \right|_0 \quad (4a)$$

This calculation is permitted because $(d\underline{V}/dt)|_0$ can be evaluated from the known grid values \underline{B}_0 and \underline{E}_0 and the particle position already specified at \underline{X}_0 . Once the new velocity has been found, \underline{X} can be integrated forward from $t = 0\delta t_{\text{radiation}}$ to $t = 3\delta t_{\text{radiation}} = \delta t_{\text{particle}}$ in a perfectly centered manner.

$$\underline{X}_3 = \underline{X}_0 + \delta t_{\text{particle}} \cdot \underline{V}_{-3/2} \quad (4b)$$

During the performance of this timestep for each particle, the new values of the sources $\underline{J}_{3/2}$ and ρ_3 are accumulated on spatial grids. These source terms are then used in integrating Eqs. (1) for \underline{E} and \underline{B} forward in time by a completely analogous leapfrog procedure.

Figure 2 shows the spatial positioning of all grid quantities in CYLRAD. A fully staggered set of four grids is used to ensure the complete centering of all spatial derivatives in Eqs. (1) and (2). This, in turn, gives second-order accuracy everywhere except perhaps on the axis. Further, by an appropriate choice of radial scale factors, the differential identities

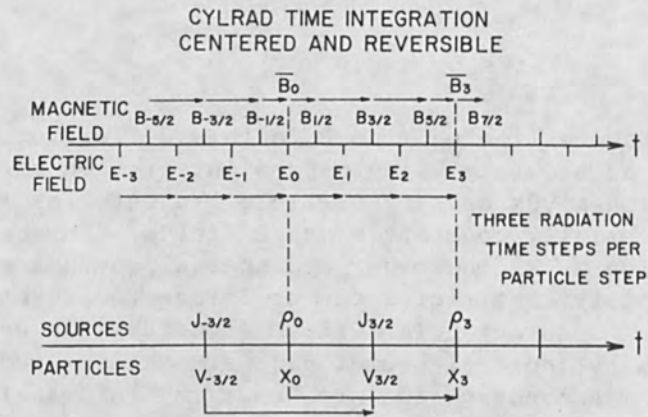


FIG. 1.--Time integration techniques for fields and particles in CYLRAD. Example shown has 3 radiations steps for each particle timestep.

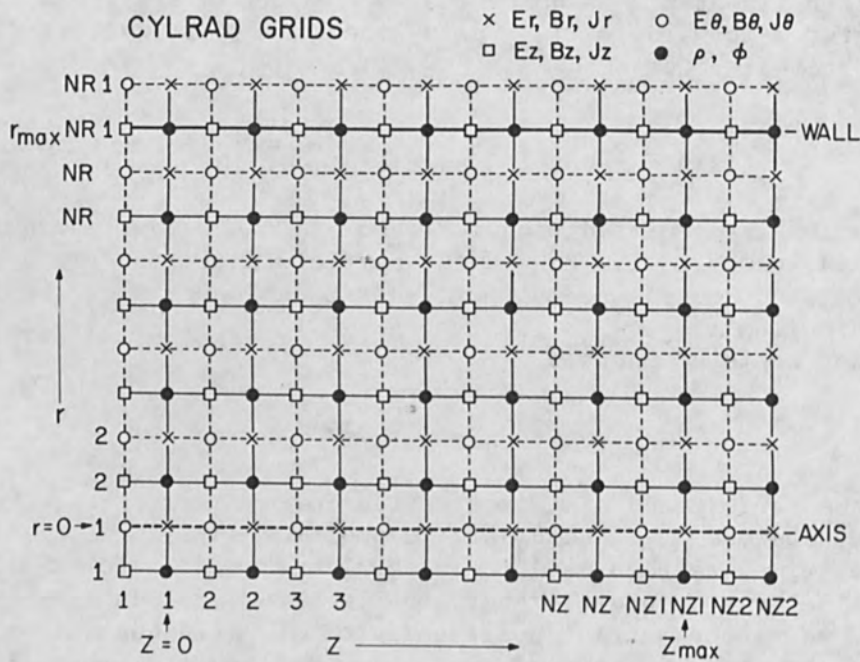


FIG. 2.--Four centered meshes of CYLRAD. Centering all field and source variables ensures second-order accuracy.

$$\underline{\nabla} \times \underline{\nabla} \varphi \equiv 0 \quad (5a)$$

$$\underline{\nabla} \cdot \underline{\nabla} \times \underline{A} \equiv 0 \quad (5b)$$

$$\underline{\nabla} \cdot \underline{\nabla} \varphi \equiv \nabla^2 \varphi \quad (5c)$$

have exact difference analogs. Thus, radiation energy is conserved in the absence of particles, for example, and $\underline{\nabla} \cdot \underline{B}$ is identically zero by Eq. (1b) for all time if it is zero initially (to round off).

Figure 3 shows the numerical and theoretical dispersion curves for CYLRAD for a case of zero plasma density ($\omega_p \delta t = 0$) and for a case of large plasma density ($\omega_p \delta t = 1$). CYLRAD uses the algorithm named "explicit" and marked by the dashed line. The model used for these dispersion curves is an infinite homogeneous two-dimensional Cartesian plasma of plasma frequency ω_p . On this is superimposed a space-time grid with cells measuring $\delta x \times \delta y \times \delta t$.

When the plasma is not relativistic, and the temperature is zero, the physical dispersion relation is

$$\omega^2 = \omega_p^2 + k^2 c^2 \quad (6)$$

In the figure $k_y = 0$ in the two cases shown. By contrast, the CYLRAD numerical algorithm has the dispersion relation

$$\sin^2 \frac{\omega \delta t}{2} = \frac{c^2 \delta t^2}{\delta x^2} \sin^2 \left(\frac{k_x \delta x}{2} \right) + \frac{c^2 \delta t^2}{\delta y^2} \sin^2 \left(\frac{k_y \delta y}{2} \right) + \frac{\omega_p^2 \delta t^2}{4} \quad (7)$$

Since $\sin^2(\omega \delta t/2)$ cannot exceed unity for stable oscillations, one has a stringent stability condition on δt ,

$$\frac{1}{\delta t^2} \geq \frac{c^2}{\delta x^2} + \frac{c^2}{\delta y^2} + \frac{\omega_p^2}{4} \quad (8)$$

In dense plasmas ω_p^2 dominates. Then $\delta t < 2/\omega_p$ is required. When the density is low, stability is satisfied roughly by requiring that light travel less than a cell per cycle, $\delta t < 1 / \sqrt{(c^2/\delta x^2) + (c^2/\delta y^2)}$.

One more feature of the CYLRAD code is that a matrix of dielectric constants is also defined on the θ grid. The dielectric constant (actually its reciprocal) at any other location in space is assumed to be defined by linear interpolation from this grid. When $1/\epsilon$ is not unity throughout the CYLRAD mesh, the Maxwell equations become

$$\frac{\partial \underline{D}}{\partial t} = c \underline{\nabla} \times \underline{B} - 4\pi \underline{J} \quad (9a)$$

$$\frac{\partial \underline{B}}{\partial t} = -c \underline{\nabla} \times (\underline{D}/\epsilon) \quad (9b)$$

$$\underline{\nabla} \cdot \underline{D} = 4\pi \quad (9c)$$

NUMERICAL DISPERSION CURVES FOR CYLRAD

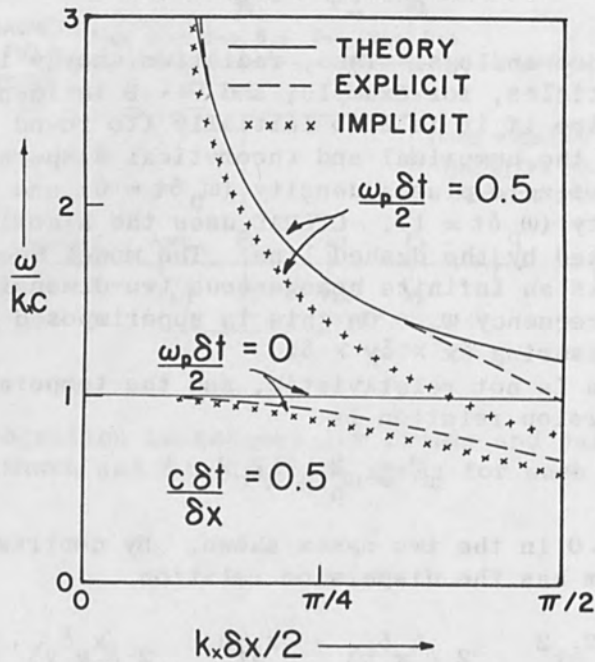


FIG. 3.--Numerical dispersion relations for CYLRAD algorithms. Theoretically correct dispersion relation and dispersion relations for implicit scheme are shown for comparison.

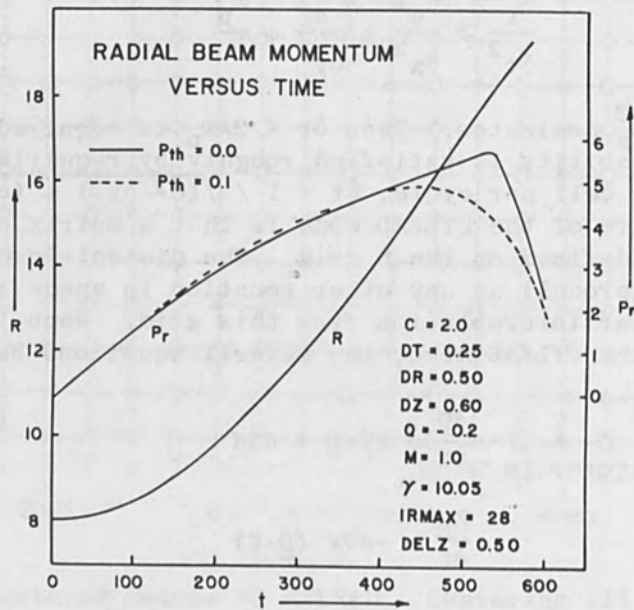


FIG. 4.--Average beam radius and total radial momentum vs time for beams with and without thermal spread in velocity.

We therefore have a very simple prescription for integrating the radiation equations in a medium of variable dielectric strength. Even greater utility arises by setting $1/\epsilon \equiv 0$ in certain regions. We then have a simple prescription for integrating Maxwell's equations in volumes containing perfectly conducting metallic objects of complicated shape. This feature is intended for use in diode design and optimization studies for electron-beam and electron-ring devices.

ELECTRON-BEAM EXPERIMENTS

In this section we describe the results of preliminary numerical beam propagation experiments.¹¹ We have investigated the dynamics of highly relativistic, infinitely long, pure electron beams with and without a magnetic guide field. The expansion of the beam agrees with the analytical theory⁷ to within a few per cent. In Fig. 4 we show the average radius and total radial momentum of the beam particles vs time for a beam with a relativistic $\gamma = 10.05$ and $v/\gamma \approx 0.1$. We considered several cases of this expansion, for various values of the thermal spread in the momenta. In Fig. 4 we display two of these cases, one for no thermal spread in the momentum and one in which the three components of the momenta all have equal thermal spread. The drifting momentum in all cases was $P_z = 20.0$, and the thermal spread in the case being discussed is $P_{th} = 0.1$. For times less than 400 the expansion proceeds as predicted by the theory. The flattening of the curve and its downward turn at about $t = 450$ are caused by the first particles reaching the perfectly reflecting outer wall of the system. This is shown dramatically in the plot of the radial momentum vs time for zero thermal spread. In the second case the particles arrive at different times due to the finite spread in momenta and the radial momentum decreases smoothly as the particles are reflected. But the finite spread in momenta has little effect on the average radius.

In Fig. 5 we show the average radius vs time for two cases that have different values of v/γ . In these two experiments the outer wall was moved sufficiently far away from the outer edge of the beam so that no particles could reach it during the experiment. The $v/\gamma = 0.1$ beam expands as expected, whereas the beam with $v/\gamma = 1.1$ quickly reaches a uniform expansion rate, since the radial velocity in the beam rest frame quickly becomes relativistic for beams with $v/\gamma \gtrsim 1$. The simple expansion theories in which γ is assumed to be constant then fail. In the beam rest frame the equation of motion for a particle in a uniform axisymmetric beam is

$$\frac{d}{dt} [\beta(1 - \beta^2)^{-1/2}] = 2c(v/\gamma_D)r^{-1}$$

where $\beta = v_r/c$, $v = \pi a^2 n_b e^2 / (m_0 c^2)$, n_b is the beam density measured in the laboratory frame, a is the initial radius of the particle, and γ_D is the relativistic γ associated with the drift velocity of the beam and is a constant. Defining $P = \beta(1 - \beta^2)^{-1/2}$ and measuring the time in the laboratory frame, we have the following set of canonical equations for the particle motion:

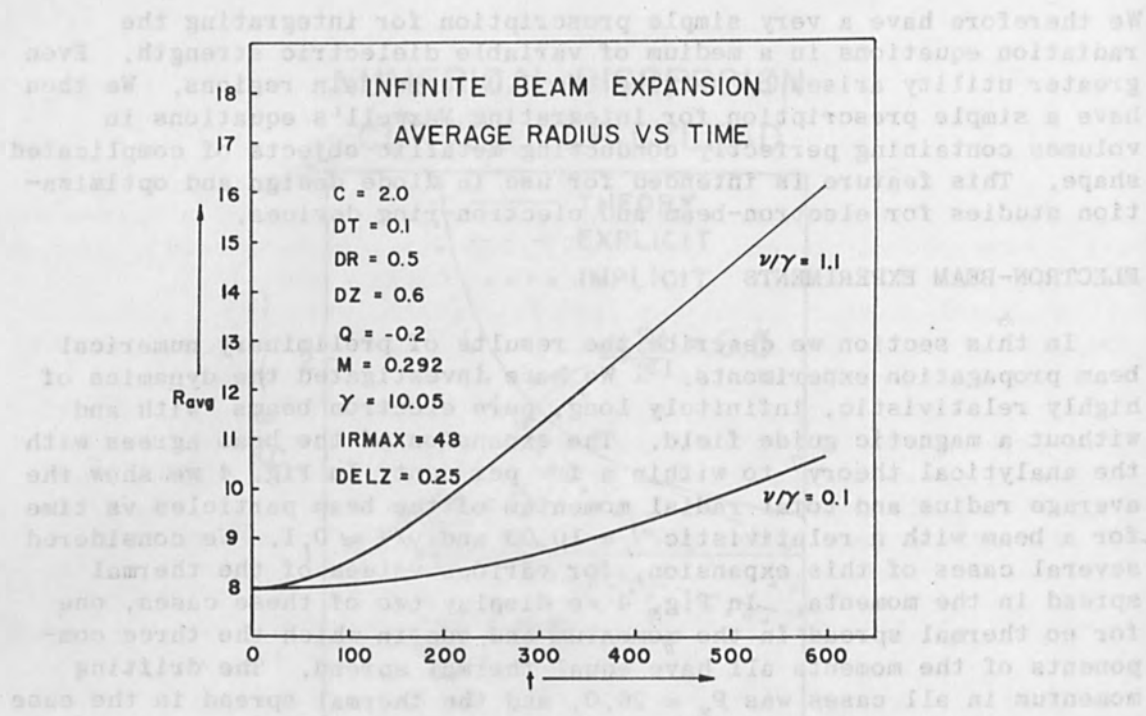


FIG. 5.--Average beam radius vs time for two values of v/γ .

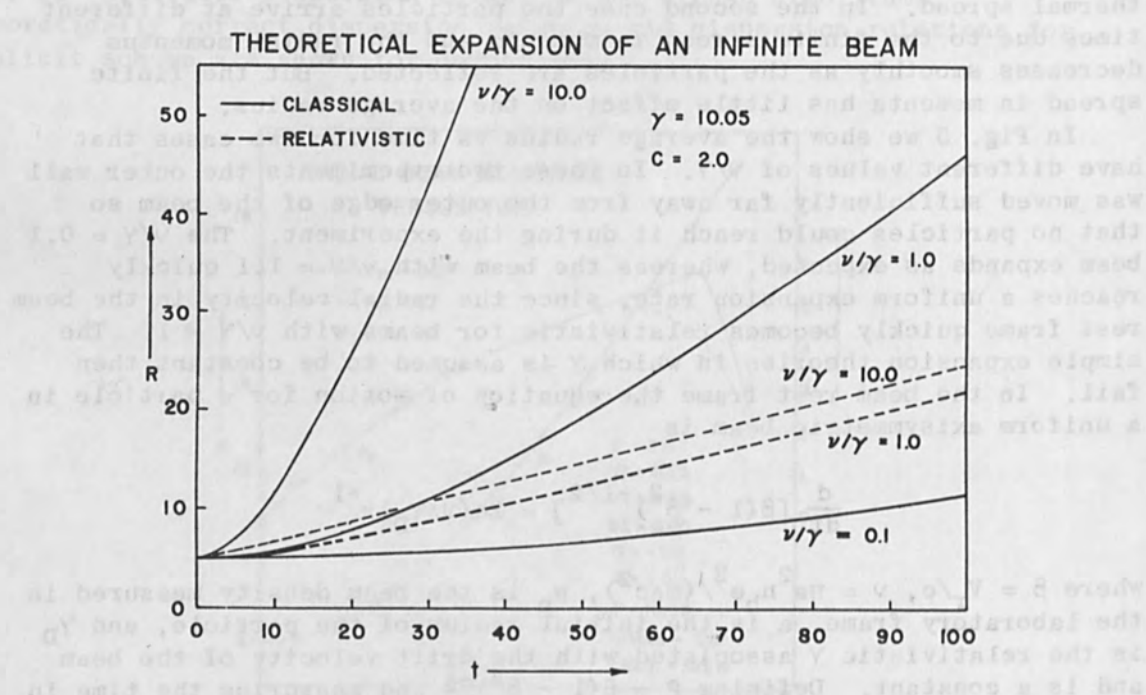


FIG. 6.--Theoretical curves of radius vs time for relativistic beam expansion.

$$\frac{d}{dt'} P = 2v c \gamma_D^{-2} r^{-1}$$

$$\frac{d}{dt'} r = c \gamma_D^{-1} P (1 + P^2)^{-1/2}$$

These equations are then integrated numerically⁸ for three values of v/γ . In Fig. 6 we present the results for two sets of conditions. The first is with the relativistic mass correction taken into account; in the second it was ignored. For $v/\gamma = 0.1$ the relativistic correction was negligible, but one sees that in the other cases in which the relativistic mass shift is ignored the results are grossly inaccurate and that relativistic dynamics are very important in the treatment of beams with $v/\gamma \gtrsim 1$. In Fig. 7 we plot the positions of a few of the particles in the simulation experiment vs time. We see that particle 16 and particle 32 reach the asymptotic expansion regime where $dr/dt = \text{constant}$ in agreement with the relativistic expansion theory.

Next we consider the expansion in a uniform magnetic guide field. Figure 8 shows the results of these simulation experiments. The beam is initialized with constant axial field and no current in the $\hat{\theta}$ direction. Because of the radial electric field and the \hat{z} magnetic field, a current in θ direction develops due to the $\vec{E} \times \vec{B}$ drift of the particles. The diamagnetic current of the beam, which is now rotating approximately as a solid body, reduces the strength of the B_z guide field inside the beam and (because we have perfectly conducting boundary conditions on the outside wall of the system) increases the B_z guide field outside the beam. Due to inertia effects the expanding beam then over-shoots the equilibrium radius. Figure 9 shows two cases where the experiment was run for a longer period of time. For $B_{z0} = 5.0$ we have followed the average radius for two bounces.

In Fig. 10 we show some very preliminary results of an experiment where a beam with a blunt head was injected into a cold background plasma. The density of the plasma is $3 \times 10^{13} \text{ cm}^{-3}$. The γ of the beam is 5 and the total current is approximately 6 KA. The beam is "injected" into the system at $z = 0$ and then propagates down the system exciting currents in the cold background plasma. In Fig. 10 we show the total current density (solid line) in the \hat{z} direction for time step 200 at a radius of 0.25 cm off the axis. The current density of the beam is also shown (dashed line). The analytical theory^{9,10} predicts that a blunt beam injected into a plasma will excite a large plasma oscillation, whose amplitude is of the same order as the beam current, at the head of the beam. The wavelength of the oscillation should be $2\pi\lambda_E$ and the wavelength of the oscillation in Fig. 10 agrees exactly with this prediction. One sees that on the average the total current (beam current plus plasma current) is zero.

ELECTRON-RING EXPERIMENTS

In this section we present calculations of relativistic electron-ring equilibria and the dynamic evolution of electron rings using CYLRAD.¹² Two major problems are addressed, the displacement of the equilibrium-ring radius due to the finite v/γ of the ring and the oscillations of the ring about the displaced equilibrium. These

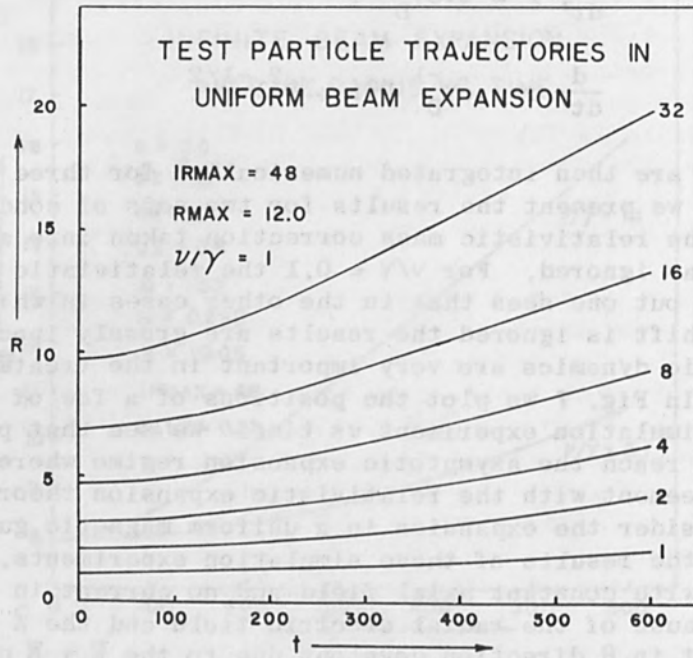


FIG. 7.--Test particle trajectories in uniform beam expansion.

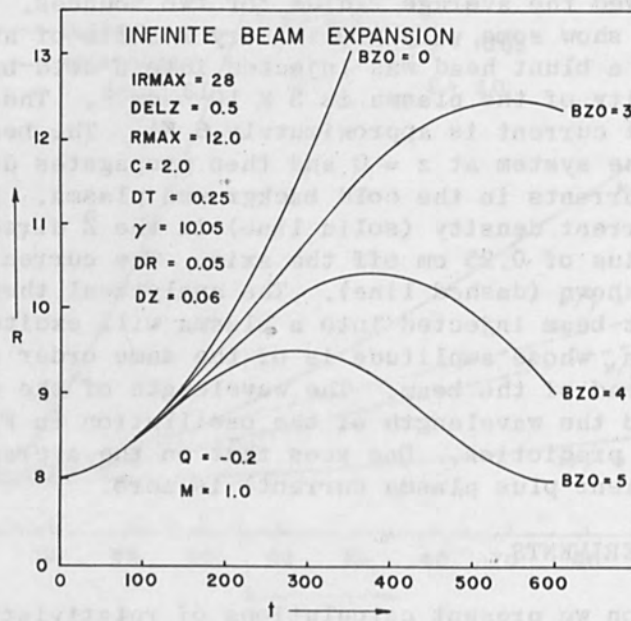


FIG. 8.--Average radius vs time of infinite beam expanding into magnetic field.

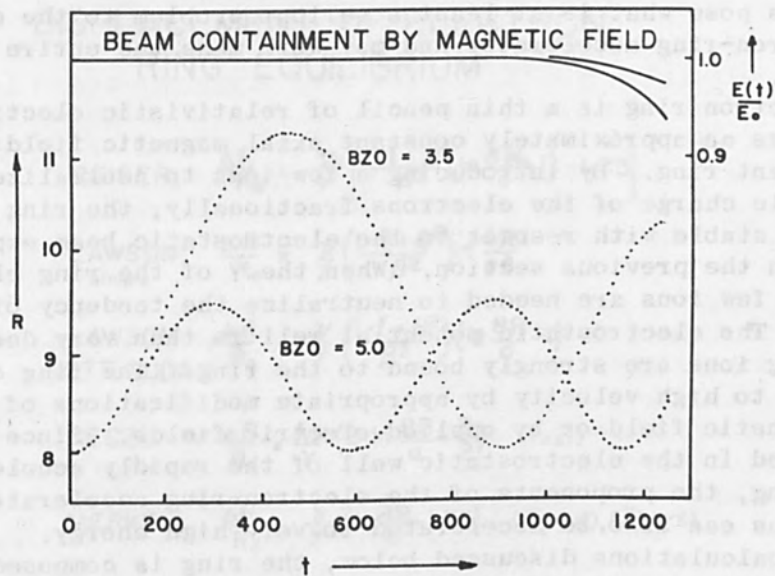


FIG. 9.--Beam containment by magnetic guide field.

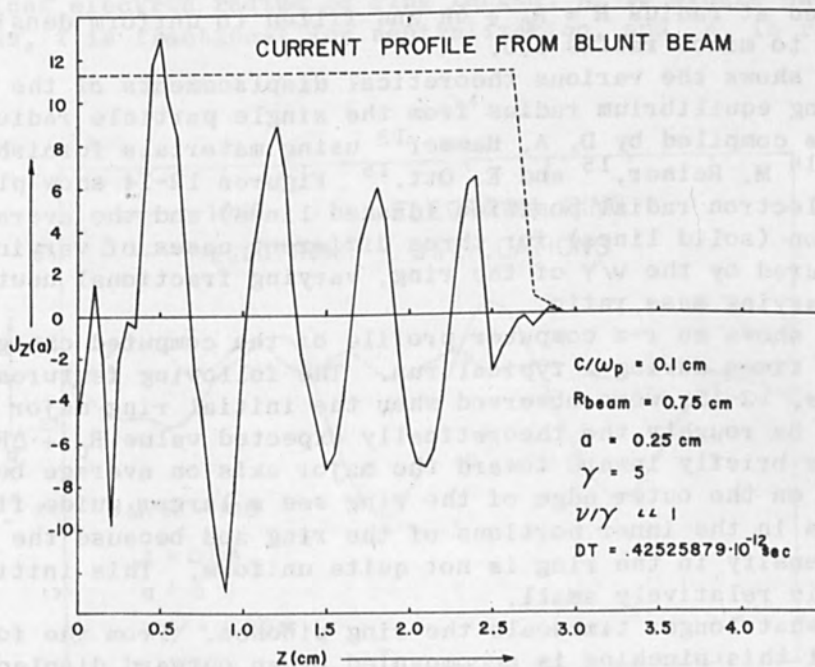


FIG. 10.--Current density vs z for blunt beam propagating in plasma.

oscillations pose what is at least a serious problem to the designers of an electron-ring accelerator and may well make the entire scheme impractical.

The electron ring is a thin pencil of relativistic electrons injected across an approximately constant axial magnetic field to form a closed current ring. By introducing a few ions to neutralize the electrostatic charge of the electrons fractionally, the ring can be in theory made stable with respect to the electrostatic beam expansion discussed in the previous section. When the γ of the ring electrons is large, very few ions are needed to neutralize the tendency of the ring to expand. The electrostatic potential well is then very deep and the neutralizing ions are strongly bound to the ring. The ring can be accelerated to high velocity by appropriate modifications of the applied magnetic field or by applied electric fields. Since the ions are entrained in the electrostatic well of the rapidly accelerating electron ring, the proponents of the electron-ring accelerator feel that the ions can also be accelerated to very high energy.

In the calculations discussed below, the ring is composed of 4000 electrons and is seeded with 400 ions. To reduce the necessary computer time the ion-electron rest mass ratios were given two values, 100:1 and 250:1. The fractional neutralization of the ring was varied by changing the ion charge (and mass) relative to the electron charge. The runs performed had $f = 0.1, 0.05, 0.02, 0.01$; results are shown for the 5 and 2-percent cases. The value of γ for all runs was 20 and the strength of B_{z0} was chosen so that the single-particle gyroradius R_0 would also be 20 in the CYLRAD units. The ring of electrons was initialized by placing the 4000 particles on a uniform polar grid (r, θ) centered at radius $R = R_0 + \delta R$ and filled to uniform density of particles out to minor radius 3.0.

Figure 11 shows the various theoretical displacements of the self-consistent ring equilibrium radius from the single particle radius R . This table was compiled by D. A. Hammer¹³ using materials furnished by J. D. Lawson,¹⁴ M. Reiser,¹⁵ and E. Ott.¹⁶ Figures 12-14 show plots of the average electron radial position (dashed lines) and the average ion radial position (solid lines) for three different cases of varying ring strength measured by the v/γ of the ring, varying fractional neutralization, and varying mass ratio.

Figure 15 shows an r - z computer profile of the computed charge density at three times during a typical run. The following features of all runs, Figs. 12-15, were observed when the initial ring major radius was chosen to be roughly the theoretically expected value $R_0 + \Delta R$. The electrons move briefly inward toward the major axis on average because the electrons on the outer edge of the ring see a larger guide field than electrons in the inner portions of the ring and because the initial charge density in the ring is not quite uniform. This initial readjustment is relatively small.

On a somewhat longer timescale the ring pinches. From the formulas in Fig. 11 this pinching is accompanied by an outward displacement of the ring because a is decreased in the $\ln(R_0/a)$ term. This outward displacement due to pinching can be seen to occur in Figs. 12-14 followed by an overshoot of the equilibrium. The electron ring then oscillates about the equilibrium position with an excursion equal to about 35 per cent of the ring minor radius a . This oscillation has a

DISPLACEMENT OF ELECTRON RING EQUILIBRIUM

REISER: $\frac{\Delta R}{R_0} = \frac{\nu}{\gamma} \left[\frac{1-f+\beta^2}{\beta^2} (\ln \frac{8R}{a} - 1) - 1.75 \right]$

LAWSON: $\frac{\Delta R}{R_0} = \frac{\nu}{\gamma} \left(\frac{1-f+\beta^2}{\beta^2} \right) \ln \frac{4R}{a}$
simple

LAWSON: $\frac{\Delta R}{R_0} = \frac{\nu}{\gamma} \left(\frac{1-f+\beta^2}{\beta^2} \right) (\ln \frac{8R}{a} - 1)$
OTT, SUDAN

KEGEL: $\frac{\Delta R}{R_0} = \frac{A\nu}{\gamma} \left(2 \ln \frac{8R}{a} - \frac{3}{2} \right) (f \ll 1)$

MERKEL: $\frac{\Delta R}{R_0} = \frac{\nu}{\gamma} (\ln \frac{8R}{a} - 1.75) (T_e \sim 0, f \sim 1/\gamma^2)$

BUDKER: DIFFERENT APPLICATION,
SIMILAR CALCULATION

SCHMIDT: SIMILAR APPLICATION,
DIFFERENT CALCULATION

FIG. 11.--Comparison of theoretical calculations by several authors of outwardly displaced ring equilibrium radius; ν is number of particles per classical electron radius of ring length, R_0 is single particle gyro-radius, f is fractional ion neutralization, and a is ring minor radius.

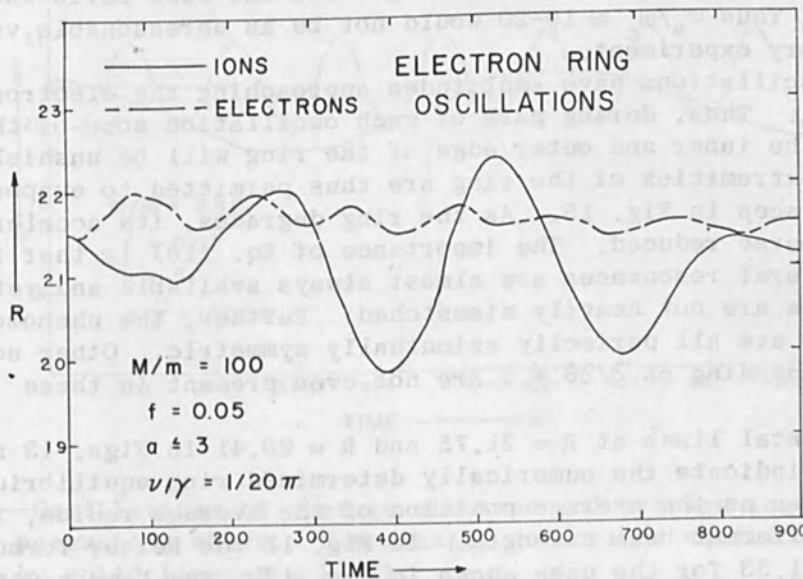


FIG. 12.--Oscillation of average electron and average ion radii with time for parameters shown.

period equal to the relativistically corrected cyclotron period as indicated by + in Figs. 13 and 14.

As the calculations continue the electron rings lose particles, causing a gradual inward adjustment of the equilibrium radius. This effect is partially counterbalanced by the pinching of the center portions of the ring as the hotter, more energetic particles are lost first. Thus $|a|$ decreases as well as v/γ in the formulas of Fig. 11 but the linear dependence on v/γ wins out over the logarithmic variation with a .

The ions play a pivotal role in the mechanism for electron loss. Due to the curvature of the ring, the minimum of the electrostatic well for the ions lies inside the equilibrium-ring radius. Thus the ions, which are initialized congruent with the electron distribution, move inward initially, whereas electrons move outward. Except in Fig. 12 where $M/m = 100$ and $f = 0.05$, the ions exert negligible effect on the radial oscillations of the electrons because they carry so little charge. The motions of the electrons on the other hand affect the ions since the ions try to track the electrostatic well of the moving electron ring. A mechanism thus exists for driving the ion oscillations to large amplitude using the electron cyclotron motion as an energy source for the radial excursions of the ions. This phenomenon depends on a resonance or near resonance between some multiple of the connected cyclotron frequency of the electrons and the "slosh" time of the ions. The ratio of frequencies is

$$\frac{\omega_s^2}{\omega_{ce}^2} = \frac{v}{\gamma} 2\gamma \frac{Q/M}{e/m} \left(\frac{R}{a}\right)^2 \quad (10)$$

For the numerical calculations of Fig. 14 we have $\omega_s/\omega_{ce} \approx 6$. For a physical ring R/a would be somewhat larger but the mass ratio would be much smaller. Thus $\omega_s/\omega_c \approx 10-20$ would not be an unreasonable value for a laboratory experiment.

The ion oscillations have amplitudes approaching the electron ring minor radius a . Thus, during part of each oscillation some of the electrons on the inner and outer edge of the ring will be unshielded by ions and the extremities of the ring are thus permitted to evaporate as seen at two places in Fig. 15. As the ring degrades, its accelerating power is of course reduced. The importance of Eq. (10) is that it shows that several resonances are almost always available and yet the two frequencies are not heavily mismatched. Further, the phenomena described here are all perfectly azimuthally symmetric. Other sorts of pathologies depending on $\partial/\partial\theta \neq 0$ are not even present in these calculations.

The horizontal lines at $R = 21.75$ and $R = 20.41$ in Figs. 13 and 14, respectively, indicate the numerically determined ring equilibrium positions, taken as the average position of the average radius, from two runs of different beam strength. In Fig. 11 the Reiser formula predicts $\Delta R = 1.33$ for the case shown in Fig. 13. The Lawson-Ott-Sudan formula predicts $\Delta R = 1.71$ when v rather than v_0 is used. Their formula errs slightly on the low side since the value of $|a|$ decreases

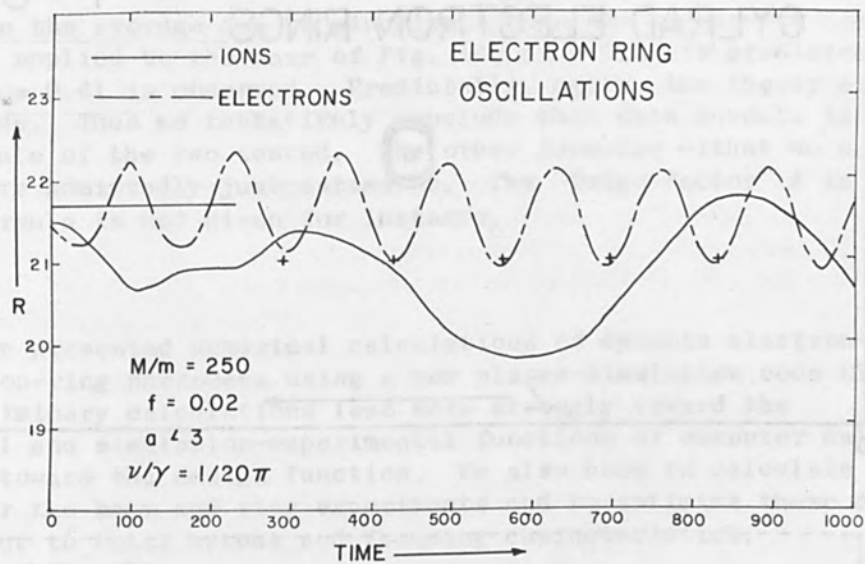


FIG. 13.--Oscillation of the average electron and average ion radii with time for parameters shown. Numerically determined equilibrium radius is shown by solid line at ≈ 21.75 .

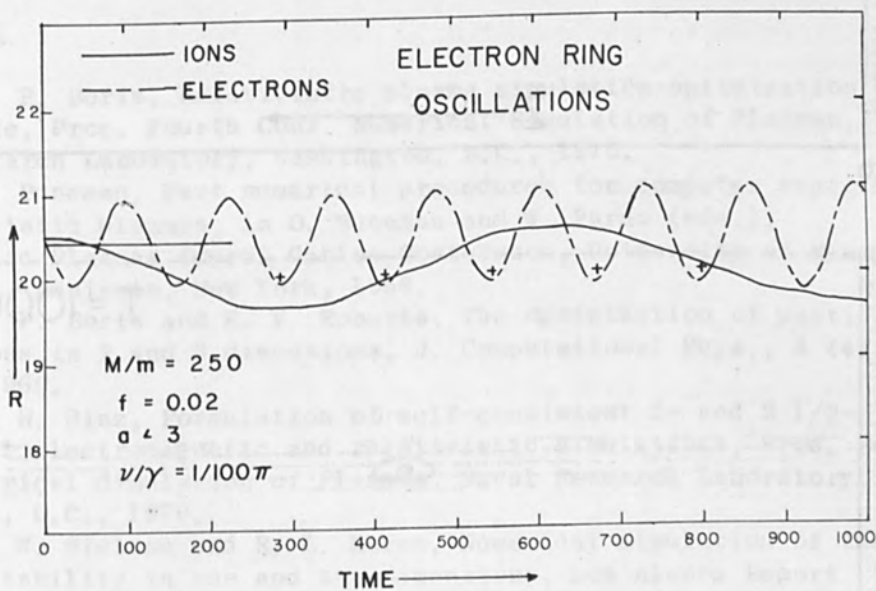


FIG. 14.--Oscillations of average electron and average ion radii with time for parameters shown. Numerically determined equilibrium radius is shown by solid line at ≈ 20.41 .

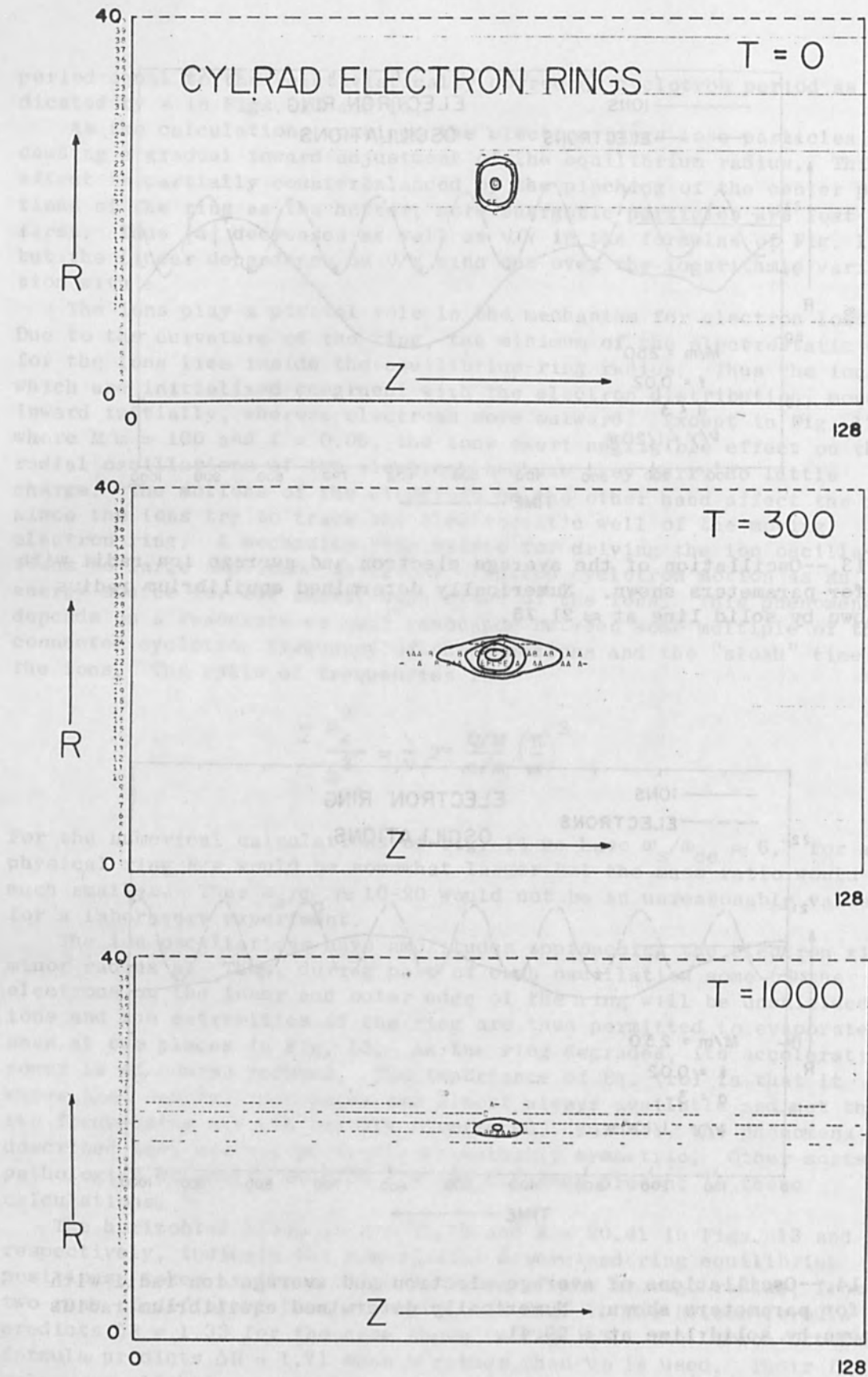


FIG. 15.--Charge density profiles of electron ring with ions at three times in calculation. Evaporation of ring due to electrostatic denneutralization from ion oscillations can be seen.

somewhat on the average due to pinching. When the Lawson-Ott-Sudan formula is applied to the case of Fig. 14, $\Delta R = 0.38$ is predicted whereas $\Delta R = 0.41$ is observed. Predictably, again, the theory errs on the low side. Thus we tentatively conclude that this formula is the more accurate of the two tested. The other formulas either do not apply or are admittedly just estimates. The "fudge-factor" A in Kegel's formula is not given for instance.

SUMMARY

We have presented numerical calculations of dynamic electron-beam and electron-ring phenomena using a new plasma-simulation code CYLRAD. These preliminary calculations lean more strongly toward the theoretical and simulation-experimental functions of computer calculation than toward the design function. We also hope to calculate diode designs for the beam and ring experiments and to optimize these designs with respect to total output and focusing characteristics.

ACKNOWLEDGMENT

The authors would like to acknowledge the help and suggestions of Ravindra Sudan, Richard Lovelace, and Leslie Levine of Cornell University and the Naval Research Laboratory during the course of this work and would particularly like to thank David Hammer of the Naval Research Laboratory for his close participation in several of the calculations and comparisons mentioned here.

REFERENCES

1. J. P. Boris, Relativistic plasma simulation-optimization of a hybrid code, Proc. Fourth Conf. Numerical Simulation of Plasmas, Naval Research Laboratory, Washington, D.C., 1970.
2. O. Buneman, Fast numerical procedures for computer experiments on relativistic plasmas, in O. Buneman and W. Pardo (eds.), Relativistic Plasmas (Coral Gables Conference, University of Miami, 1968), W.A. Benjamin, New York, 1968.
3. J. P. Boris and K. V. Roberts, The optimization of particle calculations in 2 and 3 dimensions, J. Computational Phys., 4 (4), December 1969.
4. K. H. Sinz, Formulation of self-consistent 2- and 2 1/2-dimensional electromagnetic and relativistic simulations, Proc. Fourth Conf. Numerical Simulation of Plasmas, Naval Research Laboratory, Washington, D.C., 1970.
5. C. W. Nielson and R. L. Morse, Numerical simulation of the Weibel instability in one and two dimensions, Los Alamos Report LA-4482, July 1970.
6. C. K. Birdsall and D. Fuss, J. Computational Physics, 3: 494-511, 1969.
7. J. D. Lawson, J. Elect. and Control 5: 146, 1958.
8. J. P. Boris and N. Winsor, Extrapolated numerical integration in theory and practice, Princeton Plasma Physics Laboratory Report NATT-652, November 1970.

9. D. A. Hammer and N. Rostoker, Phys. Fluids 13: 1831, 1970.
10. R. E. Lee and R. N. Sudan, Phys. Fluids 14: 213, 1971.
11. R. E. Lee and J. P. Boris, Bull. Am. Phys. Soc. 16: 573, 1971.
12. J. P. Boris and D. A. Hammer, Bull. Am. Phys. Soc. 16: 573, 1971.
13. D. A. Hammer (private communications).
14. J. D. Lanson (private communication).
15. M. Reiser (private communication).
16. E. Ott, Plasma Physics (in preparation).

ACKNOWLEDGMENT

The authors would like to acknowledge the help and suggestions of David Suter, Richard Lovelace, and Leslie Levine of Cornell University and the Naval Research Laboratory during the course of this work and would particularly like to thank David Suter of the Naval Research Laboratory for his close participation in several of the calculations and comparisons mentioned here.

REFERENCES

1. J. P. Boris, Relativistic plasma simulation-optimization of a hybrid code, Proc. Fourth Conf. Numerical Simulation of Plasmas, Naval Research Laboratory, Washington, D.C., 1970.
2. W. Suman, Fast numerical procedures for computer experiments on relativistic plasmas, in G. Buzman and W. Suman (eds.), Relativistic Plasmas (Gordon and Breach, London, 1968).
3. J. P. Boris and K. V. Roberts, The optimization of particle calculations in 1 and 3 dimensions, J. Computational Phys., 4 (4) December 1969.
4. K. H. Sims, Formulation of self-consistent 2- and 3 1/2-dimensional electromagnetic and relativistic simulation, Proc. Conf. Numerical Simulation of Plasmas, Naval Research Laboratory, Washington, D.C., 1970.
5. C. W. Nielson and R. E. Morse, Numerical solution of the Weibel instability in one and two dimensions, Los Alamos Report LA-4482, July 1970.
6. C. K. Birdsall and D. Fox, J. Computational Physics, 3: 404-411, 1968.
7. J. D. Lanson, J. Elect. and Control Eng., 1968.
8. J. D. Lanson and N. Rostoker, Extended numerical integration in theory and practice, Princeton Plasma Physics Laboratory Report NATT-852, November 1970.

CHARACTERISTICS OF COOL, HIGH v/γ ELECTRON-BEAM PROPAGATION*

LAIRD P. BRADLEY, T. H. MARTIN, K. R. PRESTWICH, J. E. BOERS, and
D. L. JOHNSON

Sandia Laboratories, Albuquerque, N. M.

and

G. COOPERSTEIN

Ion Physics Corp., Burlington, Mass.

INTRODUCTION TO COOL-BEAM APPROACH

The primary premise of this paper is that cool (low transverse energy) electron beams can be utilized for the efficient transport and concentration of high v/γ electron-beam energy. Three beam-handling concepts are of primary concern: transport, compression, and combination. Data showing the necessity and effect of coolness on each of these areas are presented. The cool, neutral-gas propagation approach is contrasted with the hot beam and with the superimposed magnetic-field approach where applicable. At the time of publication, beam transport has been obtained, using v/γ of 1 to 3 beams, with an e-folding distance of 4 to 6 m, fluence gain of 10, and 100-percent superposition with excellent uniformity.

The cool-beam approach has long been advocated by J. C. Martin of AWRE. His development of the plasma and razor edge cathodes for high-current electron-beam machines has been essential to the launching of a cool beam into neutral gas. Martin had reported¹ current neutralization ($I_{\text{net}}/I_{\text{primary}}$) of 95 percent, indicating a cool beam. He has also reported simultaneous compression and superposition of an already converging beam with a fluence gain of more than 20. The authors have conducted experiments which separately examine the aforementioned beam-handling concepts, distinguishing between such properties as compression and superposition, and arriving at functional relations for these properties. Care was taken to inject a beam which propagates with uniform cross section and then to establish the effects of compression and adding.

The propagation efficiency increases with beam coolness. An intriguing, although somewhat qualitative, trend is obtained as follows. Using data from several laboratories, the beam transverse energy is estimated for several observed e-folding distances (Fig. 1). Estimates of mean angles were determined by including type of cathode, relative pinching in diode as determined² by $(v/\gamma)/(r/2d)$, and scattering in anode foil. These estimates were compared with estimates of mean angles determined from net and primary currents and primary voltage. Note that the two Cornell data points differ essentially only by a change of anode material from 1-mil titanium to 1/2-mil Mylar. The $v/\gamma|_{\text{net}}$ is also

*This work was supported by the U.S. Atomic Energy Commission and partially by the Defense Atomic Support Agency.

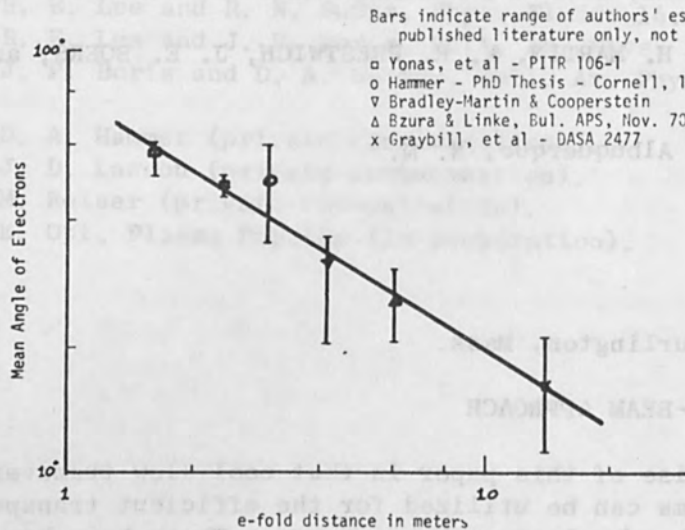


FIG. 1.--Mean electron angle $\langle \theta \rangle$ vs e-fold distance.

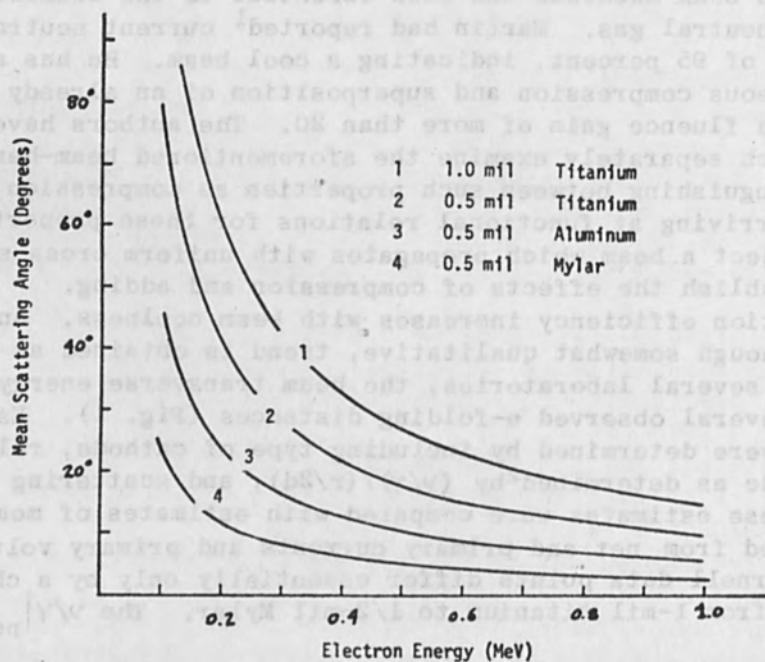


FIG. 2.--Mean scattering angle of electrons in anode material as function of electron energy.

minimized for a cool beam, being intimately related to transverse energy, ³ although $v/\gamma|_{\text{primary}}$ may be high.

BEAM INJECTION

All experimental results presented here were obtained with a plasma cathode, except one portion which employed a razor edge cathode. The plasma cathode, composed of 1/16-in. rings 1/16 in. apart, was used to produce a relatively cool beam and to provide a comparison with the work of others. The beam thus generated proved suitable for investigating limits on the appropriate beam properties. Characteristics of the electron-beam sources used in the present tests are given in Refs. 4 and 5. Characteristics of the plasma cathode and razor-edge cathode are now reasonably well understood; theoretical and experimental details will be presented elsewhere.⁶

Beam transverse energy can be probably no better than that determined by the angle of arrival of electrons at the anode compounded by the scattering in the anode material. The contributions to transverse energy would be minimized in the ultimately cool beam. For purposes of this paper, we have not attempted to obtain the ultimate case, but rather to document the contributions for a particular case and determine the effect of the known injected transverse energy on beam propagation. Where we have taken care to keep the injection angles small and to minimize scatter in the anode material, we obtain $\langle\theta\rangle \approx 30^\circ$.

Scattering in several anode materials was calculated using Moliere multiple scattering theory⁷ and is plotted in Fig. 2. An effective atomic number and atomic weight were assumed for the Mylar anodes. Although Moliere multiple scattering is valid only for mean scattering angles less than 20° and for mean number of collisions greater than 20, Fig. 2 can be used qualitatively beyond the ranges of validity.

BEAM ENERGY TRANSPORT EFFICIENCY

Preliminary experiments were conducted as a function of pressure by drifting the beam in a 6-in.-diameter plexiglass tube for 1.25 m. The optimum pressure for the beam to propagate uniformly and produce a damage spot of exactly the 1-in. cathode diameter was 3 torr. Return conductors outside the tube had no effect at this pressure, which implies that the net current was minimum. A frozen-hose instability was observed at this pressure.

This beam was then injected into a metal beamguide with an inner diameter equal to the beam diameter. The energy transport efficiency is defined as the total energy at a particular distance z relative to the energy measured at the anode plane. These measurements were made with a total stopping carbon calorimeter. Although shot-to-shot reproducibility of the energy was excellent, the diode voltage-current traces were analyzed to incorporate any slight variation for each shot.

Considering the transport efficiency parametrically, we have looked at the effect of pressure as shown in Fig. 4. Whereas hot-beam transport efficiency data^{8,9} peak at 0.5 to 0.75 torr, these cool-beam data peak toward 2 torr and are probably optimized at 3 torr. However, in the region 2.5 to 3 torr, as mentioned, a frozen-hose type of insta-

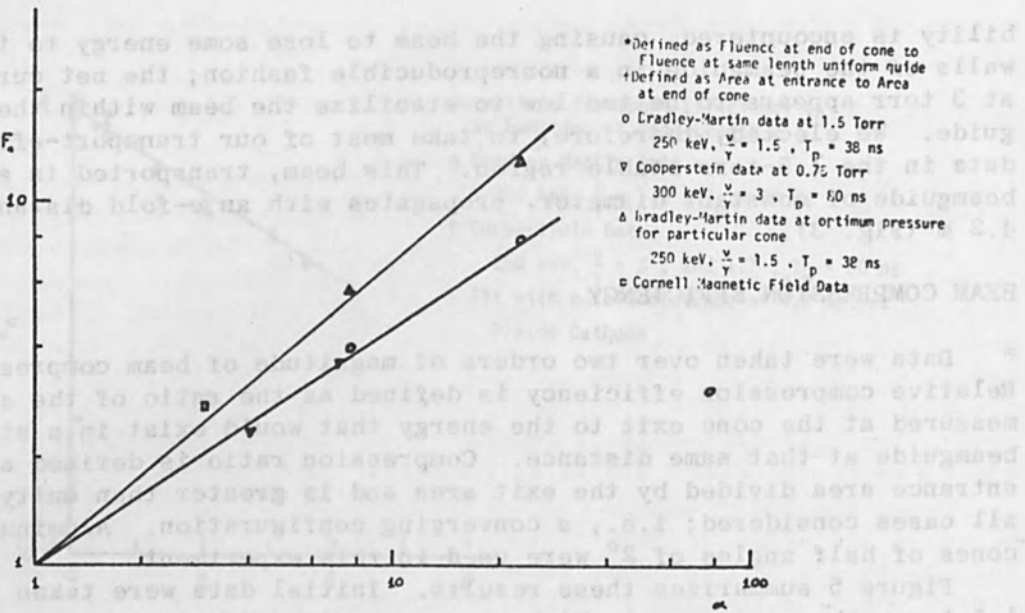


FIG. 5.--Relative fluence as function of compression ratio α .

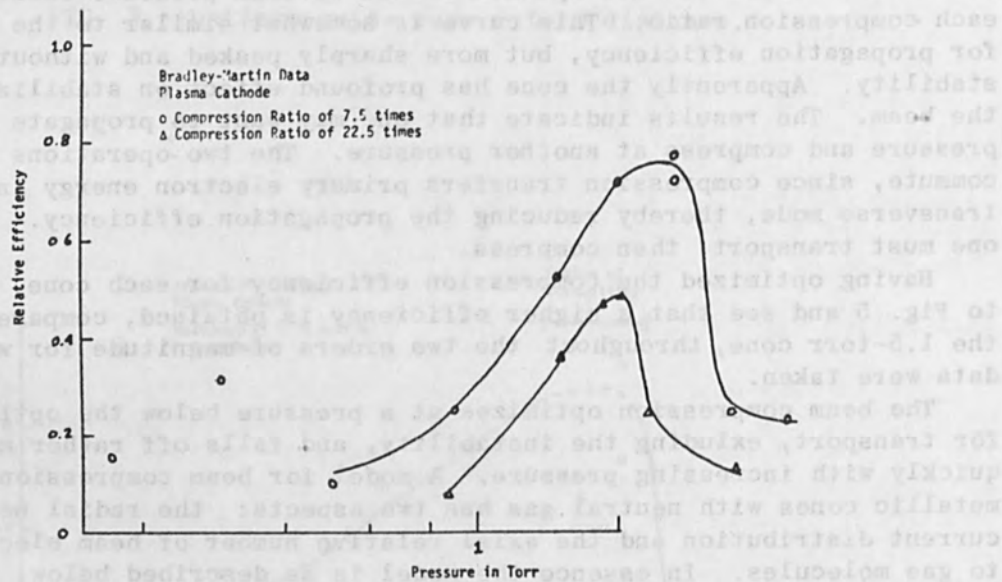


FIG. 6.--Compression data: Relative efficiency as function of pressure. (Relative efficiency defined as ratio of energy at end of cone to energy at same length of uniform guide.)

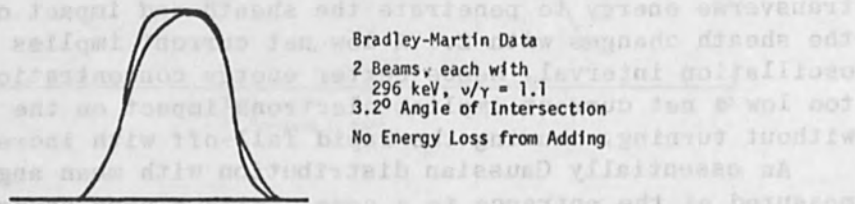


FIG. 7.--Orthogonal scans of total energy distribution at beam merger region.

at the exit. These angular distributions were measured directly by a technique somewhat similar to that employed by Clark² and indicate the increase in transverse energy as the beam is compressed in accordance with the model.

At the cone entrance, the number of gas molecules is sufficient to provide magnetic neutralization for the beam. But as the beam propagates down the cone the ratio of beam electrons to background molecules becomes exceedingly large. At some point the number of background electrons is insufficient to provide magnetic neutralization, the net current distribution changes, and efficient compression ceases. This is evident in Fig. 5 at a compression ratio of 75. Detailed discussion of this model will be presented elsewhere.

For comparison we have also plotted in Fig. 5 the best compression data reported to date utilizing magnetic¹⁰ fields (a compression of 3) and note that neutral gas compression with cones appears equally good. Attempts with hot beams⁷ produced no observable compression.

BEAM SUPERPOSITION

The result of adding moderately cool beams may be stated concisely: they add completely.

Two beams were generated by separate cathodes in one diode envelope. The beams were guided toward a common point in individual straight beamguides with an angle of intersection of 3.2° . Near the region of intersection, the beams entered a common guide with a continuous outer wall. Figure 7 contains results of orthogonal scans of the energy density⁶ in the target region; the beams merged completely. Calorimeter measurements showed no loss of energy. Experiments elsewhere¹¹ showed no addition of hot beams. We conclude that, if beams are maintained cool, they may be completely superimposed.

CONCLUSIONS

The approach to beam propagation discussed here uses a relatively low transverse energy electron beam of $v/\gamma|_{\text{primary}} > 1$. Application and extension of this approach require that electrons be emitted from the cathode at small angles, perhaps from the sharp razor edge. Diode spacings are held such that the effect of the beam magnetic field in the diode on transverse energy is minimized on the transverse energy. Anode materials are selected to minimize scatter.

With a beam thus generated, we have related transport efficiency, compression, and superposition separately to the relative transverse energy of beams. These properties are related to $v/\gamma|_{\text{net}}$, and to the rate of formation of the background plasma current and its possible spatial distribution. We have demonstrated that even with the moderately cool beam described, good transport and compression are obtained, and superposition is total. However, these operations do not commute.

Continuing work based on the aforementioned principles is aimed at optimizing transport and compression. It is based on providing initial minimal preionization and selecting injection risetime to reduce the energy loss at the front of the beam. Tailoring of net current spatial distribution and beamguide geometry are being pursued. Whereas

these data were taken with a v/γ from 1 to 3, experiments will shortly be extended to the multimegampere regime.

REFERENCES

1. J. C. Martin, DASA Review Meeting, 26-27, Jan. 1971, Washington, D. C.
2. J. J. Clark and S. Linke, IEEE Trans. 18: 322, 1971.
3. G. Yonas, P. Spence, B. Ecker, and J. Rander, PIFR-106-2, Physics International, August 1969.
4. K. R. Prestwich, Proc. 1971 IEEE Particle Accelerator Conference, 1-3, March, 1971, Chicago, Ill., to be published.
5. G. Cooperstein, DASA Review Meeting, 26-27, Jan. 1971, Washington, D. C.
6. L. P. Bradley, T. H. Martin, J. E. Boers, D. L. Johnson, and K. R. Prestwich, APS Meeting, Seattle, Wash., 25-27, Aug. 1971, to be presented.
7. Kai Siegbahn, Alpha, Beta, and Gamma Ray Spectroscopy, North Holland Publishing Co., 1966; pp. 4-7.
8. G. Yonas, B. Ecker, and P. W. Spence, Record 10th Symp. Electron, Ion, and Laser Beams, 21-23, May 1969, Gaithersburg, Md.; San Francisco Press, 1969.
9. M. L. Andrews, J. J. Bzura, H. E. Davitian, H. H. Fleischmann, and D. A. Hammer, LPS 15, Cornell University, Sept. 1969; and D. A. Hammer, Thesis, Cornell University, Sept. 1969.
10. J. Bzura and S. Linke, Bull. Am. Phys. Soc. 15: 1452, 1970.
11. G. Yonas, P. Spence, D. Pellinen, B. Ecker, and S. Heurlin, PIFR-106-1, Physics International, April 1969.

INTENSE RELATIVISTIC ELECTRON BEAM-PLASMA INTERACTIONS IN FINITE CAVITIES

SIDNEY PUTNAM

Physics International Co., San Leandro, Calif.

INTRODUCTION

Intense relativistic electron-beam propagation in neutral gas-filled drift chambers has been studied experimentally over the past several years. Depending on gas pressure and beam parameters, one observes, for example, regions of ion acceleration, relatively efficient beam transport, or highly unstable behavior.¹ To understand these different regimes, one must consider the time-varying electromagnetic (EM) beam-cavity interactions with boundary conditions appropriate to experimental configurations, as well as the beam dynamics. The full self-consistent problem is extremely complex, involving charge production processes and coupled EM-orbit equations and is probably ultimately amenable only to numerical solution. Nevertheless, most of the gross beam behavior can be understood with simple models. In this paper we discuss EM fields generated by beams in finite cavities and outline a procedure to calculate charge production in neutral gases which gives gas breakdown times in agreement with the data of Yonas and Spence.² The electrostatic field effects on low-pressure beam propagation are considered in some detail and a model for predicting transverse instability wavelengths is also given. Throughout the discussion we emphasize simple formulations of the important beam physics, which it is hoped will be of use for practical application.

ELECTROMAGNETIC FIELDS IN FINITE CAVITIES

QUASISTATIC MODEL-FIELDS BEFORE GAS BREAKDOWN. We first develop expressions for the EM fields in closed conducting cavities which include the effects of cavity endplates, variations in beam radius, charge/length, and density of background charge. Plasma effects are included only in terms of electrical (space charge) neutralization. We assume azimuthal symmetry (Fig. 1) and zero theta component of the beam current. Direct integration of the Maxwell equation

$$\nabla \times \vec{E} = -\frac{1}{c} \frac{\partial \vec{B}}{\partial t}$$

$$\text{gives } E_z = -\int_r^R \frac{\partial E_r}{\partial z} dr' - \frac{1}{c} \int_r^R \frac{\partial B_\theta}{\partial t} dr' \quad (1)$$

where we have imposed the boundary condition $E_z = 0$ at $r = R$. In the quasistatic limit we neglect the displacement current in the calculation of B_θ and assume that the radial electric field can be obtained from the electrostatic (ES) potential. We thus require that the time for light to travel twice the longest chamber dimension is small

compared to times of interest. The ES potential can be determined exactly:

$$\Phi = \int_0^R r' dr' \int_0^l dz' G(r, r', z, z') \rho(r', z') \quad (2)$$

$$\text{with } G(r, r', z, z') = \frac{8\pi}{R} \sum_{n=1}^{\infty} \frac{J_0(\lambda_n r/R) J_0(\lambda_n r'/R)}{\lambda_n [J_1(\lambda_n)]^2 \sin(\lambda_n l/R)}$$

$$\begin{cases} \sinh\left(\frac{\lambda_n}{R}\right) z \sinh\left(\frac{\lambda_n}{R}\right) (l - z'), & z \leq z' \\ \sinh\left(\frac{\lambda_n}{R}\right) (l - z) \sinh\left(\frac{\lambda_n}{R}\right) z', & z \geq z' \end{cases} \quad (3)$$

The charge density is ρ (esu/cm³) and λ_n are the roots of $J(x)$. We now make an ad hoc approximation for E_r to avoid the complications of Eq. (2): we note from the exact expression the term dropping off most slowly in z , and then find an approximate normalization factor. The chamber radius r is to be restricted to a range such that the z dependence is reasonably accurate for small z . This implies that $1 \leq R \leq 10$ length units, and henceforth we consider only such a range for R . Assuming a uniform beam current density, we write

$$\begin{aligned} E_r &= f(z) \frac{2\lambda}{a} r, \quad r \leq a \\ &= f(z) \frac{2\lambda}{r}, \quad r \geq a \end{aligned} \quad (4)$$

with $f(z) = 0, 0, l$. The beam charge/length (which may also have a z dependence) is denoted by λ . Equation (4) is exact at $z = l/2$ for λ constant. Two cases of interest are

$$\begin{aligned} \text{(i)} \quad l \leq R &> f(z) \approx \frac{4z(l-z)}{l^2} \\ \text{(ii)} \quad l &> R \end{aligned} \quad (5)$$

$$f(z) \approx \frac{1 - e^{-2.4z/R}}{(1 - e^{-2})}, \quad z \leq 2(R/2.4)$$

$$= 1, \quad 2(R/2.4) \leq z \leq [l - (2R/2.4)]$$

$$= \frac{1 - e^{-2.4(l-z)/R}}{1 - e^{-2}}, \quad [l - (2R/2.4)] \leq z \leq l$$

The E_r profiles for these two cases are sketched in Fig. 2.

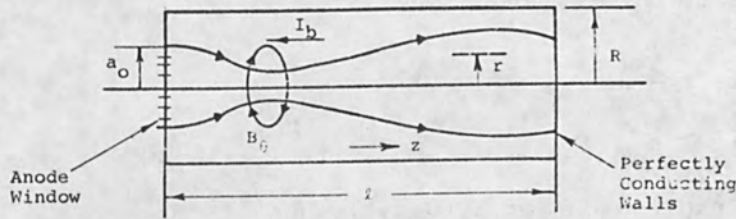


FIG. 1.--Beam chamber configuration; $a = a(z,t)$ = beam radius; l = length of cavity; R = radius of cavity; $\vec{B} = B_0 e_\theta$ = magnetic field; I_b = beam electron current.

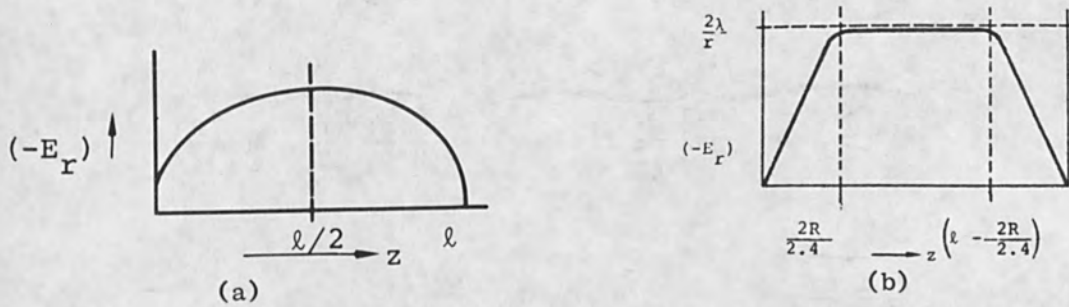


FIG. 2.--(a) Electrostatic fields for uniform electron beam in closed cavity ($l \lesssim R$); (b) Radial field for uniform beam when $l > R$.

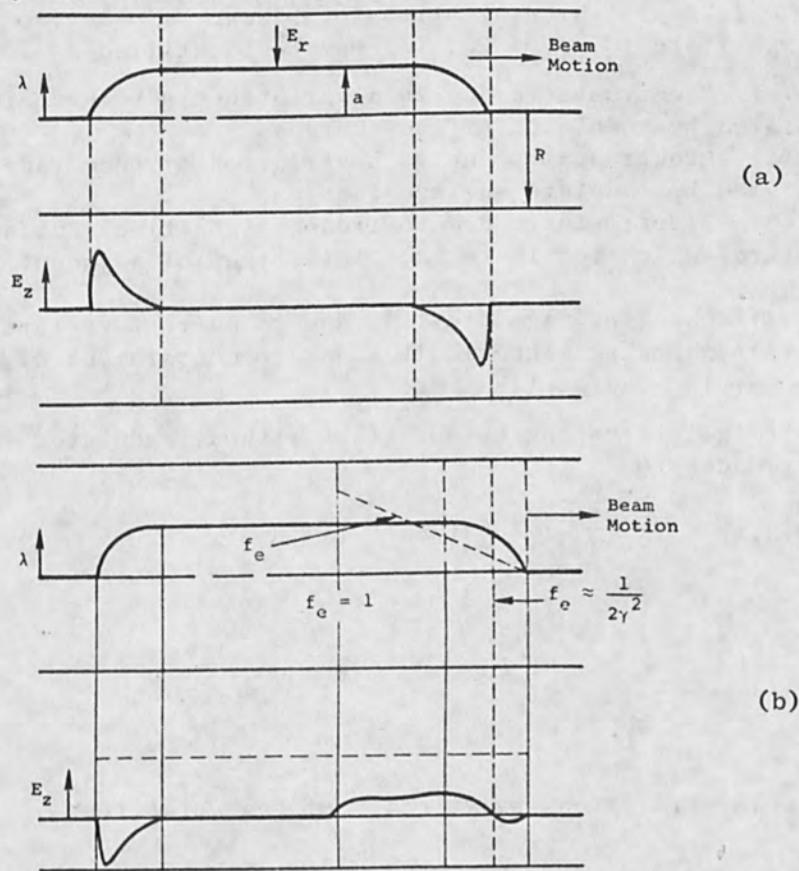


FIG. 3.--Sketches of E_z fields with and without ions: (a) long conducting pipe, no ions, $f_e = 0$; (b) long conducting pipe, f_e increases linearly behind beam front.

Returning to Eq. (1) and using

$$B_{\theta} = 2I/ca^2 r, \quad r \leq a$$

$$= 2I/cr, \quad r \geq a$$

we obtain an expression for $E_z(0, z, t)$ when $l < R$:

$$E_z(0, z, t) = - 2 \overbrace{\frac{\partial \lambda}{\partial z} \left[\frac{1}{2} + \ln \left(\frac{R}{a} \right) \right]}^{(1)} \overbrace{\frac{4z(l-z)}{l^2}}^{(2)} + \frac{2\lambda}{a} \overbrace{\frac{\partial a}{\partial z} \left[\frac{4z(l-z)}{l^2} \right]}^{(2)}$$

$$- 2\lambda \overbrace{\left[\frac{1}{2} + \ln \left(\frac{R}{a} \right) \right]}^{(3)} \overbrace{\frac{4}{l^2} (l-2z)}^{(3)} - \frac{2}{c} \overbrace{\frac{\partial I}{\partial t} \left[\frac{1}{2} + \ln \left(\frac{R}{a} \right) \right]}^{(4)}$$

$$+ \frac{2}{c} \overbrace{\frac{I}{a} \frac{\partial a}{\partial t}}^{(5)} \tag{6}$$

If $R > l$, a similar evaluation for E_z can be made from Eq. (5).

The field terms of Eq. (6) may be identified as follows:

(1) Electrostatic due to a variation in beam charge density/length modulated by endplate surface charges.

(2) Electrostatic due to a variation of beam radius with z modulated by endplate surface charges.

(3) Electrostatic due to induced (positive) surface charges at the endplates which terminate the field lines of adjacent beam (negative) charges.

(4) Changing magnetic flux due to current variation ($L dI/dt$).

(5) Changing magnetic flux due to containment of current within a time varying radius ($I dL/dt$).

It is interesting to note that without endplates (set $z = l/2$), Eq. (6) reduces to

$$E_z(0, z, t) = \frac{2}{\gamma_L} \frac{\partial \lambda}{\partial u} \left[\frac{1}{2} + \ln(R/a) \right], \tag{7}$$

$$u = \beta_L ct - z$$

$$\gamma_L = 1/\sqrt{1 - \beta_L^2}$$

$\beta_L c$ = forward streaming velocity of beam electrons

if we are not at the beam head or tail and assume a constant beam radius with varying charge/length. If we are within the current rise portion of a beam of electrons ($\partial \lambda / \partial u < 0$) streaming in the positive z

direction, E_z is in the negative z direction (i.e., in a direction to accelerate the front electrons) and is opposite in sign to the E_z field behind the head when the beam emerges from a conducting endplate. We can rewrite Eq. (7) as

$$E_z|_{r=0} \text{ (V/cm)} = \frac{(-)4}{\gamma^2 \beta_L^2} \frac{I^P \text{ (A)}}{t_r \text{ (ns)}} \left[\frac{1}{2} + \ln(R/a) \right] e^{-\alpha u} \quad (8)$$

where $I_b = I^P (1 - e^{-\alpha u})$ and (α^{-1}) is defined as a two e-folding length, $\alpha \beta_L c t_r = 2$. For $I^P = 5 \times 10^4$ A, $t_r = 20$ ns, $\gamma = 3$, $R = 6$, $a = 1$, and $\beta_L \approx 0.8$, $E_z \approx 4 \times 10^3 e^{-\alpha u}$ V/cm.

The effects of ions at rest can be easily included in the above equations by replacing λ by $\lambda(1 - f_e)$; $f_e \equiv \rho_{\text{ion}}/\rho_{\text{electron}}$ is the fractional electrical neutralization.

If we take $f_e = f_e(u)$, then Eq. (6) gives for constant beam radius

$$E_z(0, u) = + 2 \left[\frac{1}{2} + \ln(R/a) \right] \left[\frac{\partial \lambda}{\partial u} \left(\frac{1}{\gamma_L^2} - f_e \right) - \lambda \frac{\partial f_e}{\partial u} \right] \quad (9)$$

and E_z reverses sign when

$$\lambda \frac{\partial f_e}{\partial u} = \left[(1/\gamma_L^2) - f_e \right] \frac{\partial \lambda}{\partial u} \quad (10)$$

If both λ and f_e increase linearly behind the beam front, Eq. (10) is satisfied when $f_e = 1/2\gamma_L^2$. Figure 3 shows the effects of ions on E_z qualitatively.

After $f_e = 1$, only the inductive components of E_z remain and the endplates can be ignored. Thus, for $\tau_N \lesssim t < t_B$, i.e., the time between electrical neutrality τ_N and gas breakdown t_B ,

$$E_r \approx 0$$

$$E_z(0, z, t) \approx \frac{2}{c} \frac{dI}{dt} \left[\frac{1}{2} + \ln(R/a) \right] + \frac{2}{c} \frac{I}{a} \frac{\partial a}{\partial t} \quad (11)$$

and if the beam radius is approximately constant, Eq. (11) reduces to

$$E_z \text{ (V/cm)} \approx \frac{2I^P \text{ (A)}}{t_r \text{ (ns)}} \left[\frac{1}{2} + \ln(R/a) \right] \quad (12)$$

for $I = I^P t/t_r$, $t \leq t_r$.

FIELDS AFTER GAS BREAKDOWN. The time for changes in the magnetic field or the net current after gas breakdown is the magnetic diffusion time t_d , which we define as the time for the field to diffuse a distance of the order of the beam radius:

$$t_d \approx 4\pi\sigma a^2/c^2 \quad (13)$$

where σ the conductivity (sec^{-1}) after breakdown. When t_d is much longer than the remaining beam pulse width, the net current is approximately constant and an estimate of E_z can be obtained by assuming that $I_{\text{net}}(t > t_B) \approx I_{\text{beam}}(t = t_B)$, giving

$$E_z \approx \frac{I_b(t) - I_b(t_B)}{\pi a^2 \sigma} \quad (14)$$

This field places a limit on beam transport efficiency for times after breakdown, or for beams injected into pre-ionized plasmas. If we consider, for example, transport in an external B_z plasma system with a conductivity of 100 mhos/cm, corresponding to a fully ionized hydrogen plasma of a few volts temperature, a beam with current density of 10^5 A/cm would lose 100 keV/m of transport.

We have now outlined procedures to estimate EM fields at all times of interest for intense beams injected into neutral gases. We have assumed that the beam current profiles were specified and have not considered orbit or beam-envelope dynamics. The utility of the equations for beam transport problems is, of course, that one can set up EM limits on beam-transport efficiency for desired beam and chamber parameters. Moreover, if E_z is sufficiently small to ensure that the beam streaming velocity does not change appreciably over distances of interest, one can apply with confidence beam-envelope equations such as the Kapchinsky-Vladimirsky equation,³ which do not consider E_z field effects.

EXACT EM SOLUTIONS FOR A BEAM PENETRATING AN ENDPLATE IN A FINITE-RADIUS CHAMBER

The discussion above assumes that the beam has already traversed the drift chamber. We now consider exact solutions to Maxwell's equation for a beam penetrating a chamber endplate and present sufficient conditions for neglect of endplate effects. The material here is of interest for low-pressure beam transport in ion acceleration modes in which electrostatic fields dominate and it shows the importance of finite chamber boundaries. The details of the calculations are given in Ref. 4.

It turns out that an endplate has two effects on the EM fields. One, primarily electrostatic, reverses the direction of E_z near the endplate and, of course, shorts out the radial electric field. The other is the generation of a radiated field component as surface charges are accelerated by the beam. This field gives rise to precursor fields traveling at the velocity of light and to oscillatory fields near the beam front under certain conditions. The configuration used in the calculations is shown in Fig. 4.

A sufficient criterion for neglect of field oscillation is that

$$\sqrt{(ct)^2 - z_f^2} \gg R/2.4, \quad 1 \lesssim R \lesssim 10 \text{ length units} \quad (15)$$

where z_f is the beam front position. Another way of stating Eq. (15) is that the light signal must have traveled "far beyond" the beam

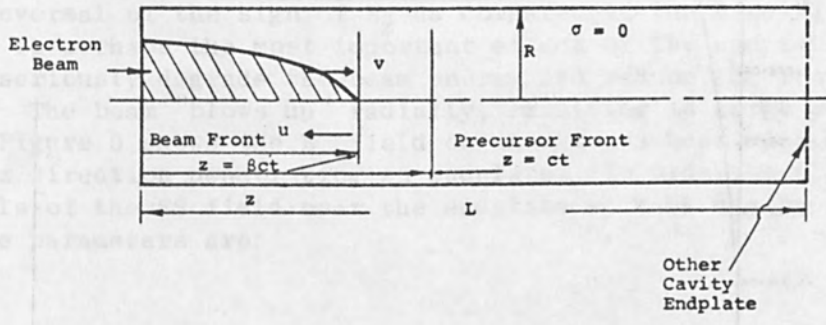


FIG. 4.--Open-ended pipe configuration.

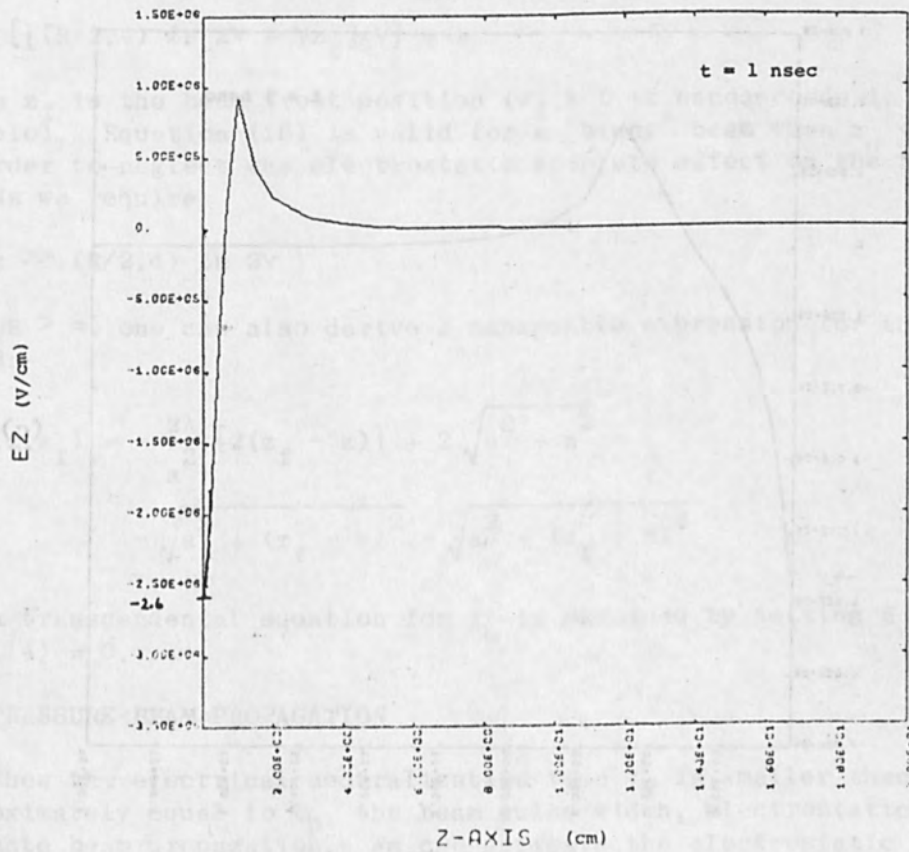


FIG. 5(a)

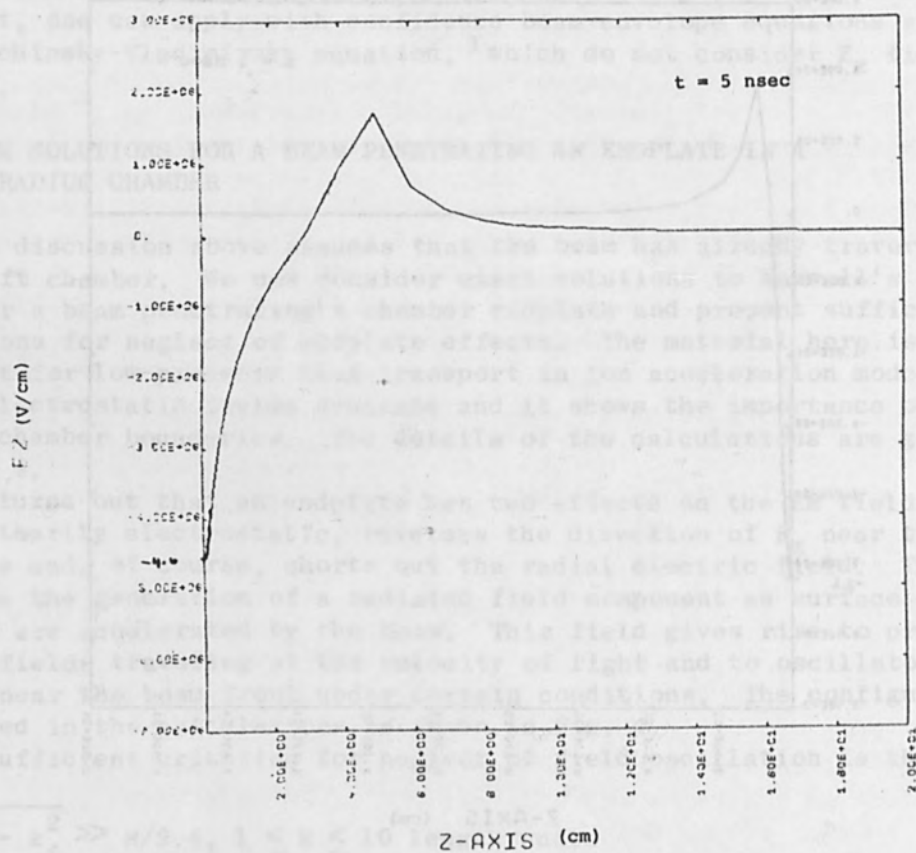
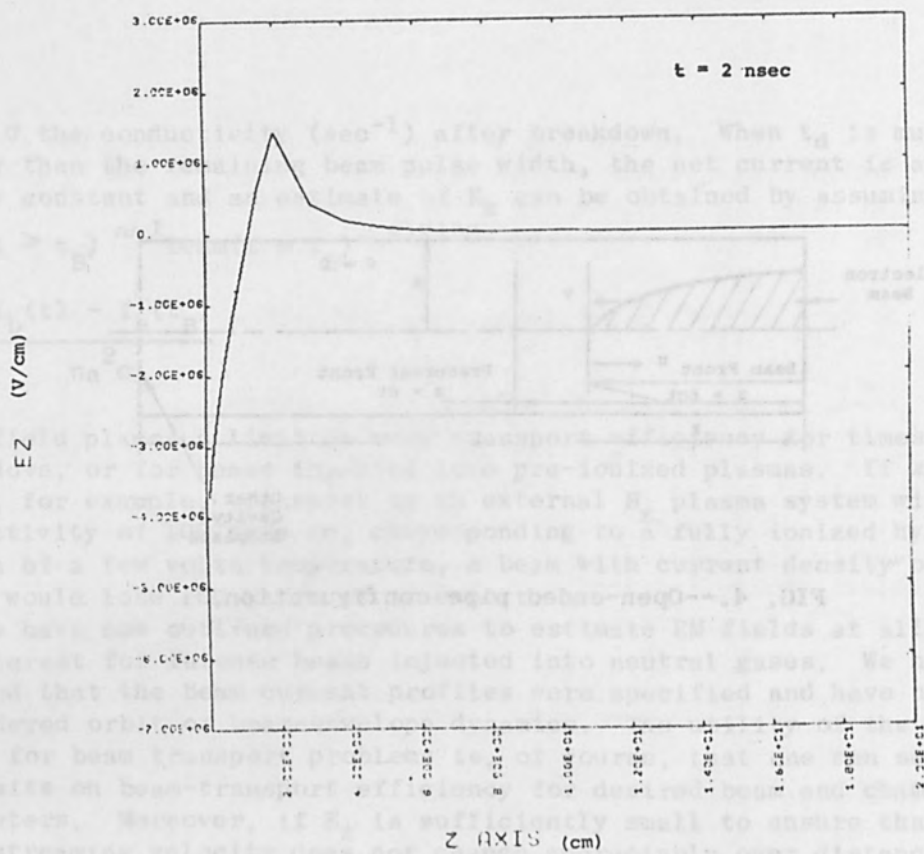


FIG. 5.--Longitudinal electric field on axis for beam penetrating endplate in finite-radius cavity: (a) $t = 1$ sec; (b) $t = 2$ sec; (c) $t = 5$ sec.

front. One would therefore not expect this effect to be important for low-energy beams. A typical oscillation amplitude, for example, would be about 10^3 V/cm with 5×10^4 A, 1 MeV beam, 20 ns risetime, and 1 cm radius in a pipe of radius 6 cm.

The reversal of the sign of E_z as compared to the case without endplates is perhaps the most important effect of the endplate, one that can seriously degrade the beam energy and reduce the front velocity. The beam "blows up" radially, resulting in large energy losses. Figure 5 shows the E_z field on axis for a beam with current in positive z direction penetrating an endplate. In order to illustrate the details of the ES field near the endplate we have chosen a "slow" beam. The parameters are:

$$\beta_L \approx 1/30$$

$$t_r \approx \text{risetime} \approx 0.1 \text{ ns}$$

$$R = 6 \text{ cm}$$

$$a \approx 1 \text{ cm (Gaussian radial current variation)}$$

$$I^P = \text{peak current} \approx 1.77 \times 10^3 \text{ A}$$

The reversal of the sign of E_z occurs at the crossover distance z_c and can be estimated from

$$z_c \approx \left\{ \left[\frac{R}{2.4} \ln 2\gamma + \gamma z_f \right] / \gamma \right\} + 1 \quad (16)$$

where z_f is the beam front position ($z_f \times t$ in nanoseconds in the above example). Equation (16) is valid for a "blunt" beam when $z_c \leq 2R/2.4$. In order to neglect the electrostatic endplate effect on the beam fields we require

$$z_f, z \gg \frac{R}{2.4} \ln 2\gamma \quad (17)$$

When $R > \infty$, one can also derive a manageable expression for the E_z field:

$$E_z(0, z, z_f) = -\frac{2\lambda}{a} \left\{ 2(z_f - z) \right\} + 2 \sqrt{a^2 + z^2} - \sqrt{a^2 + (z_f - z)^2} - \sqrt{a^2 + (z_f + z)^2} \quad (18)$$

and a transcendental equation for z_c is obtained by setting E_z in Eq. (14) = 0.

LOW-PRESSURE BEAM PROPAGATION

When the electrical neutralization time τ_N is smaller than or approximately equal to t_p , the beam pulse width, electrostatic effects dominate beam propagation. We can estimate the electrostatic potential well depth Φ for a beam penetrating a cavity approximately as

$$\Phi(V) \approx \frac{60 I(A)}{\beta_L} [(1/2) + \ln(R/a)] (1 - e^{-2.4z_c/R}) \quad (19)$$

$$z_c \lesssim 2(R/2.4), 1 \lesssim R \lesssim 10 \text{ length units}$$

If $\Phi(z_c)$ is much smaller than the beam kinetic energy, the beam propagation is not limited by the longitudinal electrical field, although space charge effects on radial motion must still be considered. However, if $\Phi(z_c) \geq$ beam kinetic energy, we define a length \bar{z}_c by $\Phi(\bar{z}_c) =$ kinetic energy and, if we approximate the exponential factor in Eq. (19) by a straight line, we obtain

$$\bar{z}_c \text{ (cm)} \approx \frac{3.4 \times 10^4}{I^P(A)} \left(\frac{t_r}{t_v}\right) \frac{\sqrt{1 + V^P} \sqrt{V^P}}{(1 + 2V^P)} \quad (20)$$

$$\cdot (R/2.4) \frac{1}{(1/2) + \ln(R/a)}, \bar{z}_c \lesssim 2(R/2.4)$$

where V^P = peak electron kinetic energy in MeV, t_r is the current rise time, t_v is the electron kinetic energy rise time, and I^P is the peak beam current. The voltage and current rise have been taken as linear and $\beta_L \approx \beta$. If $I^P \approx 30$ kA, $t_r/t_v \approx 2$, $V^P \approx 1$ MeV, $R \approx 6$ cm, and $a = 1$, we obtain $z_c \approx 1.2$ cm. One can estimate a front velocity $(\beta_{fc})^{ES}$ by assuming that the front travels a distance \bar{z}_c over a time scale of τ_N :

$$\beta_f^{ES} \approx \frac{\bar{z}_c}{c\tau_N} \quad (21)$$

This velocity is very slow for high- v/γ beams and places a severe constraint on high- v/γ beam propagation efficiency at low pressures. Ion acceleration, as proposed by Rostoker,⁵ is due to the ES field near the beam front. The front velocity accelerates as τ_N in Eq. (21) is effectively decreased by pre-ionization ahead of the beam front.

Our discussion of the longitudinal ES field suggests a qualitative picture of the beam front velocity behavior at low pressures above the ion acceleration cutoff. The beam front moves slowly according to Eq. (21) until the charge neutralization front has moved out beyond $z \approx 2(R/2.4)$. Then the endplate effect is gone and the front velocity should increase. However, the front velocity is still less than βc , and now depends on the "sharpness" of both the beam front and the space-charge neutralization front. As the beam approaches the downstream endplate an increase in front velocity is again to be expected since the field reverses direction as ES force lines start to terminate on the surface charges of the endplate.

CHARGE PRODUCTION

In order to achieve reasonable beam-transport efficiency, background gas pressure must be such that breakdown occurs over times $< t_r$. We now argue a model of charge production to estimate breakdown times and current neutralization. Secondary-electron orbit sketches and

typical field magnitudes are shown in Fig. 8 for a beam in a drift chamber. We assume that the beam front is far away from the chamber endplates ($z_f \gg 2R/2.4$). Two processes contribute to background gas ionization: direct collisional ionization by the beam electrons, and avalanching of secondary electrons by the electric field in appropriate E/P ranges, P being the gas pressure. From Fig. 6, we note that beam-driven electric fields vary several orders of magnitude from the time of front arrival to gas breakdown time t_B , and that the highest fields exist for $t \leq \tau_N$. In fact, these fields are usually sufficiently high at pressures of interest here (0.1 to 1 torr) to cause the secondary electrons to become relativistic over distances of the order of the beam radius and the ionization cross section drops to values around $\sim 10^{-18}$ cm, in comparison to typical Townsend discharge theory where cross sections are used for electrons with energies up to the kilovolt range ($\sim 10^{-16}$ cm cross section). Moreover, until $f_e \approx 1$ is achieved, the secondary electron motion is primarily radial and the flow is out of the beam channel. Thus, it seems reasonable to neglect avalanching in the beam channel until $f_e \approx 1$. When $t > \tau_N$, $|E| \approx E_z \approx 10^3$ V/cm (typically), we consider avalanche effects to be important and, as shown in the previous discussion, the electric field is inductive. With these arguments in mind, we outline an ad hoc charge production calculation procedure for high current electron beams:

(1) Calculate τ_N , the time for $f_e \approx 1$, from collisional ionization effects [$\tau_N(\text{ns}) \approx 0.7/\beta_L P(\text{torr})$ for air].

(2) From the time of beam front arrival at the point of interest up to $t = \tau_N$, secondary electrons escape instantaneously out of the beam channel and no significant electron avalanching occurs within the beam channel.

(3) From $t = \tau_N$ to $t = t_B$, the breakdown time,

$$E_z \text{ (V/cm)} \approx \frac{2I^P \text{ (A)}}{t_r \text{ (ns)}} [(1/2) + (\ln R/a)]$$

assuming a linear current rise, where R = chamber radius, a = beam radius, and t_r = beam risetime. From E_z above and the pressure of interest, determine t_i , the mean ionization time (Townsend discharge theory).

(4) Equation of charge production:

$$\frac{dn_e^s}{dt} = \underbrace{\frac{\alpha I(t)}{\pi a^2}}_{\text{collisional ionization}} + \underbrace{\frac{n_e^s}{t_i}}_{\text{avalanche}} - \underbrace{\nabla \cdot \Gamma}_{\text{transport}}$$

$\alpha = 5.8 \times 10^{17} P$ (torr) for air, n_e^s = secondary electron number density. Neglecting the transport term, and assuming E_z constant,

$$n_e^s(t - \tau_N) = \frac{I^P}{\pi a^2} (t_i/t_r) [e^{t - (\tau_N/t_i)} (t_i + \tau_N) - (t + \tau_N)]$$

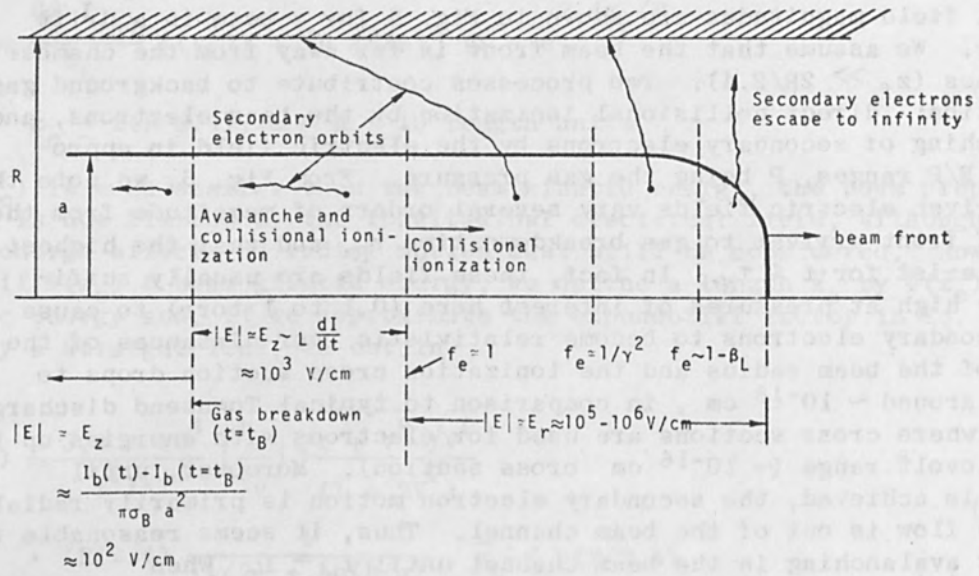


FIG. 6.--Phenomenology of charge production in neutral gas.

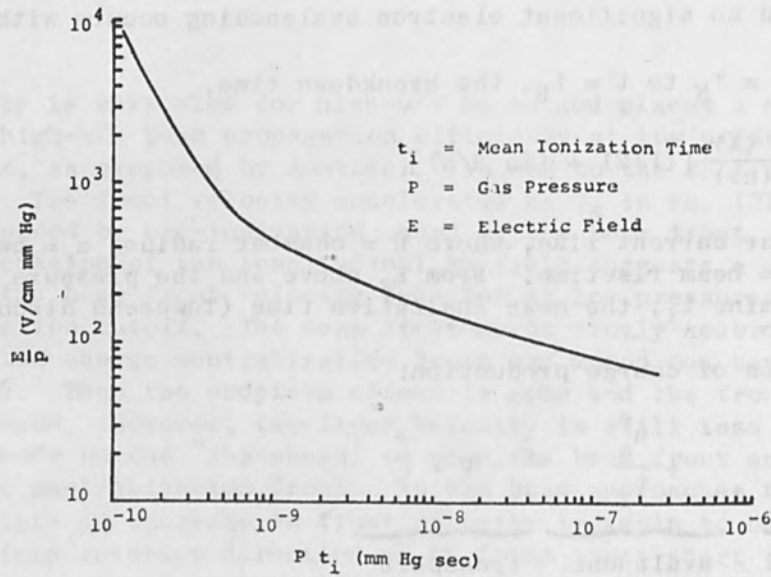


FIG. 7.--Plot of E/p versus Pt_i for air.

(5) Define breakdown as $n_e^S(t_B) = \delta n_b(t_B)$
 Empirically determined $\delta \approx 226$

(6) Obtain t_B from the transcendental equation:

$$\frac{e^{-t_B - (\tau_N/t_i)}}{t_B} \approx \frac{80}{P(\text{torr})} \frac{1}{t_i \beta_L} \frac{1}{(t_i + \tau_N)} \text{ for air (all times in ns).}$$

A plot of E/P versus $P t_i$ for air is shown in Fig. 7.

Breakdown time calculations from the above recipe are compared with the Yonas and Spence data in Table I. The beam parameter range over which the above model is relevant is not clear, inasmuch as detailed breakdown data exist only from the Yonas and Spence work. It is quite likely that widely different beam parameters at least would require adjustment of the charge multiplication factor δ .

TABLE I. Breakdown time calculations.

P (torr)	τ_N (ns)	t_i (ns)	t_B (ns) calculated	t_B (ns) measured
0.1	13.0	1.0	20.7	20
0.3	4.3	0.47	7.8	10
0.5	2.6	0.34	5.1	5
Agreement is within experimental error				

Parameters

$$I^P = 4 \times 10^4 \text{ A} \quad a^2 = 2.5 \text{ cm}^2$$

$$t_r = 20 \text{ ns} \quad \beta_L = 0.54$$

$$E_z = 2 \times 10^3 \text{ V/cm} \quad \gamma = 1.5$$

$$R = a$$

TRANSVERSE INSTABILITY

Intense relativistic beams exhibit strong transverse instabilities in appropriate pressure ranges. A typical time-integrated pinched beam self-photo at 0.1 torr is shown in Fig. 8; the beam electrons appear to follow a hose-like plasma channel. This behavior is to be contrasted with the transversely unstable high-pressure ($P > \sim 100$ torr) propagation where the beam is also pinched, but appears rapidly to blow up into a smeared, filamentary structure. Although current neutralization is small for both pinched modes, the plasma conductivity is high at low pressures ($\sigma \gtrsim 10^{13}$ - 10^{14} /sec) and very low at high pressures because of the high electron plasma collision frequency. The differences in the plasma conductivity suggest markedly different growth time regimes for



FIG. 8.--"Frozen hose" instability of a pinched beam. Instability wavelength is ~ 16 cm. Beam parameters: pressure 0.1 torr; beam current ~ 25 kA; average kinetic energy ~ 3 MeV; current risetime ~ 10 ns. Beam is traveling from right to left.

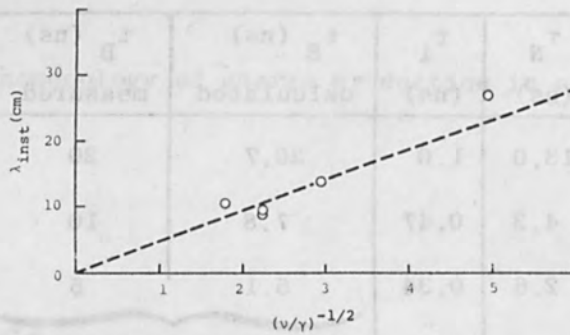


FIG. 9.--Instability wavelength as function of $(v/\gamma)^{-1/2}$, $D \gg d$. Values of v/γ are approximate and are obtained from multiple calorimetry. Beam kinetic energy is approximately 3 MeV, chamber pressure 100 μ , and $d = 2$ cm.

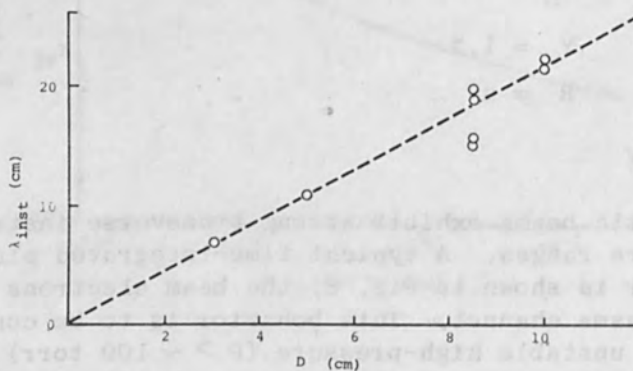


FIG. 10.--Instability wavelength in guide tube; v/γ is assumed to have approximately constant value (0.3); kinetic energy is approximately 3 MeV, chamber pressure 100 μ .

transverse instabilities. For low pressures, the high plasma conductivity after breakdown gives rise to a velocity-dependent drag force on beam "whipping" arising from the resistance of the plasma to motion of the magnetic lines of force as the beam undergoes displacement. When the angular frequency of the perturbation is much less than the plasma conductivity σ (sec^{-1}), or when the skin depth of the magnetic field penetration of the plasma is of the order of a few beam radii or less, we adopt the conventional terminology⁶ and refer to the instability as resistive. Thus, before gas breakdown in the low-pressure mode, the instability is nonresistive; after breakdown, resistive. For high pressures, a nonresistive mode would apply throughout the beam pulse.

Rather idealized theoretical models⁷ for nonresistive growth predict the wavelength of the fastest growing transverse oscillation modes:

$$\lambda_{\text{inst}} = \frac{\pi}{\sqrt{2}} \left(\frac{v}{Y}\right)^{-1/2} d \quad d \ll D \quad (22)$$

$$= \frac{\sqrt{\pi}}{2} \left(\frac{v}{Y}\right)^{-1/2} D \quad d \sim D$$

$$v = I(A)/17\,000\beta_L$$

where $d(D)$ is the beam (chamber) diameter. Figures 9 and 10 show experimentally measured wavelengths, showing reasonable agreement with Eq. (22). After gas breakdown, resistive-mode theory⁸ suggests a growth rate $\approx (t_d)^{-1}$ where t_d is the magnetic diffusion time (Eq. 13). For $\sigma \gtrsim 10^{13}/\text{sec}$, $t_d \gtrsim 100$ ns, and the beam path developed in the nonresistive mode thus appears "frozen" over times of the order of the beam pulse.

To summarize, we outline a procedure to estimate instability wavelengths for the low pressure case:

- (1) From the charge production rules given above, calculate the gas breakdown time at the pressure of interest and determine the beam current at breakdown time.
- (2) The instability wavelength may be estimated by using the above current value to determine v in Eq. (22).

REFERENCES

1. A review of the experimental observations is given by S. E. Graybill, "Dynamics of pulsed high current electron beams," IEEE Transactions on Nuclear Science, June 1971; Proceedings of the March 1971 Chicago National Accelerator Conference.
2. G. Yonas and P. Spence, in L. Marton (ed.), Record 10th Symp. Electron, Ion, and Laser Beam Technology, San Francisco Press, 1969; p. 443.
3. A. Garren, Thin lens optics with space charge, University of California Lawrence Radiation Laboratory, Berkeley, Calif. UCRL-19313, August 1969.

4. S. Putnam, Theoretical electron beam studies, Physics International Co., San Leandro, Calif., PIFR-105, April 1970.
5. N. Rostoker, Laboratory of Plasma Studies, Cornell University, Ithaca, N.Y., LPS 21, July 1969.
6. S. Weinberg, J. Math Phys. 8: 614, 1967.
7. D. Finkelstein and P. Sturrock, in J. Drummond, ed., Plasma Physics, McGraw-Hill, New York, 1961; also B. Chirikov, Plasma Physics, J. Nuc. Energy 8c: 455, 1966.
8. H. Lewis, Stability of a relativistic beam in a plasma, IDA Jason Summer Study Group Report, June 1960.

FIG. 1. Plot of the growth rate γ versus the normalized distance z/λ_D for a beam with $\beta = 0.5$. The solid line represents the growth rate calculated from the dispersion relation (13), and the dashed line represents the growth rate calculated from the asymptotic expansion (14). The growth rate is zero at $z/\lambda_D = 0$ and increases as z/λ_D increases.



where $\beta(D)$ is the beam (electron) density, β is the beam velocity, and λ_D is the Debye length. The growth rate γ is the imaginary part of the dispersion relation (13). For $\beta \leq 10^{-3}$ sec, $\beta \leq 100$ m, and the beam path developed in the asymptotic expansion (14) is valid. The growth rate γ is zero at $z/\lambda_D = 0$ and increases as z/λ_D increases.

(1) From the charge production rates given above, calculate the gas breakdown time at the pressure of interest and determine the beam current at breakdown time.

(2) The instability wavelength may be estimated by using the above current value to determine λ_D in Eq. (13).

REFERENCES

1. A review of the experimental observations is given by S. E. Graybill, "Dynamics of pulsed high-current electron beams," IEEE Transactions on Nuclear Science, June 1971, Proceedings of the March 1971 Chicago National Accelerator Conference.
2. G. Jones and S. Chou, in S. Chou, ed., Proceedings of the 1969 Electron, Ion, and Laser Beam Technology, San Francisco Press, 1969, p. 113.
3. A. Garren, "A review of the experimental observations," University of California, Lawrence Livermore Laboratory Report UCRL-7051, August 1969, p. 113.

SESSION ON ION SOURCES

ACCELERATION OF IONS BY RELATIVISTIC ELECTRON-BEAM-FORMED PLASMAS

S. E. GRAYBILL,^{*} W. H. McNEILL,^{**} and J. R. UGLUM⁺

Ion Physics Corporation, Burlington, Mass.

INTRODUCTION

This paper presents recent experimental results on the acceleration of ions by pulsed electron beams to energies greater than the electron energy. A theoretical model consisting of an accelerating potential well is discussed. In 1956, Veksler¹ proposed several theoretical schemes by which collective interactions between ions and moving beams could lead to high-energy ions with the maximum ion energy being greater than the accelerating beam by the mass ratios of the particles. These proposals led to, for example, the development of the ERA. The first observations of energetic ions that had been accelerated by intense relativistic electron beams were made by Graybill and Uglum². Since then, the following new observations have been made: (1) in some cases ion energy depends on the pressure of the neutral gas into which the beam is injected; (2) momentum analyses have determined the charge states of accelerated ions and have confirmed that the energy depends linearly on ion charge state; and (3) range measurements confirm that the ion species accelerated is always that of the neutral background gas.

ELECTRON BEAM

A dc type of electron beam generator provided the pulsed electron beam. The current peak was 30 kA, the peak voltage 1.5 MV, and the pulse length 50 ns (FWHM). This beam passed through a thin-foil transmission window in a drift tube of 15 cm diameter and 50 cm length.

TIME OF FLIGHT MEASUREMENTS

Higher time resolution in the time of flight measurements have shown that the ion energy depends on neutral gas pressure for hydrogen and deuterium. In the experimental arrangement (Fig. 1), most of the electron beam is intercepted by the end of the large drift pipe. Remaining electrons are swept to the walls of the 2.5-cm-diam drift pipe by a 3-kG magnet. Any accelerated ions are detected by a movable Faraday probe. At each firing of the machine, only one data point can be obtained. However, shot-to-shot variation in the ion pulse is only ± 1 ns. The time of flight information is obtained by measuring ion pulse arrival times at three different locations. As the probe is moved longer cables, whose electrical length had been determined by TDR techniques, are inserted between the probe and oscilloscope.

* Now at Harry Diamond Laboratories, Washington, D. C.

** Now at Simulation Physics, Inc., Bedford, Mass.

+ Now at Energy Sciences, Inc., Burlington, Mass.

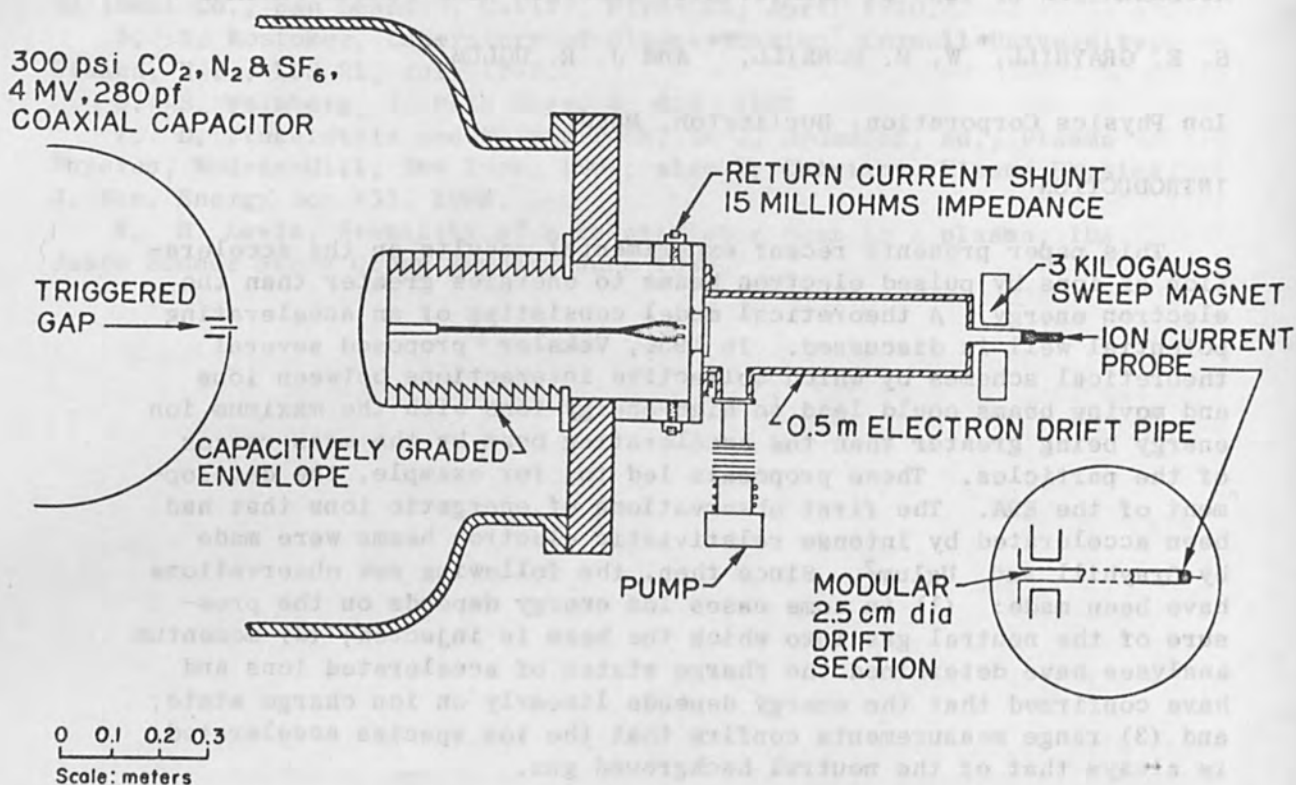


FIG. 1.--Experimental arrangement for beam plasma ion detection.

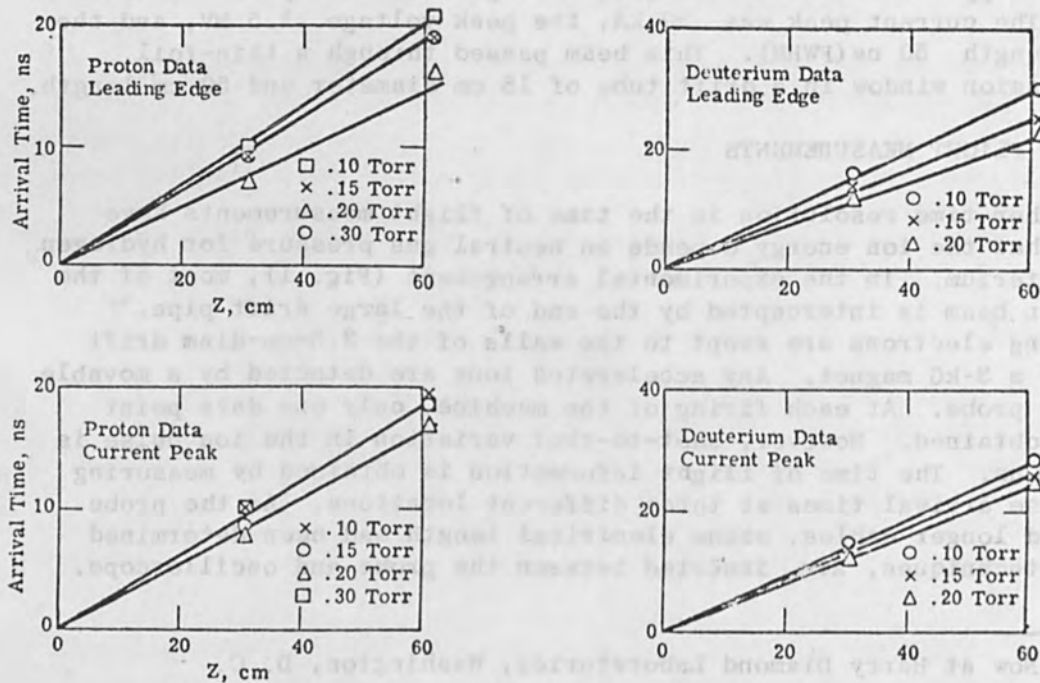


FIG. 2.--Ion time of flight for hydrogen and deuterium.

In this way a 5-ns/cm sweep rate could be maintained for all probe positions, which yielded high resolution.

The results of the time of flight measurements are shown in Fig. 2 for hydrogen and deuterium. The velocities of the leading edge of the pulse and of the current peak were measured with only slight differences. Each data point represents the average value of arrival time for two or three measurements.

The pressure dependence of proton and deuteron energies are shown in Fig. 3. Helium and nitrogen showed no pressure dependence.

RANGE-ENERGY MEASUREMENTS

Range measurements were used to confirm the identity of the accelerated ions. Various thicknesses of aluminum foil absorber were placed in front of the Faraday detector and the plots of relative transmitted current (Fig. 4) were obtained. The range for each ion species was found by extrapolating these data. The energy for each species was obtained from range-energy curves, which show that the various species have quite different range-energy curves for aluminum.

Assuming that the energetic ion species was that of the neutral gas, the energy obtained from these measurements agreed with time of flight measurements for energy.

MOMENTUM ANALYSIS

In order to understand the mechanism by which the ions are accelerated by the electron beam, the charge state of the accelerated ion must be determined by means of a magnetic spectrometer (Fig. 5). A thin slit (1 x 5 mm) was placed at the entrance to the small curved pipe attached to the end of the large drift tube. The small pipe was differentially pumped down to a good vacuum (about 10^{-5} torr). Any electrons entering the pipe are swept out by the electromagnet.

After passing through the magnetic field region, the ions must pass through another slit which is used to improve resolution. A solid-state detector was used to measure the amount of ion beam transported through the system.

Assuming only that the magnet field of the electromagnet varies linearly with applied current, the following relation holds:

$$\frac{P}{Q} = k I$$

where P is the momentum of the ion, Q its charge state, and I the electromagnet current. The system was calibrated, i.e., k was determined by changing the driving current for a series of shots with hydrogen and then deuterium. The P/Q ratios for both were already known from the time of flight work. These data are shown in the upper part of Fig. 6. The lower curves than show the results for helium and nitrogen. The arrows show where the indicated species charge states should occur from the calibration. The helium data show that only completely ionized atoms are accelerated. The nitrogen data show that highly stripped ions are formed, with the main contribution coming from six-times-ionized nitrogen.

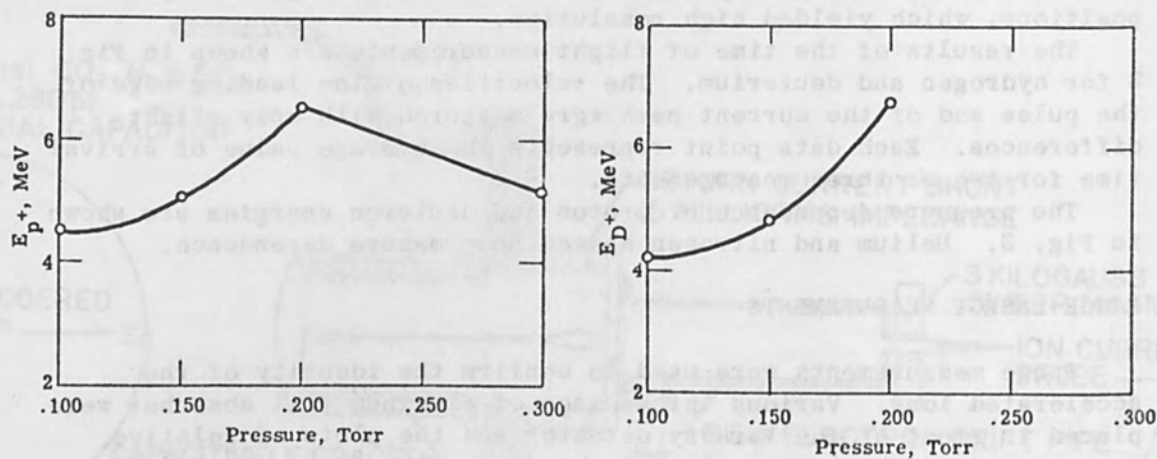


FIG. 3.--Pressure dependence of proton and deuteron energies.

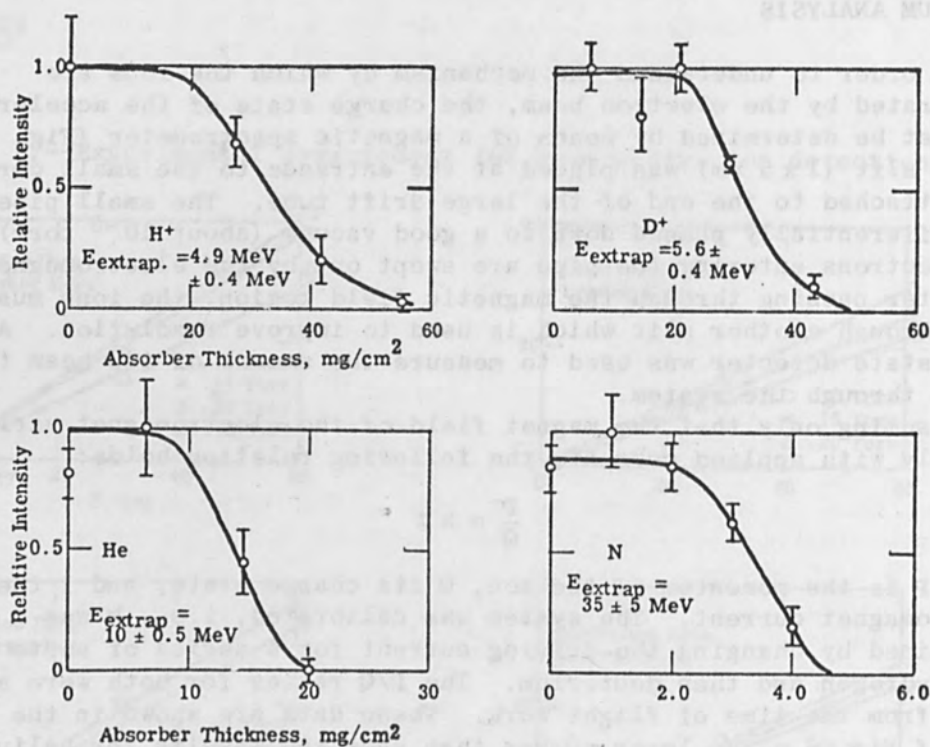


FIG. 4.--Range measurements of collectively accelerated ions.

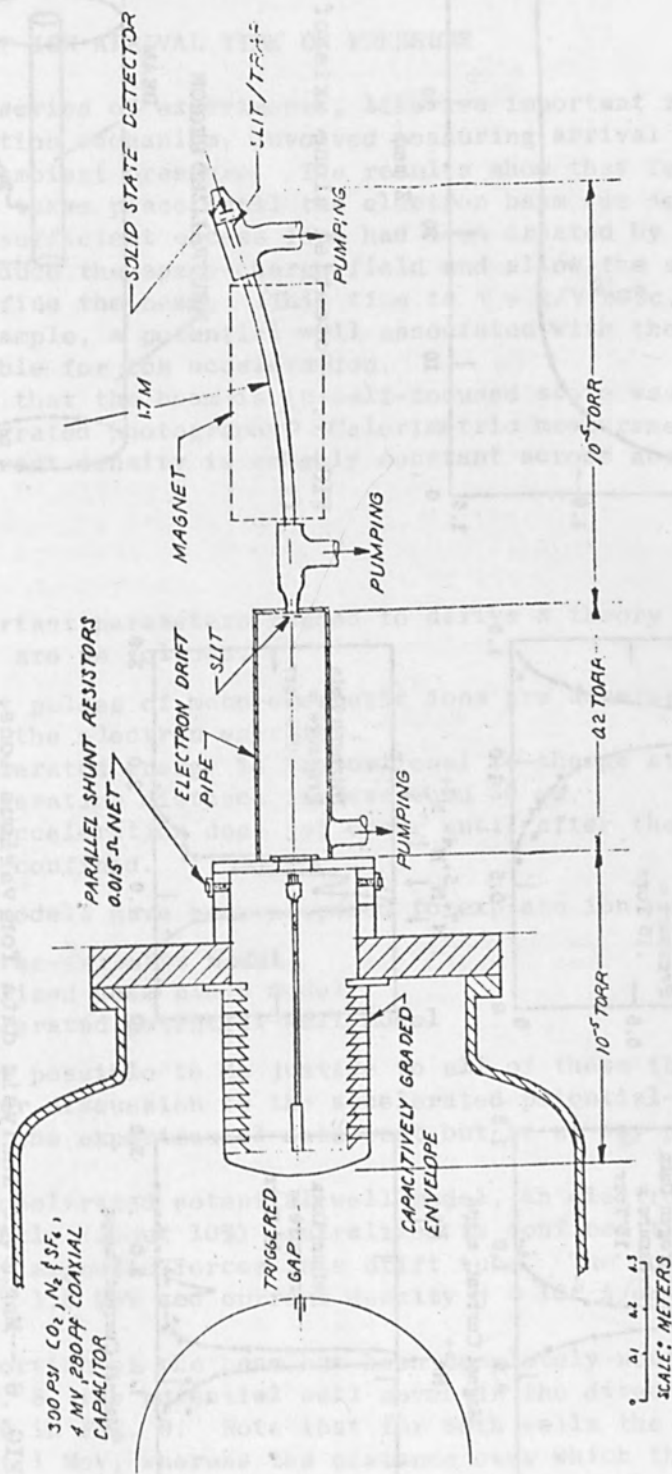


FIG. 5.--Experimental arrangement for collective accelerator momentum analysis.

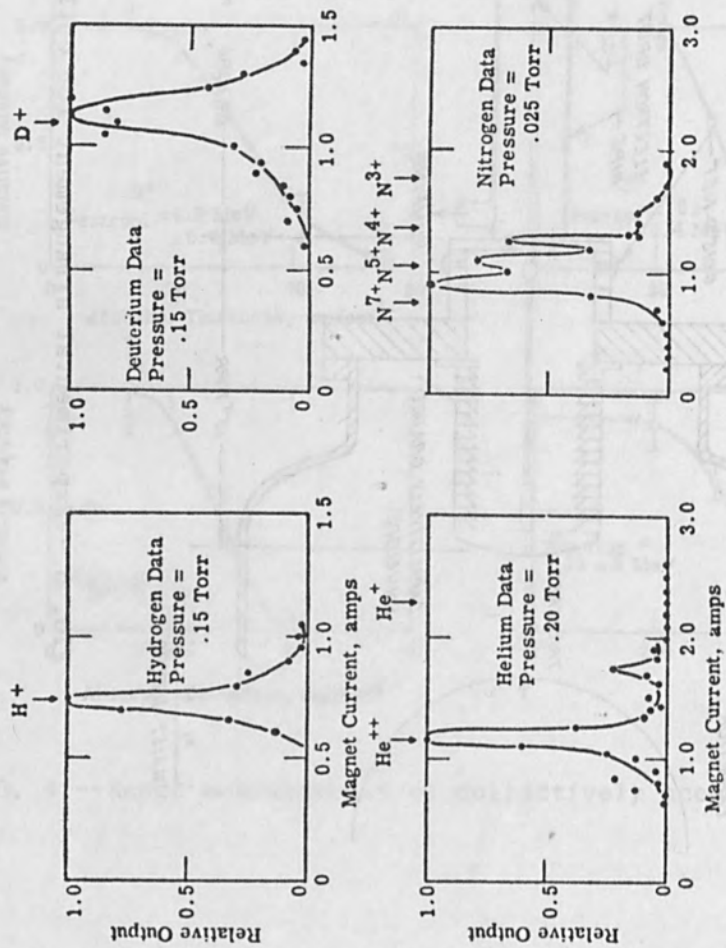


FIG. 6.--Magnetic analysis data for various ions.

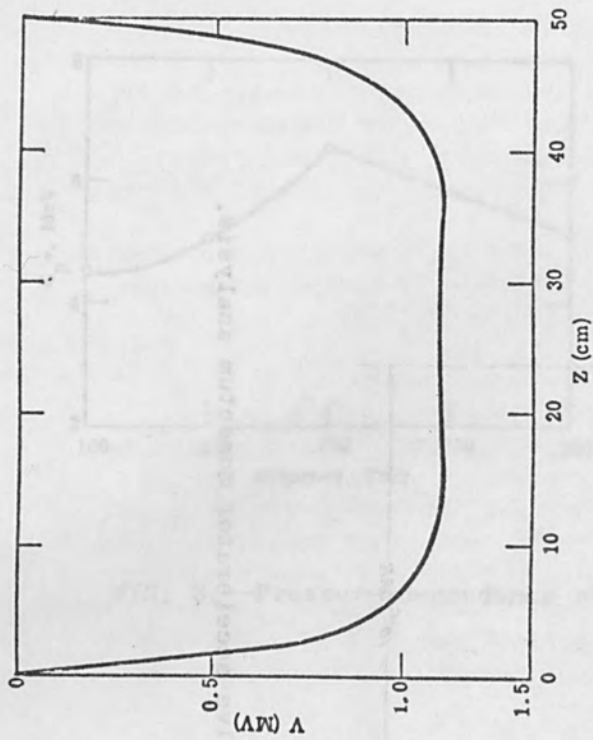


FIG. 7.--Potential along axis of drift tube ($A = 0$).

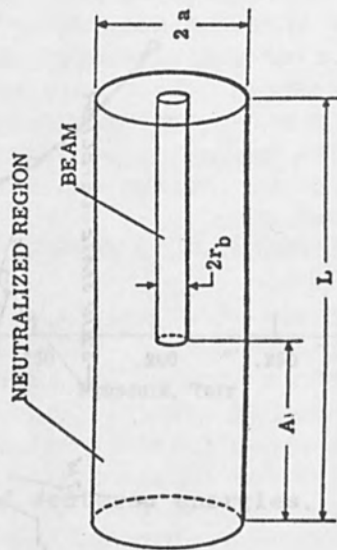


FIG. 8.--Beam-drift tube configuration.

The dependence of the ion energies on their charge state can then be determined, by combining the information obtained by momentum analysis with the energy information from the time of flight measurements. The dependence is linear. The implication of this as regards the acceleration mechanism will be discussed.

DEPENDENCE OF ION ARRIVAL TIME ON PRESSURE

Another series of experiments, likewise important in determining the acceleration mechanism, involved measuring arrival times as a function of ambient pressure. The results show that for hydrogen no acceleration takes place until the electron beam was neutralized, i.e., until sufficient excess ions had been created by primary ionization to reduce the space-charge field and allow the self-magnetic field to confine the beam. (This time is $\tau = 1/\gamma^2 n \sigma \beta c$.) Thus, for example, a potential well associated with the beam front is not responsible for ion acceleration.

The fact that the beam is in self-focused state was shown clearly by time-integrated photography. Calorimetric measurements indicate the beam current density is roughly constant across any portion of the beam.

THEORY

The important parameters needed to derive a theory to explain ion acceleration are as follows.

- (1) Short pulses of mono-energetic ions are accelerated to energies greater than the electron energies.
- (2) Accelerated energy is proportional to charge state.
- (3) Acceleration distance is less than 30 cm.
- (4) Ion acceleration does not occur until after the beam is magnetically confined.

Several models have been proposed to explain ion acceleration:

- (1) Inverse-Čerenkov model
- (2) Localized beam pinch model
- (3) Accelerated potential-well model

It is not possible to do justice to all of these theories here. We confine our discussion to the accelerated potential-well model, which seems to fit the experimental data best but in no way precludes any other theory.

In our accelerated potential-well model, an electron beam which is only slightly (about 10%) neutralized is confined to a radius about 1 cm by magnetic forces in a drift tube. The potential well for a beam of $V = 1.5$ MeV and current density $j = 10^4$ A/cm is shown in Fig. 7.

When a portion of the beam has been completely neutralized, as shown in Fig. 8, the potential well moves in the direction of the beam as shown in Fig. 9. Note that for both wells the depth of the well is about 1 MeV, whereas the distance over which the potential goes from zero to its maximum depth is about 5 cm. Thus, if that portion

of the electron beam near the entrance window is progressively neutralized, the potential well accelerates and an ion created initially in the well is trapped and accelerated.

The final energy that can be obtained by an ion accelerated by a well reaching a depth V_0 in a length L_0 is given by the following:

$$E_+ = \frac{eZ_1 V_0}{(M_1 a L_0 / eZ_1 V_0) - 1}$$

where $|a|$ is the acceleration of the well and is determined by the rate of neutralization near the entrance window.

The processes that lead to enhanced neutralization in that portion of the beam near the entrance aperture include ionization by primary beam electrons and ionization by secondary electrons. These secondary electrons are driven in a direction opposite to the beam velocity by the potential well itself. The electric field due to the potential well ($E_z \approx 200$ kV/cm) could in fact lead to an avalanche process. An acceleration rate based on extrapolating breakdown data has been determined for helium to be a 9×10^{-2} cm/ns². On the other hand, an acceleration rate has been calculated from Eq. (1), with $V_0 = 1$ MeV, $L_0 = 5$ cm, and the observed helium ion energy $H^{++} = 10$ MeV. This value is $a = 6 \times 10^{-2}$ cm/ns².

REFERENCES

1. V. L. Veksler, At. Energ. (USSR) 2: 427, 1957.
2. S. E. Graybill and J. R. Uglum, J. Appl. Phys. 41: 236, 1970.
3. J. J. Wachtel and B. J. Eastlund, Unpublished.
4. S. D. Putnam, Phys. Rev. Letters 25: 1129, 1970.
5. J. R. Uglum, S. E. Graybill, and W. H. McNeill, An accelerated potential well model to describe the acceleration of light ions by a relativistic electron beam, Bull. Am. Phys. Soc., November 1969.
6. N. Rostoker, Laboratory of Plasma Studies Report LPS 21, 1969.

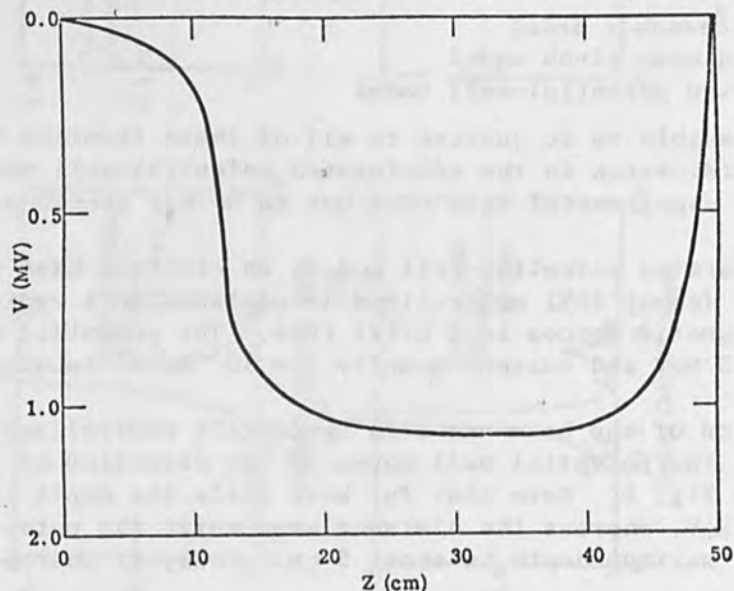


FIG. 9.--Potential along axis of drift tube (A = 12.5 cm).

LARGE-DIAMETER ION SOURCE WITH VARIABLE-BEAM CROSS-SECTION CONFIGURATIONS

BEN B. MECKEL

Physics Technology Laboratories, Inc., La Mesa, Calif.

A large-cross-section ion beam source has been developed and employed in R&D and industrial applications. The beam characteristics include variously shaped beam cross sections between 1 and 15 cm and more in breadth. Argon ion currents of 0.1 to 1.0 mA/cm² are obtained at energies of 250 to 5000 eV. The technique of attaining these values over large areas is by extracting ions from an rf-generated plasma through many apertures located in a contoured sheet electrode. Each extraction point acts as a single source or individual ion beam, and by expanding and shaping the sheet electrode surface, a wide spectrum of beam parameters and configurations can be obtained. For example, the extraction sheet can be designed to produce a focused beam or irregular cross-sectional shapes. The broad beam is space-charge neutralized by injecting thermal electrons, resulting in the reduction of coulomb spreading and charge accumulation on surfaces being bombarded. The beam is being used at present for sputter deposition of thin films, ion bombardment cleaning of metal and nonmetal surfaces, bias sputtering of films being deposited on dielectric substrates, sample thinning for electron microscopy, and surface preparation for topographical investigations. Other applications include molecular-beam studies, solar plasma wind simulation, and thermonuclear reactor ion sources.

INTRODUCTION

In many ion beam applications it would be desirable to have relatively high ion currents at low voltage over a large-diameter beam intersect area. Most ion beams at present operate on the duoplasmatron principle, in which all ions are drawn from a small orifice and must be allowed to expand in order to form large-diameter beams. In so doing the researcher loses density and density distribution control and is normally restricted to beam energies above several thousand electron volts. Several years ago members of our laboratory^{1,2} started research and development of a method for generating large ion beams of any diameter and shape using low voltages. Our results include current densities of several milliamps per square centimeter over cross-sectional beam areas of hundreds of square centimeters. The ion beams are space-charge neutralized with electrons. Movable Faraday cups are used to analyze the energy, energy distribution, density, and ion directionality as a function of position in the beam.

The following describes various apparatus designs developed for specific applications in such fields as surface bombardment for cleaning, thinning, or topographic etching of both metals and nonmetals, thin-film depositions, bias sputtering of the deposited films, production of medium energy molecular and atomic beams, solar-wind simulation, and other laboratory and applied requirements.

PRINCIPLE OF ION BEAM OPERATION

The ion beam source operates on the principle of the extraction of ions at many separate points from an rf-generated plasma. Each extraction point acts as a source of a very small individual ion beam which is aligned with references to numerous other such beams (Figure 1). Figure 2 shows this beam in operation with a few extracted beams merging into one dense beam that is 5 cm^2 in cross-sectional area. The beam is being used to etch an obliquely mounted target.

The multibeam technique reduces the inherent space-charge limitations normally encountered at low acceleration voltages. The injection of thermal electrons into the beam immediately below the ion accelerator further reduces space-charge problems, and furthermore space charge neutralizes the beam for bombardment of insulator surfaces.

The source consists of an inner dielectric cylinder around which rf coils are formed. An outer metal cylinder acts to shield against external rf radiation. The operation of the source commences with the generation of a dense plasma inside the dielectric volume. The plasma is sustained by an rf magnetically coupled field. Ions are extracted from the plasma through small multiple ports in several sequential accelerating electrodes. An arrangement is used at the accelerating electrodes so that each beam is focused through the ports to reduce ion bombardment of the high-energy electrodes. The exiting beam is at ground potential and passes into the test area at the potential of the chamber walls. The total area of the port openings in the extraction electrode ports between the plasma chamber and the beam section ranges from 0.01 to 2 cm^2 . A substantial pressure differential can be maintained between the plasma chamber and the beam chamber, which results in low test-chamber pressures with normal pumping rates.

The beam can be enlarged to any size and configuration simply by extending the plasma over larger extraction-sheet electrode arrangements. The many small beams can be focused or made parallel by shaping the electrode and made uniform or nonuniform by varying hole size, density, and placement over the electrode surface. The use of rf for plasma generation produces dense but even plasmas over large volumes. This type of source requires no hot filaments, hence oxygen and other reactive gases can be used without any detrimental effects to the system.

The source can also be used to generate beams of electrons in a similar manner as that used for ions. By simply reversing potentials, electrons are extracted from the plasma. Figure 3 shows the beam characteristic for argon ions and electrons produced by the technique. The current density was measured with a Faraday cup placed approximately 20 cm from the source. An ion current of 1 mA/cm^2 was obtained over the 5-cm^2 cross section at 2500 eV . Profile current density measurements were also made showing about ± 10 -percent variation over the 3-cm diameter. A current density of about 0.1 mA/cm^2 was obtained at an ion beam energy of 500 eV .

The electron beam characteristics from this source are also shown in Fig. 3. Here a maximum of 16 mA/cm^2 was obtained at 200 eV ; the current levels off for higher values.

The beam source operates continuously and can be varied in intensity or energy by changing the extraction potential and rf-controlled

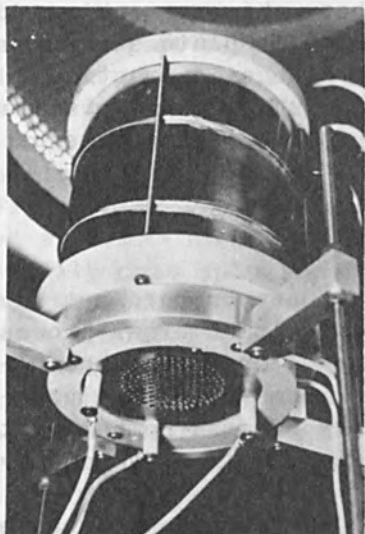


FIG. 1.--Multibeam ion source 5 cm in diameter.

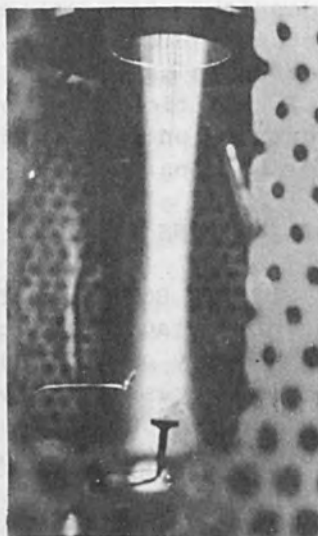


FIG. 2.--Five-KeV proton beam in operation bombarding oblique target.

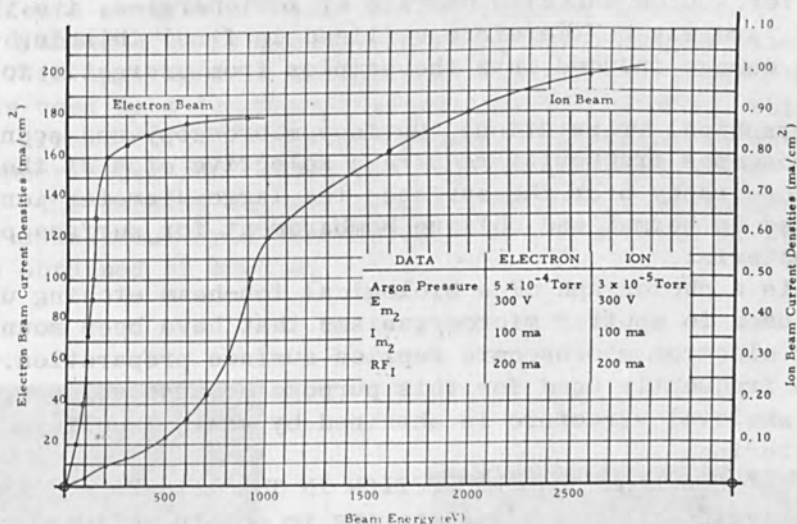


FIG. 3.--Ion and electron beam current/voltage characteristics.

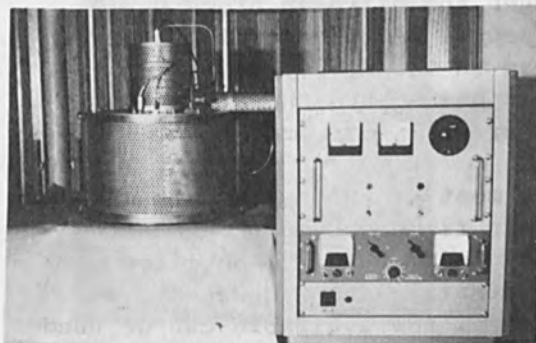


FIG. 4.--Biological ion-beam etching unit.



FIG. 5.--Ion-pumped high-purity ion-beam sputtering of silicon onto spinel.

plasma density. Large changes in density and beam chamber working pressure can be made by replacement of the extraction plate electrode with electrodes having different size or number of beam extraction ports. In addition, the contouring and otherwise shaping and placement of the extraction points can be used to obtain desired beam patterns and other beam parameters.

BEAM APPLICATIONS

A. SURFACE BOMBARDMENT. (1) Cleaning. Ion beam bombardment cleaning of surfaces in vacuum has become valuable in numerous processes. The availability of large-area ion beam coverage extends this usefulness to new processes as well as production requirements. The large-diameter ion source can be designed for a variety of area bombardment sizes and shaped, and can be used on dielectrics as well as conductive targets.

(2) Sample Thinning. Ion-beam milling is being employed for thinning targets for transmission electron microscopy target preparation.³ The beam can be applied to the preparation of many targets simultaneously. This ion source can also operate at low energies, i.e., down to 100-200 eV, and may be therefore utilized in final thinning stages to reduce the damage induced into the samples from energetic ion bombardment.

(3) Topographical Preparation. Surface microscopy and scanning electron microscopes frequently require a selective etch of the sample to obtain a topography over the surface; the large-diameter ion beam can be employed in normal and oblique bombardment for surface preparation of any material.

Figure 4 is a photograph of a biological ion-beam etching unit. This beam is used to sputter microorganisms that have been mounted and sectioned for electron microscopic replica surface preparation. Oxygen ion beams are frequently used for this purpose because selective removal of the skeletal structure is obtained by what is believed to be reactive sputtering.

B. NEUTRAL MOLECULAR BEAM PRODUCTION IN THE 1-to-25 eV RANGE. In 1962 we investigated the use of sputtering to obtain medium-energy neutral particle beams for molecular-beam applications. The initial paper⁴ published in 1965 showed that oxygen and nitrogen atoms could be obtained at velocities of 10^5 - 10^6 cm/sec with flux densities near 10^{15} atoms/cm²sec. Since that time a group in the Netherlands⁵ have used the sputtering technique for metallic beams, and the Russians⁶ have reported studies of producing beams of gas atoms from ice targets by sputtering.

C. THIN FILM DEPOSITION. One of the most useful applications of ion beams is the sputter deposition of thin films. Even though standard plasma sputtering is used extensively in thin-film deposition processes, ion beam techniques are more versatile and are necessary for certain results. The large-diameter beam now available can be used to sputter large area targets (and hence increasing deposition area). In addition, the large ion beam can be used to clean dielectric substrates before deposition and to introduce excess free energy into the film during deposition. If oblique ion impingement and low-angle

ejection are used in ion-beam deposition, the arriving atoms strike the substrate at several orders of magnitude above thermal. This application of the unique mechanism of deposition results in dense films which have good adhesion to the substrate. In addition, we have found that these conditions promote epitaxial growth of the depositing films.

Figure 5 is a 4-cm-diam ion-beam system operating on an ion-pumped system. This apparatus is being used to sputter silicon epitaxially onto spinel under high-purity conditions.

D. MISCELLANEOUS APPLICATIONS. The broad beam technique can be put into practice for numerous other applications. Ionospheric "wind tunnels" have been developed for NASA in which 2- to 10-eV ions are accelerated and mixed with thermal electrons to simulate what an earth satellite experiences as it moves in orbit. Simulation of the solar plasma wind is also accomplished by use of a hydrogen plasma and the addition of a large-diameter Bennett-type mass spectrometer to permit only the protons to enter the simulation chamber. Several versions of a 12-cm-diam solar plasma wind simulator are in use to irradiate space-based instruments and surfaces to study the charged-particle effects associated with the particulate bombardment.

Figure 6 shows a hermetically sealed source which is bakeable to 300°C. This apparatus is designed with a variety of accelerator grids and is used as a thermonuclear-reactor ion source. This primary ion beam is directed into a charge-exchange cell prior to entering the reactor chamber. Figure 7 shows the beam being tested under operating conditions. The Faraday cup and blocking-collector plate can be seen at the left downstream from the source. An ion current of 28 mA over 19.5 cm² is obtained at 1000 eV.



FIG. 6.--Glass-to-metal sealed 6-cm-diam. ion-beam source.



FIG. 7.--Thermonuclear reactor ion-beam source in operation.

SUMMARY

An ion-beam generating technique has been developed for producing large irregular diameter ion and electron beams at relatively high currents and low voltages. The technique is being used to design beams for surface-bombardment cleaning, etching, and thinning of samples; sputter deposition and activation of thin films; the production of medium-energy neutral atomic beams for cross-section research; and other applications such as solar plasma wind and ionospheric simulation, and thermonuclear reactor ion sources.

REFERENCES

1. B. B. Meckel and P. A. Harkins, The production and analysis of a large diameter plasma beam, *J. Appl. Phys.* 32; 489, 1961.
2. B. B. Meckel, Experimental study of the interactions of a moving body with a plasma, L. Talbot (ed.), *Proc. Second Intern. Symp. Rarefied Gas Dynamics*, Academic Press, New York, 1961.
3. J. J. Trillat, *Ionic Bombardment Theory and Applications*, Gordon and Breach, New York, 1964; pp. 13-50.
4. Medium Energy Neutral Molecular Beam Source, Report No. NAS5-9083, Physics Technology Laboratories, October 1965.
5. J. Politiek, P. K. Rol, J. Los, D. Onderdelinden, and J. J. Schipper, A molecular beam apparatus for the 0-50 eV region, C. L. Brundin (ed.), *Proc. 5th Symp. Rarefied Gas Dynamics*, Academic Press, New York, 1967; vol. 2.
6. V. K. Koshkin, J. A. Rijov, and B. A. Shvedov, High Energy Atomic Beams Obtained by Means of Cathode Sputtering, *Entropie* 30: 58-59, Nov.-Dec. 1969.

HIGH PRESSURE RECOMBINATION RATE MEASUREMENTS

D. H. DOUGLAS-HAMILTON

Avco Everett Research Laboratory, Everett, Mass.

A method of generating a high-pressure, high-electron-density plasma is described, and applied to measurement of electron-ion recombination rates in CO and N₂. The recombination rates are shown to be independent of pressure in the region investigated, and are given as functions of E/N.

BACKGROUND

High-pressure plasmas are of considerable current interest. A method of producing them, and of measuring the electron-ion recombination and electron-neutral attachment rates in them is described, which can be used to obtain effective rates in an arbitrary mixture of gases at arbitrary pressure. This method has been applied to a carbon monoxide plasma and to a nitrogen plasma, at pressures in which the major ionic constituent is N₄⁺.

The principle of the method is the uncoupling of the plasma electron temperature from the electron number density, and this is accomplished by external ionization of the gas using a high-energy electron beam. The swarm of secondary electrons produced by each primary electron can then maintain an electric discharge in the plasma if a field is applied. The temperature of the electrons (more exactly, the mean electron energy) can be specified by setting the external field to the appropriate value.

Measurement of ion buildup and afterglow when the electron beam is initiated and cut off provide numbers dependent on the recombination and attachment coefficients, from which these quantities are determined. A check on the results is provided by the equilibrium ionization generated by the electron beam, which depends on both the recombination and attachment (if any) coefficients, as well as the ionization cross section.

METHOD

A 100-kV electron beam is generated from a heated tungsten filament maintained at -100 kV in a 10⁻⁶-torr vacuum, and passed through a thin foil into the discharge chamber (Fig. 1). The beam penetrates a perforated plate used as cathode and enters the discharge chamber; after ionizing the gas in the chamber the beam is absorbed by the anode. The anode has an isolated central button of area 5 cm² which is used to measure the current density. Four 2-MΩ probes enclosed in glass cylinders are spaced across the discharge chamber. The central inch is bared and the voltage measurement determines the local E/N. Gas flows through the system during a run at about 300 cm/sec and is deposited in a dump tank maintained at 10⁻³ torr. The gas is made to flow in order to ensure purity: characteristic electron-ion recombination times are much shorter than characteristic flow times. A glass funnel minimizes contact with the walls until the discharge region is reached. In all

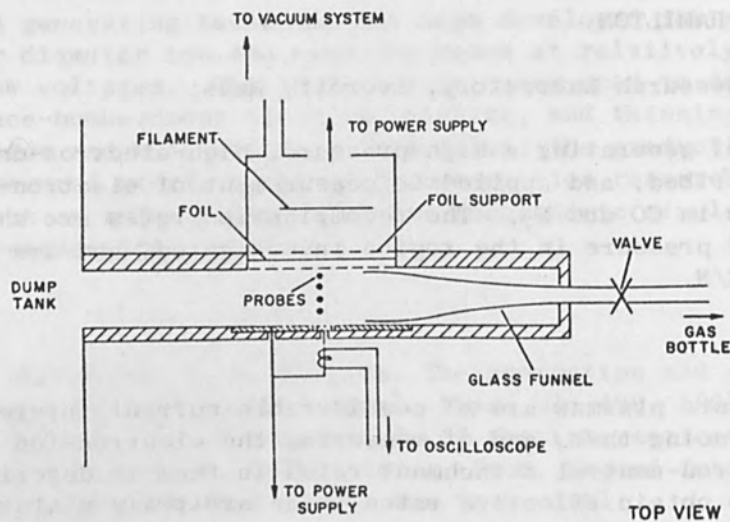


FIG. 1.--Electron-beam discharge apparatus.

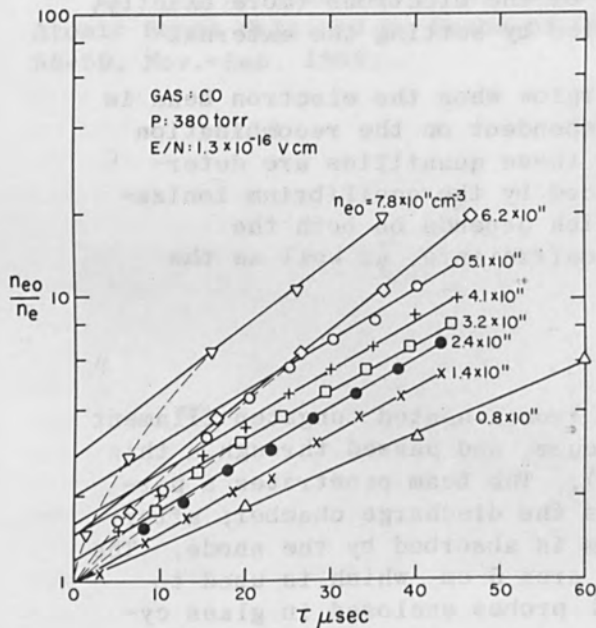


FIG. 2.--Electron density vs time at ionization cutoff in carbon monoxide.

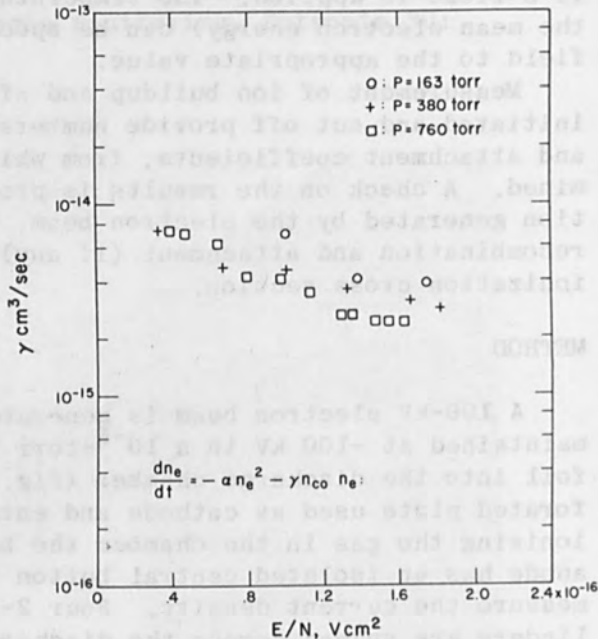


FIG. 3.--Attachment coefficient normalized to CO number density.

cases, gas temperature is 300°K.

After the flow has settled down to provide constant pressure in the discharge chamber, the chamber electric field is applied and the electron beam is pulsed on for 44 μ s (rise time < 1 μ s). Ionization onset and cutoff together with probe voltage history are measured as functions of time. Typically, the electron beam current density is 0.3 mA/cm² and the electron density produced in nitrogen is about 10¹² cm⁻³.

ANALYSIS

The electron number-density n_e in the plasma is given by

$$\frac{dn_e}{dt} = \alpha (n_{e0}^2 - n_e^2) + \beta (n_{e0} - n_e) - \sigma \nabla^2 n_e \quad (1)$$

where σ = diffusion coefficient, cm²/sec

α = electron-ion recombination coefficient, cm³/sec

β = inverse attachment time ($\beta = \gamma n_0$, where n_0 is number density of attaching neutral, and γ is attachment coefficient), sec⁻¹

n_{e0} = equilibrium electron number density, cm⁻³

We can neglect diffusion since $\tau_{\text{diffusion}} \gg \tau_{\text{recomb}}$ in the gas at high pressures (the lowest pressure used is 163 torr).

Then at cutoff, integration of the above equation yields:

$$n_{e0}/n_e = [(\alpha n_{e0}/\beta) + 1]e^{\beta t} - \alpha n_{e0}/\beta \quad (2)$$

For long times, n_{e0}/n_e has an exponential dependence on t which determines β .

At equilibrium, the ionization rate S is exactly balanced by electron loss:

$$S = \alpha n_{e0}^2 + \beta n_{e0} \quad (3)$$

Thus, knowing S , we have a check on the deduced values for α and β .

The ionization rate S is given by

$$S = \frac{nMm_p}{eE_i} j_{eb} \frac{\partial E}{\partial m} \quad (4)$$

where j_{eb} = primary electron beam current density, A/cm²

$\partial E/\partial m$ = mean stopping power, eVcm²/g

e = charge on electron, coulomb

E_i = effective ionization potential, volt

n = gas number density, cm⁻³

M = gas mean molecular weight

m_p = mass of proton

and $\partial E/\partial m$ is obtained from the table of Berger and Seltzer (published by National Bureau of Standards) of electron ranges and energy loss rates. The effective ionization potential is taken to be 35 eV.⁶

Equation (1) may be integrated at ionization onset, when the electron beam is switched on; a little rearrangement yields

$$\frac{n_e}{n_{e0}} = \frac{(\alpha n_{e0} + \beta) (e^{2\epsilon t} + 1)}{(\alpha n_{e0} + \beta) (e^{2\epsilon t} + 1) - \beta} \tanh \epsilon t \quad (5)$$

$$\text{where } \epsilon = \alpha n_{e0} + (\beta/2) \quad (5a)$$

Provided $\beta \gg 2 \alpha n_{e0}$, for large times we have:

$$n_e/n_{e0} = \tanh \epsilon t \quad (6)$$

Thus, a plot of t against $\tanh^{-1}(n_e/n_{e0})$ gives ϵ , and since β is known from the cutoff measurement, αn_{e0} is determined from Eq. (5a). The equilibrium current density $j = n_{e0} e V_D$ permits determination of n_{e0} . Drift velocity V_D is obtained from the solutions given in Refs. 1 and 2 for the transport equation in various gases, which takes account of the non-Maxwellian electron energy distribution.

In the limit $\beta \gg 2 \alpha n_{e0}$, Eq. (5) reduces to $n_e/n_{e0} = 1 - e^{-\beta t}$. Thus, in the attachment dominated case, a plot of $\ln [1 - (n_e/n_{e0})]$ against t yields β .

RESULTS

The versatility of this method is illustrated by the results obtained for the gases carbon monoxide and nitrogen. These gases are expected to have similar behavior, in that attachment should not be present in the pure gas.

A. CARBON MONOXIDE. The afterglow electron density curves obtained at fixed E/N and pressure are shown in Fig. 2. The existence of attachment is indicated by the exponential dependence of n_{e0}/n_e on t . A variation of n_{e0} from 8 to $80 \times 10^{10} \text{ cm}^{-3}$ has virtually no effect on β . This implies that attachment is not due to the accumulation of a disintegration product of CO (i.e., $\text{CO} + e \rightarrow \text{C} + \text{O} + e$), since the production rate would depend on electron number density. The secondary-electron mean energy is less than 0.7 eV in the range of E/N used, and since the CO dissociative attachment threshold is 9.6 eV,^{7,8} dissociative attachment should be unobservable. It appears, therefore, that attachment is due to an impurity initially present in the CO. The attachment rate has been measured at pressures $P = 160, 380, \text{ and } 760$ torr. It is plotted in Fig. 3 versus E/N , and has been normalized to CO number density. A. V. Phelps has suggested (private communication) that attachment in CO may be due to the presence of $\text{Fe}(\text{CO})_5$ in the carbon monoxide. Using Lee's coefficient value,³ a concentration of $\text{Fe}(\text{CO})_5$ less than 1 ppm would provide the observed attachment.

Onset curves are shown in Fig. 4 for $n_e = 8$ to $80 \times 10^{10} \text{ cm}^{-3}$. The value of α calculated from these is compared with the corresponding

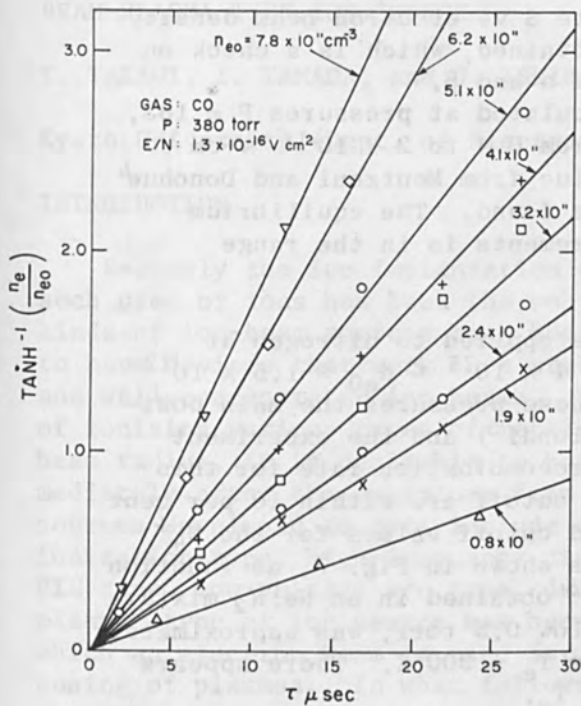


FIG. 4.--Ionization onset in carbon monoxide at various electron beam intensities.

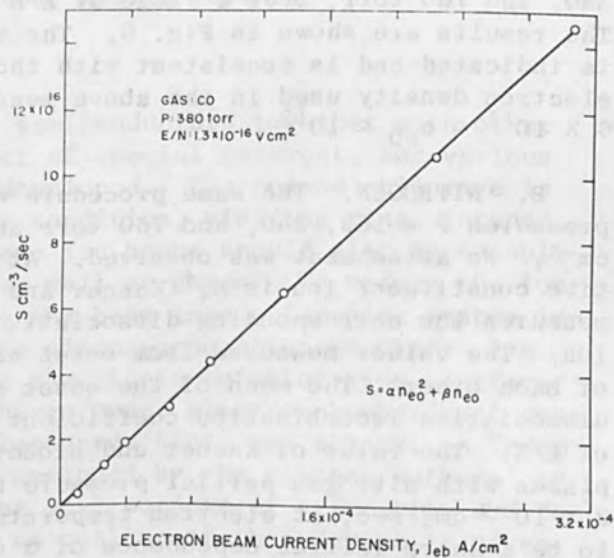


FIG. 5.--Ionization rate vs electron-beam current.

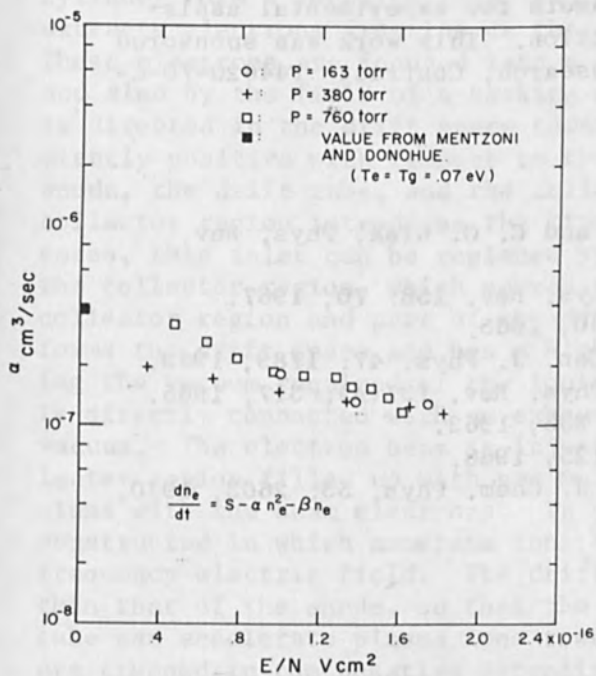


FIG. 6.--Recombination coefficient in carbon monoxide.

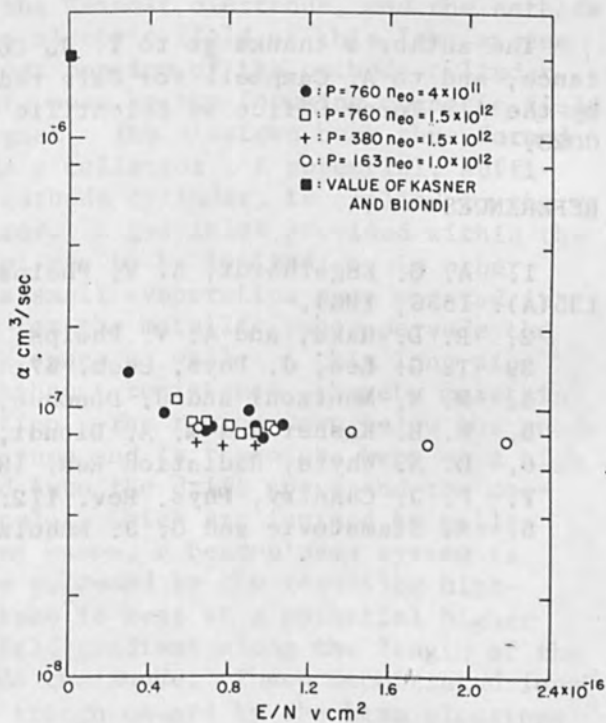


FIG. 7.-- N_4^+ recombination rate at various pressures.

value of β by plotting the ionization rate S vs electron beam density j . Figure 5 shows the linear relation obtained, which is a check on the consistency of the computed values of α and β .

The recombination coefficient is calculated at pressures $P = 163, 380,$ and 760 torr, over a range of E/N from 0.4 to 2×10^{-16} V-cm². The results are shown in Fig. 6. The value from Mentzoni and Donohue⁴ is indicated and is consistent with those found. The equilibrium electron density used in the above measurements is in the range $6 \times 10^{11} < n_{e0} < 10^{12}$.

B. NITROGEN. The same procedure was applied to nitrogen at pressures $P = 163, 380,$ and 760 torr and $4 \times 10^{11} \leq n_{e0} \leq 1.5 \times 10^{12}$ cm⁻³. No attachment was observed. At these pressures the main positive constituent ion is N_4^+ (Kasner and Biondi⁵) and the experiment measures the corresponding dissociative recombination rate for this ion. The values measured from onset and cutoff are within 10 per cent of each other. The mean of the onset and cutoff values for the N_4^+ dissociative recombination coefficient is shown in Fig. 7, as function of E/N . The value of Kasner and Biondi,⁵ obtained in an Ne:N₂ mixture plasma with nitrogen partial pressure below 0.5 torr, was approximately 2×10^{-6} cm³/sec, at electron temperature $T_e = 300^\circ\text{K}$. There appears to be a sharp initial dependence of α on T_e .

The recombination coefficient is independent of pressure or electron density, and for $E/N > 6 \times 10^{-17}$ V-cm² has the value $\alpha = 8 \times 10^{-8}$ cm³/sec. It is therefore probably the dissociative recombination coefficient for the ion N_4^+ .

ACKNOWLEDGMENT

The author's thanks go to T. J. Colameta for experimental assistance, and to A. Campbell for data reduction. This work was sponsored by the Air Force Office of Scientific Research, Contract F44620-70-C-0023.

REFERENCES

1. A. G. Engelhardt, A. V. Phelps, and C. G. Risk, Phys. Rev. 135(A): 1566, 1964.
2. R. D. Hake, and A. V. Phelps, Phys. Rev. 158: 70, 1967.
3. T. G. Lee, J. Phys. Chem. 67: 360, 1963.
4. M. H. Mentzoni and J. Donohue, Can. J. Phys. 47: 1789, 1969.
5. W. H. Kasner and M. A. Biondi, Phys. Rev. 137(A): 317, 1965.
6. G. N. Whyte, Radiation Res. 18: 255, 1963.
7. P. J. Chantry, Phys. Rev. 172: 125, 1968.
8. A. Stamatovic and G. J. Schulz, J. Chem. Phys. 53: 2663, 1970.

BEAM-PLASMA TYPE ION SOURCE

T. TAKAGI, I. YAMADA, and J. ISHIKAWA

Kyoto University (Dept. of Electronics), Kyoto, Japan

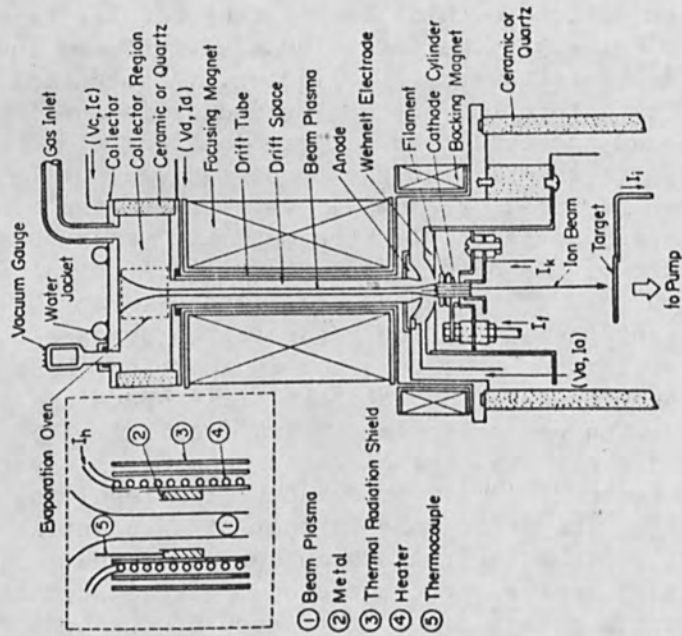
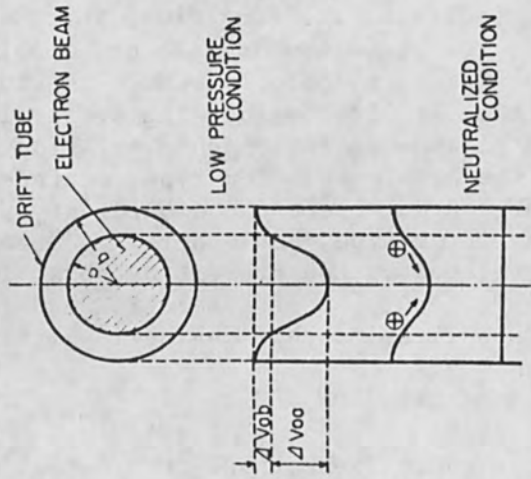
INTRODUCTION

Recently the ion implantation to semiconductors together with other such uses of ions has been the subject of special interest, and various kinds of ion-beam sources have been developed. The common objective is to have devices that work in a stable condition, yielding fine, intense, and well-concentrated ion beams. These ion beams should also be capable of ionizing various types of metals as well as gases. To reduce the ion-beam radius, it is desirable to bring the beam into a focusing system immediately after the departure from the plasma-generation chamber. Ion sources developed to date include the thermionic-emission type, surface-ionization type, high-frequency discharge type, electron-bombardment type, PIG type, low-voltage arc type, duoplasmatron type, and others. A "beam-plasma" type of ion source has been developed by the present authors¹ in which an electron beam is used for the dual purpose of generation and focusing of plasmas. In what follows, an outline of this device is given.

STRUCTURE AND OPERATION OF THE BEAM-PLASMA TYPE ION GUN

Figure 1 is the structure of the ion gun. The cathode is a metallic cylinder made of tantalum or tungsten, and is heated to a temperature appropriate for electron emission by the bombardment of electrons from filament windings. The anode electrode, the Wehnelt electrode, and the cathode cylinder form a focusing lens, and the electric field of this lens system extracts electrons from inside the upper portion of the cathode cylinder. These electrons are focused into a thin beam by the focusing magnetic field and also by the field of a backing magnet. The electron beam thus formed is directed in the drift space towards a collector. A potential, sufficiently positive with respect to the cathode cylinder, is applied to the anode, the drift tube, and the collector. A gas inlet provided within the collector region introduces the kind of gas to be ionized; or in other cases, this inlet can be replaced by a small evaporation oven mounted in the collector region, which serves to let the metallic vapor pervade the collector region and part of the drift space as well. A thin long pipe forms the drift space and has a high exhaust resistance, thereby maintaining the vacuum required of the ionization. The region down below the anode is directly connected with an exhaust pump and is therefore kept at a high vacuum. The electron beam is injected into the drift space and the collector region filled up with gas molecules, which are ionized by collisions with the beam electrons. In some cases, a beam-plasma system is constructed in which numerous ions are produced by the resulting high-frequency electric field. The drift tube is kept at a potential higher than that of the anode, so that the field gradient along the length of the tube can accelerate plasma ions towards the anode. These accelerated ions are trapped in the negative potential trough caused by the beam electrons and thus grow to an ion beam directed oppositely to the electron beam. The ions are further accelerated by means of the cathode electrode with a high negative potential, penetrate the cathode cylinder along the central axis, and proceed to the target.

FIG. 2.--Radial potential distribution of beam with various degrees of space-charge neutralization.



- ① Beam Plasma
- ② Metal
- ③ Thermal Radiation Shield
- ④ Heater
- ⑤ Thermocouple

FIG. 1.--Schematic diagram of beam-plasma type ion source.

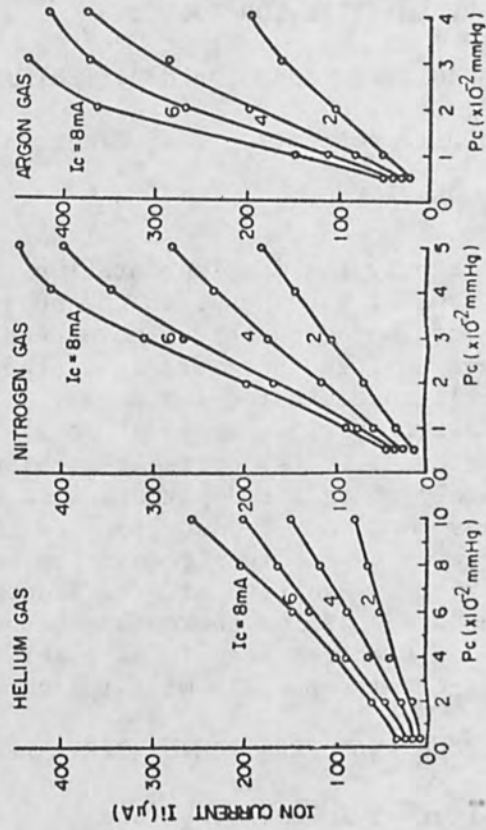


FIG. 3.--Ion current characteristics as function of pressures.

The above is the structure of our beam-plasma type ion gun. The principle of this gun is as follows.

When the residual gas pressure is sufficiently low, the potential due to an electron beam, of radius a and a uniform electron density n , in a cylindrical conductor of radius b , is given by

$$\Delta V_{ba} = \frac{qna^2}{2\epsilon_0} \ln \frac{b}{a} \quad (1)$$

$$\Delta V_{oa} = \frac{qna^2}{4\epsilon_0}$$

where the Poisson equation is used (Fig. 2). Here ϵ_0 is the vacuum dielectric constant, q the electronic charge. The potential exerted by the electron beam varies radially in approximately a parabolic way within the beam and forms a negative potential valley in relation to the tube wall. The mean energy of ions, produced by collisions between the beam electrons and the gas molecules, is $\Delta E = (2m/M) E_0$, where m and M are the electron and the ion masses, respectively, and E_0 is the energy of the electron beam. If $\Delta V_{oa} \gg \Delta E$, then the positive ions generated by collisions are completely trapped by the above negative potential valley. For example, for an electron beam of 12.5 kV and 10 mA/cm², ΔV_{oa} and ΔE are respectively 3.05 and 0.49 eV, assuming a residual gas of nitrogen. The trapped ions diffuse along the axis of the tube. The higher the gas pressure is, the shallower the potential valley becomes, since for a higher gas pressure the collisions are more frequent, yielding more positive ions. When the charge density of ions reaches the same level as that of electrons, then the potential is flattened out, and the electron beam loses the trapping ability. This critical pressure is given by Hopson² as

$$P_{scn} = (\pi^2/2L) [(q\Delta E/2)MC_i C_c^+]^{\frac{1}{2}} \quad (2)$$

where L is the axial length of the electron beam; C_i and C_c^+ are the collision frequencies, per unit gas pressure, between the electrons and the gas molecules and between the gas molecules and the ions, respectively. If the mean pressure within the domain of interest exceeds P_{scn} , the ions are not trapped by the electron beam, but they spread out as a plasma. We call this state the total-glow condition. If the mean pressure is below P_{scn} , the ions are trapped in the electron beam. We call this state the beam-confined condition.

In the collector and drift space where plasmas are generated, the total glow conditions are favorable for as many ions as possible. More specifically, we call the state the total glow condition A, in which the generation of plasmas is due to the primary beam ionization alone. In addition, the ionization can be further enhanced by the high-frequency noise, to which case we give the name of the total glow condition B. In between the anode and the cathode cylinder, a high vacuum with the beam-confined condition is maintained for effective focusing.

A. TOTAL-GLOW CONDITION A. In the drift space and the collector region, the plasma is produced by collisional ionization of the primary electron beam. Assuming part of ions are extracted from the anode, one has the following equation for the ion current:

$$I_i = I_e \left[K_1 G \int_0^{\ell_d} P_d(z) dz + K_2 G P_c \ell_c \right] \quad (3)$$

where I_e is the current carried by the beam electrons; G is the ionization efficiency; ℓ_d and ℓ_c are the dimension of the drift space and that of the collector region, respectively; P_d and P_c are pressures in the drift space and in the collector region, respectively; and K_1 and K_2 are the constants that give the ratio of these ions extracted from the anode to all of the ions generated. By adjusting the voltage applied to the anode and the drift tube, one can have $K_1 = 1$. In the drift space the gas flows almost like a molecular flow; when the pressure increases towards the upper end, Eq. (3) reduces to

$$I_i = I_e G P_c \left(K_1 \frac{\ell_d}{2} + K_2 \ell_c \right) \quad (4)$$

i.e., the ion current increases proportionally to the electron beam current, the ionization efficiency, and the pressure in the collector region as well.

B. TOTAL-GLOW CONDITION B. There are high-frequency interactions between a plasma and an electron beam that penetrates the plasma. In those frequency regions where space-charge waves and slow cyclotron waves are synchronous with plasma waves, the interaction result in various instabilities.³ With appropriate pressure and boundary conditions, the generation of high and low frequency noise is observed.^{4,5} When the potential associated with this high-frequency noise exceeds the ionization potential of the gas molecules, the efficiency of ionization becomes 10^2 - 10^3 higher than that in the absence of such noise. The result is that the ion current remarkably increases.

C. BEAM-CONFINED CONDITION. The ions extracted from the anode are trapped and guided by the duct of the negative-potential electron beam and penetrate the cathode cylinder at its central axis. Even when the ion current is intense, the ions are completely trapped in the vicinity of the cathode cylinder where the electron density is high. Thus, in any case, ion beams with a good emittance can be obtained.

CHARACTERISTICS OF THE TEST ION GUN

Consider now how the total glow condition discussed previously holds in the drift space and the collector region. For the total glow condition A to hold, the mean pressure in these regions should be higher than the critical pressure given by Eq. (2). In case of a nitrogen gas used in the test ion gun, this critical pressure of Eq. (2) turns out to be approximately 1×10^{-3} mm of Hg. On the other hand, the total glow condition B can be realized in the same regions even below this critical pressure.

The ions generated in the drift space move along the axis by diffusion. To obtain an ion beam efficiently, however, the potential of the drift tube should be higher than that of the anode, so that plasma ions are accelerated towards the anode. Over the pressure range of our experiment, saturation occurred at $V_{ad} = 2.5$ - 3.0 kV, and this value was maintained in the subsequent experiments.

In the following, the regimes of the total glow conditions A and B are separately considered concerning the operation characteristics.

A. CHARACTERISTICS OF THE TOTAL-GLOW CONDITION A. Figure 3 shows ion-beam current I_i versus pressure P_c . Here the intensity of the primary electron current is a variable parameter. The measurement was made with the use of helium, nitrogen, and argon gases. One sees, in each of these cases, that the ion current increases linearly with the pressure and the electron-beam current. The ionization efficiency improves in the order of helium, nitrogen, and argon, so that the more ion current is drawn even at a low gas pressure by use of a gas of a better ionization efficiency. Assume in Eq. (4) that all of the ions reach the ion target when there is no potential difference between the anode and the drift tube; then $K_1 = 1$. On the other hand, K_2 can be neglected since the potential gradient in the drift space, together with the resulting diffusion, does not affect the state of the collector region. Substitution of numerical values in Eq. (4) leads to good agreement with those observed. It may be inferred that the mechanism of ion production in this case is solely due to the collisional effect of the primary electron beam.

B. CHARACTERISTICS OF THE TOTAL-GLOW CONDITION B. One wants to have beam-plasma interactions in such a way that they can remarkably enhance the plasma density in the drift space, yielding a high-density ion beam. The present authors have taken special interests in this phenomenon, and have been attempting to increase the plasma density by a factor of 10^2 - 10^3 by use of this phenomenon. The boundary conditions of the plasma, required of the total-glow condition B in the drift space, can be realized by adjusting the electron or structural conditions. One way to achieve these conditions is to set the potential of the drift tube higher than that of the collector so that the ionization by secondary electrons from the collector surface can be fully utilized.

Figure 4 shows the current versus the potential difference V_{cd} between the collector and the drift tube; the gases are helium, nitrogen, and argon. When V_{cd} is above the level of ionization potential, the secondary electrons from the collector acquire energy needed for ionization. Ionization is then enhanced in the neighborhood of the junctions of the collector and the drift space, and thus the conditions required of the total-glow condition B are met. In each case, there is a notable increase in the ion current with increasing V_{cd} . In the case of nitrogen, for example, an ion current of more than 1.5 mA is observed. With the other parameters, such as pressures and currents, held constant, ion currents 75 times greater than those of the total-glow condition A are obtained. The gas pressure yielding this maximum ion current can thus be lowered. Therefore, it seems that this type of ion source is suitable to obtain a metal ion beam from material with a sufficiently low vapor pressure.

One can increase the maximum ion current by appropriately adjusting the boundary conditions of the drift space either electronically or mechanically. The gas pressure yielding this maximum ion current can thus be lowered. The junction between the collector region and the drift tube was rearranged in order to have a more stable excitation of high-frequency noise. In these conditions an ion current greater than 3 mA is obtained.

The relationships between ion-beam current I_i and pressure P_c are examined for various primary electron-beam currents. There is an optimum magnitude of the pressure to draw the maximum amount of the ion current; this optimum value becomes smaller as the electron beam current is greater. The maximum-ion current saturates at a sufficiently large amount of the electron-beam current. This result seems to confirm that the saturation level of

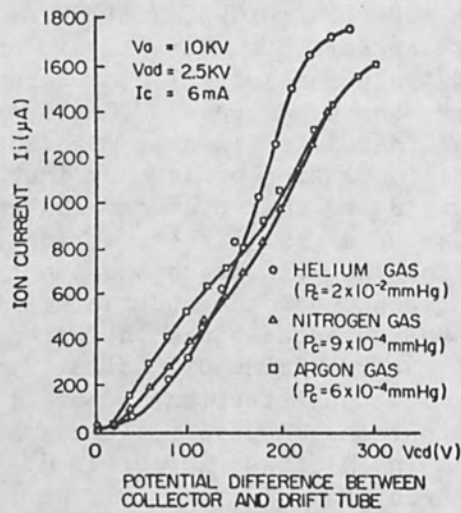
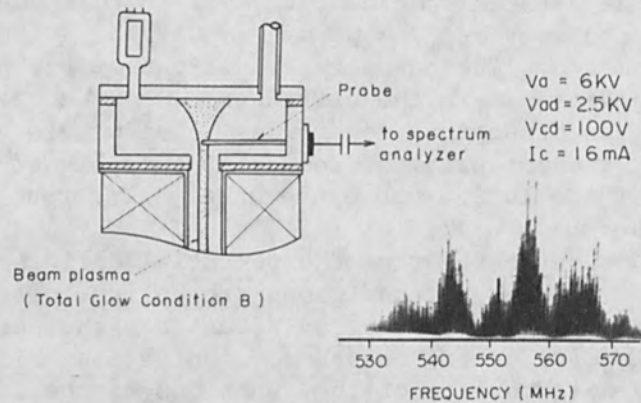


FIG. 4.--Ion current characteristics as function of potential difference between collector and drift tube.



(a) (b)

FIG. 5.--(a) Device to observe high-frequency noise and (b) noise spectrum.

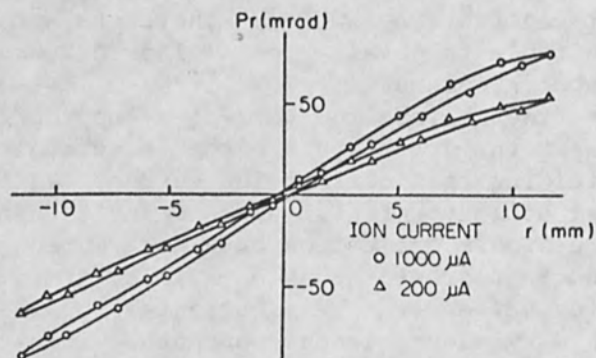


FIG. 6.--Emittances for 1000 and 200 μA ion currents.

the high-frequency noise induced by instability does not depend on the intensity of the electron-beam current.

In these working conditions, an antenna was inserted into the device, as shown in Fig. 5(a), to observe the high-frequency noise with a spectrum analyzer. Figure 5(b) is a result of this observation. The central frequency is near 550 MHz, in this example, with a width of 140 MHz, the amplitude increasing with increasing V_{cd} , i.e., the ion current. Low-frequency noise over the range of 30-100 kHz was also measured with a synchroscope.

Figure 6 is the result of an emittance measurement for 200- μ A and 1-mA ion beams at a distance of 15 cm from the cathode cylinder. It is seen that there is a divergence of 0.050-0.060 radian at the position of 10 mm beam radius. There is also very little aberration in this ion beam. For the ion-beam current of 1 mA, the emittance and average brightness, both normalized, are 3.8×10^{-8} rad m and 1.48×10^{11} A rad⁻² m⁻² respectively; these figures indicate that the beam is of good quality.

An ion beam was applied to an Al foil, which then lost its glossiness by contamination. Over an area of 20 mm in diameter this change of color was remarkable; in particular, a pin-hole of 2 mm in diameter was found at the center. Even without focusing lens systems, high-density ion beams can be evidently generated.

An evaporation oven was mounted to the collector region shown in Fig. 1, and an indium metal placed in this oven was heated up to 800°C. Metallic ions thus produced were then implanted to a silicon substrate. By radio activation analysis the amount of indium implanted was estimated at about 10^{15} cm⁻². In this amount those neutral indium particles attached to the target surface are included. From these experiments it is believed that ion guns working as sources of metallic ions can be developed.

CONCLUDING REMARKS

We have obtained various promising results concerning the beam-plasma type ion gun. The salient feature of this gun is that the electromagnetic field accelerating and focusing the electron beam also operates on the ion beam, so that the interpenetration of the two streams is made possible. In other words, the drift space that serves for a plasma production chamber and the collector region are where the beam-plasma interactions are fully exploited to enhance the plasma density by a few orders of magnitude above the level expected from the collisional ionization by the primary electron beam. The structure of our ion gun is such that the ion beam is naturally constrained in the axial direction; a very thin ion beam of small aberration can be therefore generated. In the conventional types of ion guns, such as the usual high-frequency discharge type, electron-bombardment type, PIG type, low-pressure arc-discharge type, duoplasmatron type and others, the pinhole in the plasma production chamber is covered with a plasma sheath that forms a virtual emission surface of ions. This surface seems seriously affected by the extractor potential, operating gas pressures, and other factors in such a way that the emission surface is eventually distorted, causing variations on the ion-beam structure. In our gun of the beam-plasma type, most of the above drawbacks will hopefully be removed in view of the operation mechanism on which our gun is based. Further investigations are now under way.

ACKNOWLEDGMENTS

We are grateful to Dr. Takao Tsuda and others for their discussions in the course of this study. Kind assistance offered by Professor Namba's group of Osaka University on radioactivation analysis is also appreciated. On constructing the ion guns of our type, the staff of Space Mechatronics, Inc. in Osaka did an excellent job that enabled us to accomplish our work. The present study is supported by a grant-in-aid from the Ministry of Education for 1969 and 1970.

REFERENCES

1. T. Takagi, I. Yamada, and J. Ishikawa, Beam-plasma type ion gun, Papers of The Japan Society for the Promotion of Science (132nd Committee), Oct. 1970.
2. J. E. Hopson, Beam-generated beam-plasma system, J. Appl. Phys. 34: 8, 1963.
3. R. J. Briggs, Electron-stream interaction with plasmas, M.I.T. Press, Cambridge, Mass., 1964.
4. L. D. Smullin and W. D. Getty, Generation of a hot, dense plasma by a collective beam-plasma interaction, Phys. Rev. Letters 9: 1, 1962.
5. D. A. Dunn, W. Nichparenko, J. E. Simpson, and K. I. Thomassen, Oscillations and noise generation in a beam-generated plasma, J. Appl. Phys. 36: 10, 1965.

THE DUOPLASMATRON AS A NEGATIVE HYDROGEN ION SOURCE

J. AUBERT, M. DUBARRY, G. GAUTHERIN and A. SEPTIER

Institut d'Electronique Fondamentale, Laboratoire Associé au CNRS, Orsay, France

INTRODUCTION

1.1. REASONS FOR INTEREST IN SOURCES OF NEGATIVE IONS. Negative ion sources are of interest in various branches of physics:

(i) Plasma Physics. Here, attempts have been made to synthesize plasmas free of electrons, consisting purely of positive and negative ions, by combining two oppositely charged ion beams from separate sources.

(ii) Particle Accelerators. Sources of H^- ions have already been attached to cyclotrons. A thin target placed at the periphery converts the H^- ions into H^+ ions by charge exchange; the H^+ ions are automatically ejected from the machine because the magnetic field of the machine reverses the curvature of the trajectories, which simplifies the problem of extraction.

It is, however, in the domain of electrostatic tandem accelerators that the development of negative-ion sources will be of the greatest use, since they are the essential component. The source is grounded and the negative ions are accelerated by means of a positive potential Φ_0 of a few megavolts; they then undergo charge exchange at the high-voltage electrode and the resulting protons are further accelerated, emerging with energy $W_S = 2e\Phi_0$. Since charge exchange efficiencies are always poor, the negative-ion sources must be as intense as possible, while having a low emittance, so that all the negative ions produced can be focused inside the charge-exchange system. These two factors--intensity and emittance--must be carefully studied for every type of source; that has not hitherto been done.

1.2. THE VARIOUS TYPES OF SOURCES OF H^- IONS. In low-energy nuclear physics, for protons, H^- ion sources have been developed. There are several ways of producing these ions.

1.2.1. Transformation of Positive Ions into Negative Ions Within a Gas Target by the Capture of Two Electrons. The pressure of the gas (usually hydrogen) in the charge-exchange chamber must be high enough (a few 10^{-3} Torr). There are two kinds of charge exchange sources: those with a separate chamber and those with the chamber incorporated in them.

In the first type, the beam of positive H^+ ions is extracted at a few tens of kilovolts from an ordinary gas discharge source, usually a duo-plasmatron, which can give dc currents of a few tens of milliamps. The beam is then focused onto the entry to the charge-exchange chamber. It is difficult to arrange for good transmission of the ion beam since the opening into the chamber is small, to reduce as far as possible the consumption of the target gas and the dimensions of the pumping system; moreover, the collisions between the molecules produce some angular spreading of the ion beam. Furthermore, the energy spread is wide (about 1000 eV). The useful currents of H^- ions are therefore low (10-25 μA).

In the second type, a charge-exchange tube is placed immediately beyond the exit from the source. These are hf sources, but the extraction

tube is considerably extended so that the pressure of the gas that diffuses out of the discharge region remains high for several centimeters. The positive ions in the discharge are accelerated towards the tube by the positive potential (several kilovolts) applied to the upper electrode. The beam that emerges from the tube contains both H^+ and H^- ions, which are separated by a magnetic prism. These hf sources have several advantages--long lifetime and low gas consumption--but they produce small currents of ions (a few tens of microamps) with high energy spread (several hundred eV).

1.2.2. Direct Extraction of the H^- Ions Produced in the Source. Several sources of this type have been described (Table 1), all using gas discharges. Currents of several milliamps can be obtained with reflex

TABLE 1.--Performances of various types of H^- ion sources used in particle accelerators.

References	Type of source	Gas consumption (cm ³ /min)	H^- beam current (μA)
Wittkower, Bastide, Brooks, and Rose ²	Separate charge exchange (duoplasmatron)	target : 21	23
Dandy and Hammond ³	Separate charge exchange (duoplasmatron)	target : 0.75	10
Goldie ⁴	Incorporated charge exchange (hf)	0.3	20
Sautter, Baribaud, and Dolique ⁵	Reflex	20	5000
Ehlers ⁶	Reflex	4-30	5000
Lawrence, Beauchamp, and McKibben ¹	Shifted anode duoplasmatron	0.33	120
Collins and Gobett ⁷	Shifted anode duoplasmatron	0.3	80
Dubarry and Gautherin ⁸ and our work	Shifted anode duoplasmatron	0.25-0.5	200-400

discharges and extraction by a lateral slit, which is best adapted to use in cyclotrons. The gas consumption is very high, however, and nothing is known about the emittance of the resulting beam. The electron current that is extracted at the same time as the negative ion current is considerable, but these electrons are quickly eliminated from the ion beam by the magnetic field. Extraction through a slit is inconvenient for accelerators with a straight axis, however, and J. L. McKibben et al.¹ and others have therefore suggested using a duoplasmatron with the extraction shifted in a direction normal to the axis of the discharge. The currents obtained were still rather small (about 100 μA) when we began this work, but the gas consumption is low and the energy spread is distinctly lower than that of charge-exchange sources.

We have constructed a source of this type in order to study the effect of the various geometrical and electrical parameters on the beam obtained and to analyze the characteristics of this beam: its composition, energy spectrum, and emittance.

PRINCIPLE OF OPERATION

2.1. THE SOURCE. The source is a standard duoplasmatron, of which we first give a brief account (Fig. 1). A column of dense plasma is created by a low-pressure arc between a hot cathode K and an anode A containing an extraction orifice of small diameter (about 1 mm). The discharge is concentrated in the anode region by the electrostatic effect of an intermediate electrode EI and by a strong inhomogeneous magnetic field (variable between 0 and 3 kG) between EI and A; these electrodes are made of mild steel. An examination of this source in our laboratory has shown that the discharge consists of three distinct zones: the low-density cathode plasma, situated in a region containing no magnetic field; the very dense anode plasma ($n_e \approx n_i \approx 10^{14} \text{ cm}^{-3}$); and a diffusion plasma beyond the anode, in the extraction region. The cathode plasma, which lies between the cathode sheath and the exit from the electrode EI, supplies the discharge with electrons; the latter are accelerated towards the anode plasma, in which they produce positive and negative ions. When the cathode is operating in saturated conditions, the energies of the ionizing electrons and the ions that are produced are virtually independent of the arc voltage V_{arc} since any variation ΔV_{arc} increases or reduces the potential drop in the cathode sheath. Any increase in I_{arc} is obtained by increasing the heating current of the cathode. Variations of the magnetic field B modify the diameter of the discharge column; when we wish to extract positive ions, the density of which is highest in the column, it is best to place the extraction orifice where the magnetic field produces the maximum constriction (that is, at the point where B is greatest). When negative ions are to be extracted, McKibben¹ has shown that the extraction orifice must be set off center, and it is for this reason that a mechanism has been added to our duoplasmatron to allow the combination of K and EI to be shifted relative to the anode in the transverse direction. The shift d is measured by means of a comparator with an accuracy of 0.01 mm. The movement can be carried out under vacuum, with the duoplasmatron in operation. The whole source is held at high voltage (-5 to -20 kV) and the anode, cathode region, and magnetic-field coil are cooled by a kerosene flow. The extraction orifice is cut in a molybdenum disk attached to the anode plate, so that the size or shape of the hole can be changed easily.

The extraction electrode is grounded. The beam extracted contains both negative ions and electrons; the latter are eliminated by means of a sector magnet which deflects the ions through 90° . The ion current is measured beyond the sector magnet.

2.2. CREATION AND DESTRUCTION OF NEGATIVE IONS. In a hydrogen duoplasmatron, numerous reactions occur simultaneously within a very small anode region (a few mm^3) permeated by a very inhomogeneous, high magnetic field (B may vary from 0 to 3 kG over 2-3 mm, for example). The diameter of the arc is typically 1 mm. It is clear that it is practically impossible to perform a complete theoretical analysis yielding the density and

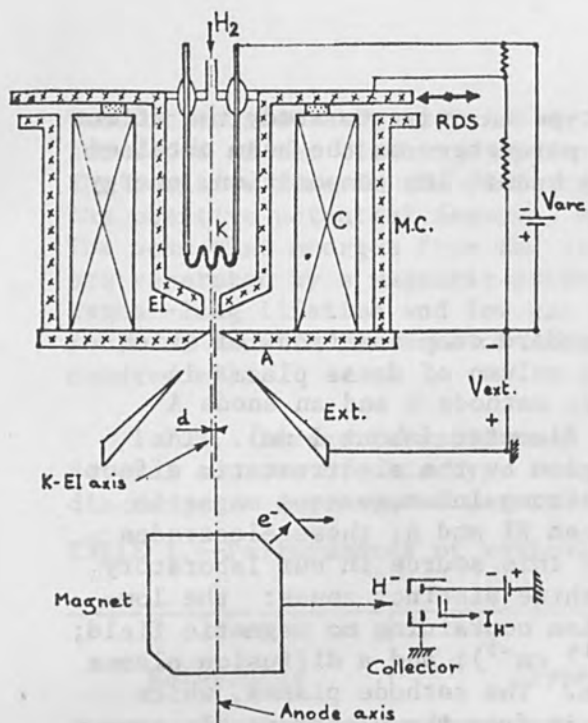


FIG. 1.--Schematic cross section of a duoplasmatron H^- source. K: cathode; EI: intermediate electrode; A: anode; C: coil; MC: magnetic circuit; Ext: extraction electrode; RDS: radial displacement system.

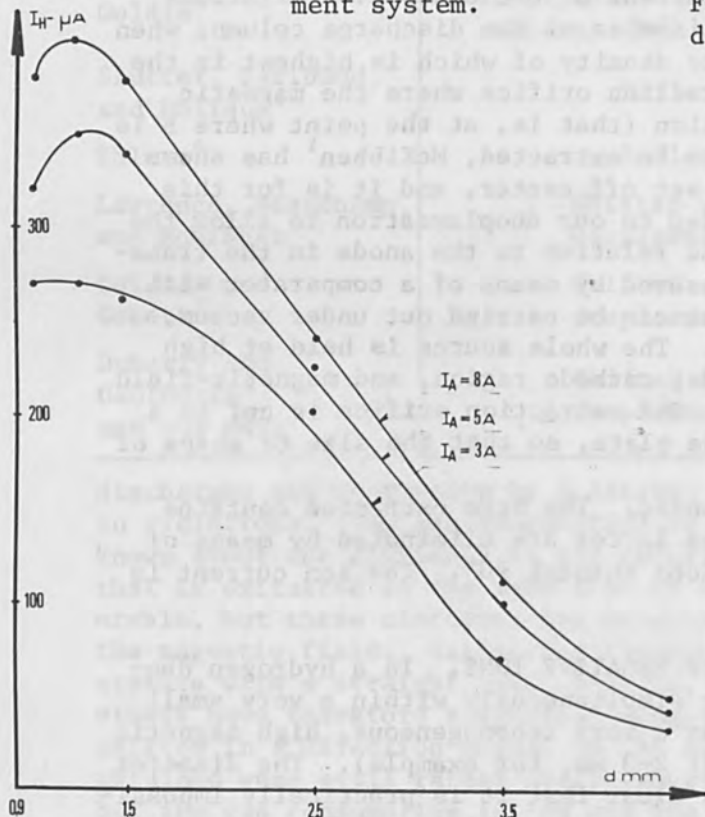


FIG. 3.--Variations of H^- beam intensity with d for different values of discharge current.

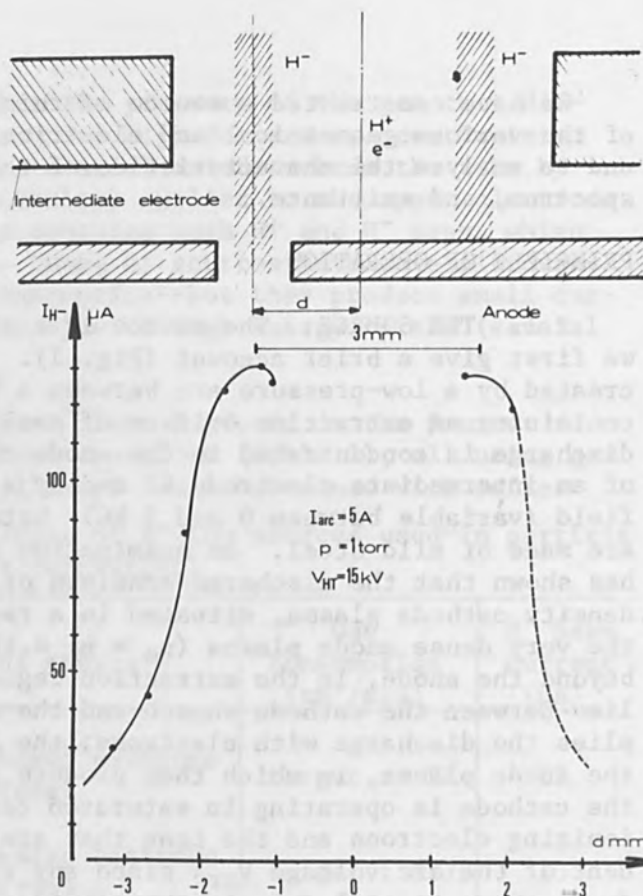


FIG. 2.-- H^- beam current versus radial displacement d of discharge axis.

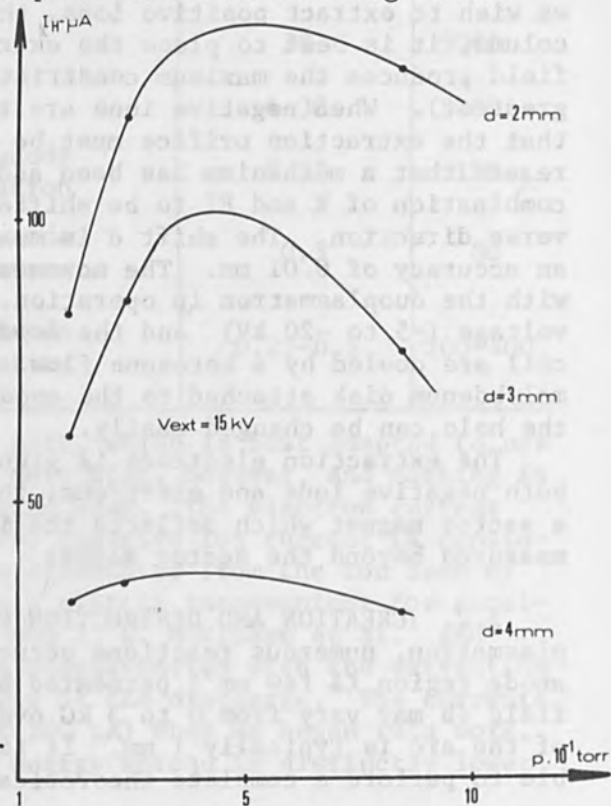


FIG. 4.--Effect of H_2 pressure on beam intensity.

distribution of the H^- ions formed. To show the complexity of the problem, we list the effective cross sections of the most probable reactions that lead to the creation of positive and negative ions (Tables 2 and 3); $E(\sigma_{\max})$ denotes the energy of the incident particle corresponding to the maximum value of the effective cross section σ_m .

TABLE 2.--Formation and destruction on H^- ions - H^* is an excited atom.

No.	Reaction	Maximum cross section σ_m (m^2)	$E(\sigma_m)$ (eV)
Formation			
1	$H_2 + e \rightarrow H^- + H$	1.2×10^{-24}	10
2	$H_2 + e \rightarrow H^- + H^*$	3.5×10^{-24}	14.2
3	$H_2 + e \rightarrow H^- + H^+ + e$	10×10^{-24}	200
4	$H + e \rightarrow H^-$	3×10^{-28}	0.75
Destruction			
5	$e + H^- \rightarrow H + 2e$	8×10^{-19}	10(e)
6	$H^- + H \rightarrow H + H + e$	10×10^{-19}	150(H^-)
7	$H^- + H_2^+ \rightarrow H + H_2$	0.2×10^{-19}	200(H^-)

TABLE 3.--Creation of H^+ ions.

No.	Reaction	σ_{\max} (m^2)	$E(\sigma_{\max})$ (eV)
8	$H_2 + e \rightarrow H_2^+ + 2e$	1.1×10^{-20}	80 (e)
9	$H_2 + e \rightarrow H + H + e$	0.4×10^{-20}	18 (e)
10	$H_2 + H_2^+ \rightarrow H_3^+ + H$	20×10^{-20}	4 (H_2^+)
11	$H_2^+ + e \rightarrow H^+ + H + e$	5×10^{-20}	20 (e)
12	$H + e \rightarrow H^+ + 2e$	0.7×10^{-20}	60 (e)
13	$H_2 + H_2^+ \rightarrow H_2 + H^+ + H$	4.6×10^{-20}	60 (H_2^+)

We see immediately from these tables that the effective cross sections for the mechanisms that are essential for producing H^- ions (reactions 1, 2, and 3) are 10^3 - 10^4 times smaller than those leading to the creation of H^+ ions and 10^4 - 10^5 times smaller than those corresponding to H^- ion destruction. We can only state that the H^- ions are created by dissociative reactions at the H_2 molecules to which fast or slow electrons from the discharge become attached, and that these ions are destroyed by collisions with fast electrons (reaction 5). Reactions 6 and 7 are very unlikely since the H^- ions travel very slowly in the anode region.

To give a full account, we should be able to take the potential distribution within the discharge into consideration; we should then know the local energy of each type of particle. We have begun a theoretical study using the computer but the results are not yet available. We cannot yet

really explain why the density of H^- ions reaches a maximum at the edge of the arc column, although this result has been found experimentally. Recent experimental results allow us to make the simplifying assumption that the discharge contains a central zone rich in electrons and positive ions and an outer region with few electrons and many negative ions (Fig. 2).

EXPERIMENTAL RESULTS

3.1. THE INTENSITY OF THE BEAM EXTRACTED. In our first series of experiments, the extraction orifice was circular with a diameter of 1 mm, with which a maximum current of 200 μA was obtained. As the orifice was gradually shifted with respect to the axis of the discharge, the radial variation of the current extracted passed through a maximum, corresponding to the maximum in the density of H^- ions, at about 1 mm from the axis (Fig. 2). The electron current, on the other hand, decreases very rapidly. The magnetic field B was held constant throughout these experiments.

The value of the maximum intensity depends on the arc current I_{arc} . At first, it varies linearly and then saturation sets in. To take the greatest advantage of the sheath of H^- ions, we then used a rectangular orifice, $6 \times 0.2 \text{ mm}^2$, tangent to the discharge. The maximum current obtained was 300 μA with $I_{arc} = 3 \text{ A}$ and 400 μA with $I_{arc} = 8 \text{ A}$ (Fig. 3), and this is at the present time the highest current extracted from a source of this type. The extraction voltage was 15 kV; its value does not affect the magnitude of the current extracted. In these conditions, the gas consumption always remains below $0.5 \text{ cm}^3/\text{min}$.

The current extracted for a given distance d between the axis of the source and the center of the extraction orifice is clearly affected by the magnetic field, which alters not only the radius r_0 of the arc column but also the volume occupied by the ion sheath. We obtain an optimum value of B for each value of d .

The ion current also depends on the distance D between the anode and the intermediate electrode, EI, and there is an optimum value, D_{opt} , at which the current is highest. In our source, $D_{opt} = 3.7 \text{ mm}$ (for H^+ ions, the source is designed with $D = 2 \text{ mm}$).

Finally, the gas pressure in the source is an important parameter. Figure 4 shows how the ion current extracted varies with the hydrogen pressure for different values of the arc intensity. It can be seen that there is an optimum pressure $P_{opt} = 0.4 \text{ Torr}$, which is about ten times higher than that usually employed in standard H^+ sources.

3.2. EMITTANCE OF THE BEAM OF H^- IONS. For a beam that is rotationally symmetric about an axis, we can always plot points in an r - dr/dz plane representing the corresponding coordinates of trajectories intersecting a transverse plane. This procedure yields the emittance diagram of the beam. If the surface area is A , the emittance is defined by the relation

$$E = A/\pi \quad (\text{rad m})$$

It is easier to compare the emittances of different sources in terms of their normalized emittances; for nonrelativistic particles, this quantity is defined by

$$E_n = Ev/c$$

where v is the particle velocity and c is the velocity of light. The brightness B_n of the beam can be derived from E_n by means of the simple relation

$$B_n = \frac{I}{\frac{1}{2}\pi^2 E_n^2}$$

in which I amperes is the beam current.

There are various ways of measuring E . We have developed a direct electrical method, in which the ion beam, from which all the electrons have been removed, falls on a plane collector in which a number of very small holes have been drilled along a diameter. A beamlet of angular aperture $\Delta r'_n$ and mean slope r'_n passes through the n -th hole, distant R_n from the axis. A probe, consisting of a tungsten wire connected to a current amplifier, can be moved at a distance L from the collector. The transverse distribution of beamlets can thus be recorded; the emittance diagram is then easily derived and its area can be measured. Figure 5 gives a typical result obtained in this way.

With a circular extraction orifice 1 mm in diameter, we found

$$E_n = 5 \times 10^{-8} \text{ rad m}$$

and for $I = 200 \mu\text{A}$,

$$B_n \approx 10^{10} \text{ A-rad}^{-2} \text{ m}^{-2}$$

This value is entirely comparable with those obtained for the same current with sources of positive H^+ ions.

We have also taken measurements with the rectangular orifice; two emittances must then be defined since the beam no longer has rotational symmetry (Fig. 6). For $I = 300 \mu\text{A}$, we obtain

$$E_n = 10^{-7} \text{ rad m} \quad \text{in the direction of the longer side}$$

and $E_n = 2 \times 10^{-8} \text{ rad m}$ in the direction of the shorter side

The mean brightness is greater than that of the beam discussed above.

Since these emittances are far lower than the acceptances of tandem accelerators, it is perfectly possible to accelerate the whole beam without loss of particles in the machine.

3.3. THE ENERGY SPREAD OF THE IONS EMERGING FROM THE SOURCE. The energy spread has been measured with the aid of an electrostatic 127° analyzer placed after the magnetic prism. The latter is very weakly excited to eliminate electrons but has almost no effect on the ion trajectories. The ion beam is focused electrostatically onto the entry slit of the analyzer. The extraction voltage is 3 kV and the energy resolution of the system is about 4 eV.

By applying a variable voltage to the plates of the cylindrical condenser, the energy spectrum of the ions is obtained at the exit. The half-width of this curve is about 45 eV when the current is 200 μA ; it increases slowly with the current, but remains close to 50 eV, which is a much smaller spread than those of charge exchange sources.

3.4. MASS DISTRIBUTION OF THE BEAM. The mass spectrum of the ions extracted can be obtained on a collector at the exit of the sector magnet.

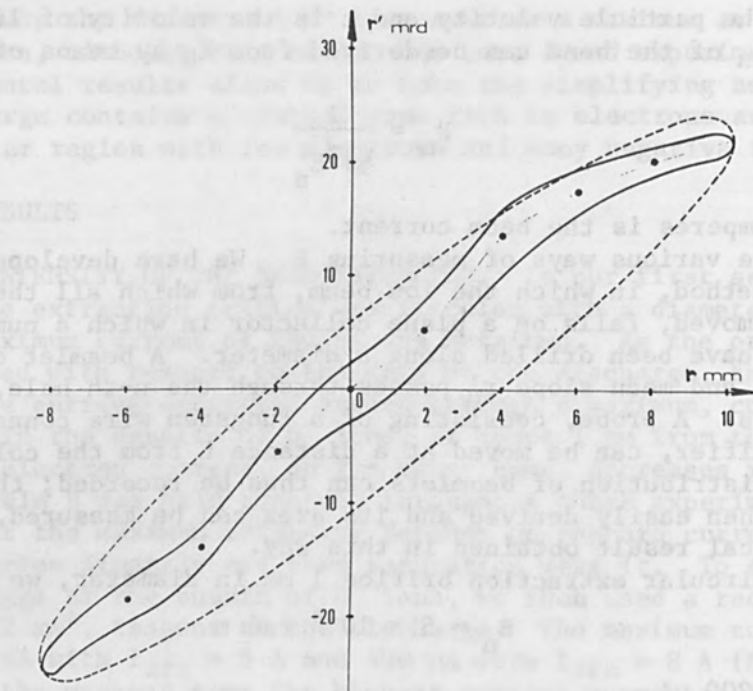


FIG. 5.--Emittance of H^- beam, for a circular anode extraction hole 1 mm in diameter; $I_{H^-} = 200 \mu A$.

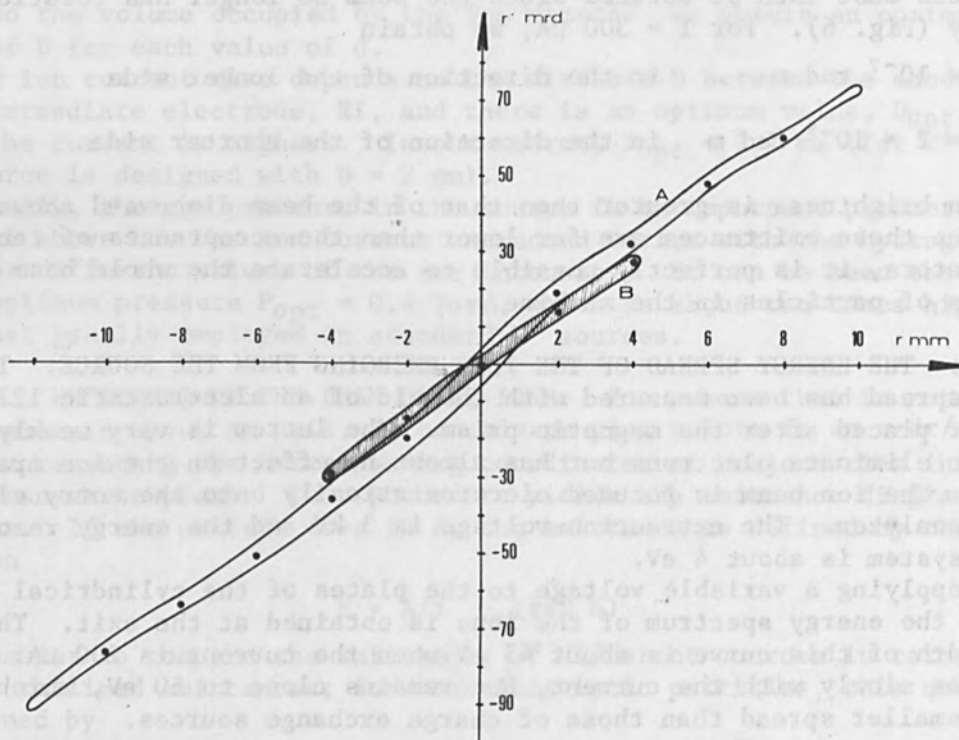


FIG. 6.--Emittance of beam, for a rectangular extraction slit of $6 \times 0.2 \text{ mm}^2$ measured at the output of magnetic prism. A, along the slit direction B, in a perpendicular direction.

In addition to H^- ions, there are numerous peaks corresponding to heavier ions (Fig. 7). We have studied the nature of the latter, their proportions relative to the H^- peak and their evolution in time. These peaks correspond to various impurities that occur as vapors in the source; they originate from the oxide cathode, neoprene joints, and traces of oil vapor from the diffusion pump (even though a liquid nitrogen trap was fitted). The negative atomic and molecular ions mostly consist of O^- , OH^- , C_2^- , C_2H^- , and CN^- . They are numerous when the source is switched on but become more sparse with time: after several hours of operation the corresponding current is about 10 per cent of the total. (The values of the H^- current given above were measured after 90° magnetic deflection so that the impurity ions were not recorded on the collector.)

A second source, identical with the first, has been constructed in a neighboring laboratory, taking advantage of the above results. With careful construction, using metal joints, the impurities have been reduced to 5 per cent, the residual ions being mainly O^- and OH^- . The source is not baked; the hydrogen gas employed is purified before being admitted. This second source is being used in practice on a tandem Van de Graaff accelerator. Its normal operating current can vary from 100 to 200 μA of H^- ions.

By using such gases as CO_2 , CO , and NO , it is possible to produce negative C^- and O^- ions but the lifetime of the cathode is shorter than with H_2 .

CONCLUSION

If we consider currents of a few hundred microamps, the advantages of this type of source over charge-exchange sources are striking: the current is higher, the energy spread of the ions is narrower, the gas consumption is low, and the emittance is small. Experiments are in progress to convert the duoplasmatron into a source of heavy negative ions by modifying the conditions of the discharge and the electron energies.

ACKNOWLEDGMENTS

We are grateful to the Compagnie Thomson-CSF for practical help while we have been studying this source, and in particular to Messrs. Warnecke and Kervizic, with whom we have enjoyed many fruitful discussions.

REFERENCES

1. G. P. Lawrence, R. K. Beauchamp, and J. L. McKibben, Direct extraction of negative ion beams of good intensity from a duoplasmatron, *Nucl. Instr. Math.* 32: 357-359, 1965.
2. A. B. Wittkower, R. P. Bastide, N. B. Brooks, and P. H. Rose, Injection of intense neutral beams into a tandem accelerator, *Rev. Sci. Instr.* 35: 1-11, 1964.
3. D. Dandy and D. P. Hammond, A pulsed negative ion beam injector, *Nucl. Instr. Math.* 30: 23-33, 1964.
4. C. H. Goldie, Terminal sources, *Nucl. Instr. Math.* 28: 139-145, 1964.
5. J. M. Sautter, M. Baribaud, and J. M. Dolique, Conception et réalisation d'une source très intense d'ions hydrogène négatifs, *C. R. Acad. Sci.* 263: 1211-1214, 1966.

6. K. W. Ehlers, Design consideration for high intensities negative ion sources, IEEE Trans. Nucl. Sci. NS-12: 811-817, 1965.
7. G. Collins and R. H. Gobett, Extraction of negative hydrogen ion from a duoplasmatron, Nucl. Instr. Math. 35: 277-282, 1965.
8. M. Dubarry and G. Gautherin, Source d'ions H^- du type duoplasmatron, Première Conférence Internationale sur les Sources d'Ions: 133-147, Saclay, 1969.

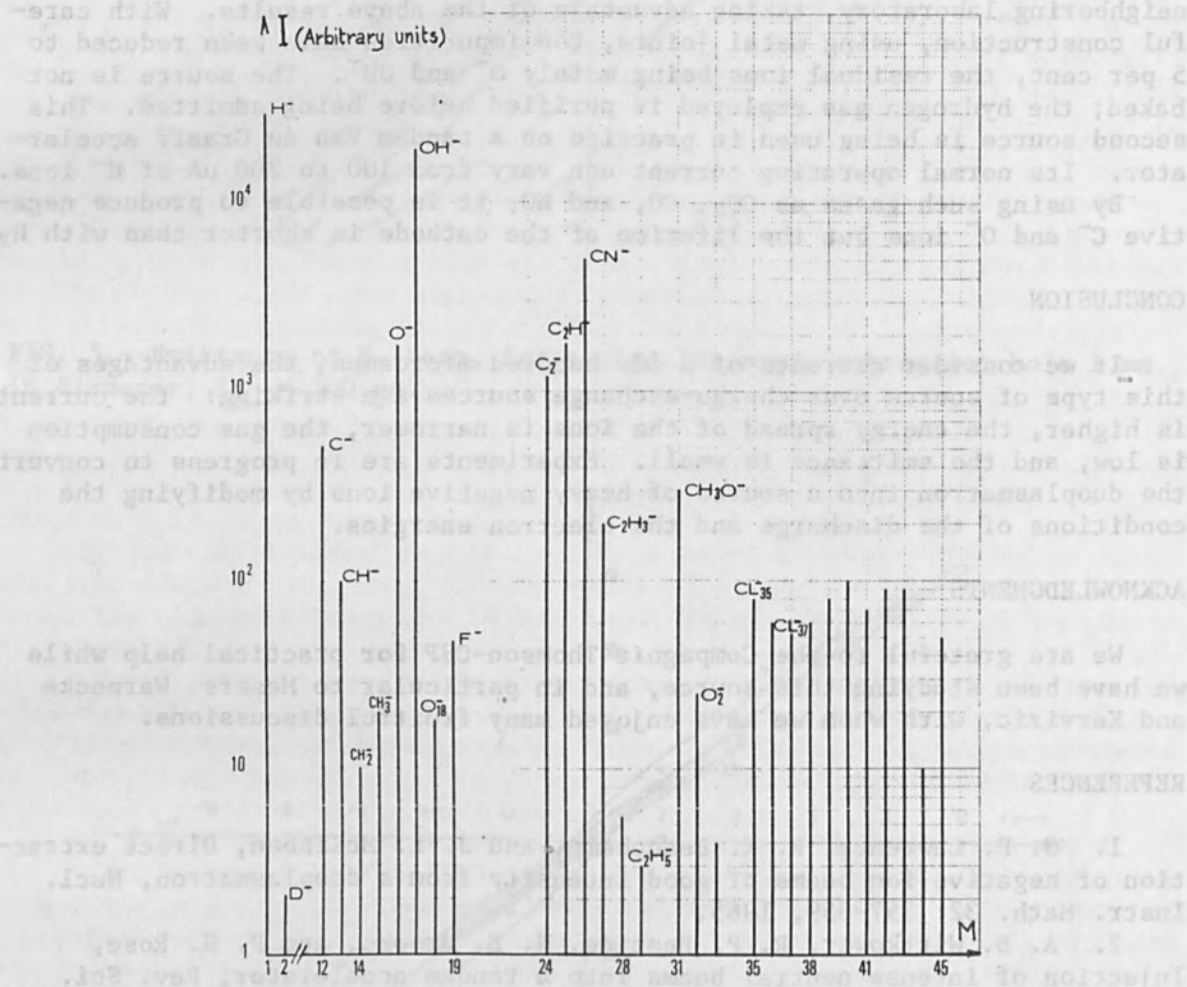


FIG. 7.--Example of a mass spectrum obtained in first hour of source working. Impurities are due to desorbed gases and organic vapors.

ELECTRON-BOMBARDMENT ION SOURCE OPERATION USING VARIOUS GASES

D. C. BYERS and P. D. READER

NASA Lewis Research Center, Cleveland, Ohio

INTRODUCTION

The electron-bombardment ion thruster^{1,2} has been the object of a research and development program³ at the Lewis Research Center and elsewhere for over a decade. The primary interest in this ion source has rested on application to advanced space propulsion systems. Two experimental space flights have been conducted with the mercury electron-bombardment ion source.^{4,5} This ion source has been operated in excess of 6000 hr in ground tests.⁵ Thrusters 5-150 cm in diameter³ have been operated and net ion energies from 0.4 to 70 kV^{3,6} have been utilized. Mercury and cesium have been the propellants used for most tests because their large atomic mass is attractive for propulsion applications. The electron-bombardment ion source can be operated with a variety of gases. An early refractory cathode thruster was operated with several gases⁷ and more recently a hollow-cathode thruster was operated with argon.⁸ Operation with materials other than mercury and cesium is of interest for a number of ground-based applications.⁹ In addition, some flight applications such as biowaste expulsion¹⁰ may be of interest. This paper describes the operation of a flight-type (Space Electric Rocket Test, SERT II) thruster with xenon, krypton, argon, neon, nitrogen, helium, and carbon dioxide. Magnetic spectrometer data were taken with some of these gases to determine the ion species ejected from the source.

APPARATUS AND PROCEDURE

The basic 15-cm-diam. thruster used in this investigation has been described previously.⁸ The thruster was a modification of the SERT II thruster⁵ and is shown in cross section in Fig. 1. The details of construction and operation have been adequately described elsewhere.¹¹ Two additional modifications were made to the thruster⁸ for some of these tests. The orifice in the hollow cathode end cap was enlarged from 0.4 to 0.75 mm. Other experiments¹² indicate that cathode erosion rates should be reduced by as much as two orders of magnitude by this enlargement. For some tests the screen grid was masked down to half radius (i.e., a beam diameter of 7.5 cm). This last modification had been done in an earlier experiment⁷ to increase the neutral density in the discharge chamber and had allowed a wider range of operation with the low molecular weight gases. The thruster operated with the masked screen is referred to here as the modified thruster.

The thruster startup procedure was nearly identical to that described by Schertler,⁸ except that a high starting voltage was applied to both the cathode keeper and the anode, rather than to the cathode keeper alone. With the low molecular weight (less than 50 amu) gases the thruster discharge often initiates directly between the cathode and anode followed by ignition of the keeper discharge. In these cases the product of pressure and distance between the cathode and the anode was

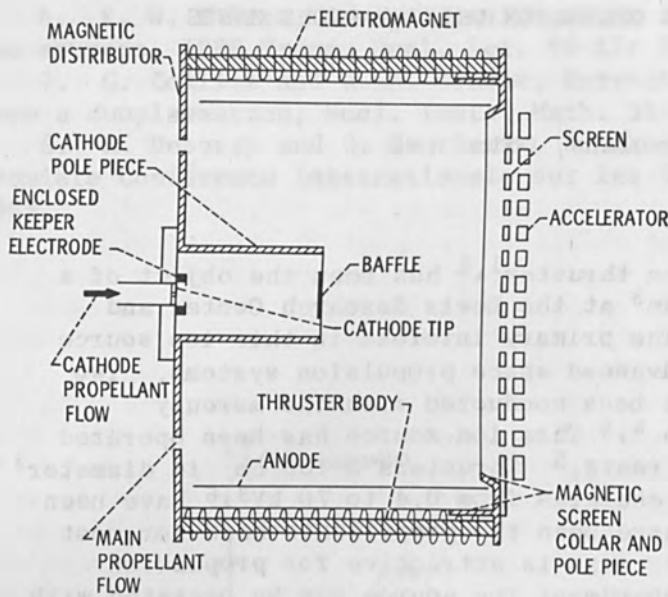


FIG. 1.--Sketch of 15-cm-diam electron bombardment thruster.

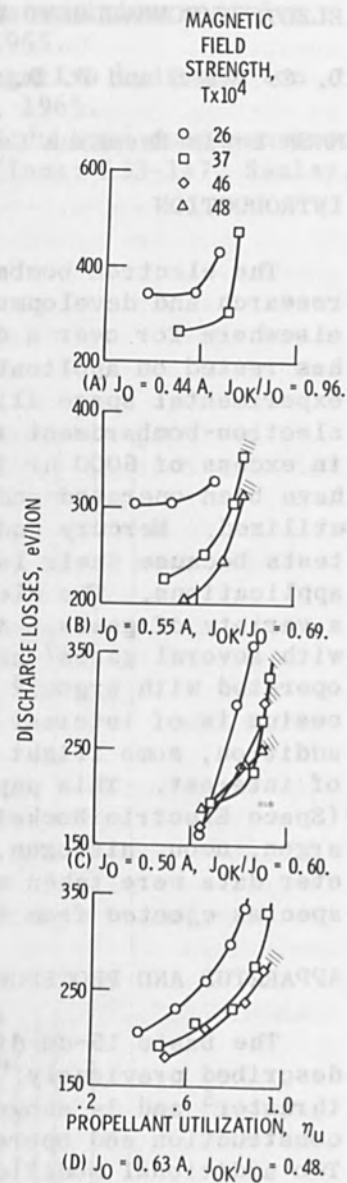


FIG. 2.--Discharge-chamber performance for xenon.

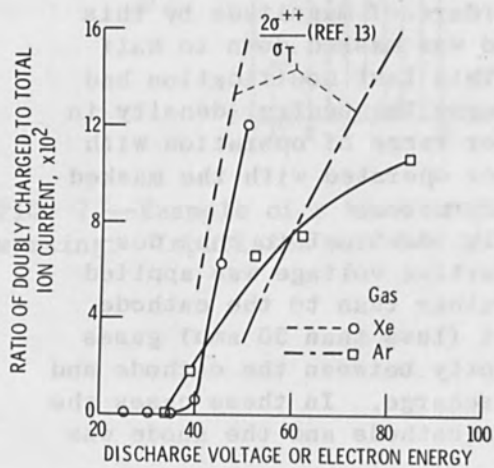


FIG. 3.--Ratio of doubly charged to total ion current for xenon and argon. Modified thruster.

closer to the Paschen minimum for the breakdown than that of the keeper region.

The magnetic field strength could be varied with the eight electromagnets described in Ref. 8 and was measured a few millimeters downstream from the cathode polepiece baffle.

After determining the performance in various gases with the basic and modified thruster, a simple mass spectrometer was installed in the facility to determine the ion species in the thruster beam. All of the spectrometer data were obtained with the modified thruster. The spectrometer consisted of a set of collimating slits positioned on the beam axis, a uniform variable magnetic field region, and an ion current collector that could be biased negatively to prevent electron collection. The magnetic field was varied so that beam ions of different charge-to-mass ratios would strike the collector located at an angle of 60° with respect to the axis of the collimating slits.

RESULTS AND DISCUSSION

Data are presented on the performance of xenon, krypton, argon, neon, nitrogen, helium, and carbon dioxide. The performance is defined in terms of discharge power dissipated per beam ion produced (eV/ion) and propellant utilization. The propellant utilization is the ratio of the ion beam current to the total inlet neutral flow rate. All neutral flow rates are expressed in equivalent amperes. The presence of multiply ionized or fractionated ions in the beam impacts both of these performance parameters. For simplicity, the graphically presented data are shown with the assumption of singly charged parent ions in the beam. Use of the magnetic spectrometer allowed evaluation of the assumption of single charge. Data are presented for the basic thruster⁸ and/or the modified thruster for the various gases. Other parameters that affect thruster lifetime or stability (for example, chamber or keeper discharges) are also discussed. The screen and accelerator extraction voltages were +3 and -2 kV respectively for all data presented herein.

XENON. Figure 2 shows the performance of the basic thruster with xenon for several values of cathode propellant flow rate J_{0k} and main propellant flow rate J_m . The total inlet flow rates, J_0 (where $J_0 = J_{0k} + J_m$), were varied over a larger range than shown but the flow rates shown gave the best performance. The upper limit on total flow rate resulted because the space-charge-limited current of the ion extraction system with xenon was about 0.6 A. At higher total flow rates it was not possible to operate at high propellant utilization. The lower limit on total flow rate for stable discharge operation was a cathode flow rate of about 0.3 A. The discharge voltages were between 29 and 40 V.

As the inlet flow rates were varied the performance shifted and was best at the conditions of Fig. 2(c), near the minimum cathode flow rate for that total flow rate. At optimum conditions the discharge losses were similar to those for mercury. The eV/ion generally decreased with increasing magnetic field at constant propellant utilization efficiency. At optimum flow conditions, however, the sensitivity of discharge losses to magnetic field variations was small. The magnetic field also affected thruster stability in that as the field strength increased the stable range of discharge current decreased. The

crosshatched areas on the figures represent regions of thruster instability.

Magnetic spectrometer data (Fig. 3) were obtained with xenon after the basic thruster had been masked down. Data obtained with argon are also shown and are discussed later. The ratio of the ion current due to doubly charged ions to the total ion current is shown as a function of discharge voltage. The ratio of twice the double ionization cross section to the total ionization cross section¹³ as a function of electron energy is shown as a dashed line. This ratio yields the relative ion current when electron-ion-inelastic collisions are neglected.¹⁴ For xenon no doubly ionized atoms were observed at discharge voltages less than 40 volts. However, the measured amount of double ionization was somewhat smaller than indicated from the cross section data. Because all the data of Fig. 2 were at discharge voltages less than 40 V, the values of discharge loss and propellant utilization are essentially those for singly charged ions.

KRYPTON. The performance of krypton is shown in Fig. 4 over a range of inlet flow rates. The upper and lower limits on flow rate due to ion extraction limits and discharge instability with krypton were about 0.9 and 0.45 A, respectively. The optimum flow rate for krypton is difficult to specify. At the lower magnet field strength the performance degraded as the cathode flow decreased. At the high magnetic field the range of discharge stability increased with decreasing cathode flow and allowed higher propellant utilizations to be achieved. At magnetic fields slightly higher than those shown, the thruster exhibited instabilities at nearly all values of discharge current.

No mass-spectrometer data were taken with krypton. All the data of Fig. 4 were taken at discharge voltages between 31 and 38 V. The ratio of double to total ionization cross section at 40 V is less than 1 per cent,¹³ so that no significant double ionization should have resulted.

ARGON. Argon was tested with the modified thruster to determine if the range of propellant flow and stability could be improved over previously published data for the basic thruster. Operation with argon is of particular interest because the gas is relatively inexpensive and easily pumped. These considerations would be of importance for several ground-based gas ion source applications.

Figure 5 shows the performance of the modified thruster with argon. The best performance obtained with argon in the basic thruster is shown by the dashed line for comparison. Masking the screen grid caused an increase of about a factor of three in the eV/ion. Such an increase might be expected because the discharge losses of this thruster type are quite sensitive to the open area of the screen grid.¹⁵ Figure 5 also shows that the modified thruster could be operated at considerably lower discharge voltage than the basic thruster. The low discharge voltages are of interest because the cathode lifetime increases with decreasing discharge voltage.

The performance of the modified thruster was quite sensitive to magnetic-field strength. An increase in the magnetic-field strength generally caused an increase in the discharge voltage and propellant utilization and a decrease in the discharge losses.

The strong dependence of discharge performance on cathode keeper power noted with the basic thruster was sharply reduced with the

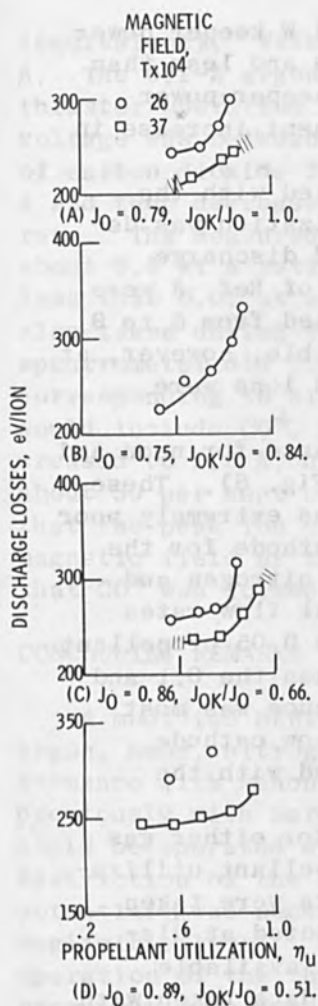


FIG. 4.--Discharge-chamber performance, krypton.

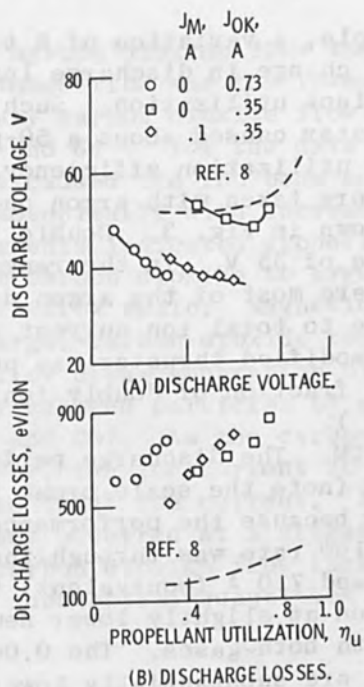


FIG. 5.--Discharge-chamber performance with argon. Modified thruster. Magnetic field strength, 26×10^{-4} T.

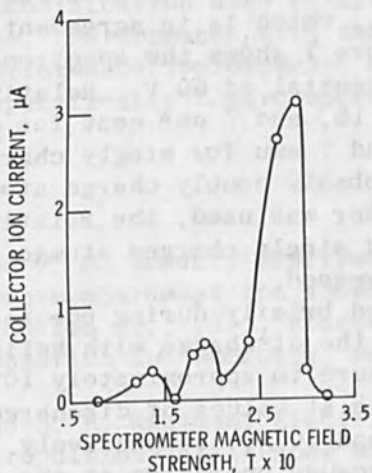


FIG. 7.--Collection ion current as a function of spectrometer magnetic-field strength with nitrogen. Modified thruster; discharge voltage, 60 V.

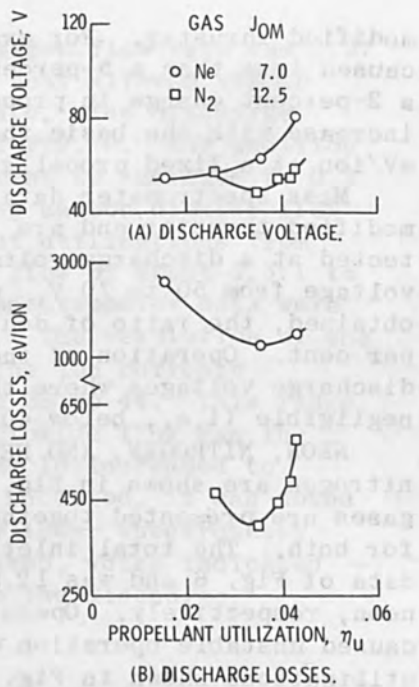


FIG. 6.--Discharge-chamber performance with nitrogen and neon. Modified thruster.

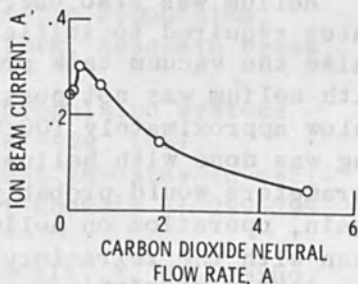


FIG. 8.--Effect of carbon dioxide flow rate on ion beam current cathode flow, argon. Modified thruster.

modified thruster. For example, a variation of 8 to 34 W keeper power caused less than a 5-percent change in discharge losses and less than a 2-percent change in propellant utilization. Such a keeper-power increase with the basic thruster caused about a 50-percent increase in eV/ion at a fixed propellant utilization efficiency.

Mass spectrometer data were taken with argon operated with the modified thruster and are shown in Fig. 3. Double ionization was detected at a discharge voltage of 35 V. In the range of discharge voltage from 50 to 70 V, where most of the argon data of Ref. 8 were obtained, the ratio of double to total ion current varied from 5 to 9 per cent. Operation of the modified thruster was possible, however, at discharge voltages where the fraction of doubly ionized ions were negligible (i.e., below 40 V).

NEON, NITROGEN, AND HELIUM. The discharge performance for neon and nitrogen are shown in Fig. 6 (note the scale break in Fig. 6). These gases are presented together because the performance was extremely poor for both. The total inlet flow rate was through the cathode for the data of Fig. 6 and was 12.5 and 7.0 A (equivalent) for nitrogen and neon, respectively. Operation at slightly lower neutral flow rates caused unstable operation with both gases. The 0.04 to 0.05 propellant utilizations shown in Fig. 6 are substantially lower than the 0.1 and 0.2 values obtained in an earlier study.⁷ This difference was most probably due to the characteristics of the present hollow cathode operating on gases of low molecular weight when compared with the thermionic refractory emitters used in that study.

Because the space-charge-limited ion beam current for either gas was less than 1 A it was impossible to obtain high propellant utilizations with stable operation. Magnetic-spectrometer data were taken with both gases. No double ionization of neon was detected at discharge voltages up to 80 V., which is in agreement with available cross-section data.¹³ Figure 7 shows the spectrometer data taken with nitrogen at a discharge potential of 60 V. Relative percentages of peak ion currents were 78, 15, and 7 per cent for charge-to-mass ratios corresponding to 28, 14, and 7 amu for singly charged ions. The peak at 7 amu equivalent was probably doubly charge atomic nitrogen. Because a magnetic spectrometer was used, the relative fractions of doubly charged diatomic and singly charged atomic nitrogen at 14 amu equivalent could not be assessed.

Helium was also operated briefly during one test. The neutral flow rates required to initiate the discharge with helium were such as to raise the vacuum tank pressure to approximately 10^{-3} torr. Operation with helium was not possible at values of discharge voltage and current below approximately 100 V and 10 A, respectively. Very limited testing was done with helium because operation at the required discharge parameters would probably result in very short cathode lifetime. Again, operation on helium with the hollow cathode was more difficult than with the refractory thermionic emitter of Ref. 7.

CARBON DIOXIDE. The modified thruster was operated with carbon dioxide, a possible biowaste propellant,¹⁰ as the main flow propellant (Fig. 1) and argon as the cathode-flow propellant. Carbon dioxide was not introduced through the cathode because of the possibility of cathode-material oxidation. Some results are shown in Fig. 8. For these data the argon flow rate was held nearly constant at 0.1 A

(equivalent). With no carbon dioxide flow the argon flow rate was 0.27 A. The 0.1-A argon cathode flow was the lowest that allowed stable thruster operation at any carbon dioxide flow rate. The discharge voltage was between 52 and 64 V for the data of Fig. 8. The addition of carbon dioxide first caused the ion beam current to increase to 0.3 A and then decrease monotonically with increasing carbon dioxide flow rate. The measured currents indicated propellant utilizations from about 0.8 at a ratio of carbon dioxide to argon flow of about 2.5:1 to less than 0.01 at a 50:1 flow ratio. Magnetic-spectrometer data were also taken during the argon-carbon dioxide test. The resolution of the spectrometer did not allow clear separation of the ion currents corresponding to singly charged particles of amu 28 to 44. This range would include CO^+ , A^+ , and CO_2^+ . As the carbon dioxide flow was increased to 1.9 A, however, the ion current at amu 16 increased to about 30 per cent of the total ion current. In addition, it was noted that the peak ion current occurred at a slightly lower spectrometer magnetic field as the carbon dioxide flow increased, which indicated that CO^+ was formed in substantial quantities in the discharge.

CONCLUDING REMARKS

A modified SERT II ion thruster was operated with xenon, krypton, argon, neon, nitrogen, helium, and carbon dioxide. The discharge performance with xenon, krypton, and argon was similar to that obtained previously with mercury.⁸ Mass spectrometer data indicated that xenon could be operated efficiently with no significant multiple ionization. Restriction of the beam area, with an associated decrease in discharge potential, was necessary to reduce multiple ionization with argon to a negligible level. This modification also resulted in more stable operation of the thruster. Performance with the remaining gases was poor, but some future performance improvements may be realizable with modifications directed specifically toward operation with gases of low molecular weights.

REFERENCES

1. H. R. Kaufman and P. D. Reader, Experimental performance of ion rockets employing electron-bombardment ion sources, in D. B. Langmuir, E. Stuhlinger and J. M. Sellen Jr., eds., *Electrostatic Propulsion*, vol. 5 *Progress in Astronautics and Rocketry*, New York, Academic Press, 1961; pp. 3-20.
2. D. J. Kerrisk and H. R. Kaufman, Electric propulsion systems for primary spacecraft propulsion, AIAA Paper No. 67-424, 1967.
3. E. A. Richley and W. R. Kerslake, Bombardment thruster investigations at the Lewis Research Center, *J. Spacecraft Rockets* 6: 289-295, 1969.
4. R. J. Cybulski, D. M. Shellhammer, R. R. Lovell, E. J. Domino, and J. T. Kotnik, Results from SERT I ion rocket flight test, NASA TN D-2718, 1965.
5. W. R. Kerslake, R. G. Goldman, and W. C. Nieberding, SERT II: mission, thruster performance, and in-flight thrust measurements, *J. Spacecraft Rockets*, 8: 213-224, 1971.

6. D. C. Byers, An experimental investigation of a high-voltage electron-bombardment ion thruster, *J. Electrochem. Soc.* 116: 9-17, 1969.
7. P. D. Reader, The operation of an electron bombardment ion source with various gases, R. Bakish, ed., *First International Conference on Electron and Ion Beam Science and Technology*, New York, Wiley, 1965; pp. 925-935.
8. R. J. Schertler, Preliminary results of the operation of a SERT II thruster on argon, *AIAA Paper No. 71-157*, 1971.
9. G. Carter and J. S. Colligon, *Ion Bombardment of Solids*, New York, American Elsevier, 1968.
10. R. V. Greco and R. M. Byke, Resistorjet biowaste utilization: evaluation and system selection, *AIAA Paper No. 68-121*, 1968.
11. D. C. Byers and J. F. Staggs, SERT II: Thruster system ground testing, *J. Spacecraft Rockets* 7: 7-14, 1970.
12. R. T. Bechtel, Component testing of a 30-centimeter diameter electron bombardment thruster, *AIAA Paper No. 70-1100*, 1970.
13. L. J. Kieffer and G. H. Dunn, Electron impact ionization cross-section data for atoms, atomic ions, and diatomic molecules: I - experimental data, *Rev. Mod. Phys.* 38: 1-35, 1966.
14. N. L. Milder, Comparative measurements of singly and doubly ionized mercury by electron-bombardment ion engine, *NASA TN D-1219*, 1962.
15. R. T. Bechtel, Discharge chamber optimization of the SERT II thruster, *J. Spacecraft Rockets* 5: 795-800, 1968.

ELECTRON-BOMBARDMENT TYPE SIMPLIFIED ION SOURCE

T. TAKAGI, I. YAMADA, and J. ISHIKAWA

Kyoto University (Department of Electronics), Kyoto, Japan

Some properties of an electron bombardment type ion source for ion implantation are studied. The magnetic field induced by the filament heating current of filament coil which emits electrons in the discharge chamber is utilized effectively. A new simplified ion source without external magnetic field is designed and operating characteristics are measured. It is shown that intense and fine ion beams can be obtained easily from various kinds of materials not only in gaseous states, but also in solid states at room temperatures, because this new ion source works stably even at high temperatures.

INTRODUCTION

Much work has been done to get high-current ion beams for particle accelerators, isotope separators, plasma apparatus, and ion implantation systems.¹ It is very difficult to produce an intense beam with a high efficiency for various kinds of ions. A particular type of gun is useful only for a particular purpose. The new simplified ion source of an electron bombardment type suitable for ion implantation is studied here. The following considerations enter.

(1) In various kinds of ion sources, the longitudinal magnetic field is often useful to increase the effective path of electrons and the rate of ion production in the source, because the electrons follow spiral trajectories before reaching the anode owing to the crossed electromagnetic fields. The longitudinal magnetic field is also effective in concentrating the plasma along the axis. In our newly designed ion source, the longitudinal magnetic field which is induced by the heating current of the filament is used instead of an external magnetic field.

(2) A central anode pipe is constructed along the axis at the center of the filament coil in order to utilize the longitudinal magnetic field effectively. The central anode pipe has a small chamber and a material to be ionized is inserted in it. The material is heated by electron bombardment and thermal radiation from the filament coil. The CCl_4 method is also available by introducing a CCl_4 gas from the opposite end of the central anode pipe.

(3) Since there are no external magnetic coils, the discharge chamber can be very small. This means that it is easy to raise the temperature and that in this way the gun will operate in a stable condition even at a high temperature. All these features are favorable for the ionization of metals with low evaporation pressures. The magnetic field resulting from the current to heat the discharge chamber can be aligned in the same direction as that due to the current of the filament coil. By this arrangement the operation can be more stabilized.

(4) It is desirable that ions extracted through a hole of the discharge chamber are concentrated originally in the longitudinal axis as narrow as possible, because it is then easy to obtain a fine and high density ion beam. A soft-iron extractor is used to extract ions and

condense the magnetic flux in the neighborhood of an extraction electrode. The plasma is concentrated under the action of the magnetic field on axis.

DESIGN AND OPERATION CHARACTERISTICS OF THE EXPERIMENTAL ION SOURCE

Figure 1 shows the equipment and the partially enlarged schematic diagram of the experimental ion source, respectively. A tantalum filament coil, a tantalum central anode pipe, a tantalum anode, a cylindrical tube made of quartz, a stainless steel base metal and a soft iron extractor are used (Fig. 1 b). The discharge chamber is surrounded by the anode, quartz tube, and base metal. A gas to be ionized is introduced through the gas inlet. When a material to be ionized is in a solid state, it is inserted into a small chamber in the central anode pipe.

Anode voltage V_a is applied to both of the central anode pipe and anode. Electric field E between central anode pipe and the filament is crossed with a longitudinal magnetic field produced by the filament heating current I_h . The electrons emitted from the filament follow spiral trajectories before reaching the central anode pipe or anode through the crossed fields. As a result, the degree of ionization in the source increases and a plasma fills the space, keeping a high intensity near the axis in the discharge chamber. The ions are extracted by means of an accelerating electrode "extractor" through a hole of the anode.

Negative voltage V_{ex} is applied to the extractor. The focusing condition changes by various source parameters such as the distance between the anode and the extractor, the shape of the extractor, the diameter of the hole of the anode, applied voltage to these electrodes, and the shape of plasma surface near the hole. By combination of these conditions, focusing of the ion beam in the extraction region can form either a convex meniscus or a concave meniscus. For a fine and intense ion beam, it is important to adjust distances, shapes, and applied voltages of the electrodes.

Some of the ions extracted by the extractor voltage V_{ex} are caught by the extractor and form extractor current I_{ex} , but most ions reach the collector through the extractor and form collector current I_c . Actually, a focus lens system is normally placed between the extractor and the collector, but in this experiment ion current I_i was measured without any focus system. I_i is the sum of extractor current I_{ex} and collector current I_c .

Because the filament coil is not only an electron emitting source, but also serves for a magnetic-field coil, the filament current and the shape and number of turns of filament coil are important factors with serious effects on the characteristics of the ion source. In this paper, the characteristics of the ion gun are studied in the following conditions:

Material: tantalum

Wire diameter: 0.6 mm

Inner diameter of coil: 9 mm

Number of turns per unit length: 5 turns/cm

Number of turns of actual filament coil in the experiment: 1.5, 4.5, 7.5, and 10.5

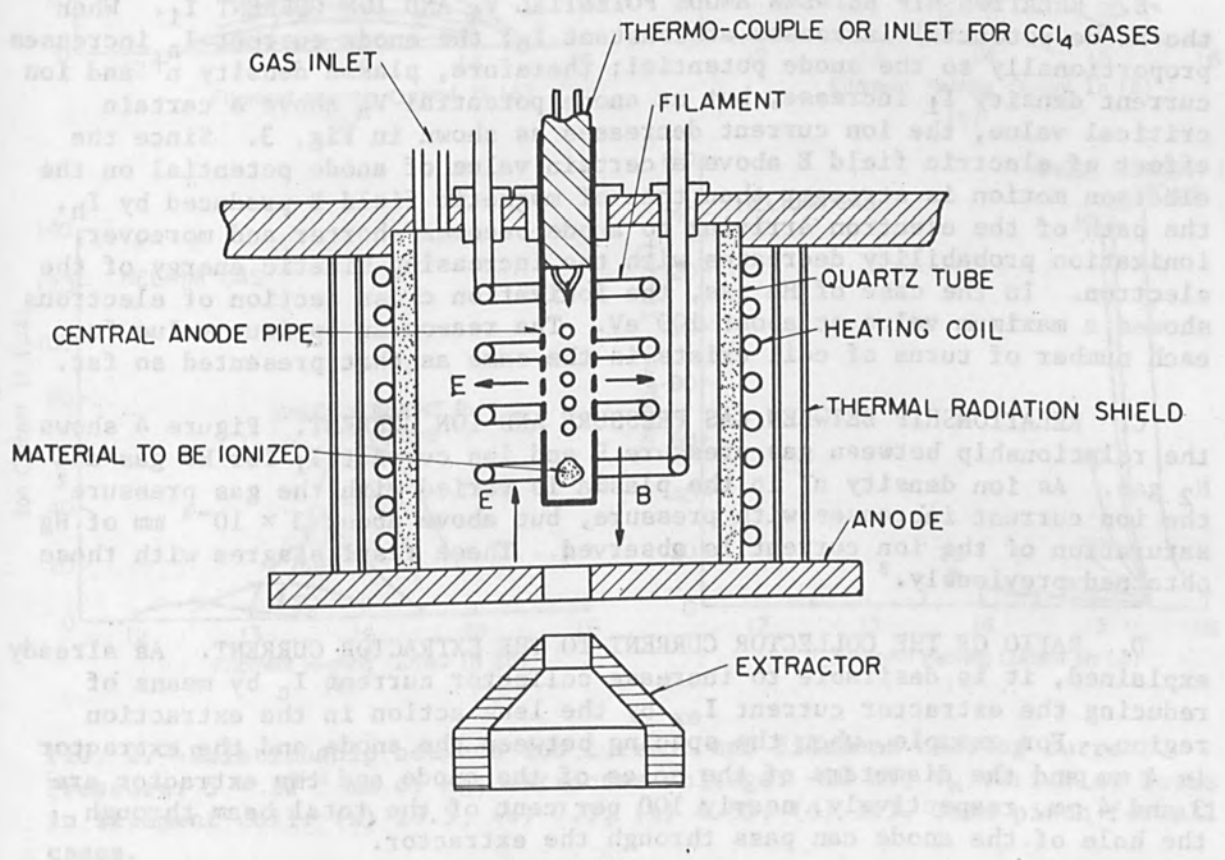
Helium and nitrogen (gases) and indium (metal) were used.

A. RELATIONSHIP BETWEEN FILAMENT CURRENT I_h AND ION CURRENT I_i . In our experiment the magnetic field produced by filament current is used for

the increase of ion production and the discharge chamber, so that it is necessary to investigate the effect of the filament current on the magnetic field. Both the amount of the discharge current and the ionization current increase with increasing filament current. The ionization current decreases with increasing filament current, as shown in Fig. 2. The ionization current for 1.5 turns seems to be the maximum value. The ionization current for 1.5 turns seems to be the maximum value of possible extraction for the filament coil increases when the number of turns increases. In view of these facts, the filament density is inversely proportional to the surface area of the filament with different number of turns. The area of the filament surface also increases with increasing number of turns of the filament.



(a)



(b)

FIG. 1.--Simplified ion source: (a) column, (b) schematic.

the increase of ion production and for the condensation of plasma in the discharge chamber, so that it is necessary to investigate the effect of the filament current on the magnetic field. Both the amount of the electron emission and the longitudinal magnetic field increase with increasing filament current. Relationships between the ion current and the filament current are shown in Fig. 2. The anode potential decreases with increasing number of turns when I_h and I_a are kept constant; V_a decreases with increasing I_h for constant I_a under the same number of turns. As shown in Fig. 2, the optimum points for operations appear. Figure 2(d) for 1.5 turns seems somewhat incomplete because it is impossible to obtain the required intensity of I_a due to the saturation of the electron emission, but if the desired I_a is obtained, Fig. 2(d) also shows the maxima exhibited in Fig. 2(a), (b), and (c). It is clearly shown in the figures that the maximum value of possible extracted ion current I_i increases with decreasing number of turns at constant I_a . The surface area of the filament coil increases when the number of turns increases. It seems, in view of these facts, that the plasma density is inversely proportional to the surface area of the filament with different number of turns used in the discharge chamber of the same volume. The area of the plasma sheath through which ions recombine on the filament surface also increases with increasing number of turns of the filament.

B. RELATIONSHIP BETWEEN ANODE POTENTIAL V_a AND ION CURRENT I_i . When the anode potential increases at constant I_h , the anode current I_a increases proportionally to the anode potential; therefore, plasma density n^+ and ion current density I_i increase, but at anode potential V_a above a certain critical value, the ion current decreases as shown in Fig. 3. Since the effect of electric field E above a certain value of anode potential on the electron motion is stronger than that of magnetic field B produced by I_h , the path of the electron arriving to anode becomes shorter and moreover, ionization probability decreases with the increasing kinetic energy of the electron. In the case of He gas, the ionization cross section of electrons showed a maximum value at about 100 eV. The reason an optimum value for each number of turns of coil exists is the same as that presented so far.

C. RELATIONSHIP BETWEEN GAS PRESSURE AND ION CURRENT. Figure 4 shows the relationship between gas pressure P and ion current I_i for He gas and N_2 gas. As ion density n^+ in the plasma is varied with the gas pressure² the ion current increases with pressure, but above about 3×10^{-3} mm of Hg saturation of the ion current is observed. These results agree with those obtained previously.³

D. RATIO OF THE COLLECTOR CURRENT TO THE EXTRACTOR CURRENT. As already explained, it is desirable to increase collector current I_c by means of reducing the extractor current I_{ex} by the lens action in the extraction region. For example, when the spacing between the anode and the extractor is 4 mm and the diameters of the holes of the anode and the extractor are 3 and 4 mm, respectively, nearly 100 per cent of the total beam through the hole of the anode can pass through the extractor.

E. NORMALIZED EMITTANCE AND NORMALIZED BRIGHTNESS. The normalized emittance for an nitrogen ion current of 60 μ A and an extractor voltage of 10 kV is 1.9×10^{-8} rad m. The normalized mean brightness in the same condition is 3.5×10^{10} A rad⁻² m⁻².

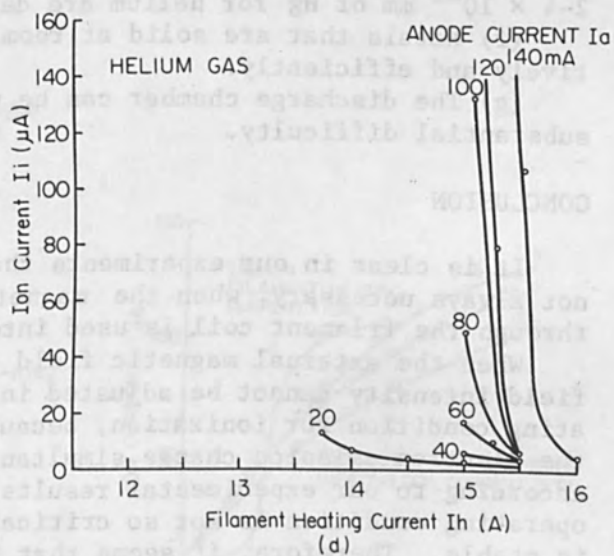
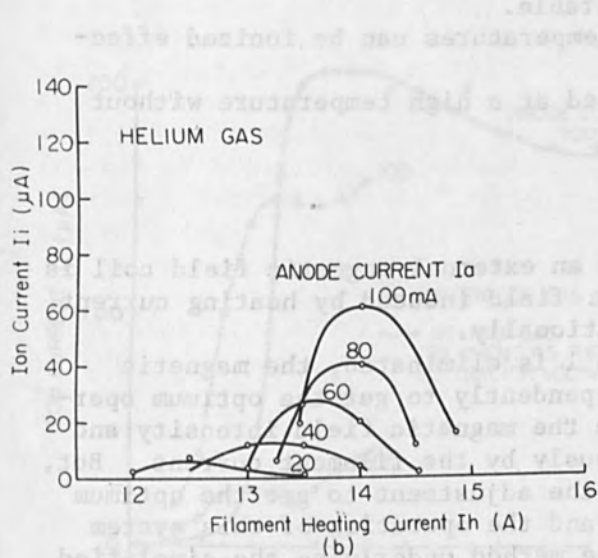
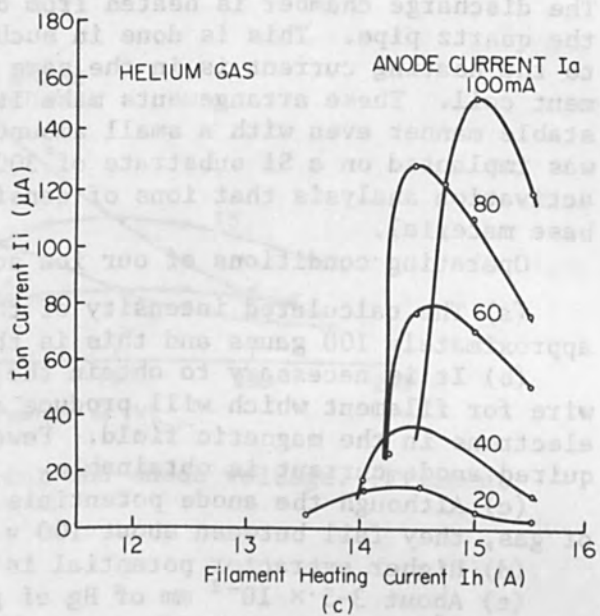
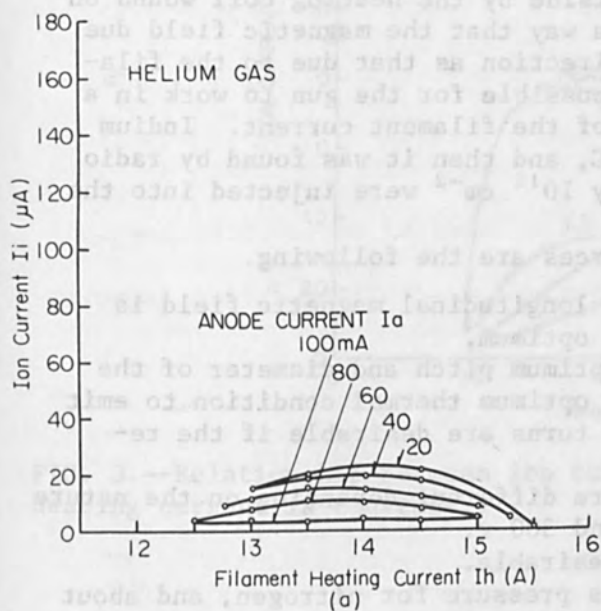


FIG. 2.--Relationship between ion current and filament heating current. Pressure: 5×10^{-3} mm of Hg; extractor voltage: -10 kV; V_a variable. Turns in filament coil: (a) 10.5, (b) 7.5, (c) 4.55, (d) 1.5. Same pitch for all cases.

Characteristics in cases where metallic vapor is ionized (the metal used is a solid at room temperature and is then heated) are as follows. An indium metal was enclosed in a small chamber within the central anode pipe, and was then heated to yield an ion current. The result is shown in Fig. 5, where the ion current is plotted against the anode current, together with the filament heating current as a parameter. An indium ion current of 100 - 150 μA was obtained at the extractor voltage of -10 kV. The discharge chamber is heated from outside by the heating coil wound on the quartz pipe. This is done in such a way that the magnetic field due to the heating current is in the same direction as that due to the filament coil. These arrangements make it possible for the gun to work in a stable manner even with a small amount of the filament current. Indium was implanted on a Si substrate of 300°C, and then it was found by radio activation analysis that ions of density 10^{15} cm^{-2} were injected into the base material.

Operating conditions of our ion sources are the following.

(a) The calculated intensity of the longitudinal magnetic field is approximately 100 gauss and this is the optimum.

(b) It is necessary to obtain the optimum pitch and diameter of the wire for filament which will produce an optimum thermal condition to emit electrons in the magnetic field. Fewer turns are desirable if the required anode current is obtainable.

(c) Although the anode potentials are different depending on the nature of gas, they fall between about 100 v and 300 v.

(d) Higher extractor potential is desirable.

(e) About $3-5 \times 10^{-3}$ mm of Hg of gas pressure for nitrogen, and about $2-4 \times 10^{-2}$ mm of Hg for helium are desirable.

(f) Metals that are solid at room temperatures can be ionized effectively and efficiently.

(g) The discharge chamber can be used at a high temperature without substantial difficulty.

CONCLUSION

It is clear in our experiments that an external magnetic field coil is not always necessary, when the magnetic field induced by heating current through the filament coil is used intentionally.

When the external magnetic field coil is eliminated, the magnetic field intensity cannot be adjusted independently to get the optimum operating condition for ionization, because the magnetic field intensity and the electron emission change simultaneously by the filament current. But, according to our experimental results, the adjustment to get the optimum operating condition is not so critical and the operation of this system is stable. Therefore, it seems that the method underlying the simplified ion source is useful in practice.

When metal ions of any kind are necessary, the discharge chamber units suitable for each metal can be provided. These units are expected to work in a stable manner and efficiently at high temperatures and form an interchangeable part of our ion implantation apparatus.

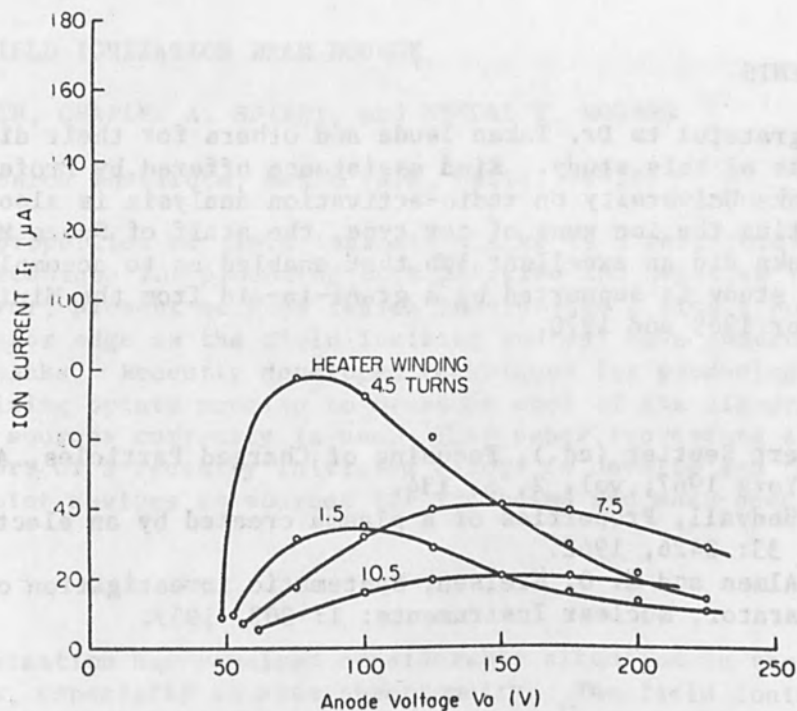


FIG. 3.--Relationship between ion current and anode voltage. (Filament heating current is constant.)

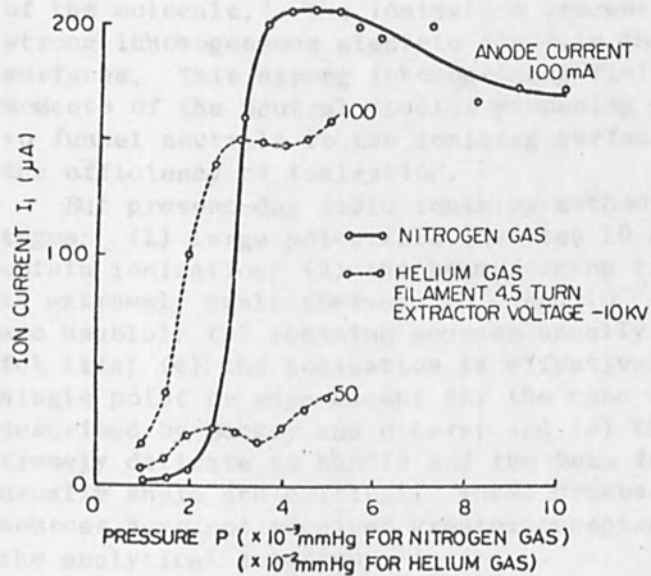


FIG. 4.--Relationship between gas pressure and ion current.

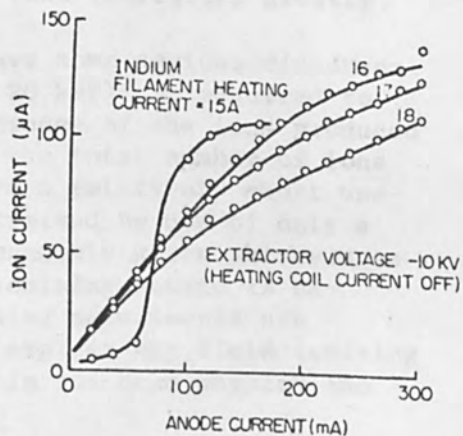


FIG. 5.--Relationship between ion current and anode current (indium):

MULTIPOINT FIELD IONIZATION BEAM SOURCE

WILLIAM ABERTH, CHARLES A. SPINDT, and KENDAL T. ROGERS

Stanford Research Institute, Menlo Park, Calif. 94025

Various properties of field ionization make it a particularly attractive technique for producing both positive and negative ion beams. However, present methods (which incorporate a single point, a wire, or a razor edge as the field ionizing source) have numerous serious drawbacks. Recently developed techniques for producing arrays of field ionizing points promise to overcome most of the disadvantages of field ion sources currently in use. This paper represents a progress report of a recently initiated effort to develop and test these multipoint devices as sources for ion beams and mass spectrometers.

INTRODUCTION

Field ionization has received considerable attention in the past several years, especially in mass spectrometry. The field ionization process does not tend to fractionate the parent neutral molecules as is typical with chemical ionization and electron bombardment. Thus, for example, the mass identification of the components of an unknown mixture is considerably simplified.

The field ionization technique uses the strong electric fields produced in the vicinity of needle points, razor edges, and extremely fine wires to ionize neutral atoms and molecules. This ionization is produced by electron tunneling through the distorted potential barrier of the molecule.¹ The ionization process is enhanced further by the strong inhomogeneous electric field in the vicinity of the ionizing surfaces. This strong inhomogeneous field interacts with the dipole moments of the neutral species producing an attractive force that tends to funnel neutrals to the ionizing surfaces, thus increasing greatly the efficiency of ionization.

But present-day field ionizing methods have some serious disadvantages: (1) large potentials (between 10 and 20 keV) are required to obtain ionization; (2) the beam-forming efficiency of the ions produced is extremely small (between 10^{-4} and 10^{-7} of the total number of ions are usable); (3) ionizing sources usually have a relatively short useful life; (4) the ionization is effectively limited by use of only a single point or edge except for the case of randomly grown whiskers as described by Beckey and others; and (5) the ionizing source is extremely delicate to handle and the beam focusing adjustments are usually sharp and critical. These drawbacks explain why field ionizing sources have not received greater acceptance in ion beam physics and the analytical sciences.

MULTIPOINT FIELD IONIZATION

A recently developed multipoint field ionizing device² promises to overcome substantially most of the above drawbacks. An array of some 3000 points spaced 0.001 in. apart is deposited on the end of a

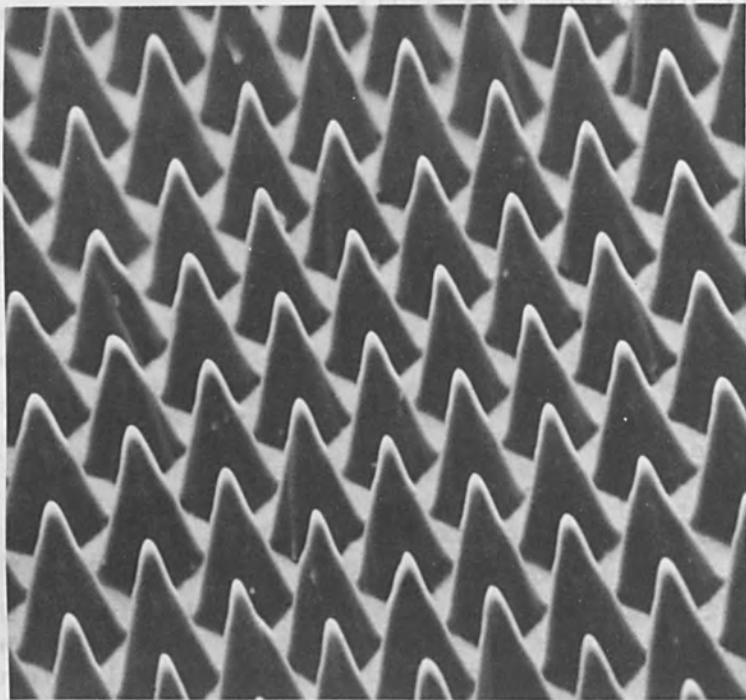


FIG. 1.--An array of field ionizing points. Points are spaced 0.001 in. apart and are 0.0015 in. high.

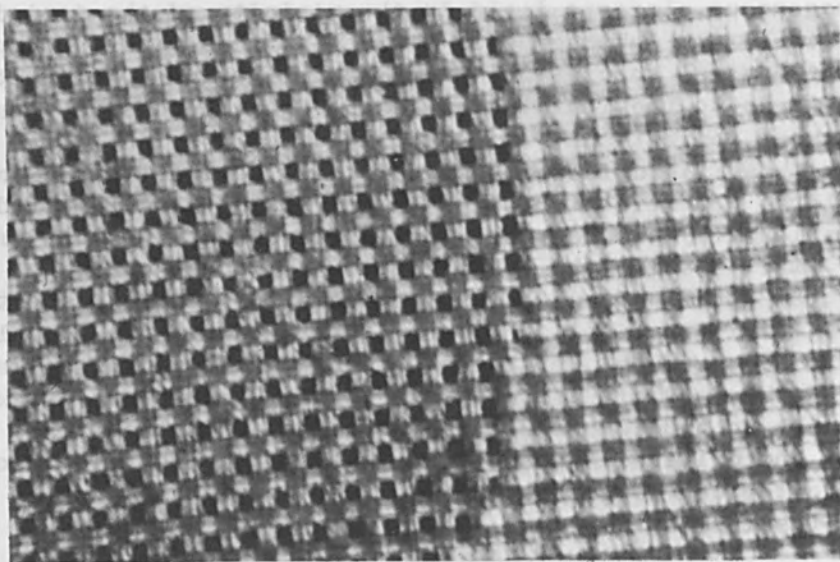


FIG. 2.--Microscope photograph of the grid-multipoint assembly. The grid wires are spaced 0.001 in. apart and are 0.002 in. above the ionizing points. Each black dot in the center of the grid squares represents a field point ionizer.

1/16-in.-diameter molybdenum rod by evaporation techniques (see Fig. 1). The points are made of molybdenum at present but other materials such as platinum or iridium could be readily substituted. Each point has a tip radius of curvature of 1000 Å or less and stands about 0.0015 in. above the substrate surface. A 1000-mesh nickel grid, well insulated from the points, is placed from 0.002 to 0.005 in. above the array and positioned in such a way that each point is registered in the center of a grid square (Fig. 2). A potential difference of about 2000 V between the points and the grid is sufficient to initiate field ionization with ionization efficiency increasing rapidly with increasing voltage. Each grid square acts like a minute electrostatic lens and thus assists in forming a well-collimated ion beam. The entire structure is rigid and shock resistant and requires no special handling procedures except the standard requirements of cleanliness.

EXPERIMENTAL ARRANGEMENT AND RESULTS

A multipoint source consisting of about 2000 points was installed in the vacuum apparatus shown schematically in Fig. 3. The grid and L_3 were kept at ground potential; L_1 and L_2 were adjusted negative and positive, respectively, for optimum focusing and the multipoint source was maintained at a positive potential. Acetone, $(\text{CH}_3)_2\text{CO}$, used as test gas, was leaked into the ion source chamber and was monitored by a Bayard-Alpert ionization gage. The initial tests used the magnetic mass selector to determine the composition of the ions emitted from the multipoint source. These tests indicated that about 95 per cent of the detected beam consisted of mass 58 and 5 per cent was mainly background pressure components of larger mass. Subsequently, a Faraday cup was placed behind the 3/16-in.-diameter bulkhead aperture (spaced 7 in. from the multipoint source), and the currents to the Faraday cup, the bulkhead, and the grid were monitored (Fig. 3). A multipoint source with a registered grid spaced 0.002 in. above the points produced an onset acetone ion beam of 2×10^{-13} A, with only 1300 V between grid and points and an absolute acetone pressure of 10^{-6} torr. Increasing this potential to 2250 V yielded the following currents: grid, 4.5×10^{-10} A; bulkhead, 7×10^{-11} A; Faraday cup, 3×10^{-11} A. Since the grid includes secondary electron current produced by the colliding ions, it is estimated to be greater than the ion current by a factor of 5 to 10 because of the high energy of the impinging ions and the large electrostatic field. Thus, it appears that perhaps 20 per cent of all ions produced are formed into a reasonably well-collimated beam. Increasing the potential difference from 2250 to 2500 V caused a short between the grid and points, terminating this series of tests. The short was apparently caused by the flexing of the grid mesh stressed by strong electrostatic attractive forces. A new grid structure (Fig. 4), described in the following section, should alleviate this problem.

The full ionization efficiency of the multipoint device has not yet been established because of the technical difficulties described. The maximum efficiency thus far achieved for acetone is 4×10^{-5} A/torr of ions collected in the Faraday cup. This efficiency should be increased greatly when changes are made in the present multipoint structure to prevent electrical breakdown between the points and grid.

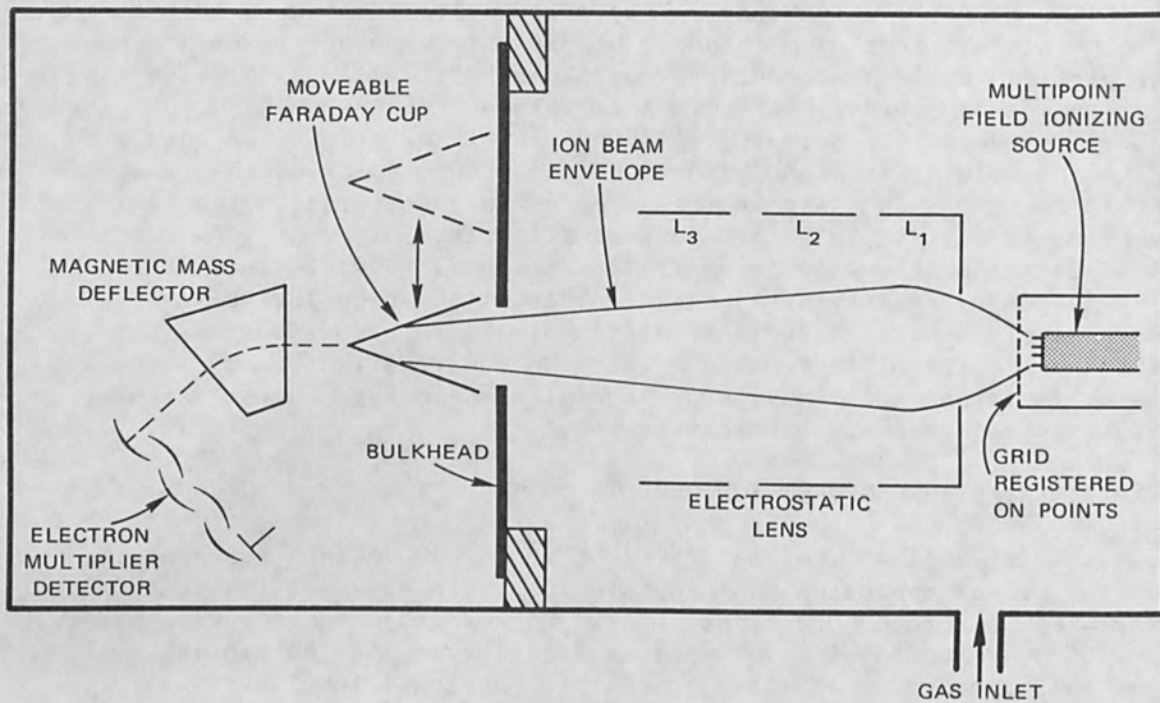


FIG. 3.--Schematic diagram of test apparatus.

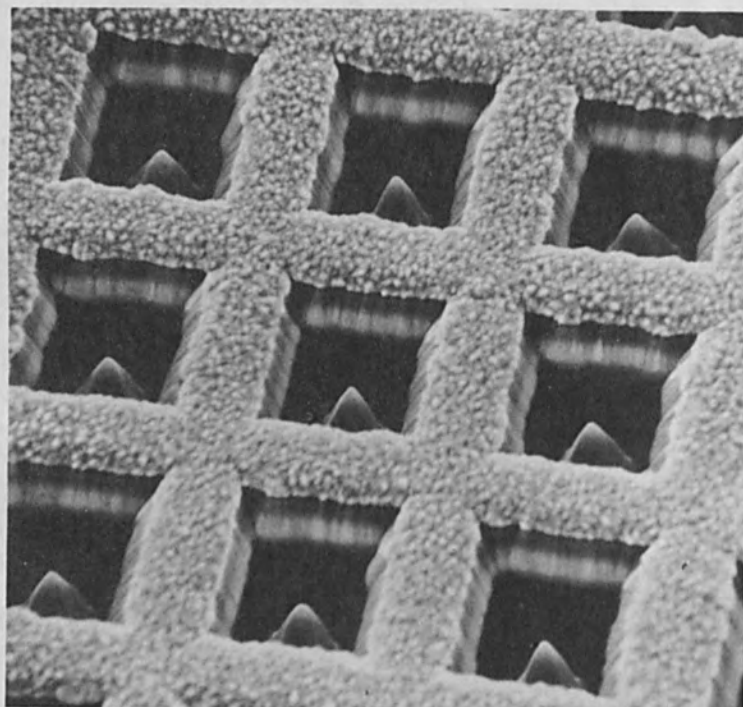


FIG. 4.--Grid structure supported on the ionizing point array base, by aluminum oxide insulation. Points are spaced 0.001 in. apart.

NEGATIVE ION PRODUCTION

The present multipoint device has proven to be an efficient field emitter^{1,3} when a reverse potential difference is applied (points negative relative to the grid) between points and grid. In this process, an electron escapes from the metal by tunneling through the potential barrier of the metal surface which has been distorted by the applied external field. If an atom or molecule with an electron affinity is at the proper separation from the metal surface, the electron can tunnel through the surface barrier and attach itself to the atom or molecule, thus forming a negative ion. The process of producing negative ions is called field attachment.

With all potentials reversed from the field ionizing arrangement, field attachment was observed in the form of three ion peaks estimated to be C^- , OH^- , and O_2^- as well as broad spectrum of peaks above mass 40. Only the ambient system background pressure of 2×10^{-6} torr was used as the ion source gas. Since the uncalibrated electron multiplier was used as the negative ion detector, no estimates are available on the negative ion production efficiency. Although the observed peaks were substantially more noisy than their positive ion counterparts, they required only about one-half of the electric field for production. It appears, however, that stable negative ion production will require bakeout pretreatment of the ionizing points as well as ultra-high vacuum operating conditions. Further work in this field will continue when these operating conditions are met.

FUTURE DEVELOPMENT

The potential development of the present techniques of field ionization will be directed toward decreasing the grid-point spacing, developing more efficient gas feeding methods, and improving the ruggedness of the grid-point structure. Work along these directions is already in progress. Figure 4 shows a grid-point structure recently constructed. The grid is supported by an insulating layer of aluminum oxide which rests directly on the base substrate. An improvement in ion beam focusing, a reduction in the voltage necessary to achieve ionization, and greatly increased grid support strength are expected. This structure should overcome the shorting problem described in the previous section.

In Fig. 5, a grid aperture has been micromachined around a field ionizing point tip. The conducting grid surface is supported on the point base by an insulating layer. The close proximity between the grid aperture and the ionizing point of this type structure should produce field ionization with a grid-point potential difference of only a few hundred volts.

ACKNOWLEDGMENTS

The authors wish to acknowledge the help of R. D. Stowell, H. Pakka, and E. Heydon in the fabrication of the multipoint devices; of R. R. Sperry, R. L. Leon, and G. M. Conklin in setting up the experiments reported here; and of L. N. Heynick in useful discussions.

REFERENCES

1. E. W. Müller, Phys. Rev. 102: 618, 1965.
2. C. A. Spindt, J. Appl. Phys. 39: 3503, 1968.
3. R. Gomer, Field Emission and Field Ionization, Harvard University Press, Cambridge, Mass., 1961.

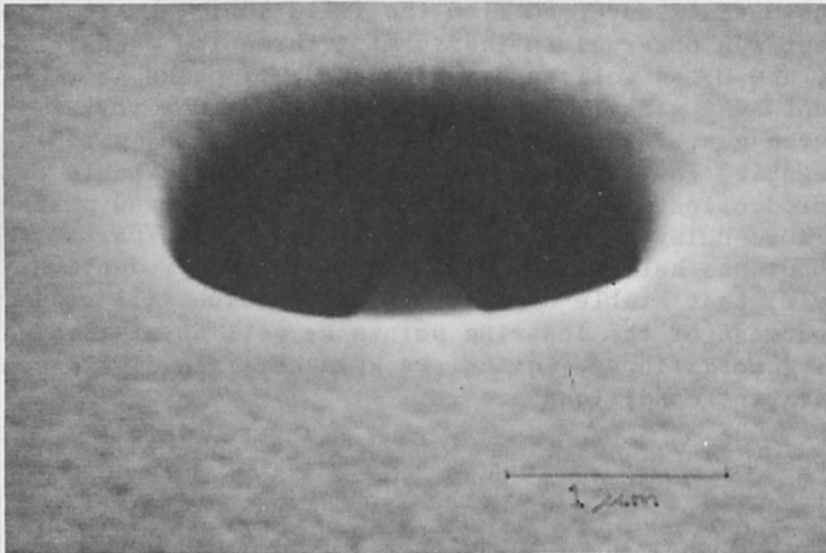


FIG. 5.--A single field ionizer with a micromachined grid aperture.

NEW ELECTRON BEAM EVAPORATOR AND ITS CHARACTERISTICS

K. MORI and T. NEMOTO

Hitachi Koki Co., Ltd., Katsuta City, Japan

Many papers have been published on the advantages of electron beam evaporation of refractory metals. But fine cracks and minute irregularities caused by reflected electrons are often observed on the surface of thin films deposited by conventional electron bombardment heating.

In order to prevent charge accumulation on the surface of thin films, the new electron beam evaporator has been developed by the authors of this paper. The evaporator consists of a Pierce gun with a grounded cathode, and it has an output power of 6 kW to increase the deposition rate.

INTRODUCTION

Usually, with guns for electron beam evaporation, the cathode is supplied with negative high voltage and both the anode and the crucible are grounded. The crucible is grounded since it must be water cooled to prevent it melting. Grounded-anode types of guns, whether of the static electric or magnetic focusing type, cause the following problem. Reflected electrons that generate from evaporating material bombarded with electrons have the same speed as the electrons accelerated by the anode, and they reach the substrate. If the substrate is an insulator such as glass, the reflected electrons charge its surface. Then they discharge over the surface of thin films to the near grounded electrode and substrate-holder. Figure 1 shows fine cracks and minute irregularities caused by the discharge of the reflected electrons.

In order to prevent charge accumulation, we constructed the evaporators in which the cathode and the metal belljar were grounded and the anode and evaporating material were kept at high potential.^{1,2}

The design of the electron gun was undertaken to increase the deposition rate and to find a way to prevent the irregularities of thin films caused by reflected electrons.

CONSTRUCTION AND CHARACTERISTICS OF NEW ELECTRON GUN

Figure 2 shows the sectional diagram of the newly designed electron gun. This horizontal Pierce-type gun has a cathode consisting of a thin tungsten plate. The cathode is grounded and both the anode and crucible are supplied with positive high voltage. The electrons emitted from the cathode are accelerated by the anode and are deflected by a set of deflecting electrodes. Then the accelerated electrons bombard the evaporating material in the crucible. We designed the special form of electrodes to get the optimum beam spot size on the evaporating material (Fig. 3). The focusing electrode has a large angle for θ_1 to increase the perveance and has a small angle for θ_2 to focus the electron beam. It was experienced that α and β must be reduced to zero to obtain the optimum beam spot size. With a view to investigating the beam patterns, we bombarded thin molybdenum plates, and melted them. Figure 3 shows the beam spots with deflection and with no deflection.

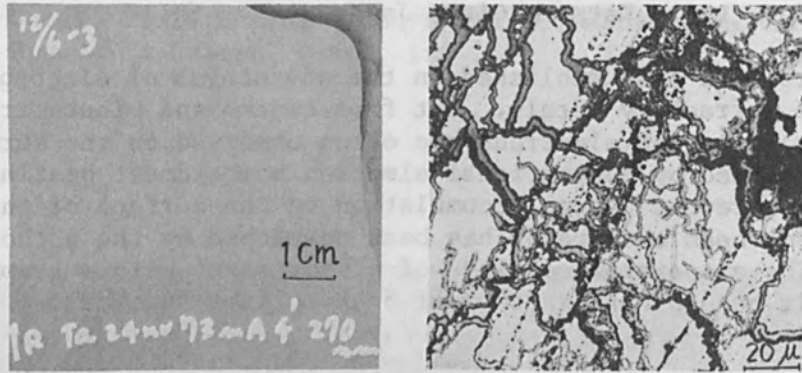


FIG. 1.--Deterioration of Ta thin films by reflected electrons.

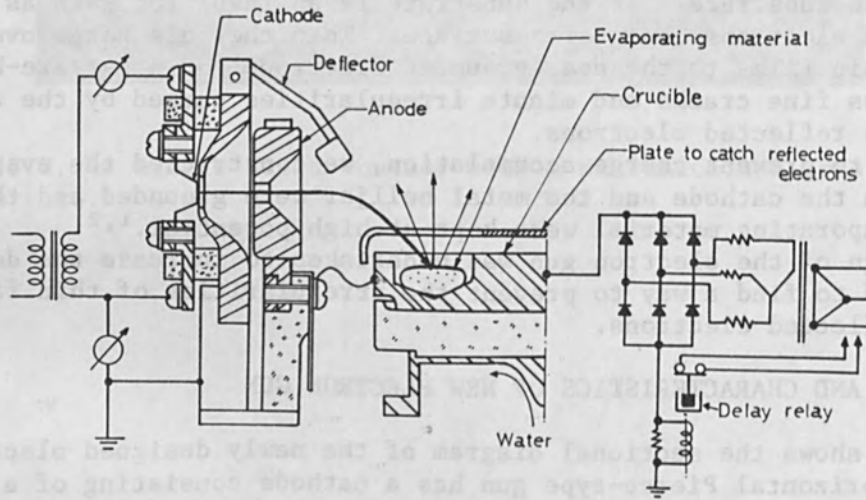


FIG. 2.--Sectional diagram of new electron gun.

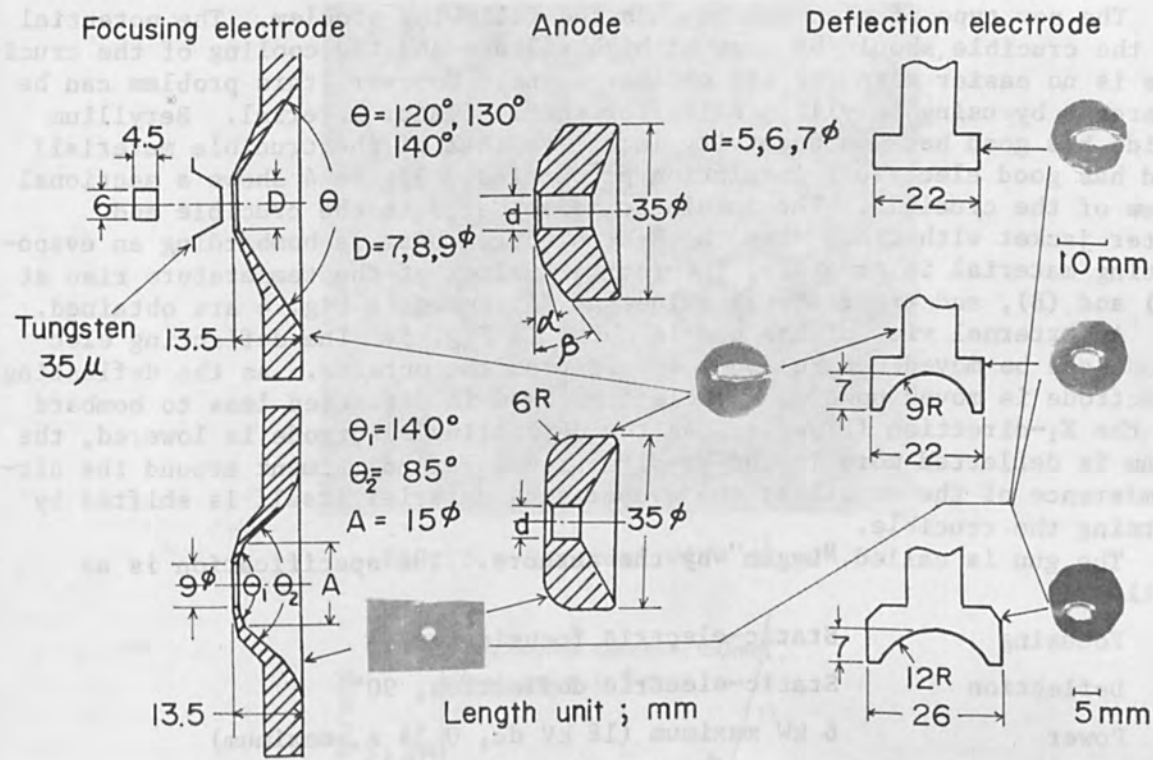
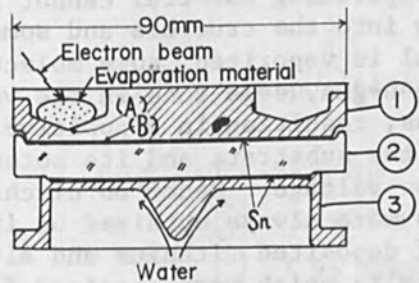


FIG. 3.--Electrode configurations for optimum spot/size, and spot shapes with and without deflection.



- (1) Crucible (Material; OFC)
Thermal conductivity ; $0.9 \text{ cal/sec}\cdot\text{cm}\cdot\text{cm}^2$
- (2) Insulator (BeO)
 $0.58 \text{ cal/sec}\cdot\text{cm}\cdot\text{cm}^2$
- (3) Water jacket (OFC)
 $0.9 \text{ cal/sec}\cdot\text{cm}\cdot\text{cm}^2$

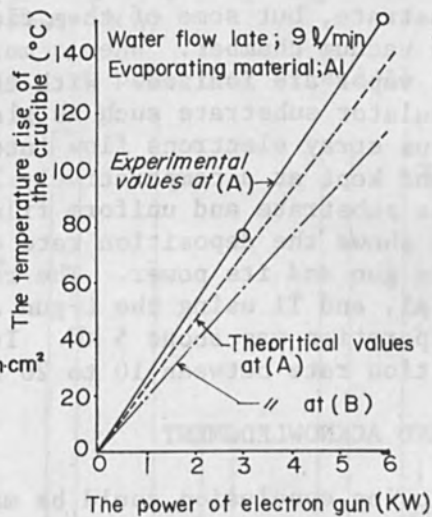


FIG. 4.--Sectional view of crucible, and temperature rise.

The new type of electron gun has the following problem. The potential of the crucible should be kept at high voltage and the cooling of the crucible is no easier than for the ordinary type. However, this problem can be overcome by using beryllium oxide for the insulator material. Beryllium oxide has good heat conductivity (equal to that of the crucible material) and has good electrical insulation properties. Figure 4 shows a sectional view of the crucible. The insulator is soldered to the crucible and water jacket with tin. When the 6-KW electron beam is bombarding an evaporating material in crucible, theoretical values of the temperature rise at (A) and (B), and experimental values at (A) shown in Fig. 4 are obtained.

An external view of the gun is shown in Fig. 5. The deflecting electrode can be moved upward and downward from the outside. As the deflecting electrode is moved upward, the electron beam is deflected less to bombard in the X_1 -direction (Fig. 5). As the deflecting electrode is lowered, the beam is deflected more in the X_2 -direction. For adjustment around the circumference of the crucible, the evaporating material itself is shifted by turning the crucible.

The gun is called "L-gun" by the authors. The specification is as follows:

Focusing	Static-electric focusing
Deflection	Static-electric deflection, 90°
Power	6 kW maximum (18 kV dc, 0.34 A, maximum)
Perveance	1×10^{-7} to 2.5×10^{-7} A/V ^{2/3}
Filament Supply	7 V ac, 35 A
Crucible	6-position turret, volume: 3.5 cm ³

In this gun, the evaporating material in the crucible is kept at positive high voltage and the substrate-holder is grounded. Therefore, the reflected electrons generated from the evaporating material cannot flow into the substrate, but some of them flow into the crucible and some stray in the vacuum chamber. When a metal is vaporized, some molecules in the metal vapor are ionized. With the L-gun, some ions in the vapor reach an insulator substrate such as glass, resulting in a positive potential. Thus stray electrons flow into the substrate and its potential is lowered and kept at a comparatively low voltage. Hence no discharge occurs on the substrate and uniform films were always obtained on it.

Figure 6 shows the deposition rate of deposited titanium and aluminum with this gun and its power. The results which were obtained for Pt, Ta, Mo, Zr, Al, and Ti using the L-gun are shown in Fig. 7. The power used for evaporation was about 5 kW. It became clear that the 6 kW gun has a deposition rate between 10 to 20 times that of the 1.3-kW gun.

CONCLUSION AND ACKNOWLEDGMENT

The following conclusion could be made after examining the experimental results.

- (1) Uniform films can be always obtained, resulting from the elimination of reflected electrons.
- (2) The same point on the vaporizing material can always be bombarded even with a wide range of accelerating voltages as no magnetic focusing and no magnetic deflection are employed.

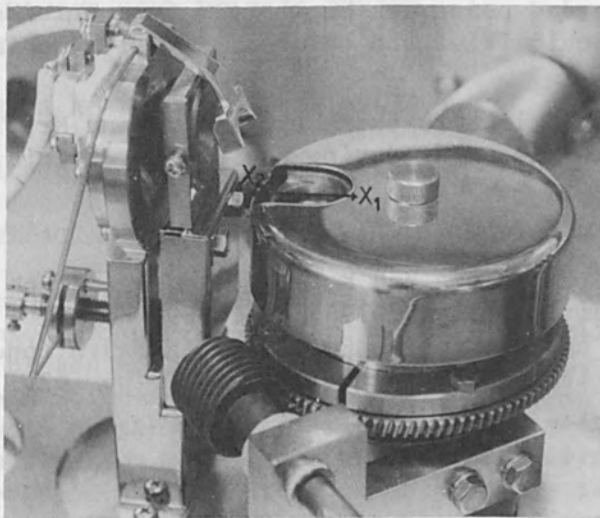


FIG. 5.--External view of gun.

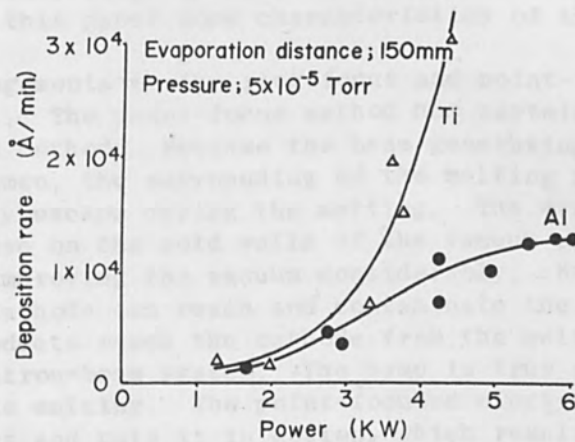


FIG. 6.--Deposition rate vs power for Ti and Al.

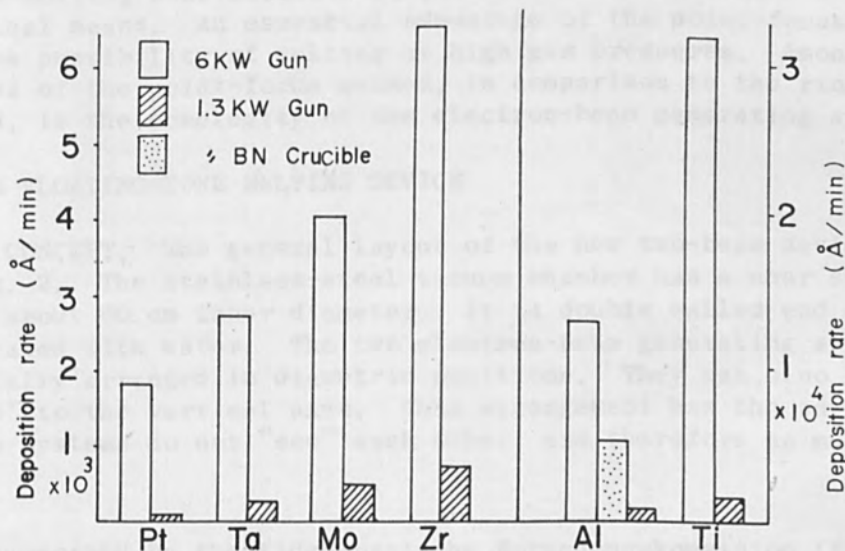


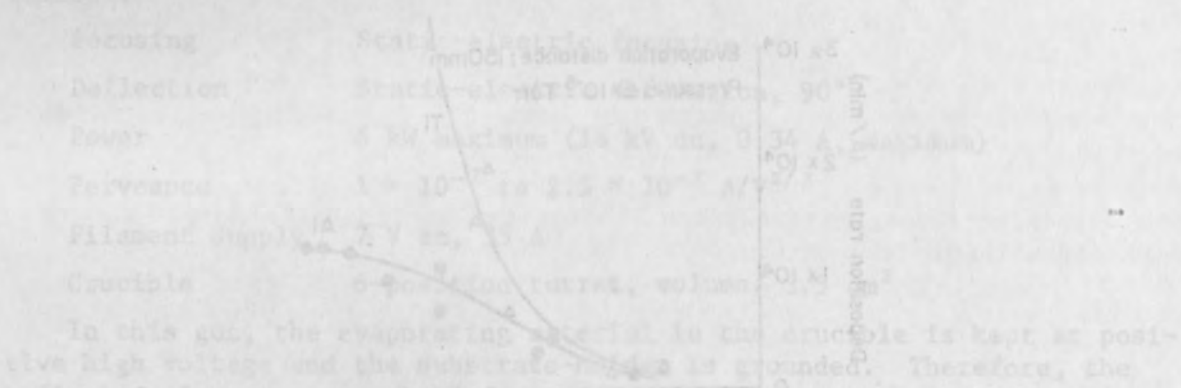
FIG. 7.--Deposition rate of metals. (Graphs for 6-kW gun are values deposited at about 5 kW power. Graphs for 1.3-kW gun are values deposited at full power.)

- (3) The bombarded point can be changed from outside.
- (4) Magnetic thin films can be obtained as there is no external magnetic field.

The authors would like to thank Dr. Kimura and Mr. Tamura, Hitachi Ltd., for help with the study during the course of this work.

REFERENCES

1. H. Kimura, H. Tamura and K. Mori, Record of 8th Symp. on Electron, Ion, and Laser Beam Technology, 1965; pp. 369.
2. H. Tamura and H. Kimura, Record of IEEE 9th Annual Symp. on Electron, Ion and Laser Beam Technology, 1967; pp. 62.



In this case, the deposition rate is almost independent of the power at high power. The deposition rate is about 3 μm/min at 2 kW power. The deposition rate is about 0.5 μm/min at 0.5 kW power. The deposition rate is about 1.5 μm/min at 1.0 kW power. The deposition rate is about 2.5 μm/min at 1.5 kW power. The deposition rate is about 2.8 μm/min at 2.0 kW power. The deposition rate is about 3.0 μm/min at 2.5 kW power.



FIG. 7. Deposition rate of metal. (Graphs for 0.5 kW and 1.5 kW are plotted at about 2 kW power. Graphs for 1.0 kW and 2.0 kW are plotted at full power.)

AN ELECTRON-BEAM FLOATING-ZONE MELTING DEVICE
FOR WORKING PRESSURES IN THE RANGE OF 10^{-7} TO 15 TORR*

E.B. BAS, P. HAFNER, A.A. LATIF, and G. WULFF

Swiss Federal Institute of Technology, Zürich

PRINCIPLES OF THE FLOATING-ZONE MELTING WITH POINT-FOCUS ELECTRON BEAMS

In the widespread standard method of floating-zone melting with electron bombardment, the ring-beam system after Calverly et al. is used.¹ In a paper presented at the 2nd International Conference on Electron and Ion Beam Science and Technology in 1966, we reported our first experiences with another type of floating-zone melting device using a point-focus electron beam and a horizontally arranged specimen.² We have further developed this point-focus method to a two-beam melting device, with vertically arranged specimen and differential pumping attachment to the electron-beam generating systems, for melting at high vacuum in the 10^{-7} -torr range as well as in a gas atmosphere up to 15 torr pressure. In this paper some characteristics of this device will be described.

The basic arrangements in the ring-focus and point-focus methods are shown in Fig. 1. The point-focus method has certain advantages over the ring-focus method. Because the beam generating system is far away from the specimen, the surrounding of the melting zone is free. The gases can easily escape during the melting. The evaporation products can condense on the cold walls of the vacuum chamber and act as a getter, thus improving the vacuum considerably. No evaporation products from the cathode can reach and contaminate the specimen. Nor can evaporation products reach the cathode from the melt and cause trouble in the electron-beam system. The same is true for the gas eruptions during the melting. The point-focused electron beam penetrates into the melt and puts it in motion, which results in very good outgasing and removal of impurities by evaporation. Free space surrounding the melting zone allows a better observation of the melting zone by optical means. An essential advantage of the point-focus method is the possibility of melting at high gas pressures. Among the disadvantages of the point-focus method, in comparison to the ring-focus method, is the complexity of the electron-beam generating system.

THE TWO-BEAM FLOATING-ZONE MELTING DEVICE

GENERAL CONCEPT. The general layout of the new two-beam device is shown in Fig. 2. The stainless-steel vacuum chamber has a near spherical form of about 60 cm inner diameter. It is double walled and can be cooled or heated with water. The two electron-beam generating systems are horizontally arranged in diametric positions. They can also be placed at 45° to the vertical axis. This arrangement has the advantage that the two systems do not "see" each other, and therefore no mutual

*Work supported by the Eidgenössische Forschungskommission (Federal Research Commission) of Switzerland.

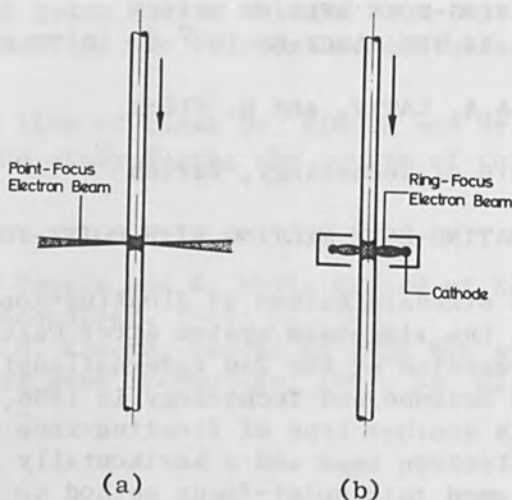


FIG. 1.--Methods of floating-zone melting by electron bombardment. (a) Point-focus method; (b) ring-focus method.

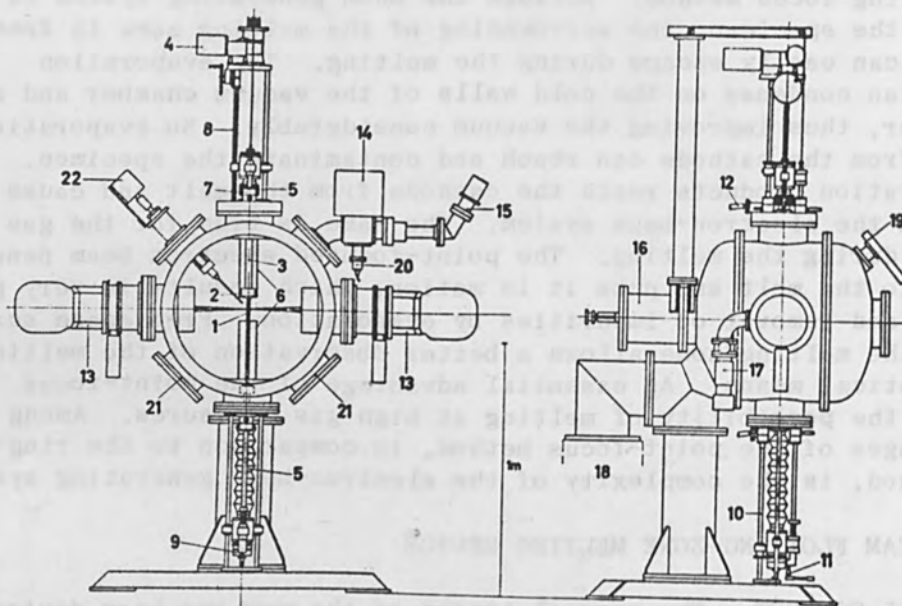


FIG. 2.--General layout of two-beam floating-zone melting device: 1 sample, 2 sample holder head, 3 water-cooled holder tubing, 4 driving motors, 5 and 6 screening, 7 coupling system, 8 driving screw for translation, 9 magnetic coupling, 10 rotation drive, 11 fine adjustment, 12 differential pumping for drives, 13 electron-beam systems, 14 trap for reflected electrons, 15 quadrupole mass spectrometer, 16 cryo-pump (N_2), 17 diffusion pump for electron gun, 18 main diffusion pump, 19 viewing port, 20 ionization gage.

damage can occur by mismanipulation. In our experiments, we are still using only the horizontal arrangement with some electronic precautions for mismanipulation. The sample-holder system is constructed as a unit that can be completely assembled outside and introduced into the melting chamber through the upper port (Fig. 3). The sample-holder tubes are water cooled up to the fixing points of the sample. The feed-throughs of the tubes into the vacuum chamber are differentially pumped. Two double-walled water cooled tubes connect the upper and lower flanges of the sample-holder system. Through one of these tubes, a solid rod connects the upper and the lower sample-holder tubes so that the same translation may be applied to both. A shaft through the second tube transmits the rotation from the upper to the lower sample holder. A magnetic coupling allows the disconnection of the lower sample-holder rotation. The driving motors for translation and rotation are electronically regulated. The translation speed can be adjusted between 0.2 mm and 10 mm/min and the rotation speed between 0 and 150 rpm. Two limit switches are attached to the translation mechanism and permit automatic stopping or reversal of the translation. This feature is especially useful during the long time needed to pre-heat the samples. When single crystals of desired orientation are being grown, a goniometric fixture is attached to the lower sample-holder head so that the seed crystal may be brought into any position and welded to the sample which is fixed at the upper holder head. The sample-holder system described above has seen many years of satisfactory operation.

ELECTRON-BEAM GENERATING SYSTEM. The electron gun is of the electrostatic ion separation type described elsewhere.^{3,4} Its chief advantage is the protection of the cathode emission surface against bombardment by energetic positive ions produced in the electron beam. The erosion of the cathode is prevented and long life possible. So-called bolt cathodes (described elsewhere⁵) are used. These are electron-bombardment-heated tungsten cathodes from $\langle 111 \rangle$ -oriented single-crystal material. They can deliver (from an emission area 2 mm in diameter) more than 400 mA at 25 kV. The emission current is stabilized to better than 1 per cent. At the crossover position of the electron gun, there is a crossover aperture 3 mm in diameter and functions as a first-stage channel of 0.3 l/s conductance for the differential pumping of the system. Although the electron-beam diameter at the crossover is less than 3 mm, the aperture cannot be made smaller because at high currents the crossover moves towards the cathode as shown in a previous paper.⁶

The electron-beam generating system (Fig. 4) is made as a compact unit which can be mounted in any position into the 180-mm ports of the vacuum chamber. The electron gun (space 1) and the drift space (space 1) behind the crossover aperture are evacuated by separate diffusion pumps. The drift space, which includes the viewing optics, makes up the second stage of the differential pumping. In this space the magnetic focusing lens and the deflection magnet act on the electron beam. A valve, just behind the crossover channel, allows the isolation of the electron gun from the drift space when the working chamber is vented. For high-pressure operation, a third pumping stage can be attached to the electron-beam generating system inside the working chamber. This stage consists of two channels. The first channel (2.4 mm in diameter,

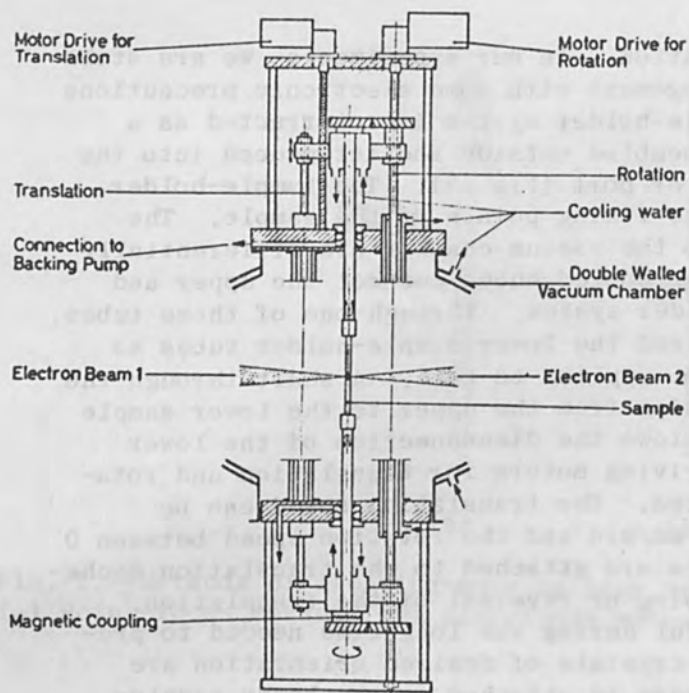


FIG. 3.--Principles of sample translation and rotation mechanism.

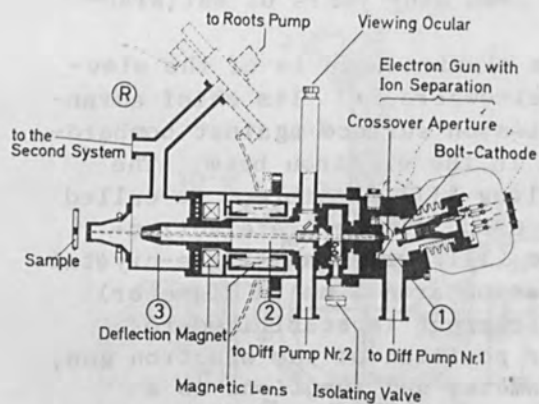


FIG. 4.--Schematic design of the electron-beam generating system with differential pumping attachment for high pressure operation.

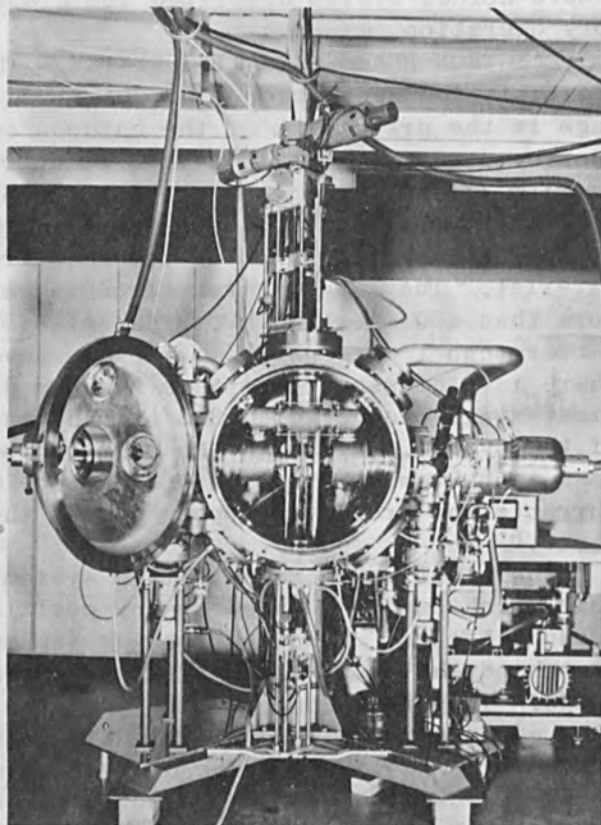


FIG. 5.--Two-beam floating-zone melting device with opened melting chamber.

6.8 mm long) is made of zone-melted tungsten and set at about 20 mm from the specimen. The second, tapered channel (5 to 7 mm in diameter, 88 mm long) is made of molybdenum and set at 50 mm from the first channel. The holders of both channels are water cooled. The high-pressure attachments of both electron-beam systems are connected together inside the working chamber and evacuated by a Roots pump. In the over-all view of the new melting device in Fig. 5, the right-hand electron-beam generating system and the high-pressure attachments inside the working chamber can be seen clearly. The high-pressure attachments can be easily removed when melting at the best achievable high vacuum. It is also possible to operate only one electron-beam system with the high pressure attachment. In this way one can, after a high-pressure pass, immediately change to high-vacuum pass using in both cases only one electron beam for the melting.

THE VACUUM SYSTEM. The schematic drawing in Fig. 6 shows the layout of the vacuum system. The 1500 ℓ/s diffusion pump, the liquid nitrogen cryo pump inside the vacuum chamber, and the gettering action of the metal deposit on the cold chamber walls make it possible to achieve a working pressure below 10^{-7} torr when melting tungsten in the high-vacuum mode. The effect of gettering of the cold chamber walls with tungsten deposit is considerable. It is possible to melt an 8-mm-diameter tungsten rod during a third zone pass at a vacuum of 1×10^{-6} torr with the main diffusion pump disconnected. Rough estimates give a pumping speed of the chamber walls above 4000 ℓ/s . In contrast, the pressure in a zone-melting device with ring-focus electron gun always rises during the melting.

For high-pressure operation, the electron-beam system is differentially pumped by the diffusion pumps of the electron guns (pressure P_1) and drift tubes (pressure P_2) and a single Roots pump at the high-pressure attachments (pressure P_3). In this way, a pressure ratio $P_R/P_1 \geq 10^5$ can be realized when argon at pressure P_R is introduced to the recipient melting chamber. Figure 7 shows the pressure variation at various pumping stages as a function of the working chamber pressure. Dashed curves give the experimental results without electron beams in operation. The solid curves are taken with two electron beams in operation, bombarding a 10-mm-diameter tungsten rod at a constant temperature of 2650°K in the bombarded zone (simulating the zone melting of a 10-mm-diameter molybdenum rod). The curve N_{EG} gives the adjusted total electron gun power (rectifier power) for this simulation. Note the big difference in these pressure characteristics for the conditions with and without electron beam. We shall come back to this point later. At 10 torr working chamber pressure, the vacuum in the cathode region is still in the 10^{-5} -torr range. It is possible to operate the system at much higher pressures. But at the highest available acceleration voltage from our power supply (25 kV), the scattering of the electrons by gas molecules in the region of the high-pressure attachment becomes very strong. A substantial part of the beam power is then lost to the apertures of this attachment. Figure 8 shows the beam transmission efficiency of the whole electron beam generation system (single-gun operation) as a function of the applied rectifier power for working chamber pressures of 4 and 8 torr. The transmission efficiency is defined as the power at the target divided by the applied rectifier power. The useful power at the target is calorimetrically

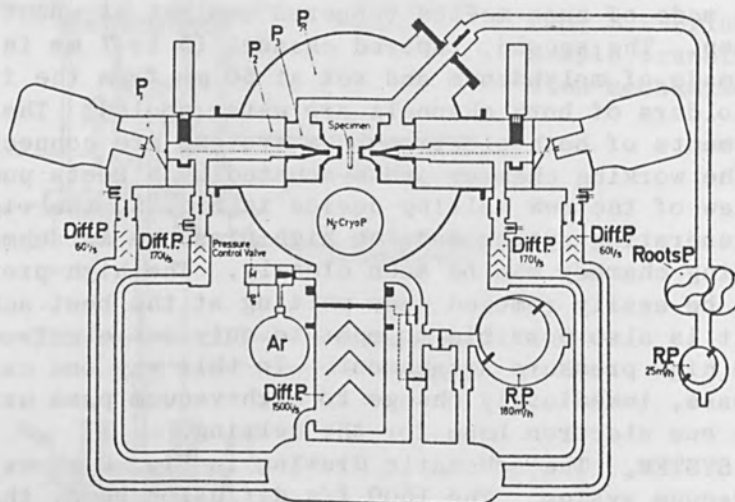


FIG. 6.--Vacuum system.

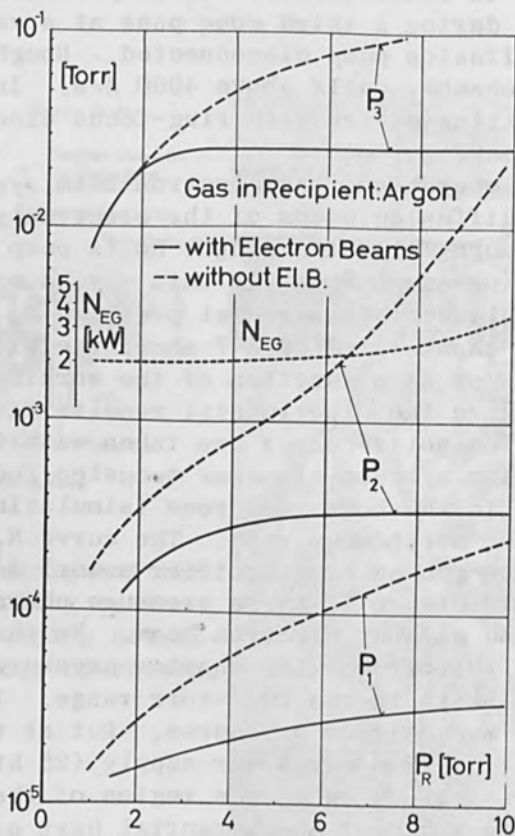


FIG. 7.--Pressures at different pumping stages as a function of the working pressure in the melting space. (Dashed lines: without electron beams; full lines: with two electron beams bombarding a 10-mm-diam tungsten rod at constant temperature of 2650°K in bombarding zone simulating the melting of a 10-mm-diam molybdenum rod.) Curve N_{EG} shows total electron gun power used.

measured because the beam current at the target is strongly affected by the plasma in this region and also the energy distribution of the electrons at the target is unknown.

The results shown in Fig. 8 are not optimum. By changing the dimensions of the second channel of the high-pressure attachment, we were able to improve the transmission considerably. Figure 8 shows some characteristics of the system. The transmission increases rapidly at higher electron gun power owing to the heating of the two channels of the high-pressure attachment. When these channels get hot, their gas flow conductivity falls, due to the rise of gas viscosity with gas temperature. As the pressure in the working chamber is held constant, the pressures in the high-pressure attachment and in the drift tube decrease considerably, as can also be seen in Fig. 7. The electron scattering by the gas molecules now becomes less effective and the transmission rises. When the electron-gun power (emission current) is further raised above a certain value, the beam aperture angle grows⁶ and more electrons are stopped by the channels, which results in a decrease of the transmission efficiency. Because of the above-mentioned temperature effect we tried at the beginning to realize a very high temperature of the exit channel by adjustment in the configuration. This solution proved to be impractical. Melt droplets produced by splashes during the melting adhered on the hot surface of the channel and gave trouble. If the surface temperature of the exit channel is not very high, say around 1000°C, the droplets are reflected. For this reason the sample side of the channel is also screened by a cooled copper aperture.

OPERATION OF THE DEVICE AT HIGH VACUUM

For melting at high vacuum with high melting power, the high-pressure attachments can be removed. In this case each electron-beam system can deliver about 10 kW melting power at an acceleration voltage of 25 kV. The experiments show that for zone melting of rod samples, the relation between the rod diameter d and the melting power N is given by:

$$N_m = kd^{3/2}$$

For tungsten $k \approx 0.19$ (d in mm and N_m in kW). According to this relation, it is possible to zone-melt a tungsten rod about 21 mm in diameter with the 20-kW melting power available in our device. The largest tungsten sample we have melted to date is 15.4 mm in diameter and about 200 mm long. The melting power for this sample was 11.6 kW. Molybdenum samples up to 20 mm in diameter are zone-melted without difficulty relative to the zone instabilities.

As is well known, the material loss when melting at high vacuum is very high. For diameter shrinkage after n zone passes, we found empirically the following relation:

$$d_0 - d_n = k_1 \frac{nh_n}{v}$$

n = number of zone passes

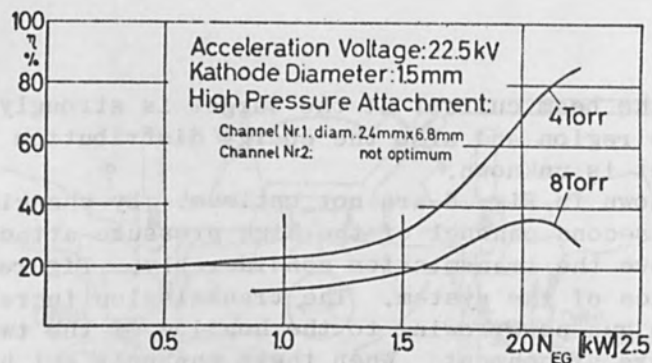


FIG. 8.--Beam transmission efficiency of entire electron beam generating system as function of electron gun power (single-gun operation).

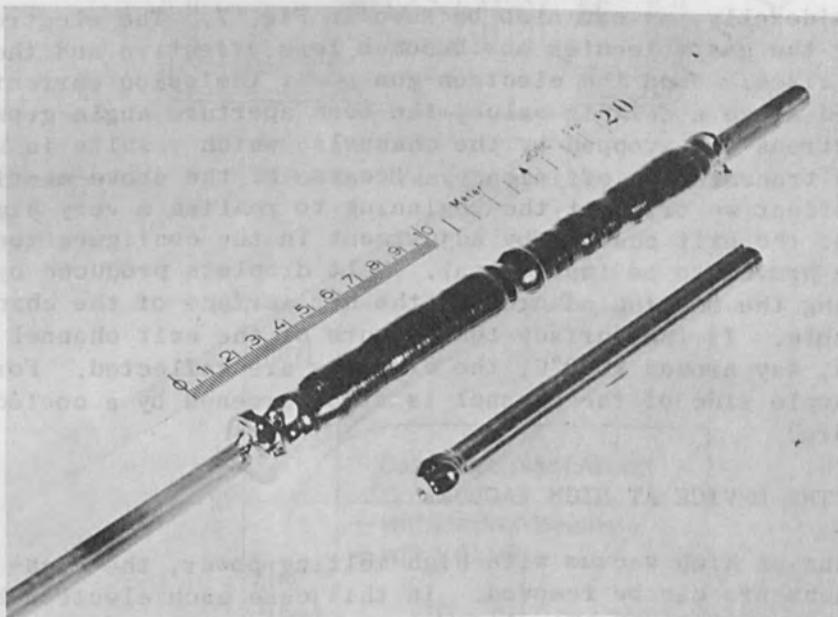


FIG. 9.--Examples for melting at high vacuum: 20-mm-diam molybdenum sample after first zone pass and single crystal tungsten prepared from three-pass sample for heat-conductivity measurements.

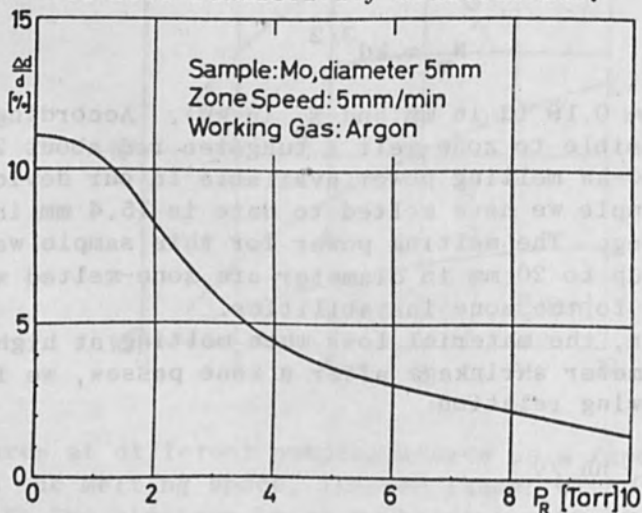


FIG. 10.--Evaporation losses as function of working pressure for zone melting of a 5-mm-diam molybdenum rod with a zone speed of 5 mm/min.

- d_0 = starting rod diameter (mm)
 d_n = diameter after the n'th pass (mm)
 h_n = zone height during the n'th pass (mm)
 v = zone velocity (mm/min)
 k_1 = material constant (about 0.6 mm/min for Mo and W)

From experimental evidence, we can write approximately

$$h_n = k_2 d_n$$

For our device, we found empirically

$$k_2 \approx 1 \quad \text{for } d_n = 1.5 \text{ to } 10 \text{ mm}$$

$$k_2 \approx 0.6 \quad \text{for } d_n = 15 \text{ to } 20 \text{ mm}$$

If we combine the above two relations, we get for the relative shrinkage after n passes,

$$\frac{\Delta d}{d_0} = \frac{k_1 k_2^{k/v}}{1 + k_1 k_2^{n/v}}$$

For example, for a Mo or W sample up to 10 mm diameter, we get, after 3 zone passes at 5 mm/min zone speed, a diameter shrinkage of about 27 per cent. For illustration some data of prepared big Mo and W single crystals are summarized in Table I. Figure 9 shows a 20-mm-diameter molybdenum sample after the first pass and a tungsten single crystal 11.4 mm in diameter prepared from a three-zone-pass sample for heat conductivity measurements.

OPERATION AT THE TORR-RANGE VACUUM

The chief advantage of melting at high pressures in an inert gas is the reduction of material loss. This is of great importance when high-vapor-pressure materials and alloys with dissimilar components are zone-melted. Figure 10 shows the reduction of material loss of molybdenum as a function of argon gas pressure in the working chamber. At a working pressure of 10 torr argon, the material loss is about 10 times lower than at high vacuum. This gain is much more pronounced when molybdenum-tungsten alloys are melted, as the experiments showed.

The second advantage of high-pressure operation is given by the possibility of introducing reactive gases into the working chamber during the melting. One can hope that in this way it will be possible to remove some impurities from the sample by selective chemical reactions. However, we have no experience in this direction at present.

The high-pressure mode of operation makes also melting of insulating materials such as oxides practicable. The plasma in the specimen region neutralizes charging of the specimen surface. The first experiments with alumina showed that the floating-zone melting is

TABLE I

Material	Mo		W	
	1	3	1	3
n				
v(mm/min)	5	5	5	5
c(rev/min)	60	60	60	60
p_0 (torr $\times 10^6$)	2.5	2.0	1.4	1.8
p_1 (torr $\times 10^6$)	12	8	9	10
p_2 (torr $\times 10^6$)	-	0.7	-	0.8
p_3 (torr $\times 10^6$)	-	0.4	-	0.35
d_0 (mm)	20	15	15.4	15.4
d_n (mm)	18.6	12	14.2	12
$R_{293}/R_{4.2}$	560	10 200	1900	20 800

straightforward but the resulting crystal has many cracks. These cracks could be eliminated by heating the solidified part of the sample by radiation from an incandescent tungsten filament, avoiding high temperature gradients. Of course, in this experiment the evaporated tungsten atoms doped the crystal, giving it a violet color. The doping can be eliminated by using an alumina tube to make the auxiliary heating oven.

The operation at high pressures allows a rapid sample cycling. After 15 min. evacuation by the roughing pump and the main diffusion pump, the vacuum in the melting chamber reaches about 10^{-5} torr and argon can be introduced to begin immediately with melting. At present, the device is used mostly in the high-pressure mode to provide experience for practical applications.

REFERENCES

1. A. Calverley, M. Devis and R.F. Lever, *J. Sci. Instrum.* 34: 142, 1957.
2. E.B. Bas and H. Stevens, in R. Bakish, ed., *Electron and Ion Beam Science and Technology*, American Inst. of Mining Metall. and Petroleum Engineers, New York, p. 167.
3. E.B. Bas, *Optik* 12: 377, 1955.
4. E.B. Bas, G. Cremosnik, and H. Lerch, *Trans. 8th Vacuum Symposium and Second Intern. Vac. Congress*, Pergamon Press, vol. 2, p. 817.
5. E.B. Bas, *Z. Angew. Phys.*, 7: 337, 1955.
6. E.B. Bas and G. Cremosnik, in R. Bakish, ed., *First Intern. Conf. on Electron and Ion Beam Science and Technology*, Wiley, New York, p. 199.

ELECTRON-BEAM WELDING IN TRANSITION

R. BAKISH

Bakish Materials Corp., Englewood, N.J.

This paper analyzes the electron beam welding process as it emerges from 1970, this critical and perhaps most devastating year of its growth since the introduction of electron beams as welding tools. The essentials of the process, problem areas, equipment trends, and industrial needs are presented together with a look into the future.

INTRODUCTION

A midyear 1971 electron-beam welding is an important welding method with outstanding capabilities, though some problem areas need attention. In fact it is not one but rather three pressure-dependent welding methods or modes, as summarized in Table I, with the essential features of the electron guns schematically illustrated in Fig. 1. Beyond the parameters given, these modes also differ in terms of suitability to the materials they process.

TABLE I

Mode	Introduced	Pressure Range (torr)	Max. Work Distance (in.)	Chamber	Accelerating Voltage (v)
Original, also referred to as hard or high vacuum	1957 ¹	0.0001 or better	30	needed	30-150
Soft, also known as commercial or partial vacuum	1962 ^{2,3}	0.1	15	needed	60-150
Nonvacuum, also referred to as IAEBW	1960 ⁴⁻⁶	760	1	not needed	150-175

The hard-vacuum mode is recommended for refractory and reactive metals subject to interstitial embrittlement and bridges the gap from welding thin films of several thousand angstroms to pieces of some alloys 9 in. thick in a single pass. It is the best of the three modes in term of heat input and depth-to-width fusion-zone ratios, and is most ideally suited for repair welding, where the very long working distance makes welding in deep cavities possible.

The partial-vacuum process, though quite satisfactory for a number of refractories, is by its nature less ideally suited to welding them. Its lower operating pressures permit important maintenance simplification and substantial efficiencies for a wide range of repetitive production operations. The IAEBW, which still permits welding of some

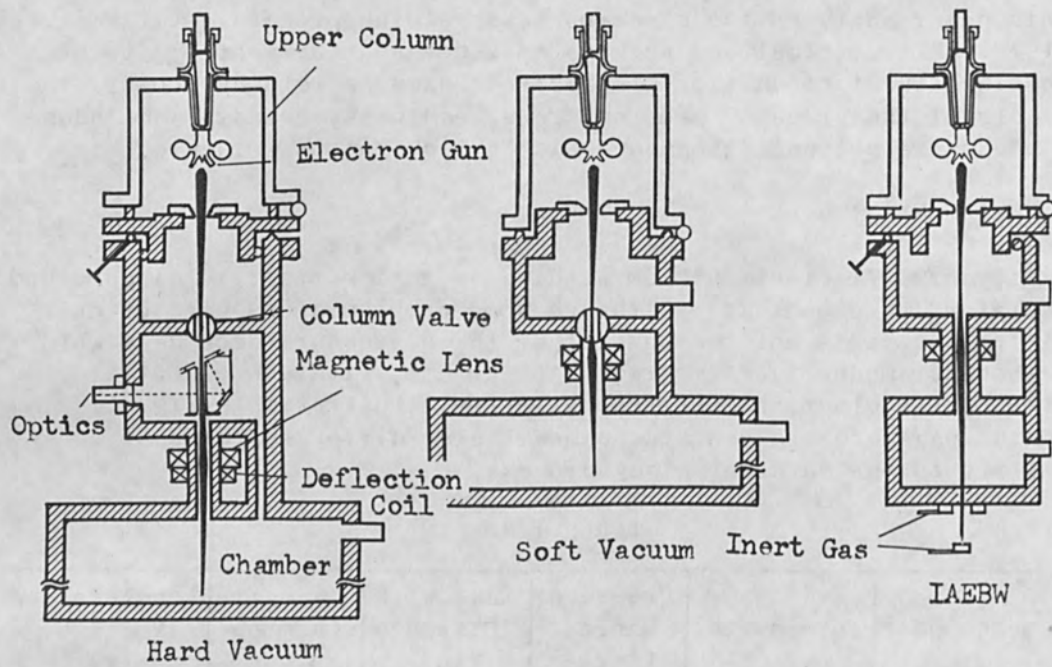


FIG. 1.--Three electron-beam welding modes.

of the refractories, is not recommended as embrittlement effects can occur. The absence of a chamber makes for processing without size limitations, yet the very small working distance available represent an important limitation on configurations that can be welded.

PROCESS PROBLEM AREAS

Despite wide acceptance of the electron-beam process (the number of electron-beam welders in the U.S. alone must be approaching 1000, and large amounts of joint-property data have been generated), much work needed for sound further growth remains undone.

The aerospace industry and aircraft manufacturers proceed to install bigger and bigger machines and set forth plans to weld a wide range of critical structural components including advanced aircraft wings, yet they still lack sufficient and reliable data on fatigue properties of electron-beam welds. Little is to be found in the literature when one seeks information on properties and reliability of thick joints, particularly in excess of 2-3 in.

No data at all on weld imperfections incidence on either partial vacuum or IAEBW are at hand, though it is certain that they exist. Yet substantial growth is expected here. The problem of partial-penetration electron-beam welding⁸⁻¹⁰ does not appear to have been resolved, though recent data apparently offer remedy at least for some situations.¹¹ The recent slow-down in research and development has not negated the need for this information. Even without U.S. government interest and with growth being confined to non-defense operations, the duty of generating concrete answers falls on the equipment manufacturers, who will derive the benefits from this growth.

THE MARKET PLACE AND THE EQUIPMENT SUPPLY

As consequence of change in economic conditions, the electron-beam welding equipment and its manufacturers have changed. Since the commercial beginnings of the process in 1959, we have witnessed both the disappearance of electron-beam welding equipment producers and the entry of the new ones.

In terms of equipment sales, indications of recovery are at hand and though sales remain sluggish, interest in equipment has increased notably. The electron-beam welding equipment suppliers are listed in Table II. The initial concept of the hard-vacuum system, i.e., a vacuum box with a worktable to move the work and a gun with power supply and controls, is no longer the important product of the equipment manufacturer.

Though this remains a viable concept, real growth will be experienced mainly by those who provide system-engineered installations with various degrees of automation. The gun and power supply here are likely to represent no more than 10-15 percent of the cost of the over-all installation regardless of the application. The precision metal-working equipment producers are likely to become more actively involved in electron-beam welding, both as users and as manufacturers of auxiliaries. Bulk of the cost in new and advanced systems are the metal-working auxiliaries on one hand and the control and automation components on the other. Metal-working equipment companies are capable

TABLE II.--Worldwide manufacturers of electron-beam welding equipment.

Producers	Country of Origin	Acc. Voltage (kV)	Power (kW)	Gun	Gun Type**	Operational Modes	Observation Modes*
Brad Thompson Industries	USA	30-60	2-5	movable	P	HV	O
Electron Research (U.C.)	USA	60	10	movable	P	HV	O
Hamilton Standard	USA	60-150	2-15	fixed & movable	S	HV, SV, IAEBW	C
Sciaky	USA	30-60	6-30 (60)	movable	P	HV, SV	O&C
Shannon/Thompson	USA	30-60	6-15	movable	P	HV	O
Thompson Welders	USA	30-60	6-15	movable	P	HV	C
Westinghouse	USA	150	6-15	fixed	S	IAEBW	O
Metropolitan Vickers	England	150	5	fixed	S	HV	C
Torvac Ltd.	England	30-60	1-10	movable & fixed	P	HV	C&O
Hawker Siddeley	England	150	2-15	movable & fixed	S	HV, SV, IAEBW	C
Alcatel	France	30-60	5	fixed	P	HV, SV	O
Sciaky	France	30-60	6-30	movable	P	HV, SV	C&O
Heraeus	W. Germany	150	6-15	fixed & movable	S	HV, SV, IAEBW	C
Steigerwald Strahltechnik	W. Germany	150	10	fixed	S	HV, SV	C
Institut M. Von Ardenne marketed in U.S. by Bakish Equipment	E. Germany	30-125	5-12.5	fixed	S&P	HV, SV	O
Paton Institute	USSR	30-150	up to 10	fixed	S&P	HV	C&O
Moscow Power Institute	USSR	30	?	?	P	HV	O
Japan Electro Optical	Japan	30-60	3-60	fixed	S	HV	C
Mech Tronics	USA	NA	NA	NA	NA	NA	NA
K/O Electron Beam	USA	NA	NA	NA	NA	NA	NA
Leader Pacific	USA	NA	NA	NA	NA	NA	NA

*C = Coaxial with beam NA = not available
 O = Oblique
 **P = Pierce
 S = Steigerwald Telefocus

of supplying system-engineered beam welders by buying guns and power supplies and automation components from their respective manufacturers. As a matter of fact even the leaders in the field often subcontract components and auxiliaries to the metal-working equipment industry, regardless of whether it is a clam-shell installation of the type extensively publicized by Grumman (one of the few nonvacuum electron-beam welding tube mills) or one of the growing number of systems being built for the automotive industry.

THE USER AND HIS NEEDS

Regardless of application there are two basic types of machines that a potential user needs for efficient operation. The first is a machine to evaluate the process and its adaptability for his new requirements; and the second, a system that permits maximum possible production rates. The job shop has a modified requirement as its needs demand the ability to maximize both versatility and good production rate capability. Let us now look at each of the three welding modes and see how these ground rules apply. In the case of hard vacuum we can come perhaps the closest to meeting the two tasks with a single machine, i.e., with the type of machine ideally needed by the job shop. This type of system can perform well and is capable of considerable production rates; yet if needs dictate surpassing these production rates, a potential user must look for full automation of the process. As options among others he can consider twin chambers with a single welding head, or tunnel-type arrangements in which the parts are brought under the gun in a tunnel-configuration chamber through gating valves and pressure stages.

In the partial-vacuum mode many of the advantages of the process in term of speed of processing can be lost in a development type of machine, since versatility in this case means essentially a larger chamber which increases the pump-down time. The automated single-part special machine has a chamber only a little larger than the parts to be welded.

When it comes to nonvacuum machines, it appears that there is only one solution: one must carry out the prototype work and establish the feasibility and economics of the process for one's task at the welding-equipment manufacturer's plant. The two active suppliers have special-purpose installations capable of generating needed data here though it appears that limited available machine time has caused scheduling problems. In nonvacuum machines a change of product to be manufactured inevitably leads to substantial costs from modification of the metal-working equipment components.

NEW DEVELOPMENTS

Relatively few major advances in equipment are apparent. Among them is the hollow (Electron Research--Linde) bombarded emitter cathode. This gun modification in principle offers potential advantages but no facts on performance are available. The need for guns that permit full reproducibility between parts or after filament change remains.

The trend is to bigger, more powerful, and complex machines, with steadily growing automation provisions, including computer controls. Hard vacuum machines up to 40 ft in length and up to 60 kW in power are being produced and still more powerful machines are in the offing. Partial and nonvacuum machines are also finding their way into highly automated production systems.

For suitable joint configurations and materials these modes permit highest possible over-all speeds and processing economy. Hard vacuum on the other hand remains as in the past the mode with the greatest capabilities. It will follow but not lag much behind.

CONCLUSIONS

By virtues of the capabilities that electron-beam welding offers the automotive, metalworking, nuclear, electrical, and to lesser extent aircraft industries, these are the areas of future growth of the process. Industrial organizations looking at the process should consider all three modes in order to select the one most advantageous for their purpose. The extreme importance of cost and production efficiencies in the highly competitive industry of the 1970s make judiciously selected electron-beam welding systems prime candidates. Despite the major capital investment needed to introduce these systems in large-scale production operations today, their very high output capability can assure proper return on investment.

REFERENCES

1. J.A. Stohr, Fuel Elements Conference, Paris, 1958; TID 7546, Book 1, p. 917.
2. J.W. Meier, in Proc. 2nd Intern. Conf. Electron & Ion Beams in Science and Technology, Gordon and Breach, New York, 1969; p. 505.
3. J.L. Solomon and H.A. James, *ibid.*, p. 553.
4. R. Kutchera, New York University Vacuum Metallurgy Conference, New York, 1962.
5. S.S. White, ASD Prog. 7-926, Final Rep. Contract, AF 33-657-7237, 1962.
6. J. Meier, *Welding Journal* 42: 63, 1963.
7. K. Hicken and W.G. Booco, in Proc. 3rd Intern. Conf. Electron & Ion Beams in Science and Technology, ECS, New York, 1968; pp. 399-411.
8. H. Tong and W.H. Giedth, in Proc. 4th Intern. Conf. Electron & Ion Beams in Science and Technology, ECS, New York, pp. 148-164, 1970.
9. D. Sandstrom, *ibid.*, pp. 165-178.
10. R.E. Armstrong, *ibid.*, pp. 179-193.
11. E.H. Bradburn, R.A. Huber, and P.W. Turner, *Weld. Res. Supplement*, AWS, pp. 1915-1935, April, 1971.

INTERACTION OF HIGH-INTENSITY LASER RADIATION WITH METALS

WILLIAM I. LINLOR

NASA-AMES Research Center, Moffett Field, Calif.

INTRODUCTION

In the approximately ten years since the advent of the Q-switched laser, much experimental and theoretical work has been done on the interaction of laser beams with solids. A convenient bibliographic summary of such work is given by DeMichelis.¹ Another reference source is the book edited by Schwarz and Hora.²

This paper considers some of the phenomena involved in absorption of high-intensity laser radiation by metals. The interaction is characterized by the production of plasma, within which the primary absorption occurs. For a Q-switched laser having a pulse duration of tens of nanoseconds, an intensity of 10^9 W/cm² or more incident on any metal produces a dense plasma in less than 1 ns; hence most of the incident radiation interacts with the electrons of the plasma. In order to illustrate these statements by an example, we list the parameters of the ruby laser that was employed for the measurements to be described (Table I).

TABLE I.--Laser parameters.

Peak power, 10^7 W
Pulse duration, 2×10^{-8} sec (full width, half maximum)
Focal spot area, 10^{-3} cm ²
Power per unit area, 10^{10} W/cm ²
Pulse energy, 2×10^{-1} joule (approximately 10^{18} eV)
Pulse energy per unit area, 10^{21} eV/cm ²
Laser light frequency, 4.32×10^{14} Hz

We note that the energy delivered per unit area is 10^{21} eV/cm². The number of electrons that absorb the incident radiation will be considered below; based on measurements to be described, let us provisionally take the number of 10^{18} for the product of path length and electrons/cm³ as being a reasonable upper limit. For this number and temperature of 10 eV (roughly 10^5 K), the product is about 10^{19} eV/cm². This is only about 1 per cent of the delivered energy per unit area, so that most of the absorption occurs via the electrons during the plasma state, compared to absorption via electrons during the solid state.

ABSORPTION OF LASER RADIATION BY PLASMA

Absorption of laser radiation by a plasma may occur by several processes. The theory of electromagnetic-wave propagation in plasmas has shown that the laser frequency must be greater than the plasma frequency if the light is to penetrate. For the laser frequency of 4.32×10^{14} Hz, the plasma electron density must be less than 2.3×10^{21} electrons/cm³ to permit penetration. For plasmas having a density gradient or for very intense beams, nonlinear effects can occur such as self-focusing of the beam, relativistic interactions, etc. Dawson and Oberman⁴ have shown that if there are large-amplitude ion waves present in a plasma, its resistivity near the plasma frequency may be enhanced by many orders of magnitude.

In this paper we shall consider only the well-known absorption process called "inverse bremsstrahlung." This procedure makes it possible to obtain an estimate of the minimum amount of plasma required to produce a certain percentage absorption, because any additional absorption effects would only enhance the absorptivity of the plasma. The usual exponential absorption relation applies:

$$I = I_0 \exp(-Kx) \quad (1)$$

where I_0 is the incident light intensity (W/cm²)
 I is the transmitted light intensity (W/cm²)
 K is the absorption coefficient (cm⁻¹)
 x is the distance within the plasma (cm)

Spitzer gives the following relation for inverse bremsstrahlung absorption:⁵

$$K = \frac{3.7 \times 10^8 n_e^2 Z^2 (1 - e^{-h\nu/kT})}{T^2 \nu^3} \quad (2)$$

where n_e is the number of electrons per cubic centimeter
 Z is the effective charger per ion in electron charge multiples
 h is Planck's constant
 k is Boltzmann's constant
 ν is the laser frequency (Hz)
 T is the electron temperature in degrees Kelvin

For $h\nu \ll kT$, we can express absorption in alternative form for ruby-laser frequency by taking the reciprocal of K (which yields the path length λ for 1/e transmission) and multiplying by the number of electrons cubic centimeter, expressing temperature in electron-volts:

$$(\lambda n_e) = \frac{1.3 \times 10^{37} T^{3/2}}{n_e Z} \text{ cm}^{-2} \quad (3)$$

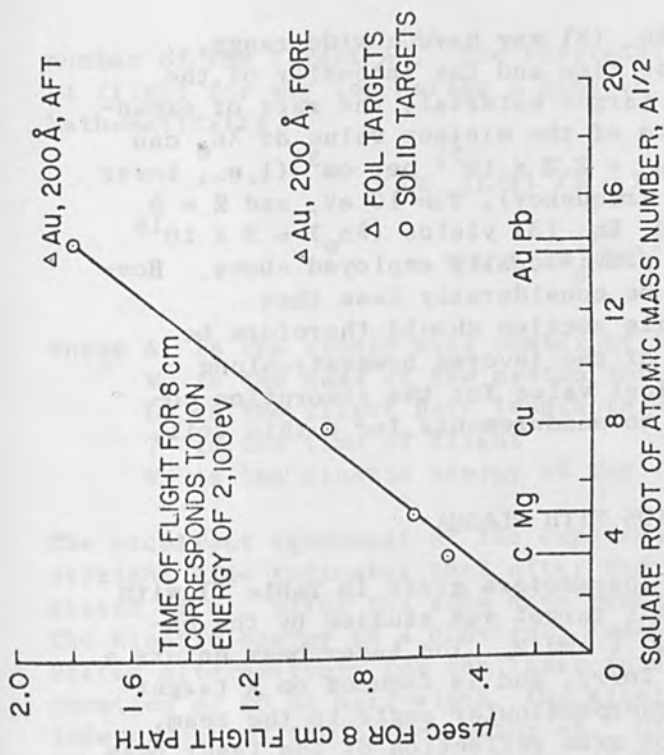


FIG. 3.--Ion time of flight for various mass numbers. (Focal spot, $10^{10}\text{W}/\text{cm}^2$; half width, 20 ns.)

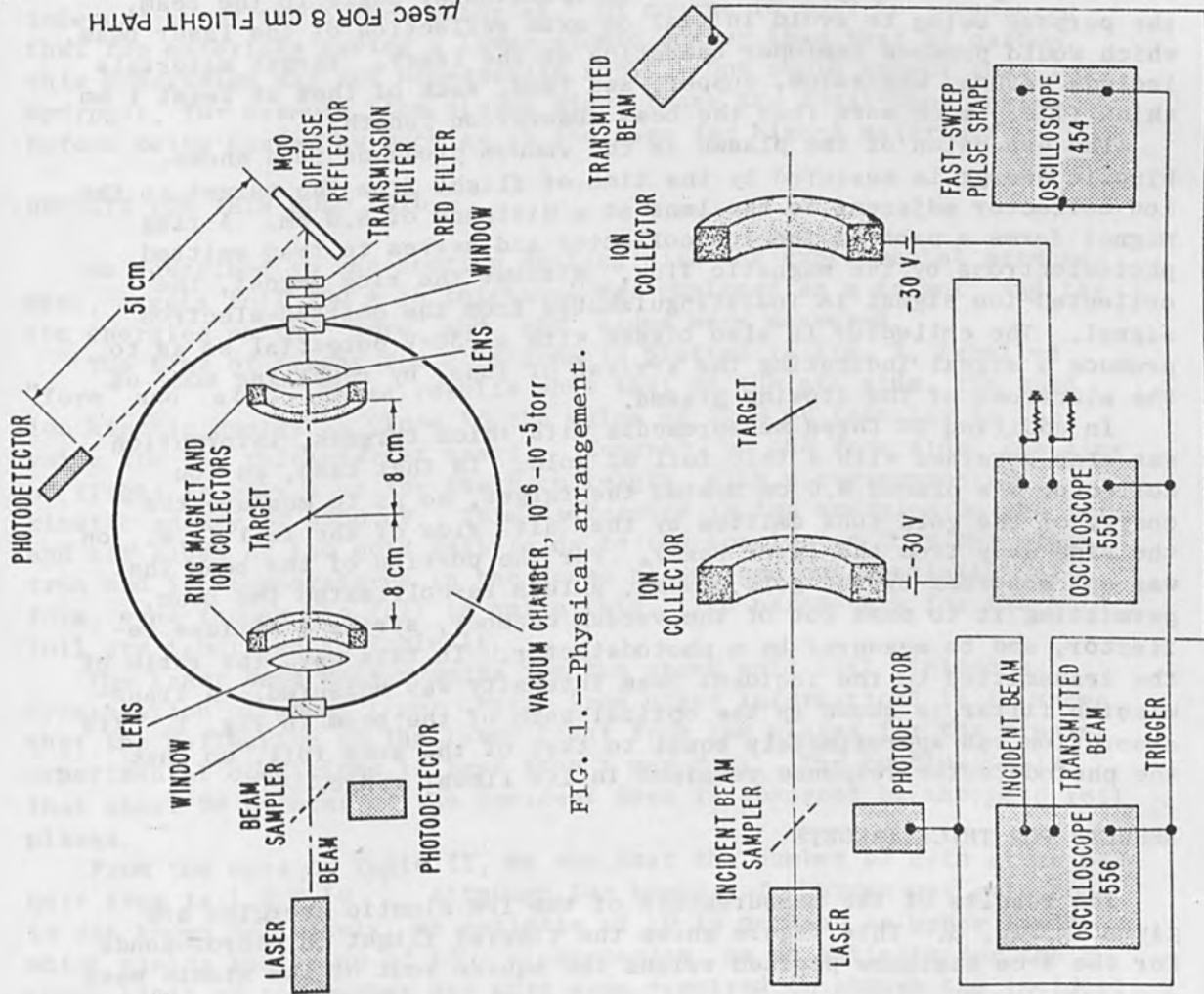


FIG. 1.--Physical arrangement.

FIG. 2.--Schematic arrangement of circuit.

The values of T , n_e , and Z for Eq. (3) may have a wide range, depending on such factors as the rise time and the intensity of the laser pulse, the composition of the target material, the rate of expansion of the plasma, etc. An estimate of the minimum value of λn_e can be obtained by selecting the value $n_e = 2.3 \times 10^{21}$ per cm^3 (i.e., laser frequency about equal to the plasma frequency), $T = 10$ eV, and $Z = 5$ (rough estimate). With these values, Eq. (3) yields $(\lambda n_e) = 3 \times 10^{16}$ cm^{-2} . This is less than the number provisionally employed above. However, the effective value of n_e may be considerably less than 2.3×10^{21} cm^{-3} . The comments of this section should therefore be interpreted as outlining the nature of the inverse bremsstrahlung process, rather than giving a numerical value for the absorption coefficient. A value for gold, based on measurements for a thin foil, will be given below.

ARRANGEMENT FOR LASER-BEAM INTERACTION WITH PLASMA

The interaction of a laser beam (parameters given in Table I) with the plasma produced from a thick metal target was studied by the experimental arrangement shown in Figs. 1 and 2. The laser beam enters a vacuum chamber (pressure about 10^{-6} torr), and is focused on a target with a lens. The target is at a nonperpendicular angle to the beam, the purpose being to avoid initial on-axis reflection of the laser beam, which would produce improper operation of the laser. Target materials include carbon, magnesium, copper, and lead, each of them at least 1 mm thick (i.e., much more than the beam absorption length).

The expansion of the plasma in the vacuum produces ions whose kinetic energy is measured by the time of flight from the target to the ion collector adjacent to the lens at a distance of 8.0 cm. A ring magnet forms a part of the ion collector and serves to trap emitted photoelectrons by the magnetic flux. Without the ring magnet, the collected-ion signal is indistinguishable from the emitted-electron signal. The collector is also biased with a -30-V potential so as to produce a signal indicating the arrival of ions, by repelling some of the electrons of the flowing plasma.

In addition to these measurements with thick targets, information was also obtained with a thin foil of gold. In that case, an ion collector was placed 8.0 cm behind the target, so as to measure the energy of the gold ions emitted by the "aft" side of the foil (i.e., on the side away from the laser beam). For the portion of the beam that was not absorbed by the gold-plasma, a lens re-collimated the beam, permitting it to pass out of the vacuum chamber, strike a diffuse reflector, and be measured by a photodetector. In this way, the ratio of the transmitted to the incident beam intensity was measured. A transmission filter is shown in the optical path of the beam in Fig. 1. Its absorption was approximately equal to that of the gold foil, so that the photodetector response remained in its linear range.

RESULTS FOR THICK TARGETS

The results of the measurements of the ion kinetic energies are given in Fig. 3. This figure shows the time of flight in microseconds for the 8-cm distance plotted versus the square root of the atomic mass

number of the target $A^{1/2}$. The straight line shown in Fig. 3 is the time of flight for any ion having a kinetic energy of 2100 eV. Mathematically,

$$AM_p (L/T)^2/2 = W = 2100 \text{ eV} \quad (4)$$

$$T = L(AM_p/2W)^{1/2} \quad (5)$$

where A is the atomic mass number of the target material
 M_p is the mass of the proton (or neutron, approximately)
 L is the flight path length (8.0 cm)
 T is the time of flight
 W is the kinetic energy of the ion (constant at 2100 eV)

The excellent agreement of the experimental flight times with the straight line indicates that after the plasma expansion has been completed (i.e., after the ions have reached their asymptotic speeds), the kinetic energy is a constant, independent of atomic number A. Stated alternatively for the laser intensity of 10^{10} W/cm², and pulse duration of 20 ns half-width, the kinetic energy of ions is 2100 eV, independent of the target material. Of course it must be remembered that for materials having a lower atomic number than that of carbon, this conclusion may not necessarily apply. One could expect that for hydrogen, for example, the plasma might leave the focal-spot region before being heated as much as is the case for high-A materials.

RESULTS FOR THIN GOLD FOIL

As described in the section dealing with the experimental arrangement, a gold foil 200 Å in thickness was employed as a target, and the ion energies on the "fore" and "aft" sides were measured.

The time of flight for gold ions is plotted in Fig. 3, labelled "fore" and "aft." These results show that on the aft side, the gold ion kinetic energy is close to the value of 2100 eV (similar to the value for the thick-target cases). However, on the fore side, the time of flight is only 1 μs for the 8-cm length, with a corresponding kinetic energy of 6300 eV. This difference in ion energies on the fore and aft sides of the gold foil leads to the conclusion that the electron and ion temperatures in the dense plasma are not spatially uniform, even though the foil is quite thin. The parameters for the gold foil are tabulated in Table II.

The laser beam measurements for the above gold foil yielded a transmission of about 1 per cent. From other information⁶ it is known that the reflection of the laser light from the plasma for the present experimental conditions is less than 1 per cent. The conclusion is that about 98 percent of the incident beam is absorbed by the gold foil plasma.

From the data in Table II, we see that the number of gold atoms per unit area is 1.2×10^{17} . Although the number of charges per gold ion is not known definitely, an estimate of 10 is perhaps an upper limit which yields the value of 10^{18} electrons/cm² as an estimate for the upper limit of the number per unit area required to absorb the incident

TABLE II.--Gold-foil parameters.

Atomic number	79
Mass number	197
Density	19.3 g/cm ³
Atoms per unit volume	6×10^{22} per cm ³
Foil thickness	200 Å
Atoms per unit area	1.2×10^{17} per cm ²
Target spot area	10^{-3} cm ²
Target spot volume	2×10^{-9} cm ³
Target spot atoms	10^{14} in focal-spot volume

beam. In the Introduction this value was selected as a reasonable one for 1/e transmission, or about 63-percent absorption. Because the actual absorption was 98 percent, it is seen that 10^{18} electrons/cm² represent upper-limit estimate for 1/e transmission for the laser parameters of this experiment.

CONCLUSIONS

The conclusions from this work are related to absorption of laser radiation by plasma. The kinetic energy of the plasma ions is independent of the material, from carbon to lead, as shown in Fig. 3. The amount of plasma required to absorb the laser beam is thus essentially constant. This should be considered to be only an order-of-magnitude conclusion, because other factors are also involved, such as plasma temperature, degree of ionization, and the expansion dynamics. As an approximate value, the upper limit for the amount of plasma to produce 1/e transmission is about 10^{18} electrons/cm², as shown by the gold-foil measurements.

For the laser parameters of this experiment, it appears that the inverse bremsstrahlung relation, Eq. (3), is consistent with the absorption process. However, the temperature, electron density, and ion charge state vary rapidly with time, and more detailed measurements are necessary to verify Eq. (3) in general.*

REFERENCES

1. C. DeMichelis, IEEE J. Quantum Electronics QE-6: 630, 1970.
2. H.J. Schwarz and H. Hora, Laser Interaction and Related Plasma Phenomena, New York, Plenum Press, 1971.
3. P. Kaw, Appl. Phys. Letters 15: 16, 1969.
4. J. Dawson and C. Oberman, Phys. Fluids 5: 517, 1962; and 6: 394, 1963.
5. L. Spitzer, Physics of Fully Ionized Gases, New York, Interscience Publishers, 1956.
6. A.W. Ehler, J. Appl. Phys. 37: 4962, 1966.

*Note added in proof: The gold foil may have had an oxide film, so that the effective average atomic number A is 88 instead of 197.

LASER WELDING: THEORY, STATUS, AND PROSPECTS

W. C. THURBER

Korad Department, Union Carbide Corp., Santa Monica, Calif.

INTRODUCTION

As is frequently the case with emerging technologies, initially envisioned growth tends to exceed the realities of the marketplace by a substantial margin. Lasers have been no exception. Although widely heralded by the scientific community since the theories of Townes and Schawlow were consummated by Maiman in 1960 with the demonstration of the first operating device,¹ lasers have fallen short as the predicted panacea for the 1960s. After a decade of intense research, development, promotion, and entrepreneurship, lasers are just beginning to bear the promised fruits.

Laser welding has developed apace with the other facets of this embryonic industry. Although used as a laboratory development tool for several years, laser welding is only now, at the beginning of the second decade since Maiman's original work, gaining modest acceptance as a true industrial device. Growth of laser welding is closely tied to the growth and diversification of the microelectronics industry. Applications in the nuclear and aerospace industries are also developing.

The purpose of this paper is: (1) to summarize briefly the theory of laser operation, particularly as it applies to welding; (2) to describe various types of laser devices that can be used for welding; (3) to cite various successful applications of laser welding; and (4) to discuss advantages, limitations, and future prospects for this equipment.

THEORY

LASER is the acronym for Light Amplification by Stimulated Emission of Radiation. Lasing action is achieved in certain solid media by optical pumping. For example, when a single crystal such as ruby (e.g., Al_2O_3 with 0.03 to 0.07% Cr) is irradiated with an intense incoherent light source such as a Xenon flashlamp, a certain fraction of the flashlamp energy is absorbed by the chromium atoms of the laser crystal and transforms these atoms from the ground state to an excited state. When there are more active atoms (i.e., chromium atoms in the case of ruby) in the excited state than in the ground state, a condition known as a population inversion is achieved. Each of these excited atoms, when it decays to the ground state, emits a photon of energy. As these photons pass through the laser crystal, they in turn stimulate other atoms to emit additional photons producing wavetrains that are in phase and a coherent cascading effect or chain reaction results. The resultant light is essentially monochromatic and extremely intense, and is emitted in a highly parallel beam. In general, one adds a fully and a partially reflecting mirror to the device to define the "cavity" of the system. Oscillations are set up between these mirrors as the coherent photon cascade passes successively through the laser crystal between

reflections from the end mirrors until the beam is finally emitted from the partially reflecting front mirror. Figure 1 is a simplified schematic drawing of a typical solid-state ruby laser.

Certain lasers, useful for welding, employ a gas mixture rather than solid material as the lasing medium. In these gas lasers, molecules are pumped from the ground state to the excited state with electrical rather than optical energy. Typically, the laser cavity is a tube filled with gas at reduced pressure and bounded on the ends by a totally reflecting and a partially reflecting mirror (Fig. 2). An electrical discharge sustained between electrodes inserted in the tube provides energetic electrons that collide with the gas molecules and excites them to higher energy states. As these excited molecules decay to the ground state, quanta of light energy are emitted in almost the same manner described previously for solid-state devices and lasing action occurs.

Basically, lasers for welding operate either in the conventional or pulsed mode; or the cw or continuous mode. Lasers can also be operated in the so-called Q-spoiled mode, in which very high peak powers (10^9 watts) are achieved in very short pulses (10^{-8} sec). The Q-spoiled mode is not suitable for welding. A comparison of these various types of lasers is shown in Table I. Although there are many other types of lasers, only those in Table I have any practical near-term significance for welding applications. The information in Table I should be further qualified in that these data do not represent state-of-the-art lasers per se, but rather practical devices suitable for industrial welding. Of the lasers described here, two can be made to operate in the cw mode at reasonable output levels--a solid-state laser, in which single crystals of yttrium-aluminum-garnet (YAG) are doped with Nd ions as the active medium (typically ~1% Nd); and a gas laser which employs a CO_2 - N_2 -He plasma (typically 6% CO_2 - 18% N_2 - 76% He) as the active medium. Continuous operation is possible with these so-called four-level systems, since those atoms which are pumped into the excited state are not required to return all the way to the ground state during stimulated emission, but rather only to an intermediate state. As a result, only a small fraction of the atoms need be pumped out of their normal ground state, greatly reducing the pumping requirements for laser action.

It is apparent that the laser designer has the choice of a number of parameters including output energy (or power), pulse length, wavelength, beam divergence, and pulse repetition rate, as well as certain optical controls that may be arranged external to the laser oscillator. It is appropriate at this point to ask the question, "what is the importance of these design parameters to the welding engineer?" How, for example, will selection of one wavelength of radiation, rather than another, permit him to better achieve his goals? What is the influence of pulse length on weld character?

A useful relationship in analyzing the performance of pulsed laser welders and elucidating many of these questions is:

$$F = 4E/\pi f^2 \theta^2 t \quad (1)$$

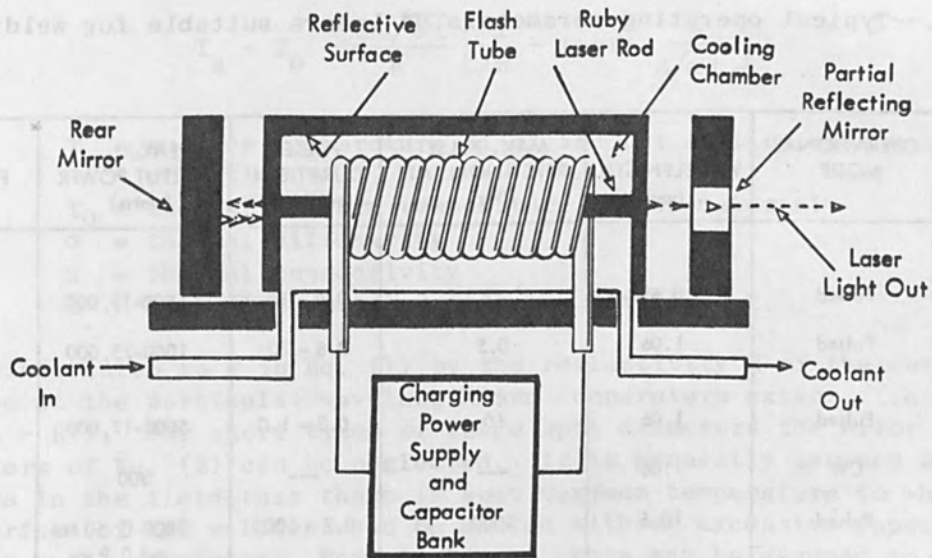


FIG. 1.--Solid-state laser system.

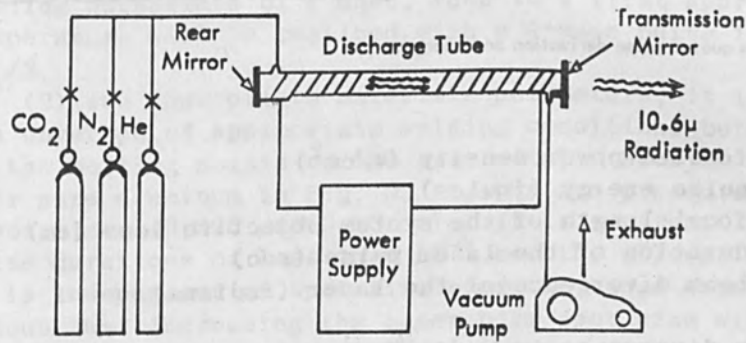


FIG. 2.--Flowing-gas system.

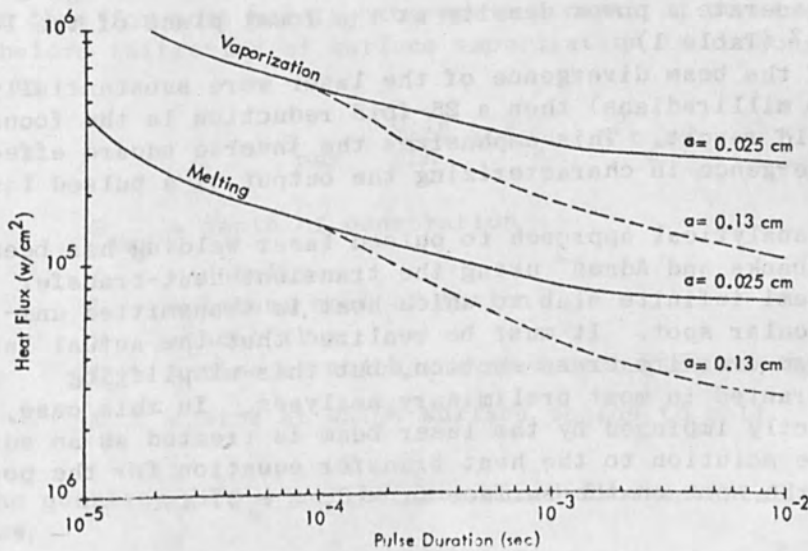


FIG. 3.--Heat flux vs pulse duration to induce melting and boiling in semi-infinite aluminum slab for various laser spot sizes.

TABLE I.--Typical operating parameters of lasers suitable for welding.

LASING MEDIUM	OPERATIONAL MODE	WAVELENGTH (nm)	MAX. PULSE REPETITION RATE (Hz)	PULSE DURATION (millisec)	PEAK * OUTPUT POWER (watts)	PULSE ENERGY (joules)
Ruby	Pulsed	0.694	2	0.8 - 10	1500-19,000	15
Nd:Glass	Pulsed	1.06	0.5	0.8 - 10	1000-75,000	60 in 0.8 ms 20 in 10 ms
Nd:YAG	Pulsed	1.06	60	0.3 - 1.0	5000-17,000	5
	CW	1.06	---	---	300	---
CO ₂ -N ₂ -He	Pulsed	10.6	5000	0.2 - 1000	3000 @ 50 Hz and 0.2 ms	0.6 in 0.2 ms
	CW	10.6	---	---	1000	---

* NOTE: Calculated from quoted pulse derivation and energy.

where F = focused power density (W/cm²)
 E = pulse energy (joules)
 f = focal length of the system objective lens (cm)
 t = duration of the laser pulse (sec)
 θ = beam divergence of the laser (radians)

If the beam divergence is defined as the cone apex angle which includes 90% of the energy flux, then F is the average power density. A ruby laser which produces a 15-joule laser pulse of 2 milliradians full angle beam divergence in 5 msec and has that beam focused through a 2-cm lens, will generate a power density at the focal plane of the lens of 2.4×10^8 W/cm² (Table 1).

Obviously, if the beam divergence of the laser were substantially greater (i.e., 10 milliradians) then a 25-fold reduction in the focused power density would result. This emphasizes the inverse square effect of laser beam divergence in characterizing the output of a pulsed laser welder.

An excellent analytical approach to pulsed laser welding has been published by Fairbanks and Adams² using the transient heat-transfer equations for a semi-infinite slab to which heat is transmitted uniformly over a circular spot. It must be realized that the actual laser beam is not uniform over its cross section, but this simplifying assumption is warranted in most preliminary analyses. In this case, the area not directly impinged by the laser beam is treated as an adiabatic region. The solution to the heat transfer equation for the point at the center of the spot on the surface (r = 0, z = 0) is:

$$T_s - T_0 = \frac{2H\sqrt{\alpha t}}{K} \left[\frac{1}{\sqrt{\pi}} - \text{ierfc} \frac{a}{2\sqrt{\alpha t}} \right] \quad (2)$$

where T_s = surface temperature of a circular spot of radius a
 at a time t
 T_0 = initial uniform temperature of the material
 α = thermal diffusivity
 K = thermal conductivity
 H = heat flux absorbed into the surface

H is related to F in Eq. (1) by the reflectivity R of the metal surface at the particular wavelength and temperature extant, i.e., $H = (1 - R)F$. For short times or large spot diameters the error function term of Eq. (2) can be neglected. It is generally assumed by most workers in the field that there is some maximum temperature to which the surface of the weldment can be heated without excessive vaporization or metal expulsion. For simplicity, this may be assumed to be the normal boiling point of the metal. If, for a given set of welding conditions, this maximum allowable temperature is obtained at a heat flux H_1 and a welding pulsewidth of 1 msec, then to a first approximation the same temperature will be realized with a 4-msec pulse if the heat flux $H_2 = H_1/2$.

From Eq. (2) and appropriate materials parameters, it is possible to define an envelope of appropriate welding conditions between the melting and the boiling points of the base metal. Such an envelope is presented for pure aluminum in Fig. 3. Graphs are presented for two different spot sizes (0.025 and 0.13 cm). It is apparent from Fig. 2 that for pulse durations of less than 10^{-4} sec the allowable heat flux for welding is independent of spot size over the range considered. It is also obvious that increasing the laser beam spot size will reduce the heat flux required to produce a phase change.

A further iteration on this semi-infinite solid heat transfer model has been made by Cohen and Epperson,³ who derived analytical solutions for the case of a constant heat flux using an analog computer. They report that for most metals, the maximum depth of penetration into the body before initiation of surface vaporization is reasonably approximated by

$$S_{\max} = \frac{0.16}{\rho LH} (H^2 t_e - H^2 t_m) \quad (3)$$

where S_{\max} = depth of penetration
 ρ = density
 L = latent heat of fusion
 H = heat flux
 t_e = time at which the surface begins to vaporize
 t_m = time at which surface begins to melt

The quantity $(H^2 t_m)$ can be determined from material properties as follows:

$$H^2 t_m = \frac{\pi T_m^2 K^2}{4\alpha} \quad (4)$$

where T_m = melting point
 K = thermal conductivity
 α = thermal diffusivity

$H^2 t_m$ can be calculated using an equivalent formula. A simplifying assumption made in deriving Eq. (3) is that the ratio $L/T_m C = 0.45$ (C is the specific heat) which is reasonable to $\pm 10\%$ for many metals.

From these relations, it is apparent that the maximum fusion front penetration can be simply represented by the equation:

$$S_{\max} = K_m / H \quad (5)$$

where K_m is a constant specific for each material. Values of K_m have been calculated as follows:

METAL	K_m^*	K_m^{**}
Cr	0.13×10^2	4.49×10^2
Cu	1.76×10^2	60.9×10^2
Au	1.89×10^2	65.4×10^2
Fe	0.31×10^2	10.7×10^2
Mo	1.51×10^2	52.2×10^2
Ni	0.34×10^2	11.8×10^2
Pt	0.61×10^2	21.1×10^2
Ag	1.60×10^2	55.3×10^2
Ta	0.42×10^2	14.5×10^2
W	1.14×10^2	39.4×10^2

* H in $\text{Btu}/\text{ft}^2\text{-sec}$ and S_{\max} in ft.

** H in W/cm^2 and S_{\max} in cm.

Obviously this equation has real meaning only for values of H sufficiently high to exceed the melting point of the material. H in turn can be obtained from Eq. (2) as discussed previously. Although H must be sufficiently high to induce melting, it must not be so high that penetration as calculated from Eq. (5) is unacceptably low. As we have previously seen, melting can be achieved at lower heat fluxes by broadening the laser pulse. It is for this reason that all good pulsed laser welding equipment contains special networks to lengthen the normal 0.5- to 1-msec pulse to values of 5 to 10 msec.

When applying this heat transfer theory to practical problems, it is of considerable interest to compare the focused power density H of laser energy sources with other more conventional welding energy sources. Typical values are presented in Table II.

TABLE II.--Comparison of heat sources for welding.⁴

HEAT SOURCE	POWER INTENSITY, W/cm ²
Laser	up to 10 ⁹
Electron beam	up to 10 ⁹
Electric arc (argon - 200 amp) ^a	1.5 × 10 ⁴
Oxyacetylene flame ^a	10 ³
Oxyhydrogen jet burner ^a	3 × 10 ³
Black body radiation, °K ^b	
6 500	10 ⁴
11 500	10 ⁵
20 500	10 ⁶
36 500	10 ⁷
65 000	10 ⁸
115 000	10 ⁹

^aExperimentally determined for heat transferred to flat surface.

^bCalculated.

Anderson and Jackson⁴ have made a number of instructive calculations comparing the efficiency of pulsed laser and arc welding. For example, a model was developed in which it was assumed that 0.001 in. of iron on the surface of a semi-infinite slab was melted with a welding arc of 10⁴ W/cm intensity and that a similar thickness of metal was melted using a pulsed laser sufficiently intense to achieve boiling at the slab surface. These calculations indicate that, with the laser, the heating time is reduced 100-fold, and the input energy by a factor of 6.5. The net result is that the extent of the weld heat-affected zone is drastically reduced. The marked differences in temperatures within the unmelted material which result from these two different energy sources are graphically shown in Fig. 4, which is taken from Ref. 4.

The discussion thus far has treated only pulsed energy sources. As indicated in Table I, cw lasers are also useful for welding. The applicable equation for the surface temperature at the center of the spot generated from a continuous source is:

$$T_s = W/\pi Ka \quad (6)$$

where W is the absorbed power and the other terms are as previously defined.⁵ This solution is exact only for situations where the material thickness is large compared to a. Firth⁵ points out that Eq. (2) approaches Eq. (6) when the pulse duration is greater than 5a²/α. For a laser beam focused to a 10-mil spot, this condition is realized at pulse durations of 0.9 msec for aluminum and 20 msec for type 304

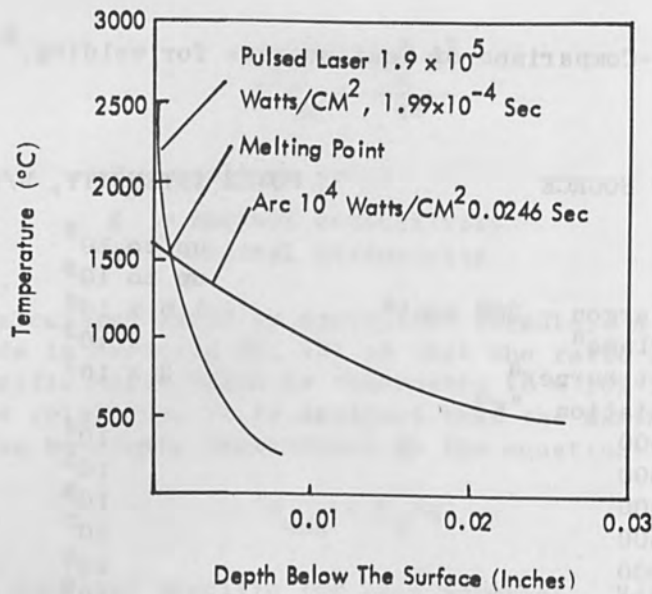


FIG. 4.--Maximum temperature reached vs depth for iron for pulsed laser and arc.

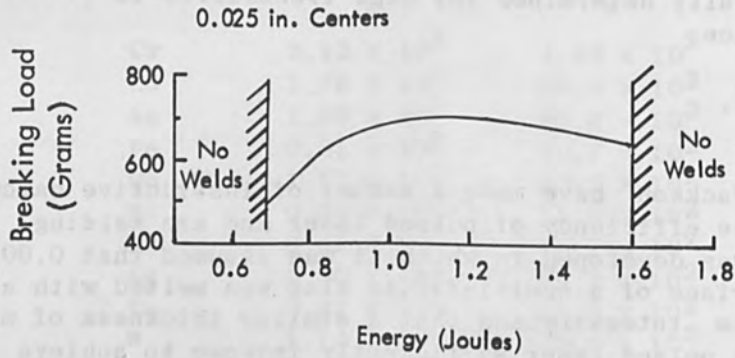


FIG. 5.--Effect of energy on strength of weld: 60° weld, edge incidence, 4.9 ms.



FIG. 6.--Kovar thermocouple gage header, co-extruded transition cylinder, and laser-welded sub-assembly.



FIG. 7.--Laser weld of Kovar thermocouple gage header to transition piece.

stainless steel. Further, the temperatures at the hemispherical surfaces of radius R from the center of the beam are given by

$$T_R = W/2\pi KR \quad (7)$$

EQUIPMENT

Most of the work done to date using lasers for welding applications has involved the pulsed ruby or glass lasers described in Table I. These solid-state lasers were developed first, so that more time has been available to convert them from laboratory devices into pilot-plant or production welding equipment. It is only recently that cw lasers, using either CO₂ or YAG, have been available with adequate power outputs to affect useful welds.

At the present time, pulsed ruby and glass lasers have been packaged into industrial devices specifically designed for welding; whereas, cw lasers have been used for welding only under laboratory conditions where the basic laser has been integrated with rudimentary optics to produce experimental weldments. A typical pulsed-laser welder consists of a work station, a power supply, and a closed-cycle refrigerated water cooler. Viewing optics are available at the work station to locate accurately the welding spot in microscope crosshairs.

Closed-circuit TV can also be used for positioning the work under the welding beam. When pulsed lasers of this type are used with ruby crystals, pulse repetition rates of up to about 60 ppm are generally obtained. It is, of course, possible to replace the ruby crystal with a neodymium-doped glass rod and obtain higher energy outputs, but the repetition rate for welding is reduced because the thermal conductivity of the neodymium-doped glass is only about 1/17 that of the single-crystal ruby. As was pointed out earlier, a YAG crystal could also be used in a similar arrangement for pulsed welding.

The components of a typical CO₂ laser system include the laser head, the power supply for excitation of the CO₂-bearing gas, and a service console which contains the gas-handling equipment and the cooling equipment. One potential advantage of this CO₂ laser is that they are extremely efficient in comparison to other laser devices. Typically, efficiencies in excess of 10 per cent are achievable with CO₂ lasers, whereas efficiencies with pulsed ruby lasers are of the order of 0.5 percent. Appropriate optics and work handling equipment must, of course, be added to make the laser into a useful welding tool. Development programs are in progress at several companies on ultra-high powered CO₂ lasers capable of cw output in excess of 10 kW. Such devices as they become available may provide welding capabilities equivalent to electron beam devices.

An existing YAG laser that might be also used for laser welding has the capability of generating 200 W of cw power from a power input of approximately 12 kW into the krypton arc lamps. Included in the photograph are the laser head, the power supply to drive the pump lamps, and the water cooling system required to remove the waste heat from the relatively inefficient energy conversion process. The YAG laser head is substantially smaller than the CO₂ laser head for equivalent power outputs. As with CO₂, appropriate optics and work handling equipment must be added to the basic YAG laser system to make it a useful welding

tool. For any of the laser systems discussed here the user has the choice of manual positioning his work under the laser beam or using automated work handling equipment, which is actuated either with numerical or computer-controlled drive circuitry.

WELDING WITH PULSED LASERS

This section summarizes typical results reported by various investigators on the application of pulsed laser welders to a wide variety of practical problems.

Results of a study on the welding of aerospace structural alloys in sheets with a pulsed ruby laser have been reported by Witt, Kaehler, and Klopper.⁶ Ease of welding was reported for Ti-8Al-1Mo-1V, Type 321 stainless steel, René 41, and Ta-10%W alloy. However, problems were encountered with cracking in 6061-T4 aluminum alloy. Parameters employed to obtain high-quality butt welds are summarized in Table III. Since, with a pulsed laser, the butt welds are created from a series of overlapping spot welds, welding speed is rather slow, in this instance varying from about 0.1 to 0.5 in./min.

One optical procedure that has been used to increase the welding speed attainable with pulsed lasers required a cylindrical, rather than a spherical, lens as the objective in the laser welder optical train. With the cylindrical lens the beam is elongated in the direction of welding, and thus the number of overlapping spots required to create a linear weld is reduced. Length-to-width ratios obtainable with the cylindrical lens are on the order to 10 to 1 or more.

In the microelectronics field Cohen et al.⁷ have reported on the feasibility of using a pulsed ruby laser for welding of an experimental plated-wire magnetic memory device. For this special application it was necessary to interconnect many 5-mil beryllium-copper wires, which were plated with 1.5 μ of Cu and 0.6 μ of the magnetic material Permalloy. The problem was made more difficult by the need to maintain a very close spacing (25 mils) between adjacent pairs of welded wires in the device. Because of these constraints, laser welding was selected. Since it was felt that the laser energy could be focused to a small spot, only simple fixturing would be required. The size of the heat affected zone and attendant changes in the magnetic properties of the wire would be minimized. The authors concluded that the pulsed ruby laser was indeed suitable for the interconnection of a multitude of fine wires and that the probability of producing short circuits even in closely spaced areas was minimal. As can be seen in Fig. 5, optimum parameters for this particular application involved energy outputs of about 1 joule with a pulse length of 5 msec from the ruby laser. Energy inputs of less than 0.6 joule were inadequate to create a weld nugget and energy inputs greater than 1.6 joules were equally ineffective, presumably resulting in vaporization rather than weld bead formation. This illustrates a fundamental problem in laser welding: defining the narrow zone between too little and too much energy.

Moorhead and Turner⁸ have discussed the use of a pulsed ruby laser for attachment of a thermocouple vacuum gage to the Apollo Lunar Sample Return Containers. These containers were designed to convey samples of the moon's surface back to the earth for analysis. For this particular application, brazing, mechanical assembly, and soldering were ruled out

TABLE III.--Laser welding conditions for producing butt welds with pulsed ruby laser.

LASER WELDING CONDITION	Ti-8Al-1Mo-1V ALLOY		321 STAINLESS STEEL		RENÉ 41	Ta-10W ALLOY	
Sheet Thickness, inches	0.023	0.062	0.005	0.027	0.025	0.025	0.025
Number of Passes	One	One	One	One	One	One	One
Spot Size Diameter, inches	0.062	0.063	0.030	0.056	0.060	0.050	0.047
Energy Output, joules	23.5	36.0	*	25.5	23.0	*	51.5
Pulse Length, msec.	18	18	9	18	18	18	18
Pulse Repetition Rate, pulse/min.	17.8	10.5	39.2	17.8	17.8	10.5	17.8
Weld Travel Speed, inches/min.	0.46	0.14	0.39	0.39	0.30	0.21	0.32 (top) 0.50 (bottom)
Spot Spacing, inches	0.026	0.013	0.010	0.022	0.017	0.020	0.012 (top) 0.028 (bottom)

* Not Measured.

on the basis of weight, contamination sources, or possible thermal damage to the container. Electron-beam welding was initially chosen as the preferred joining technique and the specific problem was to effect a structurally sound, helium leak-tight joint between a Kovar header and a Type 304 stainless steel transition cylinder (Fig. 6). Sound welds could not be produced due to unpredictable deflection of the electron beam by the magnetic Kovar pins in the header. Consequently, laser welding, which is not affected by magnetic field, was chosen and 25 subassemblies were produced by an appropriate rotary fixture. Welding parameters employed were: 6.6 joules/pulse, 5.2 msec pulse duration per pulse, 1/32-in. spot size, 30 pulses per minute, and 50% spot overlap. Of the 25 subassemblies, two were found to leak initially. However, after repair using the same parameters, all welds successfully passed the helium leak test at $< 1 \times 10^{-9}$ atm-cc/sec. The cross section of a Kovar-to-stainless steel weld is shown in the photomicrograph of Fig. 7.

In another weldability study using a pulsed ruby laser, results obtained on Type 302 stainless steel and an 18% Ni maraging steel are described by a research team at the Pennsylvania State University. With an energy input of 5 joules (other laser parameters unspecified) the welding of the stainless steel was possible in sheets of 0.005-in.

thickness, and marginal in sheets of 0.010-in. thickness; no penetration was obtained in the 0.015-in. thick sheets. However, suitable welds were made in each of the same three sheet thicknesses of the 18% Ni maraging steel and welding conditions appropriate to each thickness in terms of pulse energy and focused power density were determined. For those conditions where the input energy was inadequate or where the beam was sufficiently defocused, no penetration was observed. At the other extreme, excessive energy or a sharply focused beam will produce metal expulsion and vaporization closely akin to hole drilling. Between these extremes, various combinations of parameters were defined where reasonable welds could be effected. The difference in weldability of the Type 302 stainless steel and the 18% Ni maraging steel is probably associated with a higher thermal diffusivity in the latter alloy (4×10^{-6} versus 7×10^{-6} m^2/sec).

A significant production bottleneck in the fabrication of klystron tubes was solved with pulsed laser welding at Varian Associates of Canada, Ltd.¹⁰ In this application it was necessary to weld 0.002-in. thick tantalum sleeves to molybdenum collars. Resistance welding was initially attempted, but the welds produced were mechanically weak and the finished components were often contaminated with microscopic droplets of copper condensed from the resistance welding electrodes. Rejects ran about four in five. Laser welding was explored as an alternative and it was found to be completely successful for this particular application. The rejection rate dropped to practically zero. The weld between these two refractory metals was produced under a glass bell jar which was filled with argon to eliminate contamination and maintain the integrity of the joint. This result incidently indicates another virtue of laser welding; specifically the ability to produce joints while welding through glass. Varian also demonstrated, with this equipment, the ability to repair defective klystron tubes using this same property of the pulsed ruby welder; namely, welding through the glass envelope of the vacuum tube.

A number of successful job-shop applications using a pulsed ruby welder have been reported by workers at AiResearch Manufacturing Co.¹¹ Emphasis in this work was placed upon the ability of the laser welder to produce satisfactory welds in dissimilar metal alloy combinations. One example cited involved the successful creation of a dissimilar metal weld between a B-1113 steel feedthrough and a Type 321 stainless steel casing in a thermistor enclosure. It was necessary for the weldment to be hermetically sealed and for the heat input to be extremely low to prevent damage to a glass ceramic seal which existed in the thermistor assembly. In another production example, it was necessary to weld a Type 321 stainless steel retaining ring to a Type 440C high-temperature bearing race. Here again, it was essential to limit heat input during the welding process to prevent thermal damage to the part (i.e., softening of the martensitic stainless steel). A number of bearings were welded and tested and it was found that the laser weld between the retainer ring and the housing in no way jeopardized the performance of the component. These results substantiate in a qualitative way the laser welding advantages presented previously in Fig. 4 regarding the extent of the heat affected zone.

Many investigators have demonstrated the practicability and frequently the practicality of making sound wire-to-wire or wire-to-sheet

welds using the pulsed laser. A typical example is the precision attachment of thermocouples to an object whose temperature must be accurately measured. In the case of thermocouple welding, it is possible to simultaneously create the junction, attach the thermocouple to the substrate, and trim the rough-cut wires to exact length. Laser-produced thermocouple welds have been used to attach measuring probes to transistors, turbine blades, nuclear-reactor fuel elements, and the like.

Important considerations in these applications are the ability to produce dissimilar metal welds and very low energy input requirement in order to minimize thermal damage to adjacent materials.

Anderson and Jackson⁴ have discussed optimum procedures for welding integrated circuit flat packs to printed circuit boards in microelectronics fabrication. Figure 8 shows a typical board to which two flat packs have been welded. Figure 9 shows a close-up of two of the laser-welded interconnections between the leads and the pads of the board. Successful welds have been made to boards fabricated with nickel, copper, kovar, and multilayer claddings. These authors have also noted the laser's ability to produce attachments of insulated wires to lugs without stripping. In one example, connections of polyurethane-coated wires of a relay coil were produced by simultaneously vaporizing the organic coating and fusing the coil wire.

The Korad Department of Union Carbide Corp.¹² has conducted many applications studies with pulsed laser welders. In several instances, the ability to produce (without insulation stripping) sound welds between enameled wire and terminals has been demonstrated. Figure 10 shows an example of this. Here the 0.040-in. enameled-copper wire from the armature coil of a motor was successfully welded to a commutator segment. In this particular instance, the energy available from the 4 x 3/8-in. diameter ruby crystal ordinarily used with the laser welder did not provide adequate energy to create a sound joint. However, when the ruby crystal was replaced with a YAG crystal of the same size, the high-quality welds illustrated in Fig. 10 were easily produced. This situation stems from the fact that the conversion of pump energy to laser energy in YAG is considerably more efficient than in ruby.

Most of the pulsed welding discussion presented thus far has involved the use of ruby lasers. Ruby is generally preferred to neodymium-doped glass because the substantially higher thermal conductivity of the crystalline material permits the ruby laser to be pulsed at a higher repetition rate without exceeding thermal stress and beam divergence limitations. Hence, it is possible to achieve higher welding speeds. In addition, the higher thermal conductivity insures better shot-to-shot energy reproducibility and, weld-to-weld consistency when random welding cycles are employed. Nevertheless, fusions have been made in aluminum, carbon steel, stainless steel, molybdenum, niobium, tungsten, tantalum, titanium, Inconel, nickel, copper, and brass with glass laser welders.¹³ Unfortunately, details on welding conditions are not discussed.

WELDING WITH CONTINUOUSLY PUMPED LASERS

Virtually all work published as available literature deals with pulsed lasers (generally ruby lasers). Very little information exists

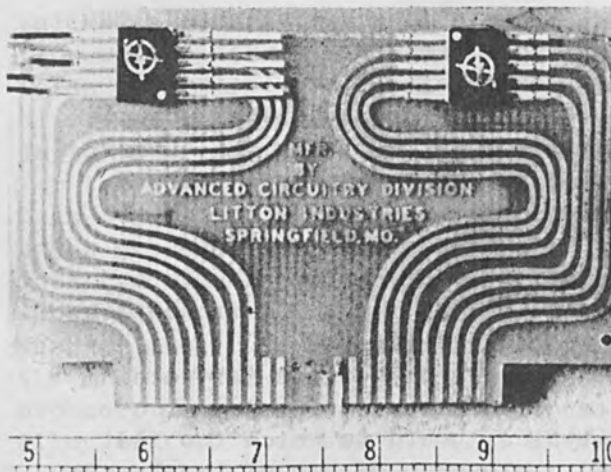


FIG. 8.--Two integrated circuits welded to a printed-circuit board.

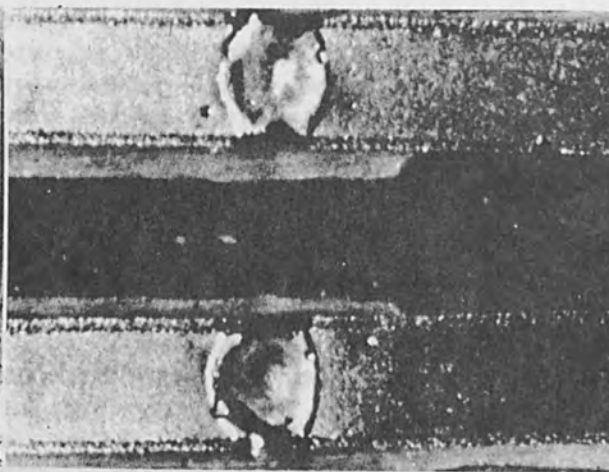


FIG. 9.--Close-up of welds shown in Fig. 8.

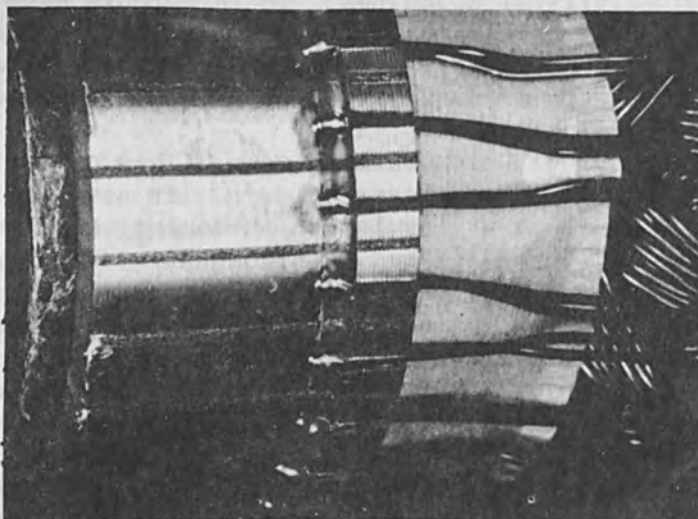


FIG. 10.--Weldments of coil wires to commutator segments in electric motor. Welds were produced with pulsed YAG laser.

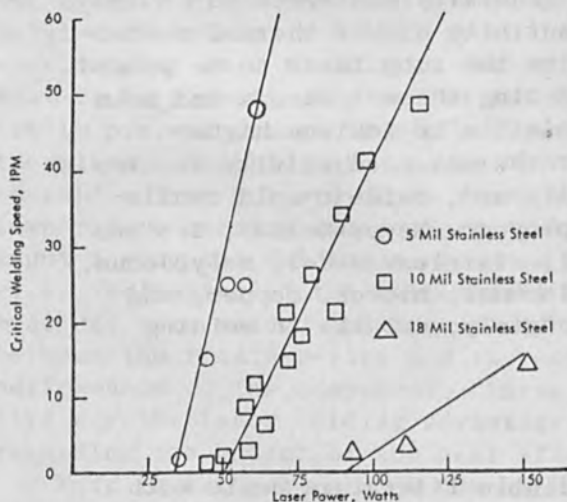


FIG. 11.--Effect of laser power on welding speed for stainless steel with YAG laser (cw pumped).

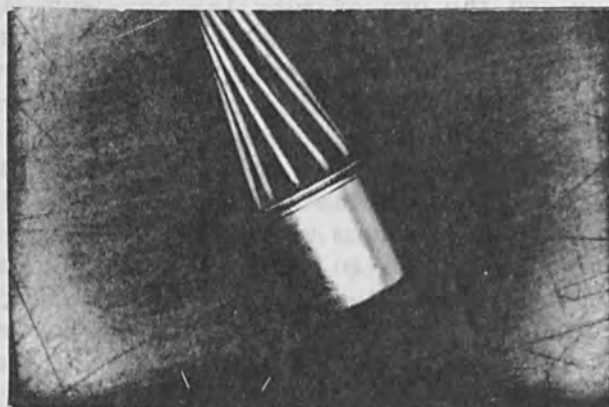


FIG. 12.--TO-5 transistor can weld produced with pulsed CO₂ laser. Welding conditions: 8.5 rpm (two revolutions), 200 pps, 25-ms pulse width, 80 W average power.

on the use of continuously pumped lasers for welding, since YAG or CO₂ lasers of adequate power for useful welding operations have not been available as long as the venerable ruby devices have been available.

An interesting comparison between the cw welding with YAG and CO₂ has been made by Jackson.¹⁴ In his developments, Jackson has defined a threshold power, which is the laser power required to sustain a molten puddle (i.e., to weld at zero speed). For power levels above the threshold power, he defines a critical welding speed, which is the maximum speed at which full penetration welds are obtained.

When welding in excess of the critical speed, less than full penetration welds are produced. Test welds were produced in Type 304 stainless steel 5, 10, and 18 mil thick using a 200-W YAG laser and an empirical correlation was developed between critical welding speed S (in./min), laser power P (W), and sheet thickness t (mils), as follows:

$$S = 3.5e^{-0.146t}(p - 22e^{0.0835t}) \quad (8)$$

Experimental results are presented in Fig. 11. Similar studies were conducted using a CO₂ laser and it was determined that power required to achieve a given welding speed was three times as great with CO₂ as with YAG. For example, to weld a 10-mil sheet at a welding speed of 30 ipm required an output of 85 W from the YAG laser and 260 W from the CO₂ laser. This trend is not surprising, since there are major differences in the absorptivity of metals to the 1.06- μ radiation emitted by YAG and the 10.6- μ radiation emitted by CO₂, the absorption being less at the longer wavelength. From the absorptivity values presented in Table IV, it is obvious that the stainless steel absorbs radiation of 1.06 μ wavelength about two times as effectively as at 10.6 μ , which supports the experimental welding observations described above. Of course, as the temperature of the workpiece increases, materials become more absorbing and the effect of these wavelength differences is less pronounced.

Further, in the context of comparison between YAG and CO₂, it should be noted that if the laser operates in the fundamental transverse mode, the beam divergence θ and thus the spot size S are proportional to the wavelength. Factoring this information into Eq. (1) reveals that the focused power density from a diffraction-limited YAG laser is 100 times greater than for a CO₂ laser with the same power output.

Preliminary studies on the welding of super alloys using a CO₂ laser have been reported by Alwang et al.¹⁸ Samples of AMS 5525 (A-286) and AMS 5544 (Waspalloy) in thicknesses ranging from 18 to 31 mils were continuously butt welded. The AMS 5544 was joined using 195 W of multimode output power focused to a 0.050-in. spot size equivalent to a power density of 15 400 W/cm². The welding speed was about 0.2-in./sec, and an argon cover gas was employed. This speed is comparable to what might be achieved by the gas tungsten arc method. Laser welds in 18 mil thick AMS 5525 were compared with electron-beam welds produced under similar conditions. Although minor differences in the chemistry and hardness of the comparison welds were noted, the two processes yielded similar results.

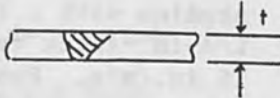

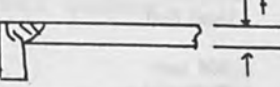
TABLE IV.--Spectral absorptance of various materials.

MATERIAL	TEMPERATURE (°F)	SPECTRAL ABSORPTANCE *		REFERENCE NUMBER
		1 μ	10 μ	
Titanium	RT	0.4 -0.55	0.09-0.12	15
Titanium	930	0.53-0.6	0.12-0.15	
Titanium	1380	0.5 -0.75	0.2 -0.25	
Type 301 SS	86	-	0.23	15
	230	-	0.3	
Type 321 SS (Electropolished)	1200	0.3	0.13	15
(Sandblasted)	1200	0.33	0.41	15
AM-350	480	- 0.7	0.42-0.49	15
	930	0.58-0.8	0.41-0.51	
	1380	0.7 -0.75	0.53-0.61	
17 - 7 PH SS	480	-0.6 -0.7	0.21-0.25	15
	930	0.56-0.65	0.21-0.25	
	1380	0.52-0.73	0.24-0.29	
Inconel X	480	-0.5 -0.7	0.27	15
	930	0.42-0.52	0.23-0.28	
	1380	0.41-0.5	0.23-0.31	
René 41	480	- 0.7	0.42-0.48	15
	930	0.56-0.6	0.48	
	1380	0.53	0.44-0.5	
Hastelloy X	480	-0.4	0.2 -0.28	15
	930	0.53-0.87	0.2	
	1380	0.65-0.7	0.23-0.47	
Haynes 25	480	-	0.29-0.32	15
	930	0.57	0.28-0.36	
	1380	0.6 -0.7	0.48-0.56	
Molybdenum	1800-2200	0.27-0.35	0.09	15
Tantalum	2200	0.3	0.1	15
Tungsten	1700	0.38	0.06	15
Al ₂ O ₃	1886	0.42	0.99	15
Aluminum	Room Temp.	0.07	0.02	17
Silver	Room Temp.	0.0064	0.0047	16
Gold	Room Temp.	0.014	0.0061	16

* Spectral Absorptance = Spectral Emittance

More recently, Webster¹⁹ has summarized welding studies using a 250-W CO₂ laser. Details of the thin-gage welding studies are presented in Table V. Webster points out that metals with high thermal diffusivity, and reflectivity such as aluminum and copper, cannot be welded with CO₂ lasers commercially available at present. Incidentally, operating costs for the 250-W CO₂ laser are quoted at \$1/hr for gas and electric power consumption. In speculating on future developments, the author alludes to the fact that an experimental CO₂ laser operating at 4.6 kW has been used to weld 1/8-in.-thick stainless steel at 14 in./min.

TABLE V.--Results of welding various materials with CO₂ laser.

MATERIAL	THICKNESS (t), IN.	RATE IN./MIN.	WELD WIDTH, IN.	REMARKS	
BUTT WELDS					
Type 321	0.005	90	0.018	Full penetration	
Type 321	0.010	35	0.028	Full penetration	
Type 321	0.0165	11	0.030	Partial penetration	
17-7 PH	0.005	110	0.018	Full penetration	
Type 302	0.005	50	0.020	Full penetration	
Type 302	0.008	30	0.020	Full penetration	
Type 302	0.010	10	0.040	Full penetration	
Inconel 600	0.004	150	0.010	Full penetration	
Inconel 600	0.010	40	0.018	Full penetration	
Nickel 200	0.005	35	0.018	Full penetration	
Monel 400	0.010	15	0.025	Full penetration	
CP titanium	0.005	140	0.015	Full penetration	
CP titanium	0.010	50	0.022	Full penetration	
EDGE WELDS					
Type 321	0.005	85	-	Weld Type I	
Type 321	0.010	25	-	Weld Type I	
Type 321	0.0165	15	-	Weld Type II	
17-7 PH	0.005	45	-	Weld Type I	
Inconel 600	0.004	160	-	Weld Type I	
Inconel 600	0.010	35	-	Weld Type I	
Inconel 600	0.0165	25	-	Weld Type II	
Nickel 200	0.005	18	-	Weld Type I	
Monel 400	0.010	25	-	Weld Type I	
Ti-6Al-4V	0.020	27	-	Weld Type II	
Ti-6Al-4V	0.010	300	-	Weld Type I	
LAP FILLET WELDS					
Tin-plated steel	0.012	20	0.025	Full penetration	
Type 302	0.016	175	0.030	Partial penetration	
Type 302	0.030	30	0.030	Partial penetration	
Type 302	0.010	15	0.025	Full penetration	
CORNER WELD					
Type 321	0.010	20	-	-	

NOTE: Welds made with Coherent Radiation's Model 41 250 w CO₂ laser equipped with a Model 141 pulsing accessory; 0.100 in. nozzle at a stand-off distance of 0.100 inc.; shielding and backing gas, argon at 15 cu. ft. per hr. All materials welded in as-received annealed condition.

In certain welding applications, the problem of high reflectivity of metal to the 10.6- μ radiation from a CO₂ laser can be overcome through the use of pulsing. When the plasma in the laser tube is electronically pulsed the peak power in the pulse is higher than the average power and the metal surface can be heated to a sufficiently high temperature that the reflectivity is reduced. Melting can then be achieved and a reasonable fusion zone sustained. Figure 12 shows an example of a microelectronics fabrication produced with a CO₂ welder. In this particular instance, a TO-5 transistor can was hermetically sealed with minimal heat input, thereby reducing the possibility of thermal damage to the circuit element.

Conti²⁰ has reported welding studies with a 100-W (cw) CO₂ laser. His results agree with those of Webster in that he was also not successful in welding materials such as copper, beryllium-copper, and aluminum which are highly reflective at 10.6 μ . Successful welding of thin sheets of stainless steels and certain copperbase alloys was accomplished, however. Results are summarized in Table VI. It will be noted that these welds were generated by operating the laser in the pulsed mode, rather than the continuous. The maximum depth of penetration obtainable from the 100-W laser operating multimode and pulsed was about 0.009 in.

Engineers at Holobeam, Inc.,²¹ have reported very limited welding studies with a 760-W (cw) Nd:YAG laser. Welds were made in bulk 1/4-in.-thick type 304 stainless steel and AISI 1030 carbon steel at 15 in./min. Penetration was only 20 mils, which is scarcely better than that quoted in Table V for a 250-W CO₂ laser. This rather surprising result may be due to the fact that the YAG laser spot size was too large in these preliminary tests.

TABLE VI.--Summary of edge-lap welds on thin metal sheet obtained with 100-W CO₂ laser.

SAMPLES WELDED	LASER POWER (% OF FULL OUTPUT)	PULSE WIDTH (SEC)	REPETITION RATE (SEC/PULSE)	TRAVEL SPEED (IN./MIN)	PARENT MATERIAL ULTIMATE STRENGTH (LBS/IN. ²)	PEEL STRENGTH (% OF ULTIMATE)
0.0045 Inch Phosphor Bronze "A" (95% Cu, 5% Sn)	95	0.30	0.35	5	49,000	65%
0.004 Inch 304 Stainless Steel Foil	95	0.0002	0.001	3	86,000	45%
0.004 Inch 304 Stainless Steel Foil	95	0.22	0.28	6.5		
0.004 Inch Silver 752" (65% Cu, 18% Ni, 17% Zn)	95	0.065	0.075	3	55,000	19%
0.004 Inch Monel (70% Ni, 30% Cu)	95	0.07	0.2	3	66,000	23%
0.004 Inch Cupro-Nickel (70% Cu, 30% Ni)	95	0.30	0.35	3	75,000	12%

LASER WELDING CHARACTERISTICS

It is apparent from the foregoing discussion that a certain range of applications exists where the unique properties of the laser beam may be used to advantage for metal joining. It is equally apparent that many jobs exist for which the laser is not suited. Basically, the

laser must be regarded as a specialty tool. Some of the specific advantages which have been alluded to previously are summarized as follows:

(1) Welds can be made in areas impossible to reach by more conventional processes, such as the bottom of blind holes. This may be paraphrased into the saw, "If you see it, you can weld it with a laser."

(2) Because of the high energy density achievable with a laser, the extent of the heat-affected zone is minimal. This reduces undesirable metallurgical changes or permits welds to be made close to heat sensitive parts.

(3) Welds can be produced in a magnetic field without deflection of the beam.

(4) The weld can be precisely located (e.g., to within ± 0.0005 in.) and the weld bead made very small (~ 0.001 in.), thus providing a process suitable for microwelding applications.

(5) Welds can be made through glass and other transparent media.

(6) No physical contact is necessary between the joining media and the workpiece. Consequently, only simple work-holding fixtures are required and the strains associated with hold-down fixtures are eliminated.

(7) Temperatures achievable with laser welding are sufficiently high to fuse all metals.

(8) Welds can be made in air, vacuum, or inert atmosphere.

(9) Dissimilar metal welds are relatively easy to make, providing the interface between the dissimilar metal does not vitiate sound metallurgical principles (e.g., with regard to formation of brittle intermetallics, etc.).

On the debit side of the ledger, the following factors must be assessed:

(1) The capital cost of the equipment is high.

(2) Deep penetration welds cannot be created with present commercially available lasers.

(3) Good fit-up between parts to be welded is required.

(4) Pulsed laser welding is considerably slower than conventional processes.

CONCLUSION

Laser welding has been successfully used for a plethora of specialty joining applications. Many of these specialty applications are in the microelectronics, nuclear, and aerospace fields, where precise weldments with limited energy input are a necessity. The laser process must be regarded by the metallurgist and the fabrication specialist as one which augments and extends our joining capabilities permitting tasks to be accomplished which are difficult to achieve by more conventional processes. It is in this light that laser welding must be considered, not as a technique to supplant the more well-established welding process, but, rather, to do jobs not otherwise possible.

REFERENCES

1. T.H. Maiman, Stimulated optical radiation in ruby, *Nature* 187: 493-494, 1960.
2. R.H. Fairbanks, Sr., and C.M. Adams, Jr., Laser beam fusion welding, *Welding Journal (Welding Research Supplement)* 43: 97-102S, March 1964.
3. M.I. Cohen and J.P. Epperson, Applications of lasers to micro-electronic fabrication, *Electron Beam and Laser Beam Technology*, 1968; pp. 139-186.
4. J.E. Anderson and J.E. Jackson, Theory and application of pulsed laser welding, *Welding Journal*, December 1965.
5. Kenneth Firth, A guide to the laser, in D. Fishlock, ed., *The Laser as a Source of Heat*, MacDonal, London, 1967.
6. R.H. Witt, W. Kaehler, and D. Kloepper, Laser welding structural alloys and parts, Grumman Aircraft Engineering Corp.
7. M.I. Cohen, F.J. Mainwaring, and T.G. Melone, Laser inter-connection of wires, *Welding Journal*, March 1969; pp. 191-197.
8. A.J. Moorhead and P.W. Tumer, Welding a thermocouple gauge to Apollo lunar sample return containers, Nuclear Division, Union Carbide Corporation, Document Y-DA-2756. (Paper presented at 50th Anniversary Meeting of American Welding Society, New Orleans, 8 October 1969.)
9. A.O. Schmidt, I. Ham, and T. Hoshi, An evaluation of laser performance in microwelding, *Welding Journal (Welding Research Supplement)* 44: 481-488S, 1965.
10. Linde Welding Progress, vol. 18, No. 2.
11. K.J. Miller and J.D. Nunnikhoven, Laser: A space age welding process, *Laser Focus*, December 1965; pp. 10-19.
12. F. Pothoven, Private communication, Union Carbide Corp., February 1970.
13. Staff Members of American Optical Corp., Glass laser technology, *Laser Focus*, December 1967; pp. 21-29.
14. J.E. Jackson, Union Carbide Corporation. (Unpublished data.)
15. Thermal radiative properties of selected materials, DMIC Report 177, 15 November 1962.
16. J.M. Bennett and E.J. Ashley, Infrared reflectance and emittance of silver and gold evaporated in ultrahigh vacuum, *Applied Optics* 4: 221-224, 1965.
17. H.E. Bennett, M. Silver, and E.J. Ashley, Infrared reflectance of aluminum evaporated in ultra-high vacuum, *J. Optical Soc. Am.* 53: 1089-1095, 1963.
18. W.G. Alwang, L.A. Cavanaugh, and E. Sammartino, Continuous butt welding using a carbon dioxide laser, *Welding Journal (Welding Research Supplement)* March 1969; pp. 110-115S.
19. J.M. Webster, Welding at high speed with a CO₂ laser, *Metals Progress* 98 (No. 5): 59-61, November 1970.
20. R.J. Conti, Carbon dioxide laser welding. Paper presented at 50th Anniversary Meeting of American Welding Society, New Orleans, La., 9 October 1969.)
21. State-of-the-art in continuous Nd: YAG laser welding, Staff Report, *Metals Progress* 98 (No. 5): 61-62, November 1970.

MATERIALS PROCESSING WITH CARBON DIOXIDE LASERS

C. M. BANAS, A. P. WALCH, and C. O. BROWN

United Aircraft Research Laboratories, East Hartford, Conn.

INTRODUCTION

At present the carbon dioxide laser provides the highest continuous output power levels and, therefore, the greatest potential for materials-processing applications, significantly enhanced by the recent development of efficient multikilowatt CO₂ laser systems.¹⁻⁴ One of these lasers, a 5-kW closed-cycle CO₂ convection laser with an output beam that is nearly diffraction limited, has been used to investigate and evaluate potential materials-processing applications with exciting and highly encouraging results.

TEST APPARATUS AND PROCEDURE

In the high-power electric-discharge closed-cycle CO₂ convection laser^{2,3} developed for welding and cutting tests, rapid gas flow is used effectively to remove waste thermal energy deposited in the gas by the electric discharge, a method that yields beam power outputs per unit volume about two orders of magnitude greater than those attainable with conventional low-mass-flow CO₂ lasers. This feature, coupled with the fact that the lasing gas is cooled and then recirculated through the laser chamber, renders this type of laser adaptable to lightweight, portable, multikilowatt units suitable for industrial or other commercial applications.

The high-quality beam and long-term stability required for materials processing are obtained by operation of the laser unit as a high-power amplifier; a beam of high optical quality from a low-power laser (about 100 W) is used as the input to the high-power amplifier. This configuration results in power amplification to the multikilowatt level with an output beam exhibiting the initial, near-diffraction-limited characteristics of the low-power input beam. Thus, focused beam power densities greater than 10^6 W/in.² are readily attainable, even with f/10 focusing optics.

In most of the tests performed, the workpiece was mounted in the horizontal plane on a three-axis positioning table having a one-axis motorized drive. The table was designed to provide smooth motion (required to prevent disruption of a stable weld zone) over a range of speeds to 150 ipm. Tests were performed on a variety of metals with and without the use of a shield gas to prevent atmospheric contamination. Reflective focusing optics, which included a 20.5-in. focal length spherical mirror and a 10-in. focal length off-axis parabolic mirror, were used.

For cutting thick materials, a small-diameter gas jet, directed as nearly coaxial with the laser beam as possible, was utilized to remove molten material and to speed the cutting process. Reactive as well as inert gases were used, depending on the nature of test material and the desired cutting characteristics.

In high-speed cutting tests of most thin materials (speeds to 1000 ft/min), gas-jet-assist was not required and, in fact, did not lead to any increase in cutting capability. For such tests the samples were mounted on a rotating arm 7 in. in radius; the arm was mounted directly on a variable-speed drive motor. The continuous laser beam output was shuttered so that only one cutting pass was made as the sample was swept through the beam.

EXPERIMENTAL RESULTS

WELDING. Since the high-power CO₂ laser available at UARL provides focused power densities and continuous power outputs comparable to those used in electron-beam welders, some of the initial tests with this system were directed toward the attainment of deep-penetration welds. In ordinary welding processes (such as MiG, TiG, oxyacetylene torch, etc.), thermal energy is supplied to the material surface and is then transported into the material by thermal conduction. Since thermal flow proceeds uniformly in all directions from the surface in homogeneous materials, the weld zone exhibits a depth-to-width ratio of approximately unity. For this reason a large heat-affected zone may result, large energy inputs are required to effect welds in thick materials, and thermal distortion often occurs.

For sufficiently high incident power densities at the workpiece surface (at present attainable only with laser and electron beams and to a limited extent with plasma arc), a void is established in the material so that energy is deposited throughout the material thickness and not only at the surface. The void generated is statically unstable, i.e., hole drilling would occur if specifically controlled relative motion did not occur between the beam and the workpiece. However, if the workpiece is moved at a speed of at least the order of 10 focused spot diameters in the time required for material expulsion, the void becomes dynamically stable and translates through the material, with solidification occurring directly behind it. Characteristics of the weld can be predicted on the basis of the assumption of a moving, line-heat source distributed through the material. The width of the weld zone is of the order of the beam-spot size and its depth is proportional to the incident power and power density. The unique characteristic of this welding process is that depth-to-width ratios substantially greater than unity can be achieved. A parallel-sided fusion zone, as demonstrated previously at UARL⁵ and in some instances interpreted as the deep-penetration phenomenon, does not necessarily satisfy the deep welding criterion. Until recently, therefore, there has been considerable doubt that deep-penetration laser welding could be achieved with a laser beam.

As described in Ref. 6, however, deep-penetration welds can be attained with the laser. A typical butt weld exhibiting the deep penetration characteristic is shown in Fig. 1. This weld, which was obtained at about 150 ipm and a laser power of approximately 3.5 kW, is characterized by a relatively small heat-affected zone and by a depth-to-width ratio of approximately 7:1. Smooth transitions from fusion zone to base material are evident at both the top and bottom surfaces, which shows that a high-quality bond was achieved. It was in fact found that selected welds, which were effected in atmosphere and

without the use of filler material, exhibited X-ray acceptable quality and excellent strength. With respect to the latter, some of the tensile test specimens failed in the base material; i.e., essentially 100-percent bond strength was achieved.

The dependence of the penetration depth on beam power and welding speed is shown in Fig. 2. The data shown represent the results of bead-on-plate tests with series 300 stainless-steel specimens. Bead-on-plate tests eliminate the requirements for weld fixturing and permit rapid generation of the required data. Penetration for a weld may be somewhat higher than for the bead-on-plate case, in part due to increased beam-power absorption caused by the existence of a crack or edge in the welding case and in part by the fact that heat sink material does not exist below the fusion zone in a full-penetration weld. With this in mind we note that welding speed is approximately proportional to power level and that the depth of penetration decreases relatively slowly as welding speed increases. The latter behavior is facilitated by a concurrent decrease in the width of the fusion zone and leads to high-speed welding with reduced thermal input per unit length of weld. The fact that such welds can be attained in atmosphere adds a significant dimension to welding technology and heralds a promising new era for CO₂ laser applications.

Another interesting and extremely important capability which stems from the high power density capability of the laser is that narrow seam welds can be made at very high speeds in thinner-gage materials. An example of this mode of operation is shown by the fillet welds in 20-gage (0.037-in.) low carbon and galvanized steel (Fig. 3), made at a laser power level of 3.9 kW and weld speeds of 150 and 120 ipm. It is noted that nearly complete penetration was obtained under these conditions. Since only partial penetration (about 50 per cent) is generally desirable for such welds, it is evident that even higher welding speeds are attainable at the same power level. Excellent results were obtained even for the galvanized-to-steel weld which is difficult to effect with conventional techniques.

Since the weld zone formed is of the order of the focused beam spot, weld speed might be anticipated to increase linearly with beam power level. Reduction in spot size would, of course, reduce the power requirements for a given weld speed but is not felt to be practical in most instances, since the requirements for seam tracking and/or fit-up would become excessive with very small diameter beams. For many production applications, therefore, focusing requirements will be dictated by cost considerations in weldment preparation and not by inherent limitations in laser optics or beam quality.

The welding speeds attained indicate that significant production tasks can be accomplished with cw CO₂ lasers operating in the range from 3 to 8 kW. The possibility of such utilization is further enhanced because (1) the CO₂ laser beam can be transmitted for appreciable distances through the atmosphere without significant attenuation or loss in optical quality, (2) the beam may be readily directed to the working area with reflective optics, (3) X-rays are not generated upon impingement of the beam on the workpiece, (4) materials transparent in the visible (glass, plexiglas, etc.) may be used to shield the working area and contain possible reflected radiation to provide the requisite safety and yet allow maximum visibility of the

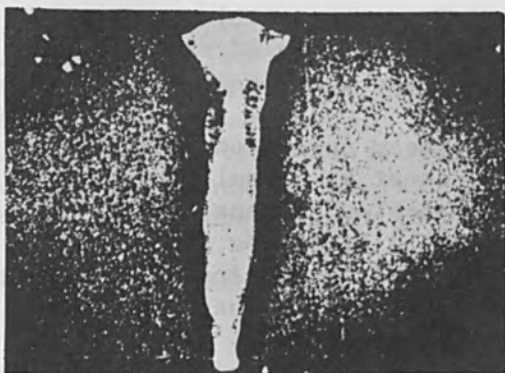


FIG. 1.--Laser butt weld in 302 stainless steel 0.5 in. thick; laser power about 3.5 kW, weld speed 50 in./min, mirror focal length 10 in., depth-to-width ratio about 7.

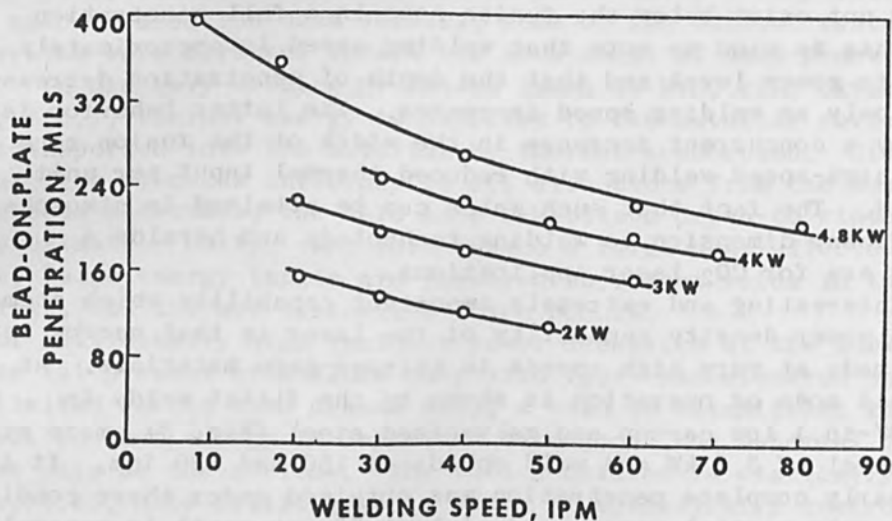


FIG. 2.--Effect of welding speed on depth of penetration in 304 stainless steel.

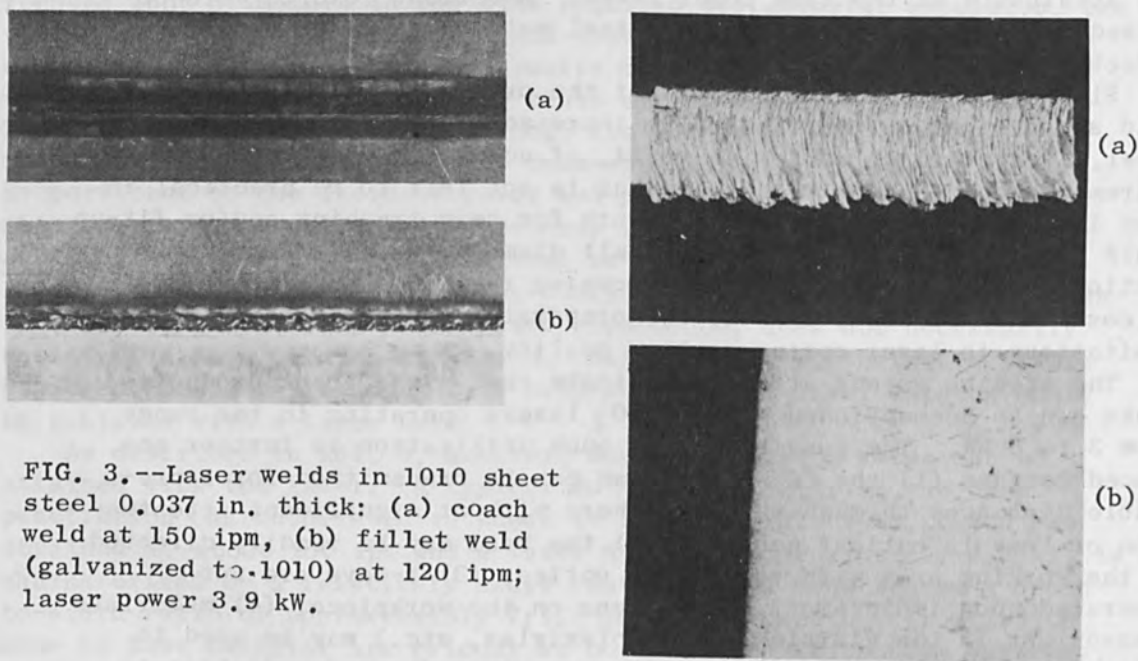


FIG. 3.--Laser welds in 1010 sheet steel 0.037 in. thick: (a) coach weld at 150 ipm, (b) fillet weld (galvanized to 1010) at 120 ipm; laser power 3.9 kW.

FIG. 4.--Laser cut in 2219 aluminum alloy 0.25 in. thick; laser power 3.8 kW, cutting speed 12 ipm, assist gas CO₂: (a) face of cut 3 X, (b) cross section 100 X (1% NaOH etch).

workpiece area, and (5) the process lends itself readily to automation.

CUTTING. In the cutting of metals in thicknesses greater than a few mils, the focused power density available with the present cw system (to 10^7 W/in.²) is not sufficiently high to permit effective removal by laser action alone; therefore, gas-jet assist must be used in conjunction with the laser beam. The gas used may react with the material to speed the cutting process (e.g., oxygen-assisted cutting of titanium⁷), the gas may be chosen on the basis of low cost for those applications in which cuts are to be made in oxidation-resistant materials, or the gas may be selected on the basis of its shielding properties if prevention of oxidation or contamination of the cut zone is required.

Since the effectiveness of oxygen-assisted cutting has been previously reported attention is directed here toward the latter two cases. An example of a gas-jet-assisted cut in 1/4-in.-thick aluminum alloy is shown in Fig. 4. This cut was obtained at a speed of 12 ipm at 3.8 kW using CO₂ as an assist and shielding gas. It is noted that a relatively oxidation-free surface was obtained, although surface roughness characteristics resembled those obtained with a plasma arc made with an improperly positioned jet.⁸ Similar results were obtained in the cutting of 0.5-in.-thick stainless steel. It is apparent from these observations that the design and performance of the gas-jet-assist device is a critical factor in the determination of cut quality.

The microstructure of the material adjacent to the cut zone (Fig. 4b) indicates a small heat-affected zone. This latter factor coupled with an improvement in surface quality of the cut could render this laser cutting process substantially competitive, especially if the requirements for postprocessing could be obviated. For the present, however, economic justification for laser use in this area can only be established in special instances such as in the cutting of extremely hard materials or in cases in which substantial savings can be realized from reduction in waste.

In contrast to the somewhat limited economic potential of current laser systems for cutting applications in thick materials, significant potential exists for applications to high speed, production cutting of thin materials. Thus, for example, a relatively low-power laser has already been adapted to production cutting of cloth in the garment industry.⁹ This cutting process is facilitated by the high absorptivity for carbon-dioxide laser radiation and the low thermal diffusivity of nonmetallics. For thin materials with relatively low energy requirements for material removal (cloth, paper, plastics, etc.) it follows that very high cutting speeds can be achieved. Further, in spite of the fact that many of these materials are quite flammable, the speed of the cutting process effectively inhibits combustion.

A typical result obtained with 0.18-in.-thick corrugated-board material is shown in Fig. 5. The cut shown was obtained at a power level of 3.5 kW and a cutting speed of 350 ft/min; essentially no benefit was derived with gas-jet-assist for this cutting mode. It is noted that the edge of the cut is very smooth with no traces of combustion. In addition, the flutes within the material have not been crushed as in the machine cut shown in Fig. 5(c). Physical inspection indicates that the laser cut material is stronger, i.e., an improved

product quality results. The potential of this process is further enhanced by its ready adaptability to automation.

Another example of a laser cutting process in which an improved end product is obtained is demonstrated by the BorsicalTM tape specimen illustrated in Fig. 6. The cut illustrated was obtained at a laser power level of 3.9 kW and a cutting speed of 100 ft/min. In addition to the relatively high cutting speed and ease of automation which are possible with this process, it is noted that the fibers have been sealed at the edge. Splitting and cracking of the edge is thus reduced and a stronger product is obtained. It has been shown that composite material fabricated from such tape may exhibit as much as 25 per cent higher tensile strength if cut by laser rather than other techniques.

Although relatively high cutting speeds were obtained in the tests described, even higher speeds are feasible at lower power levels. This fact pertains because cutting speed increases inversely with focused beam spot size (cut width). Spot size, in turn, may be decreased by utilization of lower ratios of focal length to aperture diameter in the focusing optics (f-number). Since the f-number was slightly greater than 5 in the tests reported, a substantial reduction is possible, especially if expansion optics are utilized to maintain a long focal length. A bright future for laser application in high-speed cutting is therefore indicated.

OTHER PROCESSING TESTS

In addition to the tests described, tests were also conducted to determine the efficacy of CO₂ laser cutting of rock (for possible hard-rock tunneling applications), and of hole drilling and dynamic balancing. For the latter tests, a pulsed CO₂ laser system developed at UARL was used. This system utilizes a 7-stage Marx bank to obtain high-voltage pulses in a laser tube 11 ft long and 2-in. in diameter. A high-optical-quality output of 10 J/pulse at repetition frequencies to 20 Hz is obtained with pulse durations of the order of 50 μsec.

A 5-ipm cutting speed was obtained in limestone 1.5 in. thick with the cw laser equipment at a power level of approximately 3.5 kW. It was found that gas-jet assist was not required; in other instances, in which the molten rock forms a vitreous slag (basalt, granite, etc.), gas-jet assist is necessary to remove the molten material and promote effective cutting. Although the results are encouraging, laser power requirements remain too high for significant hard-rock tunneling applications in the near term.

As for drilling, it may be noted that one of the first successful industrial applications of solid-state lasers was in the drilling of diamond wire-drawing dies. Pulsed CO₂ systems are also effective for drilling applications, especially in the case of nonmetals.¹⁰ The CO₂ laser possesses a significant advantage for hole drilling in materials such as glass, plastics, etc., which are opaque at the 10.6-μm wavelength of the CO₂ laser output, but are transparent at the shorter wavelengths of the pulsed solid-state systems. However, many potential hole-drilling applications for the laser require average power levels below 0.5 kW, so that the CO₂ laser does not command as dominant a position in this area as in those discussed previously.

TABLE I.-- Summary of predicted near-term applications potential of CO₂ laser.

Application	Approximate power range (kW)	Prospects
Very high speed cutting of thin materials	0.5-3	Most promising near-term application. Rapid development anticipated.
High-speed welding in thin-gage sheet metals	3-8	High production potential. Relatively rapid development.
Deep-penetration welding in metals to 0.5 in.	3-8	Excellent potential. Moderately rapid development.
Gas-jet-assisted cutting of thick materials	2-6	Advantageous in special applications. Limited development for specific tasks.
Hole drilling	0.2-0.6	Advantageous in specific applications. Limited development for specific tasks.
Dynamic balancing	1-4	Promising future. Requires further study.

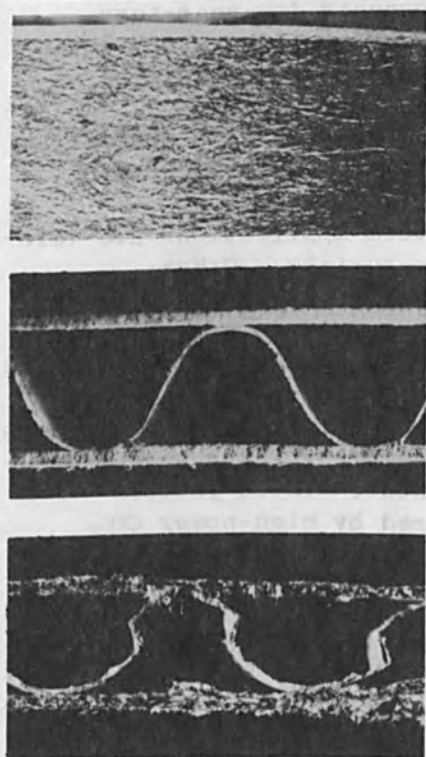


FIG. 5.--Laser cut characteristics in corrugated board 0.18 in. thick; laser power 3.9 kW, cutting speed 350 ft/min, no assist gas: (a) edge view of laser cut, (b) end view of laser cut, (c) end view of machine cut.

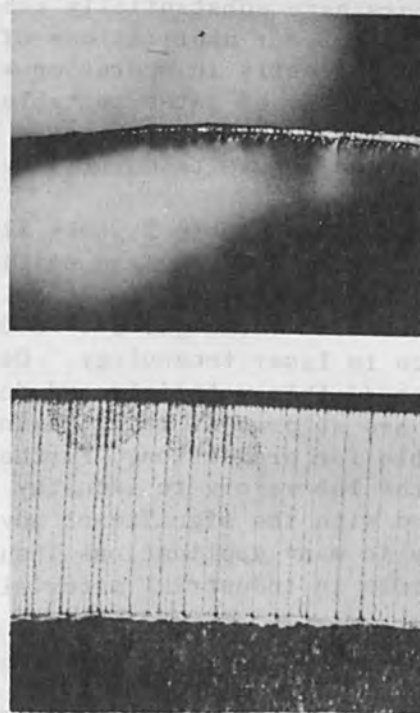


FIG. 6.--Laser cut characteristics in Borsical™ tape 0.009 in. thick; laser power 3.9 kW, cutting speed 100 ft/min, no assist gas: (a) edge view, (b) end view.

In contrast to hole drilling, many potential dynamic-balancing applications have average power requirements in the kilowatt power range; therefore, the carbon dioxide laser is currently the most promising for such applications. This position is enhanced by the fact that relatively high pulse energies can be achieved with short pulse durations, a factor important in balancing of high-speed rotating components. The primary advantage of the laser in this application is that material can be selectively removed from a part while it is rotating at design speed. Selective material removal is effected by coupling the imbalance sensing equipment to the laser system. By this arrangement balancing accuracy can be improved and the balancing time can be significantly shortened because the entire process can be accomplished in situ on the balancing machine without interruption of rotation. In tests to date on high-speed rotating samples, material removal efficiencies of 30 $\mu\text{g}/\text{J}$ were achieved, but unacceptable surfaces for stressed, rotating components were obtained. These results indicate that further investigations directed toward improvement in the nature of the laser-irradiated surface are required to permit evaluation of the full potential of the pulsed, CO_2 laser for dynamic-balancing applications.

CONCLUSION

Rapid developments in high-power laser technology within the past few years have substantially enhanced the prospects for near-term industrial laser applications of significant scale. Laboratory equipment is currently in operation with the capability for performing numerous tasks at rates suitable for production requirements. Significant applications of high-power lasers must, however, await demonstration of the requisite durability of such equipment in a production environment.

As noted in Table I, only limited, near-term applications are foreseen for hole drilling and cutting of thick materials. Other applications such as dynamic balancing require further definition and refinement in technique and hard-rock tunneling demands a substantial advance in laser technology. On the other hand, high-speed cutting and welding of thin materials and deep-penetration welding in the atmosphere are at present being performed with laboratory equipment at rates suitable for production. Further, rapid transfer of laser technology from the laboratory to industry appears imminent. These factors coupled with the significant advantages offered by high-power CO_2 lasers in many applications insure that they will soon assume a prominent role in industrial materials processing.

ACKNOWLEDGMENT

The authors gratefully acknowledge the contributions of W. G. Burwell, J. W. Davis, R. G. Tomlinson, A. C. Eckbreth, J. P. Carstens, and P. O. Erlandsen of the United Aircraft Research Laboratories to the development of the lasers used for the tests described and to the over-all materials-processing program.

REFERENCES

1. C. O. Brown, Appl. Phys. Letters 17: 388-391, 1970.
2. C. O. Brown, Plasma properties of an electric discharge convection laser, 23rd Ann. Gaseous Electronics Conf., Hartford, Conn., October 1970.
3. C. O. Brown and J. W. Davis, Electric discharge convection lasers, IEEE 1970 Intern. Electron Devices Meeting, Washington, D. C., October 1970.
4. A. C. Eckbreth, W. G. Burwell, and J. W. Davis, Electric-discharge CO₂ lasers, Rec. 11th Symp. Electron, Ion, and Laser Beam Technology, San Francisco Press, 1971.
5. C. M. Banas, The role of the laser in material processing, Canadian Materials and Processing Technology Conf., Toronto, 1969.
6. C. O. Brown and C. M. Banas, Deep penetration laser welding, AWS 52nd Ann. Meeting, San Francisco, 1971.
7. A. B. J. Sullivan and P. T. Houldcroft, Gas-jet laser cutting, Brit. Welding J., August 1967.
8. American Welding Society, Welding Handbook, New York, 1967; 5th ed., sec. 5 (81-40).
9. Lasersphere 1 (No. 4), March 22, 1971.
10. Laser drills small, accurate holes in rubber, Mat. Engg., p. 25, February 1971.

REFERENCES

1. J. C. Brown, "The Laser Drill," *IEEE Trans. Electron Devices*, ED-10, pp. 100-104, 1963.

2. J. C. Brown, "The Laser Drill," *IEEE Trans. Electron Devices*, ED-10, pp. 100-104, 1963.

3. J. C. Brown, "The Laser Drill," *IEEE Trans. Electron Devices*, ED-10, pp. 100-104, 1963.

4. J. C. Brown, "The Laser Drill," *IEEE Trans. Electron Devices*, ED-10, pp. 100-104, 1963.

5. J. C. Brown, "The Laser Drill," *IEEE Trans. Electron Devices*, ED-10, pp. 100-104, 1963.

6. J. C. Brown, "The Laser Drill," *IEEE Trans. Electron Devices*, ED-10, pp. 100-104, 1963.

7. J. C. Brown, "The Laser Drill," *IEEE Trans. Electron Devices*, ED-10, pp. 100-104, 1963.

8. J. C. Brown, "The Laser Drill," *IEEE Trans. Electron Devices*, ED-10, pp. 100-104, 1963.

9. J. C. Brown, "The Laser Drill," *IEEE Trans. Electron Devices*, ED-10, pp. 100-104, 1963.

10. J. C. Brown, "The Laser Drill," *IEEE Trans. Electron Devices*, ED-10, pp. 100-104, 1963.

11. J. C. Brown, "The Laser Drill," *IEEE Trans. Electron Devices*, ED-10, pp. 100-104, 1963.

12. J. C. Brown, "The Laser Drill," *IEEE Trans. Electron Devices*, ED-10, pp. 100-104, 1963.

13. J. C. Brown, "The Laser Drill," *IEEE Trans. Electron Devices*, ED-10, pp. 100-104, 1963.

14. J. C. Brown, "The Laser Drill," *IEEE Trans. Electron Devices*, ED-10, pp. 100-104, 1963.

15. J. C. Brown, "The Laser Drill," *IEEE Trans. Electron Devices*, ED-10, pp. 100-104, 1963.

16. J. C. Brown, "The Laser Drill," *IEEE Trans. Electron Devices*, ED-10, pp. 100-104, 1963.

17. J. C. Brown, "The Laser Drill," *IEEE Trans. Electron Devices*, ED-10, pp. 100-104, 1963.

18. J. C. Brown, "The Laser Drill," *IEEE Trans. Electron Devices*, ED-10, pp. 100-104, 1963.

19. J. C. Brown, "The Laser Drill," *IEEE Trans. Electron Devices*, ED-10, pp. 100-104, 1963.

20. J. C. Brown, "The Laser Drill," *IEEE Trans. Electron Devices*, ED-10, pp. 100-104, 1963.

The author wishes to thank the following individuals for their assistance in the preparation of this paper: J. C. Brown, D. W. Davis, R. E. Smith, and J. L. Garman.

The author also wishes to thank the following organizations for their support of this work: IBM Research Laboratories, Almaden Research Center, and the General Electric Research and Development Center, Schenectady, New York.

ACKNOWLEDGMENT

The author wishes to thank the following individuals for their assistance in the preparation of this paper: J. C. Brown, D. W. Davis, R. E. Smith, and J. L. Garman.

The author also wishes to thank the following organizations for their support of this work: IBM Research Laboratories, Almaden Research Center, and the General Electric Research and Development Center, Schenectady, New York.

AUTHOR INDEX

AUTHOR	PAGE	AUTHOR	PAGE
Aberth, W.	631	Engberg, E.	43
Ahmed, H.	111	Everhart, T. E.	483
Amboss, K.	195		
Amme, R. C.	115	Ferber, R. R.	9
Anderson, R. E.	453	Flemming, J. P.	111
Andrews, J.	141	Flinchbaugh, D. E.	259
Ashley, J. R.	157	Frame, J. M.	513
Asmus, J. F.	367	Fraser, D. L.	209
Aubert, J.	605	Fritz, R. B.	505
		Fritzke, G. P.	313
Bakish, R.	653		
Ballantyne, J. P.	495	Gamo, K.	103
Banas, C. M.	685	Ganley, T.	299
Barker, D. B.	115	Gautherin, G.	605
Barnes, F. S.	413	Gayle, D. M.	61
Bas, E. B.	643	George, T. V.	307
Benford, J.	433	Grannemann, W.	89, 93
Berkowitz, A. E.	1	Graybill, S. E.	577
Block, J.	513	Greeneich, T. E.	483
Boers, J. E.	167, 527, 553	Guyot, J.	299
Bollini, R.	359		
Boris, J. P.	535	Hafner, P.	643
Bradley, L. P.	553	Hammer, D.	513
Broers, A. N.	205, 337	Hatzakis, M.	337
Brown, C. O.	685	Heritage, M. B.	219
Buckey, C. R.	463	Herrmannsfeldt, W. B.	313
Burton, J.	513	Herzog, R. F.	483
Burwell, W. G.	247	Hewitt, J. G.	115
Buxton, L.	81	Hughes, W. C.	1
Byers, D. C.	615	Hutcheson, L.	413
Carlson, G. A.	121	Inaba, H.	385
Champney, P.	421	Ishihara, S.	103
Chang, T. H. P.	471	Ishikawa, J.	597, 623
Coane, P. J.	331	Iwaki, M.	103
Cochran, R. R.	313		
Coloff, S.	403	Johnson, D. L.	445, 553
Cooperstein, J.	553	Johnston, A. E.	313
Crawford, C. K.	131		
		Kawabe, M.	291
Davis, J. W.	247	Kim, P-H	375
Decker, D. A.	359	Kimura, I.	103
Di Chico, D.	177	Kobayasi, T.	385
Dix, C.	495	Kolb, A. C.	513
Douglas-Hamilton	591	Kudirka, P. E.	131
		Kuyatt, C. E.	177
Eckbreth, A. C.	247		
Ecker, B.	433	Latif, A. A.	643
Eisen, H.	77	Lawson, J. L.	1
Elser, T. G.	61, 209	Lee, R.	535
Emmett, J. L.	269	Levene, M. L.	69

AUTHOR INDEX (Cont'd)

AUTHOR	PAGE	AUTHOR	PAGE
Levine, S.	513	Siryj, B. W.	69
Linlor, W. T.	659	Smith, I.	421
Livesay, W. R.	505	Southward, H. D.	89, 93
Lupton, W. H.	513	Spence, P.	421, 433
		Stallings, C.	433
Martin, T. H.	553	Swinney, S.	17
Masuda, K.	103, 291		
Masuyama, A.	291	Takagi, T.	147, 597, 623
McMahon, J. M.	269	Taki, K.	375
McNeill, W. H.	577	Teepie, L. R.	53
Meckel, B. B.	585	Thiess, P.	299
Meiklejohn, W. H.	1	Thurber, W. C.	665
Meyers, W. J.	209	Ting, C. H.	345
Miley, G. H.	279, 299	Tschang, P. S.	27
Mori, K.	637		
		Uglum, J. R.	577
Nahman, N.	141		
Namba, S.	103, 291, 375	Vanderborgh, N. E.	403
Natali, S.	177	Verdeyen, J. T.	299
Nemoto, T.	637	Vitkovitsky, I. M.	513
Nixon, W. C.	495		
		Wagner, V. L.	35
Oliphant, I. M.	513	Walch, A. P.	685
Ozdemir, F. S.	331, 463	Wallman, B. A.	471
		Wang, C. C. T.	193
Parker, R. K.	453	Wilson, R. G.	351
Parks, H. G.	229	Wolf, E. D.	195, 331, 463
Pass, H. W.	53	Wulff, G.	643
Perkins, W. E.	331		
Perry, F.	81	Yamada, I.	147, 597, 623
Pfeiffer, H. C.	205, 239	Yonas, G.	421
Phillips, D. H.	89, 93		
Prestwich, K. R.	553		
Putnam, S. D.	421, 433, 561		
Reader, P. D.	615		
Reynolds, J. L.	60		
Ristau, W. T.	403		
Rogers, K. T.	631		
Rosenstein, M.	77		
Roth, O.	413		
Sample, S. B.	359		
Schroeder, C. L.	89		
Seliger, R. L.	183		
Septier, A.	605		
Shepherd, W. B.	323		
Shifrin, G. A.	351		
Shipman, J. D.	513		
Silverman, J.	77		

